C55.612/2:974-75

collected reprints- 1974-75

WAVE PROPAGATION LABORATORY

July 1976

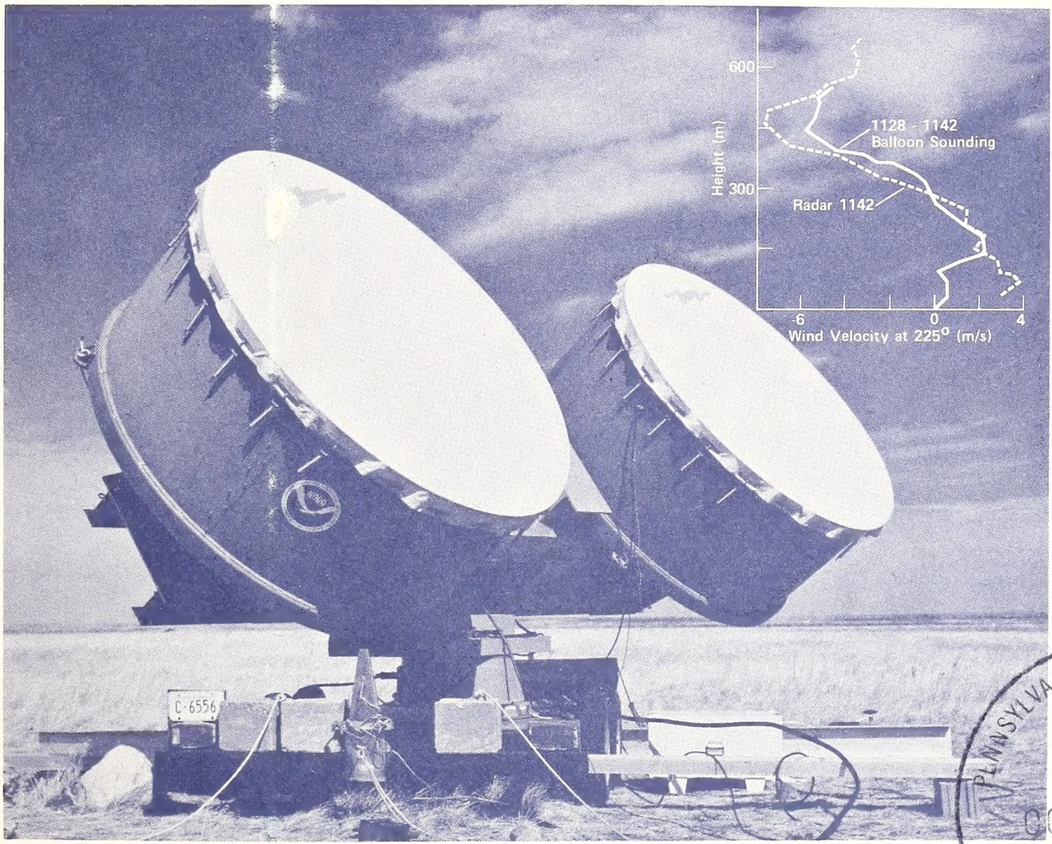

PENNSYLVANIA STATE UNIVERSITY
OCT 6 1976
DOCUMENTS COLLECTION

DEPARTMENT OF COMMERCE
UNITED STATES OF AMERICA

NATIONAL OCEANIC AND ATMOSPHERIC ADMINISTRATION / Environmental Research Laboratories

Cover: The transmitting and receiving antennas of the WPL FM-CW Doppler radar, which has successfully measured boundary-layer wind profiles in the clear air. The inset compares profiles measured by the radar in the 225° azimuth plane with that component measured by a sounding balloon tethered 300 m away. Papers 28 and 29 describe the radar and its applications.

Collected Reprints: 1974 - 75
Wave Propagation Laboratory

July 1976

U. S. DEPARTMENT OF COMMERCE
Elliot Richardson, Secretary

National Oceanic and Atmospheric Administration
Robert M. White, Administrator

Environmental Research Laboratories
Wilmot Hess, Director

U. S. Depository Copy

NOTICE

The Environmental Research Laboratories do not approve, recommend, or endorse any proprietary product or proprietary material mentioned in this publication. No reference shall be made to the Environmental Research Laboratories or to this publication furnished by the Environmental Research Laboratories in any advertising or sales promotion which would indicate or imply that the Environmental Research Laboratories approve, recommend, or endorse any proprietary product or proprietary material mentioned herein, or which has as its purpose an intent to cause directly or indirectly the advertised product to be used or purchased because of this Environmental Research Laboratories publication.

FOREWORD

The Wave Propagation Laboratory acts as the focal point within NOAA for the development and research application of new methods for remote sensing of man's geophysical environment. Since its creation in May 1967, the Laboratory has pioneered in the development and application of a large number of new remote sensing methods, involving the use of optical, radio and acoustic waves. The new techniques have many significant advantages over standard, in situ methods; in particular, it is often possible to provide the researcher with one-, two- or three-dimensional data sets possessing excellent continuity and resolution in both time and space. These new data sets are already providing important new insights into atmospheric processes.

This fourth volume of Collected Reprints comprises work published by WPL authors between 1 January 1974 and 31 December 1975. The papers included in this volume have been selected to minimize duplication or extraneous material; for this reason, only abstracts, rather than the full text, of WPL/NOAA Technical and Memorandum Reports are included.

It is hoped that this and subsequent volumes of the papers incorporating our research will provide a convenient and helpful compilation for use by colleagues in many fields. Remote sensing is still a specialized field, regarded as somewhat peripheral by most atmospheric and oceanographic research workers; we believe that these volumes will be particularly useful in demonstrating to our colleagues in these fields some of the unique advantages of remote sensing.

C Gordon Little

C. Gordon Little, Director
Wave Propagation Laboratory

Digitized by the Internet Archive
in 2012 with funding from
LYRASIS Members and Sloan Foundation

http://archive.org/details/collectedreprint00wave

CONTENTS*

Page

Foreword iii

I. Wave Propagation Studies

A. Acoustic and Gravity Wave Propagation

1. Brown, E. H., Turbulent Spectral Broadening of Backscattered Acoustic Pulses, *Journal of the Acoustical Society of America 56*, 1398-1406, November 1974. 1

2. Brown, E. H., and R. J. Keeler, Applications of Propagation Parameters to Atmospheric Echosondes, *Proceedings of 16th AMS Radar Meteorology Conference*, 272-277, April 1975. 10

3. Clifford, S. F., and E. H. Brown, Acoustic Scattering From A Moving Turbulent Medium, *Journal of the Acoustical Society of America 55*, 929-933, May 1974. 16

4. Georges, T. M., and S. F. Clifford, Estimating Refractive Effects in Acoustic Sounding, *Journal of the Acoustical Society of America 55*, 934-936, May 1974. 21

5. Gossard, E. E., and W. B. Sweezy, Dispersion and Spectra of Gravity Waves in the Atmosphere, *Journal of Atmospheric Sciences 31*, 1540-1548, September 1974. 24

6. Gossard, E. E., Reply, *Journal of Atmospheric Sciences 32*, 639-642, March 1975. 33

7. Jones, R. M., and J. J. Stephenson, A Versatile Three-Dimensional Ray-Tracing Computer Program for Radio Waves in the Ionosphere, *Office of Telecommunications Report OT 75-76*, 185 pp., October 1975. (Abstract only) 37

8. Kjelaas, A. G., E. E. Gossard, J. M. Young, and W. R. Moniger, Dispersion and Spectra of Gravity Waves Probably Generated by a Convective Storm, *Tellus 27*, 25-33, 1975. 38

B. Wave Propagation at Optical Frequencies

9. Clifford, S. F., G. R. Ochs, and R. S. Lawrence, Saturation of Optical Scintillation by Strong Turbulence, *Journal of the Optical Society of America 64*, 148-154, February 1974. 47

10. Clifford, S F., and H. T. Yura, Equivalence of Two Theories of Strong Optical Scintillation, *Journal of the Optical Society of America 64*, 1641-1644, December 1974. 54

II. Remote Sensing Concepts

A. Remote Sensing Using Acoustic and Acoustic Gravity Waves

11. Beran, D. W., Wind Measurement with Acoustic Doppler, *Atmospheric Technology*, 94-99, Winter 1974-75. 58

12. Beran, D. W., Acoustic Echo Sounding Systems: Their Potential in Forest Fire Control and Research, *Journal of Forestry 73*, 633-639, October 1975. 64

13. Beran, D. W., and F. F. Hall, Jr., Remote Sensing for Air Pollution Meteorology, *Bulletin of the American Meteorological Society 55*, 1097-1105, September 1974. 71

14. Beran, D. W., F. F. Hall, Jr., B. C. Willmarth, R. J. Keeler, and D. Hunter, Operational Test Results of Acoustic Doppler Wind Shear Detector, *Proceedings 6th AMS Conference on Aerospace & Aeronautical Meteorology*, 412-417, November 1974. 80

15. Beran, D. W., B. C. Willmarth, F. C. Carsey, and F. F. Hall, Jr., An Acoustic Doppler Wind Measuring System, *J. Acoust. Soc. Am. 55*, 334-338, February 1974. 86

16. Brown, E. H., Some Recent NOAA Theoretical Work on Echo Sounding in the Atmosphere, *Journal of Geophysical Research 79*, 5567-5571, December 1974. 91

17. Georges T. M., and G. E. Greene, Infrasound from the 29-30 April 1970 Storms, *NOAA Technical Memorandum ERL NSSL-69*, 185-193, May 1974. (Excerpt) 96

18. Georges, T. M., and G. E. Greene, Infrasound from Convective Storms. Part IV. Is it Useful for Storm Warning? *Journal of Applied Meteorology 14*, 1303-1316, October 1975. 105

19. Hall, F. F., Jr., Report on the July 1972 Workshop in Atmospheric Acoustics, *NOAA Technical Memorandum ERL WPL-8*, 25 pp., October 1973. (Abstract only) 119

20. Morris, A. L., and F. F. Hall, Jr., Remote Sensing of the Atmosphere by Sound, *Atmospheric Technology*, NCAR, 84-93, Winter 1974-75. 120

21. Neff, W. D., An Investigation of Acoustic Scatter From Small Scale Thermal Fluctuations in the Planetary Boundary Layer, *Proceedings of 16th AMS Radar Meteorology Conf.*, 263-270, April 1975. 130

22. Neff, W. D., Quantitative Evaluation of Acoustic Echoes from the Planetary Boundary Layer, *NOAA Technical Report ERL 322-WPL 38*, 34 pp., June 1975. (Abstract only) 138

23. Wescott, J. W., Acoustic Sounders for Predicting Air Pollution Over Cities, *Earth Environment and Resources Conference*, 66-67, September 1974. 139

B. Remote Sensing with Radio Waves

24. Barrick, D. E., Wind Dependence of Quasi-Specular Microwave Sea Scatter, *IEEE Transactions on Antennas & Propagation, AP-22*, 135-136, January 1974. 141

25. Barrick, D. E., J. M. Headrick, R. W. Bogle, and D. D. Crombie, Sea Backscatter at HF: Interpretation & Utilization of the Echo, *Proceedings of the IEEE 62*, 673-680, June 1974. 143

26. Chadwick, R. B., E. E. Gossard, and R. G. Strauch, Analysis of an All-Weather System for Wind Sounding up to 15 km Altitude, *NOAA Technical Report ERL 334-WPL 41*, 40 pp., June 1975. (Abstract only) 151

27. Little, C. G., Radio Probing of the Troposphere, *Radio Science 10*, 735-742, July 1975. 152

28. Miller, L. J., and R. G. Strauch, A Dual Doppler Radar Method for the Determination of Wind Velocities within Precipitating Weather Systems, *Remote Sensing of Environment 3*, 219-235, 1974. 160

29. Strauch, R. G., W. C. Campbell, K. P. Moran, and R. B. Chadwick, FM-CW Boundary Layer Radar With Doppler Capability, *NOAA Technical Report ERL 329-WPL 39*, 23 pp., May 1975. (Abstract only) 177

30. Strauch, R. G., W. C. Campbell, R. B. Chadwick, and K. P. Moran, Meteorological Applications of the FM Doppler Radar, *NOAA Technical Report ERL 351-WPL 44*, 14 pp., December 1975. (Abstract only) 178

31. Taylor, W. L., Detecting Tornadic Storms by the Burst Rate Nature of Electromagnetic Signals They Produce, *Proceedings of Ninth AMS Conference on Severe Local Storms*, 311-316, October 1975. 179

32. Westwater, E. R., J. B. Snider, and A. V. Carlson, Experimental Determination of Temperature Profiles by Ground-Based Microwave Radiometry, *Journal of Applied Meteorology 14*, 524-539, June 1975. 185

C. Remote Sensing by Optical Techniques

33. Abshire, N. L., R. L. Schwiesow, and V. E. Derr, Doppler Lidar Observations of Hydrometeors, *Journal of Applied Meteorology 13*, 951-953, December 1974. 201

34. Clifford, S. F., Remote Probing of Winds and Refractive Turbulence Using Optical Techniques, AGARD, North Atlantic Treaty Organization, *Pre-Print No. 183, Conference on Optical Propagation in the Atmosphere,* 38.1-38.10, 1975. 204

35. Clifford, S. F., G. R. Ochs, and Ting-i Wang, Optical Wind Sensing by Observing the Scintillations of a Random Scene, *Applied Optics 14*, 2844-2850, December 1975. 214

36. Clifford, S. F., G. R. Ochs, and Ting-i Wang, Theoretical Analysis and Experimental Evaluation of a Prototype Passive Sensor to Measure Crosswinds, *NOAA Technical Report ERL 312-WPL 35*, 30 pp., September 1974. (Abstract only) 221

37. Derr, V. E., M. J. Post, R. L. Schwiesow, R. F. Calfee and G. T. McNice, A Theoretical Analysis of the Information Content of Lidar Atmospheric Returns, *NOAA Technical Report ERL 296-WPL 29*, 297 pp., November 1974. (Abstract only) 222

38. Derr, V. E., M. H. Ackley, M. J. Post, and R. F. Calfee, Remote Sensing of Pollutants, Computerized Reduction of Long-Path Absorption Data, *NOAA Technical Report ERL 302-WPL 33*, 199 pp., July 1974. (Abstract only) 223

39. Hall, F. F., Jr., Laser Systems For Monitoring The Environment, *Laser Applications 2*, Academic Press, Inc., 161-225, 1974. (Index only) 224

40. Kjelaas, A. G., and G. R. Ochs, Study of Divergence in the Boundary Layer Using Optical Propagation Techniques, *Journal of Applied Meteorology 13*, 242-248, March 1974. 225

41. Ochs, G. R., S. F. Clifford, R. S. Lawrence, and Ting-i Wang, Development of a Ground-Based Optical Method for Measuring Atmospheric Turbulence Aloft, *NOAA Technical Report ERL 297-WPL 30*, 47 pp., January 1974. (Abstract only) 232

42. Schwiesow, R. L., and R. E. Cupp, Remote Doppler Velocity Measurements of Atmospheric Dust Devil Vortices, *Applied Optics 15*, 1-2, January 1976. 233

43. Slusher, R. B., and V. E. Derr, Temperature Dependence and Cross Sections of Some Stokes and Anti-Stokes Raman Lines in Ice Ih, *Applied Optics 14*, 2116-2120, September 1975. 235

44. Wang, Ting-i and S. F. Clifford, Use of Rainfall-Induced Optical Scintillations to Measure Path-Averaged Rain Parameters, *Journal of the Optical Society of America 65*, 927-937, August 1975. 240

45. Wang, Ting-i, S. F. Clifford, and G. R. Ochs, Wind and Refractive-Turbulence Sensing Using Crossed Laser Beams, *Applied Optics 13*, 2602-2608, November 1974. 251

D. Combination Methods and Comparisons

46. Strand, O. N., and E. R. Westwater, A Numerical Comparison of Two Inversion Techniques for Reomote Sensing of Atmospheric Temperature Profiles, Spring Conference, *Remote Sensing of the Atmosphere*, ThA5.1-ThA5.4, March 1975. 258

47. Wyckoff, R. J., D. W. Beran, and F. F. Hall, Jr., A Comparison of the Low-Level Radiosonde and the Acoustic Echo Sounder for Monitoring Atmospheric Stability, *Journal of Applied Meteorology 12*, 1196-1204, October 1973. 262

III. Geophysical Studies

48. Frisch, A. S., and R. B. Chadwick, Observations of Velocity Fields and Velocity Spectra in the Convective Boundary Layer Using a Dual-Doppler Radar System, *Proceedings 16th AMS Radar Meteorology Conference*, 237-242, April 1975. 271

49. Frisch, A. S., R. B. Chadwick, W. R. Moninger, and J. M. Young, Observations of Boundary-Layer Convective Cells Measured by Dual-Doppler Radar and Echosonde, and by Microbarograph Array, *Boundary-Layer Meteorology 3*, 26-39, 1975. 277

50. Frisch, A. S., and S. F. Clifford, A Study of Convection Capped by a Stable Layer Using Doppler Radar and Acoustic Echo Sounders, *Journal of Atmospheric Sciences 31*, 1622-1628, September 1974. 291

51. Frisch, A. S., L. J. Miller, and R. G. Strauch, Three-Dimensional Air Motion Measured in Snow, *Geophysical Research Letters 1*, 86-89, June 1974. 298

52. Frisch, A. S., L. J. Miller, and R. G. Strauch, Secondary Flow Fields in the Planetary Boundary Layer Estimated From Dual-Doppler Radar Measurements During Snow Conditions, *Journal of Geophysical Research 80*, 5051-5060, December 1975 302

53. Frisch, A. S. and G. R. Ochs, A Note on the Behavior of the Temperature Structure Parameter in a Convective Layer Capped by a Marine Inversion, *Journal of Applied Meteorology 14*, 415-419, April 1975. 312

54. Gaynor, J. E., Optimum Averaging Times for Short-Term Wind Prediction in the Planetary Boundary Layer, *Journal of Applied Meteorology 13*, 411-415, April 1974. 317

55. Georges, T. M., Storm, *Yearbook of Science and Technology*, McGraw-Hill, 389-391, 1975. 322

56. Gossard, E. E. and W. H. Hooke, *Waves in the Atmosphere*, Elsevier, Amsterdam, 456 pp., 1975. (Index only) 324

57. Gossard, E. E., Dynamic Stability of an Isentropic Shear Layer in a Statically Stable Medium, *Journal of Atmospheric Sciences 31*, 483-492, March 1974. 329

58. Gossard, E. E., and W. R. Moninger, The Influence of a Capping Inversion on the Dynamic and Convective Instability of a Boundary Layer Model with Shear, *Journal of Atmospheric Sciences 32*, 2111-2124, November 1975. 339

59. Greene, G. E. and J. Howard, Natural Infrasound: A One Year Global Study, *NOAA Technical Report ERL 317-WPL 37*, 156 pp., March 1975. (Abstract only) 353

60. Grossman, R. L., and D. W. Beran, An Investigation of Extreme Low-Level Wind Shear at Selected Stations in the Conterminous United States, *Journal of Applied Meteorology 14*, 506-512, June 1975. 354

61. Hall, F. F., Jr., J. G. Edinger, and W. D. Neff, Convective Plumes in the Planetary Boundary Layer, Investigated with an Acoustic Echo Sounder, *Journal of Applied Meteorology 14*, 513-523, June 1975. 361

62. Hall, F. F., Jr., and E. J. Owens, Atmospheric Acoustic Echo Sounding Investigations at the South Pole, *Antarctic Journal of the United States 10*, 191-192, July/August 1975. 372

63. Hooke, W. H., and K. R. Hardy, Further Study of the Atmospheric Gravity Waves over the Eastern Seaboard on 18 March 1969, *Journal of Applied Meteorology 14*, 31-38, February 1975. 373

64. Kjelaas, A. G., D. W. Beran, W. H. Hooke, and B. R. Bean, Waves Observed in the Planetary Boundary Layer Using an Array of Acoustic Sounders, *Journal of Atmospheric Sciences 31*, 2040-2045, November 1974. 381

65. Kropfli, R. A., and L. J. Miller, Thunderstorm Flow Patterns in Three Dimensions, *Monthly Weather Review 103*, 70-71, January 1975. 387

66. Kropfli, R. A., and L. J. Miller, Thunderstorm Flow Patterns in Three Dimensions From Dual-Doppler Radar, *Proceedings 16th AMS Radar Meteorology Conference*, 121-127, April 1975. 389

67. Kropfli, R. A., and L. J. Miller, Dual Doppler Radar Measurements within A Hail Producing Storm in Northeast Colorado, *Proceedings AMS Conference on Cloud Physics*, 277-282, October 1974. 396

68. Little, C. G., and E. E. Gossard, The 1972 Haswell, Colorado, Atmospheric Boundary Layer Experiment, *Proceedings of 3rd AMS Symposium on Meteorological Observations and Instrumentation*, 187-192, February 1975. 402

69. Mandics, P. A., F. F. Hall, Jr., E. J. Owens, and D. Wylie. Observations of the Tropical Marine Atmosphere Using an Acoustic Echo Sounder During GATE, *Proceedings of 16th AMS Radar Meteorology Conference*, 257-259, April 1975. 408

70. Mandics, P. A., and E. J. Owens, Observations of the Marine Atmosphere Using a Ship-Mounted Acoustic Echo Sounder, *Journal of Applied Meteorology 14*, 1110-1117, September 1975. 411

71. Mandics, P. A., F. F. Hall, Jr., and E. J. Owens, Preliminary Results of Acoustic Echo Sounding of the Marine Boundary Layer During GATE, *Gate Report No. 14*, Preliminary Scientific Results, Vol. II, World Meteorological Organization, 225-228, 1975. 419

72. Merrem, F. H., and R. G. Strauch, Observations of a Hailstorm with Two Doppler Radars, *Proceedings of AMS Conference on Cloud Physics*, 287-291, October 1974. 423

73. Miller, L. J., Internal Airflow of a Convective Storm from Dual-Doppler Radar Measurements, *Pure and Applied Geophysics 113*, 765-785, 1975. 428

74. Miller, L. J., J. D. Marwitz, and J. C. Fankhauser, Kinematic Structure of a Colorado Thunderstorm, *Proceedings 16th AMS Radar Meteorology Conference*, 128-133, April 1975. 449

75. Miller, L. J., and H. W. Frank, Three-Dimensional Air Motion Within A Northeast Colorado Rainstorm, *Proceedings AMS Conference on Cloud Physics*, 321-327, October 1974. 455

76. Strauch, R. G., A. S. Frisch, and W. B. Sweezy, Doppler Radar Measurements of Turbulence, Shear, and Dissipation Rates in a Convective Storm, *Proceedings 16th AMS Radar Meteorology Conference*, 83-88, April 1975. 462

77. Van Atta, C. W., and J. C. Wyngaard, On Higher-Order Spectra of Turbulence, *Journal of Fluid Mechanics 72*, 673-694, 1975. 468

78. Wyngaard, J. C., Progress in Research on Boundary Layers and Atmospheric Turbulences, *Reviews of Geophysics and Space Physics 13*, 716-720, July 1975. 490

79. Wyngaard, J. C., Modeling the Planetary Boundary Layer-Extension to the Stable Case, *Boundary-Layer Meteorology 9*, 441-460, 1975. 495

IV. Development of Instruments & Techniques

80. Bouricius, G. M. B., and K. B. Earnshaw, Results of Field Testing a Two-Wavelength Optical Distance-Measuring Instrument, *Journal of Geophysical Research 79*, 3015-3018, July 1974. 515

81. Earnshaw, K. B., G. M. B. Bouricius, and K. P. Moran, Final Report and Operations Manual for Microwave Modulated, Dual Optical Distance-Measuring Instrument, *NOAA Technical Report ERL 341-WPL 42*, 124 pp., July 1975. (Abstract only) 519

82. Hall, F. F., Jr., and J. W. Wescott, Acoustic Antennas for Atmospheric Echo Sounding, *Journal of the Acoustical Society of America 56*, 1376-1382, November 1974. 520

83. Hooke, W. H., Sensitive Microbarographs Used to Study Atmospheric Gravity Waves, *3rd AMS Symposium on Meteorology Observations and Instrumentation*, 175-178, February 1975. 527

84. Ornstein, M. H., and V. E. Derr, Prepulse Enchancement of Flashlamp Pumped Dye Laser, *Applied Optics 13*, 2100-2104, September 1974. 531

85. Ochs, G. R., G. F. Miller, and E. J. Goldenstein, The NOAA Passive Optical Crosswind Monitor, *NOAA Technical Memorandum ERL WPL-11*, 23 pp., September 1974. (Abstract only) 536

86. Owens, E. J., Development of a Portable Acoustic Echo Sounder, *NOAA Technical Report ERL 298-WPL 31*, 45 pp., May 1974. (Abstract only) 537

87. Owens, E. J., NOAA Mark VII Acoustic Echo Sounder, *NOAA Technical Memorandum ERL WPL-12*, 75 pp., June 1975. (Abstract only) 538

88. Schwiesow, R. L., and M. J. Post, Digital Data Acquisition for Laser Scattering Spectroscopy Using the Scattered-to-Incident Light Intensity Ratio, *The Review of Scientific Instruments 46*, 413-416, April 1975. 539

89. Snider, J. B., A Sensitive Two-Frequency Radiometer for Remote Sensing of Temperature Profiles, *The Review of Scientific Instruments 48*, 981-984, August 1974. 543

90. Strand, O. N., Coefficient Errors Caused by Using the Wrong Covariance Matrix in the General Linear Model, *The Annals of Statistics 2*, 935-949, 1974. 547

91. Strand, O. N., Theory and Methods Related to the Singular-Function Expansion and Landweber's Iteration for Integral Equations of the First Kind, *Siam Journal of Numerical Analysis 11*, 798-825, September 1974. 562

92. Strand, O. N., Expected Accuracy of Tropopause Height and Temperature as Derived from Satellite Radiatior Measurements, *NOAA Technical Report ERL 295-WPL 28*, 69 pp., December 1973. (Abstract only) 590

93. Westwater, E. R., and O. N. Strand, A Generalized Inversion Program, *NOAA Technical Report ERL 309-WPL 34*, 35 pp., November 1974. (Abstract only) 591

94. Willmarth, B. C., E. H. Brown, J. T. Priestley, and D. W. Beran, Beam Pattern Measurements for Large Acoustic Antennas, *Proceedings of 16th AMS Radar Meteorology Conference*, 278-281, April 1975. 592

95. Young, J. M., and W. A. Hoyle, Computer Programs for Multidimensional Spectra Array Processing, *NOAA Technical Report ERL 345-WPL 43*, 47 pp., August 1975. (Abstract only) 596

---

*NOAA publications referenced here are obtainable by request from
National Technical Information Service
Operations Division
Springfield, Virginia 22151

Turbulent spectral broadening of backscattered acoustic pulses

Edmund H. Brown

Wave Propagation Laboratory, NOAA Environmental Research Laboratories, Boulder, Colorado 80302

(Received 7 February 1974; revised 10 July 1974)

The analysis studies the broadening of the frequency spectrum of an acoustic plane-wave pulse backscattered into a finite-angle receiver by the action of a transverse mean wind which moves turbulent velocity and temperature fluctuations through the beam. The results include the frequency spectrum $I(k)$ of the acoustic pressure as a function of wavenumber and the spectral equivalent width b_s as a function of mean transverse wind speed and receiver aperture. For broad beams, both temperature and velocity fluctuations contribute to the apparent 180°-backscatter intensity, and the contributing eddy scales vary from $\lambda/2$ to $\lambda/\sqrt{2}$. Again for broad beams and for typical experimental parameters for atmospheric echosondes, the broadening effects of mean transverse wind in the scattering volume outweigh the broadening effects of turbulence trransported by a mean transverse wind during propagation to the scattering volume. However, as the receiver beam angle decreases, the spectral broadening drops to zero, regardless of mean wind. Figures are included to show the effects of wind broadening for the case of intermediate receiver beam angles.

Subject Classification: 28.40, 28.60; 20.30.

INTRODUCTION

The new technique of acoustic echo sounding provides a powerful tool for probing atmospheric structure. In simplest form—the monostatic configuration—an atmospheric echosonde operates in two steps: first, transmission of a pulse with given carrier frequency and simple envelope shape into the turbulent medium in a desired direction, and second, reception of the wave backscattered from turbulent refractivity fluctuations, using the same transducer gated to a later time determined by the desired range. The technique involves a pulse characteristic length which produces an interaction time with the scattering layer much less than the eddy turnover time. As an example, by the Kolmogorov inertial-range law, an extremely high dissipation rate of 0.04 $\mathrm{m}^2/\mathrm{sec}^3$ corresponds to an rms velocity fluctuation of about 0.5 m/sec over a 0.5-m distance (a typical wavelength). Defining the eddy turnover time as the ratio of eddy scale to velocity fluctuation gives a turnover time of approximately 1 sec. However, typical atmospheric echosonde pulse lengths range from 0.02 to 0.10 sec. Then, in zero mean wind, the backscatter process cannot change the shape, only the strength of the spectrum of the acoustic pressure. Effectively, without wind, the turbulence has no time dependence and cannot generate frequency broadening. Existence of a mean wind in the direction of the acoustic beam also leaves the spectral shape essentially unchanged. Instead, such a parallel wind produces a shift of the whole spectrum given by the familiar Doppler formula.

Introduction of a mean wind transverse to the acoustic beam alters the physical conditions. For example, turbulence with an inner scale of 1 cm moving with a moderate crosswind of 10 m/sec has an effective maximum characteristic frequency of 1000 Hz. Thus, the combination of turbulence and transverse wind creates a measurable random modulation of the pulse frequencies. In turn, such a random frequency modulation produces a nonnegligible broadening of the frequency spectrum. An earlier paper of Brown[1] obtained the general solution for an acoustic pulse propagating through moving turbulence. Two later papers of Brown and Clifford[2,3] applied the *forwardscatter* part of the general solution to the similar broadening of the power spectrum of the pressure, and the power spectrum of the amplitude by a transverse wind. This paper analyzes the effects of such a crosswind on the *backscatter* process and compares the results with the forwardscatter broadening expected in the propagation of the pulse to and from the scattering volume.

I. SCATTERED FIELD

In accordance with previous papers,[1-3] the analysis uses the following symbols: spatial coordinates x_i, $i=1, 2, 3$; spatial coordinates in the plane perpendicular to the direction of propagation of the initial wave x_α, $\alpha=1, 2$; the related three- and two-dimensional Fourier cordinates κ_i and κ_α; the mean speed of sound c_0; the time t and, for convenience, the equivalent length $\eta=c_0 t$; the related Fourier angular frequency ω and, again for convenience, the wavenumber $k=\omega/c_0$; the angular carrier frequency ω_0 and the equivalent wavenumber $k_0=\omega_0/c_0=2\pi/\lambda$, with λ the wavelength; the vector components of the mean wind $\overline{w}_i$ and their related dimensionless Mach-vector components $m_i=\overline{w}_i/c_0$; the spatial derivatives $\partial_i=/\partial x_i$, $\partial_\alpha=\partial/\partial x_\alpha$, and the Laplacian $\Delta^2=\partial_i\,\partial_i$, with repeated subscripts implying summation; the radius of the receiver aperture r (the single-scatter assumption implies that the initial sound field remains a plane wave until backscattered); and the receiver aperture radius $\rho=r/\lambda$ measured in wavelengths.

The tranformations

$$F(x_i,\ k)=(2\pi)^{-1}\int_{-\infty}^{\infty} d\eta\, e^{ik\eta} f(x_i,\eta)$$

and

$$f(x_i,\eta)=\int_{-\infty}^{\infty} dk\, e^{-i\eta k} F(x_i,k)$$

associate any function (or measure) $f(x_i,\eta)$ with its Fourier time transform $F(x_i,k)=\mathfrak{F}f(x_i,\eta)$. These transformations apply, in particular, to the acoustic

Copyright © 1974 by the Acoustical Society of America

pressure $P(x_i, k) = \mathfrak{F}p(x_i, \eta)$ and the refractive index fluctuation field $N'(x_i, k) = \mathfrak{F}n'(x_i, \eta)$. In addition, the Fourier transform associates the product of two functions $f(\eta)g(\eta)$ with the convolution product $F(k) \underset{k}{*} G(k)$ defined by

$$F(k) \underset{k}{*} G(k) = \int_{-\infty}^{\infty} dk' F(k - k')G(k') \ .$$

The sign $*$ alone usually represents the convolution product; these studies, however, require convolution with respect to a number of different variables in addition to the wavenumber k. Thus, the addition of the subscripts (such as $\underset{k}{*}$, $\underset{z}{*}$) serves to prevent confusion or lack of clarity.

When $\overline{P}$ is the initial acoustic field and P' the (singly) scattered field, the generalization of the equation given by Tatarskii[4] to the case found by Brown[1] for acoustic pulses propagating through turbulence moving with a mean wind becomes

$$\nabla^2 P' + (k + im_j \partial_j)^2 P' = 2\,\partial_i (N' \underset{k}{*} \partial_i \overline{P}) \ . \tag{1}$$

This study assumes an initial plane-wave pulse propagating through a turbulent atmosphere in the vertical or z direction:

$$\overline{p}(x_i, \eta) = d_0(z - \eta)\, e^{ik_0(z-\eta)} \ ,$$

where d_0 is the shape of the moving pulse envelope. (The idealization of the actual incident wavefront by a plane wave would seem to be reasonable when the range R is substantially larger than the outer scale L_0.) The equivalent Fourier transform is $\overline{P}(x_i, k) = D_0(\Delta k)\, e^{ikz}$, with $\Delta k = k - k_0$. The characteristic half-length l of the pulse is defined by $l = \pi D_0(0)/d_0(0)$. From Taylor's hypothesis applied to a system moving with the mean wind,

$$n'(x_i, \eta) = \int d\phi(\kappa_i) \exp[i\kappa_j(x_j - m_j \eta)] \tag{2}$$

or

$$N'(x_i, k) = \int d\phi(\kappa_i)\delta(k - m_j\kappa_j)\exp(i\kappa_i x_i) \ , \tag{3}$$

where δ is the Dirac measure and $d\phi$ is the Fourier–Stieltjes measure[4] for homogeneous turbulent refractivity fluctuations. With the additional assumption of a solely horizontal, or transverse mean wind, the backscatter part of the general solution found by Brown[1] becomes

$$P'(x_i, k) = \int d\phi(\kappa_i)\exp(i\kappa_\alpha x_\alpha) k_\alpha D_0(\Delta k_\alpha)\ \frac{\exp[iz(k_\alpha - \kappa_3)]}{k_\alpha - \kappa_3 + q_\alpha} \ . \tag{4}$$

Here k_α is an abbreviation for $k - m_\alpha\kappa_\alpha$, $\Delta k_\alpha = k_\alpha - k_0$, $q_\alpha = \pm\sqrt{k_\alpha^2 - \kappa^2}$ for $k \gtrless 0$, with $\kappa^2 = \kappa_\alpha\kappa_\alpha$ the square of the magnitude of the two-dimensional Fourier coordinate to distinguish from the three-dimensional-magnitude squared $\kappa^2 = \kappa_i\kappa_i$. (The sign change of κ_3 from that in Brown[1] facilitates the following analysis—a change which merely requires a redefinition of $d\phi$ without altering the results.)

For a given range R, represent the time-gated reception by $d_1(z + \eta - 2R)$, where d_1 has the same characteristic half-length l as d_0 but, for generality, an otherwise arbitrary shape. After transforming to the k domain, the received pressure wave $p_1 = d_1 p'$ at the ground $z = 0$ becomes

$$P_1(x_\alpha, k) = \{e^{2ikR} D_1(k)\} \underset{k}{*} P'(x_\alpha, k) \ . \tag{5}$$

If k' is the integration variable within the convolution Eq. 5, the transformation $k' \to k' + m_\alpha\kappa_\alpha$ changes the form of Eq. 5 to

$$P_1(x_\alpha, k) = \int d\phi(\kappa_i)\exp(i\kappa_\alpha x_\alpha + 2ik_\alpha R)\, Q(R, \kappa_i) \ .$$

Then, averaging over a receiver aperture of radius r to give $\overline{P}_1(k) = (\pi r^2)^{-1} \int da P_1(x_\alpha, k)$, and using the fact that $\int_a d^2 x_\alpha \exp(i\kappa_\alpha x_\alpha) = 2J_1(\kappa r)/(\kappa r)$ when $r < \infty$, yields

$$\overline{P}_1(k) = \int d\phi(k_i)[2J_1(\kappa r)/(\kappa r)]\exp(2ik_\alpha R)\, Q(R, \kappa_i) \ , \tag{6}$$

where

$$Q(R, \kappa_i) = \int dk' k' D_0(k' - k_0)\, D_1(k_\alpha - k') \times \frac{e^{-2ik'R}}{k' - \kappa_3 + \sqrt{k'^2 - \kappa^2}} \ . \tag{7}$$

When $r \to \infty$, $\int d^2 x_\alpha \exp(i\kappa_\alpha x_\alpha) \to 4\pi^2\delta(\kappa_\alpha)$ and

$$Q(R, \kappa_i) \to \int dk' k' D_0(k' - k_0)\, D_1(k - k')\ \frac{e^{-2ik'R}}{2k' - \kappa_3} \ .$$

Since $k_0 > 0$ and $k_0 l \gg 1$, the factor $D_0(k' - k_0)$ ensures that only positive values of k' contribute significantly to the k' integral Eq. 7. In addition, values of $0 \le k' < \kappa$ make the quantity $\sqrt{k'^2 - \kappa^2}$ imaginary. For such values Eq. 7 represents an evanescent wave (or damped exponential) rather than an oscillatory wave. (The case $q^2 < 0$ in the Eq. 29 of Brown[1] for the Green's function also indicates the unphysical nature of the solution.) Conversion of the k' integral to a complex contour integral as in McLachlan[5] shows that omission of the values $0 \le k' < \kappa$ corresponds to retaining the integration around the simple pole in the integrand and discarding the integration on a closed path around the two branch points $\pm i\kappa$ and the branch line between them.

Keeping only the pole in the integrand of Eq. 7 implies the following inequalities for the variables: $0 \le \kappa \le k' \le \kappa_3 \le 2k'$. For $\kappa \ne \kappa_3$, the quantity $k' - \kappa_3 - \sqrt{k'^2 - \kappa^2}$ does not vanish at the pole. Multiplying numerator and denominator of the integrand by the above quantity changes Eq. 7 to

$$Q(R, \kappa_i) = -(2\kappa_3)^{-1} \int dk' k' D_0(k' - k_0) D_1(k_\alpha - k')\, e^{-2ik'R} \times \frac{k' - \kappa_3 - \sqrt{k'^2 - \kappa^2}}{k' - k_1} \ , \tag{8}$$

where $k_1 = (\kappa_3^2 + \kappa^2)/2\kappa_3$. Converting Eq. 8 to a complex contour integral, assigning the analytic factors their values at the pole $k' = k_1$, and noting that $-\sqrt{k_1^2 - \kappa^2} = k_1 - \kappa_3$, the principal value with respect to k_1 of Eq. 8 becomes

$$Q(R, \kappa_i) = 2\pi i\, \frac{k_1(k_1 - \kappa_3)}{\kappa_3}\, e^{-2ik_1 R} D_0(k_1 - k_0) D_1(k_\alpha - k_1). \tag{9}$$

When $\kappa = \kappa_3$, $k_1 = \kappa_3$ and Eq. 9 becomes zero. Although the multiplication by $k' - \kappa_3 - \sqrt{k'^2 - \kappa^2}$ to change from Eq. 7 to Eq. 8 becomes improper when $\kappa = \kappa_3$, the rule given by McLachlan[5] that $[f(z)/g'(z)]_{z=a}$ equals the residue of $f(z)/g(z)$ at the simple pole $z = a$ of $g(z)$ gives the same zero value of Q.

When $\kappa \ll \kappa_3$, $k_1 \approx \kappa_3/2$ and $\kappa_3 \approx 2k_0$. Or, equivalently, the eddy dimension l_3 in the propagation direction becomes equal to a half wavelength, $l_3 \approx \lambda/2$. Then, P' becomes a coherent plane wave with phase $-2k_0R$, but random amplitude. Examing the phase $-2k_1R = -\kappa_3 R - \kappa^2 R/\kappa_3$ of Q shows that the initiation of appreciable phase incoherence occurs when $\kappa^2 R/\kappa_3 \approx \pi$. As κ increases, κ_3 decreases toward $k_0 = 2\pi/\lambda$. Let $L = 2\pi/\kappa$ define the transverse dimension of a refractivity eddy. Then, phase incoherence begins when L decreases to the Fresnel zone radius $\sqrt{\lambda R}$. Further reduction in L lowers the amplitude, which becomes zero at $L = \lambda$ since the factor $k_1 - \kappa_3$ in Eq. 9 vanishes for this value.

Suppose all the important eddy sizes lie between an inner scale l_0 and an outer scale L_0. To obtain solutions for electromagnetic scattering, Tatarskii[4] introduces the condition $\lambda \ll l_0$. The condition $\kappa \leq k'$ (or $\lambda' \leq L$) used in evaluating Eq. 7 implies that eddies larger than l_0 contribute to the total field as long as $\lambda' < L_0$ and, thus, $\lambda < L_0$. This result agrees with the analysis of Clifford and Brown,[6] which shows that the weaker inequality $\lambda < L_0$ replaces the requirement $\lambda \ll l_0$.

To obtain solutions, Tatarskii[4] also introduces the farfield condition $L^2 \ll \lambda R$, permissible since his analysis concerns scattering from finite volumes. Even though the pulse gating limits the vertical extent, however, a "farfield" never exists for scattering of an infinite plane wave by a semi-infinite turbulent atmosphere. Therefore, this study includes both "coherent" contributions (for $L^2 \geq \lambda R$) and "incoherent" contributions (for $L^2 < \lambda R$) to the total field. In a sense, Tatarskii's solutions and the solutions here, for the zero-wind limit, represent two complimentary theoretical approximations to experimental echo sounding techniques. The requirement of stationary solutions in the presence of a nonzero mean transverse wind underlies the different choice of physical model in this study.

II. FREQUENCY SPECTRUM

Assume an infinite sequence of pulses and their gated reception. Given an arbitrary time delay τ, the set of all time averages over a pulse length about times that are integral multiples of $2R/c_0$ represents a stationary random process. Brown and Clifford[2] give a detailed demonstration of the result that the power spectrum of such a random process is

$$I(k) = c_0 I(\omega) = (\pi/l)\langle \overline{P}_1(k)\overline{P}_1^{\dagger}(k)\rangle \ , \tag{10}$$

where the superscript † indicates the complex conjugate and the angular brackets denote ensemble averaging over the set of all received pulses. Substituting Eq. 9 into Eq. 6, the result into Eq. 10, and introducing the property of the three-dimensional isotropic turbulence spectrum Φ_n,

$$\langle d\phi(\kappa_i)d\phi^{\dagger}(\kappa_i')\rangle = \Phi_n(\kappa)\delta(\kappa_i - \kappa_i')d\kappa_i\, d\kappa_i' \ , \tag{11}$$

that (no sum on i) gives the power spectrum of the pressure in the form

$$I(k) = (\pi/l)4\pi^2 \int d^3\kappa_i \,\frac{k_1^2(k_1 - \kappa_3)^2}{\kappa_3^2}\,[2J_1(\kappa r)/(\kappa r)]^2$$
$$\times \Phi_n(\kappa)D_0^2(k_1 - k_0)D_1^2(k_\alpha - k_1) \ . \tag{12}$$

Use of k_1 as an integration variable in place of κ_3 simplifies the evaluation of Eq. 12. Also, fixing the value of k' at the pole k_1 changes the condition $\kappa \leq k'$ to the inequality $\kappa \leq k_1$. The definition $k_1 = (\kappa_3^2 + \kappa^2)/2\kappa_3$ implies $\kappa_3 = k_1 + \sqrt{k_1^2 - \kappa^2}$, and the expanded form of Eq. 12 becomes

$$I(k) = (\pi/l)\int_{-\infty}^{\infty} dk_1 k_1^2 D_0^2(k_1 - k_0)S(k_1, m) \ , \tag{13}$$

where

$$S(k_1, m) = 4\pi^2 \int_0^{k_1} d\kappa\,\kappa\,\frac{\sqrt{k_1^2 - \kappa^2}}{k_1 + \sqrt{k_1^2 - \kappa^2}}\,[2J_1(\kappa r)/(\kappa r)]^2$$
$$\times \Phi_n(\kappa)\int_0^{2\pi} d\phi D_1^2(k - k_1 - m\kappa\cos\phi) \ , \tag{14}$$

with $\kappa^2 = 2k_1^2 + 2k_1\sqrt{k_1^2 - \kappa}$, $m^2 = m_\alpha m_\alpha$, and ϕ the angle between m_α and κ_α. The κ integration adopts a more obvious physical meaning after the transformation $\kappa = k_1\sin(\pi - \theta)$, where θ is the scattering angle from an element of scattering volume dV at a distance r_s and elevation angle $\theta - \pi/2$ from the receiver. In addition, for reasonably large pulse lengths, the receiver beam-pattern factor $[2J_1(k_1 r\sin\theta)/(k_1 r\sin\theta)]^2$ does not vary strongly about the central frequency over the width of the spectrum and, thus, approximately equals $[2J_1(k_0 r\sin\theta)/(k_0 r\sin\theta)]^2$. Then the transformation changes the inner integrals (Eq. 14) to

$$S = 4\pi^2 k_1^2 \int_{\pi/2}^{\pi} d\theta\,\frac{\cos^2\theta\sin\theta}{2\sin^2\theta/2}\,[2J_1(k_0 r\sin\theta)/(k_0 r\sin\theta)]^2$$
$$\times \Phi_n\!\left(2k_1\sin\frac{\theta}{2}\right)\int_0^{2\pi} d\phi D_1^2(k - k_1 - mk_1\cos\phi\sin\theta) \ . \tag{15}$$

The elements of the scattering volume V_s which contribute to the acoustic energy flow at the receiver lie in a spheroidal shell. Define the mean radius r_s of the shell as the locus of points for which the midpoint of the initial pulse corresponds to the midpoint of the receiving gate. The mean radius r_s of this shell must satisfy the condition $r_s + r_s\sin(\theta - \pi/2) = 2R$, which implies $r_s = R/\sin^2(\theta/2)$. The thickness of the shell Δr_s satisfies $r_s \pm \Delta r_s/2 + (r_s + \Delta r_s/2)\sin(\theta - \pi/2) = 2R \pm l$, that is $\Delta r_s = l/\sin^2(\theta/2)$. Thus, the mean radius of the shell varies from $r_s = R$ at the zenith to $r_s = 2R$ at the horizon. Similarly, the thickness of the shell varies from $\Delta r_s = l$ at the zenith to $\Delta r_s = 2l$ at the horizon. A ring-shaped volume element of this shell, $dV = 2\pi r_s^2\sin\theta\Delta r_s d\theta = 2\pi lR^2\sin^{-6}(\theta/2)\sin\theta d\theta$, contributes an energy-flow component in the z direction equal to the product of $\cos^2\theta$ and the energy flow in the r_s direction. And the energy flow in the r_s direction is inversely proportional to the square of the distance r_s. Rewriting Eq. 15 in the form

$$S = \pi k_1^2 \int_{V_s} dV\,\frac{\cos^2\theta}{lr_s^2}\,[2J_1(k_0 r\sin\theta)/(k_0 r\sin\theta)]^2\Phi_n\!\left(2k_1\sin\frac{\theta}{2}\right)$$
$$\times \int_0^{2\pi} d\phi D_1^2(k - k_1 - mk_1\cos\phi\sin\theta) \ , \tag{16}$$

it clarifies the physical significance of the factors of the integrand. Except for the limit $k_0r \to \infty$, the scattering includes contributions from a range of eddy sizes, and from both temperature and velocity fluctuations. As $\kappa = 2k_1\sin(\theta/2)$ varies from $\sqrt{2}\,k_1$ at the horizon to $2k_1$ at the zenith, the eddy scale transverse to the r_s direction changes from λ_1 to ∞, and the scale parallel to r_s changes from λ_1 to $\lambda_1/2$, where $\lambda_1 = 2\pi/k_1$. Also, the major part of the coherent contributions arrive from pancake-shaped eddies near the zenith. In terms of beamwidth, the requirement $\lambda R \ll L^2$ for coherence implies the coherent contributions fall within a half-angle $\Psi \approx \sqrt{\lambda R}/L$. Equivalently, large eddies act in a similar way to a large-aperture antenna, producing a narrow-backscatter beam angle. For $k_0r = 0$ the beam-pattern weighting factor reduces to one. With increasing $k_0r = 2\pi r/\lambda$, however, scattering angles near $\theta = \pi$ receive more and more weight, while the scattering elements near the horizon $\theta = \pi/2$ becomes less and less effective. As $k_0r \to \infty$ the energy flux per unit receiver aperture area drops to zero, but the total energy flow remains constant. Wheelon[7] briefly alludes to the differences between the classical farfield and volume-averaging approximations for the scattering cross sections and the detailed description of theintensity spectrum achieved here and, for zero mean wind, obtains the cross section in the form of a series.

Returning to Eq. 15, the ϕ integrand D_1^2 has some Fourier transform f_Δ or,

$$D_1^2(k - k_1 - mk_1\cos\phi\sin\theta)$$
$$= (2\pi)^{-1}\int_{-\infty}^{\infty} d\eta f_\Delta(\eta)\exp[i\eta(k - k_1 - mk_1\cos\phi\sin\theta)]\ . \quad (17)$$

In Eq. 17, the phase $\eta(k - k_1 - mk_1\cos\phi\sin\theta)$ of the integrand differs from the approximate phase $\eta(k - k_1 - mk_0 \times\cos\phi\sin\theta)$ by much less than 2π for the significant ranges of integration. Taking $\cos\phi\sin\theta = 1$, the maximum magnitude of the phase difference $\Delta\chi$ between the exact and approximate phases becomes $\Delta\chi = m\eta|k_1 - k_0|$. The function $f_\Delta(\eta)$ decreases rapidly for η outside the range $(-2l, 2l)$. Similarly, the function $D_0^2(k_1 - k_0)$ in Eq. 13 drops quickly for $k_1 - k_0$ outside the range $(-\pi/l, \pi/l)$. Then, since $m \ll 1$ always hold for the atmosphere, $\max\Delta\chi = m\cdot 2l\cdot\pi/l = 2\pi m \ll 2\pi$. With the above phase approximation, the ϕ integration in Eq. 15 becomes

$$\int_0^{2\pi} d\phi D_1^2(k - k_1 - mk_1\cos\phi\sin\theta)$$
$$\approx \int_{-\infty}^{\infty} d\eta f_\Delta(\eta) J_0(mk_0\eta\sin\theta)\exp[i\eta(k - k_1)] \quad (18)$$
$$= D_1^2(k - k_1) \underset{k-k_1}{*} \frac{2Y[m^2k_0^2\sin^2\theta - (k - k_1)^2]}{\sqrt{m^2k_0^2\sin^2\theta - (k - k_1)^2}}\ , \quad (19)$$

where $Y(x)$ represents the Heaviside step function; $Y(x) = 0$ for $x < 0$, $Y(0) = \frac{1}{2}$, $Y(x) = 1$ for $x > 0$. The second factor in the convolution product (Eq. 19) resembles the wind-broadening factor found in Brown and Clifford.[3] When $m = 0$, the wind-broadening factor becomes $2\pi\delta(k - k_1)$, and Eq. 19 reduces to $2\pi D_1^2(k - k_1)$. For $mk_0l \leq 1$ broadening due to wind remains negligible. For typical values of l/λ, the inequality $mk_0l \leq 1$ corresponds to mean winds less than 0.5 m/sec. The remaining analysis concentrates on the case where $mk_0l \geq 1$.

In terms of the energy spectrum $E(\kappa)$ of the velocity fluctuations and the temperature-fluctuation spectrum $\Phi_T(\kappa)$, the spectrum $\Phi_n(\kappa)$ of effective refractivity fluctuations n' from Brown[1] becomes

$$\Phi_n(\kappa) = \frac{\Phi_T(\kappa)}{4T_0^2} + \cos^2\frac{\theta}{2}\,\frac{E(\kappa)}{4\pi\kappa^2c_0^2}\ . \quad (20)$$

The factor 1/4 in the temperature term Eq. 20 arises from the perfect-gas approximation $c_0/(c_0 + c') \approx 1 - T'/2T_0$, and the factor $(4\pi\kappa^2)^{-1}$ in the velocity term results from the isotropy relation between the trace of the velocity spectrum and the energy spectrum. From Tatarskii,[4] $\Phi_T = 0.033\, C_T^2\kappa^{-11/3}$ and $E(\kappa) = 0.76\, C_v^2\kappa^{-5/3}$ in the inertial subrange, where C_T and C_v represent the respective temperature and velocity structure constants. On rearranging Eq. 20,

$$\Phi_n\left(2k_1\sin\frac{\theta}{2}\right) = 0.033\, 2^{-23/6}\, k_1^{-11/3}\left(2\sin^2\frac{\theta}{2}\right)^{-11/6}$$
$$\times\left(\frac{C_T^2}{T_0^2} + 7.33\,\frac{C_v^2}{c_0^2}\cos^2\frac{\theta}{2}\right). \quad (21)$$

Unlike the forwardscatter-pressure spectrum which requires an approximation such as the von Kármán spectrum (Brown and Clifford[2]), the Kolmogorov spectrum represents a good approximation for backscatter when $\lambda < L_0$, since atmospheric turbulence usually possesses an inertial range with an outer scale L_0 of some tens to hundreds of meters. Introducing Eq. 19 and Eq. 21 into Eq. 15 changes it to

$$S = 0.033\, k_1^{-5/3} D_1^2(k - k_1) \underset{k-k_1}{*} H_m(k - k_1)\ , \quad (22)$$

where H_m represents the integral

$$H_m(k - k_1) = 4\pi^2\, 2^{-17/6}(mk_0)^{-1}\int_{\pi/2}^{\pi} d\theta[2J_1(k_0r\sin\theta)/(k_0r\sin\theta)]^2$$
$$\times\frac{\sin\theta\cos^2\theta\, Y[\sin^2\theta - [(k - k_1)/mk_0]^2}{(1 - \cos\theta)^{17/6}\sqrt{\sin^2\theta - [(k - k_1)/mk_0]^2}}$$
$$\times\left(\frac{C_T^2}{T_0^2} + 7.33\,\frac{C_v^2}{C_0^2}\cos^2\frac{\theta}{2}\right) \quad (23)$$

after taking mk_0 out of the square root. The function Y implies that H_m vanishes unless $(k - k_1)^2 \leq m^2k_0^2$. [Note that this does not imply that S vanishes for the same ranges of $k - k_1$. Outside the range $(-2mk_0, 2mk_0)$, however, the shape of the spectrum is determined by the pulse and gate spectra rather than by the turbulence.] Let $\xi = (k - k_1)/mk_0$ with $0 \leq \xi^2 \leq 1$ and replace $Y(\sin^2\theta - \xi^2)$ by $Y(1 - \xi^2)$ after changing the upper limit of integration from π to $\arccos\sqrt{1 - \xi^2}$. With the replacement of θ by $\arccos(\sqrt{1 - \xi^2}\cos\theta)$, the function H_m becomes

$$H_m(k - k_1) = \pi^2 2^{-5/6}(mk_0)^{-1}Y(1 - \xi^2)(1 - \xi^2)$$
$$\times\int_{\pi/2}^{\pi} d\theta\cos^2\theta[1 - \sqrt{1 - \xi^2}\cos\theta]^{-17/6}$$

$$\times\left\{\frac{2J_1(k_0r\sqrt{\sin^2\theta+\xi^2\cos^2\theta}}{k_0r\sqrt{\sin^2\theta+\xi^2\cos^2\theta}}\right\}^2$$

$$\cdot\left\{\frac{C_T^2}{T_0^2}+3.665\,\frac{C_v^2}{C_0^2}\left[1+\sqrt{1-\xi^2}\cos\theta\right]\right\}. \quad (24)$$

The integration (Eq. 24) becomes exact in the two limits $k_0r=0$ and $k_0r=\infty$. For $k_0r=0$, an isotropic receiver, let $1-\xi^2=[2\zeta/(1+\zeta^2)]^2$, and let $A=C_T^2/T_0^2+7.33\,C_v^2/C_0^2$ and $B=3.665\,C_v^2/C_0^2$. Then Eq. 24 becomes

$$H_m(k-k_1)=4\pi^2(mk_0)^{-1}Y(1-\xi^2)\int_{\pi/2}^{\pi}d\theta$$

$$\times\left\{A\left(\frac{1+\zeta^2}{2}\right)^{17/6}(1-2\zeta\cos\theta+\zeta^2)^{-17/6}\right.$$

$$-1/2(2A+B)\left(\frac{1+\zeta^2}{2}\right)^{11/6}(1-2\zeta\cos\theta+\zeta^2)^{-11/6}$$

$$+1/4(A+2B)\left(\frac{1+\zeta^2}{2}\right)^{5/6}(1-2\zeta\cos\theta+\zeta^2)^{-5/6}$$

$$\left.-1/8\,B\left(\frac{1+\zeta^2}{2}\right)^{-1/6}(1-2\zeta\cos\theta+\zeta^2)\right\}.. \quad (25)$$

Each of the terms in the integrand of Eq. 25 has the form $(1-2\zeta\cos\theta+\zeta^2)^{-\nu}$, with ν an arbitrary real number. Formula 22.9.3 of the NBS Handbook[8] gives expansions for such functions in Gegenbauer polynomials C_n^ν,

$$(1-2\zeta\cos\theta+\zeta^2)^{-\nu}=\sum_{n=0}^{\infty}\zeta^n C_n^\nu(\cos\theta)\;. \quad (26)$$

Integrating Eq. 26 from $\theta=\pi/2$ to π using formula 22.3.12 of the NBS Handbook,[6]

$$C_n^\nu(\cos\theta)=\sum_{h=0}^{n}\frac{\Gamma(\nu+h)\Gamma(\nu+n-h)}{h!(n-h)![\Gamma(\nu)]^2}\cos[(n-2h)\theta] \quad (27)$$

shows that the even terms vanish unless $n=2h$. Then define

$$c_n(\nu)=\int_{\pi/2}^{\pi}d\theta\,C_n^\nu(\cos\theta),\quad c_{2n}(\nu)=\frac{\pi}{2}\left[\frac{\Gamma(\nu+n)}{n!\Gamma(\nu)}\right]^2.$$

For the odd terms,

$$\int_{\pi/2}^{\pi}d\theta\,C_{2n+1}^\nu(\cos\theta)$$

$$=-\sum_{h=0}^{2n+1}(-1)^{n-h}\frac{\Gamma(\nu+h)\Gamma(\nu-h+2n+1)}{(2n+1-2h)h!(2n+1-h)![\Gamma(\nu)]^2}\;, \quad (28)$$

or, rearranging the terms of the summation,

$$c_{2n+1}(\nu)$$

$$=-2\sum_{h=0}^{n}(1-1)^h\frac{\Gamma(\nu+n-h)\Gamma(\nu+n+1+h)}{(2h+1)(n-h)!(n+1+h)![\Gamma(\nu)]^2}\;. \quad (29)$$

Using the relation $\zeta=[(1-|\xi|)/(1+|\xi|)]^{1/2}$, the exact expression for $H_m(k-k_1)$ when $k_0r=0$ becomes

$$H_m(k-k_1)=4\pi^2(mk_0)^{-1}Y(1-\xi^2)\sum_{n=0}^{\infty}\left(\frac{1-|\xi|}{1+|\xi|}\right)^{n/2}$$

$$\times\left\{A(1+|\xi|)^{-17/6}c_n(17/6)\right.$$

$$-\frac{1}{2}(2A+B)(1+|\xi|)^{-11/6}c_n(11/6)$$

$$+\frac{1}{4}(A+2B)(1+|\xi|)^{-5/6}c_n(5/6)$$

$$\left.-\frac{1}{8}B(1+|\xi|)^{1/6}c_n(-1/6)\right\}. \quad (30)$$

At the other limit, $k_0r\to\infty$, H_m approaches zero uniformly as r^{-2}. However, since the scattering volume which effectively contributes to the energy flux density at a point also decreases with r^{-2}, the total energy flow $\pi r^2 I(k)$ and the scattering cross section σ approach a constant. As $k_0r\to\infty$, πr^2 times the beam-pattern factor approaches a δ measure, concentrating all the effective scattering volume at the zenith. Using Eq. 16 instead of Eq. 23 leads to a clearer understanding of the exact behavior of $I(k)$. Setting all the slowly varying factors in Eq. 16 equal to their limits at $\theta=\pi$ gives

$$S\to\pi k_1^2\cdot 2\pi D_1^2(k-k_1)\cdot(0.033)(2k_1)^{-11/3}\;\frac{C_T^2}{4T_0^2}$$

$$\cdot(lR^2)^{-1}\int_{V_s}dV\left[\frac{2J_1(k_0r\sin\theta)}{k_0r\sin\theta}\right]^2. \quad (31)$$

The integral in Eq. 31, however, defines the effective scattering volume $\tilde{V}_s$, that is, the scattering volume V_s weighted by the beam-pattern factor. Substituting Eq. 31 into Eq. 13, and noting that the factor $k_1^{1/3}$ varies slowly during the k_1 integration compared to $D_0^2(k_1-k_0)$ in the neighborhood of k_0, gives the final form of $I(k)$ for large mk_0. Writing the integral as a convolution over $\Delta k=k-k_0$ by changing k_1 to $k'+k_0$,

$$I(k)\to\frac{\pi}{2}(\pi^2/l^2)(0.033)(2k_0)^{1/3}$$

$$\times\frac{C_T^2}{16T_0^2}\;\frac{\tilde{V}_s}{R^2}\;D_0^2(\Delta k)\underset{\Delta k}{*}D_1^2(\Delta k)\;. \quad (32)$$

Since $\int f*g=\int f\cdot\int g$ and $\int dkD_0^2(k)=\int dkD_1^2(k)=l/\pi$, the total of the energy flux density over all wavelengths approaches

$$\int dk\,I(k)\to\frac{\pi}{2}(0.033)(2k_0)^{1/3}\;\frac{C_T^2}{16T_0^2}\;\frac{\tilde{V}_s}{R^2}\;. \quad (33)$$

The power in the initial wave is $I_0(k)=(\pi/l)D_0^2(\Delta k)$ and, thus, $\int dk\,I_0(k)=1$. Then, defining the scattering cross section σ by

$$\sigma=R^2\int dk\,I(k)\Big/\left[\tilde{V}_s\int dk\,I_0(k)\right], \quad (34)$$

as in equation 35.18 of Tatarskii,[4] the backscatter cross section approaches

$$\sigma(\pi)\to\frac{\pi}{2}(0.033)(2k_0)^{1/3}\;\frac{C_T^2}{16T_0^2}\;, \quad (35)$$

which is exactly the result, equation 35.20 of Tatarskii,[4] for the case $\theta=\pi$, derived using the farfield approximation. Direct integration shows that $V_s=6\pi lR^2$. Then, for large k_0r, $\tilde{V}_s$ satisfies

$$\tilde{V}_s=\frac{1}{3}V_s(k_0r)^{-2}\int_0^1 dt\,J_1^2/(k_0rt)/t\;,$$

or, using Formula 11.3.30 of the NBS Handbook,[8]

$$\tilde{V}_s = \frac{1}{6} V_s(k_0 r)^{-2}[1 - J_0(k_0 r) - J_1(k_0 r)] ,$$

showing, in fact, that for large $k_0 r$ the effective scattering volume decreases inversely as the area of the receiver. For the case of arbitrary $\rho = rk_0/2\pi = r/\lambda$, evaluation of Eq. 24 depends on computer integration. If H_m is written as

$$H_m(\Delta k, \rho) = (mk_0)^{-1} Y(m^2k_0^2 - \Delta k^2) \times \left[\frac{C_T^2}{T_0^2} H_T\left(\frac{\Delta k}{mk_0}, \rho\right) + \frac{C_v^2}{c_0^2} H_v\left(\frac{\Delta k}{mk_0}, \rho\right)\right] \quad (36)$$

where H_T and H_v are defined by Eq. 24, then the final form of the spectrum is

$$I(k) = 0.033(\pi/l)k_0^{1/3} D_0^2(\Delta k) \underset{\Delta k}{*} D_1^2(\Delta k) \underset{\Delta k}{*} H_m(\Delta k, \rho) . \quad (37)$$

For large enough ρ, the "beam" half-angle ψ is customarily defined as the point where the square of the beam-pattern factor drops to half its maximum value. Since half the distance to the first zero of $J_1(x)$ gives a good approximation to the "half-power" point, the relation between ψ and ρ becomes

$$\rho = 0.3049/\sin\psi .$$

Figure 1 shows the wind-broadening functions H_T (for temperature fluctuations) and H_v (for velocity fluctuations) as functions of $\Delta k/mk_0$ for selected values of the parameter ρ or the beam half-angle ψ. A comparison of the ratio H_T/H_v determines the relative importance of temperature fluctuations with respect to velocity fluctuations. The computer calculations show that even for very small beamwidths ($\psi = 5°$) the effect of velocity fluctuations becomes greater than that of temperature fluctuations at a point about halfway between the center of the spectrum and the limit of influence of turbulence at $\Delta k = mk_0$.

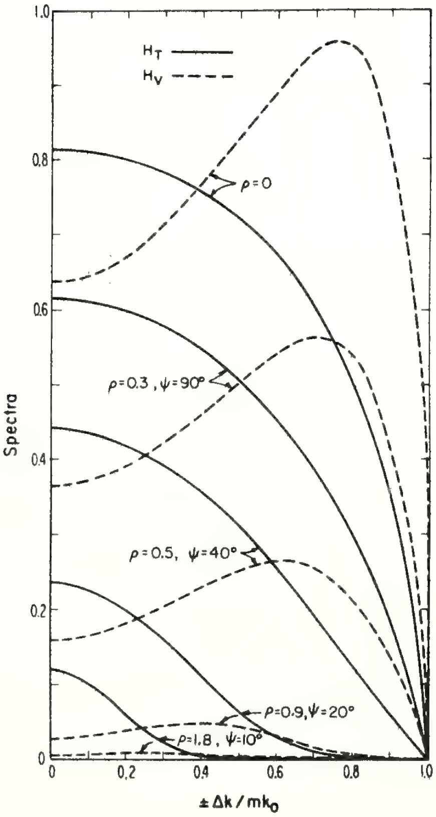

FIG. 1. Backscatter spectra H_T and H_v due to temperature and velocity fluctuations as a function of $\Delta k/mk_0$ for various receiver aperture ratios $\rho = r/\lambda$ and beam half-angles ψ.

The exact spectral shape given by Eq. 37 depends on the pulse and gate spectra D_0 and D_1. For many applications d_0 and d_1 are approximately rectangular unit pulses of length $2l$. Then, the equivalent spectral width of $D_0^2 * D_1^2$ becomes $\int dk D_0^2(k) * D_1^2(k)/[D_0^2(k) * D_1^2(k)]_{k=0} = 3\pi/2l$, just 1.5 times the spectral width of D_0 or D_1. However, $H_m(\Delta k)$ varies comparatively slowly over the interval $(-mk_0, mk_0)$. If $mk_0 l \gg 3\pi/2$ or $ml/\lambda \gg 3/4$, then $D_0^2 * D_1^2/\int dk D_0^2 * D_1^2$ acts approximately like a Dirac δ measure with respect to H_m (note that, in any case, the only interesting values satisfy $mk_0 l > 1$). As a result, the general spectrum, Eq. 37, reduces to the good approximation

$$I(k) = 0.0105\, l k_0^{1/3} H_m(\Delta k, \rho) , \quad (39)$$

where, as before, Eq. 36 gives H_m and H_T and H_v appear in Fig. 1. As a consequence of the vector character of the velocity fluctuations, the backscatter intensity when $C_T = 0$ shows a double peak in the spectrum.

For vanishing mean wind $H_m(\Delta k)$ reduced to

$$\lim_{m \to 0} H_m(\Delta k) = h_m(0, \rho)\delta(\Delta k) , \quad (40)$$

with $h_m(0, \rho)$ a function of ρ alone. The fact that $\int dk Y \times (\alpha^2 - k^2)/\sqrt{\alpha^2 - k^2} = \pi$ for any α permits evaluating $h_m(0, \rho)$ directly from Eq. 23. Again define temperature and velocity fluctuation factors:

$$h_m(0, \rho) = \frac{C_T^2}{T_0^2} h_T(0, \rho) + \frac{C_v^2}{c_0^2} h_v(0, \rho) . \quad (41)$$

The results of the computer integration of Eq. 23 are shown in Fig. 2. The zero mean wind spectrum becomes

$$I(k)\big|_{m=0} = 0.033(\pi/l)h_m(0, \rho)k_0^{1/3} D_0^2(\Delta k) \underset{\Delta k}{*} D_1^2(\Delta k) , \quad (42)$$

a spectrum with exactly the same shape as given by mirror reflection, but multiplied by a factor depending on the intensity of turbulence and the beam angle.

The integral of $I(k)$ roughly represents an energy flux density in a given direction and zero solid angle. If $d_0(\eta)$ and $d_1(\eta)$ are assumed rectangular unit pulses, then $\int d\Delta k D_0^2(\Delta k) = \int d\Delta k D_1^2(\Delta k) = l/\pi$ and again, $\int d\Delta k H_m(\Delta k) = h_m(0, \rho)$ for any m. Then, the identity $\int dk f(k) * g(k) = \int dk f(k) \int dk' g(k')$ implies that the integral of Eq. 37 is

$$\int dk I(k) = 0.033(l/\pi)k_0^{1/3} h_m(0, \rho) . \quad (43)$$

III. SPECTRAL WIDTH

The spectrum $I(k)$ given by Eq. 37 possesses a number of features. The $k_0^{1/3}$ frequency dependence results

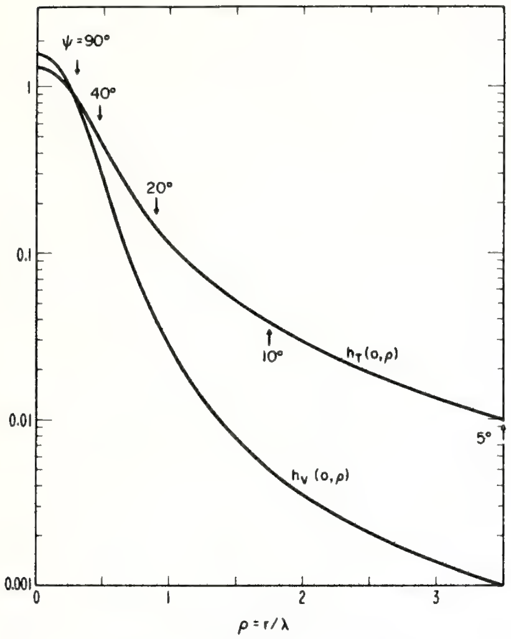

FIG. 2. Integrals of H_T and H_v as a function of receiver aperture ratio $\rho = r/\lambda$.

from the assumption of "frozen" isotropic turbulence, just as with the same frequency dependence of the zero-wind scattering cross section found by Tatarskii.[4] The assumption breaks down when the eddy turnover time becomes smaller than the pulse interaction time. Then, the random convection of $\lambda/2$-size scattering eddies by L_0-size eddies creates a Doppler broadening independent of mean wind. For this process, Ford and Meecham[9] found the frequency dependence changes to $k_0^{-2/3}$. But, such broadening does not play an important role with the customary range of parameters used for atmospheric sounding. In addition, the Doppler-shifted spectrum follows immediately from Eq. 37 on replacement of k_0 by $\hat{k}_0 = k_0/(1+m_z)$ and Δk by $\Delta\hat{k} = k - \hat{k}_0$, with m_z the mean-wind Mach-number component in the propagation direction. This replacement merely slides the entire spectrum along the k axis without change of shape or peak.

The spectral broadening produced by the convolution factor $H_m(\Delta k)$ represents the most important feature of Eq. 37. Since the convolution of two functions always has a width greater than that of either one of them, increasing mean transverse wind always implies monotonic increased broadening of the spectrum (for zero wind H_m becomes proportional to the Dirac δ measure—the "unit" for convolution products). Let a_s represent the area under the spectrum: $a_s = \int dk I(k)$. Just as with forwardscatter, a_s does not vary with mean wind, which merely acts to transfer energy flow from the spectrum peak into the wings. Then, the relation $b_s = a_s/I(0)$ defines the equivalent width b_s of the spectrum, which clearly shows that the broader the spectrum the lower the spectral peak. The assumption that $d_0(\eta)$ and $d_1(\eta)$ are both rectangular unit pulses of half-length l gives a good approximation to b_s in the general case. Then, the spectra $D_0(k)$, $D_1(k)$, and their powers all have the same equivalent width π/l. The convolution $D_0^2(k) \underset{k}{*} D_1^2(k)$, however, has the equivalent width $3\pi/2l$. Essentially, range gating a pulse broadens the spectrum because d_0 and d_1 move in opposite directions at the speed c_0, producing a shorter common interaction time. For Gaussian shapes, the factor 1.5 drops to the minimum possible $\sqrt{2}$ multiplying the equivalent width of either of the convolution factors.

Introducing the inverse Fourier transforms

$$f_\Delta(\eta) = \mathfrak{F}^\dagger D^2(k) = (l/\pi)d(\eta/2l)[1 - |\eta|/2l]$$

[for rectangular $d(\eta)$] and $h_m(\eta) = \mathfrak{F}^\dagger H_m(k)$ gives

$$a_s = \int dk I(k) = 0.033(\pi/l)k_0^{1/3} f_\Delta^2(0) h_m(0,\rho) \tag{44}$$

and

$$I(0) = 0.033(\pi/l)k_0^{1/3} \cdot \frac{1}{2\pi}\int d\eta f_\Delta^2(\eta) h_m(\eta,\rho) , \tag{45}$$

where $f_\Delta^2(0) = l^2/\pi^2$ and $h_m(\eta,\rho)$ is the inverse Fourier transform of $H_m(k,\rho)$.

In the case $\rho = 0$ (an isotropic receiver), the exact equivalent spectral width for any mk_0l follows from the use of the empirical fits.

$$\begin{aligned} &H_T(x) \approx 0.812(1-x^4), \quad x = \Delta k/mk_0 , \\ &H_v(x) \approx 0.638[9(1-x^4) - 8(1-|x|^3)] , \end{aligned} \tag{46}$$

which approximate the computer values to about 10%. Using the identities

$$\begin{aligned} &\int dx\, x^n \cos\left(\alpha x + n\frac{\pi}{2}\right) = \partial_\alpha^n \frac{\sin\alpha}{\alpha} , \\ &\int dx\, x^{n+1} \cos\left(\alpha x + n\frac{\pi}{2}\right) = \partial_\alpha^n \frac{\sin\alpha}{\alpha} - \partial_\alpha^n \frac{1-\cos\alpha}{\alpha^2} , \end{aligned} \tag{47}$$

h_m becomes

$$\begin{aligned} h_m(\eta) = {} & 1.624 \frac{C_T^2}{T_0^2}\left(\frac{\sin c\eta}{c\eta} - \partial_{cn}^4 \frac{\sin c\eta}{c\eta}\right) \\ & + 1.276 \frac{C_v^2}{c_0^2}\left[\frac{\sin c\eta}{c\eta} - 9\,\partial_{c\eta}^4 \frac{\sin c\eta}{c\eta} \right. \\ & \left. - 8\,\partial_{c\eta}^2 \left(\frac{\sin c\eta}{c\eta} - \frac{1-\cos c\eta}{c^2\eta^2}\right)\right] , \end{aligned} \tag{47}$$

where $c = mk_0$.

Substituting Eq. 47 into Eq. 45 and integrating by parts gives

$$\begin{aligned} I(0) \approx {} & 0.033(\pi/l)k_0^{1/3} \cdot (1.29) \\ & \times \frac{C_T^2}{T_0^2} g^{-1}(\mu)\left\{1 + \frac{2}{3}\gamma[1 + g(\mu)f(\mu)]\right\} , \end{aligned} \tag{48}$$

where

$$\begin{aligned} &\gamma = C_v^2 T_0^2/(c_0^2 C_T^2), \quad \mu = 2mk_0l , \\ &f(\mu) = 10(\mu^3 - 6\mu + 6\sin\mu)\mu^{-5} , \end{aligned} \tag{49}$$

and

$$g(\mu)=\frac{4}{15}\left(\frac{\mathrm{Si}\mu}{\mu}-2\,\frac{1-\cos\mu}{\mu^2}+\frac{\sin\mu-\mu\cos\mu}{\mu^3}\right.$$
$$\left.-\frac{2}{3}\,\frac{\mu^3-3\sin\mu+3\mu\cos\mu}{\mu^5}\right)^{-1}, \qquad (50)$$

with $\mathrm{Si}\mu$ representing the sine-integral function. Finally, the ratio of Eq. 44 to Eq. 48 gives the equivalent width

$$b_s=\frac{3\pi}{2l}\,\frac{(1+\gamma)g(\mu)}{1+(2/3)\gamma[1+f(\mu)g(\mu)]}\,,\quad \mu=2mk_0l\ . \qquad (51)$$

Computer-calculated curves of normalized $b_s(\mu)$ for a range of values of the parameter γ appear in Fig. 3, along with the corresponding curve for forwardscatter. As $\mu\to 0$, repeated applications of l'Hospital's rule show that $g(\mu)\to 1, f(\mu)\to 1/2$ and, thus, $b_s\to 3\pi/2l$, the unbroadened value. The function $\partial b_s/\partial\ln\gamma$ has a maximum at $\gamma=3/2$. For large mk_0l, Eq. 39 with Fig. 1, together with Eq. 41 and Fig. 2., give b_s directly. The results as a function of $2mk_0l$ for various beam-pattern parameters for the case $\gamma=3/2$ are shown by the dashed lines in Fig. 3.

IV. DISCUSSION

In an earlier paper Brown and Clifford[2] found the equivalent width

$$b_s=\frac{\pi}{l}\left(1+m\,\frac{l}{L_0}\right)$$

for forwardscatter, an equation linear in the mean wind (with ml/L_0 assumed small and the scattering assumed weak, that is, less than a radian phase change per eddy). At first glance the result (Eq. 51) for backscatter appears far more complicated. To a certain extent this complication reflects a more complex physical situation. For broad beams, the apparent 180° backscatter intensity is a sum of differential contributions from all scattering angles θ between 90° and 180°. For a horizontal mean wind, the wind component transverse to the direction of a differential scattering volume decreases with decreasing elevation angle $\theta\to\pi/2$ as $\sin(\theta-\pi/2)$. Simultaneously, the eddy dimension L transverse to the scattering direction decreases from $\infty(=L_0)$ at the zenith to λ at the horizon, implying an increase in modulation frequency with decreasing elevation angle. And, as a third factor, the amplitude of the frequency modulation also varies with elevation angle. The result (Eq. 51) expresses the sum of all these effects on the equivalent width b_s of the backscatter spectrum. As an interesting incidental result, replacing the infinite plane-wave model by narrow transmitting and receiving beams implies observation of only the very largest transverse scales near the zenith and, concurrently, the smallest modulation frequencies, giving negligible wind broadening of very narrow beams.

Returning to the plane-wave model, for typical atmospheric sounding the values of the parameter ml/L_0 determining the broadening in forwardscatter are small—perhaps less than 1/2, certainly less than one, while the values of the parameter $ml/(\lambda/2)$ determining the backscatter broadening are large, perhaps greater than ten, certainly greater than one. For such large values of $2mk_0l$, the complicated behavior of Eq. 51 disappears and b_s approaches a function linear in the mean wind. But, unlike the forwardscatter case where the effects of temperature and wind fluctuations combine in one structure constant C_n, the slope of the backscatter asymptote depends on the relative importance of C_T and C_v. Replacing $\mathrm{Si}\mu$ by its limit $\pi/2$ and keeping only first order in μ^{-1} shows that, for large $\mu=2mk_0l$,

$$b_s\to\frac{3\pi}{2l}\,\frac{1+\gamma}{1+(2/3)\gamma}\times\frac{8\mu}{15\pi}=\frac{8}{5}\,\frac{1+\gamma}{1+(2/3)\gamma}\times mk_0l\ , \qquad (52)$$

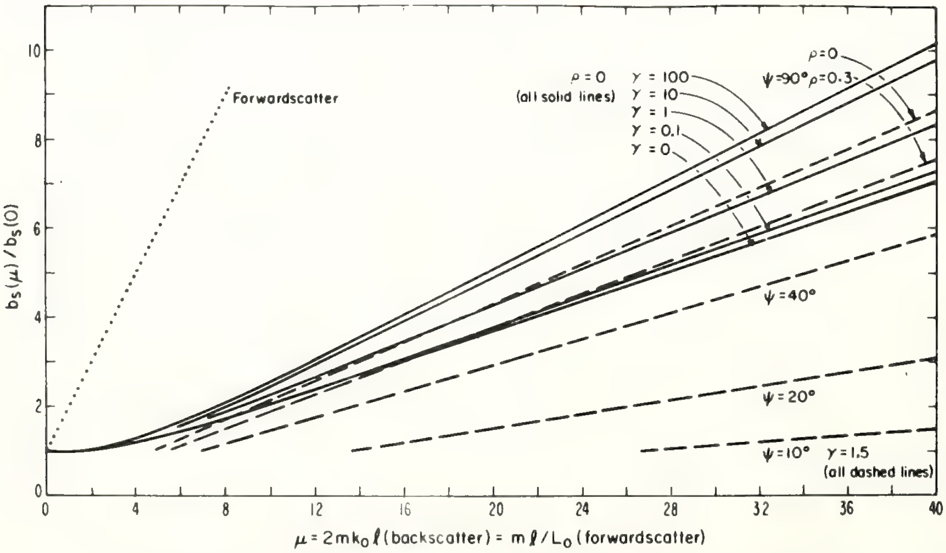

FIG. 3. Normalized equivalent spectral width $b_s(\mu)/b_s(0)$ as a function of $\mu=ml/L_0$ (forwardscatter) of $\mu=2mk_0l$ (backscatter). Solid lines are for an isotropic receiver for various $\gamma=C_v^2T_0^2/c_0^2C_T^2$. Dashed lines are for $\gamma=3/2$ and various aperture ratios $\rho=r/\lambda$.

with $\gamma = C_v^2 T_0^2/(c_0^2 C_T^2)$ as before.

Defining a time $\tau_0 = l/c_0$ proportional to the interaction time of the pulse with the turbulence permits a different viewpoint on the forwardscatter and backscatter parameters $\mu = \nu_m \tau_0$. Then, the forwardscatter modulation frequency is $\nu_m = \overline{w}/L_0$, where $\overline{w}$ is the magnitude of the mean transverse wind. Similarly, the backscatter modulation frequency is $\nu_m = \overline{w}/(\lambda/2)$. Thus, the backscatter modulation depends on the $\lambda/2$-size eddies responsible for the backscattering, while the forwardscatter modulation depends on the largest or L_0-size eddies responsible for the largest phase shifts.

Since the forwardscatter cross section is large, at moderate ranges broad beams receive contributions from waves forwardscattered through small angles before backscattering by the range-gated layer. Rosenbaum[10] has initiated a sophisticated approach to such a problem which includes both forwardscatter and backscatter effects simultaneously. However, even though violating the single-scatter assumption, a comparison of the forwardscatter broadening from Brown and Clifford[2] with the backscatter broadening (Eq. 51) permits a crude estimate of the relative importance of wind broadening during propagation and wind broadening during backscattering. As seen in Fig. 3, the forwardscatter curve of the equivalent width b_s as a function of $\nu_m \tau_0$ lies entirely above the backscatter curves. But, for typical values of $\nu_m \tau_0$ for atmospheric probing, $\nu_m \tau_0 < 1/2$ for forwardscatter, $\nu_m \tau_0 > 10$ for backscatter, the effects of backscatter on the broadening of the spectrum far outweigh the forwardscatter effects during propagation.

V. CONCLUSIONS

This paper has studied the broadening of the frequency spectrum of a backscattered broad-beam acoustic pulse by a transverse mean wind moving the scattering isotropic turbulence and temperature fluctuations through the beam. The results are expected to account for at least part of the spectral broadening obtained experimentally, such as that shown by Beran.[11] The principal results are the frequency spectrum, Eq. 37; the approximate form of the frequency spectrum, Eq. 39, with the wind broadening factor $H_m(\Delta k)$ given by Fig. 1; and the spectral width, Eq. 51 shown in Fig. 3, together with the behavior of the spectral width with receiver aperture for large $mk_0 l$.

For broad beams, both temperature and velocity fluctuations contribute to the 180° backscatter intensity, and the contributing eddy scales vary from $\sqrt{2}k_0$ to $2k_0$. Unlike forwardscatter, the effects of temperature and velocity are not combined in a single refractivity structure constant C_n, that is, C_T and C_v have different effects on the behavior of the equivalent spectral width b_s.

For typical experimental values of carrier frequency and pulse length, and for usually expected values of horizontal wind speed and outer scale of turbulence in the atmosphere, the broadening effects of mean wind during the scattering process outweigh the broadening effects of mean wind during propagation to the scattering layer.

Spectral broadening depends on beam angle. Narrow beams will result in negligible increase in the equivalent width b_s and give more accurate observations of Doppler shifts. Conversely, broad beams will increase b_s and permit more accurate observation of the maximum spectral broadening, thus providing a measurement of the magnitude of the transverse wind.

ACKNOWLEDGMENTS

The author is grateful to W. D. Neff for discussions and for the computer calculations leading to Figs. 1 and 2, and to Drs. F. F. Hall and S. F. Clifford for a number of helpful conversations.

[1] E. H. Brown, J. Acoust Soc. Am. **52**, 1391 (1972).
[2] E. H. Brown and S. F. Clifford, J. Acoust. Soc. Am. **54**, 36 (1973).
[3] E. H. Brown and S. F. Clifford, J. Acoust. Soc. Am. **54**, 461 (1973).
[4] V. I. Tatarskii, *The Effects of the Turbulent Atmosphere on Wave Propagation* (Nauka, Moscow, 1967) (in Russian); translation from U. S. Dept. Commerce, Nat. Tech. Inform. Serv., Springfield, Va. (1971).
[5] N. W. McLachlan, *Complex Variable and Operational Calculus* (MacMillan, New York, 1947).
[6] S. F. Clifford and E. H. Brown, J. Acoust. Soc. Am. **48**, 1123 (1970).
[7] A. D. Wheelon, Proc. IEEE **60**, 251 (1972) .
[8] M. Abramowitz and I. A. Stegun, Eds. *NBS Handbook of Mathematical Functions* (U. S. Government Printing Office, Washington, D. C., 1964).
[9] G. W. Ford and W. C. Meecham, J. Acoust. Soc. Am. **32**, 1668 (1960).
[10] S. Rosenbaum, IEEE Trans. **AP-20**, 618 (1972).
[11] D. W. Beran, C. G. Little, and B. C. Willmarth, Nature **230**, No. 5290, 160 (1971).

Reprinted from Preprint Volume, 16th
Radar Meteorology Conf., April 22-24,
1975, Houston, Texas. Published by
Amer. Meteor. Soc., Boston, Mass.

APPLICATIONS OF PROPAGATION PARAMETERS TO ATMOSPHERIC ECHOSONDES

E. H. Brown, and R. J. Keeler

Wave Propagation Laboratory
NOAA Environmental Research Laboratories
Boulder, Colorado 80302

1. INTRODUCTION

Atmospheric echosondes have become increasingly useful in measurements of the turbulent structure of the surface layer (the first few hundred meters of the atmosphere). Reliable extension of such measurements to the boundary layer (which may reach altitudes of 1500 meters) or to the entire troposphere requires additional knowledge of acoustic propagation parameters, such as the phase coherence length ρ_o. Figure 1 presents pictorially the deformation of a plane wave echosonde beam propagating through turbulence. The initial representation of the phase fronts as planes implies constant phase differences between any two points in a plane perpendicular to the direction of propagation. As the wave propagates through the turbulence, the random fluctuations in the acoustic refractive index produce large random fluctuations in the phase fronts. Similarly, the initial equal thickness of the lines representing the phase fronts implies constant amplitudes for points in perpendicular planes. Again, as the wave propagates, the distortions in the phase fronts imply random direction changes in the wave vectors. In turn, the interference between changed neighboring wave vectors produces random fluctuations in the amplitude of the waves.

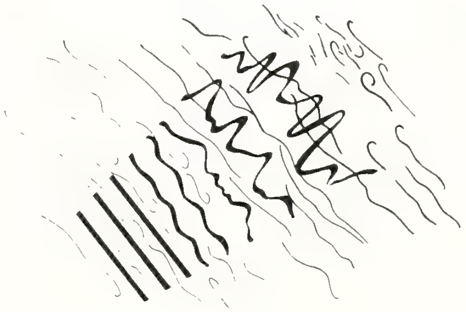

Figure 1. Propagation through turbulence

The fluctuations in amplitude and phase of an echosonde beam depicted in Figure 1 contribute both to signal (the scattered waves carrying information on the turbulent structure of the region of the atmosphere under study) and to noise (fluctuations produced in the wave by intervening regions). The noise constitutes a fundamental limitation on echosonde use, and only careful consideration of the turbulent propagation effects in echosonde design will permit measurements at higher altitudes (we can only speculate on the magnitude of the "pay-off" from an echosonde having the capability to continuously monitor wind speed, location, and direction, and turbulent intensity in jet stream systems near tropopause altitudes).

In this paper we describe measurements of such fluctuations in amplitude and phase of acoustic waves at 500, 1000, 2000, and 4000 Hz, propagating over 188 and 333 meter paths from a source on top of a 150 meter meteorological tower, and compare derived values with tower observations. The structure function of the phase fluctuations give phase coherence lengths and suggest methods for determining the outer scale of turbulence L_o. Displacements of the normalized covariance curves of the amplitude fluctuations near saturation from the theoretical intersection suggest a possible measure for gradients in the turbulent refractive index structure constant C_n.

2. DATA COLLECTION

During the last two weeks of March 1974 several groups from NOAA's Wave Propagation Laboratory, from NASA and WYLE Laboratories, and from the University of Massachusetts conducted a number of experiments at Haswell, Colorado. The Wave Propagation Laboratory's 500 foot meteorological tower, located on the flat plains of southeast Colorado at Haswell, carries standard instrumentation mounted at 100 ft altitude increments (plus an instrumented moving carriage), including instruments to measure mean temperature, mean wind speed and direction, and specialized instruments to measure the structure constant C_T of temperature fluctuations and the magnitude of wind fluctuations (which give approximate values of the structure constant C_v of velocity fluctuations). These parameters determine the structure constant C_n of acoustic index fluctuations according to the approximation

$$C_n^2 = \frac{C_T^2}{4T_o^2} + \frac{C_v^2}{c_o^2} , \qquad (1)$$

with T_o the mean temperature and c_o the mean speed of sound. The outputs of the tower instruments, plus a time code, go to a digitizer (once per second) and tape recorder for future correlation with the data from the various experiments.

Figure 2 depicts the arrangement of our experiment. Sound produced by either a JB Lansing or an Altec-Lansing driver with a sectoral horn mounted on top of the tower propagates towards the receivers. The movable receiving array stands on the ground due east of the tower at a slant range of 188 or 333 meters. Each of the four array elements includes a Realistic (Model 33-992) dynamic cardioid microphone. The microphones mount at the bottom of acoustic shields (20 gallon plastic trash containers lined with sound absorbing convoluted acoustic plastic foam) to reduce multipath effects and wind noise. The array elements lie in a horizontal line perpendicular to the direction of propagation, with spacings of 1, 2, and 4 meters (giving pair separations of 1, 2, 3, 4, 6, and 7 meters). Each array element aligns, by bore sighting, on the source at the top of the tower.

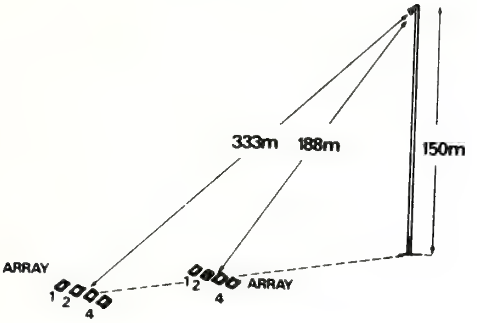

Figure 2. Experimental arrangement

CW signals at 500, 1000, 2000, and 4000 Hz, amplified to 36 electrical watts, propagate from the source. A 4-channel, 60 dB remote amplifier enhances the received signals at the array before returning the outputs to the underground equipment bunker. Then, after high-pass filtering at 500 Hz, a Vetter (Crown) Model A instrumentation tape recorder puts the received signals, plus the source and time code, on analog tape. We attempted to collect data at each frequency, and at each range, for three different conditions of atmospheric turbulence: high, $C_n^2 \approx 10^{-6}$ $m^{-2/3}$; medium, $C_n^2 \approx 10^{-7}$ $m^{-2/3}$; and low, $C_n^2 \approx 10^{-8}$ $m^{-2/3}$. Each run included 15 minutes of data to provide good averaging for the combination of large eddies and low advecting winds. An echosonde operating during the tests gave rough estimates of the amount of turbulence, providing guidance for the best periods for the collection of data.

3. DATA PROCESSING

During high-frequency, high-turbulence, long range tests we observed phase fluctuations of up to 20π radians (3600°) and amplitude fluctuations of up to 30 dB occurring with time constants of a few hundred milliseconds. We observed apparent outer scales of from 1 to 12 meters and mean winds of from 3 to 23 m/s, equivalent to time constants of from 50 milliseconds to a few seconds, that is, within the same range as the time constants of the observed phase fluctuations. Although simple envelope detectors can follow these amplitude variations, such large phase excursions require phase meters capable of quickly tracking many radians of phase change - instruments not commercially available at present. To overcome this difficulty we used two phase meters separated by a nominal 180° phase shift, a Wiltron (Model 350) and an Acton (Model 320AB) phase meter, both having a range of ± π radians. With this arrangement, when one meter's output becomes non-linear near its range limit, the other meter's output lies near the middle of its range. For every pair of signals on the analog tapes made at Haswell, we digitized the outputs of envelope detectors for each signal, and the outputs corresponding to the phase differences between the two signals from both phase meters at 100 Hz with a PDP-15 computer. Figure 3 gives a schematic diagram of amplitude and phase conversion and digitization circuits. Each 15 minute analog run required seven 15 minute digitizing runs to compare all combinations of the four receiving channels and the combination of the source and one receiving channel.

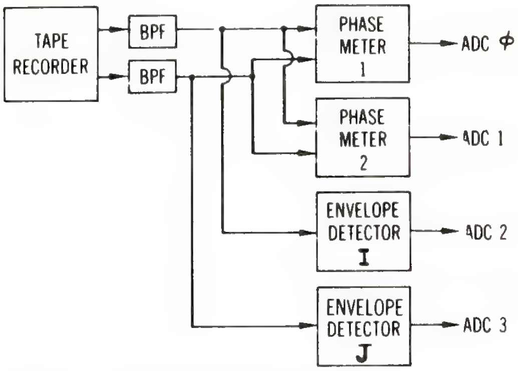

Figure 3. Digitizer Pre-Processor

Calculation of phase structure functions and phase coherence lengths required a single time series describing the phase difference fluctuations. We obtained such a time series with a "phase packing" program in which the computer selected whichever of the two previously digitized phase channels lay within certain prescribed limits. By switching back and forth between phase channels, the computer "boot-strapped" its way through many cycles of phase change. Since frequent amplitude fading occurred during periods of rapid phase changes, we included a low-amplitude detection instruction in the computer program. During such an amplitude fade, the computer held the phase constant until the signal rose sufficiently again to give reliable phase meter outputs.

4. DATA ANALYSIS

Tatarskii (1961, 1971), Lee and Harp (1969), and Clifford (1971), among others, have obtained theoretical expressions for the statistical functions associated with random amplitude and phase fluctuations of a wave. We shall need three of these quantities to express our experimental results and compare with the theory:

1) The quantity $\overline{\chi^2} = \langle [\ell n(A/A_o)]^2 \rangle$, the log-amplitude variance $\sigma_\chi^2 = \langle [\ell_n(A/A_o) - \langle \ell_n(A/A_o) \rangle]^2 \rangle$, for which, for small fluctuations compared to the mean, $\overline{\chi^2} \approx \sigma_\chi^2$, and the theoretical expression $\sigma_t^2 \approx \sigma_\chi^2$ for the case of single scatter,

$$\sigma_t^2 = 0.124\ k^{7/6}\ L^{11/6}\ \overline{C_n^2} \qquad (2)$$

with $k = 2\pi/\lambda$ the wavelength, L the one-way pathlength, and $\overline{C_n^2}$ the refractive index structure constant weighted over the path given by

$$\overline{C_n^{\,2}} = 5.544\int_0^1 du\ \left[u(1-u)\right]^{5/6} C_n^{\,2}(u), \text{with } u=Z/L \qquad (3)$$

2) The spatially-dependent log-amplitude covariance (normalized by $\sigma_t^{\,2}$) as a function of receiver separation ρ_N (normalized by a Fresnel zone $\sqrt{\lambda L}$) from Lawrence and Strohbehn (1970),

$$C_{\chi N} = 1 - 10.17\ \rho_N^{\,5/3} + 10.74\ \rho_N^{\,2} + \qquad (4)$$

$$9.125\ \rho_N^{\,17/3} - 3.158\ \rho_N^{\,4},\ \rho_N \ll 1$$

3) The spherical wave phase structure function $D_{SN}(\rho_N) = \left\langle \left[\phi_1 - \phi_2\right]^2 \right\rangle / \sigma_t^{\,2}$ (normalized by $\sigma_t^{\,2}$) as a function of normalized receiver separation,

$$D_{SN} = \begin{cases} 20.3\ \rho_N^{\,5/3} & \rho_N \ll 1 \\ 40.6\ \rho_N^{\,5/3} & \rho_N \geq 1 \end{cases} \qquad (5)$$

We use the normalization of phase differences by the geometric mean of the log amplitude variances of the two signals in order to obtain "universal" curves independent of $C_n^{\,2}$. However, such universal curves still depend on the value of the normalized outer scale $L_{oN} = L_o/\sqrt{\lambda L}$.

Assuming that the phase and amplitude sequences represent samples of random processes which satisfy the ergodic hypothesis (ensemble averages equal time averages) allows us to evaluate the following expressions:

1) Setting

$$\chi_{i\ell} = \ln\left(A_{i\ell}/A_{io}\right),\ \chi_{j\ell} = \ln\left(A_{j\ell}/A_{jo}\right),$$

$$A_{io} = \frac{1}{N}\sum_{\ell=1}^{N} A_{i\ell},\ A_{jo} = \frac{1}{N}\sum_{\ell=1}^{N} A_{j\ell}\quad ,$$

where i, j refer to the two microphones, $A_{i\ell}$ denotes the amplitude from the i^{th} microphone at sample time ℓ, and N represents the total number of samples in the average; then, for the geometric mean of the log-amplitude variances of the two signals,

$$\overline{\gamma^2} = \overline{\chi_{ij}^{\,2}} = \sqrt{\overline{\chi_i^{\,2}}\ \overline{\chi_j^{\,2}}}\quad , \qquad (8)$$

where

$$\overline{\chi_i^{\,2}} = \frac{1}{N}\sum_{\ell=1}^{N} \chi_{i\ell}^{\,2}\ ,\quad \overline{\chi_j^{\,2}} = \frac{1}{N}\sum_{\ell=1}^{N} \chi_{j\ell}^{\,2}\ ; \qquad (9)$$

2) for the normalized log-amplitude covariance

$$C_{\gamma N}(\rho_{ij}) = 1 - 1/2\ D_{\gamma N}(\rho_{ij})\quad , \qquad (10)$$

with

$$D_{\chi N}(\rho_{ij}) = \frac{1}{N}\sum_{\ell=1}^{N} \left(\chi_{i\ell} - \chi_{j\ell}\right)^2/\overline{\chi^2}\quad , \qquad (11)$$

3) for the normalized phase structure function

$$D_{SN}(\rho_{ij}) = \left\{\frac{1}{N}\sum_{\ell=1}^{N} \left(\phi_{i\ell} - \phi_{j\ell}\right)^2 \right. \qquad (12)$$

$$\left. - \left[\frac{1}{N}\sum_{\ell=1}^{N} \left(\phi_{i\ell} - \phi_{j\ell}\right)\right]^2\right\}/\overline{\chi^2}$$

We have used a 15 minute sampling interval for averaging to permit a large number of independent turbulent eddies to pass through the receiving array, thus ensuring accurate statistical estimates of the above quantities.

Due to the sensitivity of the phase measurements, jitter introduced by the tape recorder from variations in tape speed between tracks and between heads, and jitter due to delay variations in the roll-offs of the band pass filters introduce considerable noise in the phase structure functions. We measured this noise directly by recording pure tones at each of the four frequencies, and on all the channels, and then processing the recordings with the same digitization and analysis programs on the computer as the original experimental data. Assuming the signals and noise uncorrelated, subtraction of the phase variance of the jitter gives more accurate values of the phase structure functions of the signals. Other unavoidable errors arise from stretched analog tapes and other rare catastrophes affecting long-term averaging processes. We treated these mishaps by, first, partial one-minute averaging, then deleting obviously bad partial averages, and finally completing the averaging of the good data.

5. RESULTS

As indicated above, extraction of good amplitude fluctuation data presents no major problems. In Figure 4 we show some of our experimental results for $C_{\chi N}$ together with a theoretical curve for the case of negligible multiple scattering. The set of curves represent a well-behaved family parameterized by the experimental variance $\overline{\chi^2}$. Since higher values of turbulence (and C_n) lie near the ground, a spherical wave from a source on top of a tower produces greater emphasis from the smaller eddy scales (and smaller ρ_N) which, from the theory, most effectively produce amplitude fluctuations near the receivers. Increasing $\sigma_t^{\,2}$ raises the probability of multiple scatter with respect to the probability of single scatter, causing an intersection with the theoretical single-scatter curve. As a result, the experimental curves first drop more rapidly than the theoretical, then level off, dropping more slowly and crossing the theoretical at a point which moves up with increasing $\sigma_t^{\,2}$ towards the curves containing appreciable saturation in the variance. We show the $C_{\chi N}$ curves without error bars, since in all cases the standard deviation represents at most 2 percent of the mean. Note that, if transmitter and receivers were interchanged, as in the experiments of Mandics (1971), the curves for variable C_n would move above the theoretical curve rather than below it.

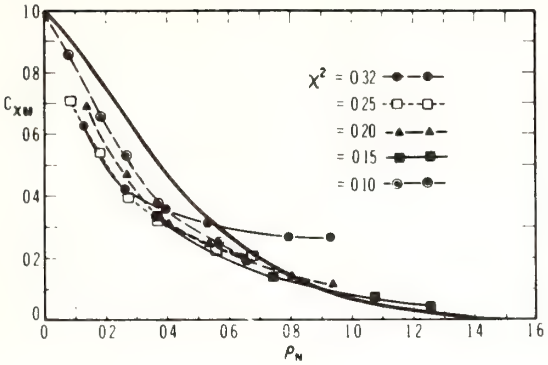

Figure 4. Experimental normalized log-amplitude covariances versus normalized lateral spacing

Equation 5 implies that the normalized phase structure function D_{SN} has two limiting forms. These two limits arise from the solution of the "wave structure function" $D_N = D_{\chi N} + D_{SN}$, the sum of the log-amplitude structure function and the phase structure function. When $\rho_N << 1$, $D_{SN} \approx D_{\chi N}$, and $D_{SN} \approx 1/2\ D_N$; but, when $\rho_N >> 1$, $D_{\chi N} << D_{SN}$, and $D_{SN} \approx D_N$. Between these limits D_{SN} varies smoothly from one curve to the other. Both these limiting forms depend on the assumption of a Kolmogorov spectrum of the refractivity fluctuation. For real atmospheres the outer scale of turbulence L_o comes into play with increasing ρ_N, forcing the D_{SN} curve to bend over and level off at some finite value. Thus, two different types of curves appear, depending on whether the outer scale (normalized by a Fresnel zone) L_{oN} satisfies the inequality $L_{oN} < 1$ or the inequality $L_{oN} \geq 1$. In the first case, the curve of D_{SN} bends over before ever reaching the higher value of slope. In the second case, the curve of D_{SN} at least begins to rise to the higher slope before the outer scale takes effect. Figure 5 shows the two expected types of D_{SN} curves as functions of $\rho_N^{5/3}$.

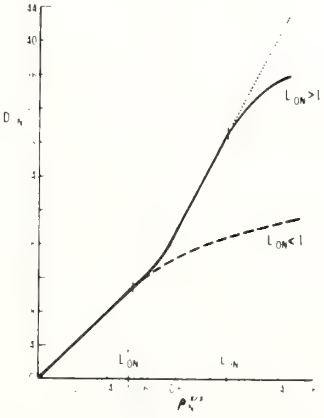

Figure 5. Theoretical phase structure functions

As implied in Section III, good phase measurements require much more effort than amplitude measurements. Figure 6 shows results for D_{SN} from three of the runs, for cases of low, medium, and high C_n^2. The error bars giving standard deviations of the data represented in all cases about 20 percent of the means. The medium variance curve represents one of the cases where, since $L_{oN} < 1$, D_{SN} bends over before any rise in slope. The high variance curve represents an intermediate case. And, the low variance case, with $L_{oN} \approx 1$, shows clear indications of an increasing slope just before the outer scale comes into play. Thus, the experimental phase fluctuation data possesses all the characteristics that we might expect from theory.

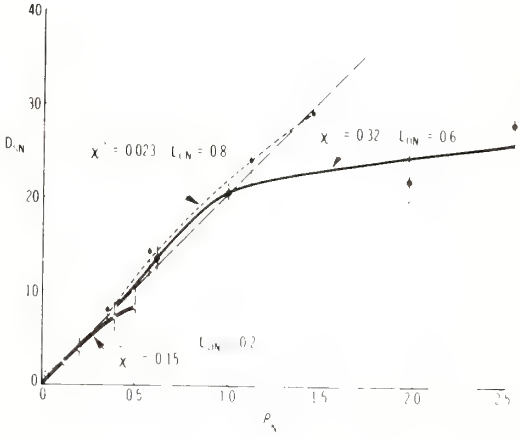

Figure 6. Experimental normalized phase structure functions versus normalized lateral spacing.

Encouraged by the agreement between our experimental results and theoretical predictions, we now briefly consider the implications for echosondes intended to reach much higher altitudes - on the order of at least 1 to 2 km. A simple model serves to illustrate the physical changes that occur with increasing range. At the scatterers, due to beam spreading, the illuminated area roughly depends linearly on the square of the effective antenna diameter D^2. Suppose that area is broken up into patches of diameter ρ; then, the total number N of patches depends on D^2/ρ^2, or $N \propto D^2/\rho^2$. For phase coherence lengths ρ_o greater than D, all the patches add coherently, so that the intensity available to scatter back to the receiver varies as N^2 times the intensity from one patch. But, if $\rho_o < D$, then setting $\rho = \rho_o$ for coherence within each patch, the available total intensity decreases towards N times the intensity from one patch; or, the intensity decreases as ρ_o^2/D^2 with decreasing ρ_o. Then even with good beam patterns, the decreasing intensity with decreasing ρ_o will eventually result in an unacceptable signal-to-noise ratio.

Long range vertical paths make consideration of the effects of varying C_n in the atmosphere obligatory. Also, Lutomirski and Yura (1971) have studied the effects of corrections due to outer scale L_o; but, we do not need these corrections for the approximations obtained here, since a typical choice takes L_o proportional to the height of the path L. Again, using the two constants for $\rho << \sqrt{\lambda L}$ and $\rho \geq \sqrt{\lambda L}$, the phase structure function becomes

$$D_S = \begin{Bmatrix} 1.089 \\ 0.544 \end{Bmatrix} k^2 L \, \rho^{5/3} \, \overline{\overline{C_n^{\,2}}} \quad , \tag{13}$$

where $\overline{\overline{C_n^{\,2}}}$ represents the weighted $C_n^{\,2}(z)$ over the path appropriate to phase measurements:

$$\overline{\overline{C_n^{\,2}}} = \int_0^1 du \, u^{5/3} \, C_n^{\,2}(u) \Big/ \int_0^1 du \, u^{5/3} , \quad u = Z/L \tag{14}$$

or for

$$C_n^{\,2}(Z) = C_{no}^{\,2} \cdot (Z/Z_o)^{-4/3} \quad , \tag{15}$$

$$\overline{\overline{C_n^{\,2}}} = 2 \, C_{no}^{\,2} \, (Z_o/L)^{4/3} \quad .$$

Assuming $C_{no}^{\,2}$ known at a height $Z_o = 1$ m and choosing $D_S = 2$ (which implies a mutual coherence function MCF = e^{-1} and defines the phase coherence length ρ_o), then (13) gives

$$\rho_o = \begin{Bmatrix} 0.951 \\ 1.440 \end{Bmatrix} L^{1/5} / (k^{6/5} C_{no}^{\,6/5}) , \tag{16}$$

or in terms of frequency f, with a nominal speed of sound c_o = 340 m/s,

$$\rho_o = \begin{Bmatrix} 115 \\ 174 \end{Bmatrix} L^{1/5} / (f^2 C_{no}^{\,2})^{3/5} \tag{17}$$

Choosing $C_{no}^{\,2} = 10^{-6} \; m^{-2/3}$, L = 1 km, and selecting the same four frequencies used in our experiment results in the following table for the minimum ρ_o:

TABLE 1

f(Hz)	ρ_o(m)
500	1052
1000	458
2000	199
4000	87

The above table clearly shows that phase coherence length will not represent a limiting factor on echosonde antenna diameter, at least for remote sensing within the atmospheric boundary layer.

ACKNOWLEDGMENTS

We would especially like to thank R. H. Gonter of the University of Massachusetts for his help in setting up and running the data acquisition part of the experiment at Haswell, Colorado. We also thank Dr. F. F. Hall, Jr., for his suggestions and support of the experiment.

7. REFERENCES

Clifford, S. F., 1971: Temporal-frequency spectra for a spherical wave propagating through atmospheric turbulence. J. Opt. Soc Amer., 61, pp 1285-1292.

Lawrence, R. S., and J. W. Strohbehn, 1970: A survey of clear-air propagation effects relevant to optical communications. Proc. IEEE, 58, pp 1523-1545.

Lee, R. W., and J. C. Harp, 1969: Weak scattering in random media, with applications to remote probing. Proc. IEEE, 57, pp 375-406.

Lutomirski, R. F., and H. T. Yura, 1971: Wave structure functions and mutual coherence functions of an optical wave in a turbulent atmosphere. J. Opt. Soc. Amer., 61, pp 482-487.

Mandics, P. A., 1971: Line of sight acoustical probing of atmospheric turbulence. Tech. Rept. No. 4502-1, Stanford Electronics Laboratories, Stanford, California.

Tatarskii, V. I., 1961: Wave Propagation in a Turbulent Medium. McGraw-Hill, New York. (transl. by R. S. Silverman).

Acoustic scattering from a moving turbulent medium

S. F. Clifford and E. H. Brown

NOAA/ERL, Boulder, Colorado 80302

(Received 7 November 1972; revised 15 February 1973)

The scattering cross section of a homogeneous turbulent layer found in the existing theory assumes that the mean motion of that layer is zero. For acoustic sounding in the real, open atmosphere the most interesting experimental results are for the case of the turbulent medium moving with the mean flow. In this case the measured Doppler shift indicates the average velocity over the scattering volume, a technique currently being used to extract vertical profiles of wind velocity. We extend the theory to the case of moving scatterers and find a modified angular dependence that, unlike the zero-wind case, predicts a nonzero cross section at a 90° scattering angle. Interestingly, there is essentially no change in the form of the backscatter cross section, i.e., there remains no contribution from wind eddies.

Subject Classification: 28.20, 28.40; 20.30; 85.88.

INTRODUCTION

The recent rapid growth of atmospheric echo-sounding research has led to a revival of interest in the propagation of acoustic waves in inhomogeneous media. In the recent book *Remote Sensing of the Troposphere*,[1] several chapters are dedicated to analyzing the state-of-the-art and future potential of this technique. The modification of the acoustic scattering properties of the atmosphere by refraction is currently of great interest to workers in this field; some progress has been achieved in these studies[2-4] and this paper is a continuation of that effort.

The early work on the scattering of an acoustic wave in a turbulent medium is due mainly to Monin[5] and Tatarski.[6] Using a homogeneous turbulence model they derived the scattering cross section for the case of zero mean flow. Recently, Brown[7] developed the scattering equations valid for a moving medium. The goal of this paper is, by applying the results of Brown, to find the analogous form of the scattering cross section valid for turbulence in motion with respect to the observer.

Figure 1 illustrates the problem considered here. A sounding is initiated in the direction of $\mathbf{k}_0$, the wave vector on the upward leg, and the echo returns along the direction of $\mathbf{k}_1$. The scattering volume, defined as the intersection of the two antenna beams, contains refractive-index fluctuations that are streaming by, advected by the mean wind $\mathbf{v}$. As before,[4] we assume horizontal stratification of the medium but not necessarily horizontal wind. By repeated application of Snell's law in this stratified medium, it becomes apparent that the only important velocity as far as refraction is concerned is the velocity difference between source and scatterer. (The effects of ray bending, i.e., the relocation of the intersection of the incident and received ray paths, are considered in detail elsewhere.[3,4] These results indicate that the change in the scattering angle produced by ray bending are of second order in v/c_0, where c_0 is the mean sound speed, whereas the changes in scattering angle, arising from Snell's law, are first order in v/c_0. Also, winds that are perpendicular to the plane defined by the scattering geometry, $\mathbf{v}_+$, produce changes in that geometry that are second order in v_+/c_0 and hence are negligible. Of course this last effect may become important if the wind velocity normal to the scattering plane is much larger than the parallel component.) This velocity difference in our model is v, since we assume zero wind at the ground. The important change in scattering geometry produced by $\mathbf{v}$ is the change in magnitude and direction of the incident wave vector from $\mathbf{k}_0$ to $\hat{\mathbf{k}}_0$, and similarly for the scattered wave vector $\mathbf{k}_1$ to $\hat{\mathbf{k}}_1$. This forces a new Bragg angle reflection condition for the scattering process as will be seen below.

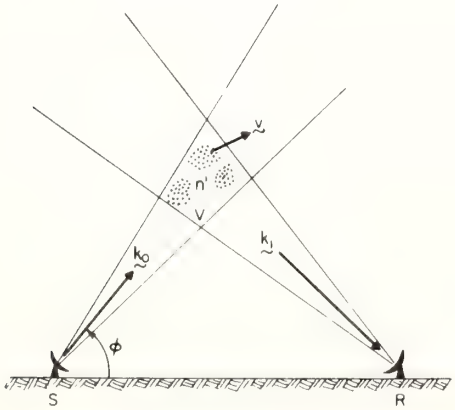

FIG. 1. A schematic drawing of the acoustic scattering process showing the sounder S and receiver R, with turbulent eddies moving through the scattering volume with a velocity $\mathbf{v}$.

I. ANALYSIS

The equations of Brown[7] show that the scattering mechanism for a *single-frequency* wave impinging on a moving volume of turbulence may be described by the scattering equations for nonmoving turbulence with the replacement of the partial time derivative, $\partial/\partial t$, by the mean substantial derivative, $d/dt = \partial/\partial t + \mathbf{v}\cdot\nabla$. This fact immediately implies that, if we are fixed with respect to the moving medium, Monin's and Tatarski's scattering results apply with the substitution of $\hat{\mathbf{k}}_0$ and $\hat{\mathbf{k}}_1$ for $\mathbf{k}_0$ and $\mathbf{k}_1$, respectively. Then, the scattering cross section as seen from the ground is found by solving for $\hat{\mathbf{k}}_0$ and $\hat{\mathbf{k}}_1$ in terms of k_0 using Snell's law.

Copyright © 1974 by the Acoustical Society of America

The scattered acoustic field as viewed in a frame moving with the mean wind is

$$P_1(r) = -(A_0/2\pi r)\exp(i\hat{k}_1 r)(\hat{\mathbf{k}}_0 \cdot \hat{\mathbf{k}}_1) \times \int_V d^3\mathbf{r}' n'(\mathbf{r}') \exp[i(\hat{\mathbf{k}}_0 - \hat{\mathbf{k}}_1)\cdot \mathbf{r}'], \tag{1}$$

where

$$n'(\mathbf{r}) = -\left(\frac{T'(\mathbf{r})}{2T_0} + \hat{\mathbf{k}}_1 \cdot \frac{\mathbf{u}'(\mathbf{r})}{\omega_0}\right). \tag{2}$$

(The form of Eq. 1 is a slight modification of the result given by Tatarski,[6] written to indicate the roles of $\hat{\mathbf{k}}_0$ and $\hat{\mathbf{k}}_1$ more explicitly.) Equation 1 is simply the spatial Fourier transform of the refractivity fluctuations, n', which are a function of the temperature and wind fluctuations T' and $\mathbf{u}'$, respectively. This equation is valid when the observer is in the farfield of the scattering volume V. The mean background temperature is T_0, and A_0 and ω_0, respectively, are the amplitude and radian frequency of the incident acoustic wave. The origin of coordinates for Eq. 1 is in the scattering volume such that the vector $\mathbf{r}$ points toward the receiver. From Eq. 1 it is apparent that the returned signal is proportional to the strength of the spatial Fourier component, $\hat{\mathbf{k}}_0 - \hat{\mathbf{k}}_1$, in the refractive index field. In the limit as $V \to \infty$, this is simply the Bragg angle reflection condition.

Following Tatarski, using Eq. 1 and the relation $\mathbf{S} = (\rho_0/2)c_0^3 P_1(r)P_1^*(\mathbf{r})\,\mathbf{e}_1$, we can calculate the flux of scattered energy (in the moving frame) in the apparent direction of the receiver as

$$\langle S\rangle = \langle \hat{\mathbf{e}}_1 \cdot \mathbf{S}\rangle = \frac{\pi\rho_0 c_0^3 A_0^2 V}{r^2}(\hat{\mathbf{k}}_0 \cdot \hat{\mathbf{k}}_1)^2 \Phi_n(|\hat{\mathbf{k}}_0 - \hat{\mathbf{k}}_1|), \tag{3}$$

where $\hat{\mathbf{e}}_1 = \hat{\mathbf{k}}_1/\hat{k}_1$ and we have ignored the smoothing of the refractive-index spectrum Φ_n by the finite size of the scattering volume. The spectrum Φ_n is defined as the three-dimensional Fourier transform of the correlation function B_n, where

$$B_n(\mathbf{r}_1, \mathbf{r}_2) = \langle n'(\mathbf{r}_1)\, n'(\mathbf{r}_2)\rangle. \tag{4}$$

In terms of the wind and temperature spectra Φ_{ij} and Φ_T, respectively,

$$\Phi_n(\mathbf{K}) = \frac{\Phi_T(\mathbf{K})}{4T_0^2} + \frac{\hat{e}_{1i}\hat{e}_{1j}}{c_0^2}\Phi_{ij}(\mathbf{K}), \tag{5}$$

where $\hat{e}_{1i}$ is a single component of the unit vector $\hat{\mathbf{e}}_1$. Next we assume statistical homogeneity and isotropy,[6] implying that $\Phi_T(\mathbf{K}) = \Phi_T(K)$ and that Φ_{ij} has the form

$$\Phi_{ij}(K) = \left(\delta_{ij} - \frac{K_i K_j}{K^2}\right)\frac{E(K)}{4\pi K^2}, \tag{6}$$

where δ_{ij} is the Kronecker delta and E is the energy spectral density of the turbulence. Equation 6 substituted into Eq. 5 and finally into Eq. 3 requires evaluation of the term

$$\frac{\hat{e}_{1i}\hat{e}_{1j}}{c_0^2}\left(\delta_{ij} - \frac{K_i K_j}{K^2}\right)\frac{E(K)}{4\pi K^2},$$

for $\mathbf{K} = \hat{\mathbf{k}}_0 - \hat{\mathbf{k}}_1$. This is easily accomplished in exact analogy to Tatarski and $\Phi_n(K)$ becomes

$$\Phi_n(|\hat{\mathbf{k}}_0 - \hat{\mathbf{k}}_1|) = \frac{\Phi_T(|\hat{\mathbf{k}}_0 - \hat{\mathbf{k}}_1|)}{4T_0^2} + \frac{(1 + \hat{\mathbf{e}}_0 \cdot \hat{\mathbf{e}}_1)}{8\pi c_0^2}\left[\frac{E(|\hat{\mathbf{k}}_0 - \hat{\mathbf{k}}_1|)}{|\hat{\mathbf{k}}_0 - \hat{\mathbf{k}}_1|^2}\right], \tag{7}$$

where $\hat{\mathbf{e}}_0 = \hat{\mathbf{k}}_0/\hat{k}_0$. The only assumption used to obtain Eq. 7 is that the wavelength of the sound in the moving medium is unchanged by the scattering process and therefore $\hat{k}_0 = \hat{k}_1$. The equality of $\hat{k}_0$ and $\hat{k}_1$ merely expresses the fact that an observer moving with the velocity of the mean wind will find the initial and scattered wavelengths identical. At this point Tatarski introduces the effective scattering cross section per unit scattering volume per unit solid angle in the form $\sigma = \langle S\rangle r^2/S_0 V$, where $S_0 = \rho_0 c_0^3 A_0^2/2$ is the incident energy flux. With Eq. 7 inserted into Eq. 3 and then normalized by $S_0 V/r^2$ we obtain

$$\sigma = \frac{\pi}{2}\hat{k}_0^2(\hat{\mathbf{e}}_0 \cdot \hat{\mathbf{e}}_1)^2\left[\frac{\Phi_T(K)}{T_0^2} + \frac{(1 + \hat{\mathbf{e}}_0 \cdot \hat{\mathbf{e}}_1)E(K)}{2\pi c_0^2 K^2}\right], \tag{8}$$

where $K^2 = 2\hat{k}_0^2[1 - \hat{\mathbf{e}}_0 \cdot \hat{\mathbf{e}}_1]$. The conventional assumption is to use the Kolmogorov spectrum[6] in Eq. 8 for $E(K)$ and $\Phi_T(K)$, where

$$E(K) = 0.76\, C^2 \epsilon^{2/3} K^{-5/3}, \tag{9}$$

$$\Phi_T(K) = 0.033 C_T^2 K^{-11/3}. \tag{10}$$

Equations 9 and 10 are valid for wavenumbers K within the so-called inertial subrange $L_0^{-1} \ll K \ll l_0^{-1}$, where l_0 is the inner and L_0 the outer scale of turbulence. The quantity C^2 is a numerical constant ≈ 1.9, ϵ is the rate of dissipation of turbulent energy, and C_T is the "structure constant" of the temperature fluctuations, a measure of their strength.

Equation 8, after inserting E and Φ_T from Eqs. 9 and 10, becomes

$$\sigma = 0.03\,\hat{k}_0^{1/3}(\hat{\mathbf{e}}_0 \cdot \hat{\mathbf{e}}_1)^2\left[\frac{(1 - \hat{\mathbf{e}}_0 \cdot \hat{\mathbf{e}}_1)}{2}\right]^{-11/6}\left\{\frac{0.13 C_T^2}{T_0^2} + \frac{(1 + \hat{\mathbf{e}}_0 \cdot \hat{\mathbf{e}}_1)C^2\epsilon^{2/3}}{2c_0^2}\right\}. \tag{11}$$

II. SCATTERING AS OBSERVED FROM THE GROUND

Equation 11 is the scattering cross section observed when moving with the scatterers. To express σ in terms of observables at the ground we must use the laws of refraction and calculate $\hat{\mathbf{k}}_0$ and $\hat{\mathbf{k}}_1$ in terms of $\mathbf{v}$, $\mathbf{k}_0$, and $\mathbf{k}_1$. First, consider $\hat{\mathbf{k}}_0$. Snell's law implies that (see Fig. 2)

$$\hat{\mathbf{k}}_0 \cdot \mathbf{e}_x = \mathbf{k}_0 \cdot \mathbf{e}_x, \tag{12}$$

i.e., the continuity of the wave-vector component along the interface. (Since we are ignoring the influence of ray bending, the refractive effects of a total wind change v can be found by assuming an abrupt discontinuity of velocity at the scatterer. This will give identical results, using Snell's law, as would be found using any continuous velocity variation with altitude of the same magnitude.) The unit vectors $\mathbf{e}_x$ and $\mathbf{e}_y$ are parallel to and normal to the interface, respectively. From the

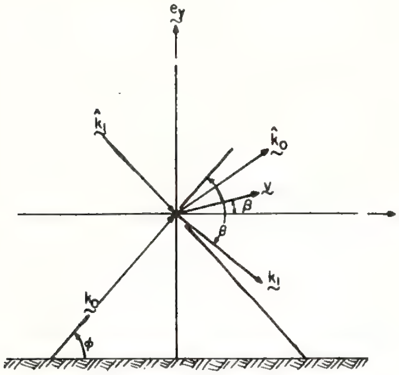

FIG. 2. The scattering geometry showing the effects of refraction on the incident $\mathbf{k}_0$ and scattered $\mathbf{k}_1$ wave vectors.

definition of the acoustic refractive index in a medium with a wave phase velocity c, $n = c_0/c$, the refractive index of the scattering volume with respect to that near the ground, due only to the motion in the medium, is

$$\hat{n} = c_0/[c_0 + \mathbf{v}\cdot\hat{\mathbf{e}}_0]\,. \tag{13}$$

The refractive index at the ground is $n = 1$. Now, $\hat{n}/n = c_0/\hat{c} = \hat{k}_0/k_0$, since $\hat{k}_0 = \omega_0/\hat{c}$ and $k_0 = \omega_0/c_0$; therefore

$$\hat{k}_0/k_0 = c_0/[c_0 + (\mathbf{v}\cdot\hat{\mathbf{e}}_0)]\,. \tag{14}$$

From Eq. 12 we have one component and from Eq. 14 the magnitude, so the total vector is obviously

$$\hat{\mathbf{k}}_0 = (\mathbf{k}_0\cdot\mathbf{e}_x)\,\mathbf{e}_x + k_0[(1+\mathbf{m}\cdot\hat{\mathbf{e}}_0)^{-2} - (\mathbf{e}_0\cdot\mathbf{e}_x)^2]^{1/2}\mathbf{e}_y\,, \tag{15}$$

where $\mathbf{m} = \mathbf{v}/c_0$. [This formula is valid only if we stay away from the critical angle defined by $(1+\mathbf{m}\cdot\mathbf{e}_0)^{-1} = (\mathbf{e}_0\cdot\mathbf{e}_x)$. When the square root becomes imaginary, total reflection occurs.] Since $m \ll 1$ in the atmosphere ($c_0 \approx 340$ m/sec for still dry air at STP), we may retain all quantities to first order in m. Then Eq. 15 becomes

$$\hat{\mathbf{k}}_0 \doteq (\mathbf{k}_0\cdot\mathbf{e}_x)\,\mathbf{e}_x + k_0[1 - (\mathbf{e}_0\cdot\mathbf{e}_x)^2 - 2\mathbf{m}\cdot\mathbf{e}_0]^{1/2}\mathbf{e}_y\,. \tag{16}$$

Note from Fig. 1 that $[1 - (\mathbf{e}_0\cdot\mathbf{e}_x)^2]^{1/2} = (\mathbf{e}_0\cdot\mathbf{e}_y)$ and therefore

$$\hat{\mathbf{k}}_0 \simeq k_0(\mathbf{e}_0\cdot\mathbf{e}_x)\,\mathbf{e}_x + k_0\left[(\mathbf{e}_0\cdot\mathbf{e}_y) - \frac{\mathbf{m}\cdot\mathbf{e}_0}{(\mathbf{e}_0\cdot\mathbf{e}_y)}\right]\mathbf{e}_y\,, \tag{17}$$

valid only if $(\mathbf{e}_0\cdot\mathbf{e}_y)^2 \gg 2\mathbf{m}\cdot\mathbf{e}_0$. From Eqs. 17 or 14, we have $\hat{k}_0 = k_0(1 - \mathbf{m}\cdot\mathbf{e}_0)$.

On the downward leg the refractive index formula analogous to Eq. 12 is $\hat{n} = c_0/\hat{c} = c_0/[c_0 + \mathbf{v}\cdot\hat{\mathbf{e}}_1]$, and consequently $\hat{k}_1/k_1 = [1 + \mathbf{m}\cdot\hat{\mathbf{e}}_1]^{-1}$. To relate k_1 to k_0 we note again that $\hat{k}_1 = \hat{k}_0$, since the wavelength in the moving frame does not change in the scattering process. With $\hat{k}_0 = k_0(1 - \mathbf{m}\cdot\mathbf{e}_0)$, then $k_1 = k_0(1 - \mathbf{m}\cdot\mathbf{e}_0 + \mathbf{m}\cdot\mathbf{e}_1)$, to first order in m. To complete the process, we again invoke Snell's law, i.e., $\hat{\mathbf{k}}_1\cdot\mathbf{e}_x = \mathbf{k}_1\cdot\mathbf{e}_x$, and then the vector $\hat{\mathbf{k}}_1$ becomes

$$\hat{\mathbf{k}}_1 \simeq k_1(\mathbf{e}_1\cdot\mathbf{e}_x)\,\mathbf{e}_x + k_1\left[(\mathbf{e}_1\cdot\mathbf{e}_y) - \frac{\mathbf{m}\cdot\mathbf{e}_1}{(\mathbf{e}_1\cdot\mathbf{e}_y)}\right]\mathbf{e}_y\,, \tag{18}$$

with $\hat{k}_1 = k_0(1 - \mathbf{m}\cdot\mathbf{e}_0)$ and $k_1 = k_0(1 - \mathbf{m}\cdot\mathbf{e}_0 + \mathbf{m}\cdot\mathbf{e}_1)$.

The resultant form of the scattering cross section is greatly simplified by using the following definitions:

$$(\mathbf{e}_1\cdot\mathbf{m}) = m_1\,, \tag{19}$$

$$(\mathbf{e}_0\cdot\mathbf{m}) = m_0\,, \tag{20}$$

$$(\mathbf{e}_0\cdot\mathbf{e}_x) = \cos\phi,\ \ (\mathbf{e}_0\cdot\mathbf{e}_y) = \sin\phi\,, \tag{21}$$

$$(\mathbf{e}_1\cdot\mathbf{e}_x) = \cos(\theta-\phi),\ \ (\mathbf{e}_1\cdot\mathbf{e}_y) = -\sin(\theta-\phi)\,. \tag{22}$$

The angle ϕ is the launch angle of the initial wave and θ is the usually defined scattering angle. [Recall that, in the presence of wind, θ is only the apparent scattering angle. The true scattering angle $\hat{\theta}$ is defined by $(\hat{\mathbf{e}}_0\cdot\hat{\mathbf{e}}_1) = \cos\hat{\theta}$.] Results 21 and 22 are easily derivable from the geometry in Fig. 2. Rewriting $\hat{k}_0$ and $\hat{k}_1$ in terms of these definitions, we have

$$\hat{\mathbf{k}}_0 = k_0\cos\phi\,\mathbf{e}_x + k_0[\sin\phi - m_0\csc\phi]\,\mathbf{e}_y \tag{23}$$

and

$$\hat{\mathbf{k}}_1 = k_1\cos(\theta-\phi)\,\mathbf{e}_x - k_1[\sin(\theta-\phi) - m_1\csc(\theta-\phi)]\,\mathbf{e}_y\,, \tag{24}$$

provided $\sin^2\phi \gg 2m_0$, $\sin^2(\theta-\phi) \gg 2m_1$. To find the cross section from Eq. 11, we must find the quantity $\hat{\mathbf{e}}_0\cdot\hat{\mathbf{e}}_1$ in terms of (θ,ϕ). Using Eqs. 23 and 24, we obtain

$$\hat{\mathbf{e}}_0\cdot\hat{\mathbf{e}}_1 = [(1 + m_0 + m_1)\cos\theta + m_0R + m_1R^{-1}]\,, \tag{25}$$

where $R = \sin(\theta-\phi)/\sin\phi$. This expression substituted into the appropriate places in Eq. 11 gives the final result for the mean wind-dependent cross section σ_m in the form

$$\begin{aligned}\sigma_m = 0.03\,\hat{k}_0^{1/3}&[(1+m_0+m_1)\cos\theta + m_0R + m_1R^{-1}]^2[a(\theta)]^{-11/6}\\ &\times\left\{\frac{0.13C_T^2}{T_0^2} + \frac{C^2\epsilon^{2/3}}{c_0^2}\left((1+m_0+m_1)\cos^2\frac{\theta}{2} - \frac{1}{2}[m_0(1-R) + m_1(1-R^{-1})]\right)\right\},\end{aligned} \tag{26}$$

where $a(\theta) = \{(1 + m_1 + m_0)\sin^2(\theta/2) - \tfrac{1}{2}[m_0(1+R) + m_1(1 + R^{-1})]\}$. (Recall that Eq. 26 is valid only for angles that satisfy the inequality presented after Eqs. 9 and 10.) In the limit as $m \to 0$, $a(\theta) \to \sin^2(\theta/2)$ and

$$\sigma_0(\theta) = 0.03k_0^{1/3}\cos^2\theta[\sin(\theta/2)]^{-11/3}$$

$$\times\left\{\frac{0.13C_T^2}{T_0^2} + \frac{C^2\epsilon^{2/3}}{c_0^2}\cos^2(\theta/2)\right\} \tag{27}$$

exactly as Eq. 23 in Chap. 2 of Tatarski's book. Figures 3 and 4 illustrate separately the angular dependence of the scattering cross section for temperature and wind fluctuations. Equation 26 for the case of a horizon-

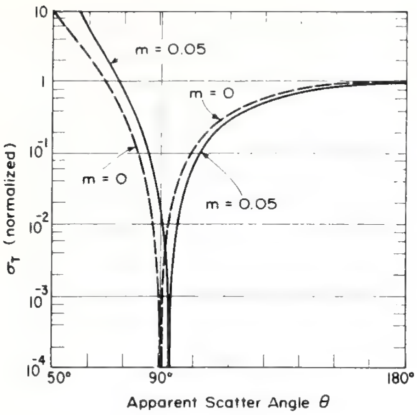

FIG. 3. Angular scattering dependence σ_T for temperature fluctuations as a function of apparent scattering angle θ, with a horizontal wind and a launch angle $\phi=\pi/4$.

tal wind with $m=0.05$ and a launch angle, $\phi=\pi/4$, is compared with the corresponding terms from Eq. 27.

III. DISCUSSION

The restriction in angle given after Eqs. 23 and 24 requires that we avoid using the formulas in the case of extremely small sounding angles $\phi \ll 2m$ or extremely small receiving angles $(\theta-\phi)\ll 2m$. These pose no difficulty for practical sounding geometries.

There are three important influences of the mean wind on the turbulent scattering process. Two of them represent a distortion of the normal radiation pattern or wind and temperature eddies and one is a modification of the Bragg angle reflection condition. These effects are admittedly small for most scattering angles, representing 5%–10% changes in total scattered power, but they take on great significance at an angle where the zero mean wind turbulence cross section is small, namely, $\theta=\pi/2$.

The first and most interesting effect is on the factor in the scattering coefficient of the wind fluctuations, $(1+\hat{\mathbf{e}}_n\cdot\hat{\mathbf{e}}_1)/2$. When $m=0$, this factor reduces to $\cos^2(\theta/2)$, which vanishes at $\theta=\pi$. Interestingly, even in the presence of a mean wind this term again vanishes (since $R=1$ where $\theta=\pi$) and there is still only backscatter from temperature eddies. Secondly, the coefficient outside the brackets in Eq. 26 that reduces to $\cos^2\theta$ in the zero wind case, producing a scattering null at $\theta=\pi/2$, no longer vanishes at $\theta=\pi/2$. Consequently, there will be scattering due to both wind and temperature fluctuations at right angles to the incident wavevector, k_0. Thirdly, the new three-dimensional spatial Fourier component that the sounder interrogates as a function of angle is

$$K(\theta,\phi,\beta)=|\hat{\mathbf{k}}_0-\hat{\mathbf{k}}_1|=2\hat{k}_0\{(1+m_1+m_0)\sin^2(\theta/2)-(m/2)\times[\cos(\phi-\beta)(1+R)+\cos(\theta-\phi+\beta)(1+R^{-1})]\}^{1/2}; \tag{28}$$

which reduces to the well-known $K=2k_0\sin(\theta/2)$ when $m=0$. In Eq. 28 we have used the result, obtained from Fig. 2, that $m_0=m\cos(\phi-\beta)$ and $m_1=m\cos(\theta-\phi+\beta)$, where β is the angle the wind makes with the horizontal For the angles of particular interest, $\theta=\pi/2,\pi$, Eq. 28 becomes

$$K(\pi/2,\phi,\beta)\simeq\sqrt{2}\,k_0\{1-(m/2)[\cos(\phi-\beta)(2+\operatorname{ctn}\phi)+\sin(\phi-\beta)\tan\phi]\} \tag{29}$$

and

$$K(\pi,\phi,\beta)\simeq 2k_0[1-m\cos(\phi-\beta)]\,. \tag{30}$$

Equations 29 and 30 show that the Bragg angle reflection condition is modified on the order of m, which has a maximum practical value of $m\sim 0.05$ ($v=17$ m/sec). Half-wavelength-size eddies still produce essentially the entire backscatter return.

The only measurable change produced by the presence of wind is a perturbation in the received signal strength. It is convenient to compare the new cross section, Eq. 26, with the zero-wind backscatter return. The backscatter cross section for zero mean wind is from Eq. 27,

$$\sigma_0(\pi)=0.004k_0^{1/3}C_T^2/T_0^2\,. \tag{31}$$

With a mean wind velocity $\mathbf{v}=\mathbf{m}c_0$, we obtain from Eq. 26

$$\sigma_m(\pi)=(1-m_0/3)\sigma_0(\pi)\,, \tag{32}$$

or less than a 2% maximum signal level change. At $\theta=\pi/2$, Eq. 26 gives

$$\sigma_m(\pi/2)=0.11\,\hat{k}_0^{1/3}h^2(\phi,\beta)[1-h(\phi,\beta)]^{-11/6}\times\left\{\frac{0.13C_T^2}{T_0^2}+\frac{C^2\epsilon^{2/3}}{2c_0^2}[1+h(\phi,\beta)]\right\}, \tag{33}$$

where

$$h(\phi,\beta)=m[\cos(\phi-\beta)\operatorname{ctn}\phi+\sin(\phi-\beta)\tan\phi]\,. \tag{34}$$

To make a meaningful comparison of Eq. 33 with the backscatter signal strength we must make some further simplifying assumptions. First let the wind be horizontal, $\beta=0$, and let $\phi=\pi/4$. Second, assume that

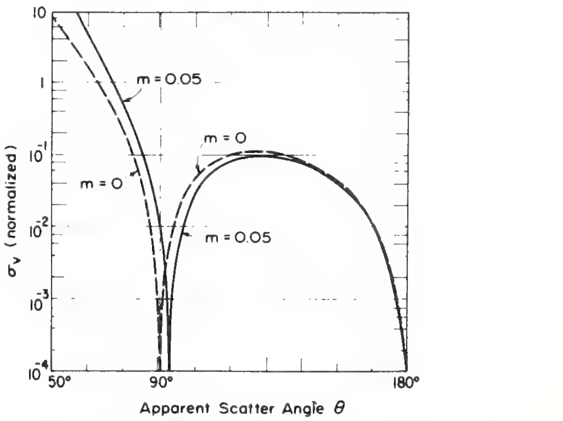

FIG. 4. Angular scattering dependence σ_v for wind fluctuations as a function of apparent scattering angle θ, with a horizontal wind and a launch angle $\phi=\pi/4$.

$C^2\epsilon^{2/3}/c_0^2 \approx 10\, C_T^2/T_0^2$, which appears reasonable from experimental work.[8] Under these conditions Eq. 33 may be written as

$$\sigma_m(\pi/2) \approx 275\, m^2\sigma_0(\pi)\ . \qquad (35)$$

For m ranging from 0.01 to 0.05 we obtain the result that $\sigma_m(\pi/2)$ is between 2.8% and 69% of the backscatter signal strength!

This result bears on the possibility, described by Little,[9] of resolving hydrometeor scattering from wind and temperature turbulent scattering. It appears that it is desirable to perform such experiments in relatively calm conditions.

It is quite easy to generalize Eq. 26 to the case of horizontally stratified temperature gradients. These, of course, produce a change in phase speed at the scattering height, $c = c_0 + \Delta c$, such that the refractive index Formula 12 is changed to $\hat{n} = c_0/[c_0 + \Delta c + \mathbf{v}\cdot\hat{\mathbf{e}}_0]$. Following through the analysis, it is immediately apparent that replacing m_0 and m_1 by $m_0 + \Delta c/c_0$ and $m_1 + \Delta c/c_0$ generalizes Eq. 26 to the nonhomogeneous temperature case.

[1] V. E. Derr, Ed., *Remote Sensing of the Troposphere* (Superintendent of Documents, U. S. Gov. Printing Office, Washington, D. C. 20402).

[2] A. N. Mahoney, L. G. McAllister, and J. R. Pollard, "The remote sensing of wind velocity in the lower troposphere using an acoustic sounder," Boundary Layer Meteorol. **4**, 155–169 (1973).

[3] D. W. Beran and S. F. Clifford, "Acoustic Doppler measurements of the total wind vector," Proc. AMS Acoust. Symposium on Meterological Observations and Instrumentation, San Diego, Calif. (1972).

[4] T. M. Georges and S. F. Clifford, "Estimating refractive effects in acoustic sounding," J. Acoust. Soc. Am. 55, 934–936 (1974).

[5] A. S. Monin, "Characteristics of the scattering of sound in a turbulent medium," Sov. Phys. Acoust. **7**, 370–373 (1962).

[6] V. I. Tatarski, *The Effects of the Turbulent Atmosphere on Wave Propagation* (National Technical Information Service, Springfield, Va., 1971) [TT68-50464].

[7] E. H. Brown, "Acoustic Doppler radar, scattering equation and general solution," J. Acoust. Soc. Am. **52**, 1392–1396 (1973).

[8] D. W. Beran (private communication).

[9] C. G. Little, "On the detectability of fog, cloud, rain, and snow by acoustic echo-sounding methods," J. Atmos. Sci. **29**, 748–755 (1972).

Estimating refractive effects in acoustic sounding

T. M. Georges and S. F. Clifford

Wave Propagation Laboratory, NOAA, Environmental Research Laboratories, Boulder, Colorado 80302

(Received 29 December 1972; revised 21 March 1973)

In an earlier paper [J. Acoust. Soc. Am. **52**, 1397–1405 (1972)], we modeled the effects of atmospheric refraction on the quantities measured in bistatic acoustic-echo sounding. Here we extend those results to the case of monostatic sounding, a configuration of particular interest experimentally. To estimate refractive displacement of the scattering volume, we have to assume linear wind and temperature profiles. Two tables show numerical values of refractive corrections, calculated for both representative monostatic and bistatic geometries.

Subject Classification: 28.20, 28.40; 20.30, 20.25; 85.88.

INTRODUCTION

In an earlier paper in this journal[1] we developed a simple model and derived formulas for estimating refractive changes of the quantities measured in active acoustic sounding of the atmosphere. Inhomogeneities in the atmospheric wind and temperature fields introduce refractive errors in measured Doppler shift, in the angular dependence of scatter by irregularities, and in the location of the atmospheric volume being interrogated. We asserted that most refractive corrections, except possibly the change in scattering angle, are normally insignificant for sounding heights presently being probed (less than 1 km), but that refractive effects would become more important for greater heights. To illustrate this we will present a table of sample calculations for two representative bistatic sounding situations.

Because monostatic sounding is of particular practical interest, and because the extension of our earlier formulas to the monostatic case is not—in all cases—straightforward, we shall develop those extensions and present sample calculations for monostatic sounding in a second table. Except where explicitly noted, notation is that introduced in the previous paper.[1]

I. CALCULATIONS FOR REPRESENTATIVE BISTATIC GEOMETRIES

A convenient bistatic sounding geometry is illustrated in Fig. 1. The sounding wave is launched vertically, and the scattered energy is detected at a 45° elevation angle ($\phi_c = 135°$ in the notation of Ref. 1). The atmosphere is represented by wind and temperature profiles that vary linearly with height, and propagation is assumed lossless. Table I shows calculations for two sounding heights, 1 and 5 km, where the horizontal wind speed reaches 10 and 50 m/sec, respectively.

The refractive corrections due to wind and temperature gradients are displayed separately so their effects can be assessed independently. In the cases illustrated, the wind and temperature effects add, but if either the wind direction or the sign of the temperature gradient were reversed, the effects would tend to cancel.

For the 1-km sounding height, refractive corrections appear to be smaller than typical observational errors, but for the 5-km sounding height, ignoring refraction could produce serious error. Note particularly the large change in scattering angle. That the last two rows contain identical numbers in each column is a result of the linear profiles.

II. MONOSTATIC SOUNDING

A. Displacement of scattering volume

In bistatic sounding, the common volume illuminated by the transmitting and receiving antennas defines the scattering volume, but in monostatic sounding it is necessary to use time-delay gating to define the scattering volume. Calculating the location of the scattering volume, given the total travel time and launch angle, appears to be difficult except for certain simple wind and temperature profiles. Specifically, linear wind and sound-speed profiles yield circular ray paths, along which the location of a point after a given travel time is readily calculated.

For a linear sound-speed profile, defined by

$$C = C_0(1 + \alpha z) , \qquad (1)$$

the ray path $x(z)$ is, to first order in αz,

$$x = z \tan\phi_a + (\alpha z^2/2)\tan\phi_a , \qquad (2)$$

where ϕ_a is the ray launch angle from vertical. We calculate the height the ray reaches after time τ_1 by first writing the differential equation

$$dz = C_0(1 + \alpha z)\cos\phi dt , \qquad (3)$$

where ϕ is the angle from vertical to the ray tangent. Then, noting that

$$d\phi \simeq \alpha \sin\phi_a \sec\phi_a dz , \qquad (4)$$

where $\alpha \sin\phi_a$ is the ray curvature, and $\sec\phi_a dz$ is (to first order) an element of length along the ray, we find that

$$\cos\phi \simeq \cos\phi_a - \alpha z \sin\phi_a \tan\phi_a . \qquad (5)$$

Substituting this into Eq. 3, eliminating higher-order terms in αz, and integrating gives

$$z = z_0 - \alpha z_0^2/2\,(\tan^2\phi_a - 1) , \qquad (6)$$

where $z_0 \equiv C_0\tau_1 \cos\phi_a$ is the "apparent" height after time τ_1 (that is, neglecting refraction). Because the ray path and travel time are the same for upgoing and downcoming paths in the absence of winds, the total travel time $\tau = 2\tau_1$. So Eq. 6 is the formula for the vertical

Copyright © 1974 by the Acoustical Society of America

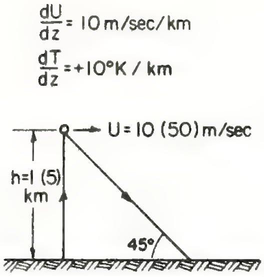

FIG. 1. The bistatic acoustic sounding geometry to which the calculations of Table I refer.

displacement in terms of τ, where $z_0 = (C_0\tau/2)\cos\phi_a$. The corresponding equation for x displacement is obtained by substituting Eq. 6 into Eq. 2, which gives

$$x = z_0 \tan\phi_a + \alpha z_0^2 \tan\phi_a - (\alpha z_0^2/2)\tan^3\phi_a \ . \tag{7}$$

The last term would normally be negligible for steep sounding angles.

Temporarily neglecting thermal refraction, we now calculate the refractive displacement in a linear profile of horizontal wind defined by

$$u(z) = C_0 \gamma z \ . \tag{8}$$

This is more difficult because the ray paths and travel times are different for upgoing and downcoming waves. The ray-path equation is

$$x = z \tan\phi_a + (\gamma z^2/2)\sec\phi_a \ . \tag{9}$$

We shall denote the arrival angle of the returning ray by $\phi_c' = \phi_a + \delta$. (The ϕ_c' we use here differs by π from the ϕ_c used in Ref. 1.) The equation for the downcoming ray is the same as for an upgoing ray launched at ϕ_c' in a wind field $u' = -u(z)$; therefore the following two equations must be satisfied by the ray intersection at the scatterer:

$$x = z \tan\phi_a + (\gamma z^2/2)\sec\phi_a \ , \tag{10}$$

$$x = z \tan\phi_c' - (\gamma z^2/2)\sec\phi_c' \ . \tag{11}$$

TABLE I. Sample calculations of refractive corrections in bistatic sounding.

QUANTITY	h = 1km			h = 5km		
	ΔT contrib.	ΔU contrib.	Total	ΔT contrib.	ΔU contrib.	Total
$\frac{\Delta f}{f_0}\Big\vert_0$	0.0	0.021	0.021	0.0	0.104	0.104
$\Delta f/f_0$ correction	0.0	0.00043	0.00043 (2.0%)	0.0	0.012	0.012 (11.5%)
Δγ change in axis of resolution	-0.488°	-0.102°	-0.59°	-2.44°	-0.511°	-2.95°
Δx displacement (km)	0.0	0.0147	0.0147 (1.5%)	0.0	0.367	0.367 (7.3%)
Δz displacement (km)	-0.0085	-0.0147	-0.0232 (2.3%)	-0.213	-0.367	-0.580 (11.6%)
Δψ change in scattering angle	-1.685°	-1.192°	-2.877°	-8.425°	-5.958°	-14.383°
equivalent $\frac{dT}{dt}\Big\vert_{av}$	1.72°K/sec			1.72°K/sec		
equivalent $\frac{dV}{dt}\Big\vert_{av}$	3.10 m/sec^2			3.10 m/sec^2		

TABLE II. Sample calculations of refractive corrections in monostatic soundings.

QUANTITY	h = 1km		h = 5km	
	ΔT contrib.	ΔU contrib.	ΔT contrib	ΔU contrib
$\frac{\Delta f}{f_0}\Big\vert_0$	0	-0.0416	0	-0.208
$\Delta f/f_0$ correction	0	0.00173 (4.15%)	0	-0.0433 (20.8%)
Δψ change in scattering angle	0	-2.38°	0	-11.9°
Δx displacement (km)	+ 0.0118 (1.18%)	+ 0.0104 (1.04%)	+ 0.295 (5.9%)	+ 0.26 (5.2%)
Δz displacement (km)	0	- 0.0104 (1.04%)	0	- 0.26 (5.2%)
δ change in angle of arrival	0	1.19°	0	5.96°

The solution of these equations for $\delta(z)$ will be used later:

$$\delta \simeq \gamma z \cos\phi_a \tag{12}$$

to first order in γz. This, by the way, is a generalization of the result given in Eq. 64 of Ref. 1 for the deflection of the arrival angle in vertical monostatic sounding.

The differential equation relating height to travel time along the ray is

$$dz = (C_0 + u \sin\phi)\cos\phi\, dt \ , \tag{13}$$

where ϕ is the angle from vertical to the ray tangent at any point. (This definition of ϕ differs slightly from that used in Ref. 1, i.e., the angle of the *wave vector* from vertical.) Since the ray's curvature is γ,

$$d\phi = \gamma\, dz \sec\phi \ , \tag{14}$$

and consequently,

$$\cos\phi \simeq \cos\phi_a - \gamma z \tan\phi_a \ . \tag{15}$$

Substituting Eqs. 15 and 12 into Eq. 13 and integrating, we get first-order equations for both rays in terms of travel time:

$$z + (\gamma z^2/2)\sin\phi_a \tan^2\phi_a = C_0\tau_1 \cos\phi_a \ , \tag{16}$$

$$z - \frac{\gamma z^2}{2}\sin\phi_a \tan^2\phi_a = C_0(\tau - \tau_1)(\cos\phi_a - \gamma z \cos\phi_a \sin\phi_a) \ . \tag{17}$$

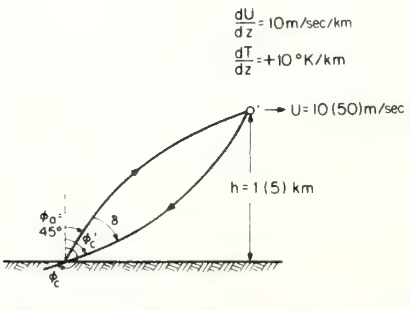

FIG. 2. The monostatic sounding geometry to which the calculations of Table II refer.

Adding and solving for $z(\tau)$ yields

$$z = z_0 - (\gamma z_0^2/2)\sin\phi_a \, , \tag{18}$$

where

$$z_0 \equiv (C_0\tau/2)\cos\phi_a \, . \tag{19}$$

Using Eq. 9 with Eq. 18 yields the x displacement

$$x = x_0 + (\gamma z_0^2/2)\cos\phi_a \, . \tag{20}$$

Equations 6, 7, 18, and 20 give the first-order refractive displacements caused by linear wind and sound-speed profiles. Displacements are relative to the "apparent" location of the scattering volume (x_0, z_0), which would be calculated from the launch angle and travel time assuming a homogeneous, still atmosphere. The displacements caused by combined linear wind and sound-speed profiles are additive to first order.

B. Doppler shift

Equation 24 of Ref. 1 becomes, in the monostatic case,

$$\Delta f = \frac{1}{2\pi}(\mathbf{K}_s - \mathbf{K}_0)\cdot\mathbf{V} + \frac{2V}{C_0}\frac{\Delta C}{C_0}\sin\beta\sec\phi_a \, . \tag{21}$$

Here $\mathbf{K}_0$ and $\mathbf{K}_s$ are the apparent incident and scattered wave vectors in the absence of refraction (see Eq. 25 of Ref. 1), β is the inclination of the wind at the scattering height, and ΔC is the difference between the sound speed at the ground and at the scatterer. This formula assumes horizontal stratification but does not require linear profiles.

Two special cases make the refractive correction to Doppler shift disappear to second order, namely, if *either* the wind at the scattering height is purely horizontal, or if there is no difference in temperature (sound speed) between the ground and the scattering height.

C. Scattering angle

With no refraction, the monostatic scattering angle ψ (between the incident and scattered wave vector) is simply $\psi_0 = \phi_c - \phi_a = \pi$. We calculate the refractive change $\Delta\psi = \psi - \psi_0$ using formula (Eq. 16) of Ref. 1:

$$\Delta\psi = (\Delta C/C_0)(\tan\phi_c' - \tan\phi_a) - (u/C_0)\{\tan\phi_c'\sin(\phi_c' + \beta) + \tan\phi_a\sin(\phi_a + \beta)\} \, . \tag{22}$$

To zero order $\phi_c' \simeq \phi_a$, so to first order

$$\Delta\psi \simeq -2(u/C_0)\tan\phi_a\sin(\phi_a + \beta) \, , \tag{23}$$

which vanishes for vertical sounding ($\phi_a = 0$). Note further that ΔC does not contribute to scattering-angle changes.

III. NUMERICAL EXAMPLE FOR A REPRESENTATIVE MONOSTATIC GEOMETRY

Table II shows the results of numerical calculations of the refractive corrections for the monostatic sounding geometry shown in Fig. 2. The same linear wind and temperature profiles used to construct Table I were used.

Note that temperature gradients contribute only to correction of the scattering volume position, and in the special case of $\phi_a = 45°$, only change its x component. The magnitudes of the Dopper-shift corrections are larger than in the bistatic case, but the changes in scattering angle are slightly smaller.

---

[1] T. M. Georges and S. F. Clifford, "Acoustic Sounding in a Refracting Atmosphere," J. Acoust. Soc. Am. **52**, 1397–1405 (1972).

Dispersion and Spectra of Gravity Waves in the Atmosphere

E. E. GOSSARD AND W. B. SWEEZY

Wave Propagation Laboratory, NOAA, Boulder, Colo. 80302

(Manuscript received 17 December 1973, in revised form 1 April 1973)

ABSTRACT

This paper describes a method for obtaining the dispersion properties of atmospheric waves from ground-based measurements of pressure and wind fluctuations. Having found the wave dispersion, we can find the displacement spectra of the waves aloft, making only minimal assumptions about the atmospheric model and without having very accurate sounding information.

We have applied the method to a pair of events for which we had fairly complete documentation. In one case, the waves aloft were observed with a vertically-pointing, high-resolution FM-CW radar, and we have compared the observed vertical displacement spectra with those deduced from ground measurements. In another case, the waves were associated with a weather front and a nearby tropical storm. The ground measurements permitted us to deduce the history of the waves aloft, and we found that the wave system before passage of the front differed dramatically from the waves present after frontal passage.

1. Introduction

In this paper we present the results of measurements and computations of atmospheric wave spectra. We show displacement power spectra deduced from pressure fluctuations at the ground and compare them with the corresponding spectra of the perturbations of the atmospheric layer structure aloft, as revealed by a vertically pointing FM-CW radar sounder. We also show measured wave dispersion curves, deduced from an analysis of the surface wind and pressure perturbations.

The measurement of wave spectra in the atmosphere presents difficulties for several reasons. The wave manifestations are most accessible to measurement at the ground. However, the fluctuations in the wave fields at the ground are large only when the waves are long compared with the height of the main wave system above the ground. Thus, the atmosphere introduces a "hydrodynamic filter" between ground level fields and fields at higher levels. This filtering can only be removed, and thus displacement deduced, by the assumption of a model atmosphere. Another difficulty is that the wave phase velocity enters directly into the equations that relate surface pressure and wind fluctuations to the displacement spectrum of the waves. If a model atmosphere is adopted, the needed phase velocity can be expressed in terms of the mean wind and temperature structure of the assumed model. However, the resulting displacement spectra depend strongly on the models assumed, so their validity is questionable unless the atmosphere happens to fit the model very well. Here we describe a method for deducing the wave phase velocity and dispersion from surface measurements of the wave-induced pressure and wind fluctuations at the ground—a method that is fairly independent of the atmospheric structure. We can then calculate the displacement power spectra making only noncritical assumptions about the atmospheric model. Since the method provides the dispersion spectrum of the waves, the wavenumber power spectrum of the waves can be deduced directly from the frequency spectrum.

In addition to the contributions from the spectrum of turbulence, major contributors to the spectrum of pressure oscillations in the mesofrequency band are convection and gravity waves (Gossard, 1960). Mechanisms for gravity (buoyancy) wave generation in the atmosphere include static instability (local convective activity) and dynamic instability (reduction in Richardson number within shear layers). The generation of wave spectra by both mechanisms has been examined theoretically by Tolstoy (1973). Tolstoy and Herron (1969) have specifically examined the generation of spectra of atmospheric pressure fluctuations by internal (untrapped) gravity waves generated by the jet stream. They treated waves with a vertical component of propagation, using the WKB approximation to solve the problem of propagation through the inhomogeneous atmosphere.

Because balloon observations indicate the presence of wind shear across isentropic or nearly isentropic layers in some cases of violent wave activity, Gossard (1974) has examined the conditions for dynamic instability in two "intensive mixing" models with shear across statically neutral, shear layers. The well-documented wave events on 10 November 1954 and 11 July 1969 were two of the observational cases showing strong shear across nearly adiabatic layers which provided the observational incentive for the theoretical examination of that model. Since surface pressure and wind data of high quality were available on both days, we used them to obtain the experimental results described in this paper.

2. Measurement and computation of spectra

We first describe the method for using the surface pressure and wind fields to deduce wave dispersion and spectra, then we explain the procedure used in analyzing the radar sounder records.

The pressure perturbations P in a wave system are related to vertical parcel displacements ζ by

$$P=\rho_s\left(\frac{\omega}{k}\right)^2\frac{\partial\zeta}{\partial z} \tag{1}$$

within layers without shear in the background wind (e.g., see Gossard and Hooke, 1974). Eq. (1) assumes that the Boussinesq approximation applies and that the amplitude-to-wavelength ratio of the waves is so small that the linearized theory also is applicable. We have defined $P=[\rho_0(z)/\rho_s]^{-\frac{1}{2}}p$ and $\zeta=[\rho_0(z)/\rho_s]^{\frac{1}{2}}\eta$, where p and η are the actual pressure perturbation and vertical parcel displacement, respectively. The ambient pressure is $\rho_0(z)$, and ρ_s is the pressure at some reference level such as the earth's surface. A two-dimensional wave system propagating in the x, z plane has been assumed, and k is the horizontal component of the wavenumber. The intrinsic frequency ω is the wave frequency noted by an observer drifting with the background wind at some level within the wave system.

We wish to obtain the spectrum of ζ, say $E_\zeta(k)$, from measurements of the temporal spectrum of P, say $E_P(f)$, measured at the ground, defining f as the wave frequency relative to the ground. Clearly, we must somehow measure ω/k, i.e., the wave phase velocity as a function of frequency, or we must calculate it from an assumed model. In addition, to obtain $\partial\zeta/\partial z$, we must also assume a model atmosphere. We naturally choose the simplest model that is realistic enough for our purposes. We therefore adopt a model made up of layers in which the Väisälä-Brunt frequency, $N=(g/\theta_0)^{\frac{1}{2}}(\partial\theta/\partial z)^{\frac{1}{2}}$, is constant (where we have defined θ to be the potential temperature). For the surface layer (subscript 1), where $0<z<H$, we assume ω, as well as N, to be constant. Thus, the wind in the surface layer is assumed to be either constant or small compared with the wave velocity. The wind in the surface layer is nearly always observed to be light when wave perturbations are prominent in the surface pressure and wind records. This is probably because of the high probability of wave encounters with critical levels when the wind velocity is comparable to the wave velocity. So

$$\zeta=\zeta_H\frac{\sin n_1 z}{\sin n_1 H},\quad \frac{N_1}{\omega}>1, \tag{2}$$

or

$$\zeta=\zeta_H\frac{\sinh\gamma_1 z}{\sinh\gamma_1 H},\quad \frac{N_1}{\omega}<1, \tag{3}$$

where ζ_H is the wave displacement at height H and $n_1=k[(N_1/\omega)^2-1]^{\frac{1}{2}}=i\gamma_1$, where $\gamma_1=k[1-(N_1/\omega)^2]^{\frac{1}{2}}$. Hence, Eqs. (1) and (2) yield, e.g.,

$$\zeta_H=\frac{H}{\rho_s\left(\frac{\omega}{k}\right)^2}\left(\frac{\sin n_1 H}{n_1 H}\right)P_0, \tag{4}$$

where P_0 is the pressure perturbation at the ground. The displacement power spectra become

$$E_{\zeta H}(f)=\left[\frac{H}{\rho_s\left(\frac{\omega}{k}\right)^2}\right]^2\left(\frac{\sin n_1 H}{n_1 H}\right)^2 E_{P_0}(f),\quad \frac{N_1}{\omega}>1, \tag{5}$$

$$E_{\zeta H}(f)=\left[\frac{H}{\rho_s\left(\frac{\omega}{k}\right)^2}\right]^2\left(\frac{\sinh\gamma_1 H}{\gamma_1 H}\right)^2 E_{P_0}(f),\quad \frac{N_1}{\omega}<1. \tag{6}$$

The "hydrodynamic filtering" enters the problem through the factors $\sin(n_1H)/(n_1H)$ and $\sinh(\gamma_1H)/(\gamma_1H)$, both of which tend to unity for $n_1H\ll1$ and $\gamma_1H\ll1$.

Gossard (1960; 1962a, b) has used Eq. (6) to deduce wave spectra assuming a simple three-layer model atmosphere in which the thickness of the middle (inversion) layer was arbitrarily taken to be zero. Then

$$\left(\frac{\omega}{k}\right)^2\approx\frac{gH\Delta\ln\theta}{\gamma_1 H\coth(\gamma_1 H)+\gamma_3 H}, \tag{7}$$

where θ is potential temperature, g the acceleration of gravity, and γ_3 applies to the top layer which is presumed to extend to infinity.

In the present approach we obtain $(\omega/k)^2$ from surface measurements, thus avoiding the most restrictive assumptions in the earlier work relating to the atmospheric model.

Gossard and Munk (1954) pointed out that the relation

$$\frac{\omega}{k}=\frac{1}{\rho_0}\frac{p}{u}, \tag{8}$$

which they termed the impedance equation, was of great value in analyzing waves aloft from surface data when p and u are measured at $z=0$. In Eq. (8), u is the velocity perturbation due to the waves and represents half the vector difference between extremes in the position of the total wind vector as it oscillates between crest and trough during wave passage. The situation is shown schematically in Fig. 1. The sign on u is arbitrary, but must be treated consistently since it determines (by its correlation or anti-correlation with pressure) the sense of the direction of wave propagation. We chose to define u as positive for clockwise rotation of the wind vector. Consequently, u and p are positively correlated when the waves are coming from the 180° sector to the left of the mean wind and are negatively correlated when they come from the right-hand 180° sector. Sign-independent correlation between u and p is a measure of gravity wave signal-to-noise.

In the present work we have extracted u throughout each time series of wave perturbations. We have then computed the power spectra of p and u and used them to deduce quantitatively the dispersive character of the waves and to obtain values of $(\omega/k)^2$ for insertion in Eqs. (5) and (6). The procedure used was to numerically filter the wind speed, wind direction and pressure data by using a running average, triangularly weighted about the center value. The filter was so chosen that it low-passed those frequencies and trends that were not a result of the wave motion. The resulting low-passed time series was used as the mean value of the wind vector. This low-passed wind vector was then vectorially subtracted from the original time series of wind velocity, and the fluctuating component caused by the waves (u in Fig. 1) was extracted and spectrum-analyzed. Obviously, there is some subjectivity in the choice of numerical filter to apply to the records. We chose to filter the 11 July records such that a wave of 15-min period would have its amplitude reduced to one-third of its true amplitude. For the 10 November record, three filters were tried in order to test the sensitivity of the filter on the result. Filters were chosen such that waves of 50-, 25- and 7.5-min periods would be one-third of their amplitude. It was found that the results for

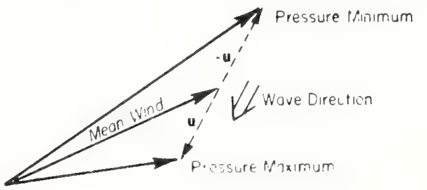

FIG. 1. Vector diagram illustrating the way a wave perturbs the atmospheric wind field. The u component is the velocity perturbation to be used in the impedance equation. When the sensors are below the level of main wave perturbation (e.g., at the ground) the maxima in pressure are under the wave crests and the sense of u at that phase determines the direction of wave propagation. The clockwise sense of u has been arbitrarily chosen as positive. Therefore, perturbations of p and u are in phase for waves propagating from the 180° sector to the left of the mean wind (as shown schematically in this figure) and out of phase for waves propagating from the 180° sector to the right of the mean wind (as in Fig. 2b).

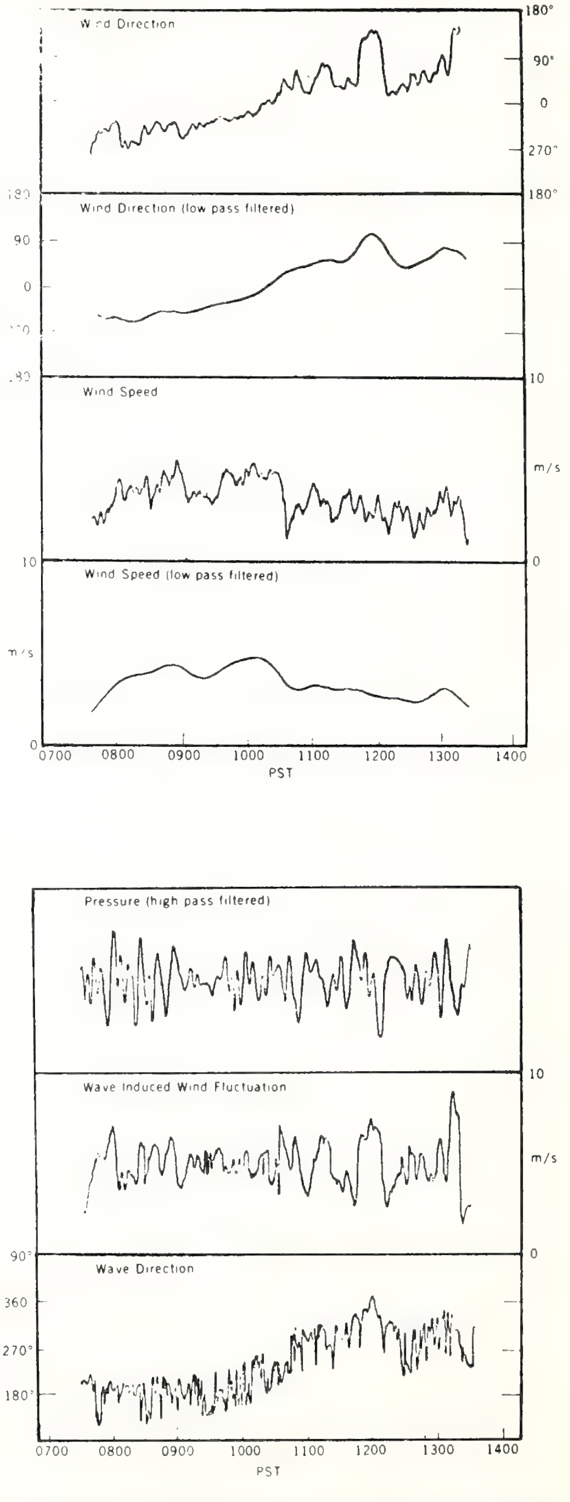

FIGS. 2a, b: Sample wind and pressure records illustrating the analysis procedure described in this paper. The middle frame of 2b is the wave component of the wind speed (u in Fig. 1). The bottom frame of 2b shows the wave direction (direction of u in Fig. 1).

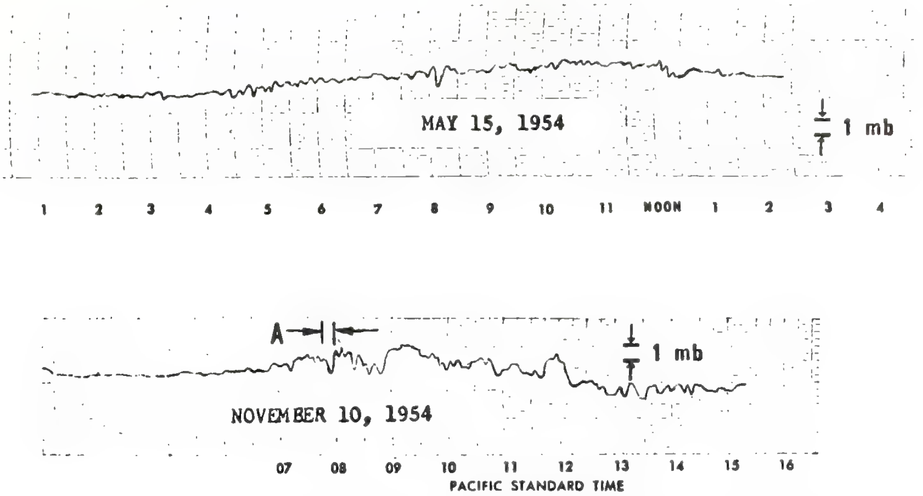

Fig. 3. Sample pressure records during wave events at San Diego. Waves were recorded on standard NWS microbarograph equipped with vibrator to minimize pen drag. Wave event in the bottom frame is analyzed in this paper using very sensitive microbarovariograph.

wave speed and direction were insensitive to the filter chosen so the middle value was chosen. However, if the waves had been strongly dispersive, more influence by the filter would, perhaps, have been found. A sample of a wind record so analyzed is shown in Fig. 2.

Of course, the power spectra of u and p are functions of frequency f relative to the fixed point where the sensors are located, rather than of the intrinsic frequency ω appearing in the impedance equation, which is the frequency relative to the mean airstream at the point where the sensors are located. Therefore, to obtain k from f, it is necessary to add algebraically the component of the airstream velocity to the intrinsic wave velocity, ω/k, and use the wave velocity relative to the ground in the transformation. Thus, if $\bar{v}$ is the component of mean velocity in the direction of wave propagation,

$$k=\frac{2\pi}{(\omega/k)+\bar{v}}f,$$

where, in general, ω/k will itself be a function of f. In this way the frequency spectra of Eqs. (5) and (6) can be transformed to wavenumber spectra. The resulting spectra will be independent of atmospheric models, except in the assumption of a constant stability N throughout the layer and the choice of a height H (within or at the top of the surface layer) at which the displacement spectra are to be evaluated. Furthermore, the spectra are insensitive to the values of N and H chosen, so they can be estimated fairly successfully from local raob data.

3. Wave events and observations

In choosing experimental data to use for the calculation of wave spectra we sought cases which were either exceptionally well documented, or cases in which the pressure and wind fluctuations were far greater than normal in the mid-frequency band (1 to 30 min period). Since in this study we were primarily interested in an accurate measure of the spectral form of atmospheric waves, we rejected two spectacular cases analyzed by Gossard (1962a, b) which were observed at San Diego. The case of 24 July 1957 was rejected because of temporal non-stationarity in the primary statistical characteristics, and that of 15 May 1954 was rejected because the inversion was so high that atmospheric filtering probably severely affected the higher wavenumber components in the surface spectra.

On the other hand, the case of 10 November 1954 was selected for re-analysis by the methods described above because it seemed to be statistically reasonably uniform throughout the day and because the temperature inversion was low; in fact, it was essentially surface-based. The average wind speed was much less than the wave speed in the surface layer, so the effect of wind shear was negligible. The pressure record of 10 November is shown along with that of 15 May in Fig. 3 as recorded on a standard, National Weather Service (NWS) barograph. The sounding data for 10 November from scheduled local raob's and pibal's is shown in Fig. 4. Unfortunately, the 0700 (all times PST) pibal was missing from NWS records so the 0147 sounding of wind is shown instead. Obviously, the wind sounding is too far removed in time from the wave event to be useful for quantitative analysis, but it clearly shows that before the wave event a condition of strong wind shear existed between 800 and 1500 m MSL where a nearly adiabatic layer is evident in the 0700 temperature sounding.

A sensitive microbarograph described by Gossard (1960) was used to obtain the surface pressure spectrum.

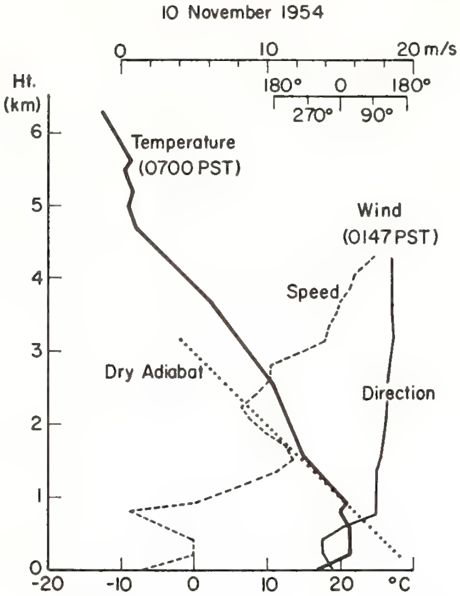

FIG. 4. Temperature and wind sounding data on 10 November 1954. No wind sounding was available at 0700 PST, so the 0147 sounding is shown. A value of $N_1 = 0.024$ was chosen to represent the region below 800 m.

The half-power points of its band-pass were 90 sec and 16 min, and the calculated spectra were corrected for the high- and low-pass characteristics of the sensors. A low-threshold cup anemometer with the same low-pass characteristics as the microbarograph was used for recording the wind speed, and a separate vane recorded the direction.

The event of 10 November was accompanied by a small hurricane or tropical storm about 1000 km west of San Diego. The coincidence in time and location of these two rather rare events suggests that they may have been related either directly or indirectly, and the 500-mb analysis showed very high winds from the south over San Diego. However, the NWS 1030 surface analysis (at that time called the WBAN analysis) showed a front passing through the San Diego area (see Fig. 5), and the results of the wave analysis (see Section 4) suggest that vertical wind shear associated with the front may have been a more direct cause.

The other case chosen for detailed analysis was that of 11 July 1969 which occurred at San Diego. This case was chosen because, in addition to the surface wind and pressure data, the waves were observed aloft using an FM-CW clear-air radar sounder developed by Richter (1969). It was also exceptionally well documented, since raob and wind soundings were obtained during the event. Several aspects of the records have already been described by Gossard *et al.* (1970). The radar record for this day is shown in Fig. 6, and the sounding data are shown in Fig. 7. The white areas seen in the radar record are showers that occurred off and on all day. Spectacular mamma clouds existed at middle cloud levels during most of the event. The light curves in Fig. 7 were obtained from a radiosonde balloon launched at the radar site at 1348 and tracked by theodolite. Unfortunately, the balloon was lost behind (or in) a rain shower. The heavy curves are the 1600 rawinsonde data obtained by the scheduled launch at Montgomery Field about 11 mi from the radar site. The 1600 sounding shows an important shear layer aloft that was missed by the 1348 wind sounding due to inability to track the balloon above 1600 m. The pressure sensor used to measure the spectrum on 11 July 1969 was a vibrotron, absolute pressure sensing device described by Gossard *et al.* (1970), and the wind fluctuations were measured with a standard aerovane. A low-pass filter with a time constant of 50 sec was applied electronically both to the vibrotron output and to the aerovane. The wind speed in the surface layer was again very small compared with the wave velocity.

In many ways, the wave system of 11 July was similar to that of 10 November. It is clear from Fig. 6 that the amplitude of the waves was very large. At an altitude of 400 m the crest-to-trough amplitude sometimes exceeded 200 m. As on 10 November, there were strong southerly winds aloft and the upper air charts showed a jet from 190° at 30 m sec^{-1}. The event also coincided with an abrupt deepening of an upper trough over the area. A satellite photograph reveals two tropical storms about 1600 km south of San Diego, but fails to establish any visual association with the wave event. It also shows what appears to be a cyclonic disturbance in the cloud structure about 500 km west of San Diego.

The wind and temperature soundings show a nearly adiabatic layer with strong wind shear across it at 2 km MSL. The Richardson number calculated for that height from the sounding data is less than 0.25, suggesting the strong possibility of dynamic instability (if not actual convective instability) at that height. The 1600 PST sounding occurred after the waves had almost ceased, and it is likely that the wind shear was even greater while the wave event was in progress.

4. Results and conclusions

When we analyzed the records of 10 November 1954 as described above, we obtained quite unanticipated results. Two distinct wave regimes were found in the records. Until about 1000, the waves were propagating from slightly west of south with a speed of about 40 m sec^{-1} (Figs. 8 and 9). After about 1030, apparently following the frontal passage, the waves came from the northwest with a speed of about 11 m sec^{-1}. The beamwidth of the earlier waves was about 30° and that of the later wave regime about 50°. During the wave event, the mean background wind averaged about 4 m sec^{-1}. It was from the northwest early in the event and thus was nearly opposed to the wave direction during the early period. However, during this period the wave

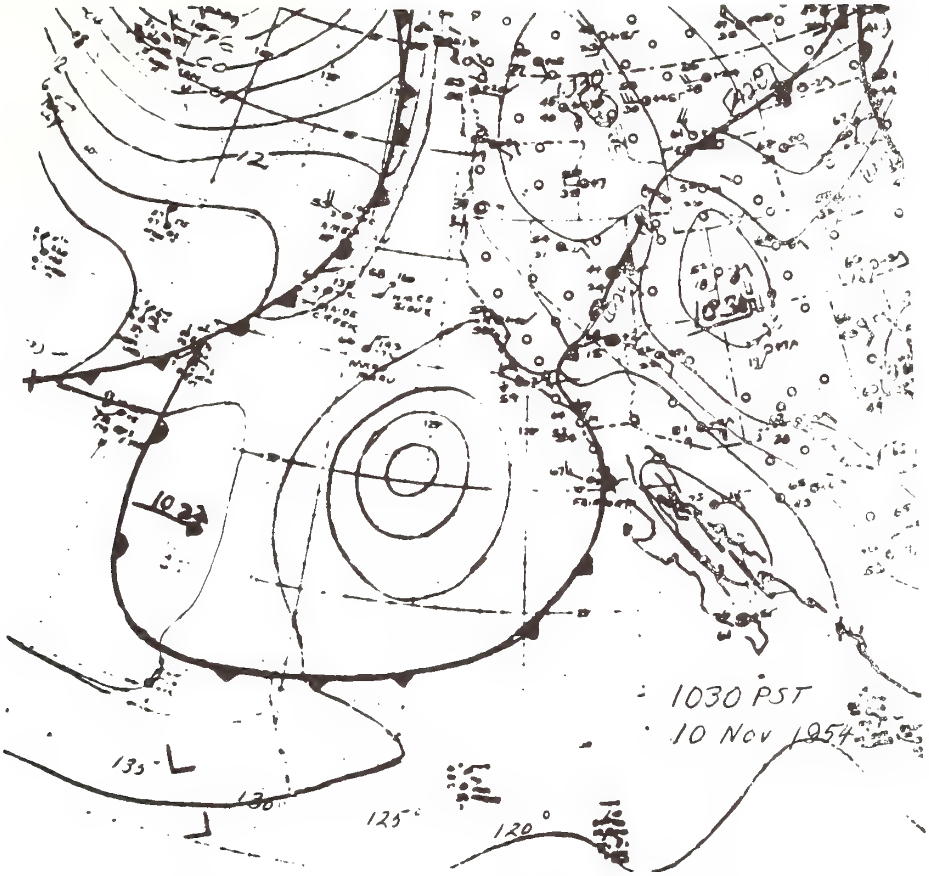

FIG. 5. Surface weather map at 1030 PST 10 November. Note weather front and tropical storm off Southern California coast.

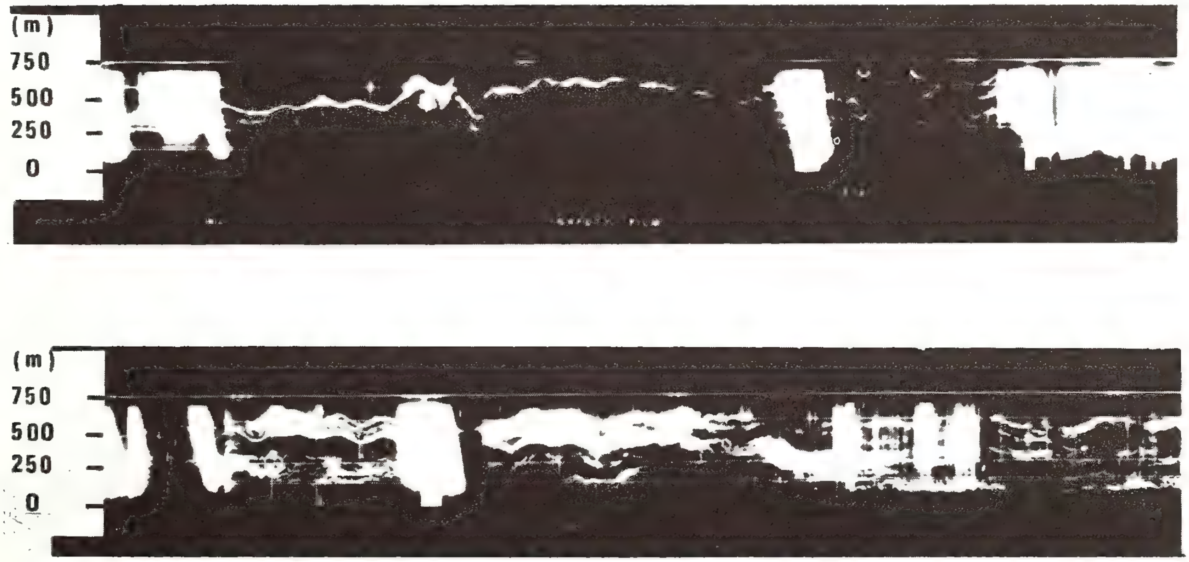

FIG. 6. High-resolution radar sounding showing waves aloft on 11 July 1969. Sounder is vertically pointing FM-CW radar (Richter, 1969). White areas are showers. Height range was shifted for a short time at about 1205. Times marked on record are daylight saving time, so one hour should be subtracted to obtain Pacific Standard Time. Horizontal lines are range markers.

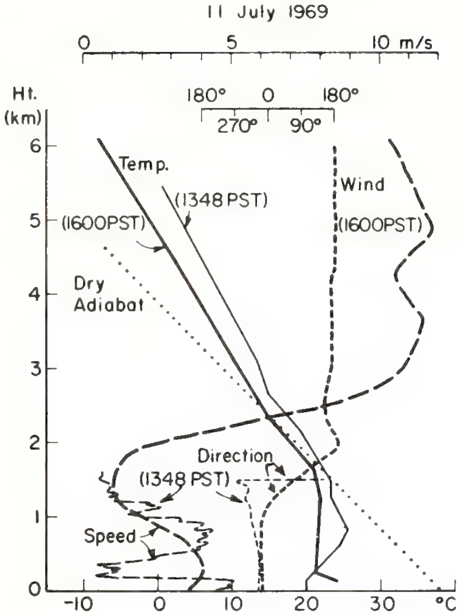

FIG. 7. Sounding data for 11 July 1969. The sounding at 1348 PST was made at the radar site, but the balloon was lost behind a rain shower and no wind data were available above about 1.6 km. The 1600 sounding was the NWS sounding from Montgomery Field, San Diego. A value of $N_1=0.025$ was chosen to represent the region below 800 m.

velocity was very high. As the event progressed, the mean wind swung gradually into the northeast and so was nearly at right angles to the waves during the later wave regime. Thus, throughout the event the intrinsic wave velocities given above were approximately the same as those of the wave relative to the ground. Since the records of 10 November consisted of two fairly distinct events they were split into two samples and separate spectra were computed. The plots of dispersion (ω vs k) are shown in Fig. 9 along with the corresponding plot for 11 July 1969.

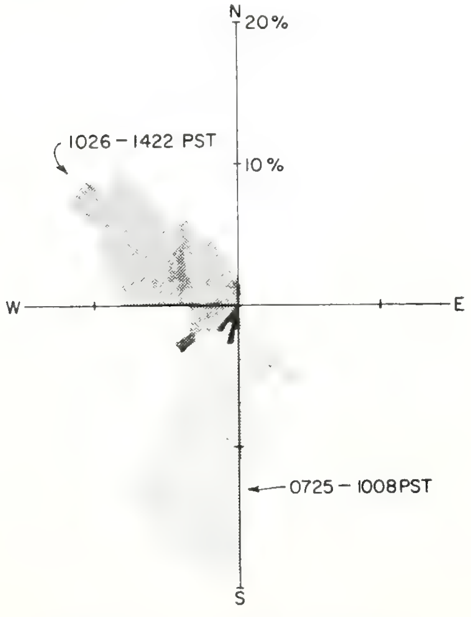

FIG. 8. Directional distribution of the two-wave systems on 10 November 1954 (see text).

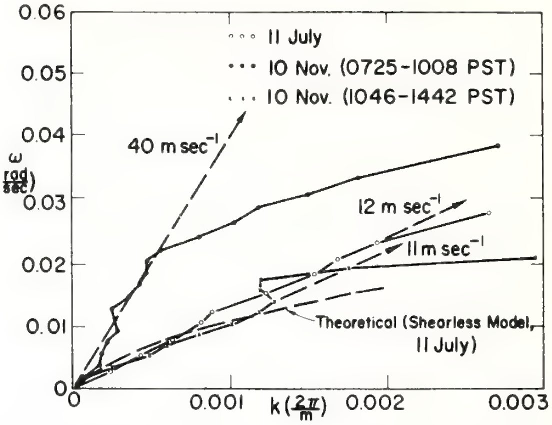

FIG. 9. Dispersion curves for 11 July 1969 and 10 November 1954 calculated from surface pressure and wind fluctuation spectra. The rapid increase in k for $\omega>0.02$ probably represents the transition from the wave-induced perturbations of wind and pressure to the turbulence regime. The pressure spectrum has dropped about two orders of magnitude at this point.

The pressure spectra plotted against frequency are shown in Fig. 10. The spectrum from an event reported by Clarke (1962) which occurred in Australia between 1200 and 1800 EST on 26 January 1960 is also shown for comparison. Clarke believed there was evidence of two "lines" in the pressure spectrum. The forms of our spectra of 10 November and 11 July tend to give some support to his view, although the 90% confidence limits for our spectra indicate the significance of the peaks to be marginal at best. However, the similarity in appearance of the 11 July spectrum and the first one on 10 November adds a little confidence to the reality of the spectral lines. Since the sampling rate, sample size, and spectral resolution were different in the two cases, there is little probability that the similar appearance results from systematic errors in the numerical analysis. In both cases the time series were detrended prior to the spectrum analysis, and in the case of 10 November the sensor also pre-whitened the data. A Hamming window was used to smooth the spectra.

The displacement spectra are shown in Fig. 11 plotted vs wavenumber. We did not attempt to calculate the displacement spectrum for the first period on 10 November because, if the waves were generated by vertical shear, they must have been generated high in the troposphere where the upper air charts showed a strong jet from the south since their phase speed was so high. Since we are interested mainly in the spectra of the wave systems near their region of generation, we would have to choose H very large during the first period and the spectrum computations from surface data are unlikely to provide realistic results for wave systems so high above the ground. On the other hand, assuming comparable wave amplitudes during the two periods, we conclude that the wave system during the second period was low in the atmosphere. This follows from Eq. (4) which shows the surface pressure perturbation to be proportional to $(\omega/k)^2/H$. Since ω/k was only 11 m sec^{-1} during this period, H (the height of the base of the shear layer) was probably of the order of 1/15 of the corresponding height during the earlier period. We have therefore calculated the displacement spectrum only during the later period and believe it to be reliable. The very large fluctuations in the spectral values at $10^{-3}<k<2\times10^{-3}$ are a result of the two higher velocity values seen on the plot in Fig. 9 at $\omega=0.016$ and 0.0175. Above $\omega=0.02$ (where the pressure spectra have fallen off by about three orders of magnitude), all dispersion curves show a rapid transition to very low velocities—probably due to a transition from wave-induced fluctuations to the turbulent fluctuation regime, so the bulge in velocity near $\omega=0.017$ is probably not significant. The rms pressure perturbation during the second period of 10 November was 0.47 mb and the rms height perturbation was more than 100 m.

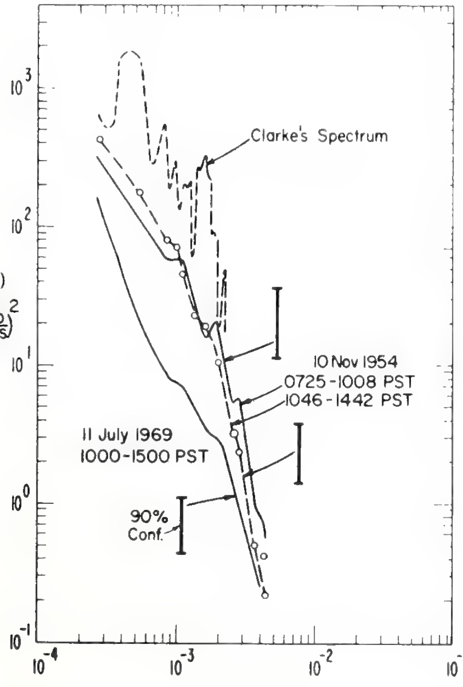

Fig. 10. Pressure spectra for 11 July 1969 and 10 November 1954. Two spectra are shown for 10 November corresponding to two wave regimes (see text). Range of 90% confidence is shown by bars. A spectrum published by Clarke (1962) is also shown, but the ordinate scale should be considered arbitrary, since we are uncertain of his units.

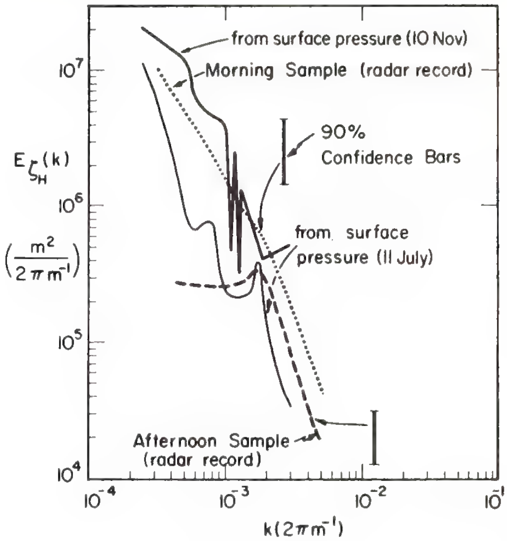

Fig. 11. Spectrum of displacement at 800 m height calculated from surface pressure records. Spectra from data scaled off of the radar records from returns at about 500 m on 11 July are also shown. Spectra are plotted in terms of wavenumber. The large perturbations which occur for $10^{-3}<k<2\times10^{-3}$ on 10 November are a result of the variation in wave speed at this point in the wavenumber spectrum (see Fig. 9).

Fig. 9 shows that the waves on 11 July were traveling with an intrinsic velocity of about 12 m sec^{-1} and were very nearly non-dispersive over the spectral range analyzed. They were coming from the southeast quadrant, tending to become more southerly as the event progressed. Since the surface wind was from the northwest at about 4 m sec^{-1}, the wave velocity relative to the ground was 7–8 m sec^{-1}. For comparison, the theoretical (dashed) curve of dispersion on 11 July for a shearless model calculated by Gossard *et al.* (apparently not very applicable in view of the 1600 wind sounding) is shown.

The displacement spectra for 11 July show evidence of the two peaks mentioned in discussing the pressure frequency spectra. In addition to the displacement spectrum deduced from the pressure record, two spectra of layer displacement taken from the radar record in Fig. 6 are shown in Fig. 11. The dotted curve is the spectrum of the time series from 1045 to 1222, and the dashed curve from 1300 to 1422. The spectra apply to the layer occurring at an average height of about 500 m. It could be traced by eye almost continuously during these intervals, even through most of the showers, if the amplitude-modulation record were used instead of the intensity-modulation record shown here. Occasionally, short segments of record were interpolated. The spectra from the radar records were sampled every 30 sec (as compared with 60 sec for the 11 July pressure record); however, the radar records were slightly less than half as long as the pressure record, so the 90% confidence range (indicated by the bars near the curves) is about the same for all three spectra. The resolution in the spectrum found from the surface pressure is about twice as good as that for the radar spectra, which may explain why distinct lines appear more clearly in the spectrum deduced from surface pressure. Clearly, the general agreement in spectral power density is good, but the morning radar spectrum shows considerably more energy in the low frequencies than that of the afternoon. Apparently, the statistical nature of the waves was not as time-stationary throughout the day as we had hoped.

The spectra we have shown here probably represent only one type of wave generation—that of dynamic instability associated with a wind-shear layer. The cases we have described were accompanied by exceptionally large pressure oscillations at the ground. In each case the soundings reveal adiabatic or nearly adiabatic layers aloft across which there is a strong vertical shear in the mean wind; in fact, both cases had essentially a 180° reversal in wind direction across the layer, with light winds below the shear layer and much stronger winds aloft. These conditions are similar to those reported by Clarke except that the Adelaide and Melbourne soundings did not show the shear to be strong across the unstable layer. Clarke reported spectacular mamma clouds during his event much like those observed during the event of 11 July 1969. In both of these events the sounding data indicated the possibility of conditional instability at or above the shear layer which is presumed to be the height of wave generation. Thus, the wave perturbation, resulting from dynamic instability in the shear layer, may have created local regions of absolute instability which led to mamma cloud formation and enhanced the generation of atmospheric waves by the release of latent heat into the system.

In conclusion, the method described in this paper seems to offer potential for using surface measurements to monitor the speed and direction of wave systems aloft, and to provide their dispersive characteristics. When they are generated low in the atmosphere their displacement spectra may also be deduced. Only the wind and pressure recorded routinely at weather stations are required, but an analog or simple digital processor would be needed for the filtering and the extraction of the u component of the wind. Only weak assumptions about the atmospheric model are necessary to extend the computations to include the displacement spectra of the waves. The two violent wave events analyzed in this paper were apparently generated by vertical shear associated with adiabatic or nearly adiabatic layers. The waves at frequencies corresponding to the highest three orders of magnitude of power density in the spectra of the wave systems we have examined here are essentially nondispersive, as would be expected for waves generated (locally) by dynamic instability due to shear across an isentropic layer when the wavelengths are not long compared with the depth of the lower layer (Gossard, 1974). However, we do not argue that shear wave generation need necessarily be always associated with isentropic layers, and the cause/effect relationship in the cases analyzed here is not clear. Such a neutrally stable layer might either be created by violent wave breaking and mixing in a shear layer or, conversely, be an important factor in the wave generation process.

REFERENCES

Clarke, R. H., 1962: Pressure oscillations and fallout downdraughts. *Quart. J. Roy. Meteor. Soc.*, **88**, 459–469.

Gossard, E. E., 1960: Spectra of atmospheric scalars. *J. Geophys. Res.*, **65**, 3339–3351.

——, 1962a: Vertical flux of energy into the lower ionosphere from internal gravity waves generated in the troposphere. *J. Geophys. Res.*, **67**, 745–757.

——, 1962b: Reflection of microwaves by a refractive layer perturbed by waves. *IEEE Trans. Antennas Propagat.*, **AP8**, 317–325.

——, 1974: Dynamic stability of an isentropic shear layer in a statically stable medium, *J. Atmos. Sci.*, **31**, 483–492.

——, and Munk, W. H., 1954: On gravity waves in the atmosphere. *J. Meteor.*, **11**, 259–269.

——, J. H. Richter and D. Atlas, 1970: Internal waves in the atmosphere from high resolution radar measurements. *J. Geophys. Res.*, **75**, 903–913.

——, and William H. Hooke, 1974: *Waves in the Atmosphere.* Amsterdam Elsevier (in press).

Richter, J. H., 1969: High-resolution tropospheric radar sounding. *Radio Sci.*, **4**, 1261–1268.

Tolstoy, Ivan, 1973: Infrasonic fluctuation spectra in the atmosphere. *Geophys. J. Roy. Astron. Soc.*, **34**, 343–363.

——, and T. Herron, 1969: Model for atmospheric pressure fluctuations in the mesoscale range. *J. Atmos. Sci.*, **26**, 270–273.

Journal of Atmospheric Sciences 32, 639-642, March 1975.

Reply

EARL E. GOSSARD

Wave Propagation Laboratory NOAA/ERL, Boulder, Colo. 80302

10 September 1974 and 21 October 1974

The purpose of my paper[1] was to work out the consequences of a new shear model atmosphere so that its predictions could be compared with observations and its representation of reality thus assessed. I therefore welcome Dr. Browning's comments and hope others will respond with additional observations.

In my paper I did not suggest that shear layers occur *only* near isentropic layers nor that the periodic structures seen by radars occur only at such layers. I do contend that shear across nearly isentropic (and even superadiabatic) layers is not an uncommon occurrence in the atmosphere, and I suggest that this condition may lead to especially active "wave" generation and perhaps to some of the exceptionally "narrow-band" patterns seen by radars.

An example of such active wave generation associated with strong wind shear across an adiabatic layer is shown in Figs. 1 and 2 taken from Gossard and Sweezy (1974). Fig. 1 shows radiosonde sounding data taken during, and at the end, of the wave event shown in Fig. 2 recorded by a vertically pointing FM-CW radar (Richter, 1969). The balloon released at 1348 PST was tracked optically and was lost behind a rain shaft (see white areas in Fig. 2) before reaching the strong shear layer revealed by the 1600 rawinsonde to exist at a height of 2.5 km—shear layer which clearly occurred at a level of minimum stability. Dramatic altocumulus mammatus middle clouds were observed during the wave event. Unfortunately, the FM-CW radar was unable to see high enough to observe the patterns within the shear layer itself, which was presumably the region of wave generation.

---

[1] I take this opportunity to point out three misprints appearing in my paper. A plus sign should be inserted before ω/k in Eqs. (9) and (15). In the line below Eq. (10a) the argument of ctn$h$ should be $\gamma_1 H$, and in Eq. (12) the last term on the left should be c instead of c^2. These errors are either typographical or misprints and are not in the final expressions nor in the results shown.

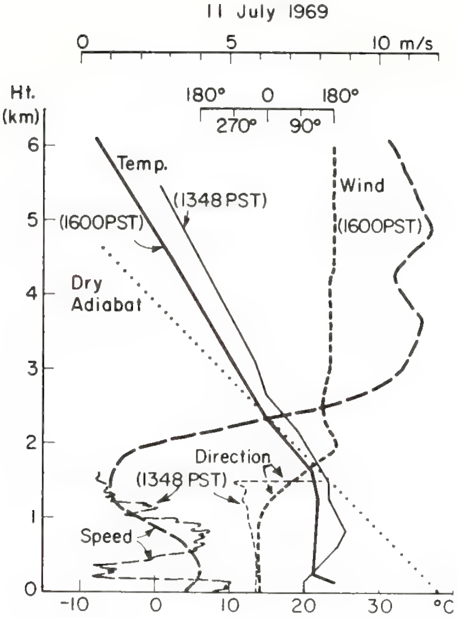

FIG. 1. Balloon sounding data on 11 July 1969. The sounding balloon launched at 1348 was lost behind a rain shower and no wind data were available above about 1.6 km. The 1600 sounding was the U. S. National Weather Service sounding from Montgomery Field, San Diego.

Other examples of shear across layers of minimum stability have been provided to me by Dr. Timothy Keliher, and are shown in Fig. 3. The soundings analyzed by Dr. Keliher were cases of exceptional wave activity as recorded on an array of microbarographs at the surface. The speed and direction of the waves, measured as they propagated across the array, are shown on each frame of the figure. In all cases the agreement is good between the speed and direction of the waves and the speed and direction of the wind in the shear layer at the height of minimum stability. (The adiabatic lapse rate is indicated by the straight line segment beside the temperature curves.) Other cases have shown the shear layer to occur at maxima in stability, but those shown here demonstrate that shear occurs not uncommonly across layers of minimal stability.

I do not consider the isentropic character of the shear layer to be the factor of primary importance in my model. The practical reason for assuming the shear layer to be precisely isentropic is the applicability then of solutions in terms of elementary functions which makes multi-layer models containing inversions tractable. The primary physical effect of this assumption is to produce a band of unstable wavenumbers at all scales of disturbances (since, obviously, the Richardson number cannot everywhere exceed $\frac{1}{4}$ in such a model). The width of the band quickly becomes infinitesimal as the Väisälä-Brunt frequency of the bounding medium becomes large or the shear becomes small.

I consider the inversions which bound the shear layer in my model No. 2 to be the characteristic of most interest. They are responsible for the narrow band of unstable wavenumbers which characterize the model. Such narrow band disturbances are evident in

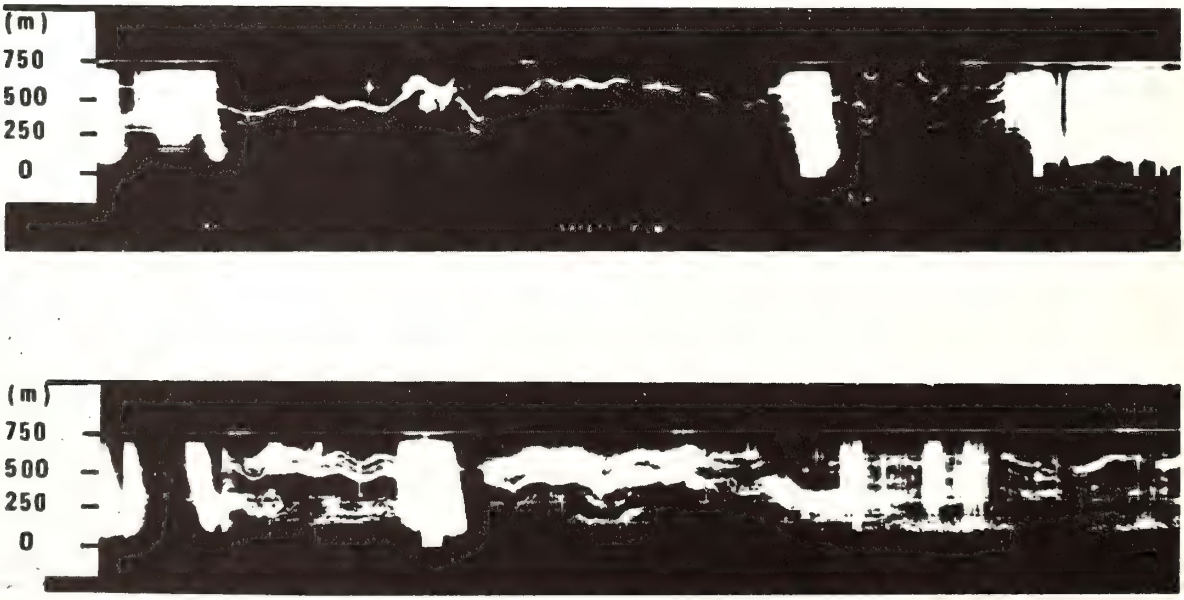

FIG. 2. High-resolution radar sounding showing waves aloft on 11 July 1969. Sounder is vertically pointing FM-CW radar (Richter, 1969). White areas are showers. Height range was shifted for a short time at about 1205. Times marked on record are daylight saving time, so one hour should be subtracted to obtain Pacific Standard Time (PST). Horizontal lines are range markers

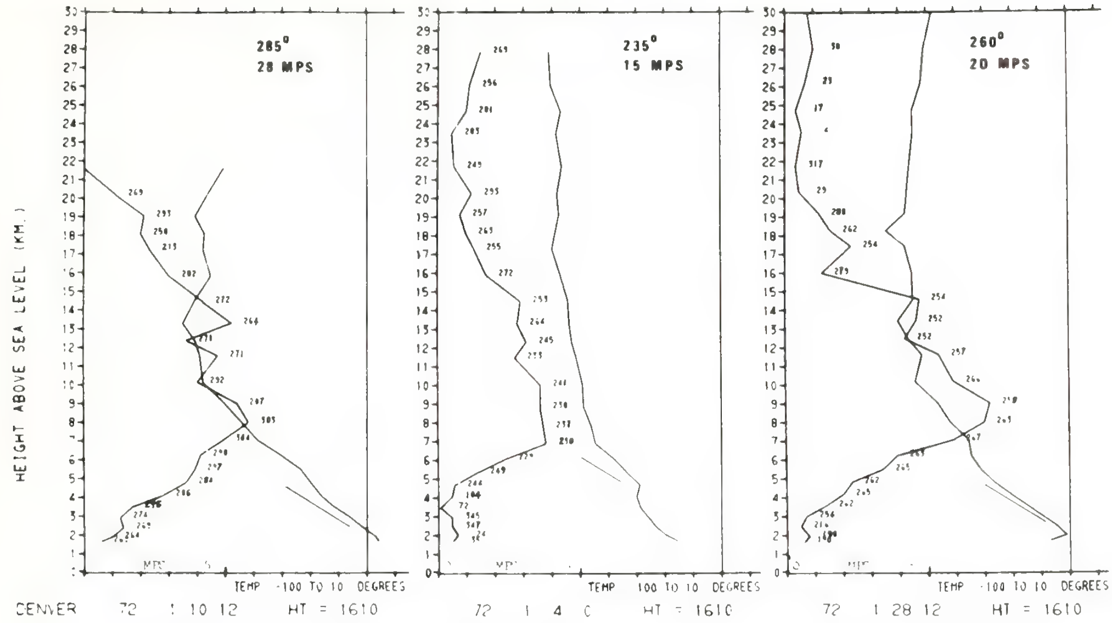

FIG. 3. Wind and temperature sounding data during significant wave events recorded on pressure arrays at Boulder, Colo. The short line segment beside the temperature curve indicates the adiabatic lapse rate. Wind directions are indicated by the figures alongside the wind speed curve. (Courtesy of T. Keliher.)

the observations of both Browning (1971) and Katz (1972). This effect is not likely to be erased by some small static stability within the shear layer, just as the cat's eye does not depend critically on the shear occurring in precisely homogeneous (isentropic) layers, although Kelvin (1880) deduced it for such layers.

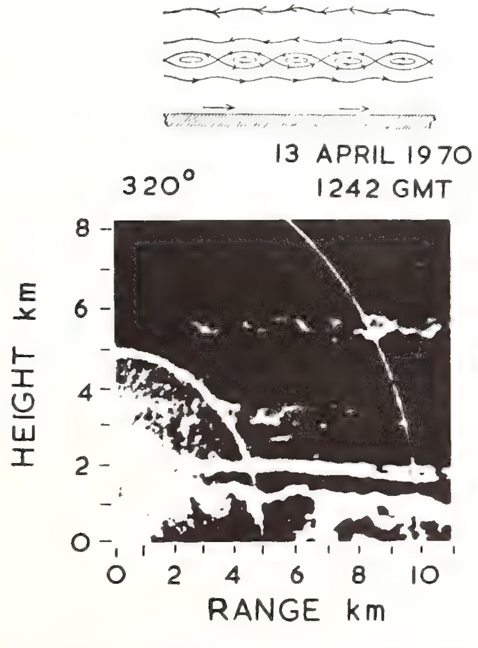

FIG. 4. Kelvin's original sketch of the cat's eye pattern displayed with the radar record from Browning's (1971) Fig. 1, for comparison.

If created by mixing in the shear layer, such bounding inversions would tend to be thin and thus not easily detected by conventional radiosondes such as those used by Browning. They may well provide the answer to Dr. Browning's question of how a well-mixed isentropic layer can give a radar return. The necessary gradients would certainly be present at the edges of the layer and would provide an explanation for the clear delineation of the cat's eye boundaries seen in Fig. 4 and similar double-echo structures commonly seen by radars. Kelvin's original sketch of the cat's eye is shown in Fig. 4 along with the radar record from Browning's Fig. 1 for comparison.

In case other workers attempt to deduce ratios of wavelength to layer thickness from radar records as Dr. Browning and I have done, it is, perhaps, well to point out that the wavelength of the intersecting sinusoids at the critical level is twice the wavelength of the disturbances generated as shown in the derivation of the cat's eye given in the Appendix of my paper, so the appropriate length is the width of the eye itself. Dr. Browning informs me that this is the length scale that he also used, so this should not lead to any discrepancy in our results. However, for the width of the layer he chose the distance between the centers of the radar echos (i.e., the eyelids in Fig. 4) whereas I chose the outer edges of the echos. In Fig. 4 this leads to a layer thickness of 400 m by his method and 700 m by mine. Thus the choice of different methods in compiling data of this kind can lead to a considerable discrepancy in the results.

REFERENCES

Browing, K. A., 1971: Structure of the atmosphere in the vicinity of large-amplitude Kelvin-Helmholtz billows. *Quart. J. Roy. Meteor. Soc.*, **97**, 283–299.

Gossard, E. E., and W. B. Sweezy, 1974: Dispersion and spectra of gravity waves in the atmosphere. *J. Atmos. Sci.*, **31**, 1540–1548.

Katz, I., 1972: The detection and study of gravity waves with microwave radar. *Proc. AGARD Conf. on Effects of Atmospheric Acoustic Gravity Waves on Electromagnetic Wave Propagation*, No. 115, 21-1 to 21-9.

Kelvin, Lord, 1880: On a disturbing infinity in Lord Rayleigh's solution for waves in a plane vortex stratum. *Nature*, **33**, 45–46.

Richter, J. H., 1969: High-resolution tropospheric radar sounder. *Radio Sci.*, **4**, 1261–1268.

OT REPORT 75-76

October 1975

A VERSATILE THREE-DIMENSIONAL RAY TRACING COMPUTER PROGRAM FOR RADIO WAVES IN THE IONOSPHERE

R. Michael Jones and Judith J. Stephenson

This report describes an accurate, versatile FORTRAN computer program for tracing rays through an anisotropic medium whose index of refraction varies continuously in three dimensions. Although developed to calculate the propagation of radio waves in the ionosphere, the program can be easily modified to do other types of ray tracing because of its organization into subroutines.

The program can represent the refractive index by either the Appleton-Hartree or the Sen-Wyller formula, and has several ionospheric models for electron density, perturbations to the electron density (irregularities), the earth's magnetic field, and electron collision frequency.

For each path, the program can calculate group path length, phase path length, absorption, Doppler shift due to a time-varying ionosphere, and geometrical path length. In addition to printing these parameters and the direction of the wave normal at various points along the ray path, the program can plot the projection of the ray path on any vertical plane or on the ground and punch the main characteristics of each ray path on cards.

The documentation includes equations, flow charts, program listings with comments, definitions of program variables, deck set-ups, descriptions of input and output, and a sample case.

Dispersion and spectra of gravity waves probably generated by a convective storm

By A. G. KJELAAS,[1] *Norwegian Defence Research Establishment, 2007 Kjeller, Norway,*
E. E. GOSSARD, J. M. YOUNG, *NOAA/ERL, Wave Propagation Laboratory, Boulder, Colorado, USA* and W. R. MONINGER, *Coe College, Cedar Rapids, Iowa, USA*

(Manuscript received February 12, 1974)

ABSTRACT

In this paper we describe a case study of progressive gravity waves in the troposphere. We deduce their propagation speed and direction, and their dispersive characteristics, from surface spectra of wind and pressure. We compare the results with direct measurements of the waves made over an array of spaced pressure sensors using cross spectrum techniques and an algorithm developed by one of us (Young). The agreement is very satisfactory and demonstrates the feasibility of monitoring atmospheric wave conditions in almost real time using only sensors (high quality) in use at standard weather observation stations. The waves in the case we describe were highly dispersive and apparently were generated by a violent thunderstorm some 100 km west of the site of observation.

1. Introduction

Atmospheric gravity waves and convective activity are important contributors to the atmospheric pressure spectrum in the band of periods from about 1 minute to 1 hour (Gossard, 1960). The form of the spectrum of displacement of the density surfaces (or isentropes), and the dispersion characteristics of propagating disturbances reveal much about the mechanism of their generation (Gossard, 1974). In this paper we measure the spectrum and the dispersion of gravity waves apparently generated by a severe convective storm on 8 August 1972 in southeastern Colorado. The wave spectra and the dispersion of the waves we will discuss are dramatically different from the spectra and dispersion of waves analyzed by Gossard & Sweezy (1974) which they concluded were generated by dynamic instability associated with shear in the middle troposphere.

A method devised by Gossard & Sweezy (1974) will be used for determining the dispersive characteristics of the observed waves, and we will compare it with direct measurements of the speed and direction of wave components across an array of spaced pressure sensors. For the latter analysis we use the digital techniques and computer algorithm devised by one of us (Young) to carry out a cross spectral analysis between spaced sensors in such a manner that the "beam" of the array is effectively steered, or swept, continouously through 360 deg of azimuth.

In addition to the usual temporal filtering commonly used to extract mesofrequency information, we have used sensors capable of spatially filtering the atmospheric spectrum, and in this paper we will discuss the merits of such spatial filtering for sorting out the contribution of atmospheric waves for analysis. We will show that by use of such a spatial averaging of the wind field, the large mesoscale features in the wind spectrum can be effectively extracted from the turbulence "noise".

2. Analytical techniques

In the method of Gossard & Sweezy (1974), the spectra of surface pressure and wind are

---

[1] This paper was prepared while the senior author was a visiting scientist at the National Oceanic and Atmospheric Administration, Environmental Research Laboratories, Boulder, Colorado, under the sponsorship of the Royal Norwegian Council for Scientific and Industrial Research.

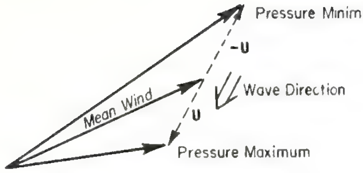

Fig. 1. Vector diagram for extracting the wind component U along the wave from fluctuations of the total wind.

combined to obtain the "spectrum" of intrinsic phase velocity of waves in the mid-frequency band of the spectra of atmospheric properties. Within the constraints of the linearized theory and the Boussinesq approximation, they point out that (e.g., see Gossard & Hooke, 1974)

$$P = \varrho_s \left(\frac{\omega}{k}\right)^2 \frac{\partial \zeta}{\partial z} \tag{1 a}$$

and

$$\frac{\omega}{k} = \frac{1}{\varrho_0} \frac{P}{U}. \tag{1 b}$$

In these equations

$$U, \zeta = [\varrho_0(z)/\varrho_s]^{1/2}\, u, \eta \quad \text{and} \quad P = [\varrho_0(z)/\varrho_s]^{-1/2}\, p,$$

where u, p, and η are, respectively, wave perturbations of the horizontal wind, pressure and isentropic surfaces; $\varrho_0(z)$ is the unperturbed density and ϱ_s is the density at some reference level such as the earth's surface. The wave frequency relative to an observer moving with the mean flow is ω (the intrinsic frequency) and the wavenumber $k = 2\pi/\lambda$ where λ is wavelength. Then the displacement spectrum at height H within a surface layer of constant Väisälä Brunt frequency N and constant wind is related to the pressure spectrum at the surface by

$$E_{\zeta H}(f) = \left[\frac{H}{\varrho_s \left(\frac{\omega}{k}\right)^2}\right]^2 B^2 E_{P_0}(f) \tag{2}$$

where B is $\sin n_1 H / n_1 H$ or $\sinh \gamma_1 H / \gamma_1 H$ depending on whether N_1/ω is greater than or less than unity. The dispersion equation for waves of infinitesimal amplitude relating n to the wave frequency ω and wavenumber k through the Väisälä-Brunt frequency $N = \sqrt{(g/\theta)\, d\theta/dz}$ (where θ is the potential temperature) is essentially (see Gossard & Hooke, 1974)

$$n = i\gamma = k\left[\left(\frac{N}{\omega}\right)^2 - 1\right]^{1/2} \tag{3}$$

for waves whose vertical wavelength is small compared with the atmospheric scale height. Also, the relation

$$\left[\frac{\omega}{k}(f)\right]^2 = \varrho_0^{-2} \frac{E_P(f)}{E_U(f)} \tag{4}$$

provides a measure of the wave dispersion when the spectra contain an important wave contribution. The wind component U must be extracted vectorially from fluctuations of the total wind as illustrated in Fig. 1. This is accomplished by choosing a suitable numerical lowpass filter to apply to wind speed and direction, thus separating the mean wind from the total wind. The same low-pass filter is applied to the pressure record. However, our pressure sensing system had its own high-pass filter, with a time constant of 50 sec, whose effect had to be removed from the final spectrum. A low-pass numerical filter was chosen such that a perturbation of 15 min period would have its amplitude reduced to one-third the true value. The time series of wind and pressure were sampled every second and then averaged over 20 sec intervals.

Young's method of processing data from spaced sensors is to azimuthally steer the array beam in either the time or frequency domains. It differs from other algorithms such as that of Mack & Smart (1972) primarily in having greater flexibility in choice of bandwidth when signal velocity is approximately independent of frequency as in the case of acoustic waves. This is accomplished by processing in terms of the wave "slowness" (defined as the inverse of velocity) rather than processing in frequency-wavenumber space. Varying the frequency bandwidth has little influence on the average within the band when "slowness" is relatively constant over the band, so the algorithm is adaptive in choosing an optimum trade-off between confidence and spectral resolution. When applied to gravity waves, the assumption of little dispersion is no longer necessarily valid as we shall see when results are discussed.

3. Observational techniques

The pressure sensors used in this study were essentially like that described by Bedard (1971), except that the filter amplifiers producing the various bandpasses shown in his Fig. 3 were not employed. Therefore the high frequency response was practically unlimited (as far as gravity waves are concerned) and the high-pass characteristic can be described by the single time constant of 50 sec. Each pressure sensor had 30 m of hose attached, into which hypodermic needles, used as orifices, were inserted at intervals of 1.5 m. The hose served to spatially filter out small scale turbulent inhomogeneities in the pressure field. The total pressure array consisted of a small array within a larger array as shown in Fig. 2. The small array was designed primarily to look at relatively small scale features within the boundary layer, and the large array was designed to observe larger scale features such as infrasound or long waves higher in the atmosphere. In the present study, additional spatial filtering of the pressure field was achieved by averaging pressure over the small array of sensors to obtain the spectrum of pressure for use in eqs. (2) and (4).

The anemometers used in the present study were bivanes with a high frequency response limited to approximately one Hz. However, our primary source of wind data was a unique system designed and built by G. Ochs and more completely described by Lawrence et al. (1972) and Kjelaas & Ochs (1974). The system uses a laser path to measure the average wind (somewhat weighted toward the center of the path) transverse to the path by measuring the velocity of the scintillation pattern at the receiver end. Clearly, only two such paths are needed to obtain a value of the total horizontal wind. However, the system was used in a triangular configuration so that horizontal mass convergence and divergence could be measured (Kjelaas & Ochs, 1974). This is also a suitable configuration for obtaining wind spatially averaged over the area of the triangle. The laser triangle is shown in Fig. 2.

The results of the analysis, using the spatially averaged pressure and winds as described above, were compared with results using point sensors. The advantage of using the laser winds was especially evident, and values of U obtained from bivane and from the laser triangle are shown for comparison in Fig. 5. Apparently the removal of small scale turbulence "noise" by the spatial filtering, accomplished by laser path averaging of the wind field, significantly improves the wave signal-to-noise.

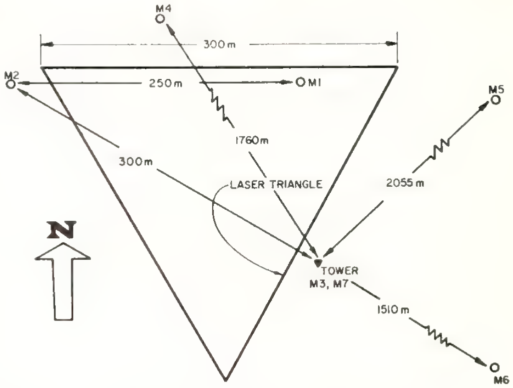

Fig. 2. Layout of the experimental configuration. The solid triangle is the laser triangle. Points marked M1, M2, M3 are the small microbarograph array, while M4, M5, M6, M7 denote the larger array. M7 is 20 m from the tower base.

4. Experimental results

The case chosen for analysis was an event which occurred in the early morning hours (0100–0230 MDT) on 8 August 1972 at Haswell, Colorado. Records of the waves of this event have been analyzed using an acoustic sounder triangle and the results published by Kjelaas et al. (1974) from whose paper the acoustic sounder records in Fig. 3, showing most of the time interval we analyzed, have been extracted. It is the purpose of our paper to analyze the dispersion and spectral characteristics using the observational techniques described above and try to deduce the mechanism of wave generation.

The pressure record and the unfiltered and low-pass filtered wind speed from the laser triangle are shown in Fig. 4. The results of carrying out the vector subtraction indicated in Fig. 1 are shown in Figs. 5 and 6. Fig. 5 shows the time series of the component U from

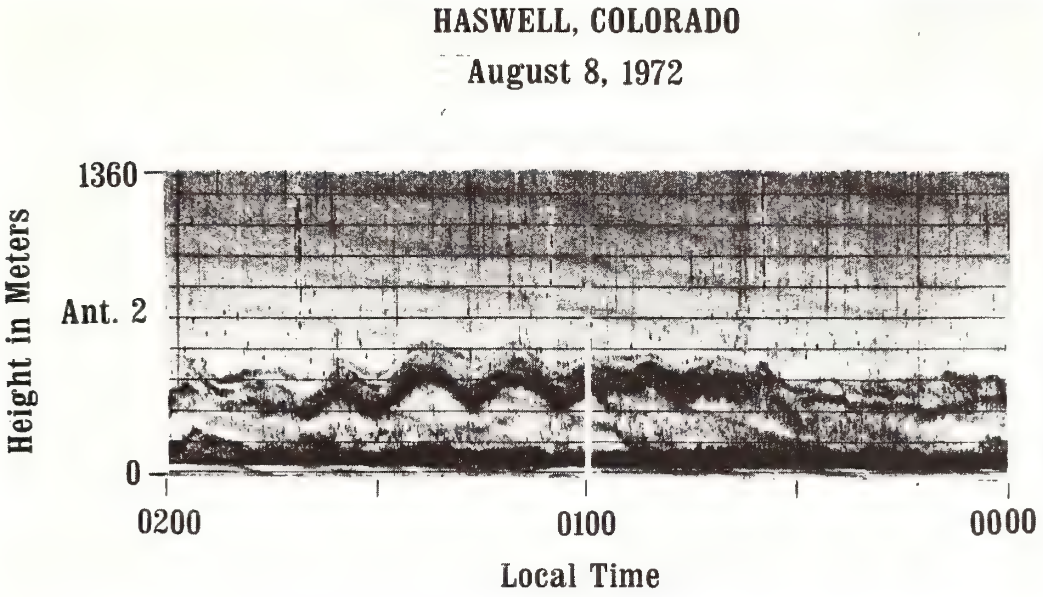

Fig. 3. Acoustic sounder record of part of the event analyzed in this paper. *LT* is Mountain Daylight Time. To convert to UT add 6 hours to LT. (From Kjelaas et al., 1974).

the laser winds along with the corresponding quantity from the bivane at 30 m elevation on a nearby tower. The fluctuating component due to the waves is much more evident in the laser wind measurements. We have chosen U as positive for clockwise rotation of the wind vector. Therefore, U and P are positively correlated when the waves come from the 180 deg sector to the left of the mean wind, but they are negatively correlated when they come from the right-hand 180 deg sector (as is the case for the principal peak in the directional distribution shown in Fig. 6). Some phase shift results from the high-pass filtering of the pressure fluctations by the pressure instrument. Fig. 6 shows the directional distribution of the waves found by the method of Gossard & Sweezy (1974). The arrows superimposed on the direction histogram show the directions obtained using Young's algorithm and the spaced array data. The arrow from 270 deg applies to the band from 21 min to 80 min, and that from 225 deg applies to the entire band from 4 to 80 min. period.

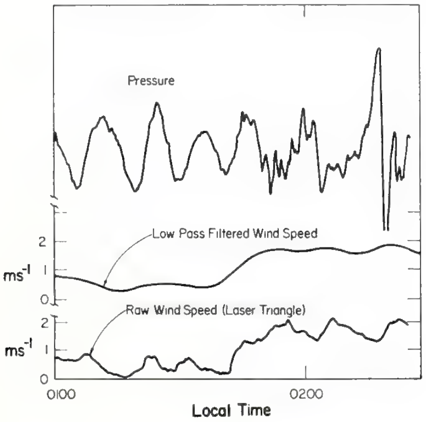

Fig. 4. Pressure recording together with the low-pass filtered and unfiltered laser wind. No scale is included for pressure since the instrument's filter characteristic has not been removed.

Fig. 7 shows the dispersion plot of phase velocity vs. frequency by the method of Gossard & Sweezy, together with the results of Young's analysis from spaced array data shown for frequency bands indicated by the bars. The spacing of elements in the array produces a high-frequency cut-off in the array spectra. The excellent agreement is a very convincing argument for the validity of both techniques. At a frequency of 2×10^{-3} Hz, the power in the spectrum (see Fig. 10) has diminished by two orders of magnitude from the peak power.

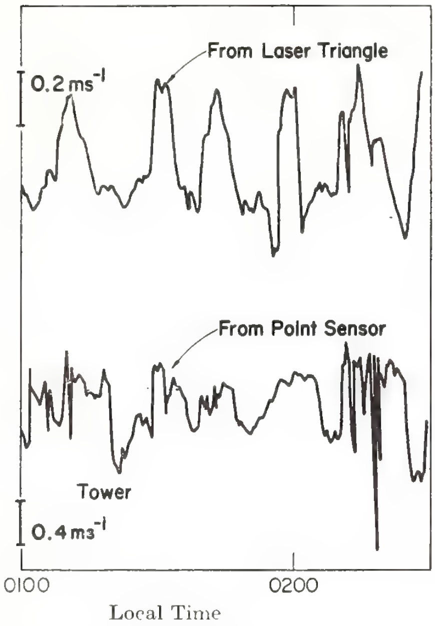

Fig. 5. Wind component U along the wave direction. Upper curve is obtained using the laser triangle, while lower curve is from the bivane at 30 m on a nearby tower.

Thus we do not consider the velocities in Fig. 7 to be significant at frequencies higher than about 2×10^{-3} Hz. During this wave event, the average surface winds were very light (about 1 m s^{-1}) and were mostly between north and east in opposition to the wave direction. We have attempted to obtain C, the true wave velocity relative to the ground, by subtracting 1 m s^{-1} from ω/k. This actually lessened the agreement in the results of the two techniques.

Fig. 8 shows the plot of ω vs. k. On this plot the slope of the line from the origin to any point on the curve represents the intrinsic phase velocity, and the slope of the tangent to the curve is the group velocity given by $d\omega/dk$.

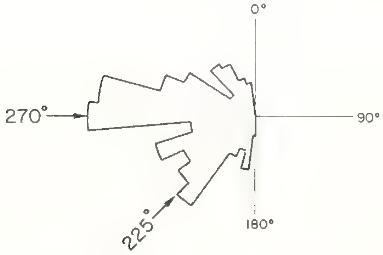

Fig. 6. Directional distribution of the waves.

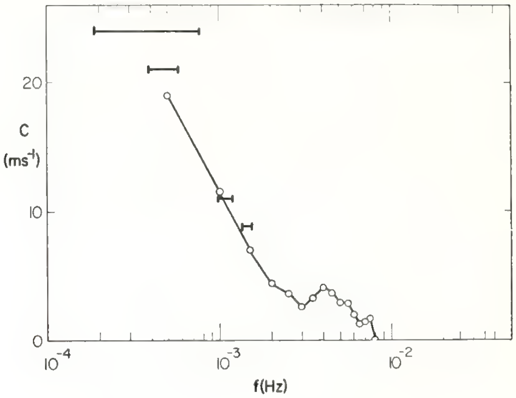

Fig. 7. Phase velocity vs. frequency. The horizontal bars are the phase velocities for different frequency bands found by applying Young's technique to the large microbarograph array. Power density of frequencies greater than $\sim 2 \times 10^{-3}$ Hz is about two orders of magnitude down from the peak in the power spectrum, so such points probably have no significance.

Fig. 9*a*, *b*, *c* shows the RAWINSONDE data obtained at 0457 MDT (the sounding nearest in time to the wave event). Unfortunately, the sounding does not well represent the lowest layers at the time of the waves, because a high surface wind sprang up at about 0400 MDT apparently due to outflow from the cool downdraft of a thundershower occurring locally at about that time. The high wind at the surface mixed the air within the radiation inversion and elevated it. We have used the surface wind and temperature data at the time of the wave event and the temperature and wind data at the top of a nearby 151 m tower (see Fig. 2)

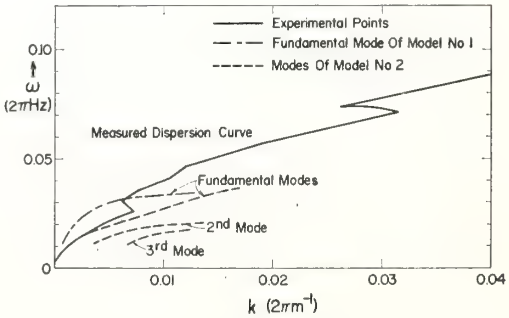

Fig. 8. Intrinsic frequency as a function of the wavenumber. Only the fundamental mode is shown for model no. 1.

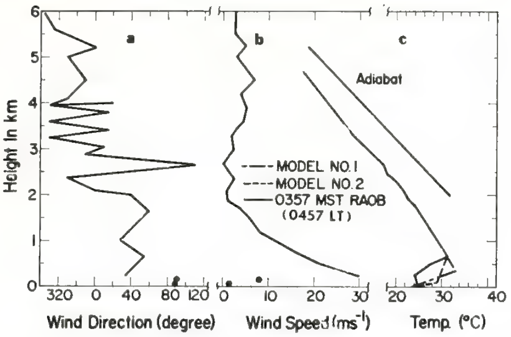

Fig. 9. Radiosonde at 0457 MDT. The circles shown are the wind and temperature data from the tower at the time of the wave event. The various atmospheric models discussed are shown as dashed curved.

to attempt to correct the sounding data back to the time of the event. The values are shown as circles, and two atmospheric models we analyze in the next section are shown as dashed and dash-dot curves in Fig. 9*c*.

Fig. 10 shows the spectrum of layer displacement at a height of 200 m calculated from eq. (2). Both the spectrum in Fig. 10 and the dispersion in Fig. 8 differ significantly from the corresponding quantities found by Gossard and Sweezy from the data taken at San Diego, Calif., under conditions of wind shear and instability aloft. The spectrum in Fig. 10 implies an r.m.s. amplitude of 38 m for the waves at a height of 200 m.

5. Comparison with models

The light winds aloft shown in Fig. 9 and the relatively low surface and tower winds at the time of the event (compared with the wave velocity of about 10 m s^{-1} at the spectrum maximum) imply that shear is not the generating mechanism for these waves. Furthermore, the waves are propagating against the background winds. Therefore it seems reasonable to compare the predictions of a shearless model with the observed dispersion.

We adopted a shearless model consisting of three layers rather than more realistic models with many layers because a three-layer model can be studied analytically whereas models with four or more layers are more effectively studied using numerical methods on high speed computers. We used a normal mode approach leading to an eigenvalue equation whose derivation is given by Gossard et al. (1970). They find that

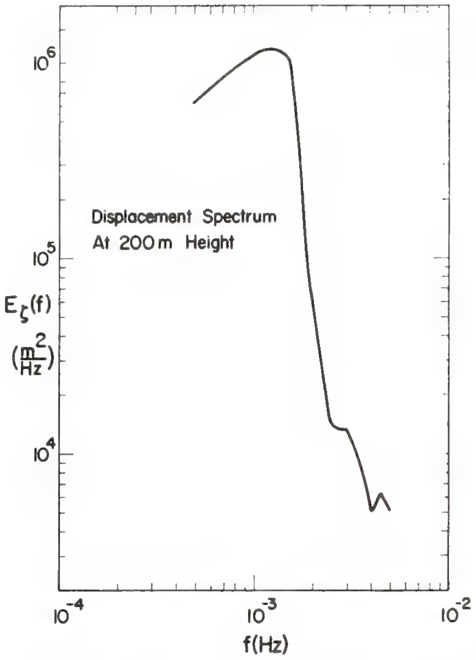

Fig. 10. Spectrum of layer displacement at a height of 200 m.

$$n_2 \cot 2n_2 \Delta H = \frac{n_2^2 - n_1 \gamma_3 \cot n_1 H}{n_1 \cot n_1 H + \gamma_3} \tag{5}$$

where the subscripts apply to the three layers of a model shown schematically in Fig. 12. Eq. (5) was applied to the two models shown by the dashed and dash-dot curves in Fig. 9*c* (see caption of Fig. 12). In model no. 1 the thickness $2\Delta H$ of the middle layer is zero so it is a two-layer model for which eq. (5) becomes (see Gossard & Hooke, 1974)

$$\tan\left(kH\sqrt{\left(\frac{N_1}{\omega}\right)^2 - 1}\right) = -\frac{\sqrt{\left(\frac{N_1}{\omega}\right)^2 - 1}}{\sqrt{1 - \left(\frac{N_3}{\omega}\right)^2}}. \tag{6}$$

The resulting dispersion curves for the two models are shown plotted on Fig. 8 for comparison with the observed values. To avoid confusion from too many curves on the plot, only

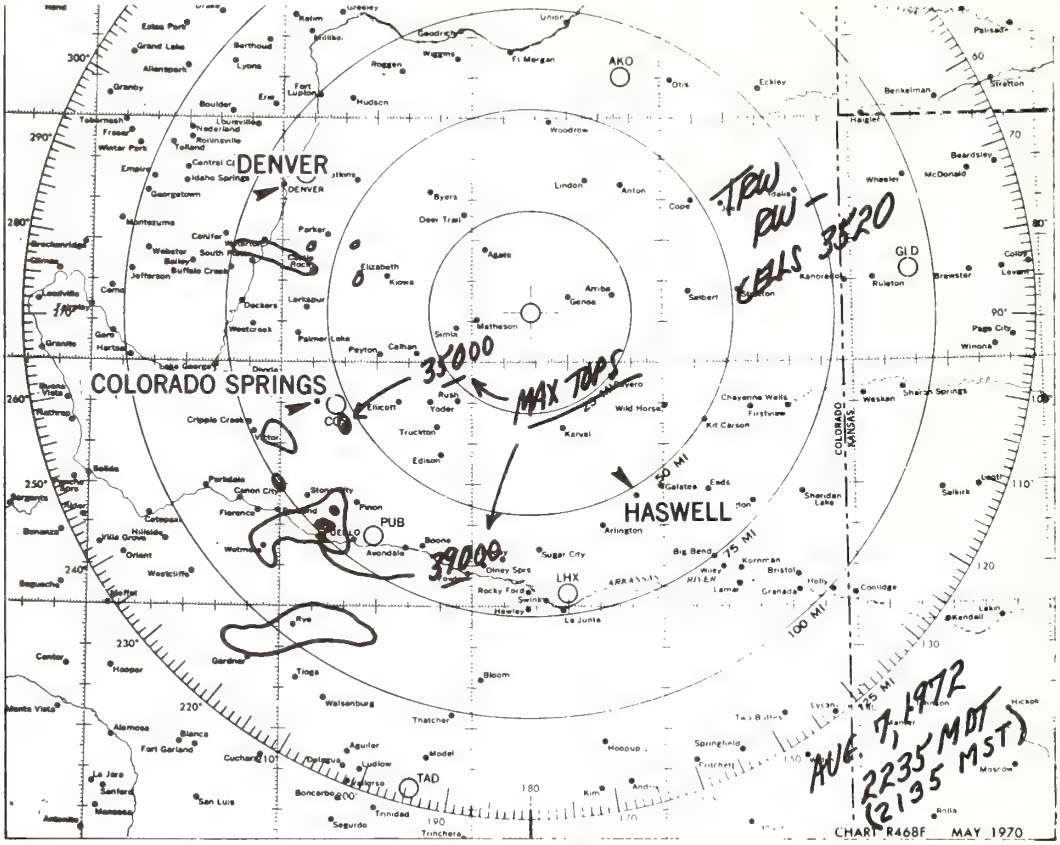

Fig. 11. Rader weather map at 2135 MST (2235 LT) obtained using the rader at Limon, Colorado.

the fundamental mode of model no. 1 has been plotted, but the second and third modes are shown for the three-layer model.

Model no. 1 provides the best fit to the gross features of the observed dispersion curve, but model no. 2 fits the low frequency portion of the curve ($\omega < 0.02$) almost exactly. In actual fact, if the waves have propagated some 100 km from the storm area, the path was undoubtedly variable, representing combinations of the various models here considered. For frequencies $\omega < N_3$, real roots to eq. (5) do not exist. This means that such waves "leak" energy upward away from the stable layers.

The important fact to note is that the observed waves are strongly dispersive as would be expected from the shearless models. If the waves had been generated by dynamic instability at a shear layer, the unstable irregularities would all travel with the mean wind speed at the center of the shear layer if the model is symmetrical with infinite upper and lower layers. If we consider a three-layer model in which the lower layer is not of infinite depth, those wave lengths long compared with its depth will no longer travel with exactly the speed of the mean wind (see Gossard, 1974), but the effect is small for the wavenumber range we consider here. The waves studied by Gossard & Sweezy (1974) displayed the non-dispersive character to be expected of wave generation by shear. The highly dispersive nature of the waves we have studied in this paper implies a different mechanism of generation. In addition, Fig. 9 shows that the shear that might have existed during the period of the event would lead to waves propagating from the northeasterly direction. They were actually propagating from the west through southwest sector (as seen in Fig. 6) with a group velocity of about 6 m s⁻¹

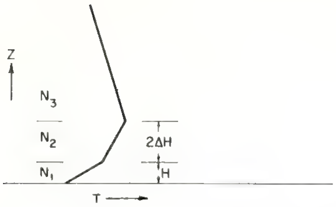

Fig. 12. The three-layer model. Model no. 1 (dash-dot curve in Fig. 8*c*) is a two-layer model, i.e., $\Delta H = O$, in which $N_1 = 0.0354$, $N_3 = 0.0111$ and $H = 200$ m. In model no. 2 (dashed curve in Fig. 8*c*), $N_1 = 0.050$, $N_2 = 0.0202$, $N_3 = 0.0111$, $H = 100$ m, $2\Delta H = 600$ m.

at frequencies corresponding with the maximum in energy of the spectrum shown in Fig. 10. If we look 100 km to the west of Haswell on the radar weather map shown in Fig. 11 taken at 2135 MST (2235 MDT) obtained by the NWS using the WSR 57 radar at Limon, Colorado we find a violent thunderstorm near Pueblo Colorado extending above 39 000 ft (11.9 km). By 2337 MDT the tops exceeded 41 000 ft (12.5 km). It seems very likely that the waves discussed in this paper were generated by the storm. The precise mechanism is uncertain. It seems possible that the storm may act like a slow explosion in the atmosphere effectively generating the low frequency gravity waves in our example. In that case the analysis of Ramm & Warren (1963) of gravity wave generation by an impulsive source may be relevant. Note that Fig. 10 shows most of the energy to be centered at a wave period of about 14 min. On the other hand it is very possible that the cool gust front associated with the strong downdraft of the storm generated the waves in the manner of a traveling disturbance.

6. Conclusion

We conclude that the methods described in this paper and that of Gossard & Sweezy (1974) provide a useful technique for observing the properties of waves in the atmosphere and of diagnosing the probable mechanism of wave generation. The method requires only single station measurements of pressure and wind. However comparison in Fig. 5 of the wind spatially averaged over the laser triangle with measurements obtained with a point sensor emphasizes the great value of spatial filtering in the extraction of large (or meso) scale features from the turbulence dominated total wind field spectrum.

Acknowledgment

The senior author expresses his sincere gratitute to Dr C. Gordon Little Director of the Wave Propagation Laboratory for providing him with the opportunity and making the facilities available to make this study while on leave from the Norwegian Defence Research Establishment.

REFERENCES

Bedard, A. J., Jr. 1971. Seismic response of infrasonic microphones. *J. of Res. Natl. Bu. of Stand. 75C(1)*, 41–45.

Gossard, E. E. 1960. Spectra of atmospheric scalars. *J. Geophys. Res. 65*, 3339–3351.

Gossard, E. E. 1974. Dynamic stability of an isentropic shear layer in a statically stable medium. *J. Atmos. Sci. 31*(2), (in press).

Gossard, E. E., Richter, J. H. & Atlas, D. 1970. Internal waves in the atmosphere from high resolution radar measurements. *J. Geophys. Res. 75*, 903–913.

Gossard, E. E. & Hooke, W. H. 1974. *Waves in the atmosphere.* Elsevier, Amsterdam (in press).

Gossard, E. E. & Sweezy, W. B. Spectra of waves in the atmosphere (submitted to *J. Atmos. Sci.*).

Kjelaas, A. G., Beran, D. W., Hooke, W. H. & Bean, B. R. 1974. Observation of waves in the boundary-layer using an array of acoustic sounders (submitted to *J. Atmos. Sci.*).

Kjelaas, A. G. & Ochs, G. R. 1974. Study of divergence in the boundary layer using optical propagation techniques. *J. Appl. Meteorol. 13*(2), 242–248.

Lawrence, R. S., Ochs, G. R. & Clifford, S. F. 1972. The use of scintillations to measure average wind across a light beam. *Appl. Opt. 11*(2), 239–243.

Mack, H. & Smart, E. 1972. Frequency domain processing of digital microbarograph array data. *J. Geophys. Res. 77*(1), 488–490.

Ramm, P. & Warren, F. W. G. 1963. Gravity-wave dispersion under wind shear in two model atmosphere. *Q. J. R. Meteorol. Soc. 89*, 349–359.

ДИСПЕРСИЯ И СПЕКТРЫ ГРАВИТАЦИОННЫХ ВОЛН, ВЕРОЯТНО ГЕНЕРИРУЕМЫХ КОНВЕКТИВНЫМ ШТОРМОМ

В данной статье мы описываем результаты наблюдений гравитационных волн, распространяющихся в тропосфере. Используя спектры ветра и давления, мы получаем скорости волн и направления их распространения, а также характеристики их дисперсии. Эти результаты мы сравниваем с данными прямых измерений волн, выполненными с помощью системы пространственно-разнесенных датчиков давления и обработанными с использованием техники взаимных спектров и алгоритма, разработанными одним из нас (Янгом). Согласие вполне удовлетворительное, что указывает на возможность прослеживания атмосферных волн практически в реальном времени с использованием только уже употребляемых высококачественных датчиков на стандартных станциях наблюдения за погодой. Волны в описываемом нами случае были сильно дисперсными и генерировались, очевидно, в области сильной грозы примерно в 100 *км* к западу от места наблюдения.

Journal of the Optical Society of America 64, 148-154. February 1974.

Saturation of optical scintillation by strong turbulence*

S. F. Clifford, G. R. Ochs, and R. S. Lawrence

National Oceanic and Atmospheric Administration, Environmental Research Laboratories, Boulder, Colorado 80302

(Received 30 July 1973)

The diffraction theory of optical scintillations has so far failed to describe the propagation of light over paths where the integrated amount of refractive-index turbulence is sufficient to cause saturation of the scintillations. We present a simple, physically based elaboration of the first-order perturbation theory and compare it with observations. Our theory reproduces in detail the observed saturation curve and the observed spatial covariance of the scintillations. In particular, we show why the fine-scale structure of scintillations persists deep into the saturation regime.

Index Headings: Scintillation; Turbulence; Atmospheric optics; Refractive index; Inhomogeneous media; Modulation transfer.

The diffraction theory of optical scintillations, suggested by Little[1] and elaborated by Tatarskii[2,3] and Fried,[4] has proven to be remarkably successful in describing the propagation of light through weak and moderate turbulence. However, it has failed to describe the saturation of scintillations that is observed when the integrated amount of turbulence along the path becomes large. Our purpose in this paper is to display some additional observations of the saturation phenomenon and to present a simple, physically based, elaboration of the Tatarski theory that succeeds quantitatively in reproducing the variance and covariance of the observed scintillations.

Lawrence and Strohbehn[5] have compared in detail, with an extensive list of references, the results of the theories[3,6–13] and observations[14–16] available before 1970. A number of attempts to generalize the Tatarskii theory produced saturation-like effects in the log-amplitude variance, with occasional qualitative resemblance to the observations, but all failed to predict in correct detail such other quantities as the distribution function and the spatial covariance function of the irradiance fluctuations.

More recently, Kerr[17] has published an extensive set of observations of the saturation phenomenon. Brown[18,19] has calculated the differential equation for the moments of the wave field and, for the case of two-dimensional geometry, has found numerical solutions for the variance and covariance of the irradiance. De Wolf[20] elaborates his original theory, one of the earliest to predict saturation, and discusses the current state of the theory in both the United States and the Soviet Union. Young[21] has presented a physically based interpretation of saturation, but his arguments lead to a disappearance of the fine-scale structure in the scintillation pattern, a conclusion contrary to observations.

The theory that we present in this paper was proposed by Ochs and Clifford[22] and has been outlined by Clifford.[23] The physical basis for the theory shows why the very smallest scales of irradiance fluctuation persist throughout the saturation region. The equations that result can be solved numerically in the realistic, three-dimensional case and so can be compared in detail with observations. We shall see that the observed variance and covariance are reproduced in detail.

EXPERIMENTAL RESULTS

We employed a continuous-wave He–Ne laser source with a 3-mW single-mode output at 0.6328 μm. The angular divergence of 2 mrad and the 1-mm transmitter- and receiver-aperture size were chosen to approximate a point source for comparison with the spherical-wave scintillation theory.[2,4,24] An earlier paper[15] describes the characteristics of our optical path and the parameters of the receiver. Supporting measurements of C_T^2 were made in the usual manner,[25] using high-speed platinum resistance thermometers with 10-cm vertical separation. Derivation of C_N^2 from C_T^2 then proceeds from the refractive-index formula.

Figure 1 illustrates the behavior of the log-amplitude standard deviation (square root of the variance), simultaneously observed at 50, 310, 500, and 1000 m,

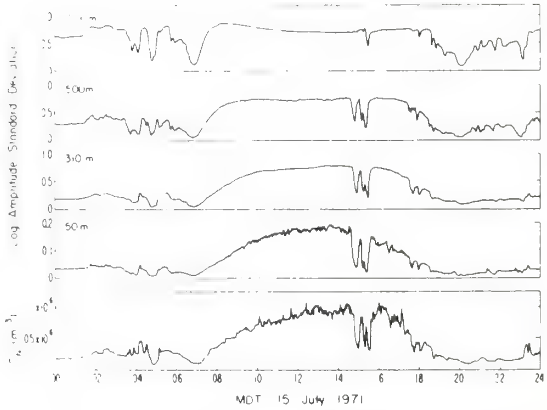

FIG. 1. The variation of the square root of the log-amplitude variance at each of four path lengths compared to the refractive-index structure parameter C_N for a 24-h period. All paths greater than 50 m show evidence of saturation.

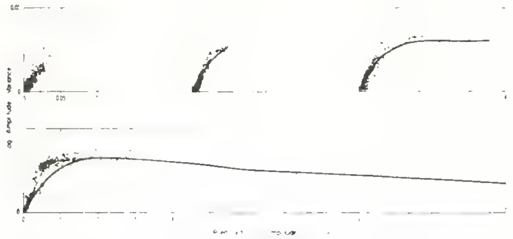

FIG. 2. Plots of the observed log-amplitude variance σ_χ^2 and the prediction σ_l^2 from the first-order theory. These data were taken simultaneously at 50 m (top left), 250 m (center), 500 m (top right), and 1000 m (bottom). The solid curve is our theoretical prediction from Eq. (13). The dashed line is a plot of Eq. (1).

for a 24-h period. Also shown is the behavior of a point measurement of the refractive-index structure parameter C_N for the same period. All of the curves were smoothed with a 100-s time constant. The spherical-wave theory,[2,4] ignoring the effects of inner scale,[24] predicts a proportionality of the log-amplitude variance, σ_χ^2, to C_N^2 and the path length, L, in the form

$$\sigma_\chi^2 = 0.124 k^{7/6} L^{11/6} C_N^2, \quad L \gg l_0^2/\lambda, \tag{1}$$

where l_0 is the inner scale of turbulence, $k = 2\pi/\lambda$, and λ is the wavelength of the light. Figure 1 clearly shows that, on all but the 50-m path, the proportionality breaks down for large values of C_N^2. From our observations, Eq. (1) is generally valid as an asymptote for values of σ_χ^2 less than 0.3, though the relation may differ as much as a factor of 2 over a period of several hours or more. Presumably, different turbulent spectra and nonuniform path distributions of C_N exist for extended periods. When σ_χ^2 exceeds 0.3 the saturation phenomenon occurs, and further increases of C_N^2 or of path length fail to produce corresponding increases of σ_χ^2. Continued increases of C_N^2 eventually produce a noticeable decrease of σ_χ^2 (supersaturation), as is shown for the 1000-m path. An interesting consequence of this effect is depicted in Fig. 1 at approximately 1500 h. Clouds passing overhead caused a precipitous decrease of C_N and a concurrent reduction in scintillation strength at 50, 310, and 500 m. Simultaneously, the log-amplitude variance at 1000 m actually increased, a strong indication that the scintillations were supersaturated at this distance.

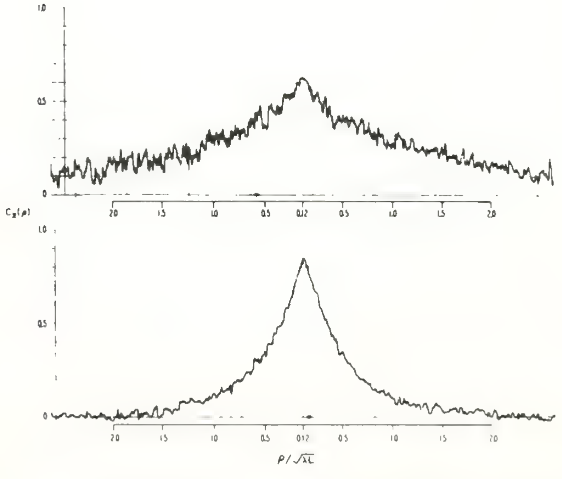

FIG. 3. Examples of direct recordings of covariance function $C_\chi(\rho_n)$ and spacing in Fresnel zones $\sqrt{(\lambda L)}$ taken on the 1000-m path.

Figure 2 provides an alternative view of similar log-amplitude observations made simultaneously at four path lengths. The log-amplitude variance is plotted against the theoretical prediction of Eq. (1), this time deriving C_N^2 from temperature probes spaced 3 cm apart, vertically. Once again, saturation appears on all but the shortest paths. Equation (1), which produces the dashed line in Fig. 2, fits the data quite satisfactorily until the predicted variance exceeds 0.3.

The log-amplitude variance is a useful but rather limited description of atmospheric optical-propagation characteristics. To learn about the spatial structure of scintillations, we measured the spatial covariance function of the log amplitude. This information is critical in the design of optical systems because it related directly to the ability of successively larger apertures to average out undesirable irradiance fluctuations. We employed two photomultiplier tubes with 1-mm apertures, the spacing of which was varied continuously in a periodic manner. Figure 3 shows a sample of such covariance measurements for a 1-km path during times of weak (bottom) and strong (top) turbulence. The ordinate is the normalized covariance function

$$C_\chi(\boldsymbol{\rho}) = \frac{1}{2T} \int_{-T}^{T} dt \chi(\mathbf{r}+\boldsymbol{\rho}, t) \chi(\mathbf{r}, t) / \sigma_\chi^2, \tag{2}$$

averaged over an interval $2T = 1$ s. The abscissa is the detector separation ρ measured in units of a Fresnel zone. Each sweep was made during an interval of approximately 10 min. Sweeps were selected for further analysis on the basis of symmetry; the symmetry indicates the degree of statistical stationarity that prevailed during the measurement.

Figures 4 and 5 summarize such covariance measurements made over 500-m and 1000-m propagation paths, respectively. The symbols a through d indicate progressively stronger levels of turbulence as measured by higher values of C_N^2. In weak turbulence (curve a), the first-order spherical-wave theory of Fried[4] shows excellent agreement with the data. As the strength of the turbulence increases, the covariance curves progressively fall off faster at spacings less than $\sqrt{(\lambda L)}/2$ and have progressively higher tails than in the weak turbulence case. The higher tails agree with the observations of Kerr,[17] as he found his correlation length increased noticeably with C_N^2. The general shapes also compare quite well with the predictions of Brown in the two-dimensional, plane-wave case. Kerr found further evidence of this result in his observation that aperture averaging was less effective than predicted and that the discrepancy increased as the strength of turbulence increased. The curves in Figs. 4 and 5 indicate that, in strong turbulence, there are relatively more of both large- and small-scale structures in the scintillation pattern than there are in weak turbulence. This result occurs because eddies the size of a Fresnel zone are made less effective as producers of scintillations by the decrease of phase coherence induced by high levels of C_N^2.

THEORY

The theoretical framework by which we propose to explain the important features of the saturation effect is a direct extension of the first-order theory of Tatarskii.[2,3] The simple physical model shown in Fig. 6 helps us to visualize the salient points of that theory.

The source S emits a spherical wave of wavelength λ that encounters a turbulent eddy of diameter $2l$ at path position z. The illuminated eddy produces a diffraction pattern, observed at L, whose size and contrast are determined by z, l, and λ and by the refractive-index fluctuation Δn of the eddy. (This qualitative explanation has been over-simplified by use of an eddy model. It would be more rigorous, though less easily visualized, to use a set of orthonormal functions to describe the turbulent medium. This is customarily done by expanding the refractive-index field in terms of Fourier components; the analytical results that follow these introductory remarks make such an expansion.)

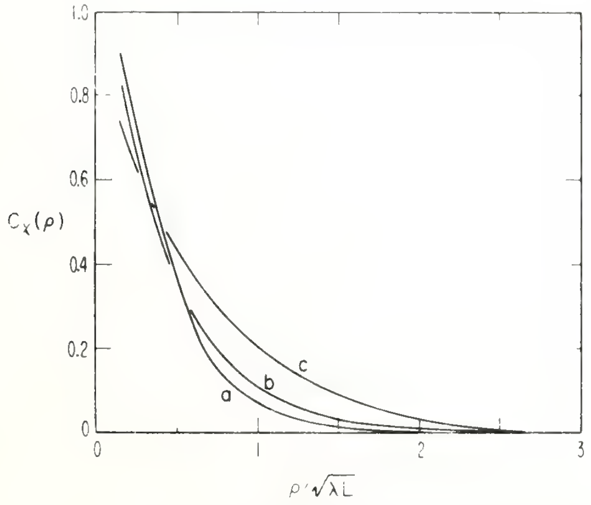

FIG. 4. Covariance functions taken at 500 m under progressively stronger (a–c) turbulent conditions. These smoothed curves represent averages of the raw data.

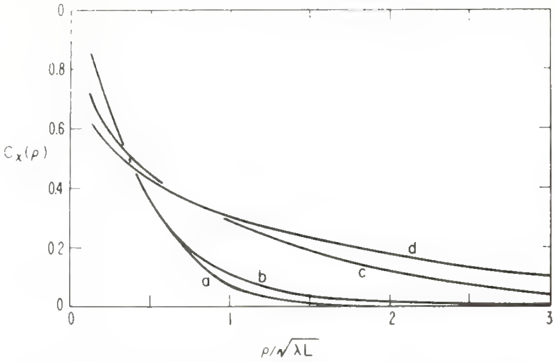

FIG. 5. Four covariance functions taken at 1000 m under progressively stronger (a–d) turbulent conditions. These smoothed curves represent averages of the raw data.

At path position z, the eddy that is most effective in producing scintillations at L is the one that satisfies the condition $SAL-SL=\lambda/2$, so that the two rays interfere destructively. Working out the geometry, we see that this Fresnel-zone-size eddy has a radius

$$l \approx (z/L)^{\frac{1}{2}}[1-(z/L)]^{\frac{1}{2}}\cdot(\lambda L)^{\frac{1}{2}}. \tag{3}$$

Smaller eddies at z produce scintillations at path positions $z<L$. Although these scintillations will persist in modified form at L, they contribute less than the others to the variance of irradiance because of the weaker refractivity fluctuation associated in the Kolmogorov spectrum with the smaller eddies. Eddies larger than a Fresnel zone will not produce strong scintillations at L because of their long focal lengths.

So far, we have considered the eddies at path position z to be acting independently of eddies at other locations along the path. Simple superposition of the effects of such independent portions of the path is, in fact, the basis of the Tatarskii first-order theory of scintillation. For sufficiently strong turbulence and long paths, the assumption of independence is no longer useful, as is shown by the failure of the first-order theory to predict saturation. To progress further, we must realize that the eddy at z is illuminated by a wavefront that is no longer spherical but has already been distorted by preceding eddies. In addition, we must realize that succeeding eddies lying between z and L will affect the wave and will modify the scintillations that might otherwise have been produced as a result of the eddy at z.

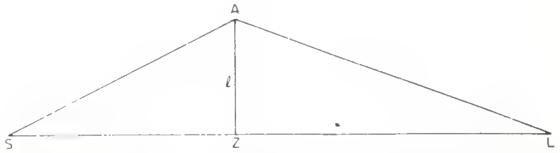

FIG. 6. The geometry of the simple eddy model used to explain the salient points of the analysis. The source at S illuminates the eddy of diameter $2l$ at z and produces scintillations that are observed at position L.

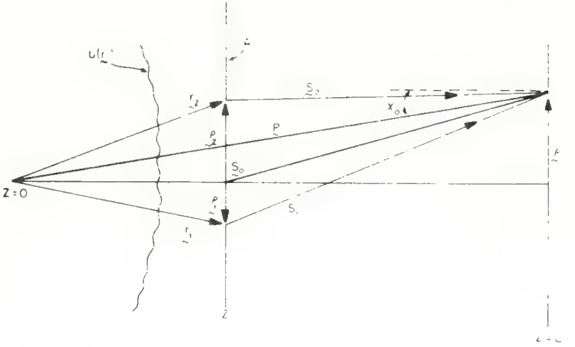

FIG. 7. The propagation geometry showing the incident perturbed field $u(r')$, the scattering at z and the ultimate field variables at $z=L$.

Let us first consider how the diffraction pattern of the eddy at z is affected by additional turbulence between the light source and the eddy. To do this it is convenient to imagine, for the moment, that the eddy is a lens focusing the light on a screen at location L. As the wave passes through the turbulence before reaching the lens, its wavefront is distorted in a random manner. Those distortions having a scale smaller than the lens will cause the resolving power of the lens to diminish and will thus increase the size of the spot observed at L. On the other hand, those distortions larger than the size of the lens will, in effect, be wave tilts and will move the spot on the screen without changing its size. Though it may not be so readily apparent, exactly the same effects will be caused by turbulence lying between the lens and the screen. Thus, it is not important to distinguish between the turbulence on the two sides of the lens, but it is, as we shall see, vitally important to consider separately the effects of the large-scale distortions of the wavefront from the effects of the small-scale distortions.

Returning to the case of the eddy, and concentrating particularly upon the Fresnel-zone-size eddies that are the most effective of all the eddies at location z, we must consider the relative lifetimes of the eddies of various sizes. Large eddies persist longer than small eddies, both because of their intrinsic lifetimes and because, for a given crosswind velocity, they take longer to pass through the line of sight. The small-scale fluctuations in the wavefront, the ones that caused smearing of the focal spot of our lens, change in detail many times during the lifetime of our eddy, so they smear the diffraction pattern of our Fresnel-zone-size eddy. On the other hand, the large-scale distortions do not change appreciably during the lifetime of our eddy. Thus, although they may have displaced the diffraction pattern, they can have no effect on the statistics of the scintillations produced by our eddy. Even the smallest details in the scintillation pattern arrive at L unaffected, that is, unsmeared by the large-scale distortions.

To calculate the smearing of the details in the scintillation pattern and the concomitant reduction of log-amplitude variance, we use the expression developed by Lutomirski and Yura[26] for the irradiance profile of an optical beam propagating through turbulence:

$$I(\mathbf{p})=\left[\frac{1+\cos\chi_0}{2\lambda s_0}\right]^2\int_A\int_A \exp[ik(s_1-s_2)+\psi(\mathbf{s}_1)+\psi^*(\mathbf{s}_2)$$
$$+\psi(\mathbf{r}_1')+\psi^*(\mathbf{r}_2')]u_0(\mathbf{r}_1')u_0^*(\mathbf{r}_2')d^2\mathbf{r}_1'd^2\mathbf{r}_2'. \quad (4)$$

Figure 7 shows the definition of each of the geometric quantities. Equation (4) is the random irradiance profile I that would be observed at location $\mathbf{p}=(\boldsymbol{\rho},z)$ from an aperture A illuminated by a random optical field u. The quantity $\exp(\psi)$ is the perturbation of the wave field, that is, $u=u_0\exp(\psi)$, and $k=2\pi/\lambda$ is the wave number of the radiation.

From the model above, we consider each Fourier component of the turbulent temperature field at z as a physical aperture that transmits a turbulence-distorted wave field through the remaining turbulent medium to a receiving plane a distance $(L-z)$ away. A critical assumption, following Young,[21] is that the effects of large integrated turbulence on the statistics of the amplitude fluctuations are adequately taken into account by a convolution of the first-order covariance function with the factor $\langle I(\boldsymbol{\rho},L)\rangle^T$ or, equivalently, the two-dimensional spectrum of the field parameters should be multiplied by the two-dimensional transform of $\langle I(\boldsymbol{\rho},L)\rangle^T$. Unlike Young, we believe that the averaging process, described by $\langle\ \rangle^T$, should proceed only over the time and spatial scales relevant to those of the log amplitude itself. (The superscript T here implies a short-term average.) As discussed above, larger-scale features produce only motion of the fine details of the scintillation pattern and not true smearing effects. A further critical assumption is that the modification of the first-order log-amplitude covariance is described in the same way, that is, as a convolution with $\langle I(\boldsymbol{\rho},L)\rangle^T$. The validity of these assumptions is borne out by the experimental results.

Equation (4) describes the spread of the focal spot at the receiver due to refractive turbulence along the path. The turbulence smears out the spatial frequencies in the received scintillation pattern by a convolution process in the spatial-frequency domain, this results in a modification of the first-order log-amplitude spectrum by a spectral filter function $H(K_p)$, that is, the two-dimensional transform of Eq. (4),

$$H(\mathbf{K}_p)=\frac{1}{(2\pi)^2}\int d^2\boldsymbol{\rho}e^{-i\mathbf{K}_p\cdot\boldsymbol{\rho}}\langle I(\boldsymbol{\rho})\rangle^T. \quad (5)$$

In Eq. (5), K_p is the spatial frequency observed in the receiving plane and $\boldsymbol{\rho}$ are the coordinates of the observation point in the plane $z=L$. Before performing the operation, we note from Fig. 7 the relations $\mathbf{s}_1=\mathbf{p}-\mathbf{r}_1'$,

$\mathbf{s}_2=\mathbf{p}-\mathbf{r}_2'$, $s_1^2=(L-z)^2+(\boldsymbol{\varrho}-\boldsymbol{\varrho}_1')^2$, and $s_2^2=(L-z)^2+(\boldsymbol{\varrho}-\boldsymbol{\varrho}_2')^2$, and in Eq. (4) make the change of variables $\boldsymbol{\xi}=\boldsymbol{\varrho}_2'-\boldsymbol{\varrho}_1'$, $2\boldsymbol{\eta}=\boldsymbol{\varrho}_2'+\boldsymbol{\varrho}_1'$. (These and the following steps are outlined in greater detail by Lutomirski and Yura.[26]) The result of this substitution, the use of the approximation $s_1-s_2\simeq\boldsymbol{\varrho}\cdot(\boldsymbol{\varrho}_2'-\boldsymbol{\varrho}_1')/(L-z)+(\boldsymbol{\varrho}_2'^2-\boldsymbol{\varrho}_1'^2)/[2(L-z)]$, and the assumption of homogeneous turbulence reduce Eq. (4) to the form

$$\langle I(\boldsymbol{\varrho})\rangle^T=\left[\frac{k}{2\pi(L-z)}\right]^2$$

$$\times\int d^2\boldsymbol{\xi}\exp\left\{\frac{ik(\boldsymbol{\varrho}\cdot\boldsymbol{\xi})}{(L-z)}\right\}M_{\mathrm{ST}}(\boldsymbol{\xi},z)M_{\mathrm{ST}}(\boldsymbol{\xi},L-z)$$

$$\times\int d^2\boldsymbol{\eta}\exp\left\{\frac{-ik(\boldsymbol{\eta}\cdot\boldsymbol{\xi})}{(L-z)}\right\}u_0^*(\boldsymbol{\eta}-\boldsymbol{\xi}/2)u_0(\boldsymbol{\eta}+\boldsymbol{\xi}/2).\quad(6)$$

The quantity M_{ST} is the appropriate short-term modulation transfer function (MTF).[27] This function is defined by[28] $M_{\mathrm{ST}}(\mathbf{r}_1,\mathbf{r}_2)=\langle\exp(\psi(\mathbf{r}_1)+\psi^*(\mathbf{r}_2))\rangle$; for homogeneous turbulence, it depends only on $\mathbf{r}_2-\mathbf{r}_1$. We consider this function in more detail later. At this point, its only important property is that the function depends on $\boldsymbol{\xi}$ alone. The existence of the product $M_{\mathrm{ST}}(\boldsymbol{\xi},z)M_{\mathrm{ST}}\times(\boldsymbol{\xi},L-z)$ in Eq. (6) is a consequence of the assumption that the integrated effects of turbulence from $z=0$ to z are independent of those from z to L, certainly a valid assumption for reasonable refractive-index correlation lengths. This assumption replaces $\langle\exp[\psi(\mathbf{s}_1)+\psi^*(\mathbf{s}_2)+\psi(\mathbf{r}_1')+\psi^*(\mathbf{r}_2')]\rangle^T$ by $\langle\exp[\psi(\mathbf{s}_1)+\psi^*(\mathbf{s}_2)]\rangle^T\langle\exp[\psi(\mathbf{r}_1')+\psi^*(\mathbf{r}_2')]\rangle^T=M_{\mathrm{ST}}(\boldsymbol{\xi},z)M_{\mathrm{ST}}(\boldsymbol{\xi},L-z)$. The appropriate next step is to make $\langle I(\boldsymbol{\varrho})\rangle^T$ a true weighting function by dividing by the average power $\int d^2\boldsymbol{\varrho}\langle I(\boldsymbol{\varrho})\rangle^T$. This normalizes the spectral-filter function to unit maximum amplitude. Substituting the normalized version of Eq. (6) into Eq. (5) and integrating gives

$$H_N(\mathbf{K}_p)=M_{\mathrm{ST}}(\mathbf{K}_p(L-z)/k,z)M_{\mathrm{ST}}\times(\mathbf{K}_p(L-z)/k,L-z).\quad(7)$$

If we assume isotropy as well as homogeneity of the turbulence, then H_N depends only on the magnitude of $\mathbf{K}_p$, that is, $H_N(\mathbf{K}_p)=H_N(K_p)$.

Fried[27] calculated short-term MTF by removing the effects of beam tilt. Tilt can be defined only in terms of the scale size of the aperture upon which the beam impinges. The plane that best fits the two-dimensional phase-fluctuation surface over that aperture then serves as an estimate of tilt and is consequently removed. As discussed previously, this same process can be approximated by high-pass filtering of the spatial-frequency spectrum used to determine MTF, so that only scales smaller than the aperture will contribute to the smearing effects described by the short-term MTF. When the aperture is a two-dimensional spatial frequency (phase screen) and the size of effective aperture is determined by the coherence properties of the incident wave, the separation between large-scale (tilting) and small-scale (smearing) components of the MTF is more difficult to define. During our calculations of the MTF of the wave incident upon the phase-retarding screen, we found that truncating the incident wave's coherence spectrum at a spatial frequency proportional to that of the phase screen accomplishes the desired result.

The long-term MTF of a spherical wave propagating through a distance z of homogeneous and isotropic refractive turbulence is given[29] by

$$M(\rho,z)=\exp\left\{-4\pi^2k^2\int_0^z dz'\times\int_0^\infty d\kappa'\kappa'\Phi_n(\kappa')\left[1-J_0\left(\frac{\kappa'\rho z'}{z}\right)\right]\right\},\quad(8)$$

where Φ_n is the refractive-index spectrum and J_0 is the zero-order Bessel function of the first kind. To proceed according to the foregoing argument, we convert the integral from one over the variable K', the spatial frequencies of the refractive-index spectrum, to one over $K_p'=K'z'/z$, that is, an integral over the spatial frequencies in the field of the wavefront variations at a position z produced by eddies at position z'. The variable K_p' represents the spatial wave numbers in the wavefront distortion that are decreased from those of the refractive-turbulence spectrum by the spherical divergence of the incident wave. Changing variables, we obtain

$$M(\rho,z)=\exp\left\{-4\pi^2k^2\int_0^z dz'(z/z')^2\times\int_0^\infty dK_p'K_p'\Phi_n(K_p'z/z')[1-J_0(K_p'\rho)]\right\}.\quad(9)$$

To modify Eq. (9) to obtain short-term MTF in line with the foregoing arguments, we truncate the integral over wave number of the wavefront perturbation below the wave number of the refractive-index turbulence K and obtain

$$M_{\mathrm{ST}}(\rho,z)=\exp\left\{-4\pi^2k^2\int_0^z dz'(z/z')^2\times\int_{\gamma K}^\infty dK_p'K_p'\Phi_n(K_p'z/z')[1-J_0(K_p'\rho)]\right\}.\quad(10)$$

The coefficient in the lower limit is $\gamma=0.35$. This arises because the tilting effects of the irregularities in the incident phase front occur at a spatial frequency somewhat lower than that of the illuminated phase screen. Numerical simulation of a random Kolmogorov phase front impinging on a screen of wave number K has indicated that $0.35K$ is a reasonable truncation point.

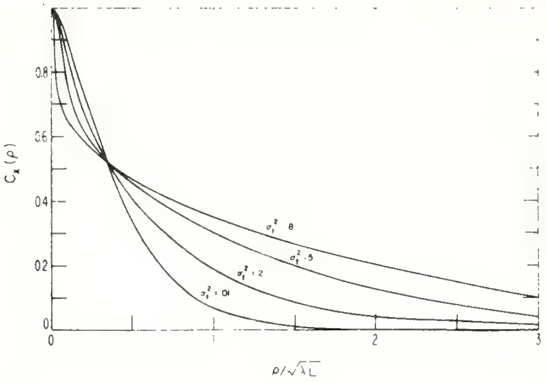

FIG. 8. Theoretical covariance curves determined from Eq. (13). Each curve results from a different amount of integrated turbulence σ_t^2.

A complete and correct calculation would, of course, produce a smooth high-pass filter in Eq. (10).

To complete the analysis, we assume the conventional spectrum for the refractivity fluctuation resulting from Kolmogorov turbulence, that is,

$$\Phi_n(K)=0.033C_N^2K^{-11/3},\quad L_0^{-1}\ll K\ll l_0^{-1}.$$

and note that we may extend the region of integration in Eq. (10) to infinity and allow K to vary from zero in the lower limit, with negligible error. [The outer scale L_0 may play a significant role here if it is unusually small, i.e., on the order of a few Fresnel zones. Its inclusion in the integral in Eq. (10) would result in higher log-amplitude variances as the amount of integrated turbulence increases.] Further, substitution of variables $u=z/L$ and $\xi=K_p\rho$, and the performance of the u integration reduces Eq. (10) to

$$M_{\mathrm{ST}}(\rho,z)=\exp\left\{-0.05\pi^2k^2C_N^2z\rho^{5/3}\times\int_{0.35K\rho}^{\infty}d\xi\,\xi^{-8/3}[1-J_0(\xi)]\right\}.\qquad(11)$$

TABLE I. A comparison of integrated-path refractive turbulence σ_t^2 as determined from temperature measurements and from fitting Eq. (13) of our present theory to the observations of Figs. 4 and 5. Here α is the rms discrepancy in C_χ between the observations and the present theory.

Curve	σ_t^2(temp)	σ_t^2(theory)	α
	500-m Path		
a	...	0	0.026
b	0.20	0.29	0.013
c	2.48	2.46	0.015
	1000-m Path		
a	0.03	0.02	0.02
b	0.62	0.58	0.015
c	3.89	4.64	0.015
d	8.68	5.83	0.038

Returning to Eq. (7) and noting the particular form of the z dependence in Eq. (11), we see that $M_{\mathrm{ST}}(\rho,z)M_{\mathrm{ST}}\times(\rho,L-z)=M_{\mathrm{ST}}(\rho,L)$.

We must now write the first-order theory for the log-amplitude covariance function and insert the spectrum modification $M_{\mathrm{ST}}(K_p(L-z)/k,L)$. From Lawrence and Strohbehn,[5] the log-amplitude covariance for a spherical wave propagating over a path L through a medium filled with Kolmogorov turbulence is determined by

$$C_\chi(\rho)=0.132\pi^2k^2LC_N^2\int_0^1du\int_0^\infty dK\times K^{-8/3}J_0(K\rho u)M_{\mathrm{ST}}(KLu(1-u)/k,L)\times\sin^2\left[\frac{K^2u(1-u)L}{2k}\right].\qquad(12)$$

In Eq. (12), we have inserted the M_{ST} function and noted that $K_p=Ku$. A change of variables from K to $y=K^2u(1-u)L/(2k)$ puts this equation in a more suggestive form in terms of the first-order log-amplitude variance, that is $\sigma_t^2=0.124k^{7/6}L^{11/6}C_N^2$. With this done, Eq. (12) takes the form

$$C_\chi(\rho_n,\sigma_t^2)=2.95\sigma_t^2\int_0^1du[u(1-u)]^{5/6}\int_0^\infty dy\frac{\sin^2y}{y^{11/6}}\times\exp\{-\sigma_t^2[u(1-u)]^{5/6}f(y)\}J_0\left[\left(\frac{4\pi yu}{1-u}\right)^{\frac{1}{2}}\rho_n\right],\qquad(13)$$

where $\rho_n=\rho/\sqrt{(\lambda L)}$ and $f(y)$ is given by

$$f(y)=7.02y^{5/6}\int_{0.7y}^{\infty}d\xi\,\xi^{-8/3}[1-J_0(\xi)].\qquad(14)$$

Equation (13) is the equation for the log-amplitude variance and covariance function in the case of strong integrated turbulence $\sigma_t^2>0.30$. Asymptotically, it reduces to the first-order result for $\sigma_t^2\leq0.30$.

COMPARISON WITH OBSERVATIONS

The results of our theory, Eq. (13), produced the saturation curve that is superimposed upon the observed points in Fig. 2. The relatively low values compared with the experimental points in the linear (unsaturated) region and in the region of high σ_t^2 result from the manner in which we chose to truncate the integral in Eq. (10). The scintillation-reducing effects do not occur abruptly, as indicated by the form of Eq. (10), but more smoothly, so that, for example, Fresnel-zone-size eddies retain some scintillation-producing effect even in strong turbulence. Thus, our abrupt truncation of the integration overstates the effects of strong turbulence on the log-amplitude variance.

A more-stringent test of the saturation theory concerns the structure of the scintillation pattern. Figures 3–5 show the observed covariance of scintillations, whereas in Fig. 8, we see a set of theoretical curves that depend on normalized spacing $\rho_n = \rho/\sqrt{(\lambda L)}$ and the first-order log-amplitude variance σ_l^2. Table I compares the σ_l^2 required for our theory to fit best each of the covariance curves of Figs. 4 and 5 with the σ_l^2 derived from point temperature measurements. The small rms discrepancies Δ indicate that observations and theory agree within the uncertainty of the measurements. Differences between σ_l^2(temp) and σ_l^2(theory) arise mostly from the failure of a single-temperature sensor to represent accurately the path-averaged temperature statistics.

Finally, our model agrees with the observation[15] that the probability distribution function of irradiance (or amplitude) is log normal in the saturation region. This statement follows directly from the central-limit theorem, because our model of the saturation phenomenon involves only linear filtering (smoothing) of the log amplitude.

In summary, we have proposed a physically based elaboration of the Tatarskii theory of propagation through turbulence; numerical results from this model agree with all observed features of the saturation phenomenon.

REFERENCES

* Invited paper presented by S. F. Clifford at the Denver meeting of the Optical Society of America, March 1973 [J. Opt. Soc. Am. **63**, 471A (1973)].

[1] C. G. Little, Mon. Not. R. Astron. Soc. **111**, 289 (1951).

[2] V. I. Tatarskii, *Wave Propagation in a Turbulent Medium*, translated by R. S. Silverman (McGraw-Hill, New York, 1961).

[3] V. I. Tatarskii, *The Effects of the Turbulent Atmosphere on Wave Propagation*, translated from the Russian (originally published in 1967) (National Technical Information Service, Springfield, Va., 1971).

[4] D. L. Fried, J. Opt. Soc. Am. **57**, 175 (1967).

[5] R. S. Lawrence and J. W. Strohbehn, Proc. IEEE **58**, 1523 (1970).

[6] V. I. Tatarskii and M. E. Gerstenshtein, Zh. Eksp. Teor. Fiz. **44**, 676 (1963) [Sov. Phys.-JETP **17**, 458 (1963)].

[7] V. I. Tatarskii, Zh. Eksp. Teor. Fiz. **46**, 1399 (1964) [Sov. Phys.-JETP **19**, 946 (1964)].

[8] V. I. Tatarskii Zh. Eksp. Teor. Fiz. **49**, 1581 (1965) [Sov. Phys.-JETP **22**, 1083 (1966)].

[9] D. A. de Wolf. Radio Sci. **2**, 1379 (1967).

[10] D. A. de Wolf. J. Opt. Soc. Am. **58**, 461 (1968).

[11] D. A. de Wolf. J. Opt. Soc. Am. **59**, 1455 (1969).

[12] W. P. Brown, Jr., in *Proceedings of the Symposium on Modern Optics*, edited by J. Fox (Polytechnic Press, Brooklyn, N. Y., 1967), p. 717.

[13] W. P. Brown, Jr., IEEE Trans. Antennas Propag. **15**, 81 (1967).

[14] M. E. Gracheva and A. S. Gurvich, Sov. Radiophys. **8**, 511 (1955).

[15] G. R. Ochs and R. S. Lawrence, J. Opt. Soc. Am. **59**, 226 (1969).

[16] M. E. Gracheva, A. S. Gurvich, and M. A. Kallistratova, Radiophys. and Quantum Electron. **13**, 40 (1970).

[17] J. R. Kerr, J. Opt. Soc. Am. **62**, 1040 (1972).

[18] W. P. Brown, Jr., J. Opt. Soc. Am. **62**, 45 (1972).

[19] W. P. Brown, Jr., J. Opt. Soc. Am. **62**, 966 (1972).

[20] D. A. de Wolf, J. Opt. Soc. Am. **63**, 171 (1973).

[21] A. T. Young, J. Opt. Soc. Am. **60**, 1495 (1970).

[22] G. R. Ochs and S. F. Clifford, J. Opt. Soc. Am. **62**, 728A (1972).

[23] S. F. Clifford, J. Opt. Soc. Am. **63**, 471A (1973).

[24] P. M. Livingston, Appl. Opt. **11**, 684 (1972).

[25] R. S. Lawrence, G. R. Ochs, and S. F. Clifford, J. Opt. Soc. Am. **60**, 826 (1970).

[26] R. F. Lutomirski and H. T. Yura, Appl. Opt. **10**, 1652 (1971).

[27] D. L. Fried, J. Opt. Soc. **56**, 1372 (1966).

[28] H. T. Yura, J. Opt. Soc. Am. **63**, 567 (1973).

[29] R. F. Lutomirski and H. T. Yura, J. Opt. Soc. Am. **61**, 482 (1971).

Journal of the Optical Society of America 64, 1641-1644, December 1974.

Equivalence of two theories of strong optical scintillation

S. F. Clifford

National Oceanic and Atmospheric Administration, Environmental Research Laboratories, Boulder, Colorado 80302

H. T. Yura

The Aerospace Corporation, P. O. Box 92957, Los Angeles, California 90009

(Received 24 May 1974)

We demonstrate that the theories of strong irradiance fluctuations of Yura and Clifford *et al*., although they start from slightly different physical models, produce the same predictions for the behavior of an optical wave propagating through strong turbulence. Both theories predict a saturation of the irradiance variance and that in the saturation regime the amplitude correlation length is equal to the lateral coherence length of the optical wave. The detailed structure of the amplitude correlation functions is also similar, showing a more-rapid decay at the origin and an enhanced tail at large separations in comparison to the results of the weak scattering theory.

Index Headings: Inhomogeneous media; Turbulence; Scintillation; Atmospheric optics; Coherence; Fluctuations of light.

The purpose of this paper is to demonstrate the physical equivalence of two theories of strong optical scintillation.[1,2] Physical equivalence of the two theories of strong scintillation is used in this paper to signify that both theories predict the same physical results in the case of strong irradiance fluctuations, and that both theories show that the turbulent eddies that are most effective in producing strong irradiance fluctuations are those that have characteristic scale sizes of the order of the lateral coherence length of the optical wave.

Recently, Yura[1] has generalized Tatarskii's[3] physical model for irradiance fluctuations to include both diffraction and the loss of lateral spatial coherence of the wave as it penetrates further into the medium. Yura's results agree with perturbation theory for $\sigma_T^2 \ll 1$ (σ_T^2 is the amplitude variance calculated on the basis of perturbation theory). For $\sigma_T^2 \gtrsim 1$, that is, in the saturation regime, he obtains a saturation of the irradiance variance, a decrease in the amplitude-correlation length for increasing σ_T, and a residual positive correlation tail. In particular, Yura shows that in the saturation region the amplitude correlation length is equal to the lateral coherence length of the wave $\rho_0(L)$, which is a decreasing function of propagation distance. That is, in the saturation regime, the amplitude and phase correlation lengths are equal. Additionally, he demonstrates that in the saturation regime turbulent eddies having scale sizes of the order $\rho_0(L)$ are the most effective in producing irradiance fluctuations (in contrast to the case $\sigma_T^2 \lesssim 1$, in which eddies having scale sizes of the order of the Fresnel length are most effective in producing the irradiance fluctuations).

On the other hand, Clifford *et al.*[2] present a simple, physically based, phenomenological elaboration of Tatarskii's perturbation results that succeeds quantitatively in reproducing the variance and covariance of their observed scintillations. At first glance, the methods and results of Refs. 1 and 2 seem different; however, we show in this paper that these two approaches to the strong-scintillation problem lead to identical physical results. In particular, we demonstrate that the log-amplitude variance derived in Ref. 2 saturates asymptotically to a constant value, independent of wavelength, path length, and parameters that describe the turbulent medium. Additionally, we will demonstrate that in the saturation regime the log-amplitude covariance function of Ref. 2 has a correlation length equal to $\rho_0(L)$ and that the eddy sizes most effective in producing the irradiance fluctuation are of the order $\rho_0(L)$, in agreement with the general results of Ref. 1.

I. VARIANCE

The results of Clifford *et al.*[2] for spherical waves and the Kolmogorov spectrum are given by

$$C_\chi(\rho_n,\sigma_T^2)=2.95\sigma_T^2\int_0^1 du\,[u(1-u)]^{5/6}\int_0^\infty dy\frac{\sin^2 y}{y^{11/6}} \times\exp\{-\sigma_T^2[u(1-u)]^{5/6}f(y)\}J_0\left[\left(\frac{4\pi yu}{1-u}\right)^{\frac{1}{2}}\rho_n\right], \quad (1)$$

where

$$\sigma_T^2=0.124k^{7/6}L^{11/6}C_n^2, \quad (2)$$

$$\rho_n=\rho/(\lambda L)^{\frac{1}{2}}, \quad (3)$$

$$f(y)=7.02y^{5/6}\int_{\alpha y}^\infty d\xi\,\xi^{-8/3}[1-J_0(\xi)], \quad (4)$$

where k is the optical wave number ($=2\pi/\lambda$, where λ is the optical wavelength), C_n is the index structure constant, and J_0 is the Bessel function of the first kind of order zero. The numerical coefficient α that appears in the lower limit of the integral in Eq. (4) could not be obtained *a priori* by Clifford *et al.* On physical grounds, it can be shown that α is nonzero and most likely is a number of the order unity. The best fit to the strong-scintillation data of Ref. 2 was obtained for $\alpha=0.7$.

The log-amplitude variance data of Ref. 2 extend out to $\sigma_T^2 \simeq 13$ and is shown in Fig. 2 of Ref. 2. For this range of σ_T^2 values, the variance, as calculated from Eq. (1), appears (see Fig. 2 of Ref. 2) to decrease asymptotically to zero with increasing σ_T^2; however, this is not the case when $\sigma_T^2 \to \infty$. We now show that σ_χ^2 asymptotically approaches a constant for $\sigma_T^2 \to \infty$.

From Eq. (1), we have

$$\sigma_\chi^2 = C_\chi(0,\sigma_T^2) = 2.95 \int_0^1 \sigma_T^2(u)\,du \int_0^\infty dy\,\frac{\sin^2 y}{y^{11/6}} \times \exp\{-\sigma_T^2(u) f(y)\}, \tag{5}$$

where

$$\sigma_T^2(u) = \sigma_T^2[u(1-u)]^{5/6}. \tag{6}$$

Consider the integral over y in Eq. (5). We have

$$\sigma_\chi^2 = 2.95 \int_0^1 du\,\sigma_T^2(u)[I_1 + I_2], \tag{7}$$

where

$$I_1 = \int_0^1 dy\,\frac{\sin^2 y}{y^{11/6}} \exp\{-\sigma_T^2(u) f(y)\} \tag{8}$$

and

$$I_2 = \int_1^\infty dy\,\frac{\sin^2 y}{y^{11/6}} \exp\{-\sigma_T^2(u) f(y)\}. \tag{9}$$

First, consider I_1. Because $y \leq 1$, we have $f(y) \approx 7.9y^{5/6}$ and $\sin^2 y \approx y^2$. It then follows that

$$I_1 \approx \int_0^1 dy\,y^{1/6} \exp[-7.9\sigma_T^2(u) y^{5/6}]. \tag{10}$$

Change variables to

$$x = 7.9\sigma_T^2(u) y^{5/6}; \tag{11}$$

thus from Eqs. (10) and (11),

$$I_1 \approx [7.9\sigma_T^2(u)]^{-7/5} \int_0^{7.9\sigma_T^2(u)} x^{-2/5} e^{-x}\,dx. \tag{12}$$

From Eq. (1) it can be seen that the main contributions to the u integral occurs for $u \approx \frac{1}{2}$; therefore, for $\sigma_T^2 \gg 1$, the upper limit on the integral in Eq. (12) can be extended to infinity. It then follows that

$$I_1 \approx 0.06[\sigma_T^2(u)]^{-7/5}. \tag{13}$$

Next, consider I_2. Because $y \geq 1$, we have $\sin^2 y \approx \frac{1}{2}$ and[4]

$$f(y) \approx 7.02y^{5/6} \int_{\alpha y}^\infty \frac{d\xi}{\xi^{8/3}} = \frac{4.2}{\alpha^{5/3} y^{5/6}}; \tag{14}$$

thus from Eqs. (9) and (14) we obtain

$$I_2 \approx \tfrac{1}{2} \int_1^\infty dy\,y^{-11/6} \exp\{-\beta/y^{5/6}\}, \tag{15}$$

where

$$\beta = \frac{4.2\sigma_T^2(u)}{\alpha^{5/3}}. \tag{16}$$

Changing variables to $q = \beta y^{-5/6}$, we obtain (note: $\beta \gg 1$)

$$I_2 \approx \frac{3}{5\beta} \int_0^\infty e^{-q}\,dq \approx 0.6\beta^{-1}. \tag{17}$$

After the definition of β from Eq. (16) is inserted, Eq. (17) is reduced to

$$I_2 \approx \frac{\alpha^{5/3}}{7.0\sigma_T^2(u)}. \tag{18}$$

From Eqs. (6), (7), (13), and (18), we can construct the asymptotic form of the log-amplitude variance

$$\sigma_\chi^2 = 2.95 \int_0^1 du \times \{0.06(\sigma_T^2)^{-2/5}[u(1-u)]^{-1/3} + 0.14\alpha^{5/3}\} \tag{19}$$

and, the u integration is performed, σ_χ^2 becomes

$$\sigma_\chi^2 = 0.36(\sigma_T^2)^{-2/5} + 0.42\alpha^{5/3}. \tag{20}$$

Therefore, according to the theory of Clifford *et al.*,[2] as σ_T^2 increases beyond unity, σ_χ^2 initially decreases as $0.36(\sigma_T^2)^{-2/5}$ and ultimately saturates at a value of $\sigma_\chi^2 = 0.23$ for $\alpha = 0.7$.[5] To compare this result with the theory of Yura,[1] we calculate the normalized variance of the irradiance $\sigma_I^2/(I_0^2)$. For log-normally distributed irradiance fluctuations, σ_I^2/I_0^2 is related to σ_χ^2 by the expression

$$\frac{\sigma_I^2}{I_0^2} = \exp(4\sigma_\chi^2) - 1. \tag{21}$$

With $\sigma_\chi^2 = 0.23$, we obtain $\sigma_I^2/(I_0^2) = 1.51$, a number of order unity, in agreement with the results of Ref. 1.

This result is also confirmed by recent experimental work in the Soviet Union.[6] Because of their extremely long path of 8.5 km, Gracheva *et al.*[6] were able to exceed $\sigma_T^2 = 400$ in their experiments. Initially, the data of Gracheva *et al.* decayed slightly for $\sigma_T^2 > 1$ and then appeared to saturate at a value $(\sigma_I/I_0)^2 \simeq 1.5$, in agreement with Clifford *et al.*[2]

In deriving the asymptotic behavior of the log-amplitude variance, we have shown that for $\sigma_T^2 \gg 1$, the main contribution to the y integral in Eq. (1) comes from I_2 around the point

$$y \sim \beta^{6/5} \sim u(1-u)(\sigma_T^2)^{6/5}. \tag{22}$$

Now, the dimensionless integration variable y is related to spatial frequency K by the relation[2]

$$y=\frac{L}{k}u(1-u)K^2; \tag{23}$$

hence, from Eqs. (22) and (23), we see that the main contribution to the strong irradiance fluctuations is obtained from spatial frequencies K_0 of the order

$$K_0 \approx \left(\frac{k}{L}\right)^{\frac{1}{2}} (\sigma_T^2)^{\frac{3}{5}} \approx \frac{1}{\rho_0(L)}. \tag{24}$$

The most-important turbulent eddies along the path are those having scale sizes of the order of ρ_0, the lateral coherence length of the wave, in agreement with the results of Ref. 1.

Another interesting property demonstrated by Eq. (19) is that, in the region of decreasing σ_χ^2 with increasing σ_T^2, the path weighting function for scintillations is $[u(1-u)]^{-\frac{1}{2}}$, highly peaked at the transmitter and receiver ends of the path and ultimately, when $\sigma_T^2 \gg 1$ it becomes completely uniform. It is interesting to compare these weighting functions to the one found in the weak-scintillation case[2] $\sigma_T^2 < 0.3$, where the most-effective region for producing scintillations is the middle of the path with a nearly parabolic taper to zero effectiveness at the receiver and transmitter ends.

II. COVARIANCE

Another important consideration is the resulting spatial structure of the scintillation pattern in strong turbulence, i.e., what scale sizes are produced in the received pattern by the most-effective eddy size ρ_0. This information is contained in the asymptotic form of $C_\chi(\rho_n,\sigma_T^2)$. Again, we split up the y integration to the region $y<1$ and $1<y<\infty$ and follow the previous analysis. After noting that I_1 in Eq. (13) will decrease with increasing σ_T^2 whereas I_2 approaches a constant value, we can write immediately for $\sigma_T^2 \gg 1$,

$$C_\chi = 1.48 \int_0^1 du\, \sigma_T^2(u) \int_0^\infty dy\, y^{-11/6} \times e^{-\beta/y^{5/6}} J_0\left[\left(\frac{4\pi y u}{1-u}\right)^{\frac{1}{2}} \rho_n\right]. \tag{25}$$

Again change variables to $q=\beta y^{-5/6}$; Eq. (25) then becomes

$$C_\chi = 1.77 \int_0^1 du \left(\frac{\sigma_T^2(u)}{\beta}\right) \int_0^\infty dq \times e^{-q} J_0\left\{\left(\frac{4\pi u}{1-u}\right)\left(\frac{\beta}{q}\right)^{\frac{3}{5}} \rho_n\right\}. \tag{26}$$

Finally, from the definition of β from Eq. (16), ρ_n from Eq. (3) and the definition of the lateral coherence length ρ_0 from Eq. (24), Eq. (26) takes the form

$$C_\chi = 0.42\alpha^{5/3} \int_0^1 du \int_0^\infty dq \times e^{-q} J_0\left\{\left(\frac{3.34u}{\alpha}\right) q^{-3/5} (\rho/\rho_0)\right\}. \tag{27}$$

The most-significant observation about Eq. (27) is that in this asymptotic form of the covariance function, the important scaling length is ρ_0 (in agreement with Ref. 1) and not the Fresnel length $(\lambda L)^{\frac{1}{2}}$.

To obtain the spatial structure in the scintillation pattern, i.e., the size of the pattern produced by the most-effective eddy ρ_0 as a function of normalized path position u, we compute the two-dimensional transform of Eq. (25).

$$F_\chi(\kappa_p) = 2\pi \int_0^\infty d\rho\, \rho J_0(\kappa_p \rho) C_\chi(\rho). \tag{28}$$

After changing variables to $r=3.34u/(\alpha q^{3/5}\rho_0)$ and noting the Bessel-function orthogonality condition,

$$\int_0^\infty d\rho\, \rho J_0(\kappa'\rho) J_0(\kappa\rho) = \frac{\delta(\kappa-\kappa')}{\kappa'}, \tag{29}$$

we see that $F_\chi(\kappa_p)$ becomes

$$F_\chi(\kappa_p) \sim \kappa_p^{-2} \int_0^1 du \left(\frac{u}{\kappa_p \rho_0}\right)^{5/3} \exp\left[-\left(\frac{3.34u}{\alpha \kappa_p \rho_0}\right)^{5/3}\right]. \tag{30}$$

Finally, we note that the largest contribution to F_χ is for $\kappa_p \sim u/\rho_0$. This implies that for $\sigma_T^2 \gg 1$ the most-effective eddy size ρ_0 produces a geometrically magnified pattern of size ρ_0/u at the receiver. The largest structure (covariance tail) will then originate from eddies at the transmitter end, and the small scale structure (initial decrease of the covariance) will be due to eddies at the receiver end.

A similar calculation on the first term involving I_1 following Eq. (25) to (30) yields the most-effective eddy size to be $[\lambda L u(1-u)]/\rho_0$ and the resultant pattern size as $[\lambda L(1-u)]/\rho_0$. The term that dominates is determined by the range of σ_T^2 as is shown in Eq. (19). The first term will dominate when $1 \lesssim \sigma_T^2 \lesssim 20$, as is shown by the data in Ref. 2. Full saturation, i.e., $\sigma_\chi^2 = 0.23$ occurs for $\sigma_T^2 \gtrsim 20$.

III. CONCLUSION

We have demonstrated the equivalence of the theories of Yura[1] and Clifford *et al.*[2]; that is, both theories predict an irradiance variance that saturates to a constant value for increasing values of σ_T^2. Furthermore, both theories predict identical amplitude correlation scales, and that, in the saturation regime, (i.e., for $\sigma_T^2 \gg 1$), the most-important turbulent eddies are those that have characteristic scale sizes of the order of the lateral coherence length of the optical wave. Thus, for example, the temporal power spectrum of the amplitude fluctuation that is implied from the results of the theory of Ref. 2 is equivalent to that which is obtained from Ref. 1 and is given explicitly in Ref. 7.

REFERENCES

[1] H. T. Yura, J. Opt. Soc. Am. **64**, 59 (1974).

[2] S. F. Clifford, G. R. Ochs, and R. S. Lawrence, J. Opt. Soc. Am. **64**, 148 (1974).

[3] V. I. Tatarskii, *The Effects of the Turbulent Atmosphere on Wave Propagation* (National Technical Information Service, U. S. Dept. of Commerce, Springfield, Va., 1971), Ch. 3.

[4] As is shown below, the main contribution to the y integral occurs for $y\ (\sigma_T^2)^{6/5} \gg 1$. Therefore, in calculating I_2, the Bessel function occurring in the expression for $f(y)$ can be neglected.

[5] The same asymptotic limit is also obtained for plane waves (assuming, of course, the same value for α).

[6] M. E. Gracheva, A. S. Gurvich, S. S. Kashkarov, and V. V. Pokasov, Akad. Nauk SSSR. Otd. Okean., Fiz., Atm. Geogr., Moscow (1973).

[7] H. T. Yura, J. Opt. Soc. Am. **64**, 357 (1974).

Atmospheric Technology, 94-99, Winter 1974-75.

Wind Measurement with Acoustic Doppler

D. W. Beran, NOAA

The signal received from sound scattered by the atmosphere contains two distinct characteristics that can be used to interpret the scattering medium. The first characteristic is the intensity of the signal. A companion article in this issue of *Atmospheric Technology* discusses ways in which scattered acoustic signal intensity can be used to study the atmosphere (Morris and Hall, "Remote Sensing of the Atmosphere by Sound"; see also Little, 1969). The second characteristic of the signal is its frequency. If the original transmitted carrier frequency is known, it can be compared with the returned signal frequency to determine a doppler shift. This doppler shift is primarily a function of the wind speed in the region where the scattering occurred, and through proper manipulation, can be converted to a measurement of that same wind speed.

Use of doppler information for measuring wind speeds represented one of the first successful attempts to derive quantitative data with the acoustic sounder (Kelton and Bricout, 1964). Earlier analysis of signal intensity led to qualitative representations of boundary layer structure. The striking detail shown by this technique was valuable for guiding other types of measurement systems and led to new insight and understanding of boundary layer processes; but quantitative information was limited to the height and time history of the events that were depicted.

Research during the past three years (Beran, 1971; Beran, Little, and Willmarth, 1971; and Beran and Clifford, 1972) has led to the development of acoustic doppler systems that are already being tested for such operational applications as low-level wind measurements at airports. While these sytems have not yet reached their ultimate development in terms of equipment sophistication, they are showing where refinements are needed and where physical limitations such as ambient background noise will prevent use of a system. This article traces the development of the acoustic doppler system from its beginning as a single-antenna instrument measuring only the vertical component of the wind to a multi-transmitter/receiver system used to measure a vertical profile of the horizontal wind. As a background to the history of this development, we should first consider the physics of sound scattering and its interaction with the doppler principle in the design of a doppler system.

Sound Scattering and the Doppler Principle

The theory of sound scattering by turbulent fluctuations in the atmosphere is adequately reported by Tatarskii (1971) and Monin (1961), and by Morris and Hall. For this reason, I will consider only those aspects of the scattering equation that are important to the design of a doppler system. In order to discuss scattering, however, it is helpful to understand the rudiments and application of the doppler principle.

Assume that we are dealing with a very simple acoustic system (see Fig. 1) that sends a sound pulse vertically into the atmosphere from a transmitter (T). The sound pulse is then scattered from some volume and arrives back at the receiver (R). If the scattering volume at point O is moving with a velocity, $\vec{V}$, the frequency, f_o, of the sound transmitted at T will be shifted to some new frequency, f_s, when it arrives at R. The difference between these frequencies, Δf, will be proportional to the velocity, $\vec{V}$. Expressing the transmitted frequency as wave vector, $\vec{K}_o$, and the scattered frequency, f_s, as wave vector, $\vec{K}_s$, we can write the difference frequency, or doppler shift, in vector form as

$$\Delta f = \frac{1}{2\pi}\left(\vec{K}_s - \vec{K}_o\right) \cdot \vec{V} \qquad (1)$$

Writing Eq. (1) in terms of the scattering angle, θ (see Morris and Hall), and the wavelength, λ_o, of the transmitted

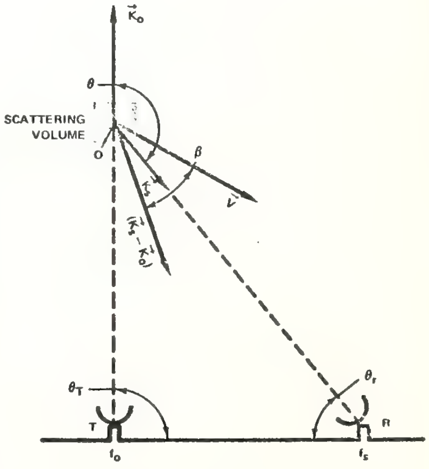

Fig. 1 Wave vector diagram showing the wind component measured by a doppler shift.

wave, and defining the angle between the total wind vector in the plane formed by the transmitter and receiver beams, we have

$$\Delta f = \frac{2V}{\lambda_o} \sin\left(\frac{\theta}{2}\right) \cos\beta \qquad (2)$$

where V cos β is now the magnitude of the wind resolved along vector, $\vec{K}_s$-$\vec{K}_o$. The direction of this doppler component is along the bisector of the angle formed by the lines TO and OR.

If λ_o is replaced by C/f_o where C is the speed of sound, the magnitude of the wind component that produced the observed doppler shift is

$$V \cos\beta = V' = \frac{C}{2 \sin \frac{\theta}{2}} \left[\frac{\Delta f}{f_o}\right] \qquad (3)$$

The diagram shown in Fig. 1 represents a bistatic system where the transmitter and receiver are separated. For the monostatic case (transmitter and receiver collocated) the vector ($\vec{K}_s$-$\vec{K}_o$) would simply rotate to the common line formed by the transmitter and receiver beams, and the doppler vector would be pointed radially along the collocated antenna beams. We also see from Eq. (2) that the magnitude of the doppler frequency shift is dependent on the sine of one-half the scattering angle θ, decreasing the observed shift at smaller scattering angles for a constant wind. Refraction effects from anomalous thermal and/or wind fields can produce errors in the measured wind (Georges and Clifford, 1972). Within ranges of less than 1 km, these errors for worst-case conditions are less than 5%.

In measuring the horizontal wind, we must settle for a non-horizontal component in the plane formed by the transmitter and receiver beams. Ideally, this component should be directed as near to the horizontal as possible. This implies that it would be best to employ a monostatic system with the antenna tilted at an elevation angle of around 45°. A bistatic system, where the measured component is along the bisector of the two antenna beams, with the receiver also tilted to 45°, would measure a doppler vector at 67.5° from the horizontal. On this basis alone, the choice of an optimum configuration seems clear; however, when the scattering characteristics are considered, the problem is less easily resolved.

In the backscatter direction (θ = 180°), the temperature fluctuations are the only effective scatterers. In all other directions, except at θ = 90° where no energy is scattered, the amount of sound scattered is a function of both temperature and wind fluctuations (see Morris and Hall). In practice, this means that for a given range, bistatic signals will be stronger than monostatic signals. In addition, the backscatter signal strength at various ranges is highly dependent on the thermal structure of the atmosphere, creating regions of strong echo intermixed with regions of weak or nonexistent signal. Scattering in other directions, where the wind fluctuations also contribute, is less structured and results in a more uniform scattering field. To achieve reasonably continuous wind measurements in both height and time, the bistatic configurations seem preferable.

The designer of an acoustic doppler system is faced with the dilemma of choosing between a tilted-beam monostatic system with its good doppler resolution angle but weak and intermittent signal, and a bistatic system with its generally good signal strength but poor doppler resolution angle. Much of the work described below has been directed toward resolving this question, and the test results help to clarify when and why each of the techniques should be used.

Doppler Experiments

The first attempt to measure winds aloft using the acoustic doppler principle was made with a vertically pointed monostatic system (Beran, Little, and Willmarth, 1971). Profiles of the vertical wind were determined by range-gating. The measurements were not compared with other wind sensors for validity; however, the continuity of the velocity field (see Fig. 2) indicated that the measurements were at least of the correct sense and that their magnitudes appeared reasonable.

Later the horizontal wind was measured with more elaborate equipment and compared with values from nearby anemometers (Beran and Clifford, 1972). Three separate and independent wind components were measured by three monostatic acoustic sounders, one pointed vertically and the other two located along orthogonal lines intersecting at the vertical antenna and tilted inward so the three antenna beams intersected at a point (see Fig. 3). Winds near this common volume were measured by the Boundary Layer Profiler (BLP) owned and operated by NCAR. Because of the intense sound reflection at a helium-air interface, the BLP could not be placed in the scattering volume; however, it was usually possible to keep the distance between the two measurement points (the BLP and the common scattering volume) to less than 100 m.

The acoustic system described above was operated in both the monostatic mode, where the three antennas used separate carrier frequencies to prevent cross talk, and in a bistatic mode, where only the vertical antenna was active, and the outlying antennas served as passive receivers. A comparison of the BLP winds and the doppler winds measured in the bistatic mode is shown in Fig. 4. These wind values were taken 200 m above the ground and have been filtered with a 2 - min time constant to eliminate variations that might have occurred as the result of the separation of the two measurement points.

These early experiments indicated that the winds at a point above the ground could be measured with either a monostatic or a bistatic system. Later work also revealed that the monostatic signal---expected to be weaker and less uniform---did not produce a continuous wind record in time.

The next step was to devise a method of measuring a vertical profile of the horizontal wind. Because of the difficulty of mechanically steering an acoustic antenna (noise from bearings and mechanical linkages is generally intolerable), a scheme using monostatic

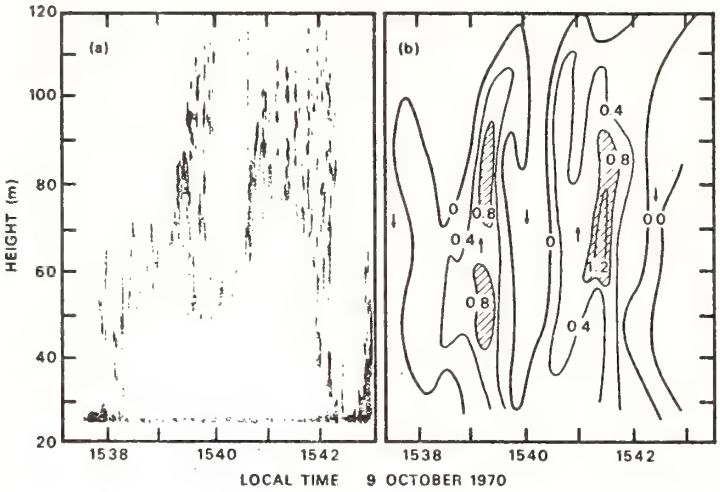

Fig. 2 Acoustic echoes (a) and doppler-derived vertical velocity field (b) during thermal plume activity. Contour interval is 0.4 m/sec, regions of velocity >0.8 m/sec are shaded, and arrows indicate direction of vertical component.

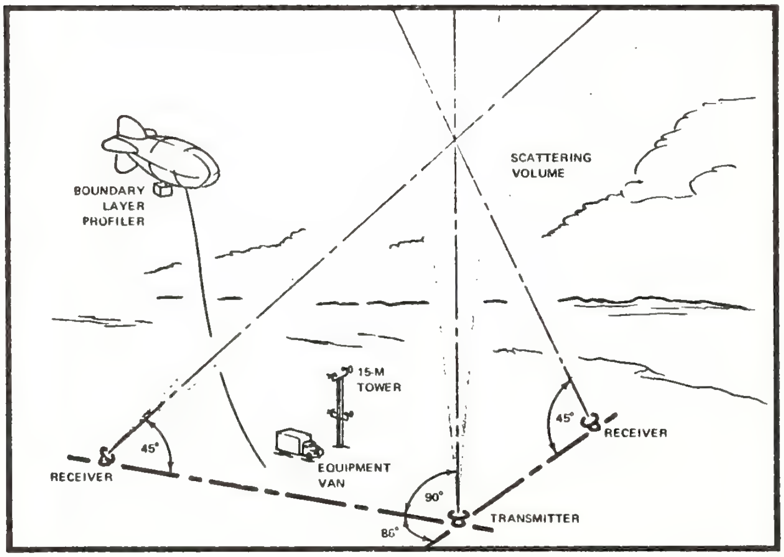

Fig. 3 Schematic of field setup for testing three-axis doppler wind technique.

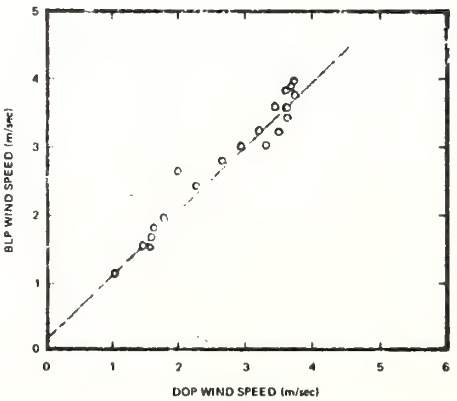

Fig. 4 Scatter diagram comparing wind measured by acoustic doppler (DOP) and the Boundary Layer Profiler (BLP). The correlation coefficient is r = 0.96 and the slope of the best-fit linear regression curve (solid line) is 0.95.

antennas in the configuration shown in Fig. 3 was tried. The monostatic signals from each of the three antennas were gated to produce three radial components at each of several altitudes. The three components were not from a common volume at altitudes other than at the point of intersection of the three beams. To compensate for this, the resulting doppler frequencies (radial components) were averaged for times long enough to make the assumption of horizontal homogeneity valid (usually about 2 min). The time-height history of the isotach field derived in this way was encouraging (see Fig. 5), but again, the weak monostatic signal made the technique useful only for the study of special events where strong thermal activity could be expected.

To achieve the strong and consistent signal necessary for continual measurement of the wind profile under a wide variety of conditions, it was necessary to employ the bistatic mode of operation. This could be done by using either fanned-beam receiving antennas, several pencil beams at different spacing or pointed in different directions, or a phased antenna that could be electronically steered. The first test of a bistatic system for measuring a vertical profile of the wind used unmodified receiving antennas spaced at various distances from the vertically pointed transmitter (see Fig. 6). The results of comparisons between the winds measured with this test setup and the same wind component measured by a slow-ascent radiosonde were very good (see Fig. 7). Later tests with a fanned beam indicated that the noise collected by the very wide beam was greater than could be tolerated.

One difficulty with the spaced-receiver configuration shown in Fig. 6 is the lack of signal at low elevations; there is no signal at scattering angles equal to 90°, and the intensity of signal near this scattering angle is very low. One solution was to add yet another receiving antenna near the transmitter; however, this only complicated the already difficult problem of switching between antennas as the signal progressed upward. A simpler solution involved using the outlying antennas in the monostatic mode during the dead period between the time when the original pulse was transmitted and the time when the scattered signal reached the first receiver. This required that only the lowest 200 m or so be covered by the monostatic mode. Despite this reduced range requirement, the monostatic portion of the pulse cycle was still found to be unacceptably inconsistent.

The latest test configuration employed two moderately wide-beamed receivers with a single main transmitter and smaller satellite transmitters located along the lines between the main transmitter and receivers (see Fig. 8). This configuration eliminated the need for switching between receiving antennas and retained the advantage of receiving bistatic signals at all elevations.

Operational Tests

A system funded by the Federal Aviation Administration used the multitransmitter configuration for operation at Stapleton International Airport in Denver, Colorado. Doppler wind profiles from this experiment have been compared with the local radiosonde winds. One such comparison is shown in Fig. 9. Operation of an acoustic system at an active airport site placed the system in one of the potentially most hostile environments. The intense noise generated by aircraft completely saturated the system, rendering it useless for periods of up to 1 or 2 min. Sophisticated data processing techniques were tested to determine if it is feasible to operate an acoustic system in this type of environment. Each range gate of each pulse was tested to determine if the signal intensity was high enough for

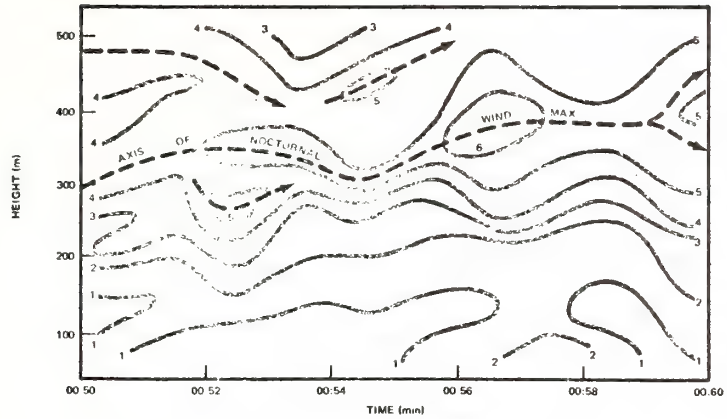

Fig. 5 Time section of isotachs for horizontal wind (in meters per second) under oscillating inversion. Winds were derived solely from acoustic doppler measurements, using three separate monostatic systems: one aimed vertically and the other two at 45°.

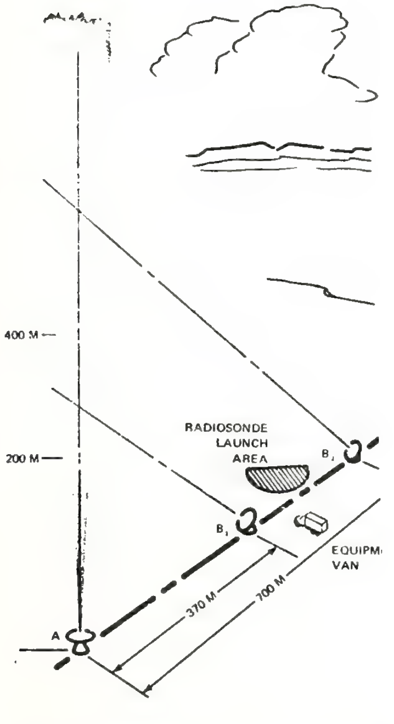

Fig. 6 Field setup used during tests of the bistatic configuration for measuring wind profiles. A is the transmitter; B_1 and B_2 are receivers.

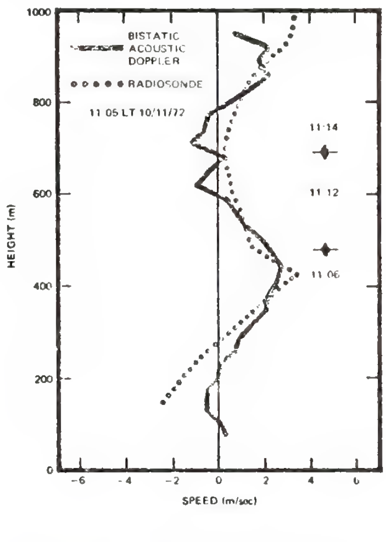

Fig. 7 Comparison of one wind component (221° azimuth) as measured by acoustic doppler and a slow-ascent radiosonde. The numbers along the right indicate the amount of time by which the doppler data were adjusted to compensate for the slow ascent rate of the radiosonde.

successful doppler tracking, the ambient background noise had not saturated the system, and the signal-to-noise (S/N) was within an acceptable range. If the data passed all of these tests, they were then averaged exponentially along with up to 5 min of previous "good" data to insure that spurious noise impulses that may have passed the tests were not given undue weight. The wind vectors were then calculated from the "cleansed" data.

These operational tests indicated that reliable wind measurements could be made even at an airport location. It was also clear that further development will be required to improve antenna design and side-lobe shielding. It appears that the optimum receiving-antenna system will consist of several rather narrow beams pointed at increasing elevation angles to form a fan shape. By progressively switching to beams at increasing elevation angles, the transmitted sound pulse can be tracked as it travels upward. The background noise collected by each of the narrow beams would, of course, be less than that which would be collected by a single fan beam covering the same vertical extent. The improved S/N should insure operation under most conditions.

Inclement weather in the form of strong surface winds and rain or hail is a limitation for the acoustic system. Eddies formed by strong winds, and hydrometeors striking the antenna face can both saturate the sensitive receivers. Because the receiving beams are pointed at an angle to the horizontal, a partial solution to these problems is to cover the antenna with a shelter to protect it from the direct impact of hydrometeors. In addition, this shelter can be constructed in the form of an underground bunker, with a level top conforming to the surrounding terrain and with the opening offset to allow the main antenna beam to project out at an angle. Reducing the size of the eddy-producing barriers minimizes the effect of strong surface winds. This type of antenna installation was used during the airport tests, but insufficient data were collected to determine its effectiveness.

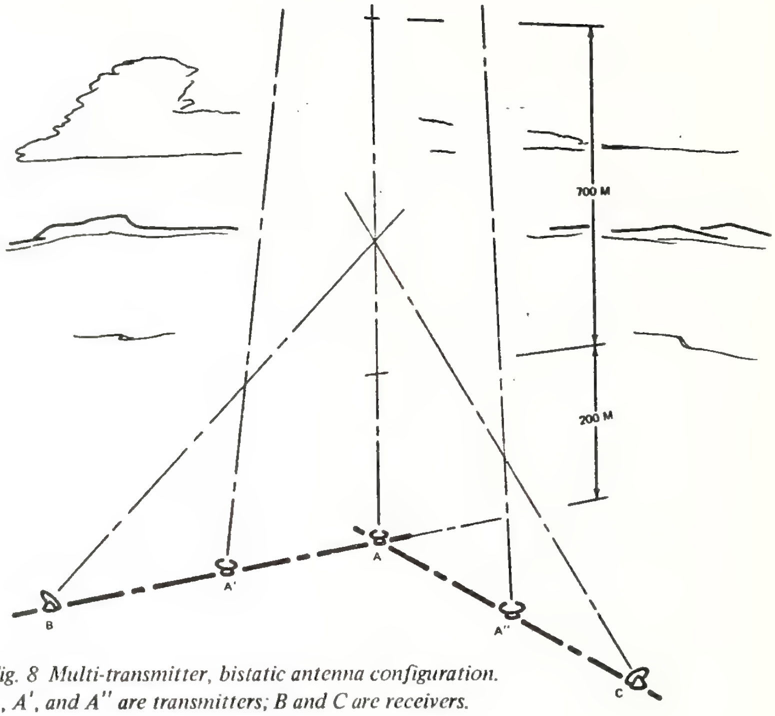

Fig. 8 Multi-transmitter, bistatic antenna configuration. A, A', and A'' are transmitters; B and C are receivers.

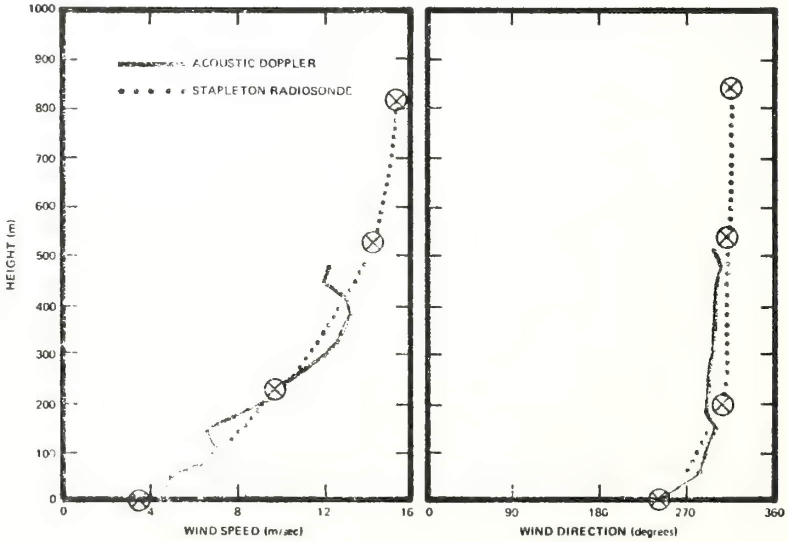

Fig. 9 Acoustic doppler wind profile (solid lines at 04:56). Stapleton Airport radiosonde winds (dashed lines) are superimposed for comparison.

It is clear that severe weather will render the system inoperative, even with the protective shelter; rain will be driven into the bunker openings, and the sound of rain impacting on the shelter may produce intolerable noise levels. Until testing is completed, the severity of these effects must remain an unknown.

A further limitation that has been observed, but not well documented, is an apparent rapid fall-off of both wind and temperature fluctuations above certain strong temperature inversions. This lack of turbulence produces signal fading; during one test involving some 300 hr of data, the signal above 500 m was found to be unreliable about 10% of the time. This effect will, of course, be a function of the season, location, and diurnal cycle of low-level stability.

Conclusions

The need exists for making continual real-time measurements of the wind profile with high spatial and temporal resolution. Such wind profiles are essential for providing pilots with a warning of hazardous low-level wind shears and as input to wake-vortex motion prediction models. The need for better wind information in mesoscale monitoring and forecasting problems, especially relating to urban air pollution, is clear and will increase as our cities become more congested and polluted.

The acoustic doppler wind-sensing technique appears to be an answer to these needs. It is still based on relatively new experimental equipment that will undoubtedly undergo many evolutionary improvements in the near future. Its limitations are recognized, if not calibrated. Many existing problems can be removed by improved design and engineering, but there are those, such as inclement weather and lack of natural tracers above strong inversions, which will remain as weaknesses to the operational application of this device. It remains to be determined just how severe these limitations will be.

For specific research applications where continual uninterrupted operation is not essential, the acoustic doppler system holds the promise of a valuable measurement tool that can provide wind information impossible to collect by contemporary methods. Its use for this type of research has already been demonstrated, and it will no doubt find increasing application as the system is refined and developed.

References

Beran, D. W., 1971: Acoustics: A new approach for monitoring the environment near airports. *J. Aircraft 8 (11)*, 934 - 936.

------, C. G. Little, and B. C. Willmarth, 1971: Acoustic doppler measurements of vertical velocities in the atmosphere. *Nature 230*, 160 - 162.

------, and S. F. Clifford, 1972: Acoustic doppler measurements of the total wind vector. *Proceedings of the Second Symposium on Meteorological Observations and Instrumentation*, American Meteorological Society, Boston, Massachusetts, 100 - 109.

Georges, T. M., and S. F. Clifford, 1972: Acoustic sounding in a refracting atmosphere. *J. Acoust. Soc. Am. 52*, 1397 - 1405.

Kelton, G., and P. Bricout, 1964: Wind velocity measurements using sonic techniques. *Bull. Amer. Meteor. Soc. 45*, 571 - 580.

Little, C. G., 1969: Acoustic methods for the remote probing of the lower atmosphere. *Proceedings of the IEEE 57 (4)*, 571 - 578.

Monin, A. S., 1961: Characteristics of the scattering of sound in a turbulent atmosphere. *Akust. Zh. 7*, 457 - 461 (English translation in *Sov. Phys. Acoust. 7*, 370 - 373).

Tatarskii, V. I., 1971: *The Effects of the Turbulent Atmosphere on Wave Propagation.* Springfield, Virginia, U.S. Dept. of Commerce, National Technical Information Service, 472 pp. ●

D. W. Beran is affiliated with the Wave Propagation Laboratory of the NOAA Environmental Research Laboratories in Boulder, Colorado. He received his B.S. degree from Utah State University in 1958, an M.S. in meteorology from Colorado State University in 1966, and his Ph.D. in meteorology from the University of Melbourne, Australia, in 1970. He has worked as a meteorologist for the U.S. Air Force (1959-1962) and for the Martin Marietta Corp. (1962-1964), and as a consulting meteorologist for Allied Research Associates (1966-1967). As a Senior Research Fellow at the University of Melbourne, he worked on the development of an acoustic sounder; at NOAA he has been involved in the development of an acoustic doppler system. Beran is a member of the American Meteorological Society, the Acoustical Society of America, and Sigma Xi.

Reprinted from the JOURNAL OF FORESTRY
Vol. 73, No. 10 October 1975

Acoustic Echo Sounding Systems:

their potential in forest fire control and research

D. W. Beran

ABSTRACT—Stability of the atmosphere at different levels is one important factor affecting the behavior of forest fires, but the measurement of stability and other atmospheric phenomena is complex and difficult. The acoustic echo sounder shows promise for measuring these parameters and for monitoring the pattern of air flow superimposed on the ambient atmosphere by an intense heat source, such as a forest fire. It is particularly well suited for monitoring the depth of stable inversion layers and for providing a qualitative indication of the degree of stability in the lower atmosphere. The addition of a Doppler capability to acoustic systems has also made it possible to sense remotely a vertical profile of the total wind vector to heights of 500 m.

The behavior of forest fires, whether wildfires or prescribed fires, is affected principally by the combined effects of fuel, slope, and the atmosphere. Fuels and slope are highly visible, and characteristics are relatively easy to measure. Some elements of the atmosphere are fairly easy to measure, at least near ground-level: direction and speed of the wind, air temperature, and relative humidity. But other important characteristics of the atmosphere frequently are more difficult for the average fire manager to measure: vertical motion of the air from ground level to several thousand feet above the fire, the elevation of inversion layers, changes in wind speed and direction at different elevations, and air turbulence caused by differential heating of the earth's surface and by the forest fire's rising column of heated air (*6*).

The acoustic echo sounder is a relatively new device that shows promise for measuring several of these atmospheric phenomena. Thermal plumes, low-level inversions, and wind profiles (*2, 3, 8*) are among the phenomena which this device has already successfully monitored. The close association between boundary-layer meteorology and the dynamics of forest fires suggests the potential use of an acoustic sounder for applications in forest fire meteorology and possibly as an aid in fire control. The purpose of this paper is to explore that potential.

How the Acoustic Sounder Operates

When a sound wave is transmitted into the atmosphere, several things happen. It is absorbed as a function of the atmospheric temperature and humidity, it spreads as a function of distance traveled, and it is scattered by the naturally occurring turbulence in the atmosphere (*5*). Scattering of a sound wave in a backward direction (180° from the direction of the original transmitted wave) is caused solely by fluctuations in ambient temperature (*7*). Scattering in all other directions, except at 90°, is a function of both turbulent wind and temperature fluctuations.

The acoustic echo sounder, when operated in its simplest configuration, relies on the backscattered sound from the fluctuations in temperature. This configuration, called monostatic (*Figure 1*), uses a single antenna which first transmits a sound pulse and then, switched to a passive receive mode, collects the backscattered sound. Variations in the intensity of the acoustic returns, which are directly related to Richardson's number or the intensity of atmospheric

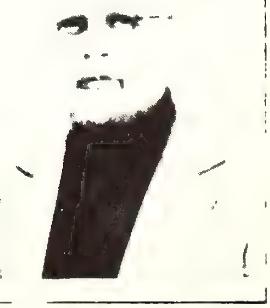

THE AUTHOR—D. W. Ber
is supervisory research met
orologist at the Wave Pro
agation Laboratory, NOA
Environmental Research La
oratories, Boulder, Colorad

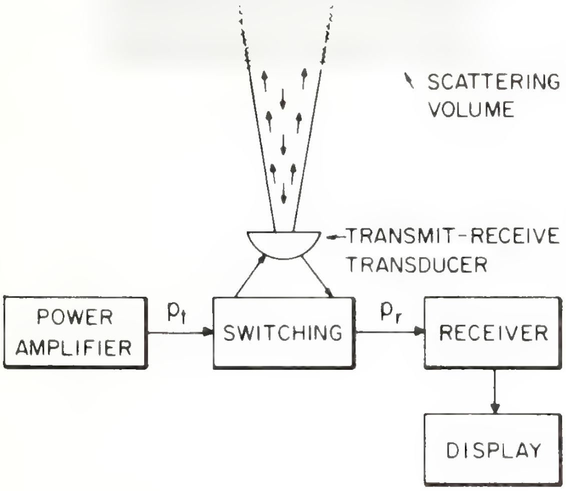

Figure 1. Components of a basic monostatic acoustic sounder.

turbulence along the path of the original pulse, are recorded as a function of time. This information can then be easily converted, through the use of the speed of sound, to the distance between the receiver and a particular level in the atmosphere where the transmitted sound wave was scattered.

If the transmitter and receiver are separated (bistatic configuration), sound scattered from fluctuations in wind can also be received. In general, the records from a monostatic configuration give a detailed picture of the thermal structure in the atmosphere while the bistatic system, having the added scattering from the wind, tends to give a more uniform distribution of returns. This difference in the returns from the two configurations can be seen by comparing *Figures 2 and 3* which illustrate, respectively, records taken with monostatic and bistatic systems.

Records from a monostatic system can be correlated with the thermal structure of the boundary layer. Dark regions (strong returns) indicate either very stable or unstable lapse rates of atmospheric temperature, while white regions (weak returns) indicate neutral stability. A comparison between a radiosonde temperature profile and a sounder record is shown in *Figure 4*. A qualitative indication of the boundary layer stability can be gained from the monostatic sounder records. For example, *Figure 5* shows the transition from stable air (the region with horizontal stratification) to unstable (the region characterized by vertically oriented dark areas).

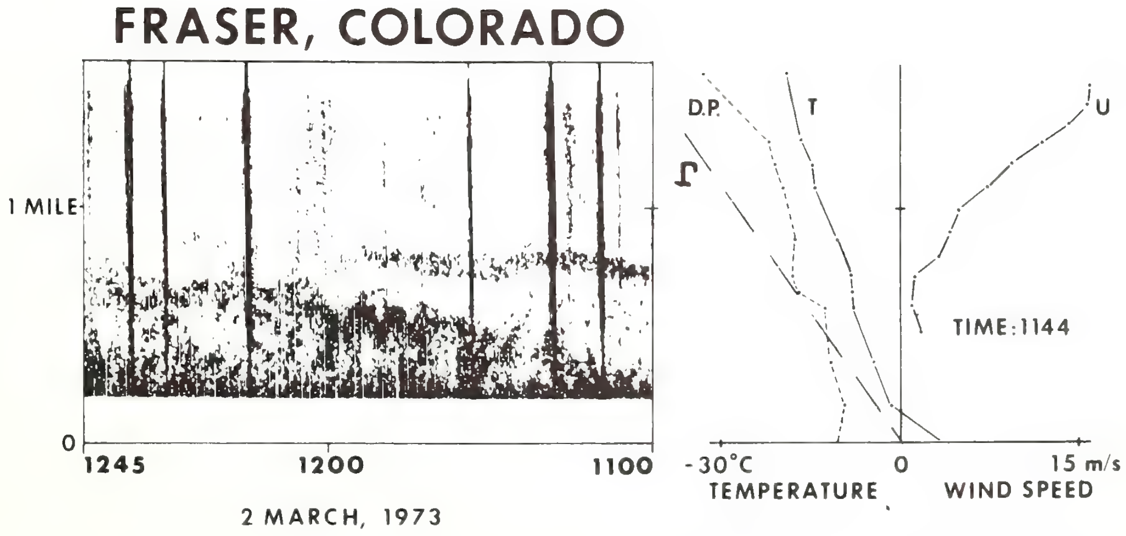

Figure 2. Facsimile record taken by a vertically pointed monostatic acoustic sounder. The temperature dewpoint and wind traces on the right were taken by a radiosonde launched some 5 miles from the sounder site.

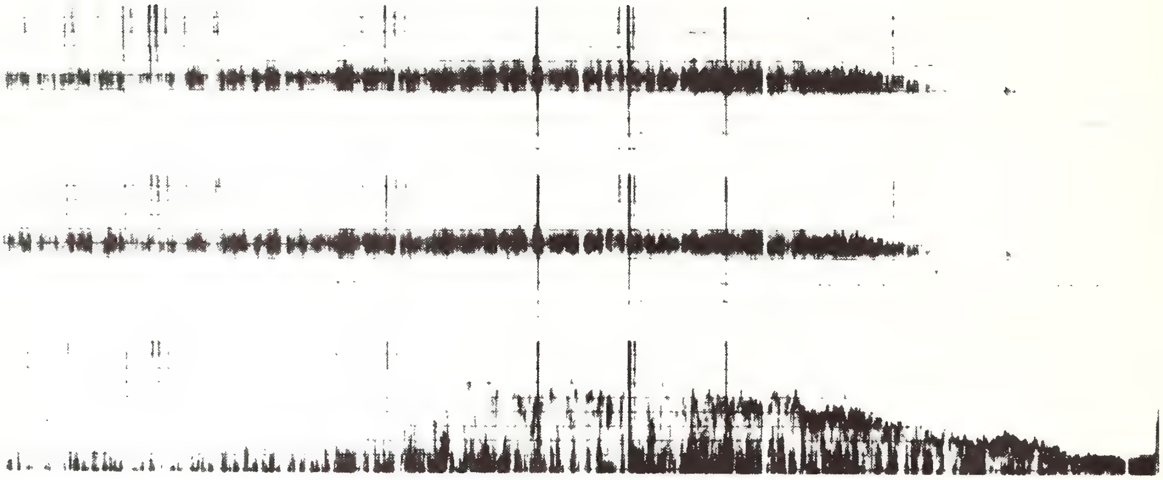

Figure 3. Facsimile record taken by a bistatic sounder (top and middle trace). The bottom trace is a monostatic record from the same region of the atmosphere. Note the lack of detail and more continuous record produced by the bistatic system.

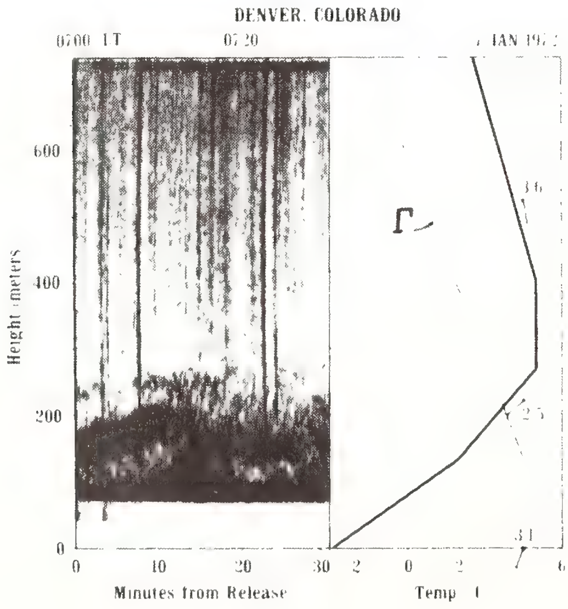

Figure 4. Comparison of a monostatic sounder record with a radiosonde temperature profile. Radiosonde-derived winds are shown by arrows (north is up). Speeds are in m/s.

The intensity of the scattered signal is used to show the details of the thermal structure and to infer the stability. The target or scattering volume which produces this signal is moving with the ambient wind. This motion produces a Doppler shift between the transmitted frequency and the frequency of the returned signal. This Doppler shift can be converted to that component of the wind velocity which is along the transmitted beam for a monostatic system (*3*). An example of vertical velocities derived from acoustic Doppler information is shown in *Figure 6*. The left side of *Figure 6* shows the facsimile record generated by thermal plumes; on the right is the Doppler-derived vertical velocity field associated with these thermal plumes.

A single monostatic system can measure (by gating) the profile of only one wind component. If three monostatic systems are properly arranged, a profile of the total wind vector can be measured (*1*). One such configuration which has been tested is shown in *Figure 7*. A comparison of the winds measured at the intersection of the three beams with an anemometer suspended from a kytoon is shown in *Figure 8*.

Because monostatic systems are well suited for detecting thermal structure and do not receive uniform returns in all regions within their range, they are not optimum for measuring the entire wind profile. Gaps in the wind record can occur in regions of neutral air stability. This problem can be overcome by adapting the bistatic configuration for wind measurements (*Figure 9*). Transmitters at points A, A′ and A″ send sound pulses upward through the beams generated by receivers at point B and C in *Figure 9*. The sound is scattered into the receiver beams, and wind-induced

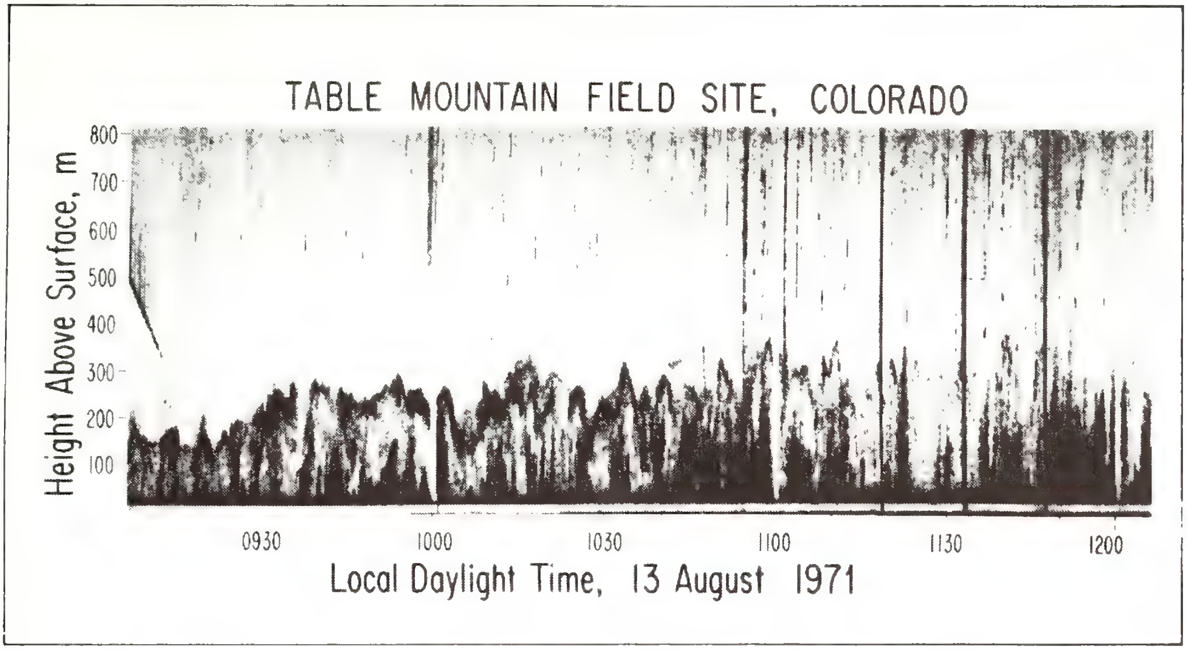

Figure 5. Monostatic sounder record showing the transition of the boundary layer from stable to unstable. The inversion is completely broken up by 1130.

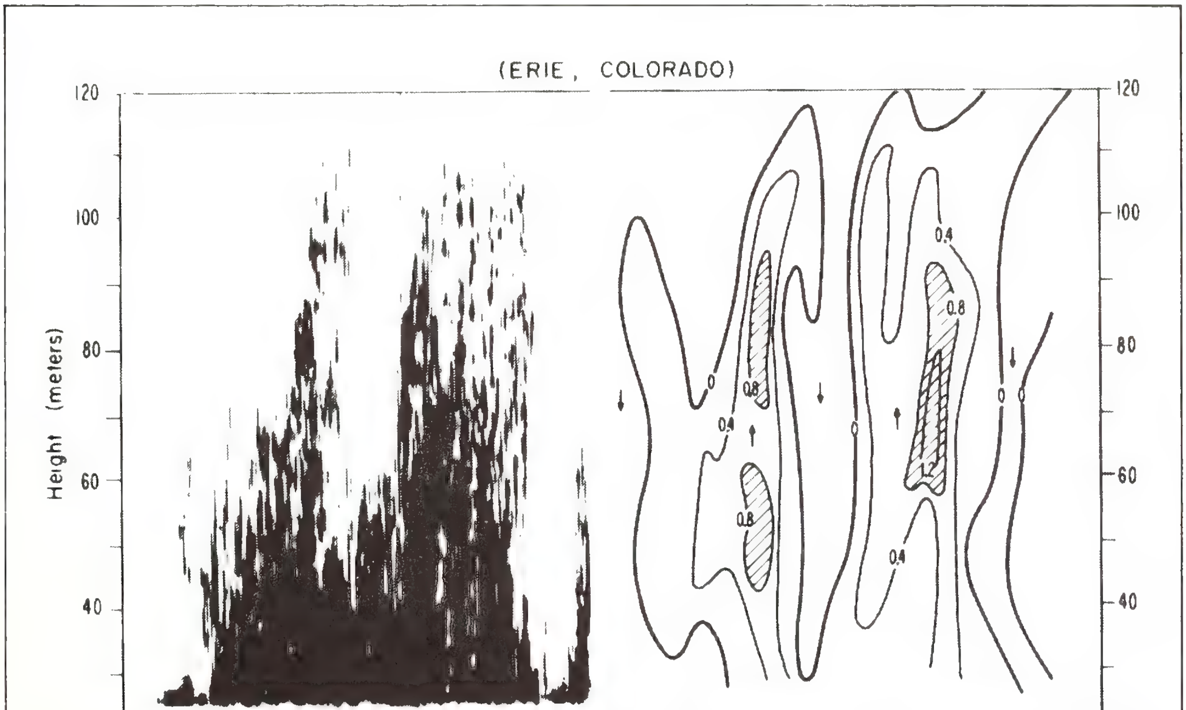

Figure 6. Doppler derived vertical wind field (m/s) taken during the thermal plume event shown on the left.

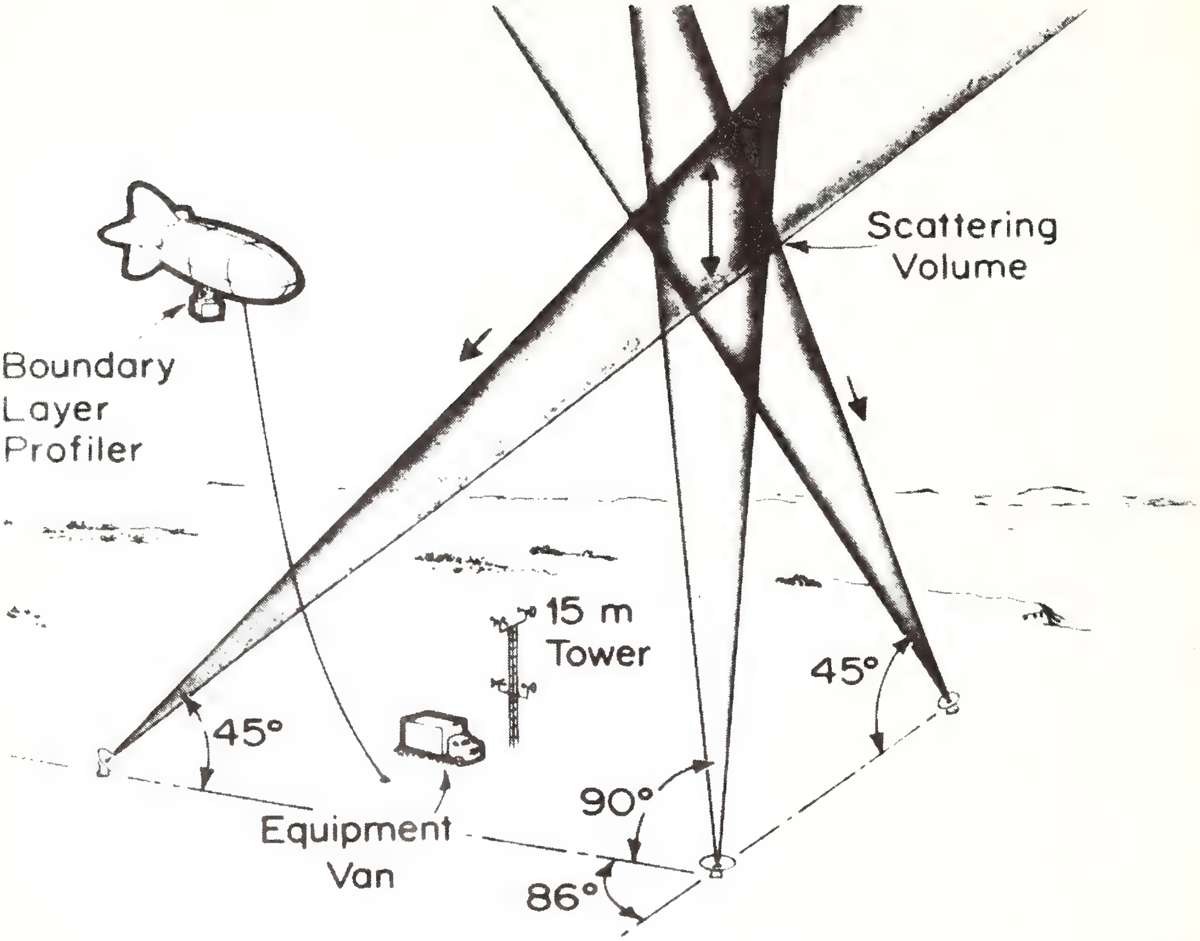

Figure 7. Field setup used for testing a three-axis acoustic Doppler system. An anemometer was suspended from the Boundary Layer Profiler (BLP) and used to check the winds measured by the Doppler system.

motion of the scattering volume is detected as a Doppler shift at B and C. By time-gating, the profile of Doppler shift (wind speed) can be determined. Tests have shown that the bistatic configuration solves the problem of non-uniform tracers; however, the measured wind component is along the bisector of the angle formed at the intersection of the transmitted and received beams. This vector is directed at an angle that is always closer to the vertical than the vector from a monostatic antenna having a similar tilt angle. This means that the horizontal wind is slightly more difficult to resolve from the bistatically measured component than it would be from a monostatically derived component. Despite this difficulty, the bistatic configuration has proved to be superior for measuring wind profiles on a continual basis. When gaps in the wind record can be tolerated, as with observations of a particular phenomenon such as the velocity in a smoke plume, the monostatic configurations can be equally successful.

Multiple antennas, arranged so that lines connecting the antennas form a closed loop, have been used to measure yet another meteorological variable, vorticity (*4*). Sound is transmitted and received through the

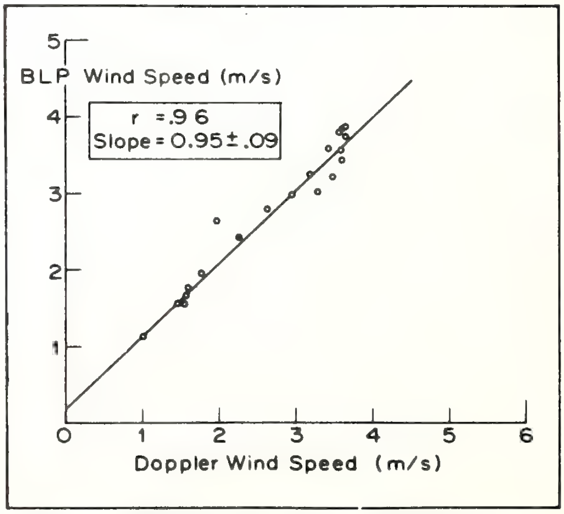

Figure 8. Scatter diagram comparing winds measured by acoustic Doppler (DOP) and the Boundary Layer Profile (BLP). Correlation coefficient r = 0.96 and the slope of the best fit linear regression curve (solid line) is 0.95.

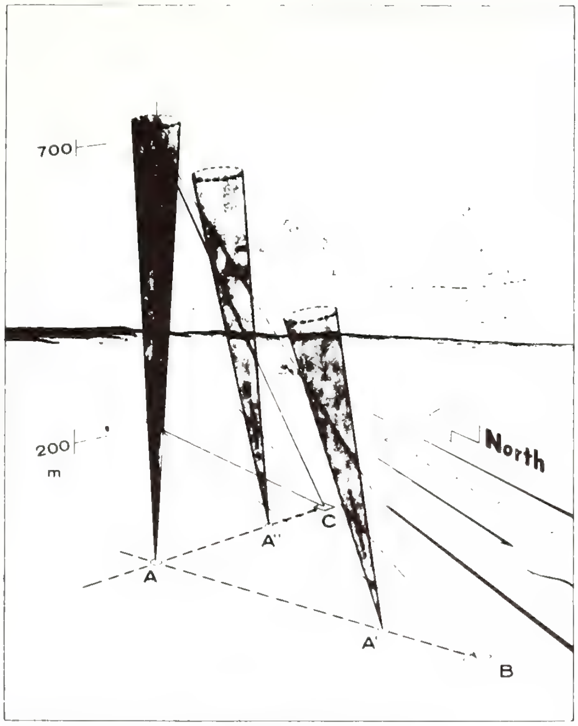

Figure 9. Bistatic acoustic Doppler configuration used for airport tests. Antennas at A, A' and A'' were active transmitters. The antennas at B and C were passive receivers[8].

sidelobes of even the best practical antennas. By measuring the transit time of the sound between adjacent antennas in both directions, the component of wind along this path can be determined. For a configuration such as that shown in *Figure 10*, this wind information provides the necessary input for calculating the circulation or vorticity of the region enclosed by the antennas. For example, if the distance, L_1, between the points A and B is known and the transit time of the sound pulse from A to B, t_{AB}, and the transit time from B to A, t_{BA}, can be determined, the wind velocity along the line from A to B is:

$$V_{AB} = L_1 \left(\frac{1}{t_{AB}} - \frac{1}{t_{BA}} \right)$$

This method has been used to calculate the vorticity associated with thermal plumes (*Figure 11*).

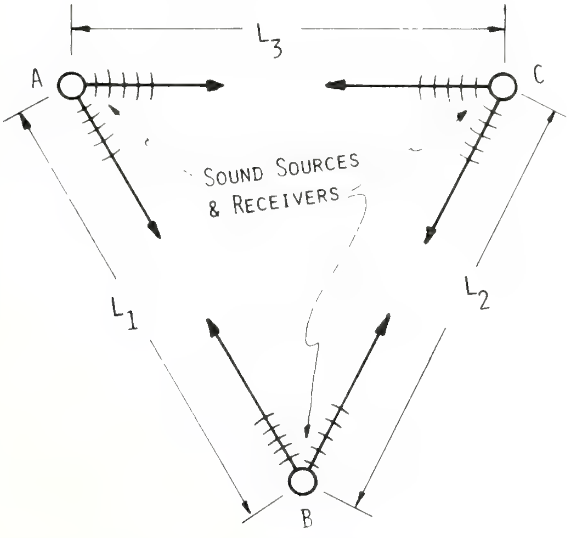

Figure 10. Schematic layout of sound sources and receivers used to measure the wind along the path AB, BC, and CB, which in turn is used to derive the vorticity.

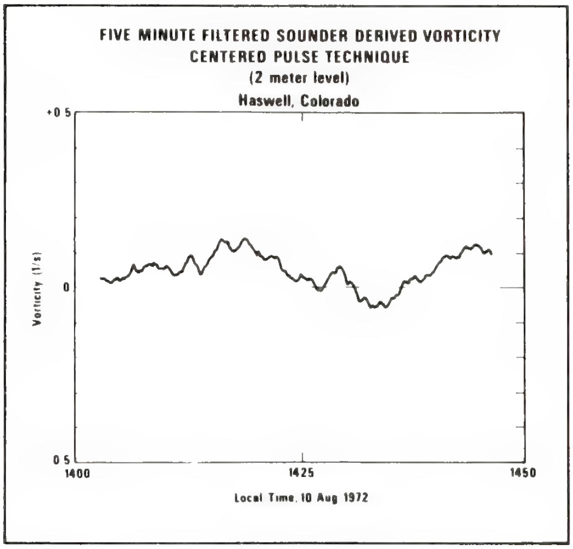

Figure 11. Record of vorticity measurements made with an acoustic triangle similar to that shown in Figure 10[6].

Applications to Fire Meteorology

The relevant question now is: How can these demonstrated capabilities of the acoustic sounder be applied to the study and application of forest fire meteorology? There are several possibilities, all related to air flow, which could be tested on wildfires or controlled burns.

First, the acoustic sounder could monitor air stability, which affects the direction, speed, and turbulence of air flow, and hence affects fire behavior. Continual monitoring of the boundary layer stability is possible with a simple monostatic acoustic sounder. The gross stability can be determined not from a temperature profile, but from the pattern observed on a facsimile record. These patterns provide an excellent indication of the state of the atmosphere. The different appearance of records during stable and unstable conditions is clearly discernable and cannot be mistaken. The degree of stability under stable conditions is somewhat more difficult to ascertain, but the intensity of convective activity, the more important parameter, is closely related to the size of the convective elements observed in the record. The actual temperature profile cannot be determined with an acoustic sounder; however, it appears quite feasible to classify the various patterns that can be seen in the record with the degree of air stability. These results differ from those obtained from use of a radiosonde; a radiosonde permits recording and plotting the temperature profile, and then obtaining a quantitative value of air stability. From the fire manager's viewpoint, it would seem that the real-time, continual output of *qualitative* information about air stability in an easily usable form could outweigh the disadvantage of not having a *quantitative* value for that parameter.

Present techniques of data transmission also make it feasible to locate an acoustic sounder at a remote site where it could operate for extended periods of time with only occasional visits for routine maintenance. Data from several acoustic sounders, located so as to give good coverage of the stability over a wide region, could be transmitted to a recorder at a convenient, central location.

Second, the acoustic sounder could sense the wind profile to heights of several hundred meters. As far as transmission of data is concerned, this type of installation could be just as feasible as the simple single-axis monostatic system. The more complex bistatic multiple-antenna system and the need for an on-line computer to process the Doppler information would, of course, make such installations more costly.

Third, the acoustic sounder could be used for remotely measuring the dynamics of air flow in and around a fire. For example, the vertical velocity of convective air flow in the smoke plume of a fire is one parameter which should be easy to measure. The intense heat from the fire would produce temperature fluctuations (the traceable parameter) in the smoke plume that are far in excess of any that would result from solar heating of the earth's surface. Because of this more intense thermal activity, it is reasonable to expect that the present range of simple monostatic systems, on the order of several hundred meters, could be extended to a kilometer or more. With this capability three or more monostatic sounders could be positioned around the perimeter of the fire with their beams directed inward to a point within the smoke plume (*Figure 12*). The Doppler shift derived from these sounders would then provide the information needed to determine the total velocity vector of air flow at points above the fire.

The indraft of air into a fire at low levels, which markedly affects the fire's intensity, also could be measured, assuming the absence of severe ray bending due to heated air. With antennas positioned around the fire, as shown in *Figure 12*, it would be possible to use sidelobe leakage of the sound pulses along the direct line of sight between adjacent antennas to measure the airflow. These measurements could then be used to determine the fire's effect on the ambient vorticity field.

Potential Problems

To provide a balanced picture about the possible use of acoustic sounders to measure forest fire meteorology, a few statements concerning the unknowns are in order. Acoustic sounders now in operation work in the audible frequency range. The noise generated by an intense fire therefore could cause the signal-to-noise ratio to reach unacceptable levels. I am not aware of published data about sound-level measurements that have been made in the vicinity of intense fires. I would recommend that if such measurements have not been made, they should be one of the first steps taken before considering an acoustic system for this application. Techniques for suppressing high-level noise that might be collected in the antenna sidelobes have been developed for use at airports, in urban regions, and onboard ships. The same techniques could be adapted to suppress the noise of a fire at the antenna.

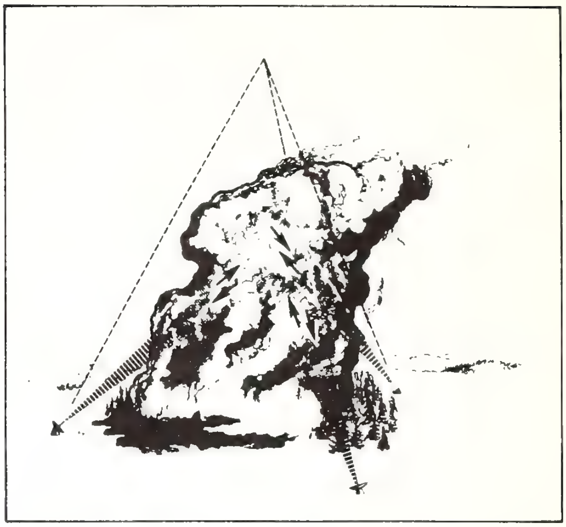

Figure 12. Artist's concept of how acoustic sounders might be used to measure the velocities in the smoke plume from a controlled fire.

Strong surface winds (above 20 knots) can also have a detrimental effect on the operation of a sounder. Again, careful attention to the preparation of shielding for the antenna and transducer can lessen this problem; however, surface winds remain an important consideration in site selection.

In summary, acoustic echo sounding appears to have several remote sensing applications which could benefit both operational and experimental aspects of forest fire meteorology. Doppler radar has been used to make smoke plume velocity measurements. With this exception, most fire-related measurements of plume velocity and vorticity are difficult to make with other contemporary techniques. Although the sounder cannot make absolute temperature measurements, its unique ability to provide continually a qualitative indication of atmospheric stability at a remote site could prove valuable for fire control measures. ■

Literature Cited

1. Beran, D. W. 1974. Remote sensing wind and wind shear systems. Report No. FAA-RD-74-3, Dep. Transportation, FAA Systems Res. and Development Serv., Washington, D. C. 115 pp.
2. Beran, D. W., and S. F. Clifford. 1972. Acoustic Doppler measurements of the total wind vector. Proceedings 2d Symp. on Meteorological Observations and Instrumentation. Symp. March 27-30, 1972. San Diego, Calif. Amer. Meteorol. Soc., Boston, Mass. 100-110.
3. Beran, D. W., C. G. Little, and B. C. Willmarth. 1971. Acoustic Doppler measurements of vertical velocities in the atmosphere. Nature *230*: 160-162.
4. Gaynor, J., F. F. Hall, Jr., J. G. Fotinger, and G. R. Ochs. Measurement of vorticity in the surface layer using an acoustic echo sounder array. (Submitted to JAM, 1975).
5. Little, C. G. 1969. Acoustic methods for the remote probing of the lower atmosphere. Proc. IEEE 57: 571-578.
6. Schroeder, M. J., and C. C. Buck. 1970. Fire weather: a guide for application of meteorological information to forest fire control operations. USDA Forest Serv., Agri. Handb. 360. 229 pp.
7. Tatarskii, V. I. 1971. The effects of the turbulent atmosphere on wave propagation (Engl. Trans. NOAA and NSF TT68-50464). Israel Program for Scientific Translations, Jerusalem. 472 pp.
8. Wycoff, R. J., D. W. Beran, and F. F. Hall, Jr. 1973. A comparison of the low-level radiosonde and the acoustic echo sounder for monitoring atmospheric stability. J. Appl. Meteorol. *12*: 1196-1204.

Bulletin of the American Meteorological Society 55, 1097-1105, September 1974.

remote sensing for air pollution meteorology

D. W. Beran and F. F. Hall, Jr.
Wave Propagation Laboratory
NOAA Environmental Research Laboratories
Boulder, Colo 80302

Abstract

The application of ground-based remote-sensing systems for monitoring those meteorological parameters of importance in urban air pollution is discussed. Typical system considerations include an analysis of site characteristics and sensor location. Examples of how remote-sensing systems might be applied to air pollution meteorology are given.

1. Introduction

This paper deals with the use of ground-based remote-sensing devices for monitoring urban meteorological parameters; however, we first consider the broader area of air pollution to define a framework within which the optimum remote-sensing system must function. For any urban region, we can equate the quality of the air at a given time to a large number of controlling factors, some constant or only slowly changing, as listed. *Constant controls:* local and surrounding terrain; type of ground cover; climatology; location and type of pollution sources; political boundaries and regulations; demography; total effluent; types of effluent.

The items presented above must be assessed periodically to determine if significant changes may have altered the general pattern over periods of months or years. There is a second set of controls, listed below, which varies from day-to-day and even from hour-to-hour. Intelligent air quality control decisions can only come about through effective real-time monitoring and accurate short-term prediction of these variables. *Variable controls:* time distribution of emissions; synoptic weather pattern; mesoscale flow pattern; inversion topography and depth; low level stability.

The controls given in the second list are those where sensors, both *in situ* and remote, are of most importance. Two classes of sensors are required: those designed to observe and classify the actual pollutants, and those used to measure the geophysical parameters that control the distribution of pollutants regardless of the type of effluent. Devices that only sense pollutants will not be dealt with here, although it should be noted that such instruments could be used as detectors of meteorological variables simply by employing the identifiable pollutants as tracers.

2. Air pollution meteorology

Most pollution-forecasting techniques are based on, and limited by, the available observations. These data typically consist of twice daily radiosonde profiles of the temperature, humidity, and wind. In addition, hourly observations of such surface parameters as pressure, wind, temperature, humidity, visibility, and cloud cover are available. Historically, these observations have been made in support of aviation and quite naturally are taken at or near an airport. As such, they may be totally unrepresentative of the urban region, perhaps several miles away. They have served well as input to forecasts of synoptic-scale motions, the primary need of aviation, but are not adequate for mesoscale urban forecasts.

Two meteorological parameters are of primary importance in controlling the level of pollution in a city. For a given set of constant controls, the level of pollution will depend on the vertical variation of temperature and the direction and strength of the low level winds (Neiburger, 1969). Present observations usually provide this type of information at only a single location and only twice per day.

The optimum rate for obtaining the mesoscale meteorological data is in part dependent on the particular parameter being measured and how it is to be used. In general, the data rate should not be so great as to clog the system with unnecessary detail, but should be rapid enough to depict significant changes taking place within the urban complex. For example, such changes as the shift from land to sea breeze, the onset or cessation of drainage winds, and the time of an inversion breakup are important for monitoring and predicting where, and how severe, pollution conditions will be. This time frame would require observations on the order of once every 10 to 20 min. The optimum density of observing points again depends on the phenomena to be observed and local terrain peculiarities which might alter or modify the urban flow pattern.

In considering remote sensors, the criterion for both time and spatial scales must be viewed in a new light. An advantage of many remote-sensing devices is their ability to rapidly scan large regions in three dimensions. Others can provide line integrals of certain parameters, giving spatially-averaged values that may be nearer to the desired measurement than a time average from a single sensor. This difference in the output of remote sensors must be a primary concern in the design of a system for monitoring the urban environment and should result in a concept other than the commonly proposed grid of sensors.

Until now it has been assumed that the classical forecasting techniques employing only the temperature and wind field would be used to make urban mesoscale forecasts. While remote-sensing devices have demonstrated the ability to measure basic parameters (temperature and wind), it should be noted that other, perhaps more valuable, information is contained in the first-order output of the sensor. For example, one of the more common products of a remote sensor is a range-dependent returned signal intensity or frequency, which is used to derive temperature or wind speed. It is conceivable that the required information for providing a forecast of future pollution concentrations is contained in the more rudimentary sensor output, and its conversion to classical meteorological variables is not always needed. Careful planning and close cooperation between developer and user will be required to use these potential resources. It is equally clear that remote sensor development should include research into new ways in which the remote sensor data can be used. This means going beyond mere speculation concerning their potential and actually developing and testing new forecasting techniques.

3. Methods of remote sensing

Recent publications (Derr and Little, 1970; Little, 1972, 1973; Derr, 1972) have dealt with the status of ground-based remote sensing. We shall borrow from these reports, which detail the many advantages of remote sensing, updating where necessary to give a brief overview of the field.

It is valid to ask why remote sensing should be used in place of, or in support of, conventional *in situ* sensors. Cost of a particular remote-sensing instrument can be high, especially when compared with a single *in situ* device. However, a more realistic analysis would compare the cost of the total number of *in situ* sensors with the cost of a remote sensor that would be required to meet the measurement objectives.

Assessment of the capability of various remote-sensing devices is complicated by the wide range of possible measurements. The *in situ* sensor is capable of, at best, a one dimensional measurement (recognizing that the atmosphere advects the measured variable past the sensor) while remote sensors have the powerful capability of multidimensional observations. This point is treated by Little (1972) in his listing of the range of measurements that are possible, going from a simple line integral to the determination of flux.

Because our primary objective in this discussion is to relate ground-based remote-sensing instruments to problems of air pollution meteorology, it would be inefficient for us to go into a detailed discussion of all types of ground-based remote-sensing devices. Rather, we shall select instruments that appear to have the proper characteristics based on our understanding of what is needed for the urban or mesoscale forecasting/monitoring problem.

4. Sensors of temperature profiles or static stability

a. Microwave radiometry

Passive, ground-based radiometers can measure thermal emission of the atmosphere by operating in any frequency band where gaseous constituents are strongly absorbing. An example is the operation of microwave radiometers in the 50–60 GHz oxygen band. The ability of such radiometers to measure quite accurately the temperature profile to heights of several kilometers has been shown (Westwater, 1972). They can also be used to determine the mixing-layer depth, discussed later (Anway, 1970).

Sophisticated data processing, involving inversion of the radiative transfer equation, is required to determine profiles up to and through ground-based inversions. Elevated temperature inversions are, however, usually smoothed over and not clearly defined. In addition, the presence of clouds in the field of view can create errors in the temperature profiles.

b. Laser temperature measurements

By measuring the ground level atmospheric pressure at a laser site and assuming that the hydrostatic equation can be used to predict pressure at greater heights, it has been shown that atmospheric temperature profiles can be directly obtained from the Raman backscatter from nitrogen (Strauch *et al.*, 1971). Another Raman method senses temperature by measuring the population of excited molecular states (Cooney, 1972).

A second possibility of temperature probing with lasers, using the distribution in the backscattered on-frequency spectrum of laser light, has been demonstrated by Fiocco *et al.* (1971).

c. Acoustic echo sounding

One of the newer remote-sensing techniques, acoustic echo sounding, relies on the scatter of sound from naturally occurring temperature and wind fluctuations in the atmosphere. Scattered sound is received at the antenna and a time-height history of the regions of strong temperature fluctuations that are advected over the sounder can be recorded as shown in Fig. 1. The enhanced acoustic scattering associated with temperature inversions is evident where the record is dark. During unstable periods, the record also shows dark areas, or regions of strong temperature fluctuation, which delineate the rising air in thermal plumes (right side of Fig. 1). This type of information cannot be used to give an absolute temperature measurement. It can, however, be used to infer the stability of the boundary layer.

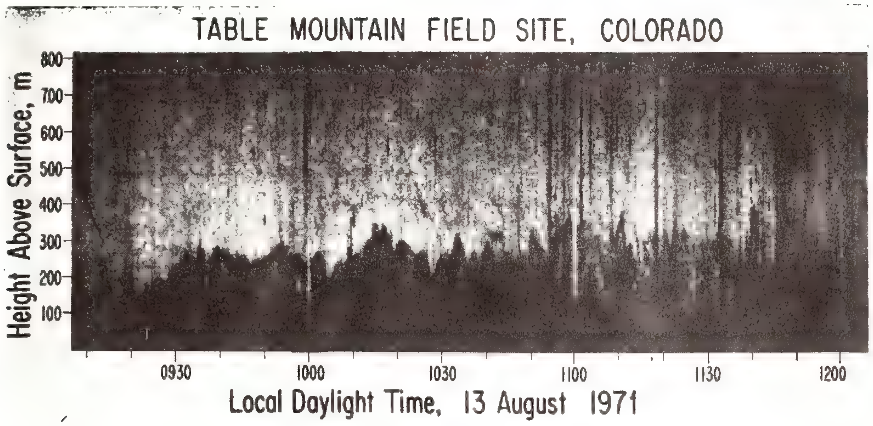

Fig. 1. Acoustic echo sounder record showing a rising temperature inversion with convective activity below. The inversion has dissipated after 11:15 local time and the pattern is dominated by typical returns from thermal plumes.

Echoes from horizontally stratified layers, usually containing evidence of organized wave structure, indicate a stable lapse rate. Neutral lapse conditions or regions where laminar flow exists will usually not produce a return and the record will be white. Vertically-oriented dark regions, associated with convective-thermal plume activity, indicate unstable lapse conditions. A direct comparison between the acoustic sounder record of an inversion and a radiosonde temperature profile is shown in Fig. 2.

Attenuation of sound energy in the atmosphere is known to be a function of temperature, humidity, pressure, and scattering caused by turbulence. It is conceptually feasible to use the measured absorption of energy to derive both temperature and humidity profiles (Gething and Jenssen, 1971). However, such techniques are still in the very early experimental stages and it will be several years before feasibility is demonstrated, and then more time before operational application.

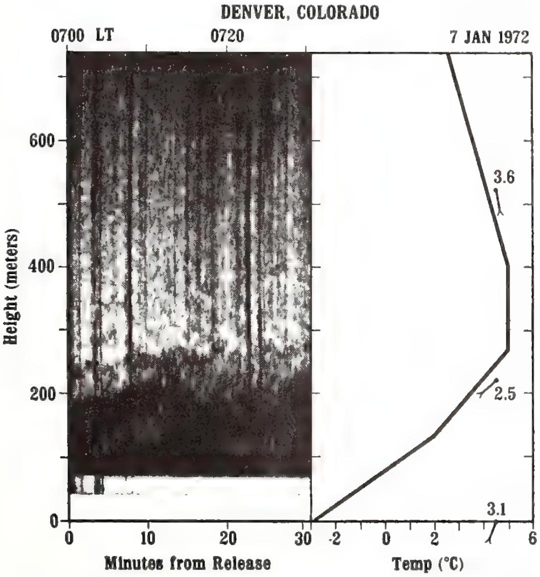

Fig. 2. Comparison of radiosonde temperature profile (right) with an inversion layer shown on an acoustic echo sounder record. The speed (m s^{-1}) and direction of the winds measured by the radiosonde are shown by the small arrows (north is up).

d. RASS

The Radio Acoustic Sounding System (RASS) (North *et al.*, 1973) is a hybrid device which uses an acoustic transducer to send a burst of sound upward into the atmosphere and a Doppler radar to track the sound wave and determine its propagation speed. Because the speed of sound is a function of the ambient temperature, the Doppler information can be used to derive a temperature profile. Recent experiments have demonstrated the feasibility of this technique for measuring temperature profiles to heights of up to 3 km. Errors caused by vertical velocities in the atmosphere can be eliminated by averaging the returned signal for periods of several minutes, a time scale commensurate with the needs of urban meteorology.

5. Wind sensing

a. Wind measurements with lasers

Laser backscattering techniques using crossed or conically scanned beams are one proposed method of measuring winds (Derr and Little, 1970); however, to date there has been no routine application of this type of system.

Another method for laser measurement of winds employs the Doppler shift of the backscattered light (Huffaker *et al.*, 1970, 1971). Because of rapid degradation of coherence in the propagated laser beam through a turbulent atmosphere, it is advantageous to use as long a wavelength as possible, and most schemes now propose to use 10.6 μm CO_2 laser radiation. Demonstrated ranges of several hundred meters indicate the technique may have application in air pollution meteorology. A Doppler wind measurement that does not require a local oscillator reference has also been described (Farmer and Brayton, 1971).

b. Radar

Pulsed Doppler radars have demonstrated their ability to measure wind fields whenever hydrometeor targets are present (Miller, 1972). The pulsed Doppler method has also been used with artificial targets (chaff) to produce excellent wind measurements. The lack of natural targets limits this method in air pollution meteorology, and it may be most useful for cloud and precipitation measurements.

c. Acoustic

Vertical wind can be measured with the single axis monostatic system described earlier. The Doppler shift of the returned signal is related to the vertical velocity of the scattering volume, which is the vertical component of the wind (Beran *et al.*, 1971b). By tilting the single monostatic antenna, a component of the horizontal wind can also be measured. A weakness in making wind measurements with a monostatic system is that the return signals are not always continuous; the lack of signal where neutral lapse conditions exist results in an intermittent sampling of the wind.

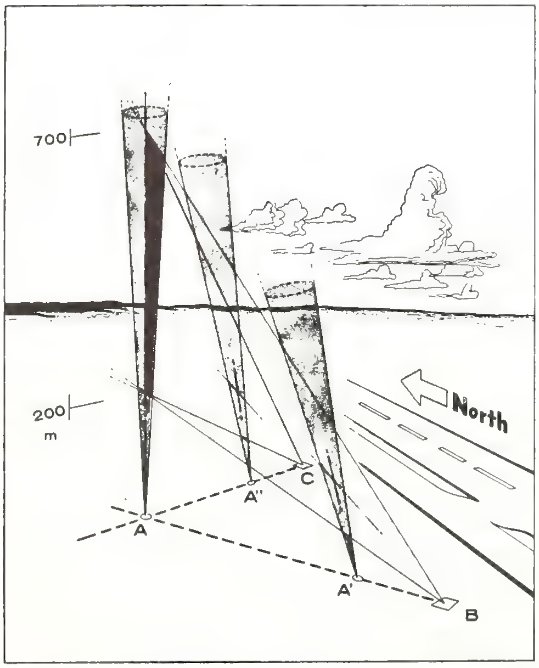

Fig. 3. A multiple transmitter acoustic antenna configuration used to measure a vertical profile of the horizontal wind. Transmitters at A, A' and A'' produce sound which is scattered to receivers at B and C.

The use of a bistatic system, where the transmitter and receiver are separated helps to solve this problem. Scatter from both wind and temperature fluctuations can be received in the bistatic mode, and the returns from wind fluctuations tend to fill in the gaps where the temperature fluctuations are weak. Bistatic configurations like that shown in Fig. 3 have been used to measure the vertical profile of the horizontal wind up to heights of several hundred meters (Beran and Clifford, 1972; Beran *et al.*, 1974). Antennas at A, A', and A'' in Fig. 3 transmit sound pulses which are scattered and received at points B and C. The Doppler shift is then related to the wind along the vertical profile.

Another method of wind sensing with an acoustic sounder is to employ the angle of arrival of the returns from a vertically pointed monostatic system (Mahoney *et al.*, 1973). This is a relatively simple method of finding the line average of the wind to heights of several hundred meters; however, it also suffers from a lack of continuous signal under some types of thermal structures.

6. Measuring the depth of mixed layers

a. Laser measurements

Most atmospheric aerosols originate from natural sources or human activities on the surface of the planet. Thus turbidity, especially in polluted regions, is usually greater within the first kilometer or so of the atmosphere where mixing is strong. The ability of the laser to monitor the depth of these mixed layers through backscattered laser light measurements has already been noted, and the actual utility of a pulsed laser system for studying the nature of polluted air has been documented (Barrett and Ben-Dov, 1967; Fernald *et al.*, 1972).

Increase in the mixed depth above a laser station can be effectively studied by displaying side-by-side a number of laser backscatter returns, documenting the intensity of the return by brightness modulation of a cathode ray tube (Collis and Uthe, 1972). This technique was used during an air pollution study in St. Louis to provide continuous information on the depth of the mixed layer (Uthe, 1972). The mixed depth has also been measured by a lidar in an experiment in Oregon (McCormick *et al.*, 1972).

b. Acoustic echo sounder

The depth of the mixed layer (see Fig. 1) is one of the most easily obtained outputs from a monostatic echo sounder. Experiments in the urban environment have shown that the inversion that caps the mixed layer can be continuously monitored on a real time basis and displayed on a simple facsimile recorder (Beran *et al.*, 1971a; Wyckoff *et al.*, 1973).

An advantage of using the acoustic system for this type of measurement is that it does not rely on the presence of artificial tracers, but uses the naturally-occurring temperature fluctuations associated with the inversion surface. This can provide a marked advantage over laser systems which require the buildup of aerosols before the mixed layer can be observed.

c. FM/CW radar

The marine inversion layer, as well as layers associated with continental radiation inversions, have been detected with FM/CW radars (Gossard and Richter, 1970; Bean *et al.*, 1973). The refractive index change that produces the signal returned to an FM/CW radar is probably more strongly a function of humidity than temperature. This system shows a great deal of potential as a monitor of the capping inversion associated with air pollution because of the humidity gradients usually associated with such structure.

7. Areal probing

The ability of certain remote sensors to provide more than measurements along a given line-of-sight by scanning a considerable area around the station within defined horizontal ranges and altitudes adds greatly to the utility of the measurements. Operation in this manner is highly dependent upon angular resolution capabilities of the remote-sensing device and its provision for a high rejection of unwanted returns in directions removed from the narrow probing main beam of waves.

a. Laser methods

Because of the high electromagnetic frequencies and the inherently coherent wavefronts used for laser probes, high angular resolution and good rejection in other directions is possible. A laser beam can be used to illuminate a narrow column of aerosols which backscatter to the aligned receiver. With available lasers, returns from distances of 10 or 20 km may be obtained. Thus, the horizontal stratification in real time may be monitored (Hall and Ageno, 1970). Until eye-safe lasers or reliable safety precautions can be developed, rapid scanning of laser beams through columns of space over cities cannot be undertaken.

b. Radar probing

Powerful radars with large antennas (20 m aperture) are able to monitor the depth of the mixed layer and detect convection patterns over ranges of 10–20 km (Battan, 1973). When operated in the range-height indicator (RHI) mode, the spatial picture of the mixed layer and convective structure can be obtained along a vertical plane. Use of the plan position indicator (PPI) mode graphically shows regions where convective structures mix through elevated inversions. Because of the large size and cost of such radar installations, none has yet been used to monitor mixed layers in regions subject to air pollution problems.

c. Transverse wind sensing with lasers

Temperature variations in the atmosphere, which give rise to acoustic backscatter, also lead to variations in the optical index of refraction. These variations influence the propagation of laser beams, and are responsible for the familiar twinkling of stars. Because such temperature variations in the atmospheric structure have a finite lifetime, the irradiance measured from a transmitted laser beam with two closely spaced apertures will show a correlation in the irradiance when the signals are time lagged an appropriate amount. This time lag is a function of the wind, which advects the temperature structure across the two adjacent paths from the laser to the two spaced apertures. Such a technique has been used (Lawrence *et al.*, 1972) to measure the average wind normal to a 15 km path. Real-time readout of the transverse wind is possible through use of a signal correlation computer. Measurements along an instrumented 1 km path have shown excellent agreement between spaced, averaged propeller-anemometer readings and the laser-derived wind. This averaged line integral of the transverse wind could provide information on the drainage across an entire valley, or with several laser paths, the wind flowing into and out of a city.

In summary, all of the important meteorological variables associated with urban meteorology can be remotely sensed by any of several different techniques. Table 1 is

TABLE 1. Rating of various techniques for sensing temperature, wind, and mixing depth.

Parameter	Category Sensor	Stage of development	Potential for all weather operation	Tracer availability	Spatial resolution	Time resolution	Accuracy	Acceptability
Temperature or stability	Acoustic	Near prototype	Medium	High	Medium	Medium	Low	High
	Laser	Experimental	Medium	Medium	High	Medium	Medium	Medium
	Microwave radiometer	Prototype	High	—	Low to medium	Medium	Medium	High
	RASS	Experimental	Medium	High	Medium	Medium	Medium	High
Wind	Acoustic	Near prototype	Medium	High	Medium	Medium	Medium	High
	Laser	Experimental	Medium	Medium	High	High	High	Medium
	Radar	Prototype	Low	Low	High	High	High	High
Mixing layer depth	Acoustic	Near prototype	Medium	High	High	High	High	High
	Laser	Near prototype	Medium	Medium	High	High	High	Medium
	Radar FM/CW	Experimental	High	Medium	High	High	High	High

a rating of the various techniques for sensing temperature, wind, and mixing depth. Each sensor or technique listed in the second column is rated in categories as follows:

The first category, "stage of development," indicates when the device might be ready for operational use. "Prototype": the system is ready for integration into a larger network; "near prototype": the system would be ready within a year; "experimental": feasibility of the system has been demonstrated but significant engineering problems remain before it is ready for use.

A second category, "potential for all weather operation," considers such factors as the possible degradation of laser signal during heavy cloud or fog and the effect of rain noise on the acoustic system. In judging a system in this and in other categories, we must keep in mind the final objective of sensing the parameter for use in air pollution-related meteorology. For example, the inability of the laser or microwave radiometer to penetrate thick clouds may not be a significant deterrent to its use for monitoring pollution-related phenomena.

"Tracer availability," the third category, is a rating of how often a sensor will be able to operate. This is important if the sensor is being considered for continual operation, and a low rating here indicates that the device is probably not acceptable for an urban air pollution application. Acceptable tracers are either natural or the result of inadvertent air pollution.

The categories of "spatial resolution" and "time resolution" give an indication of how detailed the measurements by each sensor might be. Spatial resolution is, in most cases, determined by antenna beamwidths and pulse lengths. Time resolution refers to the averaging times required to produce acceptable measurements. Small-scale turbulence measurement is not anticipated and readout of data is required on the order of every 15 to 20 min for an urban sensor network.

"Accuracy," the next to last category, is a function of the mode in which a system is operated. In addition, many of the instruments have undergone only limited testing and comparison with standard *in situ* measurements, and accuracy estimates are based on the theoretical potential rather than actual calibration. As in the previous category, it is felt that all of the instruments listed can achieve accuracies suitable for the task considered here.

The final category, "acceptability," refers to the potential nuisance or danger from a particular device. In other words, will it be acceptable for use in the urban environment? An example of a potential problem in this category would be potential eye damage from lasers.

8. Remote sensing systems

Up to this point we have discussed the urban meteorological problem and data requirements, along with a brief overview of the various remote-sensing devices which could conceivably make the measurements. It is obvious that some parameters can be measured by several techniques. What is not obvious is which of these sensors or collection of sensors would be optimum for the specific problem of improving our data-gathering methods in the urban environment. This section is devoted to an assessment of the requirements for a measurement system and an attempt is made to provide guidance in selecting the optimum set of sensors for a city.

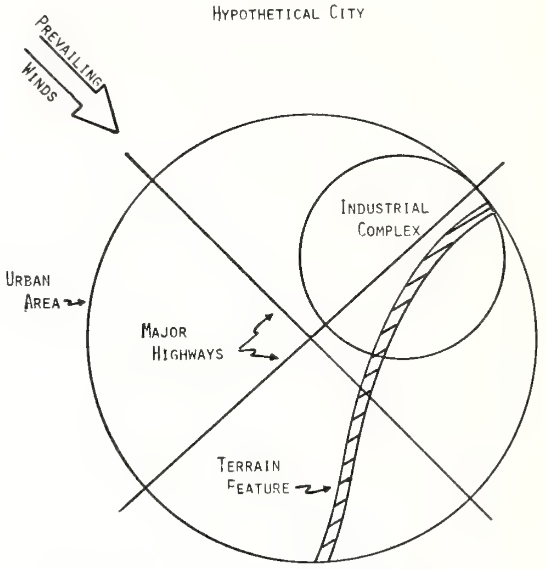

FIG. 4. A hypothetical city made up of features that are common to most urban regions.

Every urban region is a unique entity and the correct location and sensor distribution for one city may be totally unacceptable for another. Certain features are, however, common to all and can be used to generate a hypothetical city. This city then serves as a model to demonstrate the placement of sensors for air pollution monitoring. All urban regions encompass a given area. This basic area will vary in size, shape, and population density, so for a general case, we shall assume that the area is simply a circle of unit size. Figure 4 shows the hypothetical model of a city made up of several basic features.

Cities usually contain industrial regions which are a major source of pollution and as such need to be delineated in our model. Again, for the sake of simplicity we shall designate the industrial region of an urban complex as a circle, contained within the larger "area" circle.

In addition to a concentrated pollution source region, such as an industrial complex, all cities contain line sources, usually in the form of major arterial highways. For our hypothetical city we shall show these simply as crossing diagonal lines.

Terrain features are another important influence on urban meteorology, many times controlling the local flow which advects or concentrates effluent in a given region. For example, a river valley is a natural place for cold air drainage, while a coast line produces local land and sea breeze circulation, alternately cleansing a region and concentrating pollution at the sea breeze front. Without specifying the type, we shall include a terrain feature in our model as a cross-hatched band.

In the first section of this paper, climate was mentioned as an important influence on urban air pollution. It is difficult to build this feature into a general model, because of the wide range of climatic zones covered by the cities of the world. We can say, however, that all cities will have some prevailing wind direction and provide for this in our model.

Most urban regions can be reduced to a similar basic model by changing the shape and distribution of features in the model. Recalling that the primary meteorological parameters are the temperature profile (or some indication of the ambient stability) and the wind field within the boundary layer, we can now proceed with the instrumentation of our city. For temperature we can assume that conditions will be reasonably homogeneous over the urban area, but will differ over the surrounding region away from the urban heat island. Temperature profiles should be measured in each of these areas. Sensors for both regions should have a range capability that insures collection of information throughout the depth of the boundary layer.

Measurement of the wind field over the urban area is a more difficult problem. In addition to a vertical profile of the wind, we would like to monitor the trajectories of polluted air parcels, which implies the need for either several sensors at strategic locations, or the need for a single scanning sensor to map winds over a large area.

Based on experimental work to date, it is clear that the urban measurement system could be made up entirely of either acoustic or laser devices. As a starting point, we shall consider how each of these families of remote sensors might be applied.

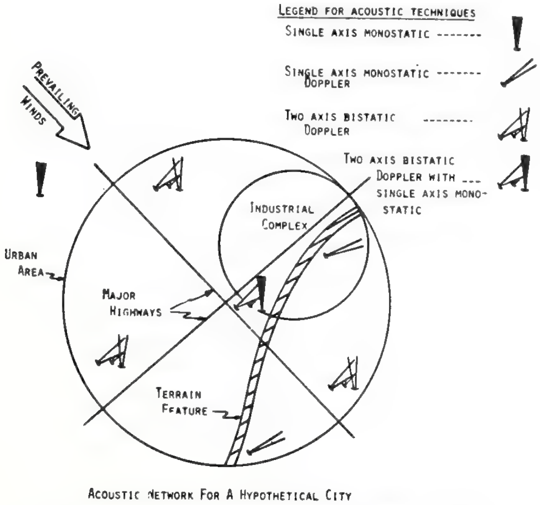
LEGEND FOR ACOUSTIC TECHNIQUES
SINGLE AXIS MONOSTATIC
SINGLE AXIS MONOSTATIC DOPPLER
TWO AXIS BISTATIC DOPPLER
TWO AXIS BISTATIC DOPPLER WITH SINGLE AXIS MONOSTATIC
PREVAILING WINDS
URBAN AREA
INDUSTRIAL COMPLEX
MAJOR HIGHWAYS
TERRAIN FEATURE
ACOUSTIC NETWORK FOR A HYPOTHETICAL CITY

FIG. 5. Proposed network of acoustic sensors placed in the hypothetical city of Fig. 4.

Looking first at acoustic devices, one can envision the core of a system being an acoustic sounder with full Doppler capabilities situated near the center of the city (see Fig. 5). This central system can also be operated in a monostatic mode providing the information on mixing depth and an indication of low level stability. The acoustic Doppler system can provide only a vertical profile of the horizontal wind. In order to determine the trajectories of air parcels it would be necessary to establish several satellite stations around the city to sense the horizontal variations in the wind field. Here it is important to consider the orientation and type of terrain features and the city size before locating the satellite sensors. While the main core system should have a full wind-profiling capability employing gating and measurement of at least two components of the horizontal wind, some of the satellite systems (for example, those along a river valley where only one component of the wind is needed) could conceivably be of a simpler design. An acoustic Doppler system which measures only the average wind from the ground to the capping inversion could provide information necessary for determining gross trajectories of parcels along or near a particular terrain feature. The depth of the mixing layer outside our urban area could be monitored by a simple monostatic system upwind of the city.

The pure acoustic system would not provide a direct indication of the temperature profile. To do this, it would require the introduction of a RASS in place of the monostatic sounder located outside of the city and possibly a second RASS near the central acoustic Doppler system. The need for measuring the absolute temperature profile must remain an open question now. If this profile is used only to derive the stability of the lower atmosphere, one must ask if there are more direct methods which do not rely on obtaining the absolute temperature, but still provide the required stability information. For example, the variance of the wind is correlated with stability, and the monostatic echo sounder record provides a qualitative indication of the stability. Because both the vertical wind profile and a record of the lower atmospheric structure can be obtained from an acoustic Doppler system, a derived stability conceivably could be obtained that might eliminate the need for more elaborate temperature profiling techniques (Baynton, 1968).

Turning now to an urban remote-sensing system based entirely on the family of laser sensors, we see some interesting differences. The ability of the laser to scan through a volume and to sense the line integral of a parameter can be applied in a variety of ways. For example, by locating a pulsed laser at some elevated point within the urban complex and scanning the beam (see Fig. 6) in a circular fashion, a complete plan position in-

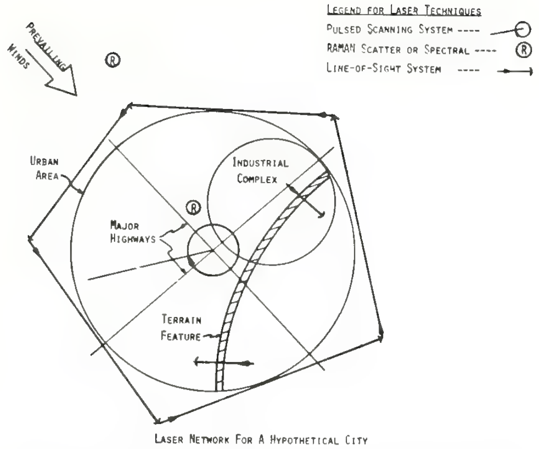
Legend for Laser Techniques
Pulsed Scanning System ----
RAMAN Scatter or Spectral ---- Ⓡ
Line-of-Sight System ----
Prevailing Winds
Ⓡ
Urban Area
Industrial Complex
Ⓡ
Major Highways
Terrain Feature
Laser Network For A Hypothetical City

Fig. 6. Proposed network of laser type sensors placed in the hypothetical city of Fig. 4.

dication of the effluent over the city could be produced. It is conceivable that a time sequence of identifiable features in this type of information could then be used to produce a trajectory analysis of the air over the urban region. The addition of a second laser at another location and the use of both lasers in a Doppler mode would make it possible to measure directly the wind field in the plane common to both beams. The temperature profile in the all-laser system could be obtained by either the Raman scatter technique or from the Doppler broadened widths of the backscattered spectrum of laser light. As in the acoustic system these devices should be located both within the urban area and in the surrounding area to measure the effect of the urban heat island. A possible weakness here would be the system located outside an urban complex where non-existence of tracers in the much cleaner air may hinder the operation of the longer wavelength Doppler laser system. The depth of the mixed layer could also be observed by vertically-pointed laser systems within the urban area; again the lack of tracers outside of the region could degrade the performance of a laser.

The ability of line-of-sight laser systems to measure the average wind component normal to the beam paths could find many unique applications within the urban region. For example, if the major terrain feature in a city is a river valley, it is important to measure the very light drainage winds that transport pollutants along the valley. An ideal method for monitoring these winds is the line-of-sight laser. One or more of these systems placed so they sense the component of the wind along the valley floor would provide a continual monitor of the average transport of air into or out of a given region. This same type of system could be installed in a ring around the city with perhaps four or five sets of transmitters and receivers to measure the low-level convergence into the urban area. The remote-sensing system based on laser techniques is shown in Fig. 6.

In developing the two "pure" systems described above, we have omitted one potentially valuable technique for measuring temperature profiles, the microwave radiometer. The advanced stage of development of this technique and its potential range of 3 km or more makes it a highly competitive device. If the actual temperature profile, and not a more direct indication of stability, is required, then the microwave radiometer might be considered as part of the operational system.

To specify the optimum system for a given city, it would be necessary to consider such important factors as the cost and the stage of development of each device. Costs are difficult to assess and the only comparison that can be made is between present research-oriented instruments. These are by their very nature more expensive than standardized production models. In general, research-oriented acoustic devices are less expensive to build and operate than lidar (optical radar) instruments. If these costs can be projected to production models, the conclusion must be that an acoustic system would be less expensive.

"Stage of development" is an equally difficult area in which to make predictions due to the uncertain nature of research projects. Some devices are very close to the operational stage, and it is safe to suggest that they should be considered first in planning for the immediate future. The microwave radiometer is one of the more advanced instruments, already tested in the urban region. Laser systems that are well advanced are those used to measure the depth of the mixing layer. The line-of-sight laser has been used to measure the average wind component over a 15 km path in the lee of a mountain range. Acoustic systems are also being tested in the urban environment under operational conditions. Single axis monostatic sounders have been used to monitor the inversion layers in cities and a full Doppler system has been placed in operation at an airport for the purpose of real-time monitoring of the wind and wind shear (Beran, 1974).

In summary, the optimum system for any given city must be the product of many considerations. A variety of techniques is available for making the required measurements and selection of a system must be based on such factors as:

a) unique requirements imposed by terrain and demography of a particular city;
b) time available before the system must be operational;
c) overall cost of the system; and
d) stage of development of the selected sensors.

It is concluded that the incorporation of remote-sensing devices into urban-monitoring systems has many advantages over presently used point sensors. In the future, remote sensing can play an important role in aiding the prediction, control, and monitoring of air pollution in cities.

References

Anway, A. C., 1970: Radiometrically measuring the mixing layer aids air pollution forecasting. 2nd International Clean Air Congress (ed. England and Beery), 999–1003.

Barrett, E. W., and O. Ben-Dov, 1967: Application of the lidar to air pollution measurements. *J. Appl. Meteor.*, **6**, 500–515.

Battan, L. J., 1973: *Radar Observations of the Atmosphere.* Chicago, Univ. of Chicago Press.

Baynton, H. W., 1968: Stability inferences from precision rawins. *Mon. Wea. Rev.*, **96**, 47–52.

Bean, B. R., R. E. McGavin, and B. D. Warner, 1973: A note on the FM-CW radar as a remote probe of the Pacific trade-wind inversion. *Bound. Layer Meteor.*, **4**, 201–209.

Beran, D. W., 1974: Remote sensing wind and wind shear system. (FAA Report) FAA-RD-74-3.

——, F. F. Hall, Jr., J. W. Wescott, and W. D. Neff, 1971a: Application of an acoustic sounder to air pollution monitoring. *Proceedings Air Pollution Turbulence and Diffusion Symposium,* Las Cruces, N.M., New Mexico State Univ., 7 p.

——, C. G. Little, and B. C. Willmarth, 1971b: Acoustic Doppler measurements of vertical velocities in the atmosphere. *Nature,* **230**, 160–162.

——, and S. F. Clifford, 1972: Acoustic Doppler measurement of the total wind vector. *2nd Symposium on Meteorological Observations and Instruments,* Boston, American Meteorological Society, 100–109.

——, B. C. Willmarth, F. D. Carsey, and F. F. Hall, Jr., 1974: An acoustic Doppler wind measuring system. *J. Acoust. Soc. Amer.*

Collis, R. T. H., and E. E. Uthe, 1972: Mie scattering techniques for air pollution measurement with lasers. *Opto-Electronics,* **4**, 87–99.

Cooney, J., 1972: Measurement of atmospheric temperature profiles by Raman backscatter. *J. Appl. Meteor.*, **11**, 108–112.

Derr, V. E., (ed.), 1972: *Remote Sensing of the Troposphere.* Wave Propagation Lab., NOAA, Boulder, Colorado, GPO (Catalog No. C55.602: T75), 809 p.

——, and C. G. Little, 1970: A comparison of remote sensing of the clear atmosphere by optical, radio, and acoustic radar technique. *Appl. Opt.*, **9**, 1976–1992.

Farmer, W. M., and D. E. Brayton, 1971: Analysis of atmospheric laser Doppler velocimeters. *Appl. Opt.*, **10**, 2319–2324.

Fernald, F. G., B. M. Herman, and J. A. Reagan, 1972: Determination of aerosol height distribution by lidar. *J. Appl. Meteor.*, **11**, 482–489.

Fiocco, G., G. Beneditti-Michelangeli, K. Maischberger, and E. Madonna, 1971: Measurement of temperature and aerosol to molecule ratio in the troposphere by optical radar. *Nature,* **229**, 78–79.

Gething, J. T., and D. Jenssen, 1971: Measurement of temperature and humidity by acoustic echo sounding. *Nature,* **231**, 198–200.

Gossard, E. E., and J. H. Richter, 1970: The shape of internal waves of finite amplitude from high resolution radar sounding of the lower atmosphere. *J. Atmos. Sci.*, **27**, 971–973.

Hall, F. F., Jr., and H. Y. Ageno, 1970: Lidar measurements of turbidity in the troposphere. *Laser Applications of the Geosciences* (ed. Gauger and Hall), North Hollywood, Calif., Western Periodicals Co., 17–32.

Huffaker, R. M., A. V. Jelalian, and J. A. L. Thompson, 1970: Laser Doppler system for detection of aircraft trailing vortices. *Proceedings of IEEE,* **58**, 322–326.

——, A. V. Jelalian, W. Keene, C. Sonnenshein, and J. A. L. Thompson, 1971: Application of laser Doppler systems to vortex measurements and detection. *Aircraft Wake Turbulence and its Detection* (ed. Olson, Goldberg and Rogers), New York, Plenum Press, 113–124.

Lawrence, R. S., G. R. Ochs, and S. F. Clifford, 1972: Use of scintillation to measure average wind across a light beam. *Appl. Opt.*, **11**, 239–243.

Little, C. G., 1972: Status of remote sensing of the troposphere. *Bull. Amer. Meteor. Soc.*, **53**, 936–949.

——, 1973: Remote sensing of the atmosphere. *Atmos. Tech.*, NCAR, **2**, 51–56.

Mahoney, A. R., L. G. McAllister, and J. R. Pollard, 1973: The remote sensing of wind velocity in the lower troposphere using an acoustic sounder. *Bound. Layer Meteor.*, **4**, 155–167.

McCormick, M. P., S. H. Melfi, L. E. Olsson, W. L. Taft, W. P. Elliott, and R. Egami, 1972: Mixing-height measurements by lidar particle counter and rawinsonde in the Willamette Valley, Oregon. NASA Tech. Note D-7103, 78 p.

Miller, L. J., 1972: Dual-Doppler radar observations of circulation in snow conditions. *Proc. 15th Radar Meteor. Conf.*, Boston, American Meteorological Society.

Neiburger, M., 1969: The role of meteorology in the study and control of air pollution. *Bull. Amer. Meteor. Soc.*, **50**, 957–965.

North, E. M., A. M. Peterson, and H. D. Parry, 1973: RASS, a remote sensing system for measuring low-level temperature profiles. *Bull. Amer. Meteor. Soc.*, **54**, 912–919.

Strauch, R. G., V. E. Derr, and R. E. Cupp, 1971: Atmospheric temperature measurements using Raman backscatter. *Appl. Opt.*, **10**, 2665–2669.

Uthe, E. E., 1972: Lidar Observations of the urban aerosol structure. *Bull. Amer. Meteor. Soc.*, **53**, 358–360.

Westwater, E. R., 1972: Ground-based determination of low altitude temperature profiles by microwaves. *Mon. Wea. Rev.*, **100**, 15–28.

Wyckoff, R. J., D. W. Beran, and F. F. Hall, Jr., 1973: A comparison of the low level radiosonde and the acoustic echo sounder for monitoring atmospheric stability. *J. Appl. Meteor.*, **12**, 1196–1204.

Proceedings 6th AMS Conference on Aerospace & Aeronautical Meteorology,
412-417, November 1974.

OPERATIONAL TEST RESULTS OF ACOUSTIC DOPPLER WIND SHEAR DETECTOR

D. W. Beran, F. F. Hall, B. C. Willmarth
R. J. Keeler and D. Hunter

Wave Propagation Laboratory
NOAA Environmental Research Laboratories
Boulder, Colorado 80302

1. INTRODUCTION

An acoustic Doppler system was tested at Denver's Stapleton International Airport between October 1973 and March 1974. This test represented the culmination of the first phases of a joint FAA/NOAA effort to develop a device capable of detecting wind shear at airports. The Stapleton system was based on designs and results from earlier development work (Beran et al., 1971; Beran and Clifford, 1971; Beran, 1971) with the added sophistication of an on-line computer for real time data processing and output.

This paper gives a brief description of the equipment and experimental configuration. For more detail the reader is referred to Beran (1974). Following the description, results of the Stapleton experiment are presented along with a discussion of design changes necessary to improve overall performance.

2. EXPERIMENTAL SYSTEM

The experimental Stapleton system was a bistatic configuration (see Fig. 1) with one main vertically pointed transmitter at A, two smaller tilted transmitters located at points A´ and A´´, and two receivers located at points B and C along two orthogonal legs intersecting at the main transmitter. Previous wind profiling experiments (Beran and Clifford, 1971) established that the bistatic antenna configuration (transmitter and receiver separated) was superior to a tilted monostatic system because of the larger and more consistent echo strengths inherent with the former. In order to detect the wind shear at any level that might be important to an approaching aircraft it was first necessary to measure a total vertical profile of the horizontal wind and then to calculate the shear across horizontal planes a predetermined distance apart. The distance between these planes, 30 m, was based on the anticipated height resolution of the acoustic Doppler system and FAA requirements. The wind profiles were calculated by measuring the Doppler frequency shift of a vertically projected pulse of sound which was "tracked" by receiving antennas B and C through the volume common to both transmitter and receiver beams (see Fig. 1). Propagation time delay was used to calculate the height and the corresponding scatter angle of the echoes. These parameters and the instantaneous Doppler shift were used to calculate the horizontal wind speeds along each leg. This wind information was then resolved into a table of wind vectors vs height (the wind profile). The secondary transmitters, at points A´ and A´´ were added to cover the levels below 200 m which were outside the volume common to the main transmitter and the two receivers.

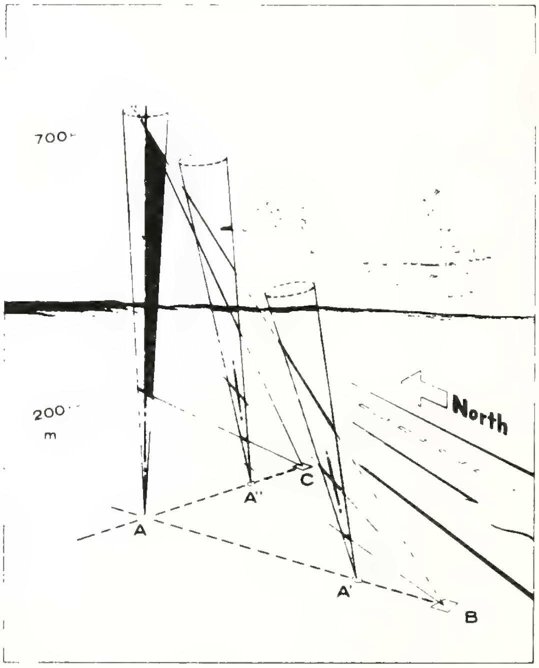

Fig. 1. Multi-transmitter bistatic antenna configuration

The functional components of the system are shown in the block diagram (Fig. 2) which is divided into four subsystems. The antenna subsystem includes the transmitting and receiving transducers, focusing reflectors, support structures, acoustic shielding, enclosures, receiving preamplifiers, and transmission lines. The receiver antennas were placed in underground bunkers similar to that shown in Fig. 3 in order to reduce the effects of ambient noise in the side lobes. The transmitting antennas were less carefully shielded as there were no people near enough to be disturbed by the sound. The main transmitting antenna (A) was a 3 m diameter parabolic reflector set in a pit about 2 m below the ground surface. The secondary transmitting antennas (A´ and A´´) were surplus army searchlights modified for use as acoustic antennas.

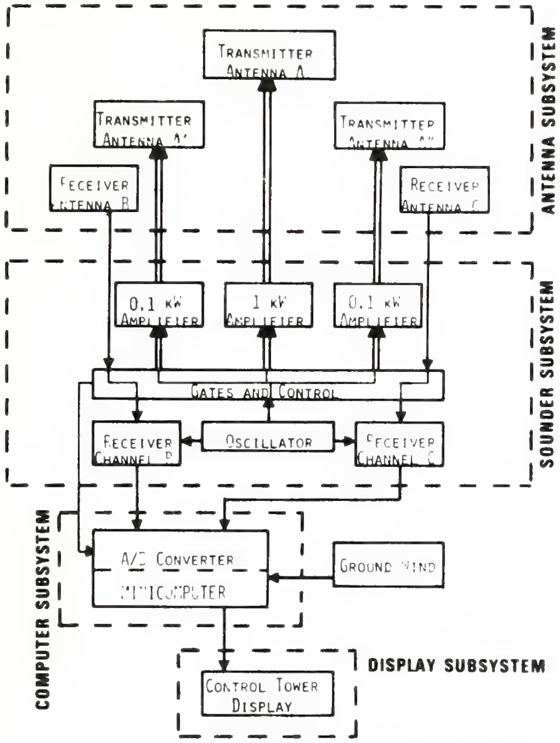

Fig. 2. Block diagram of Acoustic Doppler Wind System

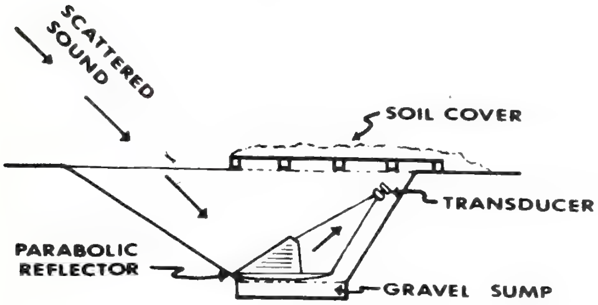

Fig. 3. Bunker installation with a horn reflector antenna

The sounder subsystem includes the transmitting power amplifiers, transmit/receive timing and frequency control functions, and a dual-channel receiver locked to the transmitted frequency. Each receiver channel had three analog voltage outputs corresponding to Doppler frequency, signal level and wideband noise level. The Doppler output was used to calculate wind vectors. The signal and noise outputs were used to estimate the reliability of the Doppler output by testing for receiver overload and S/N ratios.

The computer subsystem included a 16-bit minicomputer with 24K words of core storage, a disk unit for 2.5 million words, an eight channel A/D converter, and a CRT display terminal with hard copy unit. The A/D conversion of a data record started after the main transmitter tone burst (see Fig. 4), and continued for approximately 6 sec. The record consisted of the three outputs (Doppler, signal level, and noise level) from each of the receiving legs (B and C) plus ground wind from each leg. The receiver outputs contained three basic time segments: ambient noise sample, long range echoes, and short range echoes (third line in Fig. 4). The echoes were further divided into 30 m height gates (the number of samples per gate was dependent upon height) and averaged into a single value per gate for each of the six receiver outputs. (Ground winds were, of course, not range gated).

At this point tests for signal level and S/N ratio were applied to each set of three parameters (Doppler, signal, noise) from each range gate. The signal and noise values were used only to test for probable reliability of Doppler data (through signal level and S/N ratio tests), and the Doppler information from range gates passing these tests was used to update the stored wind profile table. Updating was done in an exponential time-averaging routine (5 min effective time constant) that weighted the latest data most heavily. This smoothing of the raw data helped to reduce the effect of spurious noise and small scale gusts, giving a more consistent picture of the winds which would affect large aircraft.

Display and Data Storage: Wind shear information, derived from these vertical profiles of the horizontal wind, was then transmitted to a display panel located in the control tower at Stapleton Airport. The format of this display panel is shown in Fig. 5. The top two rows of numbers give a readout of the maximum shear by showing the height, speed and direction of the winds just above and just below the level of maximum shear. When the maximum shear exceeded a predetermined critical value (7 knots/100 ft was used during these tests) a red shear-warning light was automatically activated. If two equal shears were detected, the one nearest the ground was selected for display. The display unit provided a digital readout of the surface wind speed and direction as determined from a surface anemometer. Surface wind gusts, determined from the variance of the ground winds, were also displayed.

To facilitate later analysis of the system performance the computer disk unit was used to store complete profiles of the measured wind along with an indication of the reliability of the information that was being archived. This information was placed in storage every 5 min and provided a complete time-height history of the system performance to be used for later analysis.

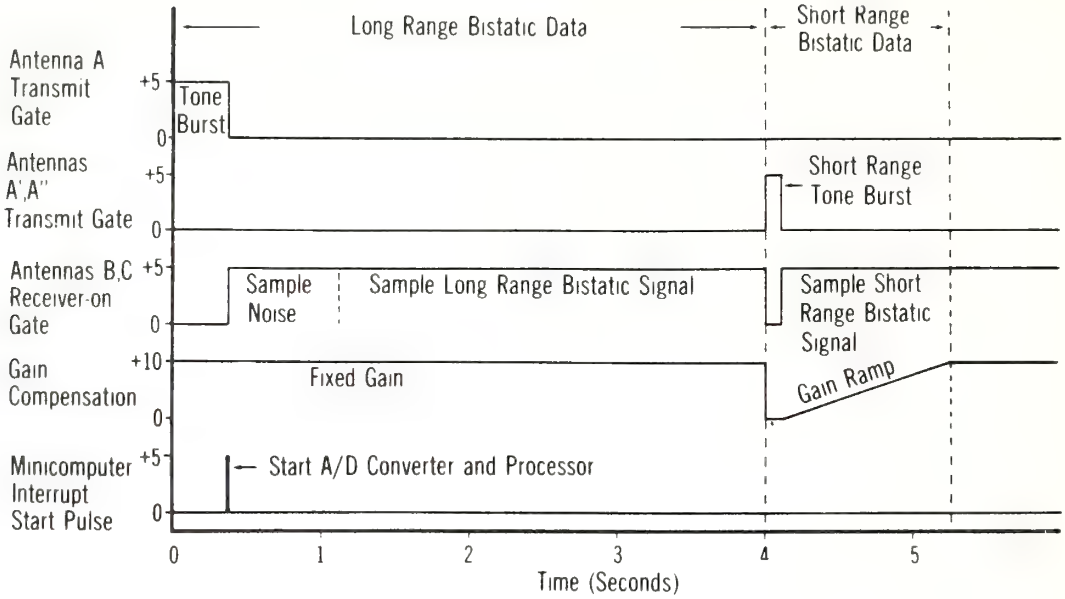
Long Range Bistatic Data
Short Range Bistatic Data
Antenna A Transmit Gate
+5
0
Tone Burst
Antennas A',A'' Transmit Gate
+5
0
Short Range Tone Burst
Antennas B,C Receiver-on Gate
+5
0
Sample Noise
Sample Long Range Bistatic Signal
Sample Short Range Bistatic Signal
Gain Compensation
+10
0
Fixed Gain
Gain Ramp
Minicomputer Interrupt Start Pulse
+5
0
Start A/D Converter and Processor
0
1
2
3
4
5
Time (Seconds)

Fig. 4. Timing diagram for Acoustic Doppler System

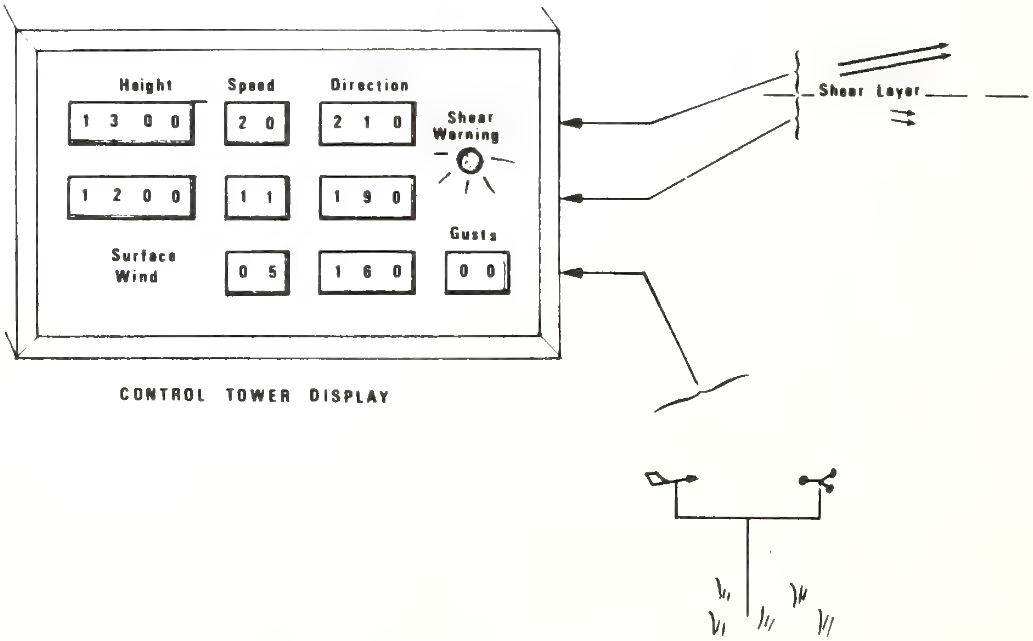

Fig. 5. Control tower display unit showing the position of wind shear and ground wind readouts

3. SITE SELECTION

Selection of a suitable site at the airport was dictated largely by the availability of land and the potential interference from construction operations associated with runway extension work at Stapleton. Noise from normal airport operations was a consideration in determining the direction that the receiver antennas would be pointed. Since one objective of the operational tests was to determine if an acoustic system could be operated in the noisy airport environment, the site selected (see Fig. 6) was exposed to the full range of airport background noise.

A second aspect of the siteing problem is the potential disturbance of local population by the sound source. Experience gained from related work with acoustic sounders (Wyckoff et al., 1973) has shown that when the proper precautions (i.e. effective side lobe suppression) are taken, that these intense sound sources can be located within a few tens of meters of normal human activity without creating an unacceptable disturbance. Nonetheless, this is an important consideration and should not be taken lightly when selecting a site and designing a transmitting antenna.

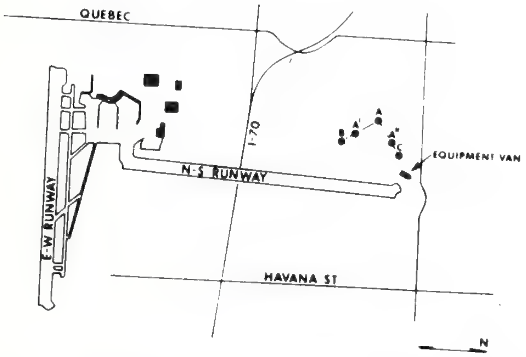

Fig. 6. General layout of Stapleton International Airport showing the position of the Acoustic Doppler Wind Measuring System.

Every airport presents a unique set of conditions including different traffic patterns, available land, and population density, each of which must be integrated into the site selection problem. Added to this is the complex question of the allowable distance between the airport operations and the point where the wind shear is actually measured. Involved here are such aspects as: a) horizontal distance over which wind shear can be assumed to be homogeneous; b) scale of wind shear which will affect a given aircraft; and c) change in scale and homogeneity with height. Some idea of the scales of shear that are important can be gained by considering the size and response time of the aircraft. Clearly, shears produced by wind eddies that are much smaller than the aircraft wing span will not have an adverse effect.

The horizontal extent of a wind shear can be estimated by observing its causal mechanism. For example, shears are often associated with low level inversions whose extent is characterized by synoptic scale features such as a frontal surface. On the other hand, strong shears have also been observed in conjunction with the cold air outflow from thunderstorms, a mesoscale feature.

Both the scale and horizontal extent of this wind related feature are closely tied to the height above the ground that the measurement is taken. Winds within a few tens of meters above the ground can be highly erratic and show large differences in only a few hundred meters horizontal distance. Winds measured at heights above the terrain-induced turbulence tend to be homogeneous over much greater distances.

Questions of scale and horizontal homogeneity have a direct bearing on the siteing problem. This problem is discussed by Grossman and Beran (1974); Gaynor (1974); and Beran (1974), and some experimental work has been done by Armendariz and Lang (1968) and Ito (1968) using two or more towers. More work using measurements over greater distances and at greater heights is needed before a definitive answer to this aspect of the siteing problem can be found. If it is demonstrated that wind measurements several miles from an airport can be used to indicate hazardous wind shear at the airport, the noise and general siteing problem would clearly become less critical.

4. STAPLETON SYSTEM PERFORMANCE

The original schedule for implementing the airport operation called for the experiment to take place during late summer and fall of 1973. For this reason, no provisions were made for cold weather operations, in particular, snow removal. Delay of the tests to the winter of 1973-1974 made it necessary to perform the experiment during less than ideal conditions and some data were lost due to heavy accumulation of snow in the antennas. Normal takeoff and landing operations resulted in intense noise of about 30 to 60 sec duration at intervals as short as one or two minutes during some heavy traffic hours. Although this resulted in rejection of the data during these times, the exponential time averaging window made operation possible. A more serious data loss occurred when jet aircraft were on the taxi strip awaiting takeoff instructions. Although this sound level was less intense than that generated during landing or takeoff, it was above the tolerable threshold and caused data losses for periods up to an hour.

While it was demonstrated that a system operating in the audible acoustic range (1 kHz) could successfully measure winds at an airport, it was equally apparent that the siteing of such a device is of primary importance. A complete airport noise survey will be essential prior to the installation of operational acoustic Doppler systems. Both ground and air traffic patterns must be considered in selecting the antenna site and beam directions.

Despite data loss due to adverse weather and high background noise, sufficient information was collected during the Stapleton operation to assess the system performance and to isolate certain weaknesses. The stored wind profiles were checked for internal consistency and continuity.

Internal consistency checks indicated that a large percentage of the wind profiles either lacked winds between the heights of 100 to 200 m or, if winds were shown, they were erratic and not consistent with the remainder of the measured profile. It will be recalled that the receiving antennas were intended to cover the range from about 200 m to 700 m with the main transmitter (A) and between 30 m and 200 m with the secondary transmitters (A´ and A´´). The section of erroneous wind estimates occurred near the transition zone, between the secondary and main transmitter ranges. A detailed computer analysis of the intersection pattern of assumed transmitter and receiver beams showed that a receiver beam which was too narrow could have caused this region of poor response. The probable signal level near the edge of the narrower beam, for uniform scattering, was some 20 dB down from that near the intersection point of the centers of the transmitter and receiver beams. This unacceptably large variation in the signal level along the vertical profile was undoubtedly responsible for the observed degradation in performance near 200 m and above 500 m height. While this problem could be cured by using a broader receiver beam, the deterioration of the S/N resulting from the greater amount of noise collected in a wide beam is an unacceptable consequence. Possible solutions are: a) to use several "pencil" beams, each directed at a slightly different angle, or b) to use a steerable phased array antenna in which a relatively narrow beam can be controlled to follow the upward traveling pulse of sound.

Measurement of the Doppler shift by the analog receiver has certain limitations. Although the instantaneous echo spectrum (for a single height gate) is not expected to exceed 10 or 20 Hz, a receiver bandwidth of about 300 Hz (30% of the transmitted frequency) is needed to allow for Doppler shifts corresponding to 30 m/sec at heights below 200 m. During noisy periods, this causes unpredictable bias in the Doppler (hence the S/N test). The dynamic range of the receiver was also limited to about 20 dB, and it was necessary to extend the range with a variable gain preamp.

An alternative signal processing technique, presently under study, would require addition of a faster A/D converter and a fast Fourier transform unit to the present digital system. The analog stage of the receiver would then merely band-pass filter the signal after which it would be digitally sampled at a higher rate and transformed into 128-line spectra for each height gate. This technique should permit more sophisticated adaptive filtering of the data, increase the dynamic range significantly, and allow operation at somewhat poorer S/N ratios.

As in most previous work with the acoustic Doppler system the lack of a suitable independent wind measurement to compare with the Doppler winds was frustrating. Some indication of the accuracy of the low level winds (lowest height gates at 45 and 75 m) could be gained from comparison with the winds measured by the ground based anemometer. The change in wind speed and direction at levels away from the surface friction effects made this only a crude guide to the system's performance.

The only wind measurements that could be used to judge the performance of the acoustic system were the twice daily radiosonde ascents taken by the Weather Service at Stapleton. These measurements were by no means comparable, as winds were reported at only 200 and 500 m above the surface, some 3 miles away from the site of the Doppler measurements. This large separation between the two wind profiles, and the unfortunate juxtaposition of the radiosonde reporting levels and the most unreliable portions of the Doppler wind profile made a detailed statistical comparison impossible. Despite these difficulties a few very encouraging comparisons were possible. The wind profiles shown in Fig. 7 are an example of remarkably good agreement between the radiosonde and Doppler derived winds. This case is especially good because it demonstrated that the acoustic system could successfully measure rather strong winds (≈14 m/sec), a feature of the system which had previously been untested.

Most acoustic Doppler wind profiles had a surprisingly jagged appearance (see Fig. 8) with deviations of one or two m/sec away from a classic smooth wind profile. At first glance this uneven appearance of the profile suggests that spurious noise might be causing the deviations. Time-height plots of the wind fields measured by the Doppler system (Beran, 1974), however, show good time continuity of these features. A second test using two parallel systems, where two receiving antennas were located side by side and aimed at a common scattering volume, indicated a high correlation between the separate systems for averaging times down to one minute. Both of these tests suggest that the observed deviations are real and that only our preconceived idea of a smooth wind profile is at fault.

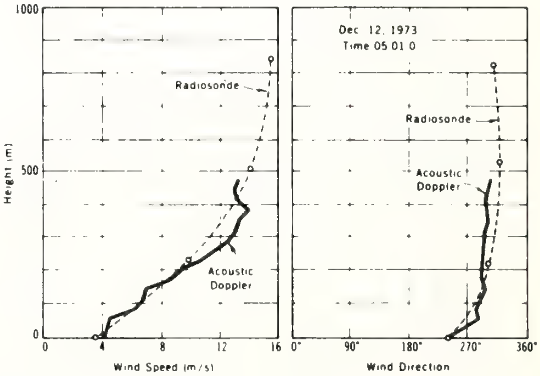

Fig. 7. Comparison of wind profiles from acoustic Doppler (solid lines) and Stapleton Airport radiosonde (dashed lines) for morning of December 12, 1973.

The radiosonde, on the other hand, does tend to smooth the wind profile because of the large distance between the balloon and the transmitter and the natural damping action of the collected balloon, string, and radiosonde package.

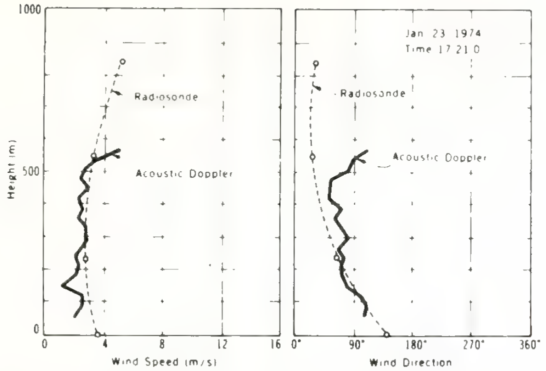

Fig. 8. Comparison of wind profiles from acoustic Doppler (solid lines) and Stapleton Airport radiosonde (dashed line) for afternoon of January 23, 1974.

5. SUMMARY AND CONCLUSIONS

The Stapleton Airport exercise represented the first full scale operational test of the experimental Acoustic Doppler Wind Measuring System. The test and the results presented here have been extremely valuable for identifying weaknesses in the system and for modifying some of the original assumptions made prior to the design of the experiment.

In practical terms a great deal was also learned about the construction and location of the equipment. The first step in locating an acoustic system at an airport is to make a complete noise survey of the area. This survey will provide a basis for later site selection that must also consider the availability and cost of land, and local terrain features which might effect the wind field. Achieving an optimum S/N ratio is, of course, the key to a successful system. Underground bunkers, designed to reduce the ambient background noise are essential. Again, such practical matters as snow accumulation and the collection of dust and other debris must be considered for an operational system. New bunker and antenna designs which incorporate heating elements for snow removal and underground sumps for collecting water are now being considered. Secondary protective measures such as sound reducing earth berms and surface wind reducing structures around the receiving antenna bunkers are also contemplated.

In summary, while the Stapleton tests indicated that several problems still exist, there does not appear to be any basic physical problem that will prevent the operation of an acoustic Doppler system at an airport site. The various recommended modifications must be tested again under operational conditions. In addition, there is a clear need for a long term comparison of the Doppler winds with a suitable set of independent wind readings to determine the full effect of diurnal changes in the scattering properties of the atmosphere. The radiosonde is just not adequate for this task. A much better set of wind profiles could be collected by anemometers on a very high tower such as one of the few 500 m towers being used for meteorological research.

REFERENCES

Armendariz, M., and V. D. Lang, 1968: Wind correlation and variability in time and space. Atmospheric Sciences Lab., White Sands Missile Range, N. M., Report ECOM-5201, 26 p.

Beran, D. W., 1971: Acoustics: A new approach for monitoring the environment near airports. *Journal of Aircraft, AIAA 8,* 934-936.

Beran, D. W., 1974: Remote sensing wind and wind shear system. Interim Report No. FAA-RD-74-3, (available from National Technical Information Service, Springfield, Virginia, 115 p.)

Beran, D. W., and S. F. Clifford, 1971: Acoustic Doppler measurements of the total wind vector. *Proc. AMS Second Symp. on Meteorol. Observations and Instrumentation.* San Diego, Calif.

Beran, D. W., C. G. Little, and B. C. Willmarth, 1971: Acoustic Doppler measurement of vertical velocities in the atmosphere. *Nature 230,* 160-162.

Ito, H., 1968: Time and space variation in meteorological elements in the aerodrome and its vicinity. *Aeronautical Meteorology,* WMO Tech. Note No. 95, 142-157.

Wyckoff, R. J., D. W. Beran, and F. F. Hall, 1973: A comparison of the low-level radiosonde and the acoustic echo sounder for monitoring atmospheric stability. *J. Appl. Meteor. 12,* 1196-1204.

An acoustic Doppler wind measuring system

D. W. Beran, B. C. Willmarth, F. C. Carsey,[a] and F. F. Hall Jr.

Wave Propagation Laboratory, NOAA Environmental Research Laboratories, Boulder, Colorado 80302

(Received 19 September 1973)

A system using the Doppler shift of audible sound waves to measure atmospheric winds to heights of 1 km above the surface is described. Planned application of the device at a commercial airport required extensive transducer and antenna shielding to reduce the effect of ambient noise. Comparisons of winds measured by both the acoustic Doppler system and standard radiosondes indicate that high accuracy and resolution can be achieved, and that the wind profiles can be continually monitored with relatively simple ground based equipment.

Subject Classification: 85.10, 85.88.

INTRODUCTION

A recent series of experiments at NOAA's Wave Propagation Laboratory demonstrated that the motion of a volume of the atmosphere can be remotely sensed by observing the Doppler frequency shift between a transmitted pulse of sound and the sound scattered from within the volume. Early work[1] with a single antenna monostatic system applied this principle to measure a vertical profile of the vertical wind component. Later experiments[2,3] using multiple antennas in a spaced configuration measured vertical profiles of the total wind vector.

This method of remotely measuring wind components has already found research application in momentum flux calculations[4] and the study of thermal plume structure.[5] In addition, an experimental acoustic Doppler system for measuring winds remotely[6] has been installed at Denver, Colorado's Stapleton International Airport for extensive feasibility tests.

This paper describes the system and presents results from some of the preliminary calibration tests which demonstrate the capability of measuring winds with the acoustic Doppler shift. The success of an acoustic system operating in high ambient noise is almost totally dependent on how well the receiving antennas and transducers can be shielded from background noise. The antennas to be used and their installation are thus discussed in some detail.

I. THEORY

An extensive bibliography covering the major contributions to the theory of sound scattering in the free atmosphere is given by Little.[7] Turbulent eddies, that produce both temperature and wind related refractive index fluctuations are the primary scattering mechanism in the atmosphere. Furthermore, the scatter of sound depends strongly on the direction in which the scattering occurs. Direct backscattering is mainly a function of the temperature eddies in a given volume, and the amount of energy backscattered is smaller than in most other directions.[8] Only backscattered energy is received by a monostatic system (collocated transmitter and receiver). Energy scattered in all other directions, referred to as oblique scatter, can be received by a bistatic system (separated transmitter and receiver). Oblique scatter is a function of the combined effect of temperature and wind eddies and is typically much more intense than backscatter, except at directions normal to the transmitted beam where no energy is scattered.

The first demonstration of wind measurement by acoustic Doppler shift was made with a spaced configuration which received scattered energy a few meters above the ground.[9] It was shown that if wind-advected scatterers induce a Doppler shift Δf on the transmitted frequency f_0, the wind speed component V that produces this Doppler shift is

$$V=[C/2\,\sin(\theta/2)]\,[\Delta f/f_0],$$

where θ is the scattering angle measured from the direction of the transmitted beam to the direction of the scattered signal, and C is the velocity of propagation. For a monostatic system, the measured velocity component is along the antenna beam, but it is in the direction of the bisector of the angle formed by the intersection of the transmitter and receiver beams in the more general bistatic case.

Several theoretical studies[10–13] have dealt with the effects of turbulence and refraction of the intervening atmosphere and the effect of the Doppler spread on the final determination of the winds. In general, the results of these studies indicate that, while many of the foregoing statements are only approximately true, potential errors in measured wind would be less than 5% for heights less than 1 km.

II. SYSTEM CONCEPT

The basic monostatic acoustic transmitter consists of a timing device, a signal generator, and a power amplifier that drives a transducer to produce pulses of sound. After emitting a sound pulse, the system is switched to a passive mode and the returning echoes are processed by a receiver. Details of the design are described by Wescott *et al.*[14] and Simmons *et al.*[15]

The Doppler frequency shift is monitored by a fast frequency tracker that measures the first moment of the Doppler spectrum. Higher-order moments are not needed for determining the wind speed, but are useful for studying turbulence in the scattering volume.

To measure a vertical profile of the wind, it is necessary to use multiple antennas arranged so they sense

Copyright © 1974 by the Acoustical Society of America

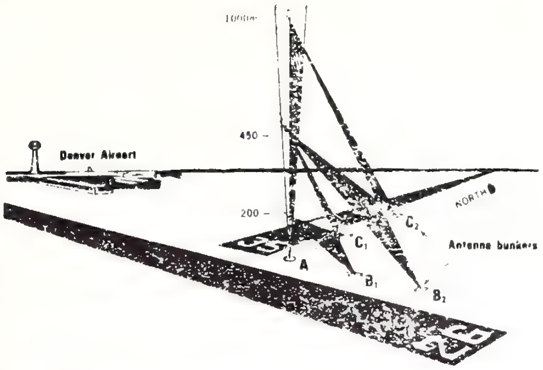

FIG. 1. Artist's concept showing the acoustic Doppler installation at Stapleton Airport in Denver, Colorado.

two components of the horizontal wind at many separate heights. A sketch of the configuration used for the calibration tests described later is shown in Fig. 1. The vertically pointing beam provides the insonification for the four antennas located on orthogonal legs that intersect at the vertically pointed antenna. The beams of the outlying antennas are wide enough to cover the height range from 200 to about 500 m (near antennas) and 500 to 1000 m (far antennas). The lack of scatter near 90°, discussed earlier, is the reason for limiting the lower range of the bistatic antenna to heights of 200 m. The region from near the ground up to 200 m is covered by pulsing antennas B_2 and C_2 simultaneously with the vertical system; then, during the dead time before the first bistatic signals reach the near antennas (B_1 and C_1), monostatic returns are received at positions B_2 and C_2. Horizontal uniformity of the wind must be assumed over an area the size of the antenna array as the altitude coverage from 30–200 m is not a common volume measurement, whereas it is from 200–1000 m. Measured winds are averaged for periods of between 2 and 7 min, thus, reducing the possible effect of nonuniform winds across the array.

The entire height range from 30 to 1000 m can be covered using this combined monostatic–bistatic approach. The sequence of events during each pulse cycle is: (a) the vertical and outlying tilted antennas (B_2 and C_2) are pulsed, (b) the two outlying tilted antennas start receiving monostatic signals from their own pulse, (c) after a little less than 2 sec, the first 200 m are probed, the receivers are switched to the near antennas (B_1 and C_1), and the bistatic echoes generated by the vertically traveling pulse are received as the pulse moves through the beams of the near antennas, (d) as the pulse reaches about 500 m, the receivers are switched back to the far antennas and they then act as passive bistatic antennas throughout the remainder of the cycle up to 1000 m. A receiver and Doppler tracker is time shared by the two stations on each of the legs.

This configuration is designed to measure only the horizontal wind component, hence, the vertically pointing antenna is not used to receive its own monostatic signals. This would be feasible if vertical wind information were required; however, the rather long averages applied to the measured wind would need to be shortened to prevent smoothing of the shorter term vertical wind oscillations. Two methods are used to avoid "cross talk" between the monostatic and bistatic echoes at the two antennas along each leg. One approach is to generate a pulsed frequency at B_1 and C_2 which is above the 1050-Hz signal produced by the vertical antenna. The 100-Hz bandwidth in the receivers, which are switched to the proper receiving frequency, will then reject the contaminating signal. A second approach is to use the same frequency at all pulsed antennas, but to generate only enough power at B_2 and C_2 to reach the 200-m altitude. The unpredictable effects of sound absorption and variation in the intensity of atmospheric scatterers makes the first approach more desirable.

Figure 2 shows a schematic of the system including the minicomputer that is required for the processing of the information provided by the sounder. The final output from the computer is the total horizontal wind vector at each 30-m height increment up to 1000 m.

The antennas for this system are of three types. The vertically pointing active system employs a 3-m-diam parabolic aluminum dish, fed by a cluster of four 100-W transducer horn combinations wired in series. They are driven with between 800- and 1000-W (electrical) peak power. The transducers are not damaged by this apparent overdriving because of the low-duty cycle and short pulse lengths. The outlying antennas are all of the off-axis paraboloid type where only a section of the parab-

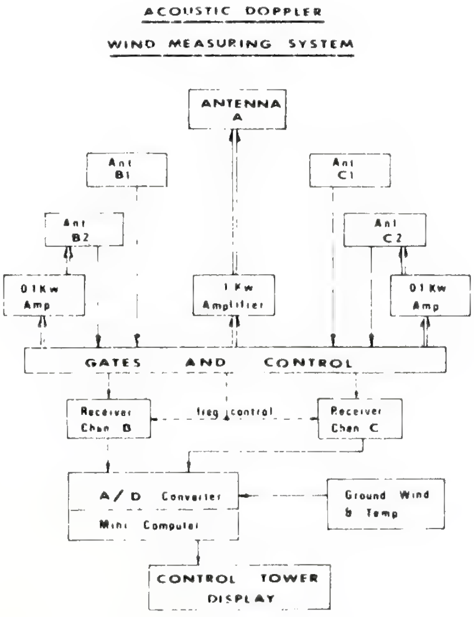

FIG. 2. Schematic diagram of the components that make up the acoustic Doppler wind measuring system. Refer to Fig. 1 for the antenna locations.

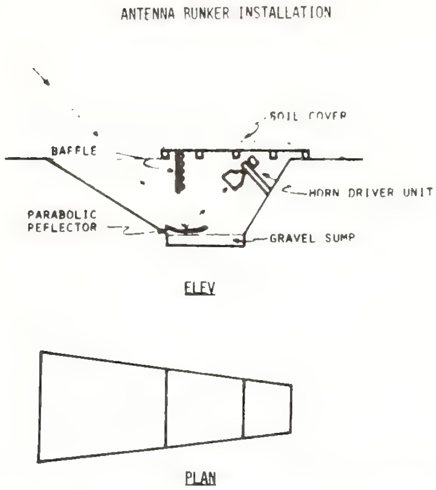

FIG. 3. Sketch of the antenna bunker and baffle used at locations B_2 and C_2.

oloid which is normal to the axis is used and is fed by a horn transducer combination at the focal point, and aimed in a direction also normal to the parabolic axis. The two outer antennas are about twice as large as those used at the near locations.

To reduce background noise that might enter through the side-lobe pattern, the receiving antennas are buried in bunkers with openings that allow the beam to project out at an elevation angle of about 45°. A sketch of the antenna installed in a bunker is shown in Fig. 3. Sound-absorbing convoluted foam plastic is added to critical areas within the bunker to increase the noise rejection characteristics. Comparison of background noise levels measured with this installation and those made with a shielded, above-ground antenna, show that between 15- to 20-dB improvement is achieved with the bunker-type installation.

It is also expected that the noise generated by aircraft, will cause oblique scattering directly into the main beam. At present, these noise sources are expected to render the system inoperative for about 50% of the time during the peak traffic periods at Stapleton Airport (i.e., one landing or takeoff per minute).

III. WIND MEASUREMENT AND CALIBRATION

During the development phases of the acoustic Doppler system, acoustically derived winds and wind measured by standard *in situ* devices were compared in several ways. The first comparison was between a two axis bistatic system and a kytoon-mounted anemometer[2] that was tethered at heights between 100 and 200 m. A second test used a three-axis monostatic system and the kytoon-mounted anemometer. The description of these early tests has been published elsewhere[3] and some of the results summarized in the scatter diagram shown in Fig. 4. This scatter diagram shows the comparison of 2-min average winds measured by the kytoon [referred to as a Boundary Layer Profiler (BLP)] and the acoustic system. The correlation coefficient of 0.96 and regression-line slope of 0.95 indicates very good agreement between the two sets of wind measurements.

Later tests, conducted near a 150-m tower equipped with anemometers, showed equally good agreement. They also demonstrated that the monostatic system was limited to ranges below 500 m, and that the strength and character of the returns from temperature fluctuations alone were highly variable and subject to long periods of fade when no wind information could be obtained.

The most recent tests, using the bistatic configuration described earlier, were designed to collect wind data throughout the total 1-km height range. Independent wind data, needed to compare with the acoustic Doppler winds, were measured with a standard GMD-1 and slow ascent radiosonde. For this test, only one leg of the two-axis system was installed along a line of azimuth 221°–41° at a field site near Boulder, Colorado. Since only one component of the wind was measured by the acoustic Doppler system, it was necessary to extract it from the radiosonde winds before comparing the two sets of data. Previous tests which compared the two-axis Doppler winds with a tower mounted anemometer indicated that the true wind direction could be measured to within 5 or 10 deg.

The computer program used to reduce the Doppler winds smoothed each height gate (30 m) with running means for period of from 2 to 7 min. The radiosonde reduction program contained three smoothing options that applied different lengths of running means along the wind profile. These smoothing operations differ in that one is time-dependent (each Doppler gate was smoothed over a number of pulses) and the other is space-dependent. This means that the Doppler information is smoothed along a horizontal direction and the radiosonde is smoothed in the vertical direction. This difference may have contributed to some of the observed error between the two sets of wind profiles.

An example of the comparison between the acoustic Doppler and the radiosonde winds is shown in Fig. 5. The two dashed curves represent both smoothed and unsmoothed radiosonde data. To obtain better resolution, slow ascent balloons, requiring from 10 to 15 min to reach 1 km, were used during these tests. The acoustic

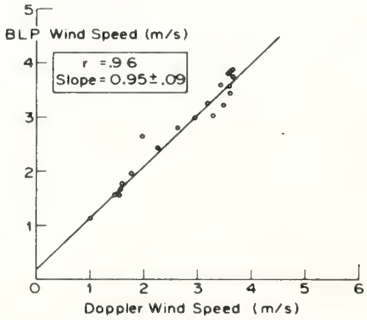

FIG. 4. Scatter diagram of the acoustic Doppler winds versus those measured by an anemometer suspended from a kytoon (BLP).[3]

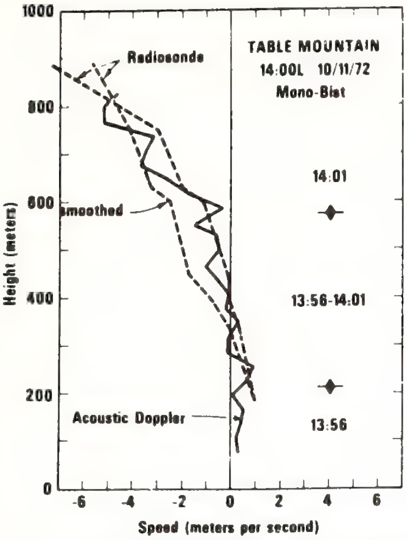

FIG. 5. Wind profiles measured by the acoustic Doppler system (solid line) and by the radiosonde (dashed line). Light and heavily smoothed radiosonde profiles are both shown.

Doppler system covered this range every 8 sec making it necessary to adjust the Doppler profiles to the time that the radiosonde balloon was in a particular height range. The resulting valid times are shown on the right side of Fig. 5. The acoustic data in each of the height increments are the average for the preceding 5 min.

Figure 6 is a similar comparison between another radiosonde and an acoustic Doppler wind profile. The acoustic data have again been time shifted to match the height–time position of the radiosonde. The portions of the profile marked "mono," "bistat 1," and "bistat 2" indicate the regions covered by the separate components of the Doppler system. The poor agreement up to 300 m is due to the combination of an error (since corrected) in the monostatic system calibration and weak signals near the lower portion of the near antenna's beam.

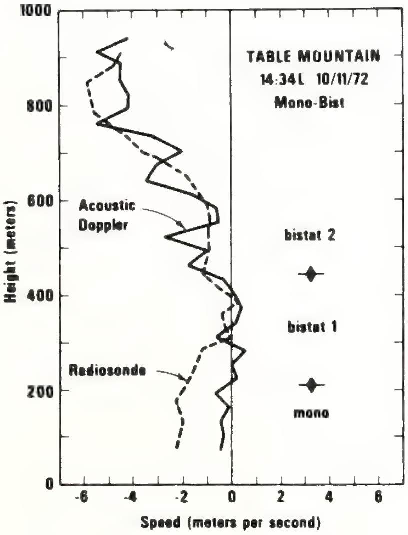

FIG. 6. Wind profiles measured by the acoustic Doppler system (solid line) and a radiosonde (dashed line). The regions separated by the diamonds on the right of the figure indicate the levels where antenna switching took place.

Wind sampled at 50-m increments on each of six profiles (two of which are shown in Figs. 5 and 6) generated during the calibration tests is plotted on a scatter diagram (Fig. 7) of acoustic Doppler (Dop) winds vs radiosonde (Rad) winds (both in msec^{-1}). The linear regression curve for this set of points is the solid line in Fig. 7. The perfect agreement line of slope 1.0 is shown as the dashed line. The 95% confidence limits on the slope of the regression line are 0.95 and 0.75, not including, but close to 1.0. The 95% confidence limits on the zero *y* intercept are 0.35 and − 0.022, including zero.

IV. CONCLUSIONS

Given the difference in resolution and the spatial separation of the radiosonde and acoustic profiles, the results of the comparisons of wind profiles are good. In all cases, the acoustic profiles suggest that the wind field contains more structure than was indicated by the radiosonde. With the test data available, it is impossible to say if the variable nature of the Doppler profiles is real or possibly a manifestation of the different smoothing procedures used on the two sets of data or of noise tracking in the receiver. It can be argued that a system consisting of a radiosonde package suspended some 20 or 30 m below a balloon will tend to act as a low-pass filter as it passes through the atmosphere. If this is the limiting factor, then the Doppler system is indeed much better than the device being used for the comparison. More testing near a fixed anemometer on a tower, or one suspended from a large kytoon, will be needed to resolve this point. These preliminary results do indicate that it will be possible to remotely determine wind profiles to altitudes of 1 km with accuracies that meet airport operational requirements.

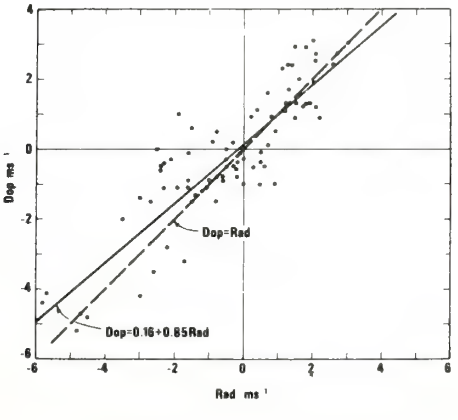

FIG. 7. Scatter diagram of acoustic Doppler winds (Dop) versus radiosonde winds (Rad). Standard error of estimate = 0.89.

ACKNOWLEDGMENTS

Support for this work has been provided by the Weather and Flight Service Station Branch, Systems Research and Development Service of the Federal Aviation Administration.

*NRC postdoctoral.

[1] D. W. Beran, C. G. Little, and B. C. Willmarth, "Acoustic Doppler Measurements of Vertical Velocities in the Atmosphere," Nature **230**, 160–162 (1971).

[2] D. W. Beran and B. C. Willmarth, "Doppler Winds From a Bistatic Acoustic Sounder," Proc. Seventh Int. Symp. on Remote Sensing of the Environment, Univ. of Michigan, **3**, 1699–1714 (1971).

[3] D. W. Beran and S. F. Clifford, "Acoustic Doppler Measurement of the Total Wind Vector," Proc. Second Symp. on Meteorol. Observations and Instrumentation, Am. Meteorol. Soc., 100–109 (1972).

[4] D. W. Beran, W. H. Hooke, and S. F. Clifford, "Acoustic Echo Sounding Techniques and Their Application to Gravity-Wave, Turbulence, and Stability Studies," Boundary Layer Meteorol. **4**, 133–153 (1973).

[5] F. F. Hall Jr., "Temperature and Wind Structure Studies by Acoustic Echo Sounding," in *Remote Sensing of the Troposphere*, NOAA/ERL (U. S. Government Printing Office, Washington, D. C., 1972), Chap. 18.

[6] D. W. Beran, "Acoustics: A New Approach for Monitoring the Environment Near Airports," J. Aircraft **11**, 934–936 (1971).

[7] C. G. Little, "Acoustic Methods for the Remote Probing of the Lower Atmosphere," Proc. IEEE **57**, 571–578 (1969).

[8] C. G. Little, "On the Detectability of Fog, Cloud, Rain and Snow by Acoustic Echo Sounding Methods," J. Atmos. Sci. **29**, 748–755 (1972).

[9] G. Kelton and P. Bricout, "Wind Velocity Measurements Using Sonic Techniques," Bull. Am. Met. Soc. **45**, 571–580 (1964).

[10] E. H. Brown, "Acoustic Doppler Radar Scattering Equation and General Solution," J. Acoust. Soc. Am. **52**, 1391–1396 (1972).

[11] T. M. Georges and S. F. Clifford, "Estimating Refractive Effects in Acoustic Sounding," J. Acoust. Soc. Am., to appear in special issue of Symp. on Atmos. Acoustics and Noise Propagation (1973).

[12] S. F. Clifford and E. H. Brown, "Acoustic Scattering From a Moving Turbulent Medium," J. Acoust. Soc. Am., to appear in special issue, Symp. on Atmos. Acoustics and Noise Propagation (1974).

[13] T. M. Georges and S. F. Clifford, "Acoustic Sounding in a Refracting Atmosphere," J. Acoust. Soc. Am. **52**, 1397–1405 (1972).

[14] J. W. Wescott, W. R. Simmons, and C. G. Little, "Acoustic Echo Sounding Measurements of Temperature and Wind Fluctuations," ESSA Tech. Memo. ERLTM-WPL 5, Boulder, Colorado (1970).

[15] W. R. Simmons, J. W. Wescott, and F. F. Hall, Jr., "Acoustic Echo Sounding as Related to Air Pollution in Urban Environments," National Oceanic and Atmospheric Admin., Tech. Rept. ERL216-WPL 17, Boulder, Colorado (1971).

USCOMM - ERL

Journal of Geophysical Research 79, 5567-5571, December 1974.

Some Recent NOAA Theoretical Work on Echo Sounding in the Atmosphere

EDMUND H. BROWN

Wave Propagation Laboratory, NOAA Environmental Research Laboratories, Boulder, Colorado 80302

This paper reviews some recent theoretical work on the effects of a nonzero mean wind on the propagation and scattering of sound by turbulent refractivity fluctuations. The paper includes a study of the deformation of the scattering cross section due to advection of the scatterers and analyses of the broadening of the frequency spectra of the acoustic pressure and pressure amplitude for forwardscatter and backscatter modes. The results have immediate applications both for determining the accuracy of echosonde measurements and for providing sensitive parameters for remote sensing of atmospheric structure.

As early as 1874 Tyndall observed, as was rephrased by *Rayleigh* [1945], 'that the very limited distances to which sounds are sometimes audible are due to an actual stopping of the sound by a flocculent condition of the atmosphere arising from unequal heating or moisture.' In addition, *Tyndall* [1874] made experimental observations on the aerial reflection (scattering) of sound by clear but turbulent air. Nearly a century passed before *McAllister* [1968] and *Little* [1969] suggested feasible echosonde techniques for remote sensing of refractive fluctuations in the atmosphere. The richness of the observations of atmospheric structure obtained by equipment of relative simplicity depends in large part on the introduction of the facsimile recorder. The techniques furnish altitude versus time charts in which the trace blackness corresponds to the magnitude of the scattering cross section, that is, to the intensity of the random fluctuations. Shortly afterward, *Beran* [1971] began the more difficult study of frequency spectra of echo sounder returns to obtain Doppler shifts corresponding to mean winds. Recently, *Hall* [1972] gave a complete state-of-the-art review of atmospheric echosonde experimental methods and results. The above brief remarks on echosonde techniques provide motivation for the following also brief review of early theoretical studies on the interaction of sound with the atmosphere.

Any theory of acoustic propagation in the real atmosphere must take turbulence into account, particularly since the latest results of Bourne (F. F. Hall, personal communication, 1974) show that turbulence, even though it is spatially intermittent, appears all the way from ground to tropopause. The combination of turbulence with tropospheric mean temperature gradients results in temperature mixing, random temperature fluctuations, and thus acoustic refractivity fluctuation fields. The theory of the interaction of sound with turbulence, just as the theory of turbulence itself, rests on the viewpoint introduced by *Taylor* [1935], which discarded deterministic modeling and treated the statistical properties of the turbulence directly. The availability of the first theoretical quantity needed for interpretation of echosonde data, the scattering cross section, also played a large part in the impetus given to the development of echosonde techniques.

In the same year that *Kolmogorov* [1941] and *Obukhov* [1941*a*] found the $\frac{2}{3}$ law for the inertial range of turbulence, *Obukhov* [1941*b*] related the scattering cross section to the general expression for the spectral density of turbulent kinetic energy. However, the neglect of gradients of the velocity fluctuations flawed the derivation and led to the missing $\cos^2 \theta$, an error continued by some later Russian researchers. *Blokhintzev* [1946] introduced the assumption that only wave numbers in the inertial range of turbulence affect the propagation of audible and high-frequency sound, thus permitting the use of the Kolmogorov spectrum in the scattering cross section. *Kraichnan* [1953] and *Lighthill* [1953] simultaneously found the correct form of the velocity-dependent part of the scattering cross section in 1953. Four years later *Batchelor* [1957] obtained the scattering cross sections used today, both the same velocity-dependent part and the part dependent on the spectral density of fluctuations of a passive additive such as acoustic velocity or temperature. Although Batchelor did not express the total cross section as the sum of the velocity-dependent and the temperature-dependent parts, such a summation is implicit in the fact that the cross section represents a normalized energy flow, and thus partial cross sections are additive.

Copyright © 1974 by the American Geophysical Union.

Evidently unaware of the earlier work, *Tatarskii* [1959] obtained the total scattering cross section expressed as the sum of a velocity-dependent and a temperature-dependent part. Unfortunately, the derivation followed Obukhov in neglecting gradients and thus omitted the factor $\cos^2 \theta$. The striking divergence in scattering angle dependence near 90° between Tatarskii's theoretical expression and the extensive experimental results of *Kallistratova* [1959] prompted *Monin* [1962] to reexamine the derivation. Monin's analysis obtained the same results found earlier by Batchelor and again expressed the total cross section as the sum of a velocity-dependent and a temperature-dependent part. In his monograph on wave propagation in turbulent atmospheres and its revision, *Tatarskii* [1959, 1971] collected a wealth of results, many from his previous papers, on the propagation and scattering of light and high-frequency sound. These results included amplitude and phase structure functions, two-dimensional spatial spectra of amplitude and phase for planes perpendicular to the propagation path, and the frequency spectrum of the amplitude fluctuations in a CW wave propagating through turbulence convected by a mean cross wind.

Most of the results of Tatarskii, mentioned above, required the condition of wavelengths λ much less than the inner scale of turbulence l_0. By calculating the two-dimensional acoustic amplitude and phase spectra for line-of-sight propagation without this condition, *Clifford and Brown* [1970] found that the theory remained valid for sound waves, at least for wavelengths up to the outer scale of turbulence L_0. Their result implies that most of the material in Tatarskii's monographs applies to sound propagation in both audible and high-frequency ranges. The present paper reviews some recent work by *Brown* [1972, 1974], *Clifford and Brown* [1974], and *Brown and Clifford* [1973*a*, *b*] on the effect that convection of turbulence by a mean crosswind has on the scattering cross section and various forwardscatter and backscatter spectra. The review makes no pretense of completeness, especially with regard to the large amount of work presently underway to deepen and strengthen the line-of-sight propagation theory by avoiding the Born single-scatter approximation.

ACOUSTIC EQUATION

Since even linearized sound propagation in a turbulent medium obeys an equation more complicated than the wave equation, convection of turbulence by a mean wind produces more changes than just the addition of a convective term to the time derivative operator. The form of the propagation equation most amendable to useful solution appears in the form of the scattering equation, the propagation equation for the scattered wave assuming the single-scatter, or Born, approximation. This approximation reduces the propagation equation to an inhomogeneous wave equation and reduces the changes introduced by a mean wind to the addition of the convection operator and an alteration of the inhomogeneous, or source term.

The most convenient form of the scattering equation appears with wave number $k = \omega/c_0$ rather than time as the independent variable (ω is arbitrary angular frequency, and c_0 the mean sound speed). The Fourier transform of a function of time, $F(k) = \mathfrak{F} f(c_0 t)$, or

$$F(k) = (2\pi)^{-1} c_0 \int_{-\infty}^{\infty} dt\, e^{ikc_0 t} f(c_0 t) \tag{1}$$

associates the product of two functions $f(c_0 t)g(c_0 t)$ with the convolution product $F(k) * G(k) = \mathfrak{F}[f(c_0 t)g(c_0 t)]$, or

$$F(k) * G(k) = \int_{-\infty}^{\infty} dk'\; F(k - k')G(k') \tag{2}$$

The operator $\mathfrak{F}$ associates the quantities $N'(k)$, $\bar{P}(k)$, $P'(k)$ with the refractivity fluctuations $n'(c_0 t)$, the mean or initial sound pressure $\bar{p}(c_0 t)$, and the scattered sound pressure $p'(c_0 t)$, respectively. Given a mean wind with the components $\bar{w}_i$, $i = 1, 2, 3$, and the related Mach vector $m_i = \bar{w}_i/c_0$, *Brown* [1972] obtained the scattering equation in the form

$$\Delta P' + (k + im_j\partial_j)^2 P' = 2\partial_j(N' * \partial_j \bar{P}) \tag{3}$$

where $\partial_i = \partial/\partial x_i$, repeated indices are summed, and $\Delta = \partial_i\partial_i$.

When isotropic 'frozen' turbulence convected by a mean wind (Taylor's hypothesis) is assumed, the spatial Fourier transform

$$N'(k) = \int d\phi\,(\kappa_i)\, \exp\,(ix_i\kappa_i)\; \delta(k - m_j\kappa_j) \tag{4}$$

relates the refractivity fluctuations $N'(k)$ over the physical space x_i to the Fourier-Stieltjes measure $d\phi(\kappa_i)$ of the fluctuations over the Fourier space with coordinates κ_i, $i = 1, 2, 3$. Here, δ is the Dirac measure satisfying the condition $\int dx\, f(x)\, \delta(x) = f(0)$ for any function $f(x)$. For isotropic turbulence with the three-dimensional spectrum of refractivity fluctuations $\Phi_n(\kappa)$, denoting the complex conjugate by a superscript dagger, $d\phi(\kappa_i)$ satisfies

$$\langle d\phi(\kappa_i)\; d\phi^{\dagger}\,(\kappa_i')\rangle = \Phi_n(\kappa)\delta(\kappa_i - \kappa_i')\; d\kappa_i\; d\kappa_i' \tag{5}$$

where κ is the magnitude of κ_i and the angle brackets denote an ensemble average.

For the case of a single-frequency CW initial wave, $\bar{P}(k)$ becomes $\delta(\Delta k)P_0(k)$, where $\Delta k = k - k_0$ with k_0 the carrier wave number; and, the source term reduces to $2\partial_j[N'(k_0)\partial_j P_0(k)]$. Then, the effects of a nonzero mean wind appear only in the addition of two convective terms, the additional operator $im_j\partial_j$ in (3), and the additional argument $-m_j\kappa_j$ of the Dirac measure in (4). The following sections discuss various useful forwardscatter, backscatter, and CW-dependent solutions of (3).

WIND DISTORTION OF THE SCATTERING CROSS SECTION

In the introduction earlier work on the farfield cross section for scattering of sound by refractivity fluctuations with zero mean wind was reviewed. Since the change in solutions of (3) with mean wind for the case of a single-frequency CW initial wave depends only on refractive effects, Snell's law relates the initial and scattered wave vectors $\mathbf{k}_0$ and $\mathbf{k}_1$, respectively, in a coordinate system fixed at the ground to the initial and scattered wave vectors $\hat{\mathbf{k}}_0$ and $\hat{\mathbf{k}}_1$, respectively, in a coordinate system moving with the mean wind. *Georges and Clifford* [1972, 1974] have studied integrated refractive effects, such as ray bending, and found them to be small, at least for echo sounding to the top of the boundary layer. *Clifford and Brown* [1974], however, obtained significant changes in the cross section for scattering angles at or below 90° due to the shifts in the wave vectors.

Assume a horizontally stratified atmosphere, that is, zero wind below a certain height, and a mean, not necessarily horizontal, wind convecting turbulence above that height. For convenience, define the unit direction vectors $\mathbf{e}_0 = \mathbf{k}_0/k_0$, $\mathbf{e}_1 = \mathbf{k}_1/k_1$, $\hat{\mathbf{e}}_0 = \hat{\mathbf{k}}_0/\hat{k}_0$, and $\hat{\mathbf{e}}_1 = \hat{\mathbf{k}}_1/\hat{k}_1$. In the moving medium the Kraichnan-Lighthill-Batchelor form of the scattering cross section becomes

$$\sigma(\hat{\theta}) = \frac{\pi}{2}\hat{k}_0^{\,2}(\hat{e}_0 \cdot \hat{e}_1)^2 \left[\frac{\Phi_T(K)}{T_0^{\,2}} + \frac{(1 + \hat{e}_0 \cdot \hat{e}_1)E(K)}{2\pi c_0^{\,2} K^2}\right] \tag{6}$$

where $\hat{\theta} = \arccos \hat{\mathbf{e}}_0 \cdot \hat{\mathbf{e}}_1$, $K^2 = 2\hat{k}_0^{\,2}(1 - \hat{\mathbf{e}}_0 \cdot \hat{\mathbf{e}}_1)$, T_0 is the mean temperature, Φ_T is the three-dimensional spectrum of the temperature fluctuations, and $E(K)$ the spectrum of the kinetic energy. For audible and high-frequency sound, and when $\hat{\theta}$ is not too close to zero, the inertial forms of the spectra give good approximations. From *Tatarskii* [1971], the inertial range forms of the spectra are $\Phi_T(K) = 0.033C_T^{\,2}K^{-11/3}$ and $E(K) = 0.76C_v^{\,2}K^{-5/3}$, where C_T and C_v are the respective temperature and velocity structure constants.

Suppose an initial acoustic beam launched at an elevation angle ϕ_0 and a scattered wave received at an elevation angle ϕ_1, with the apparent scattering angle $\theta = \phi_0 + \phi_1$. Define the magnitude of the components of the mean wind in the initial and scattered directions by $m_0 = \mathbf{e}_0 \cdot \mathbf{m}$ and $m_1 = \mathbf{e}_1 \cdot \mathbf{m}$, where m is the vector with components $\mathbf{m} = (\bar{w}_i/c_0)$. Then, for angles not too close to grazing, such that $\sin^2\phi_0 >> 2m_0$ and $\sin^2\phi_1 >> 2m_1$, use of Snell's law implies [see *Clifford and Brown*, 1974, for the details] that the scattering cross section in coordinates fixed at the ground becomes

$$\begin{aligned}\sigma(\theta) = {} & 0.033k_0^{\,1/3}(1 - m_0)^{1/3} \\ & \cdot(M \cos\theta + m_0\Sigma + m_1\Sigma^{-1})^2\chi^{-11/3} \\ & \left\{0.13\frac{C_T^{\,2}}{T_0^{\,2}} + \frac{C_v^{\,2}}{c_0^{\,2}}\right. \\ & \left.\cdot\left[M\cos^2\frac{\theta}{2} - \frac{1}{2}m_0(1 - \Sigma) - \frac{1}{2}m_1(1 - \Sigma^{-1})\right]\right\}\end{aligned} \tag{7}$$

where $M = 1 + m_0 + m_1$, $\Sigma = \phi_2/\sin \phi_1$, and the square of the log amplitude $\chi^2 = M \sin^2 (\theta/2) - (1/2)m_0(1 + \Sigma) - (1/2)m_1(1 + \Sigma^{-1})$. When the mean wind vanishes, $m_0 = m_1 = 0$, $M = 1$, and (7) reduces to equation (23) of *Tatarskii* [1971, chapter 2].

For apparent backscatter $\theta = \pi$, both Σ and χ reduce to one. Then, except for the factor $(1 - m_0)^{1/3}$, which differs only negligibly from 1 when $m_0 << 1$, the backscatter cross section becomes

$$\sigma_m(\pi) = 0.004k_0^{1/3} (1 - m_0)^{1/3} C_T^2/T_0^2 \approx \sigma_0(\pi) \qquad (8)$$

approximately the same as the backscatter cross section $\sigma_0(\pi)$ in *Tatarskii* [1971]. However, (7) gives nonnegligible wind-induced distortion of the scattering cross section at apparent scattering angles equal to or smaller than 90°. For example, for $\theta = 90°$ with a launch angle of $\phi_0 = 45°$, the wind-distorted cross section becomes

$$\sigma_m(\pi/2) \approx 275m^2\sigma_0(\pi) \qquad (9)$$

Typical values of m, ranging from 0.01 to 0.05, give the result that $\sigma_m(\pi/2)$ varies between 3 and 70% of the backscatter signal strength. Even larger percentages for $\sigma_m(\theta)$ occur as θ approaches the critical angle.

Figure 1 shows curves of the normalized scattering cross section $\sigma_m(\theta)/\sigma_0(\pi)$ as a function of apparent scattering angle θ seen from the ground, with the various values of the parameter $\gamma = C_v^2T_0^2/C_T^2c_0^2$, for the example of a 45° launch angle and a mean horizontal wind of magnitude $0.05c_0$.

FREQUENCY SPECTRA

Many assumptions such as the conditions of homogeneous isotropic inertial range and frozen turbulence permit easy solutions of acoustic scattering problems and give results that agree well with many past observations. However, the validity of the assumptions, considered as representing approximate models of the atmosphere, depends on the choice of the echosonde parameters and the true state of the atmosphere. A number of optical researchers [see *Clifford*, 1974] have found that the single-scatter assumption restricts the agreement between theoretical and experimental log-amplitude variance for line-of-sight propagation on limited path lengths and strength of turbulence. The observed variance fails to increase with increasing C_n, as is predicted by the single-scatter theory.

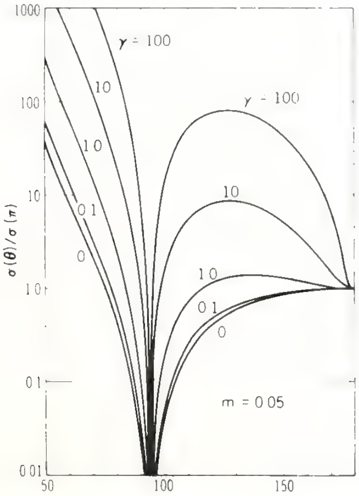

Fig. 1. Scattering cross section σ as a function of apparent scattering angle θ, with ratio m of mean wind to speed of sound and $\gamma = C_vT_0/C_Tc_0$ as parameters.

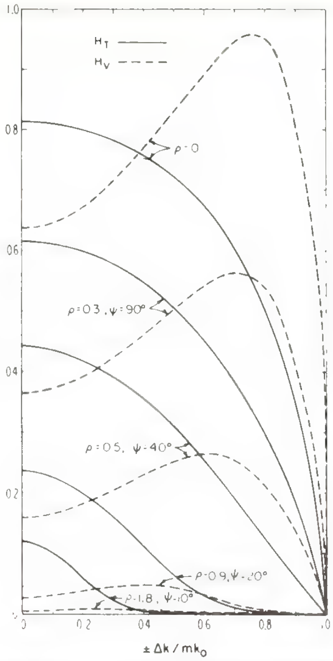

Fig. 2. Spectral factors for temperature and velocity fluctuations H_T and H_V as functions of $\Delta k/mk_0$.

Such a 'saturation' phenomenon should occur for line-of-sight acoustic beams when the quantity $k_0^{7/6}L^{11/6}C_n^2 \approx 1$, where L is the path length and C_n the structure constant of refractivity fluctuations.

One of the main purposes for the study of frequency spectra concerns the measurement of the mean wind. For the simplest configuration, the monostatic echosonde, the component of the mean wind parallel to the beam produces a proportional Doppler shift in the frequency of the spectral peak. Although it is not yet exploited and is of unknown accuracy, the broadening of the spectrum depends on the magnitude of the component of the mean wind transverse to the beam. Essentially, convection of turbulence across the echosonde beam by a transverse mean wind produces random frequency modulation of the beam frequencies and thus broadens the spectrum. More complex echosondes such as the bistatic or tristatic systems permit measurement of the complete three-dimensional vector mean wind field up to the range limit of the systems. However, measured frequency spectra also provide other atmospheric parameters, such as the structure constants of the temperature and velocity fluctuations.

Clearly, the above assumptions, such as the condition of frozen turbulence, play an important part in the theoretical study of frequency spectra. For example, in the absence of mean wind, frozen turbulence would have no time dependence and thus no spectral broadening. The study of frequency spectra represents a step in sophistication beyond that of scattering cross sections. The greater dependence of frequency spectra on the validity of the above assumptions implies a greater chance of inaccuracy in the measurements. On the other hand, frequency spectra can become powerful tools to explore the ranges of atmospheric and echosonde parameters for which the various assumptions above yield valid approximations.

SPECTRA FOR LINE-OF-SIGHT PROPAGATION

In the first considerations of a frequency spectrum, *Tatarskii* [1959] obtained the spectrum $W_{CW}(f) = W_{CW}(k)/4\pi c_0$ of amplitude fluctuations in a CW plane wave propagating through turbulence convected by a transverse mean wind ($f = \omega/2\pi$ is ordinary positive frequency, whereas k is positive or negative wave number). *Clifford* [1971] has generalized Tatarskii's results to propagation of spherical waves. The difficulty associated with including phase information in measurements of light or ultrasound and astronomical problems with scintillations of starlight led to the initial interest in the frequency spectra of the amplitude fluctuations. For plane waves, Tatarskii's result has the form

$$W_{CW}(k) = 2 \int_{k/m}^{\infty} d\xi \frac{\xi F_A(\xi\ 0)}{(m^2\xi^2 - k^2)^{1/2}} \tag{10}$$

where m is the Mach number of the transverse wind, $F_A(\xi, 0)$ is the two-dimensional spatial spectrum of the amplitude fluctuations [see *Clifford and Brown,* 1971] over the transverse Fourier space with the coordinates κ_α, $\alpha = 1, 2$, and where $\xi^2 = \kappa_\alpha \kappa_\alpha$.

Brown and Clifford [1973*a*] have studied the effect of changing from a CW wave to a pulse. For a linear system, if a sequence of operations on a wave occurs in time, the corresponding sequence in frequency becomes a set of convolution products with respect to wave number k. Since power spectra depend on the product of such sequences with their complex conjugates, in general, they will not also have the form of a sequence of k convolutions of the modulus-squared factors of the wave. However, for forwardscatter of a pulse only two operations take place: formation of a pulse with half length l having an envelope spectrum $D_0(\Delta k)$ and single scatter in the wave while it propagates through the turbulence. For stationary turbulence (including cases with a nonzero constant mean wind) the stationarity condition introduces a Dirac δ measure into the ensemble average of the modulus-squared Fourier-Stieltjes measures of the turbulent fluctuations. As a consequence the frequency spectrum of the amplitude fluctuations of a pulse, again, reduces to the form of a sequence of convolutions. In particular, *Brown and Clifford* [1973*a*] found

$$W_p\,(k) = (\pi/l)\, D_0^2(k) * W_{CW}(k) \tag{11}$$

where p is pulse. Note the shift in the center of D_0^2 from the carrier wave number k_0 to zero. Since the spectrum has a peak near the wave number $m(k_0/L)^{1/2}$ determined by the mean transverse wind and the Fresnel zone size $(\lambda L)^{1/2}$, with L the path length, the convolution operation in (12) both broadens the spectrum and shifts the peak to smaller wave numbers. (Note also that during the transformation of integration variables, *Brown and Clifford* [1973*a*] drop a factor 2, and thus their result, (23), should be doubled).

The advent of echosondes operating in the audible frequency range suggested the need for the power spectrum of the forwardscatter pressure wave itself, that is, including both amplitude and phase information. In another paper, *Brown and Clifford* [1973*b*] obtained the spectral density of the acoustic intensity due to propagation of a sound pulse through turbulence convected by a mean cross wind, and also obtained the equivalent width b_s of the spectrum as a function of the wind. When weak single scattering is assumed, the propagation broadening depends solely on the ratio of wind speed to the outer scale of turbulence L_0 and is independent of the strength of turbulence and total propagation distance L. Further, for an atmosphere with variable outer scale and with wind shear, the highest ratio of transverse wind to outer scale encountered by the pulse primarily determines the amount of broadening of the spectrum.

The remarks on the convenient effect that the stationarity condition has on the form of the forwardscatter amplitude spectrum apply equally to the spectral density of the intensity $I(k)$. Writing $\Delta k = k - k_0$ as before, *Brown and Clifford* [1973*b*] found that the frequency spectrum of the pressure for a CW wave has the form

$$I_{CW}(\Delta k) = \tfrac{1}{3} k_0^2 L C_n^2 L_0^{5/3} \frac{L_0/m}{[1 + (L_0/m)^2\ \Delta k^2]^{4/3}} \tag{12}$$

where C_n is the structure constant of the refractivity fluctuations as defined by *Tatarskii* [1959]. Using similar reasoning as that for the amplitude spectrum $W(k)$, the frequency spectrum for a pulse becomes

$$I_p(\Delta k) = (\pi/l) D_0^2(\Delta k) \underset{\Delta k}{*} I_{CW}(\Delta k) \tag{13}$$

where the symbol Δk under the asterisk indicates that the convolution is with respect to Δk rather than k. Note, moreover, that k_0 is the central wave number of both D_0^2 and I_{CW}, so that the mean cross wind broadens the spectrum without shift in the location of the peak.

The equivalent spectral width b_s gives a convenient measure of the amount of broadening produced by wind. This width is defined by the ratio $\int dk\ I(k)/I(0)$, that is, the ratio of the total scattered intensity in all wave numbers to the peak of the spectral density. For path lengths much greater than those of the outer scale $L \gg L_0$ [*Brown and Clifford,* 1973*b*],

$$b_s \approx (\pi/l)(1 + ml/L_0) \tag{14}$$

for the equivalent width of the spectrum $I(\Delta k)$. The result assumes weak scattering (less than 1 rad phase change per eddy). The most effective eddy size is the outer scale L_0, since it produces the maximum phase deviation, an effect more important for determining the change in bandwidth than the higher frequency but smaller amplitude phase modulation produced by smaller eddies drifting with the same velocity.

BACKSCATTER SPECTRA

When a mean transverse wind in the atmosphere convects turbulent eddies through the volume elements that produce the backscattered wave during echo sounding, again, a random frequency modulation and spectral broadening occurs. However, the process becomes more complicated than that in forwardscatter and depends strongly on the receiver beam half angle ψ or equivalently the effective receiver diameter-to-wavelength ratio ρ. The consideration of frequencies in the lower part of the audible range for echo sounding makes achievement of small beam angles difficult. Then, the validity of the far field approximation, that the linear dimension (measured in wavelengths) of the scattering volume is much smaller than the range (measured in wavelengths), becomes questionable.

The volume elements that contribute (with weights dependent on the beam pattern) to the signal of an isotropic receiver located on the ground lie in a spheroidal half shell. If R is the echosonde range, the mean radius of the shell varies from R at the zenith to $2R$ at the horizon. Similarly, if the echosonde uses a pulse of half-length l, the thickness of the shell varies from l at the zenith to $2l$ at the horizon. Recently, *Brown* [1974] found that the eddy scale parallel to the direction between differential scattering to element and the receiver varies from the expected $\lambda/2$ at the zenith to $\lambda/(2)^{1/2}$ at the horizon, and that the corresponding traverse scales vary from the outer scale L_0 at the zenith to λ at the horizon. Since the angle that a wind transverse to the echosonde axis makes with the above direction to a scattering element also varies with elevation, the total effect on the broadening of the frequency spectrum becomes quite complicated. For a nonisotropic receiver, only part of the scattering shell contributes effectively to the signal, and in the limit as $\psi \rightarrow 0$ the broadening drops to zero.

Fortunately, since mean winds below some value, say, 0.5 m/s, are of little interest in the problem, simpler solutions become useful approximations. For typical echosonde parameters and for winds above such a lower limit the parameter $mk_0 l$ takes on values much greater than $3\pi/2$, perhaps in the range between 10 and several hundred. For such values, Brown has obtained the following approximate solution for the frequency spectrum of the pressure as a function of wave number k and the receiver beam parameters ψ or ρ:

$$I(k) = 0.0105 l^2 k_0^{1/3} \frac{C_T^2}{T_0^2} (mk_0 l)^{-1} \cdot [H_T(\eta, \rho) + \gamma^2 H_V(\eta, \rho)] \qquad \eta^2 \leq 1 \qquad (15)$$

where $\eta = \Delta k/mk_0$, $\gamma = C_v T_0 / C_T c_0$, and the temperature and velocity dependent spectral factors H_T and H_V, respectively, appear in Figure 2. Note that if the intensity of temperature fluctuations falls much below that of velocity fluctuations, the vector character of the velocity produces a doubly peaked spectrum. Note, also, that even for very small beam angles the importance of the velocity fluctuation factor outweighs that for temperature beyond wave numbers about halfway to the limit mk_0 of influence of turbulence. By way of contrast, the backscatter broadening depends on the parameter $ml/(\lambda/2)$, that is, on the $\lambda/2$ size eddies chiefly responsible for the backscattering, whereas the forwardscatter broadening depends on the parameter ml/L_0, that is, on the largest, or L_0 size eddies responsible for the largest phase shifts.

Conclusions

Recent papers have studied a number of effects of nonzero mean wind on the scattering of sound by turbulent refractivity fluctuations. These effects include the deformation of the scattering cross section at or below scattering angles of 90° and the broadening of frequency spectra. The analysis presents specific formulas for the wind-broadened forwardscatter spectra of the pressure and the amplitude of the pressure and for the wind-broadened backscattered spectrum of the pressure. The results have immediate applications both for determining the accuracy of echosonde measurements and for providing additional sensitive parameters for remote sensing of atmospheric structure.

References

Batchelor, G. K., Wave scattering due to turbulence, Symposium on Naval Hydrodynamics, *Publ. 515*, Nat. Acad. of Sci., Nat. Res. Council, Washington, D. C., 1957.

Beran, D. W., C. G. Little, and B. C. Willmarth, Acoustic Doppler measurements of vertical velocities in the atmosphere, *Nature, 230*(5290), 160, 1971.

Blokhintzev, D. I., The propagation of sound in an inhomogeneous and moving medium, 2, *J. Acoust. Soc. Amer., 18,* 329, 1946.

Brown, E. H., Acoustic Doppler-radar scattering equation and general solution, *J. Acoust. Soc. Amer., 52,* 2391, 1972.

Brown, E. H., Turbulent spectral broadening of backscattered acoustic pulses, *J. Acoust. Soc. Amer.,* in press, 1974.

Brown, E. H., and S. F. Clifford, Amplitude spectra of acoustic pulses in the ocean, *J. Acoust. Soc. Amer., 54,* 461, 1973*a*.

Brown, E. H., and S. F. Clifford, Spectral broadening of an acoustic pulse propagating through turbulence, *J. Acoust. Soc. Amer., 54,* 36, 1973*b*.

Clifford, S. F., Temporal-frequency spectra for a spherical wave propagating through atmospheric turbulence, *J. Opt. Soc. Amer., 61,* 1285, 1971.

Clifford, S. F., and E. H. Brown, Propagation of sound in a turbulent atmosphere, *J. Acoust. Soc. Amer., 48,* 1123, 1970.

Clifford, S. F., and E. H. Brown, Acoustic scattering from a moving turbulent medium, *J. Acoust. Soc. Amer., 55,* 929, 1974.

Clifford, S. F., G. R. Ochs, and R. S. Lawrence, Saturation of optical scintillations by strong turbulence, *J. Opt. Soc. Amer., 64,* 148, 1974.

Georges, T. M., and S. F. Clifford, Acoustic sounding in a refracting atmosphere, *J. Acoust. Soc. Amer., 52,* 1397, 1972.

Georges, T. M., and S. F. Clifford, Estimating refractive effects in acoustic sounding, *J. Acoust. Soc. Amer., 55,* 934, 1974.

Hall, F. F., Temperature and wind structure studies by acoustic echosounding, in *Remote Sensing of the Troposphere,* edited by V. E. Derr, p. 18-1, U.S. Government Printing Office, Washington, D. C., 1972.

Kallistratova, M. A., An experimental investigation into the scattering of sound in a turbulent atmosphere, *Dokl. Akad. Nauk SSSR, 125,* 69, 1959.

Kolmogorov, A. N., Local structure of turbulence in incompressible fluids with very high Reynolds numbers, *Dokl. Akad. Nauk SSSR, 30,* 301, 1941.

Kraichnan, R. H., The scattering of sound in a turbulent medium, *J. Acoust. Soc. Amer., 25,* 1096, 1953.

Lighthill, M. J., On the energy scattered from the interaction of turbulence with sound or shock waves, *Proc. Cambridge Phil. Soc., 49,* 531, 1953.

Little, C. G., Acoustic methods for the remote probing of the lower atmosphere, *Proc. IEEE, 57,* 571, 1969.

McAllister, L. G., Acoustic sounding of the lower troposphere, *J. Atmos. Terr. Phys., 30,* 1439, 1968.

Monin, A. S., Characteristics of the scattering of sound in a turbulent atmosphere, *Sov. Phys. Acoust., 7,* 370, 1962.

Obukhov, A. M., Energy distribution in the spectrum of turbulent flow, *Dokl. Akad. Nauk SSSR, 32,* 19, 1941*a*.

Obukhov, A. M., Scattering of sound in a turbulent flow, *Dokl. Akad. Nauk SSSR, 30,* 611, 1941*b*.

Rayleigh, Lord (J. W. Strutt), *The Theory of Sound,* vol. 2, p. 136, Dover, New York, 1945.

Tatarskii, V. I., *Theory of Fluctuation Phenomenon for Wave Propagation in a Turbulent Atmosphere* (in Russian), Akademii Nauk SSSR, Moscow, 1959. (*Wave Propagation in a Turbulent Medium,* Engl. Transl., McGraw-Hill, New York, 1969.)

Tatarskii, V. I., *The Effects of the Turbulent Atmosphere on Wave Propagation,* U.S. Department of Commerce, National Technical Information Service, Springfield, Va., 1971.

Taylor, G. I., Statistical theory of turbulence, *Proc. Roy. Soc., Ser. A., 15,* 421, 1935.

Tyndall, J., On the atmosphere as a vehicle of sound, *Phil. Trans. Roy. Soc., Ser. A., 164,* 183, 1874.

(Received March 20, 1974;
accepted July 26, 1974.)

NOAA Technical Memorandum ERL NSSL-69, 185-193, May 1974.

INFRASOUND FROM THE 29-30 APRIL 1970 STORMS

T. M. Georges and Gary E. Greene

Wave Propagation Laboratory
Boulder, Colorado 80302

We report the observable features of infrasound recorded at Boulder, Colorado, and San Diego, California, during the subject storm. Triangulation indicates that the emissions originated in north-central Texas, not in the Oklahoma City area.

1. BACKGROUND

Infrasound is the name given to a class of acoustic waves whose frequencies are subaudible but which travel through the atmosphere at essentially the local speed of sound. A long-period limit for acoustic waves exists at the atmosphere's acoustic-cutoff period, about four minutes in the troposphere.

Many kinds of natural infrasound have now been classified, but adequate models of natural source mechanisms exist for only a few. Georges and Young (1972) review techniques for observing infrasound with arrays of microbarographs and current knowledge about many different kinds of natural infrasound.

It has been known for over a decade that certain convective storms emit infrasound powerful enough to be detected over 1500 km away, but the precise emission mechanism remains unknown. These waves typically have amplitudes of about one microbar, periods between about 10 and 60 sec, and persist for one or two hours. More recently, a connection has been found between certain severe storms and a particular class of wavelike oscillations in the ionospheric F region, 200 to 300 km above the ground. These waves were observed with ground-based radio-echo sounders and have periods between two and five minutes. Georges (1973) has recently reviewed the history and phenomenology of both of these manifestations of severe-weather infrasound.

The purpose of this paper is to report the characteristics of infrasound recorded at four microbarograph arrays during the particular storm system that is the subject of the other papers in this report. Only by comparing the details of the emissions with the spatial and temporal characteristics of storm observables, such as those presented by the companion papers in this report, is much progress toward discovery of the emission mechanism likely. Conversely, it does not seem unreasonable to hope that discovery of the mechanism might in turn shed some light on severe-storm dynamics.

2. PROCEDURE

Data recorded at four microbarograph observatories during the interval 0000 to 1500 UT (1800-0900 CST) on 29-30 April were examined for evidence of acoustic arrivals from the Texas-Oklahoma vicinity. The four observatories are at Boulder, Colorado (NOAA), Washington, D. C. (NOAA), Pullman, Washington, (Washington State University) and San Diego, California (Naval Electronics Laboratory Center). These are the only locations in the continental U. S. where suitable recordings were being made at the time and from which records are still available.

We analyzed analog tape recordings of pressure fluctuations from four microbarographs at each observatory by means of the NOAA Analog Correlator (Brown, 1963; Georges and Young, 1972), which automatically performs cross-correlation analysis to yield the speed and direction of coherent wave arrivals. In cases where acoustic wave arrivals were detected from roughly the correct direction and lasted for more than a few minutes, we measured arrival azimuth in each five-minute interval in which wave coherence (in the sense defined by Georges and Young) exceeded a certain threshold. That threshold is determined from experience in making realiable wave measurements with the analog correlator and is essentially equivalent to a broadband wave coherence of about 0.2 over the microbarograph array. Wave coherence is affected not only by propagation effects that cause "corrugations" on the wave fronts but also by non-acoustic "noise" at the sensors due to wind-advected turbulence and atmospheric gravity waves. During the intervals studied here, background noise level remained sufficiently low that we can assume that the variations in wave coherence during high S/N intervals are due primarily to variations in wave strength. (The variations during low S/N intervals may be caused by noise-level fluctuations, however.) The only exception is that high ambient noise began at Pullman at 0800 UT, precluding signal detection thereafter.

Frequency content of the waves is estimated by passing the signal through a narrow-band filter with adjustable center frequency and recording the frequencies of the two or three dominant frequency peaks that the signals usually exhibit. The portion of the wave frequency spectrum searched corresponds roughly to the 20 dB points on the overall frequency response of the recording and processing system, namely between wave periods of about 2 and 100 sec.

3. RESULTS

Strong, persistent infrasonic waves were detected at only two of the four observatories, namely Boulder, Colorado and San Diego, California. Weak waves of short or intermittent duration appeared in data recorded at Washington, D. C. and Pullman, Washington, so that it was possible to make only spot estimates of wave parameters.

Because some storm systems have been known to produce strong waves detectable several thousand kilometers away, the emissions from this system must be regarded as considerably less intense than the strongest waves observed from other storms. Maximum wave amplitude at Boulder was about 0.7 microbars and at San Diego was about 0.6 microbars.

Figure 1 summarizes the history of the important wave observables at Boulder during the period of interest, and figure 2 presents similar information for the San Diego data. The lower part of each figure is a time history of

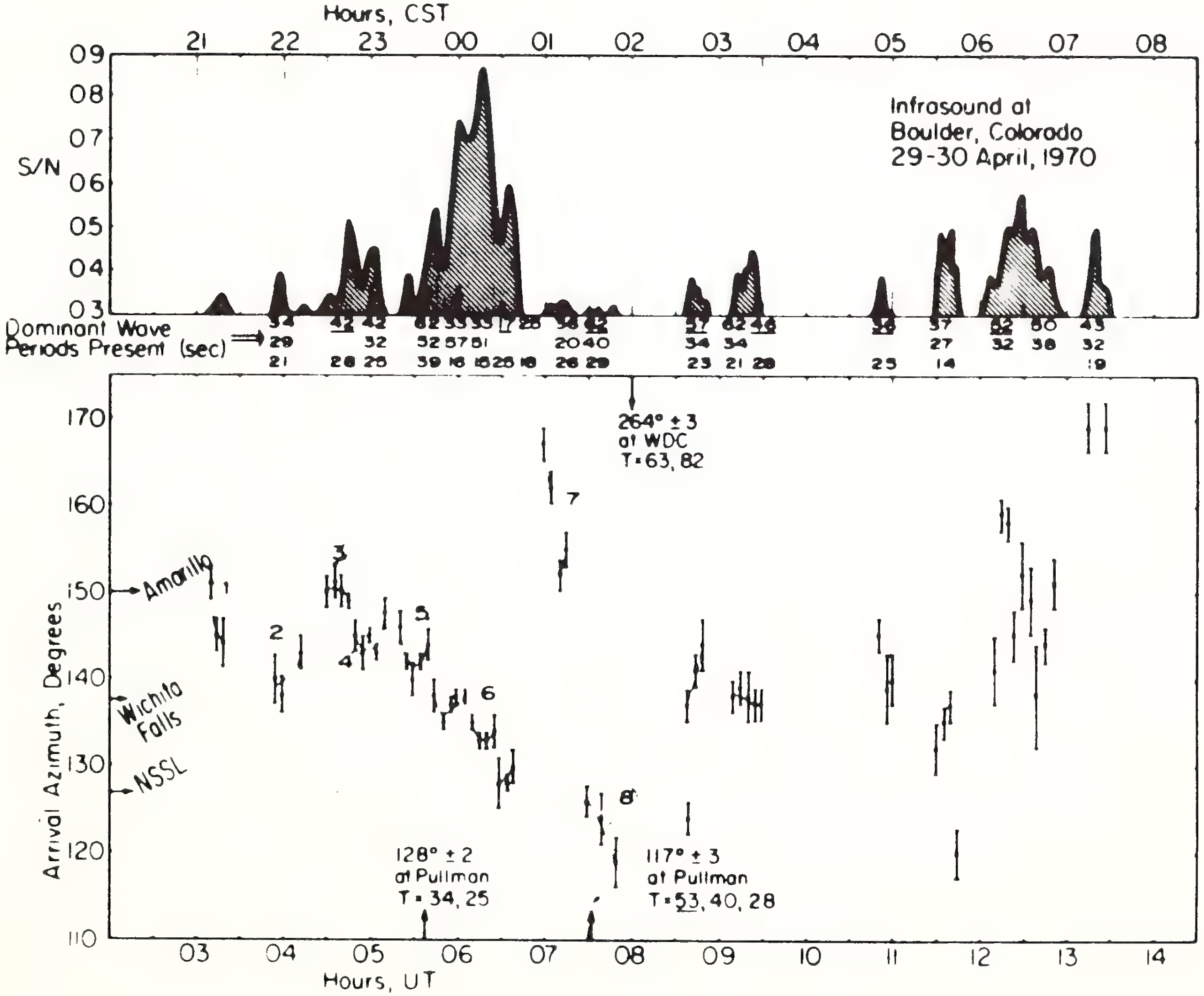

Figure 1. Time history of infrasonic wave strength (top), azimuth of arrival (bottom) and spectral content (middle) at Boulder, Colorado during the storm period.

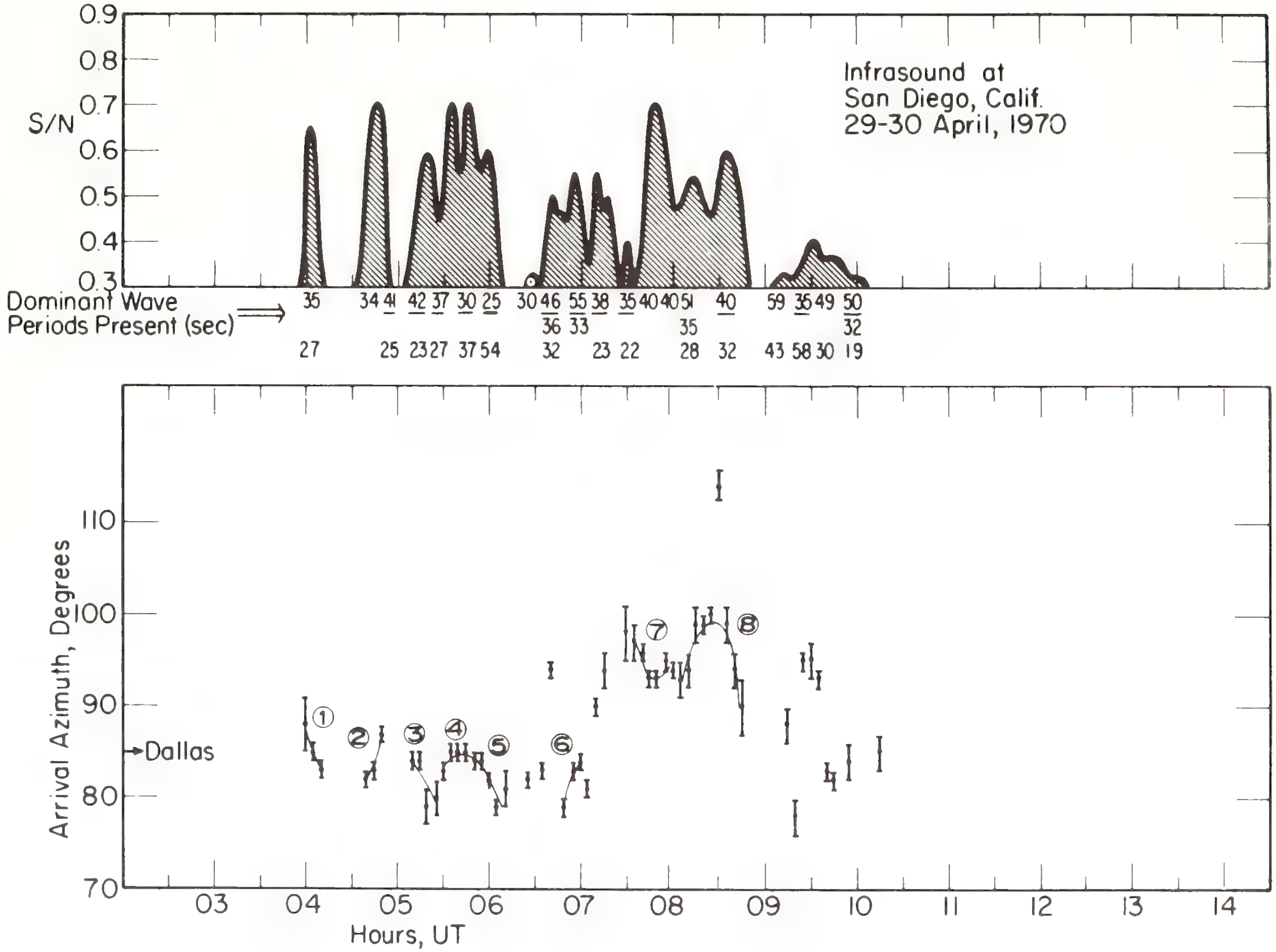

Figure 2. Time history of infrasonic wave strength (top), azimuth of arrival (bottom) and spectral content (middle) at San Diego, California during the storm period.

the azimuth of wave arrival. Reference locations are noted on the azimuth scale. Error bars indicate the probable error associated with azimuth determinations in the presence of noise and a finite sensor-array beamwidth, but are not intended to indicate errors associated with refractive effects of the propagation medium. Experience with many signals from known sources suggests that bearing errors due to propagation effects seldom exceeds 3°. Note that the indicated times are all times of wave arrival at the various observatories and have not been corrected for acoustic travel time. Such corrections usually amount to about 1100 km/hr, or in the case of propagation to Boulder, about 30 to 40 minutes and about 80 to 100 minutes to San Diego, depending on the exact source location assumed.

Brief arrivals at the other observatories are noted along the upper and lower time scales of figure 1. These estimates serve mainly to confirm the general source location in the Texas-Oklahoma area.

The top parts of figures 1 and 2 plot the "signal-to-noise ratio" at Boulder and San Diego defined by $S/N = R/(1-R)$, where R is the broadband wave coherence over each sensor array. The cause of the rather regular fluctuations in S/N is unknown; they may represent pulsations of source strength, regular fluctuations in noise level at the sensors, or propagation effects that cause amplitude scintillations at the sensors. Measurements of strong waves from nearby storms reveal similar fluctuations in source strength and direction, suggesting that the "pulsations" are a source property. Therefore, the times when S/N is largest are interpreted here as the times (when corrected for propagation time) of most intense emission.

In between the two plots of figures 1 and 2 are some numbers that give the results of wave spectrum analysis. The numbers indicate the dominant wave periods (in seconds) present at the indicated times; those underlined indicate that the spectrum is dominated by that particular wave period. In general, the spectral content varies rapidly with time, and there appears to be little relation between wave periods seen at different observatories at the same time (corrected for travel time).

Figures 1 and 2 contain enough information to permit us to calculate a time history of apparent source locations by triangulation between Boulder and San Diego. However, there is sufficient difference between the strength and azimuth histories at the two stations that there is some difficulty matching "event for event," which is necessary for meaningful triangulation. The best match seems to result from a relative time shift of about 50 minutes, (Boulder leading), which turns out to be a theoretically reasonable travel-time difference for a source in north-central Texas. Although major differences in strength exist between the two stations, it is possible to obtain a rough event-for-event match between the S/N records at Boulder and San Diego during the interval 0300-1000 UT. Between 1000 and 1400 weaker waves exhibiting greater azimuth scatter were present on Boulder records, whereas no significant waves arrived at San Diego from the direction of interest.

Using a 50-minute shift, we next calculated apparent intersections from corresponding bearings in eight 15-20 min time "blocks" suggested by azimuth groupings and S/N "pulsations." Blocks 7 and 8 yielded intersections well outside the geographical region of interest, whereas blocks 1 through 6

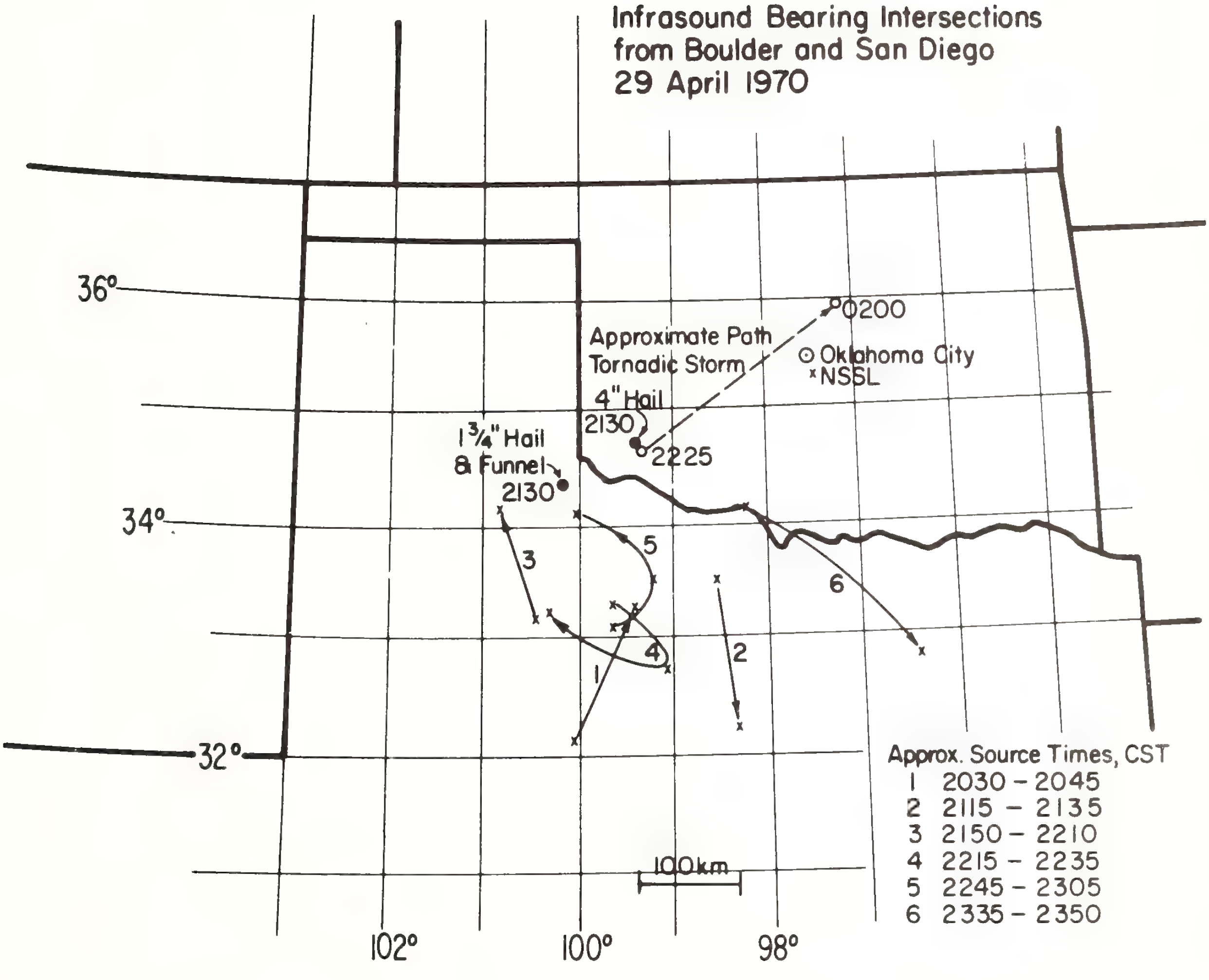

Figure 3. Tracks of infrasound bearing intersections constructed from the azimuth-time data in figures 1 and 2. Track numbers correspond to the numbered "events" in the previous figures.

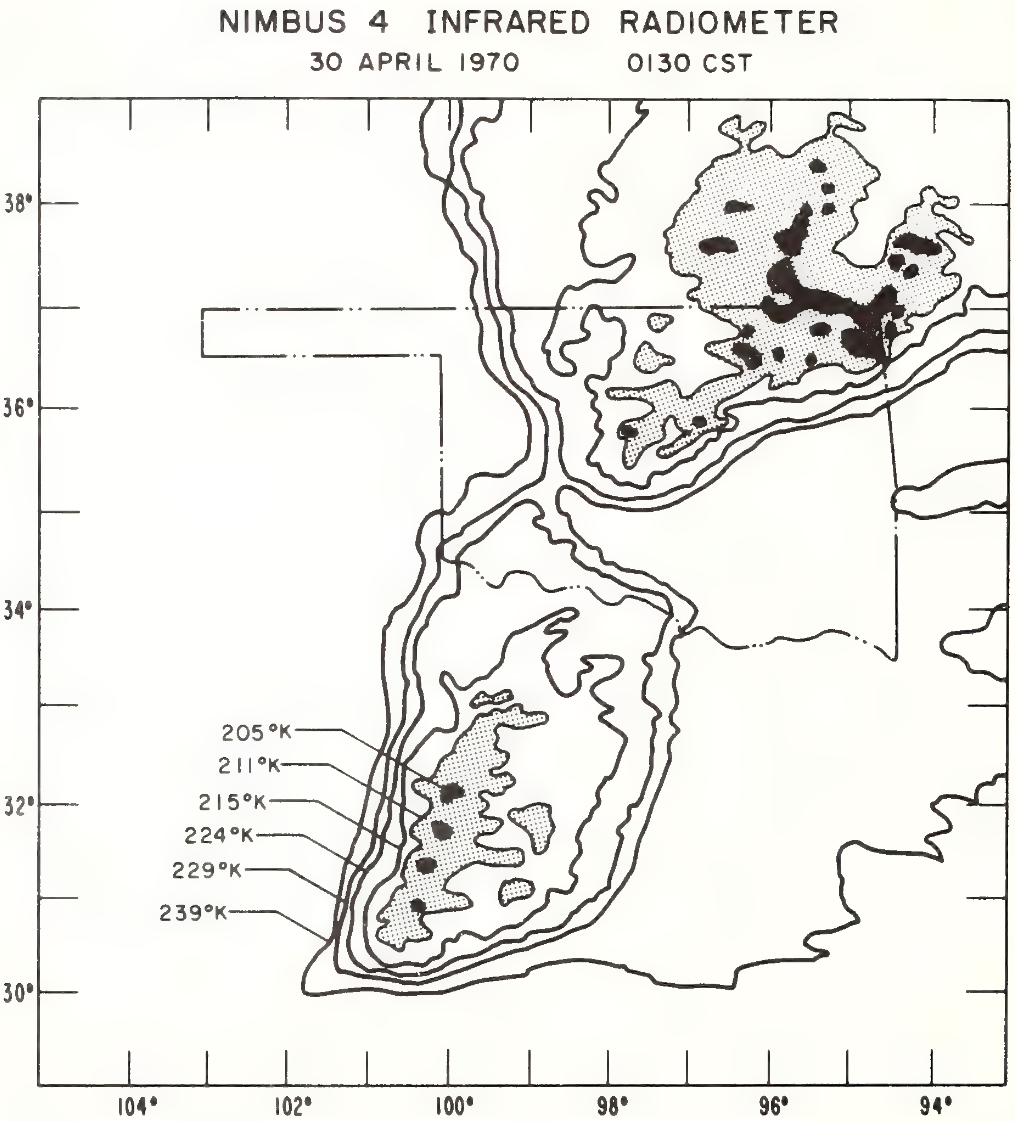

Figure 4. A partial tracing of the Nimbus 4 infrared radiometer temperature contours obtained during the passage of the frontal system across Texas and Oklahoma (outline shown).

yielded the intersection "tracks," or time histories illustrated in figure 3.

In view of the various azimuth errors inherent in both the wave propagation and in the data processing, the significance of the details of the tracks may certainly be questioned. The actual source locations should be well within 100 km of those indicated, however. For reasons arising from details of the propagation mechanism, there may be some justification for associating more accuracy with the locations at the beginning of each time block, than with those near their ends.

4. COMPARISON WITH OTHER OBSERVATIONS

Storm Data (NOAA, 1970) reports that a tornado formed in southwest Oklahoma at 2245 CST, traveled northeast and did not dissipate until reaching Stillwater at 0200 CST. Extensive damage was reported near Oklahoma City. The track connecting these beginning and end points is sketched on figure 3, although it is uncertain that the tornado followed such a track or even that only a single tornado was involved. (Such observations and reports are especially questionable when events occur at night.) This is presumably the same event studied intensively by other contributors to this volume. It seems virtually certain that the infrasonic waves recorded at Boulder and San Diego did not come from this Oklahoma storm, but rather from another storm system in northern Texas that was evidently part of the same widespread squall line.

Davies and Jones (1972) have reported observing the previously mentioned ionospheric waves during the passage of this storm system. The characteristic three-minute waves are visible between about 0400 and 1200 UT on records of his ionospheric soundings made near Oklahoma City. Davies and Jones show that at 1045 UT the waves come from the southwest of Oklahoma City, indicating possibly the same source we find.

The NOAA Radar Summary Charts show a line of storms passing across north-central Texas during the interval of infrasound generation. Several storm echoes in the line had indicated tops over 40,000 feet, with highest tops at 55,000 feet, but it has not been possible to identify specific storm echoes with the infrasound-source locations.

The Nimbus 4 infrared radiometer measurements during this storm period provide an excellent perspective of storm activity over the Texas-Oklahoma area at 0730-0737 UT (Wexler and Allison, 1972). The photograph on the cover of the Preprint Volume for the 15th A.M.S. Radar Meteorology Conference displays a color analysis of an IR photograph, reproduced in figure 4, in which the coldest temperatures indicate the locations of highest storm-cloud towers. The lower storm complex is closer to the area of infrasound emissions depicted in figure 3, but the time difference (an hour after block 6 arrived at Boulder) makes a direct association questionable.

5. REFERENCES

Brown, R. F., Jr., (1963): An automatic multichannel correlator. J. Res. NBS, 67c, 1, 33-38.

Davies, K. and J. E. Jones, (1972): Ionospheric disturbances produced by severe thunderstorms, NOAA Professional Paper No. 6, U. S. Gov't. Print. Off., Washington, D. C.

Georges, T. M., (1973): Infrasound from convective storms: examining the evidence, Rev. of Geophys. Space Phys. 11, 571-594.

Georges, T. M. and J. M. Young, (1972): Passive sensing of natural acoustic-gravity waves at the earth's surface, Ch. 21 of Remote Sensing of the Troposphere, V. E. Derr, Ed., U. S. Gov't. Print. Off., Washington, D. C.

NOAA, (1970): Storm Data, 12, 4, Environmental Data Services, Asheville, N. C.

Wexler, R. and L. J. Allison, (1972): Radar and Nimbus 4 infrared measurements of the Oklahoma City tornadoes 30 April 1970, Preprints of the 15th AMS Radar Meteor. Conf., Amer. Meteor. Soc., Boston, Mass., 77-82.

USCOMM ERL

Journal of Applied Meteorology 14, 1303-1316, October 1975.

Infrasound from Convective Storms. Part IV. Is It Useful for Storm Warning?

T. M. Georges and Gary E. Greene

Wave Propagation Laboratory, NOAA, Boulder, Colo. 80302

(Manuscript received 27 May 1975, in revised form 9 June 1975)

ABSTRACT

An experiment was carried out to collect statistics on the observability of severe-storm infrasound at three stations during the 1973 storm season. The results have been evaluated with the help of four "indices of usefulness":

- *False-alarm rate*, which tells how often infrasound from other sources is mistaken for that from storms. We devised a sorting procedure that reduces the false-alarm rate to 15–20%, and still lower rates seem achievable.
- *Detection rate*, which tells what fraction of severe storms are detected. Here the big problems are defining what we mean by "severe storm" and verifying their occurrence; we estimate a 65% detection rate for tornadic storms, a 31% detection rate for tornadoes themselves, and a 33% detection rate for storms with radar tops above 50,000 ft.
- *Timeliness*, which tells how much advance warning the waves give compared to dangerous storm effects. It was practical to consider only tornadoes from this viewpoint, and we found that the emissions tend to precede tornado onset by an hour or so.
- *Location accuracy*, which tells how well the emissions can be used to locate and track storms. This index is hard to evaluate quantitatively, as illustrated by the six cases where storms were seen at all three stations. Propagation effects and measurement uncertainty presently prevent positive identification and tracking of a particular storm, but we see ways to improve this.

The answer to the title question is that the emissions show promise as a supplement to the present warning system. A question remains about the cost-effectiveness of doing the additional required research and deploying an operational sensor network.

1. Introductory background

In the first paper of this series, one of us reviewed the evidence that certain severe convective storms radiate infrasonic pressure waves that have been detected by ground-based microbarographs thousands of kilometers away from their source and at ionospheric heights by radio sounders that detect the motions of the ionized layers there (Georges, 1973a). Then we looked at several suggested models of the emitting mechanism, in an effort to define theoretical predictions of each model that could be tested against the wave observations (Georges, 1975). Later, Jones and Georges (1975) successfully modeled the propagation effects that prevent all but a narrow-frequency band of acoustic energy from reaching the ionosphere.

Here, we ask a question of more immediate practical importance: Can the emissions be used to warn of impending severe weather (especially tornadoes) or to locate and track severe weather in progress?

Some preliminary answers have already been given (Georges, 1973b), based on data collected only at the Boulder, Colo., observatory during the 1972 storm season. We showed that over one-half of the infrasonic wave events logged during a three-month observing period could be attributed to documented convective storms, and that over one-half of those storms produced confirmed tornadoes or funnel clouds. We also displayed the diurnal and seasonal occurrence distributions of the storm-associated waves and the geographic distribution of the storms identified as sources. All were consistent with the well-known distribution statistics for tornadic storms in the Midwest. This connection suggested a possibly valuable warning capability.

With observations from only one observatory, it is possible to tell only the direction of infrasound arrival but not the distance to its source, so that ambiguities about source location sometimes occur. Furthermore, a single observatory is vulnerable to outages caused by even moderate local winds. For example, winds at the (relatively quiet) Boulder observatory during the storm season cause a background noise level greater than 1 μb amplitude about 25% of the time (see Appendix B).

We thus needed to perform a more definitive experiment, designed specifically to overcome these limitations.

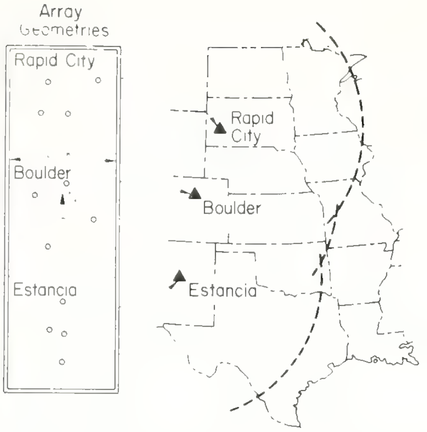

FIG. 1. Location of the three microbarograph observatories used to observe severe-storm infrasound during the 1973 storm season. The inset shows the arrangement of the four-sensor array at each station. The dashed arcs show 1000 km radii from the observatories, roughly their expected effective range.

2. The experiment

To this end, we deployed two more microbarograph arrays to record storm emissions during the 1973 season. With three observatories instead of one, we thought it should be possible to observe more storm emissions and to triangulate the sources of most of the emissions, rather than obtain only a direction of arrival. A triangulation capability not only permits a more accurate identification of a given wave as storm-related, but also is essential for evaluating the waves' storm-location potential.

Guided by the apparent concentration of emitting storms in the Midwest during the 1972 season, we located one array of four microbarographs at Rapid City, S. D., and the other at Estancia (near Albuquerque), N. M. (Fig. 1). The arrays were located to the west of the predominant source region because of a now well-known directional filtering effect on infrasound propagation caused by prevailing (westward) mesospheric winds during late spring and summer (Georges, 1973a; Bowman and Bedard, 1971). These winds reverse direction around mid-May, so that only westward propagation is favored thereafter.

Typical sensor spacing in each array was 5 to 10 km, and array geometry was irregular. The microbarographs were of the NBS type that has been described elsewhere (Matheson, 1964; Georges and Young, 1972) and has a sensitivity of about 0.01 μb (10^{-8} atm). The spectral bandpass of the sensing and processing system we used has 20 dB response points at about 2 and 100 s wave period. Spatial filters, to reduce the noise of wind-advected turbulence, were constructed of 200 ft of rubber hose with ports every 5 ft and attached to each sensor. As expected, these filters were not as effective in reducing the effects of wind noise as the more elaborate filters used at the Boulder observatory (1000 ft of iron pipe connected to each sensor). Noise statistics for each station, shown in Appendix B, illustrate this.

During the interval studied, 19 May to 31 August 1973, pressure was recorded on magnetic tape in analog form at all three stations. The tapes were processed (to yield azimuth of arrival and coherence) on the NOAA analog-correlating device that has been described elsewhere (Brown, 1963; see also Appendix A).

3. Some indices of usefulness

To provide a framework for our analysis, and also one in which to state our results, we asked the following more specific questions about the storm-identifying and storm-locating potential of infrasonic waves:

1) How often could infrasound from sources other than severe storms be mistaken for waves from storms? If this happens too often, there will be too many "false alarms" for the waves to be useful as warnings. We call the measure of this property of the emissions the *false-alarm rate*.

2) What fraction of severe storms emit detectable infrasound? If the fraction is too small, or if local noise levels at the sensors are high too often, then many severe storms would be "missed" by even an optimum infrasound-observing network, and its value as a warning system would be correspondingly small. We call the measure of this fraction the *detection rate*. Another term, the *miss rate*, or *failure-to-alarm rate*, is used. It is just 1 minus the detection rate.

3) What is the temporal relationship between the observation of storm-related waves and actual severe effects? If the waves do not often reach the sensors in advance of severe-weather effects, their warning value is nil. We use the term *timeliness* to denote this property.

4) How accurately can the emissions locate and track severe storms, and how does this accuracy depend on the number of sensors used? The term *location accuracy* refers to the measure of this ability.

In the following sections, we discuss how we quantitatively estimate these four indicators, using the three-station infrasonic wave observations during the 1973 storm season.

For future use, we define two terms: A *simple warning system* employs only information derivable from acoustic wave observations, for example, wave velocity, frequency, coherence, and even apparent source location inferred from multiple observatories. This is to be contrasted with an *augmented warning system*, which would supplement acoustic observations with other "real-time" geophysical monitors, not only weather and storm (for example, radar) information, but information related to other known infrasound sources (for example, geomagnetic activity). Such an observing and correlating system is obviously much more expensive and sophisticated than a simple one; on the other hand, it may be relatively easy to integrate acoustic information into an existing storm sensing and warning system, if such information proves useful. We will consider here mainly the capabilities of a simple warning system.

4. False-alarm rate

The way we estimate and minimize false-alarm rate is to try various objective sorting schemes for eliminating non-storm waves. The sequential scheme we developed is illustrated in the flow chart of Fig. 2. Each sorting criterion, or test, is based on our prior experience in correlating infrasonic waves with severe weather and with other geophysical phenomena. The particular order of the tests was chosen both for maximum sorting efficiency and ease of application. We tried different values of the adjustable parameters in each test, and to some extent, optimized them.

The wave events that survive this sorting process are interpreted as possible storm emissions (that is, "alarms"). Some alarms are actually storm-related, and some are not; the fraction that are not is the false-alarm rate. By comparing the wave observables with independent geophysical data, especially weather-radar charts, we estimated the most likely source of each alarm wave. We say an acoustic event is associated with a severe storm if its time of occurrence (allowing for acoustic travel time) and direction of arrival (allowing for instrument tolerances and a few degrees bearing error caused by atmospheric refraction) coincide with the time and location of a radar-indicated storm system with indicated storm tops exceeding 40,000 ft. Alarms that cannot be so identified can usually be ascribed to other known source processes, and are judged "false alarms."

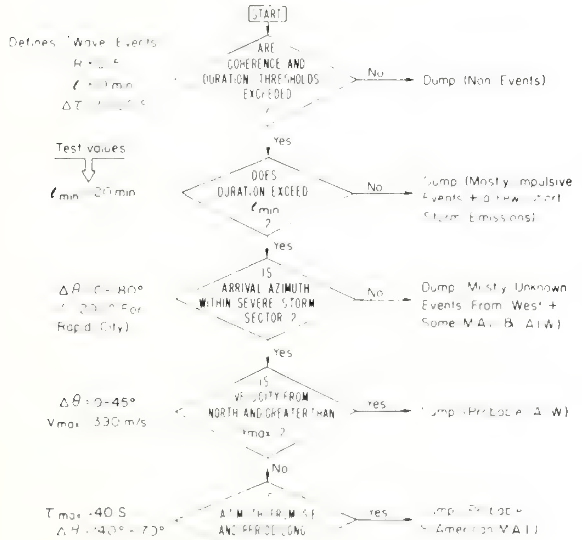
START
Defines "Wave Events"
ARE COHERENCE AND DURATION THRESHOLDS EXCEEDED ?
No
Dump (Non Events)
Yes
Test values
ℓ_{min} 20 min
DOES DURATION EXCEED ℓ_{min} ?
No
Yes
IS ARRIVAL AZIMUTH WITHIN SEVERE STORM SECTOR ?
No
Dump (Mostly Unknown Events From West + Some M.A.I. & A.I.W.)
Yes
$\Delta\theta$ = 0-45°
V_{max} 390 m/s
IS VELOCITY FROM NORTH AND GREATER THAN V_{max} ?
yes
No
T_{max} 40 S
Yes
No
Yes
No

FIG. 2. A "flow chart" of the sorting process devised for identifying severe-storm infrasound. Events that are "dumped" satisfy criteria for waves from non-severe-storm sources; those that survive the sorting are presumed to be storm emissions. We did not find the last two sorting steps useful and ultimately deleted them.

The Sorting Criteria

The first sorting test represents a definition of an "acoustic wave event," or "signal," for short. A signal is defined as a time interval of at least 10 min duration, in which wave coherence R exceeded 0.15 in the nominal system bandpass $\Delta\tau$ of 2–100 s wave period. ("Coherence" is quantitatively defined in Appendix A.) It is important to note that this definition of a signal depends not only on the strength of the acoustic wave, but also on sensor-array geometery and on the noise conditions at the sensors.)

To use data from three stations, we refined the definition of a signal to avoid duplicate identification of waves from the same source. Only a single event was identified when waves observed at more than one station coincided in time within tolerances allowed by different wave travel times. We also defined as single events some signals whose coherence dropped below 0.15 for short intervals but returned again from the same direction.

The next test eliminated short-duration signals, which seem to contain a high percentage of non-storm waves. After some experimentation, we eliminated waves of shorter than 20 min duration. Even though this also eliminated a substantial number of storm-related waves, the false-alarm rate improved considerably.

The next test is a directional filter based on prior knowledge that most emitting storms are in the Midwest. We therefore eliminated waves arriving outside the 0° to 180° azimuth sector (0° to 200° for Rapid City).

Next, a velocity and azimuth test is applied, based on prior knowledge about so-called Auroral Infrasonic Waves (A.I.W.). We sort out waves with horizontal trace speeds exceeding 390 m s^{-1} and which arrive between 0° and 45° azimuth.

The next filter is designed to eliminate the so-called "Mountain-Associated Infrasound" (M.A.I.) that comes from South America (S.A.) during the southern winter. It eliminates waves arriving between 140° and 170° azimuth and whose spectral peak τ_{max} falls at periods longer than 40 s. This cutoff was optimized experimentally.

Another coherence threshold was applied next. It wasn't clear *a priori* whether higher thresholds would

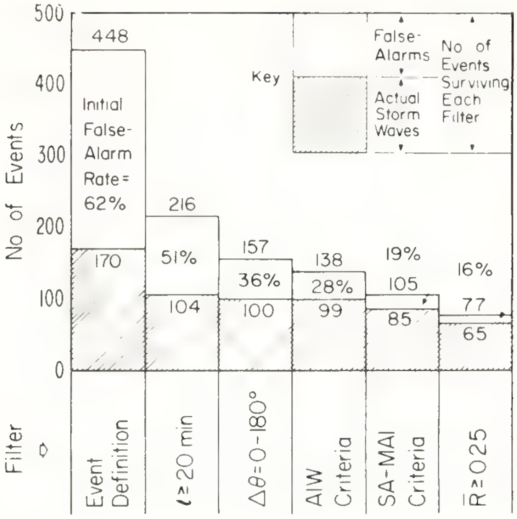

Fig. 3. Results of the sorting process for events observed at the Boulder station. The idea is that each filter should increase the ratio of actual storm waves remaining (shaded area) to false alarms remaining (unshaded area), without decreasing too much the total number in the former category.

yield lower false-alarm rates, so we experimented with a threshold R of 0.25.

Finally, we tried to apply a filter based on triangulation of source location. We thought it might help eliminate some false alarms if triangulation indicated a source location far from the usual midwestern source region of severe-storm emissions.

The effectiveness of the sorting process (excluding the triangulation test) is illustrated for the Boulder station only in Fig. 3. The shaded portion of each bar shows the fraction of the surviving events that were subsequently judged to be storm-related (based on the 40,000 ft top criterion). Compare the number of "false alarms" eliminated by each filter with the number of actually storm-related waves eliminated. Generally, the filters seem to be more effective against the false alarms than against the real storm waves. But we think the last (coherence threshold) test eliminates too many actual storm-related waves without significantly reducing the false-alarm rate. The false-alarm rates for the other two stations before the coherence filter were both 24%; after the coherence filter they were 26% (Estancia) and 21% (Rapid City).

After we accounted for duplicate observation of the same wave event on more than one station, the total number of storm-related events that survived all the filters, including the S.A.-M.A.I. filter, was 177. The total number of false alarms was 61, giving a 26% overall false-alarm rate. The false-alarm rate for the three-station network is thus greater than that for any individual station. This is mainly because false alarms tend to be events that are apparently of nearby origin and are observed only at one station (only 2 of the 63 false alarms that survived all but the last filter were recorded at more than one station), whereas a significant fraction (37 of 177) of the genuine severe storm waves were observed at two or more stations.

Because only 2 of the 63 surviving false alarms were recorded at more than one observatory, triangulation could not help reduce the false-alarm rate, and the triangulation filter was discarded.

Looking more closely at the 61 false alarms to possibly identify their nature, we find that 28 are probably associated either with nearby thunderstorms (less than 200 km from an observatory) having tops not exceeding 40,000 ft or with tornadic storm systems having no storm tops exceeding 40,000 ft. These events were therefore not classified as "actually storm-related" by our original 40,000 ft criterion, even though they probably were. Reclassifying these events gives a final three-station false-alarm rate of 16%. The need for reclassification is not the fault of the sorting process, but rather of our rigid and arbitrary definition of a "severe storm." Maybe this could be improved.

5. Detection rate

The detection rate tells how often a warning system responds to the danger it is designed to warn against. Numerically, it is the ratio of the number of events detected to the total number of events to which it is expected to respond. An effective warning system must have a high detection rate; but it is feasible to have a complex warning system that uses input from different kinds of sensors, in which the detection rate attributable to each kind of sensor is relatively low, yet that of the whole system remains high.

The process of estimating detection rate is the inverse of that for obtaining the false-alarm rate: In the former, we start with the observed storms and ask how many can be related to detected infrasound; in the latter, we start with the observed wave events and ask how many are related to actual severe storms.

a. Problems and ambiguities

A problem with evaluating any severe-storm warning scheme is that detection rate is hard to define exactly, first of all, because the term "severe storm" itself is vague: What criteria must a storm meet to be classed as "severe"? How "severe" (and how near to sensors) should an undetected storm be before it is called a "miss"?

There are also observational problems connected with setting up an experiment to measure miss rate for any severe-storm sensor. During any such test, fairly complete and accurate knowledge about the occurrence of all storms in the area under study is required. But the actual storm observing and reporting capabilities of the National Weather Service are limited in the sense of inadequate and nonuniform coverage by qualified observers. Furthermore, reporting is clearly influenced by several kinds of observational bias, such as population density, reliability of daytime versus nighttime observations, etc. Even such apparently explicitly defined events as tornadoes are, on closer examination, subject to many of the same ambiguities.

In the case of any storm-warning scheme based on infrasound emissions, minimizing the miss rate means deploying enough sensors to insure adequate geographical coverage, and also employing noise-suppression techniques to minimize sensor outages caused by local nonacoustic noise. Yet, we are attempting to estimate the miss rate with data from only three sensor arrays, two of which were deployed with less than optimum attention to noise-suppression considerations. Should we regard as "misses" events that go undetected during high noise levels at one or more observatories? If we do, then our estimate of miss rate depends very much on the "noisiness" of the particular locations we have chosen, and also upon the effectiveness of the particular noise-suppression filters we used. If we don't, that is, if we regard as our "data base" only time intervals when noise levels are below some threshold that would permit wave detection, then our estimate of miss rate will be unduly optimistic, in the sense that any real observing system would have some noise outages. Consequently, our analysis will distinguish between misses during high- and low-noise conditions.

These problems, arising mainly from incomplete data and necessarily arbitrary definitions, make all estimates of miss rate of dubious value. The best we can do is to be as careful and explicit as possible in defining what our particular estimates of the miss rate mean.

b. Storm definitions

We found that the only comprehensive and reliable source of convective storm data is the NWS weather radar network. The best single way to define a severe convective storm seems to be the radar-echo-top criterion described earlier. But we have found it impractical, if not impossible, to calculate the miss rate with respect to every storm cell with 40,000 ft or greater tops. Instead, we have defined what we call a storm "system" as a grouping of apparently related storms as indicated on radar summary charts. Often, for example, such a storm grouping falls along a squall line and lasts for many hours. Furthermore, for calculating detection rate, we had to change the 40,000 ft height criterion to 50,000 ft because of the excessive number of 40,000 ft echoes on hourly radar charts.

We say that a severe storm system is "detected" if, corresponding to the time and azimuth of the radar-indicated grouping, at least one observatory records a "severe storm emission" event, which here means one of the 177 events that survived the filtering process described in Section 4. A "miss" is defined as a radar-indicated storm system *not* accompanied by an infrasonic event at any observatory. However, a "miss" is not recorded when more than one storm system is indicated on radar, but emissions from only one source are detected. These cases are specifically identified as "other storm signals interfering." If a "miss" occurs at a time when all observatories have high noise levels, the miss is classed specifically as probably caused by noise.

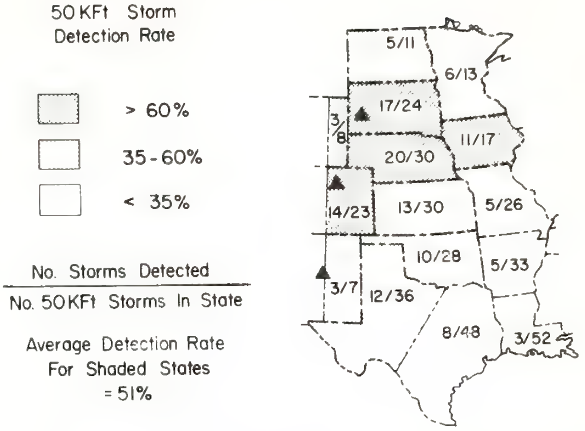
50 KFt Storm Detection Rate
> 60%
35-60%
< 35%
No. Storms Detected / No. 50KFt Storms In State
Average Detection Rate For Shaded States = 51%
5/11
6/13
17/24
3/8
11/17
20/30
14/23
13/30
5/26
10/28
5/33
3/7
12/36
8/48
3/52

Fig. 4. The geographical area selected for estimating severe-storm miss rates. The fraction shown in each state gives the number of 50,000 ft storm systems occurring in each state, compared with the number detected at one or more infrasound observatory. The shading shows how miss rate separates into three distinct groups.

To estimate detection rate, we also have to define a geographical area, within which storms are expected to produce sensor response, and outside of which they are not. Experience has taught us that virtually all severe storms that radiate infrasound strong enough to be detected more than a few hundred kilometers away are in the Midwest. So, somewhat arbitrarily, we selected as our study area that portion of the United States between the Mississippi River and the Rocky Mountains, or more specifically, the states of Texas, Oklahoma, Kansas, Nebraska, South Dakota, North Dakota, Louisiana, Arkansas, Missouri, Iowa, Minnesota and eastern parts of Colorado, Wyoming and New Mexico. Rigid geographical boundaries are, of course, arbitrary; a better scheme would use some sort of inverse-range weighting, but this seems impractical, in view of the inaccuracies in the other assumptions we are making.

c. 50,000 ft storm miss rate

We tabulated all the 50,000 ft storm systems that occurred within the specified states and calculated the detection rate based on whether acoustic waves received at one or more stations could be associated with each system. When separated by state, the detection rate seemed to fall into three ranges, separated by sizable gaps, as indicated by the shading code on Fig. 4, where the detection rate is given by state. In the double-hatched area, the average detection rate is 66%; in

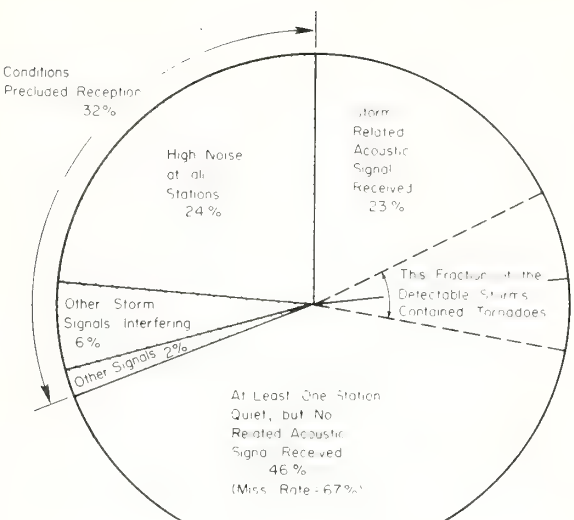

FIG. 5. Results of our attempts to relate intrasonic events with 451 storm systems containing radar echoes over 50,000 ft high. The dashed sectors are subdivisions of the solid ones. Various "detection rates" can be defined in terms of the ratios of different sectors.

the single-hatched region, it is 41%, and over both hatched regions, it is 51%. The overall detection rate is 33%. These detection rates are higher than we expected, and we cannot yet explain the particular geographic preference that the figure reveals, except that comparing Fig. 4 with Fig. 1 shows that the limits of the shaded areas tend to fit the 1000 km range circles quite well.

We counted a total of 451 systems with storms at least 50,000 ft high. Fig. 5 shows what fractions of these were detected, which were missed even though noise was low at one or more stations, and which occurred during high noise or interfering signals at all stations. In the above calculations of detection rate, the noisy periods were disregarded. We also show what fractions of the detected and undetected signals are from storms that produced tornadoes. Evidently, tornadic storms represent a significantly larger fraction of the detected than the undetected storms.

d. *Tornado detection rate*

Tornado occurrence and start times are reported in the NOAA publication *Storm Data* and in the SELS log; we take these reports as our definition of tornado occurrence. Apart from the biases and reporting difficulties mentioned earlier, the only additional problem in counting tornadoes was in classifying those attributable to the same storm system. We therefore employed the same sort of radar-grouping criteria as those used to identify a 50,000 ft storm system.

The SELS log recorded 193 tornadoes during the interval and within the geographic boundaries we have defined. Fig. 6 summarizes the results of our attempts to relate acoustic signals to each one. We realized from experience that many signals would be related in time and azimuth to tornadic storm systems, but not to the reported tornadoes themselves. Therefore, we distinguished in our tabulation between acoustic signals that could be related to the tornado occurrence itself and those that were received within ±3 h of the tornado and within 10° of the storm system that generated it. The former classification is, of course, a subset of the latter, as are a number of other cases worth distinguishing. Cases were recorded where signals were received within the 6 h interval, but not at the tornado time (corrected for acoustic travel time), either because of high noise or not. There were also signals deviating more than 10° from the tornado azimuth, but still attributable to the tornadic storm system. All of these subcases are distinguished in Fig. 6.

We can thus estimate the "tornado detection rate" as the ratio of the number of tornadoes with which we could associate acoustic signals at the tornado azimuth and time (within measurement error) to the number of tornadoes during which at least one station was capable of receiving signals (noise below 2 μb) at the tornado time. This number is 31%.

We can also estimate a "tornadic storm detection rate" as the ratio of the number of tornadic storms with which we could associate acoustic signals to the number of storms during which noise conditions were suitable at one or more stations. This number is 65%.

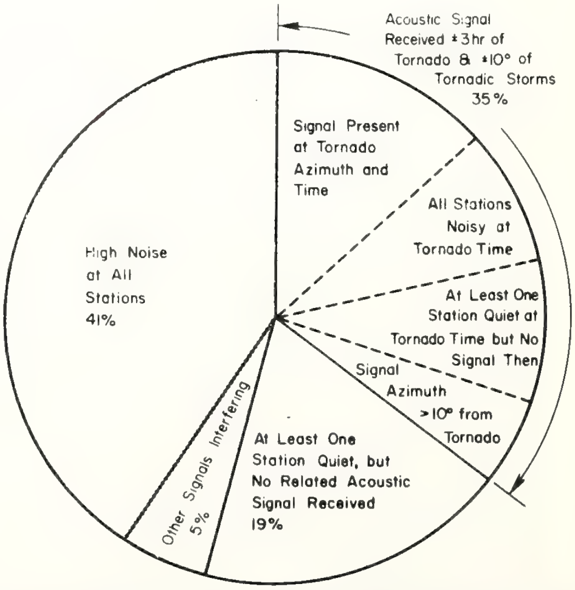

FIG. 6. Results of our attempts to relate infrasonic events with the 193 tornadoes that occurred within our temporal and geographic boundaries. The dashed sectors are subdivisions of the solid sectors. Various "tornado detection rates" can be defined in terms of the ratios of different sectors.

These numbers would, of course, be lower if the detection rate were defined to include time when high noise prevailed at all stations; on the other hand, they would be higher if receptive conditions were defined, for instance, as low noise at the nearest station or in some other way. Such are the pitfalls of trying to quantify such complex situations.

Apart from its role in determining whether the emissions are useful for storm-warning purposes, the detection rate also provides clues to the emission mechanism itself. By comparing Figs. 5 and 6, we see that the detection rate for tornadic storms is substantially higher than for 50,000 ft storms. On the surface, this reinforces earlier convictions that tornadic storms are preferred emitters. Yet, a significant fraction of the emissions appears to be unrelated to the observed tornadoes themselves. The implication is that something in tornadic storms besides tornadoes (larger scale vorticity?) is responsible for the emissions.

e. *Effect of noise level on detectability*

Next, we wanted to see what effect the background noise level has on the detectability of the emissions, and specifically to see how the diurnal fluctuations in noise level relate to the times when the emissions are most often observed.

The noise analysis of Appendix B shows that noisy or quiet conditions occur jointly at two stations about twice as frequently as they would if the occurrences were statistically independent. This must be caused at least partly by the similarity of the diurnal variability of noise level at all stations (Fig. B2). Intuitively, we expected that the emissions would be most commonly observed during the hours when both noise conditions were favorable and when the emitting storms were occurring. To see if this was so, we compared, in Fig. 7, the diurnal behavior of four numbers: the probability that the noise level at one or more stations is below the 2 μb signal-detection threshold (from Fig. B3); the number of 50,000 ft storms seen in each hourly interval; the product of the above two, indicating the joint probability of the two favorable conditions occurring; and finally the number of actual emissions observed per hour. First, we see the unfortunate tendency for the noise level to be highest during those hours when storm activity is most rapidly increasing. This is probably not accidental; the kind of afternoon convective activity that initiates thunderstorms is probably responsible for much of the wind and turbulence that interferes with the detection of acoustic waves by our sensors. Comparing the last two curves shows that the observed emissions do indeed follow the product curve, peaking at the same hour.

It thus seems likely that significant improvement of the noise-suppression devices used with the sensors would not only permit detection of many more storm emissions, but also would permit earlier detection of signals that are emitted during the high-noise hours. We have observed that a significant fraction of the signals we have studied begin with the abatement of high-background noise levels.

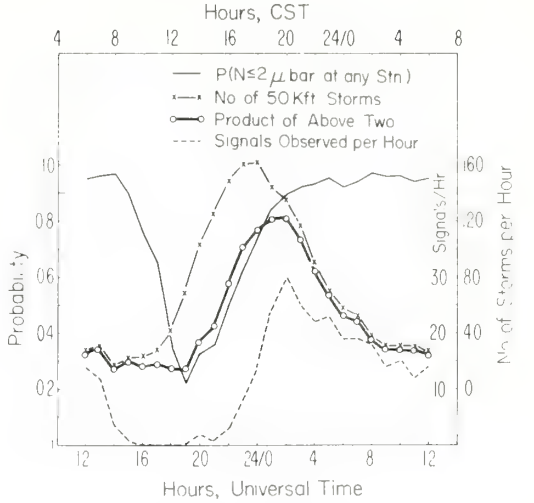

FIG. 7. Diurnal behavior of four parameters showing that the observability of severe-storm infrasound is influenced jointly by the presence of intense thunderstorms and by the existence of low-noise conditions at the sensors. The hours during which both conditions are met (corresponding to the product curve) match the hours of most frequent signal observation.

6. Timeliness

Timeliness measures how much advance warning is given by a warning system before the actual occurrence of some dangerous event. To be effective, the warning must be given early enough to permit those affected to take whatever action is required. In the case of severe convective storms, we assume that little can be done on short notice to prevent property damage by hail, high wind, heavy rainfall or tornadoes (except things like putting your car in the garage, closing the shutters, etc.). (A possible future exception might be the use of sensors to identify targets for storm modification.) However, identifying tornadic storms in their earliest stages would usually permit defensive action, where loss of life can be minimized by timely evacuations or by seeking shelter. Therefore, we will make our estimate of the advance-warning value of infrasound emissions with respect to tornado occurrence only. Another reason for considering only tornadoes is that accurate onset times for other severe features are difficult to specify and are not as frequently recorded.

a. *Acoustic propagation delay*

The relatively slow speed of acoustic wave propagation introduces a fundamental limitation on the warning value of severe-storm infrasound. At an average transit speed of about 300 m s^{-1}, the waves take almost an hour

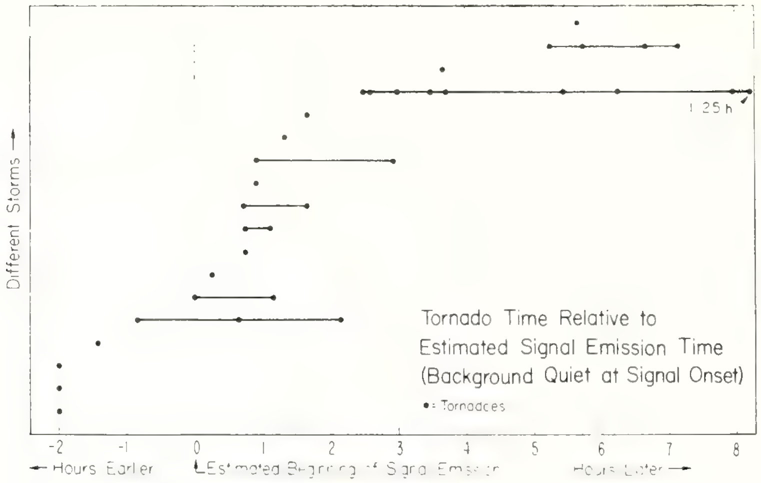

FIG. 8. Tornado time relative to estimated signal emission time for 18 tornadic storms, during which infrasound began under low-noise conditions at any observatory. The results show that the time of infrasound emission tends to precede first tornado onset by about an hour. The horizontal lines connect different tornadoes (dots) occurring within the same storm system.

to travel 1000 km. This factor, probably more than any other, would determine the minimum sensor density in any operational warning scheme.

In what follows, we have attempted to *remove* the effects of propagation delay in comparing tornado onset time with the beginning of infrasonic wave events. Otherwise, the results would contain many different delay times that would confuse the relationship we seek between the emissions and tornado occurrence. The propagation delay for any given distance is, of course, easily estimated.

b. *Does infrasound precede tornado onset?*

To answer this question, we looked at all 1973 tornadoes during which infrasound was received at any observatory from the storm system that spawned the tornado. Then we compared the reported onset time of the tornado with the time of first rise of the wave coherence above threshold. We eliminated the events that began with the abatement of high noise because their true starting time is obscured. After correcting the wave onset time for propagation delay over the distance from the storm (assuming a 300 m s^{-1} speed), we recorded the estimated wave-emission time relative to tornado onset time. Fig. 8 plots this relation for the storms whose first tornado occurred within 6 h of the estimated signal-emission time. Although the sample size is small, the plot shows a tendency for the waves to be emitted, for the median case, almost an hour before the first tornado observations.

7. Location accuracy

Some warning devices give only temporal information about some impending event, while others give spatial information as well. In the case of severe thunderstorms, it is useful not only to find the location of potentially severe weather, but also to track and predict its course.

When we can measure the arrival direction of infrasonic waves at more than one observatory, we can often locate the apparent source of the emissions by triangulation. However, we have found that several sources of error affect the accuracy of these location estimates, sometimes to the extent that many would not be useful at all.

a. *Attempts at storm location*

We think that a good way to illustrate the errors and problems actually encountered in attempts at storm location by infrasound is to look at the six cases where storm waves were recorded at all three observatories. We can see not only the relation between bearing intersections and actual storm activity, but also the geographical spread of the three possible intersections.

Fig. 9 shows six representative "snapshots" of the three infrasound bearings superimposed on maps showing the principal radar-indicated storm activity. It is not possible in any of the cases to identify the source storm unambiguously, although likely candidates can sometimes be identified. In other cases, like Fig. 9f, the infrasound bearings give no useful intersections at all. In some panels, dashed lines show how bearings from some stations changed a couple of hours later, usually in response to a new emission source rather than the motion of the original one.

If a system like the one we used were employed operationally, the source of the emissions would usually be specified no more accurately than somewhere within an area 50 to 100 km or so in diameter. Perhaps even

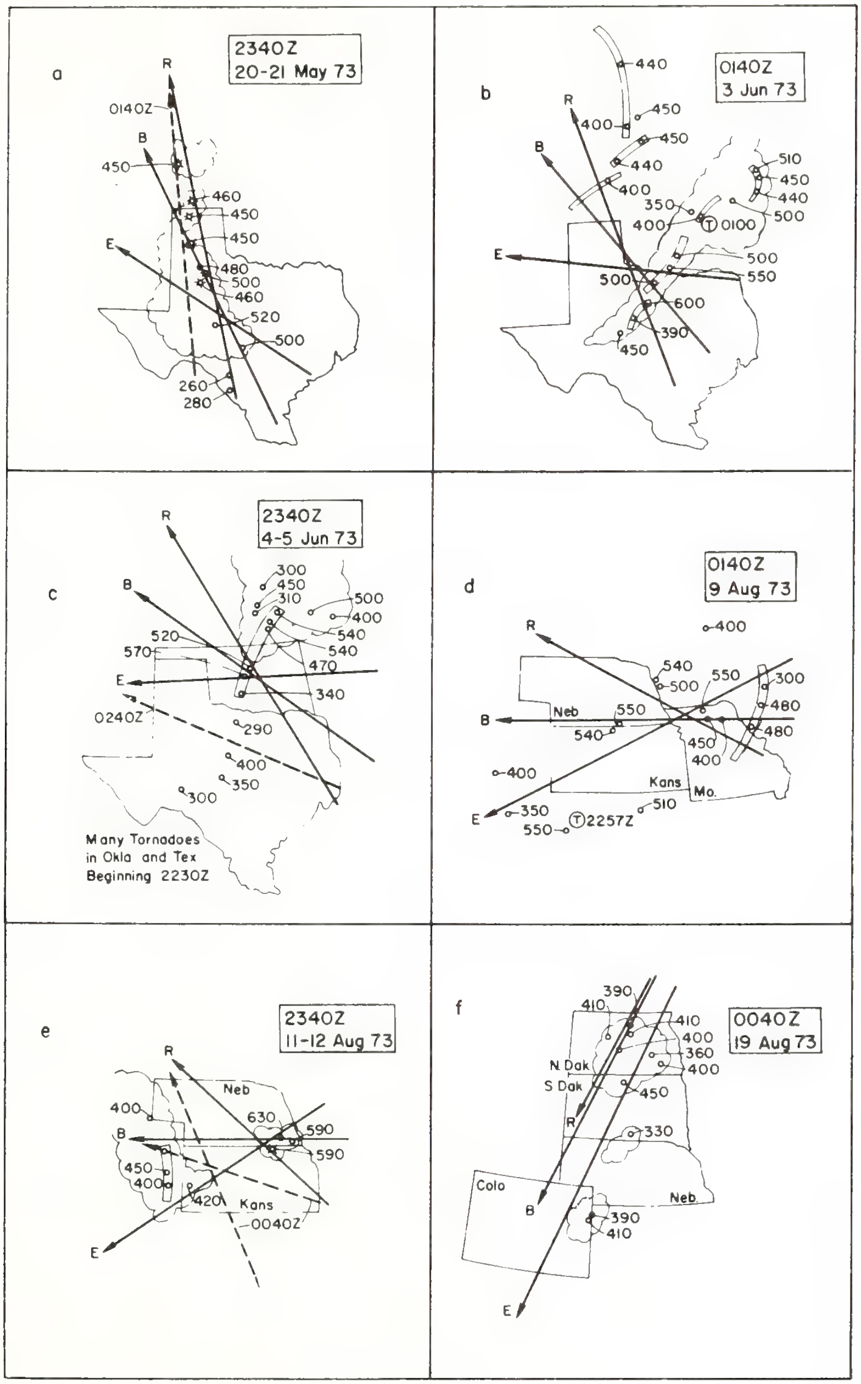

Fig. 9. Results of attempts to locate particular source storms during the six wave events that were detected at all three stations. Heavy solid lines show infrasound bearings at the time of the superimposed radar-indicated storm activity. Heavy dashed lines show infrasound bearings at some later time. The small circles are individual storm cells identified on radar and the associated numbers give the echo height in hundreds of feet. The fluffy outlines indicate areas covered by diffuse radar echoes, and the curved boxes indicate lines of radar echoes. The circled T's and accompanying times give locations and start times of tornadoes.

this accuracy would have some operational warning value.

The question of quantifying storm tracking accuracy seems academic at present because bearing errors are too great to permit single-storm identification. Furthermore, the time resolution of the hourly radar charts is not great enough to permit consistent identification of a given storm from one chart to the next; even if we had greater confidence in the intersections, these charts would not permit a good check of tracking accuracy. We would have to use the radar-scope films from individual radar stations, now available from NOAA. These films do not give echo-top height, however.

b. Sources of error

One source of error lies in the bearing estimates obtained using cross correlation when the signal-to-noise ratio is substantially less than unity. A quantitative analysis of these errors is difficult and we have not attempted one, but we have assumed that the typical bearing flucutations of 2° or 3°, observed when looking at adjacent time windows, are caused by noise contamination of the cross-correlation process.

The other major source of location error is caused by bearing errors caused by atmospheric refraction. A theoretical study by Beasley and Georges, to be published soon, shows that realistic atmospheric winds could occasionally account for bearing errors as large as 10° or more.

Another way to illustrate the effects of atmospheric refraction is to cite the bearing errors encountered in several cases where the location of an (explosive) source of infrasound is accurately known. Examples of distant events recorded at multiple observatories are the Chinese nuclear test on 27 June 1973, and the explosive volcanic eruption on the Island of Bali on 16 May 1963 (Goerke *et al.*, 1965). Bearing errors of early arrivals at seven stations for the Chinese test ranged from 0° to 9° with a mean of 5.3°; for the Bali eruption, errors at three stations ranged from 1.7° to over 30° for late-arriving portions of the signal.

Two explosions in Colorado that were recorded at Boulder indicate the kinds of errors encountered with relatively nearby sources. An explosion near Grand Junction (315 km away) on 13 November 1972 produced waves that arrived only 0.4° from the true source bearing, but later arriving portions of the same signal deviated by almost 3°. Another explosion near Crowley, Colo., on 13 December 1971 (223 km away) produced waves that deviated 6° from the source azimuth. In all of these cases, the signal was so strong that noise contamination was not a problem; the errors are almost certainly attributable to propagation effects. From both our measurement experience and our theoretical estimates, we conclude that propagation effects can easily account for several degrees of bearing error and occasionally up to 10° for medium-distance paths.

c. Reducing location errors

Although the results of our attempts to locate and track storms are not very encouraging, we recognize that some, and perhaps the most important, sources of bearing error can be mitigated. If improvements in noise-reduction techniques could be made, signal-to-noise ratios would improve and "noise" on bearing estimates would be reduced. Most refractive effects that cause bearing errors are probably caused by middle-atmospheric winds, for which we can construct reasonably accurate spatial and temporal models. Acoustic ray tracing through such models could yield corrections to be applied to the measurements. These two approaches could yield significant and possibly useful improvements in source-location accuracy. Improvements in noise suppression would also increase the number of signals seen at more than one observatory and would also make more reliable the source-location estimates based on only two bearings.

8. How multiple stations improve detectability

When we deployed two additional observatories, we expected to detect more emitting storms, but we didn't know how many more or what fraction would be observed at more than one observatory. To answer these questions, we took the 177 storm emisisons that survived the false-alarm filtering process and classified each wave event as having been observed at one, two or all three observatories. The result is illustrated in Fig. 10, where the separate areas are roughly proportional to the number of signals falling into each category. Most signals were seen at only one observatory, 18% were seen at two of the three observatories, and only 6 (3%) were seen at all three observatories.

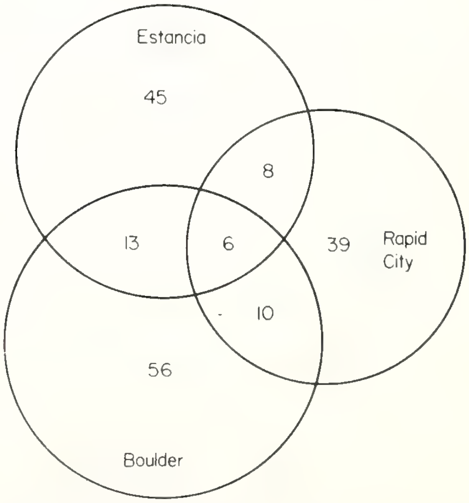

FIG. 10. Joint detectability of 177 acoustic emissions from storms with radar tops over 40,000 ft. The numbers (and roughly proportional areas) give the number of signals recorded only at one station, at pairs of stations, and at all three stations.

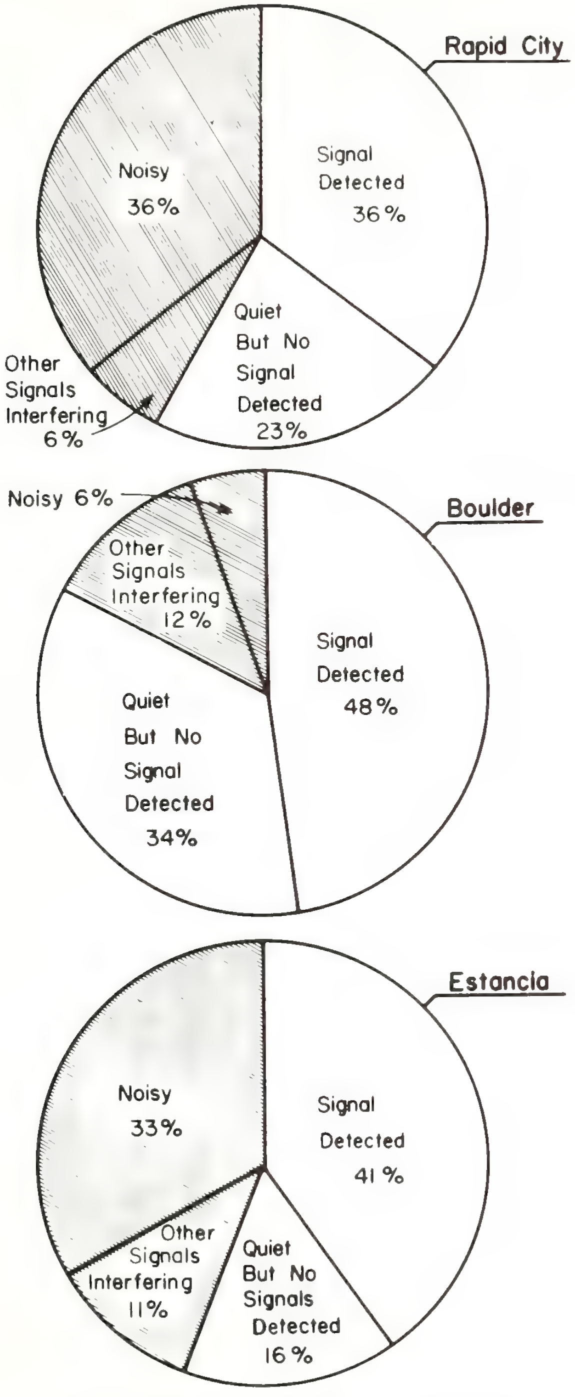

Fig. 11. Breakdown by station of the detectability of the 177 storm emissions.

Joint detectability, of course, depends on two factors: acoustic source and propagation effects that can favor one observatory over another, and coincidence in time of low-noise conditions at more than one observatory. What combination of these factors operated in the case of our three stations during this experiment?

Fig. 11 shows for each station which of the 177 emission events were detected, which were undetected because of high-noise conditions (or other acoustic interference), and which were undetected even though the background was quiet. The Rapid City and Estancia stations exhibited roughly the same statistics; the quieter Boulder station showed substantially more detected signals, but also a much greater percentage of undetected signals even when conditions were quiet. Evidently, the large fractions of noisy conditions at the Rapid City and Estancia stations are mostly replaced by the "quiet but no signal detected" condition at Boulder. This suggests that during much of the time labeled as "noisy," signals would not have been detected even if conditions were quiet, reinforcing the idea that source and propagation effects are at least as important as noise conditions in determining signal detectability. The same point is made also by considering the signals received during times when all three observatories were quiet. Of 46 such times, only 6 were seen at all three observatories, 17 were seen at two observatories, and the remaining 23 were seen at only one of the three observatories.

Propagation effects seem to combine a weak acoustic attenuation with distance (cylindrical spreading would yield an $r^{-\frac{1}{2}}$ pressure dependence) with a complicated spatial pattern of signal-strength distribution caused by focusing and defocusing of rays reflected in the middle atmosphere. It is also likely that the acoustic sources have directional radiation characteristics. We tried to uncover any obvious propagation effects by plotting the geographic distribution of the apparent sources of the 177 storm emissions. Figs. 12a, b and c are the result, where single and multiple-station observations are distinguished by the three symbols. The sources of signals seen at the Estancia and Rapid City stations, where noise level was higher, cluster more closely around the respective observatories, whereas the sources of the Boulder signals seem to be spread more evenly throughout the Midwest. Because signal levels are frequently near the noise level and have a relatively low attenuation rate with range, one might expect the sources of signals received at a quiet station like Boulder to be distributed fairly uniformly; whereas at the other locations, the more distant and somewhat weaker signals would be lost in the higher noise levels.

These results, with those of Section 5e, suggest that many more severe-storm signals would be detected if more sensor arrays were deployed and if much more effective noise-suppression techniques were used.

9. Summary and conclusions

In analyzing the results of this experiment, we encountered some results that were encouraging from a detection and warning point of view, but there were also some other results that were discouraging.

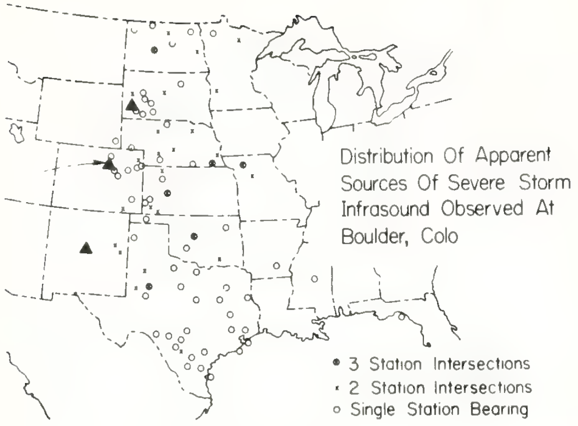
Distribution Of Apparent Sources Of Severe Storm Infrasound Observed At Boulder, Colo
● 3 Station Intersections
· 2 Station Intersections
○ Single Station Bearing

FIG. 12a. Locations of the 85 radar-indicated storms apparently responsible for the storm signals seen at the Boulder station.

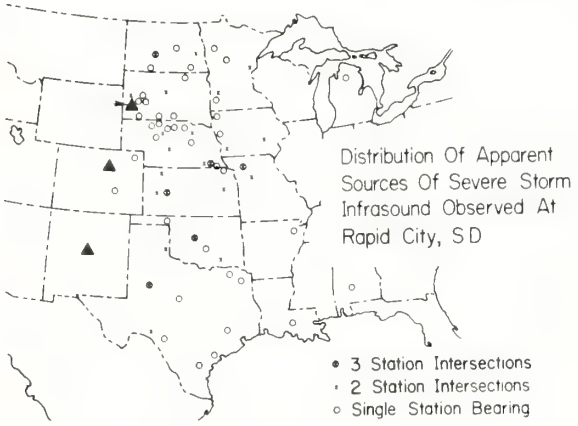
Distribution Of Apparent Sources Of Severe Storm Infrasound Observed At Rapid City, S D
● 3 Station Intersections
· 2 Station Intersections
○ Single Station Bearing

FIG. 12b. Locations of the 63 radar-indicated storms apparently responsible for the storm signals seen at the Rapid City station.

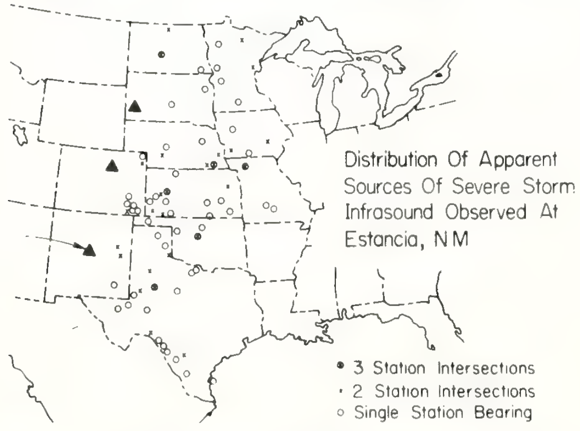
Distribution Of Apparent Sources Of Severe Storm Infrasound Observed At Estancia, N M
● 3 Station Intersections
· 2 Station Intersections
○ Single Station Bearing

FIG. 12c. Location of the 72 radar-indicated storms apparently responsible for the storm signals seen at the Estancia station.

Our ability to sort out false alarms and the percentage of severe storms detected were both better than we originally expected. The evidence that emissions tend to precede tornadoes is also encouraging; however, the acoustic propagation speed does impose fundamental constraints on the density of an operational network. Storm location and tracking ability is presently poorer than we need, but we see ways to improve this.

One of the most important lessons of this experiment is that the level of background noise is crucial to the detectability of severe-storm infrasound. Before further measurements of this type are undertaken, we need to learn more about how to improve noise-suppression devices and also how to assess in advance the effects of meteorology, terrain, vegetation, etc., on the noise level at a particular location. It might be especially fruitful to consider the effects of all these influences with respect to the time of day that the noise level reaches its maximum value. It may be possible to "engineer" a particular location where the noise level is low during the crucial late afternoon and evening hours. More research should also be done on the effectiveness of noise-reducing acoustic probes that have been developed (Smith and Bauer, 1970; Elliott, 1972).

The answer to the title question is therefore: "Yes, in principle, but the final decision must be made on economic grounds." What we have done here is to establish that the emissions are potentially useful, but that some more research is required in the areas of sensor technology, noise environments and propagation distortion. The new question is now: "Is the additional research and, ultimately, the deployment of an operational network cost-effective?" Some tools for answering this question are given by Rhodes (1975).

Acknowledgments. Most of the staff of the WPL Geoacoustics Program Area participated in the design, deployment and analysis of this experiment. Special thanks are due Michael Evans for supervising the deployment of the Rapid City and Estancia arrays. It is a pleasure to acknowledge the help and cooperation of Prof. Richard A. Schleusener and the staff of the Atmospheric Sciences Department of the South Dakota School of Mines and Technology, as well as the many hospitable citizens of Estancia without whom the experiment could not have been done.

APPENDIX A

How We Measure Wave Coherence with an Analog Correlator

We record the output of a microbarograph array (voltage analog of pressure) on 7-channel magnetic tape moving at 0.25 inch per minute. We want to measure the cross correlation between the sensor outputs as their relative time delays are varied corresponding to plane waves traversing the array from various directions and at various speeds. This is accomplished with a system of movable tape-playback heads that are mechanically programmed to vary the relative leads and lags appropriate to different wave speeds and azimuths.

We now show that suitably combining the appropriately delayed sensor outputs gives a good approximation to the broad-band cross-correlation coefficient as a function of wave speed and direction.

The *cross-covariance function* $\phi_{ij}(\tau)$ for two functions of time $X_i(t)$ and $X_j(t)$ is

$$\phi_{ij}(\tau)=\overline{X_i(t)X_j(t+\tau)}=\lim_{T\to\infty}\frac{1}{2T}\int_{-T}^{T}X_i(t)\times X_j(t+\tau)dt, \quad \text{(A1)}$$

where τ is a time shift between the two functions X_i and X_j, and $2T$ is the averaging time. The cross-correlation coefficient R_{ij} is a normalized version of ϕ_{ij} that has a maximum value of unity, i.e.,

$$R_{ij}(\tau)=\frac{\phi_{ij}(\tau)}{[\phi_{ii}(0)\phi_{jj}(0)]^{\frac{1}{2}}}, \quad \text{(A2)}$$

where $\phi_{ii}(0)$ and $\phi_{jj}(0)$ are autocovariance functions at zero lag. We can define an average cross-corrleation coefficient $\bar{R}$ for any number of time functions n as

$$\bar{R}=\frac{2}{n(n-1)}\sum_{i=1}^{n-1}\sum_{j=i+1}^{n}R_{ij}, \quad \text{(A3)}$$

which still has a maximum value of unity.

The problem with estimating $\bar{R}$ using analog processing lies mainly in performing the multiplications and divisions indicated in (A1) and (A2). We resort instead to the following tricks: First, instead of an infinite averaging time T we use a fixed value of about 10 min, which is much longer than the wave periods we are interested in. This 10 min window continuously advances in time, giving a continuous estimate of $\bar{R}(t)$. The signals from each sensor I_i are then passed through a compressor whose output is a replica of the input signal, but always has the same rms value, regardless of input; that is, each output can be expressed as

$$E_i=C[I_i/(\overline{I_i^2})^{\frac{1}{2}}], \quad \text{(A4)}$$

where $(\overline{I_i^2})^{\frac{1}{2}}$ is the rms amplitude of the input signal, and C is a constant. The E_i are then summed, squared (in a square-law detector) and averaged to give

$$E_D=\overline{(\sum_{i=1}^{n}E_i)^2}, \quad \text{(A5)}$$

which is equivalent to

$$E_D=C^2\sum_{i=1}^{n}\overline{I_i^2}/\overline{I_i^2}+2C^2\sum_{i=1}^{n-1}\sum_{j=j+1}^{n}\overline{I_iI_j}/(\overline{I_i^2})^{\frac{1}{2}}\,(\overline{I_j^2})^{\frac{1}{2}}. \quad \text{(A6)}$$

The first term clearly equals C^2n, while the second term differs by only a constant factor from the definition of the average cross-correlation coefficient for n functions I_i. Therefore,

$$E_D=C^2[n+n(n-1)\bar{R}], \quad \text{(A7)}$$

so that $\bar{R}=0$ is indicated by a detector output of C^2n, and $\bar{R}=1$ is indicated by an output of $C^2[n+n(n-1)]$, with $\bar{R}$ varying linearly for values in-between. It is thus a simple matter to construct a meter or recorder calibrated to read $\bar{R}$ directly, as the mechanical programmer steers the array pattern in wavenumber space.

The name *coherence* is given to a generalized cross-correlation coefficient that depends on frequency; but for our purposes, cross-correlation coefficient is equivalent to broadband coherence.

It is useful to combine the coherence thresholds we have used with the station noise statistics (Appendix B), to get an indication of minimum usable wave intensities in real noise environments. If we assume that non-acoustic noise is uncorrelated among the sensors and with the acoustic signal, we can show that the amplitude signal-to-noise ratio σ is related to $\bar{R}$ by

$$\sigma=\frac{\bar{R}}{1-\bar{R}}, \quad \text{(A8)}$$

so that, for example, a wave coherence of 0.5 corresponds to a unity signal-to-noise ratio. The noise amplitude-probability distribution for Boulder (Fig. B1) shows that a noise level exceeded 50% of the time is about 0.5 μb. If we assume a useful coherence threshold of 0.15 ($\sigma=0.176$), then we can say that 50% of the time the Boulder array "sensitivity" is at least $0.5\times0.176=0.088$ μb. The corresponding 50% sensitivity levels for Rapid City and Estancia stations are 0.246 and 0.194 μb.

APPENDIX B

Noise Statistics for the Three Observatories during the 1973 Experiment

Because the intensity and variability of background noise strongly influence the detectability of severe-storm infrasound, we collected statistics on the amplitude distribution and diurnal variability of noise level at each of the three observatories. The results are displayed in Figs. B1 and B2.

At each observatory, we recorded on a paper chart an estimate of the average amplitude of the ambient pressure fluctuations within the system bandpass. We averaged spatially by summing the outputs of all the sensors in an observatory's array and temporally with a peak detector and 10 min low-pass filter. Most of the time, this record indicates the level of non-propagating pressure fluctuations that we call "noise"; the fraction of the time when acoustic waves contribute much to this level is insignificant. We have defined a 2 μb noise level as a threshold above which most severe-storm infrasound is not detectable with a useful signal-to-noise

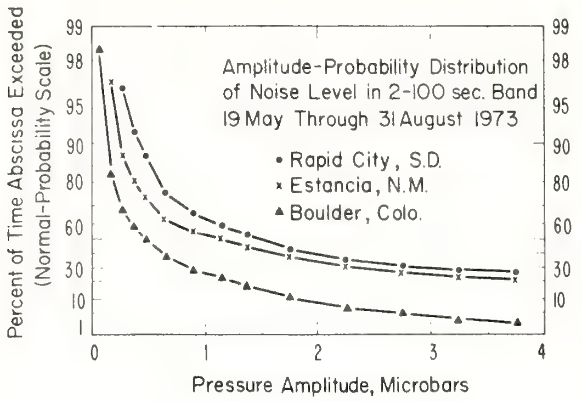

FIG. B1. Noise level amplitude-probability distributions for the three observatories during the observing season.

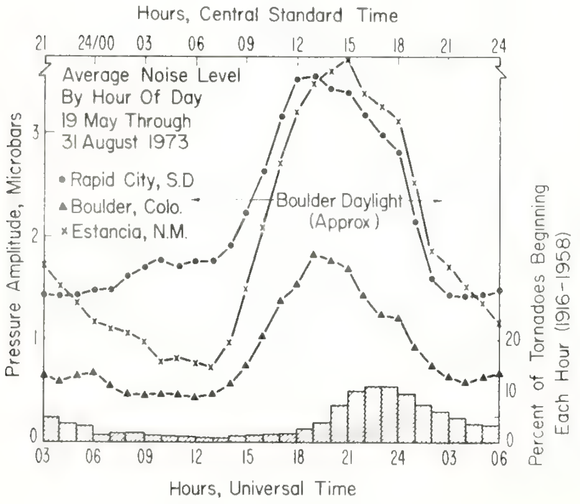

FIG. B2. Diurnal variability of observed average noise level at the three stations, compared with the historical distribution of tornado onset by hour of the day.

ratio. (Using our definition of signal-to-noise ratio from Appendix A and the coherence threshold of 0.15, this implies that most severe-storm infrasound has amplitudes less than about 0.35 μb.)

Fig. B1 gives the amplitude-probability distribution of noise level at the three stations over the entire observing period. It shows, for example, that the noise level exceeded 50% of the time is 1.4 μb for Rapid City and 1.1 ub for Estancia, but only 0.5 μb for the Boulder station. The 2 μb noise threshold level is exceeded about 39% of the time at the Rapid City station, about 33% of the time at Estancia, and only about 8% of the time at Boulder.

We believe that the lower average noise level at Boulder results mainly from the superior noise-reducing spatial-filter system used there, compared to the temporary systems used at the outlying stations.

Fig. B2 gives the diurnal distribution of noise level, averaged by hour, for the three stations. Also shown at the bottom of Fig. B2 is the hourly distribution of tornado onset, derived from NWS statistics covering 42 years and over 8000 tornado observations. This distribution matches closely the temporal distribution of severe-storm infrasound observations. Nature appears to be conspiring against the detection of tornadic storms by imposing high-noise levels at just the hours of high tornado frequency. The importance of adequate noise-reducing filters is thus doubly emphasized.

We can see from this figure that the times of quiet and noisiness tend to be correlated among the three stations. A quantitative measure of the degree of correlation can be obtained by comparing the percent of time all three stations are simultaneously quiet with the joint probability that all three are simultaneously quiet, based on their individual amplitude-probability distributions. From Fig. B1, we see that the joint probability that noise level at all three stations is less than 2 μb is $0.71\times0.34\times0.39=0.093$ (assuming statistical independence), whereas the actual fraction of the time that all three are quiet is 0.17, almost twice as great.

REFERENCES

Bowman, H. S., and A. J. Bedard, 1971: Observations of infrasound and subsonic disturbances related to severe weather. *Geophys. J. Roy. Astron. Soc.*, **26**, 215–242.

Brown, R. F., Jr., 1963: An automatic multichannel correlator. *J. Res. Nat. Bur. Stnd.*, **67C**, 33–38.

Chrzanowski, P., G. E. Greene, K. T. Lemmon and J. M. Young, 1961: Traveling pressure waves associated with geomagnetic activity. *J. Geophys. Res.*, **66**, 3727–3733.

Elliott, J. A., 1972: Microscale pressure fluctuations measured within the lower atmospheric boundary layer. *J. Fluid Mech.*, **53**, 351–383.

Georges, T. M., 1973a: Infrasound from convective storms: Examining the evidence. *Rev. Geophys. Space Phys.*, **11**, 571–594.

——, 1973b: Infrasound from severe storms. *Preprints 8th Conf. Severe Local Storms*, Denver, Colo., Amer. Meteor. Soc, 188–190.

——, 1975: Infrasound from convective storms. Part II. A critique of source candidates. (In preparation.)

——, and J. M. Young, 1972: Passive sensing of natural acoustic-gravity waves at the earth's surface. *Remote Sensing of the Troposphere*, V. E. Derr, Ed., U. S. Govt. Printing Office, Washington, D. C., Chap. 21.

Goerke, V. H., J. M. Young and R. K. Cook, 1965: Infrasonic observations of the May 16, 1963, volcanic explosion on the island of Bali. *J. Geophys. Res.*, **70**, 6017–6022.

Jones, R. M., and T. M. Georges, 1975: Infrasound from convective storms. Part III. Propagation to the ionosphere. (Submitted to *J. Acoust. Soc. Amer.*)

Matheson, H., 1964: Instructions for the operation of NBS infrasonic equipment. NBS Rept. 8519, U. S. Dept. of Commerce, Washington, D. C.

Rhodes, R. S., 1975: A preliminary study of remote sensor applications to local weather services. NOAA Tech. Rept. ERL-330-WPL 40, U. S. Govt. Printing Office, Washington, D. C.

Smith, A. M. O., and A. B. Bauer, 1970: Static-pressure probes that are theoretically insensitive to pitch, yaw and Mach number. *J. Fluid Mech.*, **44**, 513–528

NOAA Technical Memorandum ERL WPL-8, 23

October 1973

REPORT ON THE JULY 1972 WORKSHOP IN ATMOSPHERIC ACOUSTICS

F. F. Hall, Jr.

This memorandum is an information report on the proceedings of a Workshop on Atmospheric Acoustics, held in Boulder, Colorado, 6 and 7 July 1972. Primary attention is given to acoustic echo sounders, their design, construction and interpretation of the atmospheric structure they depict.

Atmospheric Technology, NCAR, 84-93, Winter 1974-75.

Remote Sensing of the Atmosphere by Sound

Alvin L. Morris, NCAR, and Freeman Hall, NOAA

In the past five years, acoustic probing of the atmosphere has undergone a sudden and spectacular growth. From 19th-century foghorn propagation studies to a 1930s interest in stadium acoustics to postwar measurements of upper atmosphere temperature profiles using rocket-borne grenades, atmospheric acoustics has found applications, but has had little real impact on meteorological research. Perhaps the acceptance of radar meteorology and the need for better understanding of the organization of the planetary boundary layer set the stage for a belated entry of this remote sensing technique. But acoustics has now arrived on the meteorological scene, with more than 50 programs active throughout the world.

This paper presents the basic relations governing the interaction of acoustic waves with the atmosphere. Examples of data from recent studies are presented to clarify the present status of atmospheric acoustics. Also, a number of references to recent publications should aid the investigator who wants to dig deeper into the subject. The paper begins with a discussion of sound propagation, condensed and brought up to date from the review by Gutenberg (1951).

Speed of Sound

Basic physics tests show that the propagation speed of longitudinal pressure waves through a fluid is determined by fluid pressure, p, and density, ρ. In the atmosphere, changes in p and ρ due to the passage of a sound wave are adiabatic, so that

$$p \alpha^{\gamma} = \text{constant}$$

in which α is the specific volume, and $\gamma = c_p/c_v$, the ratio of specific heat at constant pressure to specific heat at constant volume. Then the sound speed, c, is given by

$$c = \sqrt{\frac{\gamma P}{\rho}} = \sqrt{\frac{\gamma RT}{M}}$$

where R is the universal gas constant, equal to 8314.32 J/K (kg-mole); T is the temperature in degrees Kelvin; and M is the molecular weight of air, equal to 28.9644 kg/kg-mole for dry air and 28.9644 (1 - 0.38 e/p) for moist air (e is vapor pressure of water vapor in the air).

Substitution yields

$$c = 20.05 \left(1 + 0.19 \frac{e}{p}\right) \sqrt{T} \tag{1}$$

If the air is moving at velocity $\vec{V}$, the velocity of sound, $\vec{c}$, at a point on a wave front is

$$\vec{c}\,' = \vec{N}c + \vec{V} \tag{2}$$

where $\vec{N}$ is a unit vector normal to the wave front.

Therefore, given the distribution of e, p, T, and $\vec{V}$ in the atmosphere, it is possible to trace sound rays through the atmosphere. Conversely, given enough information about the propagation of sound in the atmosphere, it is conceptually possible to compute the distribution of e, p, T, and $\vec{V}$.

Sound Propagation

Figure 1 shows a wave front moving upward and in a positive x direction in the x,z plane. At AD it encounters a boundary between two strata of air having different values of c and $\vec{V}$. For simplicity it is assumed that the interface is horizontal and that the winds are horizontal and lie in the plane of the paper. From Fig. 1, the relationship

$$\left(\frac{c_1}{\sin \phi_1}\right) + V_1 = \left(\frac{c_2}{\sin \phi_2}\right) + V_2 = AD$$

is apparent. Additional strata can be treated in the same manner and, in general,

$$\left(\frac{c}{\sin \phi}\right) + V = \text{constant} \tag{3}$$

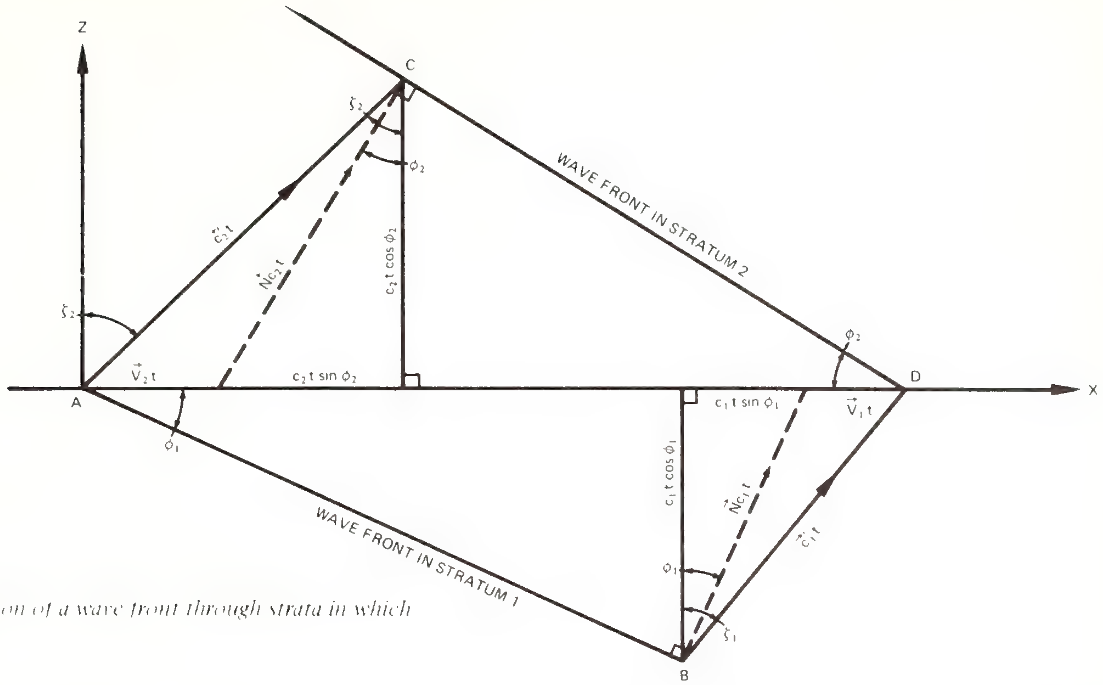

Fig. 1 Propagation of a wave front through strata in which c and V vary

Note that V can take either algebraic sign. If V = 0 everywhere, Eq. (3) becomes Snell's law, as one would anticipate.

Also from Fig. 1 it can be seen that in stratum 1

$$\tan \zeta_1 = \tan \phi_1 + \frac{V_1}{c_1} \sec \phi_1$$

and, in general,

$$\tan \zeta = \tan \phi + \frac{V}{c} \sec \phi \tag{4}$$

Thus, if c, V, and ϕ are known at any level in a horizontally stratified atmosphere, the direction of propagation, ζ, of a sound ray can be determined at any other level reached by the sound if V and c are known at that level.

It is interesting to ask what conditions must prevail to cause a ray from below to become horizontal when it reaches level n. First assume that the air is horizontally stratified and dry, and that V = 0 at all levels. Then $\zeta = \phi = \pi/2$ when the ray becomes horizontal, and

$$\frac{c_o}{\sin \phi_o} = \frac{c_n}{\sin \frac{\pi}{2}}$$

or

$$\sin \phi_o = \sqrt{\frac{T_o}{T_n}}$$

Thus any ray which leaves the surface, i.e., for which $\phi_o < \pi/2$, must encounter a stratum in which $T_n > T_o$ if it is to become horizontal in that stratum. Such a ray will then return to the surface along a path which is symmetrical with its ascent path about a vertical line drawn through the point at which it became horizontal.

If the air is dry, $V \neq 0$ and $\phi_n = \pi/2$

$$\left(\frac{c_o}{\sin \phi_o}\right) + V_o = c_n + V_n$$

Note that for a horizontal ray, $\phi_n = \zeta_n = \pi/2$. Then

$$\sin \phi_o = \frac{c_o}{\left(c_n + V_n - V_o\right)} = \frac{h\sqrt{T_o}}{\left(h\sqrt{T_n} + V_n - V_o\right)}$$

where h = 20.05 m/sec $K^{1/2}$. Evidently a ray leaving the surface may become horizontal at level n if $h\sqrt{T_o} + V_o < h\sqrt{T_n} + V_n$ or equivalently, if its horizontal speed at level n exceeds its horizontal speed at the surface.

This analysis suggests that sonic techniques used in geological surveying may have application in the atmosphere, and indeed Whipple (1923) did use such techniques to deduce that high temperatures exist in the upper stratosphere before such temperatures were measured directly. The analysis also shows a serious limitation of the method. Unless a stratum exists aloft which satisfies the condition $h\sqrt{T_o} + V_o < h\sqrt{T_n} + V_n$, sound rays propagating away from the earth will not return, and hence their interaction with the atmosphere cannot be measured by observations made at the surface.

One recent application of acoustic refraction is for determining the positions of trailing vortices behind landing aircraft (Burnham et al., 1972). A pulse of sound is propagated across the glide slope vertical plane, and when the refracting vortices are present, two pulses are heard with the ground-based receiver, one being the direct line-of-sight pulse and the other the refracted pulse. Acoustic ray paths through vortex structures have been traced by Georges (1972). Refracting effects can also influence the proper interpretation of acoustic echo sounding results, especially for returns from ranges greater than 1 km (Georges and Clifford, 1972).

Attenuation

The intensity of a sound wave is defined as the time rate of energy passage through a unit area perpendicular to the direction of wave propagation. In SI units, sound intensity is measured as watts per square meter (W/m^2). The attenuation of acoustic waves as they propagate through the atmosphere varies with the frequency of the waves but in a continuous, smooth fashion. Therefore, when small frequency ranges are considered, the intensity of a plane wave train, I, at some distance, ℓ, from a reference plane where the intensity is I_o is given by

$$I = I_o e^{-k\ell} \tag{5}$$

Here k is dimensionally the reciprocal of length, and is defined as the attenuation coefficient. It is made up of three independent components,

$$k = k_c + k_m + k_s \tag{6}$$

The subscripts stand for classical, molecular, and scattering (or excess) attenuation, respectively (Hall, 1972).

Classical attenuation of sound is caused by the finite viscosity of air, which leads to heating of the atmosphere as the sound wave passes, and by radiation and heat conduction from the high pressure regions of the sound wave. Classical absorption was first studied by Stokes (1849), and elaborated upon by Rayleigh (1896). Classical absorption varies as the frequency, f, raised to the second power, or

$$k_c = 4.24 f^2 \times 10^{-11}$$

as given by Beranek (1954). The units of k in this example are 1/m. Compared to the other two sources of attenuation, classical absorption is so small as to be essentially negligible in the audible range of frequencies under normal, temperate atmospheric conditions.

The first careful investigation to determine the cause of atmospheric absorption of sound above that predicted by the classical theory was performed by Knudsen (1931). He discovered the marked dependence of absorption on the humidity of the air. In a later investigation, he showed that the abnormally high absorption in air is determined by an interaction between oxygen and water molecules; when a test chamber was filled with only nitrogen and water vapor, it showed a much lower attenuation coefficient than when oxygen was present in the proportions found in the atmosphere (Knudsen, 1933). The mechanism by which molecular absorption occurs was explained by Kneser (1933) as the transfer of collision-excited vibrational energy, produced by the acoustic field, from oxygen molecules to water vapor molecules. The energy of the excited water molecules is then radiated away in the infrared. This transfer of energy from oxygen to water vapor is facilitated by the nearly exact overlap of energy levels in the two molecules, but while radiative decay is not possible for the oxygen molecule, this method of energy removal is highly favored by water vapor. The molecular interaction and transition rates have been studied more fully by Henderson and Herzfeld (1965).

The most comprehensive measurements of molecular absorption, studied by means of the decay of acoustic energy in closed chambers, are those of Harris (1966). Examples of data from this study are given in Fig. 2. Molecular absorption decreases with temperature, which helps explain why, in cold climates, cases of unusually long-range sound propagation are sometimes reported, although refractive ducting of sound (considered earlier) between severe arctic temperature inversions and the ground may also be important in such cases.

As an example, in comparing the importance of classical and molecular attenuation, consider a frequency of 2 kHz in air at 20C with 15% relative humidity. The classical absorption coefficient is $k_c = 1.7 \times 10^{-4}/m$. From Fig. 2,

Fig. 2 Molecular attenuation coefficients for acoustic waves in the atmosphere as a function of humidity and frequency (From Harris, 1966, p. 155.)

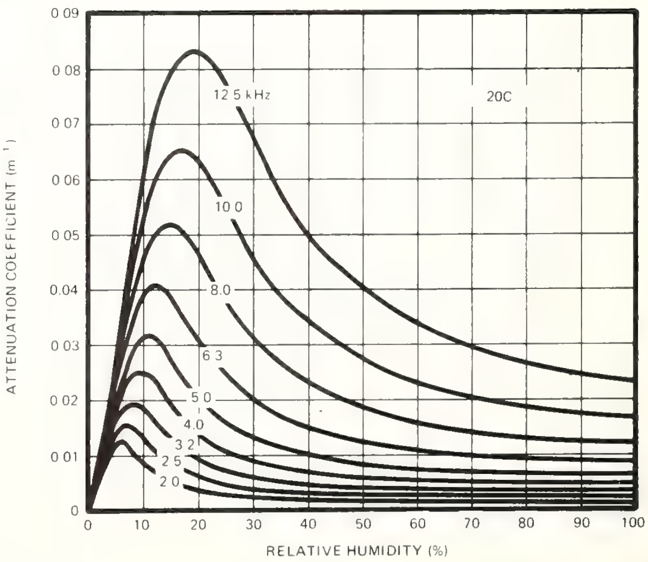

$k_m = 6 \times 10^{-3}$/m, or a factor 35 times the classical attenuation. From this comparison it is easy to appreciate why classical attenuation is usually disregarded in considering sound propagation in standard, temperate atmospheres.

Acoustic echo sounding is feasible because sound is scattered from a probing acoustic beam by temperature structure and wind turbulence in the atmosphere. Obviously, if energy is scattered from the beam the intensity of the beam will decrease. This excess attenuation, over and above classical and molecular contributions, is expressed by the third coefficient on the right side of Eq. (6). The magnitude of k_s will depend upon the structure of the atmosphere. Field tests by Beran, Reynolds, and Gething (1970), utilizing a sound source on a sailplane, indicate that excess attenuation may be negligible under some atmospheric conditions, but may be an order of magnitude larger than molecular absorption for other conditions. A similar range of variation for excess attenuation was found by Dneprovskaya, Iofe, and Levitas (1963), who measured excess values of 5 - 23 dB/km near 2 kHz. Until we know more about sound propagation and scattering in the free atmosphere, little more can be said about excess attenuation. Eventually it should be possible to predict its magnitude by observing acoustic energy scattering with an echo sounder. Accurate, quantitative interpretation of echo sounding returns depends critically upon understanding all aspects of attenuation in the real atmosphere, and more research needs to be accomplished, both theoretical and experimental, on the propagation of sound in realistic atmospheres.

Scattering

The theory of the scattering of sound caused by velocity fluctuations in the atmosphere has been discussed by Lighthill (1953) and Kraichnan (1953), while Bachelor (1957) has treated the scattering caused by temperature inhomogeneities. Monin (1961) showed that the fraction, $\sigma(\theta)$, of the incident power scattered from a unit volume per unit incident flux into a unit solid angle is

$$\sigma(\theta) = \frac{32\pi \cos^2 \theta}{\lambda^4} \left[\frac{\Phi(V) \left(\frac{4\pi}{\lambda} \sin \frac{\theta}{2} \right) \cos^2 \frac{\theta}{2}}{c_0^2} + \frac{\Phi(T) \left(\frac{4\pi}{\lambda} \sin \frac{\theta}{2} \right)}{4T^2} \right] \tag{7}$$

where θ is the scattering angle measured from the direction of propagation of the incident wave, λ is the wavelength of sound for average temperature T, $\Phi(V)$ is the three-dimensional spectral density of fluctuations in wind velocity, c_0 is the speed of sound in the undisturbed atmosphere, $\Phi(T)$ is the three-dimensional spectral density of fluctuations in temperature, and T is the average atmospheric temperature in degrees Kelvin in the scattering volume.

Both $\Phi(V)$ and $\Phi(T)$ are evaluated at the spatial scale, λ', where

$$\lambda' = \frac{\lambda}{2 \sin \frac{\theta}{2}}$$

Little (1970) calls the term $(4\pi/\lambda) \sin(\theta/2)$ the effective wave number at which an acoustic radar scattering through angle θ interrogates the medium.

In deriving Eq. (7) it has been assumed that wind and temperature fluctuations are uncorrelated and homogeneous, that the atmosphere is locally isotropic, and that humidity fluctuations are not important. Scattering from humidity fluctuations would, typically, be two to three orders of magnitude less than scattering by temperature and wind fluctuations; therefore it may be ignored. The other assumptions are not so clearly acceptable, but experience has shown that Eq. (7) does provide first-order approximations to sound scattering in the lower troposphere.

Kolmogorov (1941) studied the local structure of turbulence in an incompressible viscous fluid at very large Reynolds numbers. He concluded that, in such a fluid, energy is partitioned among the turbulent eddies in proportion to $K^{-5/3}$, where K is the wave number. Using the Kolmogorov spectrum of turbulence, Eq. (7) may be written

$$\sigma(\theta) = 0.055\ \lambda^{-1/3} \cos^2 \theta \times \left[\frac{C_V^2}{c^2} \cos^2 \frac{\theta}{2} + 0.13 \frac{C_T^2}{T^2} \right] \left(\sin \frac{\theta}{2} \right)^{-11/3} \tag{8}$$

The terms C_V and C_T are, respectively, velocity and thermal structure parameters, which are defined as follows:

$$C_V^2 = \overline{\left[\frac{V(x) - V(x + \Delta x)}{(\Delta x)^{1/3}} \right]^2}$$

$$C_T^2 = \overline{\left[\frac{T(x) - T(x + \Delta x)}{(\Delta x)^{1/3}} \right]^2}$$

where V(x) and T(x) are instantaneous wind speed and temperature at position x, and $V(x + \Delta x)$ and $T(x + \Delta x)$ are corresponding values at position $x + \Delta x$. The x-axis may be chosen in any direction which is appropriate to the experiment.

It is apparent from Eq. (8) that scattering is weakly dependent on λ, and that short waves are scattered more strongly than long waves. Equation (8) also shows that scattering is highly dependent on the scattering angle. In particular, scattering from wind velocity fluctuations is a function of $\cos^2 \theta \cos^2 (\theta/2) [\sin (\theta/2)]^{-11/3}$, a product which vanishes at $\theta = \pi/2$ and $\theta = \pi$. Hence, neither backscattering nor scattering normal to the direction of sound propagation should be expected from mechanical turbulence. Scattering from temperature inhomogeneities may be expected at $\theta = \pi$ but not at $\theta = \pi/2$. Figures 3(a) and 3(b), from Baerg and Schwarz (1966), provide a comparison of theory with experimentally determined scatter.

Acoustic Radar Equation

The useful power, P_r, returned from disturbed scattering centers in the atmosphere to a receiver located at the site of a transmitter that is transmitting power, P_t, is

$$P_r = \frac{P_t \sigma c \tau A_e L}{2R^2} \qquad (9)$$

where σ is the value of $\sigma(\theta)$ when $\theta = \pi$ [from Eq. (8), $\sigma(\pi) = 0.0072\lambda^{-1/3} \times (C_T/T^2)$], τ is the sound pulse length (time), A_e is the effective cross-sectional area of the antenna, L is a term which accounts for attenuation throughout the round trip, and R is the range to the target volume.

Consider now the power levels to which an echo sounder system receiver must respond. The theoretical limit is the acoustic noise power generated by the random thermal motion of atmospheric molecules. Under most conditions, the noise of wind across the transducer, insects, birds, and especially human transportation and industrial activities, will exceed the theoretical limits. More details on background noise are given by Simmons, Wescott, and Hall (1971).

The acoustic power return for a nominal transmitted power of 20 acoustic watts may range from near the theoretical limit at ranges of 100 m to 1 km for nonturbulent regions, to 60 or 70 dB above the noise limit for an atmosphere with a strong thermal structure function at a range of 50 m. It is therefore necessary that the acoustic echo sounding system be capable of responding over an extremely wide dynamic range.

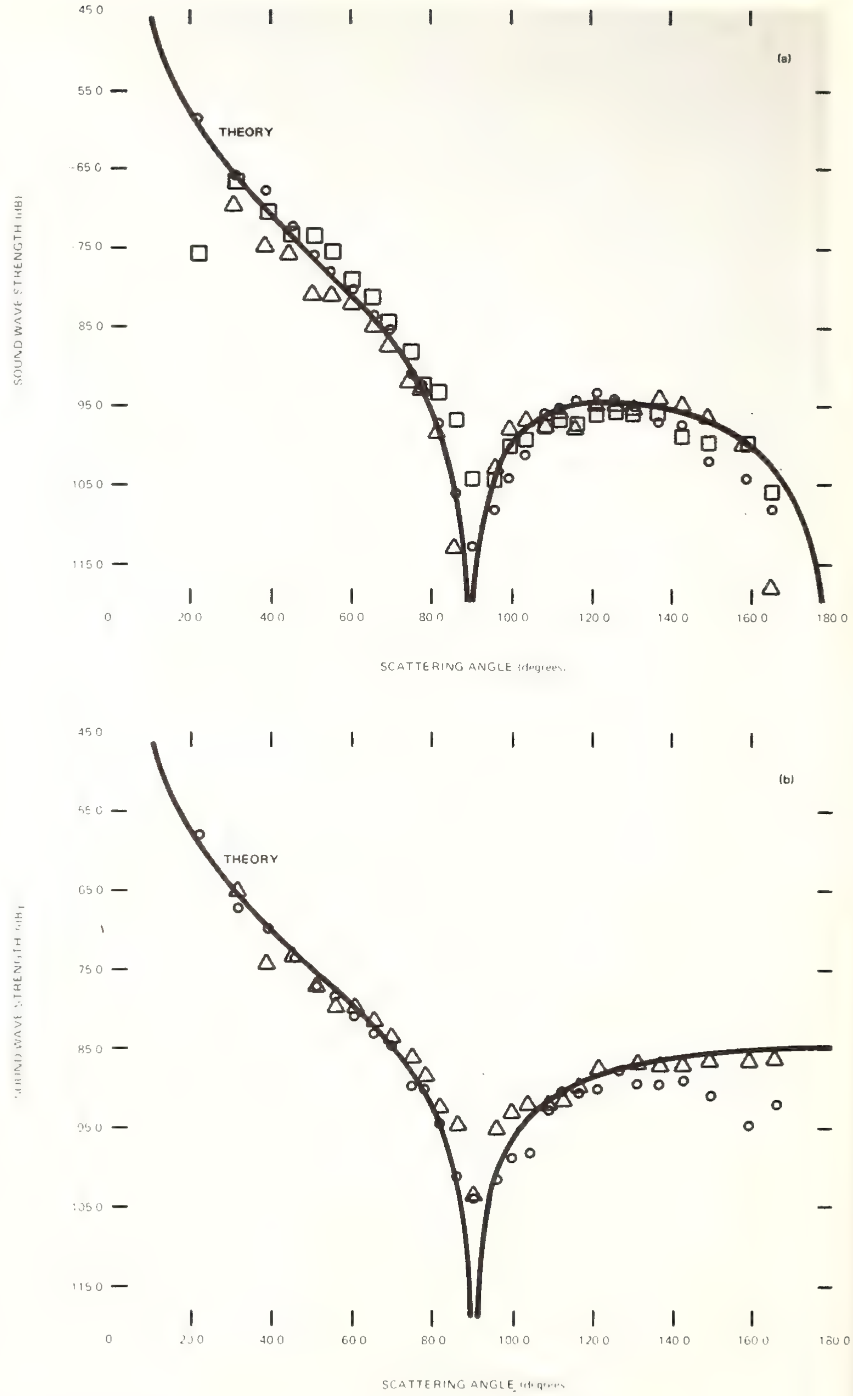

Fig. 3 Comparisons of theoretical scatter with experimental observations. Part (a) shows acoustic scatter from the velocity field; part (b) shows acoustic scatter from the temperature field. (From Baerg and Schwarz, 1966, p. 1131.)

An echo sounder system with a total dynamic range of 95 dB does not seem to exhibit saturated echoes from strong thermal structure, even at ranges as short as 30 m.

Doppler Methods

The frequency of a returned signal will be different from the frequency of the transmitted signal if there are net wind or temperature changes along the sounding path and if the scatterers in the target volume are in motion. According to Georges and Clifford (1972), however, the frequency change (doppler shift) produced by motions within the target volume dominates over the changes along the path.

The doppler frequency shift, Δf, of sound of frequency f_o scattered by a scatterer moving with the velocity, $\vec{V}$, of the wind is

$$\Delta f = \frac{1}{2\pi}\left(\vec{K}_s - \vec{K}_o\right) \cdot \vec{V} \tag{10}$$

where $\vec{K}_s$ is the wave vector of the scattered sound, and $\vec{K}_o$ is a wave vector of magnitude $2\pi/\lambda_o$ directed along the direction of propagation of the transmitted sound.

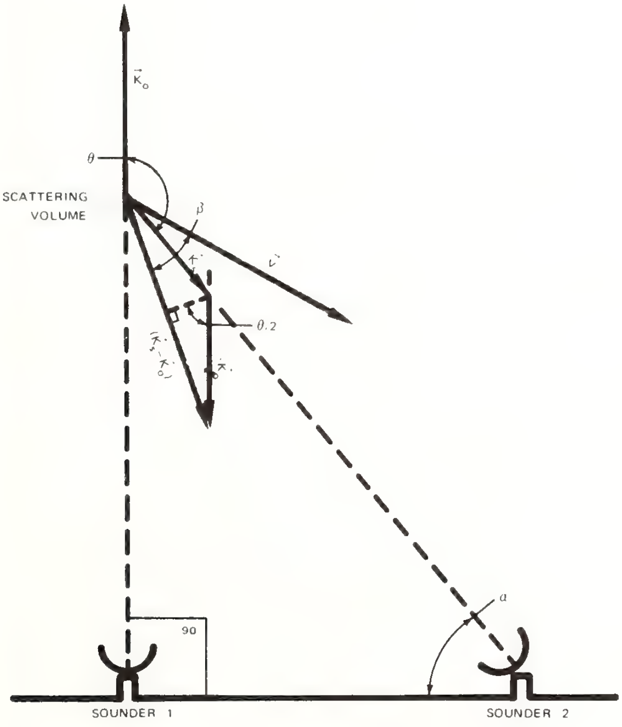

Fig. 4 Vector diagram showing the resolution of the wind in the plane of two intersecting sounder beams.

Beran and Clifford (1972) have shown how the total wind vector at the target volume can be determined using three acoustic doppler sounders. (Such an array of sounders is depicted in Fig. 3 of Beran's article, "Wind Measurement with Acoustic Doppler," in this issue of *Atmospheric Technology.*)

Figure 4 shows the geometry of the wind velocity and transmitted and scattered sound rays in such an array in a plane which includes the vertically directed sounder and either of the other sounders portrayed in Beran's Fig. 3. The vertical component of wind velocity can be determined by the vertical sounder alone. If the other sounders of a three-sounder array are also active (i.e., transmit as well as receive), it is possible to measure three components of wind simultaneously and hence the total wind vector in the intersection of the beams.

It is also possible to obtain the total wind vector with only one active sounder and two receiving antennas. A pulse transmitted vertically at the active sounder scatters continuously as it propagates upward. The scattered sound is received at the other sounders, and the time lapse after transmission serves as a measure of the height of the scattering volume. If the sound is not refracted, the wind component measured by this arrangement is directed approximately along the bisector of the antenna axes, as will be shown in the following discussion.

The vector $(\vec{K}_s - \vec{K}_o)$ is shown in Fig. 4 for sound from sounder 1 scattered by the scattering volume to sounder 2. Since $|\vec{K}_s| \approx |\vec{K}_o|$,

$$\frac{1}{2}\left|\left(\vec{K}_s - \vec{K}_o\right)\right| \approx \left|\vec{K}_o\right| \sin\left(\frac{\theta}{2}\right)$$

$$\left|\left(\vec{K}_s - \vec{K}_o\right)\right| \approx \left(\frac{4\pi}{\lambda_o}\right) \sin\left(\frac{\theta}{2}\right)$$

Substituting $|(\vec{K}_s - \vec{K}_o)| V \cos\beta$ for $(\vec{K}_s - \vec{K}_o) \cdot \vec{V}$ in Eq. (10) and solving for $V \cos\beta$ yields

$$V \cos\beta \approx \frac{\Delta f \; \lambda_o}{2 \sin\left(\frac{\theta}{2}\right)} = \frac{c_o}{2 \sin\left(\frac{\theta}{2}\right)}\left(\frac{\Delta f}{f_o}\right)$$

since $f_o \lambda_o = c_o$. The direction of vector $(\vec{K}_s - \vec{K}_o)$ is known, and $V \cos\beta$ is the component of the total wind in that direction. In general, $\vec{V}_i \cdot \vec{V} = \vec{V}_i^2$ where $\vec{V}_i$ is the vector component of the wind in any known direction. If three such vector components are known, $\vec{V}$ may be determined. This condition is fulfilled if we know the vertical wind component, the wind component in the direction of $(\vec{K}_s - \vec{K}_o)$ for sounders 1 and 2, and a similar wind component for sounders 1 and 3, where the sounders are separated by sufficient distances to provide acceptable resolution.

In the discussions above no question has been raised of our ability to measure the doppler frequency, and Δf has been used as if it were a single, well-defined value. If the many scatterers in the scattering volume do not all have the same velocity, there will be many doppler frequencies, and we must be prepared to deal with a doppler spectrum. The frequency spectrum of the returned signal is compared with that of the transmitted pulse to obtain the doppler spectrum. Figure 5, after Little (1970), shows how Δf may be obtained from the doppler spectrum. It provides a measure of the mean velocity of the scattering volume (assumed to be the wind velocity), while the broadening of the spectrum, δf, contains information about the turbulence.

Acoustic Measurements

Monostatic acoustic sounder systems (systems in which the transmitter and receiver are located together) have been used extensively in many places. They are simple and they provide many qualitative and some quantitative data that are not otherwise available; the signal can be readily recorded by facsimile recorder and viewed immediately. McAllister (1968) was first to demonstrate the dynamic, coherent patterns of atmospheric structure using a facsimile recorder, whereas an earlier study (Gilman, Coxhead, and Willis, 1946) lacked this dramatic data presentation scheme, and consequently was not widely noticed. An example of a facsimile record is shown by Fig. 6. This situation, discussed by Hooke, Young, and Beran (1972), shows several strata

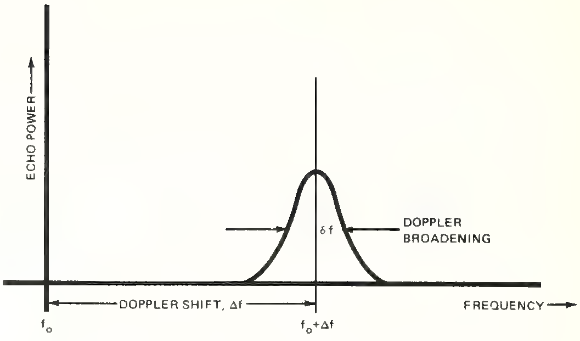

Fig. 5 The ability of the doppler radar to measure the mean radial component of velocity (proportional to Δf) and the fluctuation in that component (proportional to δf). (From Little, 1970, p. 400.)

Fig. 6 Microbarograph and acoustic sounder records for the early morning of 3 March 1971 on Table Mountain near Boulder, Colorado. As displayed above the sounder record, the pressure traces of microbarographs on the ground near the sounder have been time-shifted relative to one another so as to provide maximum cross-correlation in the time interval between 0100 and 0200 local time. As displayed below it, they have been shifted to provide maximum cross-correlation for the event occurring at about 0315 local time. The white line superimposed on the sounder record is the pressure trace of one of the microbarographs. Time scales are the same for all records. (From Hooke, Young, and Beran, 1972, p. 373.)

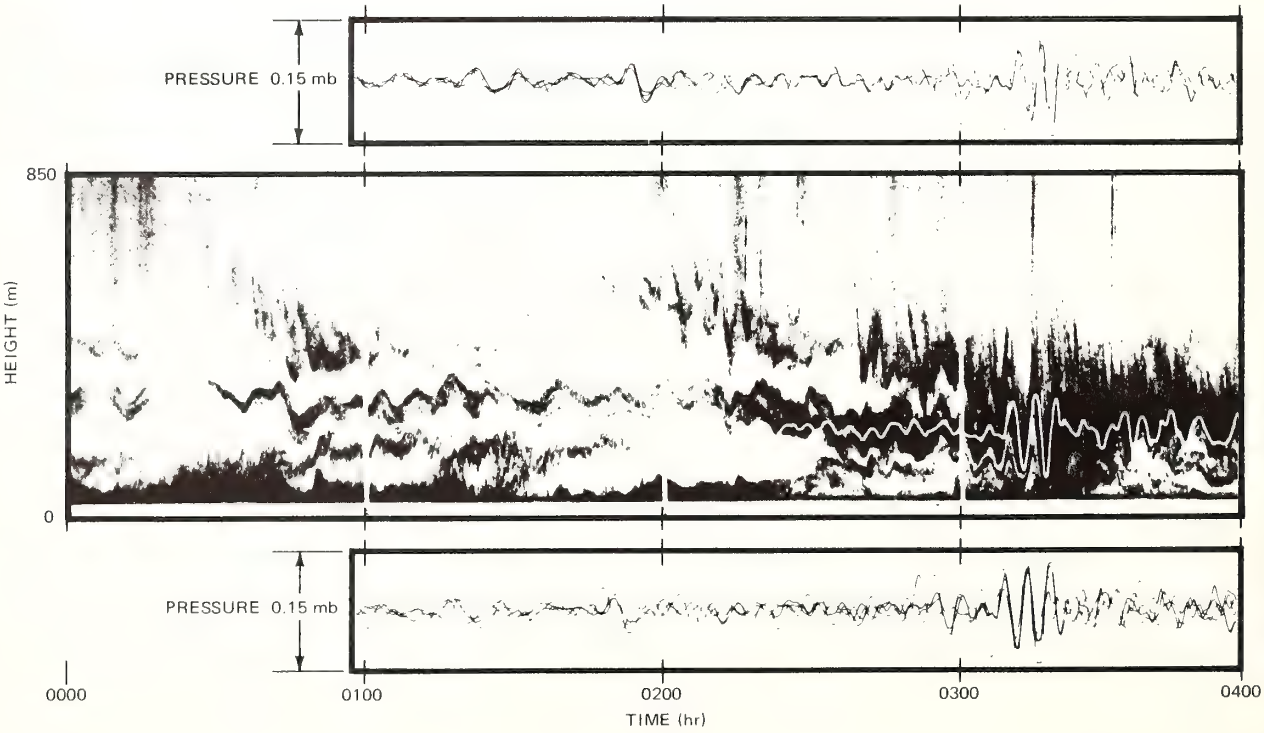

between the surface and 850 m. Since backscatter only is used by monostatic acoustic radar (wind turbulence does not scatter at $\theta = \pi$), all of the structure seen in Fig. 6 must be caused by temperature inhomogeneities. Neither absolute temperature nor temperature gradients can be determined from this type of record, but the interaction of C_T with temperature gradient and Richardson's number makes it possible to interpret the vertical temperature structure qualitatively. The regions which are dark return a strong echo and are associated with turbulent parcels of either stable or unstable lapse rates. The white areas are associated with low turbulence regions or with neutral lapse rates. This particular record shows the strata undergoing wavelike undulations. The white line superimposed on the sounder record is a pressure trace from a microbarograph located on the ground near the sounder. It is easy to show how useful even such simple acoustic sounder systems can become in boundary-layer dynamics studies (Hooke, Hall, and Gossard, 1973) and pollution studies (Wycoff, Beran, and Hall, 1973), to mention only two possibilities.

The low cost of components and the straightforward engineering involved in acoustic echo sounders make them favored projects for university research. At the University of Melbourne, a sounder has been used to study atmospheric turbulence (Beran, 1970) and the changes in lower troposphere structure during frontal passages (Shaw, 1971). Stratus cloud tops exhibit wavelike undulations in a University of Oklahoma investigation (Cronenwett, Walker, and Inman, 1972), while studies at the University of Toronto have proven the feasibility of operating sounders on top of tall buildings in noisy, urban areas (List, Bennett, and Rentsch, 1972).

Adding doppler capability to a monostatic system makes it possible to determine the vertical motion as well as to measure wave motions in the boundary layer. Beran, Little, and Willmarth (1971), using an acoustic doppler sounder, found that in thermal plumes, echo strength correlated with vertical motion (see Fig. 2 in Beran's article in this issue); however, the strongest echoes appear to be associated with the region of maximum shear between rising warm air and descending cooler air.

Winds measured by acoustic sounders in an arrangement like that shown in Fig. 4 have been compared with winds measured by a boundary layer profile (BLP) balloon system by Beran and Willmarth (1971) and Beran and Clifford (1972). See Fig. 4 of Beran's article in this issue. In that article Beran also discusses an interesting application of a doppler acoustic sounder at an airport.

Conclusion

These few examples only suggest what is evident from theory and numerous detailed observations, that enough acoustic energy is scattered in the boundary layer of the atmosphere to provide useful wind profile and thermal structure data. Complete profiles of the scattering structure may be obtained once every several seconds, with a spatial resolution of 10 m.

Experimental problems which have been mentioned are generally not serious, but they cannot be ignored. Sound transmitters and receiving antennas cannot be completely shielded from annoying interference by other audible sounds. Wind noises across the receiving antenna make even the best system inoperative when the wind exceeds 10 m/sec. Rain on the antenna can also be a problem at a time when good data might be especially desired. Thus even a system located away from population centers, where the noise produced by the transmitter is not a problem and where other noises are minimized, cannot be expected to yield acceptable data continuously.

On balance, however, a properly used acoustic sounder system is a powerful tool for atmospheric research and monitoring. Several commercial models are now available for purchase, or an innovator can build a relatively inexpensive system following guidelines available in several NOAA reports (Wescott, Simmons, and Little, 1970; Simmons et al., 1971; Owens, 1974).

Sound refraction techniques for probing the atmosphere are not as widely used as techniques that depend on scattering. They are not being ignored, however; and when low-level inversions or strong wind shears exist, they may be capable of providing information that an acoustic sounder cannot provide. Thus, the two methods may be complementary.

Theory and practice are progressing hand in hand, and improvements in both hardware and techniques can be anticipated. Clearly, acoustic echo sounders, like electromagnetic radar, produce vast quantities of data. Data handling and analysis techniques must be given high priority if the full potential of acoustic probing is to be realized.

References

Bachelor, G. K., 1957: Wave scattering due to turbulence. *Proceedings of the Symposium on Naval Hydrodynamics*, NAS-NRC Publ. 515, 409 - 430.

Baerg, W., and W. H. Schwarz, 1966: Measurements of the scattering of sound from turbulence. *J. Acoust. Soc. Am. 39*, 1125 - 1132.

Beran, D. W., 1970: *Turbulence Detection.* Ph.D. Thesis, University of Melbourne, Melbourne, Australia, 280 pp.

, R. M. Reynolds, and J. T. Gething, 1970: Sound attenuation in the free atmosphere. *Project EAR Report V*, Meteorology Department, University of Melbourne, Melbourne, Australia, 1 - 48.

——————, C. G. Little, and B. C. Willmarth, 1971: Acoustic doppler measurements of vertical velocities in the atmosphere. *Nature 230,* 160 - 162.

——————, and B. C. Willmarth, 1971: Doppler winds from a bistatic acoustic sounder. *Proceedings of the Seventh International Symposium on Remote Sensing of Environments,* Vol. III, University of Michigan, 1699 - 1714.

——————, and S. F. Clifford, 1972: Acoustic doppler measurements of the total wind vector. *Proceedings of the Second Symposium on Meteorological Observations and Instrumentation.* American Meteorological Society, Boston, Massachusetts, 100 - 109.

Beranek, L. L., 1954: *Acoustics.* New York, McGraw-Hill Book Co., 481 pp.

Burnham, D., J. Hallock, R. Kodis, and T. Sullivan, 1972: *Vortex Sensing Tests at NAFEC.* DOT - TSC - FAA - 72 - 2, Transportation Systems Center, Cambridge, Massachusetts, 65 pp.

Cronenwett, W. T., G. B. Walker, and R. L. Inman, 1972: Acoustic sounding of meteorological phenomena in the planetary boundary layer. *J. Appl. Meteor. 11,* 1351 - 1358.

Dneprovskaya, I. A., V. K. Iofe, and E. I. Levitas, 1963: On the attenuation of sound as it propagates through the atmosphere. *Sov. Phys. Acoust. 8,* 235 - 239.

Georges, T. M., 1972: Acoustic ray paths through a model vortex with a viscous core. *J. Acoust. Soc. Am. 51,* 206 - 209.

——————, and S. F. Clifford, 1972: Acoustic sounding in a refracting atmosphere. *J. Acoust. Soc. Am. 52,* 1397 - 1405.

Gilman, G. W., H. B. Coxhead, and F. H. Willis, 1946: Reflection of sound signals in the troposphere. *J. Acoust. Soc. Am. 18,* 274 - 283.

Gutenberg, B., 1951: Sound propagation in the atmosphere. *Compendium of Meteorology.* American Meteorological Society, Boston, Massachusetts, 366 - 375.

Hall, F. F. Jr., 1972: Temperature and wind structure studies by acoustic echo sounding. Chapter 18 in *Remote Sensing of the Troposphere.* Published jointly by WPL, NOAA, and University of Colorado, Boulder, Colorado.

Harris, C. M., 1966: Absorption of sound in air versus humidity and temperature. *J. Acoust. Soc. Am. 40,* 148 - 159.

Henderson, M. C., and K. F. Herzfeld, 1965: Effect of water vapor on the Napier frequency of oxygen and air. *J. Acoust. Soc. Am. 37,* 986 - 988.

Hooke, W. H., J. M. Young, and D. W. Beran, 1972: Atmospheric waves observed in the planetary boundary layer using an acoustic sounder and a microbarograph array. *Boundary-Layer Meteorol. 2,* 371 - 380.

——————, F. F. Hall Jr., and E. E. Gossard, 1973: Observed generation of an atmospheric gravity wave by shear instability in the mean flow of the planetary boundary layer. *Boundary-Layer Meteorol. 5,* 29 - 41.

Kneser, H. O., 1933: The interpretation of the anomalous sound-absorption in air and oxygen in terms of molecular collisions. *J. Acoust. Soc. Am. 5,* 122 - 126.

Knudsen, V. O., 1931: The effect of humidity upon the absorption of sound in a room, and a determination of the coefficients of absorption of sound in air. *J. Acoust. Soc. Am. 3,* 126 - 138.

——————, 1933: The absorption of sound in air, in oxygen, and in nitrogen—effects of humidity and temperature. *J. Acoust. Soc. Am. 5,* 112 - 121.

Kolmogorov, A. H., 1941: The local structure of turbulence in an incompressible viscous fluid for very large Reynolds numbers. *Dokl. Akad. Nauk SSSR 30,* 301.

Kraichnan, R. H., 1953: The scattering of sound in a turbulent medium. *J. Acoust. Soc. Am. 25,* 1096 - 1104.

Lighthill, M. J., 1953: On the energy scattered from the interaction of turbulence with sound or shock waves. *Proc. Cambridge Phil. Soc. 49,* 531 - 555.

List, R., R. C. Bennett, and U. Rentsch, 1972: Acoustic echo soundings in urban Toronto. *Atmosphere 10,* 73.

Little, C. G., 1970: Acoustic sounding of the lower atmosphere. *Meteor. Monogr. 11 (33),* 397 - 404.

McAllister, L. G., 1968: Acoustic sounding of the lower troposphere. *J. Atmos. Terr. Phys. 30,* 1439 - 1440.

Monin, A. S., 1961: Characteristics of the scattering of sound in a turbulent atmosphere. *Akust. Zh. 7,* 457 - 461 (English translation in *Sov. Phys. Acoust. 7,* 370 - 372).

Owens, E. J., 1974: *Development of a Portable Acoustic Echo Sounder.* NOAA Technical Report ERL 298 WPL 31, Boulder, Colorado.

Rayleigh, J. W. S., 1896: *The Theory of Sound, Vol. II.* Second edition. The Macmillan Company, London. Republished by Dover Publications, New York, New York, 1945, 504 pp.

Shaw, N. A., 1971: *Acoustic Sounding of the Atmosphere.* Ph.D. Thesis, University of Melbourne, Melbourne, Australia, 266 pp.

Simmons, W. R., J. W. Wescott, and F. F. Hall Jr., 1971: *Acoustic Echo Soundings as Related to Air Pollution in Urban Environments.* NOAA Technical Report ERL 216 WPL 17, Boulder, Colorado.

Stokes, G. G., 1849: On the theories of the internal friction of fluids in motion, and of the equilibrium and motion of elastic solids. *Trans. Cambridge Phil. Soc. 8,* 287 - 319.

Wescott, J. W., W. R. Simmons, and C. G. Little, 1970: *Acoustic Echo-Sounding Measurements of Temperature and Wind Fluctuations.* ESSA Technical Memorandum ERLTM-WPL 5, Boulder, Colorado.

Whipple, F. J. W., 1923: The high temperature of the upper atmosphere as an explanation of zones of audibility. *Nature 111,* 187.

Wycoff, R. J., D. W. Beran, and F. F. Hall Jr., 1973: A comparison of the low-level radiosonde and the acoustic echo sounder for monitoring atmospheric stability. *J. Appl. Meteor. 12,* 1196 - 1204.

Alvin L. Morris earned a B.S. from the University of Chicago in 1942 and an M.S. from the U.S. Navy Postgraduate School in 1953. His long career as a meteorologist has spanned a variety of activities, including scientific ballooning, the coordination of meteorological field projects, and teaching. Morris has been affiliated with NCAR since 1962. He is a member of the American Meteorological Society, the American Geophysical Union, and the American Society for Testing and Materials; he is chairman of the Meteorology Committee of the last organization.

Freeman Hall received his M.S. in physics (1957) and Ph.D. in meteorology (1967) from the University of California at Los Angeles. After 13 years of working in the area of instrument development for the aerospace industry, he has more recently specialized in the development of optical and acoustic remote sensing techniques for application to the atmosphere. He joined the National Oceanic and Atmospheric Administration (NOAA) in 1970, and is currently serving as Chief of the Atmospheric Acoustics Program for NOAA's Wave Propagation Laboratory. He is a fellow of the Optical Society of America and a member of the American Meteorological Society and the Acoustical Society of America.

Proceedings of 16th AMS Radar Meteorology Conf., 263-270, April 1975.

AN INVESTIGATION OF ACOUSTIC SCATTER FROM SMALL SCALE THERMAL FLUCTUATIONS IN THE PLANETARY BOUNDARY LAYER

William D. Neff

Wave Propagation Laboratory
NOAA Environmental Research Laboratories
Boulder, Colorado 80302

1. INTRODUCTION

Acoustic echo sounding and microwave radar techniques portray in detail the larger scale features of the planetary boundary layer (Beran et al. 1973; Gossard et al. 1971; Ottersten et al. 1973). Tracers for this technique are small scale turbulence produced refractive index fluctuations. This fine scale turbulence (scales of .05 to 1 m) and the associated behavior of passive additive scalars such as potential temperature and specific humidity are usually presumed to follow the so-called "inertial subrange" turbulence laws (Tatarskii, 1971). Such a presumption has provided the basis on which comparisons are normally made between radar reflectivities and measured refractive index spectra (Hardy and Katz (1969), Metcalf and Atlas (1973)). These comparisons have usually extrapolated measured (i.e., one dimensional) spectra to small scales or estimated the turbulent outer scale, and usually examined a single turbulence regime such as one dominated by either static stability or instability.

The acoustic measurements that are described here used redundant and multi-wavelength (0.12, 0.15, 0.19 m) echo sounding systems whose data were compared with *in situ* measurements at 92 m above the surface. These measurements spanned the transition from a turbulence regime dominated by static stability to one dominated by static instability. The comparisons were posed using a structure function approach which allows both echo sounding and *in situ* measurements to be made in the same spectral region.

The last feature is important since the analysis is then sensitive to the assumption of local statistical isotropy and homogeneity at scales of the order of 0.10 m, and not to the details of the turbulent cascade process.

This paper is based on data obtained during a remote sensing experiment carried out in August 1972 at the NOAA 152 m meteorological tower near Haswell, Colorado. This site lies at an elevation of 1307 m, on the plains of eastern Colorado. The period of the experiment was characterized by clear days with strong surface heating, followed by nights with pronounced radiative cooling.

2. EXPERIMENT INSTRUMENTATION

Acoustic echo sounding instrumentation has been described in detail by McAllister et al. (1969), and Simmons et al. (1971). The system parameters for both the single and multi-frequency channels used in the present experiment are shown in Table 1. The configuration of the sounder systems is shown in Figure 1

TABLE I

	Single Frequency	Multiple Frequency
Frequency	2250 Hz	1750,2250,2750 Hz
Pulse Length	30 ms	30 ms
Pulse Rep. Period	4 s	4 s
Efficiency	4.5 %	4.5%,4.5%,2.8%
Receiver Bandwidth	100 Hz	300 Hz
Antenna Area	1.8 m^2	1.8 m^2
Electrical Power	100 W	25 W
Vertical Range	680 m	590 m
Beamwidth (-3dB Pts.)	3.2^o	$4.5^o, 3.2^o, 2.2^o$

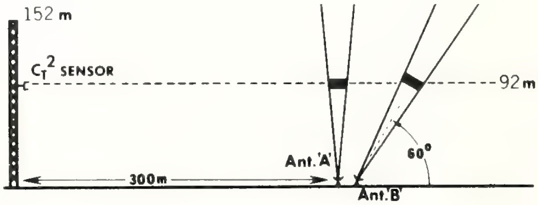

Figure 1. Sounder-Tower configuration with nominal pulse length and beam width.

Supporting meteorological data were obtained 300 m from the sounders on a 152 m tower instrumented at 30.5 m intervals. Thermistors and bivanes were located at these fixed levels and on the tower's movable carriage. In addition, the carriage and the 92 m fixed level were instrumented with "C_T" sensors (Lawrence et al., 1970.) These sensors give by analog computation the rms temperature difference between two fast-response temperature sensors spaced 0.20 m apart in the vertical. These data were digitally recorded in 1 sec integrated samples. In addition, hygrothermograph and barograph recordings were made at all the fixed levels and microwave refractivity at 61 and 92 m. These were used to calculate corrections for the attenuation of the acoustic signal.

3. THEORY AND ANALYSIS

The sounder data were analyzed using a "radar" equation approach. This yielded a value of the acoustic backscatter cross-section, σ_o, for each sounder range gate. The evaluation of the correction terms that occur in this equation is described in detail by Neff (1975) and will not be repeated here. The result of that analysis showed a possible systematic error of ± 3 dB in the evaluation of σ_o.

Following Batchelor (1957) and Monin (1962), the acoustic scattering cross section, σ_o, can be expressed in terms of the isotropic, three dimensional spectral density of temperature, ϕ_T, as

$$\sigma_o = \frac{\pi}{2} k^4 \frac{\phi_T(2k)}{T^2} \qquad (1)$$

where $k = 2\pi/\lambda$ is the incident acoustic wave number corresponding to wavelength λ, and T the local temperature ($^\circ$K).

The spectral density, ϕ_T, is related to in situ data through an analysis of the temperature structure function defined by

$$D_T(\vec{r}) = \langle (T(\vec{X}) - T(\vec{r}+\vec{X}))^2 \rangle \qquad (2)$$

where < > indicates an ensemble average and $\vec{x}$ defines the location at which D_T is evaluated for some separation $\vec{r}$. This is related to ϕ_T for a locally isotropic and homogeneous field through an expression given by Tatarskii (1971):

$$D_T(r) = 8\pi \int_0^\infty (1 - \frac{\sin kr}{kr}) \phi_T(k) k^2 dk \qquad (3)$$

where $r = |\vec{r}|$.

For inertial subrange scales of turbulence (scales between those of energy input and those of molecular dissipation) similarity theory and experiment show D_T to be proportional to r^μ where $\mu = 2/3$, $r = |\vec{r}|$ and C_T^2 is the constant of proportionality (Tatarskii, 1971):

$$D_T(r) = C_T^2 r^\mu \qquad (4)$$

The range of r over which this will be valid will depend in general on the stability of the atmosphere and the height of the measurements above the surface.

Using (4) with $0 < \mu < 2$, Tatarskii shows that (3) can be inverted to yield the following expression for the scattering cross-section

$$\sigma_o = \frac{k^4}{8\pi T^2} \Gamma(\mu + 2) \sin(\frac{\pi\mu}{2}) (2k)^{-(\mu+3)} C_T^2 \qquad (5)$$

Taking $\mu = 2/3$, this yields the result

$$\sigma_o = 0.0039 k^{1/3} C_T^2/T^2 \qquad (6)$$

Using (6) and the "radar equation", a volume averaged measure of C_T^2 at each range gate can be obtained.

A corresponding measurement of the structure function $D_T(r)$ (and hence C_T^2 through (4)) was obtained on a continuous basis from the 92 m fixed level of the tower. This output was averaged over the pulse repetition period for comparison purposes. For a period of 4 sec and a nominal wind speed of 5 ms^{-1}, this yields an average over a horizontal distance comparable with the sounder beamwidth at 92 m.

There are several significant features to this type of analysis. In Figure 2 we have plotted the fractional "error" in the ratio of C_T^2 from the sounder to C_T^2 from the tower using the "2/3" law in the application of (4) and (5) rather than some other hypothetical value of μ in (5). This is done for $0 < \mu < 2$ and several values of r and λ. As can be seen, the comparisons will not provide a sensitive test of inertial subrange spectral predictions for $\lambda \approx r$. At the same time they will not depend on spectral extrapolation to small scales or interpretation of spectral slopes from one dimensional measured spectra. Since a range of ϕ_T or alternatively an estimate of the turbulent outer scale are not required, long sampling times are not necessary and hence the comparisons can be posed in terms of "local" values of C_T^2. This then allows the use of cumulative probability distributions of C_T^2.

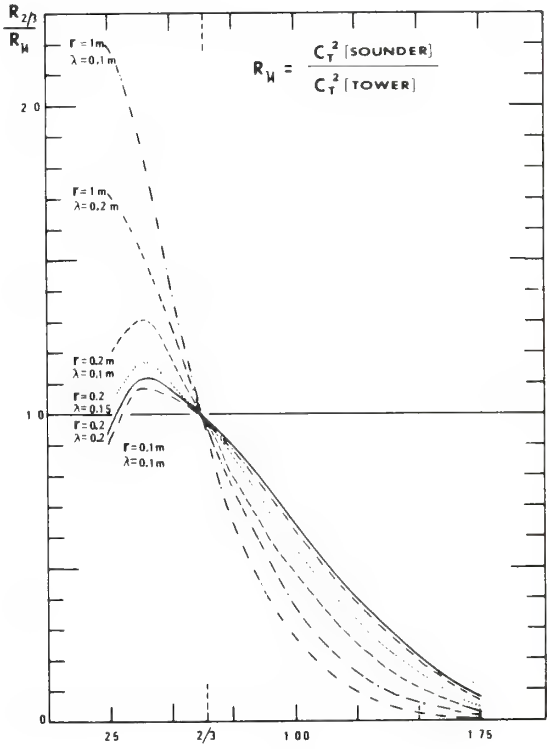

Figure 2. Fractional error in computed sounder-tower ratios of C_T^2 resulting from the use of the "2/3" power law.

Although both techniques obtain a measure of ϕ_T at the low end of the spectrum, there do remain differences in the way by which the spectrum is sampled. In particular, the sounder samples in a very narrow range about $2k = 4\pi/\lambda$ where the spectral weighting is given primarily by the Fourier transform of the incident pulse form. This very narrow band sampling of $\phi_T(K)$ then competes against the effect of the volume averaging of $\phi_T(K)$ as is implied in the cross-section calculation. To compare this with the relatively wide band sampling of $\phi_T(K)$ implied in (3), we presume that $\phi_T(K)$ is a suitably well defined function of K over the pulse volume and repetition period of the sounder. If not, then one might expect a larger sounder C_T^2 statistical variance than that derived from in situ measurements.

Inertial subrange assumptions can be tested indirectly through the form of the cumulative probability distributions. This follows from the relation between C_T^2 and other meteorological fields that arises when an inertial subrange is assumed. This relation is given by (Tatarskii, 1961; Wyngaard and Cote, (1971)

$$C_T^2 = 3.2\ N\ \varepsilon^{-1/3} \tag{7}$$

where N is the rate of destruction of the temperature fluctuations ($^{\circ}C^2 s^{-1}$) through conduction and ε is the turbulent dissipation rate of kinetic energy ($m^2\ s^{-1/3}$). Because $\ell n\ \varepsilon$ and $\ell n\ N$ should possess a Gaussian distribution (Obukhov, 1962; Kolmogorov, 1962, Gurvich and Yaglom, 1967) it follows that C_T^2 should be similarly distributed with the greatest dependence on N rather than ε (Gibson et al., 1970). In general, the apparent log-normality of the sounder and tower C_T^2 data will also depend on noise levels, electronic saturation and the number of samples in the distribution. One should also note that such probability distributions will reflect contributions from scales over which the echo intensity and in situ data are averaged.

Distributions were generated from blocks of data several hours in length, containing several thousand samples. Two adjacent time periods were chosen, each representing a fairly distinct turbulence regime. Examining the character of these distributions, the variances, and the median values one is thus able to test the calibration of the sounder against "conventional" in situ data.

4. DATA COMPARISONS

Our primary analysis period occurred on 15 August, 1972 when two sounders were collocated as shown in Figure 1. Antenna B, tilted 30° from the vertical, was operated in a multifrequency mode. This period covered a portion of a weak (2°C/100 m) nocturnal inversion followed by the development of convection and the associated rise of the inversion as revealed by the facsimile record (Figure 3). During this period, the mean wind was generally directed from the tower towards the sounders at the 92 m level. The sensors were located on the windward side of the tower.

Figure 4 shows a time series comparison of C_T^2 levels (at 92 m) where we have plotted 5 min averages of C_T^2 from the tower and the collocated-sounder-multifrequency data. These data have been low pass filtered to show a portion of the strong diurnal trend in C_T^2 levels. Figures 5a, b, show cumulative probability distributions comparing in situ and sounder C_T^2 values for the periods characterized as "inversion," and developing convection respectively. The coordinate system is logarithmic vs Gaussian. Correspondingly, lognormal data plots as a straight line with the slope related to the variance (Gibson et al., 1970).

Sounder median values and variances larger then those from the in situ sensor characterize the "inversion" case in Figure 5a. The data appears nearly lognormal despite the spread in the median values.

Slightly stable to unstable lapse rates prevail during the period of developing convection from 0730 to 1000 in the region of comparison. Figure 5b shows excellent agreement in this case. The sounder variances, as reflected in the probability distributions, also agree with those from the tower with the exception of the vertical sounder. This one exception may be due to a small multiplicative error combined with an improved signal-to-noise ratio in this channel. The disagreement in the block averaged sounder C_T^2 values following 0900 follows the excellent agreement near 0850. The only noticeable difference on the facsimile is the appearance of a series of plume "tops" near the 92 m level in the period 0910-0945. Note the decreasing correlation with the tower during this period also, particularly near 0940. This decorrelation may arise from a modulation of the convective thermal structure by vortex rolls or other instability modes in the boundary layer flow (e.g. Brown 1974).

5. DISCREPANCIES

5.1 Anomalies associated with the inversion rise

Figure 4 shows a fairly marked disagreement shortly after 0700. To examine this anomaly in more detail we computed ratios of sounder to tower median C_T^2 values in ten minute data blocks through the transition period (~0700). These ratios for each sounder and frequency appear in Figure 6. Figure 7 shows a facsimile detail and the corresponding tower potential temperature time series at 92 m and 152 m which reveal the rise of the inversion and the subsequent development of an adiabatic region. The wavelike perturbations of the inversion, particularly between 0708 and 0713, show in the 92 m temperature trace and later (~0722) in the 152 m trace.

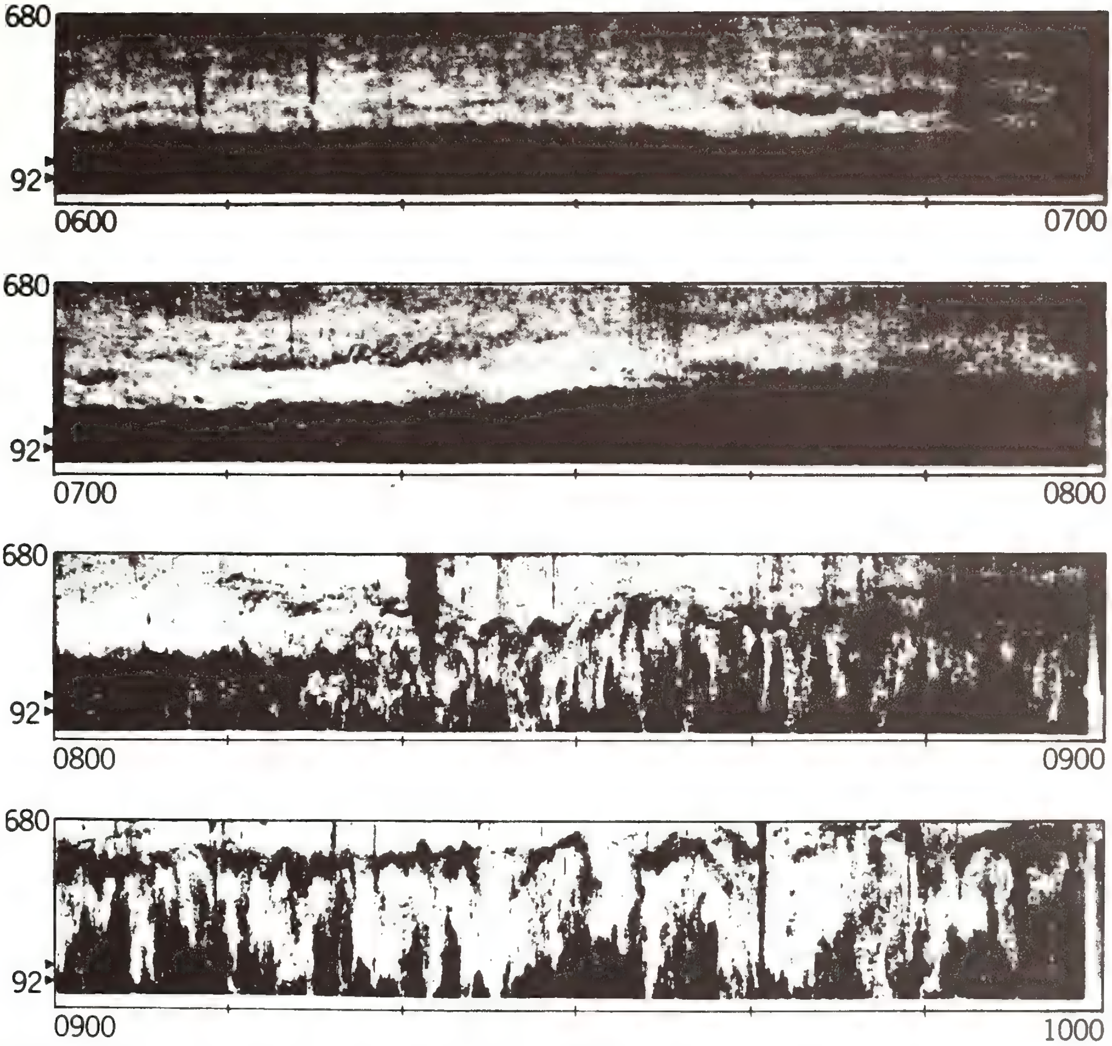

Figure 3 Vertical sounder facsimile record for the period 0600-1000, 15 August, 1972 at Haswell, Colorado. The vertical range is 680m and the height of comparison with the tower, 92m, is indicated.

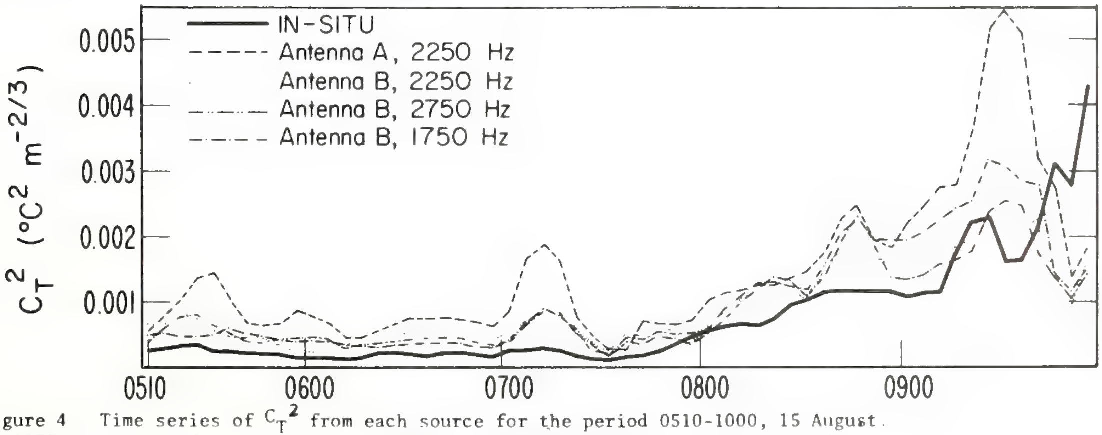

Figure 4 Time series of C_T^2 from each source for the period 0510-1000, 15 August 1972. Data was filtered with a 15 minute running average and then averaged in 5 minute blocks for plotting.

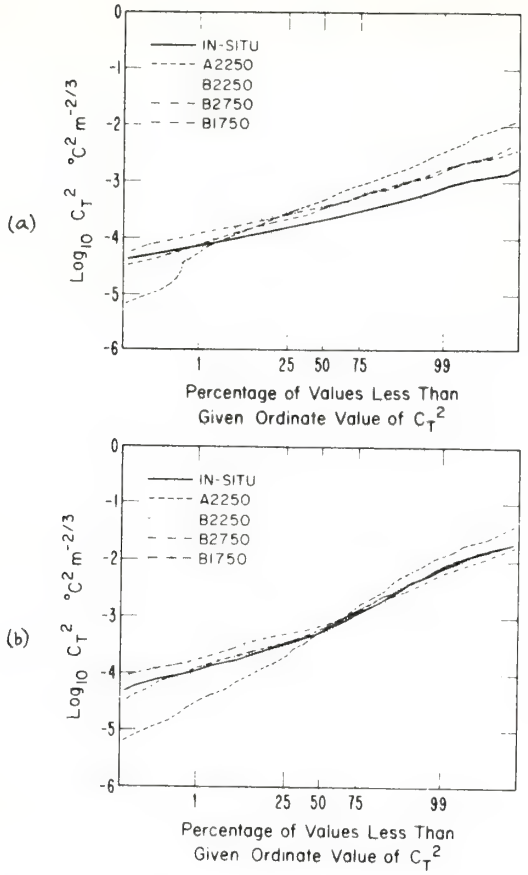

Figure 5. Cumulative probability distributions of C_T^2 from each source at 92 m for the periods a) 0510-0730, and b) 0730-1000.

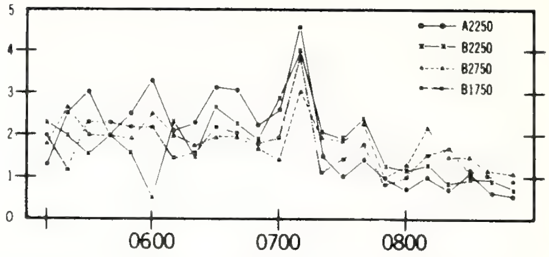

Figure 6. Ratios of sounder derived median C_T^2 to tower median C_T^2 for 10 min data blocks for each channel, 0510-0850, 15 August

As convection develops following 0730, the agreement between in situ and echo sounder-determined C_T^2 values becomes very good (seen from Figure 6). Comparison of the data in Figures 6 and 7 thus suggests a close connection between the structure of the inversion region and the observed anomaly.

Sounder data during the largest anomaly is shown in Figure 8 by 3 dB increment isopleths of C_T^2. The visual impression is that of a serie of dynamical instabilities in fairly advanced states of breakdown.

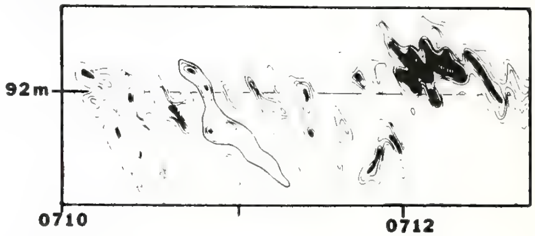

Figure 8. Isopleths of C_T^2 from the vertical sounder in 3 dB increments beginning at 0.00125 °C m$^{-2/3}$.

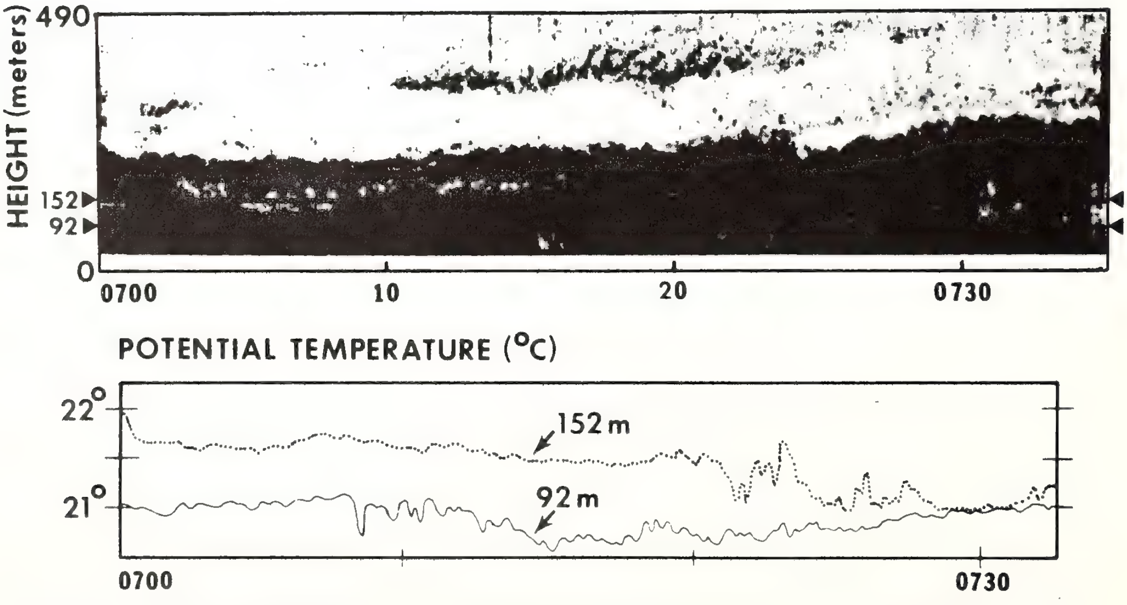

Figure 7. Facsimile record detail with potential temperature time series for the period 0700-0730

Positive identification of the sounder delineated structure in Figure 8 with corresponding measurements obtained on the tower can be approached using either time series analysis of the $C_T{}^2$ data or a more tenuous method of inference using tower temperature and velocity data, pressure array data, and assumptions about the density and velocity structure of shear instability events. This latter technique proved to be useful when a lag correlation analysis was not consistent with the assumption of advection with the mean wind. These inconsistencies were identified with the effect of a large azimuthal shear in the background flow.

These types of analyses are described by Neff (1975) and found to give fair to good results in establishing that the shear instability related fine structure ought to correlate over the tower - sounder separation in at least an ensemble average sense.

In those cases where a good correlation exists over the array, one can then postulate several explanations for the larger than expected scatter.

(1) This small scale thermal structure is non-turbulent and therefore the present scattering theory does not apply in these cases (Ottersten, 1970; Metcalf and Atlas, 1973).

(2) The internal turbulence structure can be characterized by isotropy and homogeneity, but the anisotropy sometimes associated with the patch boundaries results in an anomalously large scattering.

(3) The small scale structure has inertial subrange characteristics but the localization of the patches may introduce aliasing errors.

If cases (1) or (2) hold, then one might expect this to be revealed in the frequency dependence or aspect sensitivity of the scatter.

5.2 Aspect and frequency dependence associated with the "anomalous" scatter

To test the aspect sensitivity and the frequency dependence (from the 30° tilted sounder) we examined the region occurring just after 0712 and above 92 m in Figure 8. Figure 9 shows the vertical profiles of $C_T{}^2$ obtained from each frequency channel and averaged in 2.7 m range gates over this period. As can be seen there is no discernable frequency dependence from the tilted sounder returns. Since this comparison represented a fairly short period of data, the sounder discrete sampling rate may have introduced some aliasing. A more extensive comparison of the aspect sensitivity showed a general factor of two overestimate of $C_T{}^2$ from the vertical sounder relative to that from the tilted one throughout the stable period (0510-0710), (Neff, 1975). Although this could represent the effect of anisotropy at small scales, such an overestimate may also arise from simple geometrical effects.

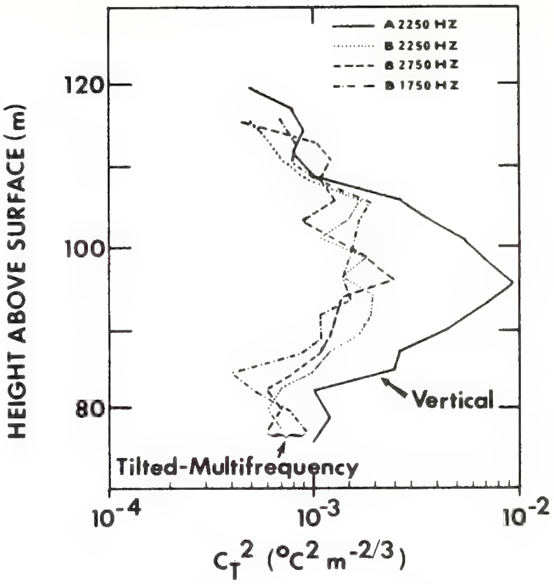

Figure 9. Vertical profiles of $C_T{}^2$ from each sounder channel during the period of maximum anomaly in the sounder-tower comparisons.

6. AN ALIASING ERROR ANALYSIS

A dominant feature of the stably stratified boundary layer is the development of quasi-horizontal, patchy lamina. At small time and space scales statistical isotropy and homogeneity might be expected to prevail. Thus, the thermal fine structure may not reveal the effect of larger anisotropic scales other than through an inhomogeneous spatial distribution. The character of this larger scale anisotropy would appear to be a function of the background static stability and the local shear (e.g. wave induced). This suggests that one ought to determine whether aliasing type errors can account for the magnitude of the observed discrepancies.

To evaluate the magnitude of such errors, we examined the patch geometry shown in Figure 10. The shaded area represents the apparent echo for a pulse length $C\tau \gg L'$ where L' is the patch (or layer) thickness. The horizontal scale over which such echoes will persist can be written $L_H = C\tau \cot \phi_o = C\tau\,(L_u+L''')/(L'+L'')$. The number of sounder sampling intervals within L_H will be $N = L_H/(u \cdot T_s)$. If the tilted layer is of infinite extent one can pose the relative sounder-tower error over the time L_H/u as

$$E_R = \frac{\frac{1}{N}\sum_{i=1}^{N}\left[\frac{L'}{C\tau/2} \cdot \frac{L_u}{L_u+L'''}\right]}{\frac{1}{N}\left[\frac{L'}{L'+L''} \cdot \frac{L_u}{u \cdot T_s} + 0\right]} = 2.$$

in the limit $C\tau \gg L'$ and with the constraint $\cot \phi_o = (L_u+L''')/(L'+L'')$.

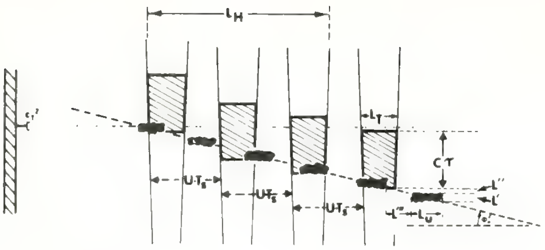

Figure 10. Schematic diagram used to compute the relative sounder-tower error for the case of turbulent patches distributed along a tilted interface. Beam dimensions, patch dimensions and spacings are indicated.

A second limiting case is that of a horizontal layer (ϕ_o=o) just below, within a distance $C\tau$ of the $C_T{}^2$ sensor. In this case $E_R \to \infty$. For a more complicated geometry such as oscillating turbulent layer at or below our 92 m comparison level one may then expect $2 < E_R < \infty$ for periods comparable with that of the oscillation.

A similar geometrical argument shows that relative beam filling effects may also account for the observed descrepancy in the aspect sensitivity (Neff, 1975).

6. CONCLUSIONS

Within an experimental error of ± 3 dB, the median echo sounder $C_T{}^2$ agreed over a considerable range of conditions with the median in situ $C_T{}^2$. The cumulative probability distributions also agreed well, showing the theoretically expected log-normal character in most cases. From the multi-frequency echo measurements no frequency dependence in the computed $C_T{}^2$ values could be discerned.

Under conditions of static stability, the vertical sounder overestimated $C_T{}^2$ relative to the tilted sounder and tower values by factors ranging from two to four. It was suggested that the quasi-horizontal spatial ordering of the small scale turbulence structure under statically stable conditions may introduce an aliasing of the in situ $C_T{}^2$ measurements relative to the finite volume echo sounding measurement. The same spatial structure may introduce errors of the magnitude observed between the vertical sounder and tilted sounder, due to relative beam filling effects.

Our analytic result suggests that such errors between tower and echo sounder values of $C_T{}^2$ can be reduced by shortening the sounder pulse length. It should also be noted that the anomalies in the stable case do not appear traceable to variations from the "2/3" power law. This is in view of our earlier result that such variations would produce only small overestimates ($r \approx \lambda$, $\nu < 2/3$)and more likely produce underestimates ($\nu > 2/3$).

Our results show the ability of echo-sounding techniques to yield a quantitative measure of the spectral density of temperature at small scales, and a consistency of the statistical isotropy and homogeneity assumptions with observed scattering cross-sections. Because of the similarity between problems of electromagnetic and acoustic scattering, our results should apply equally well to both techniques.

7, ACKNOWLEDGMENTS

Many members of WPL contributed to the success of the 1972 Haswell experiment and the data from which this paper is drawn. Discussions with, and the support and encouragement of Drs. F. F. Hall and D. W. Beran, and conversations with many other members of WPL are gratefully acknowledged.

Batchelor, G. K., 1957: Wave scattering due to turbulence. Symp. on Naval Hydrodynamics (F. S. Sherman, editor) (Wash., D. C., NAS-NRC Publ. 515) 409-430.

Beran, D. W., W. H. Hooke, and S. F. Clifford 1973: Acoustic echo-sounding techniques and their application to gravity-wave, turbulence, and stability studies. Boundary Layer Meteorol., 4, 133-153.

Brown, R. A., 1974: Analytical methods in planetary boundary layer modelling. John Wiley & Sons, New York, 146 p.

Gibson, C. G., G. R. Stegen, and R. B. Williams, 1970: Statistics of the fine structure of turbulent velocity and scalar fields at high reynolds number. J. Fluid Mech., 41, 153-167.

Gossard, E. E., D. R. Jensen, and J. H. Richter, 1971: An analytical study of tropospheric structure as seen by high-resolution radar. J. Atmos. Sci., 28, 794-807.

Gurvich, A. S., and A. M. Yaglom, 1967: Breakdown of eddies and probability distributions for small-scale turbulence. Phys. Fluids Suppl. 10 (part II), S59.

Hardy, K. R., and I. Katz, 1969: Probing the clear atmosphere with high power, high resolution radars. Proc. IEEE, 57, 468-480.

Kolmogorov, A. N., 1962: A refinement of previous hypothesis concerning the local structure of turbulence in a viscous incompressible fluid at high reynolds number. J. Fluid Mech. 13, 82.

Lawrence, R. S., G. R. Ochs, and S. F. Clifford, 1970: Measurements of atmospheric turbulence relevant to optical propagation. J. Opt. Soc. Amer. 60 (6), 826-830.

McAllister, L. G., J. R. Pollard, A. R. Mahoney, and P. J. Shaw, 1969: Acoustic sounding - A new approach to the study of atmospheric structure, Proc. IEEE 57, 579-587.

Metcalf, J. I., D. Atlas, 1973: Microscale ordered motions and atmospheric structure associated with thin echo layers in stably stratified zones. Boundary Layer Meteorol. 4, 7-35.

Neff, W. D., 1975: Quantitative evaluation of acoustic echoes and the morphology of small scale turbulence in the planetary boundary layer. NOAA ERL-WPL Tech. Rept. (to be published).

Ovoukov, A. M., 1962: Some specific features of atmospheric turbulence. J. Fluid Mech. 13, 77.

Monin, A. S., 1962: Characteristics of the scattering of sound in a turbulent atmosphere. Akust. Zh. 7, 457-461 (Sov. Phys. Acoust. 7, 370-373).

Ottersten, H., 1970: Radar angels and their relationship to meteorological factors', Swedish Res. Inst. Nat. Def., FOA Repts. 4, No. 2, Stockholm, 33 pp.

Ottersten, H., K. R. Hardy, and C. G. Little, 1973: Radar and sodar probing of waves and turbulence in statically stable clear-air layers. Boundary Layer Meteorol. 4, 47-89.

Simmons, W. R., J. W. Wescott, and F. F. Hall, 1971: Acoustic echo sounding as related to air pollution in urban environments. NOAA Tech. Rept. ERL216-WPL 17, Boulder, Colorado, 77 pp.

Tatarskii, V. I., 1961: Wave Propagation in a Turbulent Medium. McGraw-Hill Book Co. Inc., New York, 285 pp.

Tatarskii, V. I., 1971: The Effects of the Turbulent Atmosphere on Wave Propagation. (Nauka, Moscow, 1967) (in Russian) transl. from U. S. Dept. Comm. Nat. Tech. Inform. Serv., Springfield, Va.

Wyngaard, J. C., and O. R. Cote, 1971: The budgets of turbulent kinetic energy and temperature variance in the atmospheric surface layer. J. Atmos. Sci. 28, 190-201.

NOAA Technical Report ERL 322-WPL 38

June 1975

QUANTITATIVE EVALUATION OF ACOUSTIC ECHOES FROM THE PLANETARY BOUNDARY LAYER

William D. Neff

ABSTRACT

Using two acoustic echosounders (echosondes), one of which operated at simultaneous wavelengths of 0.12, 0.15, and 0.19 m, the acoustic backscatter cross-section was obtained as a function of time and height in the planetary boundary layer. The cross-sections were interpreted in terms of the temperature structure parameter C_T^2 and compared with values obtained in situ at the 92-m level on a tower located some 300 m distant. In general, excellent agreement was found between the two sets of C_T^2 values under statically unstable conditions. Under statically stable conditions, the measurements on occasion, disagreed by factors ranging from 2 to 5 with the echo-derived C_T^2 values consistently overestimating those from the tower. Our analysis suggested that the errors were due to the different spatial-sampling characteristics of the two techniques rather than a lack of isotropy and homogeneity at small scales.

Earth Environment and Resources Conference, 66-67, September 1974.

Acoustic Sounders for Predicting Air Pollution Over Cities

John W. Wescott

Wave Propagation Laboratory, NOAA Environmental Research Laboratories, Boulder, CO.

Acoustic echo sounders for remote probing of the lower atmosphere utilize natural turbulent variations in the acoustic refractive index of air that produce scattering (including substantial backscattering) of strong tone bursts radiated from narrow-beamwidth antennas. Such sounders are analogous in their operation to pulsed weather radars or sonars. The refractive index variations that cause the scattering are produced by turbulent fluctuations of temperature and wind. Thus some important characteristics of wind and temperature profiles relating to the entrapment and concentration of noxious gases and airborne pollutants over cities may be monitored continuously, in real time with acoustic sounders.

A simplified block diagram of an acoustic sounder is shown in fig. (1). Periodic tone bursts from the transmit gate of a triggered programmer are power amplified to 100 W and applied through transmit/receive (T-R) switching circuitry to an acoustic transducer and antenna which radiates each tone burst in a very narrow beam upwards into the atmosphere. The same transducer detects echoes received by the antenna at sound pressure levels from about 0 to 40 dB below the threshold of hearing. These signals pass through the T-R circuit to a preamplifier and on to a receiver gate which is programmed to conduct only during the intervals between transmit tone bursts. The echo signals are then gain swept to compensate for the normal weakening of signal strength with range. The range-compensated signal is then applied to a tuneable receiver with bandwidth adjusted for optimum S/N. The filtered signal then proceeds to a facsimile recorder which produces a real-time, three-dimensional display of echo intensity, echo range, and time of day. Note that the facsimile recorder triggers the programmer once per line scan to maintain synchronization. Also note that the tuneable receiver provides a BFO signal to the transmit gate of the programmer at the exact frequency to which the receiver is tuned.

Fig. (2) is a facsimile recording produced by the system just described. The recording chronicles a temperature inversion as it developed, intensified, and eventually caused a pollution alert in Denver, Colorado. At about 20:00 hours (local Denver time) an inversion began to develop close to the ground due to the normal radiational cooling of the earth's surface at night. Just before 03:00 a second inversion layer developed about 800 m above the surface and proceeded to descend. The descent of this layer intensified the surface inversion, within and under which the gaseous and airborne pollution of Denver was entrapped. The dark portion of the record from 08:00 to 11:00 shows the intensified surface inversion reaching to heights of 300 m. This produced an air pollution alert in Denver which was not cancelled until 14:00.

The predictive potential of a real-time echo sounder record such as fig. (2) could be utilized readily by air pollution forecasters. The descending inversion layer that intensified the surface inversion was evident for many hours before the pollution alert was called. Furthermore, the breaking up of the surface inversion by the convective effects of thermal plumes can be seen starting at 11:00, some three hours before the alert was cancelled.

Echo sounders for use by air pollution forecasters must be located in urban areas that are noisy and/or densely populated. In such cases it is essential that the sidelobe rejection of the sounder antenna be at least 50 to 60 dB at angles of 70 to 90 deg from the main beam, so that the sounder can transmit within a few hundred feet of residences without contributing noticeably to noise pollution, and can receive clean echoes from altitudes up to one mile in spite of noise from adjacent highways, airports and industry. Sidelobe rejections of 50 to 60 dB are difficult to achieve. One of the best antennas available for acoustic sounding is a microwave antenna of the conical-horn-coupled, parabolic-reflector type shown in fig. (3). A high-quality public address driver coupled to the throat of the conical horn radiates spherical waves to the parabolic reflector. The reflector transforms the spherical waves into plane waves which radiate from the antenna aperture. The conical horn prevents the driver from radiating omnidirectionally into the atmosphere, and similarly prevents off-axis background noise from reaching the driver. Thus, the conical horn plays a vital role in suppressing the sidelobes of this antenna.

Fig. (4) shows polar diagrams measured outdoors with the horn-reflector antenna at acoustic frequencies of 1 through 5 kHz. This antenna typically is operated at about 2 kHz. The aperture diameter is 4 ft or about 8 λ at 2 kHz. Fig. (4) shows sidelobe rejections of only 35 dB at angles of 70 to 90 deg from the main beam. While this is satisfactory for sounding in quiet, rural areas, it is unsatisfactory for urban area sounding. Additional sidelobe suppression was achieved by constructing an acoustically absorbent, anechoic cuff extending from the original antenna aperture to a height of about 2 aperture diameters. The cuff is built with a slight flare, as shown in figs. (5) and (6) to create a second aperture slightly larger than the first, and across which plane wave illumination is tapered radially in intensity. Sidelobe rejection at frequencies from 1 to 5 kHz was increased by 18 to 21 dB by addition of the anechoic cuff. This more than any other factor has made acoustic sounding in noisy urban areas an accomplished fact.

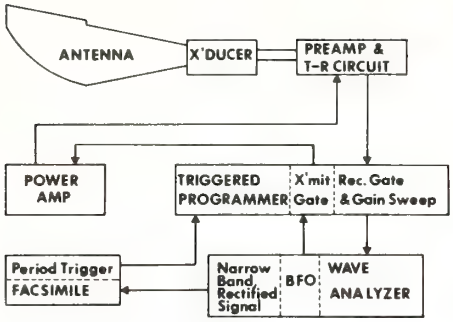

FIGURE 1. ACOUSTIC SOUNDER SYSTEM DIAGRAM

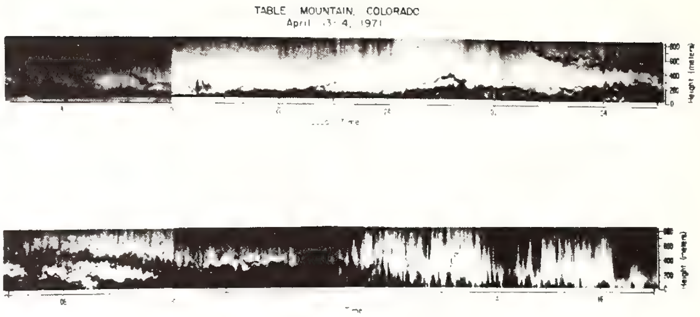

FIGURE 2. ECHO SOUNDING OF POLLUTION ALERT

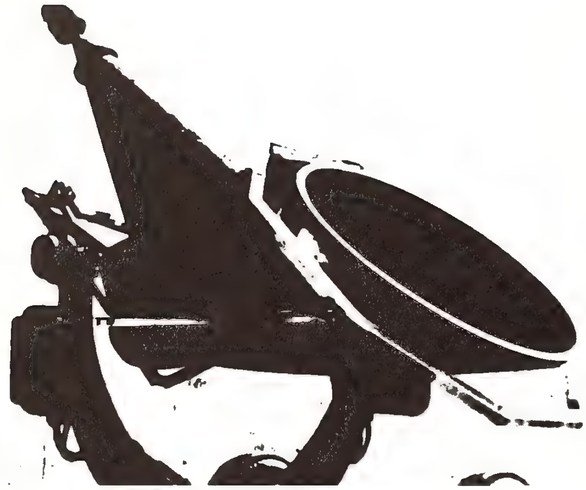

FIGURE 3. HORN REFLECTOR ANTENNA

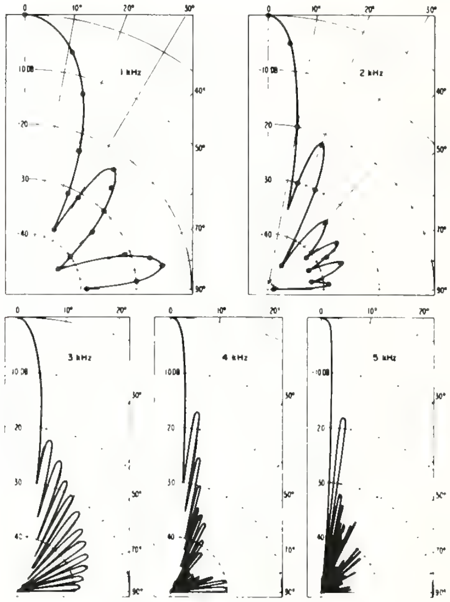

FIGURE 4. ANTENNA POLAR DIAGRAMS

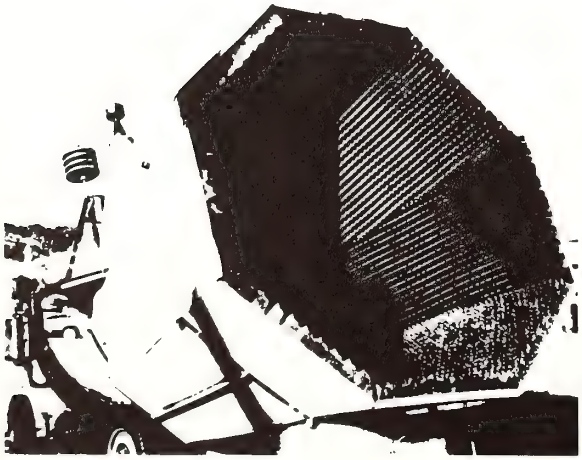

FIGURE 5. ANECHOIC CUFF TREATMENT

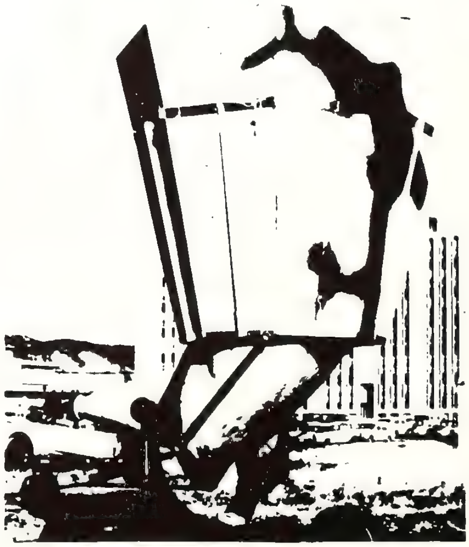

FIGURE 6. MOBILE ANTENNA AND CUFF

IEEE Transactions on Antennas & Propagation, AP-22, 135-136, January 1974.

Wind Dependence of Quasi-Specular Microwave Sea Scatter

DONALD E. BARRICK

Abstract—**It is shown that a specular-point scattering model adequately predicts the relation between the average quasi-specular microwave scattering cross section of the sea and the mean wind speed. The mean-square sea slope required in this model varies with both the upper and lower ends of the waveheight spectrum, which in themselves are functions of wind speed. Optical measurements of slopes confirm this physical relationship. Finally, the resultant scattering cross section predicted by the slope-dependent specular-point model is compared with a set of recent measurements, lending credence to the model and interpretation suggested here.**

I. INTRODUCTION

Models relating the near-vertical sea-backscattered microwave signal power to pertinent sea-state descriptors are receiving renewed interest with the advent of orbiting short-pulse radar altimeters.[1] Many independent measurements of the average backscattering cross section per unit sea area σ^0 over the past 15 yr have confirmed the angular dependence of σ^0 near the vertical (e.g., see Skolnik [1] or Barrick [2] for reviews of such data). The near-vertical angular dependence is explained by the specular-point models [3], assuming a (nearly) Gaussian distribution of surface slopes. There is considerable variance, however, between the magnitudes of σ^0 measured by the various investigators. In addition, it is not clear from the results to date to which of the various sea-surface descriptors σ^0 is most sensitive. It is the purpose of this note to call attention to an extensive well-calibrated set of measurements of σ^0 [4] and to suggest a physically meaningful relationship between σ^0 and surface wind speed via the surface slope used in the specular-point model.

A comprehensive set of measurements of σ^0 by Raytheon in the Atlantic was reported in [4]; these aircraft measurements were made at 9.0 GHz with ground-truth data taken simultaneously aboard a NASA ship beneath the aircraft. During December 1969 and January 1970 sixteen test flights were made, the data from ten of which were considered of adequate quality to be statistically reduced and presented. The data of interest here consist of averages of σ^0 in the vertical direction. Each flight typically resulted in incoherent averages over as many as 60 frames of data; each frame, recorded once per second, represented about 50 individually received, square-law-detected pulses averaged over the frame (typical travel distance per frame is ~300 ft). Most of the flights were flown at 10 000 ft with a 20-ns pulse. Radar sensitivity was calibrated and later checked dynamically by flying over ground support equipment that recorded and transponded the signal back at known power levels. The overall rms system error was estimated to be 0.9 dB.

Raytheon attempted to correlate σ^0 with the various wind and sea descriptors available from the NASA support ship. They found little or no correlation between σ^0 (at vertical incidence) and wave height, wave period, or wave direction. However, there did appear to be a definite trend between σ^0 and (surface) wind speed; this is shown in Fig. 1, where the number beside the dot refers to the flight number. A mathematical model that predicts the observed relationship between wind speed and σ^0 will be developed.

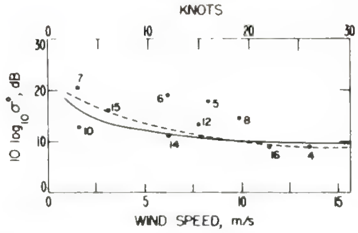

Fig. 1. Dependence of vertically incident sea backscatter on wind speed. Dots are measured values on different flights made by Raytheon [4]. Solid curve is (5) used in (2); dashed is empirical slope fit given in Conclusions.

II. SPECULAR-POINT MODEL

The specular-point model has been derived by a number of high-frequency approaches: ray optics [5]; physical optics in which averaging is done before the integration over space [6]; and physical optics in which averaging is done after integration over space [7], [3]. The latter two processes involve stationary phase integrations, where the radar wavenumber k_0 times the typical roughness height is assumed large. The last approach is equivalent to geometrical optics because the stationary phase integration over space shows that the total scattering is merely the summation of the individual returns from each specular point. Thus all of these models lead to the following result for backscatter[2]

$$\sigma^0 = \pi \sec^4 \theta p_s(-\tan \theta, 0) \mid R(0) \mid^2 \tag{1}$$

where θ is the angle of incidence from the vertical, $R(0)$ is the Fresnel reflection coefficient of the surface at normal incidence, and $p_s(\zeta_x, \zeta_y)$ is the joint probability density function of the surface slopes $\zeta_x (= \partial\zeta/\partial x)$ and $\zeta_y (= \partial\zeta/\partial y)$, with ζ being the surface height above the mean (xy) plane. It is assumed that the xz plane is the incident plane.

The interpretation of (1) is enlightening: The strength of the scattered signal is merely proportional to the probability of the surface having "specular" points, or regions tilted at slope $-\tan \theta$ so as to be normal to the incident ray. For the sea, the model is not valid for θ greater than about 15°; beyond this angle, microwave scatter is more diffuse and is describable by the Bragg diffraction model postulated in [8].

The sea surface slopes are nearly Gaussian and isotropic in their distribution, as shown in [9], and hence (1) for the sea can be written approximately as

$$\sigma^0 = (1/s^2) \mid R(0) \mid^2 \exp \{ - \tan^2 \theta / s^2 \} \tag{2}$$

where s^2 is the *total* mean-square surface slope $(s^2 = \langle \zeta_x^2 + \zeta_y^2 \rangle = 2\langle \zeta_x^2 \rangle = 2\langle \zeta_y^2 \rangle)$.

III. SEA-SURFACE SLOPE

The process by which the winds excite waves on the sea is complex and not entirely understood. A strong wind excites the longer waves whose phase velocities can just keep up with the wind velocity. However, a gusty or turbulent wind with small-scale wavenumber structure will excite short gravity and capillary waves by an air-surface resonance interaction [10]. When this turbulent wind abates, the small-scale waves will die out rather quickly due to viscous dissipation. A strong wind blowing over a very rough, choppy sea will normally become turbulent near the surface, driving the shorter waves as long as it persists.

Only the longest gravity waves contribute to the rms (or significant) waveheight, and these waves require hours to build up/die down after the application/removal of the wind. However, both the longer *and* the shorter-scale waves affect the surface slope and, in fact, in about equal magnitude. To see this, the ocean waveheight spatial spectrum in the equilibrium region can be written [11]

$$S(\kappa_x, \kappa_y) = \begin{cases} \dfrac{B}{2\pi\kappa^4}, & \text{for } \kappa_\gamma < \kappa < \kappa_v \\ 0, & \text{for other } \kappa \end{cases} \tag{3}$$

where $\kappa = (\kappa_x^2 + \kappa_y^2)^{1/2}$, with κ_x and κ_y being the spatial wavenumbers in the x and y directions. B is a dimensionless constant,

---

Manuscript received June 18, 1973; revised July 26, 1973.

The author is with the Wave Propagation Laboratory, National Oceanic and Atmospheric Administration, Environmental Research Laboratories, Boulder, Colo. 80302.

[1] The first unmanned short-pulse altimeter experiment is to be flown on NASA's GEOS-C satellite, scheduled for launch in mid-1974.

[2] The more general expression for bistatic scatter at arbitrary angles is found in [3].

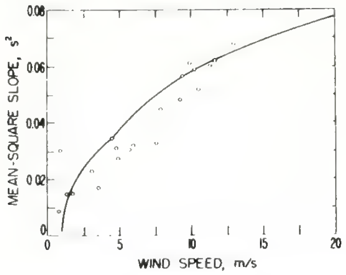

Fig. 2. Dependence of sea-surface slope on wind speed. Dots are values measured optically by glitter-point photography [11]. Solid curve is (5).

observed empirically to be $B_g \approx 0.005$ in the gravity-wave region ($\kappa < 380$ m^{-1}) and $B_c \approx 0.015$ in the capillary-wave region ($\kappa > 380$ m^{-1}). The spectrum is assumed to be semi-isotropic in direction.

The mean-square waveheight is determined by integrating (3) over all (κ_x,κ_y)-space; only the lower limit is important for κ_γ much less than κ_r and 380 m^{-1}, and this is simply $\kappa_\gamma = g/U^2$, where g is the acceleration of gravity and U is the mean surface wind speed. Thus

$$h^2 \simeq \frac{B_g}{2\kappa_\gamma^2} = \frac{B_g U^4}{2g^2} \tag{4}$$

where it is assumed that the wind has been blowing long enough to fully develop these waves. The mean-square slope, found by multiplying (3) by κ^2 and integrating, is however

$$s^2 = \begin{cases} B_g \ln\,(\kappa_r/\kappa_\gamma) & \text{for } \kappa_r < 380 \text{ m}^{-1} \\ B_g \ln\,(380/\kappa_\gamma) + B_c \ln\,(\kappa_r/380), & \text{for } \kappa_r > 380 \text{ m}^{-1}. \end{cases} \tag{5}$$

Hence the slope depends upon the upper limit κ_r and, additionally, upon whether κ_r lies in the gravity or capillary wave region. Miles [12] has studied the highest wavenumber κ_r which is neutrally stable under the influence of the mean wind and viscous dissipation. An acceptable approximation to it is $\kappa_r \sim 50\,U^{1.4}$ m^{-1}, where U is in m/s. A comparison of (5) with mean-square slope measurements obtained optically by Cox and Munk in 1954 is shown in Fig. 2 [11]. The spread in points beyond 5 m/s (where κ_r lies in the capillary region) reflects the fact that the lifetimes of these shorter waves are quite small, and hence the local variation of wind about the mean will determine how much of this upper spectral region is present at a given time in a given area. Cox and Munk also determined that the crosswind-to-upwind/downwind mean-square slope ratio s_y^2/s_x^2 was about 0.75, justifying for most purposes the isotropic assumption about the roughness statistics.

IV. Conclusions

The slope of the sea has been shown to be much more sensitive and instantaneously responsive to the wind speed than is the waveheight. With the preceding interpretation and model for s^2, we show in Fig. 1 the predicted radar cross section σ^0 at vertical incidence ($\theta = 0$) using (5) in the specular-point model (2). The Fresnel reflection coefficient of the sea at X band is also included; it is -2 dB. The agreement is good, and the spread in points about the mean is about the same as in Fig. 2. Thus the slope expression of (5),[3] when used in the specular point model of (2), offers: 1) a plausible and physically reasonable interpretation of the observed wind dependence of quasi-specular microwave sea scatter; and 2) a mathematical model useful in the analysis of altimeter/scatterometer systems as applied to oceanic sensing.

At X band and above, most of the tiny short-wave slopes present are seen by the radar; this is evident from comparing the quasi-specular return σ^0 at these frequencies with laser sea-scatter observations of σ^0 over the same angular region. At frequencies below X band, however, the smallest wavelets present may not be seen by the radar because their radii of curvature are too small. This radar limitation on the effective surface slope can be approximately included in (5) by replacing κ_r by $2k_0$ (twice the free-space radar wavenumber) as the upper limit whenever $2k_0 < \kappa_r$.

The spread in measured data points for σ^0 about a mean is about 3–5 dB, as evident from Fig. 1. Other similar measurements indicate that such spreads can usually be expected, unless averages are taken over a wide range of temporal, geographical, directional, and sea development conditions for a given wind speed. Besides the short lifetimes and small radii of curvature of the capillaries mentioned previously, other reasons for this spread include: 1) the dependence of capillary development upon the microstructure of the wind pressure spectrum; 2) the state of development of the sea, that is, whether the waves have had time to develop to their full, saturated height and slope conditions corresponding to a given mean driving wind; 3) the presence of swell along with the wind waves; and 4) the amount of foam and breaking waves present on the surface. Thus these factors will cause local measurements of σ^0 to vary about the mean predicted by the specular-point model proposed here.

References

[1] M. I. Skolnik, "Sea echo," in *Radar Handbook*, M. I. Skolnik, Ed. New York: McGraw-Hill, 1970, ch. 26.
[2] D. E. Barrick, "Rough surfaces," in *Radar Cross Section Handbook*, G. T. Ruck, Ed. New York: Plenum, 1970, ch. 9.
[3] ——, "Rough surface scattering based on the specular point theory," *IEEE Trans. Antennas Propagat.*, vol. AP-16, pp. 449–454, July 1968.
[4] *Space Geodesy Aircraft Experiment Final Report*, (NASA Contract NASW 1932, prepared by E. Genest). Sudbury, Mass.: Raytheon Co., May 1970.
[5] D. O. Muhleman, "Radar scattering from Venus and the Moon," *Astron. J.*, vol. 69, pp. 34–41, 1964.
[6] D. E. Barrick, "Relationship between slope probability density function and the physical optics integral in rough surface scattering," *Proc. IEEE*, vol. 56, pp. 1728–1729, Oct. 1968.
[7] R. D. Kodis, "A note on the theory of scattering from an irregular surface," *IEEE Trans. Antennas Propagat.*, vol. AP-14, pp. 77–82, Jan. 1966.
[8] N. W. Guinard and J. C. Daley, "An experimental study of a sea clutter model," *Proc. IEEE*, vol. 58, pp. 543–550, Apr. 1970.
[9] B. Kinsman, *Wind Waves*. Englewood Cliffs, N.J.: Prentice-Hall, 1965.
[10] O. M. Phillips, "On the generation of waves by turbulent wind," *J. Fluid Mech.*, vol. 2, pp. 417–445, 1957.
[11] O. M, Philips, *The Dynamics of the Upper Ocean*. London, England: Cambridge Univ. Press, 1966, pp. 109–139.
[12] J. W. Miles, "On the generation of surface waves by shear flows. Part 4," *J. Fluid Mech.*, vol. 13, pp. 433–448, 1962.

---

[3] A simpler empirical relationship can be fitted to the observed slopes of Fig. 2: this is $s^2 \simeq 5.5 \times 10^{-3}\,U$ for the region 1 m/s < 15 m/s.

Reprinted by permission from IEEE TRANSACTIONS ON ANTENNAS AND PROPAGATION
Vol. AP-22, No. 1, January 1974, pp. 135-136
Copyright 1974, by the Institute of Electrical and Electronics Engineers, Inc.
PRINTED IN THE U.S.A.

Proceedings of the IEEE 62, 673-680, June 1974.

Sea Backscatter at HF: Interpretation and Utilization of the Echo

DONALD E. BARRICK, MEMBER, IEEE, JAMES M. HEADRICK, SENIOR MEMBER, IEEE,
ROBERT W. BOGLE, AND DOUGLASS D. CROMBIE

***Abstract*—Theories and concepts for utilization of HF sea echo are compared and tested against surface-wave measurements made from San Clemente Island in the Pacific in a joint NRL/ITS/NOAA experiment. The use of first-order sea echo as a reference target for calibration of HF over-the-horizon radars is established. Features of the higher order Doppler spectrum can be employed to deduce the principal parameters of the wave-height directional spectrum (i.e., sea state); and it is shown that significant wave height can be read from the spectral records. Finally, it is shown that surface currents and current (depth) gradients can be inferred from the same Doppler sea-echo records.**

I. INTRODUCTION

TWENTY YEARS ago Crombie [1] observed sea echo with an HF radar, and he correctly deduced the scattering mechanism which accounted for the peculiar and unique dominant peaks in the observed Doppler spectrum. This gave rise to further research and suggested the exciting possibility of measuring sea state at great distances with HF sky-wave radars. A current joint program involving NOAA, NRL, and ITS on San Clemente Island has provided data for testing three possible applications of HF sea echo: 1) as a standard or reference target for calibrating the sensitivity of sky-wave radars; 2) as a means of deducing sea state (viz., the dominant features of the wave-height directional spectrum); and 3) as a method for measuring surface-current features. HF, as considered here, extends from the broadcast band to VHF, including radar wavelengths between 10 and 200 m.

Although the heights of ocean waves are generally small in terms of these radar wavelengths, the scattered echo is nonetheless surprisingly large and readily interpretable in terms of its Doppler features. The fact that these heights are small facilitates the analysis of scatter using the perturbation approximation. This theory [2] produces an equation which 1) agrees with the scattering mechanism deduced by Crombie from experimental data; 2) properly predicts the positions of the dominant Doppler peaks; 3) shows how the dominant echo magnitude is related to the sea wave height; and 4) permits an explanation of some of the less dominant, more complex features of the sea echo through retention and use of the higher order terms in the perturbation analysis. Hence the dominant spectral features explained by the simple, lowest order terms of the perturbation analysis are referred to as "first-order" sea echo, while the remaining, less dominant features are termed "higher order" because they arise from the smaller (i.e., second-order, third-order, etc.) terms.

By way of introduction to the basic type of HF echo records upon which the discussion in this paper is based, we show a typical received Doppler spectrum in Fig. 1. This plot represents the received signal power versus normalized Doppler shift from the carrier (the carrier being located at zero, and the predicted positions of the dominant peaks at positions ±1). Details of the conditions and system behind this spectral record will be discussed later, but for now we refer to it to illustrate how the three previously claimed applications will be subsequently developed from data such as these. 1) The dominant, first-order peak (near +1) will be tested for use as a standard or reference echo. 2) The higher order Doppler features (i.e., their shapes, peak positions, and amplitudes) will be used to deduce sea state. 3) The overall shift of the first-order echo peaks from ±1 will be used to deduce

---

Manuscript received September 12, 1973; revised January 21, 1974.

D. E. Barrick is with the Wave Propagation Laboratory, National Oceanic and Atmospheric Administration, Boulder, Colo. 80302.

J. M. Headrick and R. W. Bogle are with the Naval Research Laboratory, Washington, D. C. 20375.

D. D. Crombie is with the Institute for Telecommunication Sciences, Boulder, Colo. 80302.

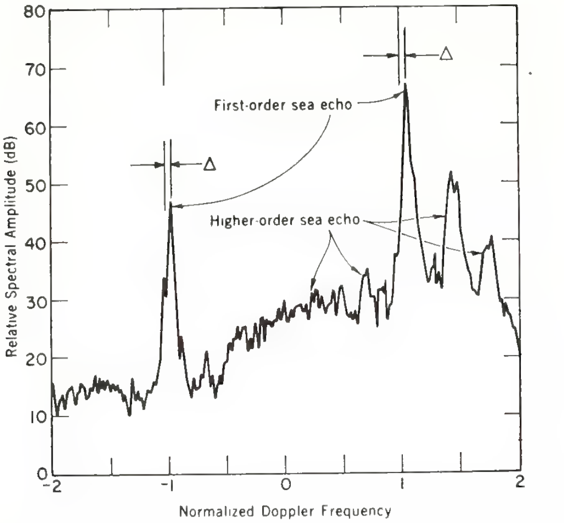

Fig. 1. Example of an averaged radar sea-echo Doppler spectrum at 9.4 MHz. Carrier would appear at center, with ±1 corresponding to Doppler shifts ±0.313 Hz from the carrier. Resolution is ~0.01 Hz.

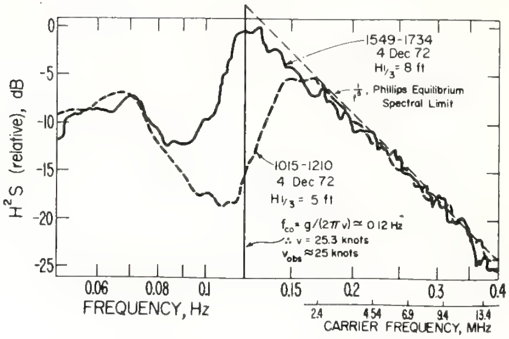

Fig. 2. Buoy-measured nondirectional wave-height spectra for morning (dashed) and afternoon (solid) of December 4, 1972. Triangle is model used in theory to approximate afternoon spectrum.

(radial) currents. Since the radar echo is produced by scatter from ocean waves, the approach taken in this paper is to relate the echo features to surface features. Ocean waves and currents are largely produced by winds, and thus one should be able to ultimately deduce wind features from these echoes; this is the approach taken in parallel analyses of HF sea echo by Ahearn *et al.* [3] and Long and Trizna [4].

II. BACKGROUND AND INTERPRETATION

Let us explain the simple interpretation of the first-order Doppler spikes of Fig. 1 as first deduced by Crombie [1]. Though the sea to a casual observer generally looks like a random, moving, scattering surface, the dominant, crisp, and equally displaced Doppler peaks lead one to believe that the radar is actually observing two targets moving radially at discrete readily identifiable velocities. The fact that these Doppler displacements are observed to vary with the *square root* of the carrier frequency suggests something unique about HF sea echo in contrast to echoes from other moving targets. Since it is well known that gravity waves in deep water travel at a phase velocity proportional to the square root of their lengths L (i.e., $v=\sqrt{gL/2\pi}$, where g is the gravitational constant), then the length of the waves producing scatter can be uniquely deduced from the radar-derived "target" velocity. This length (for backscatter near grazing incidence) is precisely one-half the radar wavelength, and explains the observed square-root relationship between the Doppler and carrier frequencies. Thus the ocean wave trains are behaving like a series of diffraction gratings, only one of which has the orientation and spacing to scatter back toward the radar (to first order). This is the double set of sea wave trains with $L=\lambda/2$ (or $\kappa=2k_0$, where λ is the radar wavelength, with $\kappa=2\pi/L$ and $k_0=2\pi/\lambda$ being the scattering ocean wavenumber and radar wavenumber, respectively) moving radially toward and away from the radar. Hence the double Doppler echo pair.

Theory [2], [5] also shows that the backscattered echo energy from this identifiable "resonant" water wave is proportional to the height of this wave component squared. Hence it is evident that measurement of the first-order radar cross section of the sea versus radar operating frequency will determine the water-wave spectrum along the radar azimuthal bearing. By looking along several bearings, one can thereby construct the "wave-height directional spectrum," a quantity which has heretofore defied simple measurement by oceanographers. However, the radar frequency region corresponding to the important long-wave portion of the gravity-wave spectrum responsible for "sea state" spans the region from about 300 kHz to 5 MHz. Constructing and calibrating an azimuthal scanning radar which sweeps over this region would be a formidable task, in addition to the difficulty that this frequency region is already heavily occupied by users (broadcast band, marine band, etc.). Furthermore, propagation at these lower frequencies is restricted to ground wave (limiting the radar range to <200 km), since ionospheric modes will be severely attenuated most of the time.

In contrast, sea scatter in the upper HF region (6–30 MHz), at which ionospheric propagation to great distances (~4000 km) is favored, is of a somewhat different character. The first-order resonant peaks are still evident and usually dominant, as shown in Fig. 1. However, other features in the Doppler spectrum are also present, and these features appear to vary more significantly with sea state than do the first-order echo peaks. These additional features are referred to as "higher order," of which "second-order" effects are felt to be the dominant contributors. On the other hand, the larger first-order echo is for the most part constant and insensitive to sea state. The reason for this is that the waves producing scatter, being half the radar wavelength, vary in length between 25 and 5 m. Waves of this length on the open oceans are nearly always present and are developed to their maximum allowable height, as limited by breaking. This region of the wave-height spectrum in which saturation occurs is called the equilibrium region; Phillips [6] has shown that the nondirectional temporal wave-height spectrum should follow an f^{-5} law (f equals wave frequency in hertz) in this region. Fig. 2 is a buoy measurement of this spectrum at two different times for 20- and 25-knot wind-driven seas in the scattering area off San Clemente Island. The f^{-5} saturation region is clearly evident in these records; a scale at the bottom shows that the radar frequencies at which first-order scatter would be observed clearly fall in this saturated equilibrium region for all operating frequencies above about 2–3 MHz. The fact that the first-order echoes at favorable ionospheric propagation frequencies originate from waves of known height characteristics suggests that these echoes can be used as a standard target for radar system sensitivity calibration. Theory [2] shows that the first-order scattering coefficient[1] σ^0 should be a constant, approximately -17 dB, independent of frequency (above some lower $-$HF limit) and sea state. In a large number of ground-wave operations on the Chesapeake Bay, σ^0 was indeed found to increase to an upper limiting value corresponding to -17 dB. Sky-wave radar operations by many groups have also confirmed the constancy and absolute value (-17 dB) of first-order σ^0.

As mentioned previously, the higher order sea-echo Doppler spectrum does appear to vary appreciably with sea state. The features of this echo take several forms: 1) secondary peaks appear around the first-order spikes, whose positions and amplitudes vary with sea state; 2) a continuum or floor around the first-order spikes appears which rises and spreads with increasing sea state; and 3) the distribution of these higher order peaks and continuum about the first-order lines varies with wave direction. A theory for the second-order contribution to these higher order echoes was advanced by Barrick [7], and the agreement thus far with experimental data is quite encouraging. A significant advantage of using second-order echo to deduce sea state at upper HF is that one is comparing this portion of the signal spectrum with the saturated first-order peaks, which serve as the reference. Hence unknown ionospheric path losses and Doppler translations do not hamper interpretation of the higher order echo in terms of sea state.

Ocean currents can also be extracted from the sea-echo Doppler spectrum. The first-order resonant Doppler peaks are often observed to be shifted equally from their predicted positions (see Fig. 1) by a small amount. This implies that the waves causing first-order scattering are superimposed on a sea surface which is physically moving due to surface currents. The radial component of this surface-current vector can thus be calculated in terms of the Doppler translation of the first-order lines to be $u = \Delta\sqrt{gc/(4\pi f_0)}$, where g is the acceleration of gravity, c is the velocity of light, f_0 is the carrier frequency, and Δ is the normalized Doppler translation, as measured in Fig. 1. Further interpretation of this concept will be undertaken later in this paper.

III. EXPERIMENTAL FACILITY

A series of HF surface-wave measurements of sea echo were undertaken in a joint experiment between NRL, ITS, and NOAA/WPL on San Clemente Island off California. Between November 1, 1972, and April 30, 1973, approximately 25 h of sea-echo Doppler spectra were gathered. The facility is located on the northwest side of the island and looks westward into the Pacific. It is capable of transmitting any number of frequencies (up to 100) simultaneously from 2 to 25 MHz in a pulse-to-pulse progression, and processing the returns on each frequency coherently. Pulsewidths available are 20, 50, and 100 μs with a 200-pulse-per-second (pps) repetition rate. The sea echo from several range gates can be processed simultaneously; to provide adequate signal-to-noise ratio, the echoes at 22.5, 30, and 37.5 km from the radar were found to be optimal, and hence most sea-echo data were recorded at these ranges. At these ranges, the water depth exceeds 1000 ft, so that bottom effects on the wave characteristics are negligible.

The transmitter provided an output power of 75-kW peak. The transmitting antenna was a twin-bay log-periodic monopole array producing vertical polarization; with a gain of 14 dB, it provided a one-way beamwidth of 60° centered on 255° T. The receiving antenna was an 850-ft-long broadside monopole array. Elements were switched in and out automatically versus frequency so that the beamwidth did not vary too drastically over the decade frequency range; as a result, the one-way beamwidth was about 15° at 3 MHz and 7° at 24 MHz. Data were processed and recorded digitally on magnetic tape, both in raw IF form and as 200-s coherent spectra.

In order to check the radar data, a Datawell Waverider buoy was moored in the scattering area. This device provided both the sea-significant wave-height and nondirectional wave-height spectra. The buoy output was confirmed and supplemented by wave hindcast tables prepared by OSI, Inc.; these data indicated wave direction and also listed the height, period, and direction of any swell present.

IV. FIRST-ORDER SEA ECHO FOR RADAR SENSITIVITY CALIBRATION

Both theory [2] and surface-wave/sky-wave measurements have shown that the first-order sea-echo energy in the upper HF region approaches a constant value for the open ocean, independent of sea state. As discussed previously, this saturation occurs because the shorter ocean waves being observed at these frequencies are developed to their maximum possible heights. Referring again to the buoy-measured wave-height spectra of Fig. 2, it is evident that for seas fully developed by 20-knot winds, frequencies above about 2 MHz are observing waves in the saturated or equilibrium range of the spectrum; for 10-knot winds, frequencies above 8 MHz will likewise fall in this region of the spectrum. For vertical polarization, the average radar cross section per unit area, σ^0, turns out to be about -17 dB, independent of frequency, and nearly independent of incidence angle in the region within about 30° of grazing.[2] This suggests using the first-order sea echo as a reference—or standard target—for calibration of sky-wave radars operating over the oceans (where winds nearly always exceed 10 knots). Such calibration is desirable and necessary because, unlike microwave radars where transmission loss is generally close to the predicted free-space value, ionospheric absorption is highly variable and unpredictable. Hence some sort of calibration (often involving the use of beacons or repeaters of known reradiation levels) is required in order to help select the optimal operating frequency and determine expected signal-to-noise ratio and/or probability of detection against a given class of radar targets.

One way of testing the concept of using first-order sea echo as a reference target over the HF band is to show that the measured value of some parameter in the radar range equation follows predictions when one uses a constant value

---

[1] The average radar backscattering cross section per unit surface area.

[2] Horizontally polarized sea echo is quite sensitive to incidence angle; near grazing, however, it is at least 20 dB lower than the vertical component. Hence it would never be used in surface-wave propagation, and would not be seen with sky-wave propagation due to the presence of the much stronger vertical return.

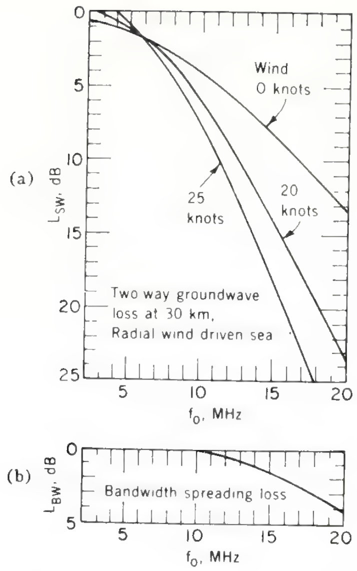

Fig. 3. Surface-wave loss and bandwidth loss factors versus radar operating frequency.

for σ^0. For this demonstration, the radar equation is rewritten in terms of the antenna gain product:

$$G_T G_R = \frac{P_R}{P_T} \cdot \frac{(4\pi)^3 R^4}{\lambda^2 \sigma^0 A} \cdot \frac{1}{L_{BW} L_{SW}} \tag{1}$$

where R is the range to the scattering area A, P_T and P_R are the transmitted and received power (in the dominant first-order Doppler echo), and L_{SW}, L_{BW} are "loss factors" accounting for two-way surface-wave propagation over the sea and Doppler line broadening, respectively. All of the factors on the right side of (1) are assumed known. The sea area A, within the resolution cell, is of course related to the antenna beamwidths (and hence gains), but in a known, calculable manner. Thus the antenna-gain product can be "measured" and compared with predictions. The excess two-way surface-wave propagation loss L_{SW} over the sea out to 30 km versus frequency and sea state is shown in Fig. 3(a), prepared from Barrick [8]. The bandwidth loss[3] L_{BW} was calculated by forming the ratio of the observed width of the dominant first-order Doppler echo with the width at the lowest operating frequency; this is shown in Fig. 3(b). Data from December 4 and December 7, 1972, were selected for this comparison, since the seas for both were driven by 20-knot (or greater) winds, predominantly from the west, and hence could be expected to produce a saturated positive first-order Doppler echo at all operating frequencies. Therefore, a σ^0 was used in (1) corresponding to -17 dB (but normalized to the ground-wave definition of antenna gains).

The comparison between calculated and "measured" values of $G_T G_R$ versus frequency is shown in Fig. 4. Data plotted as points were obtained on the two different days, for the two antenna beam positions (at 270° and 240°) at frequencies from 2.4 to 20 MHz. The solid line represents the gain product at the center of the two receiving beam positions as measured via a standard target in a small boat versus frequency; the discontinuities in the predicted gain curve arise from the fact that different receiving array elements were switched in or out at certain frequencies so as to reduce the pattern variation over the decade frequency operating range.

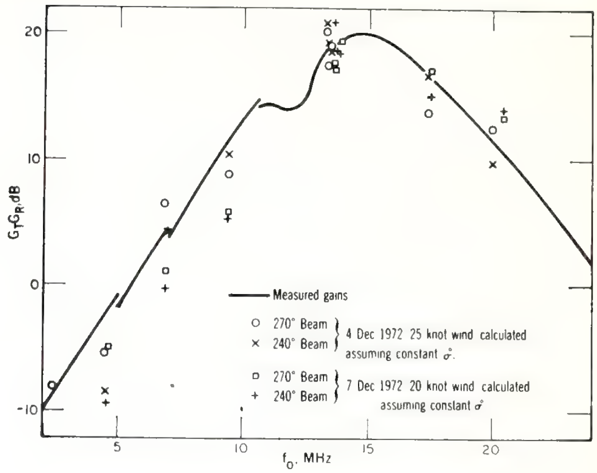

Fig. 4. Predicted (solid line) and measured (via first-order sea scatter) antenna gain product.

The comparison is favorable, and shows that the first-order echo can indeed serve as a reliable reference target. The spread in points at the lower frequencies may be due to inaccurate assumptions in the sea description. However, the spread of points near 13.4 MHz is a true index of the variation in the results, and all points lie within ±2 dB of the mean. This spread is most likely due to the fact that the 1/2 h of incoherent spectral averaging represented in obtaining each of the points was not long enough to permit observation of a large ensemble of independent, random sea surfaces within the radar resolution area; hence the points were not true means. This ±2-dB spread, however, compares favorably with the accuracies of other types of sky-wave radar sensitivity calibrators which have been used, such as beacons and repeaters (where the output power level can fluctuate due to electronic instabilities and aging) or islands/mountains whose apparent cross sections can change due to surface moisture content and Faraday polarization rotation.

V. Second-Order Sea Echo for Sea-State Determination

Theoretical explanations for second-order sea echo, present on nearly all records above 4 MHz, have been offered by Barrick [7] and Hasselman [9]; the reader is referred to these references for details of the mathematical derivation. The basic interpretation of this process is illuminating and worth some discussion. The theory shows that the radar waves interact with ocean wave trains as though the latter were diffraction gratings. Hence Bragg scatter and/or Feynman interaction diagrams are well suited to explain the various "orders" of scatter.

To first order the scattering and Doppler relationships are described in terms of Bragg scatter as follows:

$$\bar{k}^s = \bar{k}^i \pm \boldsymbol{\kappa} \tag{2a}$$

---

[3] This "loss" merely allows one to read the amplitude of the observed first-order Doppler peak, since the actual desired quantity P_R is the area under this peak.

$$\omega^s = \omega^i \pm \Omega. \tag{2b}$$

Here $\bar{k}^i$ and $\bar{k}^s$ are the two-dimensional components of the three-dimensional incident and scattered wavenumber vector lying in the mean sea-surface plane, and ω^i, ω^s are the radian temporal frequencies of the incident and scattered fields. The vector $\boldsymbol{\kappa}$ is the spatial wavenumber of the water wave responsible for scatter (i.e., $\kappa = |\boldsymbol{\kappa}| = 2\pi/L$, where L is the water wavelength), and Ω, the temporal wavenumber, is related to κ through the first-order gravity-wave dispersion tquation

$$\Omega = \sqrt{g\kappa}. \tag{3}$$

Thus, as an example, for backscatter at grazing incidence we can choose our coordinate system so that the $(-x)$ axis coincides with the propagation direction. Thus $\bar{k}^s = k_0\hat{x}$ and $\bar{k}^i = -k_0\hat{x}$ $(k_0 = 2\pi/\lambda)$, so that the scalar first-order resonance condition stated previously is established from (2a): $2k_0 = \kappa$ or $L = \lambda/2$. Then the radian Doppler shifts of the energy—defined as the difference between the incident (carrier) frequency and the actual scattered frequency—are $\omega^s - \omega^i = \pm\sqrt{g\kappa} = \pm\sqrt{2gk_0}$. Thus through simultaneous satisfaction of (2) we have established the length and direction of water waves responsible for first-order scatter, and also the unique square-root relationship for the discrete first-order Doppler echoes which had been established experimentally by Crombie two decades ago. The average spectral strength of the grazing first-order backscatter cross section per unit area (for vertical polarization) per radian/second bandwidth is found to be

$$\begin{aligned}\sigma^0(\omega) &= 2^7\pi k_0{}^4 S(\kappa_x, \kappa_y)\delta(\omega^s - \omega^i \pm \Omega)\\ &= 2^7\pi k_0{}^4 S(2k_0, 0)\delta(\omega_s - \omega_i \mp \sqrt{2gk_0})\end{aligned} \tag{4}$$

where $S(\kappa_x, \kappa_y)$ is the spatial wave-height directional spectrum for the sea.

Understanding of the extension of this interaction mechanism to second order is now straightforward; in place of (2) we have[4]

$$\bar{k}^s = \bar{k}^i \pm \boldsymbol{\kappa}_1 \pm \boldsymbol{\kappa}_2 \tag{5a}$$

$$\omega^s = \omega^i \pm \Omega_1 \pm \Omega_2. \tag{5b}$$

Now two water waves—with spatial wavenumbers $\boldsymbol{\kappa}_1$, $\boldsymbol{\kappa}_2$, and temporal frequencies $\Omega_1 = \sqrt{g\kappa_1}$ and $\Omega_2 = \sqrt{g\kappa_2}$—enter into the process. For backscatter at grazing incidence, (5a) shows that there are a whole double set of interacting water wave trains which, if they are present, can produce second-order scatter. These water wavenumber combinations, $\boldsymbol{\kappa}_1$ and $\boldsymbol{\kappa}_2$, form two sides of a vector triad whose resultant third side is $\bar{k}^s - \bar{k}^i = 2k_0\hat{x}$; hence they need not be collinear with the radar propagation direction. Imposition of the scalar Doppler condition (5b) further constrains the relationship between $\boldsymbol{\kappa}_1$ and $\boldsymbol{\kappa}_2$, reducing the number of independent degrees of freedom from two to one. Thus, in place of (4), theory shows that the second-order spectral contribution takes the form

$$\sigma^0(\omega) = 2^7\pi k_0{}^4 \iint d^2\boldsymbol{\kappa}\, |\Gamma|^2 S(\kappa_{1x}, \kappa_{1y}) S(\kappa_{2x}, \kappa_{2y}) \cdot\delta(\omega^s - \omega^i \mp \Omega_1 \mp \Omega_2) \tag{6}$$

where the variable of integration $\boldsymbol{\kappa}$ may be either $\boldsymbol{\kappa}_1$, $\boldsymbol{\kappa}_2$, or any linear combination of the two. The quantity Γ is the coupling or interaction coefficient between the two sets of water waves. Two contributions to Γ have been identified as [7]: 1) a hydrodynamic term arising from retention of the second-order (perturbational) terms in the nonlinear boundary conditions at the free water–air interface; and 2) an electromagnetic term arising from inclusion of second-order terms from the boundary perturbational expansion for the scattered fields at the water surface. The latter contribution is merely multiple scatter of the radar wave from one set of ocean waves to a second set and then back to the radar. The former contribution represents the nonlinear interaction of two water waves to form a small water-surface component with wavenumber $\boldsymbol{\kappa}_1 \pm \boldsymbol{\kappa}_2$; first-order radar scatter then takes place from this second-order water wave. Oceanographers refer to this second-order water wave as "trapped" or evanescent because it can neither carry energy away from the first-order wave spectra nor can it exist without or propagate independently of each of the first-order waves which produce it.

With the help of this theory, one can test various methods for inferring wave properties (such as significant wave height, dominant wave period, and dominant wave direction) from the second-order echo characteristics. An example of the success realized thus far in inferring significant wave height[5] from the records will be discussed here; further details on dominant wave period and directionality will be presented elsewhere.

Radar records for December 4, 1972, were selected for examination here because: 1) buoy wave-height spectra are available on that day; 2) hindcasts have determined that winds and waves were predominantly from the west, nearly along the 270° radar beam; and 3) the measured wave-height spectra have the shape characteristic of fully developed wind–wave conditions (i.e., a saturated f^{-5} equilibrium region and a fairly sharp lower end cutoff). Thus the shape of the wave spectra can be modeled by triangles, one of which is shown in Fig. 2 representing the 1630 (afternoon) wave conditions; the spectral energy omitted by this type of modeling is not significant in these two cases.

In solving the integral (6) for these wave spectra models, it is assumed that the dominant wave direction is coincident with the radar propagation direction. Furthermore, two models of azimuthal wave patterns were tested in the integration of the directional spectra $S(\kappa_x, \kappa_y)$: a cosine-squared pattern and a semi-isotropic pattern. This directional pattern has been a very difficult oceanographic quantity to measure, but the sparse data available indicate that most wind–wave patterns lie somewhere between cosine squared and semi-isotropic.

When calculating theoretical values for the integral (6), it is found that when the sea is fully developed a set of Doppler curves can be prepared as a function of a single universal parameter β: this parameter is proportional to the carrier frequency times the rms wave height $(\beta \simeq 80\pi f_0\, h/c)$. Thus Doppler spectra calculated for a given wave height but for several radar frequencies can be interpreted in terms of a single radar frequency but different wave heights. This is illustrated in Table I, where in the first set of columns the actual frequencies used on December 4 are shown. Fig. 5(a)–(c) shows calculated versus measured Doppler spectra for

---

[4] It is interesting to note that multiplication of (2) or (5) by Planck's constant gives the familiar conservation of momentum and energy equations in quantum mechanics for single and double wave–particle interactions.

[5] Significant wave height is an oceanographic term referring to the average peak-to-trough height of the highest one-third of the waves. It is related to rms wave height (for a Gaussian sea surface) h by $H_{1/3} = 4h$.

TABLE I

Parameter Interdependence Between Carrier Frequency and Significant Wave Height

Parameter β	Actual Conditions at 1630, 4 Dec. 1972		Scaled Conditions	
	f_o (MHz)	$H_{1/3}$ (ft)	f_o (MHz)	$H_{1/3}$ (ft)
1.7	2.41	7.8	18	1.0
3.2	4.54	7.8	18	2.0
4.9	6.92	7.8	18	3.0
6.6	9.40	7.8	18	4.1
9.5	13.40	7.8	18	5.8
12.3	17.40	7.8	18	7.6
14.2	20.15	7.8	18	8.7

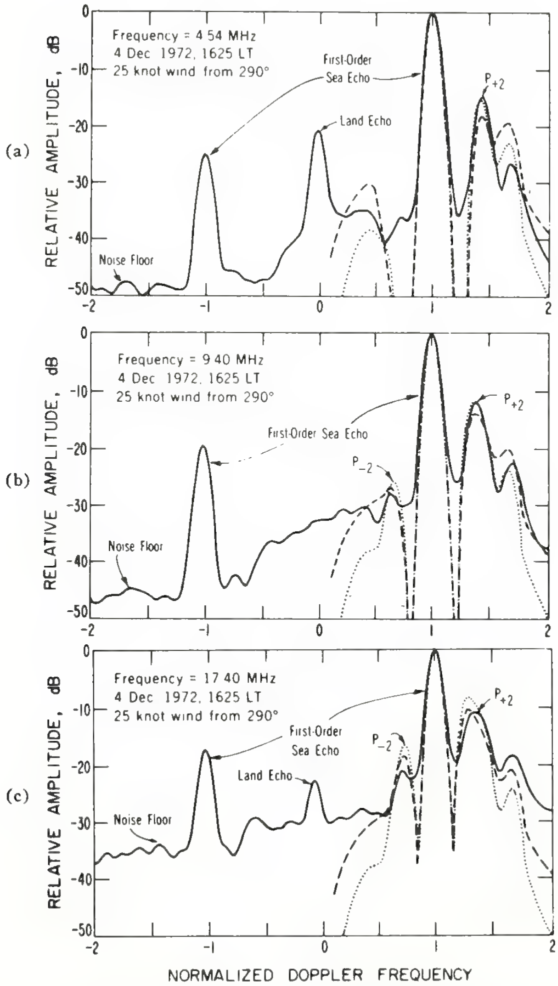

Fig. 5. Comparison of smoothed and normalized sea-echo spectra at different frequencies. Solid curves are measured (December 4, 1972), while dotted (cosine squared) and dashed (semi-isotropic) are predicted spectra for wave conditions shown in Fig. 2.

three frequencies in the afternoon of December 4; the measured spectra represent the sum of nine separate 200-s coherent power spectra, for a total of 1/2-h incoherent averaging. The theoretical spectra include both the first-order and second-order contributions; only the dominant, positive (up-

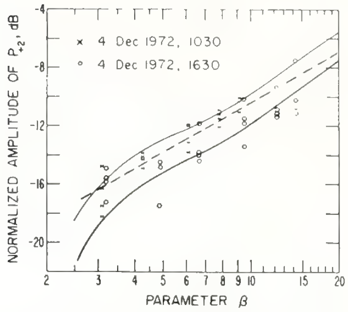

Fig. 6. Measured (points) and predicted amplitude of second-order peak P_{+2}. Upper and lower solid lines represent theoretical cosine-squared and semi-isotropic directional models, respectively. Dashed line is mean fit to measured data.

wind) sides of the spectra were calculated, with the dotted curve representing the cosine-squared and the dashed curve the semi-isotropic directional models. Both the measured and calculated spectra are normalized in frequency (with unity being the first-order Doppler position, i.e., $f_B = \pm\sqrt{2gk_0}/2\pi$), smoothed[6] by a Gaussian smoothing function of width $0.087 \times f_B$, normalized in amplitude to the top of the dominant first-order echo, and finally, the measured spectra are repositioned so that the current offset is removed. Thus Fig. 5(b) actually represents Fig. 1 after the smoothing process and removal of the current offset.

Several characteristics of the second-order echo vary with the parameter β (i.e., with frequency or wave height), as evident from Fig. 5. The amplitude and positions of the two second-order peaks designated P_{+2} and P_{-2}—with respect to the first-order peak—change with increasing β. We examine here only the amplitude of P_{+2}, and show in Fig. 6 the calculated and measured values of P_{+2} in decibels below the first-order peak. The upper line is the cosine-squared theoretical model, the lower is the semi-isotropic theoretical model, while the points comprise all of the measurements taken at 22.5-km and 30-km range at the seven frequencies and for the morning and afternoon sea conditions represented by the wave spectra of Fig. 2. Besides illustrating the good agreement between theory and measurement, this plot demonstrates a more important point. A relationship can be established between the relative height of P_{+2} and the parameter β; thus at a known radar operating frequency, the smoothed spectra could be renormalized (using the dashed calibration curve of Fig. 6) so that significant wave height can be read out directly as the height of P_{+2}. This is demonstrated in Fig. 7(a) and (b), which are the smoothed spectra for 9.4 MHz at 22.5-km range for the morning and afternoon of December 4, respectively. The significant wave heights read from the two radar records are about 5.5 and 8.5 ft, while buoy measurements and hindcasts indicated actual wave heights of 5 and 8 ft for morning and afternoon. Similar displays on the other frequencies yielded these wave heights also, with an error commensurate with the point spread in Fig. 6, caused primarily by insufficient incoherent averaging time.

---

[6] Smoothing was used for two reasons: 1) so that the widths of the first-order echoes would be broadened by a known amount beyond any system resolution and/or higher order sea dispersion effects, permitting their amplitude to be a true measure of their total energy content; and 2) because ionospheric motions are expected to introduce broadening of the spectra by approximately the amount used here.

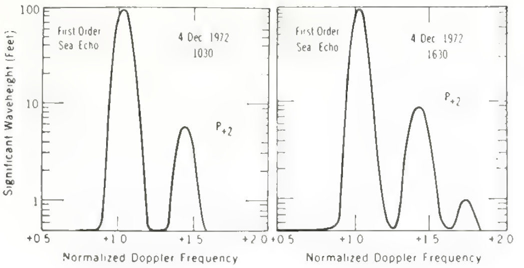

(a) (b)

Fig. 7. Upper portions of smoothed sea-echo spectra at 9.4 MHz, calibrated to show significant sea wave height (in feet) as height of P_{+2}.

VI. Current Measurement

As mentioned in the Introduction and demonstrated in Fig. 1, currents are evident in the records as an overall offset of the first-order Doppler peaks from their expected (normalized) positions at ±1. Data obtained on several days at the San Clemente Island facility have been examined from the standpoint of deducing currents. Using the relationship $u=\Delta\sqrt{gc/(4\pi f_0)}$ mentioned in the Introduction, surface currents radial to the radar were deduced and plotted in Fig. 8. These plots show the radial current component in centimeters per second along 240° (circles) and 270° (crosses) as a function of the first-order sea wavelength L corresponding to the seven operating frequencies. Error bars give an estimate of the current magnitude precision. The precision is limited by the resolution of the spectral analysis (1/200 Hz) at the longer wavelengths, while at the short wavelengths the limit is imposed by the natural broadening of the first-order lines due to higher order sea effects.

The data in Fig. 8 are for relatively high sea conditions, with the wind blowing roughly in the direction of the two antenna beams. In comparing the data in Fig. 8, several points are worthy of discussion. Note first of all that there is a considerable variability in the observed current velocities. In general, the apparent current magnitudes observed on the two bearings are different, which can be explained on the basis that the current flow is more nearly parallel to one radar beam than to the other. The data for March 13 are particularly interesting in this respect in that they show a reversal of the current in the 240° direction at the shorter sea wavelengths. On this occasion the wind was blowing roughly across the antenna beams. If the wind were coming from a direction somewhat south of west, a slight approaching velocity would be induced in the 240° record as compared with the 270° record which would be less affected by the wind. If this wind had not been blowing very long the currents produced by it would not penetrate very deeply. Thus near the surface the current would be approaching, but below the surface it could still be receding. As a result, the short waves could be expected to be most affected by the currents closest to the surface and should indicate a different current direction than the longer waves. These longer waves ought to be more influenced by the deeper currents in the opposite direction. Somewhat similar results are shown in the data for December 4.

This influence of the deeper current structure on the longer surface waves is believed to explain the dependence of velocity on wavelength exhibited in Fig. 8. Similar results have been reported by Stewart and Joy [10], who were able to compare the radar data with simultaneous observations of the drift of a submerged drogue. This effect is much like the decrease in velocity of surface waves in shallow water, and one could expect here also that surface waves should be influenced significantly by currents to a depth comparable to their wavelength. If the current changes with depth, as is usually the case, the short waves will have a different velocity than the longer waves. This has been shown by Plate and Trawle [11], following Biesel [12], who showed that the observed wave phase velocity v on infinitely deep water, having a linear vertical gradient of current velocity du/dz with depth z, could be related to the surface-current velocity u_s, and the theoretical wave phase velocity in the absence of current v_0, by

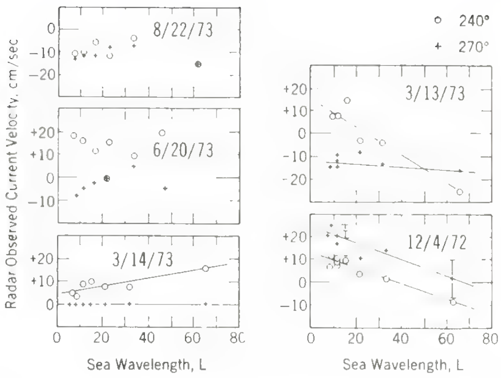

Fig. 8. Radar-inferred currents (radial to the radar) versus water wavelength being observed by radar. Relatively high sea states.

$$(v-u_s)^2+\frac{1}{\kappa}\,du/dz(v-u_s)=v_0^2 \tag{7}$$

κ being the wavenumber. Note that when $1/\kappa=L/2\pi=0$, $v=v_0+u_s$. Thus we can estimate the surface current from Fig. 8 by inspection, as wavelength approaches zero.

Likewise, the vertical current gradient du/dz can be inferred from the records by a perturbation on (7). We employ the fact that $u_s \ll v$, and set $\Delta u=u_{s1}-u_s$ where u_{s1} is the apparent "surface" velocity as measured at sea wavelength L_1 to obtain

$$\frac{du}{dz}=-\frac{4\pi\Delta u}{L_1}. \tag{8}$$

The observed currents on the open ocean are a combination of currents arising from large-scale circulation, tides, the frictional interaction between wind and the sea surface, and Stokes drift currents which are due to nonlinear wave–wave interactions [5]. The latter two components are local and transient, depending upon the local wind. Tidal components have yet to be observed and identified with this technique.

VII. Conclusions

Preliminary comparisons of theory with first-order surface-wave sea scatter lend confidence to the prospect of using this echo as a calibration standard for HF radars. This appears particularly well suited to over-the-horizon sky-wave (ionospheric) radars and/or communication systems operating over the ocean. Since path loss in such a system is highly variable and unpredictable, alternative sensitivity calibrators, including buoy beacons/repeaters or islands, will certainly be more expensive and/or sporadic in area coverage. Problems remaining to be resolved concern the expected variance in this sea echo as a function of incoherent integration (averaging) time and area of illumination. Obviously, as one increases either the incoherent averaging time (to several hours) or the geographic area over which incoherent averaging is performed (to dimensions several hundred kilometers in extent) the variance will decrease. On the other hand, the ionospheric path losses themselves will vary over such temporal and spatial extents, and hence one encounters a tradeoff between the fluctuation rates of the environmental factors and the granularity or resolution in time and space of the desired sea-echo calibration information itself. These questions will be answered by further analysis of the multifrequency surface-wave sea echo, and also by sky-wave research programs.

It appears that the important quantitative parameters describing sea state can be deduced from the characteristics of the higher order HF sea-echo Doppler spectrum. The use of this higher order echo is especially necessary with sky-wave radars because one of the first-order echo peaks is nearly always "saturated" or constant in the upper HF region in which ionospheric propagation conditions are favorable. This technique has the advantage of comparing one part of the signal spectrum with another, and hence absolute sensitivity calibration of the system, so critical for most sky-wave radar applications, is not necessary here. It is sky-wave radar which holds out the ultimate prospect of remotely sensing sea state out to several thousand kilometers from the U. S. coasts, with as few as two land-based sites. This paper has shown that significant wave height—perhaps the single most important descriptor of sea state—can be read directly from sea-echo spectral records. Further analyses of the San Clemente Island data will concentrate on deducing dominant wave period and propagation direction from the second-order echo features. A joint sky-wave radar research program is planned, which will determine the ultimate precision of such directional wave-height spectral parameters when subjected to the normal seasonal and diurnal vagaries of the ionosphere.

Preliminary success at inferring currents from the HF data must be explored further. Both surface-wave and sky-wave radars offer the prospect of current monitoring in large bays, estuaries, or near land masses. Surface-wave systems, limited in range to <200 km, can measure these currents directly from the translation of the first-order sea-echo lines from their predicted positions. Surface-wave operation at rather high frequencies ($\sim$30 MHz) might be more attractive because resolution into smaller cells by short pulses and antennas with significant angular resolution is possible. Sky-wave Doppler records, on the other hand, are often contaminated by unknown ionospheric-layer motions and multipath, and hence one must use a stable reference to remove such motions. Land or island echoes, where they are available within the resolution cell, can serve this purpose. These concepts will be tested further by both surface-wave and sky-wave experiments.

ACKNOWLEDGMENT

The authors wish to thank the Institute for Telecommunication Sciences team headed by L. Tveten, who assembled and operated the radar, for technical support. They also wish to thank J. Snider of the National Oceanic and Atmospheric Administration and L. Wagner of the Naval Research Laboratory for assistance in reduction of the data.

REFERENCES

[1] D. D. Crombie, "Doppler spectrum of sea echo at 13.56 Mc/s," *Nature*, vol. 175, pp. 681–682, 1955.
[2] D. E. Barrick, "First-order theory and analysis of MF/HF/VHF scatter from the sea," *IEEE Trans. Antennas Propagat.*, vol. AP-20, pp. 2–10, Jan. 1972.
[3] J. L. Ahearn, S. R. Curley, J. M. Headrick, and D. B. Trizna, "Tests of remote skywave measurement of ocean surface conditions," this issue, pp. 681–687.
[4] A. E. Long and D. B. Trizna, "Mapping of North Atlantic winds by HF radar sea backscatter interpretation," *IEEE Trans. Antennas Propagat.*, vol. AP-21, pp. 680–685, Sept. 1973.
[5] D. D. Crombie, "Backscatter of HF radio waves from the sea," in *Electromagnetic Probing in Geophysics*, J. R. Wait, Ed. Boulder, Colo.: The Golem Press, 1971, ch. 4, pp. 131–162.
[6] O. M. Phillips, *Dynamics of the Upper Ocean*. London, England: Cambridge Univ. Press, 1966, pp. 109–139.
[7] D. E. Barrick, "Remote sensing of sea state by radar," in *Remote Sensing of the Troposphere*, V. E. Derr, Ed. Washington, D. C.: U. S. Government Printing Office, 1972, ch. 12.
[8] ——, "Theory of HF and VHF propagation across the rough sea," *Radio Sci.*, vol. 6, pp. 517–533, 1971.
[9] K. Hasselmann, "Determination of ocean wave spectra from Doppler radio return from the sea surface," *Nature Phys. Sci.*, vol. 229, pp. 16–17, 1971.
[10] R. H. Stewart and J. W. Joy, "HF radio measurement of ocean currents," in *Proc. 1973 IEEE Conf. Engineering in the Ocean Environment*, Sept. 1973, pp. 64–67.
[11] E. Plate and M. Trawle, "A note on the celerity of wind waves on a current," *J. Geophys. Res.*, vol. 75, pp. 3537–3544, 1970.
[12] F. Biesel, "Etude theoretique de la Louille en eau courant," *Houille Blanche*, p. 279, 1950.

NOAA Technical Report ERL 334-WPL 41

June 1975

ANALYSIS OF AN ALL-WEATHER SYSTEM FOR WIND SOUNDING UP TO 15 KM ALTITUDE

R. B. Chadwick, E. E. Gossard, and R. G. Strauch

Forward-scatter radio paths are analyzed as a means of remotely measuring winds to high altitudes. The propagation problem is formulated and pertinent equations are derived. A ranging technique using pseudo-noise modulation to measure the altitude of the scattering volume is described and several possible geometries and configurations are discussed. A sample design is suggested and the performance to be expected is calculated for that design. A rough estimate is given of the equipment cost for a nationwide system capable of routinely measuring winds up to 15 km.

Radio Science, Volume 10, Number 7, pages 735-742, July 1975

Radio probing of the troposphere

C. Gordon Little

Wave Propagation Laboratory, Environmental Research Laboratories, National Oceanic and Atmospheric Administration, Boulder, Colorado 80302

(Received April 9, 1975.)

Radio wave interactions with the atmosphere and its constituents have been used to derive information on many aspects of the troposphere. Passively (i.e., in the radiometric mode), they have been used to measure temperature profiles and the water vapor and liquid water contents of the atmosphere, and to identify tornadic storms. In the active mode, three-dimensional fields of precipitation and velocity have been measured. These have permitted studies of horizontal and vertical velocities, vorticity, convergence, turbulence spectra, turbulent kinetic energy dissipation rates, and fluxes of momentum and kinetic energy, as well as studies of such atmospheric phenomena as thermal plumes, convective cells, internal gravity waves, breaking waves, and convective and orographic storms.

INTRODUCTION

Radio waves propagating in the lower atmosphere can at times be significantly affected by the presence of the atmospheric gases and hydrometeors. These interactions between the radio waves and the propagation medium have been used to derive quantitative information on the medium. This paper reviews the status of the field. In so doing, it is convenient to recognize that radio probing of the troposphere may be done either passively (as when using a microwave radiometer, or in studying "atmospherics"), or actively (as when using a weather radar).

We turn first to passive probing. At microwave frequencies, the microwave radiation from the absorbing components of the atmosphere is believed to be in thermal equilibrium with the medium. Hence, if the amount of the absorbing material is known, its temperature can be deduced from measurements of its microwave emission; alternatively, if its temperature is known, the amount of material can be calculated. The application of these passive radio probing techniques is discussed in the next section, where mention is also made of the use of lower (HF) frequencies to identify tornadic storms.

The following section deals with active radio probing systems, in which man-made radio signals are used, typically in a radar-like mode, to remotely probe the troposphere. In this case, some of the transmitted radio energy is received after being scattered by the propagation media; the scattered signal is used to derive information on the nature of the scatterer, including its spatial distribution, and (using the Doppler effect), its velocity. Typically, the scatterers are natural raindrops or snow, but man-made targets, such as chaff, may be used for studies of clear air conditions. In the case of

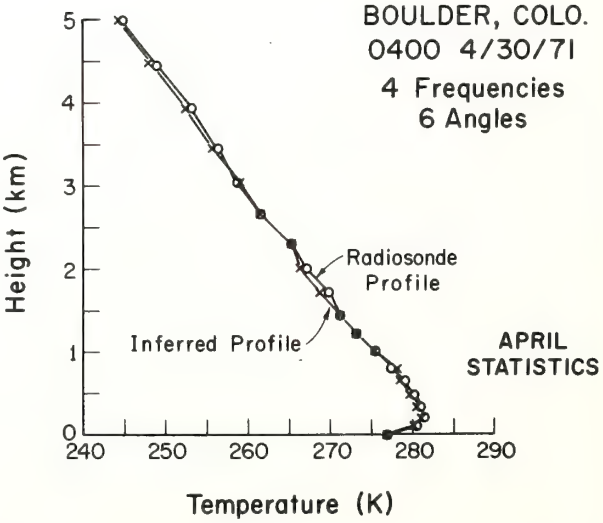

Fig. 1. Inferred and measured temperature profiles using four radiometer frequencies and six elevation angles [from *Snider*, 1972].

Copyright © 1975 by the American Geophysical Union.

modern, ultrasensitive radars, echoes obtained from the small-scale refractivity fluctuations occurring naturally in the atmosphere can be used to study the internal structure and processes of the clear atmosphere.

PASSIVE RADIO PROBING

If an antenna is immersed in a completely absorbing medium at a temperature T, the noise power available at the antenna terminals due to the thermal radiation from the propagation medium is given by the simple formula

$$P_n = kTB$$

where k is Boltzmann's constant and B is the observing bandwidth. To compute the thermal power available from an absorbing atmosphere, the distribution of temperature and absorption along the radio ray path must be known. The equivalent sky temperature, T_e, of the noise power available from a given direction is given by

$$T_e = \int_0^\infty T(s)\,\alpha(s)\exp\left[-\int_0^s \alpha(s')ds'\right]ds$$

where $T(s)$ and $\alpha(s)$ are the temperature and the absorption coefficient as a function of range s along the ray. If either $T(s)$ or $\alpha(s)$ is known, then under appropriate conditions the integral equation can be inverted to derive the other term. *Snider* [1972] has used a 4-frequency microwave radiometer in the 60-GHz O_2 absorption band to measure temperature profiles in this way. Figure 1 shows a comparison of such a radio-derived profile with that measured by a radiosonde. In general, very good agreement is found close to the ground, but elevated temperature inversions tend to be masked by the underlying absorption and to be considerably reduced in amplitude, and broadened in height.

In the absence of clouds, a microwave radiometer operating near the water vapor absorption line at about 22 GHz can be used to measure the integrated water vapor in the column above the radiometer. *Decker et al.* [1973] compare the integrated wet refractivity derived simultaneously from radio path length measurements and from passive, radiometric measurements. Their results confirm the ability of the radiometer to measure integrated water vapor content in the absence of clouds, which would cause the radiometric system to record too high an antenna brightness temperature. Recently, M. T. Decker (personal communication, 1974) has shown that the addition of a second radiometer frequency, operating well away from the water vapor line, permits correction of the water vapor measurements for

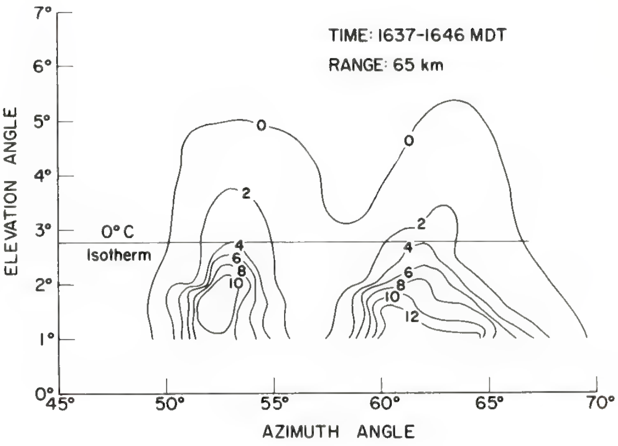

Fig. 2. Contours of liquid water content (kg m^{-2} column) of an 18 July 1967 thunderstorm near Boulder, Colorado [from *Decker and Dutton*, 1970].

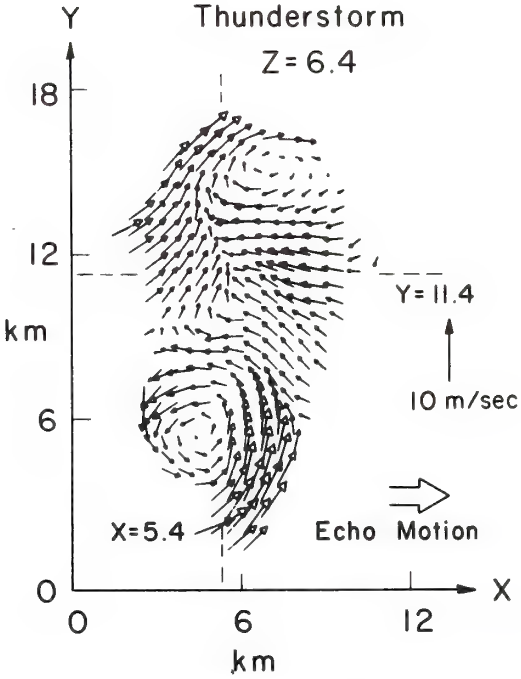

Fig. 3. Horizontal wind field at an altitude of 6.4 km revealed by dual-Doppler radar system during a Colorado thunderstorm (courtesy R. A. Kropfli and L. J. Miller).

the energy radiated by clouds in the field of view of the water vapor radiometer.

The liquid water content of clouds can be measured using a microwave radiometer tuned well away from the water vapor absorption line. Figure 2, due to *Decker and Dutton* [1970], shows a two-dimensional plot of the integrated liquid water content of a thunderstorm, obtained by scanning a 10.7-GHz radiometer across the storm. For nonprecipitating clouds, considerably greater sensitivity (to better than 1/10 mm of liquid water) can be obtained by using a frequency of about 30 GHz (M. T. Decker, personal communication, 1974). It should be noted that ice crystals show much less absorption than liquid water, and therefore are not seen by the radiometer. This suggests that microwave radiometers should be useful for monitoring the change of state of cloud particles.

It has been known since the early work of Marconi and his colleagues that appreciable radio frequency energy is radiated by lightning discharges. In recent years, these atmospherics have been studied in an attempt to find a distinguishing characteristic which could be used to automatically identify severe thunderstorms, and especially those which have tornadoes associated with them. Significant success has been obtained using measurements of the "burst rate"—the frequency of occurrence of short duration periods with very high counting rates of sferics. *Taylor* [1973] found that the general characteristic of the signals observed during nonsevere storm conditions was that of a few short-duration bursts of low sferic rates with occasional long-duration bursts of high sferic rates produced by discrete discharges. Tornadic storms typically showed enhanced sferic activity, with many bursts of high sferic rates. This enhancement in burst rate was not generally apparent at the lower frequencies (below about 300 kHz) but was easily recognized at frequencies above 1 MHz. Using a network of fifteen 3-MHz burst-rate recording systems during the 1972 tornado season, Taylor obtained data on the cumulative distributions of burst rates for five different levels of thunderstorm severity. Tornadic storms clearly showed the highest burst rates, followed by storms with funnel clouds, storms with severe wind or hail, and nonsevere thunderstorms. Approximately three out of four tornadic storms reported as occurring within 30 km of the sensors registered more than the (somewhat arbitrary) alarm criterion of 20 bursts per minute; only about one in fifteen of the nonsevere thunderstorms occurring within 30 km reached this alarm level. Work is now underway to develop an automatic direction-indicating tornadic storm detector.

ACTIVE RADIO PROBING

During the early 1930s, Marconi made some of the first measurements of the scatter of radio waves by man-made objects. From these early beginnings has grown the whole field of radar, with all its many civilian and military uses. We turn now to the use of radar for meteorological purposes. In this case, it is convenient to differentiate between three different types of studies, according to the nature of the scatterers responsible for the radar echoes. These are respectively precipitation, chaff, and regions of naturally occurring refractivity fluctuations present in the clear atmosphere.

Weather radar is by now a standard tool of many national weather services. For many years it has been used to monitor the development and motion of regions of precipitation, with some indication of the precipitation rate being derivable from the echo intensities. A recent development is project D/RADEX in which digitized data from several

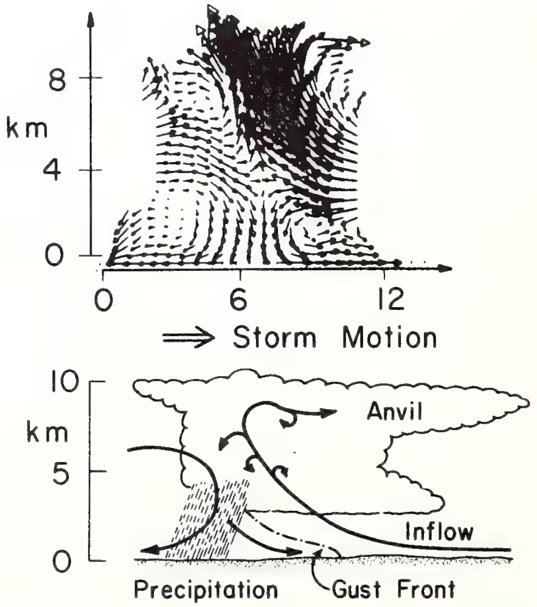

Fig. 4. Two-dimensional velocity field in a vertical plane through a Colorado thunderstorm (courtesy R. A. Kropfli and L. J. Miller), compared with typical model of a thunderstorm.

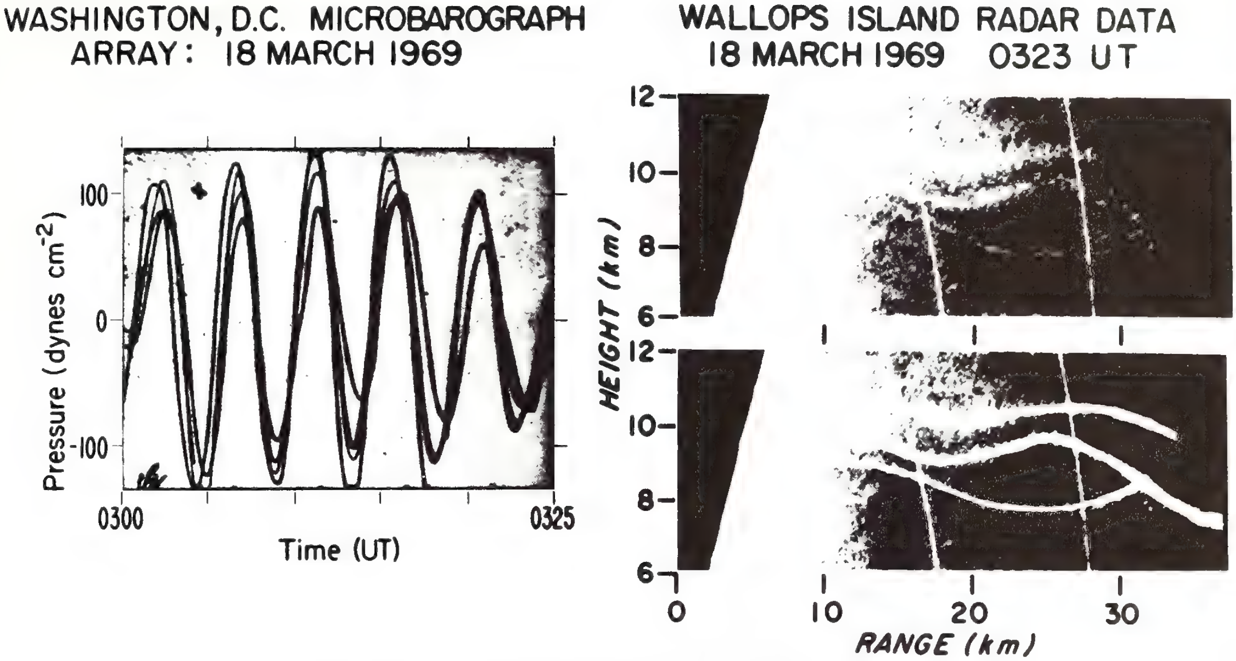

PARAMETER	MICROBAROGRAPH ARRAY DATA	RADAR DATA
λ (km)	14	15
V (m sec^{-1})	47	44 - 50
τ (sec)	300	300 - 340
A (deg)	284	(270)

Fig. 5. Comparison of recordings of gravity waves observed on a microbarograph array near Washington, D.C., and on the high power Wallops Island radar, March 18, 1969 (courtesy W. H. Hooke).

radars are transmitted to a central location by means of satellite for an essentially real-time monitoring of severe storm activity over very large areas. Also, *Eccles and Atlas* [1973] have recently shown how a two-wavelength radar system, using scaled antennas, can be used to identify the locations of regions of hail in thunderstorms.

But the most significant advance in weather radar has come with the application of the Doppler principle to determine the full three-dimensional velocity field in regions of precipitation. The displacement in frequency of the received echo relative to the transmitted frequency is directly proportional to the component of the velocity of the precipitation toward the radar. By scanning the radar in azimuth and elevation, a full three-dimensional plot of this component of velocity can be obtained. If the same volume is also scanned from a different direction by a second radar, careful processing of the two radial velocity fields permits derivation of the full three-dimensional velocity field [*Miller and Strauch,* 1974]. Some examples of results of this technique, using two 3-cm Doppler radars spaced up to about 50 km apart, are shown in Figures 3 and 4. Figure 3 shows the horizontal wind field at an altitude of 6.4 km observed during a 1973 thunderstorm. The storm motion of about 4 m/sec in the x direction has been removed. The cyclonic and anticyclonic rotations are part of rotating updraft cores, which persisted through a depth of more than 5 km. Figure 4 shows a vertical section of the same storm parallel to the direction of storm

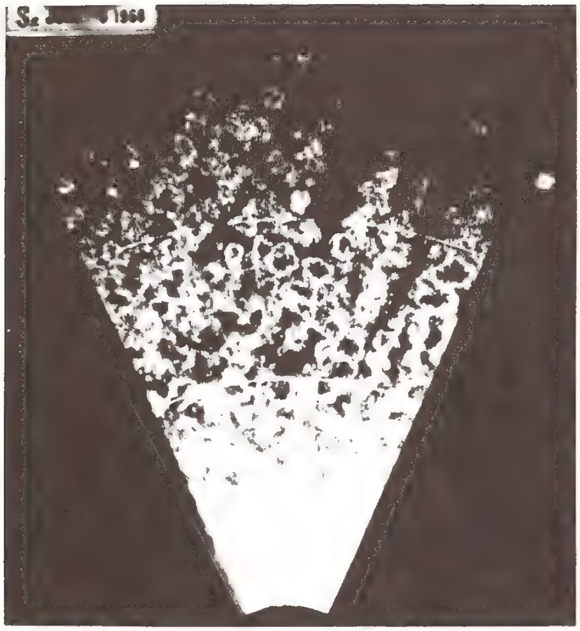

Fig. 6. PPI picture from high power 10-cm wavelength radar at Wallops Island showing convective cells. Antenna elevation angle 2°, range marks every 5 n mi [from *Konrad*, 1970].

motion. Those familiar with the simplified two-dimensional thunderstorm models will recognize the predominant features. The gust front ahead of the precipitation region is shown, as well as the mid-level inflow from the backside, lying between lower and higher levels of outflow. The updraft region is strongly identified, as is the outflow to the anvil. The simultaneous availability from this multi-Doppler radar system of the time-history of the velocity and precipitation fields in thunderstorms is giving totally new insights into their nature, and must be regarded as a major breakthrough in observational meteorology.

The Doppler radars referred to above usually use precipitation as the tracer of the velocity field, and require the presence of chaff for studies of the clear air velocity field. Ultrasensitive pulse radars [*Hardy and Katz*, 1969] and the new FM/CW radars [*Richter*, 1969] have sensitivities such that echoes can be obtained from naturally occurring fluctuations in the radio frequency refractive index of the atmosphere. In this case, the echo strength from a given volume is proportional to that Fourier component of the refractivity field in the volume which is directed toward the radar and has a spatial wavelength equal to half the radar wavelength. All other spectral components in the refractivity field are not effective in scattering a signal back to the radar. These radars may therefore be used to map regions of the atmosphere which contain relatively strong, small-scale (i.e., $\lambda/2$ size) fluctuations in refractive index. Examples of such echo patterns are given in Figures 5, 6, and 7. Figure 5, taken

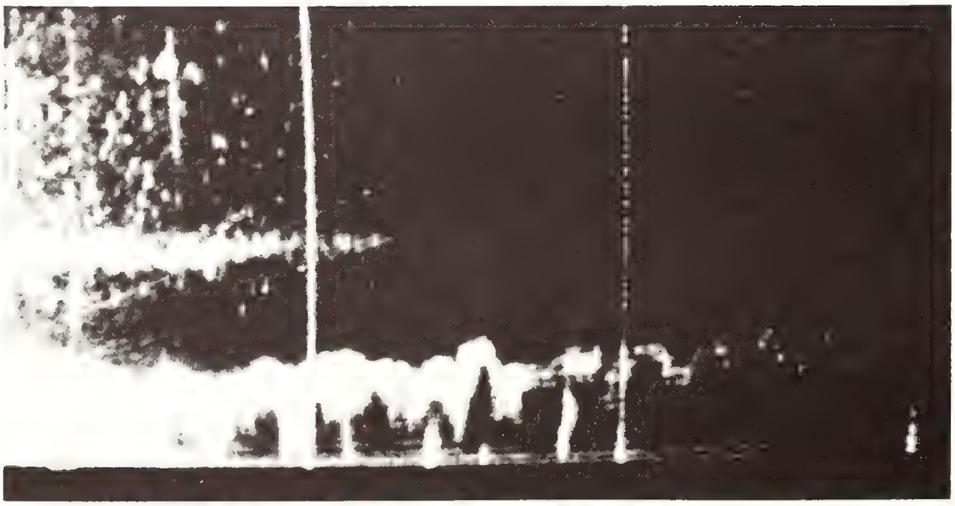

Fig. 7. RHI picture from high power 10-cm wavelength radar at Wallops Island showing convective cells. Range marks every 5 n mi. Height scale expanded approximately three times relative to horizontal scale [from *Konrad*, 1970].

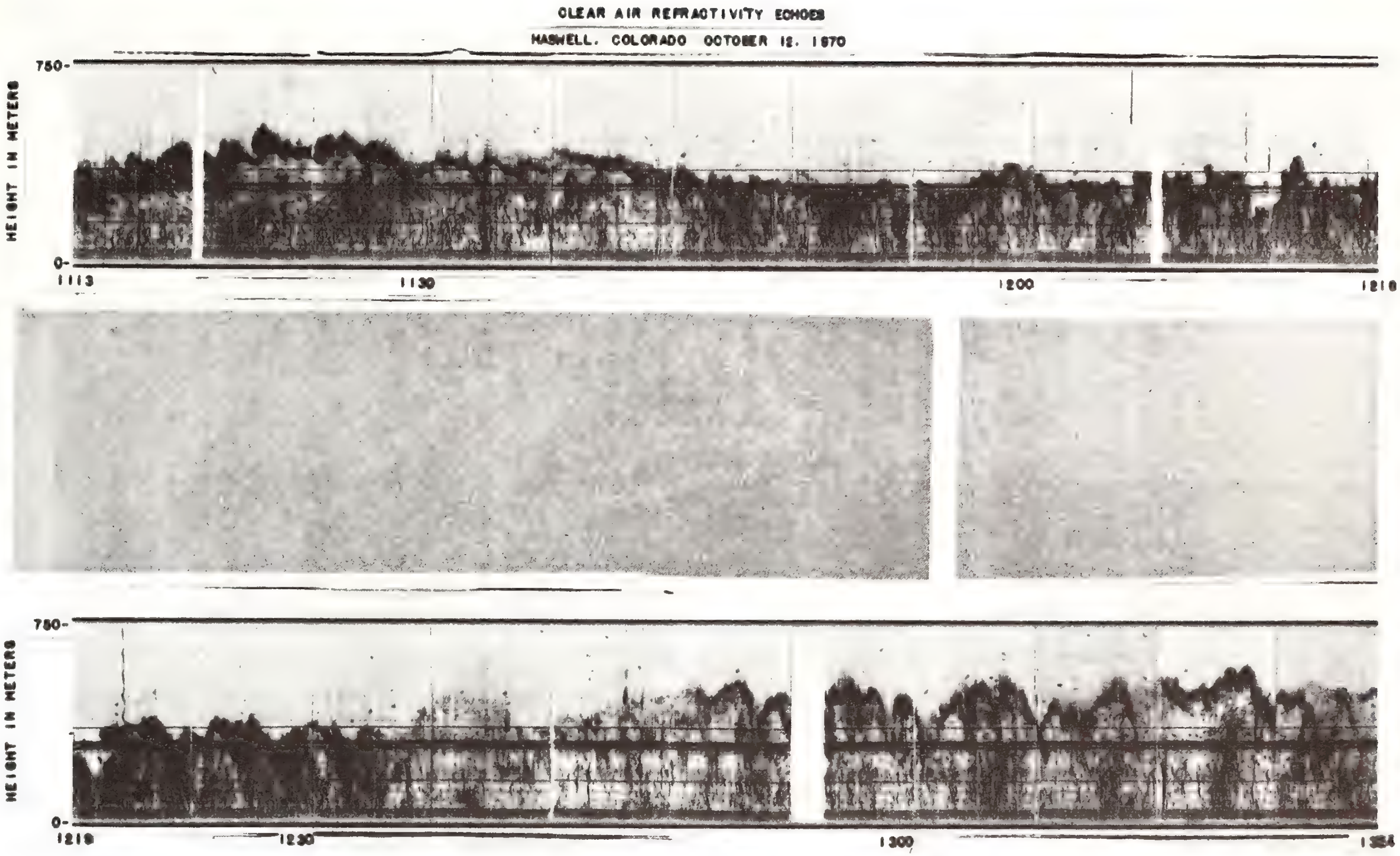

Fig. 8. Height-time recording of FM/CS radar echoes from clear air and insects during convective conditions, showing fluctuations in height of the trapping inversion [from *Bean et al.*, 1971].

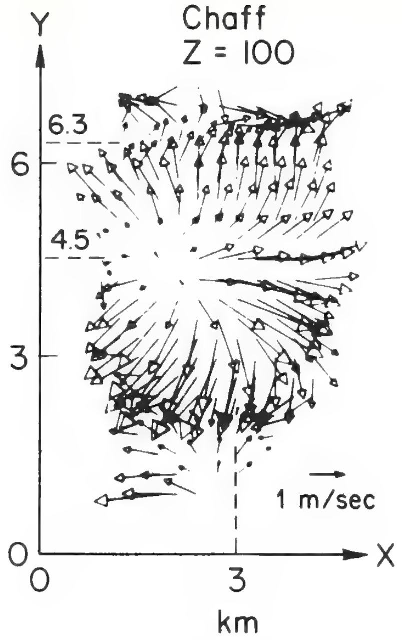

Fig. 9. Velocity field in horizontal plane at a height of 100 m, obtained during convective conditions using dual-Doppler radar system and chaff. Note the very well-defined divergence (courtesy A. S. Frisch).

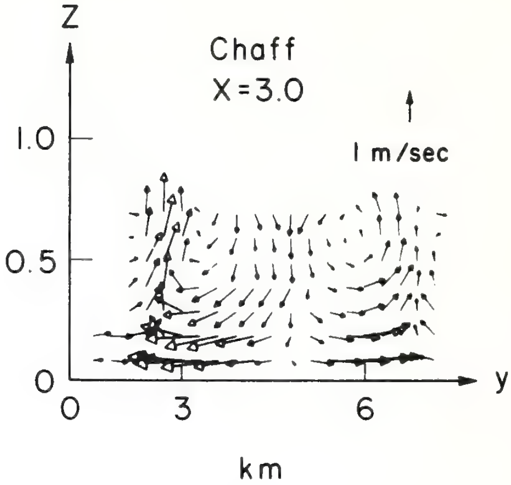

Fig. 10. Vertical cross section of velocity field during convective conditions, obtained using dual-Doppler radar system and chaff. Note the well-defined updrafts, downdrafts, and divergence (courtesy A. S. Frisch).

from a forthcoming paper by *Hooke and Hardy* [1975], includes an RHI plot of elevated layers whose height is modulated in a wavelike manner. (This echo pattern is actually characteristic of a breaking gravity wave [*Hardy and Katz,* 1969].) Also shown in Figure 5 are records taken some 200 km from the radar site on a spaced array of microbarographs. The parameters of the waves deduced from the two types of observations are shown in the table and make it plain that the two systems were observing the same wave train.

Figure 6 is a striking representation of convective cells as shown in a PPI plot from the Wallops Island radar [*Konrad,* 1970]. The donut-shaped echoes, arrayed in long lines or streets, are individual convective cells seen in cross section by the radar beam at an elevation angle of 2°. Figure 7 shows the convective plumes in vertical cross section, as obtained on the same radar, while Figure 8 shows convective activity as seen on a fixed, zenithally directed FM/CW radar. The inversion capping the convective activity is clearly identified in both figures, and is seen to be displaced vertically by the convective activity below. Figure 9, taken during clear-air convection using the dual Doppler radar system and chaff, gives a graphic representation of the divergence of the downdraft region of a convective cell in a horizontal plane 100 m above the ground. A vertical cross section of the dynamics of the cell is given in Figure 10 which clearly defines the regions of updraft, downdraft and convergence and divergence.

CONCLUSION

Thus, we see that radio waves can be used passively to measure temperature profiles, and the water vapor and liquid water contents of the atmosphere, as well as to distinguish the severity of thunderstorms. Operating actively, radar systems may be used to map (in all three spatial dimensions) clouds, precipitation, and hail, and the three-dimensional distribution of velocity, turbulence, vorticity, and divergence. In addition, ultrasensitive radars have been shown capable of monitoring clear-air phenomena such as thermal plumes, convective cells, temperature inversion layers, and gravity waves. I believe that Marconi, whose demonstrations of new radio communication capabilities repeatedly surprised the world, would himself have been surprised and pleased to see how far this frontier of radio probing of the troposphere has advanced.

Acknowledgments. I wish to acknowledge the assistance and courtesies extended to me during the preparation of this paper by many colleagues in the field of remote probing of the atmosphere, and especially by M. T. Decker, A. S. Frisch, E. E. Gossard, W. H. Hooke, R. Kropfli, R. G. Strauch, and W. L. Taylor of the Wave Propagation Laboratory, and T. Konrad of Johns Hopkins University.

REFERENCES

Bean, B. R., R. E. McGavin, R. B. Chadwick, and B. D. Warner (1971), Preliminary results of utilizing the high resolution FM radar as a boundary layer probe, *Boundary Layer Meteorol.*, *1*, 466-473.

Decker, M. T., and E. J. Dutton (1970), Radiometric observations of liquid water in thunderstorm cells, *J. Atmos. Sci.*, *27*, 785-790.

Decker, M. T., F. O. Guiraud, and E. R. Westwater (1973), Correction of electrical path length by passive microwave radiometry, Proc. Conf. Propagation of Radio Waves at Frequencies above 10 GHz, London.

Eccles, P. J., and D. Atlas (1973), A dual-wavelength radar hail detector, *J. Appl. Meteorol.*, *12*, 847-854.

Hardy, K. R., and I. Katz (1969), Probing the clear atmosphere with high power, high resolution radars, *Proc. IEEE*, *57*, 468-480.

Hooke, W. H., and K. R. Hardy (1975), Further study of the atmospheric gravity waves over the eastern seaboard on 18 March 1969, *J. Appl. Meteorol.*, *14*, 31-38.

Konrad, T. G. (1970) The dynamics of the convective process in clear air as seen by radar, *J. Atmos. Sci.*, *27*, 1138-1147.

Miller, L. J., and R. G. Strauch (1974), A dual-Doppler radar method for the determination of wind velocities within precipitating weather systems, *Remote Sensing Environ.*, *3*, 219-235.

Richter, J. H. (1969), High resolution tropospheric radar sounding, *Radio Sci.*, *4*, 1261-1268.

Snider, J. B. (1972), Ground-based sensing of temperature profiles from angular and multi-spectral microwave emission measurements, *J. Appl. Meteorol.*, *11*, 958-967.

Taylor, W. L. (1973), Electromagnetic radiation from severe storms in Oklahoma during April 29-30, 1970, *J. Geophys. Res.*, *78*, 8761-8777.

REMOTE SENSING OF ENVIRONMENT **3**, *219-235 (1974)*

A Dual Doppler Radar Method for the Determination of Wind Velocities within Precipitating Weather Systems

L. J. MILLER AND R. G. STRAUCH

NOAA/ERL/Wave Propagation Laboratory, Boulder, Colorado 80302

A method of coordinated scanning which makes use of two Doppler radars and a procedure of data reduction are described. The two radar estimates of radial velocity of the precipitation particles are combined with the equation of mass continuity and an independent estimate of the mean particle-fall velocity. This results in a complete solution for the three components of vector air motion. Examples of air motion fields which illustrate the effectiveness of this new technique in revealing the detailed structure of the winds are shown.

Introduction

Coherent or Doppler radar systems have clearly demonstrated their value in the ground-based remote sensing of mesoscale atmospheric motions. So long as air motion tracers, whether natural or man-made, are present in sufficient numbers to return a detectable signal, the pulse volume distribution of radial motions of these tracers is readily determined from an analysis of the spectrum of Doppler frequency shifts in this signal. The reflectivity-weighted average of this frequency spectrum is related to the mean particle radial motion.

Single radars have been used by numerous investigators in the determination of one-dimensional air motion during certain restricted atmospheric conditions. However, the effective determination of the complete three-dimensional vector air motion under most conditions requires the use of multiple radar systems. A method of radar scanning and a procedure of data reduction developed at the NOAA (National Oceanic and Atmospheric Administration) Wave Propagation Laboratory has demonstrated that the vector air motion fields can be determined with the use of only two radars. This paper describes the method and procedures, and shows examples of air motion fields which illustrate the power of this new technique for remotely sensing the atmospheric environment.

In our procedure, the two radar radial velocity estimates are combined with the equation of mass continuity and an independent estimate of mean terminal-fall velocity. This results in a complete description of three-dimensional air motion in space and time within the framework of the assumptions involved.

The Velocity Spectrum

As the precipitating particles comprising a distributed meteorological radar target move about, the return signal is seen to fluctuate randomly in both phase and amplitude. These fluctuations are associated with a relocation of scatterers by the relative particle motion within the illuminated volume. The time rate of change of phase ($d\varphi/dt = 4\pi\, v_R/\lambda$ where v_R is radial velocity and λ is radar wavelength) of the return signal is therefore a measure of the particle radial motion distribution (see Lawson and Uhlenbeck, 1950; Rogers, 1963).

The reflectivity-weighted average of the velocity spectrum is the mean radial velocity of the particles in the pulse volume. This average is the

© American Elsevier Publishing Company, Inc., 1974

sum of two components along the beam: (a) the radial component of the mean particle-fall velocity and (b) the mean radial air motion, assuming that the precipitating particles do indeed follow the air motion. Wilson (1970) has shown that even a hailstone as large as 2-cm diam can be expected to follow the mean horizontal air motion within ± 0.5 m $\sec^{-1}$ in a flow with vertical shear of less than 10^{-2} $\sec^{-1}$ (a reasonable value for mature convective storms). The larger particles are, however, less responsive to small scale (~ few centimeters) air motion variability. This implies that there exists an individual turbulence spectrum for each particle size.

If the incremental power returned by all scatterers moving with radial velocity between v_R and $v_R + dv_R$ is denoted by $S(v_R)\, dv_R$, the nth initial moment of the spectrum becomes

$$\overline{v_R^n} = \frac{1}{\bar{P}_R} \int v_R^n \, S(v_R)\, dv_R \, , \qquad (1)$$

where the average return power $P_R = \int S(v_R)\, dv_R$. The mean particle radial velocity is given by Eq. (1) with $n = 1$. The variance of the Doppler spectrum is

$$\sigma^2 = \frac{1}{\bar{P}_R} \int (v_R - \bar{v}_R)^2 \; S(v_R)\, dv_R . \qquad (2)$$

The measured mean radial velocity is a result of the spatial convolution of the point radial velocity function with the radar antenna illumination function (Srivastava and Atlas, 1972). Consequently, the motions being probed are low-pass filtered through the effect of pulse-volume averaging.

Coplane method

Unambiguous determination of the average vector particle motion obviously requires simultaneous measurement of mean radial velocities within a common volume from three different directions. The vector particle motion can therefore be realized by positioning three Doppler radars some distance apart and simultaneously scanning on a systematic pulse-volume by pulse-volume basis until the entire precipitating region has been probed. This method, however, does not utilize the fact that many pulse volumes along any slant range from a particular radar can be simultaneously probed for mean radial velocity estimates.

One alternative to this method would be to collect data at many range locations along each beam position in some preselected azimuthal elevation beam scan sequence. Each radar would scan independently and the radial velocity fields could be interpolated to arrive at values at common grid locations. The entire scan sequence must necessarily be completed prior to interpolation. The interpolation scheme must therefore account for temporal as well as spatial variation in the velocity fields.

This method is highly restrictive and not optimum when applied to precipitating, short-lived weather systems having considerable air-motion variability in both space and time. A more coordinated, high-speed data acquisition method is necessary for measuring motions in such weather systems. One dual radar method, COPLAN (an acronym for *co*ordinated co*plan*ar) scanning, first proposed by Lhermitte and Miller (1970) and later expanded by Miller (1972) is designed to meet these requirements. A schematic representation of the scan method is shown in Fig. 1. As will become evident, coplane scanning is a natural way of utilizing only two Doppler radars to systematically probe precipitating systems such as convective storms. Three-dimensional air motion is inferred by combining the dual radar measurements of radial particle motion with the equation of mass continuity and with an estimate of mean fall velocity obtained independently of the Doppler data.

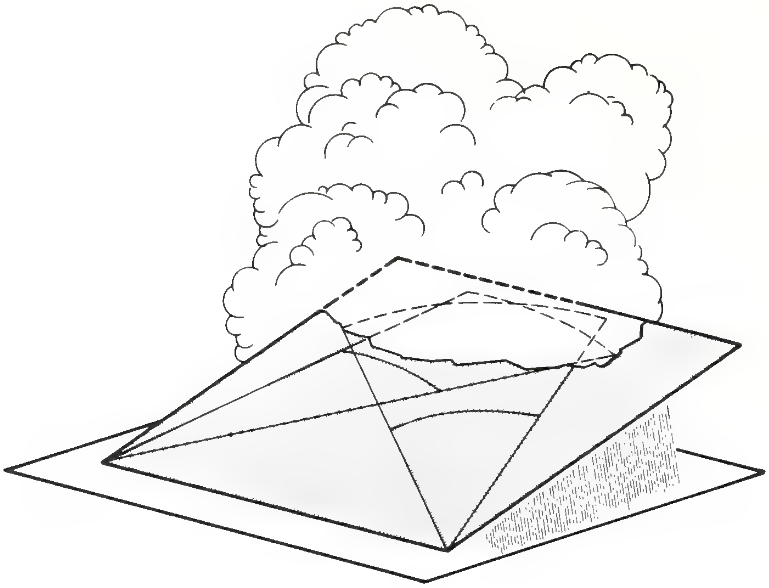

FIG. 1. Schematic depiction of dual-Doppler radar coplane scanning of a precipitating region of a convective storm.

Conventional radar scanning methods require the completion of a three-dimensional sequence of azimuth and elevation-angle scans before the measured radial particle-velocity fields can be expressed in a common coordinate system. Once these radial velocity fields are interpolated to common locations, they can be combined to give a three-dimensional vector velocity field. The particle-motion field must therefore be time-adjusted or assumed to be stationary for this total scan time. However in coplanar scanning, dual radar data to be combined for a two-dimensional motion field are initially acquired in common planes of a cylindrical coordinate system. The velocity field is then assumed stationary only for the much shorter scan time (typically one-half minute or less) of a single plane. One obvious advantage of this scanning is a better assessment of the true temporal behavior of the air motion. Data sets from a single plane can be acquired quickly and the plane rescanned periodically at a time interval much longer than the plane scan time. Moreover, interpolation procedures are two-dimensional rather than four-dimensional (space and time). This simplification of the data processing leads to a significant saving of time and money in the analysis of the large quantity of data that Doppler radars can provide.

The COPLAN method requires that data from two radars be separately evaluated for radial particle-velocity estimates at grid points in a tilted plane passing through the two radar positions. These two radial velocity fields are then linearly combined to provide an unambiguous two-dimensional particle motion vector field. When the particle-fall speed contribution is subtracted, the result is a vector air motion field in the plane. The third component of air motion normal to the plane is then estimated from an integration in cylindrical coordinates of the equation of continuity for an incompressible fluid. The velocity components are then reinterpolated for estimates in horizontal and vertical planes as needed. These new coplanar components of air motion are readily transformed to components in Cartesian coordinates.

Coordinate systems

Conventionally, weather radars have scanned in a spherical coordinate system defined by the slant range R, elevation angle θ, and azimuth angle ϕ. These coordinates are related to the conventional, local tangent-plane, meteorological system by the relations

$$R = (x^2 + y^2 + z^2)^{1/2}, \tag{3}$$

$$\theta = \tan^{-1}\left[\frac{z}{(x^2 + y^2)^{1/2}}\right], \tag{4}$$

$$\phi = \tan^{-1}\left(\frac{x}{y}\right), \tag{5}$$

for a radar located at the origin. The positive directions are, respectively, upwards from the local horizontal for the elevation angle and clockwise from true north for the azimuth angle. This system, however, is inappropriate for coordinated, high-speed scanning by two radars.

For two radars a more natural system is a right circular, cylindrical coordinate system whose axis is along the line joining the radars. As the radar antenna rotates in the azimuthal direction, the beam is constrained to a plane tilted at an angle α above the local horizontal by changing the elevation angle θ according to the relation

$$\tan\theta = \tan\alpha \, |\sin(\phi - \beta)| \, . \tag{6}$$

The quantity $(\phi - \beta)$ is the azimuth angle relative to the baseline which makes an angle β with the true north. Note that Eq. (6) requires that the coplane and elevation angles be equal in the direction perpendicular to the baseline ($\phi - \beta = 90°$) and that the elevation angle be zero for all coplane angles in a direction along the baseline ($\phi - \beta = 0°$). Obviously, this limits the scanning region to a smaller area than that useable by a single radar. But, as will be shown later, regions that cannot be scanned are those where accurate two-dimensional velocity estimates cannot be derived from the radar measurements.

The coplane or cylindrical coordinates are related to the Cartesian coordinates (x, y, z)

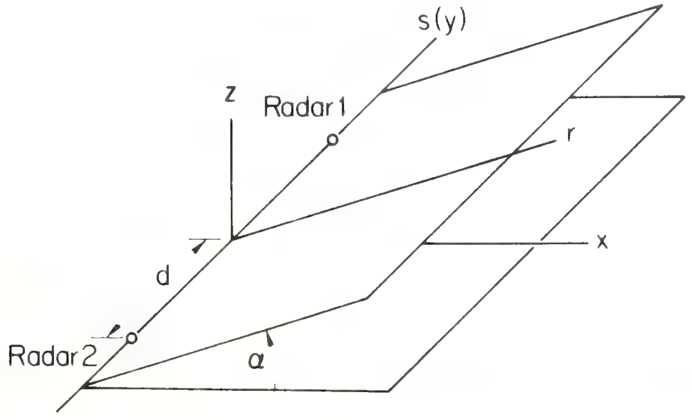

FIG. 2. Relation between coplane (r, s, α) and Cartesian (x, y, z) coordinates.

measured relative to the baseline (Fig. 2) by the following transformations:

$$r = (x^2 + z^2)^{1/2} \quad , \qquad (7)$$

$$s = y, \qquad (8)$$

$$\alpha = \tan^{-1}(z/x), \qquad (9)$$

where the tilt angle α is restricted to the interval $0 \leqslant \alpha \leqslant \pi/2$, r is the distance perpendicular to the baseline and s is the distance parallel to the baseline. Both s and r lie in the plane and the origin is at the midpoint of the baseline. The positive s-direction is defined such that the region being scanned is always to the right of the baseline when looking in the positive s-direction.

Velocities

If u and v are the respective horizontal components of air motion perpendicular and parallel to the radar baseline and w is the vertical component, the air motion components in the tilted plane are

$$u_r = u \cos\alpha + w \sin\alpha, \qquad (10)$$

$$u_s = v, \qquad (11)$$

$$u_\alpha = -u \sin\alpha + w \cos\alpha. \qquad (12)$$

The quantities u_r and u_s are, respectively, perpendicular and parallel to the baseline and u_α is normal to the plane. The inverse transformations are given by

$$u = u_r \cos\alpha - u_\alpha \sin\alpha \, , \qquad (13)$$

$$v = u_s \, , \qquad (14)$$

$$w = u_r \sin\alpha \; u_\alpha \cos\alpha. \qquad (15)$$

For particle motion one need only substitute $w + v_t$,(where $v_t < 0$ is the mean fall velocity in still air) for w in the velocity transformations, and v_r, v_s, and v_α become the respective particle-motion components:

$$v_r = u_r + \bar{v}_t \sin\alpha, \qquad (16)$$

$$v_s = u_s \, , \qquad (17)$$

$$v_\alpha = u_\alpha + \bar{v}_t \cos\alpha. \qquad (18)$$

It is noteworthy that the coplane method leads directly to the horizontal component of air motion parallel to the baseline for all planes scanned, and that v_s is independent of $\overline{v_t}$.

The first moment of the Doppler spectrum is the velocity component radial to the radar, and so is related to the velocity components above by

$$\bar{v}_R(\delta) = v_r \sin\delta + v_s \cos\delta \, , \qquad (19)$$

where $\delta = \tan^{-1}[r/(s - s_0)]$ is the angle in the plane between the baseline and the radar beam for a radar located at $(0, s_0)$. Since the particle velocity component normal to the plane does not contribute to the radial velocity, unambiguous resolution of the two-dimensional particle motion in the plane is realized from the solution of two expressions analogous to (19), one for each radar.

Measurement of two mean radial-velocity estimates, v_{R1} and v_{R2}, at the same point in the plane leads to

$$v_r(r, s) = \frac{R_1 \bar{v}_{R1}(s + d) - R_2 \bar{v}_{R2}(s - d)}{2dr} \; , \qquad (20)$$

and

$$v_s(r, s) = \frac{R_2 \bar{v}_{R2} - R_1 \bar{v}_{R1}}{2d} \; , \qquad (21)$$

where the slant ranges

$$R_1 = \sqrt{r^2 + (s-d)^2} \text{ and } R_2 = \sqrt{r^2 + (s+d)^2},$$

and $2d$ is the separation distance of the radars. The air-motion component perpendicular to the baseline, u_r in Eq. (16), is obtained from (20) by subtraction of the mean fall velocity contribution, $\overline{v_t} \sin \alpha$. As noted earlier, the air-motion component along the baseline is uniquely determined by the radar measurements and the location in the plane.

Coplane interpolation

The solutions for v_r and v_s given in (20) and (21) require knowing $\overline{v}_{R\,1}$ and $\overline{v}_{R\,2}$ at the same r, s field point. In general these estimates are not obtained at commom points so that interpolation of the measured fields is required. Most often the radar acquires data at fixed range locations as the antenna scans in the azimuthal direction. This coordinate system is orthogonal so that two-dimensional interpolation can be accomplished by first doing two one-dimensional interpolations along the arcs at each of two adjacent radar ranges to obtain new estimates at the azimuth of the r, s grid location (see Fig. 3). These estimates are then used in a one-dimensional interpolation along the radial to arrive at the needed value within the measurement range-azimuth cell. The expression for linear bivariate interpolation in the plane is given by

$$\begin{aligned}
\bar{v}_R(r, s) = {} & \\
\frac{1}{\Delta_R\, \Delta_\delta} & \Big\{ (R - R_i) \Big[(\delta - \delta_j)\, \bar{v}_R\, (i+1, j+1) \\
& + (\delta_{j+1} - \delta)\, \bar{v}_R\, (i+1, j) \Big] \\
& + (R_{i+1} - R) \Big[(\delta - \delta_j)\, \bar{v}_R\, (i, j+1) \\
& + (\delta_{j+1} - \delta)\, \bar{v}_R\, (i, j) \Big] \Big\}, \qquad (22)
\end{aligned}$$

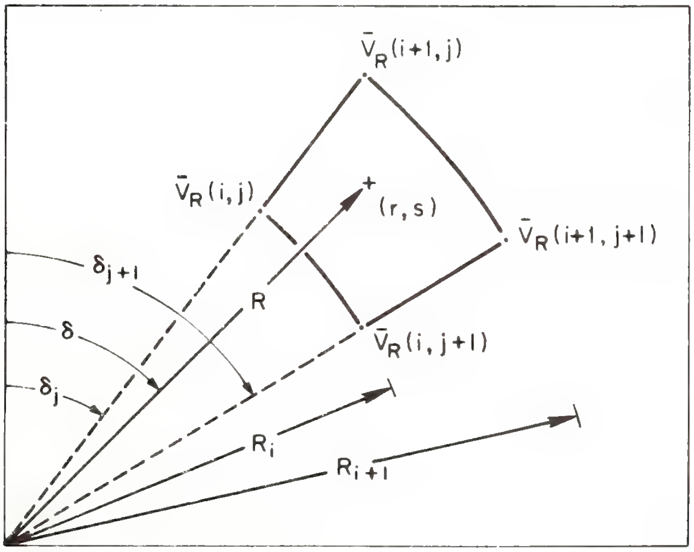

FIG. 3 Radar sampling grid for estimation of radial velocity at common r, s grid points in a plane.

where $R = \left[r^2 + (s - s_0)^2 \right]^{1/2}$ is the slant range, $\Delta_R = R_{i+1} - R_i$ is the radar range gate spacing, and $\Delta_\delta = \delta_{j+} - \delta_j$ is the azimuthal spacing in the plane. The indexing on v_R refers to the measurement locations shown in Fig. 3. Equation (22) is also the general expression for linear interpolation of any radar-measured field quantity to common grid points in the plane.

Continuity equation and the air-motion component normal to the plane

The third component of air motion, u_α, normal to the plane is obtained by integrating the mass continuity equation for an incompressible fluid (nondivergent, three-dimensional flow). In cylindrical coordinates the divergence of the vector air motion, **u**, is then

$$\nabla \cdot u = \frac{1}{r}\frac{\partial}{\partial r}(ru_r) + \frac{\partial u_s}{\partial s} + \frac{1}{r}\frac{\partial u_\alpha}{\partial \alpha} = 0. \tag{23}$$

Combining Eq. (23) with (16) and (17), the α-component of air motion at the nth plane becomes

$$u_\alpha(\alpha_n) \approx u_\alpha(\alpha_o) - r \sum_{k=0}^{n-1} (\alpha_{k+1} - \alpha_k) \left[\frac{(\mathrm{div}_\alpha\, \mathbf{v})_k + (\mathrm{div}_\alpha\, \mathbf{v})_{k+1}}{2} \right] + \sum_{k=0}^{n-1} \left\{ \frac{\left[\sin\alpha \frac{\partial}{\partial r}(r\bar{v}_t) \right]_k + \left[\sin\alpha \frac{\partial}{\partial r}(r\bar{v}_t) \right]_{k+1}}{2} \right\} \tag{24}$$

for $\alpha_{k+1} > \alpha_k$ and where

$$\mathrm{div}_\alpha\, \mathbf{v} = \frac{1}{r}\frac{\partial}{\partial r}(rv_r) + \frac{\partial v_s}{\partial s}$$

is the two-dimensional divergence of the two-dimensional particle velocity, (20) and (21), in the plane. When the lowest plane is at ground level and the ground is horizontal, the lower boundary condition requires $u_\alpha = w = 0$. If the lower bound of the summation does not coincide with the ground, or if the ground is not level, the u_α component need not be zero and consequently must be specified independently of the radar-derived quantities. Furthermore, Eq. (24) requires that the v_r, v_s, and $\bar{v}_t$ fields be stationary for the scan time of n planes. For reasonable scan times this amounts to perhaps 1-2 min. The two-dimensional divergence can be estimated by centered finite differences computed from four adjacent interpolation cells in a plane. For example, to determine the divergence at the point (r_i, s_j) in Fig. 4, we write

$$\mathrm{div}_\alpha\, \mathbf{v}\,(i,j) \approx \frac{1}{2\Delta} \left[\frac{r_{i+1}\, v_r\,(i+1, j) - r_{i-1}\, v_r\,(i-1, j)}{r_i} + v_s\,(i, j+1) - v_s\,(i, j-1) \right], \tag{25}$$

where $2\Delta = (r_{i+1} - r_{i-1}) = (s_{j+1} - s_{j-1})$, assuming a square grid of length Δ on a side. Note that Eq. (25) differs from the divergence estimate in Cartesian coordinates by the factor involving the distance away from the baseline. This is necessary to account for the divergence of the coordinate system in the r-direction.

The mean particle-fall velocity in Eq. (24) can be estimated by use of a fall velocity-radar reflectivity factor relation. Many such relations

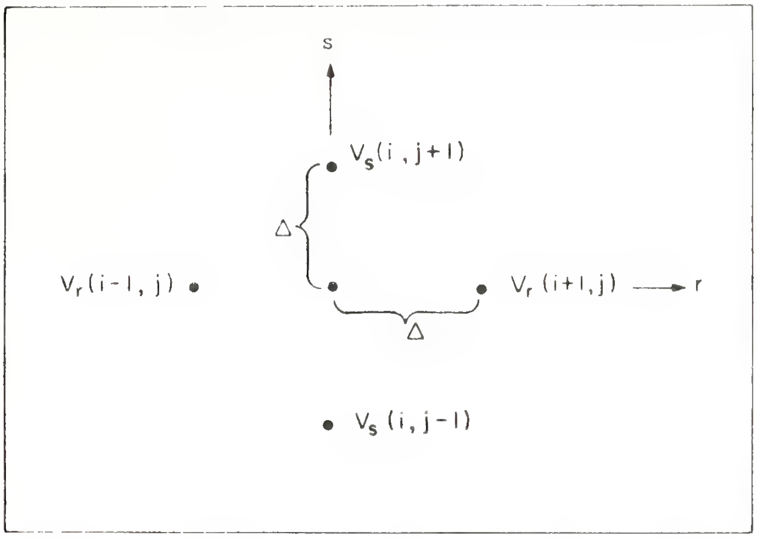

FIG. 4. Grid for centered-differences estimation of the two-dimensional divergence of the two-dimensional particle velocity in the plane.

exist in the literature and are summarized in Table 1. The radar reflectivity factor Z (proportional to total return power) is defined as the sum of the sixth power of diameters, D, per unit volume. For Rayleigh scatterers ($D \ll \lambda$ the radar wavelength, e.g., see Battan, 1973), $\bar{v}_t$ vs. Z relations can be derived (Rogers, 1964) by assuming a drop-size distribution and a fall speed-diameter relation and converting these to a theoretical velocity spectrum at vertical incidence. In the absence of vertical air motion the mean of this spectrum is related to Z. If any vertical air motion is present, the difference between the theoretical and measured Doppler mean velocity is this motion. Although the incremental return power in any particular velocity interval is not uniquely related to size at other than vertical incidence, the total return power is still related to particle sizes. The mean fall speed-reflectivity factor relation is therefore still a useful approximation. This relationship holds independently of the Doppler measure-

TABLE 1

Various Average Fall Speed-Radar Reflectivity Factor Relations of the Form $\bar{v}_t = aZ^b$ (Units of $\bar{v}_t$ are m sec^{-1} for Z in mm^6 m^{-3})

Precipitation type	*Source*	*a*	*b*	*Uncertainty (m sec^{-1})*
Stratiform rain	Rogers (1964)	3.8	0.071	±1
Thunderstorm rain	Sekhon and Srivastava (1971)	4.32	0.052	
Widespread rain	Lhermitte (1971)	2.0	0.087	±0.3
Rain (average of seven storms)	Joss and Waldvogel (1970)	2.6	0.107	±1

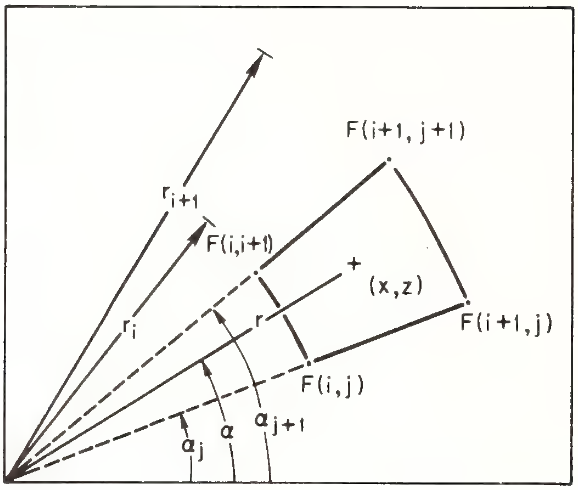

FIG. 5. Coplane grid at r, α locations used in the estimation of field values for transformation to Cartesian coordinate locations.

ments and is obtainable in a conventional, incoherent radar system capable of measurement of mean return power.

The first three entries in Table 1 are theoretical expressions based on a drop-size distribution of the form $N(D) = N_o e^{-\Omega D}$ (Marshall and Palmer, 1948). The fall velocity-diameter relationship used in each case was a best fit to the Gunn and Kinzer (1949) fall speed measurements. The Joss-Waldvogel relation is a best fit by eye to data from seven storms consisting of widespread, warm front, tropical shower, stratiform, or cold frontal thunderstorm rain. When little is known about the actual drop-size distribution, it is perhaps best to use the Joss-Waldvogel empirical relation. For measurements above ground level the fall velocity should be corrected for the change in air density. The right-hand side of the $\bar{v}_t$ vs. Z relation must be multiplied by the factor $(\rho_o/\rho)^{0.4}$, as suggested by Foote and du Toit (1969), where ρ is the air density at the observation point and ρ_o is the air density at ground level.

Interpolation to Cartesian components

Reorganization of the coplane velocity data into Cartesian coordinates requires an interpolation of this data and a conversion to Cartesian components. Linear bivariate interpolation in the xz-plane for any field value F at location x, z (see Fig. 5) can be written as

$$F(x, z) = \frac{1}{\Delta_r \Delta_\alpha} \Big\{ (r - r_i) \Big[(\alpha_{j+1} - \alpha) F(i+1, j) + (\alpha - \alpha_j) F(i+1, j+1) \Big] + (r_{i+1} - r) \Big[(\alpha_{j+1} - \alpha) F(i,j) + (\alpha - \alpha_j) F(i, j+1) \Big] \Big\} , \qquad (26)$$

where $\Delta_r \Delta_\alpha = (r_{i+1} - r_i)(\alpha_{j+1} - \alpha_j)$, $r = (x^2 + z^2)^{1/2}$ and $\alpha = \tan^{-1}(z/x)$. Interpolation in the y-direction is not needed since data are already at these grid locations. Equation (26) is applied to each of the coplane components which are then transformed according to (13), (14), and (15). Any other transformations such as a reorienting of coordinates along and perpendicular to the mean horizontal flow are easily done at this point.

Errors in the air motion estimates

The variance $\sigma^2(\bar{v}_R)$ of the estimated mean radial velocity derived from the Doppler velocity spectrum is a function of the variance σ^2 of the spectrum, signal dwell time NT (N is the number of time series samples and T is the repetition period of the radar), radar wavelength λ, and signal-to-noise power ratio SNR. This variance has been shown to be (Lhermitte and Miller, 1970)

$$\sigma^2(v_R) = \frac{\lambda\sigma}{4NT}\left(1 + \frac{1.6}{\mathrm{SNR}} + \frac{3}{\mathrm{SNR}^2}\right). \quad (27)$$

Equation (27) is based on the assumption that the spectrum is a colored spectrum from a Gaussian process contaminated by additive white noise. The spectral width must be smaller than the total unambiguous velocity range (folding at the Nyquist velocity $v_N = \lambda/4T$ due to sampling at a rate of $1/T$).

The variance of the Doppler spectrum consists of several independent components that depend on the meteorological conditions and on the parameters of the radar system. The variance can be expressed as

$$\sigma^2 = \sigma_B{}^2 + \sigma_A{}^2 + \sigma_T{}^2 + \sigma_S{}^2 + \sigma_D{}^2$$

where $\sigma_B{}^2$ is the variance resulting from the finite width of the radar beam, $\sigma_A{}^2$ is the contribution due to antenna rotation during the dwell time, $\sigma_T{}^2$ is the contribution from turbulent motions at scales smaller than the dimensions of the pulse volume, $\sigma_S{}^2$ is the spectral broadening resulting from wind shear, and $\sigma_D{}^2$ is the variance caused by the distribution of particle fall velocities due to their size distribution. At low elevation angles, $\sigma_T{}^2$ and $\sigma_S{}^2$ are the major contributors to σ^2. Typical values of the Doppler variance range from about 0.05 m^2 sec^{-2} for snow or chaff targets in weak shear ($< 10^{-4}$ sec^{-1}) to more than 9 m^2 sec^{-2} for rain in convective storms having moderate shear ($> 10^{-3}$ sec^{-1}). Using Eq. (27), typical values of $\sigma^2(\bar{v}_R)$ range from 0.01 to 0.2 m^2 sec^{-2} for a 1/8 sec dwell time and a SNR exceeding 10 dB.

Assuming that the random errors associated with the radar measurements at adjacent grid points are uncorrelated, the variance of $\bar{v}_R$ at r, s from interpolation is from (22)

$$\sigma_{rs}^2(\bar{v}_R) = \frac{\sigma^2(\bar{v}_R)}{\Delta_R^2\,\Delta_\delta^2}\left[(R - R_i)^2 + (R_{i+1} - R)^2\right] \left[(\delta - \delta_j)^2 + (\delta_{j+1} - \delta)^2\right]. \quad (28)$$

where all the variances at the radar measurement grid points are assumed to be equal. The variance of the radial velocity estimate has a value of 0.25 if r, s is in the middle of the radar measurement grid and a value of 1.0 at a sampling location. Since all values of R, δ are equally likely to occur, the expected value of the variance is the area average of $4/9\ \sigma^2(\bar{v}_R)$.

The variances of the v_r and v_s components are, from (20) and (21),

$$\sigma^2(v_r) = \sigma^2(\bar{v}_R)\left[\frac{R_1^2(s+d)^2 + R_2^2(s-d)^2}{9r^2d^2}\right]. \quad (29)$$

$$\sigma^2(v_s) = \sigma^2(\bar{v}_R)\left[\frac{R_1^2 + R_2^2}{9d^2}\right]. \quad (30)$$

Lines of constant normalized variance for the v_r and v_s components are shown in Fig. 6.

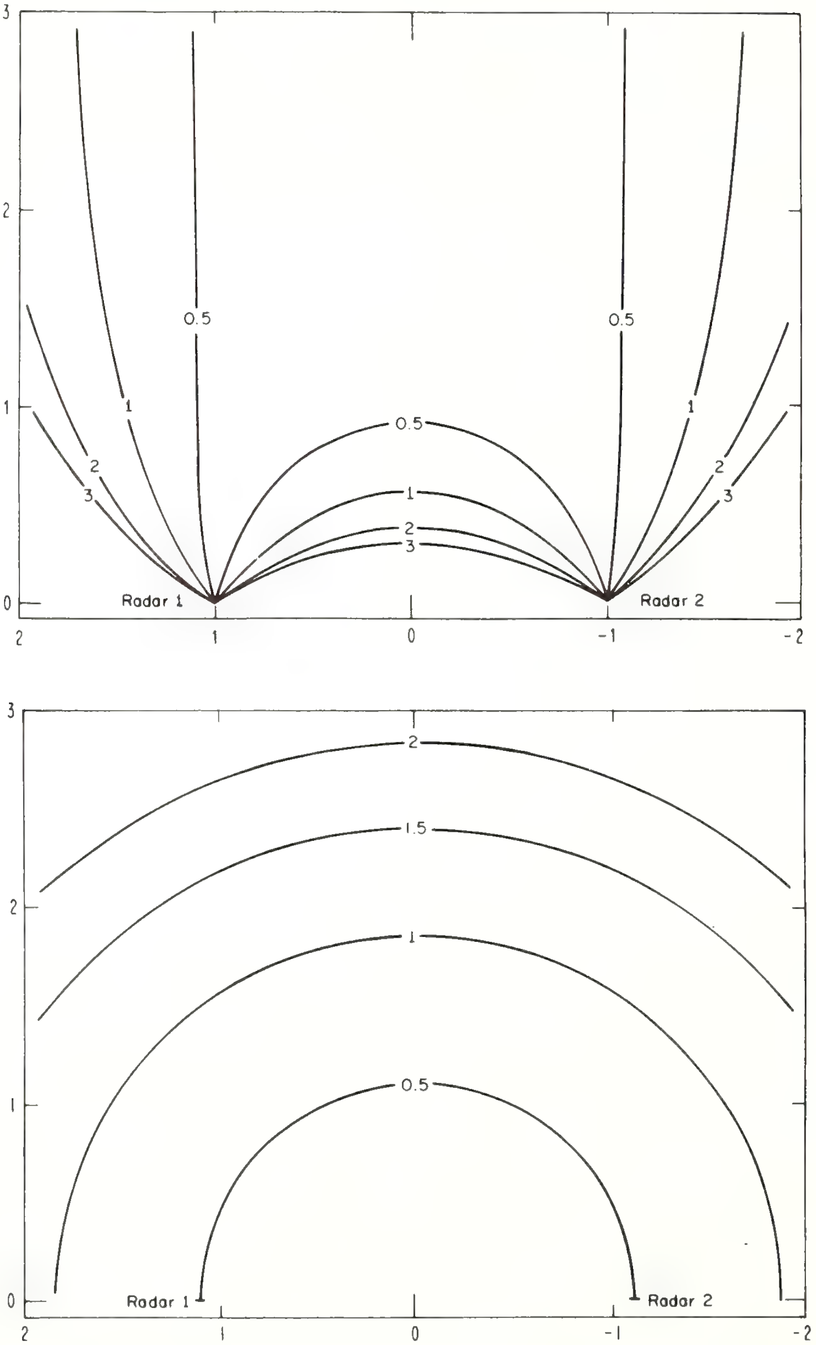

FIG. 6. Contours of constant normalized variances $[\sigma^2(v_r)/\sigma^2(\bar{v}_R)$ and $\sigma^2(v_s)/\sigma^2(\bar{v}_R)]$ for coplane particle velocity components.

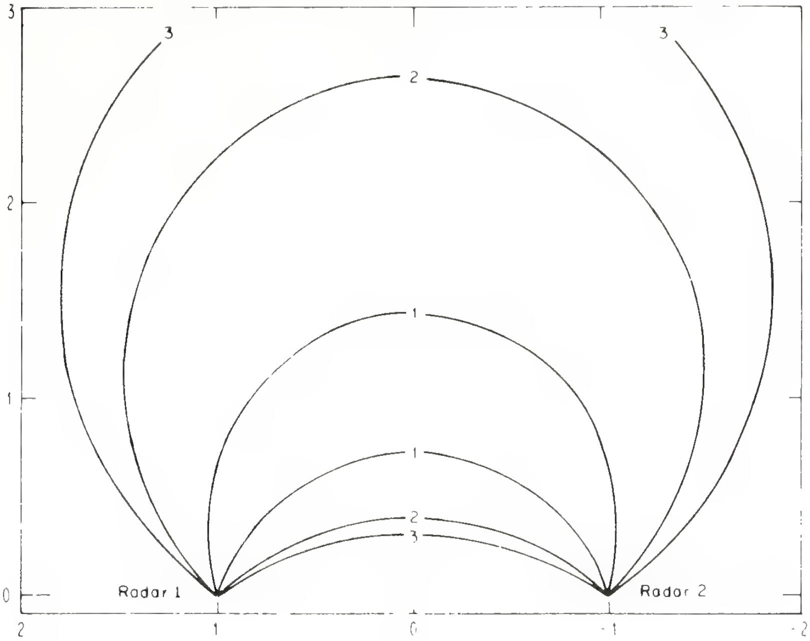

FIG. 7 Region of coplane scanning where the sum of the normalized variances of coplane components is less than a constant.

Equations (29) and (30) result when the random errors in the two radial-velocity estimates, $\bar{v}_{R1}$ and $\bar{v}_{R2}$, are assumed to be uncorrelated and equal. The latter assumption is true so long as the variance of the Doppler spectrum is independent of viewing direction. Significant wind shear across the radar beams negates this assumption and introduces a covariance term between $\bar{v}_{R1}$ and $\bar{v}_{R2}$. This covariance is a result of the relation between the variance of the mean velocity estimate and the variance of the Doppler spectrum in (27). The sum of Eqs. (29) and (30) can be used as a criteria for specifying the plane scan area where reasonable estimates of v_r and v_s are obtained. These regions are shown in Fig. 7. Data for dual Doppler analysis are acquired in the region $\sigma^2(v_r) + \sigma^2(v_s) \leqslant 16/9\ \sigma^2(\bar{v}_R)$. In this region, the angle between the two radar beam axes is between 45 and 135°.

Numerical integration of (24) results in a variance (see Fig. 8) of

$$\sigma^2(u_{\alpha_n}) \approx \frac{n\,\Delta_\alpha^2\, R_1^2\, R_2^2}{9d^2\,\Delta^2}\,\sigma^2(\bar{v}_R) \quad . \qquad (31)$$

for the α-component at the nth plane. The quantity Δ_α is the coplane tilt angle increment assumed to be the same between successive planes. Since values of v_r and v_s from the same grid location are not used in the centered finite difference technique of estimating divergence (25), there are no covariance terms involving v_r and v_s in the variance of u_α. Note that the variance of the velocity estimate derived from the continuity equation increases with each plane used in the summation. Furthermore, the expected values of the errors of all coplane velocity components are zero since we have assumed that there are no systematic errors. Equation (31) neglects the variance contribution due to fall

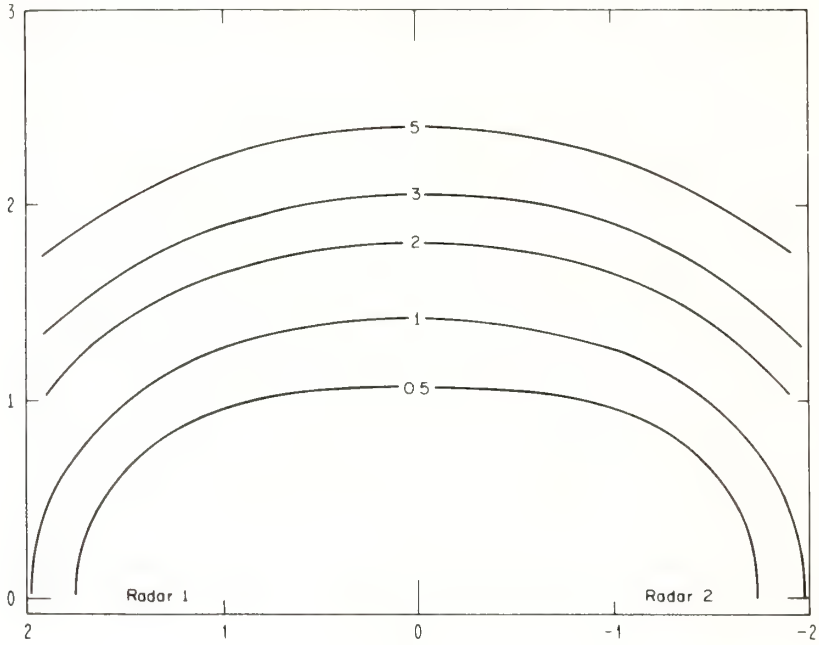

FIG. 8 Contours of constant normalized variance $[k^2 \sigma^2 (u_{\alpha n})/n\Delta_\alpha^2 \sigma^2 (\bar{v}_R)$ where $k = \Delta/d]$ of the air motion component normal to the plane at tilt angle α_n.

velocity since the sine-squared weighting at most angles ($< 15^\circ$) of interest will make $\sigma^2 (\bar{v}_t) \sin^2 \alpha \ll \sigma^2 (\bar{v}_R)$. The same is true for the variance of the air motion u_r in Eq. (16) so that (29) and (30) are approximately the variances of air motions in the plane.

Finally, we note that, although the random errors in the $\bar{v}_R$ estimates are assumed to be uncorrelated at adjacent measurement points and $\bar{v}_{R1}$ and $\bar{v}_{R2}$ are also assumed uncorrelated at the same point, the random errors in the v_r and v_s estimates are correlated. This is a consequence of their being derived from the same radar measurements, see Eqs. (20) and (21). The random errors in v_r (and v_s) may or may not be partially correlated at adjacent r, s grid points depending on whether or not the same measured values of $\bar{v}_R$ are used in the interpolation [Eq. (22)] of the radial velocity fields to common grid points. This correlation can be neglected if the interpolation and measurement spacings are comparable. Before transforming the coplane velocity components to Cartesian components, the coplane components are interpolated to Cartesian grid points according to Eq. (26). This results in a smoothing and subsequent reduction in the variances. Since all values of x, z are equally likely to occur, the expected value of the variance is the area average leading to a reduction in the variance by a factor of 4/9. Therefore, the variances of the Cartesian velocity components at Cartesian grid points are

$$\sigma^2 (u) \approx \tfrac{4}{9} \sigma^2 (v_r) \cos^2 \alpha + \sigma^2 (u_\alpha) \sin^2 \alpha, \quad (32)$$

$$\sigma^2 (v) \approx \tfrac{4}{9} \sigma^2 (v_s), \quad (33)$$

$$\sigma^2 (w) \approx \tfrac{4}{9} \sigma^2 (v_r) \sin^2 \alpha + \sigma^2 (u_\alpha) \cos^2 \alpha, \quad (34)$$

where α is the tilt angle through the x, z grid point.

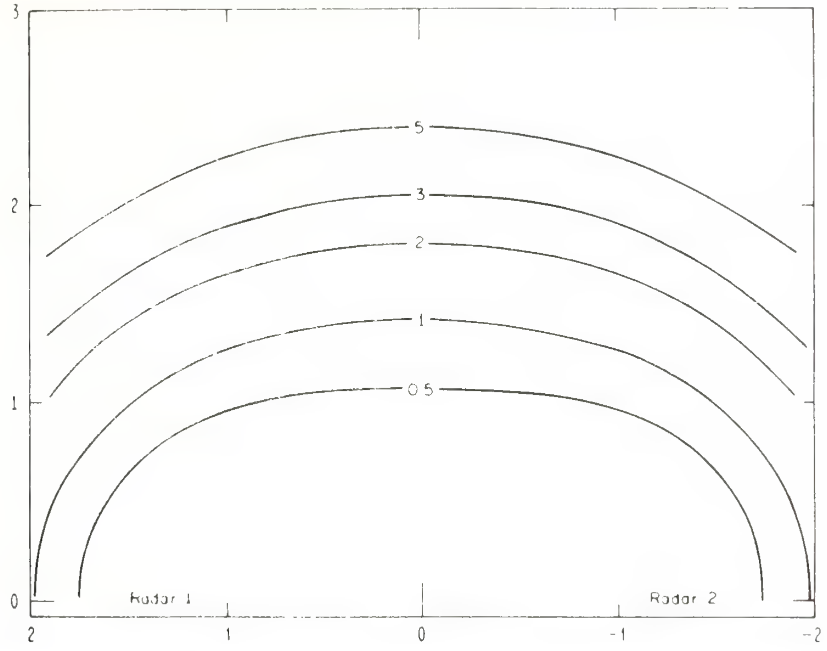

FIG. 8 Contours of constant normalized variance $[k^2\sigma^2(u_{\alpha n})/n\Delta_\alpha^2\sigma^2(\bar{v}_R)$ where $k = \Delta/d]$ of the air motion component normal to the plane at tilt angle α_n.

velocity since the sine-squared weighting at most angles ($< 15°$) of interest will make $\sigma^2(\bar{v}_t)\sin^2\alpha \ll \sigma^2(\bar{v}_R)$. The same is true for the variance of the air motion u_r in Eq. (16) so that (29) and (30) are approximately the variances of air motions in the plane.

Finally, we note that, although the random errors in the $\bar{v}_R$ estimates are assumed to be uncorrelated at adjacent measurement points and $\bar{v}_{R1}$ and $\bar{v}_{R2}$ are also assumed uncorrelated at the same point, the random errors in the v_r and v_s estimates are correlated. This is a consequence of their being derived from the same radar measurements, see Eqs. (20) and (21). The random errors in v_r (and v_s) may or may not be partially correlated at adjacent r, s grid points depending on whether or not the same measured values of $\bar{v}_R$ are used in the interpolation [Eq. (22)] of the radial velocity fields to common grid points. This correlation can be neglected if the interpolation and measurement spacings are comparable. Before transforming the coplane velocity component to Cartesian components, the coplane components are interpolated to Cartesian grid points according to Eq. (26). This results in a smoothing and subsequent reduction in the variances. Since all values of x, z are equally likely to occur, the expected value of the variance is the area average leading to a reduction in the variance by a factor of 4/9 Therefore, the variances of the Cartesian velocity components at Cartesian grid points are

$$\sigma^2(u) \approx \tfrac{4}{9}\sigma^2(v_r)\cos^2\alpha + \sigma^2(u_\alpha)\sin^2\alpha, \quad (32$$

$$\sigma^2(v) \approx \tfrac{4}{9}\sigma^2(v_s), \quad (33$$

$$\sigma^2(w) \approx \tfrac{4}{9}\sigma^2(v_r)\sin^2 a + \sigma^2(u_\alpha)\cos^2\alpha, \quad (34$$

where α is the tilt angle through the x, z grid point.

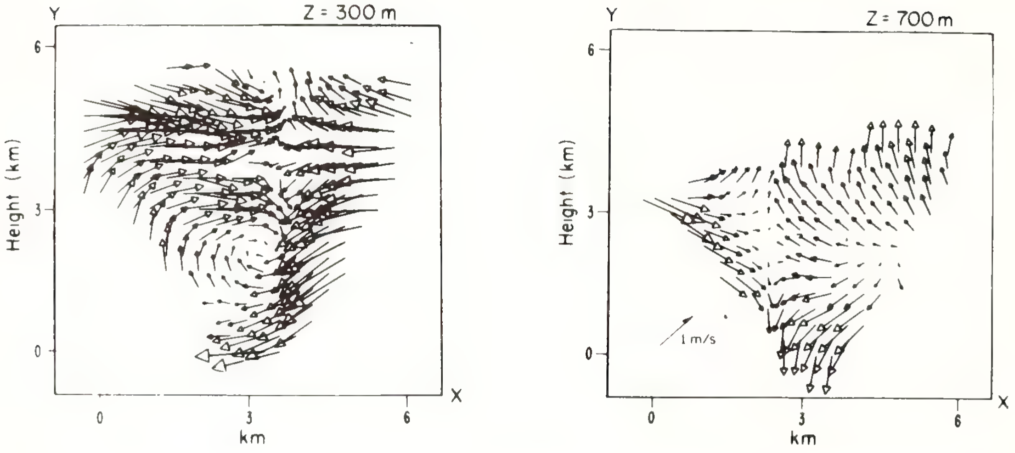

FIG. 10. Horizontal sections of air motion after subtraction of the mean flow in the lowest kilometer. The positive x-axis points in the direction of the mean flow.

Two horizontal cross sections of the spatial deviations from the mean flow are depicted in Fig. 10. These planes were at levels above the ground of 300 and 700 m. The mean flow is toward the positive x-direction. At the 300-m level there is an anticyclonic vortex upwind of the strong convergence zone. This convergence zone is shifted upwind at 700 m. The yz vertical cross sections shown in Fig. 11 are oriented normal to the mean flow and the xz vertical cross sections in Fig. 12 are oriented along the mean flow. Using the results from the previous section, we can estimate the maximum values of the variances of the wind field components. The variance of the estimate of the mean radial velocity is about 0.02 $\mathrm{m^2\ sec^{-2}}$, and the plane angles used were less than 15° so that

$$\sigma^2(u) = \sigma^2(v) < 0.01\ \mathrm{m^2\ sec^{-2}}$$

and

$$\sigma^2(w) < 0.15\ \mathrm{m^2\ sec^{-2}}.$$

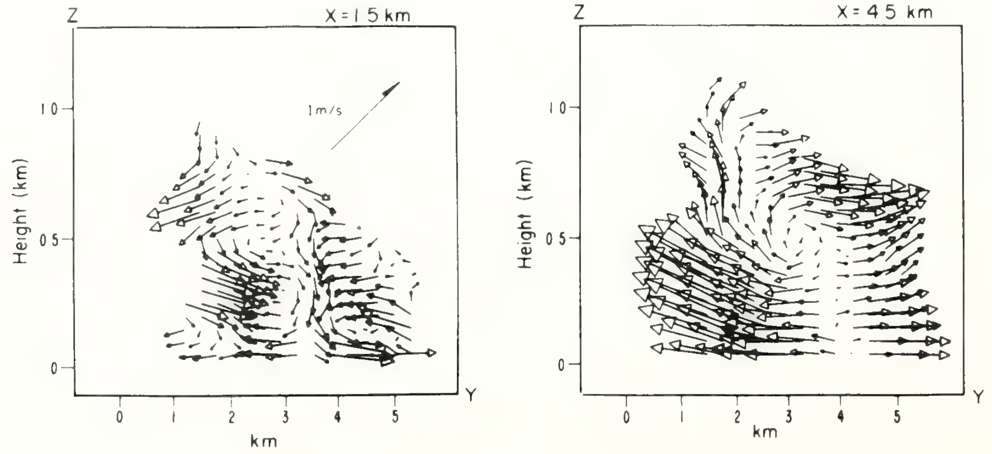

FIG. 11. Air motion in vertical planes oriented normal to the mean flow after subtraction of the mean.

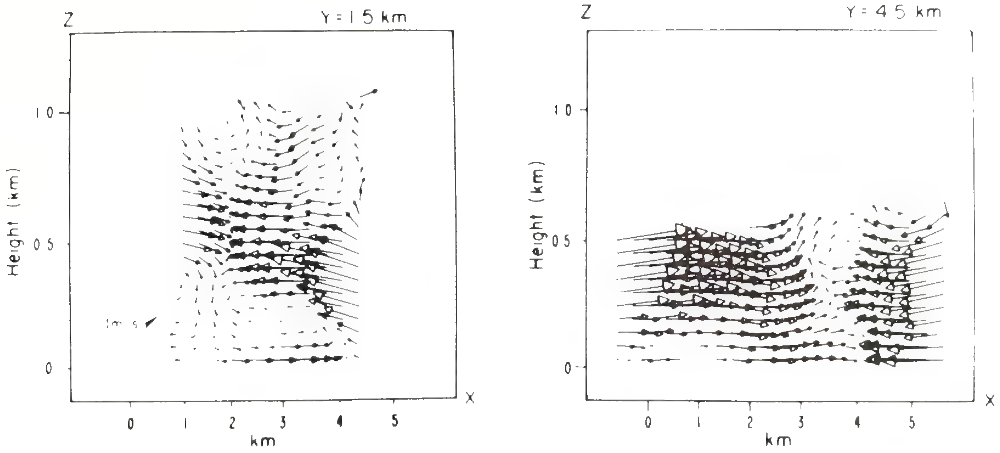

FIG. 12. Air motion in vertical planes along the mean flow.

Summary and concluding remarks

This paper has presented the COPLAN scanning and data reduction technique. The major assumptions implicit in the method are the following:

(a) Precipitating particles are tracers of the mean air motion.

(b) The reflectivity-weighted mean of the Doppler velocity spectrum represents the sum of the radial components of mean air motion and mean particle-fall velocity.

(c) Particle-fall speeds can be estimated from the measured radar reflectivity factor with sufficient accuracy for the coplane angles used.

(d) Linear interpolations of measured values to common grid points are valid.

(e) The mass continuity equation for an incompressible atmosphere is applicable at the scale sizes and heights observed by the radar.

(f) The velocity fields are stationary for the scan time of a series of n ($\sim$ 10-15) planes.

(g) The earth is assumed to be flat for the ranges ($<$ 40-50 km) covered by the two radars.

The preliminary results obtained in snow clearly demonstrate the potential of this method applied to dual-Doppler observations of atmospheric motion. No other technique presently exists whereby the meterologist and the atmospheric scientist can obtain such a complete and detailed picture of the spatial and temporal behavior of the air motion.

Compared to conventional radar-scanning methods, COPLAN scanning provides a more systematic and natural means of acquiring and reducing Doppler radar measurements of atmospheric motions. Short-duration scans of a single plane can be repeated at relatively long intervals thereby leading to a better assessment of the true temporal behavior of the circulation. Furthermore, interpolation schemes are simple two-dimensional rather than more involved four-dimensional ones thereby greatly simplifying the data reduction.

References

Battan, L. J. (1973), *Radar Observation of the Atmosphere*, Univ. of Chicago Press, Chicago.

Frisch, A. S., L. J. Miller, and R. G. Strauch (1974), Three-dimensional air motion measured in snow, submitted to *J. Atmos. Sci.*

Gunn, R., and G. D. Kinzer (1949), *J. Meteor.* **6**, 243-248.
Joss, J., and A. Waldvogel (1970), Preprint Vol., *14th Rad. Meteor. Conf.,* Am. Meteor. Soc., Boston, Mass., pp. 153-156.
Lawson, J. L., and G. E. Uhlenbeck (1950), *Threshold Signals,* McGraw-Hill, New York.
Lhermitte, R. M. (1971), *J. Appl. Meteor.* **10**, 234-246.
Lhermitte, R. M., and L. J. Miller (1970), Preprint Vol., *14th Rad. Meteor. Conf.,* Am. Meteor. Soc., Boston, Mass., pp. 133-138.
Marshall, J. S., and W. McK. Palmer (1948), *J. Meteor.* **5**, 165-166.
Miller, L. J. (1972), Preprint Vol., *15th Rad. Meteor. Conf.,* Am. Meteor. Soc., Boston, Mass., pp. 309-314.
Rogers, R. R. (1963), *J. Atmos. Sci.* **20**, 170-174.
Rogers, R. R. (1964), *Proc. 11th Wea. Rad. Conf.,* Am. Meteor. Soc., Boston, Mass., pp. 14-18.
Sekhon, R. S., and R. C. Srivastava (1971), *J. Atmos. Sci.* **28**, 983-994.
Srivastava, R. C., and D. Atlas (1972), Preprint Vol., *15th Rad. Meteor. Conf.,* Am. Meteor. Soc., Boston, Mass., pp. 297-302.
Wilson, D. A. (1970), *NOAA Tec. Report ERL 187-WPL13,* U.S. Gov't. Print. Off., Washington, D.C.

Received May 14, 1974

NOAA Technical Report ERL 329-WPL 39

May 1975

FM-CW BOUNDARY LAYER RADAR WITH DOPPLER CAPABILITY

R. G. Strauch, W. C. Campbell,
K. P. Moran, and R. B. Chadwick

A high resolution FM-CW microwave boundary layer radar has been equipped with Doppler processing. The Doppler velocity spectrum is obtained from each range resolution cell by computing the power spectrum of the signal obtained from a sequence of consecutive sweeps. Target range is measured from the signal frequency by the usual FM-CW analysis techniques. Target velocity is obtained from a measurement of the signal phase in each sweep. The velocity spectrum of meteorological (distributed) targets can be measured whereas previously only the mean velocity of point targets could be obtained from this type of radar. Results obtained with snow tracers using a variety of sweep parameters demonstrate that the Doppler spectrum is easily obtained by a microwave FM-CW radar for altitudes below 2 km.

NOAA Technical Report ERL 351-WPL 44

December 1975

METEOROLOGICAL APPLICATIONS OF THE FM DOPPLER RADAR

R. G. Strauch, W. C. Campbell, R. B. Chadwick, and K. P. Moran

Microwave FM-CW radars have been used for about 5 years to monitor the structure of atmospheric regions with large refractive-index fluctuations. We have recently devised a scheme that retrieves the Doppler velocity spectrum for each range resolution cell measured by an FM radar. In this paper we report initial results of meteorological measurements with this new capability and discuss its potential in remote sensing of the boundary layer.

Proceedings of Ninth AMS Conference on Severe Local Storms, 311-316, October 1975.

DETECTING TORNADIC STORMS BY THE BURST RATE NATURE OF ELECTROMAGNETIC SIGNALS THEY PRODUCE

William L. Taylor

NOAA/ERL
Wave Propagation Laboratory
Boulder, Colorado

1. INTRODUCTION

The development of an electromagnetic technique suitable for tornado detection was undertaken several years ago in the Wave Propagation Laboratory. Initial observations were made by Taylor (1972) during the 1969-1971 tornado seasons in cooperation with the National Severe Storms Laboratory. The results of this earlier work indicate: 1) that tornadic storms are generally associated with peculiar electrical activity characterized by many bursts of high sferic rates, 2) that the enhancement in burst rates is easily recognized only at observing frequencies above about 1 MHz, and 3) that the source of the sferics is not necessarily closely related to the tornado vortex (Taylor, 1973a). Sferics are electromagnetic signals from lightning which occur in groups or packets called bursts of a few hundred milliseconds duration. It was further concluded that the overall level of sferic activity, i.e., the manifestation of lightning activity, is closely related to the severity of a thunderstorm, which is in general agreement with the work of Hughes and Pybus (1970), Jones (1965), Lind et al. (1972), Scouten et al. (1972), Silberg (1965), and Stanford et al. (1971).

Preliminary results using burst-rate measurements to detect tornadic conditions have been reported by Taylor (1973b). These results showed that thunderstorms, as expected, produce the lowest burst rate, with hail, wind, and funnel clouds producing, in that order, increasing burst rates. Tornadic conditions were generally associated with a marked increased in burst rate relative to other severe storms, with average values in excess of 20 bursts per minute. It was concluded that most, but not all, tornadic conditions were associated with high burst rates; actually about 3 out of 4 tornadoes gave burst rates above 20 per minute. But a few severe storms, as well as some nonsevere thunderstorms, also have burst rates comparable to those associated with tornadic storms so that the "false alarm" rate was about 8 in 10.

This report will give a brief description of the electromagnetic detection equipment used during the 1972 and 1973 tornado seasons, show an example of a nominal equipment response during the period of a tornado, present results of the 1972 and 1973 observations, and give a preliminary view of the 1974 observations.

2. OMNIDIRECTIONAL DETECTOR

We developed an instrument to measure the sferic activity of thunderstorms as indicated by the sferics "burst rate," which is simply the number of clusters or groups of large-amplitude sferics occurring in a one minute period. The signals from a 1-meter long vertical monopole antenna were applied to a single-stage tuned-radio-frequency circuit with a center frequency near 3 MHz and a bandwidth of 10 percent. Two amplitude threshold levels were employed, and a burst was counted in each threshold circuit when the amplitude of a received signal was greater than the threshold level and the sferic rate exceeded 500 per second for a period greater than about 0.1 second. Burst rates were obtained from integrator circuits and presented to a multichannel event recorder to show when the burst rate exceeded 3, 10, 20, and 30 per minute. The data available consisted of eight channels of burst-rate information and one channel of time marks from a local clock.

Fifteen of these instruments, called omnidirectional tornadic storm detectors, were constructed. For the 1972 tornado season, February through August, these units were installed mostly at university and college facilities within or near "tornado alley". Amplitude threshold levels were adjusted to 5 V/m and 2 V/m, corresponding to nominal sferic amplitudes expected at ranges of 30 km and 70 km. For the 1973 tornado season, the units were installed mostly at National Weather Service Offices in the same general area covered by the 1972 observations. We increased the threshold levels to 7 V/m and 3 V/m during the 1973 season in an effort to reduce the number of "false alarms" relative to those observed during the previous year.

3. ANALYSIS AND RESULTS

3.1 Typical Detector Response

A good example of how a detector responds during typical tornadic conditions is shown in Figure 1. This record was obtained from the detector at the Oklahoma City National Weather Service Office at the Will Rogers World Airport during the period of the Union City, Oklahoma tornado on May 24, 1973. The number of bursts per minute during a 2-hour period is shown for the 70-km nominal-range threshold of 3 V/m

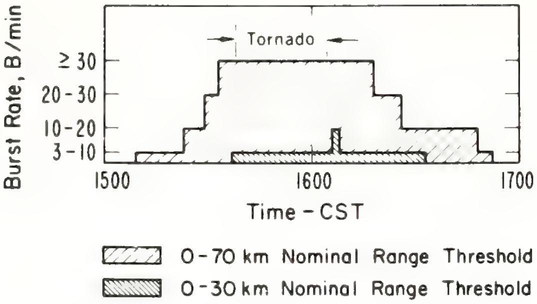

Figure 1. Detector responses during Union City tornado.

and the 30-km nominal-range threshold of 7 V/m. The time this tornado was observed on the ground is also indicated.*

Figure 1 shows that sferics exceeding the 70-km threshold produced burst rates greater than 3 per minute between 1510 and 1652 CST. (At no time during the 24 hours preceding and following this period was the minimum detector response burst rate of 3 per minute exceeded.) Beginning about 1520 CST the burst rate increased rather rapidly and exceeded 30 per minute at 1533 CST. The burst rate greater than 20 per minute, presumed to be indicative of tornado activity (Taylor, 1973b), was attained at 1529 CST, about 9 minutes before the tornado touched down. The burst remained above this 20 per minute "warning level" until 1625 CST. Very little activity was observed on the 30 km threshold records. The burst rate exceeded 3 per minute between about 1537 and 1622, but only for a brief 2-minute period around 1606 was the burst rate greater than 10 per minute.

The initial touch-down point of this tornado was about 40 km due west of our detector. The movement was toward the east-southeast, through Union City, and the tornado dissipated at a range of about 28 km. Figure 1 shows clearly that the sources of the bursts were within 70 km but greater than 30 km, since the burst rate for the 30-km threshold level was less than 3 per minute until after the tornado had formed, and the 70-km threshold level had indicated a burst rate exceeding 30 per minute. As the tornado moved closer to our detector there was a tendency for the burst rate of the 30-km channel to increase, and it actually did attain a burst rate between 10 and 20 per minute just after 1600. However, there were insufficient sources of electrical activity within the 30 km range to produce a burst rate greater than 20 per minute.

As the parent storm of this tornado continued to move closer to our detector, the burst rate continued to decrease, which indicated the enhanced electrical activity diminished rather rapidly shortly after the tornado dissipated.

3.2 Detector Response Evaluation

Analysis of the 1972 and 1973 data consisted of correlating the equipment responses 1) with the reports of thunderstorm activity from each National Weather Service Office where the equipment was located, 2) with the Severe Local Storms (SELS) Log from the National Severe Storms Forecast Center in Kansas City, and 3) with the Storm Data publications. An equipment response occurred when the burst rate exceeded 3 per minute. Verifications of selected weather conditions were also requested of the National Weather Service and subsequent corrections to the above reports were made.

Within the nominal 70 km range of the low threshold level, 509 electromagnetic equipment responses were recorded in 1973 compared with 542 during 1972. (The values for the 1972 season will be shown in parentheses for comparison.) Only 126 (225) of these responses corresponded to burst rates in excess of 20 per minute, which was presumed to be indicative of tornadic activity. Table I summarizes the 1973 (1972) results of the 3 V/m (2 V/m) low threshold level for activity within 70-km range. The difficulties of obtaining reliable severe weather observations should be noted. For example, a "funnel" report may in fact have been a tornado which touched down without being observed, or a wind, hail, or thunderstorm condition may have contained tornadic activity during the equipment response period although none was reported. Likewise, a tornado may not have actually existed during the time of a reported occurrence. The number of occurrences is the actual number of reported storm conditions within the nominal range for each threshold. The "no reports" storm condition was included to show the number of occurrences when the equipment indicated a burst rate greater than 3 per minute during periods of no reported storm activity within range. These no-report occurrences were produced probably by actual storms that were not reported, by local interference, or by equipment malfunction.

Table I

TORNADIC STORM DETECTOR DATA FOR 1973 AND (1972)
LOW THRESHOLD LEVEL - RANGE ≤ 70 km

STORM CONDITION	NUMBER OF OCCURRENCES	NUMBER ≥ 20/MIN	PERCENT ≥ 20/MIN
TORNADO	44 (41)	36 (34)	82 (83)
FUNNEL	70 (30)	11 (15)	16 (50)
WIND	63 (60)	16 (24)	25 (40)
HAIL	39 (54)	10 (26)	26 (48)
THUNDERSTORM	3461 (2738)	49 (121)	1.4 (4.4)
NO REPORTS	62 (41)	4 (5)	6.5 (12)
TOTALS	3739 (2964)	126 (225)	3.4 (7.6)

---

*Joseph H. Golden, private communication.

Another set of data from the high threshold level corresponding to a nominal range of 30 km is summarized in Table II. There were 183(238) equipment responses recorded during the year for this level, and 25(58) of these responses exceeded a burst rate of 20 per minute.

Table II

TORNADIC STORM DETECTOR DATA FOR 1973 AND (1972)
HIGH THRESHOLD LEVFL - RANGE ≤ 30 km

STORM CONDITION	NUMBER OF OCCURRENCES	NUMBER ≥ 20/MIN	PERCENT ≥ 20/MIN
TORNADO	15 (15)	9 (11)	60 (73)
FUNNEL	43 (10)	1 (4)	2.3 (40)
WIND	45 (20)	4 (4)	8.9 (20)
HAIL	26 (23)	3 (6)	11 (26)
THUNDERSTORM	641 (507)	7 (33)	1.1 (6.5)
NO REPORTS	12 (10)	1 (0)	8.3 (0)
TOTALS	782 (585)	25 (58)	3.2 (9.9)

The percentage of reported tornadoes resulting in an observed burst rate exceeding 20 per minute was slightly lower in 1973, but not significantly so. There was a noticable reduction in the percentage of other severe storms that produced burst rates above 20 per minute. The percentage of thunderstorms associated with more than 20 bursts per minute was substantially reduced.

Although only slightly fewer equipment responses were observed in 1973 relative to 1972, there were substantially fewer periods when the burst rate exceeded 20 per minute. The primary reason for this reduction in the occurrence of high-burst-rate periods is that the threshold level was set higher in 1973, in an effort to reduce the high false alarm rate caused primarily by local thunderstorms. This was quite successful, because the number of tornadoes attaining the warning level of greater than 20 bursts per minute (combining Tables I and II) remained identical at 45, while the number of false alarms dropped by more than a factor of two (from 238 to 106). The overall false alarm rate consequently dropped from about 8½ in 10 to only 7 in 10.

The effect of changing the threshold level is readily apparent upon viewing the cumulative distributions shown in Figures 2 and 3. These figures present the number of occurrences for which the burst rates exceeded the indicated values of 3, 10, 20, and 30 bursts per minute. The number of occurrences shown at the zero burst rate value is the total number of reported weather conditions within the particular observational range. Note 1) the rapid decrease in the number of thunderstorms indicated as the burst rate increases, 2) the slow decrease in the number of tornadoes as the burst rate increases, and 3) a generally intermediate decrease with burst rate for other severe storms.

Figure 2 shows the cumulative distributions for reported sources within a range of 30 km only. The nominal amplitude of signals from these storms was well above the low threshold level, and therefore a change in threshold from 2 V/m to 3 V/m should have little or no effect on the data. Indeed this is substantiated by the similarity in the distributions for each major weather condition. This similarity also indicates the burst rate characteristics of storms for the two years were essentially the same.

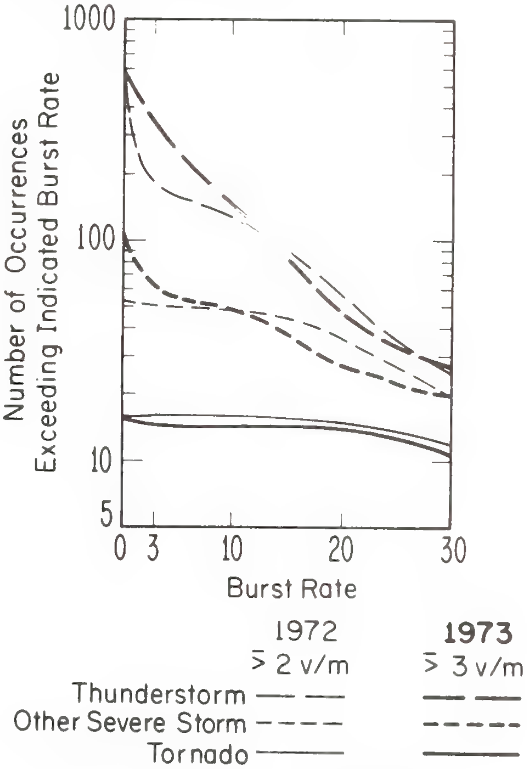

Figure 2. Cumulative distributions for sources less than 30 km range for low threshold.

The cumulative distributions shown in Figure 3 are for all sources within 70 km range. Since the nominal amplitude of signals from sources near 70 km is in the neighborhood of 2-3 V/m, we would expect to see some effect in the data upon changing the threshold level from 2 V/m to 3 V/m. So we see in this figure, for 1973 data (3 V/m) relative to 1972 data (2 V/m), a substantial decrease in the number of thunderstorms and a moderate decrease in the number of other severe storms that produced the higher burst rate values. The number of tornadoes with higher burst rates was actually greater for 1973. Therefore, the increase in threshold level during the 1973 season resulted in considerably fewer false alarms, i.e.,

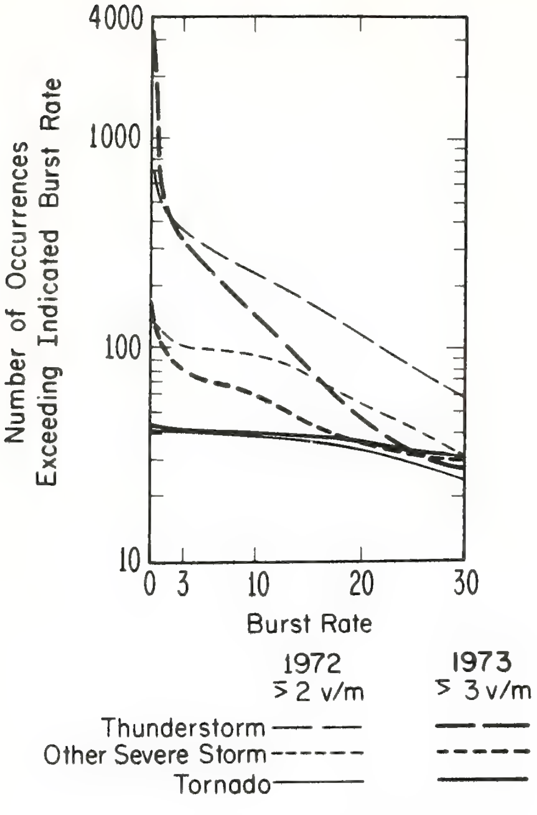

Figure 3. Cumulative distributions for sources less than 70 km range for low threshold.

warning level burst rates exceeding 20 per minute for nontornadic storms, without adversely affecting the number of tornadoes attaining the warning level.

The data contained in Figures 2 and 3 are presented in a different manner in Figures 4 and 5 to clarify some of the sferic burst rate characteristics. These figures show the number of tornadoes, other severe storms, and thunderstorms reported within a given range for which the tornadic storm detectors recorded burst rates within various intervals. It should be noted that the number of occurrences for tornadoes and other severe storms is presented on a linear scale while that for thunderstorms is on a logarithmic scale. It should also be noted that the data in Figure 5 were used to compile Table I.

If we initially disregard the burst-rate interval 0-3, which corresponds to weather events with no recorded equipment responses, we find a number of interesting aspects of these data by comparing the presentations for each year in both figures. Most noticeable is a rapid increase in the number of tornadoes partitioned into each burst-rate interval as burst rate increases. Next, there is essentially no difference in the numbers of other severe storms observed in the various burst-rate intervals. And then, there is a general decrease in the number

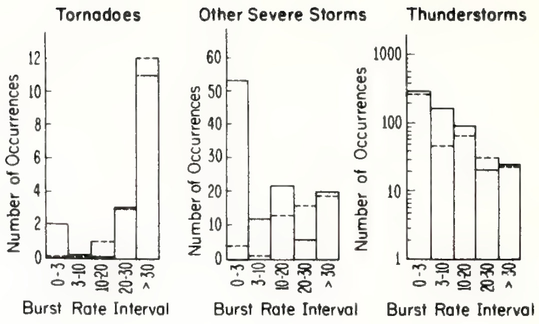

Range less than 30 km, 1972____ 1973____

Figure 4. Number of weather events partitioned into each indicated burst-rate interval for low threshold.

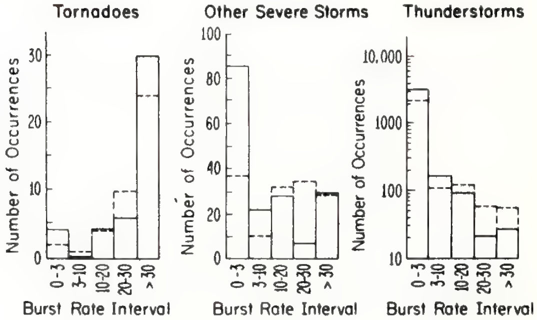

Range less than 70 km, 1972____ 1973____

Figure 5. Number of weather events partitioned into each indicated burst-rate interval for low threshold.

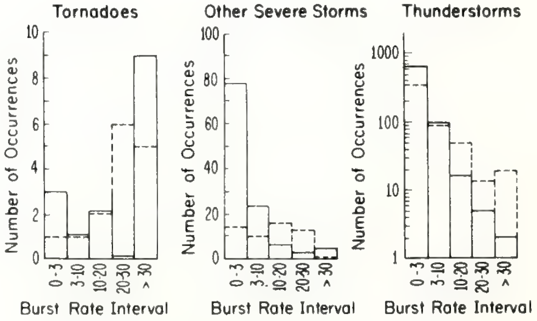

Range less than 30 km, 1972____ 1973____

Figure 6. Number of weather events partitioned into each indicated burst-rate interval for high threshold.

of thunderstorms producing burst rates within the higher intervals. No significant, systematic changes are evident between 1972 and 1973 in the distributions of burst rates of the tornadoes or for the other severe storms categories. However, in the thunderstorms category for range less than 70 km, there is a definite reduction in the number of occurrences for 1973 relative to 1972 at the higher burst rate intervals. This reduction was brought about at least in part by an increase in the threshold levels mentioned earlier as an effort to reduce the number of false alarms.

The data presented in Figure 6 contain the same reported weather conditions as found in Figure 4, but is an entirely different set of data since it was obtained from the high threshold levels, i.e., 5 V/m for 1972 and 7 V/m for 1973. Table II was compiled from the data in Figure 6. Characteristics of these data are similar to those in Figures 4 and 5 except that other severe storms show a general decrease in number of occurrences as burst rate increases. For the thunderstorm category, a very noticeable reduction in numbers is again observed in the higher burst rate intervals as a result of changing the threshold levels.

Now when we consider the 0-3 interval, we find a consistent increase in the number of occurrences for 1973 relative to 1972 for all weather categories in Figures 4, 5, and 6. This increase is caused partially by the reduction in the number of occurrences at the higher burst - rate intervals for other severe storms and thunderstorms. When the general trend of the number of tornadoes partitioned into each burst-rate interval is considered, there is a disproportionate number in the 0-3 interval for 1973 compared with 1972. This increased number of "tornadoes" in the 0-3 interval is the primary cause of the reduced percentage of tornadoes producing an alarm burst rate in 1973.

4. SECTOR-DIRECTIONAL DETECTOR

A second generation tornadic storm detector was designed and installed at 18 National Weather Service Offices during the 1974 tornado season. These directional detectors operated wideband over a frequency band extending from 10 MHz to 80 MHz and partitioned the received signals into eight 45° azimuthal sectors at an amplitude threshold of 0.5 V/m, and into a "local" category when the amplitude exceeded 2 V/m. Each detector indicated and recorded periods when the burst rates in each directional sector and in the "local" region exceeded 5 per minute and 15 per minute and periods when the burst rate was increasing. Data consisted of these 27 channels plus a time channel. A warning level was reached when one or more sectors indicated more than 15 bursts per minute. For data analysis, an equipment response was associated with the storm condition reported at that time only if the directions of the response and the storm corresponded.

5. ANALYSIS OF 1974 DATA

A preliminary analysis of the 1974 data was completed for seven locations where both the old omnidirectional detector and the new sector-directional detector were operational. Eleven tornadoes were reported within 70 km of these units. Warning level responses were associated with only 6 of these on the directional detectors and 7 on the omnidirectional units, corresponding, respectively, to 55 and 64 percent of the tornadoes producing a warning. A total of 16 alarm-level burst rates was recorded by the direction detectors while 42 were recorded by the omnidirectional units, resulting, respectively, in 62 and 83 percent of the alarms being false.

It seems rather clear, even with this limited number of tornado occurrences and equipment responses, that the two detector systems responded about equally to tornadic conditions, but the directional detector produced less than one-third the number of false alarms observed on the old omnidirectional unit. It should be remembered that these are tentative figures and the reported tornadoes have not been confirmed. Consequently, the percentage of actual tornadoes that we deteted will probably increase after clarification of weather conditons is received from the National Weather Service.

6. CONCLUSION

The primary purpose of our efforts during the past few years has been to develop an observational unit that will respond to peculiar electromagnetic signals from lightning discharge processes accompanying tornadic weather conditions. We have examined the feasibility of using sferic burst-rate measurements to supplement existing National Weather Service capabilities for warning of tornadic conditions. Ideally, of course, we would like to have a device that would warn of all tornadoes and give no false alarms. What we have found is that many, but not all, tornadic conditions were associated with high burst rates, and that some other severe storms, as well as some nonsevere thunderstorms also have burst rates comparable to those associated with tornadic storms. Coupled with these difficulties are the problems and limitations of obtaining accurate weather information, particularly in sparsely populated areas. From a practical point of view, perhaps warning for 75-80 percent of the reported tornadoes while holding the false-alarm rate to 1 in 2 or 3 will be the apparent limit in the accuracy of an electromagnetic tornadic storm detector. If this is the case, then we have closely approached that limit.

Early experience with the new directional detector led to a couple of modifications to the units prior to activation for the 1975 tornado season. First, the response to burst rates in each sector was changed from 5 and 15 per minute to 3 and 12 per minute, since 15 bursts per minute seemed a little too high for the tornadic-storm warning level. Second, the presence of short-term electrical and electromagnetic interference was a problem at some of the National Weather Service Offices at airport locations. A study of the nature of this interference led us to modify the detectors so that burst-rate activity was required to persist for several minutes before the unit responded and thereby greatly reduce, if not eliminate, the problems of local interference. Data from the early part of the 1975 season indicated these modifications were successful, and we hope that this year's observations will show a higher percentage of tornadoes producing a warning-level burst rate while further reducing the false-alarm rate.

7. ACKNOWLEDGMENTS

I wish to thank Harold Burdick and Joe Howard for much of the construction, installation, and maintenance of the detector units, Fred Guiraud for some of the design work on the directional detector, and Dave Reed for much of the data scaling and tabulation. Thanks also to the individuals in the National Weather Service, the National Severe Storms Forecast Center and the National Severe Storms Laboratory who have helped with their support. Especially I wish to thank the many people at the various National Weather Service Offices where the detectors were located without whose interest and efforts this work could not have been accomplished.

8. REFERENCES

Hughes, W. L. and E. J. Pybus, 1970: Severe storm sferics — stroke rate, Proc. 14th Radar Meteor. Conf., Amer. Meteor. Soc., Boston, Mass, 315-318.

Jones, H. L., 1965: The tornado pulse generator, Weatherwise, 18, No. 2, 78-80.

Lind, M. A., J. S. Hartman, G. S. Takle, and J. L. Stanford. 1972: Radio noise studies of several severe weather events in Iowa in 1971, J. Atmos. Sci., 29, No. 6, 1220-1223.

Scouten, D. C., D. T. Stephenson, and W. G. Biggs, 1972: A sferic rate azimuth-profile of the 1955 Blackwell, Oklahoma torando, J. Atmos. Sci., 29, No. 5, 929-936.

Silberg, P. A., 1965: Passive electrical measurements from three Oklahoma tornadoes, Proc. IEEE, 56, No. 9, 1197-1204.

Stanford, J. L., M. A. Lind, and G. S. Takle, 1971: Electromagnetic noise studies of severe convective storms in Iowa: The 1970 storm season, J. Atmos. Sci., 28, No. 3, 436-448.

Taylor, W. L., 1972: Atmospherics and severe storms, Chapter 17 of Remote Sensing of the Troposphere, V. E. Derr, Editor, Superintendent of Documents, U. S. Government Printing Office, Washington, D. C. 20402.

Taylor, W. L., 1973a: Electromagnetic radiation from severe storms in Oklahoma during April 29-30, 1970, J. Geophys. Res., 78, No. 36, 8761-8777.

Taylor, W. L., 1973b: Evaluation of an electromagnetic tornado-detection technique, Eighth Conference on Severe Local Storms, Denver, Amer. Meteor. Soc., Boston, Mass., 165-168.

Journal of Applied Meteorology 14, 524-539, June 1975.

Experimental Determination of Temperature Profiles by Ground-Based Microwave Radiometry

E. R. Westwater and J. B. Snider

Wave Propagation Laboratory, ERL, NOAA, Boulder, Colo. 80302

A. V. Carlson

Atmospheric Sciences Laboratory, U. S. Army Electronics Command, White Sands Missile Range, N. Mex. 88002

(Manuscript received 12 April 1974, in revised form 3 February 1975)

ABSTRACT

A one-week experiment was conducted to evaluate a dual-frequency microwave radiometer for recovering low altitude temperature profiles; the two-channel radiometer operated at 53.5 and 54.5 GHz. Meteorological support included radiosondes, helicopters, and an instrumented 150 m tower. Statistical inversion of 13 radiometer angular scan data sets resulted in an average rms error of 2.0 K up to 3 km for the microwave system. Significant features of thermal inversion structure were recovered. A continuous set of fixed-angle brightness observations correlated well with temperatures measured on the tower.

The statistical inversion method and the Backus-Gilbert method were applied to the analysis of the accuracy and the spatial resolution of the ground-based system. Model calculations were performed to estimate the effects of departures from horizontal stratification and of significant time variation in temperature structure during an elevation scan.

1. Introduction

Ground-based passive sensing of temperature profiles is an increasingly active field of research (Westwater, 1972a; Snider, 1972; Mount *et al.*, 1969; Waters, 1971; Miner *et al.*, 1972). In this paper we present the results of a one-week experiment designed to evaluate a dual-frequency microwave radiometric technique to retrieve thermal profiles. Participants in this experiment, held at White Sands Missile Range during the period 15–19 May 1972, were the Wave Propagation Laboratory of NOAA and the Atmospheric Sciences Laboratory of the U. S. Army Electronics Command.

Brightness temperatures were measured by a two-channel microwave radiometer operating at 53.5 and 54.5 GHz in a variable elevation angle mode. Retrieved profiles were compared with direct soundings of temperature structure made by radiosondes, helicopter flights, and temperature sensors located on a 150 m meteorological tower. Particular emphasis in the experiment was placed on the ability of the radiometric technique to recover significant features of low-altitude profiles, such as the height and intensity of ground-based inversions. In addition, it was considered important to differentiate between unstable and stable conditions by radiometric means. Consequently, the times at which soundings were made were chosen to insure that we observed the transition from nocturnal inversion to lapse conditions and vice versa.

To facilitate the data analysis and interpretation, various numerical studies are presented. To aid in interpreting profile retrievals, we studied vertical resolution via the Backus-Gilbert formalism, and expected error in retrieving via the statistical inversion method. Since tower temperature measurements occasionally indicated significant changes in the profile during an elevation scan, we computed these effects on the brightness angular spectrum for a few models.

2. Radiative transfer

Passive remote sensing of atmospheric profiles by radiometric techniques requires a functional relationship between measurements of radiant power and desired profile parameters. This relationship usually requires the solution of two problems in radiative transfer: (i) the direct problem; i.e., given the state of the atmosphere (temperature and composition profiles, etc), what is the radiant power?, and (ii) the indirect problem; i.e., given a set of radiation measurements, what is the state of the atmosphere? The solution of (ii) almost always requires the solution of (i). In this section we briefly review the formal solution to the direct problem, namely the radiative transfer equation, and discuss the uncertainties in calculations based on this equation.

The downward spectral brightness temperature T_{b_ν} emitted by a non-scattering atmosphere in local thermodynamic equilibrium is given by

$$T_{b_\nu}=(T_{b_\nu}^{\mathrm{ext}})\tau_\nu-\int_0^\infty T\frac{d\tau_\nu}{ds}ds, \tag{1}$$

where:

$T_{b\nu}^{\mathrm{ext}}$	brightness temperature external to the atmosphere (K)
τ_ν	transmission function
ν	frequency (GHz)
T	absolute temperature (K)
s	path length from surface to emitting volume (km).

In general, the transmission τ_ν is a strong function of atmospheric composition and depends only weakly on temperature. Microwave absorption in the clear atmosphere is due principally to rotational transitions of O_2 (0.5 cm) and H_2O (1.35 cm).

Although (1) represents the exact solution to the transfer equation, the functional dependence of τ_ν on atmospheric parameters must be specified before one can calculate T_{b_ν}, from radiosonde observations, for example. The absorption characteristics of a gas depend on such molecular characteristics as line strengths and positions, spectral line shape, foreign and self-collision broadening parameters, etc. The details of our calculations are given by Westwater *et al.* (1973). We use the Van Vleck-Weisskopf line shape with parameters for O_2 given by Carter *et al.* (1968), and parameters for H_2O given by Westwater (1967). The accuracy of the O_2 calculations is about 8%.

Because of the importance of an all-weather capability in a remote sensing system, the effect of clouds and rain should be discussed. As shown in Section 9, clouds showed small effect on the microwave measurements during the periods of measurement. In general, however, microwaves are affected by clouds in a manner that depends on the liquid water content and drop size distribution of the cloud (Westwater, 1972b). For nonprecipitating clouds, excellent possibilities exist to correct their effect on the total brightness temperature to give an equivalent clear air measurement. This might be achieved, for example, with a radiometer operating at say, 31 GHz, where the atmospheric emission is weakly affected by temperature and water vapor but is sensitive to clouds. A similar technique has been successful in separating water vapor and cloud emission observed from a satellite (Staelin *et al.*, 1973). The effect of rain, however, is large and would be difficult, if not impossible, to correct.

3. Inversion techniques and expected accuracy

The operational feasibility of radiometers as remote sensors of temperature profiles depends on the analytical technique used to extract profiles from radiance observations. As in many complex problems, there is no one "best" method for all situations. For example, iterative techniques that require large computer facilities would be impractical for a small field instrument whose purpose is to provide real-time profiles. On the other hand, a statistical technique allows great simplification for a real-time operation but requires a history of profiles that may not be available. In this section we discuss and compare inversion techniques that are later used in the analysis of radiometer data. A discussion of many mathematical aspects of the inversion problem is given by Westwater and Strand (1972). In addition, Colin (1972) has edited a compilation of profile inversion techniques in many fields of physics.

Statistical inversion techniques use radiation measurements to estimate, in some sense, most probable profile parameters. Although other estimation procedures are possible, we confine our attention to minimum variance estimation. Let **d** be an n-component vector of measurements (data) and **p** an m-component vector of profile parameters. For example, **d** could be a set of brightness temperatures and surface meteorological observations, while **p** could represent a temperature profile at m specified altitudes. Let the ensemble averages of a quantity V be $\langle V\rangle$ and the departure of V from its average be $V'=V-\langle V\rangle$. Furthermore, we denote the estimate of $\mathbf{V}'$ by $\hat{\mathbf{V}}'$. Then the minimum variance unbiased estimator of **p** as a linear function of **d** is (Deutsch, 1965)

$$\hat{\mathbf{p}}'=\langle\mathbf{p}'\mathbf{d}'^*\rangle\langle\mathbf{d}'\mathbf{d}'^*\rangle^{-1}\mathbf{d}'. \tag{2}$$

Here, the asterisk represents matrix transposition.

Our first inversion technique used (2) directly (see Section 9). We obtained an ensemble of 261 radiosonde profiles representing five years of May soundings at White Sands Missile Range. In contrast to many National Weather Service soundings, which are taken at 0000 and 1200 GMT, these soundings were more or less evenly distributed throughout 24 h. The brightness temperatures $\mathbf{T}_b$ at 53.5 and 54.5 GHz and 15 selected elevation angles were calculated as discussed in Section 2 for each profile in the ensemble. These 30 values plus surface observations of temperature T_0, pressure P_0 and humidity r_0 were combined to form a 33-component data vector $\mathbf{d}=[\mathbf{T}_b^*|T_0,P_0,r_0]^*$. The average of **d** was simply obtained by averaging each component over the ensemble

$$\langle\mathbf{d}\rangle\approx\frac{1}{N}\sum_{i=1}^{N}(\mathbf{d})_i, \tag{3}$$

where i refers to a member of the ensemble and N is the total number of profiles. The cross covariance matrix, $\langle\mathbf{T}'\mathbf{d}'^*\rangle$, between the temperature at m fixed altitudes and **d** was calculated by

$$\langle\mathbf{T}'\mathbf{d}'^*\rangle\approx\frac{1}{N-1}\sum_i(\mathbf{T}-\langle\mathbf{T}\rangle)_i(\mathbf{d}-\langle\mathbf{d}\rangle)_i^*. \tag{4}$$

In (4), we assumed experimental errors in **d** were uncorrelated with **T**. To calculate $\langle \mathbf{d}'\mathbf{d}'^* \rangle$ from past soundings in a way that could be applied directly to our experimental situation required knowledge of the noise properties of the radiometer. We assumed

$$\mathbf{d}=\mathbf{d}^{(\mathrm{atm})}+\boldsymbol{\varepsilon}, \tag{5}$$

where $\mathbf{d}^{(\mathrm{atm})}$ is the atmospheric contribution and $\boldsymbol{\varepsilon}$ the measurement error, and further, assumed that $\mathbf{d}^{(\mathrm{atm})}$ and $\boldsymbol{\varepsilon}$ were uncorrelated to get

$$\langle \mathbf{d}'\mathbf{d}'^* \rangle = \langle \mathbf{d}'^{(\mathrm{atm})}\mathbf{d}'^{(\mathrm{atm})*} \rangle + \langle \boldsymbol{\varepsilon}\boldsymbol{\varepsilon}^* \rangle. \tag{6}$$

We calculated $\langle \mathbf{d}'^{(\mathrm{atm})}\mathbf{d}'^{(\mathrm{atm})*} \rangle$ from our ensemble using an equation similar to (4). When we inverted radiometer data (see Section 9) the error matrix $\langle \boldsymbol{\varepsilon}\boldsymbol{\varepsilon}^* \rangle$ was estimated from assumed accuracy characteristics of the radiometer and surface observations.

The statistical inversion method allows an *a priori* estimate of the accuracy in remotely inferring profiles. As shown by Westwater and Strand (1968), this accuracy is a function of the number and kind of measurements, the instrument noise levels, and the statistical behavior of profile fluctuations. If we use minimum variance estimation, the residual, $\hat{\mathbf{T}}-\mathbf{T}$, has a covariance matrix given by (Morrison, 1967)

$$\begin{aligned}&\langle (\hat{\mathbf{T}}-\mathbf{T})(\hat{\mathbf{T}}-\mathbf{T})^* \rangle \\ &\qquad = \langle \mathbf{T}'\mathbf{T}'^* \rangle - \langle \mathbf{T}'\mathbf{d}'^* \rangle \langle \mathbf{d}'\mathbf{d}'^* \rangle^{-1} \langle \mathbf{d}'\mathbf{T}'^* \rangle. \end{aligned} \tag{7}$$

The square root of the *i*th diagonal element of this matrix represents the standard deviation of the inferred profile at the *i*th altitude. Figs. 1 and 2 show calculations of (7) for the data vector **d** of various combinations of brightness observations plus errorless surface measurements T_s, P_s, r_s. The noise matrix $\langle \boldsymbol{\varepsilon}\boldsymbol{\varepsilon}^* \rangle$ was assumed to be diagonal with brightness variance $=(1.0\ \mathrm{K})^2$. Fig. 1 compares the residual standard deviation using a total of 30 measurements at 53.5 and 54.5 GHz and 15 measurements at 53.5 GHz, with the *a priori* standard deviation about the mean temperature profile. The residual standard deviation is less than 1.4 K up to 3 km for the multi-channel radiometer. Fig. 2 shows theoretical results using the two single channels vs their combination. Note the 54.5 GHz channel gives consistently more accurate results at all altitudes than 53.5 GHz, while the combination gives moderately better results at all altitudes.

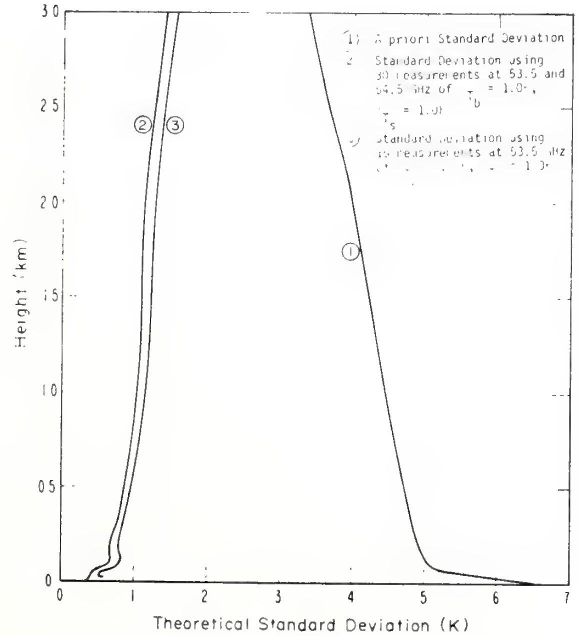

FIG. 1. Theoretical inversion accuracy for various combinations of input data.

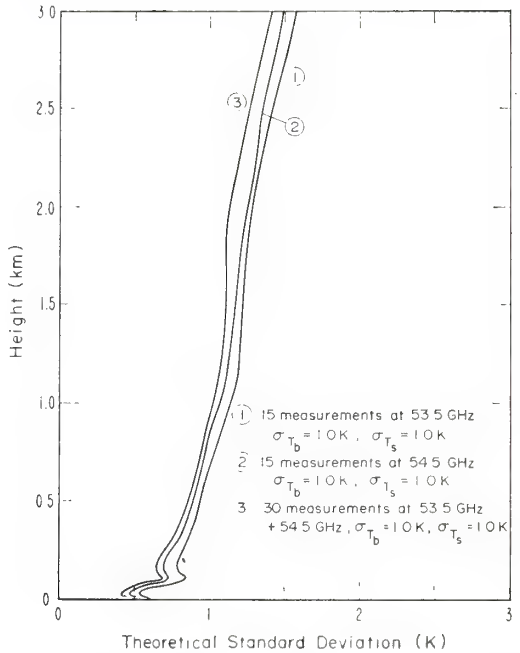

FIG. 2. Theoretical inversion accuracy for two microwave channels and their combination.

As discussed in Section 6, surface measurements were taken about 300 m from the radiometer location. We assume these locations could differ in temperature about 1.0 K and, for the remainder of this paper, we use this value to represent the noise level of the surface temperature observations. In many situations, however, accurate measurements of T_s at the radiometer location would be available. Fig. 3 shows theoretical standard deviations using errorless surface observations vs those of 1.0 K error. As is evident, the retrievals are affected only in the first 60 m above the surface.

The inversion equations (2)–(6) require initially a large amount of computer time. To reduce this time, Westwater (1972a) related a linear approximation of the brightness temperature [Eq. (1)] to the desired

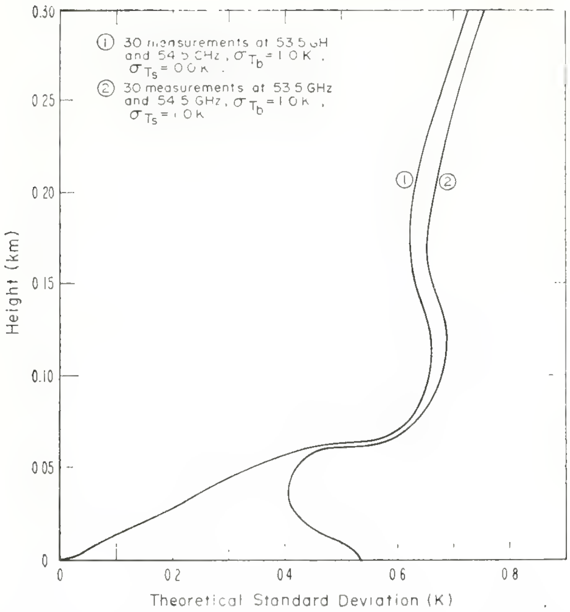

FIG. 3. Theoretical inversion accuracy with and without error in the surface temperature measurement.

profile fluctuations. This procedure requires calculations of brightness temperature and its derivative with respect to temperature, pressure and humidity for the average profile only. If we define the $n\times m$ matrix

$$(A_{\mathbf{T}})_{ij}=\left.\frac{\partial T_{b_i}}{\partial T_j}\right|_{\text{mean profile}} \tag{8}$$

with similar definitions for P and r, then the quantities required by (2) are given by

$$\langle\mathbf{T}'\mathbf{T}_b'^*\rangle\approx\langle\mathbf{T}'\mathbf{T}'^*\rangle A_{\mathbf{T}}^*+\langle\mathbf{T}'\mathbf{P}'^*\rangle A_{\mathbf{P}}^*+\langle\mathbf{T}'\mathbf{r}'^*\rangle A_{\mathbf{r}}^*, \tag{9}$$

$$\langle\mathbf{T}_b'\mathbf{T}_b'^*\rangle\approx A_{\mathbf{T}}\langle\mathbf{T}'\mathbf{T}'^*\rangle A_{\mathbf{T}}^*+A_{\mathbf{T}}\langle\mathbf{T}'\mathbf{P}'^*\rangle A_{\mathbf{P}}^*+\cdots$$
$$+A_{\mathbf{P}}\langle\mathbf{P}'\mathbf{P}'^*\rangle A_{\mathbf{P}}^*+\langle\boldsymbol{\varepsilon}\boldsymbol{\varepsilon}^*\rangle, \tag{10}$$

$$\langle\mathbf{T}_b\rangle\approx A_{\mathbf{T}}\langle\mathbf{T}\rangle+A_{\mathbf{P}}\langle\mathbf{P}\rangle+A_{\mathbf{r}}\langle\mathbf{r}\rangle. \tag{11}$$

In addition to the direct use of (2), we also used these approximate equations as an inversion algorithm after first calculating means and covariances of meteorological parameters with (2) and (4).

To compare initial computer time requirements for the exact and the approximate inversion algorithms, it can be shown that the total reduction in time achieved by the approximation is approximately $N/(6m)$, where N is the number of profiles. Thus, for five years of twice-a-day soundings, and for 25 height levels, the computer time would be reduced by a factor of about 25.

4. Spatial resolution

The statistical techniques are convenient in predicting the mean square error in an inferred profile as a function of instrument noise levels. Another important quantity is spatial resolution. Recent progress has been made in analysis of indirect sensing systems by the introduction of a quantitative measure of resolution (Backus and Gilbert, 1970). We will summarize below the portions of this theory that we apply to the ground-based temperature problem. A more complete discussion of the technique, as well as other applications, are given by Conrath (1972) and Westwater and Cohen (1973).

The value of a retrieved profile at a given point is representative of some kind of spatial average of the original profile. The effective width, or spread, of the interval over which this average extends is a convenient measure of resolution. If the value of the inferred profile at height h_0 is expressed as the integral of the product of the true function and an averaging kernel, $A(h,h_0)$, then the spread $s(h_0)$, as defined by Backus and Gilbert, is given by

$$s(h_0)\doteq 12\int(h-h_0)^2A^2(h,h_0)dh, \tag{12}$$

where the integral extends from the surface to the top of the atmosphere. This measure of resolution is normalized with the factor of 12 so that the spread of a rectangular averaging kernel with width l, height l^{-1}, and centered at h_0, is equal to l. Averaging kernels with suitable localization properties are constructed from the set of known weighting functions appropriate to the inverse problem.

To calculate the spread at various altitudes, we first must determine weighting functions. Ground-based microwave weighting functions $K_i(h)$ for retrieving temperature profiles are (approximately) given by

$$K_i(h)=[\alpha_{\nu_i}(h)/\sin\theta_i]$$
$$\times\exp\left[-\int_0^h\alpha_{\nu_i}(h')dh'/\sin\theta_i\right], \tag{13}$$

where the subscript i refers to a frequency-angle pair, α_{ν_i} is the absorption coefficient at frequency ν_i, and θ_i is the elevation angle. Fig. 4 shows selected weighting functions (in pressure units rather than height) appropriate to our choice of elevation angles and frequencies.

As Fig. 4 illustrates, the ground-based weighting functions achieve their maximum at the surface. It is not obvious whether linear combinations of these functions will achieve their maxima at higher altitudes and allow a certain degree of spatial resolution. To study this question, we determined from the basis set of 30 weighting functions the (minimum spread) averaging kernels and their associated spreads. The results of these calculations are shown in Fig. 5. Note the extremely narrow resolution near the surface and the broadening of these curves at higher altitudes. Even at 3 km, there is a degree of spatial resolution, although

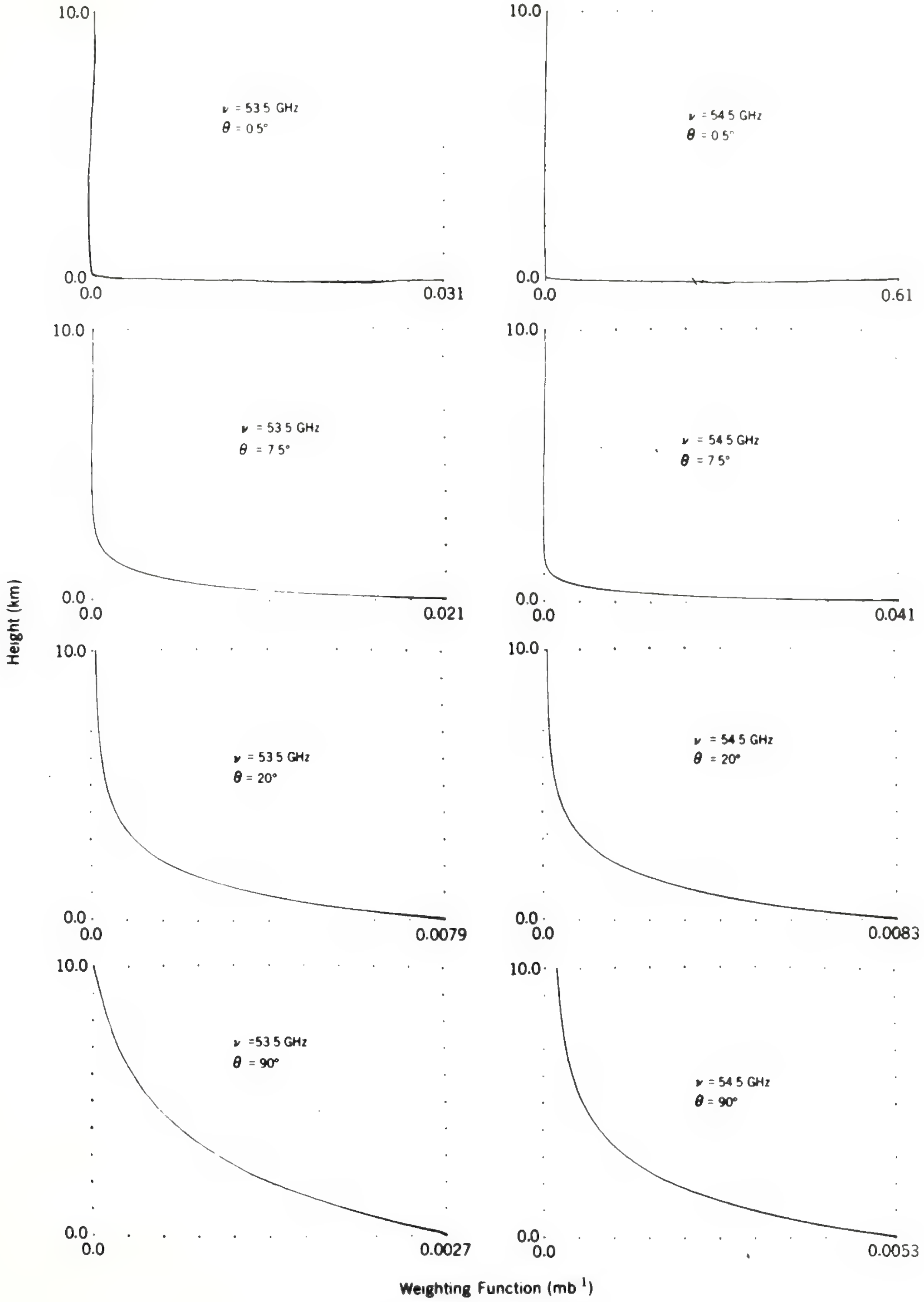

FIG. 4. Ground-based weighting functions at 53.5 and 54.5 GHz.

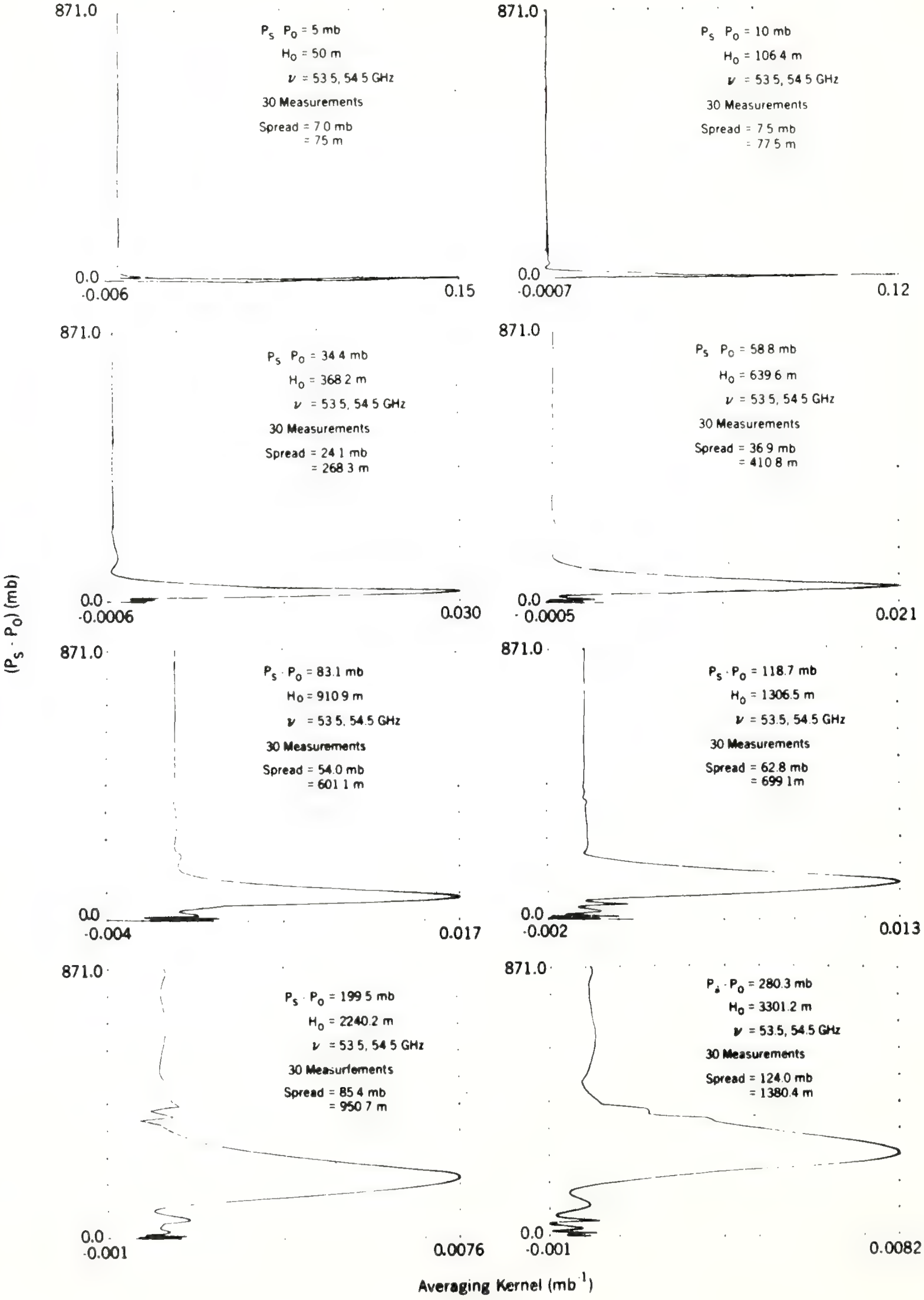

Fig. 5. Averaging kernels for 30 measurements at 53.5 and 54.5 GHz.

fine-structure of retrieved temperature profiles would be smoothed out.

5. Effect of departures from stratification and time stationarity

The angular scan technique of inferring vertical profiles requires horizontal stratification over the spatial region that contributes substantially to the brightness. In addition, since an angular scan requires a finite time to complete, substantial variations in the profile with time can affect the results. In this section, we present model calculations intended to estimate the order of magnitude of these effects.

The local terrain at the field site is uniform in all directions except for the Organ Mountains which lie about 15 km to the west. These mountains frequently induce wave phenomena which propagate downwind through the missile range. To simulate the effect of such a wave on the angular brightness temperature, we assumed a modified profile, $T(x,h)=T_0(h)+A\sin(2\pi x/L)$, where $T_0(h)$ is a standard profile, A the (constant) amplitude, L the wavelength, and x the horizontal coordinate. In Table 1 we show calculations of brightness temperature at 53.5 and 54.5 GHz for $T_0(h)$ as a lapse profile, with wave parameters $A=5.0$ K and $L=2.0$ and 20.0 km. Since the brightness temperature is approximately linear with temperature, numerical values for other choices of A can be estimated by scaling. For low elevation angles, we can compare the numerical results with those obtained from the analytical expression for δT_b when α is constant; namely

$$\delta T_b = A(k/\alpha)[1+(k/\alpha)^2]^{-1},$$

where $k=2\pi/L$. For $L=2.0$ and 20.0 km the values obtained from the analytical expression are 0.46 and 2.49 K at 53.5 GHz and 0.88 and 2.11 K at 54.5 GHz.

TABLE 1. Effect of horizontal temperature wave on brightness temperature [K] for $A=5.0$ K.

$$\delta T_b = T_b\left[T_0(h)+A\sin\frac{2\pi x}{L}\right]-T_b[T_0(h)]$$

Elevation angle (deg)	δT_b(53.5 GHz) L 2.0 km	20.0 km	δT_b(54.5 GHz) L 2.0 km	20.0 km
0.5	0.32	2.22	0.72	1.75
2.5	0.39	2.14	0.81	1.69
5.0	0.39	2.11	0.82	1.69
7.5	0.38	2.08	0.82	1.69
10.0	0.36	2.02	0.82	1.68
12.5	0.35	1.97	0.82	1.67
15.0	0.35	1.91	0.83	1.65
20.0	0.33	1.77	0.87	1.65
30.0	0.32	1.58	0.89	1.51
40.0	0.40	1.57	0.97	1.36
50.0	0.58	1.72	1.12	1.22
60.0	0.86	1.89	1.34	1.08
70.0	1.27	1.78	1.66	0.83
80.0	1.74	0.99	1.85	0.39
90.0	0.00	0.00	0.00	0.00
rms error	0.68	1.80	1.40	1.47

TABLE 2. Root mean square errors [K] to 3 km in statistical retrieval of profiles from brightness temperatures calculated from inhomogeneous atmospheres.

Radiometer noise level	Homogeneous atmosphere (lapse profile)	Temperature wave $A=5.0$ K $L=2.0$ km	Temperature wave $A=5.0$ K $L=20.0$ km	Homogeneous atmosphere (elevated inversion)	Cold front model (radiometer 1 km into front)
0.1	0.38	0.95	1.30	1.63	1.66
1.0	0.58	0.47	1.06	1.76	1.78

Another source of temperature inhomogeneity is frontal passage. We investigated a cold air mass moving under warm air with a large frontal slope of 1/50 and a temperature discontinuity across the front of 10 K. The brightness temperature difference between this model and the associated horizontally homogeneous profile depends on the position of the radiometer with respect to the front. With the radiometer 1 and 10 km into the cold sector, the maximum brightness difference exceeds 1 K at only one elevation angle; at 50 km this value had diminished to 0.4 K. These calculations suggest that the effect of departures from horizontal homogeneity induced by even an extreme frontal passage is small, except, perhaps, at the boundary of the front.

To estimate the effect of these departures from stratification on temperature profile recovery, we attempted to retrieve the vertical profiles above the radiometer from brightness temperatures calculated for the inhomogeneous models. For comparison each profile was also retrieved from the brightness temperature calculated from the associated homogeneous model. The results of inverting these data by the statistical technique assuming radiometer noise levels of 0.1 K and 1.0 K, are given in Table 2. As expected, the results for the lower noise level (0.1 K) are more sensitive to stratification errors. Since the statistical inversion equations are linear, the effect of inverting brightness data calculated from similar profiles with different magnitudes of inhomogeneity can be estimated by scaling.

As shown in Section 9, tower measurements occasionally indicated substantial (~4 K) variations of temperature structure during the time of an elevation scan (45 min). Two types of temperature variation occurred: oscillation about a mean value and a linear increase with time. To simulate the effect of such variations on the angular brightness spectrum, we computed the brightness for two cases: in the first, the temperature increased linearly with time a total of 7.5 K during a complete scan; in the second, we allowed $1\frac{1}{2}$ cycles of a sinusoidal variation of amplitude 4 K during the scan. These calculations, plus the brightness spectrum at time zero, are shown in Fig. 6. Note, in one case, the oscillatory behavior of the brightness curve about the spectrum present at time zero. This feature is present in several of the measurements discussed in Section 9.

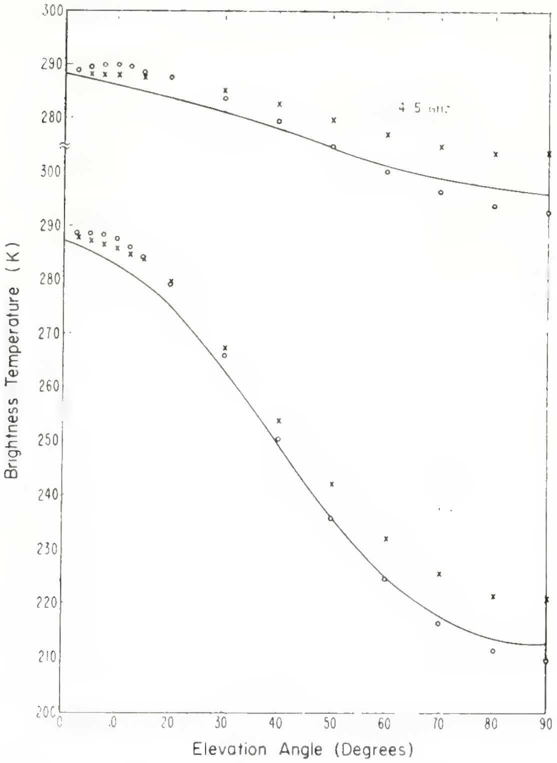

FIG. 6. Effect of time variation in temperature profile on angular brightness spectrum at 53.5 and 54.5 GHz: X's represent a linear increase in temperature with time (a total of 7.5 K during the scan); O's $1\frac{1}{2}$ cycles of a sinusoidal variation of amplitude 4 K during the scan

6. Experimental plan

Our general objective was to make ground-based remote measurements of the vertical atmospheric temperature profile using a two-channel microwave radiometer as a sensor. Profiles inferred from the radiometric data were to be compared with ground-truth information obtained by radiosondes, tower-mounted temperature sensors, and an instrumented helicopter. Our measurement site was Launch Complex No. 36 on White Sands Missile Range. The radiometer was located 500 m to the west and pointed slightly south of a 150 m instrumented tower. Radiosondes were released 300 m south of the line between the radiometer and tower while the helicopter measurements were made in an area generally south of the tower.

The radiometer measured antenna temperatures at 15 elevation angles ranging from 0° to 90°; since the dwell time at each angle was about 3 min, a complete upward scan required 45 min. A run always began at 0° elevation angle so that the radiometer would probe the lower layers of the atmosphere simultaneously with the launch of the radiosonde.

During radiometer measurements, temperatures were recorded on the tower while the helicopter measured temperature from the surface to approximately 1.5 km, and temperature at constant heights over a horizontal distance of about 8 km. The latter measurements were performed to detect departures from horizontal stratification; measurement heights were 30, 60, 150, 300, 450, 600, 900, 1200 and 1500 m. Helicopter height and position were plotted by a T-9 wind system radar.

Finally, standard surface weather observations of temperature, relative humidity, pressure and cloud cover were recorded at 30 min intervals; these data were recorded approximately 500 m southeast of the radiometer.

A primary task of our investigation was to study the ability of the radiometer to detect the presence and dissipation of temperature inversions. This requirement dictated to a large extent the measurement times; the times selected were 0500, 0800 and 1900 (all times MDT). The 0500 observation was the optimum time to detect inversions because of the strong radiation inversion characteristic of an arid region. The measurement at 0800 was selected because the radiation inversion would probably be in the process of breaking up due to solar heating of the surface and lower atmosphere. Finally, we decided to perform measurements at 1900 (approximately sundown) when the temperature profile could be expected to be in transition from the superadiabatic lapse rate typical of desert afternoons to a more nearly standard lapse condition.

7. Microwave radiometer

The microwave radiometer used to estimate temperature profiles is a two-frequency device designed and constructed in the Wave Propagation Laboratory. The system employs a switchable ferrite circulator which permits operation at two frequencies simultaneously; the system, in effect, consists of two individual switching radiometers (Dicke, 1946) connected to a common antenna and calibration system through a single switch. The radiometer is shown schematically in Fig. 7; a detailed description of the design and performance of the system is given by Snider (1974).

The antenna used with the radiometer is a conical horn reflector with 1.2 m aperture installed in an elevation over azimuth mount (Fig. 8). Antenna axes are individually controlled and the elevation and azimuth angles are displayed and recorded at the radiometer operating position. Antenna half-power beamwidth is approximately 0.3° at our operating frequencies. Primary polarization power patterns were measured to facilitate calculation of brightness temperature.

We derive brightness temperature from antenna temperature using a simple conversion factor based upon our measured antenna characteristics and a mean brightness profile calculated for the geographic area in which measurements are to be made. The process converts antenna temperature measured at a given elevation angle to a line value of brightness temperature at

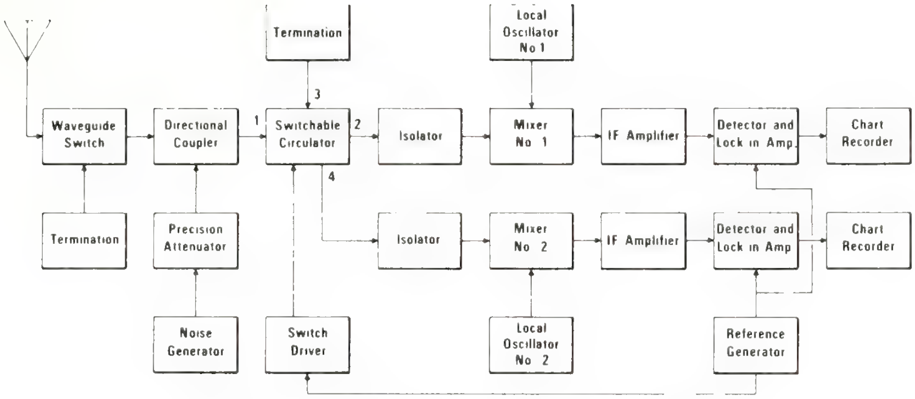

FIG. 7. Block diagram of two-frequency microwave radiometer.

the same elevation angle. We determine the conversion factor by numerically evaluating

$$T_a(\theta)=\frac{1}{4\pi}\int_{4\pi} G(\Omega)T_b(\Omega)d\Omega, \tag{14}$$

where $T_a(\theta)$ is the integrated antenna temperature at elevation angle θ and $T_b(\Omega)$ and $G(\Omega)$ are the brightness temperature and antenna gain in the direction of solid angle Ω. The mean brightness temperature profiles at our operating frequencies were computed from the history of White Sands radiosonde data described in Section 3. The conversion factor is the difference between mean brightness and the antenna temperature computed using (14). The brightness temperature measurements used as input to the profile retrieval algorithms are calculated from

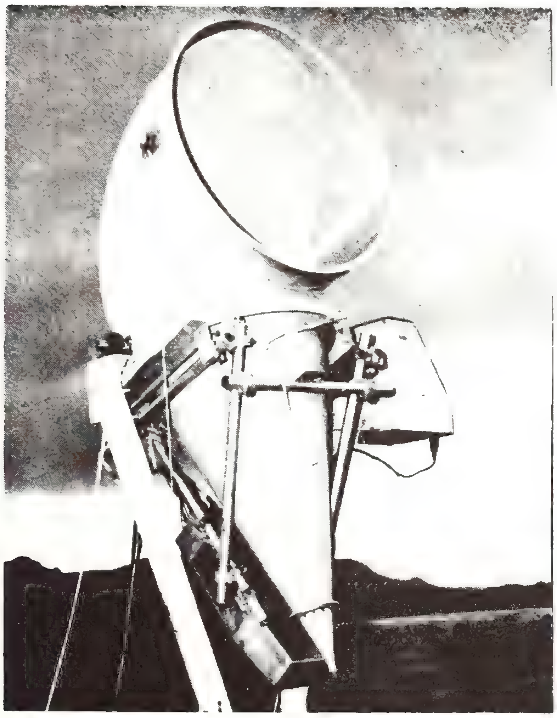

FIG. 8. The two-frequency microwave radiometer and its associated antenna.

$$T_{bm}(\theta)=T_{am}(\theta)+[T_b(\theta)-T_a(\theta)], \tag{15}$$

where $T_{bm}(\theta)$ and $T_{am}(\theta)$ are the measured brightness and antenna temperatures at elevation angle θ, and the quantity in brackets is the conversion factor.

We computed conversion factors using actual brightness profiles measured during the present experiment to estimate the possible error caused by using a mean brightness profile in (14). We found a maximum error of about 1 K for an intense surface-based inversion with the larger differences occurring at the lower elevation angles. The error when measuring a lapse profile was 0.5 K or less at all elevation angles. These calculations indicate that inferred profiles containing temperature inversions may be subject to slightly larger errors than lapse profiles. At the same time, the error is not of sufficient magnitude to justify use of more complex methods (e.g., integral equation inversion) to derive brightness temperature from antenna temperature.

Characteristics of the two-frequency radiometer are summarized in Table 3.

8. Meteorological instrumentation

Dry bulb temperatures were measured at eight levels on a 150 m tower: 4, 8, 16, 32, 60, 91, 122, 150 m.

TABLE 3. Two-frequency microwave radiometer characteristics.

LO center frequencies	53.5 and 54.5 GHz
IF passband (2 dB)	10 to 110 MHz
sensitivity ($\tau = 10$ s)	0.25 K
system noise figure*	11.4 dB
mixer noise figure	8.0 dB
antenna beamwidth (3 dB)	0.3°
estimated absolute accuracy	±3 K

* System noise figure is referred to the antenna input port.

TABLE 4. Root mean square difference [K] between measured brightness temperature and brightness temperature calculated from radiosonde data.

Date	Time	53.5 GHz	54.5 GHz
15 May	0515	3.41	2.21
	0815	2.53	1.69
	1937	2.63	1.96
16 May	0627	3.18	1.59
	0800	1.95	1.59
	1947	2.61	2.49
17 May	0516	3.29	4.07
	0800	2.90	1.63
	1935	2.44	1.97
18 May	0800	2.95	2.62
	1940	3.54	1.09
19 May	0510	2.43	2.62
	1000	3.27	1.16
rms difference for all measurements		2.92	2.19

TABLE 5. Average and root mean square difference [K] between measured and calculated brightness temperatures as a function of radiometer elevation angle.

Elevation angle (deg)	53.5 GHz		54.5 GHz	
	Average	rms	Average	rms
0	0	0	0	0
2.5	0.66	1.03	0.20	0.77
5	0.30	1.57	−0.40	1.01
7.5	0.04	2.00	−0.43	1.37
10	0.16	2.60	−0.63	1.64
12.5	0.32	2.67	−1.10	2.27
15	0.51	3.37	−0.94	2.44
20	1.78	3.42	−0.44	2.28
30	0.44	3.30	−0.46	2.77
40	0.69	2.69	0.08	1.97
50	−0.46	2.18	0.57	2.41
60	−1.99	2.74	0.14	2.02
70	−2.98	3.61	0.10	2.75
80	−3.95	4.50	0.07	2.36
90	−4.04	4.41	−1.54	3.18
All angles	−0.66	2.92	−0.34	2.19

Temperature sensors were copper-constantan thermocouples housed in aspirated radiation shields. Signals from the sensors were amplified at the tower and transmitted 680 m to a van where they were recorded on a digital tape recorder at a 10 Hz sampling rate. To reduce noise in the recorded temperatures, the sampled values were edited to remove each temperature that differed from the previous one by more than 1 K. The remaining samples were averaged over 1 min periods and then further smoothed by computing 10 min running averages; the latter values are plotted in Section 9.

Our radiosonde system was the standard rawin set AN/GMD1; temperature, humidity and wind data were recorded to a height of approximately 12 km above ground level. The radiosonde temperatures shown in Section 9 are significant level values.

A KIOWA helicopter contained sensors and recorders for air and soil temperatures; the latter quantity was measured with a downward looking infrared sensor. The air temperatures recorded on the helicopter are plotted in Section 9 with the profile comparisons.

9. Results

We now present the results of the measurements made at WSMR. We compare the brightness measurements with those calculated from theory, compare inferred and directly measured temperature profiles, and study the correlation between temperatures measured at various levels on the meteorological tower and microwave brightness measurements.

Thirteen temperature soundings using the brightness-vs-elevation-angle technique were made with simultaneous meteorological data. We first compare brightness temperatures calculated from radiosonde data (see Section 2) with measured brightness. Temperatures measured on the tower and helicopter are used as independent measures of the profile and its time variation rather than as input data for these brightness calculations. A summary of the measured and calculated theoretical brightness temperatures at 53.5 and 54.5 GHz is presented in Table 4 which lists the rms difference between measured and calculated quantities for the entire set of 15 elevation angles that comprise each run. Table 5 lists the average and rms difference between measurements and calculations as a function of antenna elevation angle; the averages are also shown in Fig. 9. A few individual sample comparisons are

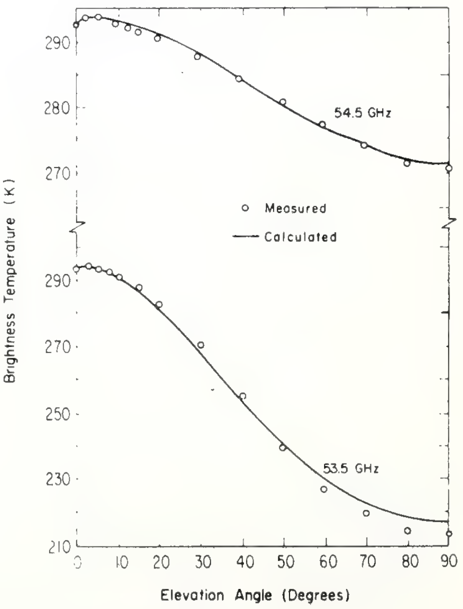

FIG. 9. Averages of measured and calculated microwave brightness for 13 profiles.

given in Figs. 10–12 which also include profile inversion results and meteorological tower temperatures that are discussed below.

Referring to Fig. 9 and Table 5, we see that agreement between measured and calculated brightness temperatures is good at 54.5 GHz and for elevation angles below 50° for 53.5 GHz. Some of the average disagreement between measurements and calculations may be caused by using an incorrect value for the stray antenna noise temperature as discussed in Section 7. Another possible cause, and one that would result in larger differences at the higher elevation angles, is incorrect absorption coefficients for H_2O and O_2.

Other possible sources of error, particularly during individual soundings, are departures from horizontal stratification and significant variation of the temperature profile during the time of measurement. The former did not seem to be important during this experiment since constant altitude helicopter flights (up to 1.5 km) indicated temperature variations of less than 1 K over a horizontal distance of ~ 8 km. Similar observations during much more extreme surface temperature differences than we encountered were reported by Businger and Frisch (1972). They measured surface temperature differences of 20 K over an extended area. However, at 30 m, maximum differences in air temperature were less than 3 K over ~ 10 km and at 100 m, the air temperature was homogeneous. We also grossly estimated the upper air horizontal temperature gradient from National Weather Service daily records of the 500 mb height contours. These records indicated maximum gradients of average temperature (to 500 mb) of less than 2×10^{-3}K km^{-1} during the week of the experiment.

As shown by the tower measurements, significant temporal variation of the temperature profile did occur at various times. Some of these cases will be discussed in detail later in this section.

Another source of error is the smoothing of low-altitude structure by the radiosonde. In several instances, the tower temperature measurements showed much more structure in the boundary layer than did the radiosonde. In all but one case, the first significant level that was reported by radiosondes was at least 100 m above the surface, while frequently much of the structure was actually below 30 m. Calculations of brightness using tower data spliced with radiosondes differed by as much as 1.5 K from those using only radiosonde data.

The cloud cover seen by the antenna main lobe during each temperature sounding was photographed and classified for subsequent qualitative estimates of effects upon the measurements. In general, cloud heights and estimated water content were such that contamination of the brightness data by cloud emission is believed to be extremely small.

We have enumerated some of the possible reasons for the observed differences in theory and experiment to indicate several limitations and uncertainties that remain in remote sensing of temperature profiles. For our immediate problem, the observed differences represent the measurement accuracy with which we must contend when estimating the temperature profile from a set of brightness data. On the basis of the average departure between measurements and theory, we have assigned a noise level of 1.0 K to the radiometer, i.e., the experimental error ε in (4) attributable to the radiometer is 1.0 K. Although the rms differences were larger than this, we felt that this larger variance was due to time variation of the profiles and did not represent radiometer error.

Temperature profiles were estimated from the brightness measurements by two methods: (a) the "exact" inversion algorithm employing Eqs. (2) through (6); and (b) the "approximate" method using Eqs. (3), (4), and (8) through (11). Input radiation data for the former method were the set of 30 measurements recorded at 53.5 and 54.5 GHz and the 15 angles listed in Table 5. The individual sets of 15 values measured at each frequency were the input data to the "approximate" inversion method; the limitation of 15 pieces of input data for the approximate method is the result of insufficient computer storage space. The statistical base from which regression coefficients, means and variances, etc. (required by both inversion algorithms) were computed, was the 5 year ensemble of WSMR radiosonde data mentioned in Section 3. The ensemble and the inversion results are independent of the 13 radiosonde profiles taken during 15–19 May 1972.

We present selected results of our profile retrievals beginning with Figs. 10–12. Part (a) of each figure shows the temperature profile (open circles) estimated by the exact procedure while the profiles measured by the radiosonde (solid line) and helicopter (crosses) are shown for comparison. The curves in part (b) present similar results for the approximate technique except that here the circles and crosses represent inferred temperatures from 53.5 and 54.5 GHz input data, respectively. The cloud type prevalent during each profile measurement is shown in parts (a) and (b). Part (c) shows measured (circles) and theoretical (lines) brightness temperatures corresponding to each inverted profile. Finally, tower temperature measurements are shown in part (d).

Fig. 10 illustrates the effect of a time-varying profile on the brightness spectrum. The first four measurements, 0° to 7.5°, were taken from 0515 to 0524 MDT 15 May 1972 while the inversion profile changed little with time. After calibration at 0527, the remaining measurements were made every 3 min from 0530 to 0600. As shown in (d), the low-altitude profile decreases to a minimum about 0545, then increases to a relative maximum again at 0600. As seen in (c), the brightness spectrum is in reasonable agreement with this trend, particularily at 54.5 GHz. The retrieved profiles, (a) and (b), reflect this feature by being close to the profile

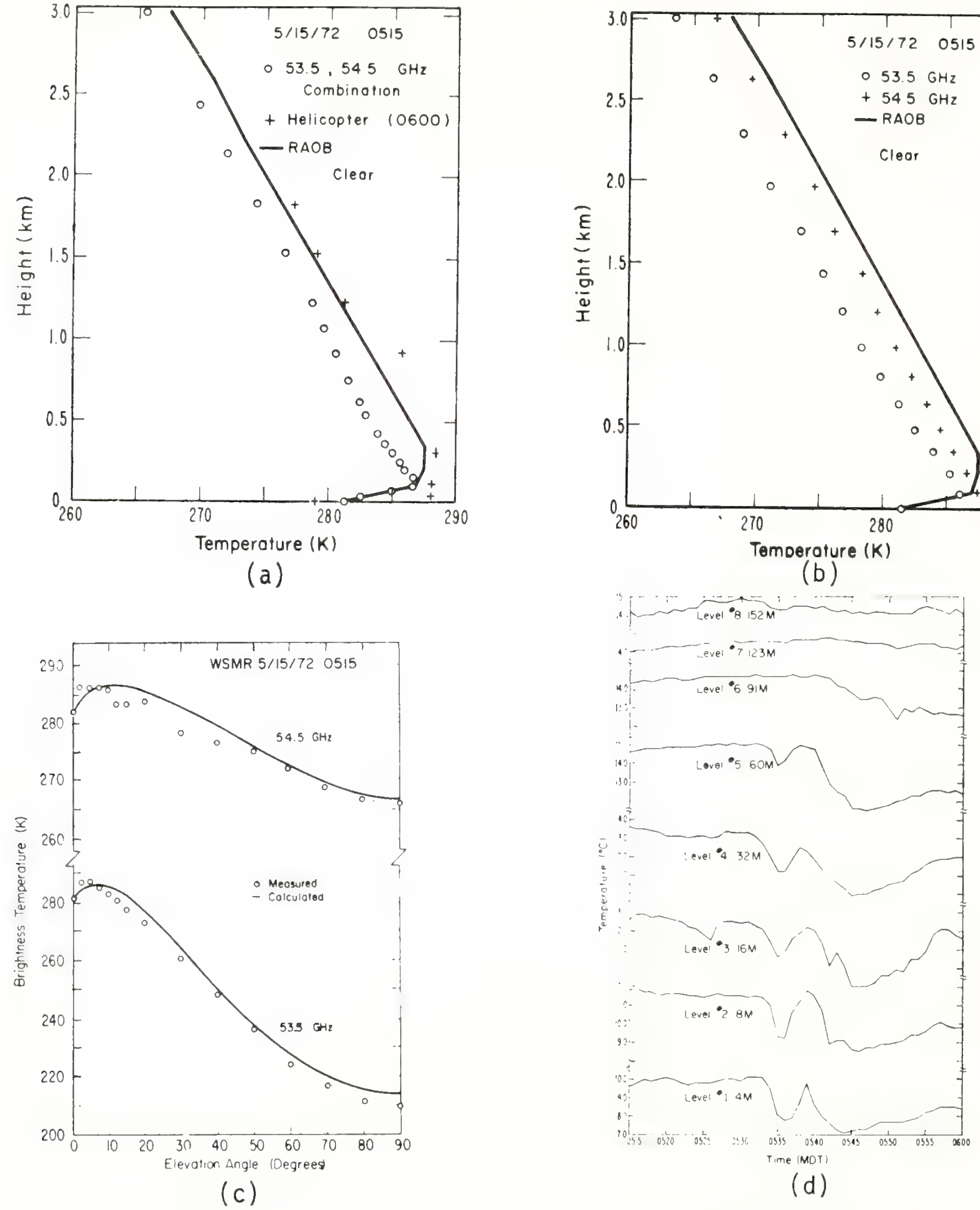

FIG. 10. Statistical inversion results for sounding begun 0515 MDT 15 May 1972. (See text for details.)

in the first several meters and then, at higher altitudes, become colder than the radiosonde profile.

Fig. 11 shows a profile retrieval from brightness measurements taken while the thermal profile (except for the first 8 m) changed little with time. The agreement between measurements and calculations is good, except for the angles above 60° at 53.5 GHz. The retrieved profiles well represent the radiosonde profile, particularly the retrieval obtained with 30 measurements.

The final case we present (Fig. 12) is an intense ground-based inversion. As is evident from the figure, the salient features of the thermal profile are well represented by the retrievals. Note that the retrieved profile is consistently warmer than the radiosonde pro-

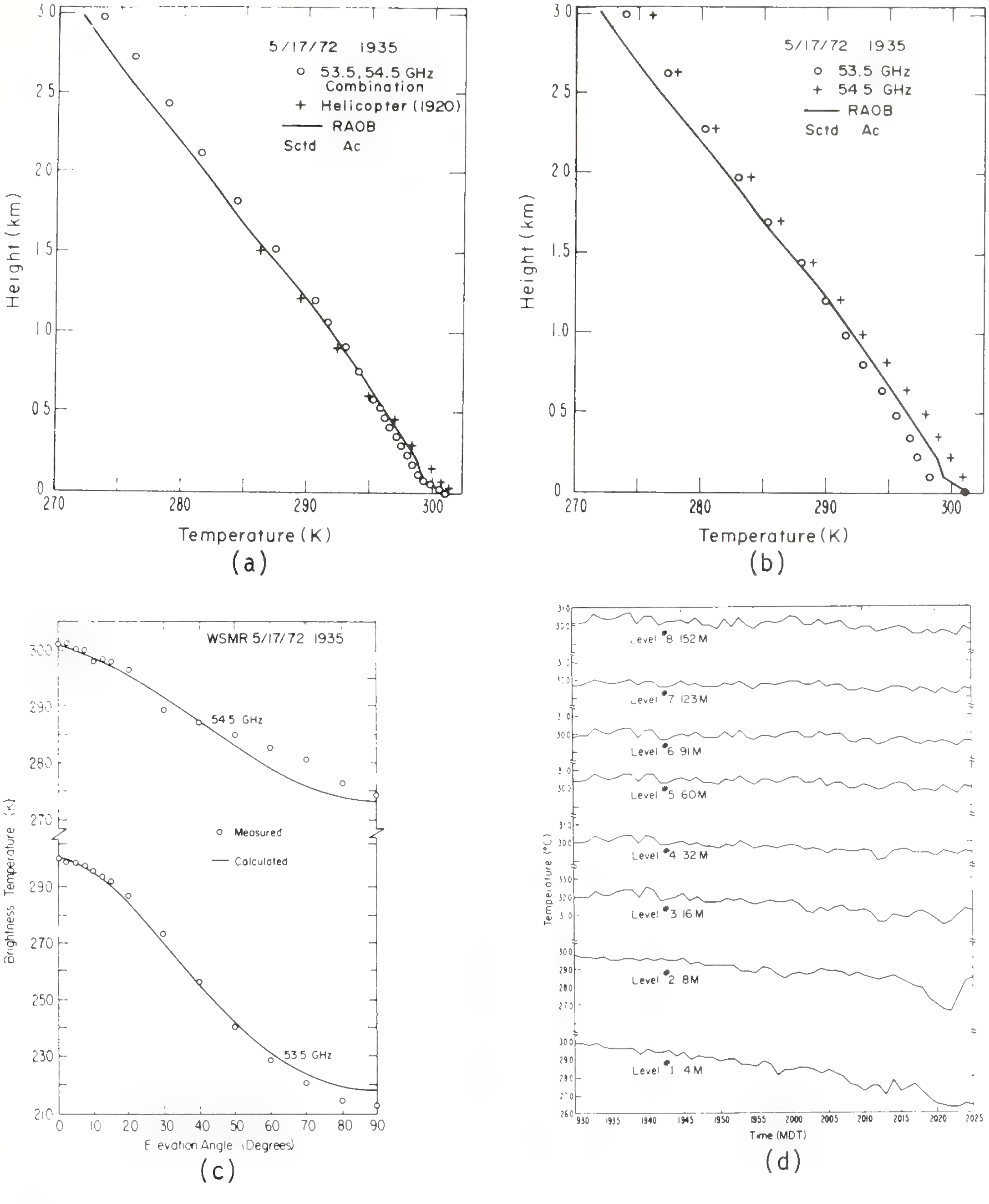

(a) (b) (c) (d)

FIG. 11. As in Fig. 10 except for 1935 MDT 17 May 1972.

file above ~60 m. This could have been caused by the profile getting warmer with increasing time due to solar heating. Unfortunately, the tower measurements were unavailable during this period.

A total of 13 profiles were inverted for the one-week set of measurements. Table 6 summarizes the retrieval results for each profile as a function of inversion method and/or input data set; the tabulated values are the rms differences between estimated and radiosonde profiles. The reduction in variance by employing 30 brightness measurements instead of 15 is about 30%. In all cases of occurrence, ground-based inversions and lapse conditions were clearly indicated. The one elevated inversion that occurred was smoothed out in the re-

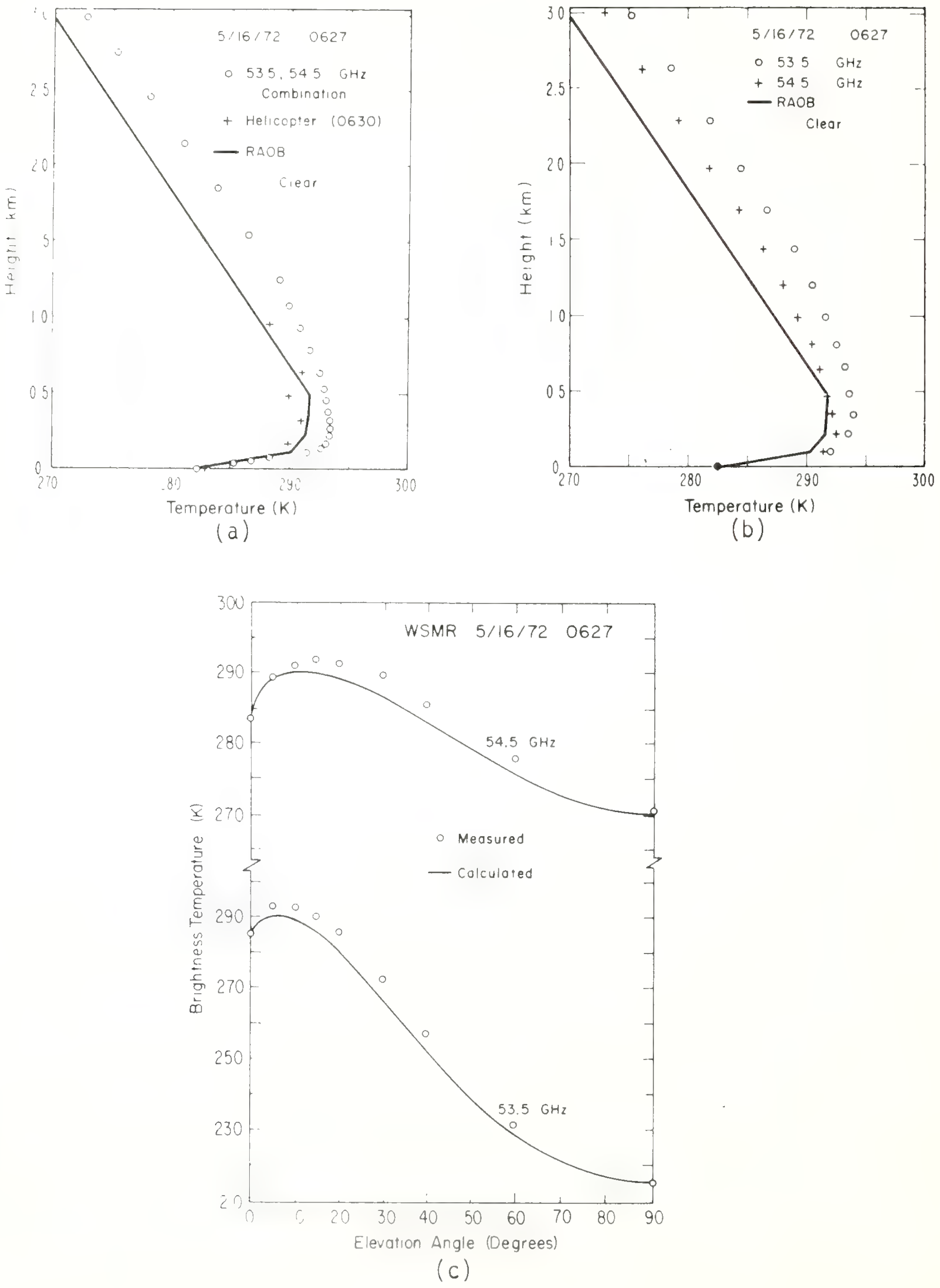

(a) (b)

(c)

FIG. 12. As in Fig. 10 except for 0627 MDT 16 May 1972.

TABLE 6. Root mean square difference [K] between measured and inferred temperature profiles over 3 km height interval.

Date	Time	53.5 GHz (15 angles)	54.5 GHz (15 angles)	Both frequencies (15 angles)
15 May	0515	3.83	1.40	2.17
	0815	1.33	2.81	2.26
	1937	1.26	1.96	1.33
16 May	0627	4.17	2.13	2.31
	0800	0.98	2.40	1.24
	1947	0.53	3.03	2.47
17 May	0516	3.62	5.16	3.94
	0800	3.58	1.16	1.62
	1935	1.04	1.52	0.52
18 May	0800	0.90	1.64	1.47
	1940	0.67	1.54	0.58
19 May	0510	1.47	1.45	2.25
	1000	2.36	1.25	1.09
ΔT_{rms} for all profiles		2.36	2.36	1.99

trieval; however, these data were suspect because of strong radio interference, presumably due to tracking during a missile launch.

During the morning of 18 May, the microwave radiometer was operated at a fixed elevation angle for approximately $2\frac{1}{2}$ h. The main purpose of this exercise was to investigate the degree of correlation between brightness at a fixed angle and the temperature measured at various levels on the meteorological tower; all microwave data were recorded at 5° elevation. Fig. 13 presents brightness temperatures at 53.5 and 54.5 GHz vs tower temperature at two levels. The sampling period was 5 min.

Note the relatively abrupt drop in microwave brightness temperature that coincides with the breakup of the inversion shortly after 0700. The observed behavior suggests the possibility that correctly interpreted direct brightness data at a fixed elevation angle may be a better indicator of atmospheric temperature at given heights than previously thought. Certainly, future experiments should evaluate this possibility by stressing brightness vs tower temperature measurements equally with angle scan measurements.

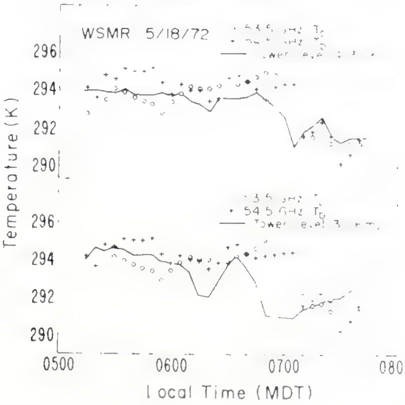

FIG. 13. Comparison of microwave brightness temperatures with tower temperatures at two levels.

10. Summary and conclusions

In this paper we have presented results of an experiment designed to compare direct and indirect soundings of vertical temperature profiles at White Sands Missile Range. Direct observations of temperature profiles were taken by radiosondes, by helicopters, and by sensors on a 150 m meteorological tower. Passive indirect soundings were obtained using a two-channel microwave radiometer operating at 53.5 and 54.5 GHz in the O_2 band. Statistical inversion of the microwave data resulted in an average rms temperature error of 2.0 K up to 3 km for 13 profiles.

The theoretical technique of Backus and Gilbert was applied to determine the vertical resolution or spread that can be achieved by our ground-based microwave radiometer operating in a variable elevation angle mode. The spread is an increasing function of altitude with values of ~75 m near the surface to ~1 km at a height of ~3 km. Theoretical estimates of accuracy in retrieving thermal profiles were less than 1.3 K up to about 3 km for radiometer noise levels of 1.0 K.

The microwave temperature retrievals exhibited generally good agreement with directly measured profiles. When there were significant departures between inferred and directly measured profiles, similar departures were present between calculations and measurements of brightness. Much of this discrepancy seems to be due to substantial changes in the low-altitude temperature profile during the period of measurements (~45 min). The available tower data tend to confirm this hypothesis. Comparison of tower data (when available) with plots of microwave brightness vs elevation angle revealed that temporal changes in the temperature profile were affecting the microwave data. Oscillations in temperature profiles gave rise to similar oscillations in the angular brightness curves. In several instances when the tower data were not available, similar features were present in the microwave plots. We may reasonably conclude that the present technique gives a poor representation of a temperature profile that is rapidly changing with time. On the other hand, the technique may give a better representation of the time-averaged temperature structure than a single radiosonde. The time required for a complete brightness scan could reasonably be reduced to 15 min with modifications of present equipment.

The ability of the microwave technique to indicate the presence or absence of ground-based temperature inversions was successfully demonstrated. In most cases, the inversion heights are accurately recovered; some differences in radiosonde and inferred measurements of the inversion intensity may be the result of rapidly changing profiles as discussed above.

The correlation between fixed angle brightness and tower temperatures at a fixed height was quite good. Future experiments should gather a much larger data base under a wide variety of profile conditions to determine to what degree and on what time scale these fluctuations can be correlated.

The success of the radiometer to retrieve, with a resolution that degrades with height, smoothed features of the thermal profile suggests that the technique could supplement satellite soundings in the first 300 mb above the surface. An automated system, with a microwave window channel, could be used in remote regions to provide profile information routinely, except during precipitation. Research is currently underway to determine the feasibility of radiometric sensing of temperature profiles from ocean-based data buoys.

Acknowledgments. The authors acknowledge Dr. Sterling E. Taylor for the operation of the helicopter in gathering temperature data. We thank Marvin A. Hamiter who was responsible for installation and operation of the meteorological tower. R. S. Lawrence offered helpful suggestions on the manuscript.

REFERENCES

Backus, G., and F. Gilbert, 1970: Uniqueness in the inversion of inaccurate gross earth data. *Phil. Trans. Roy. Soc. London*, **266**, 123–192.

Businger, J. A., and A. S. Frisch, 1972: Cold plumes. *J. Geophys. Res.*, **77**, 3270–3271.

Carter, C. J., R. L. Mitchell and E. E. Reber, 1968: Oxygen absorption measurements in the lower atmosphere. *J. Geophys. Res.*, **73**, 3121–3127.

Colin, L., Ed., 1972: *Proc. Workshop on Mathematics of Profile Inversion*, Ames Res. Center, Moffett Field, Calif., NASA Tech. Memo. TM X-62, 150 pp.

Conrath, B. J., 1972: Vertical resolution of temperature profiles obtained from remote radiation measurements. *J. Atmos. Sci.*, **29**, 1262–1271.

Deutsch, R., 1965: *Estimation Theory.* Englewood, Cliffs, N. , Prentice-Hall, Inc., 269 pp.

Dicke, R. H., 1946: The measurement of thermal radiation at microwave frequencies. *Rev. Sci. Instr.*, **17**, 268–275.

Miner, G. F., D. D. Thornton and W. J. Welch, 1972: The inference of atmospheric temperature profiles from ground-based measurements of microwave emission from atmospheric oxygen. *J. Geophys. Res.*, **77**, 975–991.

Morrison, D. F., 1967: *Multivariate Statistical Methods.* McGraw-Hill, 338 pp.

Mount, W. D., B. R. Fow, C. V. Wick and C. M. Maloy, 1969: Three radiometric data analysis techniques for measuring air temperature profiles. Sperry Rand Research Center, Sudbury, Mass., Report under Contract CPA 22-69-116, prepared for Air Pollution Control Office, EPA, Durham, N. C.

Snider, J. B., 1972: Ground-based sensing of temperature profiles from angular and multi-spectral microwave emission measurements. *J. Appl. Meteor.*, **11**, 958–967.

———, 1974: A sensitive two-frequency radiometer for remote sensing of temperature profiles. *Rev. Sci. Instr.*, **45**, 981–984.

Staelin, D. H., A. H. Barrett, J. W. Waters, F. T. Barath, E. J. Johnson, P. W. Rosenkranz, N. E. Gaut and W. B. Lenoir, 1973: Microwave spectrometer on the Nimbus 5 satellite: Meteorological and geophysical data. *Science*, **181**, 1339–1341.

Waters, J. W., 1971: Ground-based passive microwave sensing of temperatures in the stratosphere and lower mesosphere. *Proc. 7th Intern. Symp. Remote Sensing of Environment*, Ann Arbor, Mich., 1765–1776.

Westwater, E. R., 1967: An analysis of the correction of range errors due to atmospheric refraction by microwave radiometric techniques. ESSA Tech. Rept. IER 37-ITSA 37.

———, 1972a: Ground-based determination of low-altitude temperature profiles by microwaves. *Mon. Wea. Rev.*, **100**, 15–28.

———, 1972b: Microwave emission from clouds. NOAA Tech. Rept. ERL-219 WPL-18, 55 pp.

———, and A. Cohen, 1973: Application of Backus-Gilbert inversion technique to determination of aerosol size distributions from optical scattering measurements. *Appl. Opt.*, **12**, 1340–1348.

———, J. B. Snider, A. V. Carlson and J. R. Yoder, 1973: Experimental determination of temperature profiles by ground-based radiometry. NOAA Tech. Rept. ERL-289 WPL 27.

———, and O. N. Strand, 1968: Statistical information content of radiation measurements used in indirect sensing. *J. Atmos. Sci.*, **25**, 750–758.

———, and ———, 1972: Inversion techniques. *Remote Sensing of the Troposphere.* V. E. Derr, Ed., U. S. Govt. Printing Office, Washington, D. C., Chap. 16.

Journal of Applied Meteorology 13, 951-953, December 1974.

Doppler Lidar Observations of Hydrometeors

N. L. Abshire, R. L. Schwiesow and V. E. Derr

Environmental Research Laboratories, NOAA, Boulder, Colo. 80302

6 November 1973 and 24 July 1974

ABSTRACT

Significant Doppler lidar returns have been observed from snow and rain. This demonstrates the feasibility of measuring velocity and range of hydrometeors with 10.6-μm wavelength CO_2 laser lidar.

1. Introduction

The application of visible wavelength lidar to meteorological aerosol distribution problems has been reviewed by Collis (1970) and others. An extension of the lidar concept to include Doppler-shift information from aerosol particles allows remote measurement of mean wind velocity (Lawrence *et al.*, 1972). This work, based on homodyne detection (in the radar sense) of the Doppler-shifted backscatter from the aerosols, requires a CO_2 laser for ranges of 30 m or more in the turbulent atmosphere.

Our work extends the concept of lidar detection of aerosols to the detection of hydrometeors in the atmosphere. The advantages of the 10.6-μm CO_2 laser wavelength for hydrometeor lidar, compared to visible wavelengths, include such factors as: 1) lower sky background noise power, 2) eye safety, 3) much smaller refractive effects from the turbulent atmosphere, 4) larger backscatter-to-forward-scatter ratio, 5) superior haze and precipitation penetration, and 6) greater laser power conversion efficiency and frequency stability. However, water is much more strongly absorbing at a 10.6 μm wavelength than at visible wavelengths, and it was not clear from previous work that hydrometeors would yield a detectable lidar signal.

Detecting the fall velocity and particle density of hydrometeors has such applications as objectively classifying precipitation type, remotely detecting precipitation above a region of sea spray, and estimating precipitation rate.

2. Apparatus

A frequency-stable, single-longitudinal-mode CO_2 laser served as transmitter and local oscillator for the system. This unit operated at an average power of 1 W, cw. The backscattered signal was mixed with the local oscillator on a cooled Hg:Cd:Te infrared detector, which has a flat frequency response to at least 10 MHz. This detector was illuminated by using a NaCl beamsplitter set to deflect some of the laser energy through a NaCl lens to the detector element.

A 30-cm modified Gregorian telescope could be optionally used as both a transmitter and receiver element. When the telescope was used, the probed volume of the atmosphere was the small focus volume of the system, ~5 cm³. When no telescope was used, returns came from a much larger region of the precipitation, estimated to be 2 cm diameter by 15 m long. The angle of view of the horizontal optical system was directed upward at 45° elevation through an open laboratory window. Fig. 1 indicates schematically the layout.

The detector signal, after amplification by a broadband preamplifier, passed to a swept-filter spectrum analyzer. Data consisted of observed or photographed

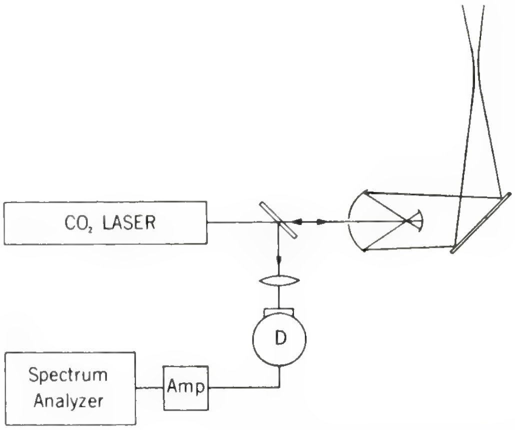

Fig. 1. Schematic of experimental apparatus. The CO_2 laser emission is transmitted either directly or through a focusing telescope. Colinear backscattered radiation is reflected from the laser output mirror and or is nonresonantly amplified in a double pass through the laser discharge. The beamsplitter samples the return together with the laser main beam as local oscillator.

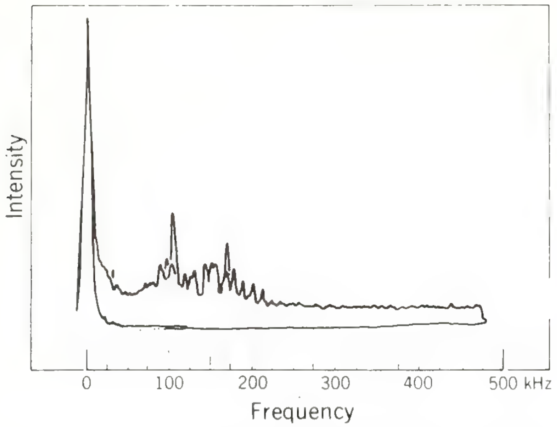

FIG. 2. Typical Doppler lidar return from snowfall for a Doppler calibration of 188.9 kHz per m sec^{-1} of radial velocity component. Analyzer scan time 20 msec, 1 kHz filter width, 500 kHz scan width.

calibrated spectrum-analyzer oscilloscope displays. Intensity peaks as a function of frequency identify the velocities of the scattering particles in the beam as well as giving more qualitative information on particle velocity and number density distributions.

3. Observations

With the telescope in the system, the Doppler signal from hydrometeors was very intermittent. At a range of $\sim$15 m with the 5 cm^3 focal volume, only individual particles were observed during a sampling period $\leqslant$1 sec. Integration of the spectrum analyzer output for 10^3 sec or more in a digital averager is required to make useful observations on particle distributions with close-focus optics. A detected Doppler burst occurred when a hydrometeor passed through the sampling region at the instant the spectrum analyzer was sweeping the frequency appropriate to the particle velocity. For a spectrum analyzer duty cycle (filter bandwidth÷frequency sweep) of 2%, the signal observation rate with the telescope was approximately 0.05 sec^{-1}, for cases similar to the snow observations discussed later.

Removing the telescope sacrifices range information for an enlarged (indefinite) spatial sampling volume. With such a sampling volume in snowfall, for example, an essentially continuous Doppler signal was observed. A significant feature was the adequate homodyne signal level, even with small collection optics of less than 5 mrad receiver aperture.

Fig. 2 is redrawn from a typical snowfall observation. Signal peaks occur at 100 and 170 kHz, although it is obvious that a wide range of frequencies from approximately 75 to 200 kHz were generated by the hydrometeor scatter. Applying the Doppler calibration factor (Lawrence *et al.*, 1972) of 188.9 kHz per m sec^{-1} for 10.59-μm radiation to the intensity peaks, radial hydrometeor velocities of approximately 0.53 to 0.90 m sec^{-1} are indicated. If we assume vertical fall with a measured 45° lidar elevation angle, hydrometeor fall velocities of 0.75 to 1.27 m sec^{-1} are suggested, which is reasonable for snowfall (Langleben, 1954).

Interpreting Fig. 2 requires some care since the data represent neither a time average nor an instantaneous average over a large number of particles in a distribution. Significant changes in the Doppler spectrum occurred over intervals of a few seconds. The two signal peaks represent aggregates of a few particles or ranges where different radial velocities occurred. Some of the substructure may have been due to orientational motion of the snow or to microscale turbulent fluctuations. The spread in observed fall velocities is larger than expected for the free atmosphere. Flow perturbations near the building affected the velocity distribution, particularly the spread.

Data similar to those in Fig. 2 were observed from rain. Of course, the signal peaks occurred at higher frequencies. Qualitatively, the rain return was less intense and more intermittent then the snow backscatter, but the rain data showed less spread in velocity space. Generally, one expects a larger percentage velocity spread for rain than for snow, in contrast to these observations. The anomalously large spread in snow data, due to flow perturbations, explains the relative differences. Rain fall velocities were in the range expected from Gunn and Kinzer (1949).

The apparatus is not yet suited to a meaningful quantitative measurement of backscattered intensity or comparison of snow and rain signal magnitudes. Mie theory is likewise not developed sufficiently to calculate snow backscatter at the large size parameters involved in the 10.6 μm lidar. The principal objective of the experiment, to test the observability of hydrometeors by means of 10.6-μm Doppler lidar, is supported by the spectrum-analyzer data.

4. Extensions and conclusions

An expansion of the sampling volume for the telescope-based system, by extending the useful range or reducing the primary mirror diameter, would reduce the intermittency problem. Even more improvement in signal rate, while still retaining the range information that is lost with the unfocused setup, would accrue from substituting a frequency-tracking heterodyne filter for the low-duty-cycle, scanning spectrum analyzer. A tracking filter operates with essentially 100% duty factor for the peak-intensity component in the frequency spectrum.

Sophistication of the optical system, including increased laser power, is an obvious possibility for increasing signal level and effective range. Our reported experiment was not signal-level limited for the close ranges studied, even in the unfocused case where the effective signal-collection optics were very small. We plan quantitative measurements of backscatter intensity from hydrometeors to clarify the signal-level question.

The addition of fall velocity information to transmissometer data on snowfall rate (Robertson, 1973) should serve to refine or possibly supplant such rate data, for example.

Hydrometeor velocities, velocity distributions, and information on number density are accessible to 10.6-μm Doppler lidar sensing techniques. Such lidar measurements have specific advantages (and limitations) with respect to visible lidar and radar probes of similar variables. Studies related to hydrometeor identification, classification, and motion in an automated, unmanned observing station as well as to severe storm investigations may well utilize the interaction of hydrometeors with CO_2 laser Doppler probes.

REFERENCES

Collis, R. T. H. 1970: Lidar. *Appl. Opt.*, **9**, 1782–1788.

Gunn, R., and G. D. Kinzer, 1949: The terminal velocity of fall for water droplets in stagnant air. *J. Meteor.*, **6**, 243–248.

Langleben, M. P., 1954: The terminal velocity of snow aggregates. *Quart. J. Roy. Meteor. Soc.*, **80**, 174–181.

Lawrence, T. R., D. J. Wilson, C. E. Craven, I. P. Jones, R. M. Huffaker and J. A. L. Thomson, 1972: A laser velocimeter for remote wind sensing. *Rev. Sci. Instr.*, **43**, 512–518.

Robertson, C. E., 1973: The reliability of an optical technique for measuring snowfall rates. *J. Appl. Meteor.*, **12**, 553–555.

Pre-Print No. 183, Conference on Optical Propagation in the Atmosphere,
38.1-38.10, 1975.

REMOTE PROBING OF WINDS AND REFRACTIVE TURBULENCE USING OPTICAL TECHNIQUES

S. F. Clifford
National Oceanic and Atmospheric Administration
Environmental Research Laboratories
Wave Propagation Laboratory
Boulder, Colorado 80302

SUMMARY

At the Wave Propagation Laboratory (WPL) of the National Oceanic and Atmospheric Administration (NOAA), we have considerable experience in the development of techniques of measuring wind and refractive turbulence C_n^2 using both active and passive optical sources. From the initial development of our path-average laser wind sensor, we have further developed systems for measuring horizontal profiles of wind and C_n^2. Recently, we have constructed a passive wind sensor that requires no active light source; It responds to fluctuations of light reflected from a target to determine the path-averaged crosswind. Finally, we have made recent progress in the application of the horizontal-path techniques to the problems of remotely sensing wind and C_n^2 profiles aloft from observations of stellar scintillations. In this paper, we analyze the principles of operation of these devices and compare their performance with more conventional meteorological instruments.

1. INTRODUCTION

In recent years, many authors (LAWRENCE, R. S. et al., 1972; LEE, R. W., 1974; WANG, T-i, et al., 1974; SHEN, L., 1970; ISHIMARU, A., 1972; MANDICS, P.A., et al., 1973; HARP, J. C., 1971; MANDICS, P. A., 1971; and KJELAAS, A. G. and G. R. OCHS, 1974) have considered the possibility of remote probing of winds over optical, microwave, and acoustic paths. At the Wave Propagation Laboratory of NOAA, we have demonstrated (LAWRENCE, R. S. et al., 1972) the feasibility of using a line-of-sight laser link to measure the path-averaged crosswind. From the initial development of our path-average laser wind sensor, we have further developed techniques for measuring horizontal profiles of crosswind and refractive turbulence (WANG, T-i, et al., 1974). More recently, we have constructed a passive wind sensor that measures wind without the need of a light source (CLIFFORD, S. F. et al, 1974). This system responds to the fluctuations of light from a naturally occurring scene such as the horizon or a hillside.

We at NOAA (OCHS, G. R., et al., 1974) and others (VERNIN, J. and F. RODDIER, 1973) have measured winds aloft from observations of stellar scintillations and we are currently testing a device to measure vertical profiles of refractive turbulence. The vertical distribution of refractive turbulence is important to know since it is refractive turbulence that limits our ability to resolve objects in orbit and produces enhanced error rates in optical communication systems. We will review progress in each of the above areas with emphasis on techniques to remotely sense meteorological information relevant to the design of optical systems.

2. THEORY OF OPERATION

Each of the techniques mentioned is an outgrowth of our path-average laser system and, because of this fact, they have quite similar principles of operation. Figure 1 shows the general configuration of our laser sensor. A laser beam, diverged to approximate a point light source, illuminates two detectors. The temperature irregularities along the optical path produce irradiance fluctuations at each of the detectors. As the wind advects these irregularities across the laser beam, the irradiance fluctuations that they produce propagate from one detector to the other in a time of the order of $\rho/v_\perp$ where ρ is the sensor spacing and $v_\perp$ is the transverse wind speed. If we time-lag correlate the signals observed by the two detectors, we obtain the normalized covariance function shown in Figure 2. The wind speed information is contained in both the time lag to the peak of the covariance function and the slope at zero time lag. We compute the slope at zero time lag to determine the wind speed rather than the peak delay because the former is a linear function of windspeed and the latter is non-linear (LAWRENCE, R. S., et al., 1974). Also, the slope technique is much less sensitive to random temporal fluctuations in the spatial scintillation pattern than the peak delay technique (LAWRENCE, R. S., et al., 1974).

Figure 3 shows a typical sample of a laser wind sensor record compared with the more conventional anemometer measurements. The top record is the reading of the optically derived wind speed transverse to a 300 m laser beam. The lower record is the average wind speed measured by six propellor anemometers spaced uniformly along the optical path. The agreement between the two curves is excellent showing that the laser wind sensor can be effectively employed to measure winds wherever a spatially-averaged value is desirable, as in determining crosswinds along airport runways, measuring the flow of pollutants down a valley, or by using a triangular array of such sensors to measure a spatially averaged divergence of the wind field.

3. THE PASSIVE WIND SENSOR

In certain applications where a two-ended system is impossible or impractical; as when one end of the optical path is inaccessible, the laser wind sensor cannot operate. To overcome this limitation we have developed a modification of our optical wind sensor (CLIFFORD, S. F., et al., 1974) that measures the path-averaged crosswind by observing the fluctuations in irradiance of a naturally illuminated scene such as a sunlit hillside, a forest, or a variety of other natural targets. Figure 4 illustrates the geometry of the passive wind sensor. Two detectors having a two-dimensional sensitivity spectrum H^2 are separated by a distance ρ and observe the fluctuations in irradiance from ambient light reflected off the target. As before, we compute the time-lagged covariance of the two detectors and determine the wind from the slope at zero delay. This technique is more complicated than the laser system because we now must specify the spectral density of the scene Q^2 to determine the weighting function for the measured wind. For example, Figure 5 illustrates the wind weighting function for the case of a trailer observed by two detectors arranged in the configuration shown in the lower left corner. The detectors are narrowband spatial filters of wavelength $2.5\sqrt{\lambda L}$, where λ is the mean frequency of the reflected light and L is the distance to the target. The tendency of the passive sensor to emphasize the winds near the receiver is characteristic of the device and applies to nearly all scene spectra. In the upper right corner of Figure 5, we show the behavior of the passive sensor compared with the average of 10 anemometers spaced uniformly along the optical path. The agreement is quite satisfactory. Finally, Figure 6 shows a similar comparison for the same target. We have plotted the reading of the passive wind sensor and the average of the five anemometers closest to the receiver. The optical system gain (upper trace) was increased to displace the curves for convenient comparison. The agreement in detail is quite remarkable.

4. WIND AND REFRACTIVE TURBULENCE PROFILING

In some applications, it may be desirable to obtain profiles of wind and refractive-turbulence intensity C_n^2. We accomplish this by crossing two laser beams (see Figure 7) so that their common volume is located at the path position that we wish to probe. (The two beams must be offset in the horizontal direction to measure wind.) If we again calculate the time-lagged covariance function of two horizontally separated sensors each looking independently at one of the beams (we accomplished this by polarization coding of the two beams--the upper detectors in Figure 7 would see only the horizontally polarized light from the lower laser and the lower detectors only the vertically polarized light from the upper laser), the resultant signal will depend only on the effects of the turbulence within the common volume of the two beams.

In Figure 8, we have plotted the theoretical path-weighting function for C_n^2(solid curve) along with experimental data points (crosses) obtained with fine wire temperature probes. We calculate C_n^2 from C_T^2, the temperature structure parameter, by using the equation (LAWRENCE, R. S., et al., 1970)

$$C_n^2 = \left[(79p/T^2)10^{-6}\right]^2 C_T^2 \qquad (1)$$

where p is the background pressure in millibars and T is the temperature in Kelvin. The fine wire probes measure the small fluctuations in temperature at two different points. The probe responses are then subtracted, squared, and averaged to obtain C_T^2, i.e.,

$$C_T^2 = \langle[T(x)-T(x+r)]^2\rangle/r^{2/3} \qquad (2)$$

where r is the separation of the two temperature sensors and the angle brackets indicate an ensemble average. (C_T^2 may be considered the mean square difference in temperature of two thermometers separated a unit distance.) The data points in Figure 8 are determined by having a computer take the five measured values of C_n^2 and multiply them by appropriate weights to maximize the correlation between the optical covariance measurement (a function of $C_n^2(z)$) and this weighted sum of C_n^2 values. So, the resulting curve depicts the relative importance of refractive turbulence at each path position for producing our optical measurement. We may increase our path resolution, i.e., narrow the weighting function, by simultaneously increasing the vertical separation of the transmitters and receivers. We change path positions by independently increasing or decreasing the transmitter's or receiver's vertical separation. We obtained the midpath crossover and the resolution shown in Figure 8 by separating the transmitters and receivers by 1.8 Fresnel zones $\sqrt{\lambda L}$, where λ is the wavelength of the radiation and L is the optical pathlength.

Similarily, we may measure transverse windspeed in the common volume of the two beams (provided they are offset slightly in the horizontal direction) by measuring the slope of the time lag covariance function at zero delay. Figure 9 illustrates the type of weighting function expected (solid line) and the experimental points derived from the measurements of five anemometers. We obtained the crossover at midpath and the path resolution shown by vertically separating the transmitters and receivers by 1.8 Fresnel zones $\sqrt{\lambda L}$ and using a horizontal beam offset of 0.3 Fresnel zones. Again, if we increase the vertical separation the peak will narrow. For further discussion and a more complete description of the systems advantages and limitations see WANG et al. 1974.

5. MEASUREMENTS OF WINDS AND C_n^2 ALOFT

There are extremely interesting applications of the above-mentioned techniques for measuring winds and C_n^2 aloft from observations of stellar scintillations. Vertical profiles of wind, remotely sensed at, say, 10 levels, provide invaluable data for weather forecasting. Remotely sensed profiles of C_n^2 provide the necessary information to determine the performance degrading effects of atmospheric turbulence on such optical systems as telescopes and optical communication links. In a recent report (OCHS, G. R., et al., 1974), we analyzed several techniques for remotely measuring wind and C_n^2 aloft.

Figure 10 is a photograph of an instrument that we designed to measure horizontal winds aloft. The system consists of four photomultipliers arranged orthogonally in pairs as shown in Figure 11. One pair (1-2) measures the slope of the time-lag covariance function at zero delay while a servo system rotates the mount so that this quantity is maintained at zero. When this pair of detectors registers zero wind speed parallel to their separation, the other two detectors (3-4) are oriented parallel to the horizontal wind. We then compute the wind speed by measuring the delay to the peak of the covariance function of the observed stellar scintillations and dividing this number into the detector separation. From the mount orientation and the delay to the peak, we can then determine the wind speed and direction.

Figure 12 shows the optically measured wind velocities compared with those determined by a rawinsonde launched 55 km away during 3 days in March 1972. From the geometry of our system, and the use of 5-cm apertures separated a distance of 6.5 cm, we expected the wind reading to be largely determined by winds near the tropopause. We then, somewhat arbitrarily, compared our velocity measurements with the average of the rawinsonde data above the tropopause. In Figure 12 there is good agreement in direction and poorer agreement in wind speed, but the overall correlation between the two sets of data is quite good considering the more than 50 km separation between the optical instrument and the rawinsonde launching site.

To measure profiles of wind or C_n^2, we must have much better height resolution than that afforded by the simple two circular aperture system. We have undertaken a theoretical study of our ability to measure profiles using narrow band spatial filtering of stellar scintillation (OCHS, G. R. et al., 1974). From the diffraction theory of the production of scintillation, we expect that at each height range one eddy size of refractive turbulence, the one that is a Fresnel zone for the rest of the optical path to the ground, will be the most important contributor to scintillation from that given height. If we adjust our spatial filter to select only that wavelength disturbance in the received scintillation pattern, then we should be observing scintillation produced by refractive turbulence primarily at that height. Of course, spatial filters have side lobes and the theory shows that other heights will contribute to the observation at a given spatial wavelength, but we would expect the weighting function to have some sort of emphasis in the desired height range. We are trying to discover how well we can determine a height profile of wind and C_n^2, i.e, how many levels and with what height averaging, by constructing a weighted sum of measurements of many different spatial wavelength detectors. By adding and subtracting these data, we can synthesize an optimum weighting function. Preliminary evidence indicates that we are able to obtain C_n^2 profiles averaged over six height ranges using observations of a single star. The height averaging interval ranges from about 2 km for the lowest altitude to 5 km for the highest altitude data.

The technique of looking at a single star can be modified in the same way as we did for our horizontal path work. For example, we could look at binary stars (ROCCA, A., et al., 1974), or two points on the limb of the sun or moon and obtain weighting functions quite analogous to our laser technique (OCHS, G. R. et al., 1974). Many modifications of the horizontal techniques have potential for vertical profile work.

6. DISCUSSION

We have discussed recent progress at NOAA in the remote sensing of winds and refractive turbulence using optical techniques. The ability to remotely sense these quantities has impact on such varied fields as weather forecasting, astronomical and satellite imaging with telescopes, ballistics and optical communication systems. Remote sensing, as opposed to in-situ measurements, provides the only hope of acquiring sufficient quality and quantity of data to understand fully and to compensate for the performance degrading effects of atmospheric turbulence on optical systems.

7. REFERENCES

CLIFFORD, S. F., G. R. OCHS, and T-i WANG, 1974, "Theoretical Analysis and Experimental Evaluation of a Prototype Passive Sensor to Measure Crosswinds", NOAA Tech. Rept. ERL312-WPL35, Supt. of Doc., U. S. Gov't Printing Office, Washington, D. C. 20402.

HARP, J. C., 1971, Ph.D. Thesis, AFCRL-71-0451, SV-SEL-71-042, Scientific Report 1.

ISHIMARU, A., 1972, "Temporal Frequency Spectra of Multifrequency Waves in Turbulent Atmosphere", IEEE Trans. Antennas Propag. *AP-20*, 10.

KJELAAS, A. G. and G. R. OCHS, 1974, "Study of Divergence in the Boundary Layer Using Optical Propagation Techniques", J. Appl. Meteorol. *13*, 242-248.

LAWRENCE, R. S., G. R. OCHS, and S. F. CLIFFORD, 1972, "The Use of Scintillations to Measure Average Wind Across a Light Beam", Appl. Opt. *11*, No. 2, 239-243.

LEE, R. W., 1974, "Remote Probing Using Spatially Filtered Apertures", J. Opt. Soc. Am. *64*, No. 10, 1295-1303.

MANDICS, P. A., 1971, "Line-of-Sight Acoustical Probing of Atmospheric Turbulence", Ph.D. Dissertation, Stanford, Univ., Stanford, Calif.

MANDICS, P. A., R. W. LEE, and A. T. WATERMAN, Jr., 1973, "Spectra of Short-term Fluctuations of Line-of-Sight Signals--Electromagnetic and Acoustic", Radio Sci. *8*, 185.

OCHS, G. R., S. F. CLIFFORD, R. S. LAWRENCE, and T-i WANG, 1974, "Development of a Ground-Based Optical Method for Measuring Atmospheric Turbulence Aloft", NOAA Tech. Rept. ERL297-WPL30, Supt. of Doc., U. S. Gov't Printing Office, Washington, D. C. 20402.

ROCCA, A., F. RODDIER, and J. VERNIN, 1974, "Detection of Atmospheric Turbulent Layers by Spatiotemporal and Spatioangular Correlation Measurements of Stellar-Light Scintillation", J. Opt. Soc. Am. *64*, No. 7, 1000-1004.

SHEN, L, 1970, "Remote Probing of Atmosphere and Wind Velocity by Millimeter Waves", IEEE Trans. Antennas Propag. *AP-18*, 493.

VERNIN, J., and F. RODDIER, 1973, "Experimental Determination of Two-Dimensional Spatiotemporal Power Spectra of Stellar Light Scintillation. Evidence for a Multilayer Structure of the Air Turbulence in the Upper Troposphere", J. Opt. Soc. Am. *63*, No. 3, 270-273.

WANG, T-i, S. F. CLIFFORD, and G. R. OCHS, 1974, "Wind and Refractive-Turbulence Sensing Using Crossed Laser Beams", App. Opt. *13*, No. 11, 2602-2608.

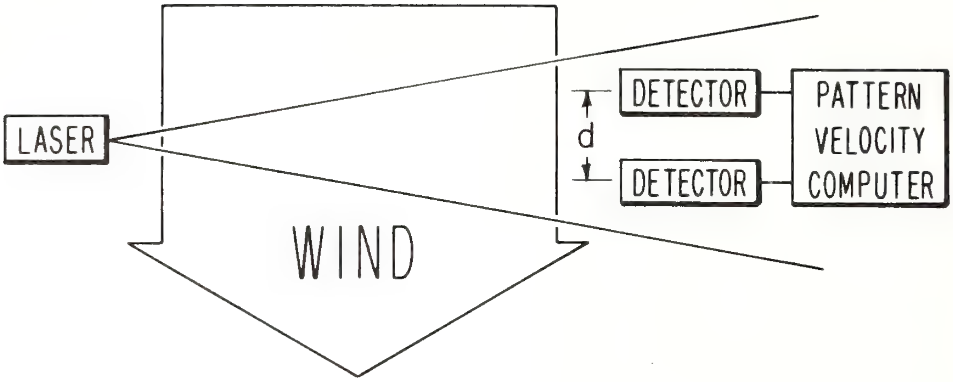

Fig. 1. The general arrangement used to measure the average component of the wind across a laser beam, parallel to the spacing of two detectors.

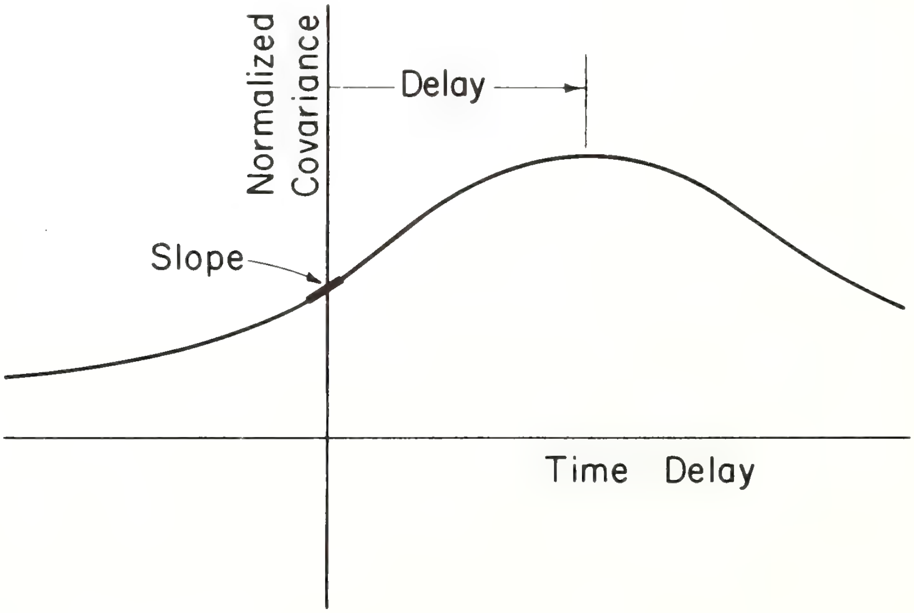

Fig. 2. A schematic of the normalized covariance function, showing the delay to the peak and the slope at zero time lag.

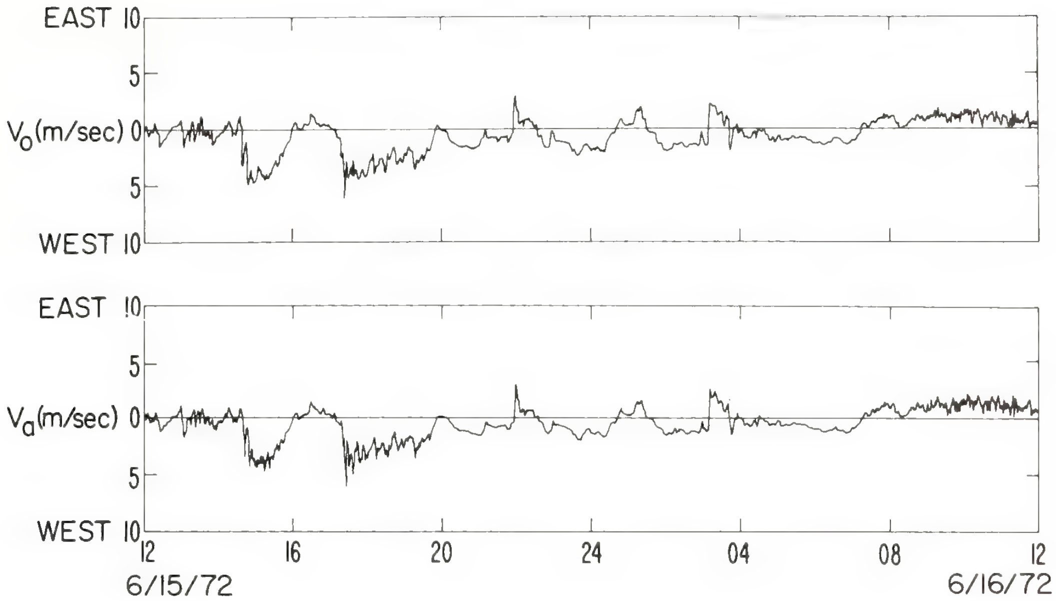

Fig. 3. A 24 hr comparison between the optically measured wind V_o and the mean of six propellor-type anemometers spaced evenly along the 300 m test path.

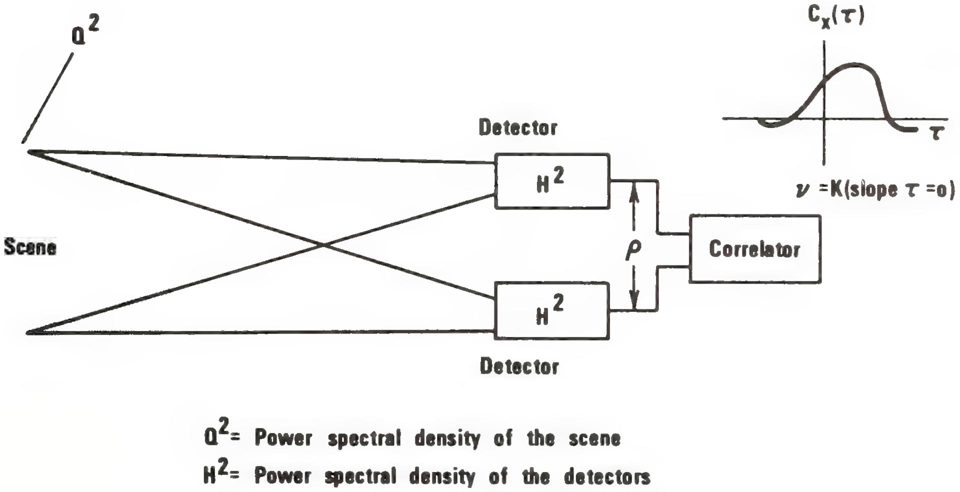
Q^2
$C_x(\tau)$
τ
Detector
H^2
ν =K(slope τ =o)
Scene
ρ
Correlator
H^2
Detector
Q^2= Power spectral density of the scene
H^2= Power spectral density of the detectors

Fig. 4. Schematic of the operation of our passive optical wind sensor showing the covariance function output of the two detectors observing a random scene.

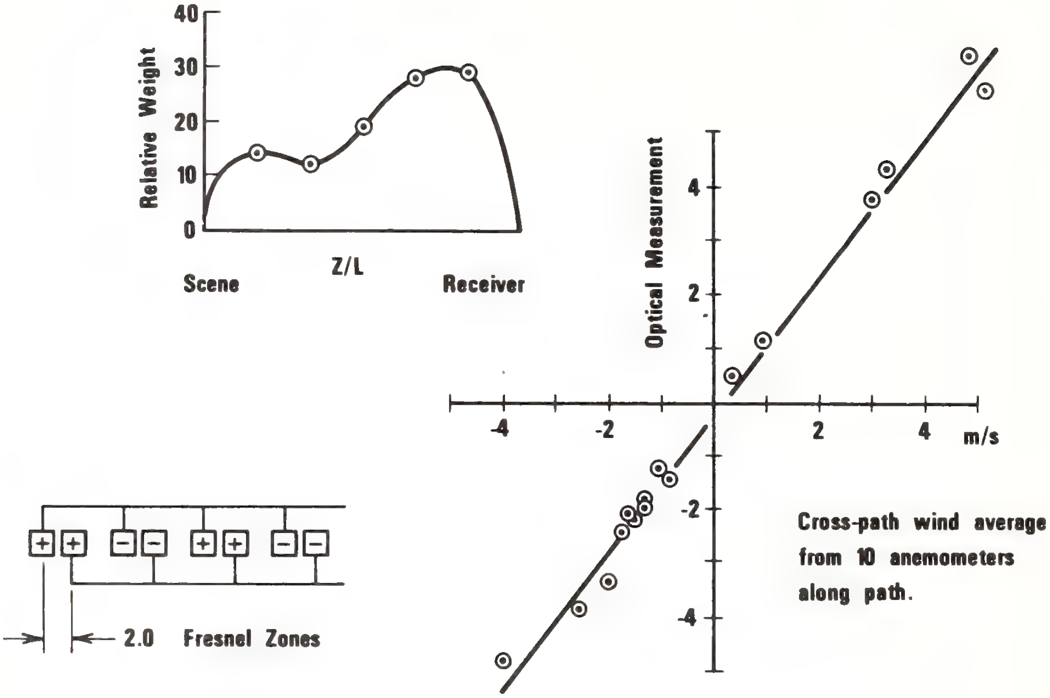

Fig. 5. Comparison of the passive wind sensor reading with the average of 10 anemometers spaced uniformly along a 500 m test path. Also shown are the detector configuration and the path weighting function.

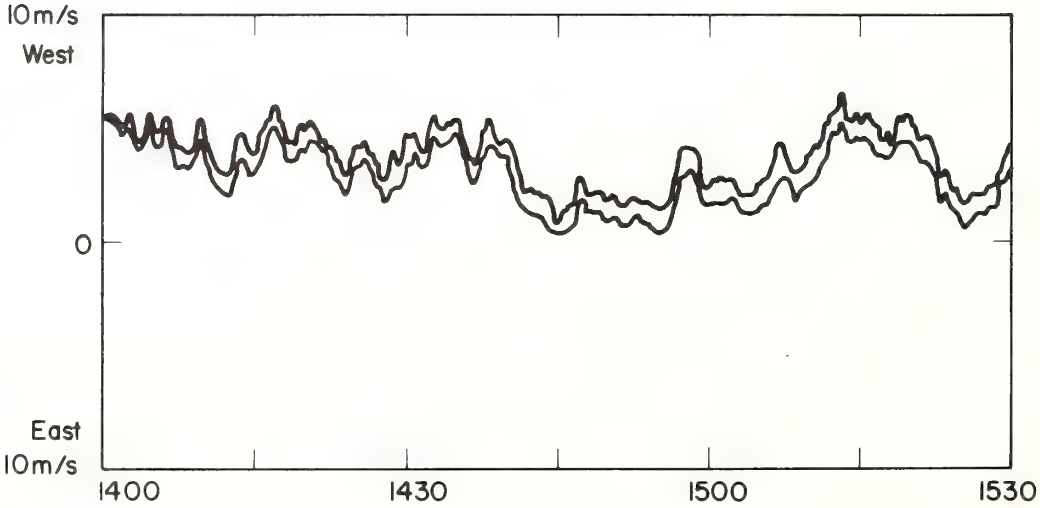

Fig. 6. Comparisons of the transverse wind speed measured by the passive optical system with the average of wind speeds measured by five anemometers equally spaced on the half of the 500 m path nearest the instrument.

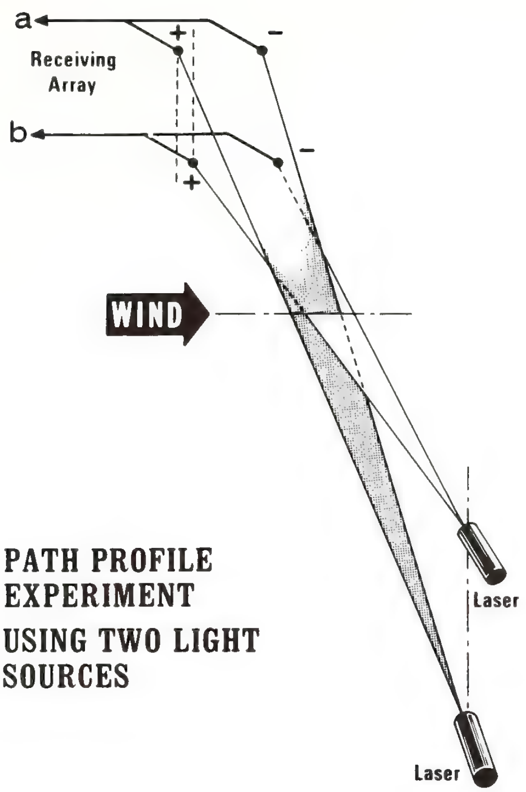

Fig. 7. Diagram of our wind profiling instrument showing two vertically separated lasers and two sets of sensor pairs separated vertically and offset slightly in the horizontal direction.

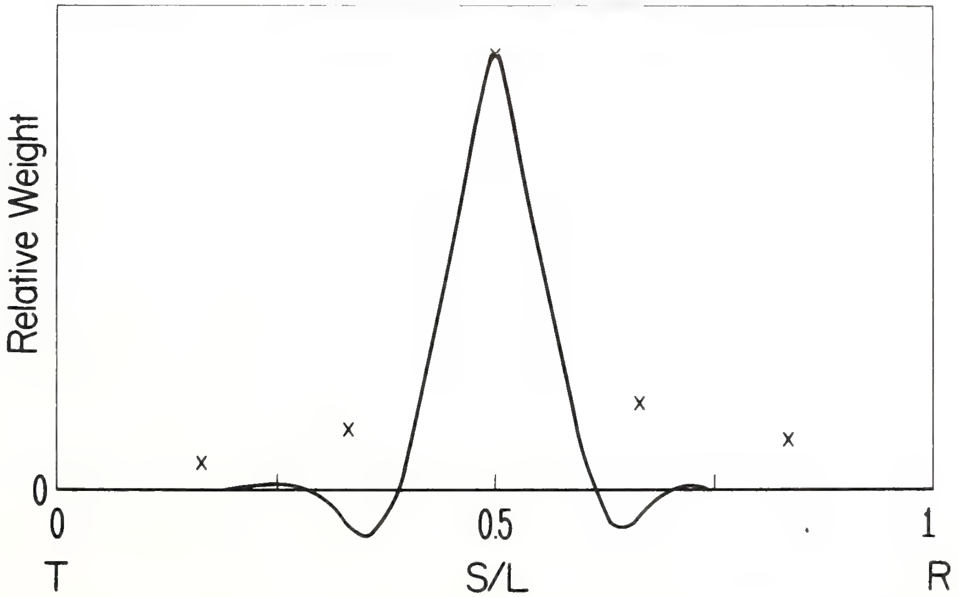

Fig. 8. Theoretical weighting function for C_n^2 (solid curve) with five experimental weights (crosses) determined by high-speed temperature sensors.

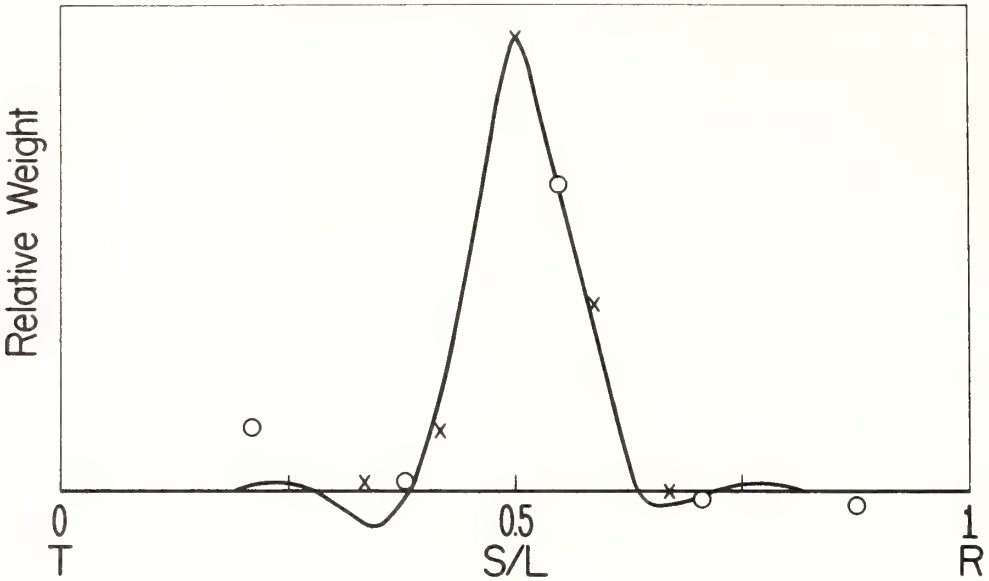

Fig. 9. Theoretical weighting function for transverse wind (solid curve) with crosses and circles representing experimental weights determined from propellor-type anemometer measurements of crosswind.

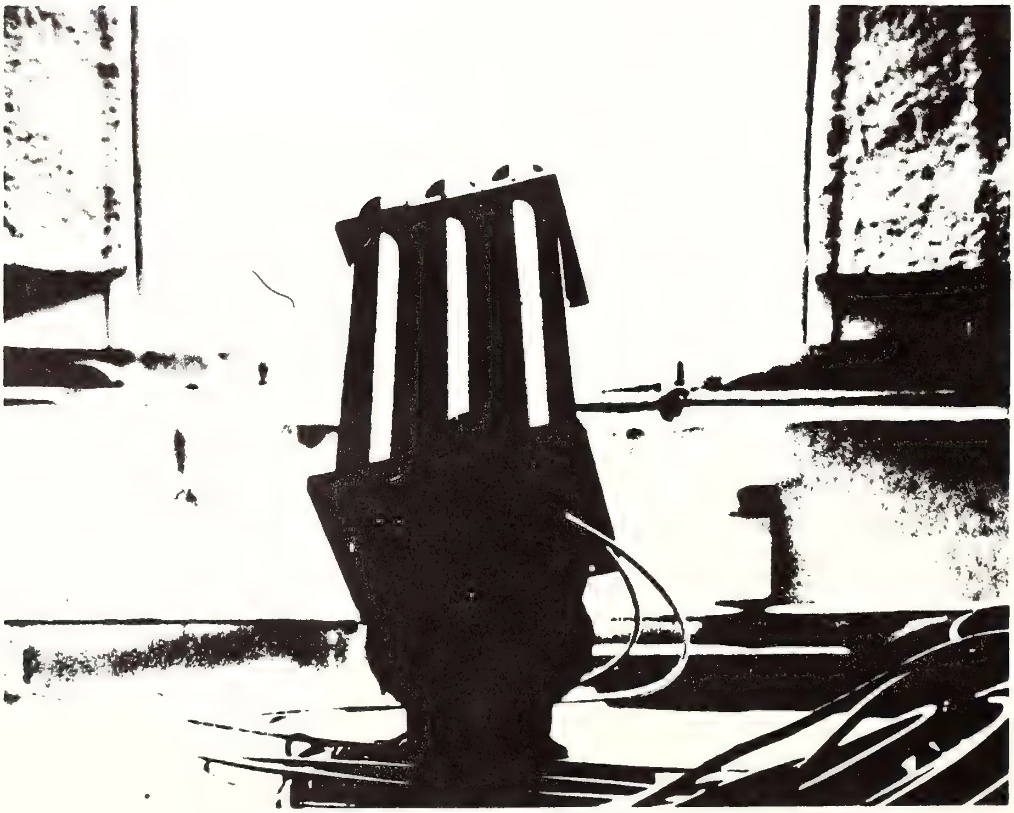

Fig. 10. Optical system for measurement of high altitude winds.

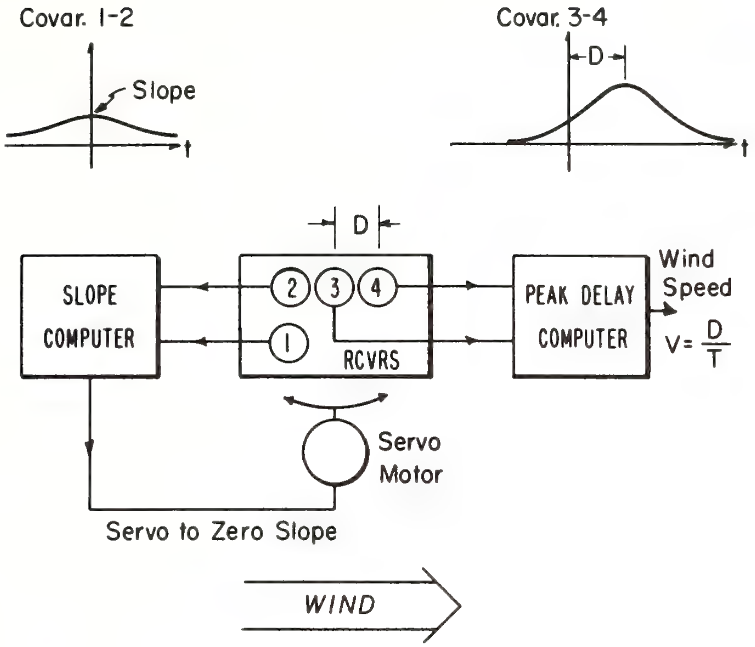

Fig. 11. Block diagram of high-altitude wind measurement system.

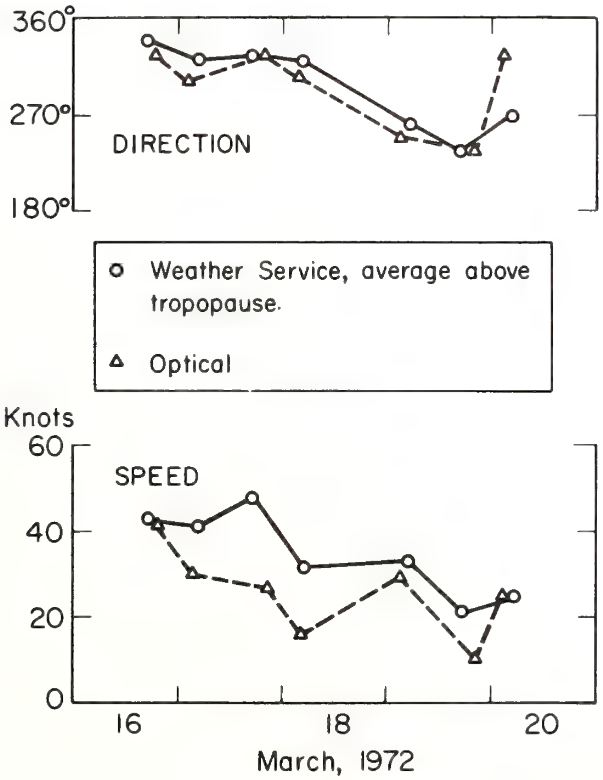

Fig. 12. Comparison of optical wind measurements and rawinsonde data during March 1972.

Applied Optics 14, 2844-2850, December 1975.

Optical wind sensing by observing the scintillations of a random scene

S. F. Clifford, G. R. Ochs, and T-i. Wang

We demonstrate the feasibility of using a naturally illuminated scene, such as a hillside or forest, as a passive optical source to measure the path-averaged crosswind between the scene and the observer. The resultant path weighting function for the crosswind cannot be varied arbitrarily, but we can obtain a useful range of weighting functions by adjusting the geometry of the receiver.

I. Introduction

In recent years, many authors[1-9] have considered the possibility of remote probing of winds over optical, microwave, and acoustic paths. We have demonstrated the feasibility of using a line-of-sight laser link to measure the average crosswind over an optical path.[1] The resulting data have produced wind information that is both more sensitive and more representative for mesoscale meteorological applications than a practical number of traditional anemometers could provide.

The use of the laser wind sensor is severely restricted in applications where terrain is rugged or where one end of the path is inaccessible. Often in some of the most interesting applications, such as measuring the flow of pollutants down a mountain valley, we encounter difficulties of this type. In this paper, we propose a modification of the laser technique that measures the path-averaged crosswind by observing fluctuations in light intensity (scintillations) of a naturally illuminated scene, such as a sunlit hillside, a forest, or buildings. This socalled passive wind sensor eliminates the need for the double-ended path, and, because of this, it has great potential for overcoming the limitations of the laser technique.

Analysis of the passive wind sensor involves the same variables as the active laser system with one additional complication: namely, we must now specify the two-dimensional spatial spectrum of the observed scene, which, in general, is not the same as the white spectrum of a laser point source.

Figure 1 illustrates a typical scene spectrum. In the theory to follow, we account for variations in scene spectra and analyze the impact of these changes on such quantities as the path weighting function and wind system calibration.

II. Theory

The general theory of passive wind sensing is derived from the analysis of the propagation geometry seen in Fig. 2. A point source light, located at $(\rho,0)$, illuminates a differential phase screen of wavenumber $\mathbf{K}$ at $\mathbf{r} = (\rho,z)$, and the scattered field is observed by a detector at (ρ_1,L). The total field, incident plus scattered, at $z = L$ is (from Lee and Harp[10])

$$dE = 1 - ikadz \exp\left[\frac{iK^2z(L - z)}{2kL}\right] \cos[\mathbf{K}\cdot\rho_1(z/L) + \mathbf{K}\cdot\rho(1 - z/L) + \mathbf{K}\cdot\mathbf{b}], \quad (1)$$

where a is the amplitude of the refractive-index fluctuation of the screen, $k = 2\pi/\lambda$, λ is the wavelength of light emitted by the point source, and $\mathbf{K}\cdot\mathbf{b}$ is an arbitrary phase offset. [In passive wind sensing, λ typically varies over a 3–1 bandwidth. In this case, the λ inserted into Eq. (1) will be the mean wavelength of the product of the background light and photodiode response, which is $\lambda \simeq 0.8\ \mu$m. This can be shown to produce results that differ in an insignificant way from those of the exact theory that incorporates the appropriately weighted sum of wavelengths.]

The parameter measured by our wind sensing device is not the total field dE, but the normalized amplitude fluctuation dP_a defined by $dP_a = |dE| - 1$. From Eq. (1) we have

$$dP_a \cong kadz \sin\left[\frac{K^2z(L - z)}{2kL}\right] \cos[\mathbf{K}\cdot\rho_1(z/L) + \mathbf{K}\cdot\rho(1 - z/L) + \mathbf{K}\cdot\mathbf{b}]. \quad (2)$$

Equation (2) is valid to first order in the refractive-

The authors are with NOAA Environmental Research Laboratories, Boulder, Colorado 80302.

Received 12 May 1975.

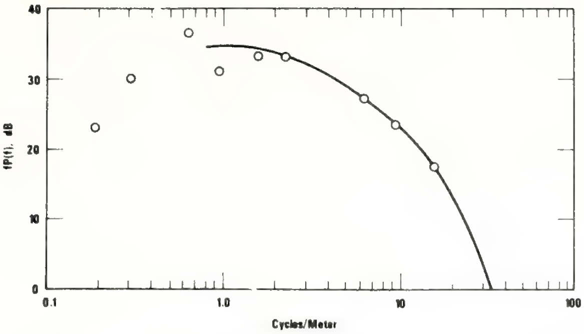

Fig. 1. One-dimensional spatial spectrum of 35-mm color slide showing two vehicles against a background of trees. The abscissa is scaled to actual dimensions at the vehicles.

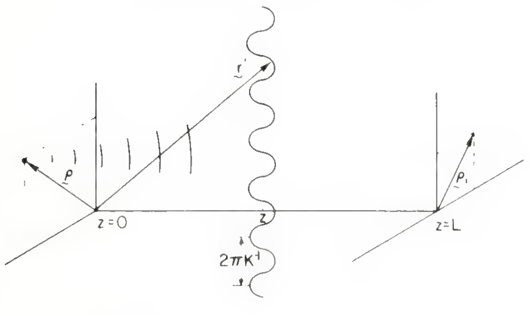

Fig. 2. Geometry of the light source and the receiver. The light at $(\rho,0)$ is perturbed by the turbulent phase screen at z to produce scintillation in the receiving plane at (ρ,L). The sinusoidal phase screen has a spatial wavenumber K.

index fluctuations a; consequently, for Eq. (2) to be a reasonable approximation, we must assume that $|a| \ll 1$. This makes our analysis valid for weak turbulence and single scattering only. If, as we assume in our model, the scene is a sum of spatially incoherent point sources with a distribution $q(\rho)$, we may add the amplitude fluctuations in the following way:

$$dP = kadz \sin\left[\frac{K^2 z(L - z)}{2kL}\right] \int d^2\rho q(\rho) \cos[\mathbf{K}\cdot\boldsymbol{\rho}_1 (z/L) + \mathbf{K}\cdot\boldsymbol{\rho}(1 - z/L) + \mathbf{K}\cdot\mathbf{b}] \quad (3)$$

to calculate the total scintillations of the scene. If these amplitude fluctuations are observed at $(\boldsymbol{\rho}_1,z)$ with a detector having a two-dimensional sensitivity $t(\mathbf{r})$, the detected scintillations will take the form

$$dP(\boldsymbol{\rho}_1) = kadz \sin\left[\frac{K^2 z(L - z)}{2kL}\right] \int d^2\mathbf{r}_1 t(\mathbf{r}_1) \int d^2\rho q(\rho) \cos[\mathbf{K}\cdot(\boldsymbol{\rho}_1 + \mathbf{r}_1)(z/L) + \mathbf{K}\cdot\boldsymbol{\rho}(1 - z/L) + \mathbf{K}\cdot\mathbf{b}], \quad (4)$$

where $\mathbf{r}_1 = \mathbf{r} - \boldsymbol{\rho}_1$ is an arbitrary displacement in the plane of $\boldsymbol{\rho}_1$.

To measure the wind we use the technique of Lawrence *et al.*[1] and determine the slope of the covariance of the amplitude fluctuations at zero time lag. Following Lee and Harp,[10] we first obtain the differential covariance function produced by a single scale-size phase screen at all path positions, i.e.,

$$dC_\chi = \left\langle \int_0^L dz_1 dP(\boldsymbol{\rho}_1, z_1) \int_0^L dz_2 dP^*(\boldsymbol{\rho}_2, z_2) \right\rangle, \quad (5)$$

where the angle brackets indicate an ensemble average, and the asterisk implies the complex conjugate. After inserting Eq. (4) into Eq. (5) and interchanging the z_1 and z_2 integrals with the ensemble averaging, we have

$$C_\chi(\boldsymbol{\rho}_1, \boldsymbol{\rho}_2) = k^2 \int_0^L dz_1 \int_0^L dz_2 \sin\left[\frac{K^2 z_1(L - z_1)}{2kL}\right] \sin\left[\frac{K^2 z_2(L - z_2)}{2kL}\right] \int d^2\mathbf{r}_1 \int d^2\mathbf{r}_2 t)(\mathbf{r}_1) t^*(\mathbf{r}_2) \int d^2\boldsymbol{\rho}' \int d^2\boldsymbol{\rho}'' q(\boldsymbol{\rho}') q^*(\boldsymbol{\rho}'') \langle a(\mathrm{K}, z_1) \cos[\mathrm{K}\cdot(\boldsymbol{\rho}_1 + \mathbf{r}_1)(z_1/L) + \mathrm{K}\cdot\boldsymbol{\rho}'(1 - z_1/L) + \mathrm{K}\cdot\mathrm{b}_1] a^*(\mathrm{K}, z_2) \cos[\mathrm{K}\cdot(\boldsymbol{\rho}_2 + \mathbf{r}_2)(z_2/L) + \mathrm{K}\cdot\boldsymbol{\rho}''(1 - z_2/L) + \mathrm{K}\cdot\mathbf{b}_2]\rangle. \quad (6)$$

Equation (6) may be simplified by following the procedure outlined in Appendixes I and II of Lee and Harp,[10] the net effect of which is to replace the quantity in the angle brackets with

$$\langle\rangle = 2F_n(K, z_1 - z_2) \cos\{\mathrm{K}\cdot[(\boldsymbol{\rho}_1 + \mathbf{r}_1)z_1 - (\boldsymbol{\rho}_2 + \mathbf{r}_2)z_2]/L + \mathrm{K}\cdot[\boldsymbol{\rho}'(1 - z_1/L) - \boldsymbol{\rho}''(1 - z_2/L)]\}, \quad (7)$$

where F_n is the two-dimensional spectrum of the refractive-index fluctuations. We now substitute Eq. (7) into Eq. (6), change variables to $2z = z_1 + z_2$ and $\xi = z_1 - z_2$, perform the ξ integration as outlined in Chap. 7 of Tatarski[11] for the case $K^2\xi/k \ll 1$, and obtain

$$C_\chi(\boldsymbol{\rho}) = 4\pi k^2 \int_0^L dz \int d^2\mathbf{K}\Phi_n(\mathrm{K}) \sin^2\left[\frac{K^2 z(L - z)}{2kL}\right] \int d^2\mathbf{r}_1 \int d^2\mathbf{r}_2 t(\mathbf{r}_1) t^*(\mathbf{r}_2) \int d^2\boldsymbol{\rho}' \int d^2\boldsymbol{\rho}'' q(\boldsymbol{\rho}') q^*(\boldsymbol{\rho}'') \cos[\mathrm{K}\cdot(\mathbf{r}_1 - \mathbf{r}_2 + \boldsymbol{\rho})z/L + \mathrm{K}\cdot(\boldsymbol{\rho}' - \boldsymbol{\rho}'')(1 - z/L)], \quad (8)$$

where $\boldsymbol{\rho} = \boldsymbol{\rho}_1 - \boldsymbol{\rho}_2$. Equation (8) has been generalized to an integral over the full three-dimensional spectrum of refractive turbulence $\Phi_n(\mathbf{K})$. (The assumption $K^2\xi/k \ll 1$ requires only that the smallest size eddy in the turbulence spectrum l_0 be much larger than the wavelength. This is a reasonable approximation for the propagation of visible light.) The integrals over $\mathbf{r}_1$, $\mathbf{r}_2$, $\boldsymbol{\rho}'$ and $\boldsymbol{\rho}''$ can most easily be performed by using the convolution theorem, which gives

$$C_\chi(\boldsymbol{\rho}) = 4\pi k^2 (2\pi)^8 \int_0^L dz \int d^2\mathrm{K} \sin^2\left[\frac{K^2 z(L - z)}{2kL}\right] \cos(\mathbf{K}\cdot\boldsymbol{\rho} z/L)\Phi_n(\mathbf{K}) \left| T(\mathbf{K}z/L) \right|^2 \left| Q[\mathbf{K}(1 - z/L)] \right|^2, \quad (9)$$

where $Q(\mathbf{K})$ and $T(\mathbf{K})$ are the two-dimensional Fourier transforms of $q(\rho)$ and $t(\rho)$, respectively, i.e.,

$$Q(\mathrm{K}) \equiv \frac{1}{(2\pi)^2} \int d^2\rho q(\rho) \exp(-i\mathrm{K}\cdot\rho) \quad (10)$$

and

$$T(\mathrm{K}) \equiv \frac{1}{(2\pi)^2} \int d^2\rho t(\rho) \exp(-i\mathrm{K}\cdot\rho). \quad (11)$$

A more straightforward but more complicated approach is to substitute the inverse transforms of t and q directly into Eq. (8) and perform the resulting integrals to obtain Eq. (9).

Equation (9) describes the covariance function of the amplitude fluctuations of an arbitrary incoherent source with spectral density Q^2 observed with two sets of detectors displaced an amount ρ and having a spectral density T^2.

To compute the measured time-lagged covariance function, we must replace ρ by $\rho - \mathbf{v}\tau L/z$ (see Clifford[12]), where τ is the time lag and $\mathbf{v}$ is the wind velocity, and normalize the expression to $C_\chi(0)$, the variance of the observed signal. This results in the expression

$$C_{\chi N}(\boldsymbol{\rho},\tau) = N^{-1}\int_0^L dz \int d^2\mathbf{K}\,\sin^2\left[\frac{K^2 z(L-z)}{2kL}\right] \cos[\mathbf{K}\cdot\boldsymbol{\rho}(z/L) - \mathbf{K}\cdot\mathbf{v}\tau]\Phi_n(\mathbf{K})|T(\mathbf{K}z/L)|^2| Q[\mathbf{K}(1-z/L)]|^2, \quad (12)$$

where

$$N = \int_0^L dz \int d^2\mathbf{K}\,\sin^2\left[\frac{K^2 z(L-z)}{2kL}\right]\Phi_n(\mathbf{K})|T|^2|Q|^2. \quad (13)$$

Finally, we determine the slope at zero time lag $m_N = \partial C_{\chi N}/\partial\tau|\tau = 0$,

$$m_N = N^{-1}\int_0^L dz \int d^2\mathbf{K}\,\sin^2\left[\frac{K^2 z(L-z)}{2kL}\right](\mathbf{K}\cdot\mathbf{v}) \sin(\mathbf{K}\cdot\boldsymbol{\rho}z/L)\Phi_n(\mathbf{K})|T)(\mathbf{K}z/L)|^2|Q[\mathbf{K}(1-z/L)]|^2. \quad (14)$$

Equation (14) is the general expression of the passive wind sensing formula. We will want to particularize the form of Eq. (14) in the next sections to study some practical systems. The factors z/L and $(1 - z/L)$, which modify the receiver and transmitter power spectral densities $|T|^2$ and $|Q|^2$, respectively, satisfy the elementary form of reciprocity, i.e., transmitter and receiver spectral densities may be interchanged to give the same result for Eq. (8) if z/L and $1 - z/L$ are also interchanged.

III. Crosswind Sensing

To obtain numerical results from Eq. (14), we must specify the form of three spectral densities, the refractive-index spectral density Φ_n, the scene spectrum $|Q|^2$, and the detector spectrum $|T|^2$. The most commonly accepted form of the spectrum of refractive turbulence is that due to Kolmogorov.[13] He postulated from dimensional analysis arguments that, within the socalled inertial subrange, defined by $L_0^{-1} \ll K \ll l_0^{-1}$, where l_0 and L_0 are the inner and outer scales of turbulence, respectively, the spectral density of the refractive-index fluctuations should have the form

$$\Phi_n(K) = 0.033C_n^2(z)K^{-11/3}. \quad (15)$$

We will use this spectrum throughout this paper.

For the detector spectrum $|T|^2$, we will discuss both the broadband and narrowband techniques in accordance with the bandpass of the spatial-spectral response of the receiver. In the broadband case, the receiver consists of two circular apertures of diameter D. The detector spectrum $|T|^2$ is then simply a lowpass filter function, i.e.,

$$|T(\mathbf{K}z/L)|^2 = \left(\frac{D^2}{16\pi}\right)^2\left[\frac{2J_1(KDz/\alpha L)}{(KDz/\alpha L)}\right]^2; \quad (16)$$

however, we found that practical difficulties are encountered in the broadband case. Temporal changes in illumination of the scene caused by movement or ac lights are not even partially canceled out and lead to large wind-estimate errors even though the light variation is of the order of one part in ten thousand of the light level of the entire scene. In addition, the broadband SNR is not as high as can be obtained with the detector arrays used in a narrowband system; therefore, we have discarded the broadband approach in favor of a spatial-filter detector or narrowband technique. In this technique, we spatially filter the received signal along one dimension transverse to the optical beam. Using an array of photodiodes, we synthesize a narrowband filter that emphasizes a single spatial frequency in that direction. By using two of these devices, separated by a phase lag of ϕ degrees in terms of the fundamental wavelength of the filter $2\pi/K_0$, we can measure the speed and sense of advection of this wavelength disturbance across the receiver.

Spatial filtering does not produce a single sinusoidal variation in time because of the many different path positions and scale sizes to which this filter is sensitive. For example, each point source of light in a scene produces a disturbance at the receiver that is a geometrically magnified version of the spatial frequency of refractive turbulence at a given path position that each source illuminates (see Lawrence *et al.*[1]). This makes the spatial-filter detector sensitive to spatial scale sizes of refractive turbulence that are larger in proportion to the distance from the scene. Therefore, because the wind profile is not uniform and because the frequency of the received disturbance is inversely proportional to the refractive-turbulence scale size, there will be many different temporal frequencies collected by the detector.

Mathematically, an ideal spatial filter oriented along the x direction has a two-dimensional transmittance

$$t(\boldsymbol{\rho}) = \cos(K_0 x + c)\delta(y), \quad (17)$$

where c is an arbitrary phase factor. The delta function implies that the elements of the filter have zero extent in the y direction and merely sample the field at $y = 0$. The theory requires that we compute the two-dimensional spectral density of t, which is

$$|T|^2 = \frac{1}{(2\pi)^1}\left|\int d^2\boldsymbol{\rho}\,\cos(K_0 x)\delta(y)\,\exp(-i\mathbf{K}\cdot\boldsymbol{\rho})\right|^2 \quad (18)$$

or

$$|T(\mathbf{K}z/L)|^2 \propto \delta[K_x(z/L) - K_0] + \delta[K_x(z/L) + K_0]. \quad (19)$$

In Eq. (19), K_x is the component of $\mathbf{K}$ in the x direction. [We need not be concerned about the coefficient in (19) because it will drop out of the normalized covariance function when substituted into Eq. (14).] Inserting Eqs. (15) and (19) into Eqs. (13) and (14), letting $K_1 = K_y z/L$, and performing the K_x integration, we obtain

$$m_N = N_1^{-1} K_0 \sin\phi \int_0^L dz C_n^2(z) v(z)(z/L)^{2/3} \int_{-\infty}^{\infty} dK_1 \times \frac{\sin^2[(K_0^2 + K_1^2)(L/z - 1)L/2k]}{(K_0^2 + K_1^2)^{11/6}} F(K_1, K_0, z/L) \quad (20)$$

and

$$N_1 = \int_0^L dz C_n^2(z)(z/L)^{5/3} \int_{-\infty}^{\infty} dK_1 \times \frac{\sin^2[(K_0^2 + K_1^2)(L/z - 1)L/2k]}{(K_0^2 + K_1^2)^{11/6}} F(K_1, K_0, z/L), \quad (21)$$

where $2F = |Q[K_0(L/z - 1), K_1(L/z - 1)]|^2 + |Q[-K_0(L/z - 1), K_1(L/z - 1)]|^2$. The phase lag $\phi = K_0 x_0$, where x_0 is the separation of the two detector arrays in the x direction. To put Eq. (20) in a form more suitable for computing, we let $u = z/L$, $t = K_1(\lambda L)^{1/2}$, and $t_0 = K_0(\lambda L)^{1/2}$, where λ, as before, is the mean wavelength of the product of the background light and photodiode response. Equation (20) then becomes

$$m_N = \frac{t_0 \sin\phi(\lambda L)^{-1/2} \int_0^1 du C_n^2(u) v(u) W_f(u)}{\int_0^1 du C_n^2(u) u W_f(u)}, \quad (22)$$

with

$$W_f(u) = u^{2/3} \int_0^{\infty} dt \frac{\sin^2[(t_0^2 + t_1^2)(1/u - 1)/4\pi]}{(t_0^2 + t_1^2)^{11/6}} F(t, t_0, u). \quad (23)$$

The assumption that C_n^2 is statistically uniform along the path allows us to cancel C_n^2 in the numerator and denominator of Eq. (22), and m_N becomes

$$m_N = \frac{t_0 \sin\phi}{A(\lambda L)^{1/2}} \int_0^1 du v(u) W_f(u), \quad (24)$$

where

$$A = \int_0^1 du u W_f(u). \quad (25)$$

Clearly from Eq. (24), we see that $W_f(u)$ is the path weighting function for the wind, i.e., the relative effectiveness of winds at each position of the path for producing the optical wind reading. If the scene spectrum is known, we can find $W_f(u)$ from Eq. (23), and, after substituting the result into Eq. (24), we can determine the path-averaged crosswind.

IV. Effects of the Scene Spectrum on Wind Weighting Functions

In this section we will consider two distinct types of scene spectra, exponential and power law, to indicate the variability of the wind weighting function $W_f(u)$, when sighting the passive wind sensor on different targets. As we shall see, the most important difference between the two types is that the exponential spectrum has a characteristic wavenumber (the equivalent of a time constant in time varying systems), whereas the power-law spectrum does not.

For the power-law scene spectrum, $|Q(\mathbf{K})|^2 \sim K^{-\alpha}$, we will vary α from 0 to 3. After substituting this spectrum into Eq. (23), we obtain

$$W_f(u) = \frac{u^{2/3+\alpha}}{(1 - u)^{\alpha}} \int_0^{\infty} dt \frac{\sin^2[(t_0^2 + t_1^2)(1/u - 1)/4\pi]}{(t_0^2 + t_1^2)^{11/6+\alpha/2}}. \quad (26)$$

Figures 3–6 show the behavior of the wind weighting function as a function of the exponent of the scene spectral power law α and the normalized wavelength of the receiving spatial filter $d_n = 2\pi/t_0 = 2\pi/[K_0(\lambda L)^{1/2}]$ for $\phi = \pi/2$. For a fixed filter wavelength, as the scene spectrum becomes steeper (higher α, i.e., contains more low frequencies), the weighting function peaks progressively closer to the receiver. For a fixed scene spectrum α, increasing the

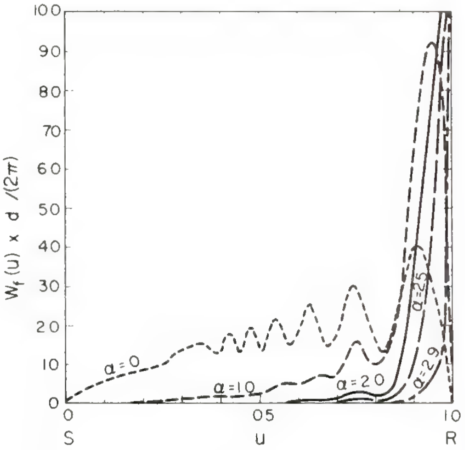

Fig. 3. Wind weighting function for a receiving array with a normalized spatial wavelength $d_n = 0.5$. The scene spectrum is assumed to follow a power-law spectrum with the slope $-\alpha$.

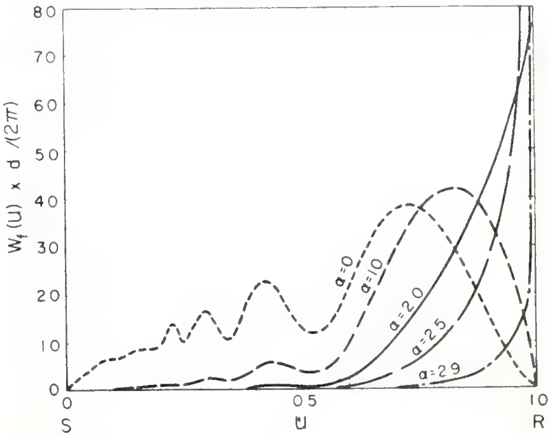

Fig. 4. Wind weighting function for a receiving array with a normalized spatial wavelength of $d_n = 1$. The scene spectrum is assumed to follow a power-law spectrum with the slope $-\alpha$.

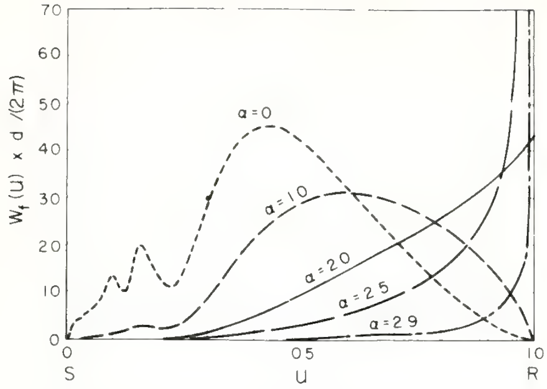

Fig. 5. Wind weighting function for a receiving array with a normalized spatial wavelength $d_n = 2$. The scene spectrum is assumed to follow a power-law spectrum with the slope $-\alpha$.

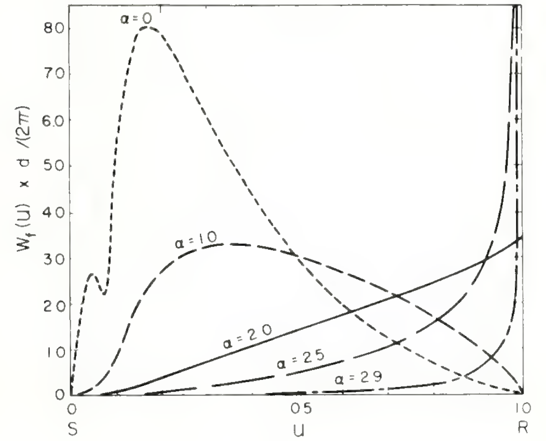

Fig. 6. Wind weighting function for a receiving array with a normalized spatial wavelength of $d_n = 4$. The scene spectrum is assumed to follow a power-law spectrum with the slope $-\alpha$.

wavelength of the filter tends to bias the weighting function back toward the scene. One caution in using these figures is that the oscillations in the curves, say for $d_n = 0.5$ and $\alpha = 0$, arise because of the assumption of monochromaticity implicit in Eq. (26). For a real scene there will be many wavelengths of light present, and these oscillations will be smeared out. For $\alpha > 2$, the weighting functions increase without limit at the receiver end. This is caused by the fact that a power-law spectrum diverges at zero frequency. If we assume an outer scale for the scene spectrum, i.e., a finite maximum scale for details in the scene, the weighting functions will go to zero at the receiver end. For different pathlengths, the relative path-weighting function will not change for a power-law scene spectrum; therefore, Figs. 3–6 can be used for any pathlength.

The variability of the weighting functions with α indicates that it is desirable to monitor the scene spectrum as closely as possible.

Inserting an exponential spectrum $|Q|^2 \sim \exp(-K/K_s)$ into Eq. (23), where K_s is a characteristic wavenumber of the scene, we obtain a wind weighting function of the form

$$W_f(u) = u^{2/3} \int_0^\infty dt \, \frac{\sin^2[(t_0^2 + t_1^2)(1/u - 1)/4\pi]}{(t_0^2 + t_1^2)^{11/6}} \exp[-(t_0^2 + t_1^2)^{1/2}(1/u - 1)/K_s(\lambda L)^{1/2}]. \quad (27)$$

To illustrate the physical validity of assuming an exponential scene spectrum, the solid curve in Fig. 1 is an exponential spectrum with $K_s = 4$ cycles/m. The data points are the spectrum of a 35-mm color slide of two vehicles against a background of trees. The fit to the data is excellent. The results of Eq. (27) are plotted in Figs. 7–9. In Fig. 7, we assume that $K_s = 4$ cycles/m, $L = 500$ m, $\lambda = 0.8$ μm, and hence $(\lambda L)^{1/2} = 0.02$ m. Figure 7 shows a family of curves with the normalized spatial wavelength of the receiving filter d_n varying from 0.5 to 4.0. Again, as we have seen for the power-law spectrum, increasing the receiver spatial wavelength tends to bias the weighting function back toward the scene. Because there is only a finite amount of energy in an exponential scene spectrum at low frequencies, the weights all go to zero at the receiver end. If we now keep the normalized receiving spatial wavelength d_n fixed and vary the normalized characteristic wavenumber of the scene $K_s(\lambda L)^{1/2}$, the relative weights are as shown in Fig. 8. As the normalized characteristic wavenumber increases, which may be either the result of the increase of the pathlength or the decrease of the scale sizes in the scene, the weighting functions move toward the target. The case for $K_s(\lambda L)^{1/2} = \infty$ is the limiting case of the scene spectrum being white noise. In this case, the weighting function coincides with the power-law spectrum of $\alpha = 0$.

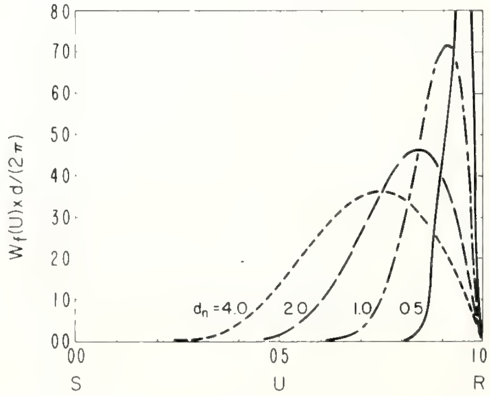

Fig. 7. Wind path weighting for receiving array normalized spatial wavelength d_n varying from 0.5 to 4.0. The scene spectrum is assumed to follow an exponential spectrum $\exp[-K(\lambda L)^{1/2}/A]$ with $A = K_s(\lambda L)^{1/2} = 0.5$ in this figure.

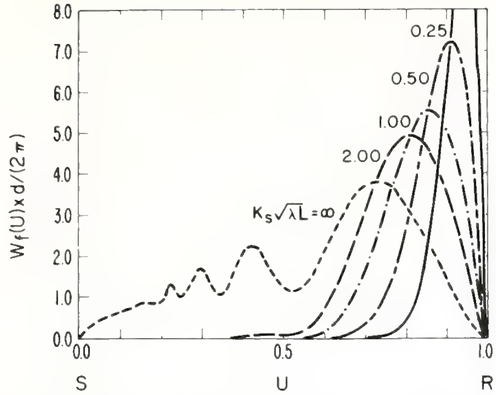

Fig. 8. Wind path weighting for a fixed receiving spatial wavelength $d_n = 1$. The scene spectrum is assumed to follow an exponential spectrum $\exp[-K(\lambda L)^{1/2}/A]$ with $A = K_s(\lambda L)^{1/2}$ varying from 0.25 to ∞.

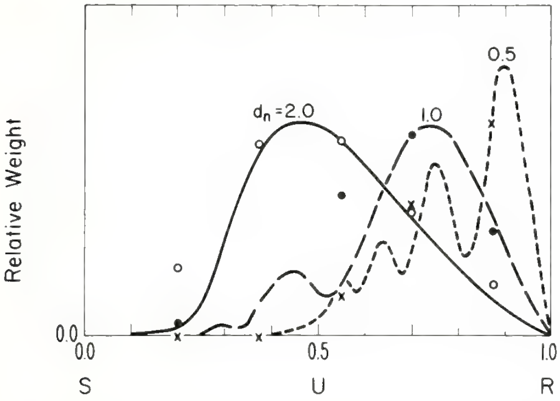

Fig. 9. Experimental and theoretical results of a ⅓ Fresnel zone circular aperture transmitter and a receiving array with spatial wavelength d_n.

V. Experimental Results

We performed an experiment on a uniform 500-m path to check the results of Eq. (23). Our path was equipped with ten propeller anemometers to measure the component of the horizontal wind at right angles to the optical path. We analyzed the data with an on-line minicomputer and compared the optical and *in situ* crosswind measurements. Data were smoothed with a 10-sec time constant and then sampled every 10 sec. The averaging period is necessary so that the anemometer measurements are more nearly like the 40-m spatial average that they are intended to represent.

If we let A_0 and A_i be the optical and the ith *in situ* measurements, respectively, the path-weighting function W_i can be defined as

$$A_0 = \sum_{i=1}^{N} W_i A_i, \tag{28}$$

where N is the number of anemometers used. Multiplying by $A_j (j = 1,2, \ldots N)$ on both sides of Eq. (28) and taking the ensemble average, we have N equations in the form

$$\langle A_0 A_j \rangle = \sum_{i=1}^{N} W_i \langle A_i A_j \rangle;\ j = 1, 2, \ldots N. \tag{29}$$

The wind weighting function W's can be obtained by solving these ten linear equations. In actuality, the ensemble average we used is the average of 88 scans of data, sampled at the rate of one scan each 10 sec.

To check the theory, we performed the experiment using a target with a known spectrum, i.e., an incandescent light source one-third of a Fresnel zone in diameter. In this case where the transmitter configuration is a circular aperture of diameter D, $|Q|^2$ is a low-pass filter function, i.e.,

$$|Q(K)|^2 \propto \left[\frac{2J_1(KD/2)}{(KD/2)}\right]^2 \tag{30}$$

Inserting Eq. (30) into Eq. (23), we obtain the path-weighting functions shown as the continuous curves in Fig. 9. The experimental results are shown by the crosses ($d_n = 0.5$), dots ($d_n = 1.0$), and circles ($d_n = 2.0$). The data agree quite closely with the theoretical predictions.

For a real scene, we chose as a target a trailer at the end of a 500-m path with a background of trees and mountains. The experimental weighting functions are shown in Fig. 10. Since we did not measure the scene spectrum in this case, we can only compare the experimental results to the theoretical prediction qualitatively. Both the theoretical results of a power-law spectrum (Figs. 3–6) with α between 2 and 2.5 and the exponential spectrum (Fig. 7) seem to agree with the experimental measurements. For a more sophisticated passive wind sensor, a monitor of the scene spectrum should be introduced. To com-

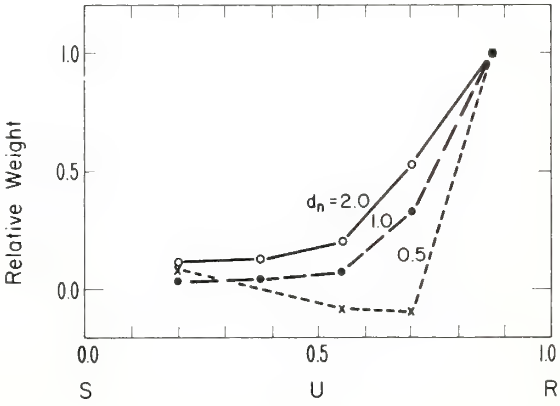

Fig. 10. Experimental wind weighting functions for a trailer in bright sunlight and the receiving array with a spatial wavelength d_n. The functions have been normalized by setting the largest ordinate of each curve to unity.

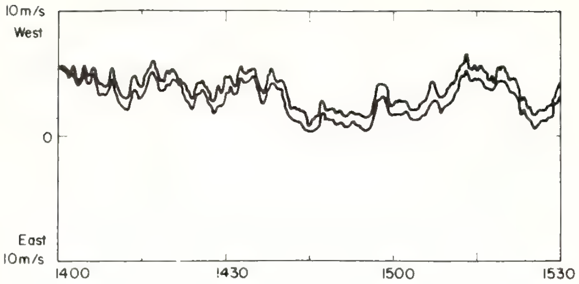

Fig. 11. A comparison of the transverse wind speed measured by the optical system (upper trace) with the average of wind speeds measured by five anemometers, equally spaced on half of the 500-m path nearest the instrument. The gain of the optical system was increased to displace the curves.

pare the optical measurement to the anemometer readings, the results of the optical measurement and the average of the outputs of the five anemometers on half of the 500-m path nearest the receiver are shown in Fig. 11. Again, they exhibit excellent agreement. The agreement on short time intervals would be even better had the anemometers been weighted according to the weighting function of the optical system. (The data shown in Fig. 11 were taken with a prototype passive-wind sensing instrument whose principles of operation were based on the theoretical analysis above. The details of the development of this instrument and the conditions of the experiment are more fully described in Refs. 14 and 15.)

VI. Summary

We have demonstrated that a naturally occurring scene can be used as a passive optical source to measure the path-averaged crosswind between the scene and the observer. The resultant path-weighting functions cannot be varied arbitrarily, but a useful variety of weighting functions can be specified.

The major difficulty with the passive wind sensor, i.e., coping with both spatial and temporal changes in scene spectra, can be overcome by introducing a scene spectrum monitor that would continuously adjust the detector spatial filter wavelength to maintain the desired wind weighting function. There is no physical reason why this cannot be done, although it may be difficult to accomplish in a practical system.

The motivation for developing this system has been to overcome the limitations of our laser beam wind sensor for applications in difficult terrain and for fast response wind measurement at a variety of azimuths. In the former case, the passive sensor eliminates the need to gain access to sites for mounting detectors or transmitters in hazardous terrain. In the latter, the passive sensor eliminates the need for locating and maintaining multiple sources to obtain wind coverage over a broad area.

This work was supported in part by the U.S. Army Electronics Command, Atmospheric Sciences Laboratory, White Sands, New Mexico 88002; T. H. Pries was the ASL Scientific Monitor.

References

1. R. S. Lawrence, G. R. Ochs, and S. F. Clifford, Appl. Opt. **11**, 239 (1972).
2. R. W. Lee, J. Opt. Soc. Am. **10**, 1295 (1974).
3. T-i Wang, S. F. Clifford, and G. R. Ochs, Appl. Opt. **13**, 2602 (1974).
4. L. Shen, IEEE Trans. Antennas Propag. **AP-18**, 493 (1970).
5. A. Ishimaru, IEEE Trans. Antennas Propag. **AP-20**, 10 (1972).
6. P. A. Mandics, R. W. Lee, and A. T. Waterman, Jr., Radio Sci. **8**, 185 (1973).
7. J. C. Harp, Ph.D. Thesis, AFCRL-71-0451, SV-SEL-71-042, Scientific Report 1 (1971).
8. P. A. Mandics, Ph.D. Dissertation, Stanford Univ., Stanford, Calif. (1971).
9. A. G. Kjelaas and G. R. Ochs, J. Appl. Meteorol. **13**, 242 (1974).
10. R. W. Lee and J. C. Harp, Proc. IEEE **57**, 375 (1969).
11. V. I. Tatarski, *Wave Propagation in a Turbulent Medium* (McGraw-Hill, New York, 1961), Chap. 7.
12. S. F. Clifford, J. Opt. Soc. Am. **61**, 1285 (1971).
13. A. N. Kolmogorov, Dokl. Akad. Nauk. SSSR **30**, 299 (1941).
14. S. F. Clifford, G. R. Ochs, and T-i. Wang, NOAA Tech. Rept. ERL 312-WPL-35 (1974).
15. G. R. Ochs, G. F. Miller, and E. J. Goldenstein, NOAA Tech. Memo ERL WPL-11 (1974).

NOAA Technical Report ERL 312-WPL 35

September 1974

THEORETICAL ANALYSIS AND EXPERIMENTAL EVALUATION OF A PROTOTYPE PASSIVE SENSOR TO MEASURE CROSSWINDS

S. F. Clifford, G. R. Ochs, and Ting-i Wang

We describe and analyze the performance of our prototype passive wind sensor. The instrument interprets the turbulence-induced optical scintillations of a random scene to infer a path-weighted transverse wind speed between scene and observer. We derive the fundamental theoretical relations on which the system is based and discuss the overall capabilities and limitations of the technique. We conclude that the system has useful application but requires a more extensive demonstration of its ability to perform with a wider variety of scene spectra and under more diverse meteorological conditions before the technique becomes operational.

NOAA Technical Report ERL 296-WPL 29

November 1974

A THEORETICAL ANALYSIS OF THE INFORMATION CONTENT OF LIDAR ATMOSPHERIC RETURNS

V. E. Derr, M. J. Post, R. L. Schwiesow,
R. F. Calfee, and G. T. McNice

The applicability of new laser technology to observation of meteorological parameters is explored in this study of the relevant information content in laser radiation after interaction with the atmosphere.

NOAA Technical Report ERL 302-WPL 33

July 1974

REMOTE SENSING OF POLLUTANTS

COMPUTERIZED REDUCTION OF LONG-PATH ABSORPTION DATA

V. E. Derr, M. H. Ackley, M. J. Post, and R. F. Calfee

ABSTRACT

Atmospheric gaseous pollutants are very numerous in industrial regions. It is estimated that 25 or more pollutant molecules may be found in the atmosphere in significant quantities. The measurement of the concentration of each gas from the complex spectrum obtained by a long-path infrared spectrophotometer requires the fitting of trial spectra composed from a library of spectra. The fitting procedure adjusts the concentrations of the trial spectra until a "best fit" in a least-squares sense is produced. This report is a description of the physical, mathematical, and calculational principles and procedures for the use of a digital computer program to determine concentrations of atmospheric gases in a path of a few kilometers. Detailed instructions for the computer program and a library of spectra are provided.

Reprinted from:
LASER APPLICATIONS, VOL. 2
© 1974
ACADEMIC PRESS, INC.

LASER SYSTEMS FOR MONITORING THE ENVIRONMENT

Freeman F. Hall, Jr.

Wave Propagation Laboratory, Environmental Research Laboratories
National Oceanic and Atmospheric Administration, Boulder, Colorado

I. Introduction . . . 161
II. Laser Systems Analysis . . . 163
  A. The Lidar Equation . . . 163
  B. Scattering of Laser Light . . . 165
  C. Signal-to-Noise Calculations for a Lidar System . . . 167
  D. Lidar Calibration Methods . . . 170
  E. Data Display and Evaluation . . . 172
  F. Safety . . . 172
  G. Group for Laser Atmospheric Probing . . . 174
III. Laser Detection of Particulate Matter in the Environment . . . 174
  A. Turbidity . . . 175
  B. Visibility Investigations . . . 185
  C. Diffusion Studies in the Atmosphere . . . 187
  D. Clouds, Fog, and Precipitation . . . 190
  E. Polarization Effects . . . 197
  F. Laser Probing of the Stratosphere and Above . . . 198
IV. Laser Sensing of Turbulence and Winds . . . 205
V. Atmospheric Constituent Analysis with Lasers . . . 211
VI. Temperature Measurements . . . 218
VII. Conclusions . . . 219
  References . . . 219

Study of Divergence in the Boundary Layer Using Optical Propagation Techniques[1]

A. G. Kjelaas
Norwegian Defence Research Establishment, Kjeller

G. R. Ochs
Environmental Research Laboratories, NOAA, Boulder, Colo. 80302

(Manuscript received 25 July 1973, in revised form 27 November 1973)

ABSTRACT

A wind-measuring system using three separate optical systems, each consisting of a 3 mW He-Ne laser and two photodiode receivers, forming an equilateral triangle 300 m on a side, has successfully measured the divergence over the area of the triangle, and the space-averaged horizontal wind vector. Good correlation was found between the flow into the triangle and occurrences of thermal plumes seen by an adjacent acoustic sounder. The flow into the triangle was proportional to the vertical velocity. During large convective activity, there was a certain periodicity in the occurrence of plumes.

1. Introduction

Reliable measurements of the divergence of the horizontal wind are difficult to achieve. Many attempts have been made to develop methods based on point measurements of wind. On the synoptic scales, Bellamy (1949) developed a technique that used a triangle of wind reports to calculate the divergence for the enclosed area; Endlich and Clark (1963) calculated divergence by linear interpolation between wind components at the vertices of the triangle of observation. Eddy (1964) improved Bellamy's triangle technique by using a computer model. He also applied a correlation technique to establish the space correlation and time persistence.

On smaller scales (i.e., those scales comparable with plumes and on up to a few hundred meters), no reliable techniques for measuring the horizontal divergence exist. Many laboratory experiments have formed the basis for different theories for entrainment into plumes. Morton *et al.* (1956) have described a model assuming that the rate of entrainment into the plumes is proportional to the vertical velocity inside the plume. Telford (1966) has developed a model assuming that the entrainment should not be related to the mean velocity but to the local level of turbulence.

Due to lack of suitable wind-measuring techniques these theories have been difficult to check in the atmosphere. Recently, remote sensing of space-averaged wind has progressed, making it possible to calculate the divergence for a small enclosed area. Lawrence *et al.* (1972) have described an optical wind sensor that uses the naturally occurring density fluctuations to obtain a spatially averaged wind. By using a correlation technique at the receiver, they are able to extract a path-averaged transverse wind speed.

This paper discusses field measurements of divergence and wind velocity based on an extension of the optical technique. A He-Ne laser triangle path (300 m on a side) was set up near a 150 m tower. The results are compared with wind velocity measured at five levels on the tower and with the occurrence of plumes as seen by an acoustic sounder located inside the triangle.

2. The optical measuring equipment

The optical technique used for wind measurement is described fully in Lawrence *et al.* (1972); however, a brief discussion is included here for completeness, since it is a recent development. The technique may be used over ranges from 300 m to more than 15 km, so that it is particularly useful for obtaining spatially averaged wind measurements. In addition, it is effective for measuring low mean wind flow in the presence of large fluctuating components.

The technique uses the drifting scintillation pattern arising from wind-transported refractive-index irregularities in the atmosphere. This drifting scintillation pattern is the cause of the twinkling, or scintillation, of starlight. With a very small, bright light source, such as a laser shining through the atmosphere, the moving scintillation pattern can be seen clearly on a screen at night. The sizes of the irregular patches of light in the pattern are determined by the diffraction of the incident beam; they result from refractive-index irregularities

---

[1] The paper was prepared while the senior author was a visiting scientist at the National Oceanic and Atmospheric Administration, Environmental Research Laboratories, Boulder, under sponsorship of the Royal Norwegian Council for Scientific and Industrial Research.

(almost entirely the result of temperature differences) at various positions along the propagation path. At each position, the diffraction process selects a most effective scale of irregularity, or eddy, whose size is sufficient to cause a half-wavelength difference in path-length to the receiver for two extreme rays passing through its edges. The diffraction effects of this particular eddy dominate over those of other eddies at the same location.

If a diverging laser beam is effectively a point source, geometric magnification increases the size of the received eddy image by the factor L/z, where z is the position along a beam of length L. The image drift rate at the receiver caused by the local eddy drift velocity, depending on the wind at position z, is also increased by the same factor. Therefore, the received optical disturbance is larger and moves faster than the eddy that produced it. Since different portions of the path contribute to the total scintillation pattern, that pattern will be continuously evolving because of the relative speeds of the different sized features it contains.

To measure the average component of the wind across an optical path, we look at fluctuations in light intensity in two small apertures spaced along the direction of movement of the pattern, as shown in Fig. 1. A function like that shown in Fig. 2 results if the normalized covariance of the logarithms of these signals is computed. For the conditions of a uniform wind at right angles to the optical path and parallel to the separation of the detectors, and for uniform refractive-index structure constant (C_n^2) along the path, some measure of the time scale of the function, e.g., the time delay to the peak or the slope of the function at zero delay, could be used to derive wind speed. For the real case, with winds of arbitrary direction and speed along the path, and with a non-uniform distribution of C_n^2 along the path, this function changes not only in time scale, but also in shape. It can be shown (Lawrence *et al.*, 1972), for uniform C_n^2 along the path, that the slope of the function at zero delay has a known relationship to the average horizontal wind across the path, even though the wind along the path is non-uniform in direction and speed. Thus, we measure the slope at zero delay to determine the average wind. The weighting function of the wind measurement for various receiver separations is shown in Fig. 3 as a function of $\beta=\rho(\lambda L)^{-\frac{1}{2}}$, where ρ is the detector spacing, λ the laser wavelength, and L the path length. For the divergence measurement reported here, $\beta=0.46$. This separation, and the use of apertures 6 mm in diameter, gave a nearly symmetrical weighting function around the center of the path.

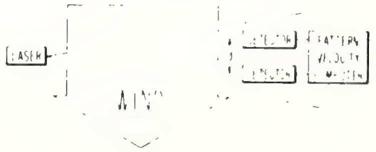

Fig. 1. The general arrangement used to measure the average component of the wind, across a laser beam, parallel to the (usually horizontal) spacing of two detectors.

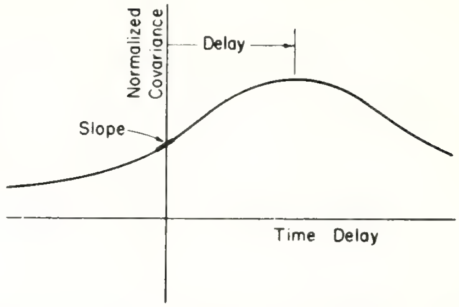

Fig. 2. A schematic diagram of the normalized covariance function, showing the delay to the peak and the slope at zero time lag. While the former is frequently used to measure pattern drift velocities, the latter is more suitable in the optical case where the pattern decays rapidly.

There are several limitations to the present optical system, but we no not believe that they affected the wind measurements reported here. The wind weighting function is strictly correct only when the wind measurement is averaged over enough time so that C_n^2 is statistically uniform over the path. This can be satisfied for a horizontal path, but if, for example, a slant path is used C_n^2 will tend to be higher at the lower end of the path, and the wind in this portion will be weighted more heavily. Random variations of C_n^2 will distort the measured average wind speed only if they are correlated with the variations in wind speed. A reasonable supposition is that turbulence is strongest at locations of maximum wind shear, not at locations of maximum wind speed. If so, the turbulence tends to be uncorrelated with the wind, and the average obtained by the

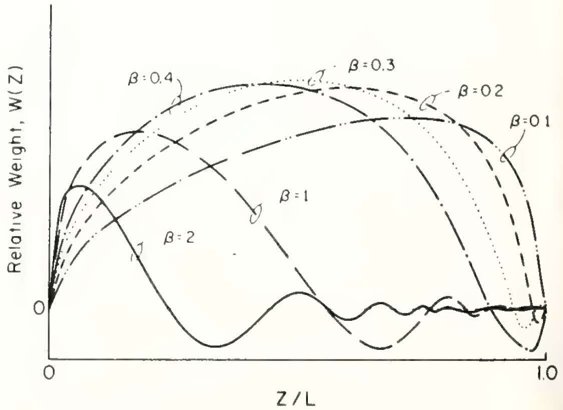

Fig. 3. The relative weights of the different portions of the path in determining the optically measured wind. The parameter $\beta=\rho(\lambda L)^{-\frac{1}{2}}$ is the separation of the sensors. These curves are calculated for point sensors; the finite area of a real sensor will tend to remove the negative weights near the receiver.

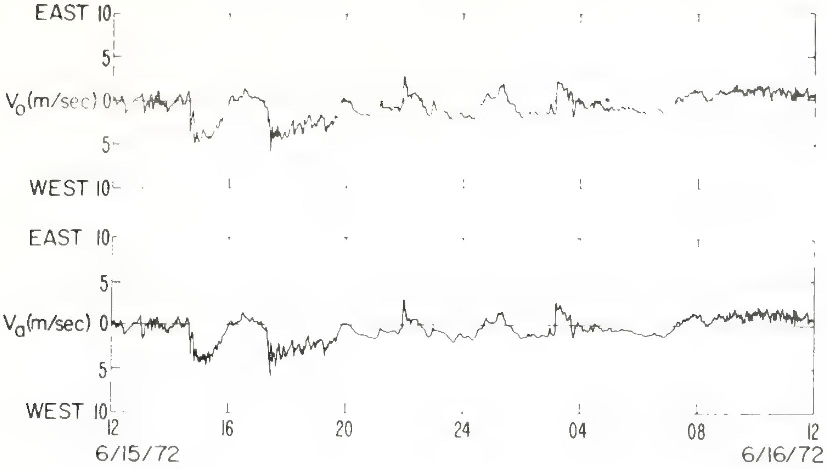

FIG. 4. A comparison of the average wind speed (V_o) measured optically, with the average of the readings of six Gill propellor anemometers (V_a) uniformly spaced along the optical path. Both the anemometers and the optical system measure the component of wind that is horizontal and at right angles to the path. The path is 300 m long, oriented north south, and 3 m above the ground.

optical system is unbiased. A second source of error may occur when there is a combination of high refractive index fluctuations and long path. Under these conditions, a so-called saturation effect occurs, in which the optical scintillation no longer increases with C_n^2. When this condition occurs, the spherical propagation equations upon which the optical wind measurement is based are no longer correct. The result is that the optical measurement will underestimate the true wind, and in severe saturation this may be by a factor of 2 or more. Saturation may be easily detected by the optical system and did not occur on the 300 m paths used in our divergence experiment.

Before undertaking the divergence experiment, we compared the average wind speed reading of one of the three optical systems, over the same height and path length that was later used, with the average of the readings of six Gill propellor anemometers uniformly spaced along the optical path. The anemometers were oriented to read the component of wind that was horizontal and at right angles to the optical path. The result for a 24-hr period is shown in Fig. 4 and appears to offer full proof of satisfactory performance.

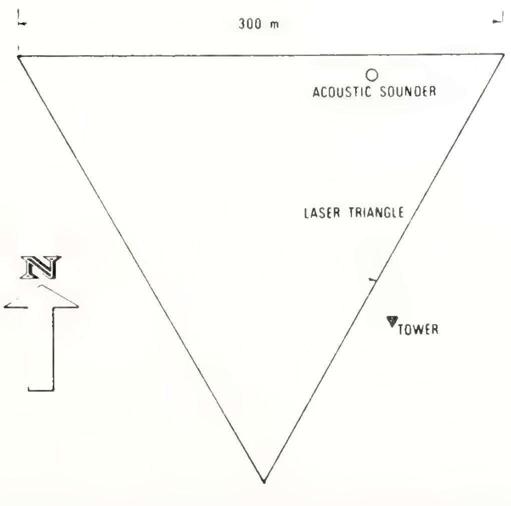

FIG. 5. The layout of the laser triangle, 150 m meteorological tower, and the acoustic sounder.

3. Measurement and data reduction

The measurements were made at Haswell, Colo., during a two-week period in the beginning of August 1972. The Haswell area has a typical high-plain meteorological regime with strong radiative cooling during the night and strong solar heating and convective activity during the day.

Three separate optical systems, each consisting of a 3-mW He-Ne laser, two photodiode receivers, and a small specialized computer providing a real-time readout of average wind speed, were used in the experiment. The optical paths formed an equilateral triangle, 300 m on a side and 2.3 m above the ground. Fig. 5 shows the location of the laser triangle relative to the meteorological tower and the acoustic sounder. The terrain near the triangle is flat and free from any obstacles for a minimum of 3 km in any direction. The area is covered with clumps of buffalo grass (~15 cm in height). Since each optical path was arranged to read an outflowing wind as positive, the sum of the readings of all three paths represents the average horizontal wind speed out of the triangle. The individual wind readings for each optical path, smoothed with a 10-sec running average, as well as the scalar sum of all three, were recorded

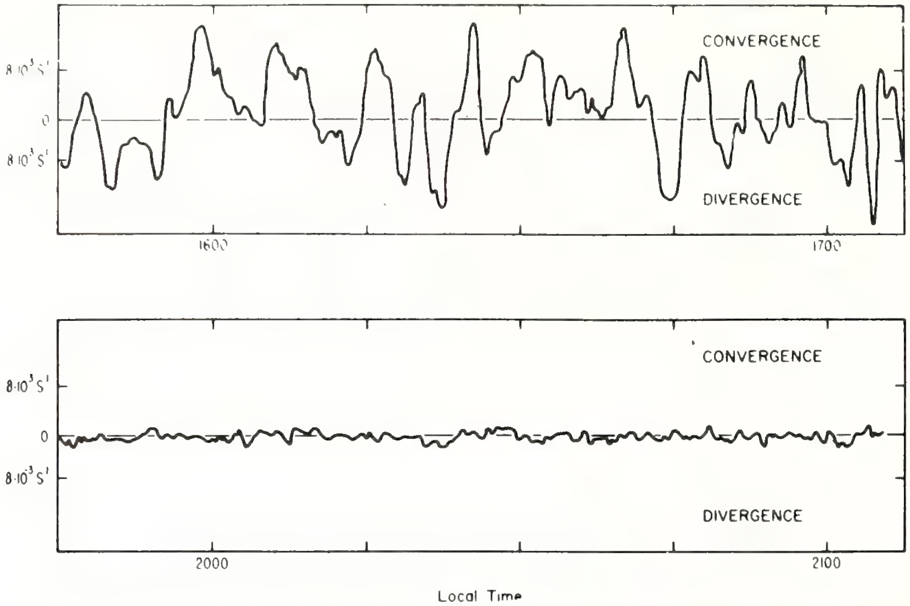

FIG. 6. Ten-second average divergence recordings for typical afternoon and night periods.

simultaneously on strip chart recorders and on a digital tape recorder.

The horizontal wind divergence is given by

$$\nabla_h \cdot \mathbf{V} = \frac{L(v_0+v_{120}+v_{210})}{A},$$

where v_0, v_{120}, v_{210} are the wind components transverse to the east-west, 30°-210° and 150°-330° triangle sides, respectively; L is the side of the triangle; and A the area of the triangle.

Typical recordings of divergence during periods of large convective activity and stable conditions are shown in Fig. 6. Convergence of 10^{-2} sec^{-1} over periods of minutes is common during daytime. During the night, values of 5×10^{-4} sec^{-1} are normal. This value may be considered the upper limit of the noise level of the divergence measurement. In the comparison between divergence and vertical velocity, a 100-sec running average was used. The space-time average wind velocity was computed by using the wind components measured over two of the triangle sides. This, of course, gives a redundant estimate of the velocity as we have three pairs of legs on a triangle.

Using, for example, the east–west and 30°-210° pair, the horizontal space average wind speed $\bar{V}_s$ can be expressed in terms of the two components v_0 and v_{120} as

$$\bar{V}_s = \left[\left(\frac{2v_{120}+v_0}{3}\right)^2 + v_0^2\right],$$

and the direction α from which the wind is blowing as

$$\alpha = \tan^{-1}\left(\frac{v_0\sqrt{3}}{2V_{120}+v_0}\right) + 180°.$$

Using the other pairs of the triangle, similar expressions are obtained.

The meteorological tower was instrumented to measure vector wind by the use of bivanes at five fixed levels: 31, 62, 93, 124 and 149 m. The acoustic sounder inside the triangle was pointing vertically, and its records were compared with the measured inflow into the triangle. All data, except the acoustic sounder data, were sampled once per second and recorded on digital tapes. The acoustic sounder data were recorded (both) on facsimile and analog tapes.

4. Results

a. Comparison of divergence and the acoustic sounder

Considerable evidence now exists that plume-like structure can be seen by an acoustic sounder (McAllister *et al.*, 1969; Beran, 1971). Fig. 7 shows an acoustic sounder record and a divergence for predominately large convective activity. The dark portions on the sounder record correspond to thermal plumes and their height indicates the height of the plumes, while the white "gaps" are interpreted as area between plumes. The solid line is the divergence measured by the optical system. Convergence is upward on the figure.

The correspondence between the measured convergence and the plumes as seen by the acoustic sounder is mostly good, although some discrepancies can be seen especially after 1440 local time. Note that while the divergence is measured at a height of about 2 m above ground, the lowest height seen by the acoustic sounder is about 50 m, making an absolute comparison between the two systems difficult.

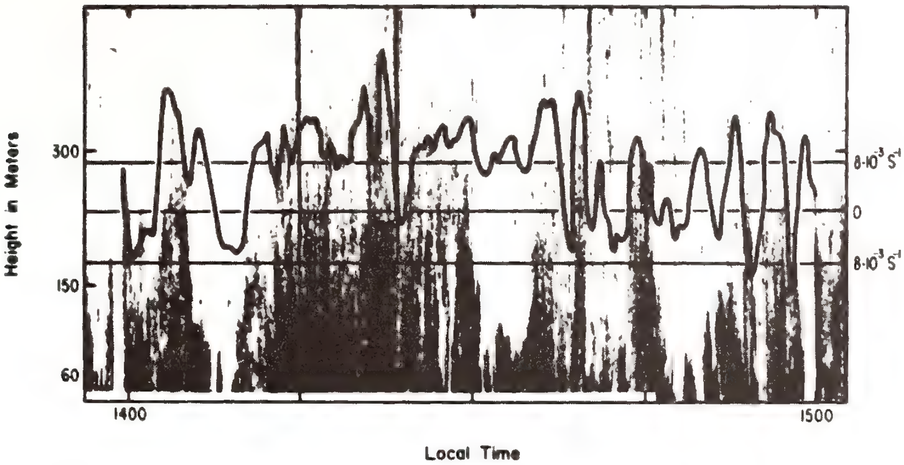

FIG. 7. Comparison between the plumes seen by the acoustic sounder and the flow into the triangle. Large plumes are associated with large convergence. The solid line is the divergence measured by the optical system.

b. Correlation of divergence and vertical wind

The vertical velocity is related to the divergence field through the equation of continuity as

$$\nabla_h \cdot \mathbf{V} = -\frac{\partial w}{\partial z}.$$

Fig. 8 shows a typical set of cross-correlation curves between the divergence and the vertical wind and gradient on the tower during strong convective activity.

Because the tower is outside the triangle, the peak in the cross correlations does not occur at zero lag but is shifted in time corresponding to the travel time between the tower and the center of the triangle. For the case chosen the wind direction was along a line between the center of the triangle and the tower. The negative lag means that the divergence is lagged behind the vertical wind on the tower.

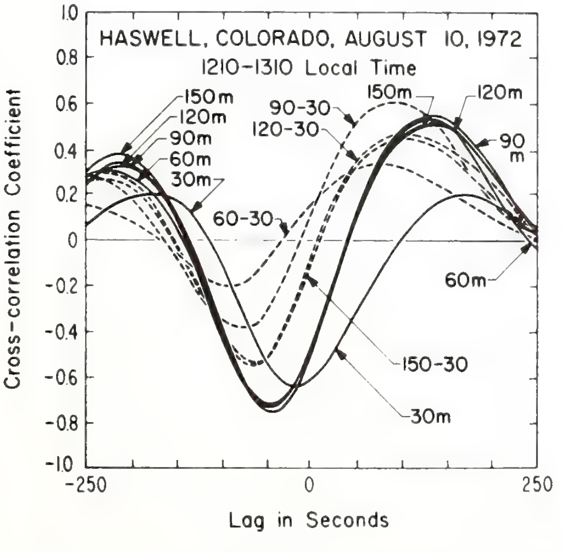

FIG. 8. Cross-correlation curves between divergence and vertical wind, and divergence and vertical wind gradient for the different levels on the tower. Solid lines are divergence vs vertical velocity and dotted lines divergence vs vertical wind gradient.

One of the interesting features in Fig. 8 is the difference in correlation between $\nabla_h \cdot \mathbf{V}$ and $-\partial w/\partial z$, and between $\nabla_h \cdot \mathbf{V}$ and w. From these curves, we see that in the case of plumes, the convergence into the plumes is more determined by the vertical wind than by the gradient of the same. These results seem to agree with Morton *et al.* (1956), who assumed that the entrainment into plumes was proportional to the upward velocity. It might be argued that this picture might have been different if we had had a measurement of the vertical wind at the same height as the divergence measurement. Due to the 100-sec running average, however, we are looking at a large population of plumes which should not differ much from 5 to 30 m, so we believe that our results give a reasonably correct picture.

Another interesting feature of these curves is the relative time shift between the peaks in the cross correlations for the vertical wind at the different levels indicating that the plumes or convective currents are tilted. The tilt is in the downwind direction. This corresponds to what Kaimal and Businger (1970) have reported for a single plume. The plumes are passing the four upper levels on the tower at about the same time but some 20–30 sec earlier than the lowest level (30 m).

In all the cases we have analyzed, the plumes were tilted in the lowest 60 m, whereas from 60 to 150 m almost no tilting was observed.

The third feature that should be observed in Fig. 8 is the periodicity in the cross-correlation curves indicating that there is a periodicity in the development of convective currents in the boundary layer. The time between the two cross-correlation maxima, which might be interpreted as the period between a set of plumes, is 360 sec.

Panofsky (1973) has recently shown that the plumes seem to move with a speed close to the local wind. In this case the wind was about 1.5 m sec^{-1} at the height of the triangle, giving us a separation in space of about 540 m between every major set of plumes. This scale size seems to agree with what Ackerman (1967) has reported for convective clouds. She found scale sizes of 400–900 m. This periodicity was only found during large convective activity. During the morning and the evening hours correlation curves like curve B shown in Fig. 9 are typical. The magnitude of the correlation between $\nabla_h \cdot \mathbf{V}$ and w seems to change very little during the day, but the plumes are released more randomly with no outstanding size contributing to the cross correlation during the morning and evening hours.

c. Daily variation of the divergence

As shown in Fig. 6, a great difference exists between the divergence during day and night. In the morning and evening, we found that the flow was out of the triangle about 60% of the time. During heavier convective activity in the middle of the day, the flow was into the triangle 60% of the time. In the middle of the day peak values in convergence (10^{-2} sec^{-1}) were found over periods of 1–2 min. The standard deviation was normally in the order of 4×10^{-3} sec^{-1}.

d. Space average of wind velocity

As shown in Fig. 4, this technique measures the transverse space-averaged wind component. By combining two components as shown in Eqs. (2) and (3), we get the total horizontal wind vector. Since three components are available, these can be combined to give three values of the wind vector. By applying a 20-min running average to the data to smooth out convective activity and comparing these three values, we have a measure of the ability of the system to obtain the space-time averaged horizontal wind vector.

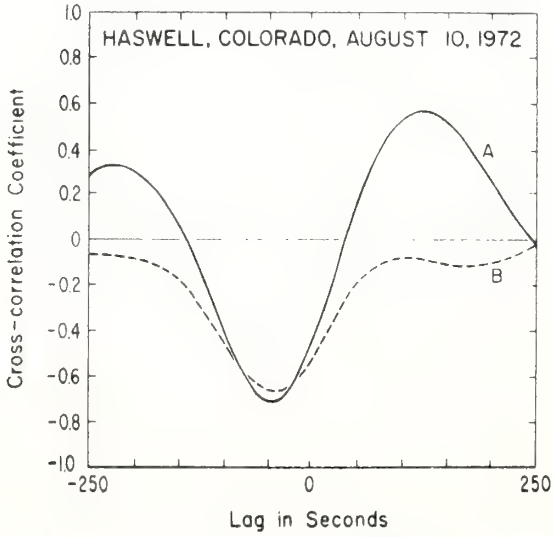

Fig. 9. Cross-correlation curves between divergence and vertical wind. The solid line is for high convective activity, and the dotted line for low convective activity.

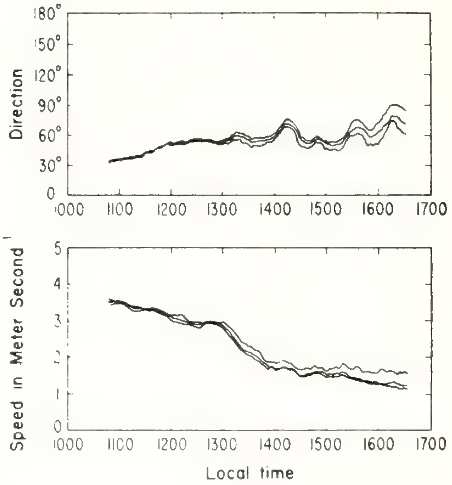

Fig. 10. A comparison of the three values of the wind vector determined from the laser triangle. Wind direction and speed are shown in the upper and lower parts of the figure, respectively. A 20-min running average has been applied to the data to smooth out the effect of convective activity.

Fig. 10 shows plots of the three values of the wind vector for nearly 6 hr, with direction and speed shown in the upper and lower parts of the figure, respectively. For a wind speed higher than about 2 m sec^{-1}, we see that it makes little difference which two of the three components are used to calculate the horizontal wind vector. When the wind speed drops below about 2 m sec^{-1} the differences increase, very likely from several causes. Due to slight differences in the terrain along the triangle legs, irregular wind patterns can persist over the triangle and be more pronounced during light wind conditions. In addition, instrumental errors appear as a fraction of the full-scale wind setting chosen, which was 10 m sec^{-1} for the case shown. Recent modifications to the instrumentation have reduced this source of error.

Figs. 11 and 12 compare the wind speed and direction calculated from the component measurement and the same quantities measured at the 30-m level on the tower. All recordings are 10-sec averages. The wind recordings at the tower are shifted 40 sec in time to compensate for the travel time from the triangle to the tower. The differences in the wind speed magnitude are expected because of the difference in height above ground. Using the logarithmic wind profile to calculate the wind speed at the 30 m level from the wind speed measured with the optical technique, we obtain the

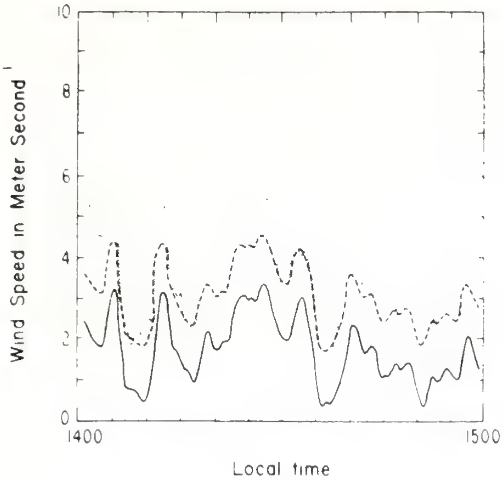

FIG. 11. Comparison of wind speed measured at the 30 m level on the tower (dotted line) with the wind speed calculated from the triangle measurement (solid line). The dashed line is the calculated logarithmic wind profile using a roughness parameter z_0 of 4 cm, and a friction velocity u_* of 20 cm sec^{-1}.

dashed line curve shown in Fig. 11. A roughness parameter z_0 and a friction velocity u_* of 4 cm and 20 cm sec^{-1}, respectively, were used. These values are regarded as reasonable for the type of ground cover and wind speed we encountered.

The correlation between the two types of measurements is very good. The larger variance of the wind measured at the tower is expected because this is a point measurement, while the optical wind measurement is an average both in time and space.

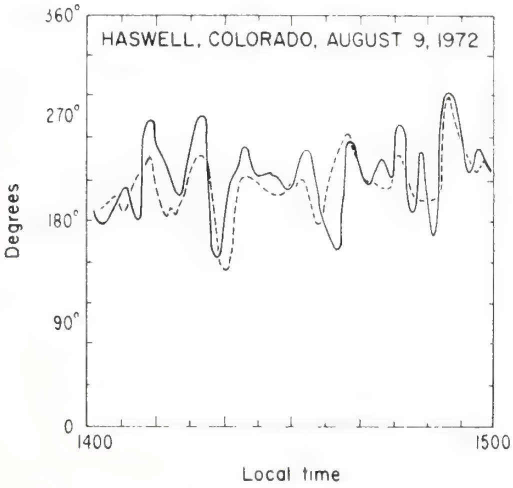

FIG. 12. Comparison of wind direction measured at the 30 m level on the tower (dotted line) and that calculated from the laser wind measurement (solid line).

5. Conclusion

It has been shown that a wind measuring system using three separate optical systems, each consisting of a 3 mW He-Ne laser and two photodiode receivers, forming a equilateral triangle, is successful in measuring the divergence over a small enclosed area. By using two of the optical systems, we can get a space-averaged horizontal wind vector. The thermal plumes as seen by the acoustic sounder and the convergence compare well. The correlation between the divergence and the vertical wind measured on the tower shows that the entrainment into plumes is proportional to the vertical velocity.

During periods with large convective activity a certain periodicity in the development of plumes is found.

Acknowledgments. The senior author expresses his sincere gratitude to Dr. C. Gordon Little, Director of the Wave Propagation Laboratory, for providing him with the opportunity and making the facilities available to make this study while on leave from the Norwegian Defence Research Establishment. The authors also thank Mr. R. S. Lawrence, who initiated this study. Finally, the senior author wants to thank the many members of the Wave Propagation Laboratory who not only contributed with helpful discussions and suggestions, but also created a stimulating environment and accepted him as one of their own.

REFERENCES

Ackerman, Bernice, 1967: The nature of the meteorological fluctuations in clouds. *J. Appl. Meteor.*, **6**, 61–71.

Bellamy, J. C., 1949: Objective calculations of divergence, vertical velocity and vorticity. *Bull. Amer. Meteor. Soc.*, **30**, 45–49.

Beran, D. W., 1971: Acoustics: a new approach for monitoring the environment near airports. *J. Aircraft*, **8**, 934–936.

Eddy, A. 1964: The objective analysis of horizontal wind divergence fields. *Quart. J. Roy. Meteor. Soc.*, **90**, 424–440.

Endlich, R. M., and J. R. Clark, 1963: Objective computations of some meteorological quantities. *J. Appl. Meteor.*, **2**, 66–81.

Kaimal, J. C., and J. A. Businger, 1970: Case studies of a convective plume and a dust devil. *J. Appl. Meteor.*, **9**, 612–620.

Lawrence, R. S., G. R. Ochs and S. F. Clifford, 1972: The use of scintillations to measure average wind across a light beam. *Appl. Opt.*, **11**, 239–243.

McAllister, L. G., J. P. Pollard, A. R. Mahoney and P. J. R. Shaw, 1969. Acoustic sounding—a new approach to the study of the atmospheric structure. *Proc. IEEE*, **57**, 579–587.

Morton, B. R., G. I. Taylor and J. W. Turner, 1956: Turbulent gravitational convection from maintained and instantaneous sources. *Proc. Roy. Soc., London*, **A234**, 1-23.

Panofsky, H. A., 1973: Structure of turbulence. *IFYGL Bull.*, No. 7, 48–49.

Telford, J. W., 1966: The convective mechanisms in clear air. *J. Atmos. Sci.*, **23**, 652–666.

NOAA Technical Report ERL 297-WPL 30

January 1974

DEVELOPMENT OF A GROUND-BASED OPTICAL METHOD FOR MEASURING ATMOSPHERIC TURBULENCE ALOFT

G. R. Ochs, S. F. Clifford, R. S. Lawrence, and Ting-i Wang

We analyze the potential of ground-based remote sensing techniques with a view toward developing a practical, continuous monitor of upper air temperature turbulence. The analysis proceeds from the crude single-aperture measurements of stellar scintillation to multiple-aperture spatial filtering and ultimately to multiple source and receiver configurations. For multiple sources we consider both resolvable and unresolvable pairs of stars. We derive, and check by observation, path weighting functions for optical refractive-index fluctuations and describe techniques for optically sharpening their peaks.

Reprinted from **APPLIED OPTICS**, Vol. 15, page 1, January 1976
Copyright 1976 by the Optical Society of America and reprinted by permission of the copyright owner

Remote Doppler velocity measurements of atmospheric dust devil vortices

R. L. Schwiesow and R. E. Cupp

ERL/NOAA Wave Propagation Laboratory, Boulder, Colorado 80302.

Received 17 October 1975.

Sponsored by F. S. Harris, Jr., Old Dominion University.

We report here what we believe to be first remote measurement of the velocity structure in a small-scale, natural atmospheric vortex. While the dust devil data are interesting in their own right, the practical demonstration of the applicability of the optical Doppler technique to field measurements on natural vortices, such as for waterspout and tornado research, is the point we wish to stress.

Basically, the cw ir (10.6-μm) Doppler system measures the line-of-sight velocity components of atmospheric aerosols within the diffraction-limited focal volume of the optical system. This sensing volume at the 3% irradiance level is approximately a cylinder $1.88 \times 10^{-3} r^2$ m long by $1.70 \times 10^{-4} r$ m diam, where r is the range in meters,[1] for our present system. At typical ranges the azimuth and elevation resolution is very good, but the range resolution element includes the entire depth of the vortex. Because the return signal is aerosol-concentration weighted, good range resolution is not required to distinguish the vortex from ambient flows. Principles of the homodyne extraction of Doppler velocity information from the return signal have been discussed elsewhere.[2-6]

The velocity spectra obtained are actually line integrals over the range resolution element, weighted by the aerosol backscatter coefficient at 10.6 μm. Although calculations on water aerosols have been done at 10.6 μm,[7] ir backscatter data for dusts are not available in a form suitable for direct use in our analysis. In general, one expects the most significant Doppler return from aerosols in the 1–10-μm diam range, whereas visual aspects are more strongly affected by smaller aerosols. Our qualitative observations have shown that some visually dense dust devils are only fair ir scatterers, though other dust devils invisible to the eye return a strong Doppler signal. Only estimates of the dimensions of the vortices were made since an investigation of dust devil morphology was not an objective of this study.

Data were collected on over forty dust devils during July 1975 at the Gila Indian Reservation south of Phoenix and at the Nevada test site of ERDA. Figure 1 reproduces velocity spectra from a small representative vortex. The vortex, at approximately 300-m range, was scanned 7 m above the surface. The visual diameter of the optically thin vortex at this height was approximately 2 m. Correlation with cinematography taken simultaneously with the velocity data reveals that the corresponding dust devil was of the broad, turbulent type (vase configuration), which often shows subvortices, rather than the narrow, intense, singular variety.[8] The mean wind of 3.5 msec^{-1} was perpendicular to the line-of-sight direction, so that ambient velocity effects are negligible in the spectra of Fig. 1.

Although the data will be analyzed in more detail later from the point of view of dust devil velocity structure, three preliminary observations can be reported.

(1) Peak horizontal velocity components in dust devils are small. We observed components up to 10 msec^{-1} near Phoenix and up to 22 msec^{-1} at the Nevada test site in these series of tests. Such values are larger than those observed with cup anemometers at other locations[9] but are not surprising in light of the very high spatial and temporal resolution of the ir Doppler system.

(2) The characteristic double-hump velocity spectrum associated with the complex vase configuration vortices, evident on two traces in Fig. 1, gives quantitative evidence for the embedded subvortices inferred by Sinclair from direction-vane data.[10] In general, subvortex tangential velocities (one-half the peak separation) were about 25% of the parent vortex rotational velocity, but one case of a subvortex velocity of 0.9 msec^{-1} in a 1.4-msec^{-1} mean rotational flow was observed.

(3) Data taken through the axis of the vortex, where only turbulent velocity components along the line of slight are expected, reveal a definite periodicity in both peak wind observed and the velocity at the spectral intensity peak. This suggests either the effect of large, slow subvortices or the existence of waves on the circumference of the main vortex itself. Such waves may be the precursor of the formation of embedded subvortices.

The characteristic behavior of the velocity spectra in dust devils as one scans across the diameter from the visual edge to the center is expressed in Fig. 1. A rather sharp tangential velocity peak at the edge of the vortex gives way to a broader spectrum as various velocity components con-

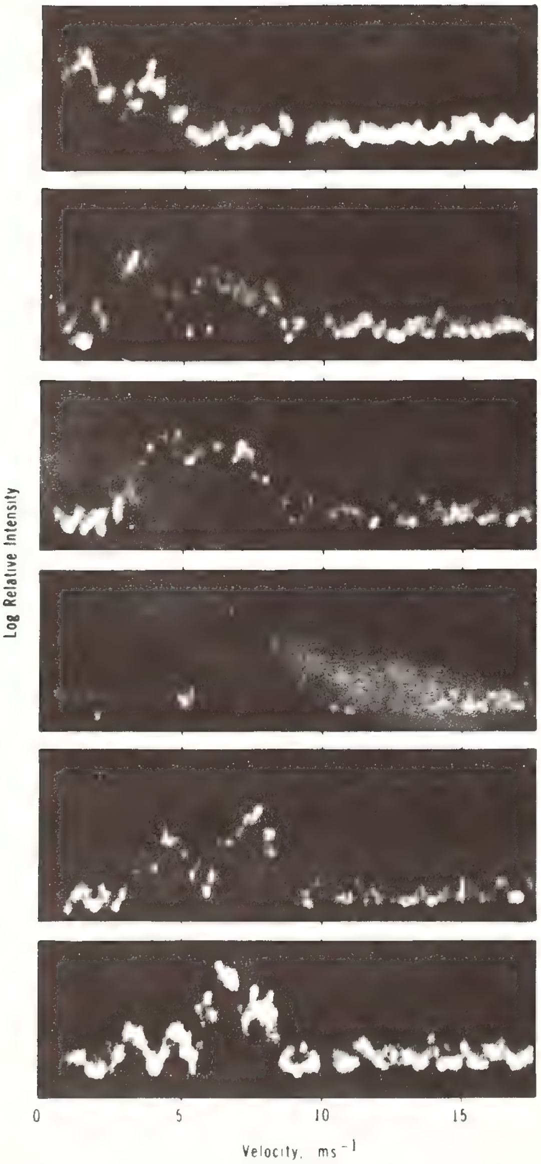

Fig. 1. Representative velocity spectra of a dust devil with spectra from the outer edge to the center of the vortex corresponding to the bottom and the top of the figure, respectively.

tribute within the sensing volume. For the vase-type vortices, the broad spectrum breaks into double peaks as subvortices are detected. As the measurement angle moves toward the vortex axis, the turbulent spectrum fills in toward zero velocity. When the mean wind is a significant fraction (20% or more) of the rotational velocity, the leading edge of the vortex (downwind side) has a more sharply defined spectrum than the upwind edge.

For practical optical applications, the remote Doppler velocity measurement system has proven utility. Experience has shown that, partly because of optical simplicity and the ir wavelengths, such a system can operate without realignments or adjustments after more than 1500-km transport on a heavy-duty, four-wheel drive vehicle. Onsite setup time was demonstrated to be less than 10 min on initial starting and less than 2 min after detector cooldown. Power requirements for such a highly mobile system allow it to be self-contained with its own 5-kW generator. It has been found that effective operation is facilitated by a two-man crew.

This reported experiment demonstrates the feasibility of the remote, ir Doppler velocity measurement of natural atmospheric vortices. Application of the system to waterspouts and tornadoes are obvious extensions of the work.

This work was supported in part by NOAA and EPA.

References

1. See, for example, R. L. Schwiesow, J. Opt. Soc. Am. **59,** 1285 (1969).
2. R. M. Huffaker, Appl. Opt. **9,** 1026 (1970).
3. R. M. Huffaker, A. V Jelalian, W. H. Keene, C. M. Sonnenschein, and J. A. L. Thomson, in *Aircraft Wake Turbulence and Its Detection,* J. H. Olsen, A. Goldburg, and M. Rogers, Eds. (Plenum, New York, 1971), pp. 113–124.
4. A. J. Hughes, J. O'Shaughnessy, E. R. Pike, A. McPherson, C. Spavins, and T. H. Clifton, Opto-electronics **4,** 379 (1972).
5. T. R. Lawrence, D. J. Wilson, C. E. Craven, I. P. Jones, R. M. Huffaker, and J. A. L. Thomson, Rev. Sci. Instrum. **43,** 512 (1972).
6. C. M. Sonnenschein and F. A. Horrigan, Appl. Opt. **10,** 1600 (1971).
7. F. S. Harris, Jr., Appl. Opt. **8,** 143 (1969).
8. S. B. Idso, Am. Sci. **62,** 530 (1974).
9. J. A. Ryan and J. J. Carroll, J. Geophys. Res. **75,** 531 (1970).
10. P. C. Sinclair, J. Atmos. Sci. **30,** 1599 (1973).

Applied Optics 14, 2116-2120, September 1975.

Temperature dependence and cross sections of some Stokes and anti-Stokes Raman lines in ice Ih

R. B. Slusher and V. E. Derr

Radiation at λ = 488.0 nm was used to obtain Raman scattering in ice Ih (atmospheric pressure, hexagonal structure). New Stokes spectra were detected for frequency shifts less than 50 cm^{-1}, and new anti-Stokes spectra were observed for frequency shifts to −212.5 cm^{-1}. Measurements of total differential Raman scattering cross sections were made for some bands in ice Ih and liquid water. The temperature dependence of the ratio of a pair of Stokes–anti-Stokes lines is given for ice Ih.

Introduction

Water (ice and liquid) was one of the first substances in which the Raman effect was demonstrated.[1] Since 1928, work on the Raman effect in ice and liquid water has been handicapped, until recent years, by the lack of high intensity light sources and efficient spectrometers that eliminate scattering from the intense illuminating lines that would otherwise obscure weaker close-lying Raman lines. Now, available spectrometers resolve low intensity lines spectrally close to the exciting radiation, and high power lasers can provide radiation whose spectral brightness is several orders of magnitude greater than that obtained from other light sources.

With these new research tools it is possible to study the Raman effect in greater detail and apply it to new fields. One such field that has attracted much interest in recent years is that of atmospheric remote sensing. With high-powered lasers as sources of intense monochromatic radiations, even weak interactions such as Raman scattering can be detected and used to measure atmospheric parameters.

The principal characteristic of Raman scattering that makes it applicable to remote sensing is the frequency shift of the scattered radiation from the incident radiation, producing a spectral separation of the weak Raman and strong Rayleigh scattering. This separation can be used advantageously in laser remote sensing by using appropriate interference filters to block the Rayleigh scattering, thus allowing detection of the Raman spectrum that uniquely identifies the scattering molecule. The use of Raman lidar (light detection and ranging) as an atmospheric remote sensing tool is described by Cooney,[2,3] Derr and Little,[4] Kobayasi and Inaba,[5,6] Leonard,[7] Schotland and Reiss,[8] Strauch *et al.*,[9,10] Derr,[11] and others.

Raman scattering parameters of ice Ih useful for atmospheric remote sensing include frequency shifts, line widths, and total differential scattering cross sections. (The total differential scattering cross section is the differential scattering cross section integrated over the line width.)

Stokes and anti-Stokes lines not previously observed are reported. In addition measurements of the ratio of the irradiance of some Stokes to anti-Stokes lines were made as functions of temperature. This article describes measurements made on Raman bands of ice Ih and liquid water selected for application to remote sensing of cloud parameters.

Experimental Arrangement

The 488.0-nm line of an argon ion laser with a power of 1 W was coupled into a clear cell of ice Ih by a 5-cm focal length lens. Scattered light normal to both the focused laser beam and its polarization vector was focused into the entrance slit of a SPEX model 1401 double spectrometer. An EM 9781B photomultiplier, operated at 750 V, was used to detect the signal at the exit slit. The signal from the photomultiplier was amplified, discriminated with a single channel analyzer, and measured by a linear ratemeter.

The sample cell of ice Ih was frozen slowly from one side so that any bubbles that formed tended to be in the water that froze last. This left a section of bubble-free ice through which the beam could propagate, and the right-angle scattering could be observed. The sample cell was kept at a constant temperature by placing it in an insulated container that was cooled by blowoff from a small liquid nitrogen

V. E. Derr is with NOAA Environmental Research Laboratories, Wave Propagation Laboratory, Boulder, Colorado 80302. R. B. Slusher is with Control Laser Corporation, 11222 Astronaut Bldg., Orlando, Florida.

Received 12 April 1975.

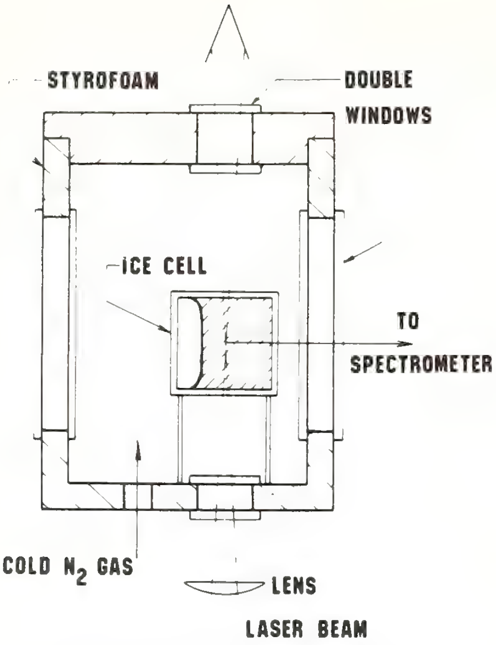

Fig. 1. Cooler and sample cell.

reservoir variably heated with a coil of nichrome resistance wire. The temperature of the container could be adjusted from −3°C to −50°C by increasing the current in the resistance wire. The container and sample cell are illustrated in Fig. 1.

Experimental Procedure and Results

The Raman spectrum of ice Ih was observed over the frequency region $\Delta\nu = -4000$ cm^{-1} to $\Delta\nu$ +4000 cm^{-1}, $\Delta\nu$ the frequency shift of the Raman spectrum from that of the pump radiation. The resolution of the spectrometer varied from 3.5 cm^{-1} at $\Delta\nu = -4000$ cm^{-1} to 1.5 cm^{-1} at $\Delta\nu = +4000$ cm^{-1}. This resolution is adequate for observing the broadbands that occur in the Raman spectrum of ice Ih; they are typically wider than 20 cm^{-1}. Table I lists the band centers observed in this region, and Fig. 2 shows the bands of interest. The Stokes and anti-Stokes bands are paired horizontally in the table although there are some discrepancies of frequency shifts. These discrepancies can be explained by the difficulty of determining the center of a broadband and also because some of these bands may be composite bands consisting of two or more bands whose Stokes to anti-Stokes intensity ratios vary differently.

The band pair at ±212 cm^{-1}, having the greatest observed anti-Stokes intensity, was chosen to measure the Stokes to anti-Stokes band intensity ratio vs temperature. Measurements of this ratio were made between −3°C and −50°C as shown in Fig. 3. A straight line fit was made to the data. The slope of the line is −2.41 IRU/°C (IRU: relative intensity ratio units of the band peaks). The accuracy of the temperature measurement varied approximately linearly from ±0.3°C at 0°C to ±1.0°C at −50°C. Intensity measurements were made with a standard deviation of 5% at the higher temperatures, increasing to 12% at the lower temperatures. The standard deviation of the data points (measured vertically) from the best-fit line is 5.9 for all points.

The data in Fig. 3 in the temperature range above −8°C is not entirely trustworthy because of the uncertainty in the freezing point of water. Dorsey[12] has shown the dependence of the freezing point on nucleation and the previous history of the sample. In this experiment, distilled water and clean vessels sometimes prevented freezing at 0°C. The presence of small amounts of liquid water was difficult to observe in the sample; the temperature was lowered until scattered light showed no evidence of water inclusions.

The 992-cm^{-1} Raman line in benzene was used as a standard to measure total differential Raman scattering cross sections. The absolute scattering cross section of this line had been measured by Skinner and Nilsen[13] using the 488.0-nm line of an argon ion laser. Their value for the peak differential scattering cross section was 1.05 (±0.08) × 10^{-29} cm^2/molecule/sr/wavenumber/plane of polarization. A comparison between the intensity of the band in liquid H_2O at 3400 cm^{-1} and the 992-cm^{-1} line of benzene was made. This yielded a value for the peak differential scattering cross section of the 3400-cm^{-1} band in water. It was then possible to compare this band with the 3200-cm^{-1} band in ice Ih. In turn those at +212 cm^{-1} and −212 cm^{-1} in ice Ih were compared to the 3200-cm^{-1} band. These comparisons, linked to the previously measured benzene standard line, yielded total differential scattering cross sections, which are listed in Table II.

In these relative scattering cross section measurements differences in number density between benzene, liquid H_2O, and ice Ih and differences in their

Table I. Observed Band Centers in Ice Ih from $\Delta\nu = -4000$ cm^{-1} to $\Delta\nu = +4000$ cm^{-1}

Stokes bands	Relative intensity[a]	Anti-Stokes bands	Relative intensity
22.9 cm^{-1}[b]	0.004	−25.0 cm^{-1}[b]	0.001
40.4 cm^{-1}[b]	0.003	−35.9 cm^{-1}[b]	0.001
54.1 cm^{-1}	0.005	−49.6 cm^{-1}[b]	0.004
212.9 cm^{-1}	1.0	−212.5 cm^{-1}	0.01
3141.6 cm^{-1}	10.0		
3264.0 cm^{-1}	7.5		
3348.0 cm^{-1}	6.5		

[a] The intensities of the band centers were measured relative to the intensity of the band center at 212.9 cm^{-1}. Slit width on the spectrometer was kept constant, and corrections were made for variations in detection efficiency. The total differential Raman scattering cross section of the band whose center is at 212.9 cm^{-1} is (from Table II) 2.3 (±0.1) × 10^{-30} (cm^2/molecule-sr).

[b] Newly observed spectra. Data taken at −19°C.

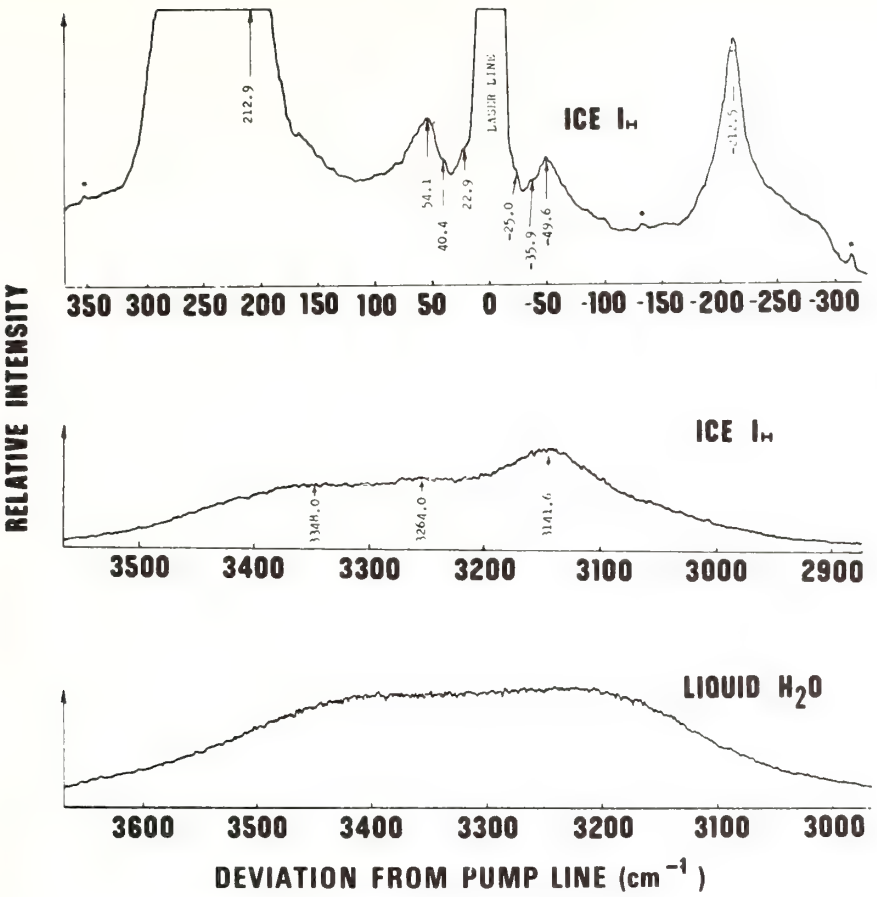

Fig. 2. Raman bands of interest in ice Ih and liquid H_2O.

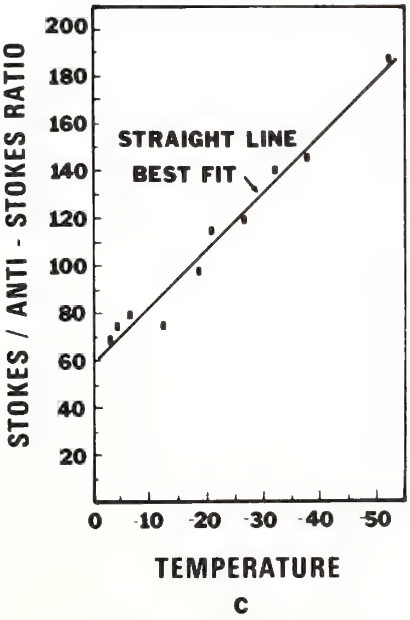

Fig. 3. Stokes to anti-Stokes scattering ratio for the ±212-cm^{-1} bands in ice Ih.

Table II. Total Differential Raman Scattering Cross Sections

Band	Cross section (cm^2/molecule-sr)
Ice Ih (2800–3700)	$2.8\ (\pm 0.2) \times 10^{-29}$
Ice Ih (100–375)	$2.3\ (\pm 0.1) \times 10^{-30}$
Ice Ih (−100 to −375)	2×10^{-32}
Liquid H_2O (2800–3700)	$4.5\ (\pm 0.3) \times 10^{-29}$

Table III. Band Designations in Ice Ih

Band center (cm^{-1})	Type of molecular motion
50	Intermolecular vibration
212	Intermolecular vibration
1000	Librations (oscillating rotary motion)
1650	Molecular vibrations
2300	Possible harmonics of librational and translational modes
3200	O–H stretching
4000	Harmonics of above motions

Table IV. Raman Bands Observed in Ice Ih Units of Spatial Frequency (cm^{-1})

This work −10°C	Taylor and Whalley (1963) 77°K	Ockman (1957) −18°C	Ockman (1957) −145°C	Maisch (1956) −150°C	Gross and Valkov (1959) −4°C	Narayanaswany (1948)
−212.5						
−49.6						
−35.9						
−25.0						
22.9						
40.4						52.0
54.1						
			68			
			83			
			100			
		122				
		163	152			
					177	
					193	
212.9		205	219		212	213.1
	225				232	
					252	
					272	
			292		299	
			330			
			356			
			373			
		458	466			
		516				
		567	566			
			659			
3142	3085	3139	3089	3159		3147
3264	3210	3259	3215	3275		3264
	3320	3307	3302			
3348		3353	3345	3370		3347
		3403	3410			

refractive indices (which affect the solid angle of light gathering by the coupling optics) were accounted for. The detection efficiency (dependent on wavelength) was determined over the entire spectral region of interest and was used to normalize the data.

Discussion

The Raman spectrum of ice Ih has been previously studied from $\Delta\nu = 20\ cm^{-1}$ to $\Delta\nu = 4000\ cm^{-1}$ by Taylor and Whalley,[14] Ockman,[15] Maisch,[16] Gross and Valkov,[17] Narayanaswany,[18] and others. The bands in this region can be classified by the probable type of molecular motion as shown in Table III, after Eisenberg and Kauzmann.[19] The spectral region in which they occur is indicative of the molecular motion involved. The bands observed below 50 cm^{-1} in this work probably result from intermolecular vibration. Table IV summarizes present and previous observations.

The use of Raman scattering to detect liquid and solid-phase (ice Ih) H_2O in the atmosphere has merit under circumstances when particle densities are sufficiently large. Conditions that prevail during snow and hail storms, for example, should supply ample scatterers to provide a detectable Raman return. The temperature-dependent ratio of Stokes to anti-Stokes Raman scattering in ice Ih might be used to measure temperature profiles in clouds.

Although the measurements of the strong Raman bands in liquid H_2O and ice Ih were made over the same region (2800–3700 cm^{-1}), the two maxima of the bands are at different frequencies. The liquid water band maximum is at 3255 cm^{-1}. The maximum of the ice Ih band is at 3142 cm^{-1}. Measuring the relative Raman scattering intensities at these two peaks would provide the ratio of liquid H_2O content to ice content. Performance (SNR vs range) may be estimated for one type of lidar system from Fig. 1 of Derr and Little.[4] Further discussion of atmospheric applications may be found in Derr *et al.*[20]

References

1. C. Y. Raman, Indian J. Phys. **2,** 387 (1928).
2. J. Cooney, Appl. Phys. Lett. **12** 42 (1968).
3. J. Cooney, J. Appl. Meteor. **9,** 182 (1970).
4. V. E. Derr and C. G. Little, App. Opt. **9,** 1976 (1970).
5. T. Kobayasi and H. Inaba, Opto-Electron. **2,** (1970).
6. T. Kobayasi and H. Inaba, Appl. Phys. Lett. **17,** 139 (1970).
7. D. Leonard, Nature **216,** 142 (1967).
8. R. M. Schotland and N. M. Reiss, in *4th Conference on Laser Radar, Tucson, Arizona* (January 1972).
9. R. G. Strauch, V. E. Derr, and R. E. Cupp, Appl. Opt. **10,** 2665 (1971).
10. R. G. Strauch, V. E. Derr, and R. E. Cupp, Remote Sensing of Environment 2, no. 2, 101 (1972).
11. V. E. Derr, Ed., *Remote Sensing of the Troposphere,* GPO Catalog C55.602:T75, stock no. 0323-0011 (Supt. of Documents, Washington, D.C., August 1972.)
12. N. E. Dorsey, Trans. Am. Philos. Soc. **38,** part 3, 248 (1948).
13. J. G. Skinner and W. G. Nilsen, J. Opt. Soc. Am. **58,** 113 (1968).
14. M. J. Taylor and E. Whalley, J. Chem. Phys. **40,** 1660 (1963).
15. N. Ockman, Adv. Phys. **7,** 199 (1958).
16. W. Maisch, Thesis, Brown University (1956).
17. E. F. Gross and V. I. Balkov, Dok. Akad. Nauk SSR **74,** 453 (1950).
18. P. K. Narayandswamy, Proc. Indian Acad. Sci. **27,** 311 (1948).
19. D. Eisenberg and W. Kauzmann, *The Structure and Properties of Water* (Oxford U. P., New York, 1969).
20. V. E. Derr, M. J. Post, R. L. Schwiesow, R. F. Calfee, and G. T. McNice, "A Theoretical Analysis of the Information Content of Lidar Atmospheric Returns," NOAA Tech. Rpt., ERL 296-WPL 29, Boulder, Col. (November 1974).

Journal of the Optical Society of America 65, 927-937, August 1975.

Use of rainfall-induced optical scintillations to measure path-averaged rain parameters

Ting-i Wang

Cooperative Institute for Research in Environmental Sciences, University of Colorado/NOAA, Boulder, Colorado 80302

S. F. Clifford

National Oceanic and Atomospheric Administration, Environmental Research Laboratories, Boulder, Colorado 80302

(Received 6 January 1975)

We apply the theory of plane-wave scattering by spheres to calculate the variance, the space–time covariance, and the temporal-frequency spectrum of the amplitude fluctuations of a light wave passing through rainfall. The development includes the effects of various sizes of raindrops and their associated terminal velocities. We show that the time-lagged covariance function of two vertically spaced sensors can provide a practical remote measurement of path-averaged rain parameters, such as drop-size distribution and rain rate, without any assumptions about the form of the drop-size distribution.

Index Headings: Scattering; Scintillation; Atmospheric optics.

Traditional techniques for measuring variables of precipitation have used point sensors, such as rain gauges. More recently, considerable effort has been devoted to the problem of the effects of precipitation on optical and infrared wave transmission through the atmosphere.[1–7] These techniques suggest that path-averaged rain parameters may be deduced from line-of-sight attenuation measurements. This has introduced a new type of space-averaged optical measurement that is more representative for mesoscale meteorology than any practical collection of rain gauges could possibly provide.

Instead of measuring attenuation, we propose to measure the rainfall-induced irradiance (or amplitude) scintillations of a laser beam. This technique seems extremely promising as a potential remote sensor of path-averaged rain parameters, such as rain-rate and drop-size distribution. This study is undertaken with a view toward using the more complicated sources and sensor geometries for rainfall measurements that have had such successful application in laser remote sensing of refractive-turbulence and wind-induced scintillation.

Because this paper contains, so far as we know, the first statistical analysis of the random fluctuations of irradiance produced by scattering of light from rainfall, in the next sections we will outline the development of the theory. First, we consider various statistical properties of irradiance scintillation, such as variance, space–time covariance, and temporal power spectrum of the amplitude fluctuations for a monodisperse size distribution. We then generalize these results to the case of a realistic raindrop size distribution and finally, we analyze the feasibility of using the space–time covariance function to monitor path-averaged rain parameters.

I. THEORY

Light scattering by raindrops may be conveniently analyzed in terms of the theoretical developments by Van de Hulst.[8] Figure 1 illustrates the geometry of an incident plane wave propagating along the x direction that is scattered by randomly located raindrops. We assume that the shape of the raindrops is spherical and that the wavelength λ of the incident wave is much smaller than the radius a of the raindrop. This problem can be treated in the same manner as the problem of light scattering by very large spheres, $a \gg \lambda$. It is well known[8] that the depolarization effect of the scattered wave can be neglected. Letting E_0 and E_s denote the electric field of the initial and scattered waves, respectively, Van de Hulst[8] gives

$$\frac{E_s}{E_0} = \frac{\exp(-ikr+ikx)}{ikr}\left[\eta^2 \frac{J_1(\eta\theta)}{\eta\theta} + O\left(\frac{1}{\xi}\right)\right] , \tag{1}$$

where r, x, and θ are coordinates (as shown in Fig. 1); $\eta = ka = 2\pi a/\lambda$ is the drop-size parameter, and $\xi = 2\eta(m-1)$, where $m = 1.33$ is the refractive index of water. The first term arises from diffraction, whereas the second term arises from the light that passes through the sphere. Because the raindrops are large compared to the wavelength (i.e., $\eta \gg 1$), the first term is the dominant term; only it will be kept. This is equivalent to assuming that the refractive index of the sphere is infinite, i.e., the sphere is considered to be opaque. Because we are interested in only the far-field solution, where the Fresnel-zone size $(\lambda x)^{1/2}$ is much larger than the drop size a and the longitudinal coordinate x is much larger than the transverse coordinate ρ, Eq. (1) can be simplified to

$$\frac{E_s}{E_0} \simeq \frac{\exp(-ik\rho^2/2x)}{ikx}\,\eta\,\frac{J_1(\eta\theta)}{\theta} . \tag{2}$$

In deriving Eq. (2), we have used the approximations, valid for $x \gg \rho$, that $|r - x| \simeq \rho^2/2x$ in the phase and $r \simeq x$ in the denominator. The first factor on the right-hand side describes the fringes of the interference pattern caused by the interaction of the incident plane wave with the scattered spherical wave that originates from the sphere. The second factor is the well-known far-field Airy-disk diffraction pattern of a sphere.

We use Tatarskii's approach[9] for a wave that propagates in a random medium to calculate the covariance and temporal power spectrum of the amplitude scintillations. We define the amplitude scintillation (normalized to the unscattered field E_0) as

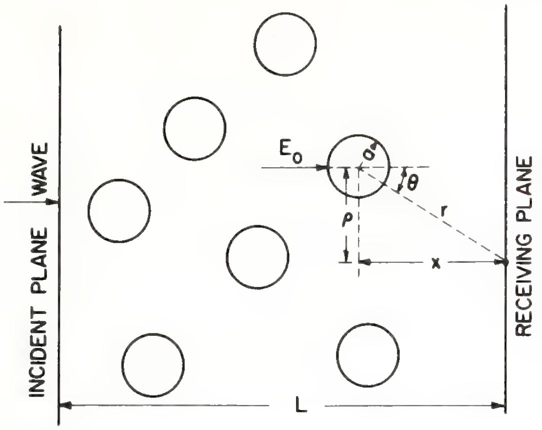

FIG. 1. Geometry of an incident plane wave scattered by randomly displaced monodisperse raindrops of radius a.

$$\chi = |(E_0+E_s)/E_0| - 1 = \{[1+\mathrm{Re}(E_s/E_0)]^2 + \mathrm{Im}^2(E_s/E_0)\}^{1/2} - 1 , \tag{3}$$

where Re and Im are, respectively, the real- and imaginary-part operators. In the weak-scattering case, $|E_s/E_0| \ll 1$, and, to first order, χ is approximately equal to $\mathrm{Re}[E_s/E_0]$. If the receiver is located at the origin of coordinates, then the amplitude scintillation $\chi(x, y, z)$ caused by a raindrop located at coordinates (x, y, z) is

$$\begin{aligned}\chi(x, y, z) &= \mathrm{Re}[E_s(x, y, z)/E_0(x, y, z)] \\ &= -\sin[k(y^2+z^2)/2x](\eta/k) \\ &\quad \times J_1[\eta(y^2+z^2)^{1/2}/x]/(y^2+z^2)^{1/2} .\end{aligned} \tag{4}$$

Equation (4) will be used to calculate the covariance function and the temporal power spectrum of the amplitude scintillations.

II. AMPLITUDE VARIANCE AND COVARIANCE FUNCTION

Because we do not wish to consider multiple scattering, only single scattering will be taken into account. This is a reasonable assumption for laser propagation through a moderate rainfall on paths of up to 1 km (see Appendix A). The time-lagged correlation function of the amplitude scintillation of a single raindrop at position x, y falling along the z axis is defined by

$$C_\chi(t) \equiv \langle \chi(x, y, z-vt)\chi(x, y, z)\rangle . \tag{5}$$

Here, the angle brackets denote an ensemble average, and v is the raindrop-fall speed. If we assume that the distance between raindrops is much larger than a Fresnel zone, which is also a reasonable assumption for moderate rainfall, the scattering can be considered incoherent. (From Appendix A, we see that, for a rain rate of 10 mm/h, the mean separation of the drops $d = 21$ cm. For a 1 km path, $(\lambda x)^{1/2} = 2.5$ cm. Clearly, in this typical case $d \gg (\lambda x)^{1/2}$.) Hence, each succeeding drop, falling in the z direction, acts as an independent member of an ensemble. Consequently, we may replace the ensemble average in Eq. (5) by an average over the z coordinate.

We now generalize Eq. (5) to the case of a differential screen of monodisperse, randomly distributed raindrops with uniform density at path position x. (We will include the effects of different sizes later.) This implies that we now integrate over the y direction, to include all drops in the plane $x = \text{const}$. With this two-dimensional array of drops, the time-lagged amplitude covariance function at the receiver takes the form

$$\begin{aligned}dC_\chi(t) &= a^2 N(x)\,dx \int_{-\infty}^{\infty} dy \int_{-\infty}^{\infty} dz \sin[k(y^2+z^2)/2x] \\ &\quad \times \sin[k\{y^2+(z-vt)^2\}/2x] \frac{J_1[\eta\{y^2+z^2\}^{1/2}/x]}{\{y^2+z^2\}^{1/2}} \\ &\quad \times \frac{J_1[\eta\{y^2+(z-vt)^2\}^{1/2}/x]}{\{y^2+(z-vt)^2\}^{1/2}} .\end{aligned} \tag{6}$$

Here, $N(x)$ is the number density of raindrops. To find $N(x)$, we let $h(x)$ denote the rain rate at x; then, the total amount of water falling into a rain gauge with uniform cross-section area A in a time period Δt is $h(x)A\Delta t$. Because we assume a monodisperse size-distribution model, the total number of water drops with radius a is $h(x)A\Delta t/(\frac{4}{3}\pi a^3)$. Also, the terminal velocities v of the raindrops are the same. In a time Δt, the volume swept out by falling raindrops is $vA\Delta t$. Hence the number density is

$$N(x) = \frac{h(x)}{4.8\pi \times 10^6 a^3 v} . \tag{7}$$

The numerical constant that appears in Eq. (7) is caused by the differing units of rainfall rate $h(x)$ (in mm/h) and the terminal velocity of raindrops v (in m/s).

It is well known that the terminal velocity of raindrops is a function of their size. Gunn and Kinzer[10] gave the relationship between the terminal velocity and the spherical drop size as

$$v^2(d) = \tfrac{4}{3} g d(\rho_w - \rho_a)/(\rho_a C) , \tag{8}$$

where g is the acceleration of gravity, d is the diameter of the sphere, and ρ_w and ρ_a denote the density of water and air, respectively. The disadvantage of Eq. (8) is that the drag coefficient, C, is also a function of drop size; however, raindrop diameters between 0.5 and 5 mm give the main contribution to the total precipitation. In this region, C is almost constant[10] and approximately equal to 0.5. In SI units, Eq. (8) is

$$v(a) = 45.4(2ga)^{1/2} = 200a^{1/2} . \tag{9}$$

(In deriving Eq. (9), we have used $\rho_w = 1$ g/cm^3 and $\rho_a = 1.293 \times 10^{-3}$ g/cm^3.) Substituting Eq. (9) into Eq. (7), we obtain the number density,

$$N(x) = 3.32 \times 10^{-10} a^{-7/2} h(x) . \tag{10}$$

Note, in Eqs. (9) and (10), that $h(x)$ is in mm/h, a is in meters, and v is in m/s.

Letting $y' = \eta y/x$ and $z' = \eta z/x$ and replacing the product of two sine functions by the difference of two cosine functions and integrating Eq. (6) with respect to x, we obtain the spatial amplitude covariance,

$$C_\chi(z_n(t))=\int_0^L dC_\chi(z_n)=\tfrac{1}{2}a^2\int_0^L N(x)[I_1(x,z_n)+I_2(x,z_n)]\,dx\ , \tag{11}$$

where

$$I_1(x,z_n(t))=-\int_{-\infty}^{\infty}dy'\int_{-\infty}^{\infty}dz'\cos[\alpha(y'^2+z'^2-z'z_n+z_n^2/2)]$$
$$\times\frac{J_1[(y'^2+z'^2)^{1/2}]}{(y'^2+z'^2)^{1/2}}\,\frac{J_1[\{y'^2+(z'-z_n)^2\}^{1/2}]}{\{y'^2+(z'-z_n)^2\}^{1/2}}\ , \tag{12}$$

$$I_2(x,z_n(t))=\int_{-\infty}^{\infty}dy'\int_{-\infty}^{\infty}dz'\cos[\alpha(z'z_n-z_n^2/2)]$$
$$\times\frac{J_1[(y'^2+z'^2)^{1/2}]}{(y'^2+z'^2)^{1/2}}\,\frac{J_1[\{y'^2+(z'-z_n)^2\}^{1/2}]}{\{y'^2+(z'-z_n)^2\}^{1/2}}\ , \tag{13}$$

$$\alpha\equiv kx/\eta^2=\lambda x/(2\pi a^2)\ ,\quad z_n=(\eta v/x)t\ , \tag{14}$$

and L is the total path length.

The variance of the amplitude scintillation is defined by $C_\chi(0)$, which from Eq. (11) is

$$\sigma_\chi^2=a^2\int_0^L N(x)\,dx\int_{-\infty}^{\infty}dy'\int_{-\infty}^{\infty}dz'\sin^2[\tfrac{1}{2}\alpha(y'^2+z'^2)]$$
$$\times J_1^2[(y'^2+z'^2)^{1/2}]/(y'^2+z'^2)$$
$$=a^2\int_0^L dx\,N(x)F_5(\alpha)\ . \tag{15}$$

If we are interested in the far-field solution, i.e., $\alpha\gg 1$, F_5 can be integrated over y' and z' by use of a stationary-phase technique (see Appendix B); then the variance of the amplitude fluctuations becomes [from Eq. (B18)]

$$\sigma_\chi^2\simeq\frac{\pi}{2}a^2\int_0^L N(x)\,dx\ . \tag{16}$$

To compare the amplitude variance induced by rain scattering with that caused by refractive turbulence, we assume that the rainfall rate is constant along a 1 km path with a value of 10 mm/h, and that the drop radius is 1 mm. From Eqs. (10) and (16), we have $\sigma_\chi^2\simeq 0.16$, which is comparable to the variance caused by moderate turbulence.[9]

III. TEMPORAL POWER SPECTRUM

The temporal power spectrum of the amplitude scintillation is defined as the Fourier transform of the temporal covariance function of the amplitude scintillation,[9] i.e.,

$$\omega_\chi(f)\equiv 2\int_{-\infty}^{\infty}\exp(-i\omega t)C_\chi(\mathbf{v}t)dt\ .$$

Here $\mathbf{v}$ is the transverse raindrop velocity and t is the time lag between observations. (A more detailed analysis and careful examination of the assumptions involved in this substitution may be found in Ref. 12.) If we assume that the wind velocity is small compared to the terminal velocity of raindrops, then $\mathbf{v}$ can be expressed by the relationship shown in Eq. (9). Inserting Eq. (11) into the above equation, we have

$$\omega_\chi(f)=a^2\int_{-\infty}^{\infty}dt\exp(-i\omega t)\int_0^L dx\,N(x)[I_1(x,z_n(t))+I_2(x,z_n(t))]$$

$$=a^2\int_0^L dx\,N(x)(F_1+F_2)\ . \tag{17}$$

It is extremely difficult to evaluate the multiple integrals in F_1 and F_2, either analytically or numerically, without introducing further assumptions; however, we are interested in only the far-field solution, i.e., we assume that the Fresnel-zone size $(\lambda x)^{1/2}$ is much larger than the drop size a. From Eq. (14), we have $\alpha\gg 1$. This is a reasonable assumption. For a typical rainfall, the mean drop radius is in the order of 1 mm. If we assume that the path length is 1 km and that the wave number is $10^7\ \mathrm{m}^{-1}$, then $\alpha=100$. Hence the trigonometric functions involved in Eqs. (12) and (13) oscillate rapidly compared with the Bessel functions. In this case, the integral can be evaluated by the method of stationary phase (see Appendix B). Inserting Eqs. (B5), (B7), (9), and (10) into Eq. (17), we obtain the temporal power spectrum of the amplitude scintillation

$$\omega_\chi(\Omega)=3.32\pi\times10^{-12}a^{-1}\Omega^{-2}\int_0^L dx\,h(x)$$
$$\times[H_1(2\Omega)+\eta J_1^2(\Omega)(\pi/kx)^{1/2}\sin(\tfrac{1}{4}\pi-kx\Omega^2/\eta^2)]\ , \tag{18}$$

where $\Omega=f/f_0$ is the normalized frequency; $f_0=v/(2\pi a)$, and $H_1(\Omega)$ is the Struve function of the first order. If we assume that there is only a sheet of rainfall between transmitter and receiver, i.e., $h(x)=h\delta(x-x_0)$; $0<x_0<L$, then the temporal power spectrum is

$$\omega_\chi(x_0,\Omega)=3.32\pi\times10^{-12}a^{-1}\Omega^{-2}$$
$$\times h[H_1(2\Omega)+\eta J_1^2(\Omega)(\pi/kx_0)^{1/2}\sin(\tfrac{1}{4}\pi-kx_0\Omega^2/\eta^2)]. \tag{19}$$

The numerical results of Eq. (19) are plotted in Fig. 2 versus the normalized frequency Ω for $x_0=10^3$ m, $a=10^{-3}$ m, and $k=10^7\ \mathrm{m}^{-1}$. The oscillation of the temporal power spectrum is caused by motion of the fringes that are produced by the interference of the incident plane

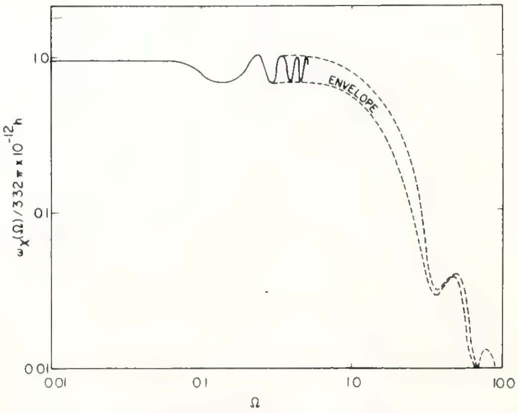

FIG. 2. Temporal power spectrum of the amplitude scintillations induced by a sheet of rainfall with a rain rate h (mm/h) located $x_0=1$ km from the receivers. The wave number of the incident plane wave is $k=10^7\ \mathrm{m}^{-1}$. A monodisperse size distribution ($a=1$ mm) of raindrops is assumed. The horizontal axis is the normalized frequency $\Omega=f/f_0$; $f_0=v/(2\pi a)$ and v is the terminal velocity of raindrops of radius a.

wave and the scattered spherical wave from each raindrop (see Sec. I). Part of the oscillation is smeared out by the effects of off-axis drops; however, the smearing is not complete. The bumps of the envelope of the temporal power spectrum in the high-frequency region are caused by the side lobes of the diffraction pattern of the raindrop. (Also see Sec. I.)

Because we have assumed that $kx/\eta^2 \gg 1$ in Eq. (18), the second term in the square brackets gives a significant contribution only for small Ω. In this case, the second term is small compared to the first term, and Eq. (18) can be further simplified to

$$\omega_\chi(\Omega) = 3.32\pi \times 10^{-12} a^{-1} \Omega^{-2} H_1(2\Omega) L\bar{h} , \tag{20}$$

where $\bar{h}$ denotes the path-averaged rainfall rate in mm/h, defined by $\bar{h} = (1/L)\int_0^L h(x)\,dx$. The magnitude of the temporal power spectrum of the log-amplitude scintillations is proportional to the path-averaged rainfall rate with a uniform path-weighting function. If the temporal power spectrum is normalized to the amplitude variance given by Eq. (16), we have

$$(\pi/2) f_0 \omega_\chi(\Omega)/\sigma_\chi^2 = H_1(2\Omega)/\Omega^2 . \tag{21}$$

The result of Eq. (21) is plotted in Fig. 3. Because we assumed that the scattering is incoherent, the final spectrum is the ensemble average of the spectra of the individual drops. Because we used a monodisperse size distribution of raindrops, we can see the bumps at the high-frequency region caused by the side lobes of the diffraction pattern of a sphere. The spectrum is relatively flat for $\Omega < 1$ (or $f < f_0 = v/2\pi a$). Note that, if the drop radius $a = 1$ mm, then $f_0 \simeq 1$ kHz. Comparing this frequency to the temporal power spectrum caused by convective and wind-induced scintillations (see Tatarskii[9]), we see that the rain-induced power spectrum is much broader and the magnitude is less.

IV. EFFECT OF MULTISIZE RAINDROPS

In the foregoing derivation, we have assumed a monodisperse size distribution of raindrops. Because it is unrealistic to assume that all raindrops are the same size, in this section we generalize our theory to include effects of different-size raindrops.

The rainfall rate defined in Eq. (7) is based on the assumption that all raindrops have the same size. For different-size raindrops, the differential rainfall rate can be expressed as $dh(a,x) = h(x)p(a,x)\,da$, where $h(x)$ is the total rainfall rate at path position x, and $p(a,x)$ is the probability-density function of raindrop size at that position. Hence the averaged quantities of interest, such as the variance, covariance function, and power spectrum, can be obtained by simply changing $h(x)$ to $dh(a,x)$ and integrating over a, i.e.,

$$\bar{F} = \int_0^\infty da\, p(a,x) F(a) . \tag{22}$$

Here $F(a)$ denotes the quantity of interest derived from a monodisperse size distribution, the quantity $\bar{F}$ is the averaged quantity over the probability-density function $p(a,x)$. Inserting Eqs. (16) and (10) into Eq. (22), we obtain the averaged amplitude variance

$$\overline{\sigma_\chi^2} = 5.22 \times 10^{-10} \int_0^L dx\, h(x) \int_0^\infty da\, a^{-3/2} p(a) . \tag{23}$$

Similarly, the averaged temporal power spectrum of the amplitude fluctuations is, from Eq. (20),

$$\overline{\omega_\chi(f)} = 1.06 \times 10^{-8} f^{-2} \int_0^L dx\, h(x) \int_0^\infty da\, p(a,x) a^{-2} H_1(\alpha_1 f \sqrt{a}) , \tag{24}$$

where $\alpha_1 = \pi/50$ and f is the frequency in Hz. In deriving Eq. (24), we have used the relationship between the terminal velocity and raindrop radius, as shown in Eq. (9). Inserting the correct density function $p(a,x)$ in Eqs. (23) and (24), we obtain the variance and the temporal power spectrum of the amplitude scintillations, including the effect of different sizes of raindrops. The probability-density function of raindrop size relates to the number-density function of raindrop size $N(a,x)$ by the formula

$$p(a,x) = \frac{N(a,x)\frac{4}{3}\pi a^3}{\int_0^\infty N(a,x)\frac{4}{3}\pi a^3\, da} . \tag{25}$$

A well-accepted raindrop number density was given by Marshall and Palmer,[11] i.e.,

$$N(a,x) = N_0 e^{-2\Lambda(x)a} , \tag{26}$$

where N_0 is the value of $P(a)$ for $a = 0$ and $\Lambda(x)$ is a function of rainfall rate $h(x)$. They found that

$$N_0 = 8 \times 10^6 \text{ m}^{-4} , \tag{26a}$$

for any intensity of rainfall, and that

$$\Lambda(x) = 4100 h(x)^{-0.21} \text{ m}^{-1} , \tag{26b}$$

where $h(x)$ is in mm/h. Inserting Eq. (26) into Eq. (25), we obtain the probability-density function of raindrop size,

$$p(a,x) = \tfrac{16}{6} \Lambda^4(x) a^3 e^{-2\Lambda(x)a} . \tag{27}$$

Substituting Eq. (27) into Eqs. (23) and (24), we have

$$\overline{\sigma_\chi^2} = 8.57 \times 10^{-5} \int_0^L dx\, h(x)^{0.685} \tag{28a}$$

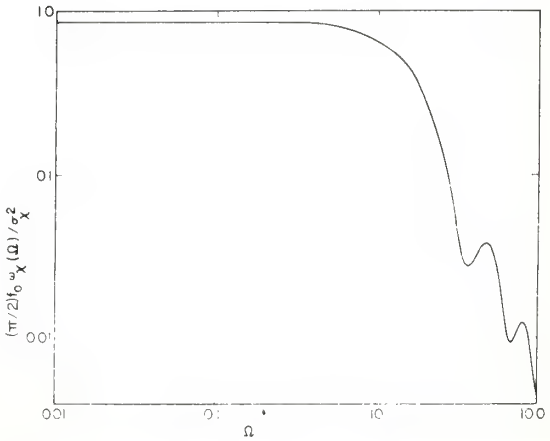

FIG. 3. Temporal power spectrum of the rain-induced amplitude scintillations of a monodisperse (a = 1 mm) rainfall normalized to the variance of the amplitude scintillations vs the normalized frequency Ω.

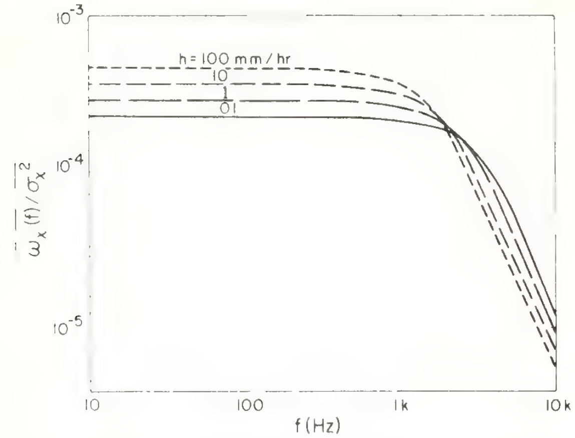

FIG. 4. Temporal power spectra of the rain-induced amplitude scintillations of a Marshall–Palmer size distribution of raindrops, normalized to the variance of the amplitude scintillations. The horizontal axis is the frequency in Hz.

and

$$\overline{\omega_\chi(f)} = \frac{0.119}{f^2}\int_0^L dx\, h(x)^{0.58}\int_0^\infty d\delta\, \delta e^{-\delta} H_1(\alpha_2 f\sqrt{\delta})\ , \qquad (28b)$$

where $\delta = 8200ah(x)^{-0.21}$ and $\alpha_2 = 6.94 \times 10^{-4}h(x)^{0.105}$. The overbars here denote the quantities averaged over all sizes. The dependence of $\overline{\sigma_\chi^2}$ and $\overline{\omega_\chi(f)}$ on the rainfall rate indicates that the contributions from the path positions with heavier rainfall rates are suppressed. This is intuitively plausible because, for the same amount of precipitation, the heavier rainfall rate contains more large raindrops, hence less scintillation. From Eqs. (28a) and (28b), the normalized temporal power spectrum is

$$\frac{\overline{\omega_\chi(f)}}{\overline{\sigma_\chi^2}} = \frac{1390}{f^2}\,\frac{\int_0^L dx\, h(x)^{0.58}\int_0^\infty d\delta\, \delta e^{-\delta} H_1(\alpha_2 f\sqrt{\delta})}{\int_0^L dx\, h(x)^{0.685}}\ . \qquad (29)$$

The disadvantage of Eq. (29) is that it is a nonlinear function of the rainfall rate at different path positions. In order to simplify the problem, we first assume that the rainfall rates are uniform along the path, i.e., $h(x) = \bar{h}$. The result of Eq. (29) is plotted in Fig. 4 for the rainfall rate $\bar{h}$ varying from 0.1 to 100 mm/h. It is clear that the bumps in the high-frequency region of the monodisperse size-distribution model are smeared out because of the effects of different sizes. Because a smaller rainfall rate has smaller drops, the temporal power spectrum has more high-frequency content. This is true because the terminal velocity is proportional to the square root of the drop size [Eq. (9)], and the cutoff frequency is on the order of the ratio of the velocity to the radius of the raindrops, i.e., $a_0^{-1/2}$, where a_0 is the mean drop size and is proportional to $\bar{h}^{0.21}$ for a Marshall–Palmer distribution. The magnitude of the low-frequency components is proportional to $a_0^{1/2}$, so that the area under the curve is unity. To illustrate the true frequency distribution of energy, we plot the normalized temporal power spectrum $f\overline{\omega_\chi(f)}/\overline{\sigma_\chi^2}$ in Fig. 5. It is obvious that for a smaller mean size a_0, or a smaller rainfall rate, the peak power is at a higher frequency. Again, the frequency of the peak power is proportional to $a_0^{-1/2}$, or $\bar{h}^{-0.105}$.

Note that the variance and temporal power spectrum of the amplitude scintillations are not dependent on the wave number k as long as the wavelength is small compared to the sizes of raindrops. Also, all of the foregoing results are based on the far-field assumption, i.e., $x \gg 4a^2/\lambda$. If we assume that the radius of the raindrops is 0.5 mm and $\lambda = 0.63$ μm, then we have $4a^2/\lambda = 1.6$ m. All of the drops, except those very close to the detector, will be sufficiently far away to satisfy the far-field condition.

The results plotted in Figs. 4 and 5 are based on the assumption that the rainfall rate is uniform along the path. Of course, this is not true for a practical case. However, from Figs. 4 and 5, we found that the temporal power spectra are not very sensitive to the rainfall rate. It seems reasonable to replace the path-dependent rainfall rate $h(x)$ by the path-averaged rainfall rate $\bar{h}$ in Eq. (29); we can show that the changes of the temporal power spectrum due to this substitution will be small. When we measure the amplitude scintillations induced by raindrops, we also measure the turbulence-induced scintillations. It is reasonable to assume that the scintillations induced by raindrops and by turbulence are uncorrelated. In this case, the total temporal power spectrum is the sum of the temporal power spectra of those two. The temporal power spectrum of amplitude scintillations induced by wind and convective turbulence was given by Tatarskii.[9] If we assume that the transverse wind speed $v_a = 2$ m/s, that the refractive turbulence-induced amplitude variance is $\sigma_{\chi a}^2 = 0.25$, that the path length $L = 500$ m and that the wavelength $\lambda = 0.628$ μm, then the temporal power spectrum of turbulence-induced scintillations takes the form shown at the left-hand side of Fig. 6. If we also assume that the path-averaged rainfall rate $\bar{h} = 7$ mm/h and the raindrop number density follows a Marshall–Palmer law, the resultant temporal power spectrum of rain-induced scintilla-

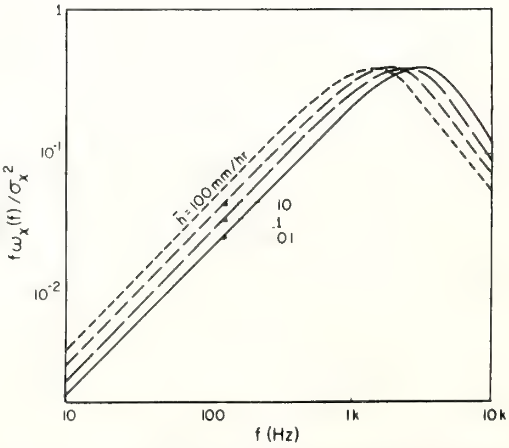

FIG. 5. Frequency distribution of energy of the temporal power spectra shown in Fig. 4.

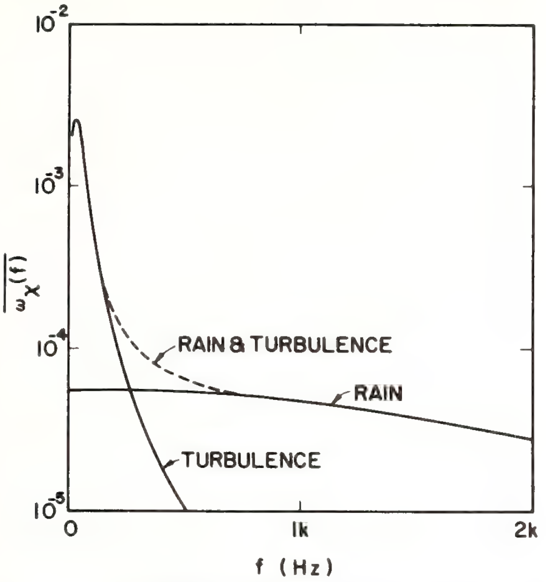

FIG. 6. The combination of the rain-induced and turbulence-induced temporal power spectra vs frequency in Hz. Here $L=500$ m, $v_a=2$ m/s, $\lambda=0.628$ μm, $\sigma^2_{\chi a}=0.25$, $h=7$ mm/h.

tion is shown at the bottom of Fig. 6. The combination of the temporal power spectrum induced by rain and turbulence is denoted by the dashed-line curve in Fig. 6. A preliminary experimental result of the measured temporal power spectrum of amplitude scintillations during a rainfall along a 500 m path is shown in Fig. 7. Although we do not know the corresponding parameters, such as the path-averaged wind speed, the variance of the amplitude scintillations produced by refractive turbulence, the rainfall rate and its associated size distribution, the result agrees qualitatively with the theoretical prediction. For different parameters, we expect that the shape of the temporal power spectrum of the amplitude scintillations will remain the same.

V. APPLICATIONS TO REMOTE SENSING

In the previous section, we have shown that the measured rain-induced temporal power spectrum is in good agreement with the theoretical prediction. Now the problem becomes: can we get any information about the path-averaged rainfall rate and the mean drop size from the measured temporal power spectrum? The mean size can be obtained from either the cutoff frequency or the peak power frequency of the temporal power spectrum (see Figs. 4 and 5). These measurements, however, are sensitive to experimental errors. If we take the second derivative of Eq. (24) with respect to f and set $f=0$, we have

$$\left.\frac{d^2\overline{\omega_\chi(f)}}{df^2}\right|_{f=0} \sim \int_0^L dx\, h(x) \int_0^\infty da\, p(a,x) = \bar{h}L \ . \tag{30}$$

In deriving Eq. (30), we have used the relationship that

$$\left.\frac{d^2}{df^2}\left[\frac{H_1(\alpha_1 f\sqrt{a})}{f^2}\right]\right|_{f=0} \propto a^2 \ . \tag{31}$$

At first glance, Eq. (30) seems well behaved. When we take the second derivative of the temporal power spectrum of rain-induced scintillation at zero frequency, we get the path-averaged rainfall rate $\bar{h}$ directly, in spite of the size distribution, but this information is contaminated by the contributions from turbulence-induced scintillation (see Figs. 6 and 7). Of course, some other techniques may be useful in the high-frequency region, where the contribution of refractive turbulence is negligible, to deduce the path-averaged rainfall rate from the spectrum. However, we have to know the correct size distribution of raindrops. Because there is a monotonic relationship between the drop size and its associated terminal velocity [see Eq. (9)], we can measure the terminal-velocity distribution instead of the size distribution.

To avoid the turbulence-induced errors in the measurement of path-averaged rain parameters, we analyze the space–time covariance of two vertically spaced sensors. Because the rain has a predominately vertical velocity and turbulence is advected primarily horizontally, the covariance of vertically spaced sensors is insensitive to turbulence effects in the frequency band of interest. For a given vertical separation, the scintillation due to turbulence will correlate only for long time lags compared with the rain, which will correlate at the much shorter time lags determined by the raindrop fall speeds. Another factor that limits the effects of turbulence is that refractive-index fluctuations for visible light are produced largely by temperature inhomogeneities in the atmosphere. These inhomogeneities occur as a result of the vertical temperature gradient that is maintained by solar heating of the ground. As cloud cover increases with the onset of rain, the temperature gradient is rapidly eliminated, which produces a concomitant reduction of the refractive-index fluctuations. For both of those reasons, the effects of refractive turbulence on our rain-

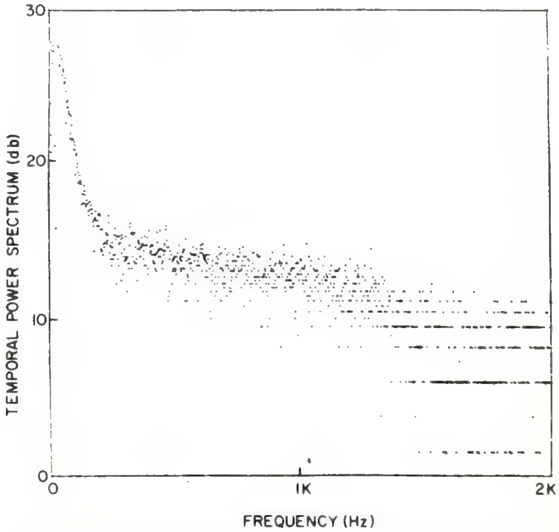

FIG. 7. Experimentally measured temporal power spectrum of amplitude scintillation during a rainfall along a 500 m path.

sensing technique will be minimized.

For an incident plane wave, the time-lagged amplitude covariance function of two detectors with a vertical separation z_0 and time lag t can be obtained by simply replacing z_0 by $z_0 - vt$ in Eqs. (11)–(14). If we assume that the raindrop size distribution at path position x is $p(a, x)$, where a is the radius of the raindrops, then the average amplitude covariance for different sizes of raindrops can be defined as

$$\overline{C_\chi(z_0, t)} = \int_0^L dx \int_0^\infty da\, \tfrac{1}{2} a^2 p(a, x) N(a, x)[I_1(x, z_0 - vt) + I_2(x, z_0 - vt)] = \int_0^L dx\,(F_3 + F_4)\,, \tag{32}$$

where the F_3 and F_4 are calculated in parts (c) and (d) of Appendix B. Inserting Eqs. (B12) and (B16) into Eq. (32), we obtain the average time-lagged amplitude covariance function,

$$\overline{C_\chi(z_0, t)} = 8.85 \times 10^{-12} t^{-1} \int_0^L dx\, h(x) p(a', x) \times [1 + 9.24 \times 10^{-6} (k/x)^{1/2} z_0^2/t^2]\,, \tag{33}$$

where $h(x)$ is the rainfall rate in mm/h at path position x, k, L; z_0 and t are in SI units; and a' is the detected size of raindrops, defined by

$$a' = z_0^2/(4 \times 10^4 t^2)\,. \tag{34}$$

Equation (33) shows that, for an incident plane wave passing through a rainfall and illuminating two detectors with a vertical separation z_0, the number of raindrops with terminal velocity $v = z_0/t$ is proportional to the time-lagged cross-correlation function of the amplitude scintillations of the two detectors with time lag t. By varying the time lag t or the vertical separation z_0, we can obtain the terminal velocity distribution of the raindrops. Because there is a monotonic relationship between the raindrop size and its associated terminal velocity, the path-average size distribution of a rainfall can be obtained.

If we assume that $L = 1$ km, $k = 10^7$ m^{-1} and the mean terminal velocity of raindrops is on the order of 5 m/s, then the second term in the square brackets is small compared to the first term. Hence Eq. (33) can be further simplified to

$$\overline{C_\chi(z_0, t)} = 8.85 \times 10^{-12} t^{-1} \int_0^L dx\, h(x) p(a', x) \sim \overline{p(a')}/t\,, \tag{35}$$

where $\overline{p(a')}$ is the path-averaged probability-density function of raindrop size.

In order to obtain Eq. (33) by the method of stationary phase, we have introduced two restrictions on the solution Eq. (35), i.e., $t \gg 0.01 (L/k)^{1/4}$ and $\sigma_v/v \gg (2L/k)^{1/2} z_0$ [See part (c) of Appendix B for details.] The physical interpretation of the former is that the vertical separation z_0 should be large enough to differentiate the different terminal velocities v and ultimately the raindrop sizes. The latter restriction implies that the raindrop size distribution cannot be monodisperse. If we assume that the largest size of raindrops of interest is $a = 2.5$ mm (the associated terminal velocity is about 10 m/s), $L = 1$ km, and $k = 10^7$ m^{-1}, the restriction on t implies that $z_0 \gg 1$ cm. Further, for a Marshall–Palmer distribution, $\sigma_v/v = 0.25$ and the second restriction implies $z_0 \gg 5.7$ cm. It is obvious that neither of these is a strong restriction.

From Eq. (35), the path-weighting function of the time-lagged amplitude covariance function is a constant. Hence Eq. (35) gives a uniform path-weighted average when we use it to measure the average size distribution. The path-averaged rainfall rate is obtained by the integration over all sizes. If we multiply Eq. (35) by t and integrate over a', we obtain

$$\int_0^\infty da'\, t\, \overline{C_\chi(z_0, t)} = 8.85 \times 10^{-12} \int_0^\infty da' \int_0^L dx\, h(x) p(a', x) = 8.85 \times 10^{-12} \bar{h} L\,. \tag{36}$$

From Eq. (34), we have (for a fixed z_0)

$$da' = -5 \times 10^{-5} z_0^2 t^{-3}\, dt\,. \tag{37}$$

Inserting Eq. (37) into Eq. (36) gives

$$\bar{h} = 5.65 \times 10^6 z_0^2 \int_0^\infty dt\, \overline{C_\chi(z_0, t)}\, t^{-2}/L\,, \quad \text{for fixed } z_0\,. \tag{38}$$

Instead of fixing the separation z_0, we can also fix the time lag t and vary the separation z_0; then we have

$$da' = 5 \times 10^{-5} z_0 t^{-2}\, dz_0\,. \tag{39}$$

Hence Eq. (36) becomes

$$\bar{h} = 5.65 \times 10^6 t^{-1} \int_0^\infty dz_0\, z_0 \overline{C_\chi(z_0, t)}/L\,, \quad \text{for fixed } t\,. \tag{40}$$

Equations (38) and (40) show that the path-averaged rainfall rate can be obtained either as the integration over time lag t of time-lagged covariance function divided by t^2 (for fixed spatial separation z_0) or the integration over the spatial separation z_0 of spatial covariance function multiplied by z_0 (for fixed time lag t). Again, from Eq.

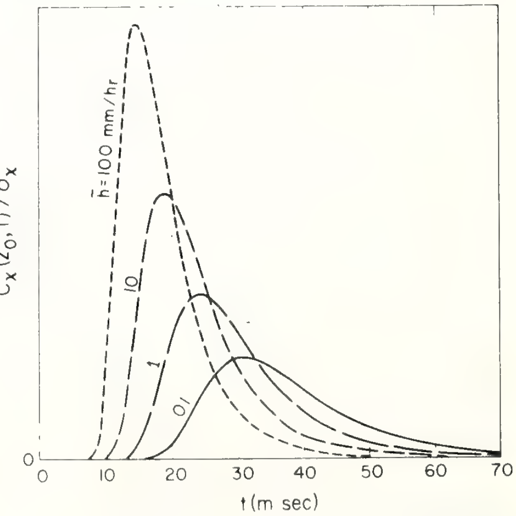

FIG. 8. The normalized covariance functions of amplitude fluctuations $\overline{C_\chi(z_0, t)}/\sigma_\chi^2$ for two detectors with a vertical separation $z_0 = 10$ cm vs the time lag t.

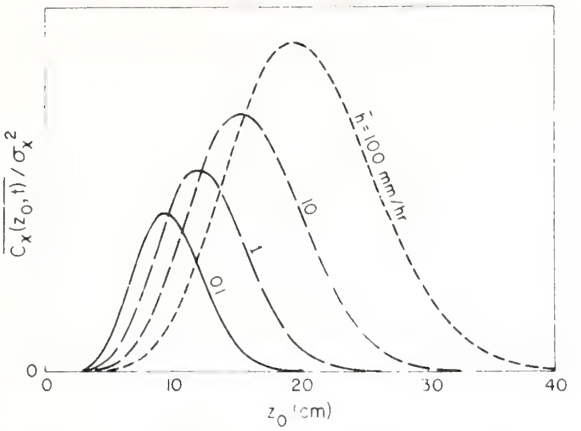

FIG. 9. The normalized covariance functions of amplitude fluctuations $\overline{C_\chi(z_0,t)}/\sigma_\chi^2$ for a fixed time lag $t=31.6$ ms vs the vertical separation z_0.

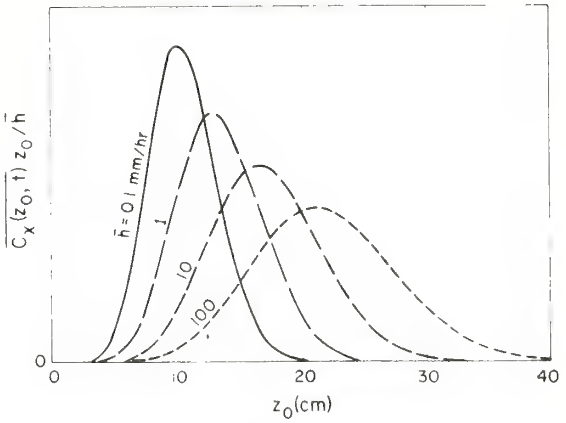

FIG. 11. The quantity $\overline{C_\chi(z_0,t)z_0/\bar{h}}$ for a fixed time lag $t=31.6$ ms vs the vertical separation z_0.

(36), a uniform path-weighting function is obtained when we measure the path-averaged rainfall rate by Eqs. (38) and (40).

There are several advantages of this space–time covariance measurement to get the path-averaged rain parameters. First, the measured quantities are not functions of the fluctuations of the rainfall rate $h(x)$ and the probability-density function of raindrop size $p(a,x)$ along the path. They are dependent on only their path-averaged values. Second, the measurements are not contaminated by the contributions from the horizontal-wind-induced scintillations, though vertical wind may still cause difficulties. If we arrange the optical path close to the ground, however, the contribution from the vertical wind will be negligible. Third, the measurement of path-averaged rainfall rate is independent of the probability-density function of raindrop size. This may be critical if we have to assume a raindrop size distribution (e.g., Marshall–Palmer distribution) in order to calculate the path-averaged rainfall rate. Fourth, the actual path-averaged probability-density function or the number-density function of raindrop size can be measured.

In order to demonstrate how we can obtain the path-averaged rain parameters, we assume that the raindrop size distribution follows the Marshall–Palmer distribution. This is only an example. Of course, the measured covariance will depend on the actual size distribution. Because the measurements are dependent on only the path-averaged values, we have only to give the path-

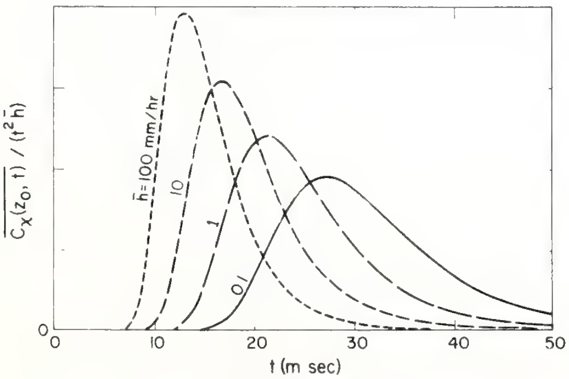

FIG. 10. The quantity $\overline{C_\chi(z_0,t)}/(t^2\bar{h})$ for a fixed vertical separation $z_0=10$ cm vs the time lag t.

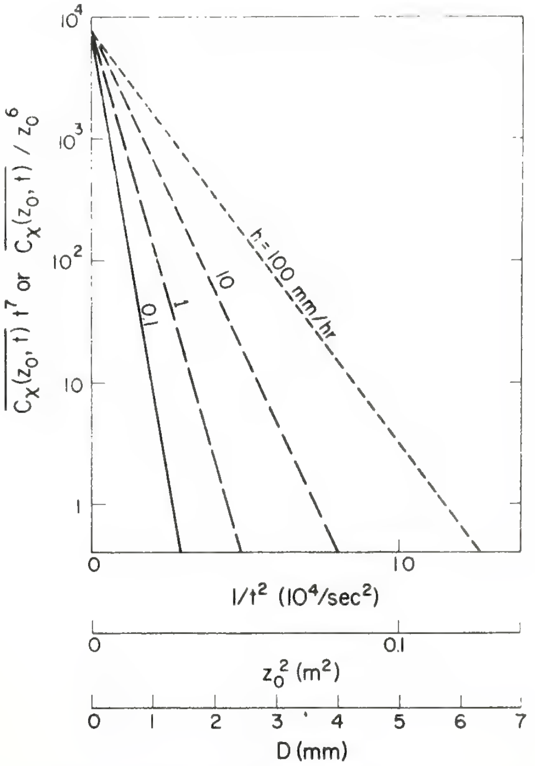

FIG. 12. The quantity $\overline{C_\chi(z_0,t)}t^7$ for fixed $z_0=10$ cm vs $1/t^2$ and the quantity $\overline{C_\chi(z_0,t)}z_0^{-6}$ for fixed $t=31.6$ ms vs z_0^2. The corresponding raindrop diameter is also shown on the horizontal axis.

averaged rainfall rate $\overline{h}$ instead of the path-dependent rainfall rate $h(x)$. The quantity $\overline{h}$ was varied from 0.1 to 100 mm/h to calculate the curves in Figs. 8–12. The normalized space–time covariance functions are shown in Fig. 8 (for a fixed separation $z_0 = 10$ cm) and in Fig. 9 (for a fixed time lag $t = 31.6$ ms). Because there are larger raindrops in the heavier rainfall rate, the peak of the covariance function has a shorter time lag (for fixed z_0) or a larger spatial separation (for fixed t) for the heavier rainfall rate. The shapes of the curves are dependent on the path-averaged raindrop size distribution. For different size distributions, we expect that the covariance function will be different. The quantities $\overline{C_\chi(z_0, t)}/(t^2\overline{h})$ (for fixed z_0) and $\overline{C_\chi(z_0, t)}z_0/\overline{h}$ (for fixed t) are plotted in Figs. 10 and 11, respectively. Again the shapes of the curves are dependent on the raindrop size distribution. The areas under the curves, however, are a constant because, from Eqs. (38) and (40), the areas under the curves of $\overline{C_\chi(z_0, t)}/t^2$ and $\overline{C_\chi(z_0, t)}z_0$ are proportional to the path-averaged rainfall rate and are independent of the raindrop size distribution.

Inserting Eq. (25) into Eq. (35), we obtain the path-averaged number-density function of raindrop size, from the space–time covariance function, i.e.,

$$\overline{N(a')} \sim z_0^{-6} t^7 \overline{C_\chi(z_0, t)} \; ; \quad a' = z_0^2/(4\times 10^4 t^2) \; . \tag{41}$$

Hence, the path-averaged raindrop number density is proportional to $\overline{C_\chi(z_0, t)}t^7$ for fixed z_0 and to $\overline{C_\chi(z_0, t)}z_0^{-6}$ for fixed t. Again, for a Marshall–Palmer distribution, the results of $\overline{C_\chi(z_0, t)}t^7$ (for fixed $z_0 = 10$ cm) vs $1/t^2$, and the results $\overline{C_\chi(z_0, t)}z_0^{-6}$ (for fixed $t = 31.6$ ms) vs z_0^2 are plotted in Fig. 12. The corresponding raindrop diameter is also shown on the horizontal axis. The results agree with the assumed raindrop size distribution. In plotting Fig. 12, we assumed that $N_0 = 8\times 10^3$ m^{-3} (mm)$^{-1}$ because we have no information about N_0 when we use Eq. (25) as the raindrop size distribution.

VI. CONCLUSIONS

We have applied the theory of plane-wave scattering by spheres to evaluate the variance, space–time covariance, and the temporal-frequency spectrum of the amplitude fluctuations produced by the interaction of an optical beam with rainfall. Further, we have shown that the time-lagged covariance function of two vertically spaced sensors can provide a practical remote measurement of path-averaged drop-size distribution and rain rate without making any assumption about the form of the drop-size distribution.

ACKNOWLEDGMENT

The authors are indebted to W. K. Klemperer, R. S. Lawrence, G. R. Ochs, and F. F. Hall for their stimulating discussions and helpful suggestions.

APPENDIX A RANGE OF VALIDITY OF THE SINGLE-SCATTERING ASSUMPTION

We estimate the range of validity of the single-scattering approximation by assuming that the onset of important multiple-scattering effects occurs when the entire laser-beam cross section is blocked, on the average, by least one falling raindrop. Then, statistically, each ray is scattered at least once before it reaches the receiving plane. If a is the drop radius, then the cross sectional area subtended by the drop is πa^2. We assume that, on the average, only one drop is contained in a cube of edge d, where d is the mean separation between drops. Because the path length L can contain L/d of these cubes, the maximum total area that the raindrops subtend is $(L/d)(\pi a^2)$. The entire optical line-of-sight will be blocked if this area approaches d^2. Consequently, a rough condition for the validity of the single-scattering assumption is

$$(\pi a^2)(L/d) \le d^2 \; . \tag{A1}$$

To reduce Eq. (A1) to a condition on path length and rain rate, we note that, if N is the number density of raindrops, then

$$d = N^{-1/3} \; . \tag{A2}$$

Substituting Eq. (A2) in Eq. (A1), we obtain

$$L \le (\pi a^2 N)^{-1} = K_m^{-1} \; , \tag{A3}$$

where K_m is the extinction coefficient. ($K_m = L_m^{-1}$, where L_m is the mean free path). Substituting the definition of N from Eq. (10) into Eq. (A3), we obtain

$$K_m(a) = 1.04\times 10^{-9} a^{-3/2} h(a) \; , \tag{A4}$$

where $h(a)$ is the rain rate attributable to drops of radius a. To relate $h(a)$ to the total precipitation rate $\overline{h}$, we have to assume a drop-size distribution. As an example, we assume that the drop sizes obey a Marshall–Palmer distribution. If $p(a)$ is the probability-density function of raindrop size as defined in Eqs. (26b) and (27) in the text, then

$$h(a)\, da = \overline{h} p(a)\, da \; . \tag{A5}$$

Substituting Eqs. (A5), and (27) into Eq. (A4), we have

$$K_m(a) = 2.77\times 10^{-9} \Lambda^4 \overline{h} a^{3/2} e^{-2\Lambda a} \; , \tag{A6}$$

where Λ is defined in Eq. (26b). Equation (A6) is the extinction that is attributable to drops of radius a. To calculate the total extinction we must integrate Eq. (A6) over drop size. After performing this operation and substituting the expression for Λ from Eq. (26b), we obtain

$$K_m = 1.7\times 10^{-4} \overline{h}^{\,0.685} \; . \tag{A7}$$

(The units of K_m are m^{-1}.)

Finally, to calculate the mean free path, we note that $K_m = L_m^{-1}$ and obtain

$$L_m = 5.9\times 10^3 (\overline{h})^{-0.685} \; . \tag{A8}$$

Note that $\overline{h}$ must be in mm/h to give L_m in meters. For a moderate rain ($\overline{h} = 10$ mm/h) $L_m \approx 1200$ m; therefore, the single-scattering assumption is valid, in this case, for paths up to 1.2 Km. In a heavy rain, $\overline{h} = 100$ mm/h, we obtain $L_m = 250$ m. These restrictions are not severe; they indicate that useful path-averaged measurements of rain parameters can be made, based on a single-scattering theory.

APPENDIX B: EVALUATION OF THE INTEGRALS IN THE TEXT BY THE METHOD OF STATIONARY PHASE

Let $F(u)$ denote an integral

$$F(u)=\int_a^b f(t)\exp[iug(t)]\,dt\ ; \tag{B1}$$

then, by the method of stationary phase,[13] as $u\to\infty$, we obtain

$$F(u)\simeq\left[\frac{2\pi}{u\,|g''(t_0)|}\right]^{1/2}\exp[i\{ug(t_0)\mp\tfrac{1}{4}\pi\}][f(t_0+0)+f(t_0-0)]/2, \tag{B2}$$

where the minus and plus signs correspond to $g''(t_0)<0$ and $g''(t_0)>0$, respectively. This result will be used to evaluate the integrals, F_1 to F_5.

(a) $F_1\equiv\int_{-\infty}^{\infty}\exp(-i\omega t)I_1(x,vt)\,dt$

$$\begin{aligned}&=-\int_{-\infty}^{\infty}dy'\int_{-\infty}^{\infty}dz'\int_{-\infty}^{\infty}dt\exp(-i\omega t)\\&\quad\times\cos[\alpha\{(y'^2+z'^2)-z'v't+(v't)^2/2\}]\\&\quad\times\frac{J_1[(y'^2+z'^2)^{1/2}]}{(y'^2+z'^2)^{1/2}}\,\frac{J_1[\{y'^2+(z'-v't)^2\}^{1/2}]}{\{y'^2+(z'-v't)^2\}^{1/2}}\,,\end{aligned} \tag{B3}$$

where $v'=\eta v/x$. Because $\alpha\gg1$, we can use the method of stationary phase to evaluate Eq. (B3). If we let $z_1=v't-z'$ in the integral over t, then Eq. (B3) becomes

$$\begin{aligned}F_1&=-\frac{2}{v'}\int_{-\infty}^{\infty}dy'\int_{-\infty}^{\infty}dz'\exp(-i\omega'z')\\&\quad\times\int_0^{\infty}dz_1\cos(\omega'z_1)\cos[\alpha y'^2+\alpha z'^2/2+\alpha z_1^2/2]\\&\quad\times\frac{J_1[(y'^2+z'^2)^{1/2}]}{(y'^2+z'^2)^{1/2}}\,\frac{J_1[(y'^2+z_1^2)^{1/2}]}{(y'^2+z_1^2)^{1/2}}\,,\end{aligned} \tag{B4}$$

where $\omega'=\omega/v'$. We also have

$$\begin{aligned}&\cos(\omega'z_1)\cos[\alpha\{y'^2+z'^2/2+z_1^2/2\}]\\&\quad=\tfrac{1}{2}\{\cos[\alpha y'^2+\alpha z'^2/2+\omega'z_1+\alpha z_1^2/2]\\&\qquad+\cos[\alpha y'^2+\alpha z'^2/2-\omega'z_1+\alpha z_1^2/2]\}\,.\end{aligned}$$

There will be no stationary-phase points for the first term with respect to z_1, for $z'>0$; hence the contribution of the first term can be neglected. The stationary phase occurs at $z_1=\omega'/\alpha$ in the second term. Substituting Eq. (B2) into (B4), we obtain

$$\begin{aligned}F_1&=-\left(\frac{1}{v}\right)\left(\frac{2\pi x}{k}\right)^{1/2}\int_{-\infty}^{\infty}dy'\int_{-\infty}^{\infty}dz'\cos\left[\frac{\pi}{4}+\alpha y'^2+\frac{\alpha z'^2}{2}-\frac{\omega'^2}{2\alpha}\right]\\&\quad\times\exp(-i\omega'z')\,\frac{J_1[(y'^2+z'^2)^{1/2}]}{(y'^2+z'^2)^{1/2}}\,\frac{J_1[(y'^2+\omega'^2/\alpha^2)^{1/2}]}{(y'^2+\omega'^2/\alpha^2)^{1/2}}\,.\end{aligned}$$

Again, using the method of stationary phase with respect to y' at $y'=0$, we have

$$F_1=\frac{2\sqrt{2}\pi\eta}{kv}\int_0^{\infty}dz'\sin\left[\frac{\alpha z'^2}{2}-\frac{\omega'^2}{2\alpha}\right]\cos(\omega'z')\,\frac{J_1(z')}{z'}\,\frac{J_1(\omega'/\alpha)}{\omega'/\alpha}\,.$$

Following a similar approach with z' at $z'=\omega'/\alpha$, we obtain

$$F_1=\frac{2\pi^{3/2}\eta^2}{k^{3/2}v}\,\frac{J_1^2(\Omega)}{\Omega^2}\sin\left(\frac{\pi}{4}-\frac{kx\Omega^2}{\eta^2}\right)\Big/\sqrt{x}\ , \tag{B5}$$

where $\Omega=f/f_0$ and $f_0=v/(2\pi a)$.

(b) $F_2\equiv\int_{-\infty}^{\infty}\exp(-i\omega t)I_2(x,vt)\,dt$

$$\begin{aligned}&=\int_{-\infty}^{\infty}dy'\int_{-\infty}^{\infty}dz'\int_{-\infty}^{\infty}dt\cos[\alpha(z'v't-(v't)^2/2)]\\&\quad\times\exp(-i\omega t)\,\frac{J_1[(y'^2+z'^2)^{1/2}]}{(y'^2+z'^2)^{1/2}}\,\frac{J_1[\{y'^2+(z'-v't)^2\}^{1/2}]}{\{y'^2+(z'-v't)^2\}^{1/2}}\,,\end{aligned} \tag{B6}$$

where, again, $v'=v\eta/x$. Using the method of stationary phase twice with respect to t and z', as previously, we finally have

$$F_2=\frac{4\pi\eta}{kv}\int_0^{\infty}dy'\,\frac{J_1^2[\{y'^2+\Omega^2\}^{1/2}]}{(y'^2+\Omega^2)}\,.$$

The integral over y' in Eq. (B6) can be performed,[14] i.e.,

$$F_2=\frac{2\pi\eta}{kv}\,\frac{H_1(2\Omega)}{\Omega^2}\,, \tag{B7}$$

where $H_1(\,)$ is a Struve function of the first order.

(c) $F_3=\int_0^{\infty}da\,p(a,x)I_1(z_0-vt)(\tfrac{1}{2}a^2)N(a,x)$

$$\begin{aligned}&=-\frac{1}{2}\int_0^{\infty}da\int_0^{L}dx\int_{-\infty}^{\infty}dy'\int_{-\infty}^{\infty}dz'\,p(a,x)a^2N(a,x)\\&\quad\times\cos[\alpha\{(y'^2+z'^2)-z'(z_0'-vt\eta/x)+(z_0'-vt\eta/x)^2/2\}]\\&\quad\times\frac{J_1[(y'^2+z'^2)^{1/2}]}{(y'^2+z'^2)^{1/2}}\,\frac{J_1[\{y'^2+(z'-z_0'+vt\eta/x)^2\}^{1/2}]}{\{y'^2+(z'-z_0'+vt\eta/x)^2\}^{1/2}}\,,\end{aligned} \tag{B8}$$

where $z_0'=z_0\eta/x$. Again, using the method of stationary phase twice with respect to y' at $y'=0$ and z' at $z'=(z_0'-vt\eta/x)/2$, we obtain

$$\begin{aligned}F_3&=2\pi k\int_0^{L}\frac{dx}{x}\int_0^{\infty}da\,p(a,x)a^4N(a,x)\\&\quad\times\sin\left[\frac{\alpha(z_0'-vt\eta/x)^2}{4}\right]\frac{J_1^2[(z_0'-vt\eta/x)/2]}{(z_0'-vt\eta/x)^2}\,.\end{aligned} \tag{B9}$$

Inserting Eq. (10) into Eq. (B9) gives

$$\begin{aligned}F_3&=\frac{1.66\times10^{-10}\pi}{k}\int_0^{L}\frac{h(x)\,dx}{x}\int_0^{\infty}da\,p(a,x)a^{-3/2}\\&\quad\times\sin\left[\frac{k(z_0-vt)^2}{4x}\right]\frac{J_1^2[ka(z_0-vt)/(2x)]}{(z_0-vt)^2/4x^2}\,.\end{aligned} \tag{B10}$$

From Eq. (8), we have $v=200\sqrt{a}$ in SI units. Then Eq. (B10) can be expressed as

$$\begin{aligned}F_3&=\frac{2.09\times10^{-7}}{k}\int_0^{L}\frac{h(x)\,dx}{x}\int_0^{\infty}\frac{dv}{v^2}p\left(\frac{v^2}{4\times10^4},x\right)\\&\quad\times\sin\left[\frac{k(z_0-vt)^2}{4x}\right]\frac{J_1^2[kv^2(z_0-vt)/(8\times10^4x)]}{(z_0-vt)^2/4x^2}\,.\end{aligned} \tag{B11}$$

The condition for the method of stationary phase to be applicable to the integration over v is that the oscillation of the sine function should be rapid compared with both the Bessel function and the probability-density function of velocity. Comparing the arguments in the sine and the Bessel function, we find that we must have $t\gg(L/k)^{1/4}/100$. It is not difficult to show also that the velocity-distribution function must satisfy $\sigma_v/v\gg(2L/k)^{1/2}/z_0$, where σ_v is the standard deviation of the terminal velocities of the different-size raindrops.

Assuming that these conditions are satisfied, we can again apply the method of stationary phase with respect to v at $v = z_0/t$ in Eq. (B11); hence, we have

$$F_3 = \frac{8.18\times 10^{-17}\sqrt{k}\, z_0^2}{t^3} \int_0^L dx\, x^{-1/2} h(x) p(a', x) \,, \qquad \text{(B12)}$$

where $a' = z_0^2/(4\times 10^4 t^2)$.

(d) $$F_4 = \int_0^\infty dz\, p(a, x) I_2(z_0 - vt)(\tfrac{1}{2}a^2)N(x) = \frac{1}{2}\int_0^L dx \int_{-\infty}^\infty dy' \int_{-\infty}^\infty dz' \int_0^\infty da\, p(a, x) a^2 N(x)$$

$$\times \cos[\alpha\{z'(z_0' - vt\eta/x) - (z_0' - vt\eta/x)^2/2\}] \frac{J_1[(y'^2 + z'^2)^{1/2}]}{(y'^2 + z'^2)^{1/2}} \frac{J_1[\{y'^2 + (z' - z_0' + vt\eta/x)^2\}^{1/2}]}{\{y'^2 + (z' - z_0' + vt\eta/x)^2\}^{1/2}} \,. \qquad \text{(B13)}$$

If we let $v = 200\sqrt{a}$ and insert Eq. (10) into Eq. (B13), we obtain

$$F_4 = 6.65\times 10^{-8} \int_0^L h(x)\, dx \int_{-\infty}^\infty dz \int_{-\infty}^\infty dy \int_0^\infty \frac{dv}{v^2} p\left(\frac{v^2}{4\times 10^2}, x\right) \cos[k\{z(z_0 - vt) - (z_0 - vt)^2/2\}/x]$$

$$\times \frac{J_1[kv^2(y^2 + z^2)^{1/2}/(4\times 10^4 x)]}{(y^2 + z^2)^{1/2}} \frac{J_1[kv^2\{y^2 + (z - z_0 + vt)^2\}^{1/2}/(4\times 10^4 x)]}{\{y^2 + (z - z_0 + vt)^2\}^{1/2}} \,. \qquad \text{(B14)}$$

Again, if we assume that $t \gg (L/k)^{1/4}/100$ and $\sigma_v/v \gg (2L/k)^{1/2}/z_0$, we can apply the method of stationary phase to Eq. (B14) with respect to v. The result is

$$F_4 = 6.64\times 10^{-8}(2\pi/kt^2)^{1/2} \int_0^L dx\, x^{1/2} h(x) \int_{-\infty}^\infty dy \int_{-\infty}^\infty dz\, p[(z_0 - z)^2/4\times 10^4 t^2, x] \cos(kz^2/2x - \tfrac{1}{4}\pi)$$

$$\times \frac{J_1[k(z_0 - z)^2(y^2 + z^2)^{1/2}/(4\times 10^4 xt^2)]}{(y^2 + z^2)^{1/2}} \frac{J_1[ky(z_0 - z)^2/(4\times 10^4 xt^2)]}{y(z_0 - z)^2/t^2} \,. \qquad \text{(B15)}$$

Using the method of stationary phase once more with respect to z, we reduce Eq. (B15) to

$$F_4 = 6.64\times 10^{-8}\frac{2\pi t}{k} \int_0^L dx\, h(x) x \int_{-\infty}^\infty dy\, p(a', x) \frac{J_1^2[kya'/x]}{y^2 z_0^2} \,.$$

From Ref. 14, page 693, we obtain

$$\int_0^\infty dy \frac{J_1^2(\alpha y)}{y^2} = \frac{4\alpha}{3\pi} \,.$$

Therefore, we have

$$F_4 = 8.85\times 10^{-12} t^{-1} \int_0^L dx\, h(x) p(a', x) \,, \qquad \text{(B16)}$$

where $a' = z_0^2/(4\times 10^4 t^2)$.

(e) $$F_5 = \int_{-\infty}^\infty dy' \int_{-\infty}^\infty dz' \sin^2[\alpha(y'^2 + z'^2)/2] J_1[(y'^2 + z'^2)^{1/2}]/(y'^2 + z'^2) = \frac{1}{2}\int_{-\infty}^\infty dy' \int_{-\infty}^\infty dz'\, J_1^2[(y'^2 + z'^2)^{1/2}]/(y'^2 + z'^2)$$

$$- \frac{1}{2}\int_{-\infty}^\infty dy' \int_{-\infty}^\infty dz' \cos[\alpha(y'^2 + z'^2)] J_1[(y'^2 + z'^2)^{1/2}]/(y'^2 + z'^2) \,. \qquad \text{(B17)}$$

Because $\alpha \gg 1$, the method of stationary phase can be applied to the second term with respect to y' and z'. From Eq. (B2), the second term is equal to zero. Letting $\rho^2 = y'^2 + z'^2$, we then have

$$F_5 = \pi \int_0^\infty d\rho\, J_1^2(\rho)/\rho \,.$$

The integration over ρ is equal to $\frac{1}{2}$. Hence, we have

$$F_5 = \pi/2 \,. \qquad \text{(B18)}$$

---

[1] T. S. Chu and D. C. Hogg, Bell Syst. Tech. J. **45**, 301 (1966).

[2] T. S. Chu and D. C. Hogg, Bell Syst. Tech. J. **47**, 723 (1968).

[3] D. Atlas, J. Meteorol. **10**, 486 (1953).

[4] R. W. Wilson and A. A. Penzias, Nature **211**, 1081 (1966).

[5] D. Atlas and C. W. Ulbrich, J. Rech. Atmos. **VIII**, 275 (1974).

[6] S. W. Kurnick, R. N. Zitter, and D. B. Williams, J. Opt. Soc. Am. **50**, 578 (1960).

[7] A. Arnulf and J. Bricard, J. Opt. Soc. Am. **47**, 491 (1957).

[8] H. C. van de Hulst, *Light Scattering by Small Particles* (Wiley, New York, 1957).

[9] V. I. Tatarskii, *The Effects of the Turbulent Atmosphere on Wave Propagation*, IPST Catalog No. 4319 (National Technical Information Service, Springfield, Va., 1971).

[10] R. Gunn and G. D. Kinzer, J. Meteorol. **6**, 243 (1949).

[11] T. S. Marshall and W. McK. Palmer, J. Meteorol. **4**, 186 (1948).

[12] S. F. Clifford, J. Opt. Soc. Am. **61**, 1285 (1971).

[13] M. Born and E. Wolf, *Principles of Optics* (Pergamon, New York, 1959), pp. 749–750.

[14] I. S. Gradshteyn and I. M. Ryzhik, *Table of Integrals Series and Products* (Academic, New York, 1965), p. 707.

Applied Optics 13, 2602-2608, November 1974.

Wind and Refractive-Turbulence Sensing Using Crossed Laser Beams

Ting-i Wang, S. F. Clifford, and G. R. Ochs

The theory of optical propagation through atmospheric turbulence demonstrates the sensitivity of such quantities as log-amplitude variance and covariance to strength of refractive turbulence and transverse wind. We exploit this sensitivity by using a crossed-path technique to derive path profiles of these quantities. The results are insensitive to changes in the spatial spectrum of the refractive-index variations. The path resolution is easily varied by changing the receiver and transmitter separations and is ultimately limited by signal-to-noise considerations. The experimental results for horizontal paths, described here, will ultimately be used to indicate the feasibility of profiling on vertical paths with passive sources.

I. Introduction

Traditional techniques for measuring meteorological variables have used point sensors. More recently,[1–6] measurements of average transverse wind have been demonstrated along optical, microwave, and acoustic paths on the order of one to several kilometers. These techniques interpret the naturally occurring atmospheric modulation of the beam intensity (scintillation) to extract the average transverse speed and direction of air motion between source and receiver. This has introduced a new type of measurement that is both more sensitive and more representative for mesoscale meteorology than any collection of anemometers could possibly provide. The scintillation technique permits measurement of the extremely small velocities prohibited by bearing friction in conventional anemometers. A single laser link can provide an estimate of windspeed along a 10-km path, one that is truly representative of the average flow across that path. An ensemble of anemometers spaced out on the same 10-km path would be subject to the limitations caused by inadequate spatial sampling, the equivalent of aliasing in time series analysis.

The average wind sensor has several promising applications. By enclosing a volume with horizontal optical paths, we can measure the outward flux or inward convergence of air,[7] a useful quantity in the monitoring for pollution events in cities. In a similar context, the mean flow of air down a valley is a critical parameter to know before initiating such pollution-causing activities as agricultural burning. In airline safety applications giving a real-time readout of the spatially averaged, cross- and parallel-runway wind components to pilots is more meaningful than the reading of a single anemometer located somewhere on the airport grounds. In general, laser wind sensors can contribute to a higher quality and more appropriate wind information in these applications.

This work describes a modification of the scintillation technique that provides transverse wind velocities and strength of refractive turbulence C_n^2 at several path positions. This technique is not only useful for providing wind and refractive turbulence profiles along horizontal or slant paths, but also provides a reasonable model for testing our ability to measure these profiles aloft,[8] using passive sources such as multiple stars or portions of the limb of the sun or moon.

II. Theory

Profiling with crossed beams is most easily analyzed in terms of the theoretical development of Lee and Harp.[9] Figure 1 illustrates the geometry of our crossed-path system. Two point transmitters aligned parallel to the y axis illuminate two detectors whose axis is oriented at an arbitrary angle. The transmitter coordinates are $(0,\rho_t/2,0)$ and $(0,-\rho_t/2,0)$, and the receiver coordinates are $(0,y_0/2,L)$ and $(x_0,-y_0/2,L)$. The z axis is perpendicular to the transmitter and receiver planes.

A transmitter, say T_a in Fig. 1, emits a spherical wave of wavelength $\lambda = 2\pi/k$ from the coordinates $(0,\rho_t/2,0)$ that illuminates a differential, sinusoidal

Ting-i Wang is with the CU/NOAA Cooperative Institute for Research in Environmental Sciences, University of Colorado, Boulder, Colorado 80302; the other authors are with NOAA Environmental Research Laboratories, Boulder Colorado 80302.

Received 7 March 1974.

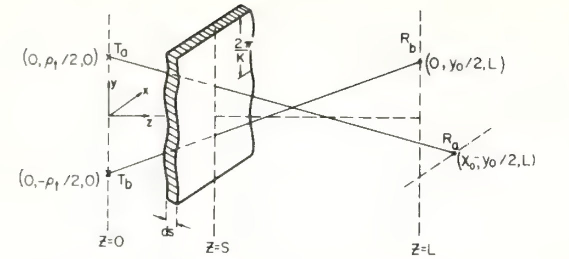

Fig. 1. Schematic of the crossed-path geometry with two laser transmitters T_a and T_b illuminating detectors R_a and R_b, respectively.

phase screen of wavenumber **K** at path position $z = s$. The phase screen imposes a sinusoidal phase perturbation on the wave. Following Lee and Harp, if the scattering from this screen is sufficiently weak, we can represent the resulting field in the receiving plane as the sum of the three spherical waves, namely, the original wave emitted from the point $(0,\rho_t/2,0)$ and two additional waves originating at $\rho_t/2 + \mathbf{K}(s/k)$ and $\rho_t/2 - \mathbf{K}(s/k)$. These waves propagate to the receiver at (ρ_0,L), where $\rho_0 = (x_0, -y_0/2,0)$. The resulting field dE_a, observed by receiver R_a from transmitter T_a, is then

$$dE_a = 1 - ikads \exp\left[\frac{iK^2s(L-s)}{2kL}\right] \cos\left\{\mathbf{K}\cdot\left[\boldsymbol{\rho}_0\frac{s}{L} + \frac{1}{2}\boldsymbol{\rho}_t\left(1-\frac{s}{L}\right) + \mathbf{b}\right]\right\}. \quad (1)$$

[In Eq. (1) we have dropped the unimportant phase factors common to all terms.] The quantity **K** is the two-dimensional spatial wavenumber of the phase screen, ds is its differential thickness, and a **(K)** is its change in refractive index from unity. The wavenumber of the radiation is denoted by $k = 2\pi/\lambda$, where λ is the wavelength, and $\mathbf{K}\cdot\mathbf{b}$ is an arbitrary phase offset. We further assume that receiver R_a observes only the radiation from T_a and R_b the radiation from T_b. This requires some form of source coding, such as polarization, frequency, and so forth, or field of view limitation.

Similarly, the signal detected by R_b from T_b is given by

$$dE_b = 1 - ikads \exp\left[\frac{iK^2s(L-s)}{2kL}\right] \cos\left\{\mathbf{K}\cdot\left[\mathbf{y}_0(s/2L) - \frac{1}{2}\boldsymbol{\rho}_t(1-s/L) + \mathbf{b}\right]\right\}. \quad (2)$$

The amplitude fluctuations produced by these signals at detectors R_a and R_b are found from the formula

$$dP = |dE| - 1 = [\mathrm{Re}^2(dE) + \mathrm{Im}^2(dE)]^{1/2} - 1, \quad (3)$$

where Re and Im are the real and imaginary parts, respectively. Substituting Eqs. (1) and (2) into Eq. (3) and ignoring terms of second order of smallness in a, we obtain

$$dP_a = kads \sin\left[\frac{K^2s(L-s)}{2kL}\right] \cos\left\{\mathbf{K}\cdot\left[\boldsymbol{\rho}_0(s/L) + \frac{1}{2}\boldsymbol{\rho}_t(1-s/L) + \mathbf{b}\right]\right\} \quad (4)$$

and

$$dP_b = kads \sin\left[\frac{K^2s(L-s)}{2kL}\right] \cos\left\{\mathbf{K}\cdot\left[\mathbf{y}_0(s/2L) - \frac{1}{2}\boldsymbol{\rho}_t(1-s/L) + \mathbf{b}\right]\right\}. \quad (5)$$

By cross correlating the amplitude fluctuations [Eqs. (4) and (5)], we obtain a signal proportional to a path-weighted average of the refractive turbulence common to the two optical paths. The differential covariance function formed in such a manner is

$$dC_{ab} = k^2\int_0^L ds_1 \sin\left[\frac{K^2s_1(L-s_1)}{2kL}\right]\int_0^L ds_2 \sin\left[\frac{K^2s_2(L-s_2)}{2kL}\right] < a(\mathbf{K},s_1)a^*(\mathbf{K},s_2) \cos\left\{\mathbf{K}\cdot\left[\boldsymbol{\rho}_0 s_1/L + \frac{1}{2}\boldsymbol{\rho}_t(1-s_1/L) + \mathbf{b}_1\right]\right\} \cos\left\{\mathbf{K}\cdot\left[\mathbf{y}_0(s_2/2L) - \frac{1}{2}\boldsymbol{\rho}_t(1-s_2/L) + \mathbf{b}_2\right]\right\} > . \quad (6)$$

The integrals over pathlength occur because we are adding up waves scattered from phase screens distributed all along the path and because the effects of different **K**'s are uncorrelated, we only consider products containing the same spatial wavenumber **K**. After we perform the operations detailed in Appendix I of Lee and Harp, Eq. (6) reduces to

$$dC_{ab} = 2\pi k^2 \int_0^L ds\Phi_n(\mathbf{K},s)d^2\mathbf{K} \sin^2\left[\frac{K^2s(L-s)}{2kL}\right] \cos\{\mathbf{K}\cdot[(\mathbf{x}_0 - \mathbf{y}_0)s/L + \boldsymbol{\rho}_t(1-s/L)]\}. \quad (7)$$

All that remains to complete the analysis is to account for the effects of all the different spatial scales at path position s and insert a reasonable refractive-index spectrum $\Phi_n(\mathbf{K},s)$.

The most commonly used spectrum is the power law proposed by Kolmogorov.[10] From dimensional analysis arguments, he found that the three-dimensional spectrum of the velocity fluctuations in a turbulent flow should decay as $K^{-11/3}$ within the so-called inertial subrange. (The inertial subrange is bounded on the large scale sizes by the requirement of isotropy and on the small scales by the onset of viscous dissipation.) By a series of arguments, Corrsin[11] shows that the same analysis should apply to temperature fluctuations and to other scalar functions that are conservative passive additives (humidity etc) and ultimately to refractive-index fluctuations. The form of the spectrum is

$$\Phi_n(K) = 0.033\,C_n^2(s)K^{-11/3};\ L_0^{-1} \ll K \ll l_0^{-1}, \quad (8)$$

where C_n^2 is the strength of the refractive-index fluctuations, and l_0 and L_0 are, respectively, the inner

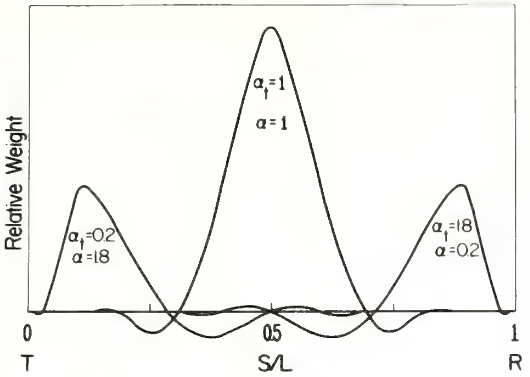

Fig. 2. Refractive-index structure parameter (C_n^2) path-weighting functions for three different transmitter-receiver configurations. The transmitter and receiver separations are α_t and α Fresnel zones, respectively, and $\beta = 0$.

and outer scales of turbulence that define the inertial subrange. [In the work that follows we have varied the power law in Eq. (8) from −9/3 to −13/3 and found negligible change in the resulting weighting functions. This is perhaps intuitively obvious in the results, because the weights are largely determined by the path geometry.] After inserting Eq. (8) into Eq. (7) and integrating over spatial wavenumber, we obtain the covariance function of the amplitude fluctuations of the crossed-path signals,

$$C_{ab} = 0.132\pi^2 k^2 \int_0^L ds C_n^2(s) \int_0^\infty dK K^{-8/3} \sin^2\left[\frac{K^2 s(L-s)}{2kL}\right] J_0[K|(\mathbf{x}_0 - \mathbf{y}_0)s/L + \rho_t(1 - s/L)|]. \qquad (9)$$

Equation (9) is the desired result. From this expression we can deduce the weighting functions for both C_n^2 and transverse wind speed.

III. C_n^2 Path-Weighting Function

The path resolution of the cross-correlation scheme becomes readily apparent if we rewrite Eq. (9) in the more suggestive form

$$C_{ab}(x_0, y_0, \rho_t) = \int_0^L ds C_n^2(s) W_{ab}(s, x_0, y_0, \rho_t), \qquad (10)$$

where W_{ab} is now the path-weighting function for C_n^2 variations, given by

$$W_{ab} = 0.132\pi^2 k^2 \int_0^\infty dK K^{-8/3} \sin^2\left[\frac{K^2 s(L-s)}{2kL}\right] J_0[K|(\mathbf{x}_0 - \mathbf{y}_0)s/L + \rho_t(1 - s/L)|]. \qquad (11)$$

To obtain a set of universal curves, we write the separations in Eq. (11) in terms of Fresnel zones $x_0 = \beta(\lambda L)^{1/2}$, $y_0 = \alpha(\lambda L)^{1/2}$, and $\rho_t = \alpha_t(\lambda L)^{1/2}$. This produces the expression

$$W_{ab} = \int_0^\infty dy y^{-8/3} \sin^2\left[\frac{y^2(s/L)(1 - s/L)}{4\pi}\right] J_0[y|(\beta - \alpha)s/L + \alpha_t(1 - s/L)|]. \qquad (12)$$

In Eq. (12), we have dropped the unimportant multiplicative factors and changed the variables to $y = K(\lambda L)^{1/2}$.

Equation (12) can be evaluated analytically in terms of confluent hypergeometric functions without any further gain in insight. The most efficient analysis is by computer, and the resultant plots are shown in Figs. 2, 3, and 4. For C_n^2 weighting, $\beta = 0$ is the optimum choice. In this case there exists a true crossover of the optical beams and, of course, the maximum correlation. This is not true for the wind-weighting function where a horizontal displacement of the two beams is essential for determining the sense of the wind. Figure 2 illustrates some typical weighting functions for emphasizing 10%, 50%, and 90% of the optical path from the transmitter. The desired location of the peak fixes the relation between α_t and α by way of the expression

$$(s/L)_{\text{peak}} = \alpha_t/(\alpha_t + \alpha). \qquad (13)$$

The characteristics of curves in Fig. 2 are a reasonably large peak-to-side-lobe ratio for the midpath case and fairly extensive side lobes for peaks near the ends of the path.

If we increase the magnitude of α_t and α while keeping the location of the peak constant, we observe the behavior shown in Fig. 3. The width of the main lobe decreases nearly linearly with increases in transmitter and receiver separation. This is a reasonable result, because increasing the angle of intersection of the two beams decreases its volume of overlap and therefore decreases the size of the region of maximum correlation along the path. Finally, to illustrate the sensitivity of the weighting functions to changes in the spectrum of refractive-index turbulence, we have the curves in Fig. 4. Even after changing the power law of the spectrum by more than 40% from −9/3 to −13/3, we observe less than a 25% change in width.

IV. Wind Weighting Function

It is quite simple to insert into Eq. (9) the time dependence caused by moving turbulence. Physically,

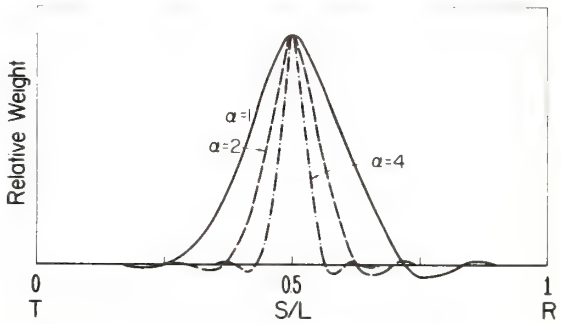

Fig. 3. Refractive-index structure parameter (C_n^2) path-weighting functions showing the variability of the path resolution with increasing angle of intersection of the two optical paths. The transmitter and receiver separations are equal, $\alpha = \alpha_t$ and $\beta = 0$.

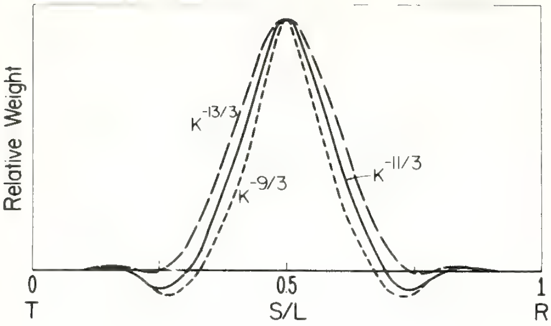

Fig. 4. Refractive-index structure parameter $(C_n{}^2)$ path weighting functions for different assumed turbulence spectra. The receiver and transmitter separations α and α_t are equal, and their displacements are in the same plane so that $\beta = 0$.

a refractive-index eddy drifts through the optical beam at path position s. The disturbance at the receiver produced by this event is enlarged by the factor L/s, and its speed is increased by the same factor. As a result, the temporal frequency of the disturbance remains Kv at both the path position where it originated and at the receiver. The proper modification of Eq. (9) to account for the temporal correlation produced by this eddy drift is to replace $(\mathbf{x}_0 - \mathbf{y}_0)s/L$ with the expression $(\mathbf{x}_0 - \mathbf{y}_0)s/L - \mathbf{v}(s)\tau$, where τ is the time lag between observations at receivers R_a and R_b. (A more detailed analysis and careful examination of the assumptions involved in this substitution may be found in Clifford.[12])

The advantages of measuring the transverse wind by means of the slope technique are fully discussed in Ref. 1. In this method, after inserting the effects of transverse wind, we derive the path-weighted velocity by computing the slope of the correlation function [Eq. (9)] at zero time lag. This process results in the expression

$$M_{ab} = \int_0^L ds C_n{}^2(s)\mathbf{v}_\perp(s)\cdot\mathbf{W}_{ab}(s), \tag{14}$$

where

$$M_{ab} = \partial C_{ab}(\tau)/\partial\tau \;_{\tau=0},$$

and

$$\mathbf{W}_{ab} = 0.132\pi^2k^2\int_0^\infty dKK^{-5/3}\sin^2\left[\frac{K^2s(L-s)}{2kL}\right]J_1(Kr)\hat{\mathbf{r}}. \tag{15}$$

The quantity $\hat{\mathbf{r}}$ is a unit vector along $\mathbf{r}$ which is given by

$$\mathbf{r} = (\mathbf{x}_0 - \mathbf{y}_0)s/L + \boldsymbol{\rho}_t(1 - s/L). \tag{16}$$

In deriving Eq. (15) we have inserted the relation $\partial J_0(z)/\partial z = -J_1(z)$.

From the path geometry in Fig. 1, we observe that the two-path crossover point occurs at $s/L = \rho_t/(\rho_t + y_0)$. Here the y-directed component of the velocity has exactly zero contribution since at this location $\hat{r}_y$ in Eq. (15) is zero. This is perhaps intuitively obvious because any eddy moving vertically (y direction) will intercept both beams simultaneously at the crossover point. This will contribute nothing to the slope at zero time lag which is a measure of the difference of arrival time of the eddy at each beam. Further, the weighting function is essentially an odd function with respect to this point since the eddy in the transmitter half of the path first intercepts the beam from T_a and then the beam from T_b. This order is reversed on the receiver portion of the path, reversing the apparent sense of the wind. Because of the zero weight at crossover and the odd-function weighting in the resolution cell, we expect that the contribution for the y-directed wind to be negligible compared to the x-directed wind. This fact is borne out by a detailed analysis of Eq. (15).

To generate a universal curve for the x-directed wind-weighting function, we again normalize to a Fresnel zone size, i.e., let $y = K(\lambda L)^{1/2}$, $x_0 = \beta(\lambda L)^{1/2}$, $y_0 = \alpha(\lambda L)^{1/2}$, and $\rho_t = \alpha_t(\lambda L)^{1/2}$, then Eq. (15) becomes

$$W_{ab} = \{1 + \beta^{-2}[\alpha - \alpha_t(L/s - 1)]^2\}^{-1/2}\int_0^\infty dyy^{-5/3}$$
$$\sin^2\left[\frac{y^2 s/L(1 - s/L)}{4\pi}\right]J_1[y\,|(\beta - \alpha)s/L + \alpha_t(1 - s/L)|\,]. \tag{17}$$

Equation (17) is plotted in Fig. 5 with α_t and α chosen to peak the weighting at each of 10%, 50%, and 90% of the path from the transmitter. In each of these cases, β was chosen to optimize the path-weighting function for a single path. An indication of the variability of the weighting with β is shown in the curves near the 10% portion of the path. Figure 6 illustrates the dependence of the width of the weighting function on the transmitter and receiver separation, namely, a marked narrowing with increasing transmitter and receiver separation. Figure 7 illustrates the sensitivity of the results to different spectra of refractive index turbulence, again, as in the case for $C_n{}^2$, showing a weak dependence.

V. Experimental Results

We performed a series of measurements at optical wavelengths on a horizontal path 1.5 m above the

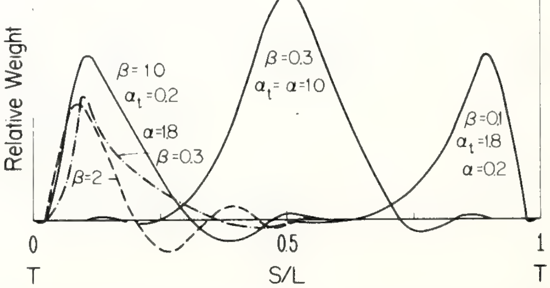

Fig. 5. Wind weighting functions for various values of transmitter separation α_t and receiver coordinates α and β.

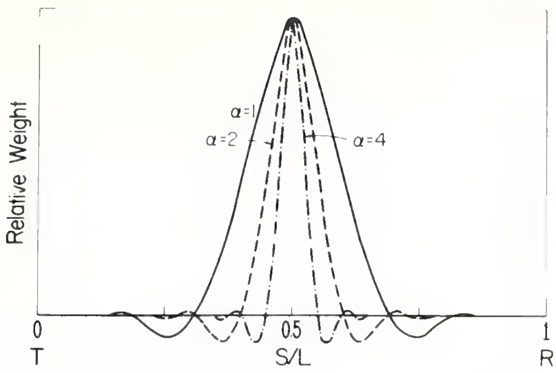

Fig. 6. Wind-weighting functions showing the variability of the path resolution with increasing angle of intersection of the two optical paths. The receiver coordinates are $\beta = 0.3$ Fresnel zones with variable $\alpha = \alpha_t$.

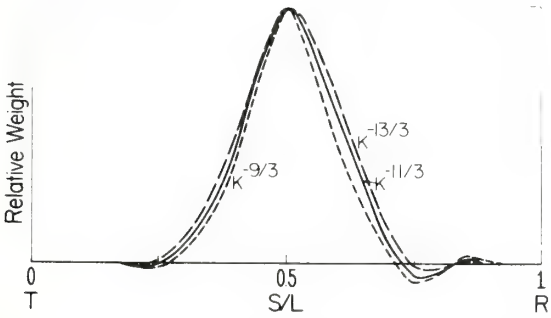

Fig. 7. Wind-weighting functions for different assumed turbulence spectra. The transmitter separation is $\alpha_t = 1$, and the receiver coordinates are $\alpha = 1$ and $\beta = 0.3$. All quantities are in Fresnel zones.

grass-covered surface of Table Mountain, a flat mesa located 12 km north of Boulder, Colorado, to test some specific cases of the theory. The test arrangement is shown schematically in Fig. 8. Two He–Ne lasers, operating at 6328 Å and vertically separated by 3.2 cm (1.8 $(\lambda L)^{1/2}$ for our 500-m path), were projected to the receiver array shown. The beams were polarization coded so that the upper beam was received only by the lower four receivers, and, similarly, the lower beam was received only by the two upper receivers, as shown. The beam size at the lasers was about 0.7 mm; the angular divergence was approximately 1.7 mrad in the horizontal by 3 mrad in the vertical. A negative cylindrical lens was used to obtain increased vertical divergence, to allow for changes in regular refraction. Square photodiode receivers, 2.7 m × 2.7 mm, were used.

The four detectors, used in the difference mode $(a - b)$, $(c - d)$, and $(e - f)$, provided signals whose covariance functions $\langle (a - b)(c - d) \rangle$ and $\langle (a - b)(e - f) \rangle$ gave the path-weighted determinations of C_n^2 and wind, respectively. This differencing scheme removes low spatial frequencies and consequently improves the SNR compared with the two-point covariances described in the theory [Eqs. (10) and (14)]. If the spacing at which the differences are computed, for example $(a - b)$, is larger than a Fresnel zone for the optical path, the effect of the resultant spatial filtering on the theory is negligible. However, in all cases when comparing theory and experiment, we assumed the exact configuration shown in Fig. 8 and modified the theory accordingly.

Ten propeller anemometers, distributed along our optical path as shown, determined the horizontal component of the transverse wind. The refractive-index structure parameter C_n^2 was derived from temperature structure-constant measurements made at five locations along the path in the manner described by Lawrence *et al.*[13]

We used an on-line computer to compare the optical and *in situ* measurements. Data were smoothed with a 10-sec time constant and then sampled every 10 sec. We then obtained the least-squares best fit values of K_i for a series of thirty-eight equations of the form

$$A_0 = \sum_{i=1}^{N} K_i A_i, \tag{18}$$

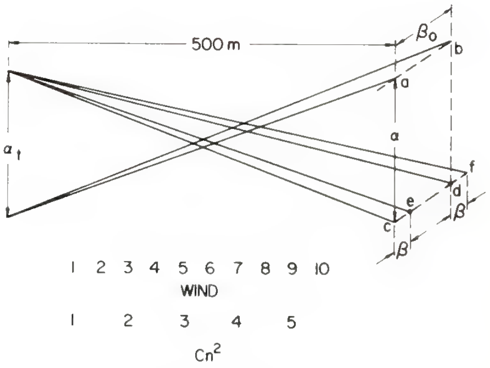

Fig. 8. Experimental arrangement to profile wind with crossed optical paths showing locations of *in situ* wind and C_n^2 measurements.

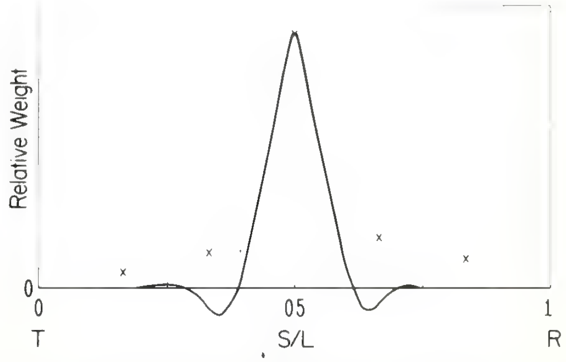

Fig. 9. Theoretical weighting function for C_n^2, where $\alpha = \alpha_t = \beta_0 = 1.8$ and $\beta = 0$ Fresnel zones (solid line). The five experimental weights (crosses) were obtained from 4 h of data.

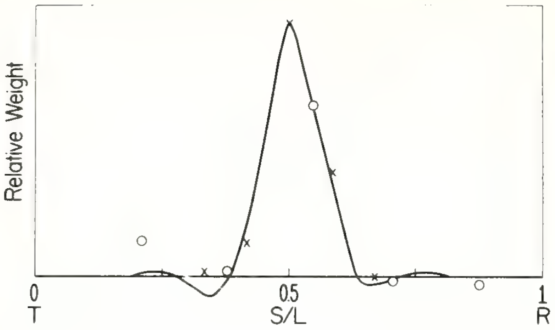

Fig. 10. Theoretical weighting function for wind where $\alpha_t = 1.8$, $\alpha = 1.8$, $\beta = 0.3$, and $\beta_0 = 1.8$ Fresnel zones (solid-line). The crosses are experimental weights using single anemometers. Circles are weights obtained from averaging adjacent pairs of anemometers. All points are derived from 2 h of data.

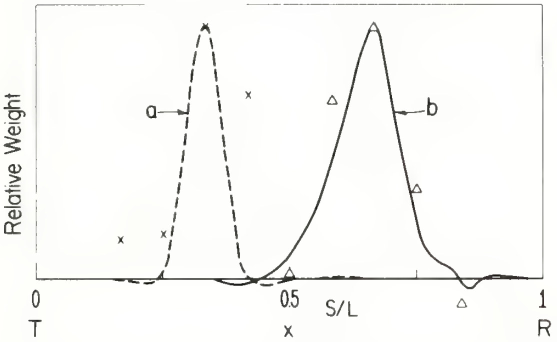

Fig. 11. Theoretical curve a is the wind weighting function for $\alpha_t = 1.8$, $\alpha = 3.6$, $\beta = 0.6$, and $\beta_0 = 3.6$ Fresnel zones. Curve b is for $\alpha_t = 1.8$, $\alpha = 0.9$, $\beta = 0.15$, and $\beta_0 = 0.9$. The experimental weights from 2 h of data are shown as crosses and circles.

where A_0 is the optical measurement, and A_i are the *in situ* measurements. The average, over the time indicated, of successive values of the K's, normalized to $K_{\max} = 1$, is the experimentally determined weighting function.

Not all the data taken in this manner can be used to evaluate the K's. When averaged over 10 sec, there is, much of the time, insufficient variation in the anemometer readings to make a determination. The 10-sec averaging period is necessary so that the point measurements are more nearly like the 40-m space average that they are supposed to represent. The system, of course, is reading the variable at the optical crossover all the time, as can be shown by correlation of the optical and anemometer readings.

In Fig. 9, five experimentally determined weights for C_n^2 are superimposed upon the theoretical-weighting function, using the crosspath arrangement shown in Fig. 8. The test was conducted from 0500 to 0900 local time. The optical measurement of C_n^2 was determined from

$$C_n^2 = B\sigma_\chi^2\rho, \tag{19}$$

where σ_χ^2 is the variance of the logarithm of the amplitude measured over one optical path using a 1-mm diam receiver. In Eq. (19), ρ is the normalized covariance of the signal $(a - b)$ with the signal $(c - d)$. The proportionality constant B was not evaluated. This method was chosen rather than a direct measurement of the cross product because it was easier to instrument accurately.

A more extensive comparison was made between theoretical and experimental wind weighting functions. In Fig. 10, we compare two sets of experimentally determined weights with the theory. In this case, the optically determined wind is considered proportional to the slope of the normalized covariance of $(a - b)$ and $(e - f)$ at zero time delay. The crosses represent weights determined over the period from 0700 to 0900 local time, from comparison with anemometers 3, 4, 5, 6, and 7 (see Fig. 8), while the circled points are determined from the average of anemometer pairs 1 and 2, 3 and 4, 5 and 6, 7 and 8, and 9 and 10 from 1400 to 1600 local time. This latter set of weights was not normalized to 1, because no anemometer pair was exactly centered on the optical crossover point.

In Fig. 11 the optical crossover point was shifted from the center of the path to positions ⅓ and ⅔ of the way from the transmitter. This was accomplished at the receiver by optically doubling and halving the receiver pattern in Fig. 8. We compared the crossover at the ⅓ position over the period from 1500 to 1700 local time with anemometers 1, 2, 3, 4, and 5 and the ⅔ crossover position over the period 0700–0900 local time with anemometers 5, 6, 7, 8, and 9.

VI. Summary

We have demonstrated the feasibility of measuring transverse winds and C_n^2 profiles with crossed optical beams. The theoretical development was from the first-order, single-scatter point of view, with no provision for the well-known saturation[14] effect. It is not expected that this effect will dramatically change the results of our weighting functions since they are so strongly dependent on the path geometry and not on the details of the diffraction process. However, we intend to check the validity of this assumption and compile observations of more weighting functions under a wide variety of meteorological conditions. Once the sensitivity of these weighting functions to variations in atmospheric parameters is determined on a horizontal test path, we propose to apply these same techniques with perhaps more modifications on vertical paths using multiple stars.

The primary support for this project was provided by RADC(OCSE), Griffiss AFB, New York 13441 under contract F 30602-73-0139. The Scientific Monitor was Raymond P. Urtz, Jr.

References

1. R. S. Lawrence, G. R. Ochs, and S. F. Clifford, Appl. Opt. **11, 239** (1972).
2. L. Shen, IEEE Trans. Antennas Propag. **AP-18,** 493 (1970).
3. A. Ishimaru, IEEE Trans. Antennas Propag. **AP-20,** 10 (1972).
4. P. A. Mandics, R. W. Lee, and A. T. Waterman, Jr., Radio Sci. **8,** 185 (1973).
5. P. A. Mandics, Ph.D. Dissertation, Stanford University, Stanford, Calif. (1971).
6. J. C. Harp, Ph.D. Thesis, AFCRL-71-0451, SU-SEL-71-042, Scientific Report 1 (1971).
7. A. G. Kjelaas and G. R. Ochs, J. Appl. Meteor., **13,** 242 (1974).
8. J. Vernin and F. Roddier, J. Opt. Soc. Am. **63,** 270 (1973).
9. R. W. Lee and J. C. Harp, Proc. IEEE **57,** 375 (1969).
10. A. N. Kolmogorov, Dokl. Akad. Nauk SSSR **30,** 299 (1941).
11. S. Corrsin, J. Appl. Phys. **22,** 469 (1951).
12. S. F. Clifford, J. Opt. Soc. Am. **61,** 1285 (1971).
13. R. S. Lawrence, G. R. Ochs, and S. F. Clifford, J. Opt. Soc. Am. **60,** 826 (1970).
14. S. F. Clifford, G. R. Ochs, and R. S. Lawrence, J. Opt. Soc. Am., **64,** 148 (1974).

Remote Sensing of the Atmosphere, ThA5.1-ThA5.4, March 1975.

A Numerical Comparison of Two Inversion Techniques For Remote Sensing of Atmospheric Temperature Profiles

Otto Neall Strand and Ed R. Westwater
National Oceanic and Atmospheric Administration
Wave Propagation Laboratory
Boulder, Colorado 80302

Introduction

Vertical temperature profiles obtained by inverting imperfect radiance observations depend strongly on the method of retrieval. Results of previous investigators (e.g., Fleming and Smith[1]) have indicated that among several contemporary inversion algorithms, no method has clear superiority over its competitors. Success in inversion is relative and weighs heavily on the choices of success criteria. In this paper, we use linear iterative methods for a numerical comparison of the generalized Landweber technique and the Backus-Gilbert technique for retrieving profiles from satellite infrared radiance observations. In particular, we compare the rms error of the retrieval methods for an ensemble of profiles, and illustrate the dependence of the solution on the initial guess and on the number of iterations.

Description of Methods

The integral form of the radiative transfer equation[1] relates radiance $I(\nu)$ at frequency ν to a weighted spatial average of the Planck radiance $B(\nu,T)$, where the temperature T is a function of the pressure P. Because of the nonlinear dependence of $B(\nu,T)$ on T, the radiance is a nonlinear functional of $T(P)$. Linear iterative methods can be applied to this equation by first expanding the integrand in a Taylor's series about an initial guess $T^{(o)}(P)$ and retaining terms to first order in $T(P)$. This yields the perturbation form of the transfer equation

$$\delta I(\nu) = \int_0^{P_o} W(\nu,P)\, \delta T(P)\, dP, \tag{1}$$

where $\delta I(\nu)$ is the departure of measured and calculated radiance, $W(\nu,P)$ is the weighting function for temperature, and $\delta T(P) = T(P) - T^{(o)}(P)$. The surface term, although not explicitly shown in Eq. (1), was included in our calculations. After solving Eq. (1) for $\delta T(P)$, we iterate by replacing $T^{(o)}(P)$ by $T^{(o)}(P) + \delta T(P)$ and relinearizing. The process is continued until the sum of squares of residuals is commensurate with the known instrumental noise.

The original Backus-Gilbert method has been applied to satellite retrieval problems by Conrath[2] and Surmont and Chen[3]. To apply this technique to a profile inversion problem requires calculation of the so-called spread tensor at each point on the profile. This expends much computer time for iterative inversion to retrieve a large number of functional values. For this reason, we constructed averaging kernels and inversion coefficients by minimizing the mean square departure from a delta function (Westwater and Strand[4]). The averaging kernels constructed by the two methods and a typical weighting function are shown in Fig. 1. Note both the much sharper resolution and the poorer side lobe response of the delta function kernels. When retrieving profiles, we choose a point on the resolution-error tradeoff curve by requiring the error variance to be less than $(2°C)^2$ at each pressure level.

The second inversion algorithm we used was of the generalized Landweber type with an iterated Twomey solution (Strand[5]). The equivalent Twomey smoothing parameter γ for n iterations was chosen to satisfy

$$(2^{1/n} - 1)\gamma = (\sigma_\varepsilon^2/\sigma^2{}_T) \tag{2}$$

where σ_ε and σ_T are estimates of the standard deviations of measurement noise and temperature fluctuations about the *a priori* curve. Here, we take $\sigma_\varepsilon = .25$ (ergs/cm²/str/cm^{-1}/s) and $\sigma_T = 10.0°C$.

Data Base

Profile retrievals were attempted on 110 profiles supplied to us by NESS. This ensemble has been described by Fleming and Smith[1] and Strand[6].

Radiances were calculated at the following wave numbers (cm^{-1}): 668.5, 677.0, 695.0, 708.0, 725.0, 747.0, 835.0 (window channel for ground information), and 535.0 (water vapor channel). Gaussian random noise of standard deviation $\sigma_\varepsilon = .25$ (ergs/cm^2/str/cm^{-1}/s) was added to the measurements.

Comparison of Backus-Gilbert vs Landweber

The Backus-Gilbert "delta function" method and the Landweber method were compared for 28 midlatitudinal profiles. Two linearizations were used for each method starting from a midlatitudinal belt initial guess. The rms errors of each of the methods and the rms departure of the true from the *a priori* standard are shown in Fig. 2. From the surface to about 50 mb,

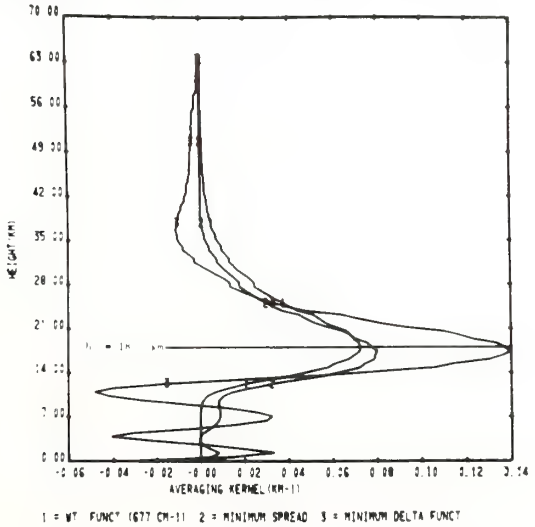

Fig. 1. Backus-Gilbert averaging kernels and weighting function centered at 18.0 km.

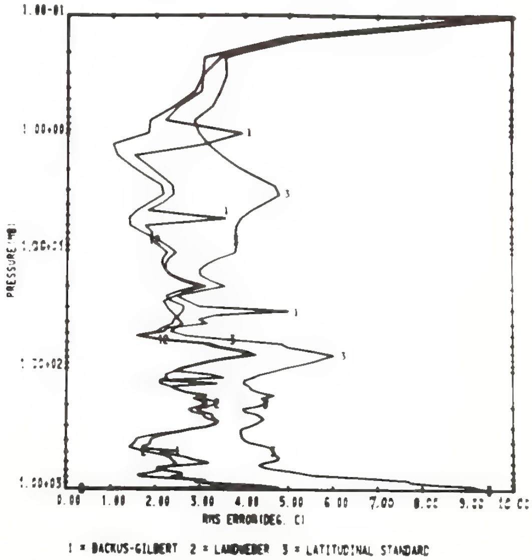

Fig. 2. Comparison of Backus-Gilbert "Delta Function" retrieval with the Landweber method.

there is little difference in the accuracy between the two retrieval methods. Above this altitude, in a region where there is very poor coverage by the weighting functions, the Landweber method gives somewhat better results. This is presumably due to the influence on the Landweber method of the weighted constraint about the a priori curve. The overall rms error for curves 1, 2, and 3 are 2.98°C, 2.75°C, and 5.66°C.

Effect of Initial Estimate

We will use the notation (L,I,γ) to denote L linearizations, each with I iterations, γ of Eq. (2) as specified. The effect of the initial profile on the retrievals was studied on 110 profiles using the Landweber technique with $(2,\ 1,\ 1.5 \times 10^{-3})$ for three sets of a priori curves. The first, unsmoothed a priori, is the appropriate latitudinal belt of the U. S. Standard atmosphere; the initial curves were smoothed by cubic spline interpolation through every ninth level to yield the second curve. Finally, the U. S. World Wide Standard (W.W.S.) was used for all retrievals to yield the remaining curve. Rms errors of retrievals based on these curves are plotted in Fig. 3. The overall rms error for curves 1, 2, and 3 are 2.97°C, 3.26°C, and 3.74°C.

Effect of Linearization

The linearization was studied for 28 midlatitudinal (m.l.) profiles (set 2) and 36 polar (p) profiles (set 4). For set 2, using the m.l. a priori, we compared retrievals using $(1,\ 2,\ 1.5 \times 10^{-3})$ with $(2,\ 1,\ 1.5 \times 10^{-3})$ to obtain an overall rms difference (sample size $n = 2800$) of 0.1°C and a max. difference of 1.2°C. By comparing these values with retrieval errors of rms = 2.8°C and max. = 15.7°C, we conclude that a single linearization about a reasonable first guess would suffice. A "worst case" study of set 4 with W.W.S. a priori using $(1,\ 2,\ 1.5 \times 10^{-3})$ and $(2,\ 1,\ 1.5 \times 10^{-3})$ gave unsatisfactory differences of rms = 1.8°C and max. = 12.7°C. Here the differences between true and a priori were rms = 16.5°C and max. = 58.6°C. We then compared $(2,\ 1,\ 1.5 \times 10^{-3})$ with $(4,\ 1,\ 3.3 \times 10^{-3})$ to obtain differences of rms = 0.5°C and max. = 2.3°C as compared with retrieval errors of rms = 4.2°C and max. = 27.0°C; thus two linearizations (as used in all retrievals in other sections) were adequate in all cases. Finally, to test Eq. (2), we compared $(1,\ 1,\ 6.25 \times 10^{-4})$ with $(1,\ 2,\ 1.5 \times 10^{-3})$ for set 2 to obtain differences of rms = 0.1°C and max. = 0.8°C.

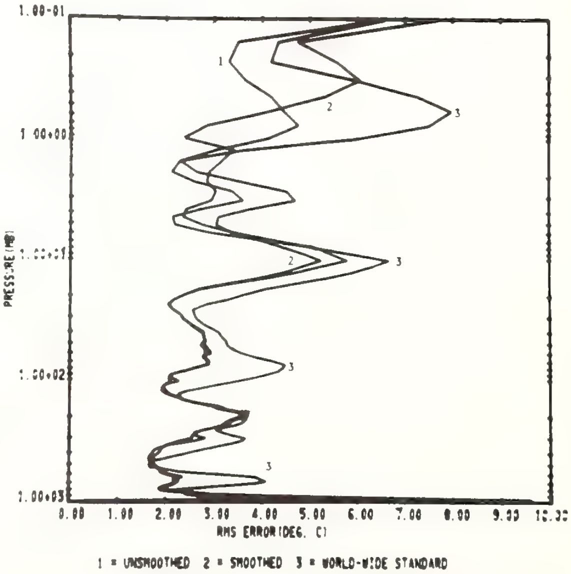

Fig. 3. Rms retrieval errors for Landweber iteration with different initial estimates.

Information Content

The accuracy of retrievals has been shown to be dependent on the initial guess; the better the guess, the better the retrieval. Since one would presumably use the best available information as an initial estimate, the information content of the radiance observations should be judged on the improvement in accuracy over the initial guess. In Fig. 4 we show both the rms error of Landweber (2, 1, 1.5 x 10^{-3}) and the rms error of the corresponding *a priori* estimate. The average reduction in overall rms error over 110 profiles is 56% (from 6.78°C to 2.97°C).

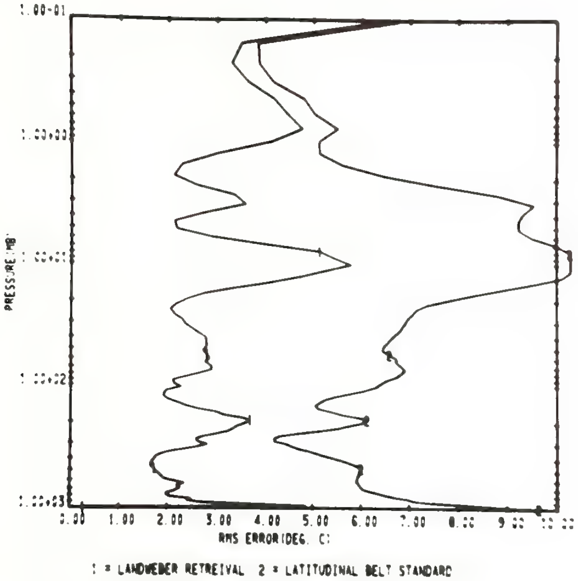

Fig. 4. Rms errors of retrievals vs rms errors in *a priori* curves.

Conclusions

Our numerical studies have indicated that (a) the Backus-Gilbert "delta function" method and the generalized Landweber method give similar accuracies in regions of good coverage of the weighting functions. In regions of poor coverage, the Landweber method is somewhat better. (b) Accuracy in retrieval was more sensitive to initial guess than to either inversion algorithm. (c) When using a good initial estimate (i.e., one of four latitudinal standard atmospheres) the accuracies of one and two linearizations were essentially the same. A poor initial estimate required two linearizations for satisfactory results. (d) For retrieving profiles, the information content of our 8 channels was quite modest (56% reduction in rms error).

References

[1] Fleming, H. E., and W. L. Smith, Inversion techniques for remote sensing of atmospheric temperature profiles, Proceedings of the Fifth Symposium on Temperature, Its Measurement and Control in Science and Industry, Washington, D.C., June 1971.

[2] Conrath, B. J., J. Atmos. Sci. 29, 1262 (1972).

[3] Surmont, J., and Y. M. Chen, J. Comp. Phys. 13, 288 (1973).

[4] Westwater, E. R., and O. N. Strand, A generalized inversion program, NOAA Tech. Rept. ERL 309-WPL 34 (1974).

[5] Strand, O. N., SIAM J. Numer. Anal. 11, No. 4, 798 (1974)

[6] Strand, O. N., Expected accuracy of tropopause height and temperature as derived from satellite radiation measurements, NOAA Tech. Rept. ERL 295-WPL 28 (1973).

[7] Twomey, S., J. Assn. Comp. Mach. 10, 79 (1963).

A Comparison of the Low-Level Radiosonde and the Acoustic Echo Sounder for Monitoring Atmospheric Stability

R. J. WYCKOFF

National Weather Service Forecast Office, NOAA, Denver, Colo. 80010

D. W. BERAN AND F. F. HALL, JR.

Wave Propagation Laboratory, NOAA, Boulder, Colo. 80302

(Manuscript received 20 April 1973, in revised form 19 July 1973)

ABSTRACT

Temperature profiles measured with a radiosonde are compared with returns from an acoustic echo sounder throughout the height range 50–700 m. In general, the sounder records indicate the temperature inversion to be somewhat lower than do the radiosonde records. Reasons for this apparent discrepancy and the advantage of the sounder, in being able to monitor continuously the inversion structure and undulations produced by wind shear, are discussed. It was proved feasible to operate the acoustic sounder in a noisy commercial district with little detrimental effect on the ability to detect atmospheric temperature structure. It is concluded from this preliminary investigation that the combination of the radiosonde and the acoustic echo sounder provides a much more valuable tool for monitoring structure in the stable planetary boundary layer than either device used alone.

1. Introduction

During the winter of 1971–72, a monostatic acoustic echo sounder was co-located with an Environmental Meteorological Support Unit (EMSU) in an industrial region of Denver, Colo. The data collected during this exercise provided a side-by-side comparison of radiosonde and acoustic echo sounder records during urban air pollution episodes.

The potential of the acoustic sounder, a relatively new remote sensing device, for monitoring the height and intensity of temperature inversions, has been discussed by McAllister (1968), McAllister *et al.* (1969), Little (1969), Beran *et al.* (1972) and Hall (1972). There was a need to demonstrate that the sounder could detect, under operational conditions, the same inversion structure that is measured by a standard radiosonde unit. In addition, it was desirable to prove that the device could operate effectively in spite of the ambient background noise found in large cities.

In principle, the acoustic echo sounder operates much like sonar, with an audible sound pulse being sent into the atmosphere. Echoes are caused by variations in the acoustic refractive index. In acoustics, the relevant refractive index variations are associated with fluctuations of both temperature and wind measured at a scale of one-half of the transmitted wavelength.

Detailed discussions of the scattering of a sound wave in the atmosphere are given by Tatarskii (1961), Kallistratova (1961), Monin (1962), Little (1969) and Tatarskii (1971). Sound energy that is directly backscattered (180° from the direction of the incident wave) is solely the result of temperature fluctuations in the scattering volume. Acoustic energy scattered in all other directions (except at 90° to the incident beam, where no scattering occurs) is the result of the combined effect of wind and temperature fluctuations.

This angular dependence of the scattering mechanism is of paramount importance to the operation of a sounder. For a monostatic configuration (co-located transmitter and receiver; scattering angle of 180°), one observes echoes that depict the temperature structure constant C_T in the atmosphere. With neutral static stability, C_T values are very low, and the scattered energy will be undetected. If a facsimile recorder is used to display the echo intensity, where each sweep of the recorder corresponds to the time required for a single sound pulse to traverse the region of interest, the record will be white when no echoes are received. As the lapse rate changes from adiabatic (either more stable or less stable), any mechanical turbulence in the air will create small-scale temperature eddies capable of backscattering some of the incident sound, and the facsimile record will be darkened in proportion to the strength of the turbulence. The monostatic sounder, therefore, gives an indication of each change in lapse rate or dynamic stability along the path of a transmitted sound pulse, producing a record with a striking amount of contrast and showing considerable detail related to the thermal structure.

For applications where the height and distribution

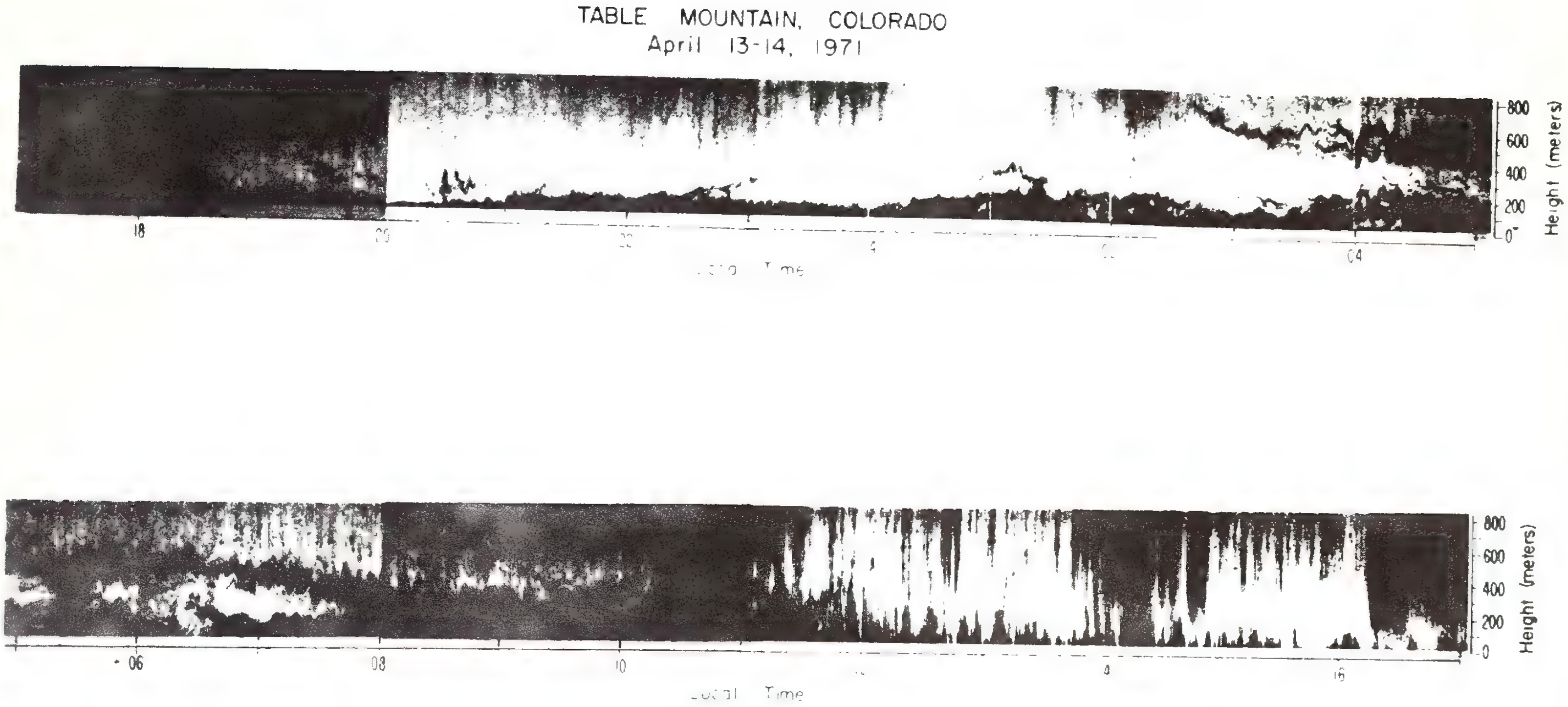

Fig. 1. Acoustic sounder record showing the evolution of the boundary layer structure before, during and after an air pollution alert (after Beran *et al.*, 1972).

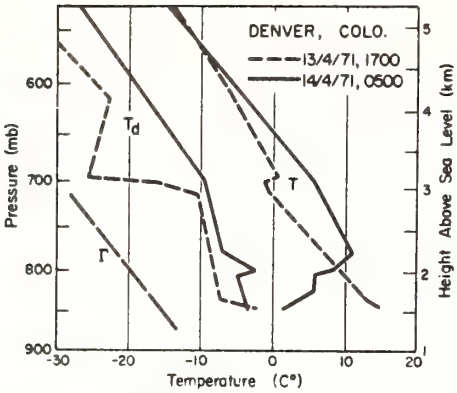

FIG. 2. Denver radiosonde records taken during the time period covered in Fig. 1 (after Beran *et al.*, 1972).

of inversion layers are important, as in air pollution monitoring, the monostatic system serves adequately. However, it should be noted that the echo intensity produced by temperature fluctuations alone is frequently much lower than that received with a bistatic system. This can be important for wind measurements since velocity fluctuations can provide the strong, continuous signals required for Doppler sensing techniques.

The potential of an acoustic sounder as a monitor of meteorological conditions which may lead to adverse pollution, is demonstrated by Fig. 1 (Beran *et al.*, 1972), which shows a 24-hr facsimile record taken by an acoustic sounder located about 50 km northwest of Denver on 13 and 14 April 1971. Despite the distance between the sounder and Denver, the mesoscale meteorological events leading to an air pollution "alert" in that city are clearly shown. From the beginning of the record, 1700 until 2000 MST on the 13th, we see a rather featureless picture with no evidence of a strong surface inversion. Following 2000, the increasing thickness of the black portion of the record indicates a deepening surface-based inversion, undoubtedly the result of radiational cooling of the ground. Just before 0300 on the 14th, evidence of a second layer appears at higher levels. This is interpreted as a subsidence inversion which is lowering, and thereby intensifying the surface inversion, a process that was complete by 0800 on the 14th. Radiosonde data shown in Fig. 2, taken at Denver, support this interpretation; the sounding at 1700 on the 13th shows an inversion at 700 mb (~1500 m above the surface), which has lowered to 800 mb (~500 m above the surface) by 0500 on the 14th. The comparison between Denver's radiosonde and the acoustic record is meant only to convey the general synoptic pattern and should not be taken as proof of the height of a given layer. The solid dark region of the record, reaching up to heights of 300 m between 0800 and 1100 on the 14th, indicates a very strong surface-based inversion that produced an air pollution alert in Denver.

After 1100, surface heating starts to break up the inversion. Note the change from predominantly horizontally stratified layers to vertical structure. This is characteristic of the pattern associated with a transition from stable to unstable lapse rates. By 1200 the appearance of the record has completely changed; the inversion is seen to have dissipated, and 2 hr later the air pollution alert was removed.

If this type of information had been available in real time the forecaster could have monitored the events as they developed; he might have given an earlier warning of the impending pollution conditions. The knowledge of the inversion breaking up and the removal of the alert might also have been moved up by as much as 2 hr.

2. The experiment

Having observed the case described above, we decided to make further controlled tests of the acoustic system at the Denver Environmental Meteorological Support Unit (EMSU) site. This site is located ~200 m south of Interstate Highway 70 and 100 m east of a railroad switching area. The Platte River, an important controlling feature in the distribution of effluent in the Denver area (Riehl and Herkhof, 1972), runs nearly parallel to the rail lines next to the EMSU site.

Locating the acoustic sounder at the EMSU site provided an excellent opportunity to test the system in a high background noise environment (traffic noise from both the highway and the railroad was at times above 70 dBA[1]). In addition, the acoustic records could be compared with the profiles provided by the EMSU radiosonde, launched twice per day at around 0700 and 1200 MST.

The sounder used for this exercise was of the simplest type, consisting of an audio oscillator and power amplifier, a control unit for timing, a single vertically pointing antenna operated in the monostatic mode, a receiving amplifier, and a facsimile recorder (Wescott *et al.*, 1970). The sounder was placed in operation in early December 1971 and ran on a nearly continuous basis throughout the entire winter air pollution season, through March 1972. During this time data on two stagnation episodes were taken and the inversion height measurements from the radiosonde and sounder were compared on a daily basis.

3. Comparison of radiosonde and sounder records

First we examine a few cases that compare the information derived from a radiosonde with that inferred from the acoustic sounder record; the dark and light portions of the facsimile record enable a pattern recognition type of analysis. Based on the lapse rates measured by the radiosonde, the cases fall into one of two general categories: strong surface based inversions, and elevated inversions with less stable air below.

---

[1] dBA refers to the frequency response curve of standard sound level meters designed to approximate the frequency response of the human ear (Bragdon, 1971).

Fig. 3 is an example of the first category, a strong ground-based inversion. The format of Fig. 3 shows the sounder record starting when the balloon was released and continuing for 20–30 min. The radiosonde temperature trace for this time is on the right. The winds, as measured by optically tracking the radiosonde, are indicated by the small arrows at the readout heights, giving the wind direction with reference to north (the top of the figure) and the speed (m sec^{-1}) shown next to each arrow. The sounder record in Fig. 3 is typical of a strong inversion, with the very dark echoes extending from the ground up to the break point where isothermal conditions start. Even though the sounder and radiosonde were separated by only a few tens of meters, it is still difficult to draw a one-to-one comparison between the height of a particular inflection as shown by the two methods. This is because the balloon-borne radiosonde provides only a single temperature profile, while the sounder effectively gives a continuous temperature structure profile every 4 sec. "Where did the balloon go through a particular feature?" is important and difficult to answer, especially, as will be shown later, when the inversion or structure of interest is undulatory. Despite this difficulty, the sounder record in Fig. 3 indicates the presence of more than one layer (note the variation in the darkness of the returns). The radiosonde does show one small break at about 200 m, which suggests the layers seen in the sounder record.

In a previous section, we stated that a monostatic sounder would see only fluctuations in refractive index structure due to small-scale temperature changes.

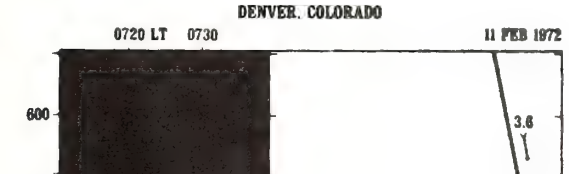

FIG. 3. Acoustic sounder record (left) compared with radiosonde temperature and wind profile (right) showing the pattern typical of a strong ground-based temperature inversion. The arrows represent wind direction (north is the top of the page) and speed (m sec^{-1}).

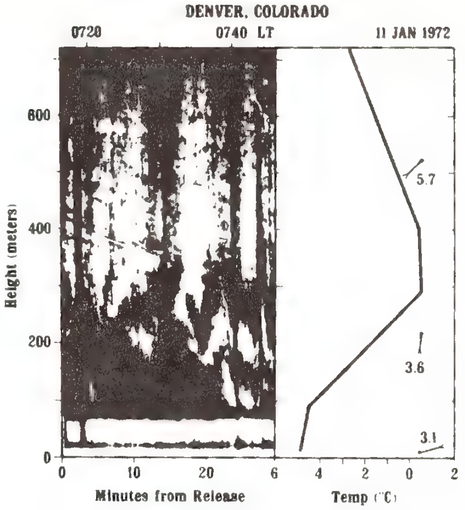

FIG. 4. Acoustic sounder record (left) compared with radiosonde temperature and wind profile (right) showing the pattern typical of a moderately strong inversion containing gravity waves.

While this is indeed true, it should not be concluded that wind shear is an unimportant influence on the sounder record. Wyngaard *et al.* (1971) have shown that the temperature fluctuations that produce the acoustic echoes are a function of Richardson's number, or the ratio of buoyancy to the square of the wind shear. Because of the shear term in the denominator, the darkness of an acoustic record may be closely related to the dynamic instability as well as to the static instability.

The production of gravity waves, or larger scale boundary layer features, is also related to wind shear. An example of this type of wavy structure is shown in Fig. 4. Again there is a rather strong, surface-based inversion, but in this case, a moderate wind shear is present at about 200 m. Patterns of this type vividly display the difficulty of using a single profile to determine the inversion depth. During the half-hour period shown in Fig. 4, the maximum depth of the inversion varies by nearly 150 m, a factor that could lead to considerable error in predicting the time of inversion breakup if conventional forecast methods are used.

The second general category of cases, inversions aloft, is typified by the record shown in Fig. 5. Here we see a rather diffuse pattern of returns, extending from about 100 m up to 450 m, with no distinct horizontal layering that can be identified as a contiguous top of the inversion. The radiosonde, on the other hand, shows a very sharply defined break in the temperature profile between 350 and 400 m. Although this is near the top of the diffuse echo region shown by the sounder, the radiosonde does not show the full complexity of the structure. Again, wind shear across the apparent boundary is responsible for wave motions, vestiges of

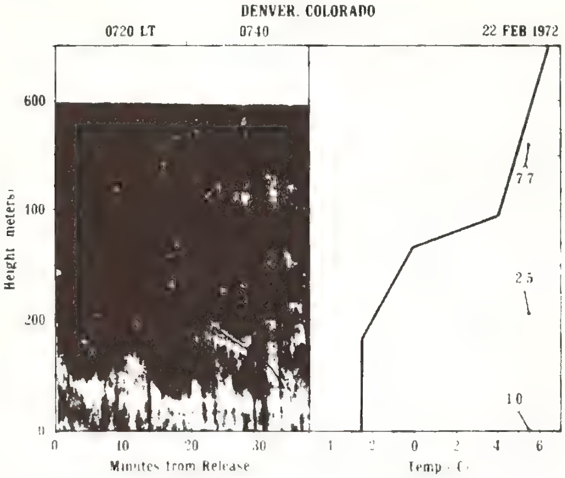

FIG. 5. Acoustic sounder record (left) compared with radiosonde temperature and wind profile (right) showing the pattern typical of an elevated inversion with waves.

which can be seen near 400 m, about 10 min after the radiosonde launch time.

A second example of an elevated inversion, but at a later stage of development, is shown in Fig. 6. In this case, surface heating has progressed to where the lowest levels are approaching instability and echoes from small thermal plumes are starting to appear at the bottom of the record. Note that the sharp inversion appearing on the temperature trace at 300 m is evident in the acoustic records as an oscillating dark band.

During the period of operation 19 cases were selected where the inversion height measured by the radiosonde was compared with that from the acoustic sounder. A scatter diagram comparing these two heights appears in Fig. 7. The lack of a one-to-one agreement could result from any of several reasons. First, as pointed out earlier, it is very difficult to determine exactly which part of an oscillating inversion surface has been penetrated by the radiosonde. This factor could account for the rather large scatter of some of the points in Fig. 7. A second factor that contributes to the presence of a systematic bias error (the radiosonde typically shows the inversion to be higher than the acoustic sounder) is the assumption of a constant speed of sound based on surface temperature when scaling the acoustic records. For example, if the speed of sound were assumed to be 325 m sec^{-1} (as would be the case for a temperature of −10C), and the temperature aloft was 6C, the speed of sound would be too low by 10 m sec^{-1}. This factor would cause only about a 3% error and would not account for the total observed bias. In more detailed analysis this error could be eliminated by using an acoustic propagation speed derived from vertical temperature profiles.

It should also be recognized that the radiosonde heights are subject to error due to the inherent lag in the pressure sensor and the possibility of an incorrect assumption of rise rate or pressure surface (Middleton and Spilhaus, 1953). Inversion height errors of several tens of meters can result from the temperature and pressure sensor lags as a radiosonde passes through a sharp change in temperature gradient. A previous study (Emmanuel *et al.*, 1972) demonstrated that the height of inversions as measured by a fixed tower compared well with the height determined from the acoustic sounder. This further suggests that the source of the bias error observed during this experiment is the radiosonde data.

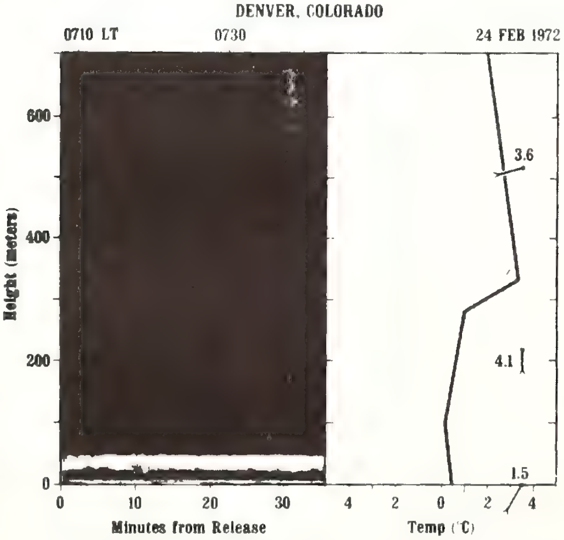

FIG. 6. Acoustic sounder record (left) compared with radiosonde temperature and wind profile (right) showing the pattern typical of the later stages of an elevated inversion with waves.

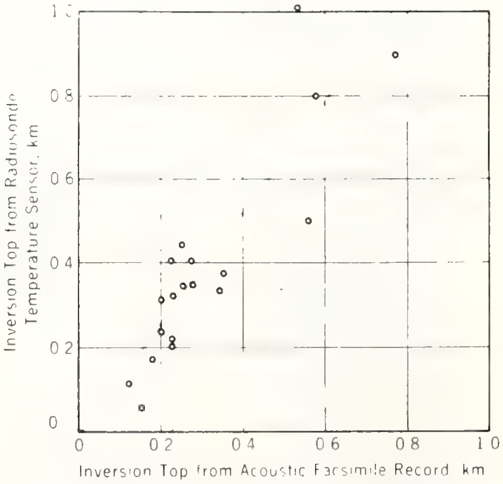

FIG. 7. Scatter diagram comparing inversion heights as determined from acoustic sounder records with those from radiosonde temperature traces.

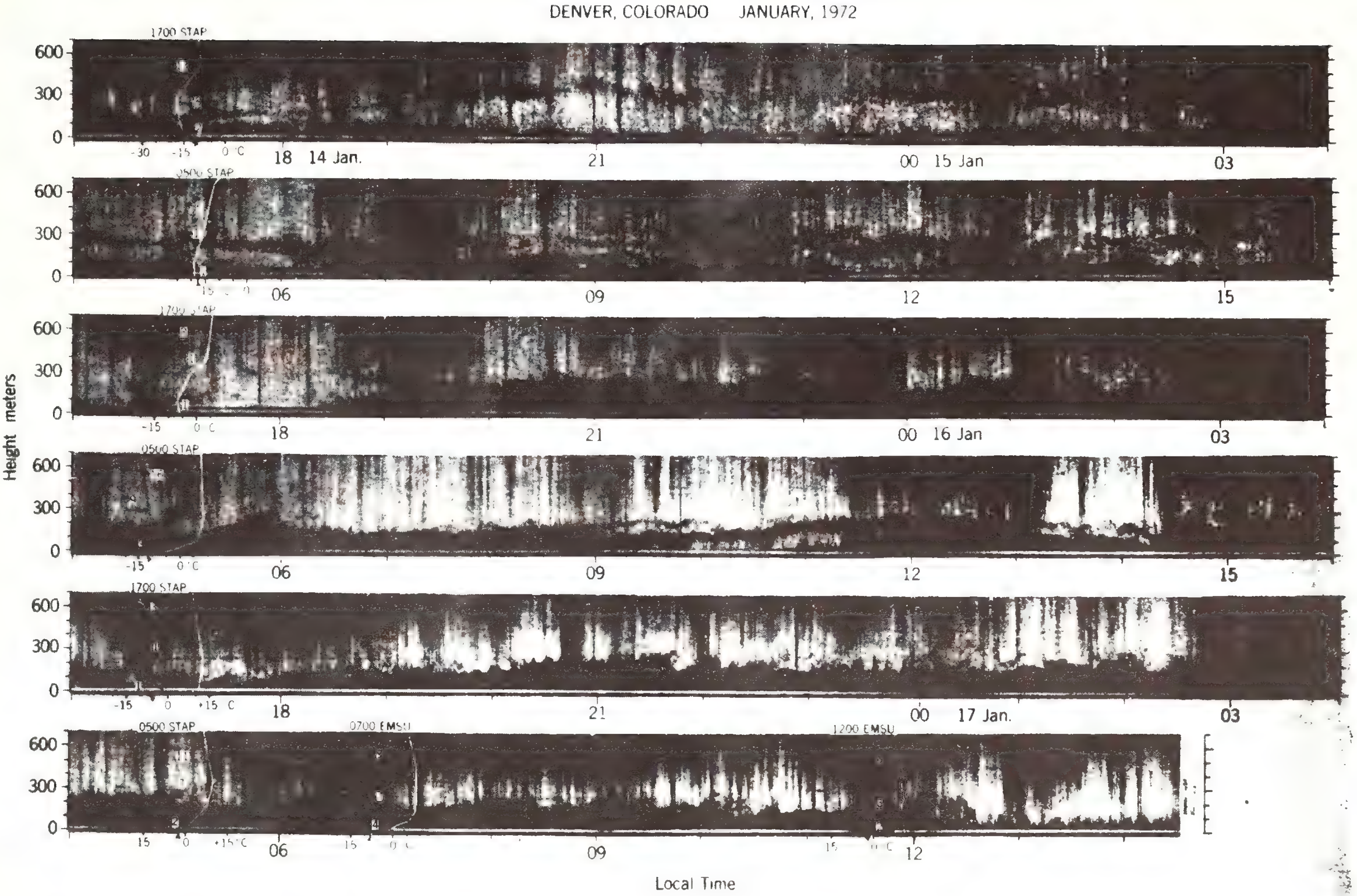

FIG. 8. Acoustic sounder record taken at Denver EMSU site during an air pollution episode. The superimposed temperature and dew point traces marked "STAP" were taken at Stapleton airport, about 8 km from the site. The traces marked EMSU were taken at the EMSU site. Wind speeds (m s^{-1}) are shown by the arrows (a north wind would be from the top of the figure).

4. A pollution episode

Two pollution episodes occurred during the experiment. One began on 23 December 1971 and lasted for less than 24 hr. The second started on 14 January 1972 and was of much longer duration, lasting until around noon on the 17th. This period covered a weekend when the EMSU radiosondes were not launched; however, the rather long duration and striking manner in which the low-level thermal structure was displayed by the sounder make this case worth some discussion.

Nearly 70 hr of continuous sounder record taken between 1600 on 14 January and 1430 on 17 January 1972 are shown in Fig. 8. Two EMSU radiosonde soundings were taken on Monday, the 17th; these temperature and humidity traces along with the low-level winds are superimposed on the sounder record at 0700 and 1200. (The black bands at these times are caused by electronic interference during the radiosonde baselining procedure.) Radiosonde temperature and winds taken by the National Weather Service at Stapleton Airport, some 8 km east of the sounder site, were available during the weekend and are also shown in Fig. 8. The greater distance between the Stapleton radiosondes and the sounder eliminates the possibility of a one-to-one comparison of the inversion height, but they do indicate the general thermal structure over the city during the episode.

The record in Fig. 8 shows that the episode was characterized during the first day by an elevated inversion forming a cap that varied in height from 200 to 400 m. The 1700 Stapleton radiosonde taken on 14 January shows this elevated layer to be higher than that observed at the EMSU site. The second Stapleton profile contained a break in the temperature profiles at a level above the sounder's range, but did not indicate a thermal structure that would have produced the strong echoes at around 300 m seen by the sounder. It is possible that this layer was not present at the higher airport site. Between 1600 and 1930 on 15 January, the acoustic echo became very weak with only subtle vestiges of the layered structure that appeared in the Stapleton profile. This lack of strong echoes is attributed to an accumulation of snow in the acoustic antenna, a problem that has since been solved by heating that parabolic antenna during wintertime operation. Later, during the night of 15–16 January, the echo intensity became very strong with many horizontal layers in evidence. This structure eventually evolves into a steep surface-based radiation inversion, as depicted by the Stapleton sounding at 0500 MST 16 January. At 0930 on the 16th, we see evidence of some surface heating, which begins to lift the strong inversion layer. This heating was not intense enough to break the inversion or to dissipate the accumulated pollutants.

Again on the night of 16–17 January the radiative cooling reestablished the strong surfaced-based inversion, responsible for the very dark echoes that last until the morning hours of the 17th. Both the Stapleton sounding (0500 MST 17 January), and the morning EMSU sounding show the very strong surface-based inversion. Finally at around 0930 on the 17th, we see the first indication of the impending inversion breakup. At this time, there is evidence of surface heating (the echo layer is lifting) and a rather long-period, large-amplitude wave is present. By 1200 the inversion layer can be seen to deteriorate significantly and by 1230 the typical thermal plume pattern, indicating convective activity with no capping inversion, marks the end of the pollution episode.

5. Conclusions and recommendations

The limited objective of this experiment was to place a simple monostatic acoustic echo sounder in an urban environment near standard instrumentation to determine 1) if it was feasible to operate this type of system in the noise environment characteristic of an urban area, and 2) if the acoustic records would indicate the depth and intensity of inversion measured by accepted standard methods. It was our earlier theoretical prediction that nearly continuous records can be obtained in a noisy city by taking precautions with acoustic shielding to reduce antenna side lobes (Simmons *et al.*, 1971). Judging from the records taken at the Denver site, this prediction was confirmed, since background noise was only occasionally intense enough to obliterate the acoustic returns, and efficient operation was possible during more than 99% of the time. The small amount of time when noise would ruin a record is insignificant when the usable record length is compared with the observing time of a radiosonde which gives only a brief look at the thermal structure, normally only twice per day.

Our data show that an exact one-to-one comparison of inversion height was not always possible. The reason for this can be attributed in part to the nature of the radiosonde and its quick, one-time look, while the acoustic sounder continually monitors the oscillation in the inversion height. It is very difficult to determine the exact time and position of the radiosonde as it penetrates an inversion surface, making a comparison of the sounder record and radiosonde trace, at best, subjective.

The measured heights also showed a bias toward higher values for the radiosonde data. This error is most probably due to the inherent lag of the radiosonde temperature and pressure sensors. A second, but smaller error, could be introduced by the assumption of a constant speed of sound through an atmosphere having a varying temperature.

The comparison could also be affected simply because the thermal structure measured by a radiosonde does not indicate all of the parameters involved in producing acoustic scattering. Indeed, a much more valid comparison could be made to Richardson's number (Emmanuel *et al.*, 1972), which has been shown to be directly related to the structure constant C_T for temperature fluctuations (Wyngaard *et al.*, 1971). This type of comparison was not made because the rather gross scale of the radiosonde winds and temperature would not relate well to the fine scale shown in the sounder records. This is not to suggest that research along this line would be unfruitful. The value of monitoring a stability parameter like Richardson's number on a continual basis could lead to new insight into the mechanism and evolution of boundary layer inversion dynamics.

When compared with most other meteorological instruments, the acoustic sounder is in its infancy; we have much to learn about optimum methods for applying this new method of collecting data. One needs little imagination, however, to see ways of applying the device as a research tool in solving problems relating to urban air pollution. This is especially true if the Doppler wind measuring capability is added to the system (Beran *et al.*, 1971; Beran and Clifford, 1972). An acoustic system, involving only slightly more complexity, could measure a profile of the vertical velocity, in addition to the inversion depth. A three-axis acoustic system, with two tilted antennas and Doppler receivers, can measure a vertical profile of the total wind vector to heights of 1 km. These more sophisticated systems should prove valuable in a study such as that reported by Riehl and Herkhof (1972) and would make it possible to measure the turbulent transport of pollutants, a term that could only be estimated in Riehl and Herkhof's work.

Operational applications of the sounder also appear highly feasible. It can be argued that sounder records give only a qualitative estimate of the inversion strength; the records, therefore, are only good for use in conjunction with standard temperature profiling techniques. This is true if taken in the context of presently used boundary layer models, where forecasts of inversion breakup times are based on the amount of heating required to remove the stable part of the profile. This argument loses sight of the fact that the sounder presents an entirely new view of the boundary layer structure on a time scale that has never before been available.

The relatively few records taken to date already demonstrate that it is a simple matter to identify and categorize stable and unstable conditions. This same method of pattern recognition may also enable using sounder records to forecast inversion breakup a few hours before it occurs. In the earlier discussion of the January pollution episode, we mentioned that the first indication of the impending inversion breakup was visible some 2–3 hr prior to the actual occurrence. This prediction was based on the observation that an ascending layer having a long-period, large-amplitude wave was visible in the sounder record prior to breakup.

A thorough study has not yet been made; however, examination of the few cases that are available seems to indicate that the inversion breakup is preceded by long-period wave motion in the boundary layer. Although it is nothing more then speculation at present, a study of the connection between such wave motions and the dynamic instability of the boundary layer may lead to the identification of a useful precursor of inversion breakup. The success of this type of approach could lead to the development of new forecasting techniques based solely on acoustic sounder records.

Acknowledgments. The personnel of the Denver EMSU, R. Roe and J. Robinette, gave valuable assistance in monitoring and adjusting the acoustic sounder facsimile machine; and J. Harding helped in the comparison of wind records and sounder traces. D. Henderson, EPA Regional Office Meteorologist, gave assistance in data analysis. This four-month long experiment was carried out with a developmental, sometimes temperamental, acoustic echo sounder, and the help provided by B. C. Willmarth, J. W. Wescott, E. J. Owens and C. E. Case of WPL was indispensable. Partial funding support was provided by the Division of Meteorology, EPA.

REFERENCES

Beran, D. W., and S. F. Clifford, 1972: Acoustic Doppler measurements of the total wind vector. *Preprints, Second Symp. Meteor. Observations and Instruments*, San Diego, Calif., Amer. Meteor. Soc., 100-110.

——, C. G. Little and B. C. Willmarth, 1971: Acoustic Doppler measurements of vertical velocities in the atmosphere. *Nature*, **230**, 160-162.

——, F. F. Hall, Jr., J. W. Wescott and W. D. Neff, 1972: Application of an acoustic sounder to air pollution monitoring. *Proc. Symp. Air Pollution, Turbulence and Diffusion*, H. W. Church and R. E. Luna, Eds., Sandia Labs., Albuquerque, N. M., 66–72.

Bragdon, C. R., 1971: *Noise Pollution.* Philadelphia, University of Pennsylvania Press, 54–56.

Emmanuel, C. B., B. R. Bean, L. G. McAllister and J. R. Pollard, 1972: Observations of Helmholtz waves in the lower atmosphere with an acoustic sounder. *J. Atmos. Sci.*, **29**, 886–892.

Hall, F. F., Jr., 1972: Temperature and wind structure studies by acoustic echo sounding. *Remote Sensing of the Troposphere*, V. E. Derr, Ed., Washington, D. C., Govt. Printing Office, 18-1 to 18-26.

Kallistratova, M. A., 1961: Experimental investigation of acoustic wave scattering in the atmosphere. *Tr. Akad. Nauk SSSR Inst. Fiz. Atmos.*, No. 4, 203–256. (English translation USAF FTD TT-63-441.)

Little, C. G., 1969: Acoustic methods for the remote probing of the lower atmosphere. *Proc. IEEE*, **57**, 571–578.

McAllister, L. G., 1968: Acoustic sounding of the lower troposphere. *J. Atmos. Terr. Phys.*, **30**, 1439–1440.

——, J. R. Pollard, A. R. Mahoney and P. J. R. Shaw, 1969: Acoustic sounding—A new approach to the study of atmospheric structure. *Proc. IEEE*, **57**, 579-587.

Middleton, W. E. K., and A. F. Spilhaus, 1953: *Meteorological Instruments.* University of Toronto Press, 260-261.

Monin, A. S., 1962: Characteristic of the scattering of sound in a turbulent atmosphere. *Sov. Phys. Acoust.*, **7**, 370–373.

Riehl, H., and D. Herkhof, 1972: Some aspects of Denver air pollution meteorology. *J. Appl. Meteor.*, **11**, 1040–1047.

Simmons, W. R., J. W. Wescott and F. F. Hall, Jr., 1971: Acoustic echo sounding as related to air pollution in urban environments. Tech. Rept. ERL 216 WPL 17, NOAA, Boulder, Colo.

Tatarskii, V. I., 1961: *Wave Propagation in a Turbulent Medium* (translated by R. A. Silverman). New York, McGraw-Hill, 285 pp.

———, 1971: *The Effects of the Turbulent Atmosphere on Wave Propagation.* (English translation NOAA and NSF TT68-50464, p. 472.)

Wescott, J. W., W. R. Simmons and C. G. Little, 1970: Acoustic echo-sounding measurements of temperature and wind fluctuations. ESSA Tech. Memo. ERLTM-WPL 5, Boulder, Colo., 24 pp.

Wyngaard, J. C., Y. Izumi and S. A. Collins, Jr., 1971: Behavior of the refractive index structure parameter near the ground. *J. Opt. Soc. Amer.*, **61**, 1646–1650.

USCOMM - ERL

Proceedings 16th AMS Radar Meteorology Conference, 237-242, April 1975.

OBSERVATIONS OF VELOCITY FIELDS AND VELOCITY SPECTRA IN THE CONVECTIVE BOUNDARY LAYER USING A DUAL-DOPPLER RADAR SYSTEM

A. S. Frisch and R. B. Chadwick

NOAA/ERL/Wave Propagation Laboratory
Boulder, Colorado 80302

1. INTRODUCTION

Knowledge of the velocity field in the convective boundary layer can be useful for such things as predicting pollutant diffusion and understanding dynamics of the boundary layer. During August 1972, the Wave Propagation Laboratory carried out a large scale field experiment near Haswell, Colorado, in which many remote sensing devices were operated simultaneously near a 152 m meteorological tower. This paper presents the results of observations in a convective boundary layer using a dual-Doppler radar system. This system was used to determine the velocity field over an area of approximately 5x5 km to a depth of approximately 1 km by using chaff as an air motion tracer.

2. MEASUREMENT AND ANALYSIS TECHNIQUES

Some results of three-dimensional air motion by dual-Doppler radar have been presented by Frisch et al. (1974), Miller and Frank (1974), and Kropfli and Miller (1974). This work used the COPLAN method originated by Lhermitte and Miller (1970) and Miller (1972). The techniques used for the total three-dimensional wind field measurements will only be summarized here. An extensive discussion can be found in Miller and Strauch (1974).

To obtain velocity estimates of the air motion, each radar needs targets that follow the air motion reasonably well. These targets can be chaff (a reflective coated mylar filament cut to 1/2 wavelength) or precipitation. Since the targets move randomly within the radar pulse volume, the return signal fluctuates in both phase and amplitude. This signal is converted to a spectrum of the velocity component parallel to the radar beam axis.

This spectrum is weighted by the backscattering cross section of the particles moving at a particular velocity within the pulse volume. The weighted average of the velocity spectrum is the mean radial velocity of the particles in the pulse volume.

In the Wave Propagation Laboratory's system, the radars are scanned in a series of tilted planes. The measured velocities in each plane are combined to provide the two-dimensional particle motion vector field. The particle fall velocity component in each plane is subtracted to give the vector air motion field. The third component is calculated, normal to each plane, by integrating the equation of continuity and assuming the third component to be zero at the ground. Since the resulting velocity field is in cylindrical coordinates, the velocity field is transformed into the more useful Cartesian coordinate system, with two of the axes parallel to the ground.

Spatial spectra of the velocity fields were calculated with the maximum entropy spectral analysis technique because, for short data samples, it provides better spectral estimates than classical methods (Burg, 1967; LaCoss, 1971; Markel, 1972; Ulrych, 1973; Chen and Stegen, 1974). Generally, better frequency resolution is obtained by increasing the length of the data sample. However, in the case under consideration here, the length of data is determined by the size of the area covered with chaff and is not under control of the experimenter; thus the resolution can not be increased in the conventional way. Because of this, the maximum entropy spectral analysis was used to obtain good resolution.

The maximum entropy spectral analysis relies on the fact that the estimated autocorrelation function can be extended in a manner other than the conventional extension by zeros. The extension is such that the entropy (in the information theory sense) of the data having the extended autocorrelation is maximized. The constraint that the extended autocorrelation must agree with the estimated autocorrelation function over its range is also imposed. It is important to note here that the extension of the autocorrelation function in the maximum entropy manner is not equivalent to manufacturing new data any more than the more conventional methods of estimating spectra which require that the autocorrelation function be extended by zeros. The maximum entropy technique does provide a logical, systematic method of making nonzero extensions of the autocorrelation function.

The extension in the maximum entropy manner is actually indirect and is never explicitly calculated. What is calculated is a time domain filter that will "whiten" the data. That is, a filter that will transform the data signal into a signal with a spectrum that is constant with frequency. It is clear that the reciprocal of the power transfer function of this filter is proportional to the power spectrum of the data signal.

Dual-Doppler radar data were processed so that spatial autocorrelation functions of the 2 horizontal components of wind were obtained. These estimates were then used in the maximum entropy spectral algorithm to obtain estimates of the spatial spectra of the wind components. Some inconsistencies were noted and further study indicated that the method was extremely sensitive to the validity of the estimated autocorrelation function. The details of this are discussed by Chadwick (1974) where it is demonstrated that one must continually check the validity of the estimated autocorrelation function. An algorithm to check the validity was developed and it became clear that the data could be tapered in an unconventional way to improve the stability of the maximum entropy technique. This technique will be reported in the near future (Strand and Chadwick, 1975). All of the spectra contained in this paper this "tapered" version of the maximum entropy technique.

3. EXPERIMENT AND RESULTS

The 152 m tower near Haswell, Colorado, was the site for the measurement program and radar positions relative to this tower are shown in Fig. 1. The radar chaff (aluminum coated mylar fibers--1-1/2 cm long and 0.0025 cm in diameter) were dispersed from an airplane at about 1230 MDT on 10 August 1972. As soon as the chaff had diffused enough to fill most of dual-Doppler scan volume, radar data were taken.

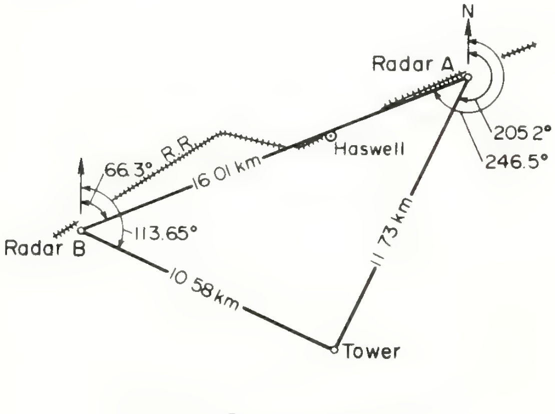

Location of Radars A and B relative to the 150m Tower

Fig. 1. Location of the radar relative to the 152 m meteorological tower. The measurement area was approximately 5x5 km adjacent to and north of the tower.

3.1 Velocity Fields

Velocity fields are displayed by projecting each vector into sets of planes, with the volume averaged velocity removed to show more detail in the velocity structure. Figs. 2 and 3 show the velocity vectors projected into a series of horizontal planes. Starting at z = 100 m, the horizontal field diverges over most of the area measured. As z increases, a more organized vortex-like pattern emerges. This is particularly apparent at z = 600 m, where the vortices are approximately 2 km in diameter.

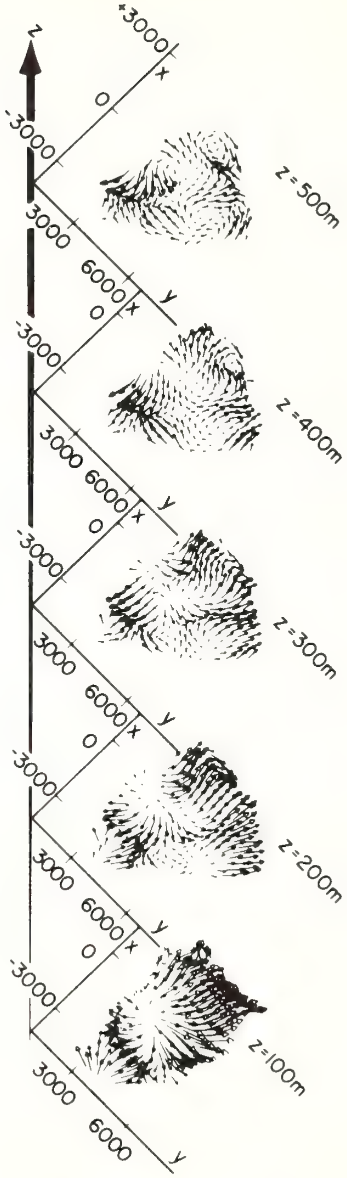

Fig. 2. Projections of the velocity vectors on a series of horizontal planes. The volume-averaged wind (5 m/sec) has been removed. The volume-averaged wind is in the x-direction.

Figs. 4 and 5 are projections of the velocity vector in planes approximately parallel to the volume-averaged wind. In the plane y = - 900 m (Fig.5), two downdraft regions approximately 3.5 km apart are apparent, with vertical components slightly less than 1 m/sec. Adjacent to the left hand region of downward moving air is upward moving air. The magnitude of this updraft is somewhat less than that of the downdraft. This feature is coherent through planes

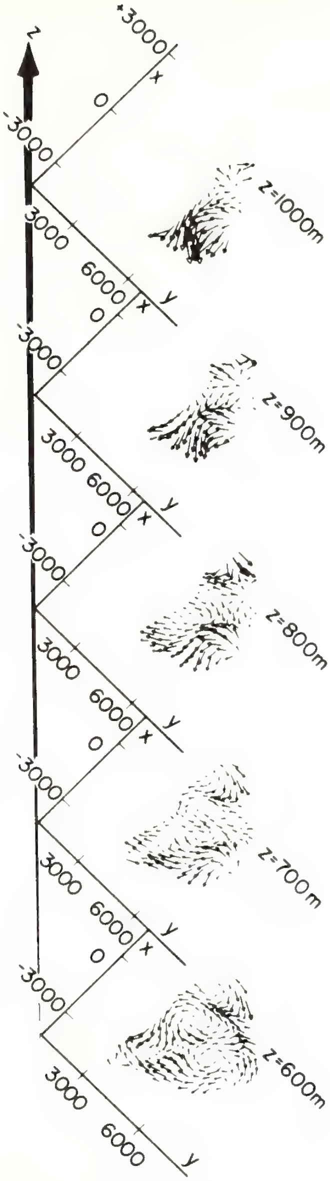

Fig. 3. Projections of the velocity vectors in a series of horizontal planes. The volume-averaged wind (5 m/sec) has been removed. The volume-averaged wind is in the x-direction.

y = - 600 m and y = - 300 m, with some rotational features appearing in these latter two planes. These rotational features appear between x = 5400 m to x = 7200 m and z = 800 m to z = 1200 m in the y = - 600 m plane. Another rotating feature can be partially seen in the y = 0 plane at z = 0 to z = 700 m for x > 6300 m. At y = - 300 m this rotation is even more apparent and this type of motion can be traced to the y = 600 m plane (Fig. 4).

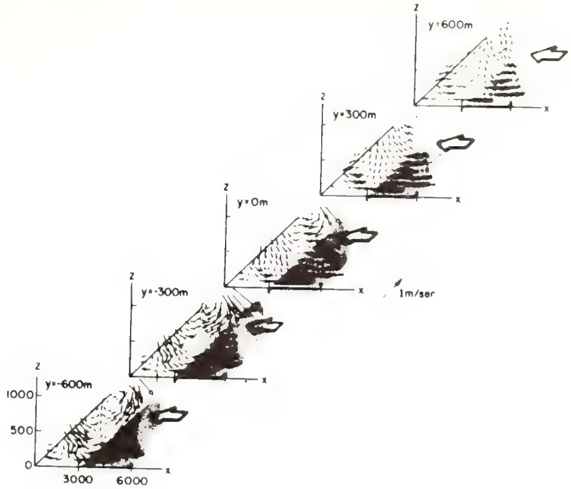

Fig. 4. Projections of the velocity vectors on vertical planes parallel to the volume-averaged wind. The volume-averaged wind has been removed from each vector. The y scale gives the relative location of each plane.

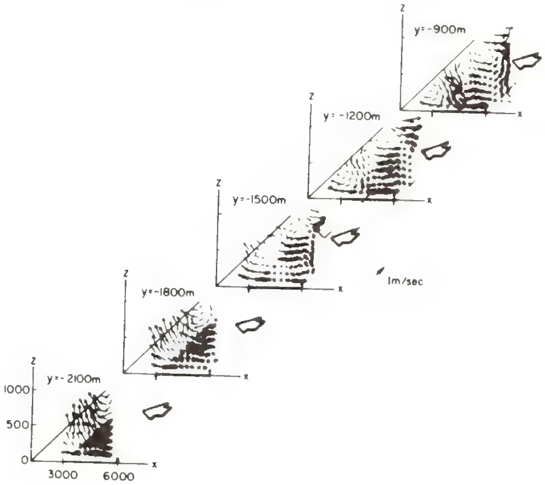

Fig. 5. Projections of the velocity vectors on vertical planes parallel to the volume-averaged wind. The volume-averaged wind has been removed from each vector. The y scale gives the relative location of each plane.

Figs. 6 and 7 show the projections of the velocity vectors onto vertical planes perpendicular to the volume-averaged mean wind. In the planes between x = 3300 m (Fig. 7) and x = 5100 m (Fig. 6), distinct updraft and downdraft regions appear. These extend from the lowest plane, z = 100 m, to a height of z = 800 m. The updrafts are approximately 2 km apart in the y direction. At x = 4200 m, a rotary motion is evident from y = 0 m to y = 2100 m and z = 300

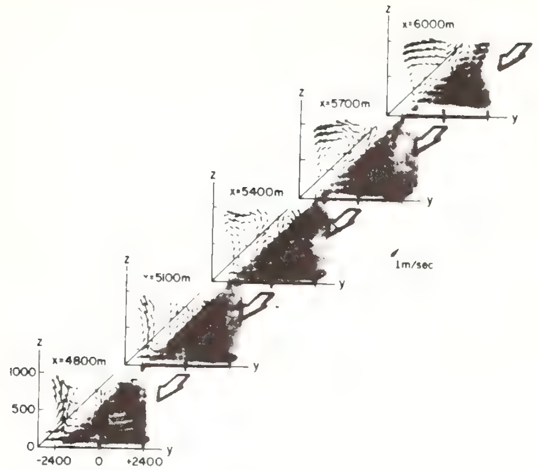

Fig. 6. Projections of the velocity vectors on vertical planes perpendicular to the direction of the volume-averaged wind. The volume-averaged component of wind has been removed from each vector. The x scale gives the relative location of each plane.

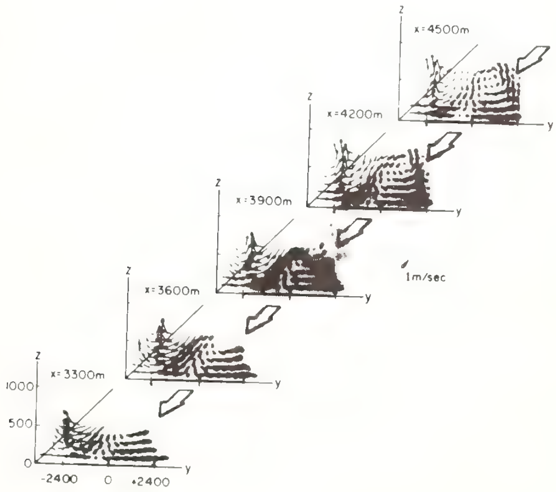

Fig. 7. Projections of the velocity vectors on vertical planes perpendicular to the direction of the volume-averaged wind. The volume-averaged component of wind has been removed from each vector. The x scale gives the relative location of each plane.

m to z = 700 m. This motion is consistent through to z = 6000 m before it disappears at x = 6300 m. In addition, at x = 4800 m, another vortex-like motion appears, counter-rotating to the other.

The velocity spectra of wind components parallel and perpendicular to the volume-averaged wind direction show most of their energy to be at scales comparable to the vortex scales. Fig. 8 shows the u, or along wind spectrum, for 600 m height in the x or cross wind direction. This is plotted as fP(f) vs. logf, where P(f) is the spatial spectral density and f is the spatial frequency or wavenumber.

These spectra show two peaks, one at 2 km, and one at 5 km. Similarly, the spectra of the v component (vv,x) along the x direction at 600 m has a peak at 3.0 km.

In the y direction, the u spectrum has one major peak at 3.5 km with a smaller peak at 1.8 km. The v spectrum in this direction (Fig. 8) has a peak at 5 km, and a smaller one at 2 km.

The apparent shift in these peaks with components and direction may be due to the fact that the spectra are calculated from a very limited sample of the atmosphere, since the chaff was dispensed over an area of approximately 5x5 km, and the dominant wavelengths appear to be somewhat between 2-3 km with another one at 5 km. In Fig. 3 at z = 600 m, there are vortex-like motions with scale sizes of 2 km to 2.5 km, which would give a corresponding wavelength of 4 to 5 km. One of the vortices appears to have a smaller size, approximately 1200 m. and this could account for some of the spectral energy at 2.4 km.

4. SUMMARY AND CONCLUSION

The use of chaff as an air motion tracer for a dual-Doppler radar system has revealed large scale motions in a convective boundary layer. Near the ground (100 m), only a divergent feature appeared in the horizontal plane. At 500 m height, the motion was rotary, showing distinct counterrotating vortices, with diameters of about 2 km. The projections of the velocity vectors into vertical planes also showed a vortex-like motion, with a vertical scale of 1 km and the maximum vertical velocities on the order of 1 m/sec. The horizontal components of velocity spectra at 600 m showed definite peaks between 2 and 5 km both along and across wind.

REFERENCES:

Burg, J. P., 1967: Maximum entropy spectral analysis, 37th Annual Intl. SEG Meeting, Oklahoma City, Okla., Oct 31, 1967.

Chadwick, R. B., 1974: A caution on the use of maximum entropy spectral analysis, submitted to J. Geophys. Res.

Chen, W. Y. and G. R. Stegen, 1974: Experiments with maximum entropy power spectra of sinusoids, J. Geophys. Res., 79(20), 3019-3022.

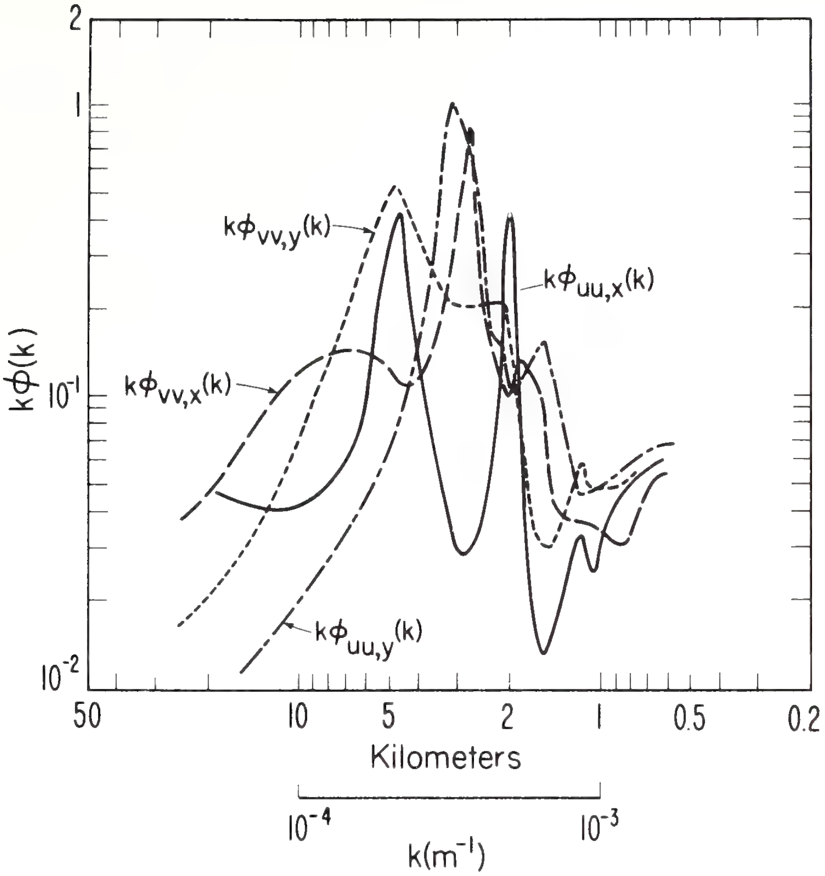

Fig. 8. Wavenumber times wavenumber spectra for the components perpendicular and parallel to the mean wind. (Here the mean wind (v component) is in the y direction.)

Frisch, A. S., L. J. Miller, and R. G. Strauch, 1974: A study of convection capped by a stable layer using Doppler radar and acoustic echo sounders, J. Atmos. Sci., 31, 1622-1628.

Frisch, A. S., L. J. Miller, and R. G. Strauch, 1974: Three-dimensional air motion measured in snow, Geophys. Res. Letters, 1(2), 86-89.

Kropfli, R. A. and L. J. Miller, 1974: Dual Doppler radar measurements within a hail producing storm in northeast Colorado, Preprint Vol., AMS Conf. on Cloud Physics, Tucson, Ariz., Oct 21-24, 1974, 277-282.

LaCoss, R. T., 1971: Data adaptive spectral analysis methods, Geophysics, 36(4), 661-675.

Lhermitte, R. M. and L. J. Miller, 1970: Doppler radar methodology for the observation of convective storms, Preprint Vol., AMS Proc. 14th Radar Meteorol. Conf., 133-138.

Markel, J. D., 1972: Digital inverse filtering--a new tool for formant trajectory estimation, IEEE Trans. Audio Electroacoustics, AU-20(2), 129-137.

Miller, L. J. and H. W. Frank, 1974: Three-dimensional air motion within a northeast Colorado rainstorm, Preprint Vol., AMS Conf. on Cloud Physics, Tucson, Ariz., Oct 21-24, 1974, 321-327.

Miller, L. J. and R. G. Strauch, 1974: A dual-Doppler radar method for the determination of wind velocities within precipitating weather systems, to appear in Remote Sensing of Environ.

Miller, L. J., 1972: Dual-Doppler radar observations of circulation in snow conditions, Preprint Vol., AMS Proc. 15th Radar Meteorol. Conf., 309-314.

Strand, O. N. and R. B. Chadwick, 1975: Maximum entropy spectral analysis from the standpoint of matrices and determinants, in preparation for publication in 1975.

Ulrych, T. J., 1972: Maximum entropy power spectrum of truncated sinusoids, J. Geophys. Res., 77(8), 1396-1400.

OBSERVATIONS OF BOUNDARY-LAYER CONVECTION CELLS MEASURED BY DUAL-DOPPLER RADAR AND ECHOSONDE, AND BY MICROBAROGRAPH ARRAY

A. S. FRISCH, R. B. CHADWICK, W. R. MONINGER, and J. M. YOUNG
NOAA/ERL/Wave Propagation Laboratory, Boulder, Colo., U.S.A.

(Received in final form 30 September, 1975)

Abstract. Three-dimensional air motion, observed with radar in a convective planetary boundary layer under light wind conditions, is organized in cellular structures scaled from 2 to 5 km; simultaneous acoustic echosonde measurements indicate that near the ground there are smaller cells than those observable by the radar. At heights of 400 m, cell scales become as large as those observable by the radar. Pressure fluctuations at the ground measured with spatial pressure transducers, at the same time as the radar and echosonde observations, traveled at the same speed and direction as the radar volume-averaged wind. The length scale determined at the ground with pressure fluctuation data was between 1.2 and 2.4 km, smaller than the largest radar-measured motion scales.

1. Introduction

Measurements of the wind field in the planetary boundary layer can help us determine diffusion properties, length scales that contain maximum energy (and thus knowledge as to how energy is input), and the nature of atmospheric motions.

The way the energy is distributed in the boundary layer depends on the type of atmospheric motion which in turn depends on atmospheric properties such as wind speed and temperature gradient. For example, when Woodcock (1942) observed the soaring habits of gulls over the ocean, he found their patterns dependent upon the temperature difference between the air and ocean-surface temperature and the horizontal wind speed. At low wind speeds, the soaring was circular, changing to line soaring at high wind speeds. The circular soaring indicated presence of large convection cells at lower wind speeds.

Taylor (1958) observed that near the ground during day-time convection, there was evidence of organized thermal structures extending vertically for several metres superimposed on a background of random disturbances. Vulf'son (1961) considered these small thermals as jets and with a statistical model, he inferred the average diameter to be on the order of 50 to 100 m to heights of 3 km. Telford and Warner (1964) examined how the vertical temperature flux was carried by eddies much smaller than the thermals which were the obvious feature of the temperature records. However, the importance of these smaller eddies in the transport of temperature fluctuations decreased with height. In a later paper, Warner and Telford (1967) found temperature pulse widths to be about 300 m in diameter below a height of 3 km. While these diameters were at variance with Vulf'son's observed diameters, lapse rate data were not available to compare the effects of thermal stability between the two sets of observa-

Boundary-Layer Meteorology **3** (1975) 199–226. *All Rights Reserved*
Copyright © 1975 by D. Reidel Publishing Company, Dordrecht-Holland **75–42T**
26 1

tions. The lapse rate has a particularly important effect on the diameters at low levels as shown by Frisch and Businger (1973). High-power radar observations by Hardy and Ottersten (1969) and by Konrad (1970) showed convection cells originating several hundred metres above the surface with disorganized returns having scale sizes between 100 and 200 m in diameter near the surface, increasing to well-developed cell structures 1 to 3 km in diameter at heights of over a kilometer. With an instrumented aircraft, Lenschow (1970) found convection scales 800 m in diameter. With wind shear present, the types of motion can change dramatically. For example, LeMone (1973) found two-dimensional horizontal roll vortices 2 km wide in the convective boundary layer when the wind speed was in excess of 7 m s^{-1}.

Our calculations use data from a dual-Doppler radar system, an acoustic echosonde, and a microbarograph array to describe features of the convective boundary layer. The Doppler radar system determined the three-dimensional wind fields over a horizontal area of 5×5 km^2 to a height of 1 km. Chaff was used as an air motion tracer. The echosonde was used to infer the spatial scales of the fluctuations of temperature variance observed in the convective boundary layer, for comparison with the velocity spatial scales observed by the dual-Doppler radar system. The micro-barograph array gave the size, direction, and speed of pressure disturbances at the ground.

2. Measurement and Analysis Techniques

2.1. Dual-doppler radar.

This work used the COPLAN scanning method originated by Lhermitte and Miller (1970). The dual-Doppler techniques used for the total three-dimensional wind field measurements are summarized here; a comprehensive discussion of them can be found in Miller and Strauch (1974).

To obtain velocity estimates of the air motion, each radar needs targets that follow the air motion. These targets can be chaff (a reflective coated mylar filament cut to $\frac{1}{2}$ wavelength) or precipitation. Since the targets move randomly, the return signal fluctuates in both phase and amplitude. The signal is converted to a spectrum of the velocity component parallel to the beam axis of each radar. The spectrum is weighted by the backscattering cross-section of the particles moving at each particular velocity within the pulse volume. The weighted average of this velocity spectrum is the mean radial velocity of the particles. We obtain the true air motion by combining radar radial velocity measurements with the equation of mass continuity and an independent estimate of the mean terminal fall velocity of the radar targets. Such determinations of three-dimensional air motion by dual-Doppler radar have been presented by Frisch *et al.* (1974), Miller and Frank (1974), and Kropfli and Miller (1974).

We calculate the spatial spectra of the velocity fields with the maximum entropy spectral analysis technique because, for short data samples, it provides spectral estimates with higher resolution at a given confindence level than classical methods do (Burg, 1967; LaCoss, 1971; Markel, 1972; Ulrych, 1972; Chen and Stegen, 1974). In many problems, better frequency resolution can be achieved by increasing the length of the data sample. However, in our case the length of the data sample is determined by the size of the area covered with chaff, which is not under the complete control of the experimenter.

When we first calculated spectra from the dual-Doppler radar data, using the conventional maximum entropy technique described by Burg (1967), the limited sample size introduced large errors into the estimates of the autocorrelation functions. Such errors can make the function mathematically inadmissible. Under certain conditions the inadmissible autocorrelation functions caused invalid peaks in the maximum entropy spectrum that could easily lead to a complete misinterpretation of the spectra. Therefore, a more general algorithm was developed that safeguards against these errors. This algorithm tapers the possible inadmissible estimate of the correlation function in an unconventional manner that causes it to be admissible. This allows use of more lags in the autocorrelation function for a given data sample size. This new processing procedure is described by Strand and Chadwick (1975). All spectra in this study were calculated with this 'tapered' version of the maximum entropy technique.

2.2. Echosonde

The theory of acoustic sounding has been discussed by Little (1969) and its potential uses described by Beran and Hall (1973). An echosonde system similar to the one used in this experiment has been described by Owens (1974). The echosonde was operated in a direct vertical backscatter mode. The intensity of the backscattered acoustic waves may be calculated as a function of the magnitude of the fluctuations in the refractive index of the medium if it is assumed that the fluctuations result from siotropic turbulence. The theory of interactions of sound waves with the turbulent atmosphere has been investigated by many authors (e.g., Tatarski, 1961). In the direct backscatter mode, the scattering cross-section is a function only of **Cp**, which depends on the turbulent kinetic energy dissipation rate, ε, and on the rate of destruction of temperature fluctuations. Such actions between acoustic waves and the atmosphere have been used to investigate atmospheric phenomena such as gravity waves and plumes (Bean *et al.*, 1973; Emmanuel *et al.*, 1972; Hooke *et al.*, 1973; Wyckoff *et al.*, 1973; Frisch and Clifford, 1974; Kjelaas *et al.*, 1975). When the boundary layer is unstable, the echosonde shows large values of **Cp** intermittent in time and coherent from a height of about 50 m to a few hundred metres. These have been associated with plumes or families of plumes that are generated in the surface layer and carried aloft by some scale of motions larger than the plumes, as suggested by LeMone (1973) and Kjelaas and Ochs (1974).

2.3. Microbarograph array

The microbarograph used in this study (Cook and Bedard, 1971) consisted of a variable-capacitance differential pressure sensor in conjunction with an acoustic high-pass filter. This instrument measures pressure fluctuations with periods from 1 to 1000 s and has a noise level of 10^{-3} μbar. The data from a triangular array of microbarographs spaced about 300 m apart were used to determine the correlation distance, speed, and direction of arrival of pressure fluctuations at the ground. This was done by 'steering' the array beam; i.e., by systematically varying the phase relationships between different sensors (see Gossard and Hooke, 1975, pp. 337–341). For the analysis of our pressure data, we used Young's algorithm for digital array processing (Young and Hoyle, 1975). The technique has been described by Kjelaas *et al.* (1975) who used it to study a storm-generated system of gravity waves.

3. Experiment and Results

A site near Haswell, Colorado, was the location of the measurement program. We determined the average value of the Richardson number from measurements on a 152-m tower and from a laser triangle located 2 m above the ground (Kjelaas and Ochs, 1974). The tower and laser triangle were in the vicinity of the echosonde and microbarograph array. Radar targets, consisting of aluminium coated mylar rods 1–$\frac{1}{2}$ cm in length and 0.0025 cm in diameter, were dispersed from an airplane at about

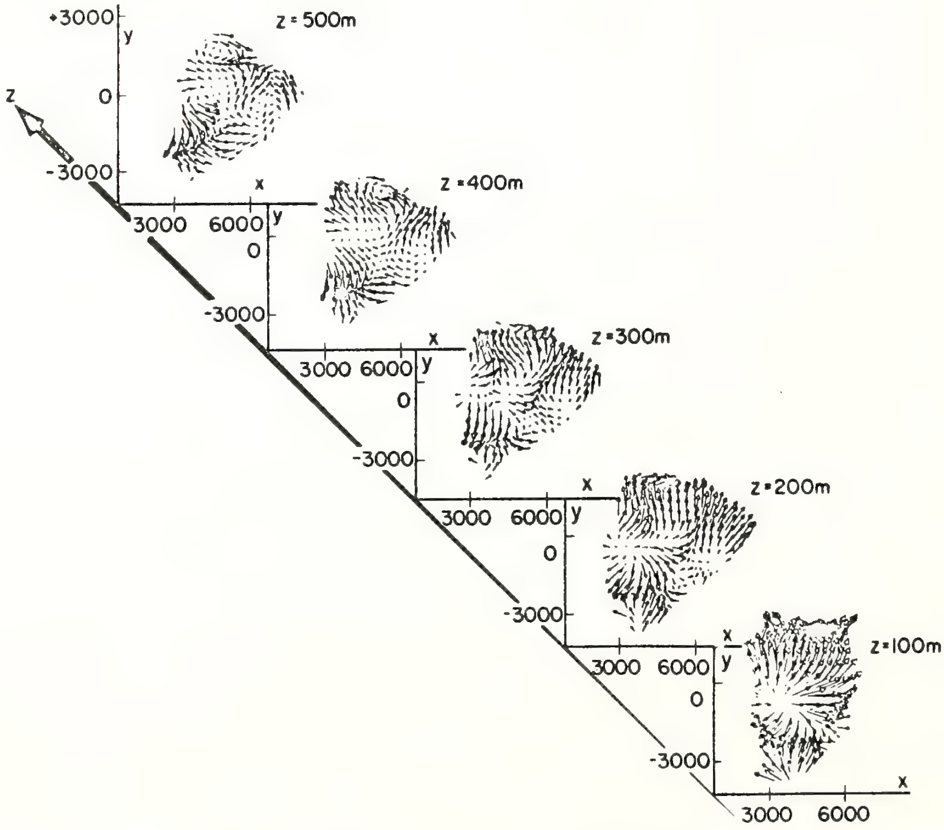

Fig. 1. Projections of the velocity vectors in a series of horizontal planes. The volume-averaged wind (5 m s^{-1} in the negative x-direction) has been removed. Dimensions are in metres.

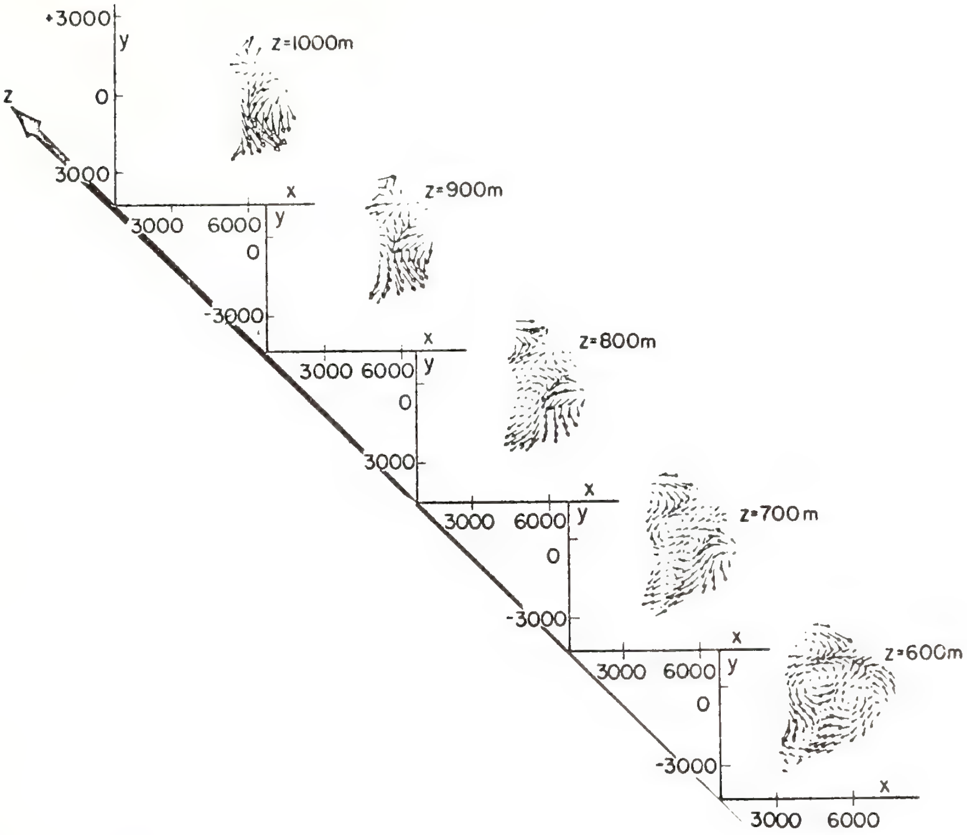

Fig. 2. Projections of the velocity vectors in a series of horizontal planes. The volume-averaged wind (5 m s^{-1} in the negative x-direction) has been removed. Dimensions are in metres.

1230 MDT on 10 August 1972. As soon as the chaff had diffused enough to fill a significant volume (after a tine of about 25 min), radar data were taken in conjunction with data from the acoustic echo sounder and microbarograph array. The wind speed was about 5 m s^{-1} from the SE, and the Richardson number, measured between 33 and 2 m, was -2.

3.1. VELOCITY FIELDS

The mean wind velocity was obtained by averaging all of the radar velocity measurements in the scan volume (about 5 km × 5 km × 1 km). Velocity fields are displayed by projecting the vector field onto sets of orthogonal planes: one set parallel to the ground, and two vertical sets parallel and perpendicular to the volume-averaged wind direction. To display more detail in the velocity field, the volume-averaged velocity was removed from each velocity vector to obtain a fluctuation field. The errors in the estimate of these fluctuations are less than 4 cm s^{-1} in the horizontal and less than 15 cm s^{-1} in the vertical.

Figures 1 and 2 show the velocity vectors projected onto a series of horizontal planes. The data are plotted in a coordinate system whose origin is the center of the baseline joining the radars. The x-axis is horizontal and perpendicular to the baseline. The z-axis is vertical. At $z = 100$ m, the horizontal field diverges over most of the area measured. As z increases, an organized rotational pattern in the velocity fluctuation field emerges. This is especially apparent at $z = 600$ m, where two complete vortices and a third incomplete vortex may be seen within the chaff cloud. The largest has a diameter between 2.5 and 3.0 km and the smallest has a diameter of about 1.2 km.

Figures 3 and 4 are projections of the velocity vectors onto planes approximately parallel to the volume-averaged wind. In the plane $y = -900$ m (Figure 3), convective cellular structure is apparent, with two downdraft regions approximately 3.5 km apart having vertical velocities slightly less than 1 m s^{-1}. Adjacent to the left-hand region of downward moving air is upward moving air. The magnitude of this updraft is somewhat less than that of the downdraft. This feature is coherent through all planes between $y = -600$ and 600 m. In Figure 4 some closed vortices are to be seen in the

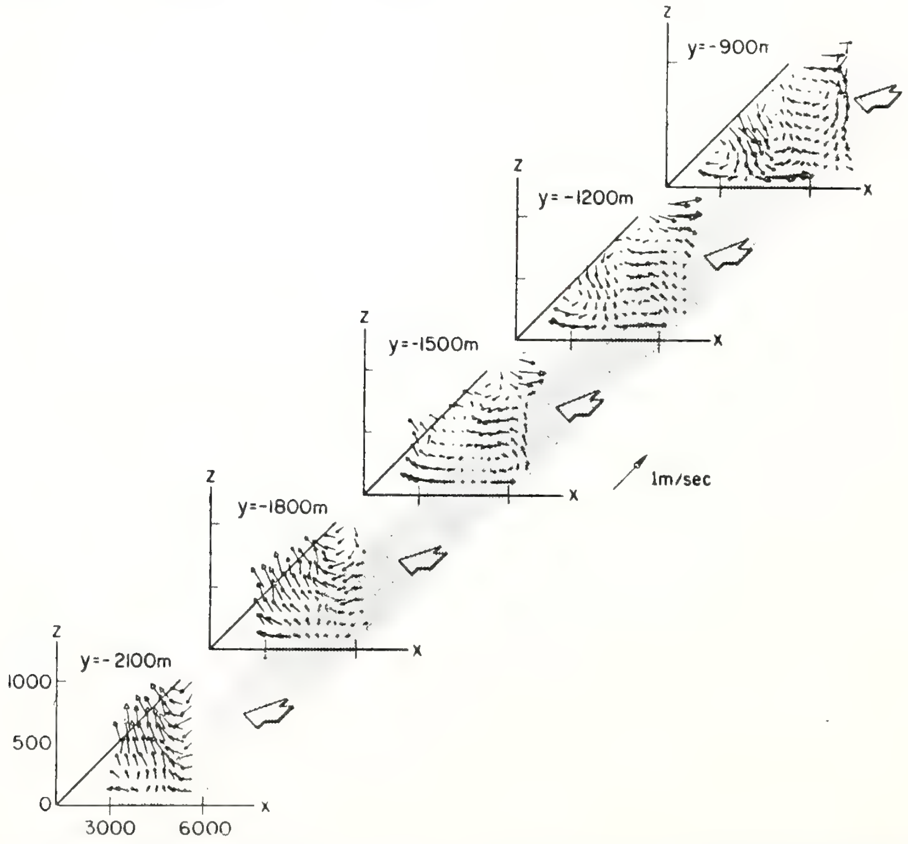

Fig. 3. Projections of the velocity vectors on vertical planes parallel to the volume-average wind. The volume-averaged wind has been removed from each vector. The y scale gives the relative location of each plane. Dimensions are in metres.

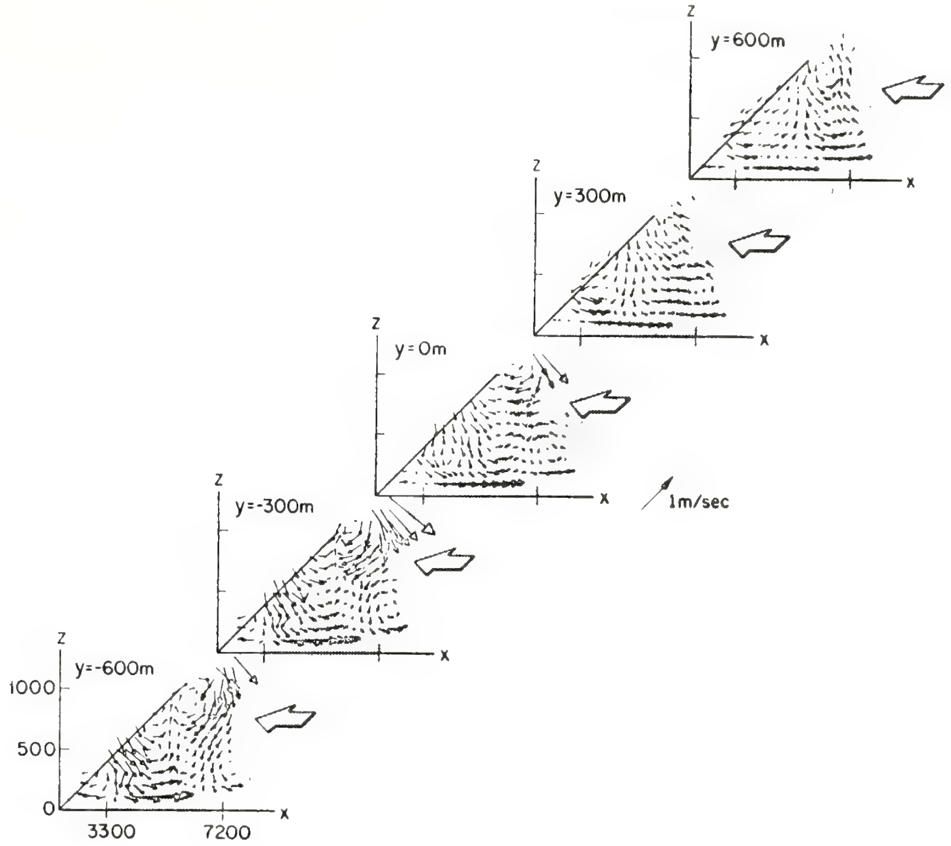

Fig. 4. Projections of the velocity vectors on vertical planes parallel to the volume-averaged wind. The volume-averaged wind has been removed from each vector. The y scale gives the relative location of each plane. Dimensions are in metres.

plane $y = -600$ m between $x = 5400$ m and $x = 7200$ m from $z = 800$ m to $z = 1200$ m. Part of another rotating feature can be seen in the $y = 0$ plane at $z = 0$ to $z = 700$ m for $x > 6300$ m. At $y = -300$ m this rotation is even more apparent and this type of motion can be traced to the $y = 900$ m plane.

Figures 5 and 6 show the projections of the velocity vectors in vertical planes perpendicular to the volume-averaged wind. Between the planes $x = 3300$ m (Figure 5) and $x = 5100$ m (Figure 6), one can again see a cellular structure with distinct updraft and downdraft regions. The cells extend from the lowest plane, $z = 100$ m, to a height of $z = 800$ m. Their scale in the y direction is approximately 2 km. A portion of this cell can be seen at $x = 4200$ m, where a rotary motion starts to appear from $y = 0$ to 2100 m and from $z = 300$ to 700 m. This motion is coherent through $x = 6000$ m before it disappears at $x = 6300$ m. In addition, at $x = 4800$ m, part of another cellular-like structure appears with the motion field counter-rotating relative to the other cell.

3.2. VELOCITY SPECTRA

Spatial power spectra of velocity give the distribution of kinetic energy density as a function of wavelength. Such spectra have been estimated from velocity measurements obtained from instrumented towers or aircraft (e.g., Lumley and Panofsky, 1964; Panofsky, 1973; Pasquill, 1972). Because the Doppler radar measurements yield a three-dimensional velocity field over a volume of the planetary boundary layer, it is possible to calculate estimates of the spatial velocity spectra within that volume. Comparing these spectra with spectral estimates found by other techniques under similar atmospheric conditions, we can judge the genreality of our observations. We chose the horizontal plane 600 m above the ground for analysis and calculated the spectra of the orthogonal velocity components u, v (Figure 7). We calculated spectral estimates of only the u and v components, since they are much less sensitive to errors in the integration of the equation of continuity than the vertical component (Miller and Strauch, 1974). The results are shown as $k\phi_{uu,}x(k)$, etc., vs $\log k$, where k is the wavenumber in the x direction (depending on the subscript after the comma in ϕ).

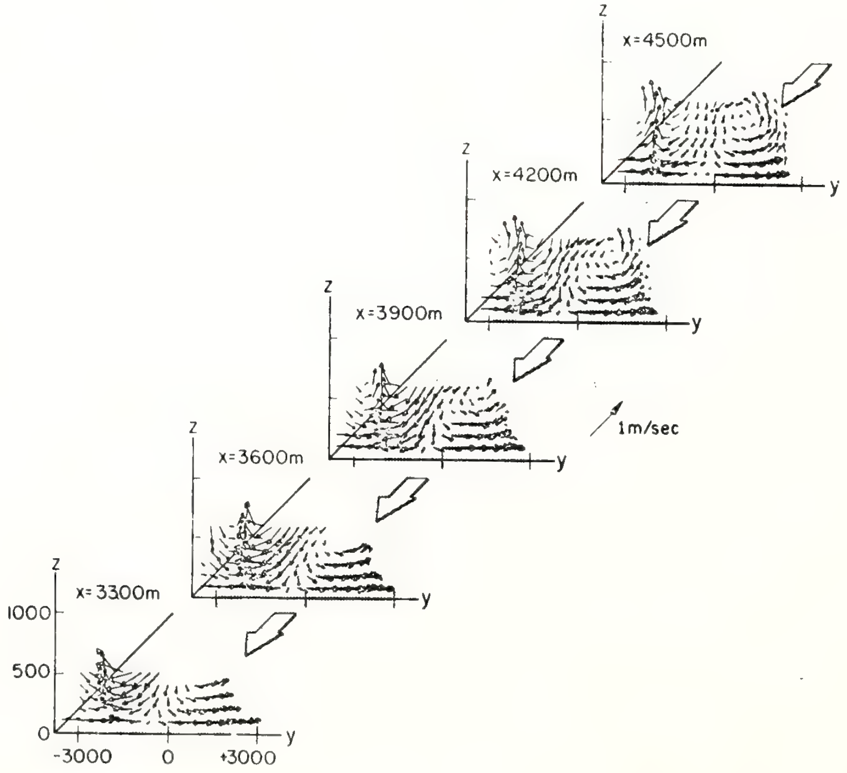

Fig. 5. Projections of the velocity vectors on vertical planes perpendicular to the direction of the volume-averaged wind. The volume-averaged wind has been removed from each vector. The x-scale gives the relative location of each plane. Dimensions are in metres.

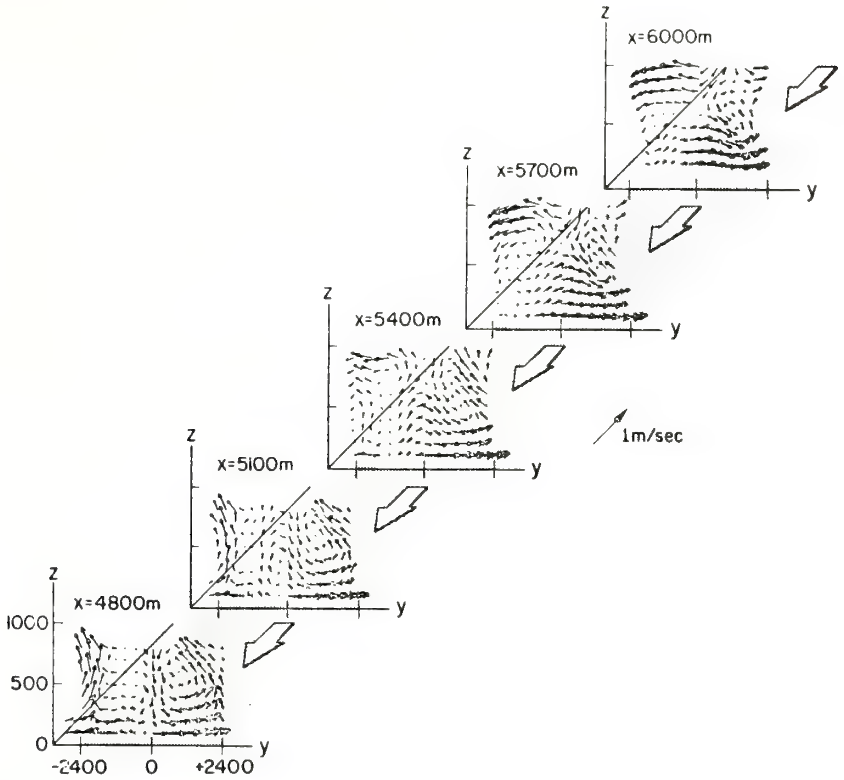

Fig. 6. Projections of the velocity vectors on vertical planes perpendicular to the direction of the volume-averaged wind. The volume-averaged wind has been removed from each vector. The *x*-scale gives the relative location of each plane. Dimensions are in metres.

The spectrum of the *u* component in the *x* direction shows two peaks, one at an approximate wavelength of 5 km, and the other at 2 km. Examining the $z=600$-m plane in Figure 2, one can see parts of three counter-rotating features. In the smaller cell, located at $x=6000$ m and $y=0$, the *u* component reverses itself in a distance of 1 km, which corresponds to a wavelength of 2 km. Considering the features centered at $x=4000$ m and $y=0$, the *u* component reverses itself in a little over 2.5 km which would give a wavelength of 5 km, corresponding to the second peak in the $\phi_{uu,x}(k)$ spectrum. The *v* component spectrum appears to behave in a similar manner in the *x* direction although the spectral peaks are shifted toward longer wavelengths compared to the *u* spectral peaks. The spectra of the *u* component in the *y* direction show a major peak at slightly greater than 3 km with a smaller one slightly under 2 km. Again looking at the velocity field projection in Figure 2 at 600 m, the *u* component in the larger cell reverses itself within about 1.5 km in the *y* direction and about 1 km in the smaller cell. These correspond to scale sizes of 3 and 2 km, respectively. Similarly, the *v* spectrum in the *y* direction has peaks at 5 and 2 km, associated with scales appearing in Figure 2.

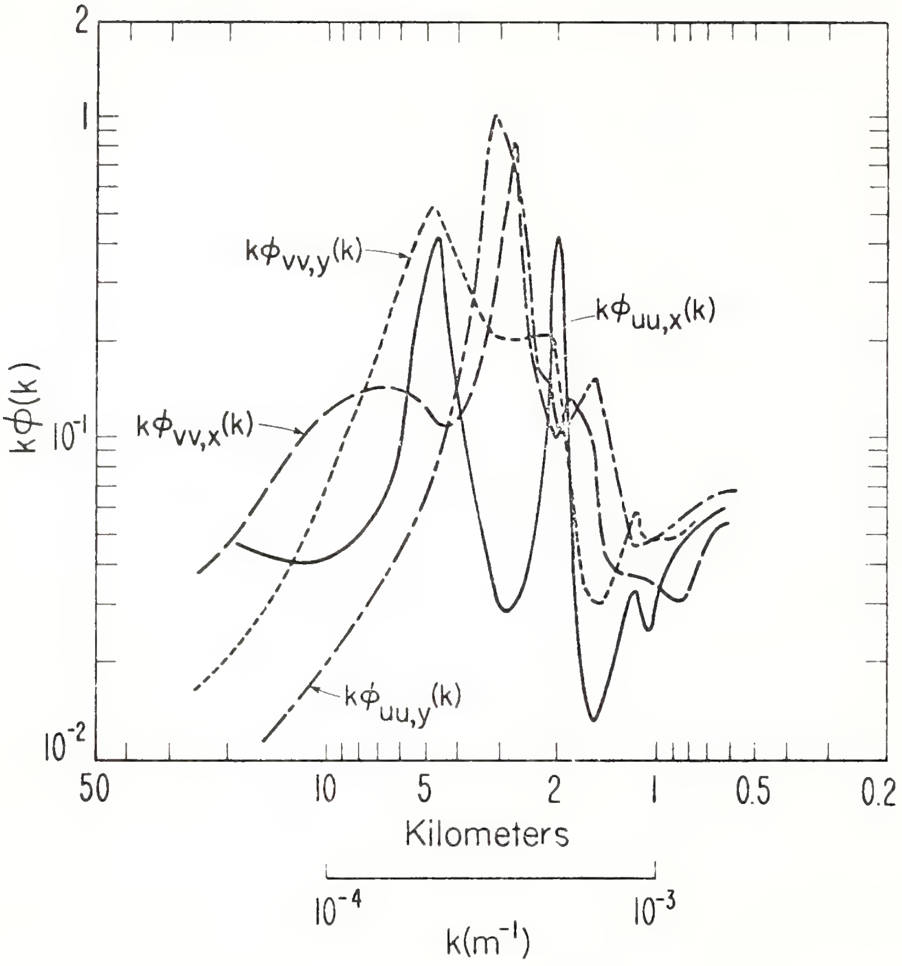

Fig. 7. Wavenumber vs. wavenumber spectra for the components perpendicular and parallel to the mean wind. (Here the mean wind (v component) is in the Y direction.)

3.3. ECHOSONDE DATA

The echosonde was located at approximately $x = 8000$ m and $y = 300$ m in the radar coordinate system in which the origin is at the center of the radar baseline. The x-axis is horizontal and perpendicular to the baseline. Figure 8 shows the echosonde facsimile record for a time interval that includes that of the dual-Doppler radar observations. The darker the record, the stronger the backscattered signal. Thus the plot displays echo strength as a function of time and height. It shows the acoustic intensity increasing and then decreasing over periods of a few minutes except near the ground (< 100 m) where the intensity is more continuous. Near the ground the periods are shorter. Furthermore, the larger values of C_T^2 seem to last longer than do weak values of C_T^2. Since there is an updraft in the convective boundary layer less than 50% of the time.

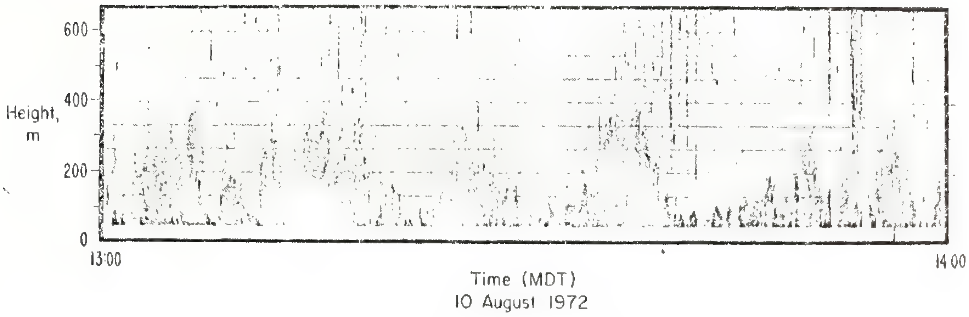

Fig. 8. Acoustic backscattered intensity vs time and height.

(Frisch and Businger, 1973), either some of the temperature fluctuations causing the large acoustic echoes are in part of the downward moving air, or the angular resolution of the acoustic beam is insufficient to separate the structure in the lower part of the records.

Higher in the boundary layer, acoustic Doppler measurements have indicated that most of the larger values of Cp are associated with upward moving air (Beran *et al.*, 1971). Unfortunately, the chaff did not fill the region above the echosonde (as can be seen in Figure 1, recalling the fact that the echosonde was at $x = 8000$ m and $y = -300$ m). Thus it is not possible to compare directly the echosonde data with the radar measurements. Adopting Taylor's hypothesis using 5 m s^{-1} as the mean wind speed, one can see that near the ground the fluctuations of C_T^2 are of much smaller scale than the distances between updrafts in the radar data. The radars can only resolve features larger than 300 m, and thus may be filtering out the smaller scales resolved by the echosonde.

At approximately 400 m, the echosonde record shows two very strong echoes at 1300 and 1318 MDT (rouhly the time of the Doppler radar measurements). Again using Taylor's hypothesis, the separation distance is roughly 5 km – comparable to the distance between updrafts observed by Doppler radar. Although these are only two events, a similar scale was observed by Fitzjarrald (1975) using more echosonde data and longer time intervals. The similarity of the updraft separation distances to the separation distances between the large values of C_T^2 indicates that the large-scale updrafts may be important in transporting the temperature fluctuations upward above the surface layer, as suggested by LeMone (1973) and Kjelaas and Ochs (1974).

3.4. MICROBAROGRAPH ARRAY

Because of high noise in the pressure data and because the chaff volume was not over the array (located near the echosonde), it was not possible to compare the pressure fluctuations directly with patterns seen in the radar data. Using cross spectrum analysis to process the micro-barograph array data, we found that most of the energy of coherent pressure fluctuations was in a frequency band between 8.8×10^{-4} and 4.7×10^{-3} Hz. The propagation velocity of these coherent fluctuations was the same as the radar volume-averaged wind. The corresponding scales of the pressure disturbances were between 1.2 and 2.4 km, i.e., in the same range as one of the spectral peaks of $\phi_{uu,x}(k)$. However, at lower frequencies (longer wavelengths) the spectral estimates were unusable because of contamination by contributions due to power line fluctuations.

4. Discussion and Conclusions

The observations we have described show the kinematic structure of convection cells in the boundary layer. The maximum kinetic energy in the residual velocity field in a horizontal plane 600 m above the ground was at scales between 2 and 5 km, with slightly more energy in the along-wind component than in the transverse component. Pennell and LeMone (1974) found that most of the momentum flux in the unstable trade-wind boundary layer over the ocean occurred at scales between 800 m and 10 km, with two peaks at 800 m and 6 km, comparable to the peaks in our spectral data (Figure 7). During BOMEX, Grossman (1973) observed similar scales in the u and v spectra with peaks occurring in the 2 to 3 km wavelength range. The echosonde data indicate that near the ground, scales smaller than the radar grid resolution are important, with a transition to the dominance of the larger scale motion as the height above the ground increases. This is in agreement with observations of Telford and Warner (1964) showing that near the ground, small scales are important in transferring temperature fluctuations vertically, with larger scales becoming more important with-increasing height.

The surface pressure data indicate that there is at least one scale size in the range between 1.2 and 2.4 km that propagates at the same speed and direction as the wind velocity averaged over the first kilometre of the atmosphere. We cannot say with certainty from the present data whether or not the velocity features revealed by the Doppler radar are correlated with the pressure fluctuations at the ground.

Comparison of our spectral results with those of other investigators (Grossman, 1973; Pennell and LeMone, 1974) suggests that the velocity patterns or structures in the unstable boundary layer may be similar over the ocean and over land.

References

Bean, B. R., Frisch, A. S., McAllister, L. G., and Pollard, J. R.: 1973, 'Planetary Boundary-layer Turbulence Studies from Acoustic Echo Sounder and *in situ* Measurements', *Boundary-Layer Meteorol.* 4, 449–474.

Beran, D. W. and Hall, F. F., Jr.: 1973, 'Remote Sensing Applications in Air Pollution Meteorology', *ISA Proc. 2nd Joint Conf. on Sensing of Environmental Pollutants*, 231–246.

Beran, D. W., Little, C. G., and Willmarth, B. C.: 1971, 'Acoustic Doppler Measurements of Vertical Velocities in the Atmosphere', *Nature* 230, 160–162.

Burg, J. P.: 1967, 'Maximum Entropy Spectral Analysis', *37th Annual Intl. SEG Meeting*, Oklahoma City, Okla.

Chen, W. Y. and Stegen, G. R.: 1974, 'Experiments with Maximum Entropy Power Spectra of Sinusoids', *J. Geophys. Res.* 79, 3019–3022.

Cook, R. K. and Bedard, A. J.: 1971, 'On the Measurement of Infrasound', *Geophys. J. R. Astr. Soc.* **26**, 5–11.

Emmanuel, C. B., Bean, B. R., McAllister, L. G., and Pollard, J. R.: 1972, 'Observations of Helmholtz Waves in the Lower Atmosphere with an Acoustic Sounder', *J. Atmos. Sci.* **29**, 886–892.

Fitzjarrald, D. E.: 1975, 'A Field Observation of Atmospheric Free Convection', submitted to *J. Appl. Meteorol.*

Frisch, A. S. and Businger, J. A.: 1973, 'A Study of Convective Elements in the Atmospheric Surface Layer', *Boundary-Layer Meteorol.* 3, 301–328.

Frisch, A. S. and Clifford, S. F.: 1974, 'A Study of Convection Capped by a Stable Layer Using Doppler Radar and Acoustic Echo Sounders', *J. Atmos. Sci.* **31**, 1622–1628.

Frisch, A. S., Miller, L. J., and Strauch, R. G.: 1974, 'Three-Dimensional Air Motion Measured in Snow', *Geophys. Res. Letters* **1**, 86–89.

Gossard, E. E. and Hooke, W. H.: 1975, *Waves in the Atmosphere*, Elsevier, Amsterdam, 456 pp.

Grossman, R. L.: 1973, 'An Aircraft Investigation of Turbulence in the Lower Layers of the Marine Boundary Layer', Ph. D. Dissertation, Colorado State University, 182 pp.

Hardy, K. R. and Ottersten, H.: 1969, 'Radar Investigation of Convective Patterns in the Clear Atmosphere', *J. Atmos. Sci.* **26**, 666–672.

Hooke, R. H., Hall, F. F., Jr., and Gossard, E. E.: 1973, 'Observed Generation of an Atmospheric Gravity Wave by Shear Instability in the Mean Flow of the Planetary Boundary Layer', *Boundary-Layer Meteorol.* **5**, 29–41.

Kjelaas, A. G. and Ochs, G. R.: 1974, 'Study of Convergence in the Boundary Layer Using Optical Propagation Techniques', *J. Appl. Meteorol.* **13**, 242–248.

Kjelaas, A. G., Gossard, E. E., Young, J. M., and Moninger, W. R.: 1975, 'Dispersion and Spectra of Gravity Waves Probably Generated by a Convective Storm', *Tellus* **27**, 25–32.

Konrad, T. G.: 1970, 'The Dynamics of the Convective Process in Clear Air as Seen by Radar', *J. Atmos. Sci.* **27**, 1138–1147.

Kropfli, R. A. and Miller, L. J.: 1974, 'Dual-Doppler Radar Measurements Within a Hail Producing Storm in Northeast Colorado', *Preprints, AMS Conf. on Cloud Physics*, 227–282.

LaCoss, R. T.: 1971, Data Adaptive Spectral Analysis Methods', *Geophysics* **36**, 661–675.

LeMone, M. A.: 1973, 'The Structure and Dynamics of Horizontal Roll Vortices in the Planetary Boundary Layer', *J. Atmos. Sci.* **30**, 1077–1091.

Lenschow, D. H.: 1970, 'Airplane Measurements of Planetary Boundary Layer Structure', *J. Appl. Meteorol.* **9**, 874–884.

Lhermitte, R. M. and Miller, L. J.: 1970, 'Doppler Radar Methodology for Observation of Convective Storms', *Preprints, AMS Proc. 14th Radar Meteor. Conf.*, 133–138.

Little, C. G.: 1969, 'Acoustic Methods for the Remote Probings of the Lower Atmosphere', *Special Issue on Remote Environ. Sensing. Proc. IEEE-7*, 571–578.

Lumley, J. L. and Panofsky, H. A.: 1964, *The Structure of Atmospheric Turbulence*, Wiley, London, 239 pp.

Markel, J. D.: 1972, 'Digital Inverse Filtering – A New Tool for Format Trajectory Estimation', *IEEE Trans. Audio Electro-acoustics, AU-20*, 129–137.

Miller, L. J. and Frank, H. W.: 1974, 'Three-dimensional Air Motion Within a North-East Colorado Rainstorm', *Preprints, AMS Conf. on Cloud Physics*, 321–327.

Miller, L. J. and Strauch, R. G.: 1974, 'A Dual-Doppler Radar Method for the Determination of Wind Velocities Within Precipitating Weather Systems', *Remote Sensing of Environ.* **3**, 219–235.

Owens, E. J.: 1974, 'Development of a Portable Acoustic Echo Sounder, *NOAA Tech. Report, ERL 258-WPL 31*, U.S. Dept. of Commerce.

Panofsky, H. A.: 1973, 'Boundary Layer Above 30 m', *Boundary-Layer Meteorol.* **4**, 252–264.

Pasquill, F.: 1972, 'Some Aspects of Boundary-layer Description', *Quart. J. Roy. Meteorol. Soc.* **98**, 469–494.

Pennell, W. R. and LeMone, M. A.: 1974, 'An Experimental Study of Turbulence Structure in the Fair-Weather Trade Wind Boundary Layer', *J. Atmos. Sci.* **31**, 1308–1323.

Strand, O. N. and Chadwick, R. B.: 1975, 'A New Procedure for Computing and Analyzing Whitening Filters and Maximum Entropy Spectral Estimates', submitted to *Math. of Computation.*

Tatarski, V. I.: 1961, *Wave Propagation in a Turbulent Medium*, McGraw-Hill, New York, 285 pp.

Taylor, R. J.: 1958, 'Thermal Structures in the Lowest Layers of the Atmosphere', *Australian J. Physics* **11**, 168–176.

Telford, J. W. and Warner, J.: 1964, 'Fluxes of Heat and Vapor in the Lower Atmosphere Derived from Aircraft Observations', *J. Atmos. Sci.* **21**, 539–548.

Ulrych, T. J.: 1972, 'Maximum Entropy Power Spectrum of Truncated Sinusoids', *J. Geophys. Res.* **77**, 1396–1400.

Vulf'son, N. I.: 1961, 'Convective Motions in a Free Atmosphere', Isreael Program for Scientific Translations, Jerusalem (Trans. 1964), Clearinghouse, U.S. Dept. of Commerce, π64–11017, 188 pp.

Warner, J. and Telford, J. W.: 1967, 'Convection Below Cloud Base', *J. Atmos. Sci.* **24**, 374–382.

Woodcock, A. H.: 1942, 'Soaring over the Open Sea', *The Scientific Monthly* **55**, 226–232.

Wyckoff, R. J., Beran, D. W., and Hall, Jr., F. F.: 1973, 'A Comparison of the Low-level Radiosonde and the Acoustic Echo Sounder for Monitoring Atmospheric Stability', *J. Appl. Meteorol.* **12**, 1196–1204.

A Study of Convection Capped by a Stable Layer Using Doppler Radar and Acoustic Echo Sounders

A. S. Frisch and S. F. Clifford

Wave Propagation Laboratory, Environmental Research Laboratories, NOAA, Boulder, Colo. 80302

(Manuscript received 27 January 1974)

ABSTRACT

Simultaneous atmospheric acoustic echo sounding and Doppler radar measurements were used to study some of the characteristics of an unstable boundary layer capped by an inversion. The resultant set of observations shows that the turbulent energy dissipation rate was constant with height up through the inversion layer. Since production from buoyancy and shear were found to be negligible in the upper part of the convective layer, the turbulent energy must be supplied by energy flux convergence. The stress at the top of the momentum layer was estimated to be approximately 2.5 dyn cm^{-2}, assuming the energy flux divergence term was small above the inversion. In addition, the height where the downward heat flux above the inversion went to zero and the height where the shearing stress went to zero were different. For the case analyzed in this paper, the apparent height at which the heat flux went to zero was 0.6 times the height where the shearing stress became zero.

1. Introduction

Meteorological measurements needed to study the dynamics of a heated atmospheric boundary layer, capped by a stably stratified or neutral atmosphere, are not easily acquired. Wind speed and direction are usually obtained from a meteorological tower, by aircraft, or by tracking a balloon. The measurement of various turbulence quantities such as stress, buoyancy production, and turbulent dissipation rate require sophisticated instrumentation and platforms. Most sensors yield only time series of point measurements; consequently, the interpretations of these measurements are limited by the nonstationarity of the atmosphere. Even more importantly, *in situ* techniques lack the spatial sampling capability and overall flexibility characteristic of remote sensors.

The two atmospheric remote sensing techniques used in this case study were atmospheric acoustic echo sounding and meteorological Doppler radar. Using these techniques simultaneously, we were able to measure the turbulent dissipation rate, the vertical wind profile, and to locate regions of production and dissipation of turbulent temperature eddies. With these data we were able to infer the relative importance of the transport of turbulent kinetic energy and pressure fluctuations, and the stress across the top of the inversion layer. The utility of these remote sensors in this work arises from two facts: 1) the intensity of the backscattered acoustic signal is proportional to C_T^2, where $C_T^2=N\epsilon^{-1/3}$*, and 2) the first moment of the backscattered Doppler radar signals is a function of the mean wind field and, under conditions to be specified, the second moment is a function of the turbulent dissipation rate.

Some of these parameters appear in the turbulent kinetic energy equation [Eq. (1)], and if they are known we can deduce the relative importance of various terms in this equation using the acoustic sounder and Doppler radar measurements. The turbulent kinetic energy equation may be written as

$$\frac{\partial\bar{e}}{\partial t}=\underset{\text{I}}{\frac{\boldsymbol{\tau}_s}{\rho}\cdot\frac{\partial\bar{\mathbf{V}}}{\partial z}}+\underset{\text{II}}{\frac{g}{T}\overline{w'\theta'}}+\underset{\text{III}}{\frac{\partial\overline{w'(e+p'/\rho)}}{\partial z}}-\underset{\text{IV}}{\epsilon}=0, \tag{1}$$

where $\mathbf{V}=u\mathbf{i}+v\mathbf{j}+w\mathbf{k}$ is the wind vector, p' pressure, $\boldsymbol{\tau}_s$ shearing stress, ρ air density, θ potential temperature, w vertical velocity, g gravity, and z the height coordinate. The overbar indicates a time average and primes

---

* In this expression N is the rate of destruction of the turbulent temperature fluctuations. Under stationary and horizontally homogeneous conditions, N may be expressed as

$$N=-\overline{w'\theta'}\frac{\partial\bar{\theta}}{\partial z}-\frac{\partial\overline{w'\theta'^2}}{\partial z}$$

[for a more complete discussion see Tatarski (1961)]. In the first term on the right-hand side $\overline{w'\theta'}$ is the vertical flux of potential temperature (w' is the fluctuation in vertical velocity and θ' is the potential temperature fluctuation) and $\partial\bar{\theta}/\partial z$ is the vertical gradient of the mean potential temperature. The second term on the right-hand side is the vertical transport of the temperature variance. In the surface layer (usually the first few tens of meters above the ground), the first term on the right-hand side is dominant compared to the second term (Wyngaard and Coté, 1971). However, above the surface layer, this term may become significant (Lenschow, 1970). This will be discussed in more detail as we examine the data for our case.

denote deviations from that average. We have assumed that the turbulence is stationary in time and is horizontally homogeneous. The terms are defined as follows: I is called the "shear production term"; II is the buoyancy production term; III represents the divergence of (i) the vertical kinetic energy flux given by $e = \frac{1}{2}(u'^2+v'^2+w'^2)$, and (ii) the vertical flux of pressure fluctuations; and IV is the turbulent dissipation rate, i.e., the rate at which turbulent energy is lost through molecular viscosity (see, e.g., Lumley and Panofsky, 1964).

2. The Doppler technique

The measurement of the turbulent dissipation rate using Doppler radar has been described by Gorelik and Mel'nichuk (1963, 1968). This technique uses the fact that the width and shape of the Doppler spectrum is determined by the distribution of radial velocities of the scatterers in the pulse volume. They show that spectral width is influenced by the finite beam width, wind shear, distribution of fall velocities of the scatterers and by turbulence. If the effects of the first three are negligible, then the turbulent dissipation rate can be determined from the width of the Doppler spectrum.

By using the first moment, we estimated the effect of radial wind shear using the method of Sloss and Atlas (1968) and found that under most conditions the shear broadening amounted to less than 0.05 $\mathrm{m}^2\ \mathrm{sec}^{-2}$ and was entirely negligible compared with broadening by turbulence. Measurement from the two Doppler radars reinforce this conclusion. On one occasion there was a radial shear of $5\times10^{-3}\ \mathrm{sec}^{-1}$ affecting one radar and almost no shear affecting the other. Both observed a common volume and yet their dissipation values derived from Doppler spread were essentially identical.

Because of spectral broadening by radial wind shear, Gorelik and Mel'nichuk (1968) restricted their measurements of dissipation to vertical beams. This would enhance the contribution of the fallspeed distribution of the scatterers to the velocity variance. If, as was true in our case, low slant angles are used, the fall velocity contribution is greatly reduced. For example, limiting the slant angle to less than 17° above the horizon reduces the spectral broadening due to fall velocity variance by an order of magnitude compared to that at vertical incidence. The low fall velocity of the chaff used as a tracer also reduces this contribution significantly.

Previous work (Gorelik and Mel'nichuk, 1968) on the Doppler technique did not consider the high-pass spectral filtering of the turbulence spectrum due to the finite transverse extent of the radar beam. This restricted dissipation measurements to ranges where the pulse length was much larger than the transverse beam width. We use the fact that the antenna beam pattern and pulse shape of our Doppler radar may be accurately fitted by two Gaussian curves. The theoretical calculation of the second moment of the Doppler spectrum then depends upon the transverse dimensions of the scattering volume as well as the pulse length and dissipation rate. This additional dependence allows a determination of turbulent dissipation from the minimum (~1 km) to the maximum range of the radars.

3. Theory

Srivastava and Atlas (1972) determined the spatial spectrum of the wind velocity averaged over the pulse volume, in terms of the true velocity spectrum, in the form

$$\Phi_{\bar{v}}(\mathbf{k}) = (2\pi)^6\Phi_v(\mathbf{k})\,|F_P(\mathbf{k})|^2, \tag{2}$$

where $\Phi_{\bar{v}}$ and Φ_v are, respectively, the spectral densities of the volume-averaged and point-measured radial velocities, and $F_P(\mathbf{k})$ is the Fourier transform of the antenna illumination pattern P as a function of spatial wavenumber $\mathbf{k}$. We assume that the condition of narrow beam width holds sufficiently well that the radial velocity may be considered everywhere parallel to the beam axis. Therefore,

$$\Phi_v(\mathbf{k}) \approx \Phi_{11}(\mathbf{k}), \tag{3}$$

where $\Phi_{11}(\mathbf{k})$ is the radial component of the spectral density tensor of the velocity field.

The variance of the radial velocity measured *within* the volume, i.e., from measurements of Doppler spread, expressed in terms of the point-measured and volume-averaged velocity variance is

$$\sigma_{11}^2 = \sigma_{\mathrm{point}}^2 - \sigma_{\mathrm{vol}}^2, \tag{4}$$

or, in terms of their spectra,

$$\sigma_{11}^2 = \int d^3\mathbf{k}\,\Phi_{11}(\mathbf{k})[1-(2\pi)^6|F_p(\mathbf{k})|^2]. \tag{5}$$

We fitted the antenna illumination pattern with a three-dimensional Gaussian distribution

$$P(x,y,z) = \frac{\exp\{-[(y^2+z^2)/(2\alpha^2)+x^2/(2\beta^2)]\}}{(2\pi)^{3/2}\beta\alpha^2}, \tag{6}$$

where x is the direction along the beam axis, and y and z are coordinates transverse to the beam. The constants α and β relate to the beam width and pulse length respectively. The filter function $|F_P(\mathbf{k})|^2$ derives from

$$|F_P(\mathbf{k})|^2 = (2\pi)^{-6}\exp\{-[(k^2-k_x^2)\alpha^2+k_x^2\beta^2]\}, \tag{7}$$

where $k^2=k_x^2+k_y^2+k_z^2$. The assumption of an isotropic tensor for the turbulence spectrum implies that

$$\Phi_{11}(\mathbf{k}) = \frac{E(k)}{4\pi k^2}\left(\frac{k_x^2}{k^2}-1\right), \tag{8}$$

and if the scale sizes of interest are in the inertial subrange, then

$$E(k)=A\epsilon^{\frac{2}{3}}k^{-5/3}, \tag{9}$$

where A is the universal constant [$A\approx 0.47$ (Lumley and Panofsky, 1964)] and ϵ the rate of turbulent energy dissipation. Substituting (7) and (8) into (5), we obtain

$$\sigma_{11}^2=\frac{A\epsilon^{\frac{2}{3}}}{4\pi}\int d^3\mathbf{k}k^{-11/3}\left[1-\left(\frac{k_x}{k}\right)^2\right]$$
$$\times\{1-\exp[-(k^2-k_x^2)\alpha^2-k_x^2\beta^2]\}. \tag{10}$$

Changing to spherical coordinates $(k,\ \theta,\ \phi)$ where $k_x=k\cos\theta$, and integrating, Eq. (10) reduces to

$$\sigma_{11}^2=\tfrac{3}{2}\Gamma(5/3)A(\epsilon\alpha)^{\frac{2}{3}}\left[1-\frac{\gamma^2}{15}-\frac{\gamma^4}{105}\right], \tag{11}$$

where $\gamma^2=1-(\beta/\alpha)^2$ with the restriction that $(\beta/\alpha)\leqslant 1$. For the range of γ of interest in our experiment we need only retain terms of at most order γ^2 in (11) and invert to find

$$\epsilon\approx\alpha^{-1}\left[\frac{\sigma_{11}{}^2}{1.35A\left(1-\frac{\gamma^2}{15}\right)}\right]^{\frac{3}{2}} \tag{12}$$

For the case $(\beta/\alpha)>1$, the equation for the dissipation becomes

$$\epsilon\approx\beta^{-1}\left[\frac{\sigma_{11}{}^2}{1.35A\left(1+\frac{\xi^2}{15}\right)}\right]^{\frac{3}{2}},\quad\text{where}\quad \xi^2=1-(\alpha/\beta)^2. \tag{13}$$

Eqs. (12) and (13) allow the determination of ϵ for the full range of pulse lengths β and beam widths α.

A potential problem in estimating ϵ appears if the maximum wavelength of the inertial subrange is smaller than the largest dimension of the radar pulse volume. Measurements by Myrup (1969) indicate that the spectral slope may differ from the $k^{-5/3}$ law if the measurements are made above the inversion base where the atmosphere is stably stratified. One of his spectra in the stable layer showed the inertial subrange to begin at about 69 m though his averaged spectra of many measurements showed the inertial subrange for this stable layer to begin at a wavelength of about 400 m. The largest effective dimension contained within our beam at 10 km range for our radar was about 150 m.

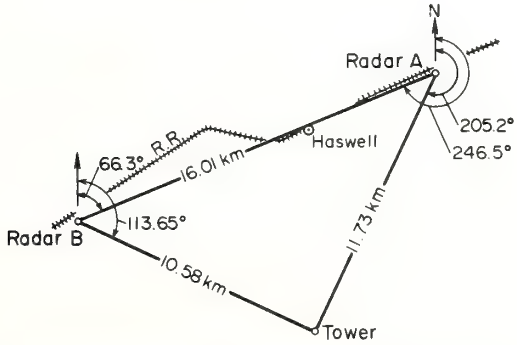

FIG. 1. Haswell site: Radars A and B relative to the 150 m tower.

4. Comparisons with *in situ* measurements

We compared dissipation measurements derived from (12) and (13) with direct observations from the top of a 150 m tower located near Haswell, Colo. The tower stands in the center of a shallow bowl, approximately 75 m deep and 25 km in diameter. The vegetation around the site was buffalo grass about 15 cm high. Fig. 1 shows the relative locations of the two Doppler radars and the tower. Chaff dispensed from a small aircraft acted as a tracer of the atmosphere's turbulent motions. In addition to the Doppler radars, an acoustic sounder (McAllister *et al.*, 1969), located near the tower and operated in the backscatter mode, continuously monitored the local inversion height (Wyckoff *et al.*, 1973).

From the tower data we estimated the dissipation by first time-lagging the vertical component of velocity as measured by a bivane. Then assuming Taylor's hypothesis we calculated the spatial structure function of vertical velocity in a manner similar to that of Record and Cramer (1966). The dissipation rate in the inertial subrange was then calculated from the velocity structure function D_w, using the formula

$$D_w(r)=\overline{[w(x)-w(x+r)]^2}=B\epsilon^{\frac{2}{3}}r^{\frac{2}{3}}. \tag{14}$$

In (14), B is a universal constant, w is the vertical velocity, and the overbar denotes a time average. The displacement r is the effective separation of the two velocity measurements given by $r=\bar{u}\Delta t$, where $\bar{u}$ is the mean wind speed and Δt the time lag. Several time lags were used to determine the extent of the inertial subrange.

To reduce the radar data, the second moment of the Doppler spectrum was estimated by fast Fourier transforming 512 complex radar return signals. The Doppler spectrum was then extracted from the complete signal spectrum by assuming a noise threshold and frequency window which eliminated ambiguities due to folding. The power threshold level was set equal to a fraction (typically $\frac{1}{2}$ to 1) of the average power of the noise contaminated spectrum. Then noise, ground return and image spectra that still remained above the threshold level were removed, retaining only the set of spectral points that formed a continuous set above the threshold. Once the second moment was determined, we estimated the standard deviation of these moments for each height interval, and rejected moments exceeding one standard deviation. Eqs. (12) and (13) were used

TABLE 1. Radar parameters.

Parameter	Radar A	Radar B
Slant angle	0 to 4°	0 to 4°
Azimuth angle	196 to 230°	115 to 130°
Radar range (km)	8.9 to 12.3	8.5 to 12.3
α (m)	0.0084×range	0.0084×range
β (m)	90	90

to estimate ϵ from the radar data. The values of ϵ were averaged over 100 m height intervals. The radar parameters used for this comparison are shown in Table 1. For the tower measurements of dissipation, the bivane was lagged by 5 sec and by assuming Taylor's hypothesis the observed 5 m sec^{-1} wind speed yielded an equivalent separation of 25 m which was used to compute the structure function. Eq. (14) with $B\approx 1.4$ then gave the dissipation rate. Table 2 shows the results of this comparison.

In Table 1, the biggest discrepancy between ϵ computed from the tower data and that computed from the radar observations appears in the data taken with radar A. One possible cause could be ground return in the received signal which would give a contribution to the Doppler variance.

In addition to the Doppler radar measurements of ϵ, there are acoustic Doppler techniques (Beran and Clifford, 1972) that might be used. In a comparison between values of ϵ measured with an acoustic echo sounder and measurements made with a Doppler radar, Gaynor (1974)[1] found good agreement up to 400 m above ground level (AGL). Above 400 m the intensity of the backscattered acoustic signal dropped to values that were too small to achieve an accurate Doppler velocity estimate.

5. Results and discussion

A qualitative picture of a convective layer topped by a stable layer is provided by a facsimile recording of the backscattered acoustic echo (as seen in Fig. 2). The light areas correspond to little backscattered acoustic signal, and the dark areas correspond to larger values. The recording shows a gradual deepening of the thermal plume layer with time (~100 m at 0800 becoming about 300 m thick at 1000 (all times MDT)). Above this layer is a lighter echo region extending approximately 50–100 m above the plume echoes. Immediately above the lighter echo region is a second echo region about 50–100 m thick, and fairly continuous in time. Finally, above the second darker echo region, there is another region of little echo extending from a height of about 400 m to the maximum range of the acoustic sounder. To facilitate the discussion, these layers (see Fig. 3) have been labeled as regions A (30 to 300 m), B (300 to 400 m), C (400 to 500 m) and D (>500 m) at 1000 MDT.

TABLE 2. Comparison of radar dissipation rate (cm^2 sec^{-3}) estimates with instrumented tower for 9 August 1972.

Time (MST)	Radar A	Radar B	Tower
0950 to 1000	21	34	31
1230 to 1245	82	60	61

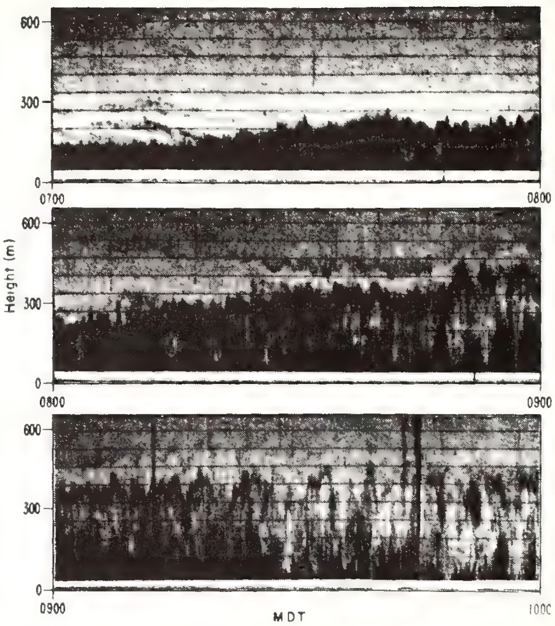

FIG. 2. Backscattered intensity of acoustic signal vs height and time. These data were taken within a few meters of the tower at Haswell on 9 August 1972.

The turbulent kinetic energy dissipation rate ϵ measured with two pulse Doppler radars using chaff targets is shown in Fig. 4. These measurements show that ϵ is essentially constant from a height of 100 m AGL to about 500 or 600 m, where it rapidly decreases to very small values at 0945 to 1000.

One should also note that in region C, the layer thickness is less than the Doppler radar beam width (~120 m thick). Under this condition, ϵ could be under-

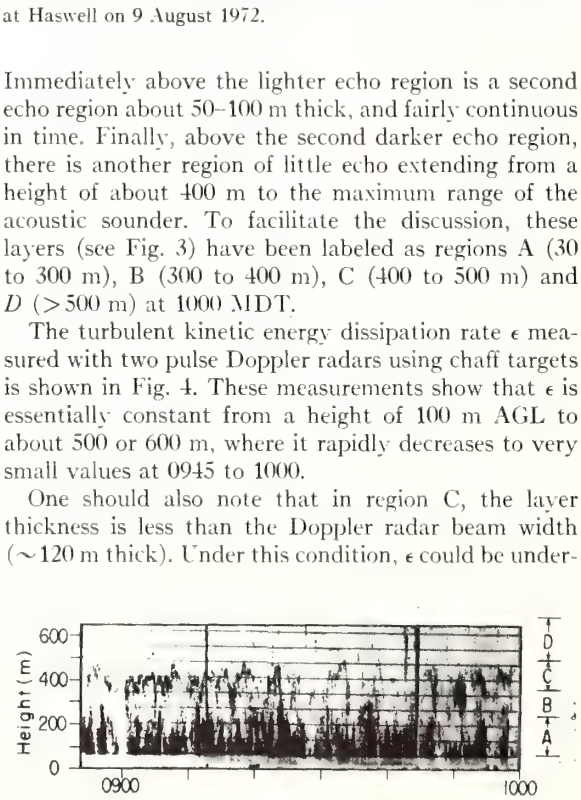

FIG. 3. Expanded scales of the 9 August 1972 backscattered intensity of acoustic signal vs height and time for 0900 to 1000 MDT. Note the inversion height at 400 m just before 1000. These data were taken within a few meters of the tower at Haswell.

---

[1] Private communication.

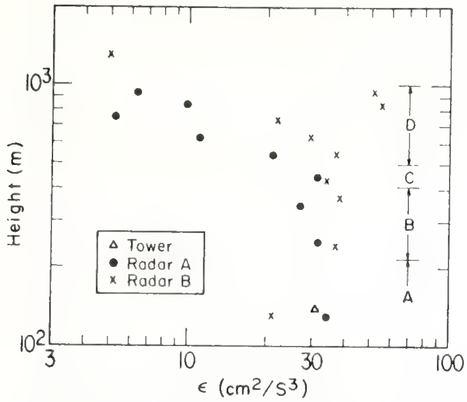

FIG. 4. Dissipation rate vs height for 0950 to 1000 MDT 9 August 1972, near Haswell.

estimated. If ϵ is actually larger in C compared to A and B, this large value could be due to the presence of Kelvin-Helmholtz billows formed in the inversion (Readings *et al.*, 1973).

Part of the shear production term of the turbulent kinetic energy balance equation [term I of Eq. (1)] may be obtained from measurements of mean wind velocity as a function of height using the Doppler radar data (Fig. 5). We use the Doppler radar data for estimates of the mean wind speed and direction since the nearest sounding was taken at 0803, 2 hr prior to the chaff drop. These measurements indicate that $\partial\bar{U}/\partial z$ is very small in region A, increasing in region B, and increasing to large values in regions C and D, and finally becoming very small in the upper part of region D. Thus in region A, term I should be small, while in the other regions it could have relatively large values depending upon the magnitude of $\boldsymbol{\tau}_s/\rho$. A summary of the various acoustic and radar parameters are shown in Table 3 for 1000.

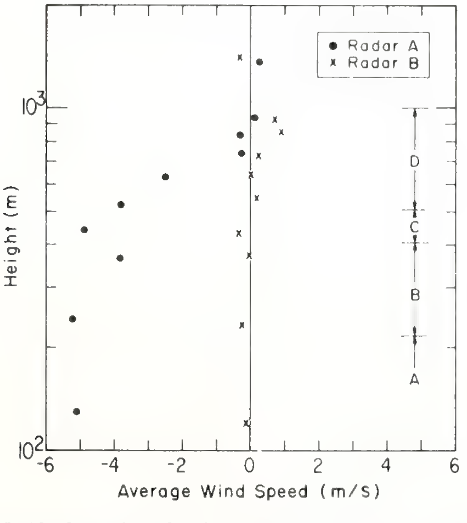

FIG. 5. Wind speeds vs height for 0950 to 1000 MDT 9 August 1972, near Haswell. These two components are approximately perpendicular to each other.

TABLE 3. Parameters at 1000.

Regions	A	B	C	D
C_T^2	large	small	large	small
ϵ	~30	~30	~30	~30 to 5
$\dfrac{\partial\bar{\mathbf{V}}}{\partial z}$	small	large	large	large decreasing to small

The qualitative behavior of term II Eq. (1) may be determined by examination of the acoustic sounder records, measurement of ϵ, and the rawinsonde temperature data taken at 0803 and at 1700. Fig. 1 shows similar patterns at 0800 and at 1000. The main difference is the height and thicknesses of regions A, B, C and D at the two times. The sounding at 0803 shows region B to have an adiabatic lapse rate ($\partial\theta/\partial z\approx 0$). Region C, at the same time, has a very stable potential temperature gradient, and in region D the gradient is less stable. We do not have a sounding at 1000, but we can confidently assume that the adiabatic layer located approximately between 200 and 300 m at 0800 had lifted to the height corresponding to region B at 1000. Between 0945 and 1000, the dissipation rate ϵ (Table 1) was constant through regions A, B, may have increased in C, and decreased with height in D. Since $C_T^2\equiv N\epsilon^{-\frac{1}{3}}$, ϵ is almost constant, then $N\sim C_T^2$. Therefore, from Table 1, we can say that in region A, N is large; in region B, N is very small; in region C, N is large; and in D, N is very small. Now

$$N\approx -\overline{w'\theta'}\frac{\partial\theta}{\partial z}-\frac{\partial\overline{w'\theta'^2}}{\partial z}.$$

Since N is very small in region B, both terms on the right-hand side are small since one would not expect a lack of destruction of temperature variance in the presence of a source of production $[-\overline{w'\theta'}(\partial\bar{\theta}/\partial z)]$. (This is supported by the 0803 sounding which shows that $\partial\theta/\partial z$ changes sign in the region of no acoustic echo and is thus passing through zero in this region.) Comparisons by Neff (1974)[2], of *in situ* tower observations with acoustic echo sounding in a case similar to ours, show that $\overline{w'\theta'}=0$ in the region of weak echoes.

If advection on the large scale is negligible, evaluation of term II in Eq. (1) can be accomplished by assuming $d\theta/dt=\nabla\cdot\mathbf{V}=0$. With these assumptions, we can write

$$\frac{\partial\bar{\theta}}{\partial t}=-\frac{\partial\overline{w'\theta'}}{\partial z}.$$

---

[2] Private communication.

Below the inversion, where $\partial\bar{\theta}/\partial t$ is independent of height, integration yields a linear variation of $\overline{w'\theta'}$ with height, which has been confirmed by Lenschow (1970) and Pennel and LeMone (1974). We can evaluate $(g/T)\overline{w'\theta'}|_{z_s}$ by using two soundings (Fig. 6) at 0803 and 1700. This gives an average value of 33 cm² sec^{-3}.

Assuming steady state and recalling that shear production is small, we find for region A that

$$\frac{\partial}{\partial z}\overline{w'(e+p'/\rho)}=(g/\theta)\overline{w'\theta'}|_{z_s}(1-z/z_i)-\epsilon$$
$$\approx 33(1-z/z_i)-31 \text{ cm}^2 \text{ sec}^{-3}. \quad (15)$$

Thus, the height divergence of the vertical flux of the sum of kinetic energy and pressure fluctuation is positive near the ground, changing sign at about $0.1z_i$ and then becoming even larger near the top of A. This behavior of the divergence is consistent with aircraft observations of Lenschow (1970) and Pennel and LeMone (1974). In region C, there is a strong echo, and Fig. 6 indicates that there was a stable temperature gradient associated with this layer at 0803. Thus, there would be a negative heat flux in this region associated with the entrainment of air from the stable layer. This would not be reflected in the soundings since $\overline{w'\theta'}$ represents an average over most of the day. At the bottom of region D, the turbulent dissipation rate is large decreasing with height to small values near the top.

Since $\partial V/\partial z$ also approaches zero with height at the top of layer D, and assuming energy dissipation to be equal to mechanical production, we estimate the component of $\boldsymbol{\tau}_s$ parallel to the wind shear to be on the order of 2.5 to 3.0 dyn cm^{-2}.

6. Comparisons with Tennekes' model

The non-zero value for ϵ at the inversion height is different from that assumed by Tennekes (1973). In his model for the inversion height, he assumed $\epsilon=0$ near the inversion. It is interesting, however, to compare the height of the inversion vs time using his model. For the morning case, his model gives the inversion height as

$$h\approx\left[\frac{7}{5}\frac{(\overline{\theta'w'})_n}{\gamma\tau}\right]^{\frac{1}{2}}t, \quad (16)$$

where γ is the lapse rate and τ the time scale of the initial increase of $\overline{w'\theta'}$ with time at sunrise. He estimates τ from Deardorff's (1967) measurements to be ~ 10^4 sec. The turbulent temperature flux $(\theta'w')_n$ is evaluated at noon. From the soundings at 0803 and 1700, the average value of $\overline{w'\theta'}$ was 0.10 m (°C) sec^{-1}. Since this includes the early morning in the average, it is undoubtedly underestimating the noon values. With $\gamma\approx10^{-2}$ (°C) m^{-1} and sunrise at 0700, the 1000 MDT value of h would be 380 m as compared with about 400 m for the inversion height indicated by the sounder.

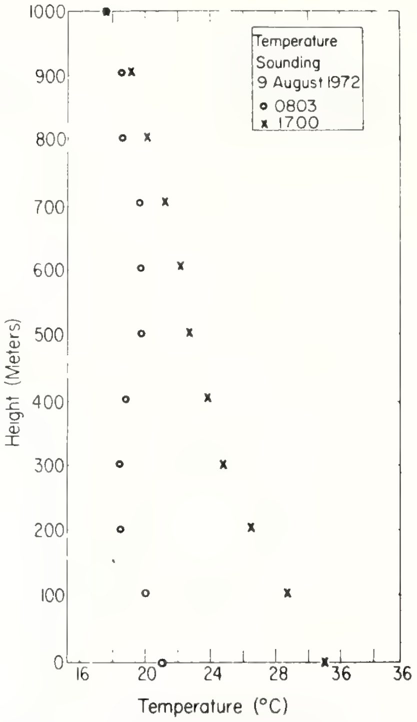

FIG. 6. Temperature soundings for 0803 and 1700 on 9 August 1972.

7. Conclusions

We see that the use of simultaneous acoustic echo soundings and dual Doppler radar observations can provide useful quantitative measurements within the planetary boundary layer. For our particular case, the acoustic echo sounder was used to delineate the height of the inversion base, and the height at which the heat flux became essentially zero. The Doppler radars were used to measure the mean wind as a function of height and also to measure the turbulent dissipation rate. For the first time, comparisons were made between the Doppler-radar-measured dissipation rate and the dissipation rate measured from an instrumented tower. Good agreement was found between the two.

The dissipation rate was constant with height through the convective layer and remained large for about 200 m above the inversion base. In addition, the wind shear was very small within the convective region. By using this information, and the fact that $\partial\bar{\theta}/\partial t$ was independent of height in the convective layer, we infer that there must be a convergence of both the vertical flux of turbulent kinetic energy and pressure fluctuations as the inversion base is approached from below.

Also, it appears that the height where the downward heat flux above the inversion base becomes very small (at the top of C where the acoustic echo goes to zero) is lower than the height where the turbulent dissipation rate drops to very small values (see Fig. 3).

Acknowledgments. The authors would like to thank N. M. Kohn and F. H. Merrem for their skillful programming; R. G. Strauch, L. J. Miller and E. E. Gossard for many helpful discussions; F. F. Hall and his co-workers for the use of the acoustic sounder data; and R. S. Lawrence for his skillful piloting of the chaff dispensing aircraft.

REFERENCES

Beran, D. W., and S. F. Clifford, 1972: Acoustic Doppler measurements of the total wind vector. *Preprints Second Symp. Meteorological Observations and Instrumentation*, San Diego, Calif., Amer. Meteor. Soc., 100–109.

Deardorff, J. W., 1967: Empirical dependence of the eddy coefficient for heat upon stability above the lowest 50 m. *J. Appl. Meteor.*, **6**, 631–643.

Gorelick, A. G., and Yu. V. Mel'nichuk, 1963: Radar study of dynamic process in the atmosphere. *Tr. Vses. Nav. Meteor. Souesh.*, No. 5.

—, and —, 1968: A new method for measuring dissipation rate of turbulence in clouds and precipitation using conventional radar. *Proc. Third All-Union USSR Radar Meteor. Conf.*, 150–156.

Lenschow, D. H., 1970: Airplane measurements of planetary boundary layer structure, *J. Appl. Meteor.*, **9**, 874–884.

Lumley, J. L. and H. A. Panofsky, 1964: *The Structure of Atmospheric Turbulence.* London, Wiley, 239 pp.

McAllister, L. G., J. R. Pollard, A. R. Mahoney and P. S. R. Shaw, 1969: A new approach to the study of atmospheric structure. *Proc. IEEE, Special Issue Remote Environ. Sensing*, 579–587.

Myrup, L. O., 1969: Turbulence spectra in stable and convective layers in the free atmosphere, *Tellus*, **3**, 341–354.

Pennell, W. T., and M. A. LeMone, 1974: An experimental study of turbulence structure in the fair weather trade wind boundary layer. *J. Atmos. Sci.*, **31**, 1308–1323.

Readings, C. J., E. Golton and K. A. Browning, 1973: Fine-scale structure and mixing within an inversion. *Boundary-Layer Meteor.*, **4**, 275–287.

Record, F. A., and H. E. Cramer, 1966: Turbulent energy dissipation rates and exchange processes above a non-homogeneous surface. *Quart. J. Roy. Meteor. Soc.*, **92**, 519–532.

Sloss, P. W. and D. Atlas, 1968: Wind shear and reflectivity gradient effects on Doppler radar spectra. *Preprints 13th Radar Meteor. Conf.*, Montreal, Amer. Meteor. Soc., 44–49.

Srivastava, R. C., and S. D. Atlas, 1972: The effects of a finite radar pulse volume on turbulence measurements. *Preprints 15th Radar Meteor. Conf.*, Urbana, Ill., Amer. Meteor. Soc., 297–302.

Tatarski, V. I., 1961: *Wave Propagation in a Turbulent Medium.* New York, McGraw-Hill, 285 pp.

Tennakes, H., 1973: A model for the dynamics of the inversion above a convective boundary layer. *J. Atmos. Sci.*, **30**, 558–567.

Wyckoff, R. J., D. W. Beran, and F. F. Hall, 1973: A comparison of the low level radiosonde and the acoustic echo sounder for monitoring atmospheric stability. *J. Appl. Meteor.*, **12**, 1196–1204.

Wyngaard, J. C., and O. R. Coté, 1971: The budgets of turbulent kinetic energy and temperature variance in the atmospheric surface layer. *J. Atmos. Sci.*, **28**, 190–201.

Geophysical Research Letters 1, 86-89, June 1974.

THREE-DIMENSIONAL AIR MOTION MEASURED IN SNOW

A. S. Frisch, L. J. Miller, and R. G. Strauch

NOAA/ERL/Wave Propagation Laboratory
Boulder, Colorado 80302

Abstract. In this letter, we present the results of a method that uses two Doppler radars to observe the three-dimensional wind field during light snowfall. These radars are designed to scan in a series of tilted planes, passing through the two radar positions. From the mean Doppler shifts in the frequency spectra we can determine average radial velocities within the pulse volumes. Since the two radars do not observe the same volume increments at the same time, spatial interpolation is needed before the radial velocities can be combined into a two-dimensional velocity field at a set of common coordinates within each plane. The estimated terminal fall velocity of the snow is subtracted from the particle velocity to obtain the true air motion in the plane. The air motion component normal to the plane is obtained by integrating the equation of continuity in cylindrical coordinates starting with the surface boundary condition at the plane of zero elevation. The velocity field in the common planes scanned by the radars is then transformed into a rectangular coordinate system with one axis oriented parallel to the average wind direction. After the mean wind field is removed from the results, a well organized "eddy" wind field is evident.

Radar Equipment

The two-dimensional particle velocity field in a plane is obtained from measurements made in the plane by two nearly identical coherent radars. The radar beams scan over each tilted plane in 16, 32, or 64 azimuthal increments each of which is sampled in 24 range gates. After scanning a plane, the radar antennas are stepped up 1 deg to another plane. In this manner, the two-dimensional velocity field in a predetermined volume of space can be measured. The time needed to scan each plane is 32 sec, and a scan of the whole volume typically requires approximately 3.5 min.

The bipolar video data from two phase-quadrature channels is recorded on digital magnetic tape for off-line Doppler processing and analysis. For the data we present here, 512 radar pulses were used to sample each range "bin" (0.262 sec dwell time at a PRP of 512 μsec). This dwell time is enough to keep the standard deviation of the mean radial velocity estimate to less than 0.1 m/sec (Lhermitte and Miller, 1970) for the wavelength (3.2 cm) and signal-to-noise power ratio of these Doppler radar systems.

Copyright 1974 by the American Geophysical Union.

Mean Radial Velocity

The Doppler frequency shift was estimated from the discrete Fourier transform of the complex time series of the phase-quadrature signals from each range gate. The Doppler spectrum was extracted from the complete frequency spectrum by choosing an empirical noise power threshold and frequency window which eliminated the additive noise portion of the spectrum. The power threshold level was set to a fraction (typically 0.5 to 1) of the average power of the noise-contaminated spectrum. Ground return and image peaks caused by small errors in the 90 deg phase shift demodulation were removed by the frequency window. The mean Doppler shift and the spread of the Doppler spectrum were estimated from the remaining set of spectral points.

Coordinate System and Velocity Calculations

Two radial velocity estimates, derived from two radars scanning a common plane of given tilt angle, are sufficient to resolve the two-dimensional vector velocity in that plane. The particle velocity components are perpendicular and parallel to the radar baseline (Miller, 1972), and are initially expressed in a cylindrical coordinate system. The two-dimensional particle velocity field is converted to a two-dimensional air motion field by subtracting the estimated terminal fall velocity of the snowflakes. Integration of the continuity equation ($\vec{\nabla} \cdot \vec{v} \approx 0$) in cylindrical coordinates yields the component of air motion normal to the plane.

Mapping the wind field by simultaneous observation of the same volume by both radars is impractical, but if the field can be assumed to change little during the time required to scan a single plane (typically $\leq 1/2$ min), each radar can scan that plane independently. Spatial interpolation is applied to the two radial velocity fields to obtain new values at common grid points which can be combined to obtain total velocity in cylindrical coordinates. After integrating the continuity equation in cylindrical coordinates, the velocity field is transformed into a Cartesian coordinate system with the x, y plane chosen parallel to the local ground plane.

Turbulent Dissipation Rate Estimate

In addition to the first moment information provided by the Doppler spectrum, we can use the second moment information to estimate the turbulent dissipation rate, ϵ. We use the technique described by Gorelick and Mel'nichuk (1968) and modified by Frisch and Clifford (1974). They found that ϵ is related to the variance of the

Doppler spectrum, σ^2, by

$$\epsilon \simeq \alpha^{-1}\left\{\frac{\sigma_{11}{}^{2}}{0.68(1-\gamma^{2}/15)}\right\}^{3/2}$$

where $\gamma^2 = 1-(\beta/\alpha)^2$ and α and β are functions of the beam width and pulse length.

Among the sources of errors in this measurement are (a) spectral broadening due to the finite width of the radar beam, (b) non-uniform distribution of reflectivity within the pulse volume, and (c) spectral broadening due to wind shear parallel to the beam. For our measurements, the last source is probably the most important. Using the method of Sloss and Atlas (1968), we find this effect to be small with the values of wind shear found in the mean wind field, especially between 100 and 400 m.

Experiment and Results

The two radars were located near Boulder, Colorado (see Fig. 1). The data were taken during a light, steady snow on 3 January 1972 from 1127 to 1141 MST. There was a NNE wind at 5 m/sec. The Denver sounding (at 1100) showed a negative potential temperature gradient below 200 m, while above 200 m this gradient was slightly positive. The scanning of the common plane was 8 deg to 0 deg to 8 deg in 1 deg increments. Since it took approximately 30 sec to scan each plane, we used the two sequences of plane scans (8 deg to 0 deg and back to 8 deg) and interpolated each plane angle to a common time. The total observed field covered a volume in space approximately 6x6x1 km, thus for brevity, we show only a few of the possible planes.

Figs. 2 and 3 show the projection of the vector velocity fluctuation field relative to the mean velocity in the pulse volume in several of the yz and xz planes, which are separated by 300 m. The xz planes are vertical planes parallel to the mean wind, and the yz planes are vertical planes perpendicular to the mean wind. We show the velocity deviation fields because it is difficult to see any organized structure in the total vector wind field while clear patterns appear when the average wind over the volume is subtracted from the field of total velocity. For example, Fig. 2 shows coherent velocity patterns in the form of an elliptical rotor (note that the height scale is 5 times the horizontal scale). Fig. 3 consists of planes approximately parallel to the mean wind, and shows a zone of convergence that is coherent for at least 900 m in the y direction and tilted

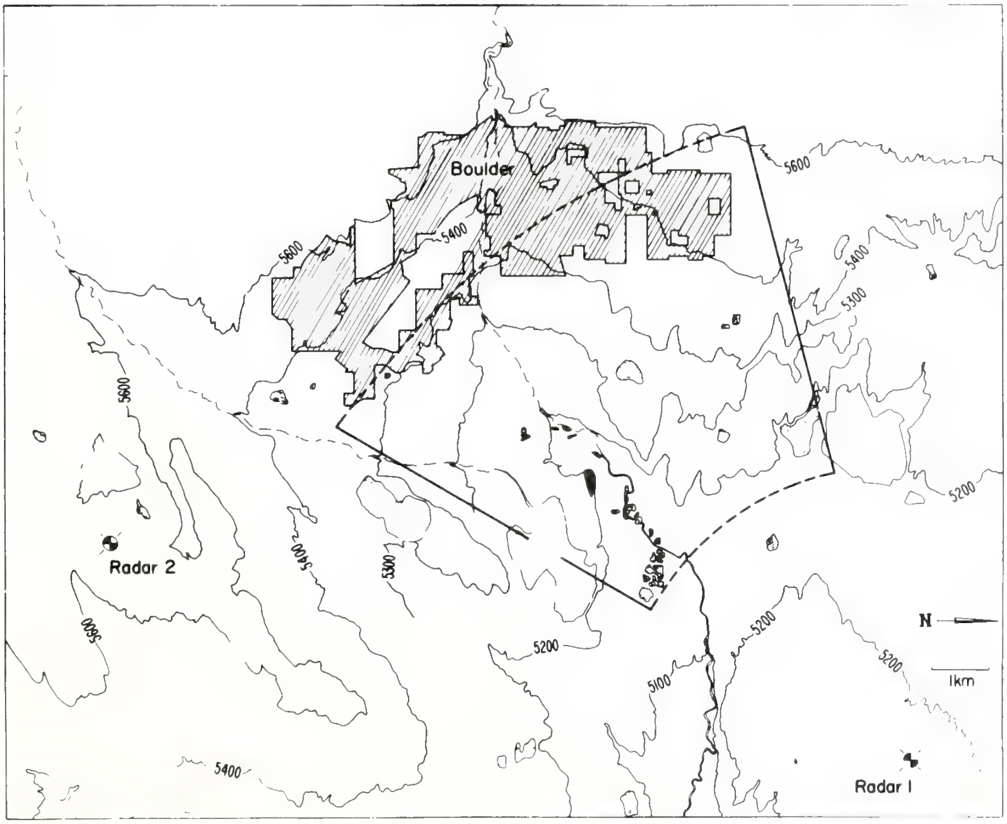

Fig. 1. Radar positions relative to area scanned.

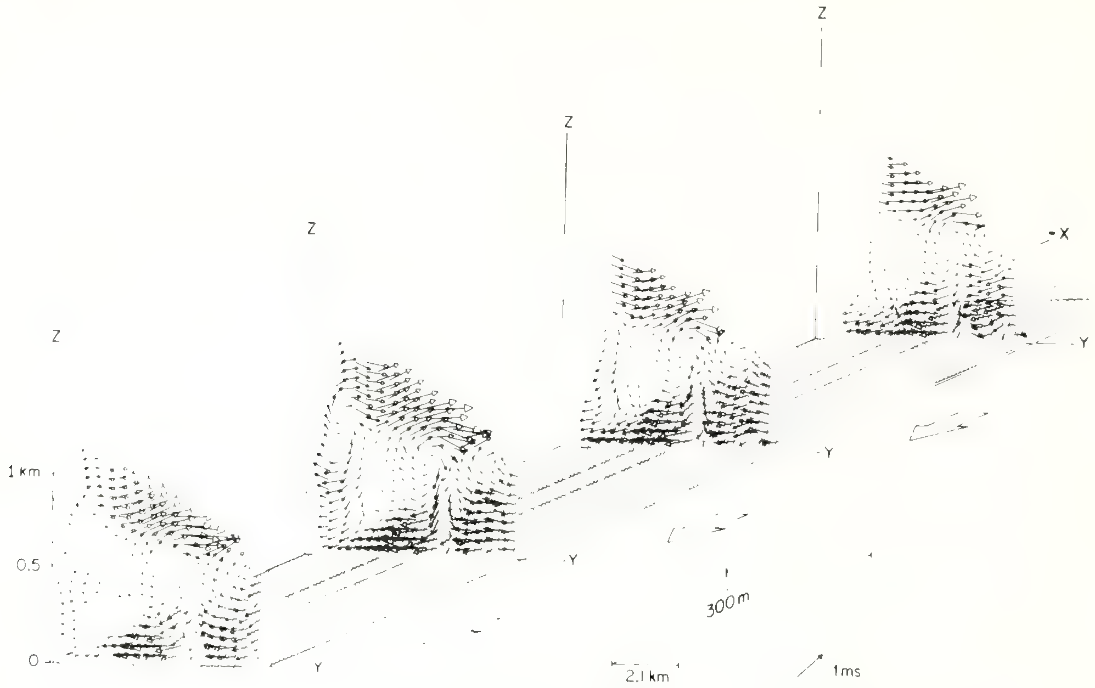

Fig. 2. z-y components of velocity fluctuations in planes approximately perpendicular to the mean wind. Note that the horizontal scale is compressed 5 to 1 relative to the vertical scale. The dashed lines show the location of the other set of planes.

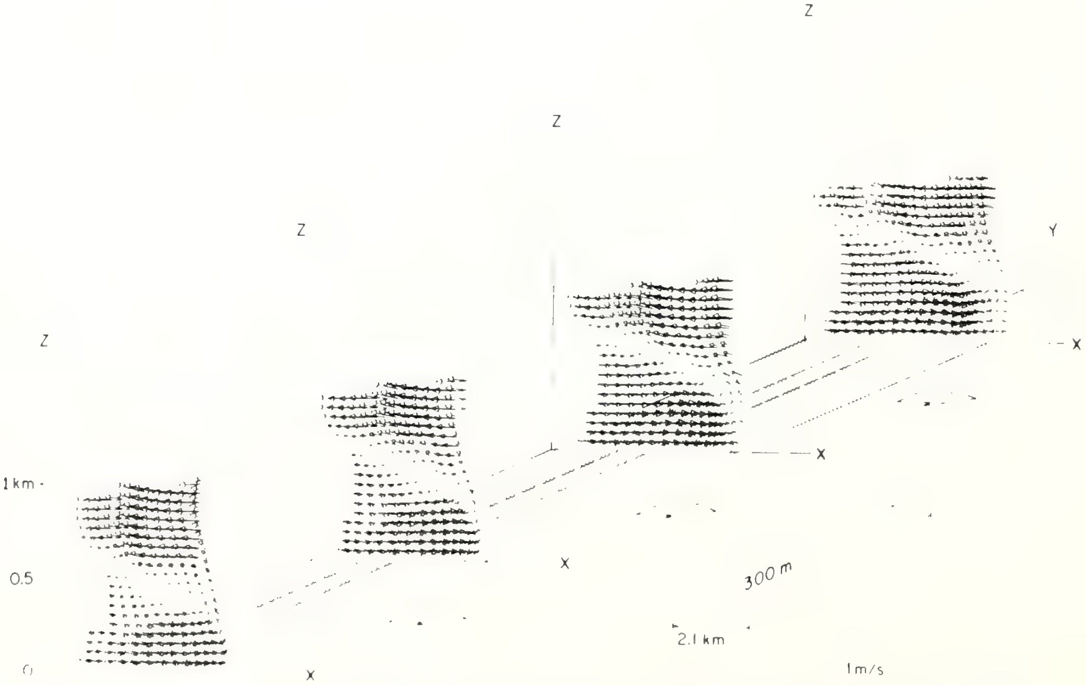

Fig. 3. z-x components of velocity fluctuations in planes approximately parallel to the mean wind. Note that the horizontal scale is compressed 5 to 1 relative to the vertical scale. The dashed lines show the location of the other set of planes.

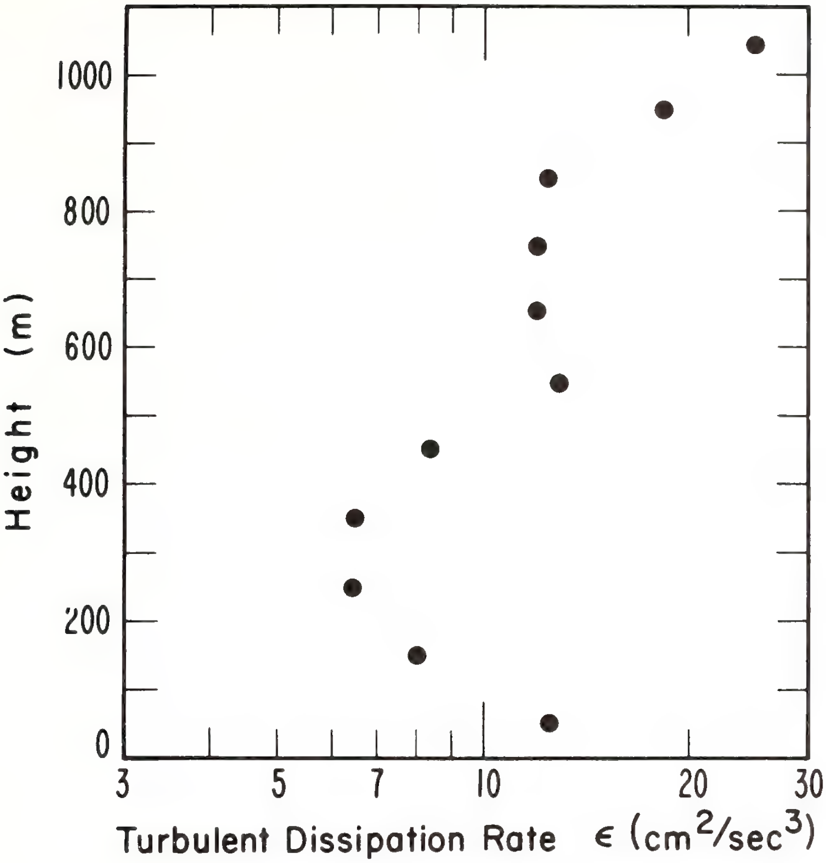

Fig. 4. Dissipation rate of turbulent kinetic energy, ϵ, as a function of height.

at approximately 20 deg from the horizontal. The dashed lines in the center of Fig. 2 show the relative position of the planes in Fig. 3 and vice versa.

The calculations of ϵ, shown in Fig. 4, are averaged over 100 m height increments. From the ground, ϵ decreases with height up to 300 m, where it starts increasing. The increase with height continues (from 7 to 13 cm^2/sec^3), up to 500 m near the center of the elliptical patterns. Above 550 m, ϵ is constant to 850 m, where it again increases with height (from 13 to 22 cm^2/sec^3). However, there are less data at greater heights, and the sampling error is larger. These results differ from those of the convective boundary layer studied by Frisch and Clifford (1974), who found that ϵ was approximately constant with height from near ground to the base of an elevated inversion.

Thus one can see some of the potential value of the dual Doppler system in obtaining data in the atmospheric mesoscale range. At the present time there are no other techniques that are capable of yielding the detailed spatial velocity structures provided by the dual Doppler technique. These results show that there is a large amount of middle scale structure that needs to be studied to determine how important these structures are and the role they take in the atmosphere.

References

Frisch, A. S., and S. F. Clifford, A study of convection capped by a stable layer using Doppler radar and acoustic echo sounders, accepted for publication by J. Atmos. Sci., 1974.

Gorelick, A. G., and Yu. V. Mel'nichuk, A new method for measuring dissipation rate of turbulence in clouds and precipitation using conventional radar, Radar Meteor. Proc. of the Third All-Union Conf., Moskva, NOAA Transl., U.S. Dept of Commerce IPST Cat. No. 5809, 1968.

Lhermitte, Roger M., and L. J. Miller, Doppler radar methodology for the observation of convective storms, AMS Proc. 14th Radar Meteor. Conf., 133-138, 1970.

Miller, L. J., Dual-Doppler radar observations of circulation in snow conditions, AMS Proc. 15th Radar Meteor. Conf., Boston, Mass., 309-314, 1972.

Sloss, P. W., and D. Atlas, Wind shear and reflectivity gradient effects on Doppler radar spectra, AMS Proc. 13th Radar Meteor. Conf., 44-49, 1968.

(Received April 18, 1974;
accepted May 17, 1974.)

Journal of Geophysical Research 80, 5051-5060, December 1975.

Secondary Flow Fields in the Planetary Boundary Layer Estimated From Dual-Doppler Radar Measurements During Snow Conditions

A. S. Frisch, L. J. Miller, and R. G. Strauch

Wave Propagation Laboratory, Environmental Research Laboratories, NOAA, Boulder, Colorado 80302

In this paper we present observations of the secondary flow patterns in the planetary boundary layer by using a dual-Doppler radar system with snow as an air motion tracer. The results show definite patterns of flows, with scale sizes, and the distribution of energy consistent with a secondary flow model of Brown (1970) The sense of rotation is different, but this may be due to the lack of a wind speed high enough to obtain a fully developed secondary flow. The Doppler-derived turbulent dissipation rate shows an initial decrease with height followed by an increase in an elevated shear layer.

Introduction

In this paper we present detailed velocity fields measured in the planetary boundary layer using snow as an air motion tracer for dual-Doppler radars. We have calculated profiles of the average wind, variance of the three wind components, and the turbulent dissipation rate to help interpret the air motion.

Some initial results of three-dimensional air motion measurement using the dual-Doppler technique were presented by *Frisch et al.* [1974], and a description of the method used was given by *Miller and Strauch* [1974]. Several steps are needed to obtain estimates of the three components of wind velocity.

1. The radars are scanned in a series of common planes [*Lhermitte and Miller*, 1970], each plane taking between 10 and 30 s for a scan. For our data it took 30 s to scan each plane. The radar was gated to give 24 pulse volumes along each radial beam, and 16 beams were used per plane. Each pulse volume was about 75 m long, and its dimension transverse to the beam varied from 100 to 250 m in diameter. There was a 300-m separation along each beam between each pulse volume.

2. The raw data were converted to radial velocity fields relative to each radar.

3. Finally, through a series of manipulations involving interpolation, differentiation of the velocity field, and integration of the mass continuity equation the final three-dimensional wind fields were obtained.

The measurement of the turbulent dissipation rate by a Doppler radar was described by *Frisch and Clifford* [1974]. The dissipation measurement relates the variance estimate of the velocity spectrum within each radar pulse volume. It assumes that the largest dimension of the radar pulse volume is smaller than the largest scale of the inertial subrange for velocity. Aircraft measurements by *Myrup* [1969] indicate that this is a reasonable assumption for our pulse volume dimensions.

Experiment and Results

We wanted to know if it is possible to distinguish between organized secondary flow motion and random turbulence in the planetary boundary layer. With such ability we could obtain information about the scales and how the secondary motions are produced. In turn, from these scales and their distributions we could learn about the source of energy of the air motions. The secondary flow energy production is expected to come either from inflection point instabilities located throughout the boundary layer or from convective instability predominantly at the surface. There is evidence in the data of both convective-induced motion and motion associated with inflection point instability in the upper portion of the boundary layer.

Our two radars were located near Boulder, Colorado. The data were taken during a light, steady snow on January 3, 1972, from 1127 to 1141 MST. The wind was 5 m s from NNE. The Denver temperature sounding (Figure 1), whose release point was approximately 30 miles (48 km) from the radar experiment, showed a slightly unstable temperature gradient below 200 m and a stable temperature gradient from 200 m to about 3 km. During this time the radar-scanned planes tilted from 0° to 8° in 1° increments. The Doppler frequency shift at each radar was estimated from signals in each range gate. The radial dimension of each range gate was approximately 75 m, the beamwidth was about 0.9°, and there were 16 azimuthal beams made up of 24 range gates. For the data we present here there are 512 radar pulse samples from each range gate (0.262-s dwell time at a pulse repetition period of 512 μs). The standard deviation of error in the mean radial velocity estimate at each range gate is less than 6 cm/s [*Lhermitte and Miller*, 1970] for this sample length. Additional smoothing of the data is done by interpolating the radar data to grid points in a cylindrical coordinate system which reduces the error to less than 3 cm/s [*Miller and Strauch*, 1974]. At this stage in the processing one has a two-dimensional velocity field in each plane. The divergences in these two-dimensional fields are then calculated, and the velocity component perpendicular to each tilted plane is found by integrating the

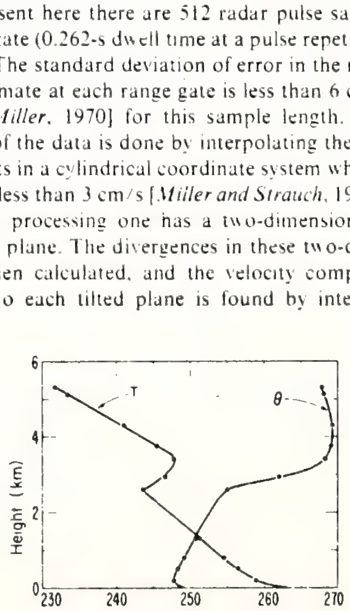

Fig. 1. Denver sounding for January 3, 1972, at 1103 MST; *T* is temperature and *θ* is the potential temperature.

Copyright © 1975 by the American Geophysical Union.

equation of continuity in the anelastic form $\nabla \cdot \rho \mathbf{v} = 0$, where ρ is ambient density and $\mathbf{v}$ is the velocity perturbation. The date, time, and scanning geometry are given in the tabulation below. The data were converted from the cylindrical coordinate system to a series of velocity vectors projected into horizontal planes at different heights and to a series of orthogonal vertical planes.

Date	January 3, 1972
Time	1127–1141 MST
Base line angle	194.6° (14.6°)
Common plane angles used	0°–8°
Minimum range	5.805 km (both radars)
Maximum range	12.71 km (both radars)

Some secondary flow models [e.g., *Brown*, 1970] and measurements [e.g., *LeMone*, 1973] are split into a mean and a perturbed, or secondary, flow, with the mean of the horizontal wind $\bar{U}(z)$ removed at each height. Therefore we treated our wind fields in the same manner. This enabled us to isolate the secondary flow patterns from any influence due to the changes of the mean wind with height. The mean horizontal wind at each height was the average of the wind at all available grid points in each horizontal plane. This average was then subtracted from the value at each grid point. For our observations we chose the x direction parallel to the volume-averaged horizontal wind direction within the measured volume (this volume is approximately 5 × 5 km in area at the base and a little more than 1 km in height). Figure 2 shows the velocity projec-

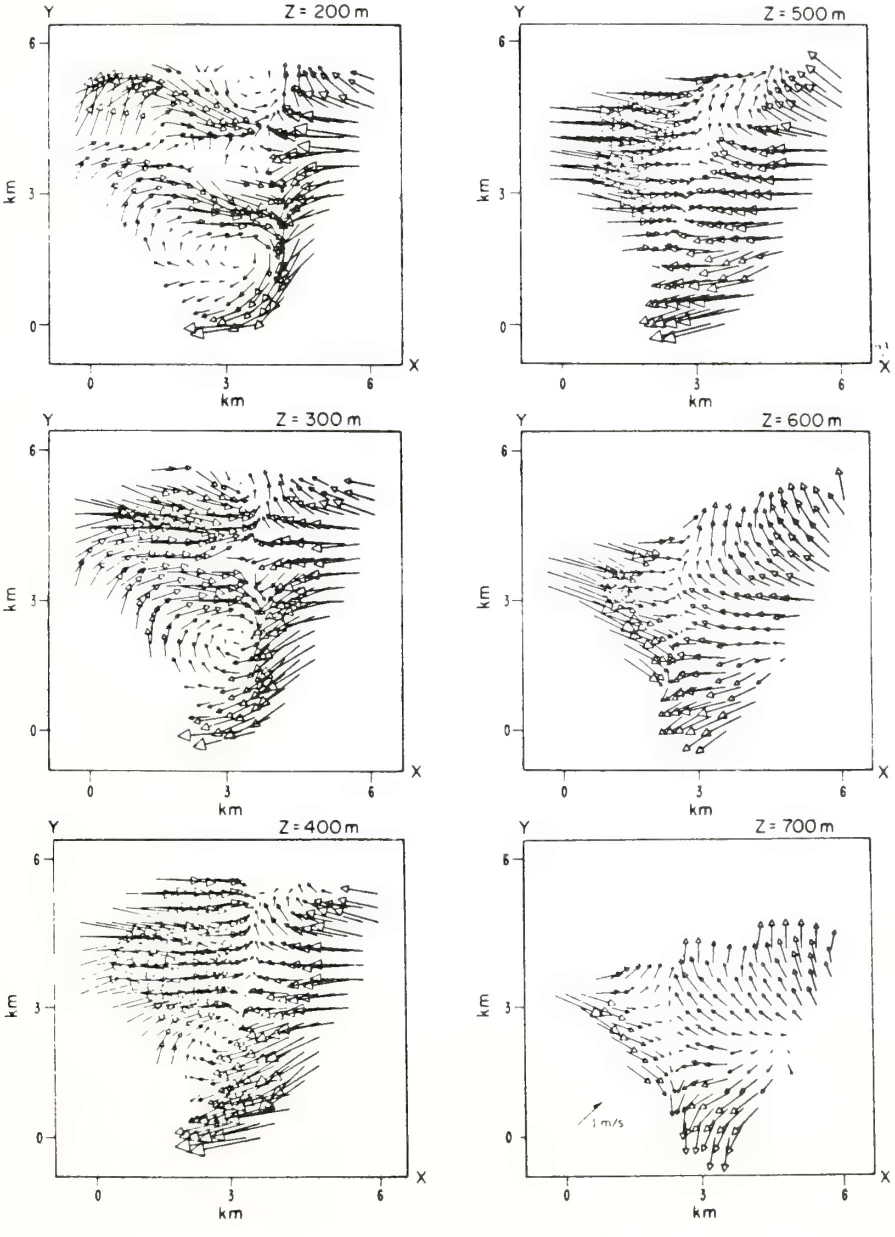

Fig. 2. Velocity vector projections into a series of horizontal planes. The mean velocity in each plane has been removed.

tions in horizontal planes; Figures 3 and 4 show the flow in vertical planes parallel and perpendicular to the mean flow. At every height there were regions of convergence starting with a zone of convergence aligned almost perpendicular to the mean wind at 200 m, which gradually rotated clockwise with increasing height, reaching an angle of about 30° at 500 m. Figure 3 shows the projection of the wind velocity on vertical planes parallel to the mean wind. In Figure 3*b*, at Y = 2.4 km, the components of velocity indicate counterrotating vortices at heights above 500 m. Figure 4 shows planes perpendicular to the mean wind direction. Again, there were regions of rotation, convergence, and divergence. One region of rotation appeared at X = 1.8 (Figure 4*b*) centered at Y = 2 km and Z = 500 m. This rotation remained coherent through X = 5.1 km (Figure 4*c*). Its horizontal cross section was elliptical, with a 2-km horizontal axis and a 600-m vertical axis. Adjacent to this feature motion (Figure 4*b*) at X = 3.0 km, Y = 4.5 km, and Z = 300 m one can see a smaller elliptical-shaped vortexlike motion rotating in the same direction. Figure 5 shows the average wind that was removed in calculations to obtain the secondary flow fields. This shows that most of the wind shear is in the x direction, with a very weak shear transverse to the volume-averaged flow direction at 600 m.

Having the spatial distribution of the separate components of the velocity field, we can determine how the kinetic energy of the secondary flow is concentrated among the components

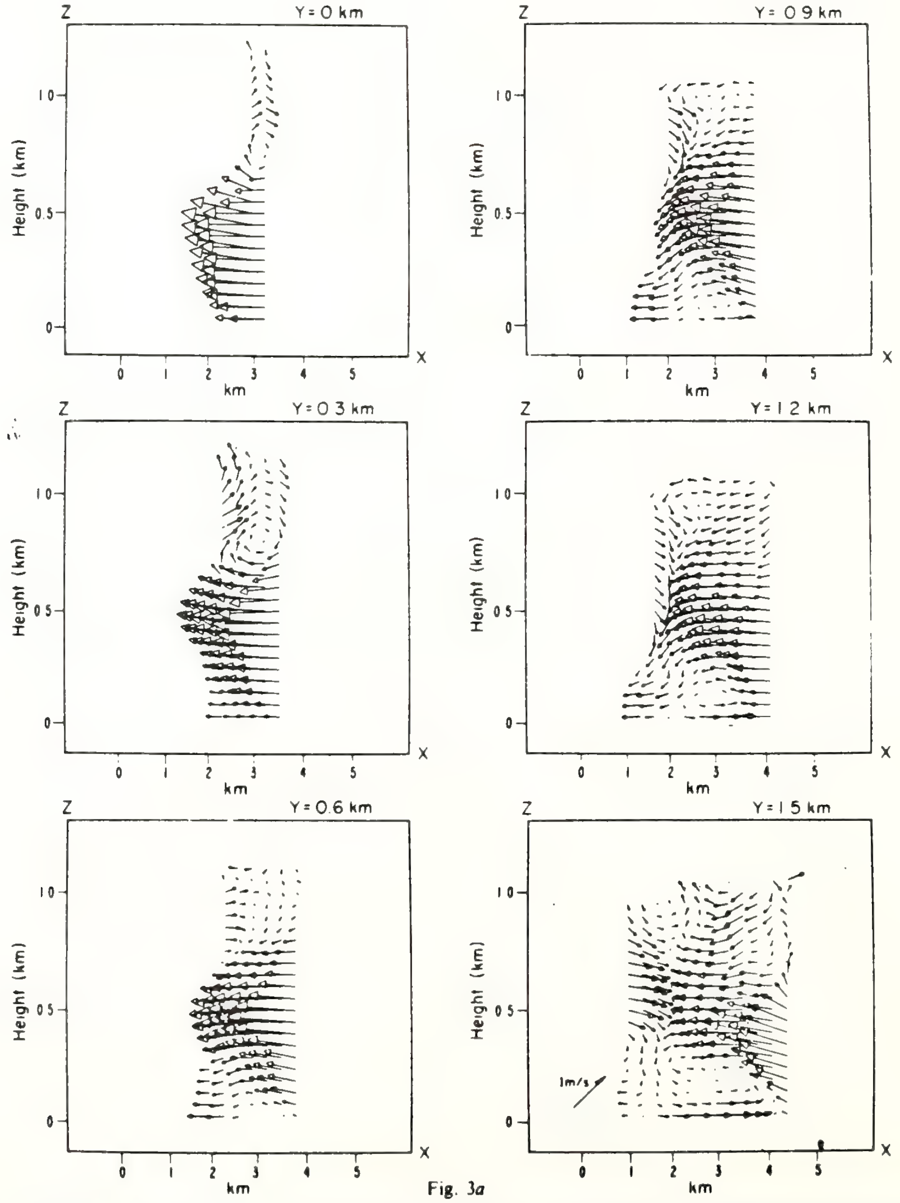

Fig. 3a

Fig. 3. Velocity vector projections in a series of XZ planes, parallel to the volume-averaged wind direction and separated by 300 m. The mean wind velocity at each height has been removed.

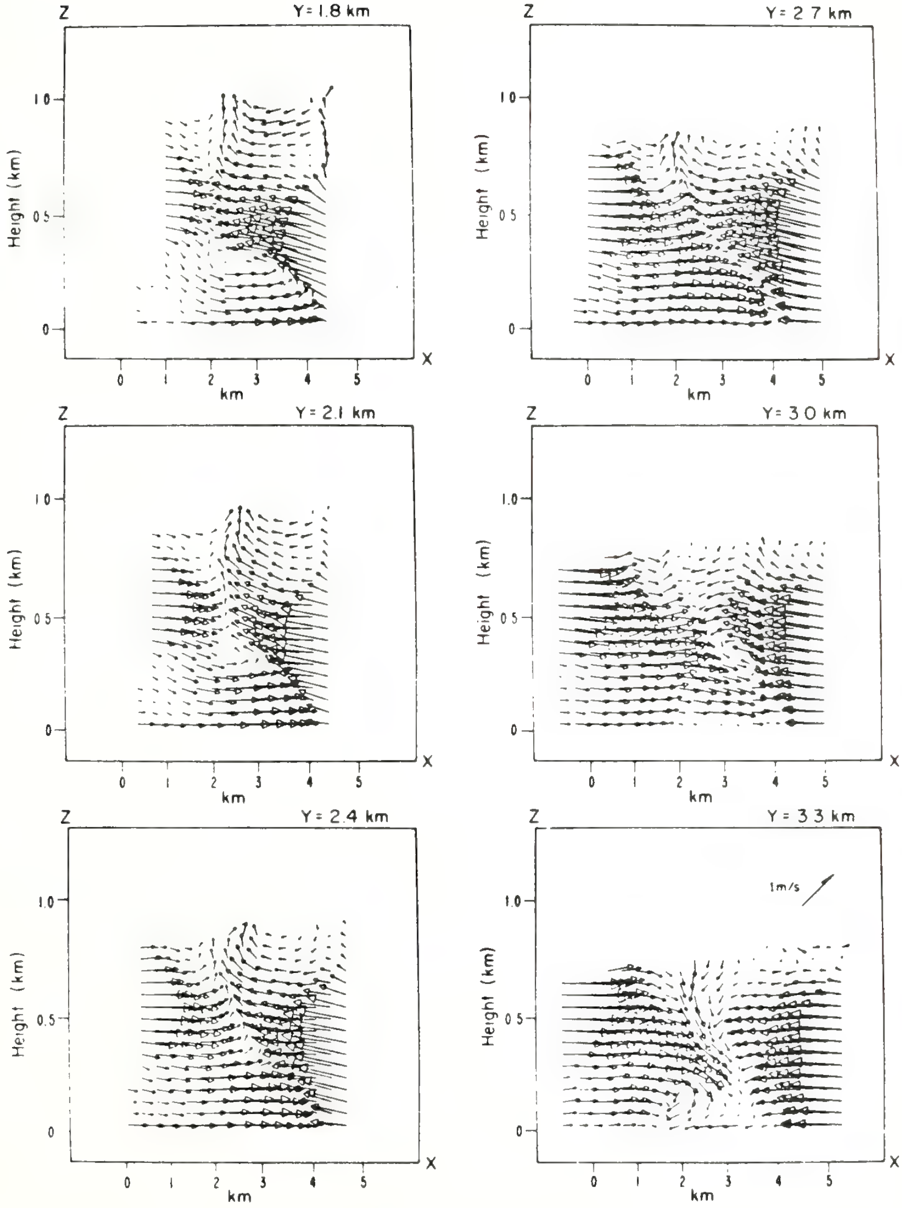
Z
Y= 1.8 km
Height (km)
1.0
0.5
0
X
0 1 2 3 4 5
km
Z
Y= 2.7 km
Height (km)
1.0
0.5
0
X
0 1 2 3 4 5
km
Z
Y= 2.1 km
Height (km)
1.0
0.5
0
X
0 1 2 3 4 5
km
Z
Y= 3.0 km
Height (km)
1.0
0.5
0
X
0 1 2 3 4 5
km
Z
Y= 2.4 km
Height (km)
1.0
0.5
0
X
0 1 2 3 4 5
km
Z
Y= 3.3 km
1m/s
Height (km)
1.0
0.5
0
X
0 1 2 3 4 5
km

Fig. 3*b*

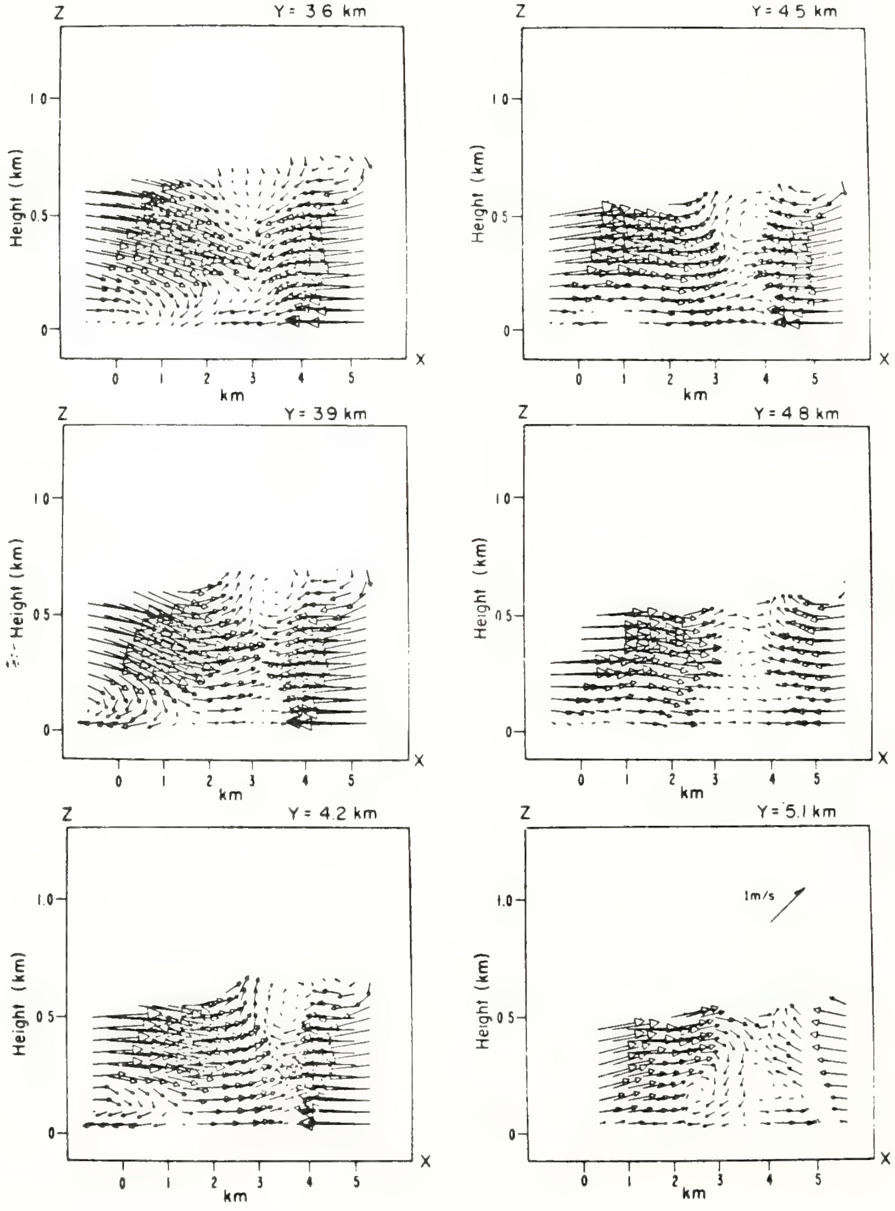
Y = 3.6 km
Y = 4.5 km
Y = 3.9 km
Y = 4.8 km
Y = 4.2 km
Y = 5.1 km
Z
X
Height (km)
1.0
0.5
0
km
0
1
2
3
4
5
1m/s

Fig. 3c

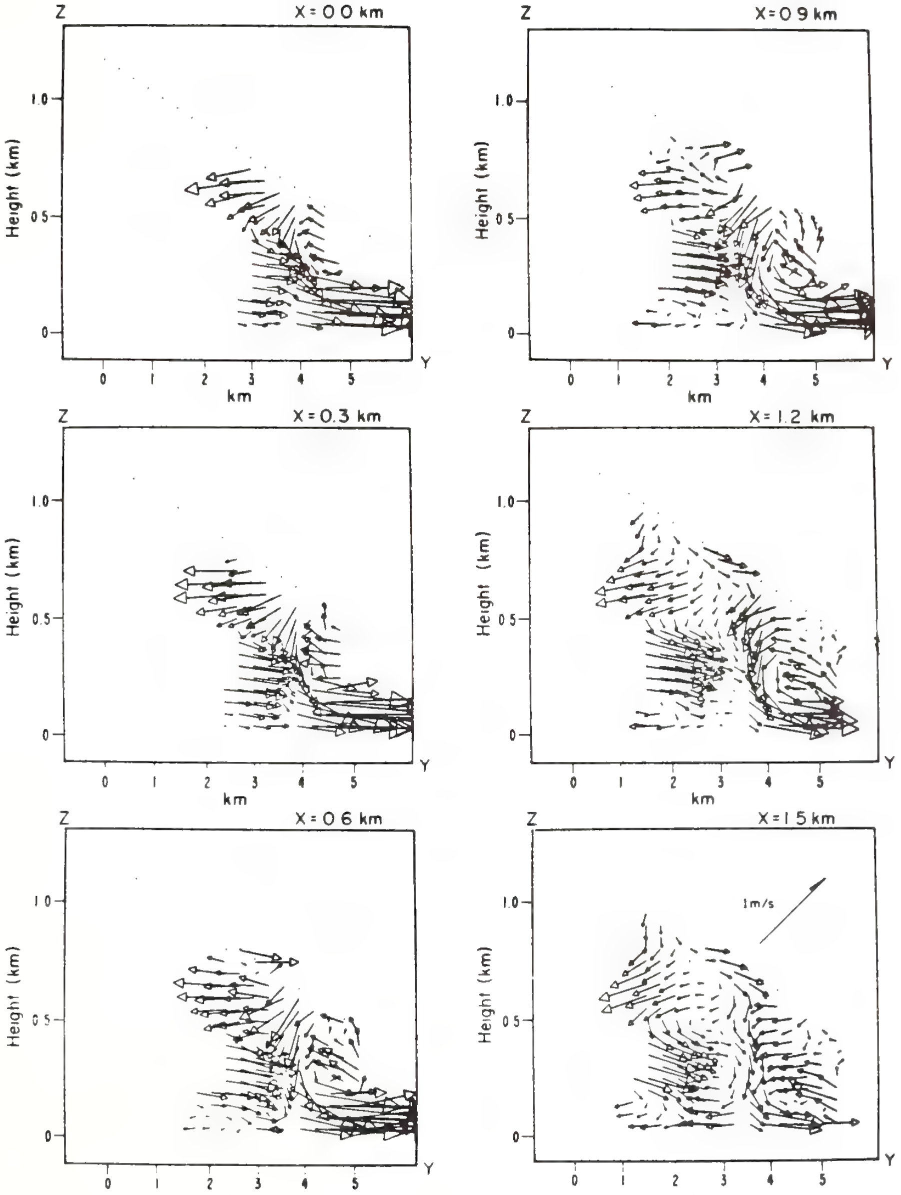

Fig. 4a

Fig. 4. Velocity vectors projected in a series of *YZ* planes, perpendicular to the volume-averaged wind direction and separated by 300 m. The mean wind velocity at each height has been removed. Note that the lengths of the vectors have been changed on this figure from Figures 2 and 3 to improve the visibility of the pattern.

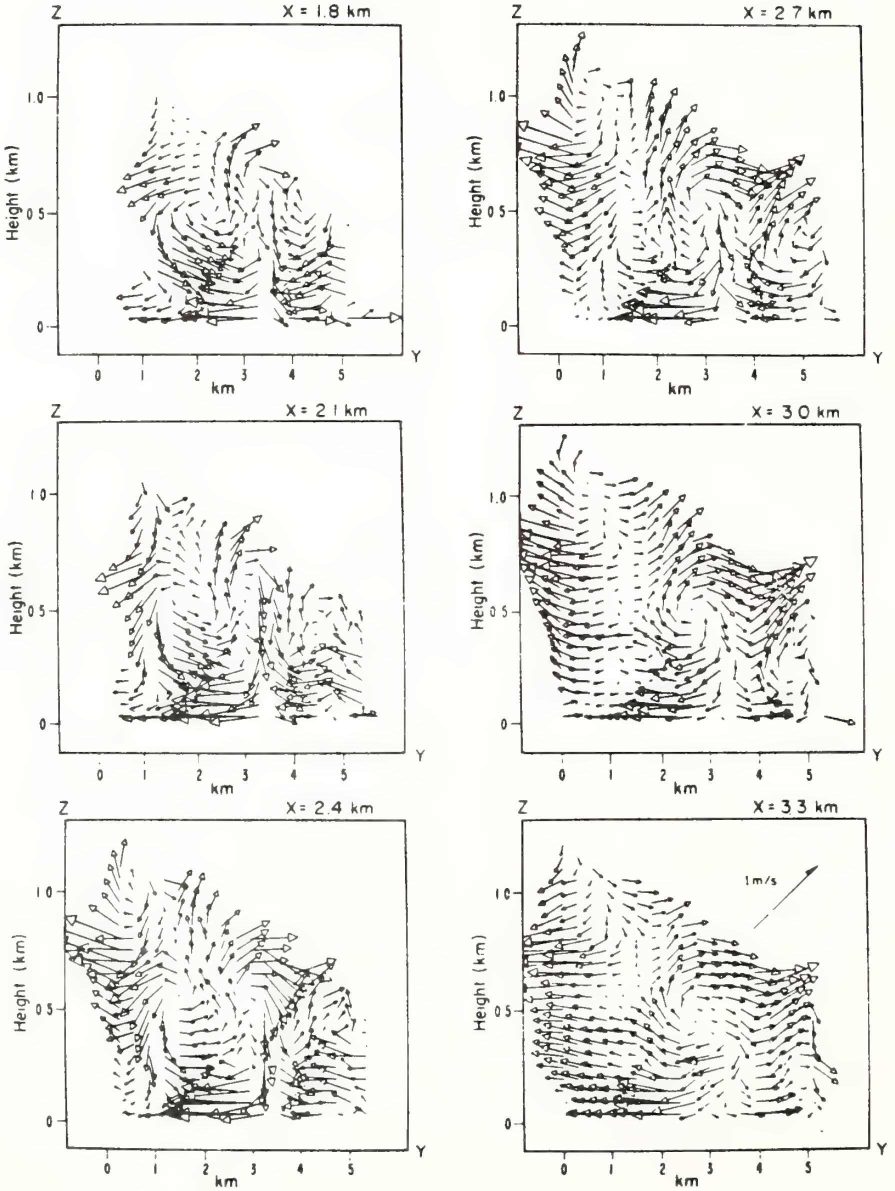
Z
X = 1.8 km
Height (km)
1.0
0.5
0
Y
0 1 2 3 4 5
km
Z
X = 2.7 km
Z
X = 2.1 km
Z
X = 3.0 km
Z
X = 2.4 km
Z
X = 3.3 km
1 m/s

Fig. 4b

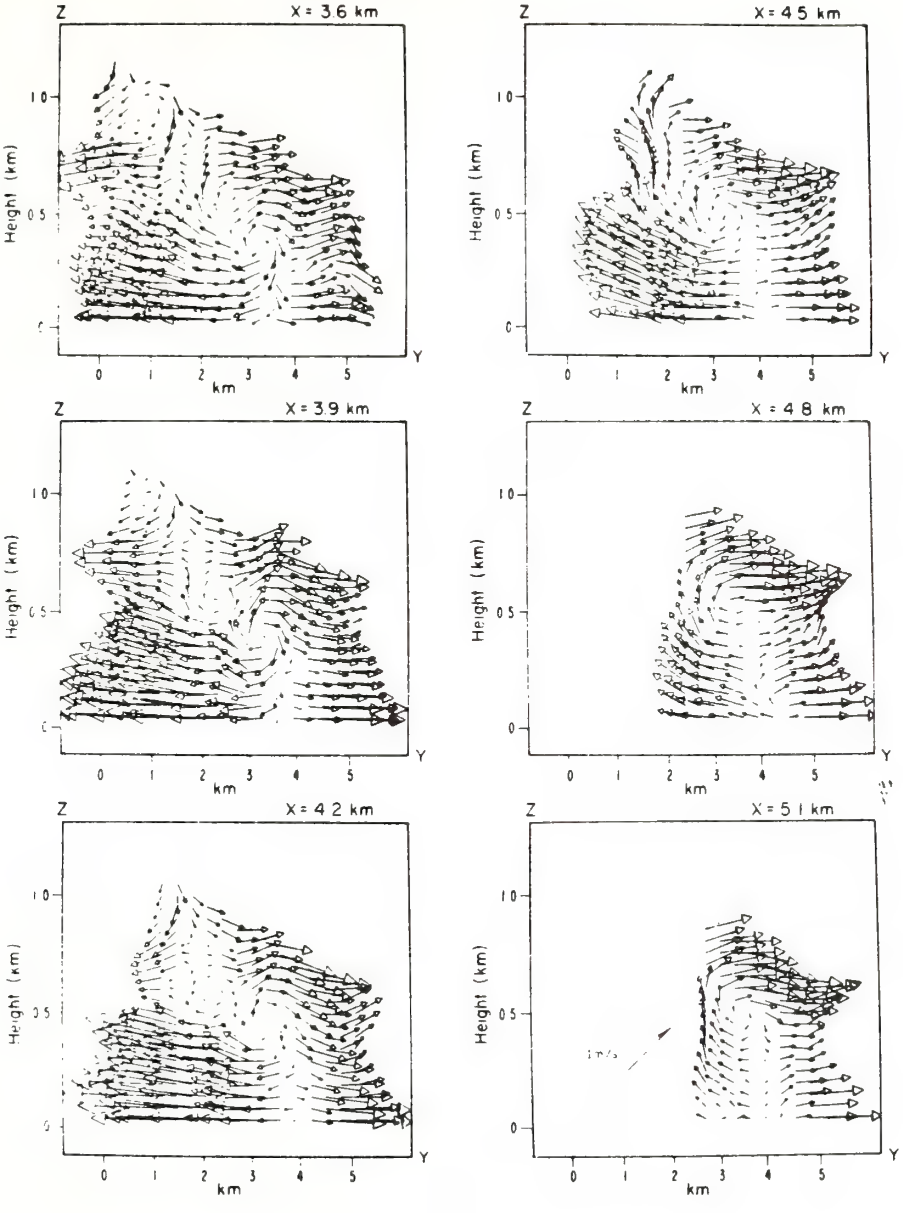

Fig. 4c

and how it is distributed with height, i.e.,

$$\langle u'^2(z)\rangle = \langle [u(z) - \langle u(z)\rangle]^2\rangle$$

etc., for $v'^2(z)$ and $w'^2(z)$, where the angle brackets represent a horizontal average. These calculations show that most of the kinetic energy of this secondary flow was in the longitudinal component of the flow.

Since the local Richardson number (*Ri*) is the single parameter best representing the effects of stratification and shear, we calculate it using the closest rawinsonde available, i.e., the Denver sounding. *Miles* [1961] and *Howard* [1961] have shown that a necessary condition for dynamic instability is that *Ri* be locally less than ¼ somewhere in the flow. The Denver sounding shows that the local *Ri* above 200 m is never less than 1.2. However, this sounding is approximately 30 miles (48 km) away from our radar observations and may not be representative. Therefore the possibility that these motions result from dynamic instability cannot be ruled out. The temperature profile (Figure 1) suggests that a definite layer of uniform temperature gradient exists between the convective layer and the very stable layer at about 2.8 km. The inflection point instability leading to vortex flow has been shown [*Brown*, 1972; *Kaylor and Faller*, 1972] to be theoretically possible in stable as well as unstable boundary layers. *Brown* [1970] solved the equations of motion to produce an equilibrium flow that consists of a modified Ekman spiral mean flow plus a helical secondary flow. His model shows that the modified mean flow exhibits less turning with height than the flow unmodified by secondary flow. In his solutions the longitudinal component of the secondary flow is the largest, a maximum being predicted at

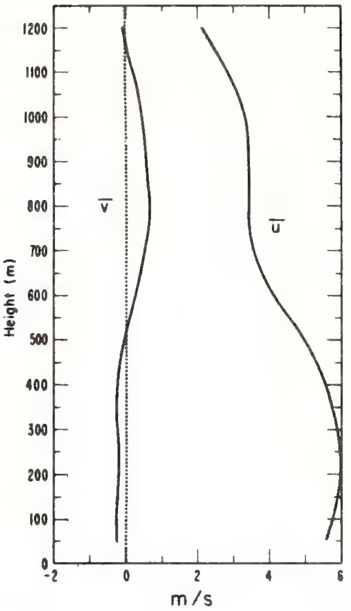

Fig. 5. Horizontal wind speed components averaged over each horizontal plane versus height.

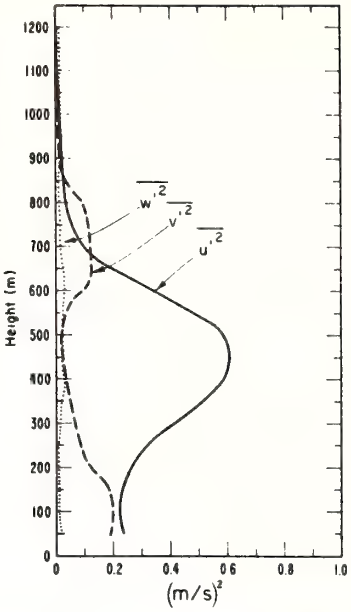

Fig. 6. Variance of u, v, and w versus height after removing the average wind profile.

about 500 m. Typical predicted wavelengths for these instability waves are about 1–2 km. Our observations indicate that the maximum energy is at 500 m (Figure 6), near the center of the vortexlike motion, and that most of the energy is in the component parallel to the mean flow, as predicted by Brown's model.

The secondary flow in the lateral plane is maximum at the lowest levels and reaches a minimum at about 0.5-km height, in agreement with theory. The completely developed equilibrium secondary flow predicted patterns do not appear. This is probably because of the relatively low mean velocity and the variable stratification. *Brown* [1972] found evidence of large distortion to the basic secondary flow patterns when stable stratification was present.

We also tried to determine if the horizontal rotary wind pattern was related to the orography. Figure 7 shows the projection of the wind velocity vectors in a horizontal plane approximately 100 m above the height of the radar base line, superimposed upon a contour map of the measurement area. There is no obvious correlation between the horizontal wind fluctuation patterns and the topography. There is a power plant located at $X = -1$, $Y = 4$ in the coordinate system of Figure 2. This might be considered a potential source of energy driving the secondary flow. However, the wind is from NNE (from the positive x direction), so the plant is downwind from the area where the data were taken; therefore it seems unlikely that it could have had an appreciable influence on the observed patterns.

The horizontally averaged turbulent dissipation rate versus height (Figure 8) was obtained from the second moment of the radial Doppler velocity spectrum as described by *Frisch and Clifford* [1974]. The dissipation rate shows a decrease with height from the ground to 350 m, where it starts increasing again. This increase occurs above the wind maximum, where the magnitude of the wind shear (Figure 5) starts to become large. There is a second increase in ϵ above 850 m, where the magnitude of the wind shear again increases. The first increase in the dissipation rate is most likely to occur as the result of shear production above 350 m. This increase in the value of ϵ in the region from 350 to 800 m is also in the same height range as the vortexlike motion, and both may be related to the wind shear in this height range. The second increase in ϵ also may result from the wind shear above 850 m. However, since the snow started at a height slightly above 1 km, the distribution of scatterers within the radar pulse volume might have been

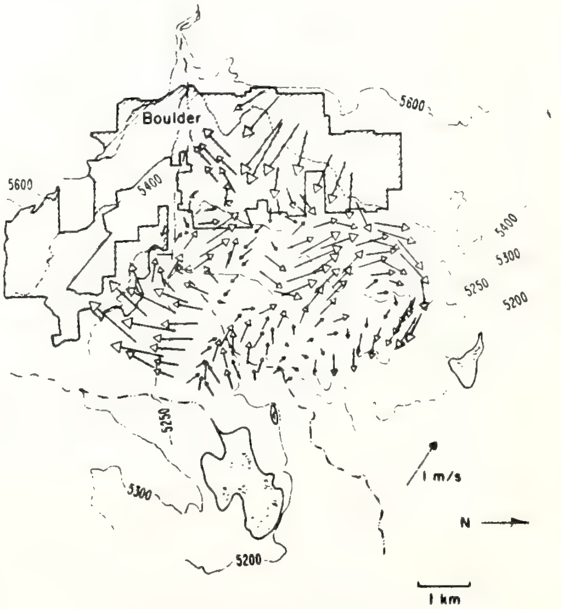

Fig. 7. Comparison of horizontal wind fluctuations at approximately 100-m height above the radar base line and terrain contours (where the contours are in feet). The mean wind was from the NNE at approximately 5 m/s.

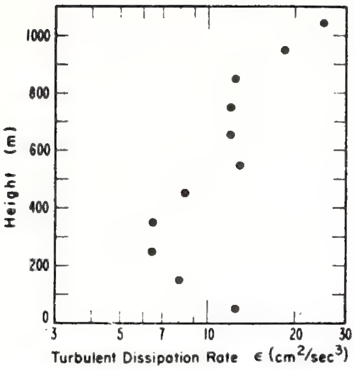

Fig. 8. Turbulent dissipation versus height, averaged over 100-m height intervals.

more inhomogeneous in this region than at the lower heights. This could cause a significant error in the estimate of ϵ in this height region.

SUMMARY AND CONCLUSIONS

By using a dual-Doppler radar system with snow as the air motion tracer we were able to observe the three wind components in a large volume of space near the ground. After mean wind velocity values were removed in each horizontal plane, a complex structure of secondary motions was visible. In that structure, numerous vortices appeared with a typical scale of 1-2 km. One of these motions, with major axis parallel to the mean wind, had a cross section 0.5 km in height, 2 km in width, and extended for more than 5 km downward. This motion occurred in a stably stratified atmosphere at the height of a weak inflection point in the lateral mean velocity profile, although the two-dimensional horizontal roll vortices predicted in theory did not appear in the weak mean flow. There were many indications of sporadic production of secondary flows with wavelengths of secondary flow components that are in agreement with theory. *LeMone* [1973] has found that roll production is sporadic at low mean velocities, becoming dominant only at larger mean flows (>7 m/s).

The Doppler spectral width shows that the turbulent dissipation rate initially decreased with height near the surface. In a region of shear, above the surface layer, the dissipation rate increased. The increase took place near the height of the centers of the ellipsoidal motions, becoming relatively large toward the top. This suggests the generation of nonsurface layer turbulence associated with shear aloft.

Acknowledgments. The authors wish to thank Frank Merrem and Nathan Kohn for their programing assistance and Harold Frank for help in obtaining the data.

REFERENCES

Brown, R. A., A secondary flow model for the planetary boundary layer, *J. Atmos. Sci., 27,* 742-757, 1970.

Brown, R. A., On the inflection point instability of a stratified Ekman boundary layer, *J. Atmos. Sci., 29,* 850-859, 1972.

Frisch, A. S., and S. F. Clifford, A study of convection capped by a stable layer using Doppler radar and acoustic echo sounders, *J. Atmos. Sci., 31,* 1622-1628, 1974.

Frisch, A. S., L. J. Miller, and R. G. Strauch, Three-dimensional air motion in snow, *Geophys. Res. Lett., 2,* 86-89, 1974.

Howard, L. N., Note on a paper of John W. Miles, *J. Fluid Mech., 10,* 496-508, 1961.

Kaylor, R., and A. J. Faller, Instability of the stratified Ekman boundary layer and the generation of internal waves, *J. Atmos. Sci., 29,* 497-509, 1972.

LeMone, M. A., The structure and dynamics of horizontal roll vortices in the planetary boundary layer, *J. Atmos. Sci., 30,* 1077-1091, 1973.

Lhermitte, R., and L. J. Miller, Doppler radar methodology for the observations of convective storms, Proceedings of the 14th Radar Meteorology Conference, pp. 133-138, Amer. Meteorol. Soc., Boston, Mass., 1970.

Miles, J. W., On the stability of heterogeneous shear flows, *J. Fluid Mech., 10,* 496-508, 1961.

Miller, L. J., and R. G. Strauch, A dual-Doppler radar method for the determination of wind velocities within precipitating weather systems, *Remote Sensing Environ., 3,* 219-235, 1974.

Myrup, L. O., Turbulence spectra in stable and convective layers in the free atmosphere, *Tellus, 3,* 345-354, 1969.

(Received May 1, 1975;
revised July 30, 1975;
accepted September 5, 1975.)

Journal of Applied Meteorology 14, 415-419, April 1975.

A Note on the Behavior of the Temperature Structure Parameter in a Convective Layer Capped by a Marine Inversion

A. S. Frisch and G. R. Ochs

NOAA ERL Wave Propagation Laboratory, Boulder, Colo. 80302

12 April 1974 and 2 December 1974

ABSTRACT

Aircraft measurements of C_T^2 in an unstable marine boundary layer suggest a modification of the surface layer free-convection model. This modification is given by a function of z/z_i, where z is the observation height and z_i the height to the inversion base. This variation of C_T^2 with height may be expressed as $z^{-4/3}[1+0.84(z/z_i)+4.13(z/z_i)^2]$ for $0 \leqslant z/z_i \leqslant 0.8$.

1. Introduction

The optimum design of optical systems for outdoor use requires knowledge of the turbulence and the associated refractive index fluctuations of the atmosphere. The relevant refractive-index structure parameter C_n^2 (Tatarski, 1961) is related to the temperature structure (in a dry atmosphere) by

$$C_T^2 = (79 \times 10^{-6} P/T^2)^{-2} C_n^2,$$

where P is the pressure and T the temperature of the

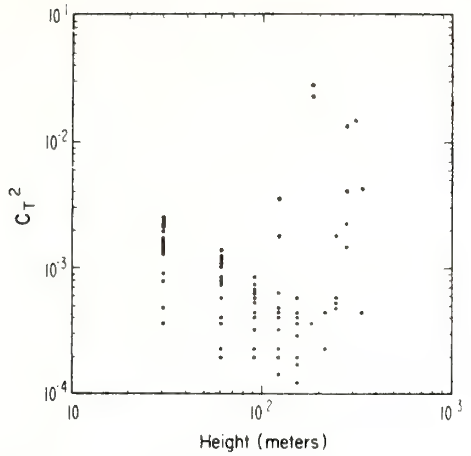

FIG. 1. Variation of C_T^2 with z/z_i for all measurements.

atmosphere. The temperature structure constant can be determined from temperature-fluctuation measurements. In the presence of water vapor, the description of C_n^2 is more complicated (Gossard, 1960) and may require consideration of the correlation or anti-correlation of the fluctuations of temperature and water vapor (Friehe *et al.*, 1972).

The behavior of C_T^2 as a function of other meteorological variables in the atmospheric surface layer, or constant-flux layer (about 10 to 100 m deep), has been studied by Wyngaard *et al.* (1971). Their measurements show that C_T^2 is a function of the Richardson number, defined by

$$\mathrm{Ri}=(g/\bar{T})(\partial\bar{\theta}/\partial z)/(\partial\bar{u}/\partial z)^2, \qquad (1)$$

where g is the acceleration of gravity, $\bar{T}$ the mean temperature, $\partial\bar{\theta}/\partial z$ the mean potential temperature gradient, and $\partial\bar{u}/\partial z$ the mean wind speed gradient.

Ri can be related to the height z above the surface through a nondimensional parameter z/L (Businger *et al.*, 1971), where L (the Monin-Obukhov length) is defined as

$$L\equiv\frac{-u^{*3}\bar{T}}{kgQ}. \qquad (2)$$

Here u_* is the frictional velocity scale, k the von Kármán constant, and Q the surface temperature flux.

The purpose of this note is to show that a similar relation can apply to heights above the surface layer. We use measurements of C_T^2, taken by an instrumented aircraft over the ocean in the vicinity of a floating instrument platform (*Flip*). Simultaneous measurements made on *Flip* determined the Monin-Obukhov length.

The temperature sensor mounted on the aircraft was a platinum resistance-wire thermometer with high-frequency response (Ochs and Lawrence, 1972). The measurements from *Flip*, 100 km off the coast of San Diego, were made by personnel from the University

TABLE 1. Measured values of C_T^2 [(°C^2 m$^{-2/3}$)$\times10^3$].

Date (1972)	Time	z_i (m)	C_T^2 30 m	60 m	80 m	120 m	150 m	180 m	210 m	240 m	270 m	300 m	330 m
23 Feb	1717	360	2.1	1.2	0.84	0.48	0.58						
	1747	360	2.2	1.0	0.63	0.33	0.36						
24 Feb	1452	240	0.78	0.40	0.23	0.23	0.40						
	1539	240	0.90	0.23	0.20	0.20	0.19						
25 Feb	1345	240	0.36	0.20	0.20	0.14	0.12						
	1440	240	0.48	0.23	0.20	0.20	0.17						
27 Feb	0640	270	1.44	0.78	0.68								
	0656	270	1.33	1.2									
28 Feb	0642	330	2.4	1.2	0.58	0.44	0.44						
		330	2.4	0.78	6.9								
	0715	330	2.4	0.84									
28 Feb	1301	510	1.7	0.78	0.53	0.40	0.40						
	1339	510	1.6	1.0	0.4	0.44	0.25						
20 Apr	1224	240	1.5	0.78	0.73	0.40		0.36	0.44		2.2		4.2
	1327	240	1.4	0.73									
20 Apr	1750	210	1.5	1.4		3.5		27.2		0.02			
	1833		1.7					22.5					
21 Apr	1234	270	2.3	0.84		0.44				0.53	4.0	14.4	0.44
	1318		1.5	1.1		0.63				1.8	13.2		
	1800	270	1.4	0.78	0.40		0.19		0.23	0.48	1.4		
	1856		0.73	0.58	0.32	0.32				0.58			

of California at San Diego. Five-minute, level flights past *Flip* were made at various altitudes below and through the marine inversion. The lowest flights were 30 m above the water. The height of the marine inversion was determined by climbing flights.

2. Results and discussion

The times, dates and measured values of C_T^2 appear in Table 1, and a plot of C_T^2 vs height is shown in Fig. 1.

During the times of measurement, the boundary layer was unstable, with a Monin-Obukhov length of ~ -30 m (Friehe, 1972, personal communication). Above the boundary layer, there was an inversion layer with a height varying from 210 to 510 m. Because of these conditions, we consider it reasonable to adopt the results of Wyngaard *et al.* (1971) near the surface, modifying it empirically in terms of the ratio of height to inversion base height, z/z_i.

When $L \approx -30$ m it was found by Wyngaard *et al.* (1971) that

$$C_T^2 = [4/(3k^{\frac{2}{3}})](\bar{T}/g)^{\frac{2}{3}}(\overline{w'\theta'})^{\frac{4}{3}}z^{-\frac{4}{3}}, \quad \text{for } -7z/L \gg 1. \quad (3)$$

where $\overline{w'\theta'}$ is the covariance between the fluctuations of the vertical velocity component w' and of temperature θ'. If z_i, the height of the inversion base, is another relevant scaling parameter (see, for example, Deardorff, 1972), then proceeding in a manner similar to that of Wyngaard *et al.*, we may modify his Eq. (3) by using an additional similarity function, $G(z/z_i)$. Thus, Eq. (3) becomes

$$C_T^2 = [4/(3k^{\frac{2}{3}})](\bar{T}/g)^{\frac{2}{3}}(\overline{w'\theta'})^{\frac{4}{3}}z^{-\frac{4}{3}}G(z/z_i), \quad (4)$$

where $G(z/z_i) = 1$ for $z/z_i \ll 1$, because we require that (4) reduces to (3) in the surface layer.

To test the validity of Eq. (4), we normalize each series of measurements to those at the lowest height, 30 m for this series of runs. Using Eq. (4) we have

$$\frac{C_T^2(z/z_i)}{C_T^2(30/z_i)} = \frac{G(z/z_i)}{G(30/z_i)}\left(\frac{z}{30}\right)^{-\frac{4}{3}}. \quad (5)$$

Because $30/z_i < 0.15$ for all our measurements, we can assume that $G(30/z_i) \approx 1.0$. Thus we can use (5) to find $G(z/z_i)$, i.e.,

$$G(z/z_i) = \frac{C_T^2(z/z_i)}{C_T^2(30/z_i)}(z/30)^{\frac{4}{3}}.$$

A plot of C_T^2 vs z is shown in Fig. 1. In Fig. 2 we plot $G(z/z_i)$ vs z/z_i. By using this transformation, the scatter is reduced significantly over that shown in Fig. 1. For $z/z_i > 0$, with the constraint that $G(0) = 1$, a least-squares fit for the data yields

$$G(z/z_i) \approx 1.0 + 0.84(z/z_i) + 4.13(z/z_i)^2, \quad \text{for } 0 \leqslant z/z_i < 0.8. \quad (6)$$

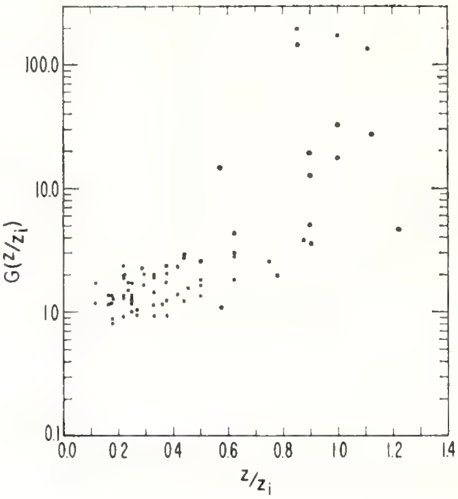

Fig. 2. Variation of $G(z/D)$ with z/D for all measurements.

This would give

$$C_T^2 \approx [4/(3k^{\frac{2}{3}})](\bar{T}/g)^{\frac{2}{3}}(\overline{w'\theta'})^{\frac{4}{3}}z^{-\frac{4}{3}} \times [1.0 + 0.84(z/z_i) + 4.13(z/z_i)^2], \quad \text{for } 0 \leqslant z/z_i \leqslant 0.8. \quad (7)$$

There is a significant departure from a $z^{-\frac{4}{3}}$ law for values of $z/z_i > 0.1$. This indicates that the atmosphere is no longer in the "free convection" regime, but is affected by the lid on the convective layer at z_i. This effect would restrict the integral scale of the turbulent temperature fluctuations with height compared to the free convection value. In addition, because of the large-scale circulation and mixing, the temperature variance should be greater than the free-convection variance. These effects will increase the value of C_T^2 relative to the free-convection prediction.

The scatter of $G(z/z_i)$ vs z/z_i is most likely caused by uncertainty in z_i, which was obtained from the aircraft sounding. By definition, z_i is the height where $\partial\bar{\theta}/\partial z = 0$. Acoustic echo sounding observations (Wyckoff *et al.*, 1973) of shallow inversion layers indicate oscillations of about 100 m amplitude. Such oscillations would cause an appreciable error in the determination made from an airplane, especially for the smaller values of z_i (~ 210 m).

Since $C_T^2 \propto z^{-\frac{4}{3}}G(z/z_i)$, one would expect $G(z/z_i)$ to decrease as z/z_i approaches 1. The fact that $G(z/z_i)$, shown in Fig. 2, does not become small near $z/z_i = 1$, could be the result of two factors. The abrupt transition of $G(z/z_i)$ at $z/z_i = 0.8$ seen in Fig. 2 could result from a combination of convective mixing in the boundary layer and the large temperature gradient above this transition which should lead to a large temperature variance above the inversion base that diffuses downward. In addition, the spatial variability

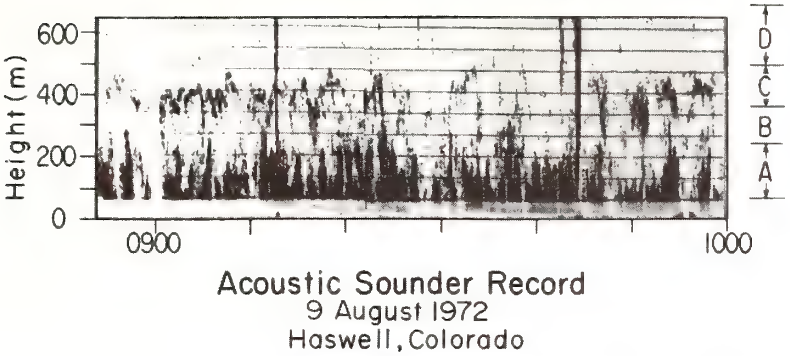

FIG. 3. An example of an acoustic sounding in a convective layer capped by an inversion. The backscattered signal intensity is proportional to the degree of darkening in the record. This intensity is also a function of C_T.

of the inversion base height and the fact that the aircraft traverses a large horizontal distance as it passes through the base would tend to produce a large temperature variance. Fig. 3, taken from Frisch and Clifford (1974), shows an example of an acoustic echo sounding taken in a convective boundary layer capped by a stable inversion. The backscattered intensity is presumably proportional to C_T^2. Thus the dark lower part of the record (region A) corresponds to high values of C_T^2, while the lighter part of the record (region B), which is changing height with time, shows very low values of C_T^2. In B, $\partial\bar{\theta}/\partial z \approx 0$, while the strong echo above occurs in the region of a large positive temperature gradient in the lower part of the inversion base. The height of the weak echo corresponding to the layer adjacent to and just below the inversion base (region B) changes with time. This time-height variability is partially related to some horizontal variability in the height of the inversion base. Hence horizontal measurements of C_T^2 by an instrumented aircraft near an inversion base could be in error. Thus in the neighborhood of $z/z_i = 1.0$, our values of $G(z/z_i)$ may be incorrect. Since the scatter in the data up to $z/z_i \approx 0.8$ is relatively small, we used only the values of $G(z/z_i)$ for $0 \leqslant z/z_i \leqslant 0.8$ for our fit of the data.

Tsvang (1969) reported a $z^{-4/3}$ height dependence of C_T^2 up to 500 m over land. His measurements could be explained if they were made when the inversion was considerably higher than the marine inversion layer off San Diego. Over land, the height of the inversion base capping the mixed layer is typically 1 or 2 km (e.g., Lenschow, 1970).

3. Conclusions

We have extended the surface layer analysis of Wyngaard *et al.* (1971) to 0.8 times the height of the inversion layer by use of a function involving z/z_i where z_i is the height of the base of the inversion layer. The resulting variation of C_T^2 with height was

$$C_T^2 \approx [4/(3k^{4/3})](\bar{T}/g)^{2/3}(\overline{w'\theta'})^{4/3}z^{-4/3}$$
$$\times[1.0+0.84(z/z_i)+4.13(z/z_i)^2].$$

Because of potential errors in determining z_i, the valid range for this relationship should be restricted to $0 \leqslant z/z_i \leqslant 0.8$.

Acknowledgments. The authors would like to thank J. C. Wyngaard for the helpful discussions and C. A. Friehe for making the *Flip* measurements available. This work was partially supported by the Rome Air Development Center under Contract F30602-7-f-0317.

REFERENCES

Businger, J. A., J. C. Wyngaard, Y. Izumi and E. F. Bradley, 1971: Flux-profile relationships in the atmospheric surface layer. *J. Atmos. Sci.*, **28**, 181–189.

Deardorff, J. W., 1972: Parameterization of the planetary boundary layer for use in the general circulation models. *Mon. Wea. Rev.*, **100**, 93–106.

Friehe, C. A., C. H. Gibson and G. F. Dreyer, 1972: Effects of temperature and humidity on density and refractive-index fluctuations over the open ocean (abstract). *J. Opt. Soc. Amer.*, **62**, 1340.

Frisch, A. S., and S. F. Clifford, 1974: A study of convection capped by a stable layer using Doppler radar and acoustic echo sounders. *J. Atmos. Sci.*, **31**, 1622–1628.

Gossard, E. E., 1960: Power spectra of temperature, humidity and refractive index from aircraft and tethered balloon measurements. *IRE Trans. Antennas Propagat.*, **8**, 186–201.

Ochs, G. R., and R. S. Lawrence, 1972: Temperature and C_n^2 profiles measured over land and ocean to 3 km above the surface. NOAA Tech. Report ERL 251-WPL 22, Environmental Research Laboratories, Boulder, Colo., 39 pp.

Lenschow, D. H., 1970: Airplane measurements of planetary boundary layer structure. *J. Appl. Meteor.*, **9**, 874–884.

Tatarski, V. I., 1961: *Wave Propagation a Turbulent Medium.* McGraw-Hill, 285 pp.

Tsvang, L. R., 1969: Microstructure of temperature fields in the free atmosphere. *Radio Sci.*, **4**, 1175–1177.

Wyckoff, R. J., D. W. Beran and F. F. Hall, Jr., 1973: A comparison of the low-level radiosonde and the acoustic echo sounder for monitoring atmospheric stability. *J. Appl. Meteor.*, **12**, 1196–1204.

Wyngaard, J. C., Y. Izumi and S. A. Collins, 1971: Behavior of the refractive-index-structure parameter near the ground. *J. Opt. Soc. Amer.*, **61**, 1646–1650.

Journal of Applied Meteorology 13, 411-415, April 1974.

Optimum Averaging Times for Short-Term Wind Prediction in the Planetary Boundary Layer

J. E. Gaynor

Wave Propagation Laboratory, NOAA Environmental Research Laboratories, Boulder, Colo. 80302

6 June 1973 and 5 February 1974

ABSTRACT

Root-mean-square error statistics were applied to tower wind data to find the optimum average times of the wind and azimuth to be used as predictors of a 2-min mean wind speed and direction, 0-10 min in the future. The data were divided into classes of stable and unstable boundary layers, and although the predictability was the same, the results showed the difference in the frequency distribution of the atmospheric wave structure for stable and unstable conditions. As opposed to the conclusion of previous studies, beyond the 1-min forecast interval, simple persistence is the best predictor of both the wind speed and direction at the three levels.

1. Introduction

The advent of more sophisticated and larger aircraft, along with a large increase in air traffic at the world's airports, has made wind data near runways more important. In addition to real-time winds, there is a need for predicting winds several minutes ahead in time; allowing the pilot to anticipate the wind speed and direction at touchdown while he is still on his approach, and thus make corrections that will better insure a safer landing.

The International Civil Aviation Organization (ICAO) Fifth Air Navigation Conference (1967) defined the surface wind given to the pilot as a 2-min-mean wind direction and speed. This information is provided when a pilot is in, or near, the traffic pattern. It would be more desirable if a prediction of the conditions at touchdown (a few minutes later) could be given. Hardware for on-line analog averaging exists (Koren, 1972), and it remains to find a predictor of the 2-min averaged winds.

Simple persistence values have been used with root-mean-square (RMS) statistics for evaluating predictions with relatively long-term forecast schemes (Thompson, 1961). Rachele and Armendariz (1967) used root-mean-square error (RMSE) statistics for short-term prediction and found that 6-min averaged wind speeds and directions measured within 1 min of a rocket launch were their best predictors of a 4-sec mean wind 4.2 m above the ground. Using towers aligned nearly parallel with the average wind direction, Armendariz and Lang (1968) found a 1-min wind average to be a good predictor up to a lag of 1 min; beyond that, the 4- or 5-min average was preferable. Employing tower winds and assuming the descending path of an aircraft, Sparks and Keddie (1971) showed that the minimum error is made when a 4–5 min average wind is used for a 10-min forecast interval.

In general, wind sensors are not located at the point of aircraft touchdown. Armendariz and Lang suggest the sensor should be located at an average upwind or downwind location, a difficult situation for a multiple runway airport. It is encouraging to note that Ito (1968) demonstrated remarkable horizontal homogeneity of low-level winds for distances of a few kilometers. His results suggest that a single point sensor may be acceptable for most airports.

The statistical method used in this study precludes predicting sudden changes in wind speed and direction caused by migratory synoptic phenomena, such as occurs in the vicinity of thunderstorms or frontal activity (Donald Lenschow, personal communication). Important parameters to include for the prediction of wind during such occurrences would be surface pressure and vorticity changes, which should have a statistical relation to short-period wind changes. The precise relation would, of course, be very difficult to obtain. Although these parameters may improve the prediction techniques, they would also be somewhat difficult to measure and include on-line at an airport.

The same results that will be presented here may possibly be obtained from a careful power spectra analysis of wind speed and direction. However, the intent of this study is to present a simple on-line method of wind analysis at airports, with the results discussed as a check on the validity of this method.

2. Method of analysis[1]

Wind data from three levels (30, 91 and 152 m) of a tower at Haswell, Colo., were sampled at a rate of 1 Hz, separated into high- and low-variance cases, corre-

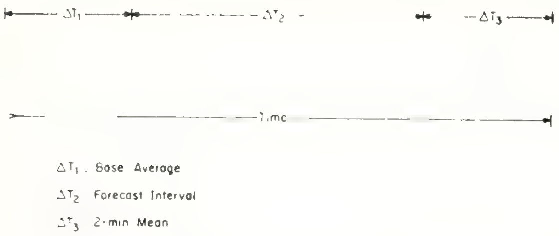

FIG. 1. Schematic representation of the forecasting problem.

sponding to stable and unstable thermal structures (Singer and Smith, 1953).

Predictability was determined by using an RMSE approach normalized by the standard deviation of the 2-min running average, represented by

$$r(t,\tau)=\frac{\{\Sigma[x_2-x_t(\tau)]^2/N\}^{\frac{1}{2}}}{\sigma_2}, \qquad (1)$$

where x_2 is the 2-min running average of the wind speed or direction, the variable we wish to predict. The x_t value is the ($\frac{1}{2}$, 1, 2, 3, 4, 5 min) running average of the wind speed or direction, σ_2 is the standard deviation of the 2-min running average, and N the number of data points. Using the above equation and lagging x_2 from $x_t(\tau)$ for times (τ) of 0 to 10 min (the forecast interval) at 1-min increments, a total of 11 RMS errors for each of the six running averages were collected. With $x_t(\tau)=x_2$, the RMSE values, $r(2,\tau)$, for the various forecast intervals (τ) represent the "persistence" values or simply the error between the actual 2-min average of the wind speed or direction and the 2-min mean extrapolated ahead in time. The forecast interval is from the end of the period of the current average to the beginning of the period of the 2-min mean verifying wind speed or direction (Fig. 1). Standard deviations from the average of all the sample RMSE values, $r(t,\tau)$, in each of the two variance classifications and for each value of t and τ were calculated and tested for significance with the standard one-sided t-test.

3. Discussion of results

Table 1 shows the hourly averaged 5-min running wind speed variance for the high- and low-variance cases at each level. High and low variances are separated by nearly an order of magnitude. The averages of the high variances show a marked decrease in magnitude above the 30 m level. This is reasonable in that gustiness decreases with height in an unstable atmosphere (Monahan and Armendariz, 1971; Fichtl *et al.*, 1969; Davis and Newstein, 1968).

TABLE 1. Sample average of the hourly averaged high and low 5-min running wind speed variances separated by level.

Level (m)	11 low-variance samples ($m^2\ sec^{-2}$)	8 high-variance samples ($m^2\ sec^{-2}$)
30	0.034	1.187
91	0.053	0.507
152	0.032	0.707

The 12 cases were categorized as follows:

1) Three levels (30, 91, 152 m).
2) Wind speed and direction.
3) High and low variance.

The RMSE statistics were computed using Eq. (1) for each of the above cases for six running averages ($\frac{1}{2}$, 1, 2, 3, 4, 5 min) and at forecast intervals from 0 to 10 min at 1-min intervals.

Only the four cases for the 30 m level are presented here, since the results are similar for each of the respective cases at the two higher levels. Each of the following graphs contains six curves, one for each running average. The first two graphs are averages of the 8 high-variance samples and the next two are averages of the 11 low-variance samples. One standard deviation is represented by the bars on the persistence curves as well as by bars

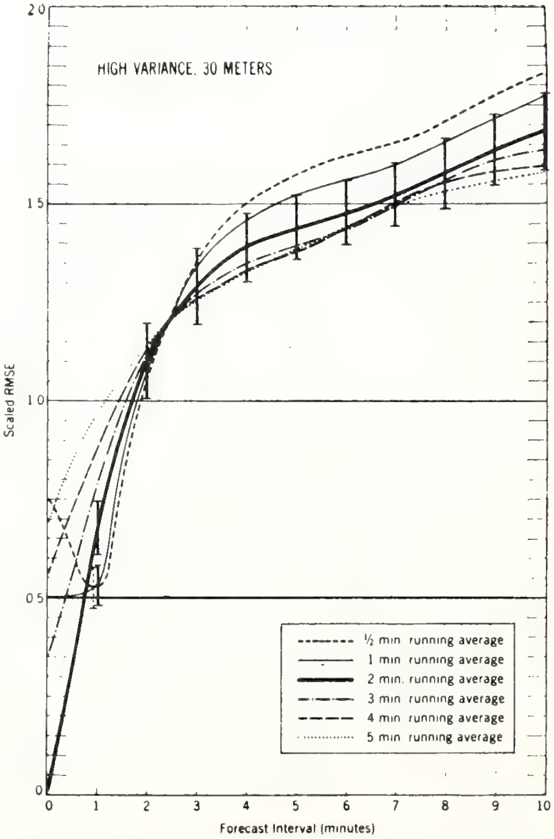

FIG. 2. Normalized RMSE of the wind speed from Eq. (1) for each forecast interval at the 30 m level (averaged over the 8 high-variance samples). The vertical bars are the 1σ sample averages, using 2-min running means (persistence).

on the ½- and 1-min running average curves at the 1-min forecast interval. To avoid confusion, the standard deviation bars for the ½-min averages have been offset slightly to the left.

Fig. 2 (high variance, 30 m level wind speed) shows that the ½- and 1-min running averages are better predictors of the 2-min mean wind out to about the 2-min forecast interval. After this, the curves cross and the 3–5 min averages drop below persistence, becoming better predictors out to the 10-min forecast interval.

Results for wind speed and direction were essentially the same at the higher levels except for the point the curves cross the persistence line. Note the similarity between the high-variance wind speed (Fig. 2) and the high-variance wind direction (Fig. 3). The graphs for the low-variance, 30 m level wind speed and direction (see Figs. 4 and 5) look dramatically different from those for the high variance. The departure between high and low variance can be explained by the difference in the frequency distribution of the atmospheric wave structure between the stable and unstable boundary layer. The high- and low-variance criterion has clearly separated the two stability classifications. The stable boundary layer nearly always contains waves, commonly with periods anywhere from 4 to 10 min (Hooke *et al.*, 1972). For moderate wind speeds, the spectra of turbulence near the surface (Kaimal *et al.*, 1972) have shown maximum energy for the periods corresponding to those of the gravity waves. Superimposed on these lower frequency waves are higher frequency oscillations with less energy content. The apparent correlation between the ½- and 1-min running averages with the 2-min presistence could well be due to the fact that the longer period oscillations are not filtered out. Gravity waves are also present in the "persistence" time series, but most of the gravity wave energy has probably been filtered out with the 3–5 min running averages. For this reason, the comparison between persistence and these longer averages is not good at the various forecast intervals, shifting these curves above the persistence value on the low-variance graphs.

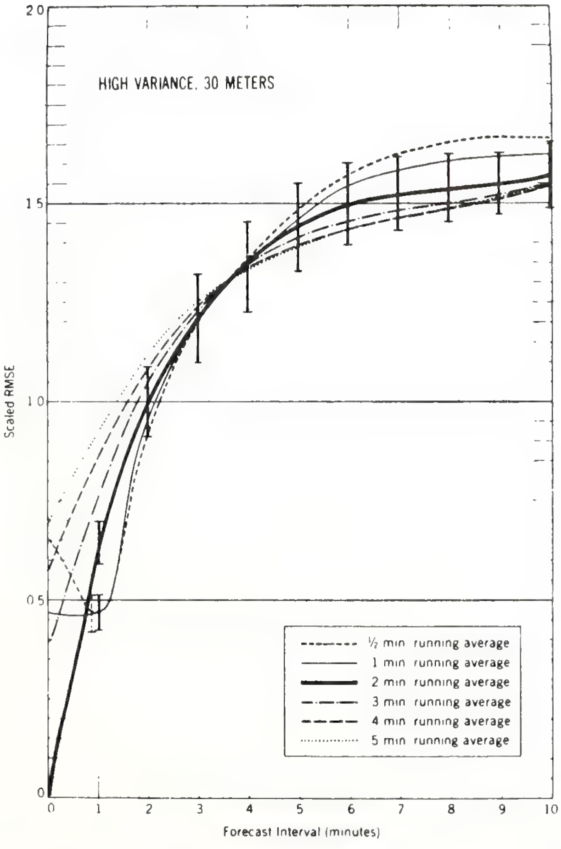

Fig. 3. As in Fig. 2 except for wind direction (averaged over the 8 high-variance samples).

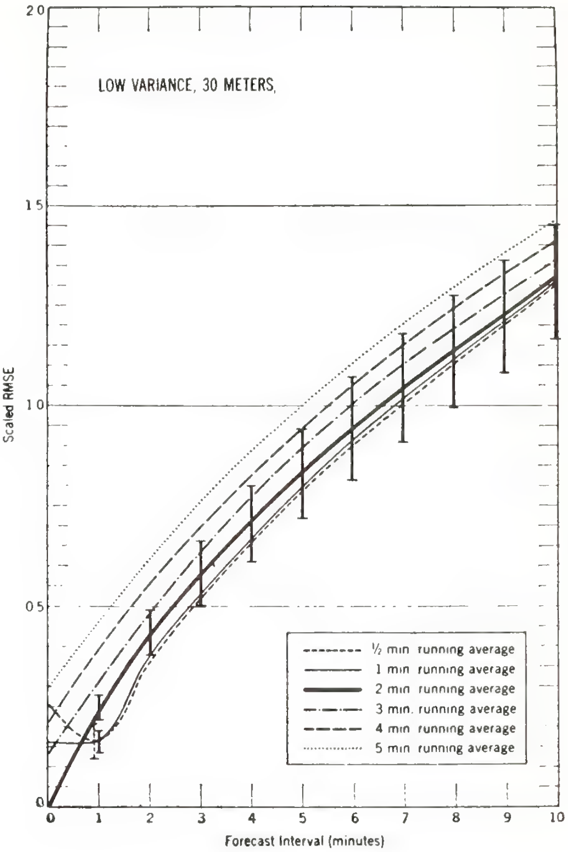

Fig. 4. As in Fig. 2 except for wind speed (averaged over the 11 low-variance samples).

The crossing of persistence by the high-variance curves is a more difficult feature to explain. Kaimal *et al.* show that shorter period oscillations during an unstable regime contain more energy than shorter oscillations during stable periods. This greater energy occurs at periods of about 2 min. Kaimal *et al.* also show that longer period waves contain even more

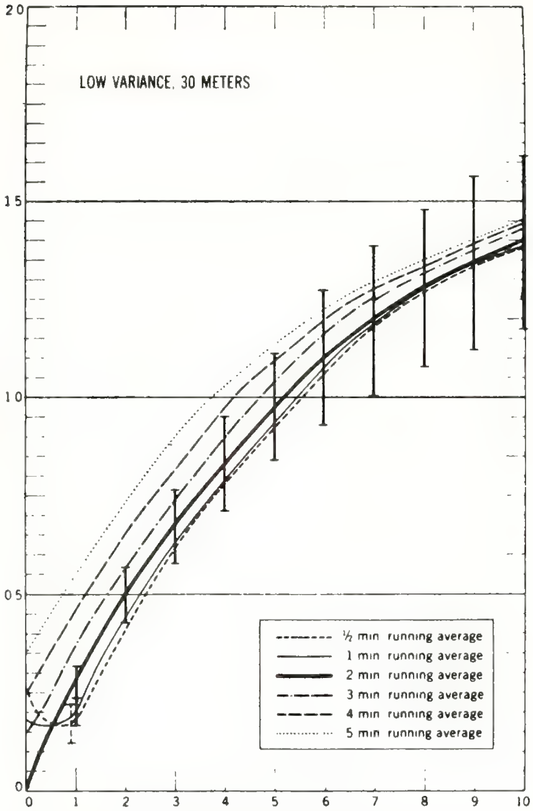

FIG. 5. As in Fig. 2 except for wind direction (averaged over the 11 low-variance samples).

energy than the shorter periods when the boundary layer is unstable, and much more energy than the corresponding longer periods in the stable atmosphere. According to a hypothesis raised by Businger (1972), these larger scale oscillations may be induced by convective activity with periods of many minutes, which may not be filtered out even by our largest averaging periods. Table 1 indicates that we have separated the data into quite stable and quite unstable boundary layer cases. Nevertheless, we cannot rule out the possibility that some of the low-frequency energy may be caused by roll vortices which, if they occur at all, are nearly always embedded in the near-neutral or slightly unstable boundary layer with moderate to strong wind (LeMone, 1972). For small forecast intervals, the RMSE may be low, since the small-scale oscillations have not been completely filtered out. If the shorter time oscillations are not periodic, then at longer forecast intervals the lag correlation becomes low for shorter averages, and the curves eventually cross above the persistence line. Short periods have been filtered out by the 3–5 min running average. At the shorter forecast .intervals, the RMSE of the longer averages is not good. For longer intervals, the longer periods are the dominant lag correlating factor and the comparison with persistence becomes relatively good.

Tables 2 and 3 show the significance of the data for the predictability conditions on the 2-min mean wind speed and direction using the t-test. We can say with 90% confidence that the $\frac{1}{2}$- or 1-min averages are better predictors than persistence of the 2-min averaged wind speed and direction 1 min ahead. The exception is the 91 and 152 m high-variance wind direction where the confidence of the $\frac{1}{2}$-min average drops below 90%. In general, the 1-min averaged wind speed and direction gives slightly better confidence of prediction than the

TABLE 2. Accepted data from the t-test for the running average less than persistence at the 90% confidence level for the high variance case containing eight samples (cutoff at $t=1.415$).

Level (m)	Forecast interval (min)	Running average (min)	Student's t
		Wind speed	
30	1	$\frac{1}{2}$	2.527
	1	1	2.967
91	1	$\frac{1}{2}$	1.844
	1	1	2.609
152	1	$\frac{1}{2}$	1.727
	1	1	3.819
		Wind direction	
30	1	$\frac{1}{2}$	3.537
	1	1	3.491
91	1	1	1.898
152	1	1	2.537

TABLE 3. Accepted data from the t-test for the running average less than persistence at the 90% confidence level for the low-variance case containing 11 samples (cutoff at $t=1.372$).

Level (m)	Forecast interval (min)	Running average (min)	Student's t
		Wind speed	
	1	$\frac{1}{2}$	2.736
30	1	1	3.305
	2	$\frac{1}{2}$	1.543
91	1	$\frac{1}{2}$	2.477
	1	1	2.300
152	1	$\frac{1}{2}$	1.830
	1	1	2.119
		Wind direction	
30	1	$\frac{1}{2}$	2.464
	1	1	2.795
91	1	$\frac{1}{2}$	2.105
	1	1	2.050
152	1	$\frac{1}{2}$	2.317
	1	1	2.340

$\frac{1}{2}$-min average. For the 30 m low-variance wind speed, the $\frac{1}{2}$-min average proved to be a better predictor of the 2-min mean wind 2 min ahead. However, with this one exception, the confidence drops rapidly after the 1-min forecast interval.

Little or no difference exists between wind speed and direction, between the levels and between stabilities with respect to the predictability conditions. For the limited sample which was analyzed we conclude that after 1 min, simple persistence is the best predictor of the 2-min mean wind.

Acknowledgments. The author acknowledges the helpful ideas that D. W. Beran and R. L. Grossman contributed to this study. This study was partially supported by the Aviation Weather Systems Branch, FAA.

REFERENCES

Armendariz, M., and V. D. Lang, 1968: Wind correlation and variability in time and space. Rept. ECOM-5201, Atmos. Sci. Lab., White Sands Missile Range, N. M., 26 pp.

Businger, J. A., 1972: The atmospheric boundary layer. *Remote Sensing of the Troposphere*, WPL ERL, Dept. of Engineering, University of Colorado, Chap. 6.

Davis, F. K., and H. Newstein, 1968: The variation of gust factors with mean wind speed and with height. *J. Appl. Meteor.*, **7**, 372–378.

Fichtl, G. H., J. W. Kaufman and W. W. Vaughan, 1969: Characteristics of atmospheric turbulence as related to wind loads on tall structures. *J. Spacecraft*, **6**, 1396–1403.

Hooke, W. H., J. M. Young and D. W. Beran, 1972: Atmospheric waves observed in the planetary boundary layer using an acoustic sounder and a microbarograph array. *Boundary Layer Meteor.*, **2**, 371–380.

ICAO, 1967: Report of the Fifth Air Navigation Conf. Montreal Doc. 8720, AN-CONF/5.

Ito, H., 1968: Time and space variation in meteorological elements in the aerodrome and its vicinity. *Aeronautical Meteorology*, WMO Tech. Note No. 95, 142–157.

Kaimal, J. C., J. C. Wyngaard, Y. Izumi and O. R. Coté, 1972: Spectral characteristics of surface layer turbulence. *Quart. J. Roy. Meteor. Soc.*, **98**, 563–589.

Koren, O., 1972: Digital output wind system for airport use. *Preprints Second Symp. Meteorological Observations and Instrumentation*, San Diego, Calif., Amer. Meteor. Soc., 262–266.

LeMone, M., 1972: The structure and dynamics of the horizontal roll vortices in the planetary boundary layer. Ph.D. thesis, University of Washington.

Monahan, H. H., and M. Armendariz, 1971: Gust factor variations with height and atmospheric stability. *J. Geophys. Res.*, **76**, 5807–5818.

Rachele, H., and M. Armendariz, 1967: Surface wind sampling for unguided rocket impact prediction. *J. Appl. Meteor.*, **6**, 516–518.

Singer, I. A., and M. E. Smith, 1953: Relation of gustiness to other meteorological parameters. *J. Meteor.*, **10**, 121–126.

Sparks, W. R., and B. Keddie, 1971: A note on the optimum averaging time of wind information for conventional aircraft landings. *Meteor. Mag.*, **100**, 129–143.

Thompson, P. D., 1961: *Numerical Weather Analysis and Prediction.* New York, Macmillan, 170 pp.

Yearbook of Science and Technology, McGraw-Hill, 389-391, 1975.

Storm

Many recent advances in the understanding of severe thunderstorms and in the ability of meteorologists to forecast them flow from developments in the new field of meteorological remote sensing. Radar is an example of an active remote sensor; in storm research, Doppler radars illuminate storms with microwave electromagnetic energy and process the echoes to chart air currents inside storms. Electromagnetic sensors are also used passively to listen to waves that the storms themselves emit. For example, a kind of radio receiver that monitors the "atmospherics" emitted by lightning strokes and other electrical activity inside storms is now being developed into a tornado-warning device. Even satellite photography, used for tracking storm activity on a global scale, might be called a passive optical (or, in some cases, infrared) remote-sensing tool.

Still another remote-sensing technique that has been recently used to study severe storms measures their emissions of ultra-low-frequency acoustic waves called infrasound (Fig. 1). At the moment, no one knows why certain storms radiate infrasound and others do not, but scientists at the National Oceanic and Atmospheric Administration (NOAA), who have been observing the waves for more than a decade, are trying to find out what these waves can reveal about the internal dynamics of storms, and whether the emissions have any practical value, specifically as advance indicators of storm severity

Pressure waves. Infrasonic waves are pressure fluctuations that travel in the atmosphere at essentially the local speed of sound—about 340 m/sec under standard conditions—but their frequencies lie below the nominal 20-Hz limit of human hearing. The infrasound from severe storms typically has wave periods in the tens of seconds; one usually speaks of wave period, the duration of 1 wave cycle, when the frequency of the wave is below 1 Hz. Since atmospheric absorption is much lower at these frequencies than it is for audible sound, infrasound can travel great distances with little loss of strength. Thus, the infrasound from some severe storms has been detected several thousands of kilometers from its source, and waves from more powerful sources, like nuclear bombs have been detected after several circuits around the Earth.

Because the pressure fluctuations associated with the waves that storms emit are very weak—only about one-millionth of an atmosphere—arrays of very sensitive microphones (called microbarographs), with special filters to reduce the noise caused by wind, are required to detect them. Even then, pressure fluctuations must be cross-correlated between several microphones before the storm's signal is recognizable (Fig. 2).

Ionospheric waves. Acoustic waves from severe thunderstorms can also travel into the upper atmosphere and cause observable effects by moving its layers of electrically charged ions up and down. These ionospheric motions, occurring about 250 km above the Earth, are detectable with certain radio-sounding devices that bounce radio waves off the layers.

In 1967 NOAA scientists first identified certain peculiar wavelike motions in the ionosphere as the effects of acoustic emissions from severe thunderstorms. Since these waves have somewhat longer periods than those of the infrasound observed at ground level—3–5 min compared to tens of seconds—an immediate connection between the two effects was not made. But recent theoretical studies of the frequency-filtering effects of the atmosphere on the two different kinds of propagation path have explained how the two different observations can be just different manifestations of some broad-band emission process. Indeed, detailed case studies of storm events that produced both kinds of effects have lent credibility to the hypothesis of a common emission mechanism.

Both the ionospheric waves and the ground-level pressure fluctuations attributable to severe storms are seen almost exclusively during the late after-

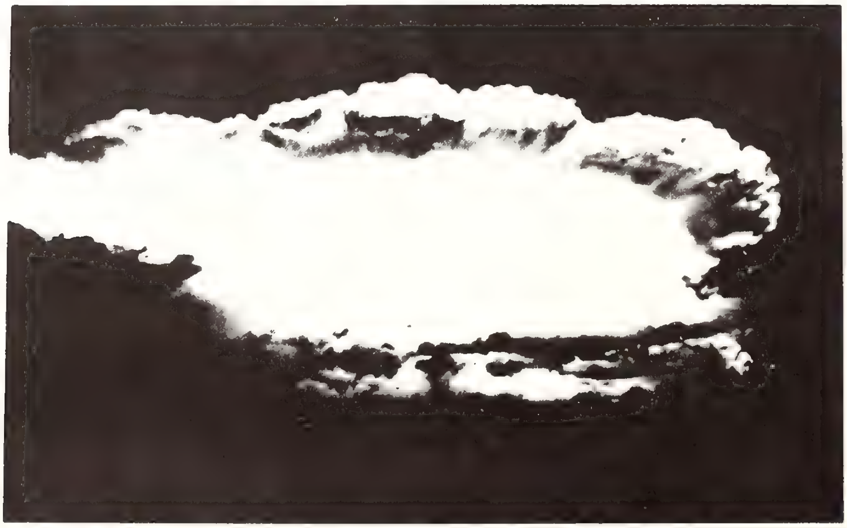

Fig. 1. Photograph of a cumulonimbus near Boulder, CO; its top reached 40,000 ft (12,200 m). At the time this photograph was taken, infrasound from the direction of the storm was being recorded by NOAA microbarographs near Boulder

noon and early evening of the spring and summer months. The average duration of the emissions is about 2 hr. The wave sources, when identifiable, seem to be predominantly in the Midwest—most frequently in Oklahoma and Texas. Whereas the waves observed at the ground generally contain many superimposed frequencies, those detected in the ionosphere invariably appear as nearly sinusoidal oscillations whose frequencies are confined to the narrow band between 2- and 5-min wave periods.

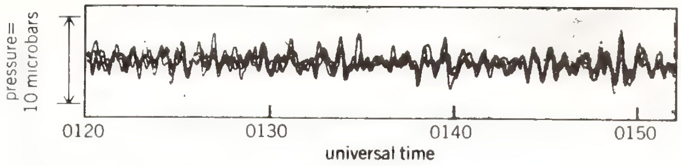

Fig. 2. Superimposed pressure versus time records from four microbarographs at Boulder, CO, during severe storm activity in Oklahoma.

Source models. Although the exact emission mechanism remains unknown, several reasonable theoretical models have been advanced and are currently being subjected to observational tests. Among them are electrical mechanisms for generating "infrasonic thunder," various kinds of oscillations in latent heat release and of air circulation in storm cells, and the aerodynamic noise of turbulence inside storms. The most promising mechanism, in terms of the detail with which it conforms to the phenomenology of the observed waves, is drawn from the theory of sound radiation from vortex motion. Whereas steady vortex flow emits no sound, vortex flow that contains irregularities, instabilities, or secondary vortexes can be shown to radiate acoustically somewhat like the rotating propeller of a fan. There is ample evidence for the presence of irregular vortex flow and of secondary vortexes within larger vortex flows in the atmosphere, specifically in observations of tornadoes and dust devils. But such observations are rare, and no specific instance has yet been associated with observed infrasound. It seems likely, however, that such visible effects represent only the "tip of the iceberg," in the sense that invisible, yet intense, vortex motion abounds in and around convective storms, particularly the severe ones that occur when squall lines pass through the Midwest.

The most powerful storms emit up to 100,000,000 W of acoustic power, equivalent to the electrical power consumed by a city of 100,000; yet the acoustic emissions still represent an insignificant fraction of the total energy of a storm. Such high power levels present one difficulty in the search for a suitable source model.

Practical value. To find out whether the emissions have any practical value, NOAA conducted tests of the storm-detecting abilities of its sensitive microphones during the 1972 and 1973 storm seasons. During 1972, with only one array of microphones at Boulder, CO, NOAA recorded about 86 infrasonic events that were subsequently identified as storm-related by comparison with independent weather data. More than half of those events were identified with storms that produced confirmed tornadoes or funnel clouds. More than two-thirds of the emitting storms were in Texas, Oklahoma, Kansas, Nebraska, or South Dakota. At least 87% of the detected storms produced some documented severe effects, such as large hail, heavy rains, high winds, and tornadoes. In some instances, when radar indicated a grouping of storms with similar echo characteristics (for example, echo height), infrasound emissions appeared to select the location of most severe effects (large hail, heavy rainfall, tornadoes).

During the 1973 season, tests were conducted with two additional infrasound observatories, one near Albuquerque, NM, and the other near Rapid City, SD, to increase detection reliability and to permit storm triangulation (Fig. 3). Preliminary results indicate that well over a hundred storms were detected and located from bearing intersections of infrasound received by at least two of the observatories. More detailed analysis of these data should provide the information needed to assess the value of infrasound in simulated storm-warning situations.

At least two limitations on such practical uses of infrasound are imposed by the atmosphere itself. One is that the waves travel at the relatively slow speed of sound, about 1200 km/hr. If the sensors are located too far away, their warning value is obviously diminished. The other limitation is the distortion of the waves' propagation paths by atmospheric winds, which can cause the measured source direction to differ by several degrees from its true direction. Uncorrected bearing intersections can thus be up to tens of miles in error. If atmospheric winds are roughly known, however, bearing corrections can be estimated.

For background information *see* THUNDERSTORM; WEATHER FORECASTING AND PREDICTION in the McGraw-Hill Encyclopedia of Science and Technology. [T. M. GEORGES]

Bibliography: K. Davies and J. E. Jones, *NOAA Profess. Pap. no. 6*, 1972; T. M. Georges, *Rev. Geophys. Space Phys.*, 11:571–594, 1973.

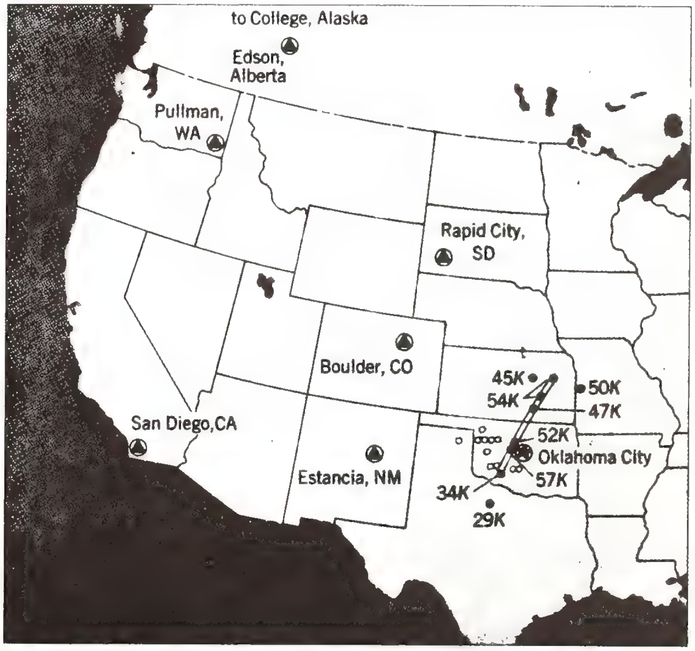

Fig. 3. Map of the western United States showing the intersections of infrasound bearings from seven observatories (the seventh observatory is in College, Alaska) made on June 5, 1973, at 0100 universal time. Locations of thunderstorm radar echoes and their heights are shown in the vicinity of the intersections. Line of radar echoes near Oklahoma City indicates presence of a squall line.

WAVES IN THE ATMOSPHERE

E. E. Gossard and W. H. Hooke

Published by Elsevier, Amsterdam

CONTENTS

Preface V
Acknowledgments IX

CHAPTER 1. INTRODUCTION 1

1. Historical review 1
2. Recent developments in wave sensing 9
3. Names and nonsense 13
4. Glossary of symbols and definitions 15
5. Vertical distribution of atmospheric properties 13
6. Typical values of wave parameters 25

CHAPTER 2. THE FUNDAMENTAL EQUATIONS 27

7. Introduction 27
8. A little thermodynamics 27
   The first law 27
   Equation of state 28
   Specific heat 30
   Internal energy 31
   Work done by external forces 32
   Adiabatic processes 33
   Isothermal processes 33
9. Continuity equation 34
   Conserved properties 34
   Conservation of matter 35
   Continuity equation in the ionosphere 37
   Production and loss in the ionospheric continuity equation. 38
10. Equations of motion 39
   Conservation of momentum 39
   The stress tensor 40
   The shearing stresses 41
   The Reynolds' stresses and eddy viscosity 45
   The Coriolis force 46
   Inertial oscillations 50
   Scale analog of a rotating earth 51
   The force of gravity 52
11. The electromagnetic forces 55
12. Ohm's law in the ionosphere 58
13. Maxwell's equations 60
14. The high-frequency approximations 60
   Electromagnetic waves 60
   Electrostatic waves 64
15. The low-frequency equations 65
16. The perturbation equations 66
17. Speed of sound 70
18. Potential temperature and the Väisälä-Brunt frequency 71
19. Gravity waves 75

20. The Lagrangian equations 77
Equation of continuity 78
Equations of motion 80

CHAPTER 3. RELATIONSHIPS BETWEEN FIELD VARIABLES 89

21. The basic equations 89
Eckart's coefficient — the Boussinesq approximation 90
Some dynamic relationships 92
The impedance equation 93
Lamb waves 95
Rossby waves 96
The polarization equations 97
22. Energy and momentum 100
Wave energy and energy flux 100
Wave momentum flux 108

CHAPTER 4. WAVE EQUATIONS AND DISPERSION EQUATIONS 111

23. Compressible model with earth rotation, no vertical shear, non-ionized medium . 111
Some special cases 112
The propagation diagnostic diagram 113
The acoustic cut-off frequency (diagnostic diagram Branch A) 113
Buoyancy waves (diagnostic diagram Branch B) 115
The propagation surfaces 117
Interpretation of the dispersion equation for buoyancy-inertial waves 118
Group velocity and energy flow 118
24. Model with vertical shear, no earth rotation 121
25. Ionized, incompressible, inviscid model; no collisions; no earth rotation . . . 124

CHAPTER 5. SOME BOUNDARY VALUE PROBLEMS 129

26. Introduction 129
Layered models 129
Continuous-function models 130
Arbitrary models 130
27. The kinematic boundary condition 130
28. The dynamic boundary condition 131
29. Eigensolutions, models discontinuous in density 132
Model with no shear, density discontinuous 132
Model with wind and density discontinuous 136
The Wegener hypothesis 138
Model with two wind and density discontinuities 141
Model with constant shear, one density discontinuity 143
Model with constant shear, two discontinuities in density 144
Model with one density and two wind gradient discontinuities 146
Model with two density and wind gradient discontinuities 147
30. Eigensolutions, models continuous in density 149
Homogeneous model with shear 149
Three-layer model continuous in density and temperature, no shear 150
Two-layer model, surface-based inversion 156
Three layers continuous in density, temperature, and wind 156
General three-layer model; homogeneous shear layer 157
31. Models continuous in gradients of velocity and density 162
Model with smooth density profile, no shear (Groen's model) 162
Model with tanh wind profile; exponential density 166

Model with tanh wind profile; $\rho = \rho_s \exp(-S \tanh z/d)$ 167
32. The WKB approach 168
33. Critical levels 170
Introduction 170
The Kelvin cat's eye pattern 171
The cockeyed cat's eye of G.I. Taylor 172
Streamline pattern near critical layer with static stability 175
Wave encounters with critical levels 176

CHAPTER 6. DYNAMIC STABILITY OF ATMOSPHERIC WAVES 183

34. Introduction 183
35. Stability in fluid with linear wind, exponential density 185
36. Richardson number 188
Introduction 188
Ri-distribution in a wave in medium with no shear 189
Ri-distribution in a wave in medium with shear 197
37. The stability of homogeneous shear flow 198
Inflection point instability 199
Howard's semicircle theorem 200
38. The stability of heterogeneous shear flow 202
Observations of dynamic stability of atmospheric layers 210

CHAPTER 7. WAVE PROPAGATION IN A DISSIPATIVE ATMOSPHERE 215

39. Introduction 215
40. Minimum wave scale sizes permitted in the presence of viscosity and thermal conductivity 218
41. Buoyancy and acoustic waves in viscous or thermally conducting atmosphere — limiting approximations 224
Buoyancy waves in a viscous incompressible atmosphere 225
Acoustic waves in a viscous atmosphere — gravity neglected 230
Buoyancy waves in a thermally conducting, inviscid incompressible atmosphere 231
Acoustic waves in a thermally conducting atmosphere — gravity neglected 232
42. Waves in a windless isothermal atmosphere with constant kinematic viscosity 233
43. Waves in a windless isothermal atmosphere with constant kinematic thermal conductivity 234
44. Wave propagation in a windless, isothermal atmosphere with constant viscosity or thermal conductivity 235
45. Energy transport in a viscous atmosphere 236
46. Waves in a viscous, thermally conducting isothermal atmosphere 237
47. Wave propagation in a windless atmosphere with Rayleigh friction 238
48. Atmospheric wave propagation in a partially ionized atmosphere 238
49. Wave propagation in an atmosphere with radiative damping 247
50. Wave dissipation — effects on the mean atmospheric flow 249

CHAPTER 8. MOUNTAIN LEE WAVES 251

51. Introduction 251
52. Linear problem for flow over an obstacle 252
The eigenfunctions and field variables 252
53. The lower boundary 254
Sinusoidal boundary 254
Boundary perturbation concentrated on y-axis 255
Bell-shaped boundary perturbation 256

54. One-layer models . . . 257
  Case when $k >> k_N$ . . . 257
  Case when $k \simeq k_N$ . . . 257
  Case when $k_N >> k >> k_\Omega$ . . . 261
  Case when $k \simeq k_\Omega$ . . . 262
  Case of $k << k_\Omega$ . . . 265
  Concluding remarks . . . 265
55. Two-layer model . . . 265
  Isolated mountains and ridges . . . 268
56. Models with three or more layers . . . 269
57. Wind shear . . . 270
58. Non-linear flow and lee waves . . . 272
59. Vertical energy and momentum transport by mountain lee waves . . . 278

CHAPTER 9. INFRASOUND . . . 283

60. Introduction . . . 283
61. Sources of infrasound . . . 283
  Auroral emissions from magnetic substorms . . . 287
  Infrasonic emissions from severe weather . . . 289
  Infrasonic emission from the sea surface (microbaroms) . . . 295
  Infrasound of unknown origin . . . 300
62. Propagation of infrasound — the normal mode approach . . . 304
  Formulation for numerical solution by normal modes . . . 305
  Impulsive point source . . . 312
  Examples of numerical solution by normal modes . . . 319
63. Propagation of infrasound — ray tracing . . . 322
64. Structure of the atmospheric wave guide . . . 326
65. Reception and analysis of infrasound . . . 328
  Power-spectrum analysis — general . . . 329
  The covariance function . . . 330
  Power-spectrum computation — transform of $R(\tau)$ . . . 331
  Power-spectrum computation — Fast Fourier Transform (FFT) . . . 332
  Cross-power spectrum . . . 333
  Applications of cross-spectrum analysis to spatially separated recordings . . . 335
  Beam steering of phased arrays . . . 337
  Beamwidth of signal . . . 341
  Velocity bandwidth . . . 348
  General solution . . . 352
  Example . . . 356

CHAPTER 10. PROGRESSIVE BUOYANCY WAVES IN THE LOWER ATMOSPHERE . . . 359

66. Introduction . . . 359
67. Review of proposed wave sources and source mechanisms in the lower atmosphere . . . 359
  Orography . . . 359
  Squall lines and frontal systems . . . 360
  Turbulence . . . 360
  Penetrative convection . . . 362
  Wave—wave interactions . . . 362
  Geostrophic adjustment . . . 362
  Shear instability . . . 363

Ekman-layer instability 363
Wave generation by boundary-layer turbulence 363
68. Case studies — introduction 364
Long waves on elevated layers 364
Waves generated by shear instability in the troposphere 386
Waves in the boundary layer 387
Small-scale waves and vortices 389

CHAPTER 11. WAVES IN THE UPPER ATMOSPHERE 399

69. Introduction 399
70. Buoyancy waves manifested in the neutral upper atmosphere 402
71. Atmospheric waves manifested in the ionized upper atmosphere 406
Traveling ionospheric disturbances 406
Spread F 413
Sporadic E 414
D-region ionospheric irregularities 417
72. Propagation in the upper atmosphere 417
73. Sources of buoyancy waves in the upper atmosphere 418
74. Wave dynamics in the upper atmosphere 420
Wave energy and momentum deposition in the upper atmosphere 420
The quasi-biennial oscillation 422

References 423

Appendices 441

Author Index 443

Subject Index 449

Journal of Atmospheric Sciences 31, 483-492, March 1974.

Dynamic Stability of an Isentropic Shear Layer in a Statically Stable Medium

EARL E. GOSSARD

Wave Propagation Laboratory, NOAA/ERL, Boulder, Colo. 80302

(Manuscript received 19 July 1973, in revised form 1 November 1973)

ABSTRACT

Two theoretical models of shear layers in the atmosphere are examined. The conditions for their dynamic stability are found and their predictions of wavelength to layer-thickness ratio are compared with classical models and with available observational data. Although the models are only rigorously applicable to incompressible fluids, it is suggested that they also represent conditions in the atmosphere, and clear-air returns published by Katz from the high-power pulse radar at Wallops Island are especially emphasized. Model 2 appears to be able to account for the narrow band characteristic of many of the observed events and also to explain better than other models the observed wavelength to layer-thickness ratios.

1. Background

The wave equation for small perturbations of a statically stable, incompressible fluid undergoing shear is [see e.g., Taylor, 1931, Eq. (6)]

$$\frac{d^2W(z)}{dz^2}+\left[\frac{N^2}{(u_0-C)^2}-k^2-\frac{u_0''}{(u_0-C)}-\frac{2\Gamma u_0'}{u_0-C}-\Gamma^2\right]W(z)=0. \qquad (1)$$

In the above equation $W=[\rho_0(z)/\rho_s]^{\frac{1}{2}}w$, where w is the vertical velocity perturbation, ρ_0 the ambient density of the fluid, and ρ_s the density at some reference height that may be arbitrarily chosen within each layer. This transformation replaces the more common transformation of variables which only involves the factor $(\rho_0)^{\frac{1}{2}}$, and it retains the dimensions and approximate magnitudes of the variables. We have chosen to use the notation of Eckart (1960), for the Väisälä-Brunt frequency N and for $\Gamma=(g/2c_s^2)(1-N^2c_s^2/g^2)$. Since the sound velocity c_s for an incompressible fluid is infinite, $\Gamma=-N^2/2g$. Primes indicate height differentiation of the ambient velocity u_0 of the fluid. The phase velocity C is defined to be σ/k where the solutions in x and t are of the form $\exp i(kx-\sigma t)$. The influence of compressibility on atmospheric stratification can be included in Eq. (1) by expressing N and Γ in terms of potential temperature instead of density, but in applying it to the atmosphere it is required that terms in C/c_s be negligible and the acoustic solutions are therefore lost from the model.

In the following, Eq. (1) will be considered to apply to the atmosphere. Then $N^2=(g/\theta)\partial\theta/\partial z$ where θ is potential temperature. Furthermore, we will assume $u_0''=0$ (linear profile) and adopt a classical approximation that neglects the terms involving Γ. In the earth's atmosphere Γ is very small, being of the order of $g/2c_s^2$, since the dimensionless number $N^2c_s^2/g^2$ is always fractional. For an incompressible fluid, Γ is precisely zero if $N=0$, so under those conditions (1) is just

$$\frac{d^2W(z)}{dz^2}-k^2W(z)=0, \qquad (2)$$

with solutions which are some combination of terms of the form

$$W=W_0e^{-kz}. \qquad (3)$$

In order to make the argument that (2) is applicable in the compressible atmosphere we must justify the neglect of $2\Gamma u_0'/[u_0(z)-C]$ compared with k^2 even when $u_0(z)\rightarrow C$. If we are just concerned with the neutral curves, this is most easily done by permitting C to have a small imaginary component, i.e., consider conditions of some instability. Except for the effect of compressibility on stratification, our model will be treated as incompressible, and while its applicability to the atmosphere is suggested, the precise conditions for its justification are not pursued further. The fact that instability structures similar to those seen in the atmosphere are also found in the oceans implies that compressibility is not the primary consideration. However, since the atmosphere is more accessible to observation than the oceans, data to check the models come mostly from the atmosphere.

Eq. (2) has been used by many investigators, including Rayleigh, Kelvin, Taylor and Goldstein, to study problems in shear flow. In particular, Rayleigh (1894) examined the problem of the stability of a homogeneous fluid undergoing shear. Kelvin (1880) described the shape of the streamlines near the level where $C=u_0$, deducing the now famous "Kelvin cat's

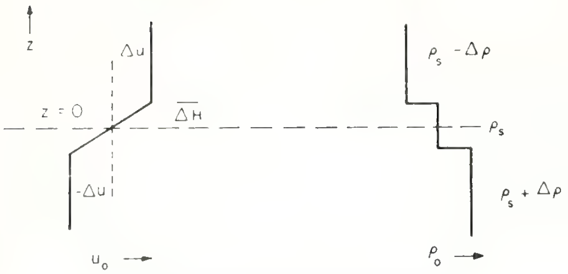

FIG. 1. Goldstein's three-layer model.

eye" pattern. Taylor (1931) and Goldstein (1931) examined several multilayer models; one is shown schematically in Fig. 1. Of course, the value of these models arose from the fact that simple solutions such as Eq. (3) could be assumed. When the dynamic and kinematic boundary conditions at the layer boundaries were satisfied, eigenvalue equations for the model were obtained which were then examined to determine the stability of perturbed flows. Models such as that in Fig. 1 were not physically realistic, but were useful in providing insight. For example, they demonstrated the importance of layer thickness on shear wave instability.

On the other hand, a model with no shear in which $N \neq 0$ has the wave equation

$$\frac{d^2W}{dz^2} - k^2\left(1-\frac{N^2}{\omega^2}\right)W = 0, \tag{4}$$

where, in general,

$$\omega = k[C - u_0(z)], \tag{4a}$$

but in the shearless model u_0 is constant.

Like Eq. (2), this equation has simple solutions, i.e. of the form

$$W = W_0 \exp\{-k[1-(N^2/\omega^2)]^{\frac{1}{2}}z\}. \tag{5}$$

Unlike the Taylor/Goldstein model of Fig. 1, this "no shear" model can include the static stability (in terms of N) in all layers of the model shown in Fig. 2. It was treated by Gossard and Munk (1954) who used it to analyze gravity waves in the lower atmosphere in Southern California. They found the eigenvalue equation

$$\gamma_2 \operatorname{ctnh}(2\gamma_2\Delta H) = \frac{-\gamma_2^2 - \gamma_1\gamma_3 \operatorname{ctnh}(\gamma_1 H)}{\gamma_1 \operatorname{ctnh}(\gamma_1 H) + \gamma_3}, \tag{6}$$

where $\gamma = k(1-N^2/\omega^2)^{\frac{1}{2}}$ and the subscripts on γ go with those on N. For a model in which $H=\infty$ and $N_1 = N_3 = N$, Eq. (6) becomes

$$\operatorname{ctnh} 2\gamma_2\Delta H = -\frac{\gamma^2+\gamma_2^2}{2\gamma\gamma_2}. \tag{6a}$$

For models of interest, N_1 or N_2 are greater than ω so that γ_1, γ_2, or both, are pure imaginary. If wind shear is included in a model like that of Fig. 2, waves generated within the region of shear are either unstable or cannot exist if their phase velocity is anywhere equal to the wind speed (e.g., Scorer, 1951). Much effort has gone into the analysis of models with wind shear across such stable layers in an effort to determine the range of initial instability and the most unstable wavenumber at the onset of instability. We mention recent papers such as Miles and Howard (1964) who analyzed a model with profiles made up of linear segments, Drazin (1958) who analyzed a hyperbolic tangent wind profile and an exponential density profile, and Holmboe (1960) who analyzed profiles both of which were hyperbolic tangent in form. All such studies are mathematically difficult because of singularities at the critical level, where $C = u_0$, which require some form of solution of a hypergeometric differential equation. If the results of such analyses of the linearized equations [such as Eq. (1)] are applicable to the real atmosphere, they are likely to apply only at the onset of a disturbance when the perturbations are still very small. The whole subject of shear instability is very completely summarized by Drazin and Howard (1966).

Many of the recent results were anticipated in earlier papers by Taylor (1931), Goldstein (1931) and Sekera (1948). After examining the general (linearized) problem of the dynamic stability of an inviscid, statically stable layer under shear, Sekera concluded that billow clouds were a result of waves at a shear layer, and that they must occur at levels in the atmosphere where the static stability vanishes, i.e., an isentropic region, in order to account, within the linear theory, for the stability of their patterns. In this paper we explore isentropic models, and suggest that wavelike disturbances arising from shear wave instability tend to create such a model and steady patterns.

2. Model 1

For the models to be examined in this paper, the solutions (3) and (5) are applicable. A limiting form (i.e., $H=0$) has been used by Ramm and Warren

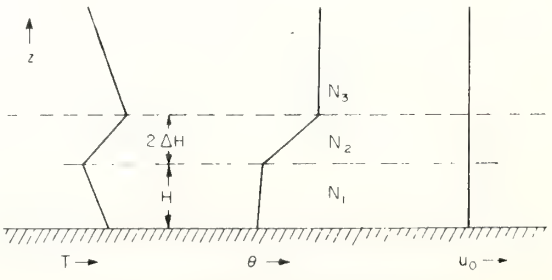

FIG. 2. Gossard-Munk three-layer model.

(1963) to examine the effect of an impulse on gravity wave generation and dispersion. Our first model is one in which a shear layer of statically neutral stability is imbedded in a medium which is otherwise statically stable and whose stability can be described by a constant Väisälä-Brunt frequency N. Then the solution applies within the shear layer and the solution [Eq. (5)] applies elsewhere. The model is shown schematically in Fig. 3, where

$$\left.\begin{array}{ll} u_0=-\Delta u, & \theta=\theta_s\exp[(N_1^2/g)z], \quad \text{for } z<H \\ u_0=-\Delta u+\beta(z-H), & \theta=\theta_s\exp[(N_1^2/g)H], \\ & \qquad \text{for } H<z<H+2\Delta H \\ u_0=\Delta u, & \\ \quad \theta=\theta_{H+2\Delta H}\exp[(N_3^2/g)(z-H-2\Delta H)], & \\ & \qquad \text{for } z>H+2\Delta H \end{array}\right\}$$

Solutions for the various layers are of the form

$$W_1=A\sinh\gamma_1 z, \qquad z<H, \tag{7a}$$

$$W_2=B_1e^{kz}+B_2e^{-kz}, \quad H<z<H+2\Delta H, \tag{7b}$$

$$W_3=De^{-\gamma_3(z-2\Delta H)}, \qquad z>H+2\Delta H. \tag{7c}$$

The kinematic boundary condition to be satisfied at the layer interface is (for small perturbations)

$$W_1=W_2, \quad W_2=W_3,$$

and the dynamic condition is $p_1=p_2$ and $p_2=p_3$, where p is total pressure. Then

$$\frac{dp_1}{dt}=\frac{dp_2}{dt}, \quad \frac{dp_2}{dt}=\frac{dp_3}{dt};$$

therefore,

$$\left(\frac{\rho_0}{\rho_s}\right)^{\frac{1}{2}}\left(\frac{DP}{Dt}-\rho_s gW\right) \tag{8}$$

must be continuous across fluid interfaces. D/Dt is the Stokes operator

$$\frac{D}{Dt}=\frac{\partial}{\partial t}+u_0\frac{\partial}{\partial x}=-i\omega,$$

and $P=(\rho_0/\rho_s)^{-\frac{1}{2}}p'$, where p' is the pressure perturbation. The unperturbed density is ρ_0, and ρ_s the density at some reference level. For convenience the x direction is chosen to be the direction of horizontal propagation. In condition (8), it is convenient to express P in terms of W using

$$\frac{DP}{Dt}=\rho_s\frac{\omega}{k}\left[\beta W+\frac{\omega}{k}\frac{\partial W}{\partial z}\right], \tag{9}$$

where $\beta=du_0/dz=\Delta u/\Delta H$ and where ω, k is defined by Eq. (4a). Letting $\alpha=k\Delta H$, one finds from Eq. (4a) that $\omega/\beta=\sigma/\beta\pm\alpha$ in the lower (+) and upper (−) layers,

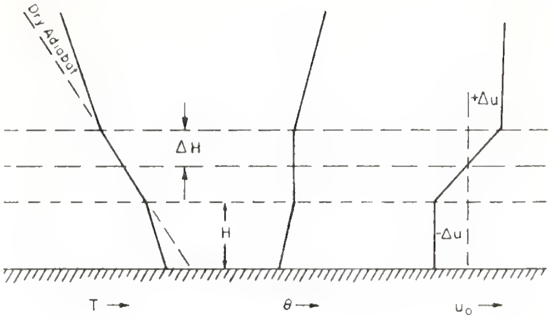

FIG. 3. Model 1.

and

$$\frac{\omega}{\beta}=\frac{\sigma}{\beta}+\alpha\left(1-\frac{z-H}{\Delta H}\right), \quad H<z<H+2\Delta H,$$

in the shear layer. Therefore,

$$\gamma_1=k\left[1-\left(\frac{N_1/\beta}{\frac{\sigma}{\beta}+\alpha}\right)^2\right]^{\frac{1}{2}}, \quad \gamma_3=k\left[1-\left(\frac{N_3/\beta}{\frac{\sigma}{\beta}-\alpha}\right)^2\right]^{\frac{1}{2}}.$$

Applying the solutions given in Eq. (7) to the condition (8), we find at the lower boundary

$$\left[\alpha_1-\alpha\frac{1-(B_2/B_1)e^{2\alpha}}{1+(B_2/B_1)e^{2\alpha}}\right]\left(\frac{C}{\Delta u}+1\right)=1, \tag{10a}$$

where we have let $\alpha_1=\gamma_1\Delta H$ ctnh~~β~~H. At the upper boundary, if we let $\alpha_3=\gamma_3\Delta H$ γ

$$\left[\alpha\frac{1-(B_2/B_1)e^{-2\alpha}}{1+(B_2/B_1)e^{-2\alpha}}+\alpha_3\right]\left(\frac{C}{\Delta u}-1\right)=-1. \tag{10b}$$

Elimination of B_2/B_1 reveals the eigenvalue equation for the model of Fig. 3 to be

$$\left[\left(1+\frac{\alpha_1\alpha_3}{\alpha^2}\right)\tanh 2\alpha+\frac{\alpha_1+\alpha_3}{\alpha}\right]\left(\frac{\sigma}{\beta}\right)^2$$
$$+\left[\left(\frac{\alpha_1-\alpha_3}{\alpha}\right)\tanh 2\alpha\right]\left(\frac{\sigma}{\beta}\right)+(2\alpha-\alpha\alpha_1-\alpha\alpha_3)$$
$$-(1+\alpha^2-\alpha_1-\alpha_3+\alpha_1\alpha_3)\tanh 2\alpha=0. \tag{11}$$

If $N=0$, the model is a three-layer homogeneous medium with the middle layer under constant shear and is one of a class of homogeneous models studied extensively by Rayleigh. Then $\alpha_3=\alpha$ and $\alpha_1=\alpha$ ctnhkH. Thus, Eq. (11) is of the form

$$a\left(\frac{\sigma}{\beta}\right)^2+b\frac{\sigma}{\beta}+c=0, \tag{12}$$

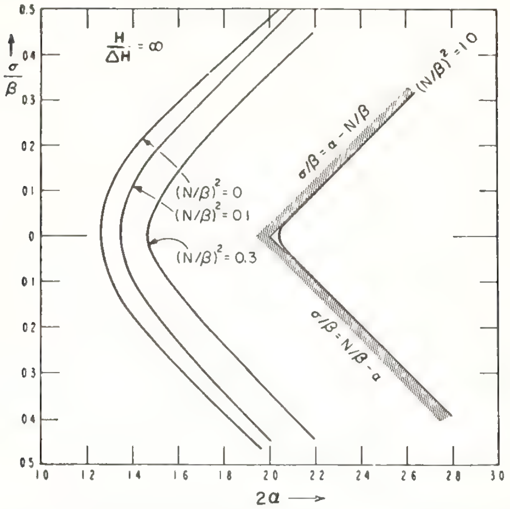

FIG. 4. Eigenvalue plots, Model 1, parametric in N^2/β^2; $H/\Delta H=\infty$. Beyond shaded lines $|\alpha\pm\sigma/\beta|<N/\beta$ and energy leaks away from layer.

where

$$\left.\begin{aligned}a&=(1+\operatorname{ctnh}kH)(\tanh 2\alpha+1)\\ b&=(\operatorname{ctnh}kH-1)\tanh 2\alpha\\ c&=\alpha[2-\alpha(\operatorname{ctnh}kH+1)]\\ &\qquad-[1+\alpha(\alpha-1)(1+\operatorname{ctnh}kH)\tanh 2g]\end{aligned}\right\}.$$

The question of stability is therefore decided by the sign at b^2-4ac.

The most widely quoted result of Rayleigh is found for the model in which $H=\infty$ so that (12) reduces to

$$\left(\frac{\sigma}{\beta}\right)^2=\frac{\tanh 2\alpha}{2(\tanh 2\alpha+1)}-\alpha(1-\alpha). \tag{13}$$

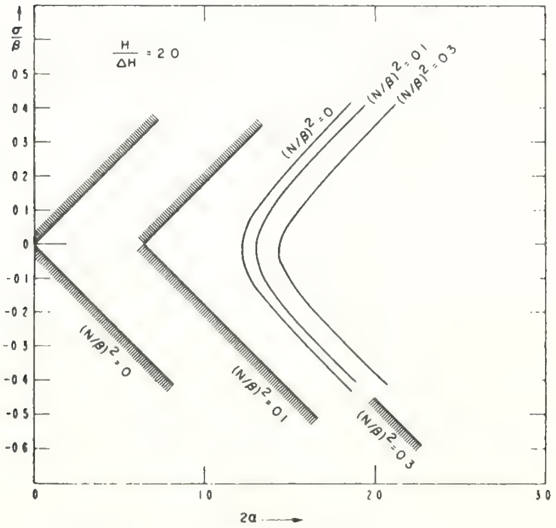

FIG. 5. Eigenvalue plots, Model 1, parametric in N^2/β^2; $H/\Delta H=2$.

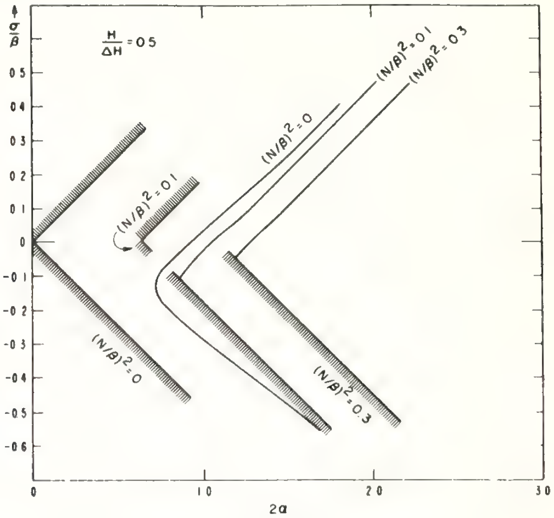

FIG. 6. Eigenvalue plots, Model 1, parametric in N^2/β^2; $H/\Delta H=0.5$.

Recalling that $\tanh 2\alpha=(1-e^{-4\alpha})/(1+e^{-4\alpha})$, one finds the Rayleigh condition for stability [σ real and $(\sigma/\beta)^2$ positive] for this model to be

$$(2\alpha-1)^2-e^{-4\alpha}>0,$$

which yields the critical ratio of wavelength to layer thickness to be

$$\frac{\lambda}{2\Delta H}=\frac{2\pi}{1.28}=4.90.$$

Rayleigh further found the most unstable wavelength [that wavelength for which $(\sigma/\beta)^2$ reaches its largest negative value] to be given by the ratio

$$\frac{\lambda}{2\Delta H}=\frac{2\pi}{0.8}=7.85.$$

At the other extreme, when $\beta=0$ (i.e., $\Delta u=0$), the "no shear" limit of Eq. (11) reduces to the Gossard-Munk equation (6) which applies to a nonhomogeneous atmosphere. If $N_2=0$, $N_1=N_3=N$, and $H=\infty$, one finds from (6) that

$$\operatorname{ctnh} 2\alpha=-\frac{\alpha^2+\alpha_0^2}{2\alpha\alpha_0},\quad\text{where}\quad \alpha_0=\alpha[1-(N/\sigma)^2]^{\frac{1}{2}}. \tag{14}$$

The plots of σ/β vs 2α, from (11), are shown in Figs. 4–6 for various values of $H/\Delta H$, assuming in all cases that $N_1=N_2=N$. The curve designated as $N^2/\beta^2=0$ is that of the Rayleigh homogeneous model [Eq. 12]. The other curves represent a generalization of the homogeneous model in which a statically neutral shear layer is imbedded in a statically stable medium.

Although N^2/β^2 is superficially like a Richardson number, N describes the stability of the medium *outside* the layer while β describes the shear *across* the layer. For values of 2α to the left of the nose of the curves, only imaginary or complex values of the frequency σ can be roots of (11) and such solutions represent unstable disturbances. On the shaded side of the straight lines, the radical in γ_1 or γ_3 becomes imaginary, i.e., $|\alpha\pm\sigma/\beta| < N/\beta$. Beyond $\sigma/\beta=\pm(N/\beta+\alpha)$, it would again become real.

The plot of σ/β vs 2α is shown parametric in $H/\Delta H$ for $N/\beta=0$ in Fig. 7. As $H\rightarrow 0$

$$\left.\begin{aligned} a&=1+\tanh 2\alpha \\ b&=\tanh 2\alpha \\ c&=-\alpha^2+\alpha(1-\alpha)\tanh 2\alpha \end{aligned}\right\}\text{ in Eq. (12).}$$

For this special case σ/β is real for all α and the flow is stable. This result is in accord with Rayleigh's general conclusion on "inflection point instability," since change in slope of the velocity profile has only one sign when $H=0$. The "nose" of the eigenvalue curve in this case dips in to the origin. Clearly the presence of a boundary must be considered when it is less than a wavelength from the shear layer. When it is less than 0.1 wavelength away from the layer, it is very important. The boundary effect is even more striking in Fig. 8 in which the value of $(b^2-4ac)/4a^2$ is plotted vs 2α, parametric in $H/\Delta H$. When $(b^2-4ac)/4a^2$ is negative, the frequency has an imaginary part and perturbations are unstable, growing exponentially. Its maximum negative value represents a most unstable value of 2α. The dashed curves in Fig. 8 show the real part of the ratio $C/\Delta u$ (see model) in the unstable range of $2k\Delta H$ for various values of $H/\Delta H$. When $H=\infty$, $C=0$, so the waves move with the mean wind speed within the shear layer, i.e., zero. When $H/\Delta H$ becomes small, $C/\Delta u$ becomes significantly negative, so the waves tend to move with the wind in the lower layer.

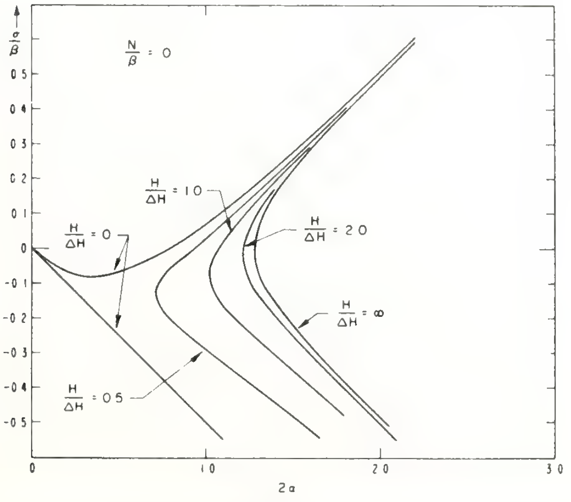

FIG. 7. Eigenvalue plots, Model 1, parametric in $H/\Delta H$, $N/\beta=0$.

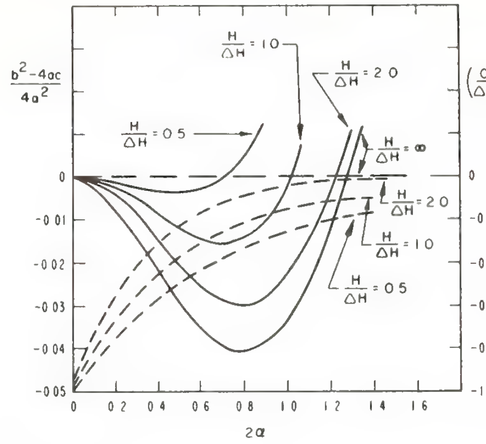

FIG. 8. Curves describing real (dashed) and imaginary (solid) components of $C/\Delta u$; parametric in $H/\Delta H$.

3. Model 2

Suppose we seek a model that may be representative of intense mixing in a layer imbedded in a stable medium, and treat the model shown in Fig. 9. This model can be thought of as a generalization of the Goldstein model (Fig. 1) with a lower boundary—one in which the upper and lower layers are no longer required to be homogeneous. This model contains discontinuities in temperature (inversions) at the layer boundaries, so the boundary condition (8), taking into account the density discontinuity, requires continuity of

$$\rho_s\frac{\omega}{k}\left(\beta W+\frac{\omega}{k}\frac{\partial W}{\partial z}\right)-\rho_s g W. \tag{15}$$

Proceeding as before, applying the solutions (7), and neglecting $\Delta\rho$ compared with ρ_s (or $\Delta\theta$ compared with θ) except when it appears as a product of g, one finds

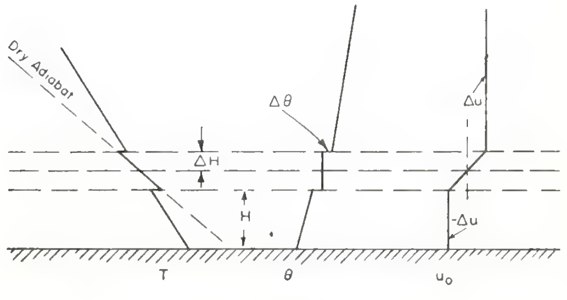

FIG. 9. Model 2.

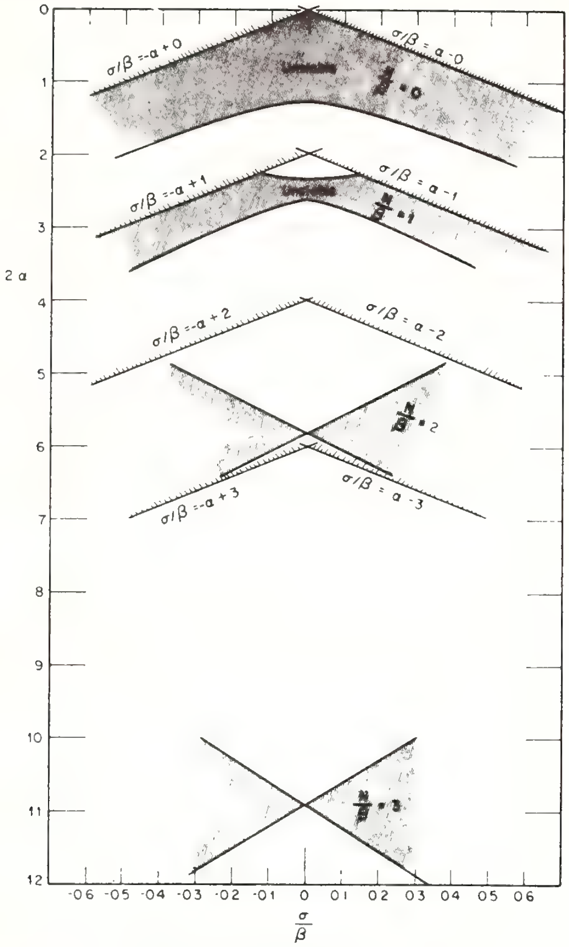

FIG. 10. Eigenvalue plots, Model 2, parametric in N^2/β^2; $H/\Delta H=\infty$.

that

$$e^{4\alpha}\left[\frac{-R_U+\left(\dfrac{C}{\Delta u}-1\right)^2(\alpha_3+\alpha)+\dfrac{C}{\Delta u}-1}{R_U+\left(\dfrac{C}{\Delta u}-1\right)^2(\alpha-\alpha_3)-\dfrac{C}{\Delta u}+1}\right]$$

$$=\left[\frac{R_L+\left(\dfrac{C}{\Delta u}+1\right)^2(\alpha-\alpha_1)+\dfrac{C}{\Delta u}+1}{-R_L+\left(\dfrac{C}{\Delta u}+1\right)^2(\alpha+\alpha_1)-\dfrac{C}{\Delta u}-1}\right],$$

where $R_{U,L}=g(\Delta\rho_s)_{U,L}\Delta H/(\rho_s\Delta u^2)$ is a kind of Richardson number for the upper (U) and lower (L) discontinuities, and $\Delta\rho_s$ is the density difference across each discontinuity. As before, we equate $\Delta\rho_s/\rho_s$ and $\Delta\theta/\theta$. Choosing the special case of $R_U=R_L=R$ and remembering that $C/\Delta u=\sigma/\alpha\beta$, it can be written

$$a\left(\frac{\sigma}{\beta}\right)^4+e\left(\frac{\sigma}{\beta}\right)^3+b\left(\frac{\sigma}{\beta}\right)^2+f\left(\frac{\sigma}{\beta}\right)+c=0, \qquad (16)$$

where

$$a=\frac{1+\alpha_1\alpha_3/\alpha_2}{\alpha^2}\tanh 2\alpha+\frac{\alpha_1+\alpha_3}{\alpha^3},$$

$$e=\frac{\alpha_1-\alpha_3}{\alpha^3}\tanh 2\alpha,$$

$$b=-\left[\frac{(R-1)(\alpha_1+\alpha_3)}{\alpha^2}+1+2(1+\alpha_1\alpha_3/\alpha^2)\right]$$
$$\times\tanh 2\alpha-\frac{2}{\alpha}[R-1+(\alpha_1+\alpha_3)],$$

$$f=\frac{\alpha_1-\alpha_3}{\alpha^3}\{1-2(1+R)\}\tanh 2\alpha,$$

$$c=[(1+R-\alpha_1)(1+R-\alpha_3)+\alpha^2]$$
$$\times\tanh 2\alpha+\alpha(\alpha_1+\alpha_3)-2\alpha(1+R).$$

Inspection of Fig. 9 shows that $R=N^2/\beta^2$ which greatly simplifies the parameterization of the problem when $N_1=N_3$.

When the medium in which the layer is imbedded is of neutral stability, $\alpha_1=\alpha_3=\alpha$ and the model is that shown in Fig. 1 and treated by Goldstein (1931).

The eigenvalue curves for Model 2 are shown in Fig. 10. It is apparent that as N/β increases from zero the domain of instability moves out toward larger α in a rapidly narrowing *band* of unstable wavenumbers as shown in Fig. 11 for $\sigma/\beta=0$. By the time $N/\beta=2$, the unstable range is almost pinched out and is essentially monochromatic so that wave excitation should be

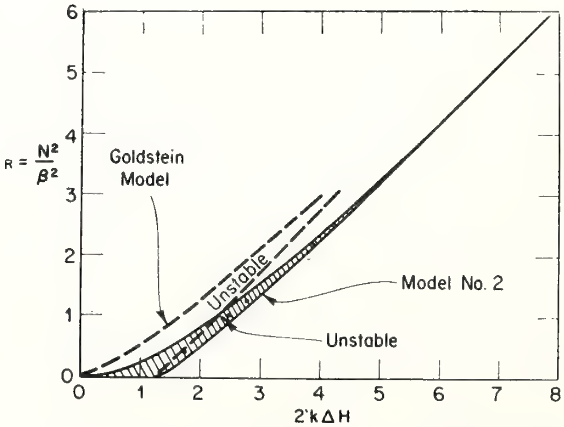

FIG. 11. Neutral curves, Model 2, for $\sigma=0$ ($C=0$). Dashed curves refer to Goldstein's model (Fig. 1). Dots are experimental values from Katz' data plotted in unstable region without regard to N/β.

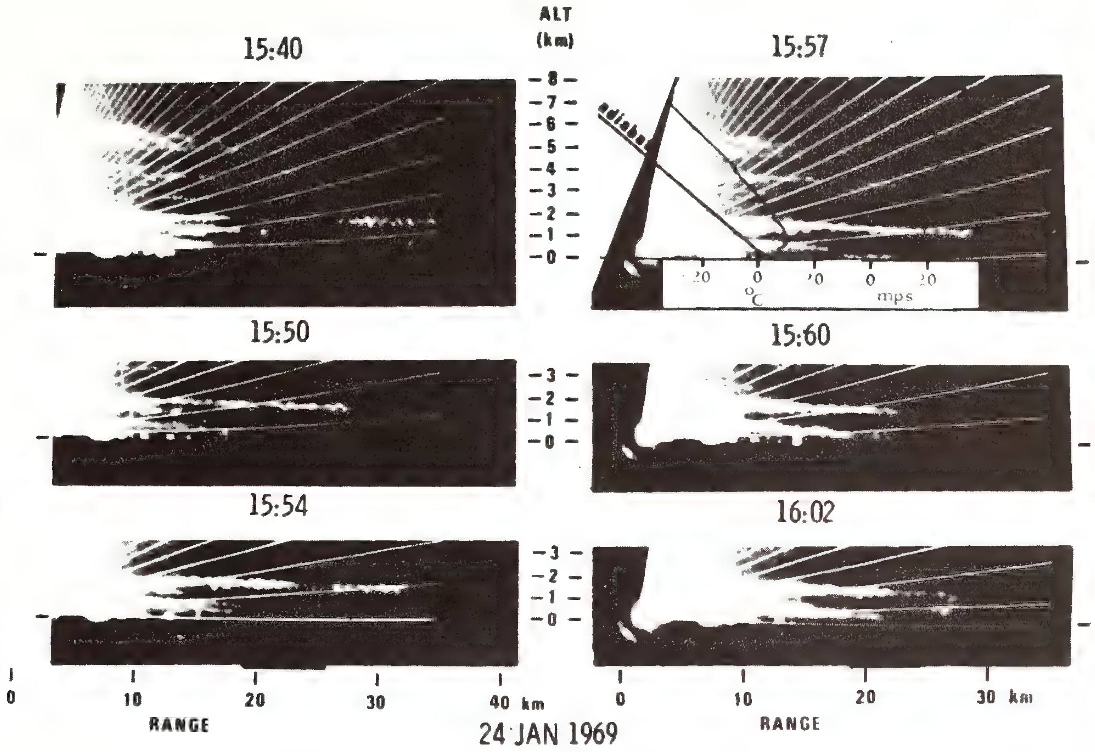

Fig. 12. Radar returns from the clear atmosphere taken from Katz (1972) for radar located at Wallops Island. The 1830 EST temperature and wind sounding at Wallops Island is shown in the 1557 EST frame of the figure. Note strongly super-adiabatic layer at about 1500 m.

highly selective in wavelength. Even for N/β as small as 1.0, the ratio of wavelength to total layer thickness ranges only from 2.4 to 2.7. However, the *magnitude* of maximum instability decreases as the band narrows, so one would expect to observe those wavelengths which lie within the region of appreciable bandwidth. Because of the spatial symmetry of the model with infinite lower and upper layers, it is natural to suppose the real part of the wave velocity C_r to be zero (and therefore $\sigma_r=0$). This can be proved in special cases; e.g., Tollmien (1935) proved that $C=u_0$ at the inflection point of a monotonic profile of velocity for a neutral disturbance in a flow of uniform density.

The above model only describes a limiting condition toward which the real atmosphere would tend when violent mixing occurs, caused perhaps by dynamic instability from shear within the medium. The extent to which the model is pertinent to the observed layer structure within the real atmosphere should be determined by observation.

4. Observations of structure on layers

A variety of models with shear layers imbedded in stably stratified media have been analyzed in recent years. For example, Drazin (1958) analyzed a model with a hyperbolic tangent wind distribution and exponential density decrease. Holmboe (1960) analyzed a model with hyperbolic tangent wind distribution and hyperbolic tangent exponent of the density distribution. Miles and Howard (1964) analyzed a three-layer model in which both wind and density were composed of linear segments, piecewise continuous. The symmetrical or nearly symmetrical models of both Holmboe (1960) and Miles and Howard (1964) give a ratio of wavelength/layer thickness of about 6.5 for the "most unstable wave," and the nonsymmetrical (density) model of Drazin gives about 4.5.

Few reliable measurements exist against which to compare the various models. From acoustic sounder data and *in-situ* tower data, Emmanuel *et al.* (1972) found ratios of 5.2 and 4.0 for features in the boundary layer. From similar data on another event, Hooke *et al.* (1973) found a ratio of 3.5. Gossard *et al.* (1970) found a ratio of 3.2 for features on an elevated layer using FM-CW radar data and radiosonde sounding data. The above investigations suggest that observed ratios tend to be smaller than those implied by the major instability models for stable layers. However, all of the above observations were indirect in the sense that the horizontal scale had to be inferred from the wave velocity. Sometimes (Emmanuel *et al.*, 1972) the wave

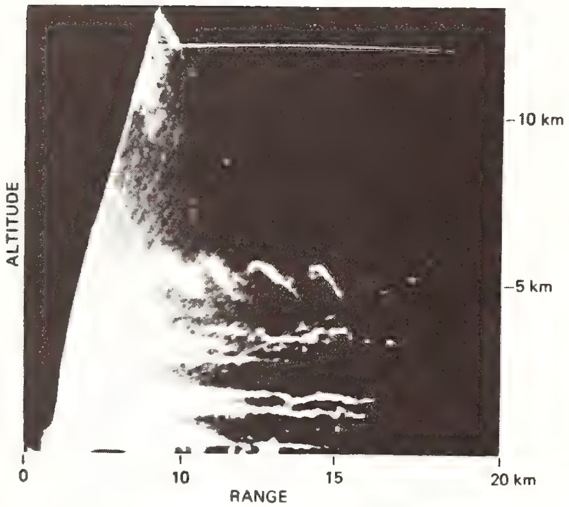

FIG. 13. Radar returns from the clear atmosphere taken from Katz (1972). Same day as in Fig. 14 but time is different.

velocity was assumed to be that of the wind at the height of the wave structure; sometimes (Hooke *et al.*, 1973) the wave velocity was deduced from the ratio of pressure perturbation to wind perturbation through the impedance equation, or (Gossard *et al.*, 1970) through the ratio of velocity perturbation components by use of polarization relations.

Table 1 is compiled from data that were published by Katz (1972). They should be more reliable than any of the earlier data referenced because the measurements of the spatial scales are direct.

Figs. 12–15 show radar returns from the clear atmosphere obtained by the powerful pulse radar of NASA at Wallops Island on a wavelength of 10 cm. From data such as these the ratio of spatial wavelength to echo layer thickness may be scaled directly. The main uncertainty concerns the question of whether the braided or wavelike features completely fill the layer and are thus a true measure of layer thickness. However, underestimation of layer thickness would *increase* the estimated ratio. The ratios so deduced are presented in Table 1.

TABLE 1. Ratios of wavelength to layer thickness from observations published by Katz (1972). Figures in parentheses are corresponding values of 2α.

Date	Figure number	Time (EST)	High layer	Middle layer	Low layer
24 Jan. 1969	14	1540	2.9(2.2)	1.5(4.2)	
		1550		2.3(2.7)	
		1554		1.6(3.9)	
		1557	4 (1.6)	1.6(3.9)	
		1560		1.5(4.2)	
24 Jan. 1969	15		2.7(2.3)		
16 May 1968	16			2.7(2.3)	
20 Dec. 1968	17				3.8(1.7)

The values of 2α are shown in parentheses in the table and are plotted in Fig. 11 (Model 2) as solid dots without regard to observed values of N^2/β^2. Reliable estimates of N^2/β^2 were impossible from the available wind sounding data, since the balloon release time was 3 hr after the radar observations. However, it is evident that the cases fall in the "narrow band" region of the graph and in a range of N^2/β^2 which is easily attained in the atmosphere. Table 1 indicates a clear tendency for the observed ratios of wavelength to layer thickness to be significantly less (average 2.3) than those predicted for the most unstable wave for shear layers in stable media. Furthermore, Model 2 provides a mechanism for strong selectivity of wavelength, as observed, whereas other models provide only weak selectivity associated with the broad peak of the neutral curves.

The sounding data for the 1830 EST (2330 GMT) balloon release on 24 January is shown in the 1557 EST frame of Fig. 12 in which the layer structure is clearest. The sounding data are too remote in time from the radar observations to provide reliable quantitative data; however, the layer structure revealed is qualitatively similar to that observed by the radar, and the presence of super-adiabatic and near-adiabatic layers in the vicinity of the radar echo layers is obvious, especially at the most periodic of the layers near 1.5 km.

In several of the references listed above, acoustic echo soundings and FM-CW radar soundings are shown which reveal structures within statically stable regions of the troposphere which appear to be unaccompanied by significantly increased temperature lapse rates according to radiosonde temperature soundings through the layers. However, such layers in the lower troposphere are thin, and these sounders cannot probe the deeper layer structure of the higher atmosphere. Since the response of the radiosonde temperature element is poor, it cannot be expected to adequately resolve such thin layers. However, the humidity element responds much faster, and the corresponding humidity distribution (or radio refractive index) invariably shows regions of small gradient in the neighborhood of thin echo layers. Since such regions of small gradient are usually (as expected) bounded by regions of large gradient, very precise matching of the height of the radiosonde with the height of layer echoes is required to establish the relationship between atmospheric structure and layer echoes. The double-echo structure often seen on sounder records may represent returns from the bounding regions of large gradient in this model. Certainly, observations using the lower tropospheric sounders do not rule out the "intense mixing" model we suggest, and the powerful pulse radars probing deeper layers of the atmosphere tend to support this model.

The observations shown in this paper tend to favor Model 2 (the limit of intense mixing in a statically

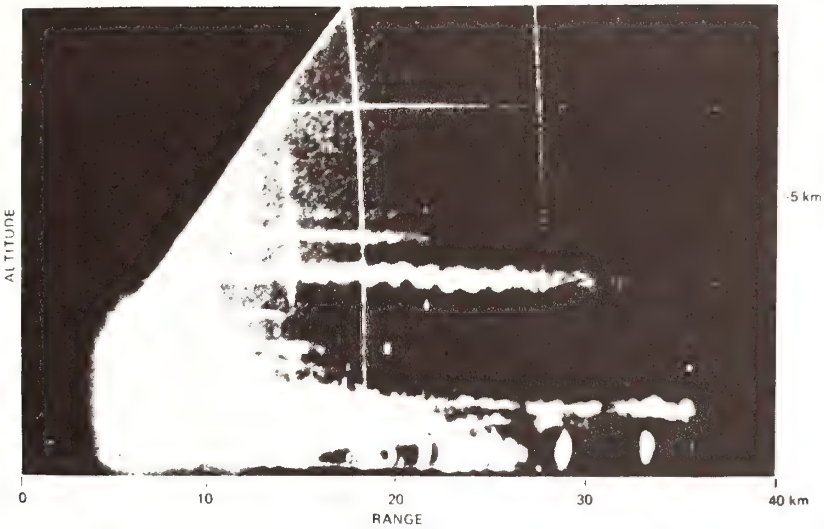

Fig. 14. Radar returns (16 May 1968) from the clear atmosphere taken from Katz (1972).

stable medium) rather than Model 1. However, Model 1 may also fairly well represent some cases of wave generation when the isentropic or nearly isentropic layer is a result of air mass dynamics or thermodynamics. In this case, the bounding inversion discontinuities might be expected to be absent as assumed in Model 1. Broad-band wave generation of this type may be the explanation of pressure oscillations of a class observed in the eastern United States which has been attributed (Madden and Claerbout, 1968) to wave generation by dynamic instability due to shear in the upper atmosphere associated with the jet stream. If the temperature lapse is nearly isentropic in such a region of shear, Model 1 may be fairly realistic.

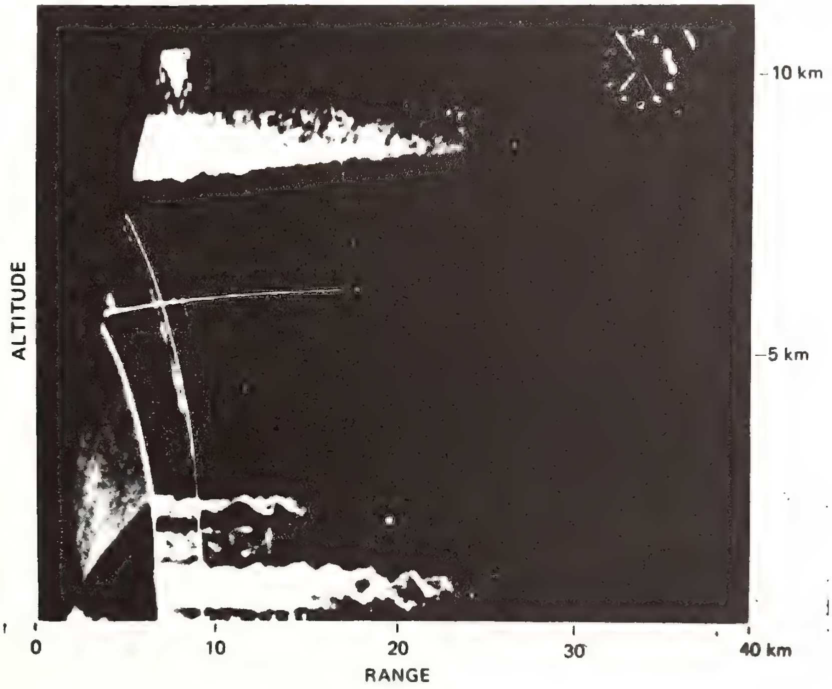

Fig. 15. Radar returns from the clear atmosphere taken from Katz (1972). Layer at about 8 km is cirrus cloud.

5. Streamlines of the flow

To find eigensolutions for the homogeneous region, either Eq. (10a) or Eq. (10b) is solved for B_2/B_1, and $C/\Delta u$ is then eliminated using Eq. (11). For an infinitely deep lower layer, and $N_1=N_3$, Eq. (10b) becomes

$$\frac{B_2}{B_1}=e^{2\alpha}\frac{(\alpha_3+\alpha)\left(\dfrac{C}{\Delta u}-1\right)+1}{(\alpha-\alpha_3)\left(\dfrac{C}{\Delta u}-1\right)-1},$$

where $\alpha_3=\gamma\Delta H$. For a homogeneous model, $\alpha=\alpha_3$ and

$$\frac{B_2}{B_1}=-e^{2\alpha}\left[2\alpha\left(\frac{C}{\Delta u}-1\right)+1\right],$$

where

$$\left(\frac{C}{\Delta u}\right)^2=\frac{(2\alpha-1)^2-e^{-4\alpha}}{4\alpha^2}, \tag{17}$$

which gives

$$\frac{B_2}{B_1}=-e^{2\alpha}\{[(2\alpha-1)^2-e^{-4\alpha}]^{\frac{1}{2}}+(1-2\alpha)\}.$$

The origin is chosen at the height where $C-u_0=0$. For the condition $C=0$, $B_2/B_1=\pm 1$, so Eq. (7b) gives

$$W_2=2B_1 \cosh kz.$$

Since $C=0$, the wave system is stationary in this model and $u_0=0$ at $z=0$. Within the Boussinesq approximation (and neglecting earth rotation), $U=ik^{-1}\partial W/\partial z$. Therefore, if U_s is the amplitude of the perturbation of the horizontal wind,

$$U_2=U_s \sinh kz,$$

so the total wind in the middle layer is

$$U=\beta z+U_s e^{ikx} \sinh kz,$$

where we have now included the factor periodic in x. The streamfunction is therefore

$$\psi=\int_0^z U(z)dz=\beta\frac{z^2}{2}+\psi_s e^{ikx} \cosh kz.$$

Then, for small kz, the displacement z of the streamlines is

$$z\approx\pm(2/\beta)^{\frac{1}{2}}(\psi-\psi_s e^{ikx})^{\frac{1}{2}}.$$

When $\psi=\psi_s$, this plots as a pattern of interlacing sinusoids of wavelength 2λ centered on the height $z=0$. When $\psi>\psi_s$, the streamlines are simple sinusoids. When $\psi<\psi_s$, they are closed curves within the interlaced sinusoids. The pattern is essentially the cat's eye pattern of Kelvin.

Acknowledgments. The author expresses his appreciation to I. Katz of the Applied Physics Laboratory, The Johns Hopkins University, for the use of the radar records—a crucial part of the paper—and for his helpful discussions of their interpretation.

REFERENCES

Clarke, R. H., 1962: Pressure oscillations and fallout downdraughts. *Quart. J. Roy. Meteor. Soc.*, **88**, 459–469.

Drazin, P. G., 1958: The stability of a shear layer in an unbounded heterogeneous inviscid fluid. *J. Fluid Mech.*, **4**, 214–224.

, and L. N. Howard, 1966: Hydrodynamic stability of parallel flow of inviscid fluid. *Advances in Applied Mechanics*, Vol. 9, New York, Academic Press, 1–89.

Eckart, C., 1960: *Hydrodynamics of Oceans and Atmospheres.* New York, Pergamon Press, 290 pp.

Emmanuel, C. B., B. R. Bean, L. G. McAllister and J. R. Pollard, 1972: Observations of Helmholtz waves in the lower atmosphere with an acoustic sounder. *J. Atmos. Sci.*, **29**, 886–892.

Goldstein, S., 1931: On the stability of superposed streams of fluid of different densities. *Proc. Roy. Soc. London*, **A132**, 524–548.

Gossard, E. E., and W. H. Munk, 1954: On waves in the atmosphere. *J. Meteor.*, **11**, 259–269.

, J. H. Richter and D. Atlas, 1970: Internal waves in the atmosphere from high-resolution radar measurements. *J. Geophys. Res.*, **75**, 903–913.

Holmboe, J., 1960: Unpublished lecture notes (see Miles, 1963).

, 1962: On the behavior of symmetric waves in stratified shear layers. *Geophys. Publ.*, **24**, No. 2, 67–113.

Hooke, W. H., F. F. Hall, Jr., and E. E. Gossard, 1973: Observed generation of an atmospheric gravity wave by shear instability in the mean flow of the planetary boundary layer. *Boundary Layer Meteor.*, **5**, 276–288.

Katz, I., 1972: The detection and study of gravity waves with microwave radar. *Proc. AGARD Conf. No. 115 on Effects of Atmospheric Acoustic Gravity Waves on Electromagnetic Wave Propagation*, 21-1 to 21-9.

Kelvin, Lord, 1880: On a disturbing infinity in Lord Rayleigh's solution for waves in a plane vortex stratum. *Nature*, **33**, 45–46.

Madden, T., and J. Claerbout, 1968: Jet stream-associated gravity waves and implications concerning jet stream instability. *Acoustic-Gravity Waves in the Atmosphere*, U. S. Govt. Printing Office, 121–134.

Miles, J. W., 1963: On the stability of heterogeneous shear flows. Part 2. *J. Fluid Mech.*, **16**, 209–227.

, and L. N. Howard, 1964: Note on heterogeneous shear flow. *J. Fluid Mech.*, **20**, 331–336.

Ramm, Pauline, and F. W. G. Warren, 1963: Gravity-wave dispersion under wind shear in two model atmospheres. *Quart. J. Roy. Meteor. Soc.*, **89**, 349–359.

Rayleigh, J. W. S., 1945: *The Theory of Sound*, Vol. 2 (reprint of 2nd ed. of 1894). New York, Dover, Chap. 21.

Scorer, R. S., 1951: On the stability of stably stratified shearing layers. *Quart. J. Roy. Meteor. Soc.*, **77**, 76–84.

Sekera, Z., 1948: Helmholtz waves in a linear temperature field with vertical wind shear. *J. Meteor.*, **5**, 93–102.

Taylor, G. I., 1931: Effect of variation of density on the stability of superposed streams of fluid. *Proc. Roy. Soc. London*, **A132**, 499–523.

Tollmien, W., 1935: Ein allgemeines Kriterium der Instabilität Laminarer Geschwindigkeitsverteilungen. *Nachr. Ges. Wiss. Göttingen, Math.-Phys. Kl.*, **50**, 79–114 (translated as NACA, Tech. Memo., No. 792, 1936).

Journal of Atmospheric Sciences 32, 2111-2124, November 1975.

The Influence of a Capping Inversion on the Dynamic and Convective Instability of a Boundary Layer Model with Shear

EARL E. GOSSARD

Wave Propagation Laboratory, NOAA, Boulder, Colo. 80302

WILLIAM R. MONINGER

Coe College, Cedar Rapids, Iowa 52402

(Manuscript received 31 March 1975, in revised form 15 July 1975)

ABSTRACT

The dynamic instability and the kinematics of a multi-layer, shear model of a convective boundary layer are analyzed. Important features of the model include a capping temperature inversion that may or may not be accompanied by a wind discontinuity, a surface-based superadiabatic layer, and a statically stable upper atmosphere. It is shown that the capping inversion can result in a relatively narrow band of dynamically unstable wavenumbers that depend on shear layer thickness, implying a strong selection of scale in growing disturbances. The influence of the various model parameters on selection of the "most unstable" scales is shown and their corresponding propagation velocities are calculated.

A simple form of the model is also used to examine the characteristics of the convectively unstable modes. It is found that two-dimensional disturbances aligned transverse to the wind shear are most dynamically unstable, whereas two-dimensional disturbances parallel to the wind shear are most convectively unstable.

The vorticity and general kinematics of the disturbances are affected in an important way by the presence of a critical level within the height range occupied by the disturbance.

1. Introduction

The current literature contains innumerable papers on the dynamic and kinematic structure of the convective boundary layer. These are mostly numerical investigations requiring the use of high-speed computers. Many have concerned themselves with Ekman layer instabilities in which wind profiles representative of an Ekman planetary boundary layer are assumed. A few examples of studies of this kind are those of Lilly (1966), Brown (1970, 1972), Kaylor and Faller (1972), Gallagher and Mercer (1965), Maslowe and Thompson (1971) and Deardorff (1965). Observational data have been provided by LeMone (1973). There is also a large literature on such subjects as numerical modeling of severe storms, cloud physics, and wet convection.

In addition to the investigations listed above, which are primarily numerical in nature, various analytic studies of simple models have been carried out. A few of these include the work of Case (1960), Kuo (1963) and Asai (1970) who analyzed the stability of two- and three-dimensional disturbances in a thermally unstable shear flow; Ramm and Warren (1963) who examined the dispersive character of impulsively generated waves in two-layer models with a surface-based adiabatic layer under shear; and Gossard (1974) who investigated the dynamic stability of both surface-based and elevated adiabatic shear layers within a stable atmosphere.

In some ways analytic models have advantages over numerical models, although numerical models can, of course, be more complicated and therefore can be more realistic. Analytic approaches often provide more physical insight, and they can usually be parameterized in a simple enough way so that the contribution of the various elements composing the model can be seen more clearly. We consider that much of the value of the model we have analyzed lies in the insight it can provide for numerical models that may include viscosity, nonlinear effects, and gaseous and liquid water.

Our model differs from others listed above in that it includes a capping temperature inversion, a surface-based superadiabatic layer, and a wind shear layer of varying height above the ground. Our model is three-dimensional, and we examine not only the conditions for dynamic instability but the kinematics of the initially most unstable disturbances and the influence of a critical level on the velocity fields and vorticity. As in most of the analytic studies listed above, our approach is to solve the boundary value problem by the method of normal modes.

2. The model

Our primary purpose is to examine the effects of a capping inversion on the dynamic stability of a boundary layer under shear. We choose to study a model

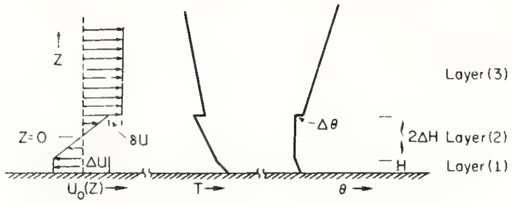

FIG. 1. The model. θ is potential temperature.

(Fig. 1) in which the shear layer is adiabatic because it has mathematically simple solutions such that fairly complicated layered models, including a capping inversion, can be synthesized by satisfying the dynamic and kinematic interfacial boundary conditions. Such a model is not representative of steady, horizontally homogeneous conditions because the large momentum flux that accompanies strong mixing in a shear layer will tend to erase the shear unless sources and sinks of momentum external to the system are maintained. Therefore, we do not claim this to be a general or typical representation of real boundary layers, but we do believe that real environments resemble it often enough so that it is worthwhile working out the consequences of the model and examining the way the various parameters of the model affect its dynamic instability. Of course it is unlikely in nature that the shear will ever coincide with a precisely adiabatic layer. In reality a transition zone between a superadiabatic region below and a somewhat stable region above, as seen in Fig. 2, is more likely. We hope the essential physics is not lost by representing the transition zone as an adiabatic layer. Beneath the shear layer we choose a neutral or superadiabatic layer without shear (except, of course, in a thin layer next to the ground which we neglect). In the analytic development we allow for a temperature discontinuity at the base of the shear layer as well as at the top, but in the numerical calculations we have assumed the lower discontinuity to be zero as shown in the schematic representation of our model in Fig. 1.

We believe the model may sometimes also be representative of environments that can lead to large-scale convective development and severe storms. Fig. 2 shows such an example. The "capping" inversion at 500 mb in this example is due to subsidence and is a common feature of soundings in this area and season. It is typically accompanied by an abrupt decrease in humidity with height. In the afternoon of the case shown, widespread cumulonimbus development occurred with damaging hail. The progression of the cells was from southwest to northeast which is in the direction of principal shear (x,z plane) having an azimuth of 230°;

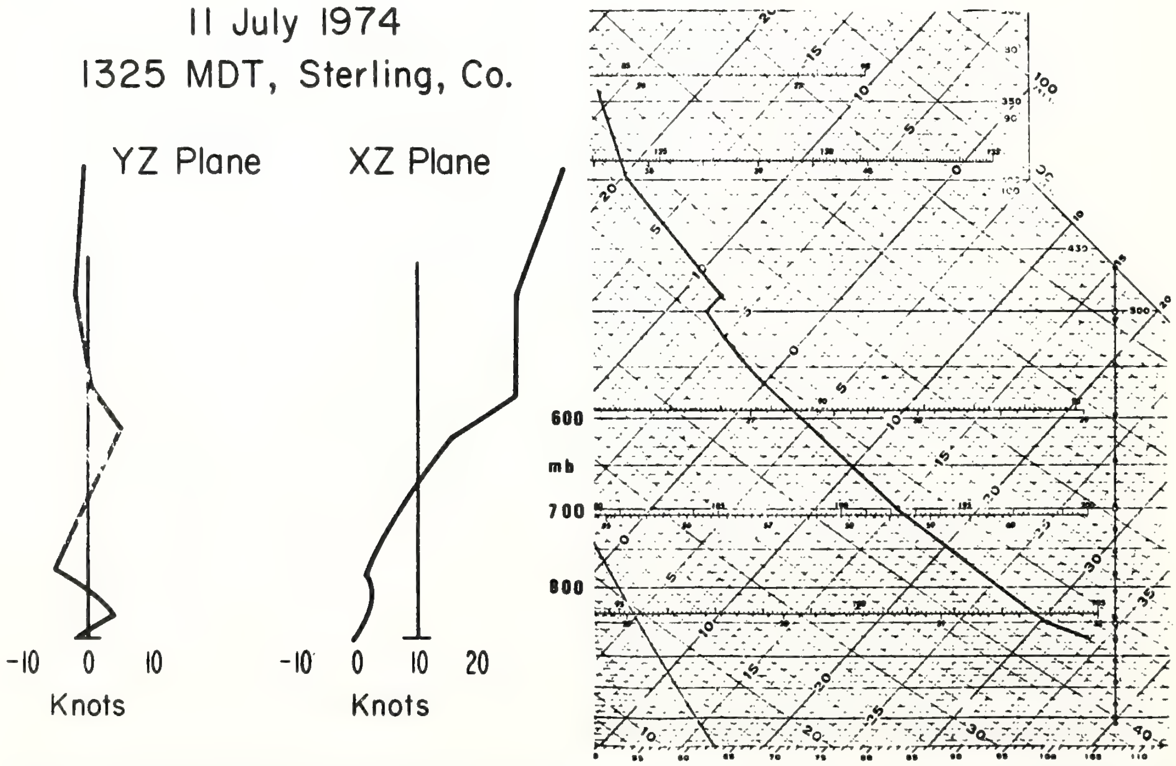

FIG. 2. Wind and temperature soundings made in severe storm conditions. Large-scale cumulonimbus development occurred in the afternoon. Cells moved from southwest to northeast. The x,z plane (the plane of principal shear) was oriented 230° in azimuth. Wind and temperature are plotted to the same height scale.

Clearly, the presence of the dynamic instability we discuss is not sufficient to ensure the development of convective storms. Factors such as the available moisture supply in the low-level air as well as convergence and vorticity in the mesoscale flow patterns will largely determine whether the "trigger" we propose will be effective in initiating large-scale convection.

The key characteristics of the model that lead to the important consequences are the inflection point in the wind profile which is the primary cause of the dynamic instability, and the capping inversion that confines the instability to a relatively narrow band of wavenumbers.

3. The linearized equations including shear

For a basic flow with vertical shear ($\partial u_0/\partial z$) in the x direction, the linearized equations of motion, continuity and energy conservation for adiabatic processes are

$$\frac{D}{Dt}\left(\frac{\partial u}{\partial x}\right)+\frac{1}{\rho_0}\frac{\partial^2 p}{\partial x^2}+\frac{\partial u_0}{\partial z}\frac{\partial w}{\partial x}=0, \tag{1}$$

$$\frac{D}{Dt}\left(\frac{\partial}{\partial y}\right)+\frac{1}{\rho_0}\frac{\partial^2 p}{\partial y^2}=0, \tag{2}$$

$$\frac{Dw}{Dt}+\frac{1}{\rho_0}\frac{\partial p}{\partial z}+g\frac{\rho}{\rho_0}=0, \tag{3}$$

$$\frac{D\rho}{Dt}+w\frac{\partial\rho_0}{\partial z}+\rho_0\nabla\cdot\mathbf{v}=0, \tag{4}$$

$$\frac{D\rho}{Dt}+w\frac{\partial\rho_0}{\partial z}=\frac{1}{c^2}\left(\frac{Dp}{Dt}+w\frac{\partial p_0}{\partial z}\right), \tag{5}$$

where u, v, w, ρ, p are small perturbations of the x, y, z components of wind, and of density and pressure. Zero subscripts indicate unperturbed quantities, and c is sound velocity. We have chosen the x direction as the direction of the undisturbed flow, so $v_0=w_0=0$ and the operator $D/Dt=\partial/\partial t+u_0(z)\partial/\partial x$.

It is convenient first to eliminate ρ between Eqs. (4) and (5). We then adopt the transformation

$$U,\ V,\ W,\ P^{-1}=(\rho_0/\rho_s)^{\frac{1}{2}}[u,\ v,\ w,\ p^{-1}], \tag{6}$$

where $\rho_0(z)$ is the distribution of the unperturbed density with height, and ρ_s is the density at some reference level such as the surface. The resulting partial differential equations are linear and homogeneous, and a solution representing one of the simplest forms of three-dimensional disturbance is

$$U,\ V,\ W,\ P=\tfrac{1}{2}[U(z),\ V(z),\ W(z),\ P(z)] \\ \times[\exp i(kx+ly-\sigma t)\pm\exp i(kx-ly-\sigma t)], \tag{7}$$

which requires the following phasing of the variables:

$$P=P(z)\cos ly\sin(kx-\sigma t) \tag{8}$$

$$U=U(z)\cos ly\sin(kx-\sigma t) \tag{9}$$

$$V=V(z)\sin ly\cos(kx-\sigma t) \tag{10}$$

$$W=W(z)\cos ly\cos(kx-\sigma t). \tag{11}$$

Elimination of $P(z)$, $U(z)$ and $V(z)$ leads to the ordinary differential equation in $W(z)$:

$$\frac{d^2W(z)}{dz^2}-\left\{m^2-\frac{u_0''k}{[C-u_0(z)]}-\frac{(Nm/k)^2}{[C-u_0(z)]^2}\right\}W(z)=0, \tag{12}$$

where $m^2\equiv k^2+l^2$, $u_0''\equiv d^2u_0/dz^2$. The phase velocity in the x direction is $C=\sigma/k$. In deriving Eq. (12), we have defined $N^2\equiv-g(\rho_0^{-1}d\rho/dz+g/c^2)=(g/\theta_0)d\theta/dz$, where N is the Väisälä-Brunt frequency (Väisälä, 1925; Brunt, 1927) and θ is potential temperature. Furthermore, we have neglected the quantity $(2\rho_0)^{-1}d\rho_0/dz+g/c^2$ compared with the operator $\partial/\partial z$ applied to the field variables, and we have assumed $C\ll c$. This is a form of the Boussinesq approximation and implies that we have assumed the scale depth of the atmosphere to be large compared with the scale depth of the disturbance. Eq. (12) is exactly the same as the wave equation for a two-dimensional disturbance except that k has been replaced by m and N has been replaced by (Nm/k).

From (7) we see that $D/Dt=-i\sigma+iku_0(z)\equiv-i\omega(z)$, which defines the intrinsic frequency $\omega=k[C-u_0(z)]$, where $C=\sigma/k$ is the velocity of the disturbance in the x direction. Thus ω can become zero at a "critical level" where $u_0=C$.

Then in terms of ω, $W(z)$ is related to the other variables as

$$U(z)=-\frac{k}{m^2}\left(\frac{\partial}{\partial z}-\beta\frac{k}{\omega}\frac{l^2}{k^2}\right)W(z), \tag{13}$$

$$V(z)=-\frac{l}{m^2}\left(\frac{\partial}{\partial z}+\beta\frac{k}{\omega}\right)W(z), \tag{14}$$

$$P(z)=-\rho_s\frac{\omega}{m^2}\left(\frac{\partial}{\partial z}+\beta\frac{k}{\omega}\right)W(z), \tag{15}$$

where $\beta\equiv\partial u_0/\partial z$.

If the coefficient in Eq. (12) is constant, it has very simple solutions which are some combination of exponentials. The coefficient is constant if both u_0''/ω and $(N/\omega)^2$ are constant or zero, but (12) will have annoying singularities at any height where $\omega=0$. In 1880 Lord Kelvin discussed this "disturbing infinity in Lord Rayleigh's solution for waves in a plane vortex stratum." He pointed out that if u_0'' is zero (and the fluid is homogeneous, i.e., $N=0$) "we evade entirely the consideration of this infinity." The simple solutions then apply, and Kelvin proceeded to deduce the now famous Kelvin's cat's eye pattern at the critical level from purely kinematic considerations.

In the model we analyze here, the atmosphere will be assumed to be adiabatic and the wind shear to be constant in the layer containing the critical level. As pointed out by Kelvin, we thus avoid the difficulty with singularities if we deal with vertical velocity. The simple solutions then apply and we can synthesize fairly complicated models by satisfying appropriate boundary conditions between the several layers of the model. However, although W is well behaved, the particle displacement is given by W/ω and would thus become infinite as ω goes to zero. Consequently, Kelvin's artifice does not allow us to "evade entirely" the problem of infinities at the critical level. However, confidence in the approach may be derived from the "reasonable" results deduced from such models as those examined by Taylor (1931), Goldstein (1931), Howard (1963), Holmboe (1962) and Gossard (1974). The singularities arise primarily because of the absence of viscosity in our model, and complete justification of the results must be found in a comparison with results found in models in which viscosity is included. Hazel (1967) solved numerically the full sixth-order differential equation including viscosity for flux-matching conditions across the critical level. He compared his results with those found for a model without viscosity by Booker and Bretherton (1967) and concluded that the results were identical within the limits of numerical truncation errors. We will now proceed to analyze a model made up of layers in which $u_0''=0$ and $(N/\omega)^2$ is either zero or constant.

4. The boundary conditions

To proceed with the solution of (12) for the multilayered model shown in Fig. 1, the eigensolutions which satisfy certain boundary conditions must be found.

At the surface, assumed to be level and rigid, $w=0$. At the interfaces between layers 1 and 2 and between 2 and 3, we satisfy the kinematic conditions $w_1=w_2$, $w_2=w_3$; and the dynamic conditions $p_{T1}=p_{T2}$ and $p_{T2}=p_{T3}$, where p_T is total pressure. The latter conditions can most conveniently be applied by requiring continuity in dp_T/dt where

$$\frac{dp_T}{dt}=\frac{Dp}{Dt}+w\frac{\partial p_0}{\partial z}=\left(\frac{\rho_0}{\rho_s}\right)^{\frac{1}{2}}\left(\frac{DP}{Dt}-\rho_s gW\right),$$

in which we have used the hydrostatic relation $\partial p_0/\partial z=-\rho_0 g$ and the transformation (6). If there is a discontinuity in the wind profile, the conditions of continuity in W and dp_T/dt are only exactly true in the long-wavelength (or small-amplitude) limit (see Gossard and Hooke, 1975). A somewhat more precise statement is that the displacement (and therefore W/ω) is continuous across boundaries. However, this condition is applied at the undisturbed position of the interface and therefore it also is only true in the small-amplitude limit. The degrees of approximation are comparable and either set of conditions leads to the same result. If we choose the interface to be the reference level of ρ_s, we have at the interface $\rho_{01}=\rho_{s1}$ and $\rho_{02}=\rho_{s2}$ so we require continuity in $DP/Dt-\rho_s gW$ across the interfaces. Letting β be the shear, the basic equations (8), (11) and (15) yield the differential relation

$$\frac{DP}{Dt}=-\frac{\rho_s\omega^2}{m^2}\left(\frac{\partial}{\partial z}+\frac{k}{\omega}\beta\right)W,$$

so that the dynamic boundary condition expressed in terms of W requires continuity of

$$\rho_s\frac{\omega^2}{m^2}\left(\frac{\partial}{\partial z}+\frac{k}{\omega}\beta\right)W-\rho_s gW. \tag{16}$$

Therefore, both the kinematic and dynamic boundary conditions at the interfaces can be satisfied by restrictions on W only. Because $\omega=k[C-u_0(z)]$ for a model with vertical shear, we readily see from Fig. 1 that

$$\left.\begin{array}{lll} u_0(z)=-\Delta u, & \omega=k(C+\Delta u), & z<-\Delta H \\ u_0(z)=\dfrac{\Delta u}{\Delta H}z=\beta z, & \omega=k\left(C-\dfrac{\Delta u}{\Delta H}z\right), & -\Delta H<z<\Delta H \\ u_0(z)=\Delta u+\delta u, & \omega=k(C-\Delta u-\delta u), & z>\Delta H \end{array}\right\},$$

so that $\omega_1/\beta=(k/m)\alpha(\xi+1)$, $\omega_3/\beta=(k/m)\alpha(\xi-1-\delta)$, where $\beta=\Delta u/\Delta H$, $\alpha=m\Delta H$, $\xi=C/\Delta u$, and $\delta=\delta u/\Delta u$.

Finally, we require that the modified vertical velocity W not become infinite at infinity.

5. The eigensolutions

If we choose the origin to be at the center of the shear layer, i.e., at $H+\Delta H$, solutions which satisfy the boundary conditions in the various layers are:

$$W_1=W_H\frac{\sinh\gamma_1(z+H+\Delta H)}{\sinh\gamma_1 H} \tag{17}$$

$$W_2=W_H\frac{\sinh mz+A\cosh mz}{-\sinh m\Delta H+A\cosh m\Delta H}$$

$$\equiv W_{H+2\Delta H}\frac{\sinh mz+A\cosh mz}{\sinh m\Delta H+A\cosh m\Delta H} \tag{18}$$

$$W_3=W_{H+2\Delta H}\exp[-\gamma_3(z-\Delta H)]. \tag{19}$$

Satisfying the condition (16) at the lower boundary of the shear layer we find for A that

$$A=\frac{(\xi+1)^2(\alpha_1\tanh\alpha+\alpha)-(\xi+1)\tanh\alpha-R'(m/k)^2\tanh\alpha}{(\xi+1)^2(\alpha_1+\alpha\tanh\alpha)-(\xi+1)-R'(m/k)^2}; \tag{20}$$

and from the condition at the upper boundary

$$A=-\frac{\alpha_3(\xi-1-\delta)^2\tanh\alpha+\alpha(\xi-1)^2+(\xi-1)\tanh\alpha-R(m/k)^2\tanh\alpha}{\alpha_3(\xi-1-\delta)^2+\alpha(\xi-1)^2\tanh\alpha+(\xi-1)-R(m/k)^2}, \tag{21}$$

where $\xi=C/\Delta u=(\sigma/\beta\alpha)\ (m/k)$, $C=\sigma/k$ is the velocity of the disturbance, $\alpha_1=\gamma_1\Delta H \text{ ctnh } \gamma_1 H$, $\alpha_3=\gamma_3\Delta H$,

$$\gamma_3=[1-(N_3/\beta)^2/(\omega_3/\beta)^2]^{\frac{1}{2}}m,$$

$$\gamma_1=[1-(N_1/\beta)^2/(\omega_1/\beta)^2]^{\frac{1}{2}}m,$$

$$R=-\frac{g\Delta\rho}{\rho_0}\frac{\Delta H}{\Delta u^2}\approx\frac{g\Delta\theta}{\theta_0}\frac{\Delta H}{\Delta u^2}$$

where θ is potential temperature, and $\Delta\theta$ the potential temperature discontinuity at the top of the shear layer, and

$$R'=\frac{g\Delta\theta'}{\theta_0}\frac{\Delta H}{\Delta u^2},$$

where $\Delta\theta'$ is the potential temperature discontinuity at the base of the shear layer ($\Delta\theta'=0$ in Fig. 1).

Equating (20) and (21) yields the eigenvalue curves for the model, i.e., the relation between ξ and α for assumed values of N_3/β, δ, R and $H/\Delta H$. It is similar to Eq. (16) in the paper by Gossard (1974) except that we here express the relations in terms of hyperbolic rather than exponential functions. We have generalized the earlier model by including a wind discontinuity δu at the top of the shear layer and by permitting the lower layer to be superadiabatic.

Because $\omega\propto k$, we see in Eqs. (12), (20) and (21) that buoyancy terms in N^2 and R always appear multiplied by $(m/k)^2\equiv 1+l^2/k^2$. Therefore, the three-dimensional model is derivable from the two-dimensional case simply by introducing a modified Väisälä-Brunt frequency and a modified R, which are the unmodified quantities multiplied by m/k and $(m/k)^2$ respectively. It is immediately seen from Eq. (12) that the buoyancy term is minimum for the two-dimensional case, i.e., $m=k$. Therefore, for a statically stable layer ($N^2>0$), the two-dimensional model is least stable because the stabilizing effect of the buoyancy term is minimum. However, when $N^2<0$, the destabilizing effect of buoyancy becomes larger as l/k becomes larger, so there will be a tendency for disturbances oriented along the x direction (parallel to the direction of shear) to grow most rapidly.

It should also be noted that the conditions (20), (21) apply to a two-dimensional perturbation propagating at an angle to the shear as well as to the three-dimensional disturbance described by Eq. (7).

6. The unstable roots

It is of primary interest to inquire what value of the frequency σ has the largest imaginary component and to determine the associated value of α. This will indicate the scale of the most rapidly growing disturbance. (Actually, since $\alpha=m\Delta H$, it indicates the ratio of scale to layer thickness.) We have therefore plotted the dispersion relation in terms of σ rather than ξ, noting that $\sigma/\beta=\alpha\xi k/m$. In this kind of analysis it is presumed that the initially most rapidly growing disturbance will remain the dominant scale after the original approximations of the small-amplitude, inviscid theory are no longer applicable.

The real roots of Eqs. (20), (21) can be easily found using any modern, programmable desk calculator. The complex roots were found by use of a high-speed computer and a search algorithm modified from one originally written by Lewis (1966; see Moninger, 1974).

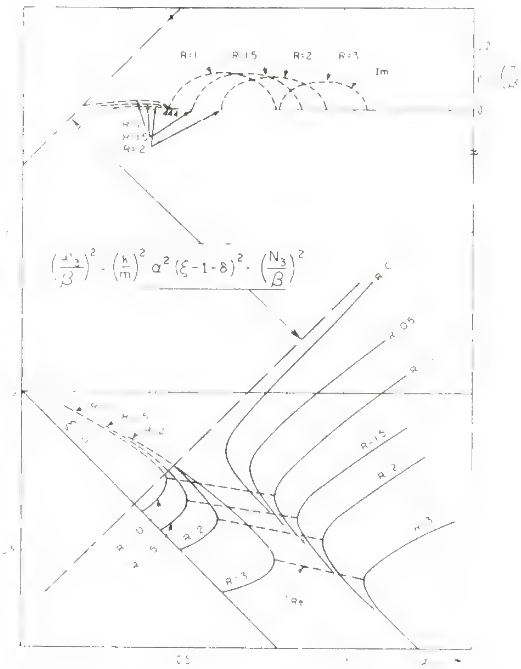

FIG. 3. Example of eigenvalue curves for the conditions shown on the figure. Solid lines represent loci of real roots; short dashed lines represent the real and imaginary parts of complex roots. Long dashed lines indicate boundaries within which $|\omega|<N_3$. Top frame: The imaginary parts are shown in the top frame of the figure. There are generally two domains of nonzero imaginary part (indicated by curved arrows) separated by a region of real roots. Both positive and negative values of the imaginary part are solutions but they have been arbitrarily plotted as positive. Bottom frame: Hyperbola-like solid curves and the straight line sloping down to the right are loci of real roots. The interval of α between noses of branches of hyperbolas is the domain of dynamic instability and yield the stability boundaries plotted in the next figures. The model is two-dimensional so $m=k$; $H/\Delta H=1$, $\delta=0$, $(N_3/\beta)^2=0.5$, $(N_1/\beta)^2=-0.1$.

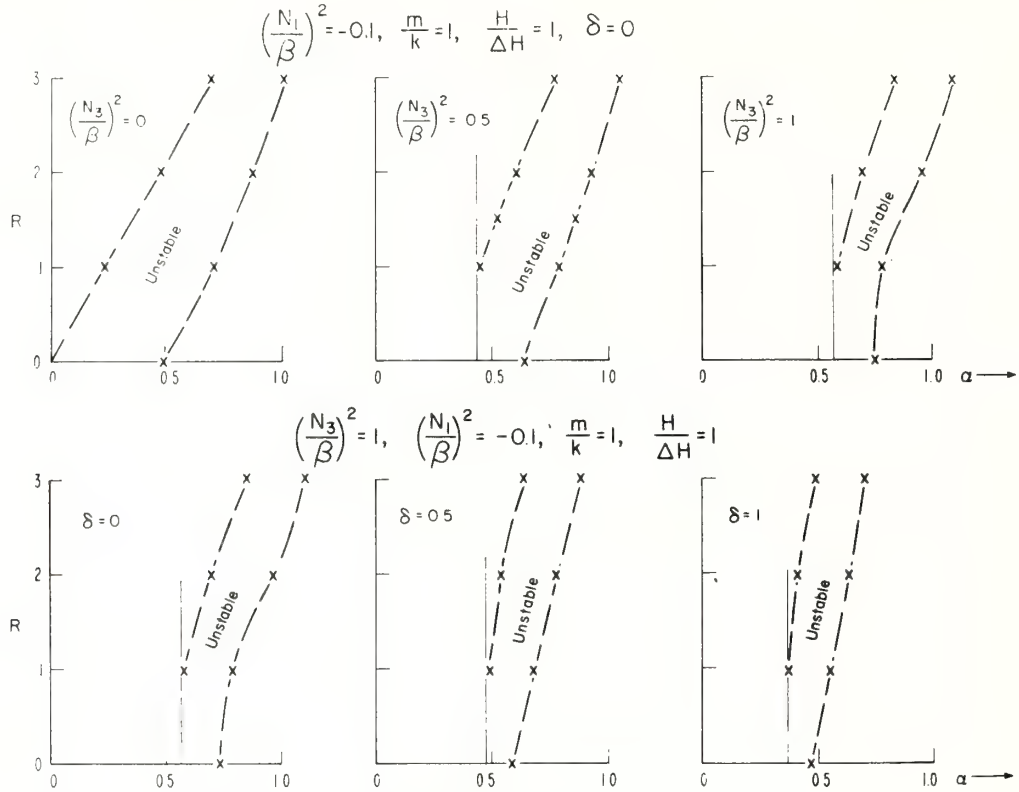

FIG. 4. Stability boundaries for various values of model parameters for the two-dimensional case, i.e., $m=k$. The figure demonstrates the influence of static stability in the upper layer of the model and the effect of a wind discontinuity at the top of the shear layer. $\delta=\delta u/\Delta u$. Points actually calculated are shown as X's. γ_3 is not real for values of α less than the intercept with the thin vertical line.

a. Bandwidth of the instability

Fig. 3 shows an example of the loci of the roots found by equating (20) and (21) for conditions indicated in the caption. Purely real roots are indicated by solid lines. The real and imaginary parts of complex roots are indicated by short dashes. Above the lower line composed of long dashes, the radicand of γ_3 becomes negative, i.e., $(k/m)^2\alpha^2(\xi-1-\delta)^2<(N_3/\beta)^2$. Physically, this indicates the existence of vertical fluxes of energy and momentum resulting from internal gravity waves in the upper layer of the model and implies relative dissipation of disturbances in this domain of the figure due to leakage of energy away from the shear layer. For R greater than about unity, this domain of complex roots in Fig. 3 is separated from that representing dynamic instability. (Note separation of arrowheads showing the "foot" of the curves for $R=1.5$ and $R=2$ in the upper frame of the figure.) At smaller values of R, the two domains merge. Above the upper line of long dashes the radicand of γ_3 again becomes positive. If roots exist in this domain, such high-speed disturbances would have their energy trapped within the lower regions of the model like those in the domain below the lower dashed line.

The loci of the real part of the complex roots in the unstable domain link the noses of the branches of the hyperbola-like curves representing the real roots. This region delineates the instability boundaries, and these instability boundaries are shown in Figs. 4–6 for many combinations of the various parameters describing the model.

We see that there is, in general, a relatively narrow band of unstable wavenumbers. The narrow-band character of the instability is a result of the temperature discontinuity at the top of the shear layer, and the scale and bandwidth of the unstable disturbances depend significantly on R. The width of the unstable band shrinks to zero as H tends toward zero because when $H=0$ there is no inflection point in the velocity profile (see Fig. 1). Because we have chosen a model in which the stability (described by N) is precisely zero in the shear layer, there is instability for some scales at all values of R. The width of the band of unstable wavenumbers also depends importantly on the intensity of the superadiabatic layer as described by N_1/β, the stability of the upper atmosphere, N_3/β, and the height H of the base of the shear layer. As seen from Fig. 6, the lower layer need not be superadiabatic for this kind of

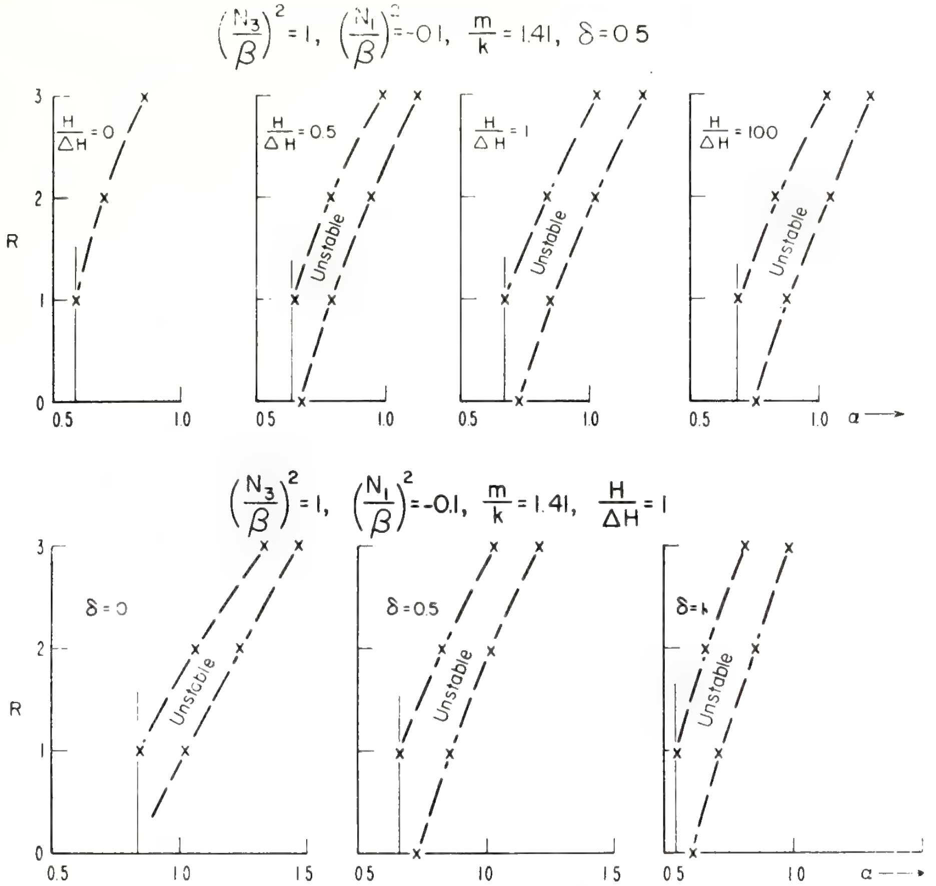

FIG. 5. Stability boundaries for various values of model parameters for the three-dimensional case in which $k=l$, i.e., $m=1.41k$. The figure demonstrates the influence of height of the base of the shear layer above the surface and the influence of a wind discontinuity at the top of the shear layer. Otherwise see caption for Fig. 4.

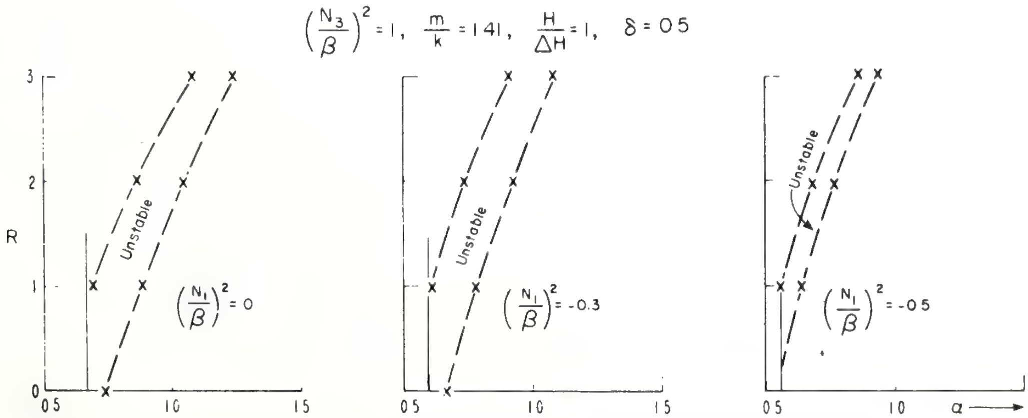

FIG. 6. Stability boundaries for various values of model parameters for the three-dimensional case, showing the influence of intensity of the superadiabatic surface layer. Otherwise see captions for Figs. 4 and 5.

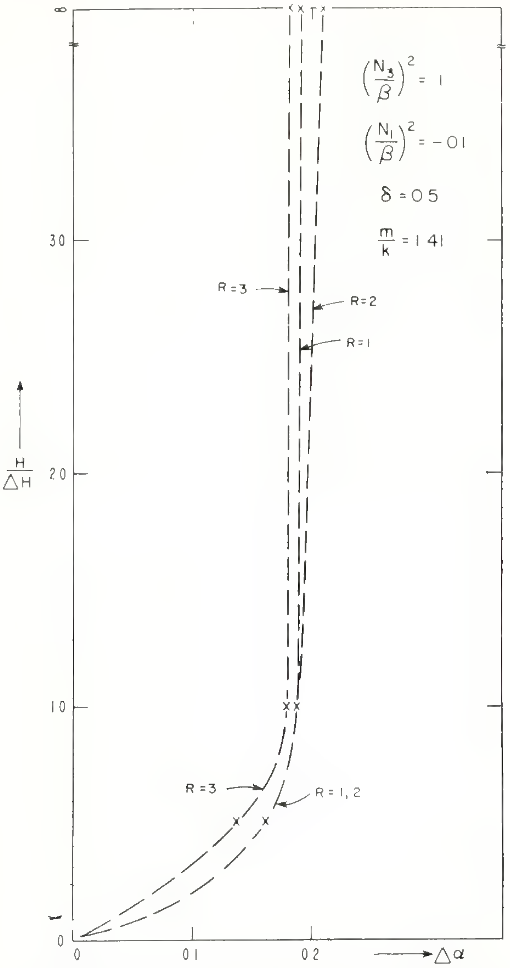

FIG. 7. Dependence of bandwidth of unstable disturbances, $\Delta\alpha$, on the ratio of the height of the base of the shear layer to its half-thickness ΔH.

instability to occur. In fact, below $(N_1/\beta)^2 = -0.5$ the bandwidth of instability shrinks to zero at $m/k = 1.41$. The bandwidth dependence on H and R is shown in Fig. 7. The main effect of δ is to shift the position of the band.

b. Propagation velocity

Relative to the background wind, the velocity of the most unstable disturbance is given by the real part of ξ and is shown plotted in Figs. 8–11 for various combinations of model parameters. We see that the disturbance propagates more slowly as the base of the shear layer lowers, becoming equal to the ambient velocity of the wind in the lower layer as H shrinks to zero. Likewise, the propagation velocity decreases as the lowest layer becomes more intensely superadiabatic. The propagation velocity becomes that of the wind in the lower layer when $(N_1/\beta)^2$ reaches approximately -0.5. Typically, values of $C/\Delta u$ are in the vicinity of -0.6, which means that the disturbance moves considerably slower than the average background wind, i.e., about 0.4 of the wind speed at the center of the shear layer.

c. Convective instability and roll orientation

Until now, we have considered only dynamic instability. However, if $(N_1/\beta)^2$ is negative, solutions representing convective instability also exist. As $(N_1/\beta)^2$ becomes increasingly negative, it seems likely that a point will be reached at which convective instability will assume the dominant role. In order to examine the relative roles played by these two kinds of instability it is convenient to simplify the model to permit simpler parameterization. We therefore let $R_1 = R_2 = (N_3/\beta)^2 = \delta = 0$. The static stability, shear and orientation are then represented in the single parameter (N_1/β) (m/k). There is thus an equivalency between static instability N_1/β and disturbance orientation m/k, and the results we will present may be interpreted in terms of either parameter. However, it must be remembered that m/k appears also in the dependent variable $\xi = C/\Delta u = (\sigma/\beta\alpha)(m/k)$ in Eqs. (20) and (21). We have chosen to parameterize the results shown in Fig. 12 in terms of orientation of the disturbance, assuming $(N_1/\beta)^2 = -0.05$. The figure can also be used to describe the results in terms of $(N_1/\beta)^2$, assuming $m/k = 1$, if the values of $(\sigma/\beta)_{r,i}$ for each curve in the figure are multiplied by their indicated m/k. Then the curves in increasing order of the indicated m/k correspond to $(N_1/\beta)^2 = -0.05, -0.45, -1, -1.8, -5$, respectively.

In Fig. 12, loci of pure-real roots are labeled "real." All others are complex, with the imaginary part plotted above zero on the σ/β scale and the real part plotted below. Because $R = 0$, only the right-hand branch of the hyperbola-like real roots (see Fig. 3) are seen in Fig. 12a.

There are several points of interest in Fig. 12:

1) As m/k varies, two regions are evident. One region, shown in Fig. 12a, has a set of roots exhibiting a rather well-defined most-unstable scale. These roots represent dynamic instability and in this region of m/k and α dynamic instability dominates. The band of unstable wavenumbers if fairly broad because $R = 0$. For $m/k = 1,3$ there is another set of roots whose loci in this region are nearly straight lines passing through the origin. These roots represent convective instability, and have no most unstable scale. In the region in Fig. 12b where $m/k \geqslant 4.5$, or $(N_1 m/\beta k)^2 \leqslant -1$, only roots for convective instability exist in this model. Here the instability increases steadily as α increases (scale size decreases). In reality, viscous damping would take over at some small scale size yielding a most unstable scale at some high wavenumber. Thus, there may be two initially most rapidly growing scales of disturbance: one dynamic and one convective, with the dynamic having a much larger scale size. It seems not unreasonable that the larger scale dynamic instability may sometimes be the trigger that initiates large deep convection.

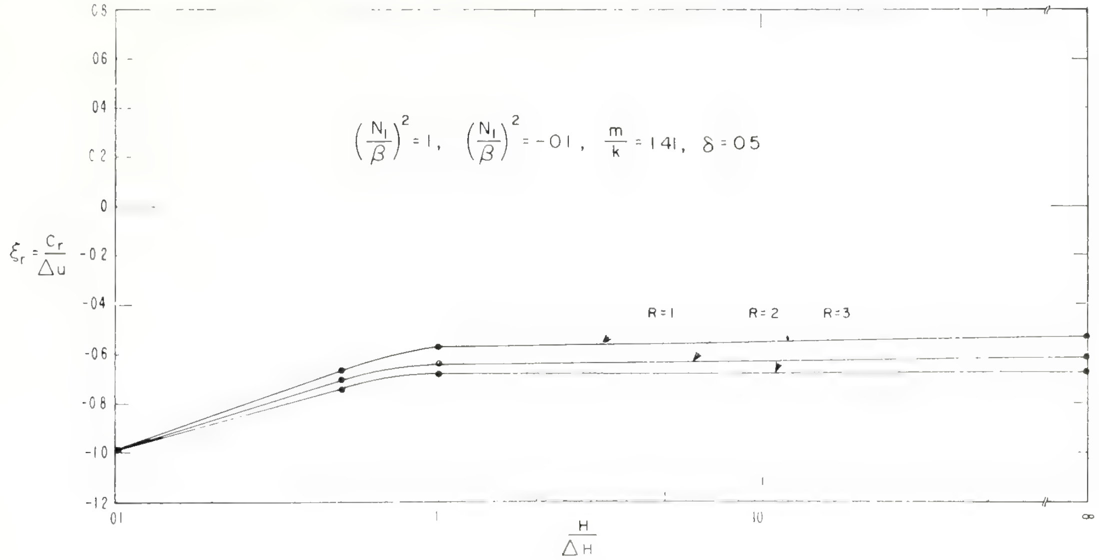

FIG. 8. Influence of the height of the base of the shear layer on the phase velocity of the most unstable disturbance: $C_r/\Delta u = -1$ when the velocity of the disturbance is 0 relative to the ground; $C_r/\Delta u = 0$ when the velocity of the disturbance is that of the wind at the center of the shear layer.

The real roots also exhibit a characteristic behavior in the two domains. In Fig. 12a, the right-hand branch of the hyperbola-like loci, typical of the real roots in Fig. 3, are to be seen at the lower right. At the value $m/k = 4.5$, where dynamic instability is cut off, the lower part of the hyperbola no longer bends back toward larger α, and in the convective domain (Fig. 12b) they loop in the origin. This conclusion is quite general and is not altered by letting N_3/β, R or δ be non-zero. However, if R' is not zero it is no longer true.

2) In the domain dominated by dynamic instability the most unstable configuration is a two-dimensional disturbance transverse to the shear ($m/k = 1$) and is probably the explanation of those cloud streets observed to be oriented transverse to the mean wind shear.

3) In the domain of convective instability the most unstable configuration is a two-dimensional disturbance aligned along the shear ($m/k = \infty$) and is probably the explanation of those cloud streets aligned along the mean wind shear.

4) Making $(N_1/\beta)^2$ more negative increases the convective instability but decreases the dynamic insta-

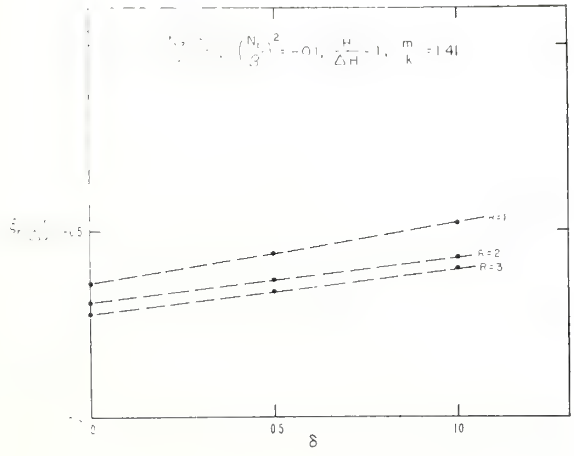

FIG. 9. Influence of wind and temperature discontinuity on the phase velocity of the most unstable disturbance. $\delta = \delta u/\Delta u$. For interpretation of ordinate scale, see caption for Fig. 8.

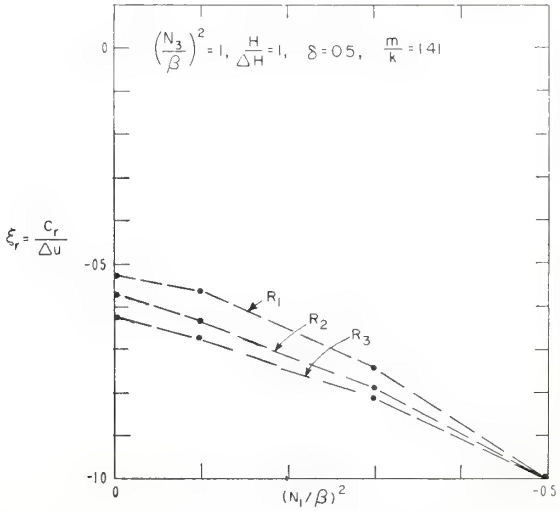

FIG. 10. Influence of intensity of superadiabatic layer on the phase velocity of the most unstable disturbance. For interpretation of ordinate scale, see caption for Fig. 8.

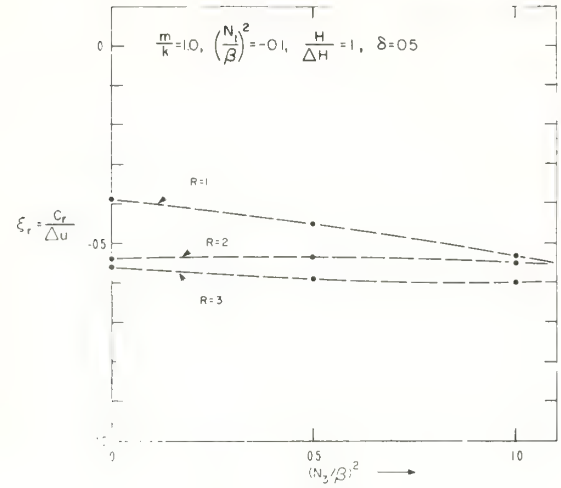

FIG. 11. Influence of static stability of the upper atmosphere on phase velocity of the most unstable disturbance for the two-dimensional model. For interpretation of left-hand scale see caption for Fig. 8.

bility until it is cut off for $(N_1 m/\beta k)^2 \leqslant -1$. Thus shear increases the dynamic instability while it stabilizes the convectively unstable modes. There are multiple solutions for the convective type of instability, representing higher order modes. In Fig. 12 we have shown only the most unstable roots of this type.

The conclusions above are remarkably similar to results obtained by Asai (1970) for a very different model. Asai chose a model with mean flow between parallel, free boundaries across which a linear, statically unstable temperature profile was assumed to exist. The profile of the mean flow, which had an inflection point, was described by $u_0(z)=\frac{1}{2}[1-(2z-1)^2]^n$, $n=1, 2, \ldots$. In contrast, our model has no shear across the statically unstable lower layer, within which the momentum is assumed to be intensely mixed, but instead the shear is across a statically neutral layer above. Furthermore, these two layers are capped with a statically stable region. Asai called the dynamically unstable domain "inertially unstable," and the convectively unstable domain "thermally unstable."

The four points listed above are not altered fundamentally when R and $(N_3/\beta)^2$ are not zero. The main effect of R is to narrow the band of dynamically unstable wavenumbers while leaving the convective domain virtually unchanged. The principal effect of increasing stability above the shear layer is to shift everything to the right along the α axis. For example, the most unstable wavenumber in the dynamically unstable domain is shifted toward larger wavenumbers much as shown in Fig. 4. The magnitude of the static instability at transition $[(N_1 m/\beta k)^2=-1]$ does not vary with upper level stability, or $R\neq 0$, but the position of the transition shifts to the right on the α axis. At $\sigma/\beta=0$ the real root is at $\alpha=0.5$ when $(N_3/\beta)^2=0$, but is at $\alpha=0.72$ and 1.0, respectively, when $(N_3/\beta)^2$ is 0.45 and 1.0.

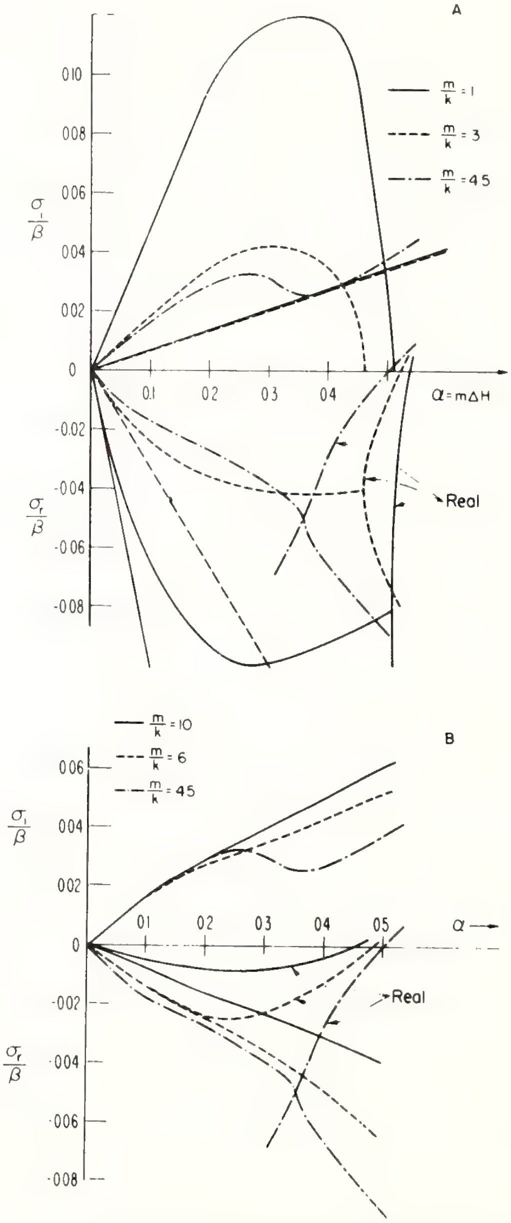

FIG. 12. Effect of orientation of perturbation on instability. Plots are the loci of roots for a model in which $H/\Delta H=1$, $(N_1/\beta)^2=-0.05$, $R=R'=N_3/\beta=0$. Pure-real roots are labeled "real." The other curves are complex roots with the imaginary part plotted above zero on the σ/β axis and the real part is plotted below. The top frame shows the domain of m/k in which dynamic instability is dominant. The bottom frame shows the domain in which only convective instability exists. The curves can also be interpreted in terms of strength of static instability in the lower layer instead of orientation (see text). The four major conclusions to be drawn from this figure are listed in Section 6 in the subsection on convective instability and orientation.

7. Discussion

We have taken no account of transient conditions in our formulation of the problem because our goal was limited to finding the conditions for the onset of dynamic instability of infinitesimal disturbances. By the nature of the assumptions, such disturbances will initially grow exponentially with time. Much theoretical work has been done on the way the boundary layer evolves after sunrise. Recent papers in this category include those of Tennekes (1973), Stull (1973) and Carson (1973). These models have been concerned with the heat budget in the boundary layer as the day progresses, i.e., they consider the effects of solar heating of the surface, entrainment of air across the interfacial (capping) inversion, and (sometimes) subsidence, on the rate of increase in depth of the convective boundary layer. They do not explicitly include the effects of shear, advection, evaporation or (usually) radiation. In contrast, we explicitly focus on the effects of shear and the capping inversion, and we will only qualitatively consider how the developing boundary layer might create the inflection point in the wind profile needed to generate this kind of dynamic instability.

Thus one might imagine the following sequence of events to occur following sunrise. As the night ends, assume that the lower atmosphere is characterized by a surface-based shear layer such that the wind profile has no inflection points. Because shear always appears in dimensionless quantities along with the Väisälä-Brunt frequency N or the temperature discontinuity $\Delta\theta$, note that this kind of instability is possible even though the shear be made arbitrarily small—but not zero. As surface heating proceeds, an intensely mixed layer forms next to the ground, and the resulting large rate of transfer of momentum leads to a nearly constant wind throughout the lower layer (except, of course, in the constant flux layer next to the ground ignored in our model). The base of the shear layer is then approximately at the top of the intensely mixed layer, and the resulting inflection point in the profile leads to dynamic instability. This situation might resemble that shown in Fig. 2. As the base of the shear layer rises, the strength of the dynamic instability increases until a height of about $h = \Delta H$ is reached, after which there is little further increase. As it increases, the instability may become sufficient to overcome the frictional resistance in the system and large-scale perturbations may be initiated which will presumably modify the environment and invalidate the linearizing assumptions used in predicting the conditions for the initial onset of the instability. It is even possible that, if the lower atmosphere contains an adequate moisture supply and favorable mesoscale circulation, the perturbation may be sufficient to trigger the thermodynamic processes needed to bring about large deep convection associated with storms.

We should not expect the above eigenvalue relations or even the predicted kinematics of the flow to be valid later in the convective development when the inviscid and small perturbation assumptions no longer hold. However, with that disclaimer, we will proceed to calculate the flow patterns hoping the reader will exercise suitable caution in comparing them with real convective systems, especially near the critical level.

8. Flow patterns, vorticity, and divergence

The behavior of the flow patterns near the critical level in the three-dimensional, inviscid shear model is interesting. Infinities occur in U, V and vorticity at the critical level that are not found in two-dimensional models. To show this we first express all velocity components in terms of the perturbation in W at the top of the shear layer [i.e., $W_{H+2\Delta H}$ in Eqs. (18) and (19)]. Letting the total velocity $u_T = u_0(z) + U$, where u_0 is the unperturbed and U the perturbed component of the velocity in the x-direction, we find from Eqs. (13) and (14) that

$$u_T = u_0(z) - \frac{k}{m^2}\left(\frac{\partial}{\partial z} - \frac{k}{\omega}\beta\frac{l^2}{k^2}\right) W(z) \cos ly \sin(kx - \sigma t), \quad (22)$$

$$V = -\frac{l}{m^2}\left(\frac{\partial}{\partial z} + \frac{k}{\omega}\beta\right) W(z) \sin ly \cos(kx - \sigma t), \quad (23)$$

$$W = W(z) \cos ly \cos(kx - \sigma t), \quad (24)$$

where $W(z)$ is given by Eqs. (17)–(19). We again remind the reader that the origin of the height coordinate is at the center of the shear layer (see Fig. 1) so that in the shear layer $u_0(z) = \beta z$ where β is the shear factor—assumed here to be constant.

It is important to note that the 2nd term in the parentheses of Eqs. (22) and (23) becomes infinite where $\omega = 0$. If ω is real, this occurs at the level where the disturbance velocity is equal to the environmental flow velocity, i.e., the critical level. Consequently, U and V there become infinite even though W and its height derivative do not and even though there are no singularities in the wave equation in W. This is a result of the three-dimensional nature of the model, as seen from the fact that when $l = 0$, i.e., the wave propagates precisely in the direction of the shear vector, the terms in ω^{-1} drop out and the infinities disappear. They also disappear even in the three-dimensional case if there is no shear, i.e., $\beta = 0$.

From (18) and (19) we can calculate the vorticity and divergence. In the horizontal plane, the vertical component of vorticity is

$$\mathrm{vor}_H = \frac{\partial V}{\partial x} - \frac{\partial u_T}{\partial y} = +\frac{\beta l}{\omega} W$$

and the divergence is

$$\mathrm{div} = \frac{\partial u_T}{\partial x} + \frac{\partial V}{\partial y} = -\frac{\partial W}{\partial z}.$$

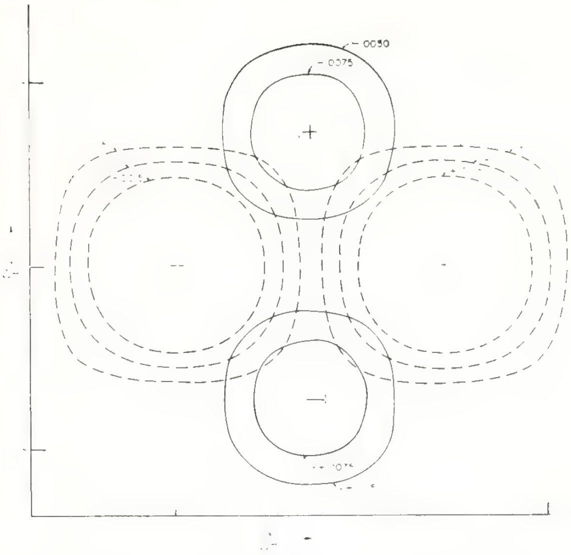

FIG. 13. Vorticity pattern (solid curves) and divergence pattern (dashed curves) at the base of the shear layer ($z/\Delta H=-1$) of a model in which $H/\Delta H=1$, $(N_3/\beta)^2=1$, $(N_1/B)^2=-0.1$, $k=l$, $\delta=1$, $R=1$ and $2\Delta u/W_H=4$. Then $\alpha_r=0.62$, $A=-1.21$ and the critical level is at a height of $z/\Delta H=-0.48$.

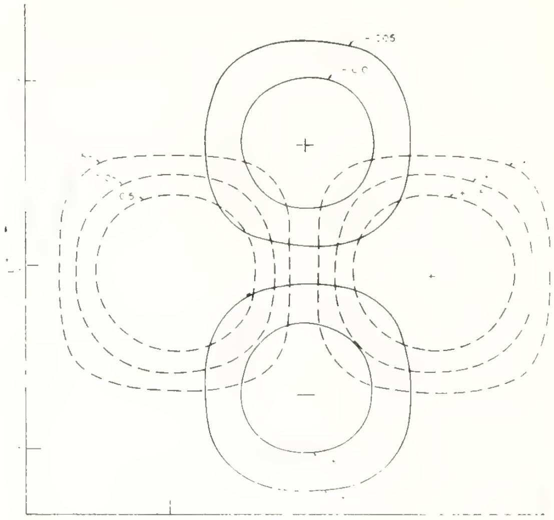

FIG. 14. As in Fig. 12 except $z/\Delta H=-0.8$.

If ω is real, we see that vorticity becomes infinite at the critical level [unless $W(z)$ goes to zero as fast or faster than ω as $z\rightarrow z_c$] while divergence remains well behaved.

In the middle layer, where $\omega/\beta=(k\alpha/m)(\xi-z/\Delta H)$,

$$u_T=\beta z-\frac{k}{m}\left[\frac{1}{m}\frac{\partial W(z)}{\partial z}-\frac{l^2}{k^2}\frac{W(z)}{\alpha\left(\xi-\dfrac{z}{\Delta H}\right)}\right]\times\cos ly\sin(kx-\sigma t),\qquad(25)$$

$$V=-\frac{l}{m}\left[\frac{1}{m}\frac{\partial W(z)}{\partial z}+\frac{W(z)}{\alpha\left(\xi-\dfrac{z}{\Delta H}\right)}\right]\times\sin ly\cos(kx-\sigma t),\qquad(26)$$

$$\mathrm{vor}_H=-\left(\frac{l}{k}\right)\frac{W(z)}{\Delta H\left(\xi-\dfrac{z}{\Delta H}\right)}\sin ly\sin(kx-\sigma t),\qquad(27)$$

where

$$W(z)=W_{H+2\Delta H}\frac{\sinh mz+A\cosh mz}{\sinh m\Delta H+A\cosh m\Delta H},\qquad(28)$$

$$\frac{\partial W(z)}{\partial z}=m\frac{\cosh mz+A\sinh mz}{\sinh m\Delta H+A\cosh m\Delta H}W_{H+2\Delta H}.\qquad(29)$$

It is readily seen from Eq. (27) that the presence of a critical level has an important effect on vorticity when 1) the disturbance is three-dimensional and 2) vertical shear exists in the background wind. If the disturbance is two-dimensional ($l=0$), or if there is no shear ($\Delta u=0$, $\xi=\infty$), $\mathrm{vor}_H=0$ in this model. Contours of vorticity (solid curves) and divergence in four horizontal planes bracketing the critical level (taken to be at $z/\Delta H=-0.48$) are shown in Figs. 12–16. At the critical level the vorticity becomes infinite and reverses sign, but in the real atmosphere both viscosity and nonlinear effects must have an important influence at this level. However, in spite of the defects associated with the linear theory, it seems clear that vorticity can occur in such three-dimensional systems even when large-scale

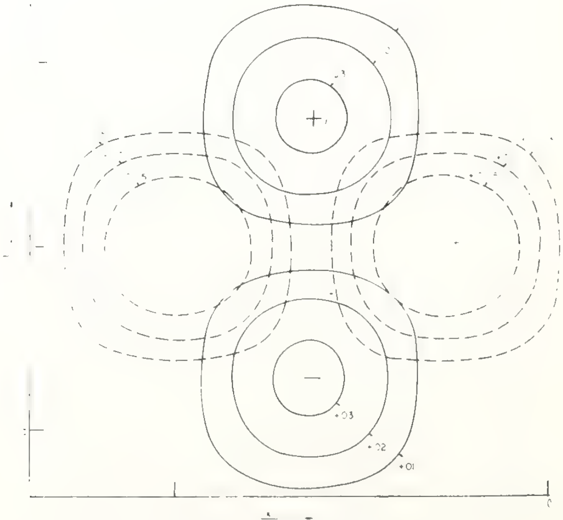

FIG. 15. As in Fig. 12 except $z/\Delta H=-0.6$.

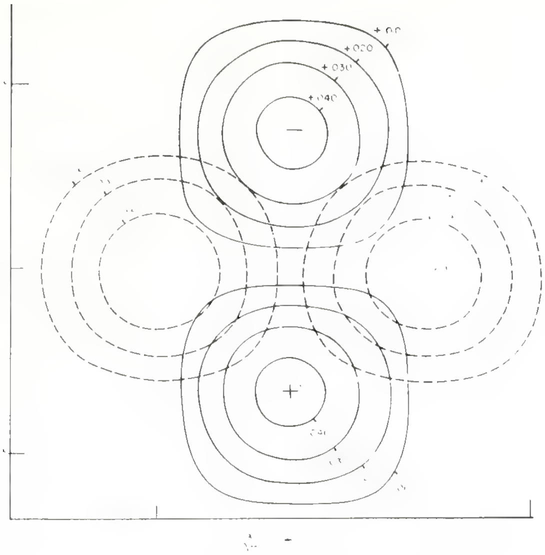

Fig. 16. As in Fig. 12 except $z/\Delta H = -0.4$.

horizontal gradients of velocity are absent and without any particular concentration of vorticity in the background flow by the disturbance itself.

9. Conclusions

We have analyzed the dynamic stability and kinematics of a sheared convective boundary layer capped by a temperature and wind discontinuity; a neutral or unstable surface layer lies beneath an adiabatic layer under shear. We find that the capping inversion can lead to a narrow band of unstable wavenumbers that depends on shear layer thickness. The bandwidth and propagation speed of these "most unstable" scales is closely related to the height of the shear layer above the surface. In fact, the width of the band of instability shrinks to zero when the shear layer becomes surface-based or when the intensity of the thermal instability of the lower layer becomes high. The static stability above the shear layer determines what scales of disturbance can leak their energy away from the shear layer by internal gravity wave propagation into the upper atmosphere, because it determines the position of the long-dashed lines in Fig. 3.

Whereas there is a most unstable wavelength associated with dynamic instability, convective instability is greater the higher the wavenumber, in the absence of viscosity; so dynamic instability will tend to be dominant at the larger scales. The shear needed to produce dynamic instability actually reduces the magnitude of the convective instability. Two-dimensional disturbances aligned transverse to the wind shear are most dynamically unstable, while two-dimensional rolls aligned along the wind shear are most convectively unstable.

We have shown that the kinematics and vorticity of initially "most-unstable," three-dimensional disturbances under shear depend importantly on the presence of a critical level within the growing disturbance. Infinities occur in the three-dimensional, inviscid shear models that do not occur in the two-dimensional models.

Acknowledgments. We wish to express our appreciation to Dr. Franco Einaudi for giving us his modified version of the Lewis algorithm used in searching the complex plane, and for helpful discussions. We wish also to thank Drs. Stanley Barnes, Dan Fitzjarrald, William Hooke, James Deardorff, and Tzvi Gal-Chen for reading the manuscript and offering suggestions.

.REFERENCES

Asai, Tomio, 1970: Stability of a plane parallel flow with variable vertical shear and unstable stratification. *J. Meteor. Soc. Japan*, **48**, 129–139.

Booker, J. R., and F. P. Bretherton, 1967: The critical layer for internal gravity waves in a shear flow. *J. Fluid Mech.*, **27**, 513–539.

Brown, R. A., 1970: A secondary flow model of the planetary boundary layer. *J.' Atmos. Sci.*, **27**, 742–757.

——, 1972: On the inflection point instability of a stratified Ekman boundary layer. *J. Atmos. Sci.*, **29**, 850–859.

Brunt, D., 1927: The period of simple vertical oscillations in the atmosphere. *Quart. J. Roy. Meteor. Soc.*, **53**, 30–32.

Carson, J. D., 1973: The development of a dry inversion-capped convectively unstable boundary layer. *Quart. J. Roy. Meteor. Soc.*, **99**, 450–467.

Case, K. M., 1960: Stability of inviscid plane Couette flow. *Phys. Fluids*, **3**, 143–148.

Deardorff, J. W., 1965: Gravitational instability between horizontal plates with shear. *Phys. Fluids*, **8**, 1027–1030.

Gallagher, A. P., and A. McD. Mercer, 1965: On the behaviour of small disturbances in plane Couette flow with a temperature gradient. *Proc. Roy. Soc. London*, **A286**, 117–128.

Goldstein, S., 1931: On the stability of superposed streams of fluid of different densities. *Proc. Roy. Soc. London*, **A132**, 524–548.

Gossard, Earl E., 1974: Dynamic stability of an isentropic shear layer in a statically stable medium. *J. Atmos. Sci.*, **31**, 483–492.

——, and William H. Hooke, 1975: *Waves in the Atmosphere*. Amsterdam, Elsevier 480 pp.

Hazel, Philip, 1967: The effect of viscosity and heat conduction on internal gravity waves at a critical level. *J. Fluid Mech.*, **30**, 775–783.

Holmboe, J., 1962: On the behavior of symmetric waves in stratified shear layers. *Geophys. Publ.*, **24**, No. 2, 68–113.

Howard, L. N., 1963: Neutral curves and stability boundaries in stratified flow. *J. Fluid Mech.*, **16**, 333–342.

Kaylor, R., and A. Faller, 1972: Instability of the stratified Ekman boundary layer and the generation of internal waves. *J. Atmos. Sci.*, **29**, 497–509.

Kelvin, Lord, 1880: On a disturbing infinity in Lord Rayleigh's solution for waves in a plane vortex stratum. *Nature*, **33**, 45–46.

Kuo, H. L., 1963: Perturbations of plane Couette flow in a stratified fluid and origin of cloud streets. *Phys. Fluids*, **6**, 195–211.

LeMone, M. A., 1973: The structure and dynamics of horizontal roll vortices in the planetary boundary layer. *J. Atmos. Sci.*, **30**, 1977–1091.

Lewis, L. D., 1966: U. S. Department of Commerce, NOAA/ERL/SEL unpublished computer subroutine.

Lilly, D. K. 1966: On the instability of Ekman boundary flow. *J. Atmos. Sci.*, **23**, 481–494.

Maslowe, S. A., and J. Thompson, 1971: Stability of a stratified free shear layer. *Phys. Fluids*, **14**, 453–458.

Moninger, W. R., 1974: The search for most unstable scales of disturbances in three-layer atmospheric models with shear and static stability—procedure and results. NOAA Tech. Rept. ERL 314-WPL 36.

Ramm, Pauline, and F. W. G. Warren, 1963: Gravity-wave dispersion under wind shear in two model atmosphere. *Quart. J. Roy. Meteor. Soc.*, **89**, 349–359.

Stull, R. B., 1973: Inversion rise model based on penetrative convection. *J. Atmos. Sci.*, **30**, 1092–1099.

Taylor, G. E., 1931: Effect of variation in density on the stability of superposed streams of fluid. *Proc. Roy. Soc. London*, **A132**, 499–523.

Tennekes, H., 1973: A model for the dynamics of the inversion above a convective boundary layer. *J. Atmos. Sci.*, **30**, 558–567.

Väisälä, V., 1925: Uber die Wirkung der Windschwankungen auf die Pilot-Beobachtungen. *Soc. Sci. Fenn. Commentat. Phys.-Math.*, **2**, 2–46.

NOAA Technical Report ERL 317-WPL 37

March 1975

NATURAL INFRASOUND: A ONE YEAR GLOBAL STUDY

Gary E. Greene and Joe Howard

Using continuous pressure records from eight infrasonic observatories around the world, we have compiled statistics on infrasound occurrence and on the background noise distribution that affects the detectability of infrasound. With triangulation, the source locations for over 200 infrasonic events have been established. The most frequently detected sources appear to lie in or near certain mountainous regions throughout the world.

An Investigation of Extreme Low-Level Wind Shear at Selected Stations in the Conterminous United States

ROBERT L. GROSSMAN[1] AND DONALD W. BERAN

Wave Propagation Laboratory, NOAA Environmental Research Laboratories, Boulder, Colo. 80302

(Manuscript received 1 May 1974, in revised form 9 January 1975)

ABSTRACT

The occurrence of extreme low-level wind shear at 10 stations in the conterminous United States is investigated by applying a bivariate frequency-distribution analysis to rawinsonde and pibal data. Data for Denver, Colo., received additional analysis and showed that extreme wind shears were associated with particular synoptic conditions. Many stations indicated variation of extreme shear with season. Large values of extreme wind shear were found to correlate well with mean storm tracks in the conterminous United States.

1. Introduction

Characteristics of the vertical variation of the horizontal wind component have been extensively investigated in the lowest layers of the atmosphere. Most of these studies have dealt with the general characteristics of low-level wind shear, with little emphasis on occurrences of extreme values. In recent years, the effect of wind shear on aircraft takeoff and landing has come under review (Gera, 1971; Melvin, 1970; Watson, 1969), and extreme wind-shear incidence and aircraft accidents have been shown to correlate. As early as 1964, the International Civil Aviation Organization Commission for Aeronautical Meteorology (CAeM/III) asked member states to investigate low-level wind shear conditions, with emphasis on the occurrence of extreme values, in the vicinity of aerodromes.

The results of several studies conducted at airfields and meteorological towers since 1964 have direct applicability to aircraft operations. Some of these studies can be found in two World Meteorological Organization (WMO) Technical Notes: Aeronautical Meteorology (1969) and Vertical Wind Shear in the Lowest Layers of the Atmosphere (1969). The work presented in these WMO Technical Notes emphasizes that no true climatology of low-level wind shear exists for the United States.

The work reported here provides a statistical background on the climatological aspects of extreme low-level wind shears at various points in the conterminous United States and explores the applicability of such information to aircraft operations.

2. Models of wind shear and its extremes

Three approaches may be used in modeling wind shear and its extremes. These are 1) physical models, which treat the motion equations either analytically or numerically; 2) statistical models, which treat characteristics of the population distribution of wind shear; and 3) meteorological models, which deal with meteorological conditions associated with observations of extreme wind shear. We will be concerned with the latter two. Those interested in physical modeling are referred to Taylor (1970) and Arya (1972), among others.

For statistical modeling, we must first determine the type of population distribution which applies to wind shear. Second, we must determine whether this distribution is universal. If it is, then the next step is to discover the relationship between statistics of the distribution, from which extreme values can be found, and easily measured meteorological parameters. An alternate method would be to concentrate, in a similar manner, only on the extreme value distributions. It is not known at this time whether or not the wind shear distribution is universal. In fact, the exact form of wind shear distributions in specific areas has not been conclusively determined.

Fichtl (1971), using a limited data set from Cape Canaveral, treated statistical modeling of wind shear from the similarity view of turbulent motions. His approach was to universalize certain statistical parameters by proper scaling and to associate the variation of these scaled parameters with certain external dimensionless parameters which include combinations of sensor separation, measurement height, Coriolis parameter, friction velocity, and Monin-Obukhov stability length.

Most statistical results reported so far should be considered as background material because they have not attempted to relate the statistics of a distribution to meteorological parameters or variables. In contrast, as we have done, they have dealt with the gross characteristics of the distribution, such as frequency of occurrence using relatively long-time series covering a wide variety of meteorological conditions.

---

[1] Present affiliation: Advanced Study Program, National Center for Atmospheric Research. The National Center for Atmospheric Research is sponsored by the National Science Foundation.

Reports resulting from the original CAeM/III request show that individual component differences of 5 m s^{-1} in the first 30 m (the critical value established by CAeM/III, 1964) make up about 1% of the total number of occurrences. These same reports provide little information on persistence of extreme wind shear. This characteristic should be included in a working model. Kusano *et al.* (1967) cited a case of extreme wind shear persisting for 22 h, indicating that some cases are more heavily influenced by mesoscale and synoptic-scale events than, for instance, by local stability.

The object of meteorological wind shear modeling is to determine the set(s) of meteorological conditions under which extremes of wind shear exist and the extent to which these conditions influence or are associated with persistence of the extreme shear occurrence. For planning purposes, the statistical approach is probably the most useful; for operations, the meteorological approach is better because the conditions under which extreme shears may occur could be recognized by an experienced meteorologist, especially at stations where low-level wind profiles are not routinely measured.

It is recognized that large values of low-level wind shear are associated with the low-level wind maxima (Abramovic and Glazunov, 1969; Rider and Armendariz, 1966) paralleling the observation of jet-stream-linked strong wind shears in the free atmosphere (Reiter, 1961). Strong wind shears in the boundary layer are often found in stable rather than unstable atmospheric stratification (Mashkova, 1967; Pettitt and Root, 1969; Rijkoort, 1969; Tsverava, 1967). In an apparent contradiction, Marwitz (1971) and Colmer (1971) noted strong wind-shear conditions existing in the cold air outflow of cumulonimbus; however, the cold air outflow provides for local stability in the boundary layer even though the atmosphere is unstable through a deeper layer (Zipser, 1969). Boucher *et al.* (1965), Jefferson (1966) and Sowa (1972) reported strong wind-shear occurrences in the vicinity of frontal surfaces. In Japan, Kusano *et al.* (1967) correlated strong wind shear with the following synoptic conditions: cold fronts, outbursts of winter monsoon, high pressure areas (possibly agumented by a land-sea breeze circulation), and typhoons. They noted that low visibility is unlikely to be accompanied by strong wind shear.

In summary, existing literature suggests these meteorological characteristis of strong wind shear: 1) associated with stable rather than unstable boundary-layer conditions; 2) frequently seems to be caused by changes in wind direction with height rather than with changes in wind speed with height, direction remaining constant; and 3) often found in the vicinity of frontal zones which carry with them the characteristics of stable conditions in the lowest layers and the wind direction shifts noted in 1) and 2) above.

3. Effect of wind shear on aircraft

Consider an aircraft during the critical landing operation. The aircraft is moving horizontally as it descends making the horizontal wind parameter of interest,

$$\frac{\Delta}{\Delta x}\left[\frac{\Delta \mathbf{V}}{\Delta z}\right], \quad \text{where} \quad \mathbf{V}=u\mathbf{i}+v\mathbf{j}. \tag{1}$$

The Δ is used to emphasize data acquisition restraints. Generally, the principle of horizontal homogeneity is invoked, and the operative parameter becomes $\Delta\mathbf{V}/\Delta z$, measured at one point near the landing strip. Data acquisition requirements lead to

$$\frac{\Delta \mathbf{V}}{\Delta z}=\left[\frac{\overline{\Delta \mathbf{V}}}{\Delta z}\right]+\left[\frac{\Delta \mathbf{V}}{\Delta z}\right]', \tag{2}$$

where the overbar denotes a time average and the prime a departure from the mean, or a "shear gust."

In turbulence theory, an acceptable averaging time is one in which the average of the deviations is nil. Wind shear data acquisition for aircraft operations may compromise this important criterion. Furthermore, it is possible, considering studies of vertical shear in the free atmosphere, that the correct averaging time for application to (2) would be a function of Δz (Reiter and Lester, 1967).

Some assumptions can be made that lead to an estimate of the averaging time, and Δz to be used for most major airport operations. Refinements of these estimates ultimately depend upon the aerodynamic response of a given aircraft. If an aircraft is descending at about 3 m s^{-1} with 85 m s^{-1} ground speed, and if it takes a pilot approximately 1 s to decide to correct for an approach problem, 1 s to act upon it, and still another second for the aircraft to respond, then the aircraft has traversed 9 m vertically and about 255 m horizontally. The above estimates are crude, but they give some idea of the spatial and temporal limits (i.e., $\Delta z > 9$ m and an averaging time >3 s). These types of limits will hold even if the aircraft responds to a smaller space interval and averaging time. Furthermore operational averaging time may depend in part on the persistence of small shear layers. In addition, Burnham (1970) suggested that a pilot may not be able to distinguish between the gustiness of the horizontal wind field and a sudden wind vector change on his descent through a shear layer. Various investigators [see the two WMO Technical Notes (1969) mentioned earlier] gave results on data averaged from 5 s to 60 min. Suggestions for optimum averaging times ranged from "nearly instantaneous" to less than 4 min.

4. Method of analysis

Three questions were relevant to determing the method of analysis. First, what is the best way to present a frequency distribution of a vector field? Second, given the data set (see Section 5), how should the CAeM extreme wind-shear criterion be applied? Third, how should this criterion be applied to aircraft operations to produce results consistent with the CAeM standard format of wind shear statistics? We will take up each of these questions in turn.

a. Frequency distributions of vector fields: The bivariate frequency table

Wind shear, like wind velocity, is a vector quantity. It can be described by two scalar variables: either a direction and magnitude or x and y components. Marginal frequency distributions of either scalar variable (i.e., distribution of x components and distribution of y components) force one to view the scalar parameters as independent of one another. This may be true over very short periods of time when trends are small (Panofsky and Crutcher, 1951), but it is probably not true when wind shear components are treated in a climatological sense. Previous wind shear studies have not considered the probability that the two scalar variables are interdependent.

Crutcher (1957) discussed the use of the bivariate frequency distribution as applied to vector wind fields in the free atmosphere, where the two variables were the x and y components of the wind velocity. Crutcher and Baer (1962) used this approach to develop an elliptic bivariate normal distribution model of a climatological series of upper wind data.

To comply with CAeM wind shear formats, the vector wind was broken into x and y components, as in Fig. 1, and component differences between levels were then taken. All shear values were given as wind speed differences (m s^{-1}) for a known Δz. A bivariate table was constructed using the component differences as in Fig. 2.

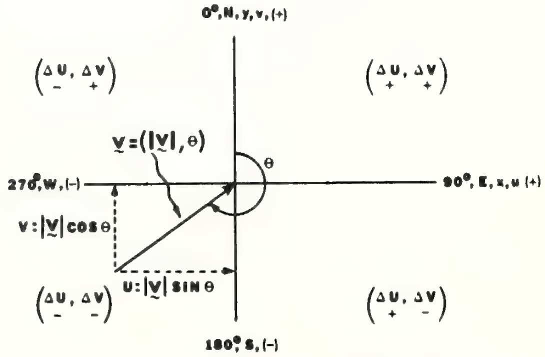

FIG. 1. The wind vector and its components. Example shown is for a southwest wind. This figure is based upon the National Climatic Center Winds Aloft Summary format.

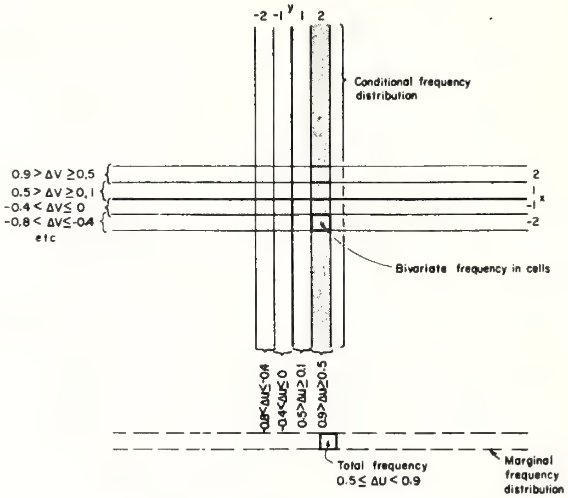

FIG. 2. Format of bivariate frequency table used as basis for this study. Bivariate classes (at top and on right side of figure) form cells representing the bivariate frequency in percent of total occurrences. Marginal frequency distributions are at bottom (for Δu, m s^{-1}) and on left-hand side (for Δv, m s^{-1}). Other information on the table includes station, month, period of observation, sample number, log of methods of observation, number of calms, layer considered, and mean shear vector in component form.

The values in the table were normalized so that

$$\int\int P(x,y)dxdy = 100,$$

where $P(x,y)$ is the percent occurrence for x, given y, or vice versa.

To find the frequency of occurrence of shear vectors originating between angles $\alpha_2 \leqslant \alpha \leqslant \alpha_1$ and having a magnitude $|\Delta\mathbf{V}|$ between $|\Delta\mathbf{V}_2| \leqslant |\Delta\mathbf{V}| \leqslant |\Delta\mathbf{V}_1|$, one needs to perform the integration

$$\int_{\alpha_1}^{\alpha_2} \int_{|\Delta\mathbf{V}_1|}^{|\Delta\mathbf{V}_2|} P(\alpha, |\Delta\mathbf{V}|) d\alpha \, d|\Delta\mathbf{V}|, \qquad (4)$$

which is shown graphically in Fig. 3. In practice, the bivariate frequencies in each cell of the table are summed to give the frequency of occurrence within the desired limits. The bivariate frequency table is well suited for operational use. Airport operations personnel might want the shear vector components with respect to a certain runway alignment (i.e., alongwind and crosswind components) rather than for standard meteorological coordinates. The percent occurrence of extreme crosswind and alongwind shears can be found by using the overlay shown in Fig. 4. Marginal frequency distributions, such as those given in the two WMO Technical Notes are given by summing each row and column of the bivariate frequency table. In this study, computer roundoff errors caused Eq. (3) to be slightly different than 100.

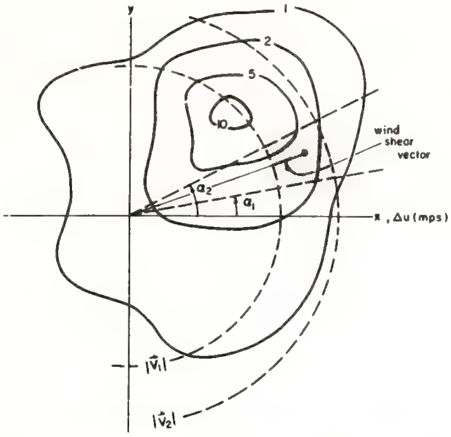

FIG. 3. Graphical depiction of integration limits for finding frequency of occurrence (sum of cell frequencies within shaded area) of wind shear vectors whose magnitude was between $|\mathbf{V}_1|$ and $|\mathbf{V}_3|$ and whose origin was between angles α_1 and α_2. Contours are in percent occurrence. Note shear vector is drawn from a point in shaded area to the origin.

b. Criterion for extreme wind shear

For data used in this study, the first winds aloft measurement level was 150 m above the ground making it necessary to draw a relation between the CAeM criterion of 5 m s^{-1} vector difference over the first 30 m and the results of this work.

Wind shears have traditionally been modeled by the power law relationship

$$\frac{V_2}{V_1}=\left(\frac{z_2}{z_1}\right)^n,\quad z_2>z_1. \tag{5}$$

Ekhardt and Newell (1964) report extreme wind shear conditions for military aircraft for $n\approx 0.3$. If we define $\Delta V\equiv V_2-V_1$ and $\Delta z\equiv z_2-z_1$, then using (5),

$$\Delta V=V_1\left[\left(\frac{\Delta z}{z_1}+1\right)^n-1\right]. \tag{6}$$

With the restriction that $\Delta z\gg z_1$, (6) can be reduced to

$$\Delta V\approx V_1\left[\left(\frac{\Delta z}{z_1}\right)^n-1\right]. \tag{7}$$

To give a general guideline on relating the CAeM criterion to the radiosonde measurements, the ratio

$$\frac{\Delta V_{150}}{\Delta V_{30}}=\frac{\left(\dfrac{150}{z_1}\right)^{0.3}-1}{\left(\dfrac{30}{z_1}\right)^{0.3}-1}, \tag{8}$$

was formed. The subscripts on ΔV refer to the separation distance; taking $z_1=2$ m yields $\Delta V_{150}\approx 10$ m s^{-1}.

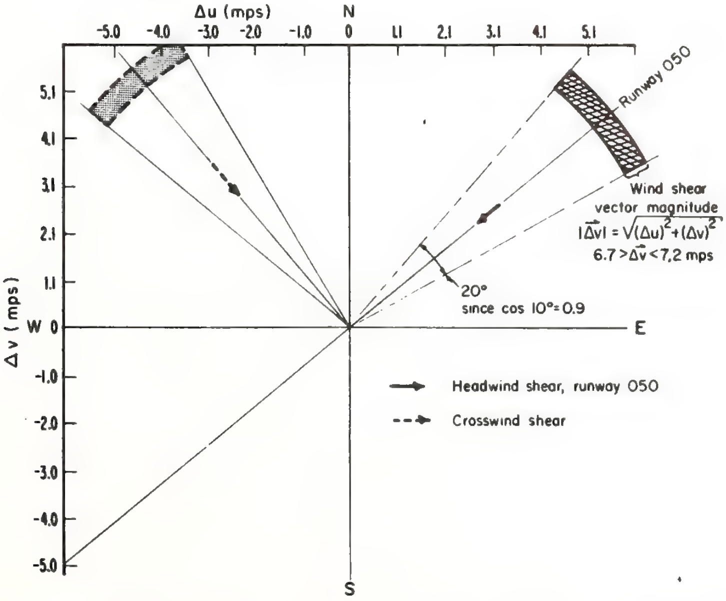

FIG. 4. Overlay scheme to be used with bivariate frequency tables to obtain percentage occurrence of wind shear along and perpendicular to a given runway. To obtain percent occurrence, add all values in shaded areas. In this case, 6.7 > $|\Delta\mathbf{V}|$ > 7.2 m s^{-1}.

Based on the above results, a pilot study on the wind shear environment of Denver, Colo., and the results of previous studies an extreme wind shear criterion for a 150 m separation was chosen to be $|\Delta\mathbf{V}| \geqslant 6.5$ m s^{-1}.

c. *Use of the bivariate frequency table*

To obtain statistics on the occurrence of extreme low-level wind shear, an overlay was constructed as in Fig. 5, and percentage occurrence was summed within the overlay corresponding to $\Delta V > 6.5$ m s^{-1} and ±45° around north, south, east and west. An example of these results for Denver is given in Fig. 6.

5. The data set and its limitations

The data set comprises wind sounding data from 10 stations chosen within the conterminous United States. Three criteria were used in the selection of a station: area representativeness, data availability (chiefly length of record), and classification by the Federal Aviation Administration as a major airport. Table 1 lists the stations chosen.

The wind sounding data (taken mostly by rawinsondes or radisondes) between the years 1956–64 were made available by the National Oceanic and Atmospheric Administration National Climatic Center (NCC). Frequency of the soundings at any one station varied from 2 to 4 soundings per day. Standard measurement levels were at the surface, 150 m above the surface, 300 m above the surface, and at the first standard level above sea level that was greater than 300 m above the surface. Therefore, the Δz of the first two layers was 150 m, while the Δz of the last layer varied from station to station. Calm winds were not included when computing shear statistics [the number of calms at each level was noted in the bivariate frequency table output (see Fig. 2)].

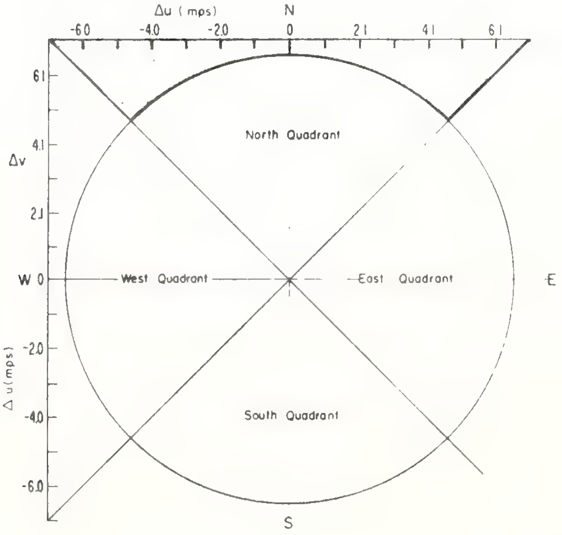

FIG. 5. Schematic of overlay used in extreme wind-shear analysis. Quadrants are as shown. Circle defines $|\Delta\mathbf{V}| \geqslant 6.5$ m s^{-1}. For example, north-quadrant percentage extreme wind shear is found by summing all cell percentages in shaded area.

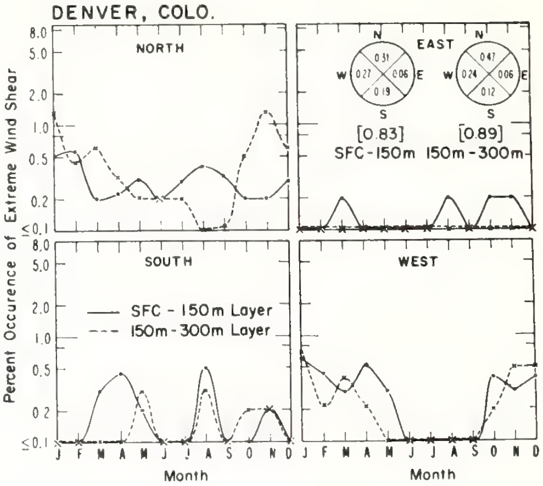

FIG. 6. Summary of extreme wind-shear (i.e., $|\Delta\mathbf{V}| \geqslant 6.5$ m s^{-1}) statistics at Denver, Colo. Results are given by quadrant; abscissa is climatological month; ordinate is percent occurrence of extreme wind shear; and circles in the upper right give values for the entire climatological year for the different quadrants. The figure in brackets below the circle gives the percent occurrence of extreme wind shear irrespective of quadrant.

In addition to smoothing errors caused by time averaging of the radar data the data set was subject to two error sources. These errors resulted from improper coding and keypunching and from radar lock-on difficulty in the lower boundary layer. The latter was an especially difficult problem in built-up areas and under strong wind conditions. The Denver case study discussed below indicates that these errors were small. However, the knowledge that the errors are present suggests that caution should be used in interpreting the results.

6. Denver case study

Stapleton International Airport at Denver has been selected for an extensive field program to determine the applicability of acoustic Doppler wind-measuring techniques in an operational environment (Beran *et al.*,

TABLE 1. Stations selected for low-level wind shear analysis.

Station	Major airport
Tatoosh Island, Wash.	No
Oakland, Calif.	Yes
Salt Lake City, Utah	Yes
Carswell AFB, Tex.	No
Denver, Colo.	Yes
Topeka, Kans.	No
Athens, Ga.	No
Dayton, Ohio	Yes
Green Bay, Wisc.	No
Nantucket, Mass.	No

1973). To provide some background information for this field program, Stapleton Airport was also chosen for a more detailed examination of extreme wind-shear occurrence.

To investigate the auditing errors mentioned above, all extreme wind profiles for the first two layers were examined on a hodograph. Over a 9 year period, 176 extreme wind shears were observed in the first two layers. Of these, 41 were judged to be suspect. These 41 cases were then subjected to an audit at NCC; four were found to be mispunched and 10 were logged improperly. The 27 remaining suspect shears generally received a "questionable surface wind" comment from the auditor. It is possible that these suspect profiles reflect local winds, not uncommon in Denver. The tracking or lock-on error was investigated using the remaining 27 profiles. Of these, 13 had surface winds of less than 5 m s^{-1}, 13 had surface winds of between 5 and 7 m s^{-1}, and only one had a surface wind above 7 m s^{-1}, suggesting that lock-on errors during high surface-wind conditions were unlikely. Even if 10 of the 27 remaining cases had lock-on errors, that number represents only about 5% of the total number of extreme wind shears. It was concluded from the above analysis that the Denver statistics are relatively free of error.

The marginal distributions of u and v for each layer and for each month at Denver were checked for normality, and in general showed Gaussian characteristics. There was some deviation from normal at the extremes, an expected result from a finite (and in this case, relatively small) data sample, but overall a linear relation existed between cumulative probability and class irrespective of month or layer. This is a necessary but not sufficient requirement for modeling Denver's low-level wind shear in terms of an elliptical bivariate distribution (Crutcher and Baer, 1962). The distribution of extreme wind shear, by direction, month and level for Denver is shown in Fig. 6.

Five cases of extreme wind shear at Denver were chosen on the basis of those having the largest wind shears for the 9-year period. Table 2 summarizes some of the information about the five cases of extreme shear occurrence. The strongest shear occurrences were confined to the first two layers and the frequency of occurrence was nearly equally divided between the lowest layer and the layer just above.

A consistent pattern was apparent between the synoptic situation and the soundings associated with the cases studied. The shear always resulted from changes in wind direction rather than in wind speed. The synoptic pattern was generally one in which a weak ridge or shallow high was present near the Denver area. Clear skies generally prevailed and visibility was well above the minimum for aircraft operations (for the map time analyzed). At 500 mb, the wind field generally showed strong westerly winds either directly over Denver or over southern Wyoming. The temperature-humidity sounding showed strong radiation inversions in every case. The directional wind shift causing the shear occurred across the inversion surface. Below the inversion, the flow appeared to be the result of local circulation, with the wind having some easterly component. Most of the directional shifts in the wind profile were due to backing winds rather than veering winds.

TABLE 2. Extreme wind-shear cases chosen for synoptic analysis.

Time (GMT)	Date	$\|\Delta V\|$ (m s^{-1})	Layer
1200	1 Feb 61	11.1	Sfc–150 m
0600	12 Oct 62	12.0	150 m–300 m
1800	20 Nov 62	11.0	150 m–300 m
0600	28 Nov 62	12.0	150 m–300 m
0600	13 May 63	11.1	Sfc–150 m

7. Results and conclusions

Table 3 summarizes the results from all stations studied with respect to the total percentages of extreme wind shear. Four out of 10 stations showed little difference between the extreme shear in the surface to 150 m layer and in the 150 to 300 m layer; one station showed a larger percentage of extreme shear in the higher rather than the lower layer. These results suggest that extremes of wind shear do not always fit boundary-layer models which predict stronger shears in the lowest layer (as was the case for 5 of the 10 stations). The highest frequency of extreme shear was shared by Athens, Ga., and Nantucket, Mass., while the lowest frequency was at Oakland, Calif.

The results of the literature review, the seasonal march of extreme wind-shear occurrence, and the fact that extreme shears are not necessarily confined to the lowest layer allow one to speculate that the major portion of extreme shear occurrence is closely tied to synoptic (or large mesoscale) conditions (where many present boundary-layer concepts break down). This is further demonstrated in Figs. 7 and 8 which present the total percentage occurrence of extreme wind shear for the 10 stations, with the major mean cyclone tracks over the conterminous United States superimposed. The correlation between high incidence of extreme wind shear and passage of cyclonic storms is evident in both layers. The occurrence of extreme wind shears shows large variation with season at almost all stations, with

TABLE 3. Total percentage of occurrence of extreme wind shear

Station	Surface to 150 m layer	150 to 300 m layer
Oakland, Calif.	0.35	0.28
Tatoosh Island, Wash.	2.07	1.37
Green Bay, Wisc.	2.30	2.29
Nantucket, Mass.	4.65	2.32
Salt Lake City, Utah	0.89	0.55
Denver, Colo.	0.83	0.89
Topeka, Kans.	3.55	3.38
Carswell AFB, Tex.	3.05	0.76
Dayton, Ohio	2.05	3.09
Athens, Ga.	4.64	2.11

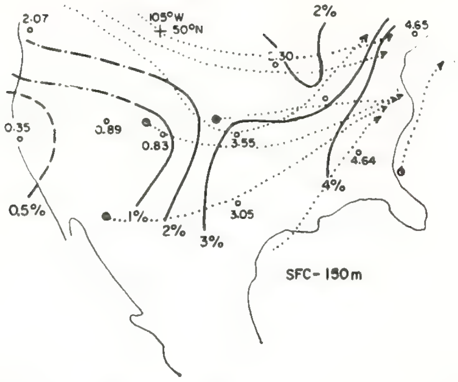

FIG. 7. Total annual percentage of extreme wind shears for the 10 stations analyzed. Dotted arrows are mean cyclone tracks (circle denotes origin of cyclone track) for the conterminous United States. Layer considered is surface to 150 m. The dash-dotted line denotes uncertainty due to mountainous terrain.

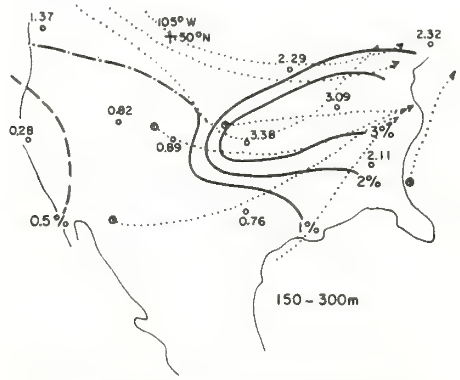

FIG. 8. As in Fig. 7 except for layer 150 to 300 m.

the greater percentage of extreme shears occurring in late fall through early spring. The lowest percentage occurrence is found from late spring through late summer.

Acknowledgments. The authors wish to acknowledge their fruitful discussions with Dr. Harold Crutcher. The bivariate frequency tables were constructed by the Applied Climatology Division, National Climatic Center. We also thank Ms. Pam Sedillo and Mr. Mike Sanchez who prepared Fig. 6.

This study was funded under a joint agreement between the Federal Aviation Administration and the Wave Propagation Laboratory.

REFERENCES

Abramovic, K. G., and V. G. Glazunov, 1969: Wind shear in the lower atmosphere. WMO Tech. Note No. 93, 195–202.

Aeronautical Meteorology, 1969: WMO Tech. Note No. 95.

Arya, S. P. S., 1972: The critical condition for the maintenance of turbulence in stratified flows. *Quart. J. Roy. Meteor. Soc.*, **98**, 264–273.

Beran, D. W., B. C. Willmarth, F. D. Carsey and F. F. Hall, Jr., 1973: An acoustic Doppler wind measuring system. *J. Acoust. Soc. Amer.*, **55**, 334–338.

Boucher, R. J., R. Wexler, D. Atlas and R. M. Lhermitte, 1965: Mesoscale wind structure revealed by Doppler radar. *J. Appl. Meteor.*, **4**, 590–597.

Burnham, J., 1970: A brief review of R.A.E. research on wind and gust effects relevant to landing and takeoff. Roy. Aircraft Est., Tech. Memo. Aero. 1201, 12 pp.

Commission for Aeronautical Meteorology (CAeM/III) International Civil Aviation Organization, 1964: WMO Rept. 157, Vol. 1 (abridged).

Colmer, M. J., 1971: On the character of thunderstorm gust fronts. *Proc. Intern. Conf. Atmospheric Turbulence*, 18–21 May 1971, London, England, Roy. Aero. Soc., 11 pp.

Crutcher, H. L., 1957: On the standard vector-deviation wind rose. *J. Meteor.*, **14**, 28–33.

——, and L. Baer, 1962: Computations from elliptical wind distribution statistics. *J. Appl. Meteor.*, **1**, 522–530.

Eckhardt, H. D., and J. S. Newell, 1964: Study of tactical army aircraft (TAALS). Task 1—Atmospheric studies. RCA Corp. Tech. Rept., 56 pp. [AD 433632].

Fichtl, G. H., 1971: Standard deviation of vertical two-point longitudinal velocity differences in the atmospheric boundary layer. *Boundary-Layer Meteor.*, **2**, 137–151.

Gera, J., 1971: The influence of vertical wind gradients on the longitudinal motion of airplanes. NASA-TN-D-6430, N71-34022, 19 pp.

Goldman, J. L., 1969: Analysis of wind field conditions adversely affecting vehicle operations. NASA Contractor Rept. CR-61286, N69-34881, 103 pp.

Jefferson, G. J., 1966: An incident of severe low-level elements in the study of eddy structure. *Meteor. Mag.*, **95**, 279–285.

Kusano, K., Y. Suzuki and H. Takei, 1967: Vertical wind shear in the lower layers at the Tokyo International Airport. *Geophys. Mag. Tokyo*, **33**, 239–256.

Marwitz, J. D., 1971: Severe storm types in relation to wind shear. *Preprints 7th Conf. Severe Local Storms*, Kansas City, Mo., Amer. Meteor. Soc., 240–243.

Mashkova, G. B., 1967: Wind profiles during low cloudiness at a height of less than 300 m. *Tr. Akad. Nauk SSSR Inst. Prin. Geofiz*, **10**, 39–43.

Melvin, W. W., 1970: Wind shear on the approach. *Shell Aviation News*, **393**, 16–20.

Panofsky, H., and H. Crutcher, 1951: Horizontal momentum flux due to small-scale turbulence. *J. Meteor.*, **8**, 420–421.

Pettitt, R. B., and R. G. Root, 1969: Vertical wind shear in the boundary layer. WMO Tech. Note No. 93, 1–30.

Reiter, E. R., 1961: *Jet Stream Meteorology*. The University of Chicago Press, 515 pp.

——, and P. F. Lester, 1967: The dependence of the Richardson number on scale length. Atmos. Sci. Paper No. 111, Colorado State University, 39 pp.

Rider, L. J., and M. Armendariz, 1966: Low-level jet winds at Green River, Utah. *J. Appl. Meteor.*, **5**, 733–736.

Rijkoort, R. J., 1969: Dependence of observed low-level wind shear on averaging period and lapse rate. WMO Tech. Note No. 93, 185–194.

Sowa, D. F., 1972: Turbulence plot program. *Shell Aviation News*, April, 16–19.

Taylor, P. A., 1970: A model of airflow above changes in surface heating flux, temperature and roughness for neutral and unstable conditions. *Boundary-Layer Meteor.*, **1**, 18–39.

Tsverava, V. G., 1967: Investigation of vertical wind vector shears based on observations on a 300 m meteorological tower. *Meteor. Gidrol.*, **2**, 82–84.

Vertical wind shear in the lowest layers of the atmosphere, 1969. WMO Tech. Note No. 93, 250 pp.

Watson, I. A., 1969: Report of an investigation into low-altitude wind structure for automatic landing. WMO Tech. Note No. 95, 61–96.

Zipser, E. J., 1969: The role of organized unsaturated convective downdrafts in the structure and rapid decay of an equatorial disturbance. *J. Appl. Meteor.*, **8**, 799–814.

Journal of Applied Meteorology 14, 513-523, June 1975.

Convective Plumes in the Planetary Boundary Layer, Investigated with an Acoustic Echo Sounder

F. F. HALL, JR., J. G. EDINGER[1] AND W. D. NEFF

Wave Propagation Laboratory, ERL, NOAA, Boulder, Colo. 80302

(Manuscript received 1 May 1974, in revised form 17 January 1975)

ABSTRACT

The turbulent temperature structure and winds in thermal convective plumes over prairie grassland have been investigated with an acoustic echo sounder system. Three spaced acoustic antennas, with two inclined at 45° elevation, were used to provide plume shape information and Doppler-derived total wind-vector patterns between heights of 70 and 500 m. Supporting *in situ* measurements were made on a 15 m tower, with a tethered balloon-supported Boundary Layer Profiler, and from a light aircraft. The most probable orientation of the plumes was nearly vertical, but frequent upwind and downwind tilts were also observed. Maximum positive vertical velocities in the plumes at midday were near 2 m s^{-1}, while maximum downward currents were one-half this value. Acoustic echoes from regions above the mixed layer, corresponding in height to an elevated temperature inversion, correlate well with regions of maximum wind shear.

1. Introduction

The object of this investigation was to map the turbulent temperature structure and the wind in convective plumes generated by solar heating of prairie terrain. It is concluded that an array of acoustic echo sounders can provide significant information on plume size, shape and velocity, and on how the stable planetary boundary layer is modified by convection.

From the earliest days of atmospheric acoustic echo sounding, large returns from the turbulent, convective daytime atmosphere have been observed (Gilman *et al.*, 1946). When facsimile recorders capable of displaying the backscattered intensity as a function of height and time were added to sounders, it became apparent that these daytime echoes were associated with vertically oriented plume structures (McAllister *et al.*, 1969). A typical facsimile recording of the unstable atmosphere, where the darkness of the record is proportional to the intensity of the echo, is shown in Fig. 1. This is the convective plume pattern for clear sky, light wind conditions, and direct solar heating of dry grassland terrain. Such plumes typically reach maximum development shortly after noon and may not show much seasonal structure dependence under certain specialized prairie conditions (Hall, 1972). The disappearance of the plumes with height on the facsimile records is not necessarily because the mixed layer extends no higher. Above several hundred meters, the temperature fluctuations are much weaker than near the ground, and there is additional absorption of transmitted and scattered acoustic energy at longer ranges, making the echoes indiscernible.

The acoustic scattering equation for a turbulent atmosphere was derived by Batchelor (1957), and in a different form by Tatarskii (1960), later corrected by Monin (1962); the application of this scattering theory to acoustic echo sounding has been analyzed by Little (1969). In the investigation reported here, the direct backscattering of sound, attributable to the temperature structure parameter C_T^2, was measured, where

$$C_T^2 = \overline{(T_1 - T_2)^2}/r^{\frac{2}{3}}, \tag{1}$$

with r being the distance separating the two points where the temperatures T_1 and T_2 are measured. A more complete discussion of C_T^2 and its relation to physics of the planetary boundary layer is given by

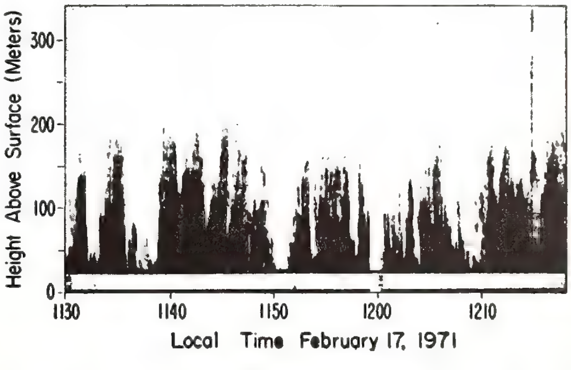

FIG. 1. A typical acoustic facsimile recording of thermal plume structure for a clear day with light wind conditions over dry grassland terrain.

---

[1] Also at Department of Meteorology, University of California, Los Angeles.

Neff (1975). The power backscattered from a unit volume, per steradian, for unit incident flux is then given by

$$\sigma = 7.2\times10^{-3}\lambda^{-\frac{1}{3}}\frac{C_T^2}{T^2}. \qquad (2)$$

By use of the acoustic "radar equation" (Little, 1969), C_T^2 is determined from the echo power received. It is important to note that the scattering equation (2) assumes a Kolmogorov spectrum of turbulence and that the probing acoustic energy of wavelength λ acts as a single-frequency analyzer of this turbulence with a spatial scale $\lambda/2$ (Kallistratova, 1962).

2. Experiment description

The experiment was conducted during August 1971 at the NOAA Table Mountain Field Site, 10 km north of Boulder, Colo. The topography of this flat, low mesa has been described by Hooke *et al.* (1972). At the time of the tests, the ground was covered by mixed dryland grasses approximately 15 cm high, scattered yucca somewhat higher, and occasional bare rock and sandy areas. Because of the close proximity to the first range of foothills of the Rocky Mountains about 5 km to the west and to the sloping sides of the mesa some 30 m high, the site cannot be considered typical of uniform, flat prairie land; there were undoubtedly orographic effects from the sloping terrain and nearby hills.

The arrangement of the acoustic antennas is shown in Fig. 2. Each sounder was operated monostatically at a different frequency (1750, 1900, 2150 Hz) and with pulse durations of 40 ms. The sounder system design was essentially that described by Simmons *et al.* (1971). The sloping antennas were located 200 m from the vertically pointed beam so that two nearly orthogonal planes were defined with a mutually probed scattering volume located 200 m above the vertically directed antenna. Clearly, within this scattering volume, the total wind vector may be derived by analyzing the Doppler-shifted return in each of the three beams (Beran and Clifford, 1972). Because the winds were averaged over 2 min and because the scale of structures exhibiting vertical velocity was greater than the antenna separations, the vertical velocity measured in the vertically pointed beam was assumed to be the same as that within the sloping beams; using this assumption the total wind vector (u, v, w) was derived between 70 and 470 m height. *In situ* measurements of wind as well as dry and wet bulb temperatures were provided by a kytoon-mounted package on a Boundary Layer Profiler (BLP), kindly provided by the National Center for Atmospheric Research (NCAR) Facilities Laboratory. In addition, winds were recorded at 2 and 15 m on a tower; temperature, humidity and pressure were recorded in a standard instrument shelter; and solar radiation was monitored by a Robitzsch-type pyranometer.

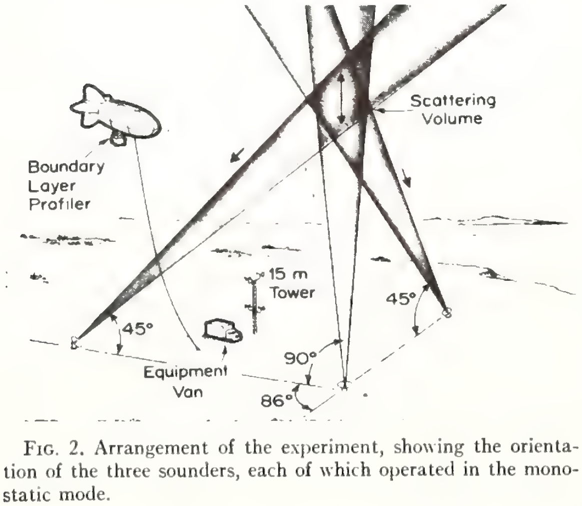

FIG. 2. Arrangement of the experiment, showing the orientation of the three sounders, each of which operated in the monostatic mode.

The sounder system had been previously calibrated against spaced, fine-wire temperature sensors, used for the *in situ* measurement of C_T^2 during an experiment at the Haswell, Colo., field site in 1969 (Hall, 1972). In addition, the calibration of the sounder equipment was continuously checked during the course of the experiment by flying a fast-response temperature sensor, mounted on a light aircraft, over the antenna at heights of 100, 200 and 300 m; the temperature sensor has been described by Lawrence *et al.* (1970). Aircraft passage over the sounder causes vertical, dark, noise lines to appear on the facsimile recording similar to the one at 1215 in Fig. 1.

The acoustic echoes from the atmosphere were recorded on facsimile machines for qualitative interpretation of the atmospheric structure and quantitatively on a multi-channel analog magnetic-tape recorder. The selected magnetic tapes were then digitized; the acoustic attenuation values were computed from temperature, pressure and humidity measurements; and the absolute intensities of the returns were calculated. The line-of-sight wind vectors along the three beams were computed by a frequency analysis of the return signals, using a bandpass filter, phase-shift Doppler derivation technique. The final computer output was a grid of C_T^2 values and of u, v, w wind-component values that could be overlaid on the facsimile records.

3. Observed characteristics of convective plumes

A close examination of the plume pattern in Fig. 1 reveals several characteristics of convective patterns as depicted by the sounder. It is apparent that within the plume boundaries, there are localized regions of much greater temperature structure, or plumes within plumes. The assumption of a statistically uniform plume interior, as modeled by Telford (1970), is not borne out by observation.

Another feature shown on the facsimile record are the small, but very dark, "vigorous" plumes of high C_T^2;

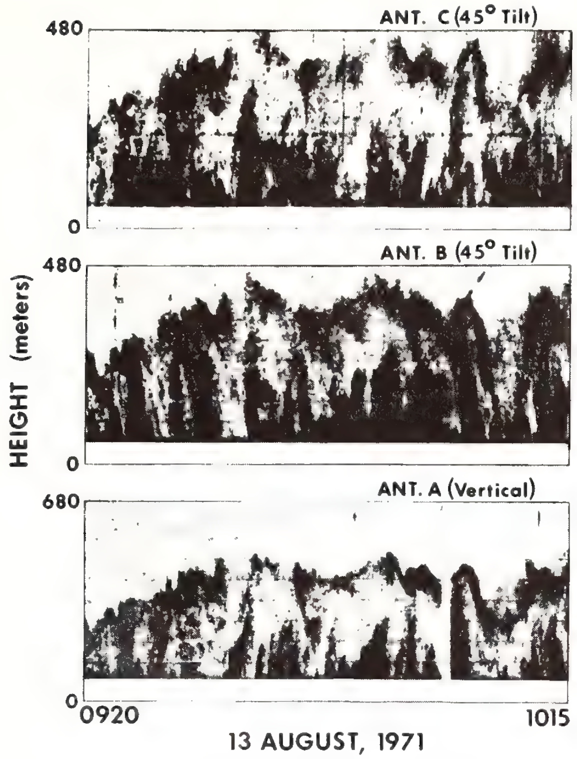

FIG. 3. Facsimile records from three sounders oriented as shown in Fig. 2. Returns from the sounder pointed vertically (A), pointed upward 45° toward the east (B), and pointed upward 45° toward the south (C) illustrate the differences in appearance enabling the derivation of plume velocity vectors.

two examples occur in Fig. 1 between 1132 and 1133, a taller one at 1136.5 and a shorter example at 1138. It was found from repeated aircraft passages through the larger plume families that the lifetime of such family groupings was at least 10 min. However, vigorous "hot spots" found on one pass would be indistinguishable on successive passages through the same plume family only 2 min apart. These observations on the merger of small vigorous plumes with larger plume families are in accordance with the numerical investigation of Deardorff (1972) who shows, in a time sequence of plume vertical velocity contours, the growth and merger of small plumes into older, larger plumes. However, the *spatial* distributions plotted by Deardorff may not be exactly comparable to the *temporal* cross sections of plumes recorded by the sounder. The facsimile of Fig. 1 presents only what the mean horizontal flow advects past the vertically directed acoustic transceiver.

Note also that the upwind plume edge, occurring later in time, is generally more sharply defined than the earlier downwind edge. Echo returns are more intense from the upwind edge, indicating greater temperature fluctuations at this location. This finding is in agreement with aircraft observations of plume temperature structure, reported by Myrup (1967) and by Lenschow (1970).

The ease by which individual convective plumes or plume families may be recognized on the facsimile records is demonstrated by the results in Fig. 1. Because these are temporal records, the shape and orientation of the plumes are not accurately depicted. Depending upon the gain and dynamic range of the facsimile machine, the location of the plume edges is somewhat ill-defined. A feature of the facsimile record which seems less susceptible to a subjective judgment of plume edges is the slope of the central axis of the plume returns. Fig. 3 illustrates the facsimile appearance of plumes seen with the vertically pointed sounder (A), with the sounder pointed upward 45° toward the east (B), and with the sounder pointed upward 45° toward the south (C). Because the beams from the three sounders point in significantly different directions and because the facsimile records present time versus height representations of the echo returns, the plumes must be tilted on at least one channel of data and usually on all three.

In Fig. 4, we show an isometric view of the geometry of the sounder array. The plane P is defined by the plume axis and by a line normal to the plume direction of motion. This plane is shown at two different times in the figure: at the moment when it intersects the common volume of the three sounder beams 200 m above the ground, and at that later time when it passes just above the antenna of the vertically directed sounder. Let T_H be the time required for the plane to traverse from the intersection of the beams downward to the ground. This time will depend upon the horizontal velocity v_H of the plane and its tilt angle β.

Additional time is required for the plane to complete its traverse down the beams of the other two sounders. The times required for these traverses from the 200 m level to the ground are called T_C and T_B. Three relevant equations to compute the plume slope β, speed v_H and

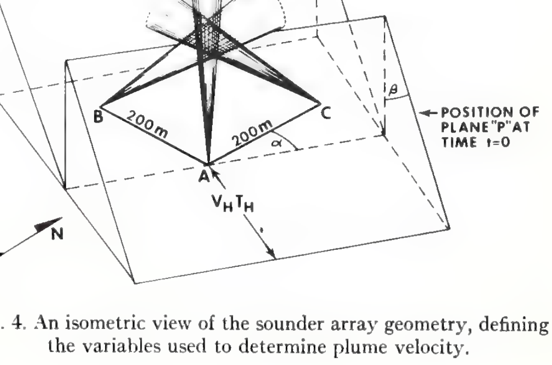
POSITION OF PLANE "P" AT TIME t=T_H
POSITION OF PLANE "P" AT TIME t=0
β
B
200m
200m
C
α
A
V_H T_H
N

FIG. 4. An isometric view of the sounder array geometry, defining the variables used to determine plume velocity.

direction α are then:

$$\left.\begin{aligned}\beta&=\tan^{-1}[(v_H T_H)/200]\\ v_H&=\frac{200\sin\alpha}{T_C-T_H}\\ \alpha&=\tan^{-1}\left(\frac{T_C-T_H}{T_B-T_H}\right)\end{aligned}\right\}$$

Using data from 1149 to 1422 (all times MDT) on 11 August 1971, a clear, sunny day with light winds, it was possible to identify 24 plume features that passed through the beams of all three sounders and for which it was possible to determine the slopes. Before 1130, a capping inversion existed near the 200 m level over the test site, but BLP probes showed that the inversion was destroyed after 1130. All convective plumes analyzed occurred in an atmosphere with an adiabatic lapse rate from 30 to 500 m.

The tilt angles for the plumes are shown in the histogram (Fig. 5). The maximum upwind tilt was 31° and the maximum downwind tilt 43°, with the greatest clustering of tilts occurring in the region from vertical to 10° downwind. The average tilt was 0°; the average plume was vertical.

Although Fig. 4 shows the plume-tilt reference plane extending to the ground, it should be noted that tilt measurements were actually made from 30 to 500 m. Plumes are known to tilt downwind in the lowest few tens of meters altitude from tower investigations (Kaimal and Businger, 1970). The lack of a consistent tilt direction at the higher levels does seem to rule out the possibility of optimally locating a solar observatory, whereby the most probable line-of-sight would be parallel to the tilted plumes, as suggested by Webb (1964). The low wind speeds existing during the experiment eliminate the possibility that the plume slope was influenced by convective organization into horizontal helical roll vortices (LeMone, 1973); the lack of such roll structure is also evidenced by the absence of large bursts of convective activity observed by Haugen *et al.* (1971) over grassy terrain with moderately high wind speeds.

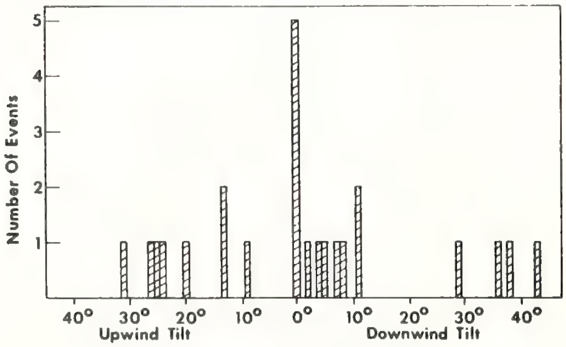

FIG. 5. A histogram of the tilt angles for 24 thermal plumes observed with the three-sounder array during conditions of free convection.

The velocity vectors, averaged over the 200 m height interval for the 24 plumes, were plotted end-to-end, and the resultant mean velocity of these features was found to be 3.0 m s^{-1} from 110°. Individual plumes passing the sounder array departed from this track by as much as 45°. For the same time period, the BLP measured an average wind from 30 to 200 m of 3.3 m s^{-1}, while the 15 m tower indicated wind direction from 108°. Acoustic Doppler derived winds were 2.9 m s^{-1} from 123°, with little shear averaged over the same height range as the BLP data. It therefore appears that the plumes do advect essentially with the mean wind field, averaged over the height range from 30 to 200 m.

As an independent measure of the horizontal dimensions of the convective plumes, the light aircraft, equipped with a fast-response temperature sensor, was flown through the volume probed by the sounder array. Twenty-two passes were obtained during the time interval 1149 to 1422 on 11 August 1971. One-half of the traverses were made in the downwind direction, and the other half across the wind direction. As was the case with the acoustic sounder plume features, the identification of the plume boundaries was somewhat subjective. Using the envelopes of the larger temperature fluctuation segments of the record as the boundaries of the convective plumes, a mean downwind dimension of 392 m and a crosswind dimension of 280 m were determined for the plumes, measured at 200 m above the terrain. This elongation of plumes along the wind direction has also been detected by Lenchow (1970) and by Frisch and Businger (1973).

In addition to the qualitative information on plume shape yielded by facsimile records, sounders may now be absolutely calibrated with respect to ***in situ*** measurements of the temperature structure (Hall, 1972; Neff, 1975). An analysis of the Doppler shift in frequency of the returns allows a determination of the velocity of the scattering parcel to be made (Beran *et al.*, 1971).

Typical maximum vertical velocities measured with the acoustic Doppler system in freely convective plumes, after the BLP indicated a neutral or unstable lapse rate to 500 m above terrain, were near 2.0 m s^{-1}, and the heights at which these maximum velocities were measured were usually between 200 and 300 m. Smaller plumes, possibly representing developing thermals which had not yet merged with larger families, displayed lower maximum vertical velocities and occurred at lower heights. An approximate relation between the maximum vertical velocity (m s^{-1}) in plumes and the height (m) at which it is measured is

$$w_{\max}=z/120,$$

at least to $z=250$ m.

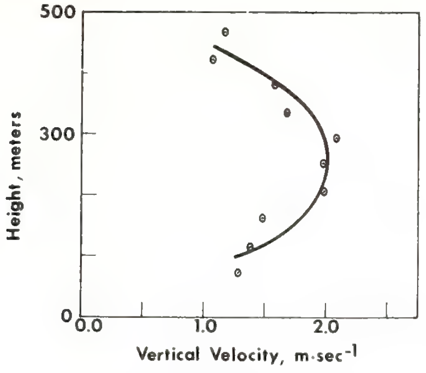

FIG. 6. Plot of typical maximum vertical velocities in a plume family as a function of height above the surface.

The distribution of vertical velocities in a typical large plume family is shown in Fig. 6. This plot represents a vertical slice through the plume and clearly indicates the buildup to maximum velocities between 200 and 300 m and the falloff to lower *w* values at greater heights.

The vertical velocity profile in Fig. 6 was recorded at 1300 on 11 August 1971. By extrapolating the rate at which the mixed layer depth increased between 0800 and 1100 when the elevated inversion echo was discernible, it is estimated that the depth of the mixed layer at 1300 was 600 m. The shape and magnitude of the plot of the maximum plume vertical velocities in Fig. 6 then agrees very well with numerical predictions shown in Fig. 28 in the study by Deardorff (1972). In a private discussion, Deardorff has pointed out that if the rms vertical velocity is about one-half the maxima of Fig. 6, then for a mixed layer depth of 600 m, one obtains a surface kinematic temperature flux of 0.20 m s^{-1} °C by working backward from his numerical results. This is a reasonable flux value for summer prairie conditions.

After a clear, sunny morning on 13 August, thunderstorms developed over the Rockies, just west of the experiment site, in the early afternoon. At 1405, the sun abruptly disappeared behind a dense anvil cloud, and within 1 min all signs of ground-based plumes disappeared from the sounder facsimile record. One elevated rising bubble, detached from its earthly origin, drifted by in the low-level easterlies at 1407, but with that all signs of convection ceased. The dry prairie terrain obviously had a low heat capacity.

4. Evolution of the mixed layer

One principal reason for conducting the experiment was to investigate the modification of the early morning, stable planetary boundary layer by convective activity. A typical facsimile recording of this modification, taken from the vertically directed sounder, is presented in Fig. 7. The increase in thermal plume activity during the course of the record is clearly indicated, but the explanation for the darker "envelope echo" above the plumes, apparently located at the elevated inversion was unexplained in previous studies (McAllister *et al.*, 1969). This envelope is termed the "convective front" by Rosset *et al.* (1973). It was known from investigations by Gossard *et al.* (1970) and by Emmanuel *et al.* (1972) of the statically stable atmosphere that such dark streaks on FM/CW radar or acoustic sounder facsimile records could correlate with regions of turbulence generated by shear instabilities where the Richardson number is less than 0.25. It was not certain if this was the proper explanation when the boundary layer was being modified by heating from below, and where neutral or unstable lapse rates extended up to a shallow, elevated inversion.

a. In situ measurements with balloon-borne sensors

The dark sloping streak, starting at a height of 500 m at 0905 in Fig. 7, is not atmospheric, but is caused by the echo from the BLP balloon which was descending at the time and happened to drift into the acoustic beam or a side lobe of the beam. The temperature trace

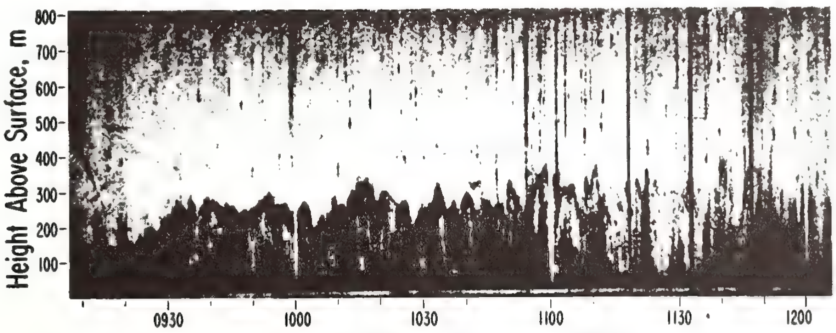

FIG. 7. Facsimile record of thermal plume activity lifting and modifying the planetary boundary layer from one of static stability at sunrise to one exhibiting free convection near noon.

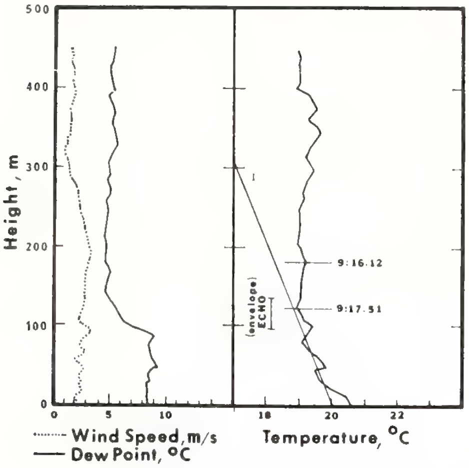

FIG. 8. Temperature, dew point and wind profiles obtained with the BLP on 13 August 1971 in the time interval from 0906 to 0925 MDT.

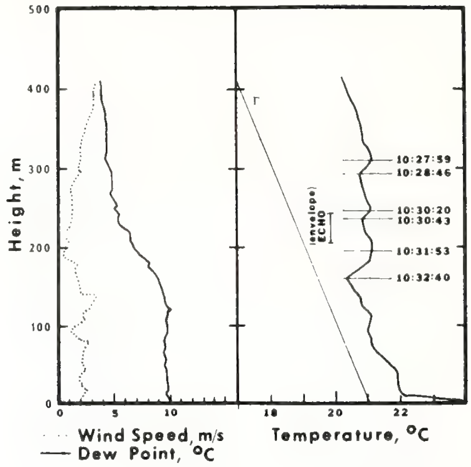

FIG. 10. As in Fig. 8 except for 1022–1038 MDT.

obtained with this balloon sounding is shown in Fig. 8, and it can be seen that the envelope echo does correlate with an inversion near the 100 m level. (The dew point, also shown in Fig. 8, abruptly increased 4°C just below 100 m. In most BLP probes, the wet bulb readings were very helpful in identifying the depth of the convectively mixed layer.) Notice that solar heating has already produced superadiabatic lapse rates in the lowest 30 m. The diagonal line in Fig. 8 is the adiabatic slope, and the time markers indicate the height of the BLP at different times.

By 0950, the envelope echo was above 200 m; the temperature and wind sounding for this time period is shown in Fig. 9. This echo region again corresponds to statically stable layers, while heating from below has raised the average temperature and the height of the superadiabatic lapse region. The balloon trace of this ascent is just visible in Fig. 7.

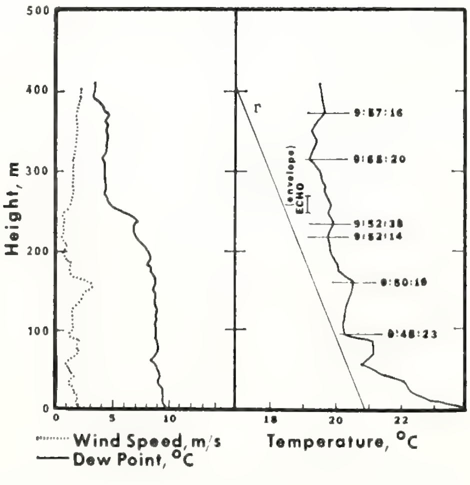

FIG. 9. As in Fig. 8 except for 0944–1007 MDT.

Not much change in the envelope echo height occurred before the next descent of the balloon through the envelope at 1030. The balloon sounding for this time period is shown in Fig. 10. Again, the envelope echo is near a region of static stability through which the BLP passed at 1030. That this is the inversion is clearly revealed by study of the wet bulb readings which frequently are a less ambiguous tracer of the mixed layer below the inversion. In the next balloon ascent through the envelope region at 1045 (Fig. 11), the envelope echo has been somewhat weakened, although a statically stable region was detected by the balloon at approximately 240 m.

b. *Richardson number calculations*

The rates of ascent and commutation of data of the BLP allowed a resolution in Δz of 5 m for wind, dew point and temperature. This is a sufficiently fine vertical resolution to allow reliable calculations of the Richardson number in the atmosphere and, in fact, matches the criterion for such measurements proposed by Woods (1969). Averaging times for these measurements were 15 s, or probably several times the lifetime of the dominant eddies or coherent turbulent structure in the inversion. The sounder was pulsed every 4 s with 40 ms tone bursts, capable of resolving 6 m eddies, and a careful examination shows fine-scale changes with each probing of the inversion, and in plumes as well. Table 1 lists the times that the inversion was penetrated by the BLP and the values for the height, potential temperature, and gradients of wind and potential temperature for the uppermost, statically stable layers in the inversion. (These layers were primarily identified by the sharp change in wind and dew point.) From these values, the resulting gradient Richardson number is calculated; it is shown in the last column of Table 1. For all five measurements, the Richardson number within the inversion is less than 0.25, so that we would expect shear instability turbulence to be generated. With the positive gradient of potential temperature through the inversion, a downward turbulent transfer of heat must occur, a mechanism hypothesized by Ball (1960).

c. Conditions above the planetary boundary layer

It is not surprising that the turbulent overturning of the statically stable air leads to acoustic echoes, for this is just the process which will produce C_T. However, an examination of the air temperature above the inversion in Figs. 8–11 shows that the average temperature in the height region from 300 to 500 m increased at a rate of 2.3×10^{-4}°C s^{-1} during the 2 h from 0910 through 1110. This implies a net heat flux into this region given by

$$H=\int_{h_1}^{h_2} c_p\rho\frac{dT}{dt}dz, \qquad (3)$$

or $H=45$ W m^{-2}. This is more than one-half of the heat flux value for the same period of time for the 0 to 200 m height range below the inversion where $H=85$ W m^{-2}. If the downward turbulent transfer of heat through the inversion were a continuous process, this heating of the air above the inversion could not have occurred in the absence of other mechanisms.

We now investigate possible heating mechanisms for the air above the lifting inversion. One possible mechanism is the horizontal advection of heated air in the 1 m s^{-1} easterly wind. To produce the observed heating rate would require a horizontal temperature gradient of 0.23°C km^{-1}, a rather large temperature gradient in the absence of a frontal surface. No fronts passed through the Colorado region on 13 August 1971.

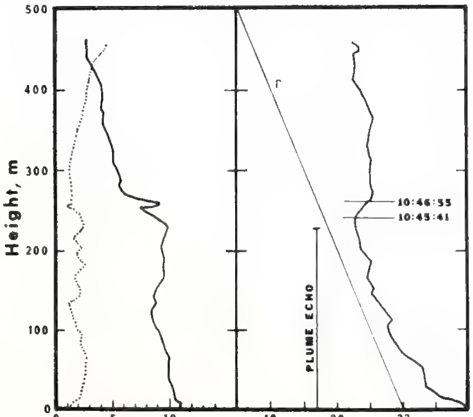

FIG. 11. As in Fig. 8 except for 1038–1054 MDT.

TABLE 1. Characteristics of the elevated temperature inversion that shows as the more intense acoustic "envelope" echo in Fig. 7.

Time (MDT)	Height (m)	θ (K)	$d\theta/dz$ (K m^{-1})	du/dz (s^{-1})	Ri
0920	79–92	293	0.038	0.077	0.21
0953	247–254	295	0.038	0.080	0.20
1031	220–230	296	0.016	0.058	0.16
1047	245–256	296	0.029	0.100	0.10
1116	232–240	297	0.072	0.107	0.21

Another possible mechanism is the radiative heat-flux divergence. Thompson and Neiburger (1953) have shown that the absorption of solar radiation may lead to an air mass temperature rise as great as 1°C per day, although long-wavelength cooling effects usually reduce this value. The observed rate of temperature increase here is nearly 20°C per day, far in excess of increases that would be expected from radiative mechanisms.

The most probable heating mechanism is air mass subsidence. To accomplish the observed increase in temperature requires a sinking velocity of only 2.3×10^{-2} m s^{-1}. On the day in question, there was a weak trough extending from Mexico over Colorado to a low centered in the Dakotas, whereas Petterssen *et al.* (1947) found that 80% of the investigated cases of subsidence were associated with anticyclonic vorticity. In addition, a temperature inversion may develop at the base of the subsiding air (Izumi, 1964), and such inversions are detectable with the acoustic sounder (Hall, 1972). No such subsiding inversion surface was detected on 13 August. BLP data on the time variation of temperature above and below the envelope inversion were also gathered on 5, 9 and 11 August. On the 11th, there was a 1020 mb high over Colorado when stronger subsidence might have been expected, but the rate of change of temperature above the inversion was somewhat *less* than on the 13th. The acoustic sounder record for the 11th does not show quite as strong an envelope echo as that for the 13th. The heating rates on the other two days, 5th and 9th, were also comparable to that on the 13th, although on the 9th a weak trough extended through the area and on the 5th the entire United States was dominated by high pressure.

In spite of seeming contradictions and arguments against subsidence, it seems probable that the close proximity of the experiment site to the Rocky Mountains and the weakness of the troughs on the 9th and 13th may counter the statistics of Petterssen *et al.* (1947). The failure of the mixed layer to increase much in depth between 0940 and 1130 in Fig. 7 is probably explained by subsidence. We have seen many facsimile records taken at the NOAA field site at Haswell, Colo., 200 km from the Rockies, where the mixed layer depth increases nearly linearly with time starting 1–2 h after sunrise. The weak subsidence required to produce the heating measured above the inversion may not have produced a sharp temperature discontinuity at the base of the subsiding air, especially since the heating rates in the mixed layer did clearly exceed those which might have been produced by adiabatic sinking. Therefore, the reader is cautioned to look upon the 13 August data analysis as an interesting case study, one used to test the ability of acoustic methods to study the boundary layer, but a case not necessarily representing a completely typical prairie situation.

The BLP sounding from 1159 to 1215, after all indications of the envelope echo have disappeared from the facsimile recording, showed a neutral-stability lapse rate above 30 m at a potential temperature of $\theta = 298$ K. For this sounding, the Richardson number is essentially zero because of the numerator term.

d. Sounder derived isopleths of C_T^2 and wind

From an examination of Fig. 7, it appears that breaks in the inversion follow periods of enhanced turbulence and waves in the layer, and perhaps even a thickening of the inversion. This thickening might serve to reduce the shear, increasing the Richardson number to a value at which turbulence is no longer sustained. Such patchy turbulent shear zones are also observed in the thermocline in the ocean (Woods, 1969). It is unfortunate that BLP penetrations of the gaps in the inversion, as revealed by the sounder, were not made. It may be significant that the strength of the inversion, $\sim 1°$C, seemed to remain constant until dissipation after 1116; the same intensity of the inversion was observed at 0711 in the first BLP profile obtained during this day, before any convective activity was detected by the sounder. It is apparent that any successful analytical modeling of inversion surfaces above convective activity must explain the feedback mechanism by which Ri near 0.25 is maintained.

A quantitative evaluation of the acoustic sounder echoes for the time period from 0900 to 1100, corresponding to the first 2 h of the facsimile records shown in Fig. 7, is given in Fig. 12. The solid line isopleths indicate regions of equal acoustic intensity with the contour interval of C_T^2 equal to 5×10^{-3} °C^2 m^{-3}. Values of C_T^2 greater than 2×10^{-2} °C^2 m^{-3} are shaded with a square pattern in the figure. These shaded regions thus correspond closely to the black regions in the original facsimile (Fig. 7). For example, note the slender thermal plume just before 0930 that merges with a strong envelope echo, continuing until 0935.

The dashed isopleths in Fig. 12 connect heights of equal horizontal wind shear with height; the contour interval is 1 m s^{-1} for each 44 m increment of height. Shear values greater than 2 m s^{-1} per 44 m are shaded with a diagonal cross-hatch pattern. The solid circles indicate the position of the BLP; the data displayed in Figs. 8–11 correspond to the four flights shown in Fig. 12. The stretched-out time scale of Fig. 12, compared to Fig. 7, more accurately depicts the true spatial orientation of the structures seen with the sounder. The frequent sloping attitudes of the plumes are more accurately shown, and the lateral spread of the plumes below the inversion is more accurately portrayed, as at 0918, 0933, 1000 and 1025. Frequently, where the plumes spread below the inversion, the wind shear is enhanced through rather significant depths. The spatial resolution and the lack of *in situ* temperature data for these periods do not permit the calculation of the Richardson number, but it appears obvious that the more intense envelope echoes are associated with strong, deep shear zones. The apparent gaps in the envelope that occur follow such events. These gaps may represent regions where stable air is entrained down into the mixed layer. Since the entrained stable layer is essentially nonturbulent on a small scale, it carries low C_T^2 downward.

A better understanding of the winds may be obtained from a streamline analysis of the acoustic Doppler-derived velocity, as shown in Fig. 13. Here it is apparent that the inversion surface decouples the horizontal wind above the inversion from the more complex vertical motions in the convective mixed layer. The strong vertical motion within the plumes is apparent, and shear, convergence, or overturning vortex structure associated with the plumes and the stronger envelope echoes also occur. Note that the wind below the inversion changed from a downslope westerly wind during the first hour to an upslope easterly wind after 1000. The easterly wind was quite constant above the inversion during the entire course of the experiment. This reversal in the lower mixed region is shown by the 1 h average of acoustically derived winds in Fig. 14. Even with this change in wind direction, undoubtedly orographically influenced, the shear at the inversion nonetheless retained the proper value to maintain the gradient Richardson number at values just below 0.25.

We have seen with the sounder the very similar, hummocky, patchy envelope echoes above the developing convective layers, even at our Haswell field site where the prairie grassland is essentially flat for many kilometers in all directions. High-power radars have seen what appear to be identical inversion structures in England (Browning *et al.*, 1973). It would appear for the rather weak radiative inversions which develop in Colorado that the characteristics of the boundary layer, as it is modified by convection in the early morning hours, are little influenced by the detailed topography of the site and that similar patterns would probably be observed over most relatively flat, grassy terrain.

5. Conclusions

The combination of acoustic remote sensing techniques with *in situ* temperature and wind measurements provides new information on convective plume

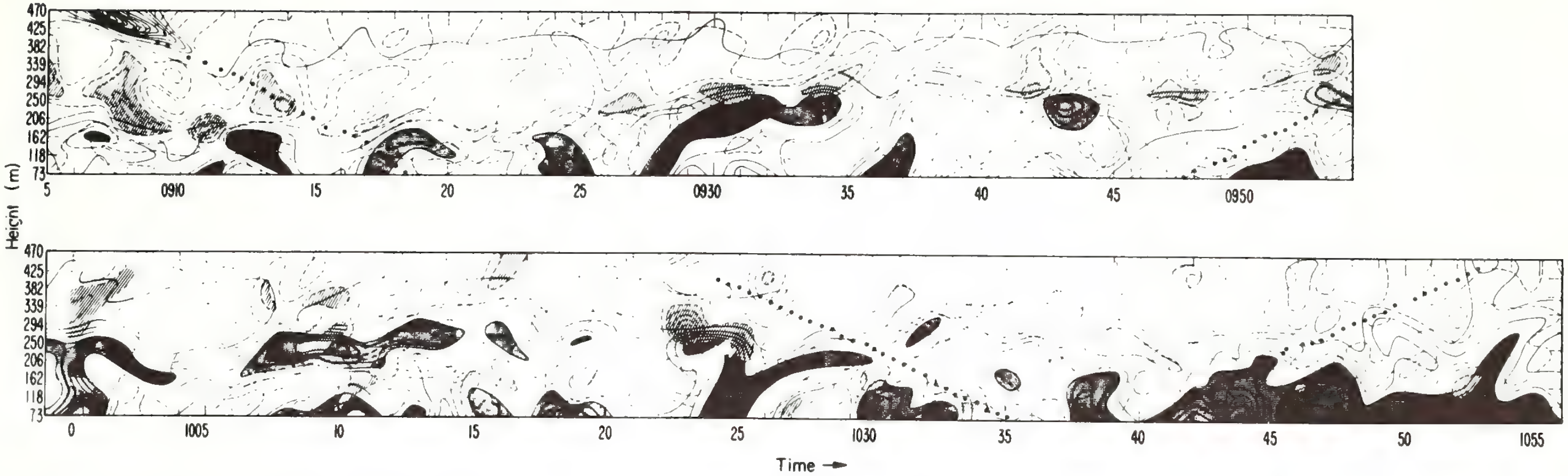

FIG. 12. Quantitative evaluation of the 13 August 1971 acoustic sounder returns. The solid line isopleths indicate regions of equal acoustic echo intensity using a contour interval of $C_T^2=5\times10^{-3}$ °C² $m^{-\frac{2}{3}}$. The dashed isopleths connect regions of equal horizontal wind shear, with the contour interval being 1 m s⁻¹ for each 44 m of height increment. The dots indicate the temporal trajectory of the BLP balloon.

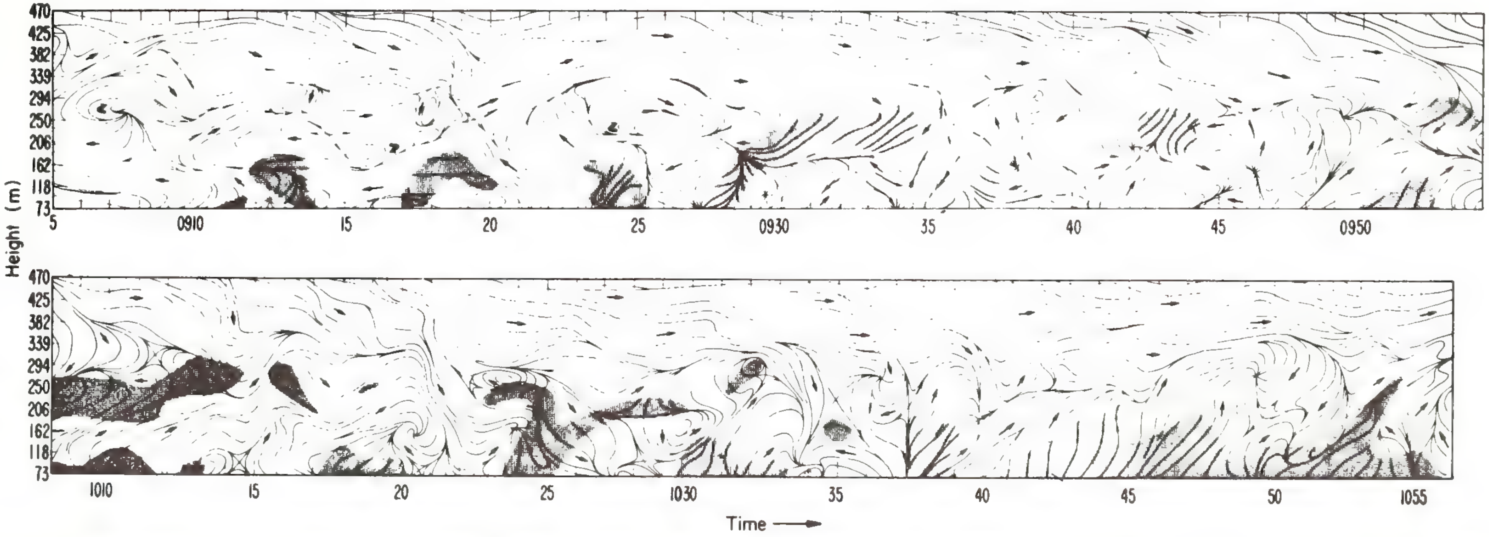

FIG. 13. Streamlines for the 13 August 1971 planetary boundary derived from acoustic-sounder Doppler analysis. Location of the stronger acoustic echoes is indicated by the shaded regions.

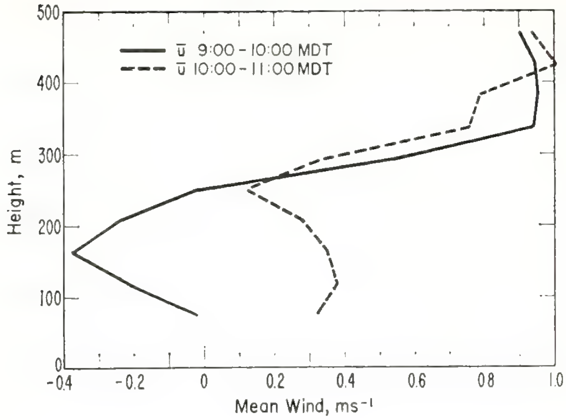

FIG. 14. Hourly wind-profile averages in an east-west plane derived by the acoustic array, showing the maximum wind shear at the height of the elevated inversion and the reversal of winds below the inversion during the morning.

morphology. The typical convective plume in the height range between 30 and 300 m is vertical, although it may slope into or with the wind, and the plume advects with the mean wind field. Plumes are vertically contiguous structures, but with continuously changing shapes as smaller plumes join the larger plume families.

A three-axis, Doppler acoustic system is capable of mapping the wind fields to heights of at least 500 m. Upward velocities within convective plumes may reach 2 m s^{-1} during the summer over dry, prairie terrain.

As convective plumes interact with the stable planetary boundary layer in the early morning hours, an elevated inversion develops which is characterized by a hummocky shape and by a Richardson number of less than 0.25. The hummocks or waves in the inversion have lengths that are 15–20 times the inversion thickness (assuming Taylor's hypothesis and wave speed equal to the wind in the inversion), so they are probably not pure Kelvin-Helmholtz billows but may have their shapes modified by the convective plumes impinging on the stable interface from below. The capping inversion surface is evidently not continuous, and air from the stable region above the inversion is entrained downward through the gaps.

Acknowledgments. The BLP was provided by NCAR through the efforts of H. W. Baynton; it was operated during the experiment by R. B. McBeth who also aided in reducing the temperature and wind data. Aircraft were piloted by R. S. Lawrence and R. W. Fegley; setup and operation of the acoustic system were accomplished with the assistance of D. W. Beran, R. W. Krinks, J. W. Wescott and B. C. Willmarth of the NOAA Wave Propagation Laboratory. The support of all of these individuals was a great help in completing his investigation. Discussions with and comments by J. W. Deardorff, W. H. Hooke and C. G. Little while preparing this paper were most useful.

REFERENCES

Ball, F. K., 1960: Control of inversion height by surface heating. *Quart. J. Roy. Meteor. Soc.*, **86**, 483–494.

Batchelor, G. K., 1957: Wave scattering due to turbulence. *Proc. Symp. Naval Hydrodynamics*, F. S. Sherman, Ed., NAS-NRC Publ. 515, Washington, D. C.

Beran, D. W., C. G. Little and B. C. Willmarth, 1971: Acoustic Doppler measurements of vertical velocities in the atmosphere. *Nature*, **230**, 160–162.

, and S. F. Clifford, 1972: Acoustic Doppler measurements of the total wind vector. *Preprints 2nd Symp. Meteorological Observations and Instrumentation*, San Diego, Amer. Meteor. Soc., 100–109.

Browning, K. A., J. R. Starr and A. J. Whyman, 1973: The structure of an inversion above a convective boundary layer as observed using high-power pulsed Doppler radar. *Bound. Layer Meteor.*, **4**, 91–111.

Deardorff, J. W., 1972: Numerical investigation of neutral and unstable planetary boundary layers. *J. Atmos. Sci.*, **29**, 91–115.

Emmanuel, C. B., B. R. Bean, L. G. McAllister and J. R. Pollard, 1972: Observations of Helmholtz waves in the lower atmosphere with an acoustic sounder. *J. Atmos. Sci.*, **29**, 886–892.

Frisch, A. S., and J. A. Businger, 1973: A study of convective elements in the atmospheric surface layer. *Bound. Layer Meteor.*, **3**, 301–328.

Gilman, G. W., H. B. Coxhead and F. H. Willis, 1946: Reflection of sound signals in the troposphere. *J. Acoust. Soc. Amer.*, **18**, 274–283.

Gossard, E. E., J. H. Richter and D. Atlas, 1970: Internal waves in the atmosphere from high-resolution radar measurements. *J. Geophys. Res.*, **75**, 3523–3536.

Hall, F. F., Jr., 1972: Temperature and wind structure studies by acoustic echo-sounding. *Remote Sensing of the Troposphere*, V. E. Derr, Ed., U. S. Govt. Printing Office, Washington, D. C., 26 pp. (Cat. No. 0323-0011).

Haugen, D. A., J. C. Kaimal and E. F. Bradley, 1971: An experimental study of Reynolds stress and heat flux in the atmospheric surface layer. *Quart. J. Roy. Meteor. Soc.*, **97**, 168–180.

Hooke, W. H., J. M. Young and D. W. Beran, 1972: Atmospheric waves observed in the planetary boundary layer using an acoustic sounder and a microbarograph array. *Bound. Layer Meteor.*, **2**, 371–380.

Izumi, Y., 1964: The evolution of temperature and velocity profiles during breakdown of a nocturnal inversion and a low level jet. *J. Appl. Meteor.*, **3**, 70–82.

Kaimal, J. C., and J. A. Businger, 1970: Case studies of a convective plume and a dust devil. *J. Appl. Meteor.*, **9**, 612–620.

Kallistratova, M. A., 1962: Experimental investigation of acoustic wave scattering in the atmosphere. *Tr. Akad. Nauk SSSR, Inst. Fiz. Atmos.*, No. **4**, 203–256 [USAF FTD translation TT-63-441].

Lawrence, R. S., G. R. Ochs and S. F. Clifford, 1970: Measurements of atmospheric turbulence relevant to optical propagation. *J. Opt. Soc. Amer.*, **60**, 826–830.

LeMone, M. A., 1973: The structure and dynamics of horizontal roll vortices in the planetary boundary layer. *J. Atmos. Sci.*, **30**, 1077–1091.

Lenschow, D. W., 1970: Airplane measurements of planetary boundary layer structure. *J. Appl. Meteor.*, **9**, 874–884.

Little, C. G., 1969: Acoustic methods for the remote probing of the lower atmosphere. *Proc. IEEE*, **57**, 571–578.

McAllister, L. G., J. R. Pollard, A. R. Mahoney and P. J. R.

Shaw, 1969: Acoustic sounding—A new approach to the study of atmospheric structure. *Proc. IEEE*, **57**, 579–587.

Monin, A. S., 1962: Characteristics of the scattering of sound in a turbulent atmosphere. *Sov. Phys. Acoust.*, **7**, 370–373.

Myrup, L. O., 1967: Temperature and vertical velocity fluctuations in strong convection. *Quart. J. Roy. Meteor. Soc.*, **93**, 350–360.

Neff, W. D., 1975: Quantitative evaluation of acoustic echoes from the planetary boundary layer. NOAA ERL-WPL Tech. Rept. (to be published).

Petterssen, S., P. A. Sheppard, C. H. B. Priestley and K. R. Johannessen, 1947: An investigation of subsidence in the free atmosphere. *Quart. J. Roy. Meteor. Soc.*, **73**, 43–64.

Rosset, R., P. Mascart, H. Isaka and R. G. Soulage, 1973: Mode d'epaissisement d'une basse couche convective matinale en ciel clair. *C. R. Acad. Sci. Paris*, **B276**, 223–226.

Simmons, W. R., J. W. Wescott and F. F. Hall, Jr., 1971: Acoustic echo sounding as related to air pollution in urban environments. NOAA Tech. Rept. ERL 216-WPL 17, Boulder, Colo., 77 pp.

Tatarskii, V. I., 1960: *Wave Propagation in a Turbulent Medium*. McGraw-Hill, 285 pp.

Telford, J. W., 1970: Convective plumes in a convective field. *J. Atmos. Sci.*, **27**, 347–358.

Thompson, A. H., and M. Neiburger, 1953: The radiational temperature changes over the eastern North Pacific Ocean in July 1949. *J. Meteor.*, **10**, 167–174.

Webb, E. K., 1964: Daytime thermal fluctuations in the lower atmosphere. *Appl. Opt.*, **3**, 1329–1336.

Woods, J. D., 1969: On Richardson's number as a criterion for laminar-turbulent-laminar transition in the ocean and atmosphere. *Radio Sci.*, **4**, 1289–1298.

Antarctic Journal
of the United States 10,
191-192, July/August 1975.

Atmospheric acoustic echo sounding investigations at the South Pole

F. F. HALL, JR., *and* E. J. OWENS
Wave Propagation Laboratory
Environmental Research Laboratories
National Oceanic and Atmospheric Administration
Boulder, Colorado 80302

The objective of this investigation is to monitor the structure of the planetary boundary layer at the South Pole using a monostatic acoustic echo sounder. An improved knowledge of the turbulent mixing depth characteristics will allow better estimates to be made of the atmospheric heat flux into the ice. By comparing the turbulent and solar input to the ice to the heat loss measured by spacecraft radiometers, we may be able to understand long-term variations in ice temperatures, and study the effect of such variations on climate dynamics.

The typical facsimile recording of acoustic echo intensity we obtained at the Pole shows rather closely spaced, descending turbulent layers. The Richardson numbers calculated from Pole radiosonde temperature and wind gradients in such layers are of the order 1.0, whereas values less than 0.25 were to be expected. Based on some previous prairie observations, we feel the waves observed may be closely related to Tollmien-Schlichting waves, produced by the surface stress. A comparison of the depth of the "herringbone" pattern of echoes with radiosonde ascents at the Pole shows a strong correlation with the most stable portion of the ground based inversion. From 431 hours of acoustic sounder records obtained between January 20 and February 12 at the Pole, a surface based inversion existed during 420 hours.

The mean depth of this turbulent inversion layer was 114 meters, with a standard deviation of 59 meters. The potential temperature of an air parcel at the top of this layer averaged 4°K. higher than the surface shelter temperature during clear January conditions, but only 2°K. higher under cloud cover. In early February the magnitude of the inversion increased to 9°K.

Surprisingly, during 11 hours of the 431 for which records are available, or for 2.6 percent of the time, the sounder detected convective plumes originating at the ice surface. Three separate such events occurred, each during a rapid decrease in surface shelter temperatures. We hypothesize that relatively warmer air had heated the ice surface, and the rapid intrusion of colder air found the ice warmer than the atmospheric surface layer, thus setting off the convection. The radiosonde ascent at 1115 on February 9, 1975, showed a super-adiabatic lapse rate in the lowest 138 meters of the atmosphere, but some of the plumes detected by the sounder extended to more than 200 meters, undoubtedly because of convective overshoot. Other types of atmospheric events observed with the sounder include gravity waves in elevated inversion layers and abrupt spikes in the turbulent return (possible hydraulic jumps associated with frontal passages?), rising from the surface based inversion to heights of 200 meters or more. Approximately 6 hours of such transient spikes were detected.

Situation reports from the Pole indicate the sounder was operating through June with minimum down time. With the aid of the wintering National Oceanic and Atmospheric Administration technicians, Kenton Martinsson and Richard Maestas, we hope that the sounder will accumulate a 1-year record of surface structure characteristics for further evaluation.

This research was supported by National Science Foundation grant 74-24415.

Journal of Applied Meteorology 14, 31-38, February 1975.

Further Study of the Atmospheric Gravity Waves over the Eastern Seaboard on 18 March 1969

William H. Hooke
Wave Propagation Laboratory, NOAA, Boulder, Colo. 80302

Kenneth R. Hardy[1]
Air Force Cambridge Research Laboratories, Bedford, Mass. 01730

(Manuscript received 14 February 1974, in revised form 17 September 1974)

ABSTRACT

Washington, D. C., microbarograph records for 18 March 1969 reveal gravity-wave-associated pressure oscillations which appear to be directly related to upper tropospheric wave structure observed at the same time with a Wallops Island 10-cm wavelength radar. The consistency between the two sets of data provides new observational support for a hypothesis of long standing in the microbarograph community; namely, that shear instability in the upper tropospheric flow is indeed the mechanism responsible for the generation of such waves. The comparison presented here suggests that microbarograph arrays might be useful adjuncts to future radar studies of upper tropospheric wave dynamics, supplying such wave parameters as phase velocity and wavelength in favorable cases. A closer examination of the radar data pertinent to this event reveals an apparent vertical wave phase variation, permitting a very approximate and somewhat uncertain estimate of the wave-associated vertical flux of horizontal momentum, which is found to be $\sim$4 dyn cm^{-2}. While approximate, this illustrative calculation yields a value several times greater than the annual average flux at temperate latitudes, and since microbarograph data show such events to be fairly common wintertime phenomena, we are tempted to infer that wave generation by shear instability in the upper tropospheric air flow and the resulting vertical momentum transport may be an important element of the global atmospheric momentum budget. More extensive and conclusive studies are obviously indicated.

1. Introduction

Recently Reed and Hardy (1972; hereafter referred to as RH) published the results of a case study of persistent, intense clear-air turbulence (CAT) in an upper level frontal zone over the eastern seaboard on 18 March 1969. Using data from research and commercial aircraft, a sensitive 10-cm wavelength radar at Wallops Island, Va., and conventional synoptic charts and reports, RH concluded that the CAT and the mesoscale gravity-wave motions they observed were generated by dynamical instability of the shear flow in the baroclinic zone. Because such "jet-stream-associated" gravity waves have been detected for many years using ground-based microbarograph arrays (Kuettner, 1952; Flauraud *et al.*, 1954; Claerbout, 1967; Madden and Claerbout, 1968; Claerbout and Madden, 1968; Herron and Tolstoy, 1969; Herron *et al.*, 1969), the RH study motivated one of us (W. H. H.) to examine microbarograph records for that date obtained by the staff of the Geoacoustics Research Program Area of NOAA's Wave Propagation Laboratory at a Washington, D. C., site roughly 190 km NW of Wallops Island (see Fig. 1).

Here we present these microbarograph observations, which reveal wave-associated pressure fluctuations directly related to the waves observed by RH. We also correct a computational error which led to an incorrect estimate by RH of the wave phase speed at cirrus cloud heights; the revised estimate of the phase speed brings it into essential agreement with those at lower levels. We then note that the Wallops Island radar data reveal an apparent vertical wave phase variation, not discussed by RH, whose sense is consistent with wave generation by shear instability below the cirrus cloud level, and which we use to estimate (very approximately, and with some degree of uncertainty) the wave-associated momentum transport. The argument is similar to that presented by Donn *et al.* (1973) for the same case; their estimate was published when a draft of this manuscript was being revised.

2. The microbarograph observations compared with the radar data

The Washington, D. C., pressure measurements reported here were made using microbarographs located roughly 5–10 km apart at the positions marked by dots in Fig. 1. For a discussion of the equipment and the general type of processing used the reader is

---

[1] Present affiliation: Environmental Research & Technology, Inc., Concord, Mass. 01742.

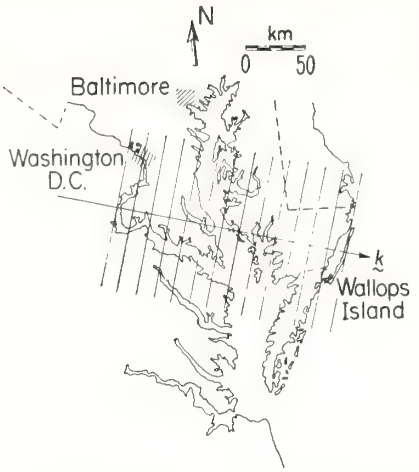

FIG. 1. The experimental geometry in the Del Mar Va peninsula area. Dots indicate the locations of the four microbarographs in the Washington, D. C., microbarograph array. Also indicated are the direction of wave propagation over the observing sites and surfaces of constant wave phase. The wave propagation direction coincides with the wind direction at the height of the wave critical level.

referred to the recent review by Georges and Young (1972) and the references therein.

Fig. 2 shows the four microbarograph records superimposed (after being time-shifted for maximum cross correlation) for the 0100–1600 (all times GMT) interval on 18 March 1969. The sporadic generation of large-amplitude waves having periods of roughly 5 min is quite evident on these records, even though the microbarograph system used was designed for the study of acoustic waves and strongly filtered the low-frequency gravity-wave pressure fluctuations. Of particular interest for present purposes is the wave packet of about five cycles detected just after 0300; this is the event we associate below with the RH data. As Fig. 2 shows, however, there are at least four intervals spaced several hours apart throughout this particular day when wave-associated pressure fluctuations of large amplitude are observed. Table 1 gives the values of the wave parameters deduced from the microbarograph array data (by determining the time shifts of the individual pressure traces required to maximize the cross correlation of the four microbarograph records) for these intervals. It shows that throughout this 15 h period, wave parameters varied relatively little from event to event.

Fig. 3 shows the wave event occurring just after 0300 in somewhat more detail, along with the values for the wave parameters determined from the array data; these are compared with an RHI photo of the wave structure observed by the Wallops Island radar and the wave parameters deduced therefrom by RH. [While this particular RHI photo was not published by RH, it has appeared subsequently in papers by Katz (1972) and Hardy and Reed (1972)]. We see that:

1) There is substantial agreement between the radar and array estimates of the horizontal wavelength λ (15 km, 14 km). This is measured directly by the radar, but with some uncertainty since the azimuth of the radar scan may not coincide exactly with the direction of wave propagation (see below); it is indirectly but rather accurately measured by the microbarograph array, by multiplying the horizontal wave phase velocity computed from the time shifts by the wave period.

2) There is good agreement between the two estimates of the wave period τ (300–340 s, 300 s). This is measured directly by the microbarograph array; it is indirectly measured using the radar by examining time sequences of the RHI photos to determine the wave phase velocity V (see below) and dividing λ by V.

3) There is good agreement between the two estimates of the horizontal wave phase speed V (44–50 m s^{-1}, 47 m s^{-1}). This is measured by the time shifts required to maximize cross correlation of the four microbarograph records; it is estimated from time sequences of the radar photos by following the motion of the wave structure from photo to photo. A comment is in order here. RH reported originally that the radar wave structure in the vertical consisted of two waves, of similar wavelength but having different horizontal wave phase speeds. Specifically, the wave structure at cirrus cloud level was reported to be moving at 67 m s^{-1}, while that revealed by the lower clear-air echoes was reported to be moving at 44 m s^{-1}. We find after reexamining the radar photos and repeating the procedure used to determine the wave phase speed that although the 44 m s^{-1} estimate was essentially correct, there had been a computational error in the original estimate of the wave phase speed at the cirrus cloud level which amounted to a factor of $\frac{4}{3}$. When we divide the original estimate by this factor, we find a phase speed $V \approx 50$ m s^{-1}. This corrected figure, the 44 m s^{-1} estimate made from the wave structure at lower levels, and the 47 m s^{-1} estimate from the microbarograph data agree within the experimental uncertainties in these estimates ($\sim 10\%$). The three estimates are supported as well by an independent estimate of the wave phase speed made using two other (unpublished) radar photos of the same event (which in fact led to the discovery of the original error).

4) There is good agreement between the two estimates of the azimuth A (270°, 284°) from which the wave is coming. The RH estimate is the cruder of the two, since radar elevation scans were made for only a few azimuths; it is probably accurate only to within ±20°. Fortunately, two of the radar scan azimuths (90° and 270°) happened to be very nearly

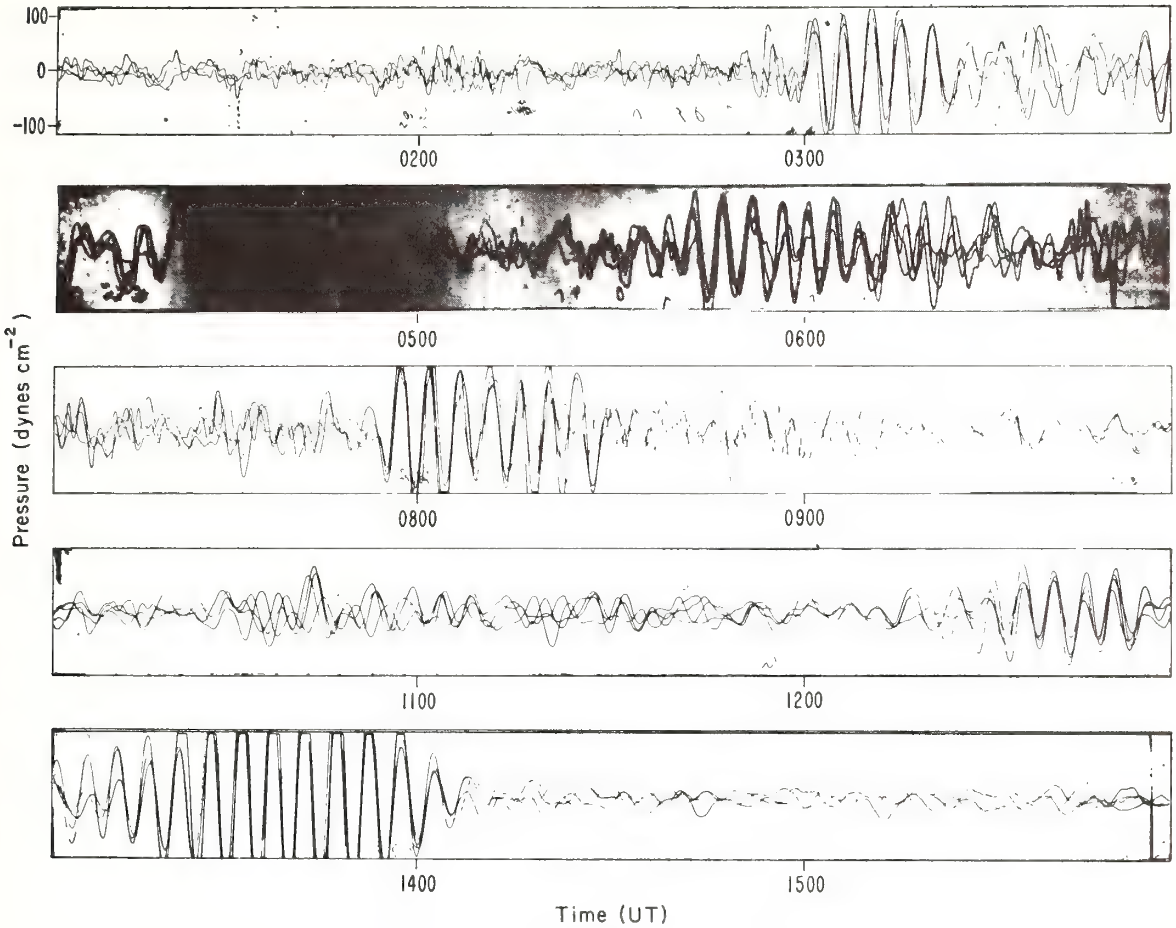

Fig. 2. The four microbarograph records for the 0100–1600 GMT interval on 18 March 1969. The records have been shifted by times of several minutes for maximum cross correlation and superimposed. Note the sporadic wave activity at 5 min and longer periods occurring at about 0300, 0600, 0800 and 1300. Table 1 gives the wave parameters determined from these data. Certain short segments of the microbarograph records at the break points are not shown. The gray pattern in the 0400–0700 interval arises from a photographic difficulty.

in the direction of the upper tropospheric winds and the wave travel.

5) The wave event occurs nearly simultaneously at the two locations. Using the estimated horizontal wave phase speed (47 m s^{-1}) and a propagation azimuth of 284°, we find that the wavefronts simultaneously passing over the two sites (roughly 190 km apart) must differ in phase by about 12 wave cycles, so that the propagation time between the two sites is about 1 h. Hence none of the wavefronts observed by the microbarograph array (which were seen only after 0300) could have passed over Wallops Island before 0400. Thus the very same wavefronts were not observed at both Washington and Wallops Island. It is likely instead that the airflow over the region encompassing the two sites went unstable everywhere with respect to the wave generation nearly simultaneously. The wave train generated might then have been some 10 15 wavelengths long as indicated in Fig. 1. This is not an unreasonably large number of cycles if we can judge from satellite and ground-based photographs of similar wave phenomena in clouds. The momentum transport associated with the wave generation (see below) and the CAT could have subsequently returned the tropospheric shear flow to a stable condition, terminating the event after about half an hour. (It

Table 1. Wave parameters from microbarograph data.

Approximate time (GMT)	λ (km)	V (m s^{-1})	τ (s)	A (deg)
0300	14.1	47	300	284
0600	12.9	49	260	272
0800	10.8	40	270	276
1300	12.6	42	300	272

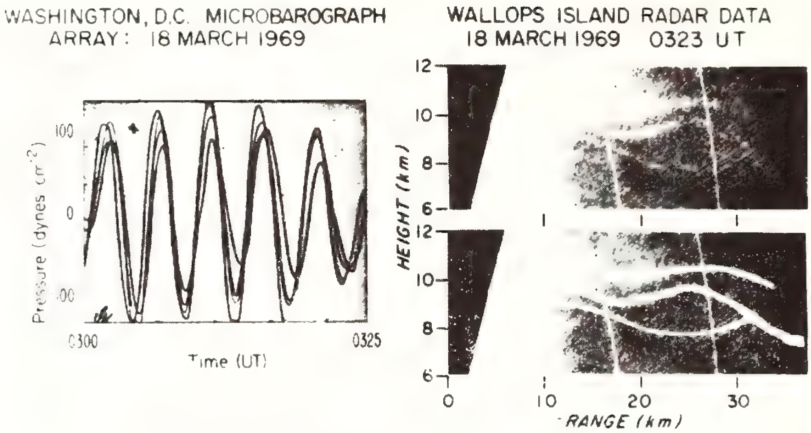

PARAMETER	MICROBAROGRAPH ARRAY DATA	RADAR DATA
λ (km)	14	15
V (m sec^{-1})	47	44 - 50
τ (sec)	300	300 - 340
A (deg)	284	(270)

FIG. 3. A more detailed view of the microbarograph wave event occurring just after 0300, together with the values for the horizontal wavelength λ, horizontal phase speed V, period τ, and azimuth A from which the wave was propagating. These are compared with the waves observed by the 10.7-cm wavelength radar at Wallops Island shown in the portion of an RHI photo taken along an azimuth of 270°. (The bottom radar photo has been retouched from the original.) The radar-derived wave parameters given in the table were determined from this and other RHI photos. Several independent estimates of the wave phase velocity between heights of 8 and 10 km yield values ranging between 44 and 50 m s^{-1}. The wave period given here was calculated from the corrected RH estimates of λ and V. (See the discussion in the text.)

is of interest to note that the event at Washington occurred between 0300 and 0325, at Wallops between 0317 and 0350. We can thus conclude that either the "velocity of propagation of the disturbed region" is in the direction of the background wind, in which case it must exceed 140 m s^{-1} which in turn exceeds the maximum wind speeds by 50 m s^{-1} or so, or it must be in a direction quite different from that of the background wind. It must, therefore, be of the nature of a phase rather than a material velocity.)

6) There appears to be some degree of consistency between the wave amplitude observed at the height of the radar echo strata and the amplitude observed at ground level. A definitive comparison would require a full-wave calculation using accurately known background (or unperturbed, or mean) temperature and wind profiles, using, for example, methods analogous to those developed by Vergeiner (1971); however, the radiosonde data available do not provide such profiles for the actual time of the radar and microbarograph observations, nor do they permit separation of the background wind and temperature profiles from the instantaneous wave-induced perturbations of these profiles. For these reasons, and because our requirements are not very demanding, we have contented ourselves with two very approximate comparisons using the approaches suggested by Tolstoy and Herron (1969) and Gossard and Sweezy (1974). Neither of these approaches is free from difficulties.

Following Tolstoy and Herron, we note that the lowermost of the three radar traces appears to be centered at a height of 8.3 km. From Fig. 4, which is a composite of wind and temperature profiles taken hours before and after this event, we find that the background wind speed at this height is 39 m s^{-1} (although see the qualifying remarks below). Now the "intrinsic" frequency Ω of the wave, i.e., the wave frequency measured by an observer moving with the background wind, is defined by

$$\Omega(z)=\omega-kU(z)=[V-U(z)]k, \qquad (1)$$

where $\omega=2\pi/\tau$ is the angular wave frequency as measured by a stationary observer on the ground, $k\equiv2\pi/\lambda$ is the horizontal wavenumber, and U is the background wind speed (we use the scalar formulation here rather than the vector because in this example the direction of wave propagation essentially coincides with that of the wind, and because the changes in the wind direction with height are negligible). Thus, taking $V=47$ m s^{-1} and $\lambda=15$ km, we find Ω (8.3 km) $=3.4\times10^{-3}$ s^{-1}. This corresponds to an intrinsic wave period of ~31 min. The wave-associated vertical parcel velocity amplitude w is related to the amplitude ζ of the wave-associated vertical displacement by

$$w=\zeta\Omega; \tag{2}$$

taking $\zeta=680$ m from the radar photo, we find $w=2.3$ m s^{-1}. To proceed further, we assume that the wave propagation can be described approximately using a WKB treatment; for small-scale plane waves propagating in an isothermal or slowly-varying atmosphere, the amplitude u of the wave-associated horizontal parcel velocity fluctuations is given in terms of w by (e.g., Hines, 1970)

$$u=\left|\frac{n}{k}\right|w, \tag{3}$$

where n is the vertical wavenumber, given to the same approximation by (e.g., Gossard and Munk, 1954; Hines, 1960)

$$n=k[(N/\Omega)^2-1]^{\frac{1}{2}}, \tag{4}$$

where N is the Brunt-Väisälä frequency $\{\equiv[(g/\theta)d\theta/dz]^{\frac{1}{2}}$, where θ is the potential temperature and g the acceleration of gravity$\}$; these last two equations are valid only for waves of vertical wavelength or skin depth small compared to the atmospheric scale height or the scale of wave refractive index variations. From data in Fig. 4 we find $N=1.2\times10^{-2}$ s^{-1} at 8.3 km; thus we find $|n/k|=3.4$ at a height of 8.3 km, giving $u(8.3 \text{ km})=7.8$ m s^{-1}. The order of magnitude of the amplitude p_s' of the wave-associated surface pressure fluctuations in terms of u (8.3 km) is then (Tolstoy and Herron, 1969)

$$p_s'=\left(\rho_0\rho_s V\left|\frac{n_s}{n}\right|u\right)^{\frac{1}{2}}\left|\exp\left[-i\int_0^{8.3 \text{ km}} n(z)dz\right]\right|, \tag{5}$$

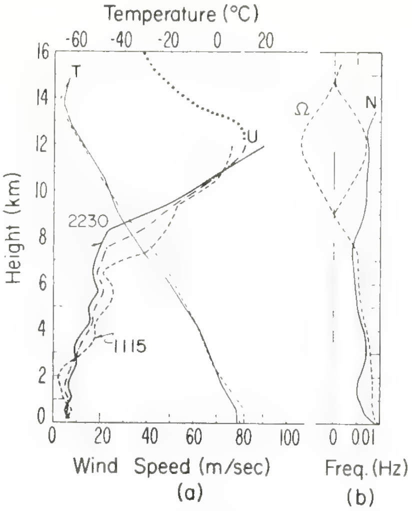

Fig. 4a. Wind and temperature profiles at Wallops Island at 2230 GMT 17 March 1969 (solid curves) and 1115 GMT 18 March 1969 (dashed curves). The broken curve is the wind profile for 0300 GMT 18 March, obtained by linear interpolation; it is this profile that is used in the calculations. It should be clear that the uncertainties introduced by this procedure are considerable, particularly in the shear region of interest. The temperature profiles were sufficiently similar so that no interpolation was deemed necessary. Wallops Island wind data were unavailable for heights greater than 12 km; the Washington, D. C., wind data for the same time interval were used to estimate the wind profile at higher levels, indicated by the dotted portion of the wind profile.

Fig. 4b. The intrinsic wave frequency Ω, its absolute value, and the Brunt-Väisälä frequency N averaged over 1 km height intervals. Note that $|\Omega|<N$ at all heights above 8 km.

where ρ_0 and ρ_s are the background atmospheric densities at 8.3 km and at the surface, respectively, and n and n_s are the corresponding vertical wavenumbers. We find from the data in Fig. 4 that n is imaginary for heights $z\lesssim8$ km, with an average magnitude between the surface and 5 km of $\sim2.4\times10^{-4}$ m^{-1}. Thus the wave is not freely propagating in the vertical through this region; rather it is evanescent, with the exponential factor in (5) implying an amplitude decreasing with decreasing height. Using $\rho_s=1.3\times10^{-3}$ g cm^{-3} and $\rho=4.7\times10^{-4}$ g cm^{-3}, Eq. (5) gives $p_s'=144$ dyn cm^{-2}, which compares quite favorably with the observed value of perhaps 100–120 dyn cm^{-2}. However, this apparent good agreement is misleading for a number of reasons. Most obviously, the estimate of the average height of the radar echo stratum and the estimate of the background wind at that height are subject to considerable uncertainty, implying a corresponding uncertainty in the computed values of Ω, n/k and u, which are quite sensitive to the values chosen for the measured parameters. More fundamentally, however, the WKB approximation made here should itself break down, because (i) the properties of the background medium in the 8 km region vary significantly over vertical distances of less than one wavelength, (ii) the Richardson number in this region is small, (iii) there is a turning point, i.e., a height for which $n(z)=0$ in this region, and (iv) because the estimate fails to include the effect of wave reflection at the earth's surface. The last of these effects is allowed for in the analysis by Gossard and Sweezy (1974), who find that (changing notation slightly)

$$p_s=\left(\frac{\bar{\Omega}}{k}\right)(\rho_s\rho_0)^{\frac{1}{2}}\frac{i\bar{n}}{\sinh i\bar{n}h}\zeta h,$$

where the overbar refers to an average value over the height interval h in question, which in this case is from the surface to 8.3 km. Taking $\bar{\Omega}/k=32$ m s^{-1} and $i\bar{n}=2.4\times10^{-4}$ m^{-1}, we obtain $p'_s=40$ dyn cm^{-2}.

The good agreement between the microbarograph records and the Reed and Hardy data in the six respects discussed above leaves little room for doubt that the Washington, D. C., microbarograph array and the Wallops Island radar sensed the same wave train. Because RH were able to establish shear instability in the jet-stream airflow as the generating mechanism, the close association between the two sets of records supports earlier evidence put forth by Claerbout (1967) and Madden and Claerbout (1968) suggesting this origin for the jet-stream-associated waves observed using microbarographs.

The usefulness of microbarographs in studies of gravity-wave motions in the planetary boundary layer has been well established (Gossard and Munk, 1954; Gossard *et al.*, 1970, 1971; Hooke *et al.*, 1972, 1973); the present results suggest that microbarograph arrays may be useful adjuncts in radar and aircraft studies of mesoscale gravity waves and CAT in the upper troposphere as well. As Eqs. (4) and (5) imply, the arrays are best suited for the study of the larger-scale wave motions at these altitudes (wavelengths comparable to the height or greater), since the ambient tropospheric wind shears tend to make the smaller-scale waves evanescent outside a very narrow height range, greatly reducing the wave amplitude at the earth's surface. Nevertheless, the evidence suggests that these large-scale motions often coexist with the smaller-scale turbulence that represents a direct inconvenience and hazard to aircraft.

Indeed, Hodge and Volz (1968) have suggested that microbarograph arrays might be used to detect CAT and have supplied some data to support this contention. Future joint radar, aircraft and microbarograph studies could confirm or deny this possibility. In addition, it appears that microbarograph arrays could be used to indicate in real time the presence of wave motions of interest that might be detectable by radar as well as the wave propagation direction or optimum radar scan azimuth. In the absence of such information, radar operators must scan in a variety of azimuths to search for the wave structure or identify the azimuth of wave propagation; this is a rather time-consuming process.

3. Reexamination of the radar data: An estimate of the wave-associated momentum flux

While there are a number of echo strata revealed by the RHI photo of Fig. 3, only three are useful for analysis of the wave propagation. Two features of these three radar echo strata are striking. The first is that the lowermost of the three traces can apparently be interpreted most naturally as forming a partial "cat's eye" pattern with the intermediate trace: such patterns are characteristically found at wave critical levels z_c. Taking $V=47\pm5$ m s^{-1} and remembering the uncertainties in the linearly interpolated wind profile of Fig. 4 we find that there is fair consistency on this point.

The second is that the upper two strata appear to exhibit a small vertical phase variation, amounting to some 60° or 1 rad in a height inverval of 1.4 km. (We can gain some confidence in the existence of this vertical phase variation when we examine Fig. 3 of RH, which shows that it appears consistently from cycle to cycle in a drawing made at a time when its significance was not realized.) This would imply, then, an average "vertical wavelength" at this height $\lambda_z=8.4$ km. The term is put in quotes here because it is large compared to the scale of the wind speed gradient, which from (1) and (4) implies corresponding large variations in the true vertical wavelength in this 2 km interval. It follows, of course, that WKB concepts do not strictly apply, as indicated earlier, but if we proceed anyway to use these equations to estimate the vertical wavelength expected theoretically, we find, taking $\bar{U}=60$ m s^{-1} as the average background wind speed in this height interval, that $\lambda_z=12$ km. The discrepancy here seems reasonably small. [We note parenthetically that our estimate of the vertical wavelength is just greater than half the value given by Donn *et al.* (1973), who found λ_z 15 km; while we had the original data at our disposal and have some confidence in our value, this difference should serve to indicate the uncertainties involved.]

The associated vertical phase propagation is upward as seen by an observer fixed on the ground. That is, if we define a coordinate system so that ω and ω/k are positive, and z is positive upward, then ω/n is positive as well. At heights above z_c, $V<U$, so that Ω is negative and Ω/n is also negative. Thus, as seen by an observer moving with the background wind speed at cirrus cloud level, the vertical wave phase velocity is downward, implying that the height of wave generation must be below the height of the upper two radar traces (see, e.g., Eckart, 1960; Hines, 1960; Hines and Reddy, 1967). This constitutes additional support for the RH contention that the wave studied here was generated by shear instability in the tropospheric airflow at a height of roughly 9 km, i.e., below the cirrus cloud level.

Now the vertical wave phase variation also implies that the wave motion is not purely evanescent or trapped; instead it is at least to some extent freely propagating in the vertical direction, and must therefore produce a corresponding vertical flux of horizontal momentum (Hines, 1970). This is consistent with the profiles of N and Ω shown in Fig. 4, where we see that although Ω approaches N in this region, it never quite exceeds it. Thus, according to the WKB approximation the wave energy will propagate upward

Table 2. Velocity amplitudes for the upper two radar traces of Fig. 3.

z (km)	U (m s^{-1})	Ω (s^{-1})	ζ (m)	w (m s^{-1})	n/k	u (m s^{-1})	M (dyn cm^{-2})
10.7	70	-9.6×10^{-3}	200	1.9	1.1	2.1	-7
9.3	51	-1.7×10^{-3}	310	0.5	8.2	4.1	-4
8.3	39	3.4×10^{-3}	680	2.3	3.4	7.8	

past the wind maximum. Note that the wave must apparently encounter another critical level at a height of between 15 and 16 km, where its energy and momentum are presumably returned to the mean flow (Booker and Bretherton, 1967). It is very easy to estimate the magnitude M of this flux if we assume that the wave is entirely freely propagating, i.e., there is no partial reflection or imperfect wave ducting. In this case it will be given by

$$M=\tfrac{1}{2}\rho uw. \tag{6}$$

Calculating the velocity amplitudes u and w for the upper two radar traces in the same manner as we did for the lowermost trace (see Table 2), we find M (10.7 km) = 7 dyn cm^{-2} and M (9.3 km) = 4 dyn cm^{-2}. [Again, to appreciate the large uncertainties in these estimates, the reader should compare them with the estimate of Donn *et al.* (1973), who found $M=1.6$ dyn cm^{-2}. They did, however, use the incorrect RH value of the horizontal wave phase speed.] These will be downward fluxes of positive horizontal momentum if we use the coordinate system defined above. The magnitude of these fluxes is obviously rather large, being several times the annual average of the downward flux of momentum at temperature latitudes. which amounts to some 1 dyn cm^{-2} [see, e.g., Palmén and Newton (1969) and the references therein].

Before considering this point, however, we must emphasize that if the wave in question were indeed freely propagating between 9.3 and 10.7 km as hypothesized, and not interacting with the medium between these two heights in any way, then M should have a constant value, which it apparently does not. It is tempting to dismiss this discrepancy as experimental error, since by changing U (9.3 km) by small amounts we can eliminate the discrepancy entirely, and since the uncertainties in $U(z)$ are considerable. But we can also increase the apparent discrepancy by similar means, and in any event we know that the inhomogeneities in the medium will induce partial reflections and interactions.

In any event, the large value of the flux estimated in this case is not out of line with more direct measurements of the wave-associated momentum flux produced during several similar wave-generation events in the planetary boundary layer [Hines, 1970 (2 dyn cm^{-2}); Hooke *et al.*, 1972, 1973 (5 dyn cm^{-2}); Beran *et al.*, 1973 (1 dyn cm^{-2})]. All these fluxes are comparable to the lee-wave momentum fluxes (7 dyn cm^{-2}) measured by Lilly (1971), whose divergence has been suggested to be of some importance in limiting the intensity of jet-stream winds (Lilly, 1972). In view of the microbarograph observations that show jet-stream-associated atmospheric waves to be a fairly common wintertime occurrence over regions of broad longitudinal extent (see the references cited at the beginning of this paper), we are tempted to infer that wave generation by shear instability may be as important as lee wave generation in producing the vertical transport of momentum at temperate latitudes required for global atmospheric momentum balance. Indeed, this was the explanation put forth by Helmholtz (1888) nearly a century ago to account for the absence of excessively high winds at temperate latitudes [the instability that bears his name; see also Lorenz (1967), who puts this work in context]. We feel it important to attempt to confirm or deny this inference through more careful and extensive observational studies of the type only illustrated above. These would require more timely measurements of the background temperature and wind profiles and direct measurement of the wave-associated velocity perturbations. In addition, statistical studies should be made to determine the occurrence frequency of such events, and the nature of the wave-associated momentum transport both in individual cases and on the average.

The wave-associated vertical energy flux in the 10 km region for this event may also be calculated. It is (e.g., Hines and Reddy, 1967; Hines, 1970)

$$\tfrac{1}{2}pw=\tfrac{1}{2}\rho_0(V-U)uw\approx 8000 \text{ ergs cm}^{-2}\text{ s},$$

again a very large value.

Acknowledgments. We wish to thank Dr. David Atlas of NCAR and Dr. Richard J. Reed of the University of Washington for helpful comments on the draft form of the paper.

Mr. G. E. Greene of NOAA's Propagation Laboratory recovered and analyzed the microbarograph data. Certain aspects of the research were carried out by W.H.H. at the Cooperative Institute for Research in the Environmental Sciences (CIRES), an institute run jointly by the University of Colorado and NOAA, and were supported in part by the National Science Foundation, under Grant GA-32604. The research conducted using the Wallops Island radar facility has

been supported in part by the National Aeronautics and Space Administration.

REFERENCES

Beran, D. W., W. H. Hooke and S. F. Clifford, 1973: Acoustic echo-sounding techniques and their application to gravity-wave, turbulence, and stability studies. *Bound. Layer Meteor.*, **4**, 133–153.

Booker, J. R., and F. P. Bretherton, 1967: The critical layer for internal gravity waves in a shear flow. *J. Fluid Mech.*, **27**, 513–539.

Claerbout, J. F., 1967: Electromagnetic effects of atmospheric gravity waves. Ph.D. thesis, Massachusetts Institute of Technology.

——, and T. R. Madden, 1968: Electromagnetic effects of atmospheric gravity waves. *Proc. Acoustic-Gravity-Wave Symp.*, T. M. Georges, Ed., U. S. Govt. Printing Office, 135–155.

Donn, W. L., S. D. Gedzelman and N. K. Balachandran, 1973: Atmospheric waves and the energy of the jet stream. *Bull. Amer. Meteor. Soc.*, **54**, 633–636.

Eckart, C. H., 1960: *Hydrodynamics of Oceans and Atmospheres*. Pergamon, 290 pp.

Flauraud, E. A., A. H. Mears, F. A. Crowley, Jr., and A. P. Crary, 1954: Investigation of microbarometric oscillations in eastern Massachusetts. AFCRC Tech. Rept. 54-11.

Georges, T. M., and J. M. Young, 1972: Passive sensing of natural acoustic-gravity waves at the earth's surface. *Proc. Remote Sensing of the Troposphere*, V. E. Derr, Ed., U. S. Govt. Printing Office, Chap. 21.

Gossard, E. E., and W. H. Munk, 1954: On gravity waves in the atmosphere. *J. Meteor.*, **11**, 259–269.

——, J. H. Richter and D. Atlas, 1970: Internal waves in the atmosphere from high-resolution radar measurements. *J. Geophys. Res.*, **75**, 3523–3536.

——, D. R. Jensen and J. H. Richter, 1971: An analytical study of tropospheric structure as seen by high-resolution radar. *J. Atmos. Sci.*, **28**, 794–807.

——, and W. B. Sweezy, 1974: Spectra of waves the in atmosphere. *J. Atmos. Sci.*, **31**, 1540–1548.

Hardy, K. R., and R. J. Reed, 1972: Wave patterns and clear air turbulence. *Preprints 15th Radar Meteor. Conf.*, Champaign-Urbana, Amer. Meteor. Soc., 262–267.

Helmholtz, H., 1888: Uber atmospharische Bewegwigen. *Sitz.- Ber. Akad. Wiss. Berlin*, 647–663. English translation: Abbe, C., The mechanics of the earth's atmosphere. Washington, D. C., The Smithsonian Institution, 58–66 (1893).

Herron, T. J., and I. Tolstoy, 1969: Tracking jet stream winds from ground level pressure signals. *J. Atmos. Sci.*, **26**, 266–269.

——, —— and D. W. Kraft, 1969: Atmospheric pressure background fluctuations in the mesoscale range. *J. Geophys. Res.*, **74**, 1321–1329.

Hines, C. O., 1960: Internal atmospheric gravity waves at ionospheric heights. *Can. J. Phys.*, **38**, 1441–1481.

——, 1970: Comments "Internal waves in the atmosphere from high resolution radar measurements." *J. Geophys. Res.*, **75**, 5956–5959.

——, and C. A. Reddy, 1967: On the propagation of atmospheric gravity waves through regions of wind shear. *J. Geophys. Res.*, **72**, 1015–1034.

Hodge, M. W., and D. T. Volz, 1968: Possible relations of mesoscale surface pressure waves to the jet stream region and to clear air turbulence. *Preprints Third Natl. Conf. Aerospace Meteor.*, New Orleans, Amer. Meteor. Soc., 557–564.

Hooke, W. H., J. M. Young and D. W. Beran, 1972: Atmospheric waves observed in the planetary boundary layer using an acoustic sounder and a microbarograph array. *Bound. Layer Meteor.*, **2**, 371–380.

——, F. F. Hall, Jr., and E. E. Gossard, 1973: Observed generation of an atmospheric gravity wave by shear instability in the mean flow of the planetary boundary layer. *Bound. Layer Meteor.*, **5**, 29–41.

Katz, I., 1972: The detection and study of gravity waves with microwave radar. *Proc. AGARD Conf., Effects of Atmospheric Acoustic Gravity Waves on Electromagnetic Wave Propagation*, Wiesbaden, Chap. 21.

Kuettner, J., 1952: On the possibility of soaring on traveling waves in the jet stream. *Aeronaut. Eng. Rev.*, **11**, No. 12, 1–7.

Lilly, D. K., 1971: Observations of mountain-induced turbulence. *J. Geophys. Res.*, **76**, 6585–6588.

——, 1972: Wave momentum flux—a GARP problem. *Bull. Amer. Meteor. Soc.*, **53**, 17–23.

Lorenz, E. N., 1967: *The Nature and Theory of the General Circulation of the Atmosphere*. World Meteorological Organization, Geneva.

Madden, T. R., and J. F. Claerbout, 1968: Jet-stream-associated gravity waves and implications concerning jet stream stability. *Proc. Acoustic-Gravity-Wave Symp.*, T. M. Georges, Ed., U. S. Govt. Printing Office, 121–134.

Palmén, E., and C. W. Newton, 1969: *Atmospheric Circulation Systems*. Academic Press, 603 pp.

Reed, R. J., and K. R. Hardy, 1972: A case study of persistent, intense, clear air turbulence in an upper level frontal zone. *J. Appl. Meteor.*, **11**, 541–549.

Tolstoy, I., and T. J. Herron, 1969: A model for atmospheric pressure fluctuations in the mesoscale range. *J. Atmos. Sci.*, **26**, 270–273.

Vergeiner, I., 1971: An operational linear lee wave model for arbitrary basic flow and two-dimensional topography. *Quart. J. Roy. Meteor. Soc.*, **97**, 30–60.

Waves Observed in the Planetary Boundary Layer using an Array of Acoustic Sounders

A. G. KJELAAS,[1] D. W. BERAN,[2] W. H. HOOKE[2] AND B. R. BEAN[3]

(Manuscript received 27 December 1973, in revised form 3 June 1974)

ABSTRACT

Three acoustic sounders, with antennas having vertically-pointed beams located at the vertices of a triangle about 300 m on a side, have been used successfully to calculate horizontal phase velocities of gravity waves in the lowest 1000 m of the atmosphere. The wave parameters obtained were compared with those obtained by an array of microbarographs. The results from the two independent techniques agreed well in all cases where the waves were detected by both methods. However, the acoustic-sounder array was also able to detect gravity waves propagating in an inversion overlying the convective boundary layer that were undetected by the microbarograph array because of wave attenuation in the convective region.

Wave-associated vertical-velocity fluctuations inside the undulating structure were measured using Doppler techniques to an accuracy of about ± 0.1 m sec^{-1}. Vertical-velocity fluctuations of about ± 0.5 m sec^{-1} were measured inside one wave with displacement amplitude of 120 m and wavelength of 5.5 km. From wave-associated vertical-velocity fluctuations, displacement amplitude and wave period, we could calculate the wind speed component along the wave propagation direction. This calculated wind speed component agreed reasonably well with the value derived independently from radiosonde measurements.

1. Introduction

During the summer of 1972, the staff of NOAA's Wave Propagation Laboratory (WPL) mounted an experimental program at the Haswell field site in Colorado lasting several weeks. During the observing period, this area was characterized by a typical High Plains meteorological regime: strong radiative cooling at night and strong heating and convective activity during the day. The program had the dual objectives of (i) checking the operation of a variety of remote sensing systems and calibrating them against data gathered from a 150 m instrumented meteorological tower, and (ii) studying the Haswell atmospheric boundary layer.

Included among the remote-sensing systems and meteorological instruments were three acoustic echo sounders and an array of microbarographs. The acoustic echo sounders operate like sonars: they transmit acoustic pulses and detect the echoes resulting from boundary-layer turbulent wind and temperature fluctuations (Tatarski, 1961; Monin, 1962). In this way, these sounders can measure boundary-layer turbulence intensity (e.g., Little, 1969; Bean, 1971; Emmanuel *et al.*, 1972; Beran *et al.*, 1973; McAllister, 1968) as a function of height and time, as well as the three components of the boundary-layer wind, which can be determined from the Doppler shift of the acoustic echoes when two of the three antenna beams are directed at angles off the vertical (Beran *et al.*, 1971, 1973; Beran and Clifford, 1972). The microbarographs supported the remote-sensing studies of boundary-layer gravity waves, by measuring wave-associated pressure fluctuations at the earth's surface. From these records we determined wave parameters such as wave period, horizontal wavelength, phase velocity and azimuth of propagation [for illustrations of previous studies see, e.g., Hooke *et al.* (1972) and Beran *et al.* (1973)].

During most of the observing period, the acoustic echo sounder data were gathered primarily to evaluate the relative merits of various antenna configurations in Doppler wind measurements. However, we were also interested to see whether we could operate the sounders in a mode analogous to that of the microbarograph array in order to study boundary-layer wave motions. To test this possibility, we operated the sounders for short intervals several hundred meters apart with all beams directed vertically. Then to determine horizontal wavelengths, wave phase speeds and propagation directions, we used the cross correlation between corresponding features of the acoustic echo returns recorded by the three sounders (i.e., the cross correlation between the height-time echo intensity patterns), and the time lags required to maximize this cross correlation. These values were compared

---

[1] Norwegian Defence Research Establishment, Kjeller, Norway.

[2] Wave Propagation Laboratory, NOAA Environmental Research Laboratories, Boulder, Colo.

[3] Office of Weather Modification, NOAA Environmental Research Laboratories, Boulder, Colo.

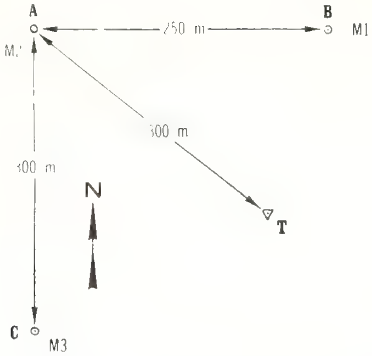

FIG. 1. The layout of the experimental configuration. Points marked A, B, C show the positions of the three acoustic echo sounders, and M1, M2, M3 the microbarographs.

with those obtained from the microbarograph cross-correlation analysis as well as with those obtained by using the so-called impedance relation (Gossard and Munk, 1954), which gives the wave phase speed and direction from an analysis of the wave-associated pressure and velocity fluctuations measured at a single point.

In this paper, we summarize the results of using an array of three vertically-pointing acoustic echo sounders in calculating the phase velocity, period, and hence the horizontal wavelength of gravity waves. The results illustrate the advantages and limitations of this application of acoustic echo sounding. In addition, we show that from sounder measurements of 1) wave period, 2) wave-associated vertical-velocity perturbations (as revealed by Doppler shifts of the acoustic echo returns), 3) vertical parcel-displacement perturbations (as revealed by fluctuations in height of the strata of strong echo returns), and 4) horizontal wavelength (calculated from measurements of wave period and phase velocity), we can determine the mean wind speed component in the direction of wave propagation. We can therefore check the data still further for consistency by comparing the value of the mean wind speed calculated in this manner with that measured directly from a radiosonde and on the tower. Thus, we have demonstrated in principle that acoustic echo sounders can use boundary-layer gravity waves as tracers in wind profiling.

2. The experiment

The experimental configuration is shown in Fig. 1. The points marked A, B, and C are the positions of the three acoustic echo sounders, which form a right triangle with legs roughly 300 m in length. The points marked M1, M2, and M3 denote the positions of the three microbarographs and T the location of the 150 m meteorological tower. This size and configuration was adequate for the gravity-wave studies here; however, to study larger-scale waves with higher phase velocities, we would have needed a larger triangle.

The three sounders (A, B, C) were operated at center frequencies of 2750, 1750 and 2250 Hz, respectively, in order to avoid cross talk. The other sounder parameters are given in Table 1. Both the intensity of the backscattered energy and the Doppler frequency shift for each sounder were recorded on analog tapes and digitized at a sampling rate of 62.5 sec^{-1}. In addition, facsimile recordings were made of the acoustic echo returns as functions of boundary-layer height and time. The tower was instrumented to measure wind and temperature at 30, 60, 90, 120 and 150 m; and to measure wave-associated pressure fluctuations at 90 and 150 m. Radiosonde wind and temperature profiles were also obtained.

3. Theory of wind speed determination from gravity-wave observations

For any fluid motion the vertical parcel velocity w is instantaneously related to the vertical parcel displacement ζ by

$$w=\frac{D\zeta}{Dt}, \tag{1}$$

where D/Dt denotes the time derivative following the parcel motion. That is,

$$\frac{D}{Dt}\equiv\frac{\partial}{\partial t}+\mathbf{u}\cdot\nabla, \tag{2}$$

so that for a sinusoidal wave of frequency ω (as measured by an observer fixed with respect to the ground) and wave vector $\mathbf{k}$, and of perturbation amplitude

$$\frac{D}{Dt}=\omega-\mathbf{k}\cdot\mathbf{U}_0\equiv\Omega. \tag{3}$$

The frequency Ω is the so-called "intrinsic" wave frequency, i.e., the wave frequency that would be measured by an observer moving, relative to the ground, with the background wind velocity $\mathbf{U}_0$. In general, $\mathbf{U}_0=\mathbf{U}_0(z)$ and $\Omega=\Omega(z)$, where z is the height. Thus, at any height z, we have the relation

$$w^*(z)=\Omega(z)\zeta^*(z), \tag{4}$$

TABLE 1. Acoustic echo sounder parameters.

Peak power	10 W (acoustic)
Pulse width	100 msec
Pulse repetition frequency	0.125 Hz
Maximum range	1360 m
Carrier frequency	variable from 1750–2750 Hz
Antenna diameter	152 cm
Antenna beamwidth	±5° to 3-dB points
Beam direction	vertical
Receiver bandwidth	100 Hz

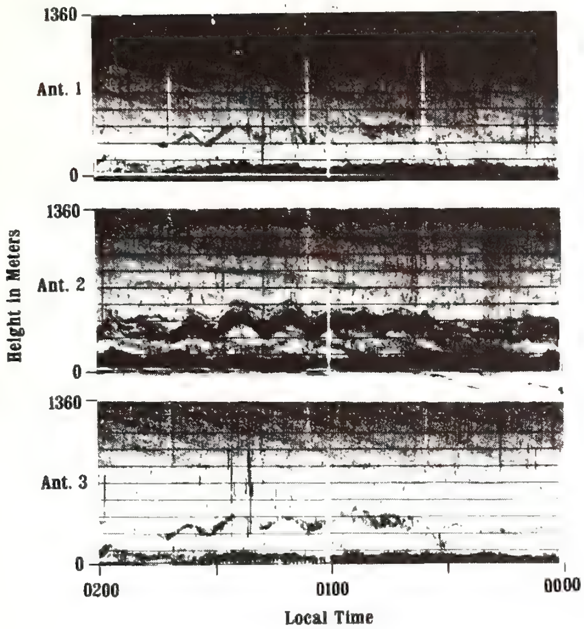

FIG. 2. Facsimile records from each of the sounders for 0000–0200 LT 8 August 1972: Case I.

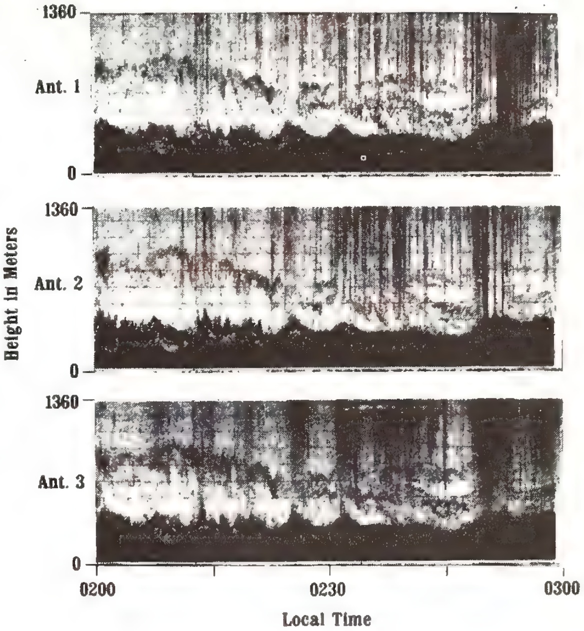

FIG. 3. Facsimile records from each of the sounders for 0200–0300 LT 23 July 1972: Case II.

where the asterisks denote *amplitudes* of the wave-associated fluctuations. We have then that

$$U_{0k}(z)=\frac{\omega}{k}-\frac{w^*(z)}{k\zeta^*(z)},$$

$$=\frac{\omega}{k}\left(1-\frac{w^*}{\omega\zeta^*}\right), \tag{5}$$

where $U_{0k}\equiv(\mathbf{k}\cdot\mathbf{U}_0)/k$. This value of U_{0k} can then be compared with the one obtained from radiosonde.

4. Analysis

Three periods [0100–0140 LT 8 August 1972 (Case I); 0215–0235 LT 23 July 1972 (Case II); 0820–0850 LT 23 July 1972 (Case III)] were selected for detailed analysis. The facsimile records from each of the three sounders for each of the three cases are shown in Figs. 2–4. To determine the horizontal wave phase speed and direction of propagation of the waves revealed by the undulating strata of strong echo returns shown in Figs. 2–4, a simple time-lagged cross-correlation analysis between the intensity patterns of the strong echo return above the nocturnal inversion for the three sounders was performed. In general, the peak in the cross correlations does not occur at zero time lag, but is shifted in time. These shifts correspond to the travel time of a wave from one sounder to another. From this travel time both phase speed and direction of propagation can be derived (Briggs *et al.*, 1950).

The accuracy in the derived phase velocity depends on the accuracy with which the different travel times can be estimated. Since the pulse repetition frequency,

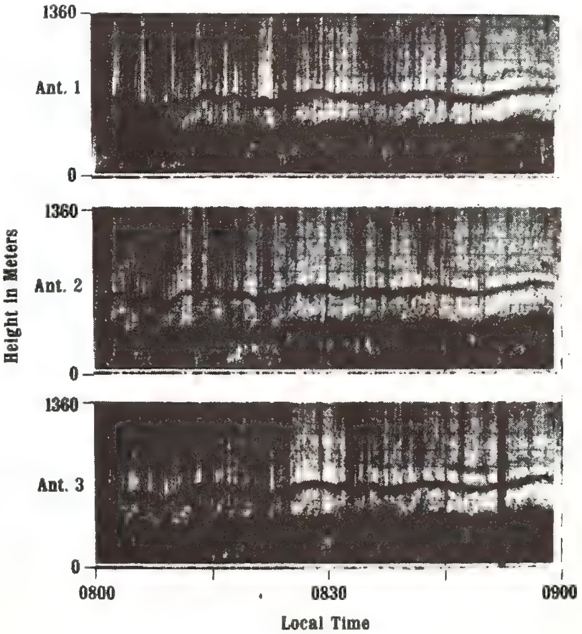

FIG. 4. Facsimile records from each of the sounders for 0800–0900 LT 23 July 1972: Case III.

which can be interpreted as the sampling frequency, is 0.125 Hz in our case, the position in time of the peak of the cross correlation cannot be estimated more accurately than ±4 sec. This should give an accuracy in the calculated phase speed of the order of ±1 m sec^{-1} and approximately ±10° on direction for a wave travelling with a speed of 10 m sec^{-1} over the array. An increase in phase speed will increase the estimated errors. For Case I, Doppler data were used to estimate the wave-associated vertical-velocity fluctuations. For this purpose the echo returns from five vertical height intervals totalling about 11 m were time-averaged over 10 consecutive pulses (80 sec). The vertical velocity resolution, assuming that the signal must be observed for 0.0588 sec and that one-quarter of the period is needed to track the Doppler, was found to be ±0.1 m sec^{-1}.

a. Case I

In Case I (Fig. 2) we have an apparently stable undulating stratum of strong echo returns well separated from the nocturnal surface boundary-layer inversion below. The wave motion appears to be nearly sinusoidal, and the wave parameters for this time interval calculated from both the acoustic-echo-sounder array data and the microbarograph array data are shown in Table 2. Table 2 also gives the horizontal wave phase speed ω/k and propagation direction computed from tower data on the amplitude of the wave-associated pressure fluctuations p' and horizontal velocity fluctuations $\mathbf{u}'$ (where prime denotes the wave-associated departure from the background value k), using the "impedance relation" (Gossard and Munk, 1954)

$$\frac{\omega}{k}=\frac{p'(z)}{\rho_0(z)u'(z)}-U_{0k}(z). \tag{6}$$

No significant differences appear between the results obtained from the microbarograph array and the acoustic echo sounder array as far as wave period and horizontal phase speed are concerned; both give a period of about 715 sec and a phase speed of about 8 m sec^{-1}. The difference in the observed direction of arrival is larger, about 25°; however, because the wavelength is an order of magnitude greater than the dimensions of the array, the direction determined is subject to uncertainties larger than ±10°.

TABLE 2. Wave parameters for the events of Case I.

Wave parameters	Acoustic sounder array	Microbarograph array	Impedance relation
Period	715 sec	717 sec	
Horizontal phase speed	7.5 m sec^{-1}	8.0 m sec^{-1}	7.7 m sec^{-1}
Horizontal wavelength	5.4 km	5.7 km	
Direction of arrival	245°	220°	
Average height of the wave	400 m		
Amplitude of the wave	120 m		

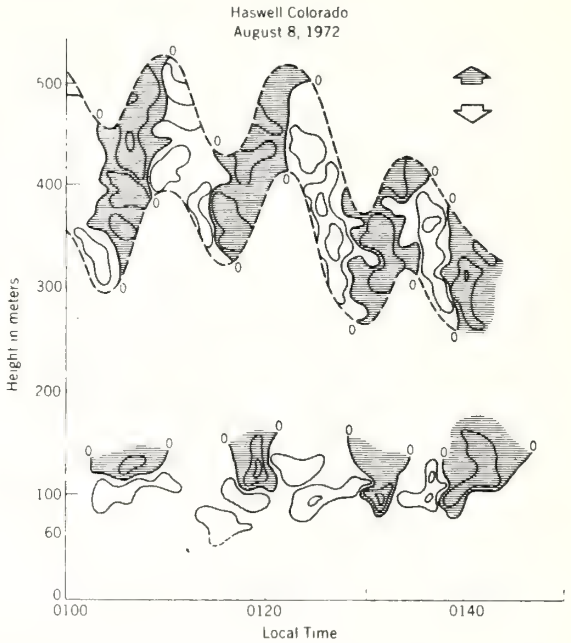

FIG. 5. Doppler-derived vertical velocities for the case shown in Fig. 2. The darker cross-hatched portions indicate upward vertical velocity, while lighter stippled portions correspond to areas with downward vertical velocity. The heavy line is the zero vertical velocity contour; the ±0.1 and ±0.3 m sec^{-1} contours are also shown. The dotted lines are the boundaries of the stratum of strong echo return.

The Doppler-derived vertical velocities for Case I are shown in Fig. 5. The hatched portions indicate height-time intervals of positive (i.e., upward) vertical velocity, while the stippled portions correspond to areas with negative (i.e., downward) velocity. The heavy line is the zero vertical velocity boundary; the ±0.1 and ±0.3 m sec^{-1} contours are also shown. For clarity, the boundaries of the stratum of strong echo return (dotted lines) are also shown.

The Doppler-derived vertical velocity for the descending portion of the wave between 0109 and 0115 was found to average -0.25 m sec^{-1} with a maximum value of -0.35 m sec^{-1}. Between 0123 and 0129, the Doppler method gave about -0.35 m sec^{-1} with a maximum of -0.48 m sec^{-1}. This agreement is very good. The low signal-to-noise ratio precluded our deriving the vertical velocity for that part of the atmosphere between the stratum of strong echo returns and the nocturnal inversion below; therefore, we were unable to determine whether this part of the atmosphere was oscillating in phase with the wave motion above. However, by examining the vertical velocity fluctuations at the top of the nocturnal inversion, as shown in the bottom of Fig. 5, we see that periods with significant upward vertical velocities correspond to the periods of upward vertical velocity inside the stratum of strong echo returns. The facsimile record in Fig. 2 also gives evidence that the height of the nocturnal inversion is oscillating in phase with the wave motion.

Using the wave parameters shown in Table 2 together with Eq. (5), we obtained a wind component of 6 m sec^{-1} along the propagation direction of the wave. The radiosonde gave a component of about 5.5 m sec^{-1}. Unfortunately, the radiosonde we used was released about 2 hr before the wave event. During the time between the radiosonde and the wave event, no significant changes in wind speed or direction were observed on the nearby tower. This may indicate that the radiosonde data were representative of values prevailing at the time of the event, at least in the first few hundred meters. Taking into account the difference in time between the radiosonde and the wave event, the agreement between the wind component measured by the radiosonde and the one calculated from acoustic sounder data is quite good. This appears to confirm the potential of acoustic echo sounder observations of boundary-layer gravity waves for measuring boundary-layer wind speeds.

b. Case II

In Case II (Fig. 3) the wave is clearly within the nocturnal inversion. The wave parameters calculated both from the acoustic sounder and the microbarograph array are shown in Table 3.

As we see, an excellent agreement exists between the two systems. In this case the wavelength is much shorter, only about 3.5 km, which gives us better accuracy. In addition, even at only 250 m above ground the wave has a relatively large amplitude, giving us a good signal-to-noise ratio in the pressure fluctuations observed on the ground.

c. Case III

Case III (Fig. 4) is a common morning situation in which the nocturnal inversion is eliminated when a convective layer develops with the onset of solar heating. The rising plumes within this convective layer appear to induce a wave structure at its top. There is some evidence of vertical wave phase variation, indicating a wave-associated vertical energy and momentum transport within the overlying inversion. These wave parameters are shown in Table 4. For this event, we were only able to calculate the wave parameters from the acoustic sounder array; the wave was not detected by the microbarograph array. The reason for this can be seen from the gravity-wave dispersion equation which, in the Boussinesq and WKB approximations can be written as (e.g., Hooke *et al.*, 1973)

TABLE 3. Wave parameters for the events in Case II.

Wave parameters	Acoustic sounder array	Microbarograph array
Period	368 sec	365 sec
Phase speed	9.7 m sec^{-1}	10 m sec^{-1}
Wavelength	3.5 km	3.6 km
Direction of arrival	330°	322°
Amplitude	~100 m	

TABLE 4. Wave parameters for the events of Case III.

Wave parameters	Acoustic sounder array
Period	205 sec
Horizontal phase speed	5.2 m sec^{-1}
Horizontal wavelength	1.1 km
Direction of arrival	278°
Amplitude of the wave	~50 m

$$n^2=k^2\left(\frac{N^2}{\Omega^2}-1\right), \tag{7}$$

where we have assumed that the wave-associated velocity and pressure perturbations vary as

$$\exp i(\Omega t-kx-nz),$$

and where $N^2\equiv gd(\ln\theta)/dz$ is the square of the Brunt-Väisälä frequency N. Since for the most part the temperature structure within the convective planetary boundary layer is adiabatic, $N\approx 0$, which implies from Eq. (7) that $n=\pm ik$. Thus, we find that the wave amplitude at ground level is only a few percent of what it is in the overlying inversion; this causes it to be undetectable in the presence of the large pressure fluctuations associated with the thermal plumes.

5. Conclusion

We have shown that three vertically-pointing acoustic sounders arranged in a triangle about 300 m on a side can be successfully used to calculate horizontal wavelengths, phase velocities, and direction of arrival of gravity waves in the lower 1000 m of the atmosphere. The gravity waves analyzed had horizontal wavelengths ranging from about 1 km to almost 6 km with horizontal phase velocities from 5 to 10 m sec^{-1}. Comparing these results with a collocated array of microbarographs gave a good agreement.

Using estimates of the wave-associated vertical-velocity fluctuations and vertical displacements together with the wave period and horizontal wavelength, we were able to determine the mean wind speed component along the wave propagation direction.

Acknowledgments. The authors thank Gary E. Greene and John W. Wescott who aided in various aspects of the data acquisition and analysis.

The senior author, a member of the Norwegian Defence Research Establishment, expresses his sincere gratitude to Dr. C. Gordon Little, Director of the Wave Propagation Laboratory, for providing the opportunity and facilities for him to be a visiting scientist and complete this study.

He also expresses his thanks to the many other scientists within WPL who not only contributed with helpful discussions and suggestions, but also created a stimulating environment and accepted him as one of their own.

His contributions to this work were sponsored by the Royal Norwegian Council for Scientific and Industrial Research.

REFERENCES

Bean, B. R., 1971: Comparisons of remote and in-situ measurements of meteorological parameters and processes. *Statistical Methods and Instruments in Geophysics*, A. G. Kjelaas, Ed., Oslo, Teknologisk Forlag, 181–196.

Beran, D. W., and S. F. Clifford, 1972: Acoustic Doppler measurements of the total wind vector. *Preprints Second Symp. Meteorological Observation and Instruments*, San Diego, Amer. Meteor. Soc., 100–110.

——, C. G. Little and B. C. Willmarth, 1971: Acoustic Doppler measurements of vertical velocities in the atmosphere. *Nature*, **23**, 160–162.

——, W. H. Hooke and S. F. Clifford, 1973: Acoustic echo sounding techniques and their application to gravity-wave turbulence and stability studies. *Bound. Layer Meteor.*, **4**, 133–153.

Briggs, B. H., G. S. Phillips and D. H. Shinn, 1950: The analysis of observations on spaced receivers of fading radio signals. *Proc. Phys. Soc. London*, **B63**, 106–121.

Emmanuel, C. B., B. R. Bean, L. G. McAllister and J. R. Pollard, 1972: Observations of Helmholtz waves in the lower atmosphere with an acoustic sounder. *J. Atmos. Sci.*, **29**, 886–892.

Gossard, E. E., and W. H. Munk, 1954: On gravity waves in the atmosphere. *J. Meteor.*, **11**, 259–269.

Hooke, W. H., J. M. Young and D. W. Beran, 1972: Atmospheric waves observed in the planetary boundary layer using an acoustic sounder and a microbarograph array. *Bound. Layer Meteor.*, **2**, 371–380.

——, F. F., Hall, Jr. and E. E. Gossard, 1973: Observed generation of an atmospheric gravity wave by shear instability in the mean flow of the planetary boundary layer. *Bound. Layer Meteor.*, **5**, 29–41.

Little, C. G., 1969: Acoustic methods for the remote probing of the lower atmosphere. *Proc. IEEE*, **57**, 571–578.

McAllister, L. G., 1968: Acoustic sounding of the lower atmosphere. *J. Atmos. Terr. Phys.*, **30**, 1439–1440.

Monin, A. S., 1962: Characteristics of the scattering of sound in a turbulent atmosphere. *Akust. Zh.*, **7**, 457–461 (*Sov. Phys.–Acoust.*, **7**, 370–373).

Tatarski, V. I., 1961: *Wave Propagation in a Turbulent Medium.* New York, McGraw-Hill, 285 pp.

Monthly Weather Review 103, 70-71, January 1975.

Thunderstorm Flow Patterns in Three Dimensions

R. A. Kropfli and L. J. Miller

Wave Propagation Laboratory, NOAA, Boulder, Colo. 80303

(Manuscript received 16 October 1974)

The dual-Doppler radar system at the Wave Propagation Laboratory of NOAA has recently revealed in unprecedented detail the three-dimensional velocity structure within a severe thunderstorm during the mature and dissipating stages. These observations were obtained during the National Hail Research Experiment (NHRE) in northeast Colorado on 28 July 1973 when hail was reported at the ground. Data acquisition and reduction procedures described by Miller and Strauch (1974) were utilized in producing these results.

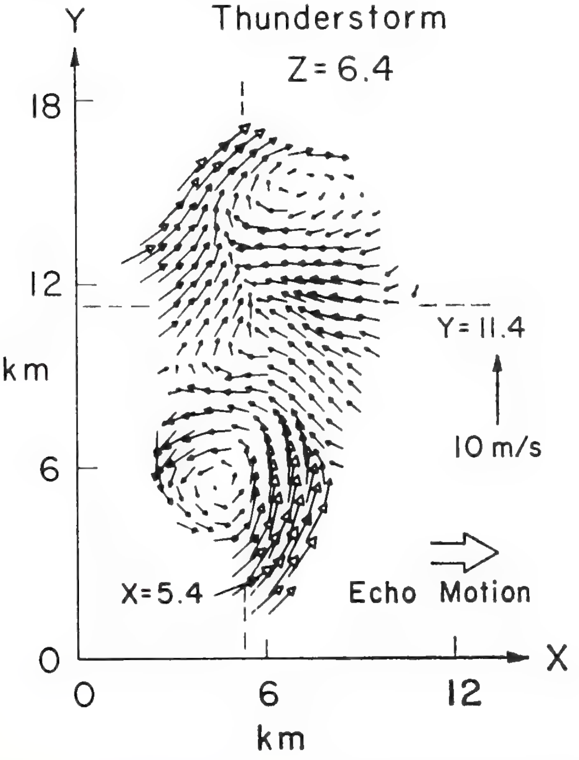

Fig. 1. Horizontal flow relative to moving storm at 6.4 km above ground. Lengths of arrows are proportional to relative wind speed.

At 1730 MDT, the storm was located directly over the NHRE mesonet in which meteorological parameters were recorded at 30 ground stations. Relative to the two Doppler radars, the storm's location was 40 km east of the baseline between the radars which were positioned near the northwest and southwest corners of the NHRE protected area. The separation distance of the two radars was 50 km.

Shown in Figs. 1, 2, and 3 (top) are projections of the vector wind field onto three orthogonal planes within the storm. Arrow lengths are proportional to wind speed. A 10 m/s reference arrow is shown on each figure. The mean horizontal echo motion of 3.9 m/s toward the east has been removed from all three displays in order to display flow relative to the moving storm. Figure 1 is the relative flow in a horizontal plane at a height of 6.4 km above ground level with the y-axis directed north. Figures 2 and 3 are flow patterns in vertical planes along the dashed axes indicated in Fig. 1. The xz plane of Fig. 3 is aligned approximately along the inflow direction.

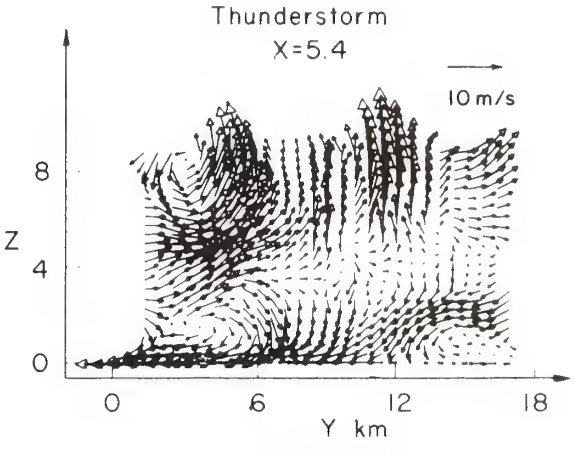

Fig. 2. Vertical flow in yz plane at $x = 5.4$ km as indicated in Fig. 1.

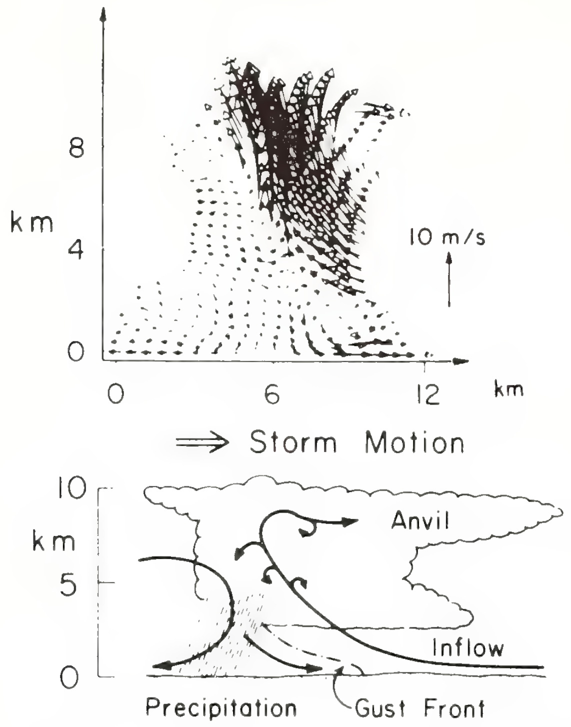

FIG. 3 Top: Vertical flow in xz plane at $y = 11.4$ km as indicated in Fig. 1; Bottom: Schematic representation of flow pattern in vertical plane corresponding to top figure.

Despite the complexity of these patterns and the obvious three-dimensionality of the flow, Fig. 3 exhibits several clearly identifiable features such as the backward sloping updraft overriding a precipitation-filled downdraft, middle-level intrusion of cold, dry air into which the precipitation can fall, and a well defined gust front. The schematic representation in Fig. 3 (bottom) identifies these features.

Several characteristics that had not been anticipated are also apparent. For example, Fig. 1 shows two distinct counterrotating vortices aloft which are aligned approximately along a north-south axis. Other horizontal planes not shown indicate that three high-vorticity regions extend vertically through a significant portion of the storm and are separated by two strong sloping updraft cores in the middle and upper levels.

An intensive analysis of these data is presently underway and we plan to soon publish comprehensive quantitative results.

REFERENCE

Miller, L. J., and R. G. Strauch, 1974: A dual-Doppler radar method for the determination of wind velocities within precipitating weather systems. *Remote Sensing of Environment*, 3, 217–233.

Proceedings 16th AMS Radar Meteorology Conference, 121-127, April 1975.

THUNDERSTORM FLOW PATTERNS IN THREE DIMENSIONS FROM DUAL-DOPPLER RADAR

R. A. Kropfli and L. J. Miller

NOAA/ERL/Wave Propagation Laboratory
Boulder, Colorado 80302

1. INTRODUCTION

It has been widely recognized that a comprehensive understanding of severe storms must have as a basis the interaction of microphysical and dynamical processes. As emphasized by Mason (1969), "Progress has been hindered by a poor appreciation of interrelations between the air motion and the microphysical events which, acting in concert, culminate in the release of precipitation." Laboratory investigations have added greatly to our understanding of the microphysical processes involved in the formation of raindrops, snowflakes, and hailstones. However, these investigations usually have been performed in a controlled environment of uncertain relevancy to the real atmosphere. In addition, numerical calculations of microphysical processes have also been performed and again the weakness has been a lack of knowledge of the environment in which these processes actually take place. In particular, incomplete information about kinematics, for example the updraft and downdraft profiles, has been a shortcoming.

The three-dimensional wind field described here for a hail producing storm in northeast Colorado is a first step in an analysis plan that will eventually include the microphysics. As of this time we have computed air parcel trajectories through a storm velocity field measured with the NOAA/Wave Propagation Laboratory X-band dual-Doppler radar system. These trajectories can give only an approximate picture of where growing precipitation particles would travel within the storm. A terminal velocity component that varies with time and space will eventually be included in the trajectory calculations to give more realistic precipitation and cloud particle trajectories. This study is being pursued jointly with the National Hail Research Experiment (NHRE) since such particle trajectories clearly have implications regarding optimal seeding for hail suppression and/or precipitation enhancement.

In acquiring the data we have utilized the COPLAN method of scanning first described by Lhermitte and Miller (1970). Further discussion of the data acquisition and reduction procedures used here is given by Miller and Strauch (1974) and the X-band Doppler radar characteristics are given by Miller (1972).

The analysis presented here is for the first of six COPLAN scans through the hailstorm of 28 July 1973 during the NHRE in northeast Colorado. The observations were made at 1730 MDT (all times are given as Mountain Daylight Time) while the storm was centered over the NHRE mesonet in which temperature, pressure, humidity, wind speed and direction were measured and hail samples were collected. Two and one-half minutes were required for the complete dual-Doppler scan through the storm.

It should be pointed out that there are significant differences between this storm and a storm observed in the same area only a few days later as reported by Miller et al. (1975). These differences emphasize the pitfalls encountered in generalizing indiscriminantely from a few case histories. A comparison of data such as these should lead to a more complete understanding of environmental conditions which ultimately produce a particular kinematic structure and precipitation distribution.

2. STORM ENVIRONMENT

The storm of 28 July 1973 was traveling slowly toward the east at about 3 m/s at 1730. Fig. 1 shows the environmental winds relative to the moving storm. Note that the relative winds are directed toward the origin. This hodograph represents the average of 5 soundings released at 1800 from locations a few tens of kilometers outside of the NHRE protected area. The convective condensation level (CCL) determined from these rawinsonde releases was 610 mb or 4.1 km above mean sea level (MSL) at 1800. This was unchanged from the CCL 90 min earlier.

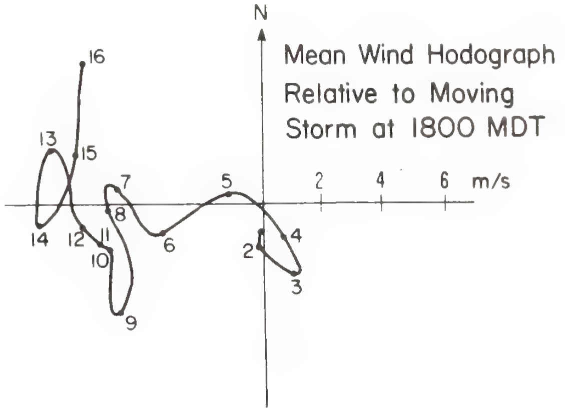

Figure 1. Mean wind hodograph determined from 5 rawinsondes at 1800 MDT. A 3 m/sec component toward the east has been removed. Heights are in km above MSL and velocities are toward the origin.

From Fig. 1 it can be seen that the subcloud winds were light (< 3 m/s) and that the winds above cloud base were somewhat stronger (~ 10 m/s) and from the west. Moderate shear of 2×10^{-3} sec^{-1} existed from just above cloud base to 7 km (MSL). The interval from cloud base to 14 km was weakly sheared with a value of 8×10^{-4} sec^{-1} being indicated in Fig. 1.

The mixing ratio in the lower half of the subcloud layer was also determined from the five radiosonde releases at 1800 and five others at about 1620. It was found that the subcloud mixing ratio was nearly time invariant and constant over the area at a value of 6.2 g/Kg. The temperature excess of a parcel lifted adiabatically from near the surface to the CCL and then moist adiabatically to 500 mb was about 3°C at this time.

Earlier soundings also revealed that a layer of air centered at the 5 km (MSL) level had a relatively low equivalent potential temperature of less than 326°K compared with values greater than 330°K near the surface. This potentially cool layer aloft contributed to storm development this day and its movement out of the area after 1700 preceded the decay of the storm by 45 min.

3. STORM EVOLUTION

The storm was scanned by the NHRE 10 cm radar at Grover, Colorado, from near 1600 until storm dissipation at about 1814. Fig. 2 shows the reflectivity structure at 15 min intervals centered at the time of the NOAA/WPL dual-Doppler measurements, i.e., 1728. These data were produced from 1.9° elevation angle scans with the Grover radar and represent the 2.3 km (AGL) level through the storm. The contours shown start at 20 dBZ and increase in 10 dB increments. Portions of the NHRE protected area and the area of Doppler coverage are also shown in the figure.

Fig. 2 shows that while the storm was moving eastward from 1659 to 1730 it was diminishing in size though not in intensity. Values of reflectivity slightly in excess of 50 dBZ are indicated by both the 10 cm and the Doppler systems at 1730. From 1730 to 1814 the storm continued to diminish rapidly in area and also decreased in reflectivity. The Doppler data therefore represent the last few minutes of the storm's mature stage. Other Doppler scans not reported here were taken during the next 10 min and show rapid decreases in the updraft speed and reflectivity.

4. KINEMATICAL DESCRIPTION

A series of horizontal projections of flow relative to the moving storm is shown in Fig. 3. A 3 m/s component to the east has been removed from the display. Below the flow patterns are shown both the reflectivity contours (solid lines) obtained from the Doppler systems and updraft contours (dashed lines). Shaded areas indicate where vertical velocity estimates were made. We assume that the vertical velocity at the surface is zero as a boundary condition. The attenuation problem, which can be severe when X-band radar is used to observe storms, is reduced by the use of the larger of the reflectivity estimates from the two Doppler systems.

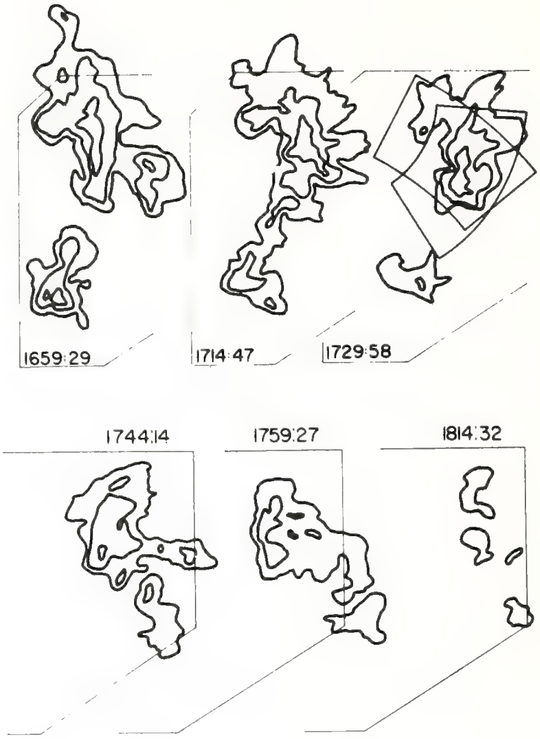

Figure 2. Evolution of reflectivity structure from S-band radar at Grover. Lowest contour is 20 dBZ. Increments are 10 dB.

In some regions of the flow patterns, the velocity component normal to the coplane, i.e., before transformation to Cartesian coordinates, could not be estimated because of missing data in lower planes. Thus the vertical integration of the continuity equation could not be performed to that level. Since the coplane angles are less than 15°, this normal component contributes little to the horizontal field. Horizontal projections for which this normal component has been neglected in Fig. 3 are indicated by arrows with half tips except in the plane at the surface. Half-tipped arrows in the surface plane indicate that no divergence calculation was possible at those locations because of data missing at the edge of the pattern.

The coordinate system used in Fig. 3 has its origin at the midpoint of the baseline between the radars and since the baseline is only 5.9° away from north, the x axis is approximately eastward. A vector representing 10 m/s is displayed in the figure.

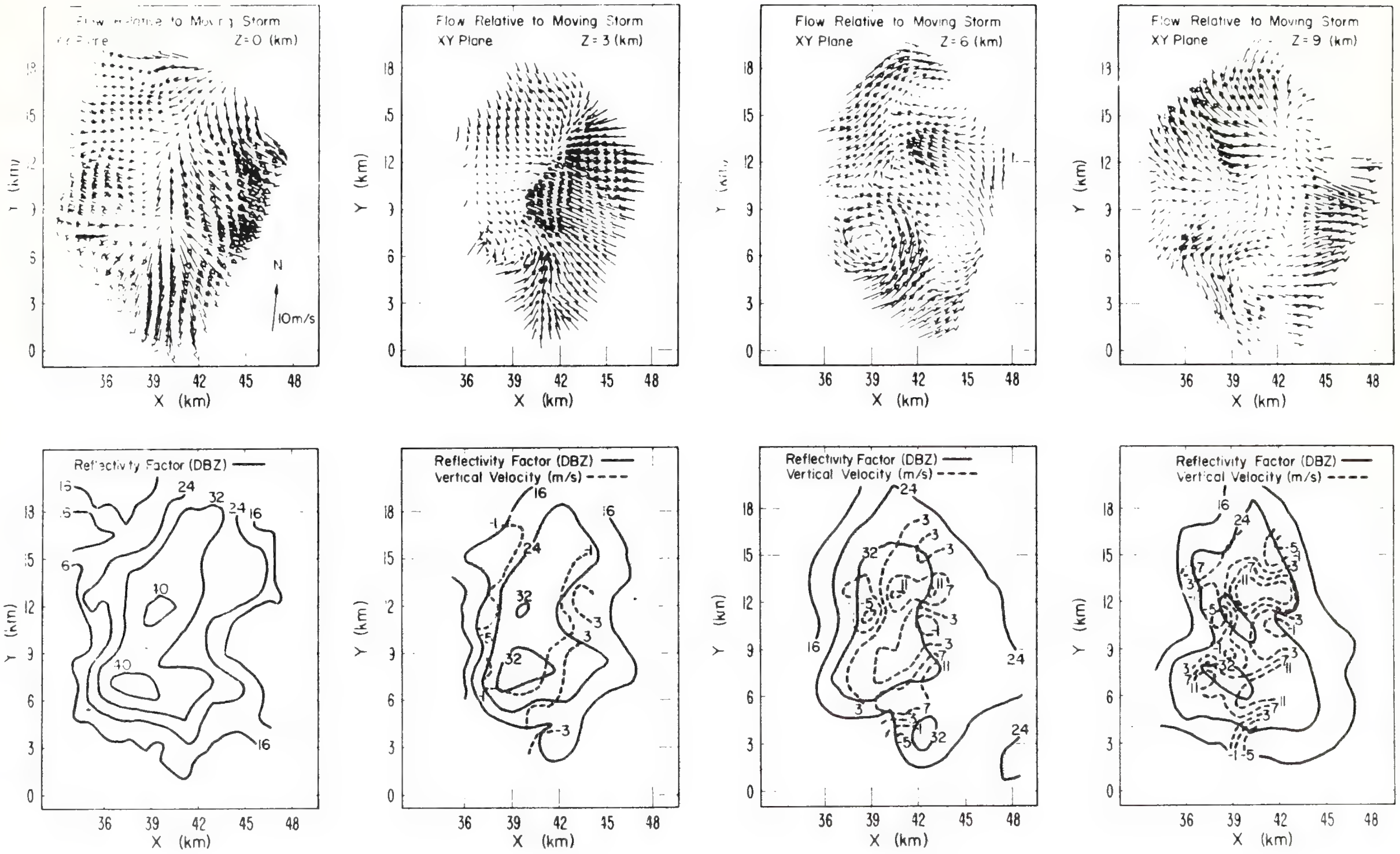

Figure 3. Relative flow, reflectivity, and vertical velocity contours at heights of 0, 3, 6, and 9 km above the surface.

The most apparent feature of the plane at the surface in Fig. 3 is the highly divergent flow pattern coincident with the high reflectivity region. A peak divergence of $8x10^{-3}$ sec^{-1} is found about 1 km east of the southernmost 40 dBZ contour. There exists a similar correspondence of divergence with reflectivity for the 40 dBZ contour to the north. A local maximum of $4x10^{-3}$ sec^{-1} is found less than 1 km northeast of the northern 40 dBZ contour. This correspondence of divergence with reflectivity is expected at the base of a precipitation induced downdraft.

The plane at z = 3 km clearly shows the inflowing air from the ESE direction on the eastern half of the storm. This air enters the storm from the east as the lower edge of the updraft but is caught in the precipitation. Consequently, it is descending at about 4 m/s in the center of the storm at this level. It can be seen that the inflowing air enters the storm from the east, crossing the 24 dBZ contour with an updraft speed of about 3 m/s.

At 6 km the inflow air is somewhat less apparent in the flow pattern but perhaps more clearly defined in the vertical velocity contours. The figure shows that the inflowing air has penetrated the eastern two-thirds of the storm at this level. The 3 m/s contour runs from the xy coordinate (42, 17) to the position (38, 6) with the entire region to the east of this line in a vigorous updraft. Several regions of high vorticity can be seen in the flow pattern. Vorticity in excess of $4x10^{-3}$ sec^{-1} extends vertically throughout most of the depth of the storm and does not tilt with the updraft. An explanation of the cause of the northernmost and southernmost vorticity cores is offered below.

Near the top of the storm at z = 9 km a somewhat more symmetrical flow pattern is observed. A divergence pattern near the northern portion of the updraft is clearly seen, indicating a weakening of the updraft. A peak divergence value of $5x10^{-3}$ sec^{-1} is observed here. Two updraft cores in excess of 11 m/sec oriented nearly north south are also indicated at this level. Also revealed in this plane is the relative flow out into the anvil within the eastern third of the storm.

A column of cyclonic vorticity is seen in the southern portion (right flank) of the storm from below cloud base (~ 2 km AGL) to the highest level of the Doppler data, 10 km AGL. The peak vorticity observed in this column is $1.0x10^{-2}$ sec^{-1} at 4 km AGL. To the north (left flank) is a corresponding column of anticyclonic vorticity. This column is generally weaker, having a peak vorticity of $.7x10^{-2}$ sec^{-1} between 7 km and 8 km, and it extends from 4 km AGL to the highest observed level within the precipitation-filled volume.

One possible explanation for these cyclonic and anticyclonic vorticity columns is the suggestion that the storm acts, to some extent, as an obstacle to the environmental wind. The result is cyclonic curvature on the right of the storm and anticyclonic curvature on the left when the environmental wind flows past the storm from behind as suggested by Newton and Newton (1959). Other explanations, including vorticity production by the tilting term in the vorticity equation, are presently being pursued.

Vertical cross sections of the flow patterns in the x and y directions are shown in Figs. 4 and 5 respectively. The xz plane

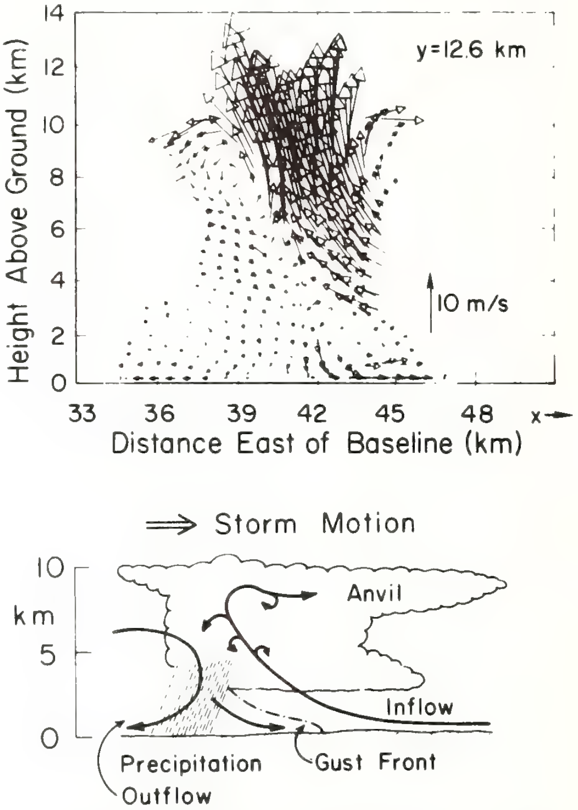

Figure 4. Vertical (xz) cross section of relative flow at y = 12.6 km with corresponding schematic shown below.

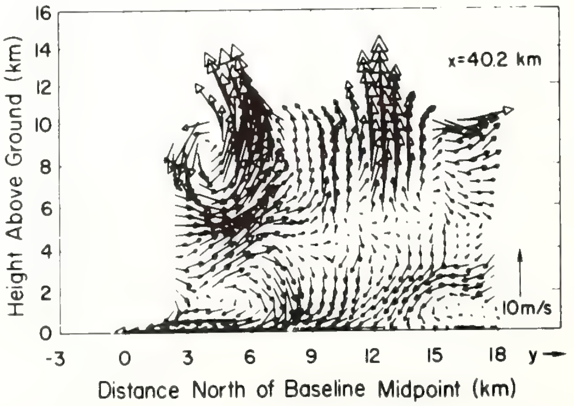

Figure 5. Vertical (yz) cross section of relative flow at x = 40.2 km.

is approximately along the inflow direction within the northern updraft core and shows excellent correspondence with the schematic representation in Fig. 4b. Fig. 5 is a vertical plane along the north-south direction and emphasizes the three dimensionality of the flow. It also displays the two strong updraft cores in the upper levels.

Fig. 6 shows the surface wind relative to the moving storm measured by anemometers in the NE portion of the NHRE mesonet at 1730. The anemometers east of the storm show significant surface flow away from the storm at this time. Several minutes earlier the relative wind at these locations was light (< 3 m/s) and variable. This sudden wind increase at 1730 is the gust front preceding the echo by 10-15 km and is accompanied by a rapid decrease in equivalent potential temperature, θ_e, from 335° at 1715 to 326° at 1745. The 1629 MDT sounding taken at Grover shows that air with $\theta_e = 326°$ was found at the 4 km level above the surface. This is consistent with Fig. 7 which shows air forming the gust front is brought down from near 4 km (AGL).

Air parcel trajectories through a steady state velocity field were calculated for initial points near the storm edge. Fig. 7 displays a sampling of these steady state trajectories or streamlines that begin at the 4 km level. Wide arrows simply indicate that several trajectories which follow approximately the same path are combined and that a larger volume of air is involved in the flow. The indicated times specify the amount of time an air parcel takes in following a trajectory until it exits the velocity field near the arrow tip. The 25 dBZ contour derived from the Doppler radars is indicated by a dashed line at the surface and at the 4 km level.

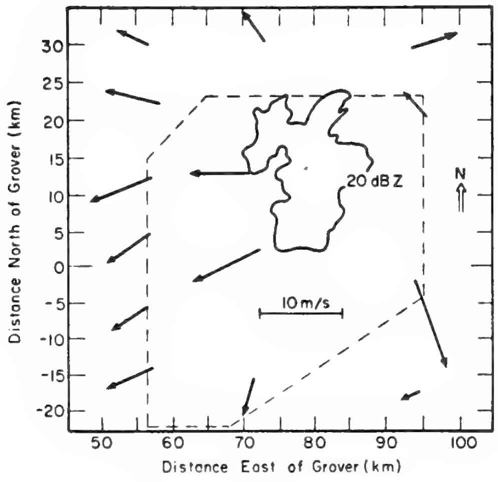

Figure 6. Relative winds at surface from NHRE mesonet at 1730 MDT with superimposed 20 dBZ contour.

The first point to be made from Fig. 7 is that the gust front on the storm's right forward flank has its source on the left rear flank near the 4 km level. Air descends anticyclonically from the left rear portion of the storm and exits under the southern portion of the updraft at the surface. Notice that the northern portion of the gust front has, as a source, air starting from the left forward flank that becomes entrained into the anticyclonic downdraft. This portion of the gust front also originates from the left rear flank at this level. Air at the 4 km level on the right rear flank descends with little rotation and exits at the rear and about .5 km from the surface. Some of the inflowing air that starts at the lower edge of the updraft becomes entrained in the downdraft and also exits near the surface on the right rear flank. Air starting on the right flank and right forward flank moves upward with cyclonic curvature and exits the measured velocity field near the 10 km level. Most of the broad sheet of upward moving air near the forward central edge of the storm at this level moves directly upshear with little rotation, eventually exiting near the x, y, z coordinates (40, 13, 10). However, the northern portion of this sheet splits off, turns anticyclonically and exits the left rear flank at the upper levels.

Other trajectories which begin at the 2 km and 6 km levels have been computed but are not shown. Most trajectories starting near the periphery at 6 km exit the top levels of the storm but some air starting near the point (32, 11, 6) becomes entrained into the downdraft and descends to the 3 km level. At this level it splits into one portion that is carried to the 10 km level by the updraft and another portion that continues downward and becomes part of the gust front near the southeast edge of the storm. All parcels starting near the periphery of the velocity field at the 2 km level (not shown here) are carried to the surface.

It should be noted from Fig. 7 that different air parcels starting from points separated by as little as 1 km at the 4 km level may end up on opposite sides of the storm. Thus there are regions of the storm in which the trajectory followed by an air parcel is sensitive to its exact starting point. Other air parcel trajectory calculations are now in progress.

5. QUANTITATIVE RESULTS

In addition to a qualitative description of kinematic structure within thunderstorms, much quantitative information can be provided by a dual-Doppler system. Software has now been developed at this laboratory to compute the average of any of the computed data fields over the updraft or downdraft regions. If desired, these averages can also be computed over an area in which any other field assumes a specified range of values. The amount of quantitative information now available is awesome. Only a brief sample can be presented here.

Table I displays mean values of the indicated parameters. These averages represent nearly 6000 samples over a 2-1/2 min period within the precipitating volume of 10^3 km^3. As in the

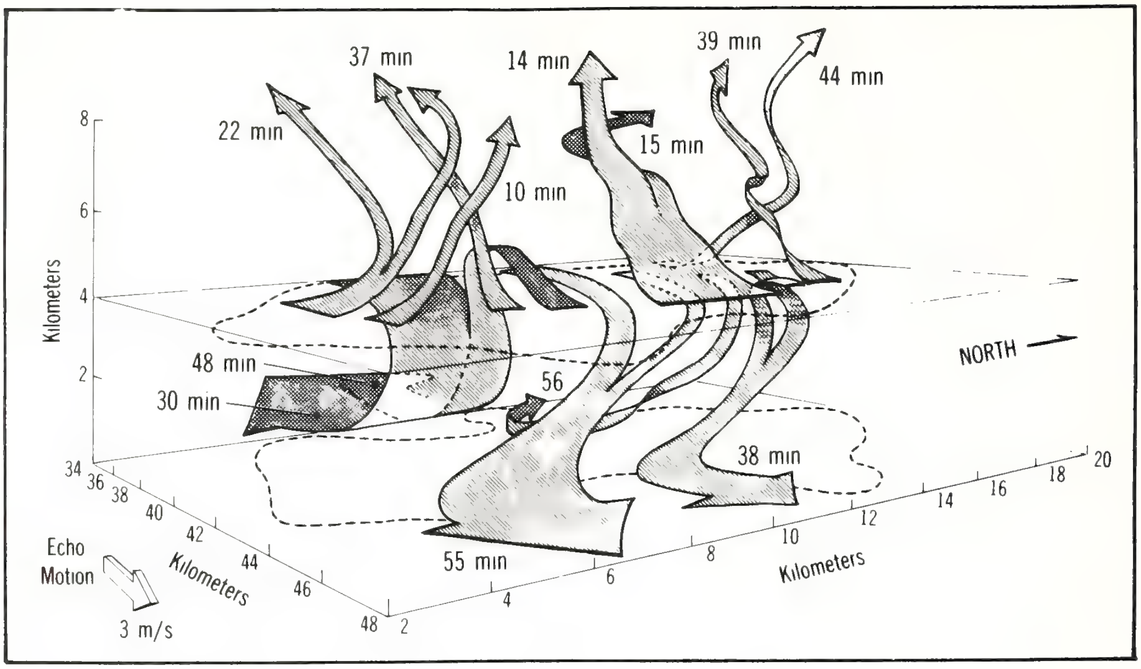

Figure 7. Streamlines starting at the 4 km level. Dashed contours indicate the 25 dBZ reflectivity level.

patterns, a 3 m/s storm motion toward the east has been removed before all calculations were made.

The small mean values for the east and north components, $\bar{u}$ and $\bar{v}$, respectively, indicate that the echo advection speed was nearly equal to the mean Doppler-derived speed which confirms that the flow patterns are indeed relative to the storm. The average vertical velocity over the storm is quite large and is heavily weighted by the presence of the strong updraft to be discussed later. Consistent with the net upward motion in the storm at this time is the net convergence in Table I. COPLAN scans taken only several minutes later reveal a dramatic reduction in the updraft core and the mean vertical motion within the storm is downard at this later time. The time history of this storm will be fully discussed in a later paper.

Although vorticity and updraft cores were not coincident, vorticity was found to be positively correlated with the updraft velocity. The entire downdraft volume had a mean vorticity of $-.47\text{x}10^{-3}$ sec^{-1}, the entire updraft had a mean of $.43\text{x}10^{-3}$ sec^{-1} and the strong updraft (> 5 m/s) had a mean of $1.04\text{x}10^{-3}$ sec^{-1}.

The last item in Table I is the mean kinetic energy measured within the storm; it is probably an underestimate because it includes only the precipitating region. As we have seen in Fig. 6, there are significant velocity perturbations as far ahead of the precipitation as 15 km. Nevertheless, the number we have calculated is not in serious disagreement with Sellers (1972) who estimates the kinetic energy of an "average" summer thunderstorm to be $1.5\text{x}10^{14}$ joules. The basis for his estimate is not given.

The components of total momentum flux in the x and y directions were also computed. The mean vertical flux of easterly momentum ($\overline{\rho uw}$) is -17 dynes/cm^2 and the flux of northerly momentum ($\overline{\rho vw}$) is 18 dynes/cm^2. If not the magnitudes, at least the signs on these quantities are consistent with the environmental winds of Fig. 1 in which the wind vectors are directed toward the origin. Knowing that the storm is effective in the vertical exchange of air, we

TABLE I

Quantities Averaged over Storm Volume

$\bar{u}$	$\bar{v}$	$\bar{w}$	$\nabla \cdot \vec{v}$	$\nabla \times \vec{v}$	$\overline{KE}$
-.3 m/s	.2 m/s	1.2 m/s	$-.1\text{x}10^{-3}$ sec^{-1}	$.02\text{x}10^{-3}$ sec^{-1}	$3.0\text{x}10^{13}$ joules

expect air from aloft to have a component toward the east-southeast relative to the lower levels. This would explain the negative correlation between u and w and the positive correlation between v and w.

Fig. 8 illustrates the core updraft cross section as a function of height at 12.6 km north of the radar baseline midpoint. The flow pattern in this xz plane is given in Fig. 4. The upshear tilt of the updraft can be clearly seen. From the profiles in Fig. 8, the locus of points defining the centroid of the updraft in this plane is tilted about 25° from the vertical. The double peaked structure of this updraft core is found at nearly all levels of the storm.

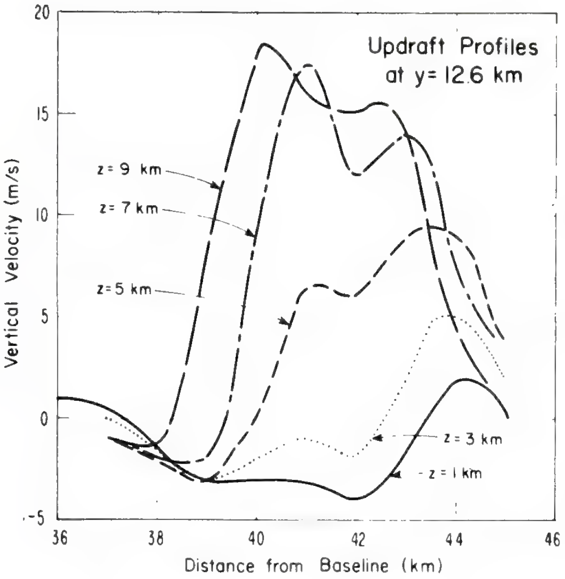

Figure 8. Vertical velocity profiles along y = 12.6 km for various heights above ground.

Updraft profiles were also determined in the southern updraft core at y = 6.6 km. These profiles (not shown) show a similar tilt of the updraft in the shear direction up to at least 10 km; however, the eastern portion of the updraft core is not observed because of attenuation suffered by the northern Doppler radar.

6. SUMMARY

The NOAA/WPL dual-Doppler radar system has been used to determine the kinematic structure of a hailstorm in a weakly sheared environment during the late-mature stage. Two nearly parallel updraft cores were observed to be tilted upshear about 25° from the vertical. Located near the right and left flanks of the storm were columns of positive and negative vorticity respectively. A plausible explanation for these vortex columns is that the mass of air within the storm acts, to some extent, as an obstacle to the environmental air flowing around the storm.

Three-dimensional streamlines were calculated for air parcels starting at different points around the storm periphery at the 4 km level. The source of inflow air was near the surface and up to 15 km ahead of the right forward flank of the precipitation. The kinetic energy and vertical flux of momentum were also determined for the entire storm. Finally, a positive correlation was found to exist between the updraft speed and vorticity when averaged over the entire storm.

7. ACKNOWLEDGEMENTS

Much of the credit for these results must be given to the Meteorological Radar Group at the Wave Propagation Laboratory, for it was indeed a team effort extending over several years. In particular, the engineering effort of Richard Strauch, the computer programming of Nate Kohn, and the art work of Don Valentine deserve recognition here. The authors are also grateful for the valuable discussion with Keith Browning. Supporting data used in Figs. 1, 2, and 6 were made available by the NHRE.

REFERENCES:

Lhermitte, R. M. and L. J. Miller, 1970: Doppler radar methodology for the observation of convective storms, Preprint Vol., AMS 14th Radar Meteor. Conf., 133-138.

Mason, B. J., 1969: Some outstanding problems in cloud physics--the interaction of microphysical and dynamical processes, R. Meteor. Soc., 95, 449-485.

Marwitz, J. D., 1973: Trajectories within the weak echo regions of hailstorms, J. Appl. Meteor., 12, 1174-1182.

Miller, L. J., 1972: Dual-Doppler radar observations of circulation in snow conditions, Preprint Vol., AMS 15th Radar Meteor. Conf., 309-314.

Miller, L. J. and H. W. Frank, 1974: Three-dimensional air motion within a northeast Colorado rainstorm, Preprint Vol., AMS Conf. on Cloud Physics, 321-327.

Miller, L. J. and R. G. Strauch, 1974: A dual-Doppler radar method for the determination of wind velocities within precipitating weather systems, Remote Sensing of Environ., 3, 217-233.

Newton, C. W. and H. R. Newton, 1959: Dynamical interactions between large convective clouds and environment with vertical shear, J. of Meteor., 10, 483-496.

Sellers, W. D., 1972: Physical Climatology, Univ of Chicago Press, Chicago, p. 13.

Proceedings AMS Conference on Cloud Physics, 277-282, October 1974.

DUAL DOPPLER RADAR MEASUREMENTS WITHIN A HAIL PRODUCING STORM IN NORTHEAST COLORADO

R. A. Kropfli and L. J. Miller
NOAA/ERL/Wave Propagation Laboratory
Boulder, Colorado 80302

1. INTRODUCTION

The success of any cloud seeding program depends critically upon knowledge of winds within the storm, particularly the storm updraft and downdraft structure. Since storms of primary interest (the hail and tornado producers) are extremely violent, it is usually difficult if not impossible to penetrate these storms with aircraft to the extent that wind fields can be determined. Single Doppler radar measurements require assumptions about the stationarity of the storm over several tens of minutes.

The dual Doppler radar technique that provided the data described here yields the three-dimensional wind field within a storm and requires that the wind field pattern remain unchanged for less than 2 min while the storm is being scanned.

The observations were taken with the NOAA/WPL dual X-band Doppler radar system during the National Hail Research Experiment (NHRE) in Northeast Colorado on 9 July 1973. Two complete scans of the forward half of a hailstorm complex were taken 3 min apart. During this time the storm was spawning two cells along its forward edge, one of which eventually grew to a reflectivity value in excess of 50 dBz. These two cells were probed in detail by other NHRE participants, using aircraft.

It is noteworthy that the data presented here exhibit a great deal of consistency, both internally and with other independent observations. For example, the flow relative to the storm agrees with the meso-network of anemometers. Updraft velocities feeding the main cell at 1625 MDT agree to within a few meters/sec with aircraft observations in the vicinity. Updrafts and downdrafts are found to occur in expected locations. And finally, the two completely independent sets of dual Doppler data taken about 3 min apart reveal essentially the same velocity and reflectivity structure, merely translated in position.

2. THE COPLANE METHOD OF SCANNING

The coplane method for coordinated scanning with two Doppler radars is fully described by Miller and Strauch (1974). Only a quick overview is presented here for completeness. Fig. 1, taken from the reference, indicates the scanning geometry. Two radars are synchronized to scan the same plane simultaneously and then move up to the next plane until the entire precipitating region is probed. Common planes are tilted with respect to the horizon and intersect the horizontal plane along a line joining the two radars.

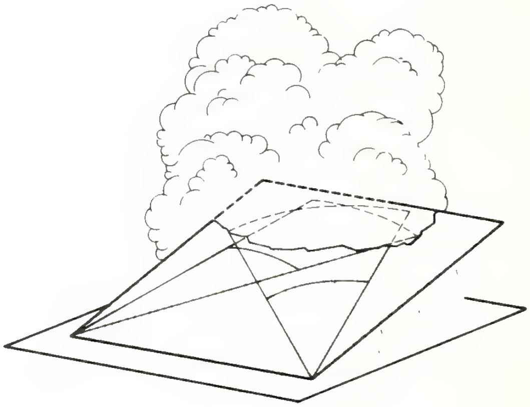

Figure 1. Coplane geometry

Doppler spectra computed by the Fast Fourier Transform provide estimates of the mean radial velocity for each radar, and these radial velocities are vectorially combined to yield the two-dimensional velocity field for each plane. To obtain the component normal to each plane, the continuity equation for incompressible fluids is integrated in a cylindrical coordinate system with the axis along the radar baseline. A boundary condition that vertical velocity vanishes in the 0° coplane is assumed. Finally, an interpolation procedure is used to transform wind fields to a Cartesian coordinate system. This interpolation program provides plots of velocity, divergence, vorticity, and reflectivity, samples of which are provided below for the 9 July hailstorm.

3. ENVIRONMENTAL CONDITIONS

Radiosondes released from five nearby locations at 1554 MDT and 1725 MDT were used to define the environment in which the storm was propagating. Three of the release points are indicated in Fig. 2 while the two others, Sidney and Sterling, are just off the figure to the east and southeast, respectively. The dual Doppler observations were taken near 1625 MDT. Table 1 indicates the average mixing ratio up to

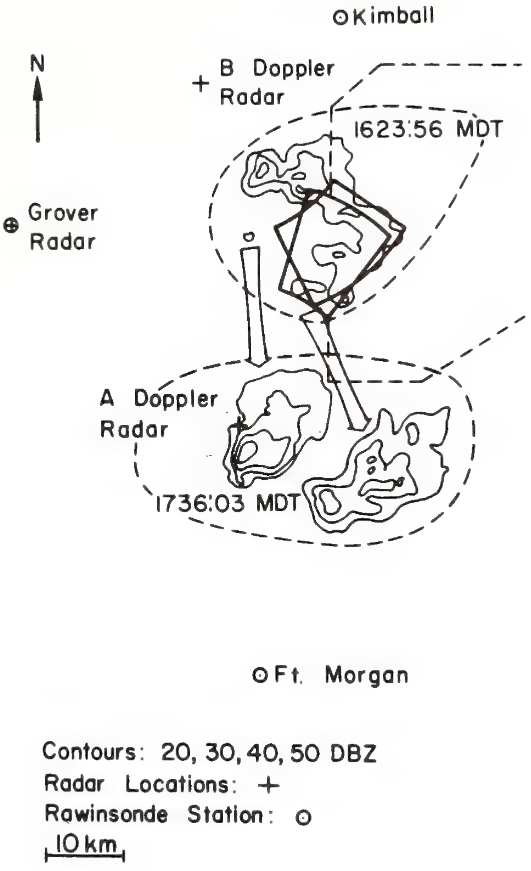

Figure 2. Evolution of storm echo from 1623:56 to 1736:03 with superimposed coplane coverage at 1623:10.

cloud base (∿ 630 mb) computed from these soundings. A gradual influx of moisture into the region is noted from the table in all the soundings except for Kimball. The decrease noted there was the result of the storm passage over that station with the removal of moisture in the form of precipitation. Note that the Grover station, the farthest to the west, remained dry during this period.

Table I

Average mixing ratio (g/Kg) up to cloud base

	1554 MDT	1725 MDT	Average
Kimball	9.3	8.2	8.7
Sidney	8.1	9.7	8.9
Sterling	6.9*	9.3	8.1
Ft. Morgan	9.4	9.9	9.6
Grover	5.5	6.0	5.7

*Released at 1630 MDT

Fig. 3 shows that the environmental winds were backing from 70° at the surface to 260° at 10 km MSL. The storm complex was moving due south so that its motion was to the right of the winds above 4.2 km MSL (2.7 km AGL), while flow below cloud base was bringing in moisture from the ENE direction. The wind speed profile shown in Fig. 4 indicates moderately strong speed shear of about $4x10^{-3}$ sec^{-1} at about 7 km above MSL which may have been a factor in maintaining the storm system for over a 2 hr period. The low level flow relative to the storm was from the SE as indicated by the meso-network of anemometers and the Doppler data.

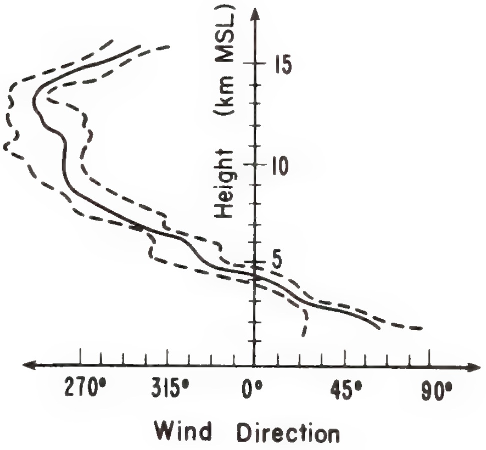

Figure 3. Environmental wind direction showing mean and extreme values for soundings at 1600 MDT.

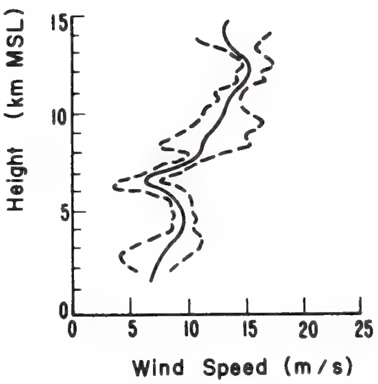

Figure 4. Environmental wind speed showing mean and extreme values for soundings at 1600 MDT.

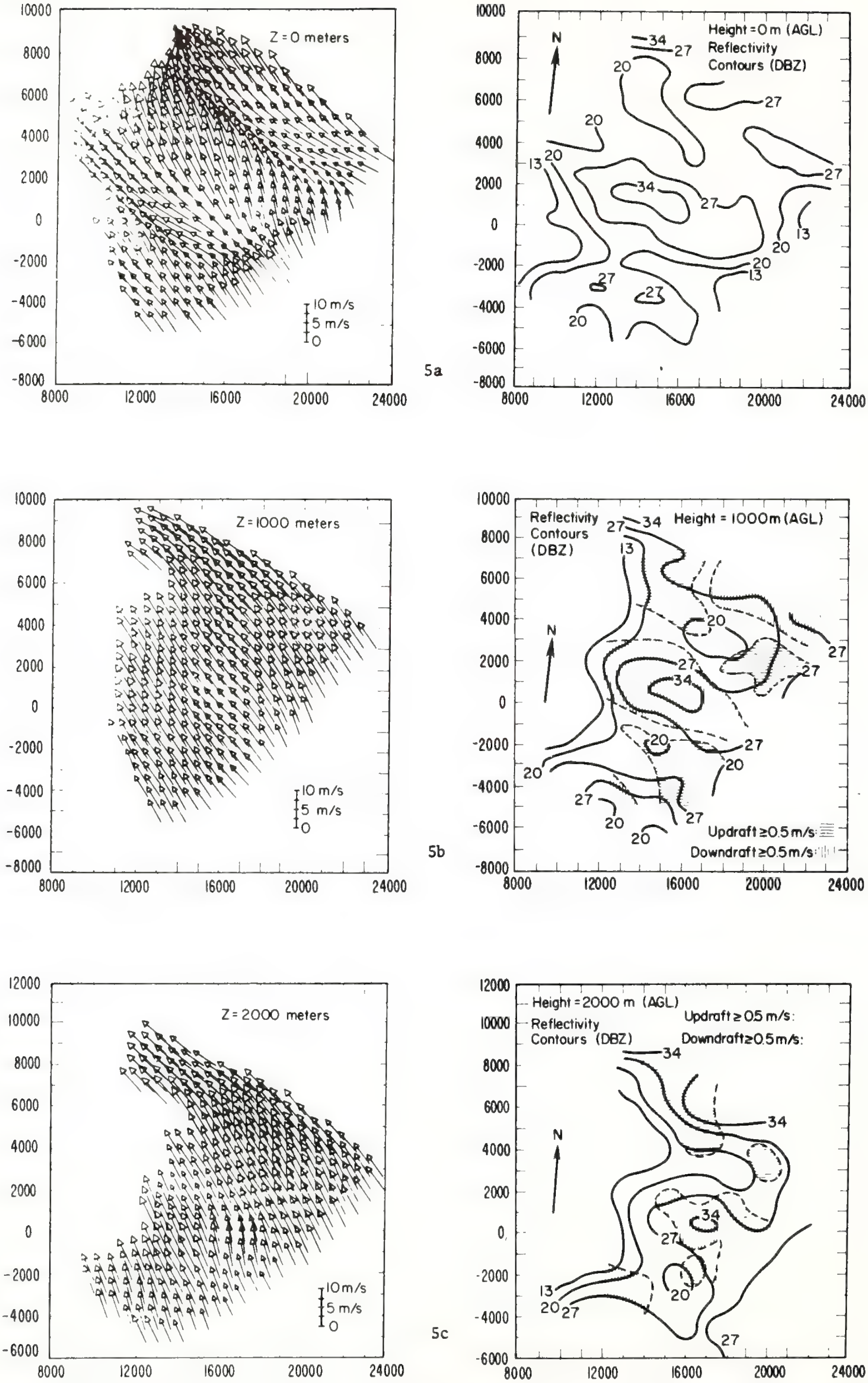

Figure 5. Horizontal (vector) wind field relative to storm, reflectivity and vertical velocity structures at the surface, 1 km and 2 km for coplane scan beginning at 1623:10. Ordinate and abscissa are labeled in meters with the origin at the midpoint of radar baseline.

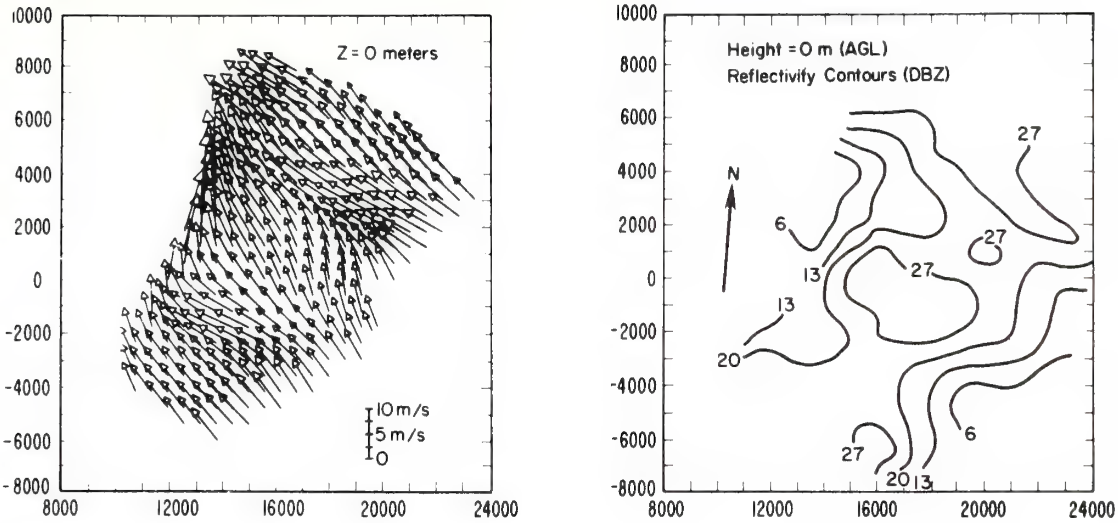

Figure 6. Horizontal (vector) wind field relative to storm, reflectivity and vertical velocity structures at the surface, 1 km and 2 km for coplane scan beginning at 1623:10. Ordinate and abscissa are labeled in meters with the origin at the midpoint of radar baseline.

4. WIND AND REFLECTIVITY STRUCTURE OF THE 9 JULY HAILSTORM

Observations of the storm by the Grover radar at 1609 MDT revealed a weakly reflecting system (∿ 35 dBz) near the northwest corner of the NHRE protected area. Fig. 2 shows its structure later at 1623:56, the time of the first dual Doppler radar observations, and again at 1736:03. As indicated in the figure, the two cells near the forward sector of the system grew from 20 dBz minicells into two major systems. These two cells were probed by other NHRE participants and the western cell was observed by the A Doppler radar pointed vertically at 1725. Results of these later observations are reported elsewhere.

Also shown in the figure is the coplane scanning area. The scanned area covers the region of low level inflow into the intense cell to the north. Two complete coplane scans were performed within the indicated region, the first of which was begun at 1623:10 and the second at 1625:52.

Figs. 5a through 5c show horizontal fields of reflectivity, vertical velocity, and the horizontal wind field at kilometer intervals from the surface to 2 km obtained from the first coplane scan. Basic features of this scan were reproduced by the second coplane scan as can be seen by comparing the surface fields of Fig. 6 with Fig. 5a. Other heights show similar agreement.

The echo motion of 10 m/s to the south has been removed from the velocity field so that the vectors represent flow relative to the storm. The Cartesian coordinate system used here has its origin at the midpoint of the baseline between the radars and the y axis is oriented nearly north-south.

Several features are immediately apparent from these figures. In Figs. 5b and 5c, the central downdraft is coincident with the area of relatively high precipitation (∿ 40 dBz) which is forcing the downdraft by evaporative cooling. Similarly, along the upper right corner of these figures is a region of higher reflectivity which again is coincident with a downdraft. In contrast to this, the very northernmost portion shows reflectivities ≈ 40 dBz within the strongest observed updraft. This is the updraft feeding the most intense cell existing at this time and the updraft penetrates into the region of high reflectivity gradient but probably not into the peak reflectivity just north of the Doppler coverage shown in Fig. 2.

Figs. 5 show that the flow relative to the storm below cloud base (∿ 2200 m AGL) was from the SE in close agreement with the anemometer mesonetwork. This relative inflow from the SE was the source of moist unstable air for the most intense cell to the north and the effect of the central downdraft on this inflow is apparent in the vector fields of Figs. 5a and 6. The downdraft impedes the inflow as would a solid object and the inflow is diverted to either side. This diversion is caused by downward momentum transport from aloft.

The reduction of the inflow by this downdraft is the probable cause for the decay of the most active cell at this time. Also, the spreading out of this descending air near the surface most probably initiated the lifting of moist unstable air out in front of the complex, as is indicated by the new growth there.

Fig. 7 shows the vertical velocity profile of the main updraft region in the northern portion of the Doppler scan. The entire updraft was not observed here and these data represent only values of vertical velocity observed along the eastern portion of the updraft. These values of vertical velocity are consistent with aircraft observations in the vicinity and with the second set of Doppler observations.

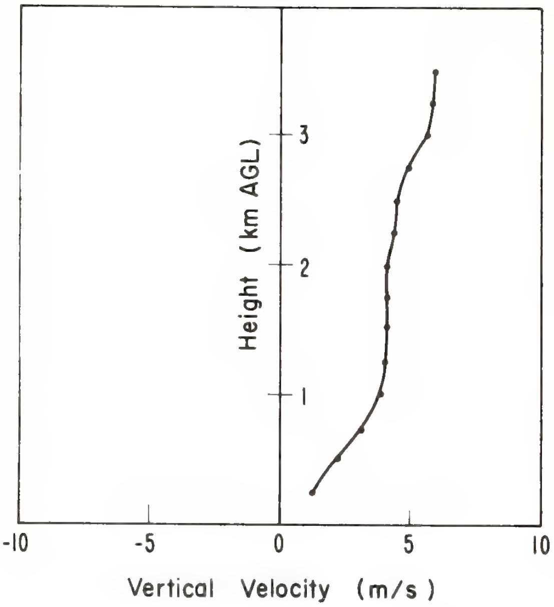

Fig. 7. Vertical velocity profile of the eastern edge of the main updraft determined from first coplane scan.

An interesting feature of the observed flow is revealed in Fig. 8 in which a region of reflectivity > 34 dBz within the central downdraft of Figs. 5b and 5c is superimposed over the flow pattern in a vertical plane orthogonal to the inflow direction. This plane is oriented along an azimuth of 39°. A significant horizontal component of vorticity along the inflow direction is produced by the precipitation. A similar vortex is partly displayed along the right of this figure. This second high vorticity region is a consequence of the main cell just off to the north of the Doppler coverage, the edge of which just appears as the broken 34 dBz contour on the right. A portion of the main updraft feeding this cell is indicated by the upward sloping arrows on the right at a height of 4.5 km.

A comparison of Figs. 9 and 10 reveals a high degree of similarity between the Browning-Ludlam hail-cloud circulation model taken from Fujita (1963) and the relatively weakly reflecting cell in the central portion of Fig. 5. The flow pattern in Fig. 10 is a vertical slice along the inflow direction, i.e., at right angles to the plane used in Fig. 8. The similarity, except for scale, is surprising in view of the applicability of the Browning-Ludlam model to severe hail producing cells in contrast to the cell illustrated in Fig. 8 which is a less intense portion of a more severe storm complex. Fig. 10 shows that the cell is tilted in the direction of inflow.

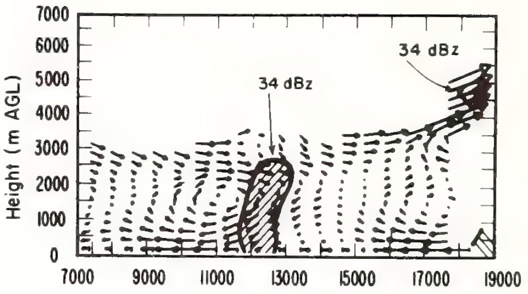

Fig. 8. Wind field projection onto plane perpendicular to inflow with superimposed 34 dBz reflectivity contour.

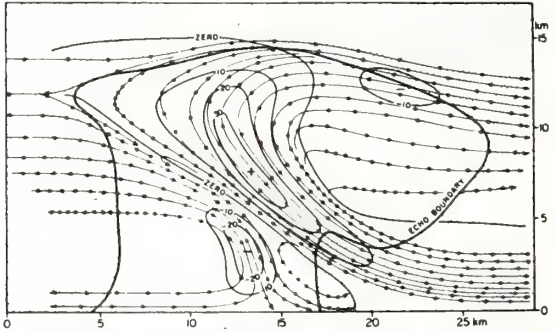

Fig. 9. Browning and Ludlam's model of hail-cloud circulation from Fujita (1963).

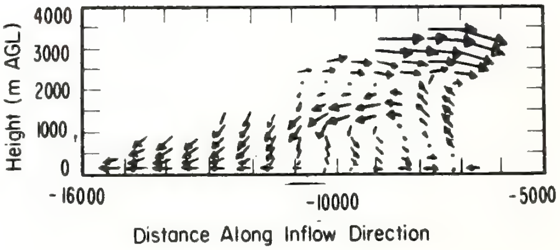

Fig. 10. Wind field projection onto plane parallel to inflow from the right.

5. SUMMARY

Many interesting features of a hail producing storm have been revealed by two Doppler radars operating in the coplane mode. A precipitation induced downdraft near the leading edge of the storm complex was seen to have an active role in the evolution of the storm, not only by impeding the inflow to the main cell and causing its decay, but also by contributing to the new growth along the leading edge of the complex that eventually became the most active and persistent cells of the day. A portion of the main updraft was observed to penetrate into a region of high reflectivity gradient. The measurements were confirmed by a second coplane scan, by a surface network of anemometers and by aircraft observations.

6. REFERENCES

Miller, J. L. and Strauch, R. G. (1974), A Dual-Doppler Radar Method for the Determination of Wind Velocities Within Precipitating Weather Systems, submitted to Remote Sensing of Environment.

Fujita, T. (1963), Analytical Mesometeorology: A Review, Meteorological Monographs, Vol. 5, p. 103.

Proceedings of 3rd AMS Symposium on Meteorological Observations and Instrumentation, 187-192, February 1975.

THE 1972 HASWELL, COLORADO, ATMOSPHERIC BOUNDARY LAYER EXPERIMENT

C. Gordon Little and Earl E. Gossard

Wave Propagation Laboratory
Environmental Research Laboratories
National Oceanic and Atmospheric Administration
Boulder, Colorado 80302

1. INTRODUCTION

This paper describes the boundary layer experiment conducted by the Wave Propagation Laboratory at Haswell, Colorado, during the period August 1 to August 15, 1972.

From the outset, the purpose of the experiment was two-fold: (a) to test, evaluate and compare a wide range of remote sensing instrumentation, in a well-instrumented meteorological environment, and (b) to utilize the unique combination of remote sensing and in situ instrumentation to study the structure and processes of the atmospheric boundary layer during both stable and unstable conditions, and also during the transition between stable and unstable regimes. As such, it was the largest and most complex of the series of WPL field experiments conducted since 1969.

The Haswell site was selected for the experiment because of (a) valuable previous experience in using the site, (b) the 500 ft. high meteorological tower at the site, and (c) because of the simple terrain. The site is located approximately 100 miles east of the Rockies in a wide shallow bowl, some 70 meters deep and 20-30 km across, with the immediate terrain around the site very flat and sparsely covered with clumps of buffalo grass (~15 cm in height). The Haswell area has a typical high-plains meteorological regime, with strong radiative cooling at night and strong solar heating and convective activity during the day.

2. THE OBSERVATIONAL SYSTEM

The unique combination of instrumentation assembled at the site is listed in Table 1. The meteorological tower was instrumented at five fixed levels (100 ft., 200 ft., 300 ft., 400 ft., and 500 ft.) with thermistors and with fast response bivane anemometers giving wind speed, elevation angle and azimuth angle. The top 100 ft. of the tower also included a closely spaced array of anemometers which measured horizontal wind speed and azimuth angle, at 425 ft., 450 ft., and 475 ft. The microwave radio-frequency refractive index of the ambient air was measured using microwave refractometers at the 200 ft. and 300 ft. levels. In addition, an instrumentated carriage which moved up the exterior of the tower carried

TABLE 1. WPL 1972 HASWELL EXPERIMENT INSTRUMENTATION

Parameter / Instrument	VELOCITY								GRAVITY WAVES			TEMPERATURE				HUMIDITY			
	Surface Velocity	Surface Divergence	Surface Vorticity	Vertical Profile	Structure Constant Profile	Spectrum of Turbulence	Momentum Flux	3-D Velocity Field	Velocity	3-D Spectrum	Dispersion	Vertical Profile	C_T Profile	Spectrum	Heat Flux	Vertical Profile	C_e Profile	Spectrum	Water Vapor Flux
A. In Situ																			
Tower	X			X	X		X					X	X			X	X		
Tetroon									X										
Aircraft						X	X							X	X			X	X
Radiosonde				X								X				X			
Surface network	X																		
B. Remote Sensing																			
3-D Microphone Array									X	X	X								
Acoustic Sounder Array			X	X	X				X	X	X		X						
Laser Beam Array	X	X																	
Doppler Radars		X	X	X	X	X	X	X											
0_2 Radiometer												X							

sensors for three-dimensional wind, temperature, radio frequency refractive index and the structure constants of radio refractive index, wind velocity and temperature. The 300 ft. level also carried sensors for the structure constant of temperature. Microphones at the base of the tower and at the 100 ft. and 500 ft. levels were used to sense pressure fluctuations, such as those associated with gravity waves. In all, the meteorological tower supplied 43 channels of in situ data, designed to give profiles of standard meteorological parameters and also of the small scale structure constants of temperature, velocity and humidity important to the scatter of acoustic and radio waves.

Meteorological information at heights above the tower were obtained by standard GMD radiosonde releases once per six hours from the site. In addition, the NCAR Buffalo aircraft was used to define the horizontal properties of the atmosphere at various heights.

A network of eight 100 foot towers was set-up by the Air Resources Laboratory Field Research Office, Idaho Falls. These towers were placed in a diamond grid within a square 80 km on a side, and centered on the 500 foot high Haswell tower. An aerovane at the 50 foot level provided nearly continuous wind speed and direction from May until September.

Constant volume balloon (tetroon) flights were made during a 3 week period in August. The tetroons were released in pairs from the same site with a time interval between release of about 1 minute. The 39 pairs of tetroons were set to float at a height of 500 feet, and were released generally between 4 a.m. and noon. Each tetroon was located at 1-second intervals by an M-33 radar. The purpose was to detect the presence of gravity waves and, from the paired release, an estimate of gravity wave speed.

The above array of in situ instrumentation provided a well-monitored environment in which to test and evaluate a unique set of WPL remote sensing instruments. These included an array of three acoustic echo sounders, located at the corners of a triangle of roughly 300 meters on a side. These sounders were directed vertically and used in the monostatic mode to measure profiles of vertical velocity and C_T (the structure constant of temperature), or were operated in an off-vertical configuration to obtain Doppler wind profiles according to five alternate operational plans aimed at acquiring data on thermal plumes, gravity waves and high plains convective storms. Leakage of acoustic energy between the different sounders permitted the measurement of vorticity over the triangle. In addition, C_V (the structure constant of velocity) was measured utilizing the differences in Doppler-derived vertical velocity as a function of separation of range gates, and from measurements of the echo strength measured on bistatic systems.

A triangular array of horizontal laser beams was used to enclose an equilateral triangle of side 300 meters; this array was used to provide triply-redundant measurements of space-averaged wind speed and direction and (more important) of the horizontal convergence and divergence of air into the triangle, at a height of 2.3 meters above the ground. A total of seven microphones (plus the two on the tower) were used to monitor the pressure fluctuations around the site, in a close-spaced array of roughly 200 meters on a side and a wide-spaced array of about 2 km on a side. In addition, two 3 cm wavelength Doppler radars spaced 16 km apart, were used as a coordinated pair to track chaff released over the site, and hence to define the three-dimensional velocity field over an area of 100 square kilometers surrounding the site. Finally, a microwave radiometer, tuned to the O_2 absorption band at about 5 mm wavelength, was used to monitor the temperature profile in the lowest kilometer or so of the atmosphere.

Thus the combination of standard and novel in situ and remote sensing instrumentation provided a totally new opportunity to evaluate device performance, and to observe the structure and processes of the boundary layer at scales ranging from a few centimeters to many kilometers.

3. NEW TECHNOLOGICAL RESULTS

As indicated above, one of the main purposes of the experiment was to test and evaluate the performance of several new remote sensing concepts. We turn now to a brief description of four of the most significant technological experiments.

3.1 Quantitative Check of Acoustic Scatter Theory

Acoustic scatter theory shows that the scattered power, per unit volume, per unit incident flux, per unit solid angle for a plane acoustic wave scattered from a Kolmogorov spectrum of turbulent temperature eddies is given by $\sigma\ (\theta) = 0.0039\ C_T^2/T^2$ where C_T is the structure constant defining the strength of the small scale temperature eddies and T is the mean temperature of atmospheric scattering volume. It is obviously important to check the validity of this theory since $\sigma\ (\theta)$ is clearly a fundamental parameter essential to the design of acoustic echo-sounding systems.

A careful quantitive test of this scattering theory was performed by Mr. W. D. Neff, by comparing the C_T measurements made on the meteorological tower with those derived from measurements of the acoustic echo strength at the same height in the vicinity of the tower. The acoustic sounding systems were calibrated at several frequencies against a standard corner reflector target mounted for the purpose on the tower instrumentation carriage. The C_T measurements were obtained by recording the rms difference in air temperature at two points spaced 20 cm apart vertically, using very high speed metal filaments (Lawrence et al., 1970). Typical results obtained under convective conditions are shown in Figure 1, which compares the distributions of C_T measured on the tower at 92 m height and by two of the sounders. The agreement is obviously very good, the median C_T values observed typically agreeing to within the experimental error of about 2 decibels. This must be regarded as a very satisfactory confirmation of the acoustic scatter theory under conditions when the Kolmogorov theory, which assumes the presence of isotropic, homogeneous turbulence, is likely to be applicable. The results obtained under stable conditions, when the atmosphere is likely to show strong horizontal stratification, are less conclusive. Earlier results had indicated that on occasion the echo strengths observed under stable situations exceeded those predicted from the tower measurements by several decibels. However, under these conditions it is difficult to be sure that the C_T measurements on the tower are really

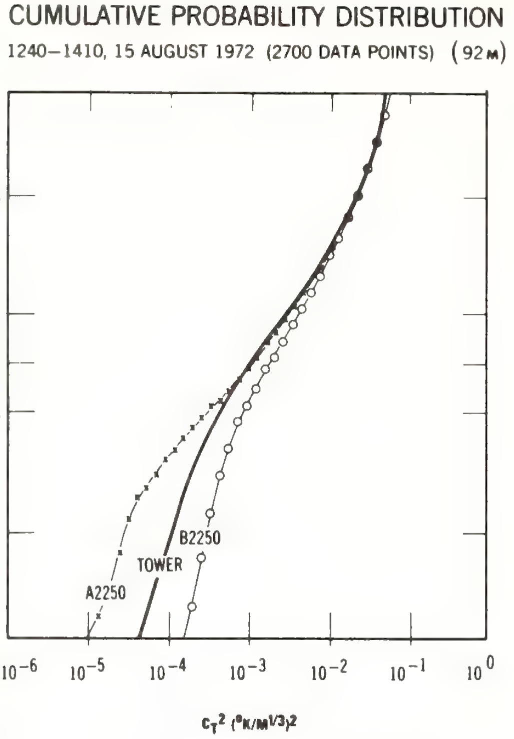

Fig. 1 Cumulative probability distributions of C_T^2 at 92 m height observed during convective conditions by two acoustic sounders and the tower instrumentation.

representative of the much larger volumes interrogated by the acoustic sounder. The Haswell 1972 data indicates that much of this discrepancy disappears when shorter acoustic pulses (and therefore smaller interrogation volumes) are used. This improved agreement suggests that the $\frac{\lambda}{2}$-size (~15 cm) temperature eddies are quasi-isotropic even under stable conditions, a result which is supported by the observed absence of any significant aspect-sensitivity of the frequently observed thin echoing layers.

Thus the experiment demonstrated that the existing acoustic scatter theory gives accurate estimates of scattered power under unstable atmospheric conditions, and is probably also applicable under stable conditions.

3.2 Measurements of Space-Averaged Wind Velocity and Divergence

Earlier work with a single laser beam had shown the optical scintillations introduced by the atmosphere could be used to measure the average wind speed across the beam (Lawrence et al., 1972). At the Haswell 1972 experiment, the technique was extended to provide space-averaged values of mean wind speed and direction, and of convergence and divergence. The results of this work using a triangular configuration of laser beams, have already been published (Kjelaas and Ochs, 1974). Since only two paths at different angles are required to provide space-averaged wind speed and directions, the triangular array provided triply redundant values of the air velocity. Excellent agreement was obtained, except under conditions of low and varying wind speeds when, as might be expected, correlation between the wind speeds measured at the three corners of the triangle decreased.

Of particular technological importance is the demonstrated ability of the laser beam array to measure the divergence or convergence of air into the enclosed triangle. Figure 2 is typical of the recordings of divergence under convective and stable regimes.

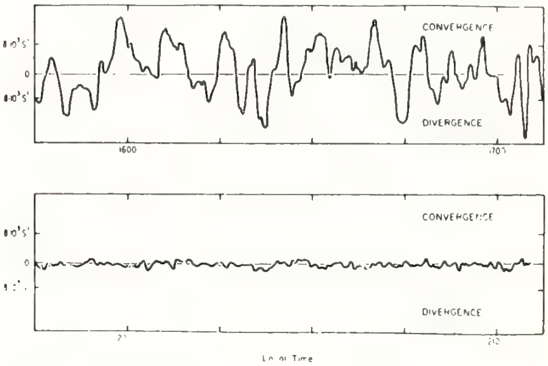

Fig 2 Daytime (top) and night-time (bottom) records of convergence of air as measured by the laser-beam triangle.

3.3 Acoustic Measurement of Vorticity

The availability of three acoustic echo sounders in a triangular array approximately 300 meters on a side provided a unique opportunity to measure the vertical component of atmospheric vorticity, using the circulation theorem (Gaynor et al., 1975). The three acoustic sounders were synchronized but operated on different frequencies; by measuring the time of arrival at each sounder of the leakage pulse from the other two sounders the "ring-around" time of acoustic energy in each direction around the triangle could be determined. The difference in the "ring-around" time in the two directions is a direct measure of the circulation of the air, and by dividing by the area of the triangle gives the vorticity. As an example of the results of this new technique, Figure 3 gives the spectral density of the acoustically measured vorticity some 2 meters above the surface of the earth.

3.4 Measurement of the Three-Dimensional Velocity Field Using Chaff

The use of two microwave Doppler radars to measure the three-dimensional atmospheric velocity field, using precipitation as the tracer of atmospheric motions, has already been described (Miller and Strauch, in press). These studies had hitherto been limited to regions of precipitation, and it was therefore decided that tests would be made during the 1972 Haswell experiment of the feasibility of using chaff (thin, artificial, metal coated fibers, cut to λ/2 in length) as tracers of the atmospheric motions in clear air.

These tests were highly successful under convective conditions. A small aircraft was used to dispense the chaff at an altitude of about 1 km. Typically, a series of 25 shotgun shells loaded with chaff were fired over a 5 km by 5 km area, and were allowed to disperse for about 20

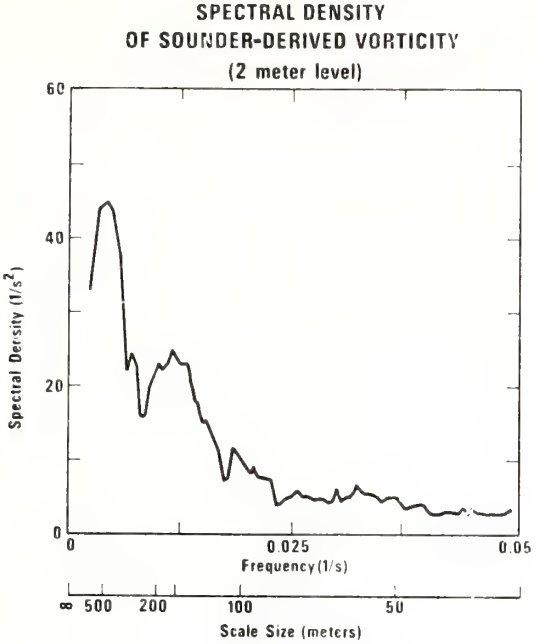

Fig. 3 Spectral density of the vertical component of vorticity, measured acoustically during convective conditions.

minutes prior to recording the radar data. Figure 4 is an example of the resultant data, and dramatically demonstrates the divergence of air in a plane 100 meters above the ground as revealed by the two Doppler radars. More recent tests during the 1974 National Hail Research Experiment in northeast Colorado showed that chaff could be released by hand from the surface and would rapidly diffuse under convective conditions, reaching an altitude of 2 km after several minutes.

On the other hand, chaff released at Haswell under stable, night-time conditions did not disperse, and no equivalent night-time boundary layer velocity fields were obtained by this method.

4. OBSERVATIONS OF CONVECTION

This section summarizes some of the principal results of the observations of the atmospheric convection, taken under clear sky, daytime conditions.

4.1 Convergence/Divergence under Convective Conditions

Convergence values of 10^{-2} sec^{-1} over periods of 1 to 2 minutes were common during daytime convective conditions, as opposed to typical night-time values of 5.10^{-4} sec^{-1}. Periods of strong convergence usually corresponded well with strong thermal plume echoes on the acoustic echo sounder located just inside the laser beam triangle, with periods of divergence corresponding to weak acoustic echoes. The occasional exception to this relationship may be attributable to the fact that the convergence was measured close to the surface, whereas the minimum height of the acoustic echoes was about 50 meters.

Figure 5 shows the cross-correlation curves between divergence and vertical wind as measured on the tower. The solid line is for high convective activity, and shows evidence of a strong periodicity at a period of about 400 seconds; the dashed line, for low convective activity periods, typically during early morning or late afternoon hours, shows little evidence of periodicity of the thermal plumes. Comparison of the divergence measurements with vertical wind measurements at the different levels on the tower indicated that the plumes were tilted in the forward direction in the lowest 30-60 meters, but were essentially vertical at greater heights. For further details of the laser-beam divergence measurements, the reader is referred to Kjelaas and Ochs (1974).

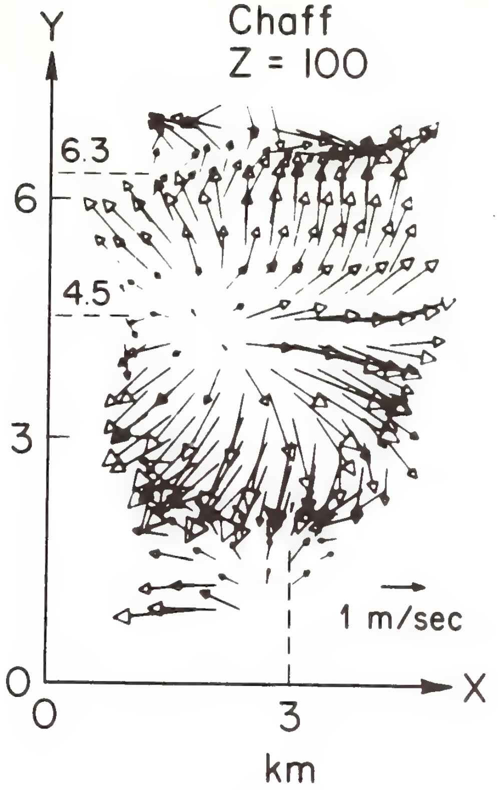

Fig. 4 Divergence of air in a horizontal plane 100 meters above the ground, measured during convective conditions by two Doppler radars.

4.2 Vorticity Under Convective Conditions

The acoustic measurements of vorticity are in the process of publication (Gaynor et al., 1975). Peak vorticity values near $0.5\ S^{-1}$ were observed using 12 second averaging of the data; in some cases the peaks were seen to coincide in time and sign with the passage of relatively small dust devils across the 3.75×10^4 m^2 triangle. During the 50 minute period analysed, the vorticity was observed to be cyclonic, and in good agreement with the environmental vorticity estimated from surface synoptic charts of about $0.05\ S^{-1}$. These spectra of near-surface vorticity show a maximum at periods of about 250 seconds, with a subsidiary maximum at about 85 seconds (see Figure 3). The 250 second period is somewhat smaller than the periods of 330 to 380 seconds found for the spectral peaks of vertical velocity and C_T measured

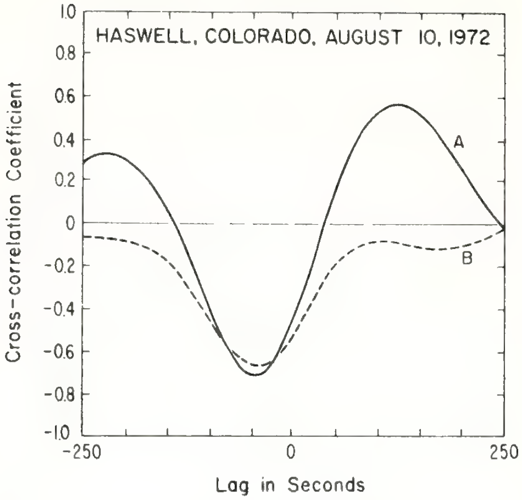

Fig. 5 Time-lagged cross-correlation curves between divergence measured on the laser-beam triangle and the vertical wind measured on the tower.

acoustically and on the tower, and on the laser-beam divergence measuring system.

Thus, these measurements can be taken as clear evidence of the fact that thermal plumes do rotate, and that the dust devils embedded in a plume predominantly rotate in the same sense as the plume.

4.3 Velocity Patterns in Convection

The dual-Doppler radar observations of convection, using chaff, are planned for publication in a forthcoming paper by Frisch et al., (1975). Figure 4, referred to earlier, shows the horizontal divergence of air as the downdraft region of a convective cell reaches the 100 meter level; Figure 6 shows a vertical cross section through the cells in a plane normal to the mean flow, and shows clearly the regions of updraft and downdraft. The dual-Doppler data also contain information on the vorticity and divergence fields, on the spectra of turbulence, and on the spatial dimensions of the convective cells. Analysis of these data is continuing.

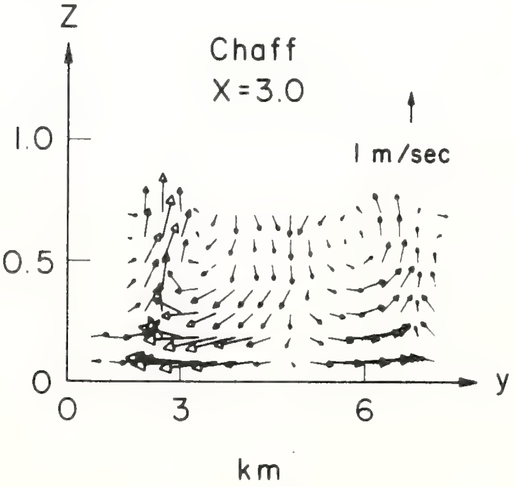

Fig. 6 Vertical cross-section of velocity field in a plane normal to the mean flow, measured during convective conditions using two Doppler radars.

4.4 The Transition Between Stable and Unstable Conditions

The transition between stable (night-time) and unstable (daytime) conditions, as observed using the Doppler radars and the acoustic echo sounder, is discussed in the paper by Frisch and Clifford (1974). Figure 7, taken from their paper, shows the capping inversion overlying thermal plume activity, for the period 0900-1000 on August 9, 1973. The turbulent energy dissipation rates measured by the microwave Doppler radar, the acoustic Doppler sounders and the meteorological tower were in good agreement at a value of about 30 $cm^2\ s^{-3}$. The Doppler radar showed this dissipation rate to be constant with height in and below the capping inversion. Comparison of the Doppler radar data permitted the interpretation of the acoustic record at 0955 as divided into four regions; a region A, of low wind shear, reaching to about 250 meters height in which thermal plumes carried heat upwards and gave strong acoustic echoes; a region B, extending from about 250 to 350 meters, in which shear increased and energy dissipation remained high, but acoustic echoes were absent, indicating a quasi-adiabatic temperature profile; a region C, from about 350 m to 450 m, of high wind shear and turbulent energy dissipation and strong echoes, identifying the temperature inversion capping the convective activity; and a region D above the inversion in which the wind shear and turbulent energy dissipation decreased with height, and in which the absence of acoustic echoes indicated a near-adiabatic temperature profile.

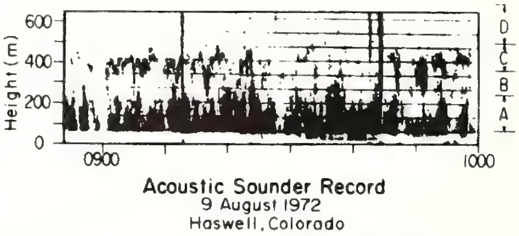

Fig. 7 Acoustic echo-sounding record showing thermal plume activity capped by an overlying temperature inversion.

5. GRAVITY WAVE OBSERVATIONS

Gravity waves crossing the Haswell site were registered primarily by the microbarograph arrays (through the associated pressure fluctuations), by the acoustic echo sounders (as oscillations in the height of quasi-horizontal echoing strata), and by the laser beam triangle (as oscillations in mean wind speed and direction). This section summarizes the results of two studies, comparing these data.

5.1 Comparison of Gravity Wave Observations Made Using Acoustic Echo Sounder and Microbarograph Arrays

The results of this study have already been published (Kjelaas et al., 1974a). The two independent acoustic sensing arrays, one passive, one active, gave excellent agreement in their measurements of wave period, horizontal phase speed and direction, and horizontal wavelength(see Table 2). The acoustic sounder array was able to detect gravity waves propagating in an inversion overlying the convective boundary layer that were undetected by the microbarograph array because of the wave evanescence in the underlying convection region. On one occasion, wave-associated vertical velocity oscillations of up to ± 0.5 ms $^{-1}$ were observed using the acoustic sounders in the Doppler mode.

TABLE 2

Comparison of Wave Parameters Observed on Acoustic Sounder Array and Microbarograph Array

Wave Parameter	Acoustic Sounder	Microbarograph
Period	368s	365s
Phase Speed	9.7ms $^{-1}$	10 ms $^{-1}$
Wavelength	3.5 km	3.6 km
Direction of Arrival	330°	322°
Amplitude	100 m	-

5.2 Dispersion and Spectra of Gravity Waves, Derived From Surface Measurements of Wind and Pressure

One of the most significant advances of the 1972 Haswell experiment was the demonstration of the ability to derive the spectra and dispersion characteristics of gravity waves crossing the site, using surface measurements of wind and pressure (Kjelaas et al., 1974b). In that paper, the spectrum and dispersion of gravity waves apparently generated by a severe convective storm on 8 August 1972 in southeastern Colorado were derived by two methods (a) from analysis of the data from the microbarograph array, and (b) from application of the Gossard-Sweezy method (Gossard and Sweezy, 1974) to observations of the wave-associated fluctuations of pressure and mean wind speed and direction, as observed on the laser beam triangle. Figure 8 indicates the excellent agreement between the two methods of deriving the variation of phase velocity with frequency. Critical to the success of the Gossard-Sweezy method was the ability of the laser-beam triangle to provide space-averaged values of the wave associated fluctuations in wind speed and direction, thereby filtering out much of the local turbulent fluctuations registered on point sensors.

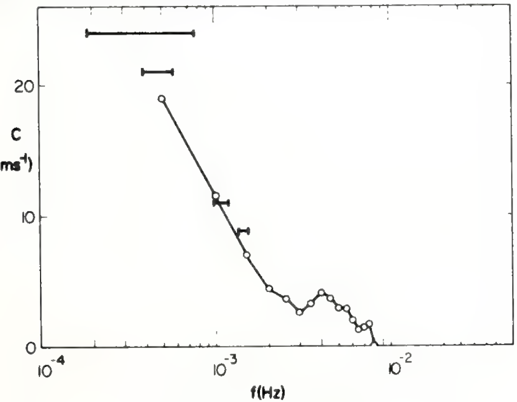

Fig. 8 Phase velocity vs. frequency, derived from microbarograph array (horizontal bars) and from measurements of wave-associated fluctuations in pressure and wind (full line).

Thus, this test indicates that the spectra and dispersion of lower tropospheric gravity waves passing overhead can be derived from surface measurements from one location, and that the laser beam averaging of velocity can be used to eliminate the need for an array of microbarographs.

6. SUMMARY

The above is a brief account of some of the results of the Haswell 1972 experiment. The technological and scientific progress that was made is largely due to the unique combination of a meteorological tower surrounded by remote sensing instrumentation, a combination which the Wave Propagation Laboratory plans to extend by the creation of a new year-around field site, equipped with a 500 meter meteorological tower, located some 20 to 40 kilometers east of Boulder, Colorado. To judge by the successes of Haswell 1972, we hope and expect that this new facility, which will be available continuously for widespread use by other atmospheric scientists, will have major impact on the future of atmospheric science and atmospheric technology in the U. S.

References

Frisch, A. S. and S. F. Clifford, 1974: A study of convection capped by a stable layer, using Doppler radar and acoustic echo sounder. J. Atmos. Sci. 31, 1622-1628.

Frisch, A. S., R. B. Chadwick, W. R. Moninger and J. M. Young, 1975: Observations of the convective boundary layer using simultaneous measurements by a dual-Doppler radar system, acoustic echo sounder and a microbarograph array. (To be submitted to J. Atmos. Sci.)

Gaynor, J. E., F. F. Hall, Jr., J. G. Edinger and G. R. Ochs, 1974: Measurement of vorticity in the surface layer using an acoustic sounder array. (Submitted to J. Amer. Meteor.)

Gossard, E. E. and W. B. Sweezy, 1974: Dispersion and spectra of gravity waves in the atmosphere. J. Atmos. Sci. 31, 1540-1548.

Kjelaas, A. G., D. W. Beran, W. H. Hooke and B. R. Bean, 1974: Waves observed in the planetary boundary layer using an array of acoustic sounders. J. Atmos. Sci. (Paper in press)

Kjelaas, A. G., E. E. Gossard, J. M. Young and W. R. Moninger, 1975: Dispersion and spectra of gravity waves probably generated by a convective storm. Tellus, Jan. 1975 issue.

Kjelaas, A. G. and G. R. Ochs, 1974: Study of divergence in the boundary layer using optical propagation techniques. J. Appl. Meteorol. 13, 242-248.

Lawrence, R. S., G. R. Ochs and S. F. Clifford, 1972: The use of scintillations to measure average wind across a light beam. Appl. Opt. II, 239-243.

Lawrence, R. S., G. R. Ochs and S. F. Clifford, 1970: Measurements of atmospheric turbulence relevant to optical propagation. J. Opt. Sci. 60, 826-830.

Miller, L. J. and R. G. Strauch, 1974: A dual-Doppler radar method for the determination of wind velocities within precipitating weather systems. Remote Sensing of Environ. (Paper in press)

Proceedings of 16th AMS Radar Meteorology Conference, 257-259, April 1975.

OBSERVATIONS OF THE TROPICAL MARINE ATMOSPHERE USING AN ACOUSTIC ECHO SOUNDER DURING GATE

P. A. Mandics, F. F. Hall, Jr., and E. J. Owens

Wave Propagation Laboratory
NOAA Environmental Research Laboratories
Boulder, Colorado 80302

and

D. Wylie

Department of Meteorology
University of Wisconsin
Madison, Wisconsin 53701

1. INTRODUCTION

Acoustic echo sounders (or echosondes) have been used successfully over land to probe remotely the structure of the planetary boundary layer. Thermal plumes, inversion layers, and their dynamic behavior have been studied in detail by using the intensity of the echo returns (Hall, 1972). More recently, the Doppler frequency shift of scattered signals has been analyzed to determine the wind velocity (Beran, 1974). The use of echo sounders in the marine atmosphere is a relatively new development (Ottersten et al., 1974).

In support of the boundary-layer subprogram of the Global Atmospheric Research Program Atlantic Tropical Experiment (GATE) we have installed an acoustic echo sounder aboard the NOAA Ship OCEANOGRAPHER. Our objective was to measure the wind velocity profile and to obtain data on the structure of the tropical subcloud layer.

2. THE EXPERIMENT

Figure 1 shows the acoustic antennas mounted in the bow of the ship. Short acoustic pulses were projected into the atmosphere using three 1.2-m diameter parabolic-dish antennas. One antenna was pointed vertically while the other two were elevated at 45° with respect to the horizontal and separated by 90° in azimuth. The Doppler frequency shift of the backscattered signals along the three axes made it possible to determine the wind velocity. The echo intensity from the vertically-pointed antenna provided information about the structure of the atmosphere. The antennas were mounted on a gyro-controlled stable platform which corrected for the ship's pitch and roll. An accelerometer, attached to the vertical antenna, was used to eliminate aliasing caused by the ship's up and down motions from the Doppler-derived vertical wind velocity. Because of the high mechanical vibration levels encountered on the ship, it was necessary to separate the antenna platform assembly from the deck by a vibration isolator. To reduce the received acoustic noise level and to decrease acoustic interference caused by the operation of the sounder, the antennas were enclosed by 1.5-m tall absorbing, foam-lined shielding cuffs (Strand, 1971).

The signal-conditioning and control circuitry were similar to those described by Simmons et al. (1971). Typical sounder parameters used during GATE were as follows: transmitted carrier frequency 2950 Hz, transmitted acoustic power 10 W, transmitted pulse duration 200 ms, pulse interval 5 s, antenna half-power beamwidth 10°, vertical-antenna receiver bandwidth 30 Hz, and tilted-antenna receiver bandwidth 100 Hz. The backscattered acoustic returns were recorded on a multi-channel analog magnetic tape recorder for later data analysis. In addition, a facsimile recorder was used to produce time-height records of the echo intensity from the vertical antenna.

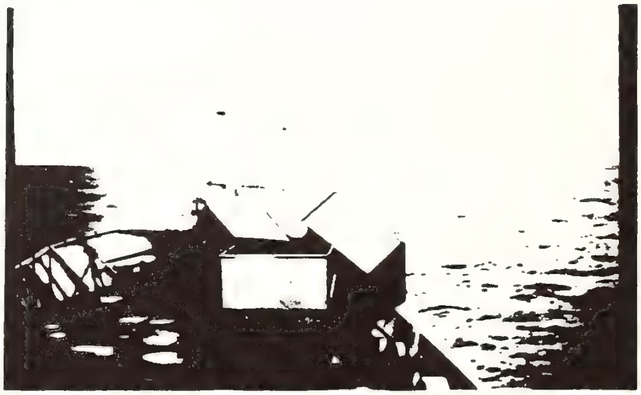

Figure 1. Echo sounder antennas mounted in the bow of the ship

3. EXPERIMENTAL RESULTS

To date only facsimile-recorded echo intensity data have been analyzed. These records proved to be useful for studying different aspects of the boundary layer up to and including the subcloud transition layer. Garstang and Betts (1974) present an up-to-date review of the structure of the tropical boundary layer.

Figure 2 shows typical time-height echo intensity data taken during undisturbed weather conditions. In the figure, darker regions indicate strong scattering while white areas correspond to a lack of scatter. To compensate for the geometrical spreading of the acoustic beam, a gain ramp was incorporated in the receiver circuit (Simmons et al., 1971). A gradual darkening of the record with height resulted from amplification of the received ambient background noise by the gain ramp. The dark, spiky traces extending from the bottom of the record to 200-300 m height were caused by convective plumes rising from the surface of the water. Because undisturbed weather conditions prevailed most of the time in the GATE area, plumes like those shown in Figure 2 were observed during a large percentage of the time. In general, these plumes had characteristics similar to the ones recorded over dry land (Hall et al., 1975). For example, assuming that the plumes were advected by the 4.5 m s^{-1} mean wind, we estimated their along-the-wind dimension from Figure 2 to be between 200 and 500 m near the surface. Measurement of the Doppler frequency shift of the returns indicated that typical updraft velocities were about 1 m s^{-1} within the plumes. No obvious upwind or downwind plume tilts were noted during GATE, however. Also, the usual dry-land diurnal pattern (convective plumes during the day, more stable, layered structures at night) was not seen in the marine environment, because here the energy input was controlled by the sea-air temperature difference; generally plumes formed as long as this quantity remained positive. There were numerous occasions during GATE when plumes were observed 24 hours a day for several consecutive days.

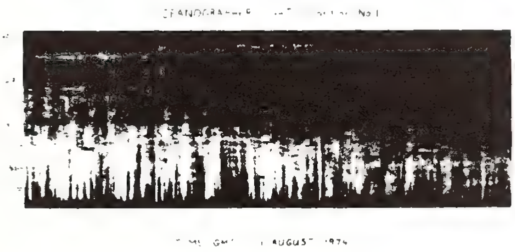

Figure 2. Facsimile record of echo intensity during undisturbed conditions

Figure 2 also shows patchy returns from the subcloud transition layer located between 400 and 700 m. Frequently, these returns were quite weak or entirely absent, indicating the low level of turbulence associated with this nominally stable layer or the total absence of the layer itself. When present, these returns conveniently delineated the vertical extent of the mixed layer. The pronounced dark horizontal traces at 780, 740, 590, and 400 m were caused by reflections from the Boundary Layer Instrumentation System (BLIS) balloon and three of its sondes. Echoes of this kind were used to determine accurately the height of the BLIS sondes.

Using estimates of the sensible heat flux over the tropical ocean, we calculated the expected intensity of acoustic returns. The results shown in Figure 2 and most of the data obtained during undisturbed time periods indicated return strengths that were in close agreement with the predicted values.

Under disturbed, enhanced convective conditions, substantial changes take place in the structure of the tropical marine boundary layer (Garstang and Betts, 1974). The destruction of the trade-wind inversion and cloud-induced mixing can result in the direct coupling of sea surface processes with the high troposphere. Furthermore, in some areas the subcloud layer may become quite stable. Figure 3 illustrates a typical situation three hours after the passage of an intense squall line. A low-level, very strong inversion formed which limited the depth of the mixed layer. For example, at 1725 the top of the mixed layer was at only about 100 m. Because of the increase in mechanical turbulence, plume activity subsided considerably. The subsidence event around 1800 reinforced the inversion and waves with over 100 m amplitude are seen near the end of the record. The significance of strong inversions such as the one shown in Figure 3 is that they produced a barrier to the vertical transport of latent and sensible heat. Consequently, no new disturbances were expected to develop until after the inversion has weakened and lifted. In this particular case it took about 12 hours for the inversion to rise and plume activity to resume. Figure 4 shows the inversion ascending from 300 to 600 m. Wind-shear induced breaking waves can be seen on the inversion layer from about midnight until the end of the record.

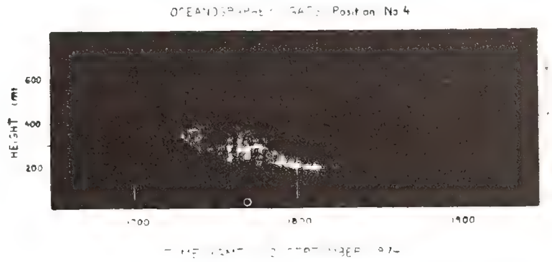

Figure 3. Facsimile record of echo intensity during disturbed conditions

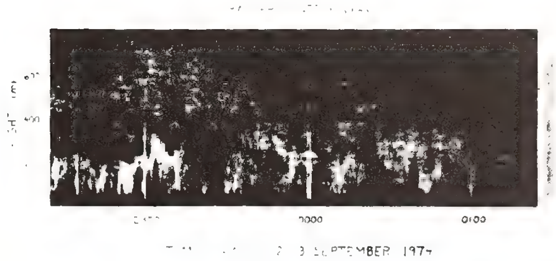

Figure 4. Facsimile record of echo intensity during transition from disturbed to undisturbed conditions

The effects of a less-intense disturbance are shown in Figure 5. At the beginning of the record plumes characteristic of undisturbed conditions are seen. Suddenly, at 2213 the intensity and height of the echo returns increased substantially as a result of cold air outflow from a nearby storm. Again, a low-level, multi-layered, undulating inversion formed which persisted for about six hours. Plume activity gradually built back up to the usual 300 m height level during this period.

Comparison of acoustic facsimile recordings with BLIS-measured meteorological data provided valuable insights into processes taking place in the boundary layer. For example, simultaneous observations of an inversion layer with the echo sounder and BLIS verified that warmer, less-moist air existed above the inversion than was found just below it. The sounder records provided ready explanation for changes in meteorological variables when the sondes made multiple passes through undulating inversion layers in the profiling mode. BLIS wet-bulb and dry-bulb temperatures and wind velocities closely correlated with patchy returns indicated by the sounder such as those seen in Figure 2.

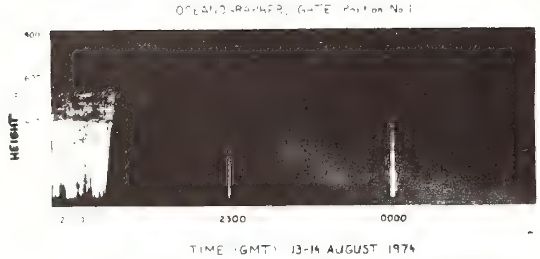

Figure 5. Facsimile record of echo intensity at the onset of disturbed conditions

4. CONCLUSIONS

In spite of the severe limitations imposed by the high ambient noise level of the ship, the acoustic echo sounder proved to be a unique and valuable tool for investigating the structure of the tropical marine boundary layer. The echo sounder records vividly depicted changes in the boundary layer caused by mesoscale phenomena such as squall lines and showers. Future, detailed quantitative data analysis will include the determination of wind velocity profiles, the intensity of mechanical turbulence and temperature variations, and surface heat flux.

5. REFERENCES

Beran, D. W., 1974: Remote sensing wind and wind shear system. Interim Rept., Systems Research and Development Service, Federal Aviation Administration, Dept. of Transportation, Rept. No. FAA-RD-74-3, available from NTIS, Springfield, Virginia 22151, 115 pp.

Garstang, M., and A. K. Betts, 1974: A review of the tropical boundary layer and cumulus convection; structure, parameterization, and modeling. Bull. Amer. Meteor. Soc., 55, 1195-1205.

Hall, F. F. Jr., 1972: Temperature and wind structure studies by acoustic echo-sounding. Remote Sensing of the Troposphere, V. E. Derr, Ed., U. S. Dept. of Commerce, Superintendent of Documents, U. S. Government Printing Office, Washington, D. C. 20402.

Hall, F. F. Jr., J. G. Edinger, and W. D. Neff, 1975: Convective plumes in the planetary boundary layer, investigated with an acoustic echo sounder. (to be published in J. Appl. Meteor.).

Ottersten, H., M. Hurtig, G. Stilke, B. Brümmer, and G. Peters, 1974: Shipborne sodar measurements during JONSWAP II. (to be published in J. Geophys. Res.).

Simmons, W. R., J. W. Wescott, and F. F. Hall, Jr., 1971: Acoustic echo sounding as related to air pollution in urban environments. NOAA Tech. Rept. ERL 216-WPL 17, U. S. Dept. of Commerce, Superintendent of Documents, U. S. Government Printing Office, Washington, D. C. 20402, 77 pp.

Strand, O. N., 1971: Numerical study of the gain pattern of a shielded acoustic antenna. J. Acous. Soc. Amer., 49, 1698-1703.

Journal of Applied Meteorology 14, 1110-1117, September 1975.

Observations of the Marine Atmosphere Using a Ship-Mounted Acoustic Echo Sounder

P. A. Mandics and E. J. Owens

Wave Propagation Laboratory, NOAA Environmental Research Laboratories, Boulder, Colo. 80302

(Manuscript received 27 June 1974, in revised form 6 March 1975)

ABSTRACT

A monostatic acoustic echo sounder with a vertically-pointed antenna was installed aboard the NOAA research vessel *Oceanographer* and was tested during a recent cruise in the Pacific and Caribbean Oceans. Acoustic returns produced by turbulence-induced temperature fluctuations were received from up to 300 m in height. The data revealed the existence of a rich variety in the structure of the marine atmosphere. Thermal convective plumes were usually observed when the sea water temperature exceeded the air temperature by as little as 1°C. Under more stable conditions the echo sounder detected the presence of layered structures associated with temperature inversions that were often perturbed by gravity waves or wind shear. Doppler frequency shift of the returned echo signals was used to estimate the vertical velocity of atmospheric scatterers.

The results of the tests indicate that it is possible to probe remotely the lower layers of the marine atmosphere from a moving ship using acoustic echo sounding techniques. Wind-generated noise, ambient acoustic noise, and structure-borne vibrations proved to be the major limitations on the performance of the echo sounder.

1. Introduction

The strong interaction of acoustic waves with the turbulent atmosphere makes it possible to exploit the scattering of sound waves to probe the atmospheric structure remotely. McAllister (1968) and McAllister *et al.* (1969) demonstrated the feasibility of acoustic echo sounding, and Little (1969) analyzed various methods for remote acoustic probing. Numerous improvements during the past few years resulted in highly sophisticated systems which made it possible, among other things, to observe atmospheric waves in the boundary layer (Hooke *et al.*, 1973) and to monitor atmospheric stability (Wyckoff *et al.*, 1973). Recently, Beran *et al.* (1971), Beran and Clifford (1972) and Beran (1974) have demonstrated that the Doppler frequency shift of the returned acoustic echo may be used to measure wind velocity.

With the notable exception of the recent ship-based measurements made by Ottersten *et al.* (1974), all previous acoustic echo sounders have been operated over dry land. Because echo sounders of this kind have the potential to give an equally unique description of the marine atmosphere, a sounder was installed on the National Oceanic and Atmospheric Administration (NOAA) ship *Oceanographer* for the Global Atmospheric Research Program Atlantic Tropical Experiment (GATE). GATE is a large-scale international experiment aimed at studying cloud clusters and the transports of heat, water vapor and momentum in the tropical Atlantic off the West Coast of Africa during the summer of 1974. In addition to providing a description of the atmospheric structure, the system planned for GATE will also measure the wind velocity in the subcloud layer (below 600 m). Because of the limited size of the oceanic platform, monostatic sounder geometry will be used; the same antennas will serve for both transmission and reception. A cluster of three antennas, one pointed vertically and two others elevated at 45° and separated by 90° in azimuth, will be used to resolve the total wind vector. During a preliminary sea trial conducted in February 1974 a single, vertically-pointed antenna was installed onboard the *Oceanographer*. The following is a report on some of the results obtained during the cruise from Seattle, Wash., to Miami, Fla. First, we will discuss the scatter of sound waves in the marine atmosphere, and from this information we will estimate the expected maximum range of the acoustic system. After a brief description of the experimental apparatus, we will present and discuss a sampling of the preliminary results.

2. Scatter of sound in the ocean atmosphere

According to Batchelor (1957) and Monin (1962) acoustic backscattering is produced by irregularities in scalar atmospheric properties (temperature and humidity). The fraction of acoustic intensity, $d\sigma$, which is backscattered into a cone of solid angle $d\Omega$ per unit volume of temperature inhomogeneities, is given by

$$\frac{d\sigma}{d\Omega}=0.0075\lambda^{-\frac{1}{3}}\frac{{C_T}^2}{T^2}, \qquad (1)$$

where λ is the acoustic wavelength, C_T the temperature structure parameter (indicating the intensity of temperature variations), and T the mean absolute temperature. Eq. (1) indicates that the scattering is weakly dependent on the acoustic wavelength. Consequently, the optimum operating frequency is determined by a compromise between propagation losses and ambient background noise level. The former increase with increasing frequency while the latter decreases under the same condition.

Measurements of C_T over dry land under strong convective conditions yield $C_T \approx 0.25$ K m$^{-1/3}$ (Hall, 1972). For more stable conditions C_T may decrease by a factor of 10 or more. Because the sensible heat flux H is about an order of magnitude smaller over even the tropical oceans than over dry land (Lenschow, 1970; Holland, 1972), and because $C_T{}^2 \sim H^{4/3}$ for a given height in the free convective surface layer (Wyngaard *et al.*, 1971), we may conclude that $C_T \lesssim 0.05$ K m$^{-1/3}$ over the ocean. Direct measurements of C_T in a convective marine boundary layer indicate that this is a reasonable upper limit for C_T (Frisch and Ochs, 1975). For a typical probing frequency of 2 kHz ($\lambda \approx 0.17$ m) and $T = 293$ K, the backscattering cross section thus becomes $d\sigma/d\Omega \lesssim 4 \times 10^{-10}$ m^{-1}.

Moisture fluctuations are usually unimportant when operating a sounder over land. Because the latent heat flux can exceed the sensible heat flux by an order of magnitude over the tropical ocean (Holland, 1972), water vapor variations could produce a significant contribution in this case.

We may apply the radar equation (Skolnik, 1970) to a monostatic sounder to calculate the returned signal power as

$$P_R = P_T \eta^2 \left(\frac{D\lambda^2}{4\pi}\right) \frac{1}{R^2} \left(\frac{c\tau}{2}\right) \frac{d\sigma}{d\Omega} L, \qquad (2)$$

where P_T and P_R are the transmitted and received electrical signal powers, respectively, η is the efficiency of the transducer, D the directivity of the antenna, λ the acoustic wavelength, R the range to the scattering volume, c the speed of sound in air, τ the transmitted pulse duration, $d\sigma/d\Omega$ the scattering cross section per unit solid angle per unit volume, and L a loss term caused by atmospheric absorption which accounts for propagation losses to and from the scattering region. Although sound absorption in the atmosphere is a complicated function of frequency, temperature and humidity (Harris, 1966), we may take 0.01 dB m^{-1} as a reasonable value for $f = 2$ kHz at a temperature of 20°C and relative humidity of 40% or higher.

The ultimate success of an echo sounder depends on the signal-to-ambient-noise ratio of the returned signal. Alternately, we may inquire what the expected maximum range of the sounder is in a particular noise environment. Recent measurements onboard the NOAA ship *Discoverer* (sister ship of the *Oceanographer*) revealed that the airborne acoustic noise pressure spectrum level at 2 kHz is typically 22 dB relative to 20 μN m^{-2}. Following the technique of Simmons *et al.* (1971), we calculate that for commonly used acoustic antennas and transducers (antenna directivity $D = 400$; slide-lobe reduction of 55 dB between 70° and 90°; transducer efficiency $\eta = 0.1$) the received electrical noise power is $P_N = 4.4 \times 10^{-17}$ W Hz^{-1}.

For the above estimates of scattering cross section, received noise power, attenuation, sounder parameters of $P_T = 150$ W, $\eta = 0.1$, $D = 400$, $\lambda = 0.17$ m, $\tau = 50$ ms, receiver bandwidth 30 Hz, and received signal-to-noise ratio of 10 dB, we find from (2) that the maximum range is approximately 300 m. Under conditions of less intense scattering, the maximum range will be shorter and/or the received signal-to-noise ratio will be reduced. The above calculation shows that, in spite of the high ambient noise level of the ship, it should be possible to probe the lower layers of the maritime atmosphere using a ship-based acoustic echo sounder.

3. Experimental apparatus

The *Oceanographer* is the largest oceanographic survey ship in the NOAA fleet. The ship is 92 m long, 16 m wide, has a draft of 6 m, and displaces about 4000 tons. To reduce the incident ambient acoustic noise level to the minimum, the echo sounder antenna was located on the forward weather deck near the bow approximately 10 m above the water's surface. Fig. 1 shows the acoustic antenna mounted on its pedestal. Approximately 100 m length of cable connected the antenna/preamplifier unit with the rest of the electronics located aft in the Oceanographic Laboratory.

The echo sounder consisted of a 2 kHz signal source, power amplifier, transducer feeding a 1.2 m diameter parabolic dish antenna (Fig. 2) used for both transmission and reception, preamplifier, and a tuned narrowband receiver. Additional timing circuits were provided for generating the transmitted tone burst and for gating the receiver. The detected echo signal from the receiver was recorded on a facsimile recorder to provide a time vs height presentation of the scattering intensity. All the significant experimental parameters were also recorded on a multi-channel analog magnetic tape recorder for later digitization and quantitative computer analysis. Echo sounder components and electronic circuitry similar to that used in the present experiment were described in more detail by Simmons *et al.* (1971).

Because the ship pitches and rolls, a sound pulse transmitted from a fixed antenna in a given direction could return at a later time when the antenna is pointed in a new, and sufficiently different direction that the return echo signal would not be within the receiver beam pattern. To circumvent the above difficulty, the acoustic antenna was mounted on a pitch- and roll-stabilized platform, also shown in Fig. 1, capable of correcting for ±7° excursions in pitch and for ±30°

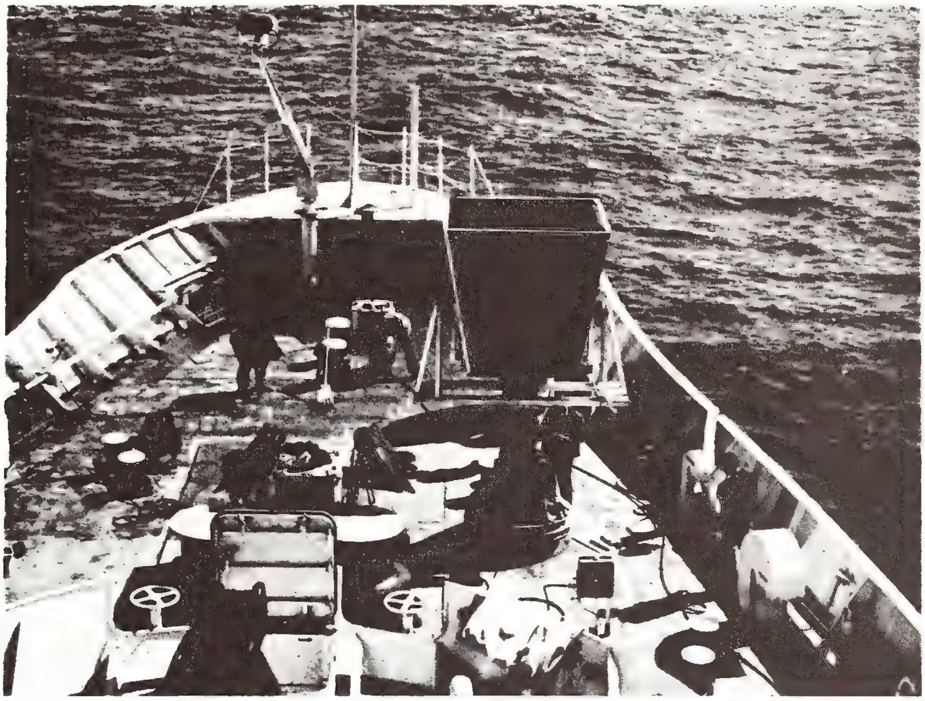

Fig. 1. View of the deck with the acoustic antenna mounted on its pedestal.

excursions in roll. In addition, the entire antenna assembly was mechanically decoupled from the ship's deck by placing it on top of a vibration isolator. The isolator was designed to provide for approximately 30 dB reduction in vibration-induced noise at 2 kHz.

To reduce the interference from airborne ambient

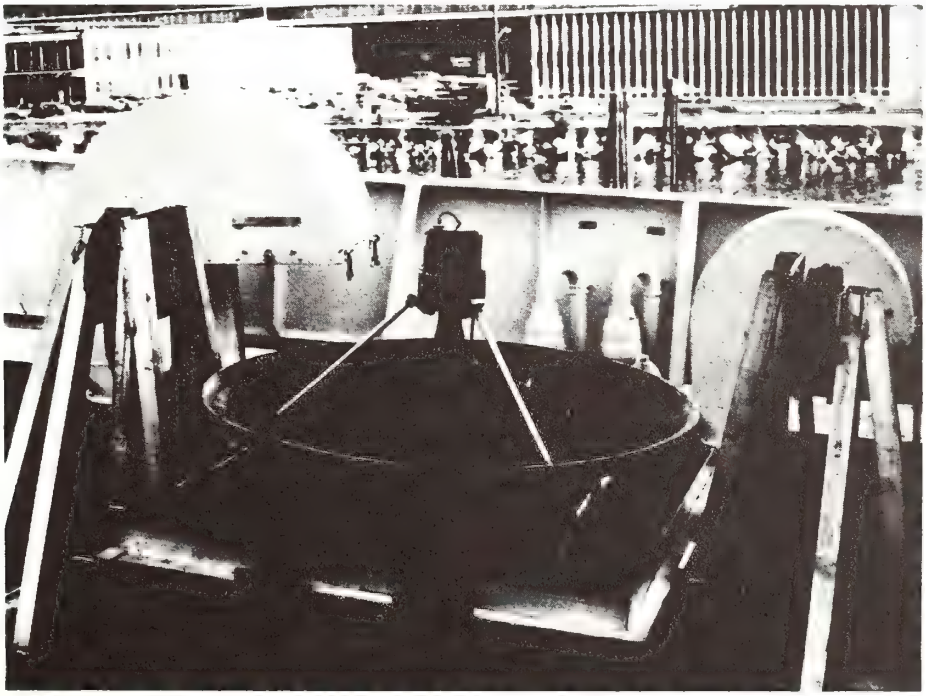

Fig. 2. Parabolic dish antenna, transducer, and feed horn without shield.

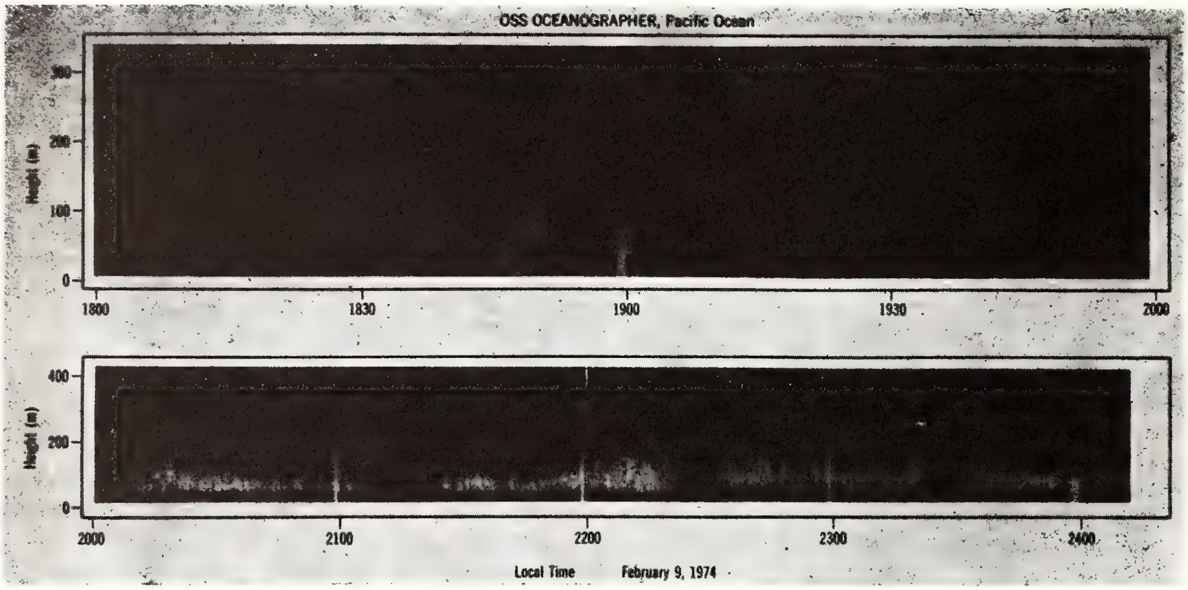

FIG. 3. Facsimile record of atmospheric structure taken with a vertically-pointed monostatic acoustic echo sounder. Ship is in the vicinity of 26°0′N, 115°30′W, approximately 140 km off the coast of Baja California.

noise and to keep the transmitted tone burst from annoying the ship's personnel, the dish antenna was placed inside a 1.8 m tall shielding cuff similar to the type discussed by Strand (1971). The cuff was made of four trapezoidal panels, 1.2 m wide at the bottom and flaring to 1.8 m at the top. For maximum strength and minimum weight, the panels and an additional bottom cover were constructed of corrugated paper sandwiched between thin layers of fiberglass. The inside of the cuff was lined with 6 cm thick convoluted polyurethane foam to provide additional sound absorption. Although no accurate beam pattern measurements were performed on the shielded antenna, it was estimated from the measured receiver noise power output that the side-lobe level between 70° and 90° was of the order of −55 dB relative to that of the main lobe.

4. Experimental results

Because of the schedule of the *Oceanographer*, essentially all the echo soundings had to be taken while the ship was steaming at full speed (8 m s^{-1}). This meant that in addition to the ambient noise produced by the ship's engines, the sounder had to contend with the wind-generated noise as well. Depending on the wind speed and direction, interference from this latter source of noise ranged from negligible to the point where sounding became impossible. Usually, good acoustic returns were obtained as long as the relative wind speed did not greatly exceed 12 m s^{-1}. In spite of these difficulties, acoustic echoes were received during a large percentage of the time when the sounder was in operation.

Only a very limited amount of *in-situ* meteorological data were gathered aboard the ship. Wind speed and direction were measured on the mast 30 m above the water using a Bendix Model 120 Aerovane system. Sea-surface temperature measurements were taken only every 6 h with the help of a mercury glass bucket thermometer. In-between water temperature values were obtained from a continuously-recording sensor located 4 m below the water line. The agreement between these two temperature measurements was usually 0.5°C or better. The air temperature was recorded once every hour on the bridge 12 m above the water using a mercury glass thermometer enclosed in an instrument shelter. Because of the inadequate instrumentation, we estimate that our determination of the sea-air temperature difference was accurate only to within ±0.5°C.

The echo sounder system was placed in operation shortly after leaving Seattle. The acoustic antenna and shield were assembled and were at first placed directly on the deck. No acoustic returns were observed, however, because the received noise level was exceedingly high. Echo sounding became possible only after the antenna was mounted on the vibration-isolated stable platform which resulted in a significant reduction in the received noise level.

Fig. 3 illustrates a 6 h altitude vs time facsimile record of the intensity of acoustic scattering taken off the coast of Baja California. The following sounder parameters were used: transmitted frequency $f = 2$ kHz, transmitted electrical acoustic peak pulse power $P_T = 100$ W, pulse duration $\tau = 50$ ms, pulse repetition rate 2 s, and receiver bandwidth 30 Hz. At this frequency the half-power beamwidth of the antenna was

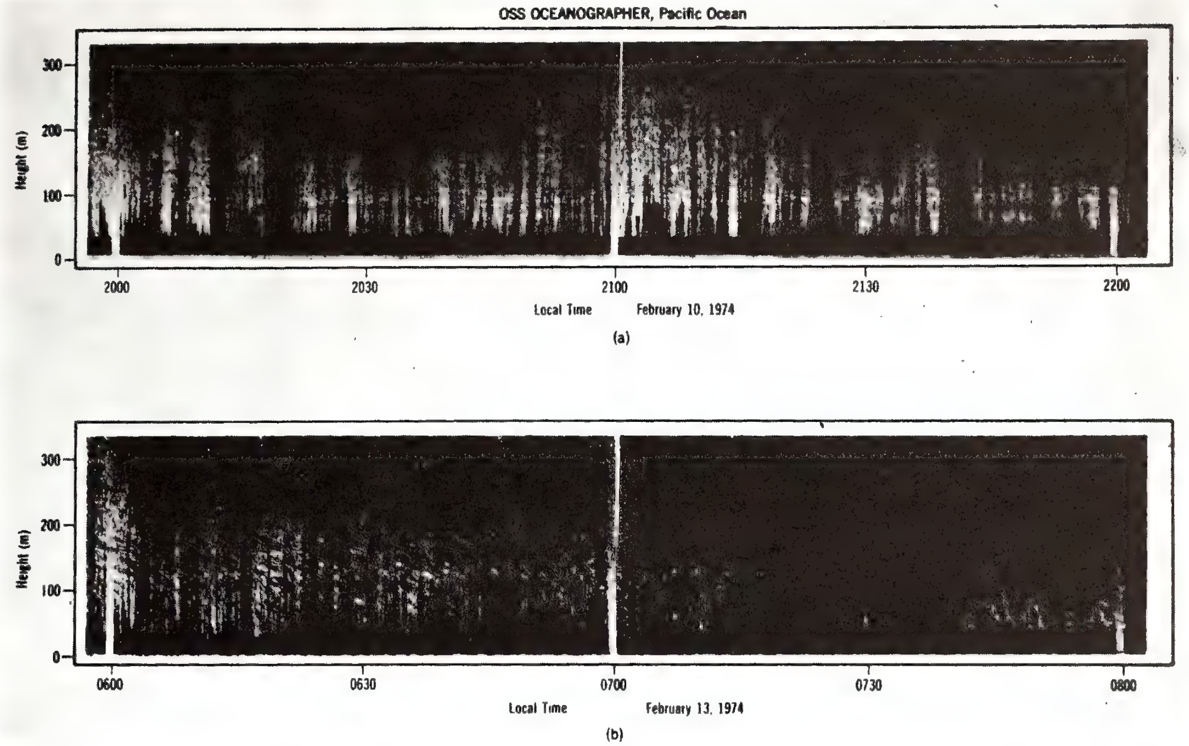

FIG. 4. Facsimile record of atmospheric structure taken with a vertically-pointed monostatic acoustic echo sounder: (a) in the vicinity of 22°10′N, 110°20′W, approximately 100 km off the southern tip of Baja California. (b) in the vicinity of 13°30′N, 97°0′W, approximately 260 km off Puerto Angel on the Mexican coast.

approximately 10° and the transducer efficiency was 10%. The darker regions in the figure correspond to more intense scattering, while the white areas indicate the lack of scatter. The ambient acoustic noise manifested itself as a uniform gray background which became progressively darker with increasing height because the receiver gain was varied inversely with range to compensate for the spreading of the acoustic beam. The transmitter was turned off for 1 min at the end of each hour to provide a time mark on the facsimile record. Because the receiver remained connected to the antenna, these 1 min periods also allowed for a qualitative, visual inspection of the received signal-to-noise ratio. Permanent echoes, apparently caused by the ship's superstructure and mast, were recorded as horizontal lines at 20 and 34 m. The "spiky" echoes seen in the early portion of the record were caused by convective thermal plumes rising from the surface of the water and are similar to such plumes observed in daytime over the land (McAllister *et al.*, 1969). Some of these thermals were tracked up to 150 m in height. During this time the air temperature was 15°C, the water temperature 16°C, and the true wind speed 4 m s^{-1}. At about 1900 the convection subsided considerably and an inversion layer started to form at 200 m. Correspondingly, the sea-air temperature difference decreased and the true wind speed gradually increased to 7 m s^{-1}. Wind-shear induced fluctuations of the layer, which at times reached 200 m in magnitude, are clearly visible from 1915 to 2000. At 2000 the 2 s sweep period was changed to 5 s which compressed both the height and time scales. Also, the transmitted power was increased from 100 to 150 W. One, sometimes two, undulating layers were observed for the next several hours. The finestructure seen near 100 m in the upper portion of the figure is caused by wrinkles in the recording paper and not by acoustic returns.

Fig. 4a shows thermal plumes ascending from the water's surface at night. In this case the air temperature was 20°C, the water temperature was approximately 1°C higher, and the true wind speed varied between 1 and 3 m s^{-1}. Strong convection persisted until next morning when the sounder had to be turned off because of interference from routine ship maintenance. Occasionally, a capping inversion was also detected at the top of the convective layer, as can be seen between 2120 and 2130.

Another interesting situation is depicted in Fig. 4b. After intense convection all night long, a temperature-inversion layer developed at 150 m around 0700. The convection entirely ceased by 0740. The sea-air tem-

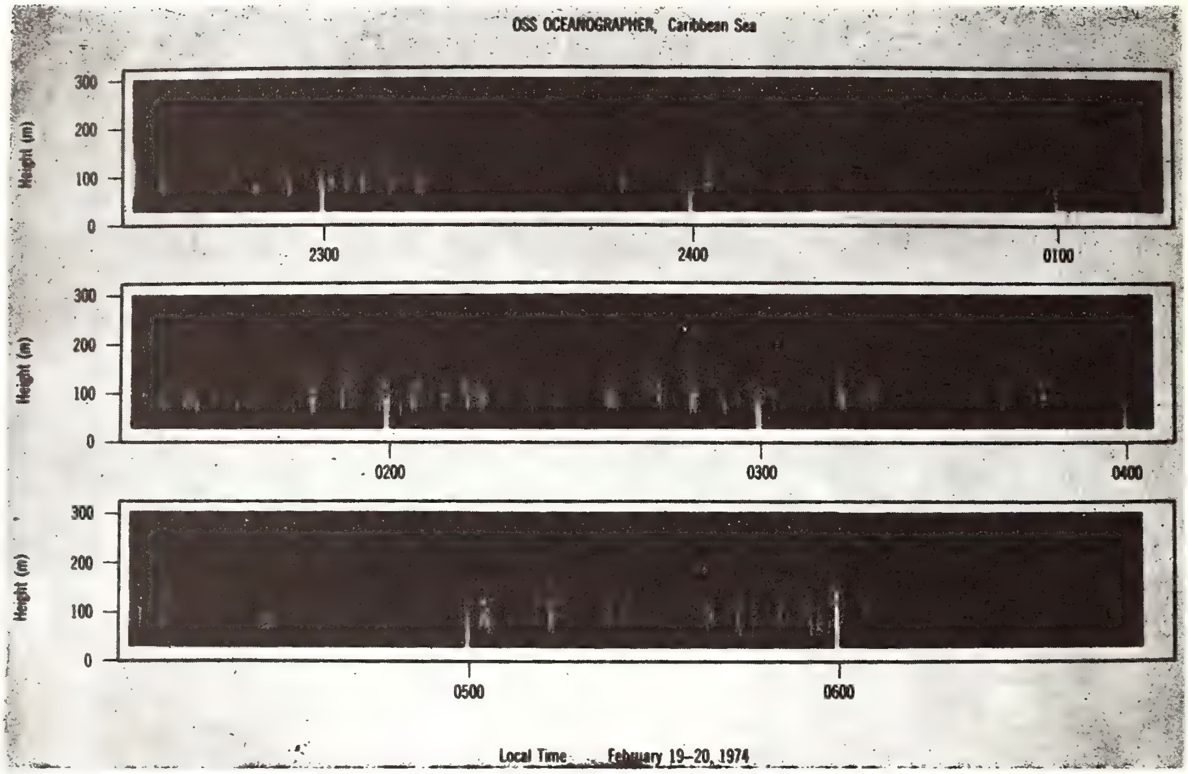

FIG. 5. Facsimile record of atmospheric structure taken with a vertically-pointed monostatic acoustic echo sounder. Ship is in the vicinity of 21°25′N, 85°20′W, near Cuba.

perature difference remained fairly constant at around +2°C throughout the entire period even though the air temperature gradually decreased from 26 to 23°C. The true wind speed increased from 2 to 5 m s^{-1} around 0700. The same sounder settings were used here as in Fig. 3, except that the transmitted power was kept at 150 W and the pulse repetition rate was 2 s for both portions of Fig. 4.

A longer record of nighttime convection is shown in Fig. 5. For these tests the dish antenna was replaced by a square array consisting of one hundred 0.12 m square horns fed by 25 drivers. The main advantage of the array antenna was that it allowed for a higher power input; in this case $P_T = 800$ W. All the other system parameters were the same as before. Relatively strong convective activity was observed throughout the night even though the sea-air temperature difference was $\leqslant +1$°C. The sea-water temperature was 25°C and the true wind speed varied between 6 and 8 m s^{-1}.

Fig. 6 illustrates the intensity of the acoustic echoes and the corresponding vertical velocity field inferred from the Doppler frequency shift of the returns during a convective period. The sea water and air temperatures were both near 26°C and the true wind speed was 7 m s^{-1}. Again, the array antenna was used with $P_T = 800$ W. In the velocity record, white regions indicate an updraft of 1 m s^{-1} (or greater) and black ones correspond to a downdraft of 1 m s^{-1} (or greater). Velocity values that fall between ± 1 m s^{-1} are depicted by intermediate shadings of gray; zero velocity is represented by neutral gray. Although the facsimile record gives only a rough, qualitative idea of the vertical velocity field, it is clear that thermal plumes are associated with ascending parcels of air. Sinking air motion was detected near the edges of and between plumes and occasionally within plumes. The velocity data were contaminated by the ship's pitching motion; however, at the location of the acoustic antenna, this velocity error did not exceed ± 0.4 m s^{-1} during the period shown in Fig. 6.

5. Conclusions

Although the high ambient noise environment of the ship placed severe limitations on the performance of the echo sounder, we have demonstrated that it is possible to obtain acoustic returns from up to 300 m in height using a moving ship as the antenna platform. The variety of phenomena observed (thermal plumes, undulating layers, etc.) indicates that the atmosphere over the ocean is quite rich in structural detail. We feel that echo sounders of this type could become valuable tools for remotely probing the lower layers of the marine atmosphere.

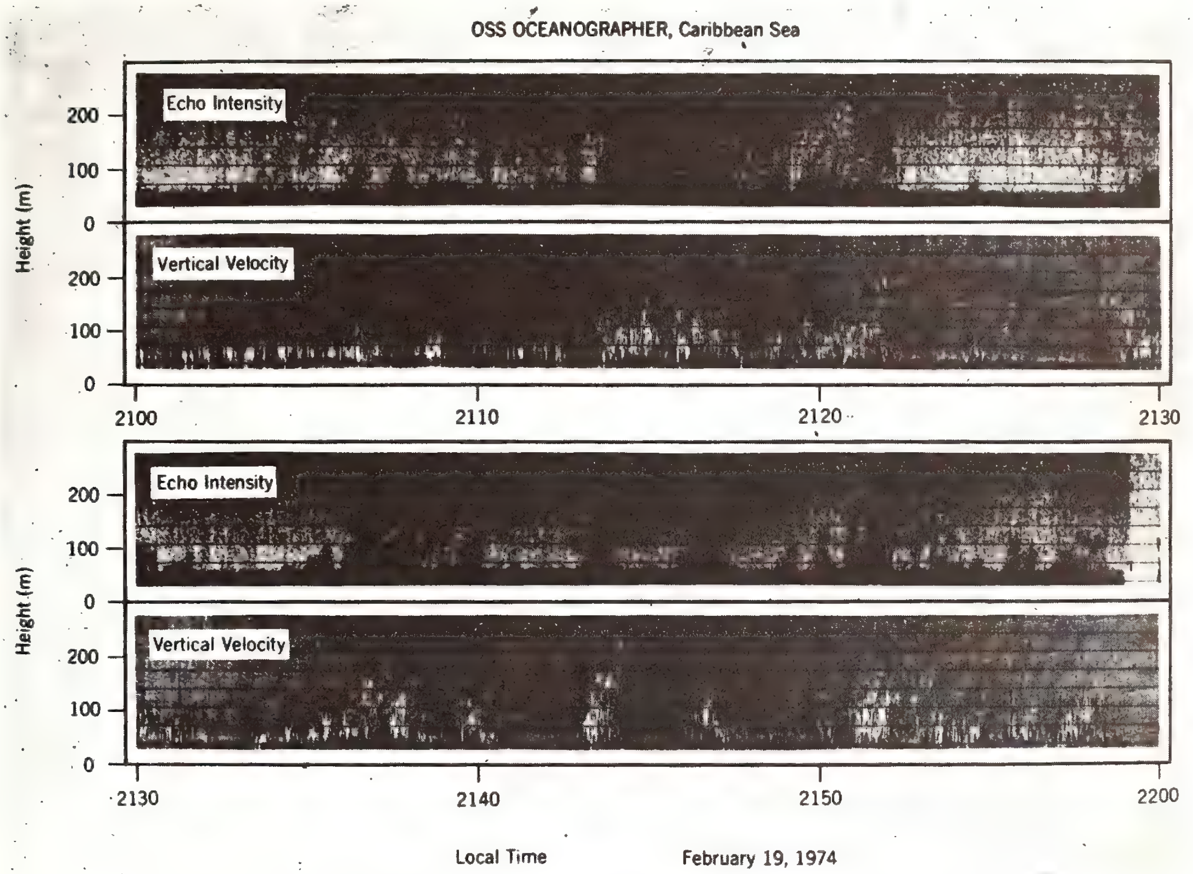

FIG. 6. Facsimile record of the intensity of scattering and vertical velocity field. Ship is in the vicinity of 20°28′N, 84°19′W, approximately 120 km south of Cuba.

The maximum range achieved was near to that estimated earlier in the paper. Not too much significance should be attached to this fact because of the uncertainties involved in estimating several important parameters used in the calculations.

The lack of more detailed meteorological data made the interpretation of the acoustic records subjective. Nevertheless, a clear and predictable pattern emerged; whenever the sea water temperature exceeded that of the air by as little as 1°C, thermal convective plumes were usually observed. The Doppler frequency shift produced by the scatterers allowed the determination of the vertical velocities associated with the plumes. The acoustic returns showed layered structure, indicating more stable stratification, when the water temperature was less than the air temperature.

The importance of mechanically isolating the transducer from the ship's vibrations cannot be overemphasized. Because of the vibration-induced noise, no acoustic returns were observed at all when the antenna was attached directly to the deck. Similarly, we feel that the antenna shielding cuff significantly reduced the airborne acoustic noise and helped to minimize the wind-generated noise, as well.

During the cruise, seas were calm enough so that the roll and pitch motions of the ship seldom exceeded $\pm 10°$ and $\pm 3°$, respectively, and were usually considerably less. Most of the data were taken with the stable platform in the locked position. Consequently, we are not able to conclude whether the stabilization of the acoustic antenna improved the performance of the sounder or not, or whether pitch and roll compensation is even necessary.

Acknowledgments. The authors would like to thank Captain W. D. Barbee, the officers, and the crew of the *Oceanographer* for their cooperation during the testing of the acoustic echo sounder. Mr. B. C. Willmarth's help with the Doppler frequency analysis of the data and the assistance given by Messrs. R. W. Krinks and L. A. Vohs during various phases of the experimental program are gratefully acknowledged. Messrs. K. B. Earnshaw, T. L. Wilson and Dr. D. W. Beran provided valuable help in the design and construction of the antenna shield and support structure. The advice and encouragement of Dr. F. F. Hall, Jr., is sincerely appreciated.

REFERENCES

Batchelor, G. K., 1957: Wave scattering due to turbulence. *Proc. Symp. Naval Hydrodynamics*, F. S. Sherman, Ed., NAS-NRC Publ. No. 515, 409–430.

Beran, D. W., 1974: Remote sensing wind and wind shear system. Rept. No. FAA-RD-74-3 [National Technical Information Service, Springfield, Va.], 115 pp.

——, and S. F. Clifford, 1972: Acoustic Doppler measurements of the total wind vector. *Preprints Second Symp. Meteorological Observations and Instrumentation*, Amer. Meteor. Soc., 100–109.

——, C. G. Little and B. C. Willmarth, 1971: Acoustic Doppler measurements of vertical velocities in the atmosphere. *Nature*, **230**, 160–162.

Frisch, A. S., and G. R. Ochs, 1975: A note on the behavior of the temperature structure parameter in a convective layer capped by a marine inversion. *J. Appl. Meteor.* (in press).

Hall, F. F., Jr., 1972: Temperature and wind structure studies by acoustic echo sounding. *Remote Sensing of the Troposphere*, V. E. Derr, Ed., Govt. Printing Office, Washington, D. C.

Harris, C. M., 1966: Absorption of sound in air versus humidity and temperature. *J. Acoust. Soc. Amer.*, **40**, 148–159.

Holland, J. Z., 1972: Comparative evaluation of some BOMEX measurements of sea surface evaporation, energy flux and stress. *J. Phys. Oceanogr.*, **2**, 476–486.

Hooke, W. H., F. F. Hall, Jr., and E. E. Gossard, 1973: Observed generation of an atmospheric gravity wave by shear instability in the mean flow of the planetary boundary layer. *Boundary-Layer Meteor.*, **5**, 29–41.

Lenschow, D. H., 1970: Airplane measurements of planetary boundary layer structure. *J. Appl. Meteor.*, **9**, 874–884.

Little, C. G., 1969: Acoustic methods for the remote probing of the lower atmosphere. *Proc. IEEE*, **57**, 571–578.

McAllister, L. G., 1968: Acoustic sounding of the lower troposphere. *J. Atmos. Terr. Phys.*, **30**, 1439–1440.

——, J. R. Pollard, A. R. Mahoney and P. J. R. Shaw, 1969: Acoustic sounding—A new approach to the study of atmospheric structure. *Proc. IEEE*, **57**, 579–587.

Monin, A. S., 1962: Characteristics of the scattering of sound in a turbulent atmosphere. *Akust. Zh.*, **7**, 457–461 [*Sov. Phys. Acoust.*, **7**, 370–373].

Ottersten, H., M. Hurtig, G. Stilke, B. Brümmer and G. Peters, 1974: Shipborne sodar measurements during Jonswap 2. *J. Geophys. Res.*, **79**, 5573–5584.

Simmons, W. R., J. W. Wescott and F. F. Hall, Jr., 1971: Acoustic echo sounding as related to air pollution in urban environments. NOAA Tech. Rept. ERL 216-WPL 17, Govt. Printing Office, Washington, D. C., 77 pp.

Skolnik, M. I., Ed., 1970: *Radar Handbook*. McGraw-Hill.

Strand, O. N., 1971: Numerical study of the gain pattern of a shielded acoustic antenna. *J. Acoust. Soc. Amer.*, **49**, 1698–1703.

Wyckoff, R. J., D. W. Beran and F. F. Hall, Jr., 1973: A comparison of the low-level radiosonde and the acoustic echo sounder for monitoring atmospheric stability. *J. Appl. Meteor.*, **12**, 1196–1204.

Wyngaard, J. C., Y. Izumi and S. A. Collins, Jr., 1971: Behavior of the refractive-index-structure parameter near the ground. *J. Opt. Soc. Amer.*, **61**, 1646–1650.

Gate Report No. 14, Preliminary Scientific Results,
Vol. 11, World Meteorological Organization, 225-228, 1975.

Preliminary Results of Acoustic Echo Sounding of the Marine Boundary Layer During GATE

P. A. Mandics, F. F. Hall, Jr., and E. J. Owens

Wave Propagation Laboratory
NOAA Environmental Research Laboratories
Boulder, Colorado 80302

An acoustic echo sounder was installed aboard the NOAA Ship OCEANOGRAPHER to study the lower layers of the tropical marine atmosphere during GATE. A pitch- and roll-stabilized cluster of three antennas, one pointed vertically, the other two elevated at 45° above the horizontal and separated by 90° in azimuth was used. Acoustic backscattering produced by temperature inhomogeneities approximately of the size of one-half the acoustic wavelength ($\lambda/2 \approx 0.06$ m) provided information about the vertical structure of the atmosphere. Magnetic tape recordings of the Doppler-frequency-shifted acoustic returns along the three axes will be used during the subsequent data reduction to determine vertical profiles of wind velocity.

Facsimile recordings of the acoustic echo intensity showed that the undisturbed tropical atmosphere was characterized by convective plumes to heights of 300-400 m. In Figure 1b the dark, "spiky" traces extending to 200-300 m illustrate convective plumes during a typical suppressed period. Depending on the wind speed, the apparent size of plumes displayed by the facsimile records varied greatly. However, assuming that the plumes were translated by the mean horizontal wind, we found that plume dimensions at their bases were typically between 100 and 250 m in the downwind direction. Similar findings were observed in earlier acoustic experiments conducted over dry land. Acoustic returns from the trade inversion located between 450 and 800 m also were observed part of the time. Comparison of acoustic data with Boundary Layer Instrumentation System (BLIS) measurements provided ready interpretation for temperature and humidity changes registered by BLIS sensors when convective plumes penetrated a fixed BLIS sonde level. Although plumes invariably contained more moisture than the air surrounding them, the dry bulb temperature frequently decreased within plumes. Convective plumes were observed around the clock during a large percentage of the time through all three phases of GATE.

The sounder records vividly depicted changes in the atmospheric boundary layer caused by mesoscale phenomena such as squall lines and showers during disturbed conditions. Cold air outflow from storms frequently limited the mixed layer to depths of 100 m; the resultant stronger mechanical shear at times entirely eliminated the convective plumes. Slowly rising, undulating inversion layers followed these events and usually it took several hours for the mixed layer to re-establish itself to 500 m or greater depth. Figure 1a shows an example of a stably stratified boundary layer. The inversion layer capping the plumes rose from less than 100 m at 1020 to about 400 m at 1225. Also seen in the figure are heavy dark lines that were caused by strong acoustic returns from the BLIS balloon and its instrument package.

Two particularly intense squall lines with winds gusting over 35 kts passed over the ship on 11 and 12 September. In each case strong, low-level, multi-layered inversions formed which persisted for about 10-15 hours. The continuous facsimile recordings of these two events clearly illustrated the effects of this type of disturbance on the boundary layer; Kelvin-Helmholtz breaking waves and dramatic changes in inversion height were among the phenomena observed. BLIS profiles taken in stably stratified atmospheres often indicated substantial differences in parameters such as inversion height between ascents and descents separated by only 20 minutes. Simultaneously recorded acoustic data clearly showed the changes in atmospheric structure that were responsible for these differences.

During the February 1974 sea trial of a single channel of the acoustic echo sounder, we demonstrated that the Doppler frequency shift of the returns can be used to estimate vertical wind velocity. Figure 2 shows simultaneous facsimile recordings of the intensity of returns and Doppler-derived vertical velocity. In the velocity record, white regions indicate upward motions of 1 m s^{-1} and black ones correspond to downdrafts of equal magnitude. In-between velocity values are depicted by intermediate shadings of gray; zero velocity is represented by neutral gray. Although Figure 2 gives only a rough, qualitative picture of the velocity field, by comparing the echo intensity and vertical velocity records one may observe that plumes are associated with ascending parcels of air.' Sinking air motion was detected near the edges of and between plumes and occasionally within plumes. Monitoring of the acoustic returns during GATE indicated that good Doppler tracking was usually obtained to heights of 200 to 300 m. Subsequent computer analysis of the data should allow us to determine wind velocity profiles to these heights.

In summary, the acoustic echo sounder proved to be a unique and valuable tool for investigating the structure and dynamics of the tropical marine boundary layer. In addition to determining wind velocity, the acoustic data will be analyzed to obtain a quantitative measure of the intensity of mechanical turbulence and temperature variations, and a measure of the surface heat flux.

Figure Captions

1. Facsimile recordings of the intensity of acoustic scattering.
   (a) Stably stratified atmosphere with an undulating inversion layer.
   (b) Convective plumes during suppressed conditions.
   Ship is at Position #4, 8^{o} 30' N 23^{o} 30' W.

2. Facsimile recordings of the intensity of acoustic scattering and Doppler-determined vertical velocity field. Ship is in the vicinity of 20^{o} 28' N 84^{o} 19' W, approximately 120 km south of Cuba.

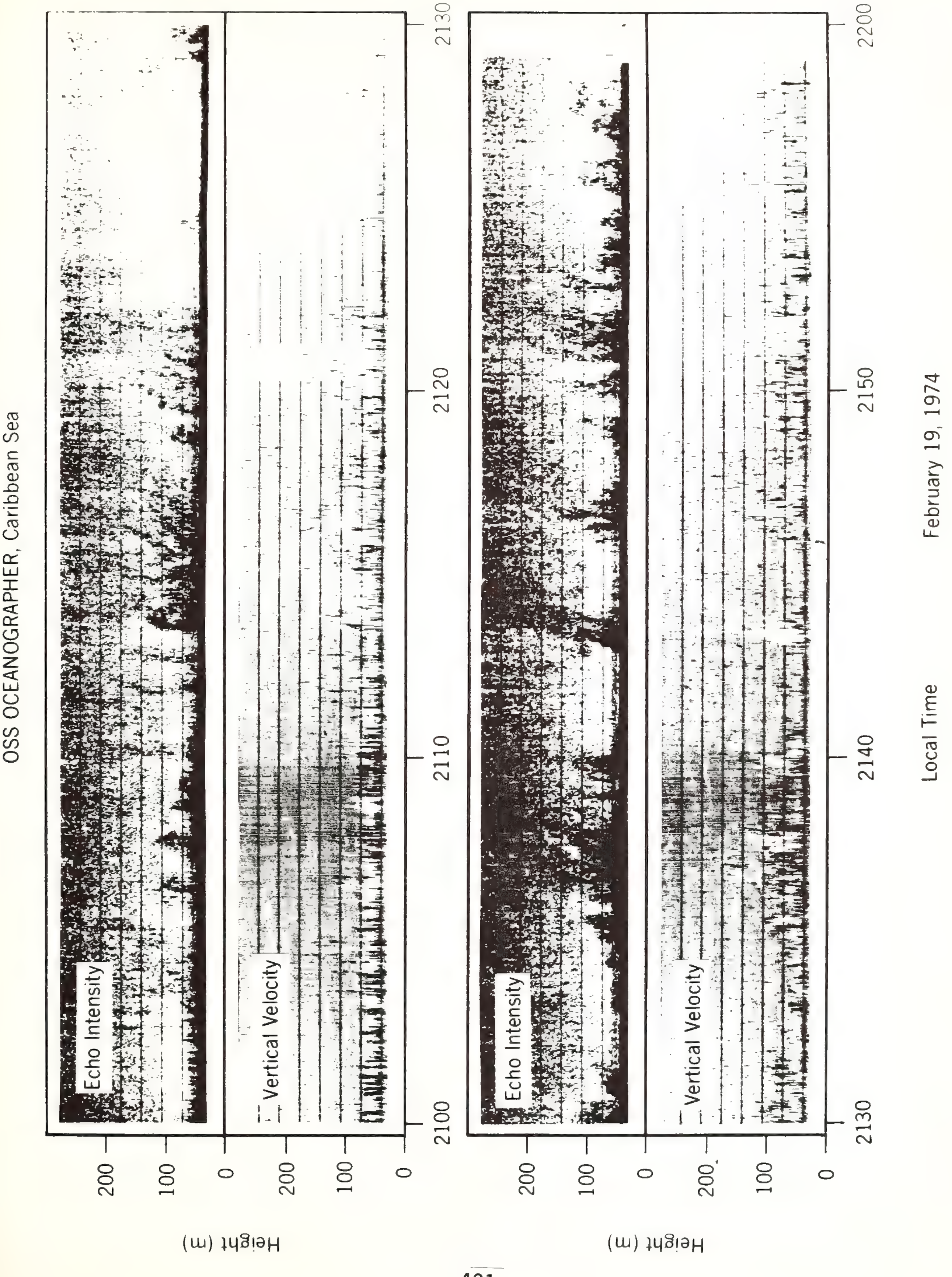
OSS OCEANOGRAPHER, Caribbean Sea
Echo Intensity
Vertical Velocity
Echo Intensity
Vertical Velocity
Height (m)
Height (m)
200
100
0
200
100
0
200
100
0
200
100
0
2100
2110
2120
2130
2130
2140
2150
2200
Local Time
February 19, 1974

OSS OCEANOGRAPHER, Atlantic Ocean

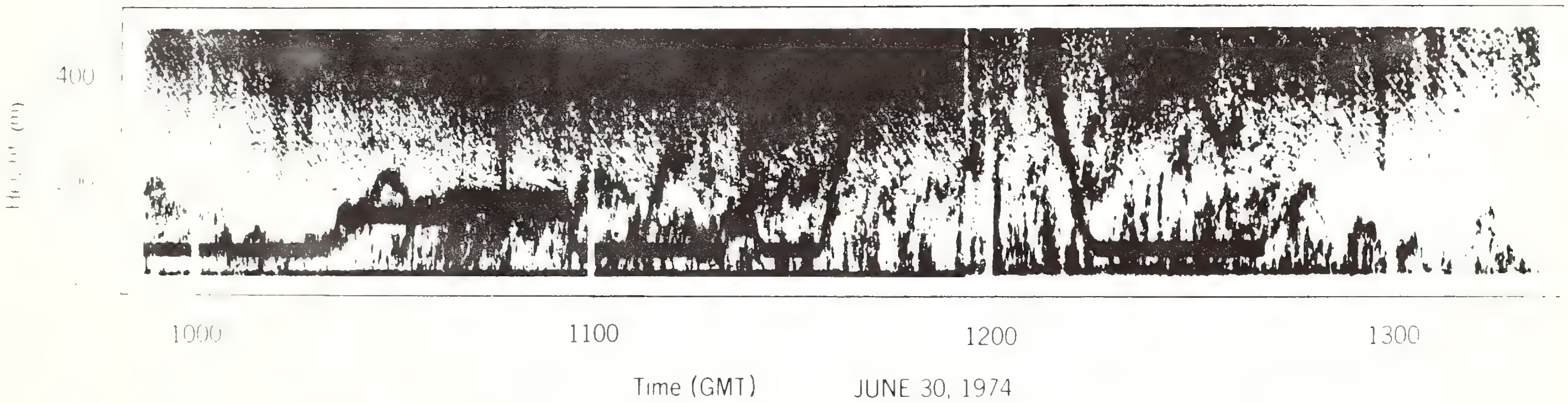

(a)

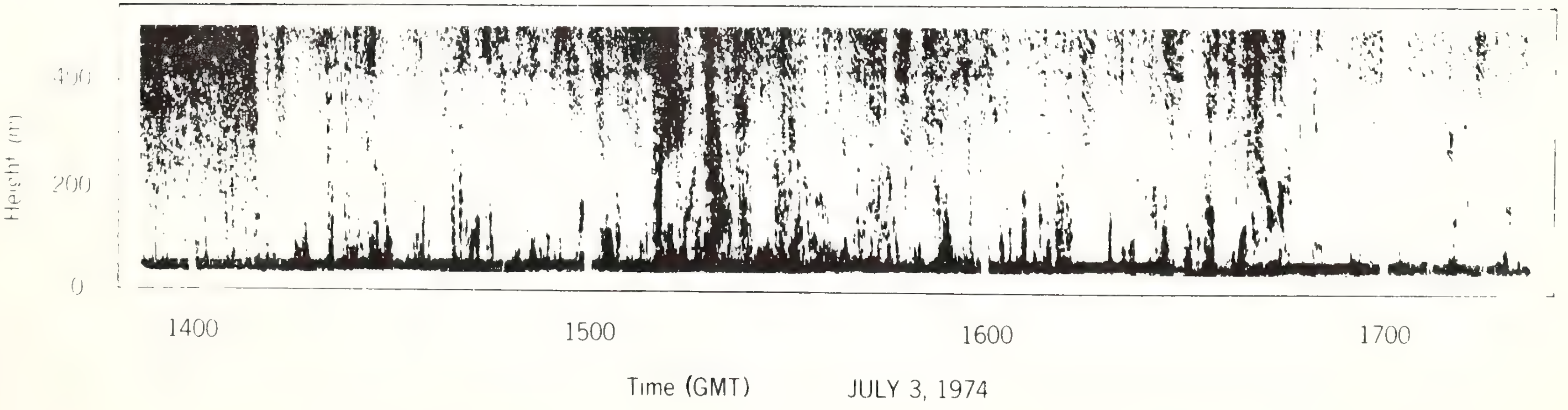

(b)

Proceedings of AMS Conference on Cloud Physics, 287-291, October 1974.

OBSERVATIONS OF A HAILSTORM WITH TWO DOPPLER RADARS

F. H. Merrem and R. G. Strauch
NOAA/ERL/Wave Propagation Laboratory
Boulder, Colorado 80302

1. INTRODUCTION

Vertical air motion fields in convective storms have been studied by both aircraft and zenith-pointing Doppler radars. Neither of these observation methods can depict the entire vertical air motion field, but both methods can add an important insight into the interpretation of the overall storm dynamics as well as microphysical processes inside the storm. The apparent structure of the storm observed by a zenith-pointing radar depends largely upon the location of the radar relative to the storm. Other information is required to determine the part of the storm that the radar observed. The detailed information contained in the zenith-pointing Doppler radar spectra can be used to deduce the drop size distribution and vertical air velocity (Atlas et al., 1973) for a particular volume of space, whereas the air velocity estimates for contiguous volumes, as a function of time, yields information on the overall dynamics of the storm as it advects overhead.

Two 3-cm mobile Doppler radars were used during the 1973 field program of the National Hail Research Experiment (NHRE) in Northeastern Colorado. These radars were operated as a dual Doppler system whenever storms were located in a region suitable for deducing three-dimensional wind fields. During the field program of NHRE several severe convective storms passed directly over one of the radars. Whenever this occurred one radar operated in a zenith-pointing mode while the other radar scanned an azimuth sector in a stepped elevation raster mode. Several hours of data of this type were obtained, including some cases in which hail fell at the location of the zenith-pointing radar.

2. THE 9 JULY OBSERVATIONS

On 9 July 1973, a hailstorm passed over the radar located at Raymer, Colorado. Kropfli and Miller (1974) summarized the environmental conditions for this storm and have presented data obtained by the dual Doppler method approximately one hour prior to the data obtained in the zenith-pointing mode. During the period 1725:55 to 1737:54 (MDT) vertical data were acquired by the Raymer radar while the second radar, located approximately 51 km north, was scanning the entire radar echo in azimuth sectors at elevation angles of 0 to 15 deg in 1 deg steps. Fig. 1 shows the 10-cm slant range radar reflectivity contours measured by the Grover radar for the start and end of the 3-cm radar observations. The echo motion is approximately south at 9 m sec^{-1} during this period.

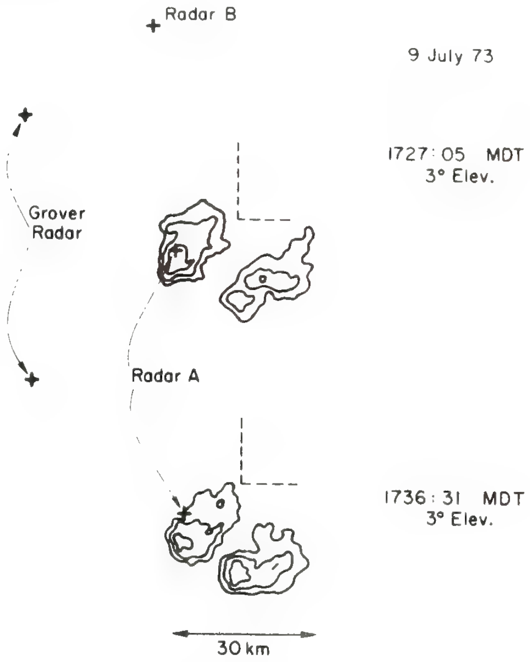

20, 30, 40, 50 dBz Contours

Figure 1. 10-cm reflectivity contours from Grover radar near start and end of 3-cm vertical observations. The slant range PPI's are taken near cloud base.

Hail fell at the ground immediately after the start of the observation period. The hail was pea sized, mixed with rain, with a few larger stones of up to 1.5 cm in diameter. Data were recorded by the raster scanning radar for 384 (16 azimuth x 24 range) radar resolution cells for each fixed elevation step. The sequence of elevation steps was repeated every 2.5 min. The zenith-pointing radar acquired data at 24 fixed height locations, and a spectrum was obtained for each height location at about 100 times per minute. One hundred twenty-eight radar samples were used for each Doppler spectrum with a dwell time of 0.065 sec. The radar beamwidth of 0.9 deg provided a horizontal resolution of less than 250 m at the maximum altitude. The radar height resolution was 75 m. The heights sampled were separated by 600 m during the period 1725:55 to 1728:05 with the lowest height gate centered at 400 m and the highest centered at 14.2 km. From 1728:05 to 1737:54 the height gates were spaced by 300 m, with the closest centered at 400 m and the highest at 7.5 km. The in-phase and quadrature video signals were recorded on digital magnetic tape for off-line computer analysis.

3. ANALYSIS PROCEDURE

The analysis of the digitized Doppler signals was performed on a CDC 3800 at NOAA/ERL (Boulder). The data were first analyzed using an FFT algorithm to obtain the power density spectrum, an estimate of the first and second moments of the spectrum, and an estimate of the average returned power. The vertical data were Fourier analyzed with a velocity interval of +8 to -24 m sec^{-1} (positive velocity is upwards). Since each data tape contained information for 10^4 Doppler spectra, automated methods of selecting the signal spectra from the signal plus noise were used. The results were examined to find any data points where the spectrum was folded or where the automated algorithms failed to properly select the signal spectrum. The data from the scanning radar were analyzed using methods developed for processing dual Doppler radar measurements.

The vertical air velocity, w, was estimated by correcting the measured mean Doppler particle velocity, V, for the fall velocity V_T, where V_T is an estimate of the mean Doppler velocity in still air. V_T was estimated using the empirical relation $V_T = 2.6\ Z^{0.107}$ of Joss and Waldvogel (1970) as suggested by Atlas, et al. (1973). It is readily seen that a simple equation involving only radar reflectivity is not strictly applicable because the radar scatterers are of a rain-hail mixture. The terminal velocities of hailstones can considerably exceed those of raindrops and will be dependent on the hailstone shape, size, and composition. In the case of rain alone, the V_T-Z relationship should yield estimates of w to within ± 1 m sec^{-1}. If hail is present the terminal velocity will be underestimated, resulting in an overestimation of downdrafts and an underestimation of updrafts.

Two-dimensional wind profiles above the zenith-pointing radar were obtained by combining the estimates of vertical air motion obtained by the zenith-pointing radar with radial velocity estimates from the scanning radar. The radial velocity estimates were corrected for the contribution of vertical air motion. In addition the scanning radar provided detailed radial velocities and reflectivity estimates for the major part of the storm echo.

4. RESULTS

The echo motion was in a southerly direction 9 m sec^{-1} during the observation period. From 1725 to 1727, when hail was observed at the ground, the echo tops were at about 13 km. Although the 10-cm radar (Fig. 1) showed the highest reflectivity regions had already passed the zenith-pointing radar, the 3-cm scanning radar (Fig. 2) showed the highest reflectivity region of the storm was just starting to pass the zenith-pointing radar. This discrepancy is probably due to the averaging of the 10-cm data which tends to shift the echo relative to the recorded azimuth angle. From 1727 to 1735 the height gates used did not extend to the echo top and the termination of the updraft was, unfortunately, not recorded.

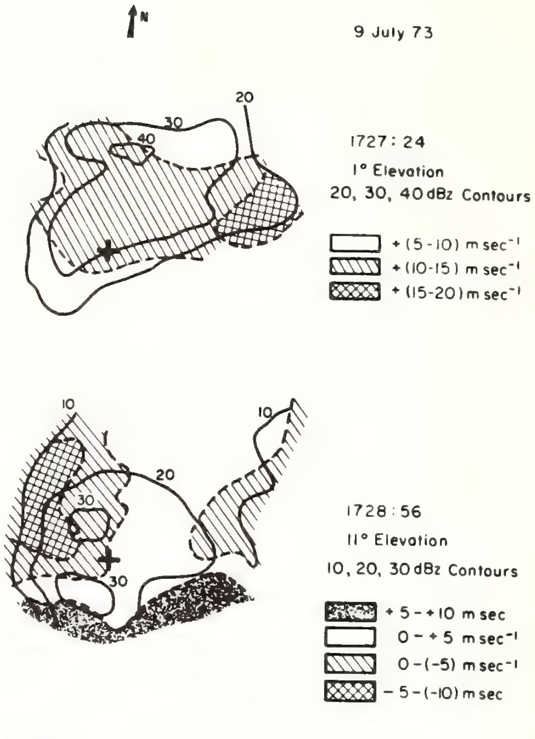

Figure 2. Reflectivity and radial velocity fields measured by 3-cm scanning radar. Upper illustration shows fields below cloud base and lower illustration shows fields at a mean altitude of 10 km (AGL).

Examples of vertical particle velocities recorded by the zenith-pointing radar are shown in Fig. 3. Sixty-four data points taken over a 40 sec interval while hail was observed are shown for 3 heights in Fig. 3a. In the upper trace moderate updrafts are observed with a particle velocity change of 6 m sec^{-1} occurring in 8 sec. If a frozen horizontal translation of 9 m sec^{-1} is assumed, the corresponding horizontal shear of the updraft is 8×10^{-2} sec^{-1}. The middle trace of Fig. 3a shows data from the high velocity gradient region generally between the updraft and downdraft. The lower trace shows data taken in the downdraft region. Fig. 3b shows data taken later in the observation period when only downdrafts were observed. The error bars denote the standard deviation of the radar estimates of mean velocity calculated from

$$\bar{\sigma}_V = \frac{\lambda\bar{\sigma}}{4T_D}\left(1 + \frac{1.6}{\rho} + \frac{3}{\rho^2}\right)$$

used by Lhermitte and Miller (1970) when T_D is the dwell time (0.065 sec), $\bar{\sigma}$ is the average standard deviation of the Doppler spectra and

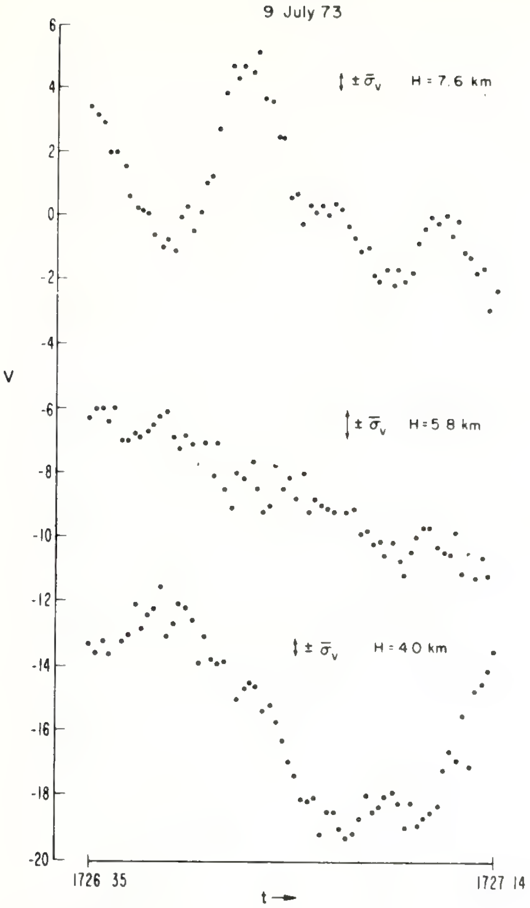

Figure 3a.

ρ is the signal-to-noise ratio. The data shown in Fig. 3 indicate that for these observations, a sampling rate of about 1 sample every 4 sec would be sufficient for meaningful temporal resolution.

Fig. 4 illustrates profiles of vertical particle velocity taken during the early (Fig. 4a) and later (Fig. 4b) parts of the observation period. Particle velocities as high as +12 m sec^{-1} (+ denotes upward) were measured. The strongest updrafts were sometimes observed in only 1 height gate. It is evident from these data that the spatial resolution of the data (600 m height spacing for the period 1725 to 1727) is not sufficient to adequately describe the velocity profile. A height sampling interval of about 150 m would be desirable. Also evident from these profiles is the importance of measuring the velocity profile to the top of the echo as some updraft regions were missed from 1728 to 1730.

Fig. 2 shows the radial velocity and reflectivity contours observed by the scanning 3-cm radar during the first part of the observation period. It should be noted that the scanning radar was observing velocity components generally

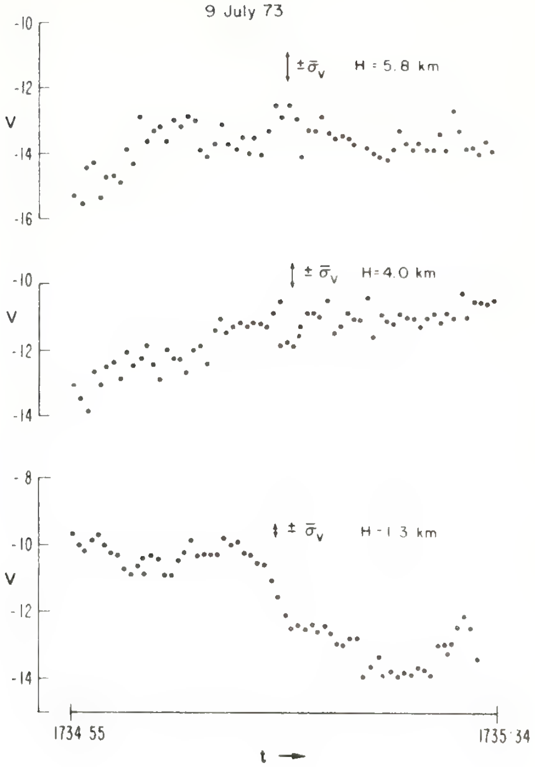

Figure 3b.

Figure 3. Vertical particle velocity samples, early (a) and late (b) in the observation period.

in the direction of the echo motion. In the low levels, 1 deg scan, the radial velocity fields from the scanning radar indicate significant differences from the flow patterns observed by Kropfli and Miller (1974) an hour earlier in other parts of the storm. The horizontal flow pattern, even though difficult to infer from a single radar, is generally opposite that observed by Kropfli and Miller, particularly in the SE region of the echo. When an echo motion of 9 m sec^{-1} is removed, the low level flow remains generally toward the south. This may be chiefly due to the influence of the cell 25 km SE of the storm being scanned. The 11 deg elevation scan shows the upper level contours in the updraft region (mean altitude of 10 km) and here the wind direction relative to the ground is northerly indicating that the tilt of the updraft is opposite to the direction of motion of the storm echo. The direction of the tilt is substantiated by Fig. 5 where two-dimensional wind vectors in a vertical plane through the two radars are shown. The tilt of the updrafts is toward the north while the low level winds are in the direction of the echo motion. The upper level flow has a strong northerly component relative to the echo motion. At 1731 the strongest downdrafts are observed in the trailing edge of the high reflectivity region.

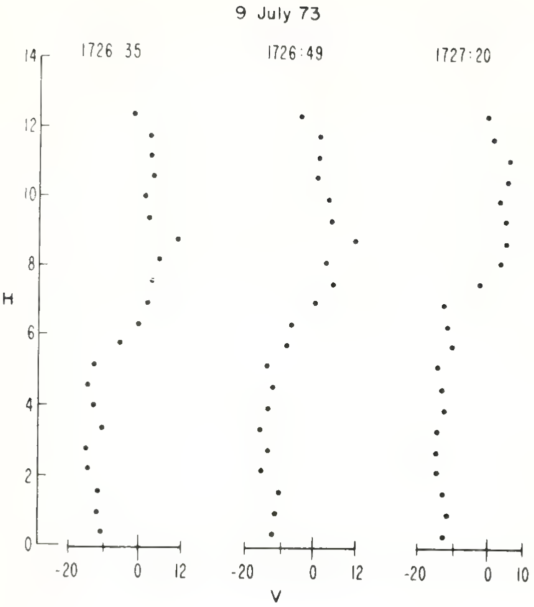

Figure 4a.

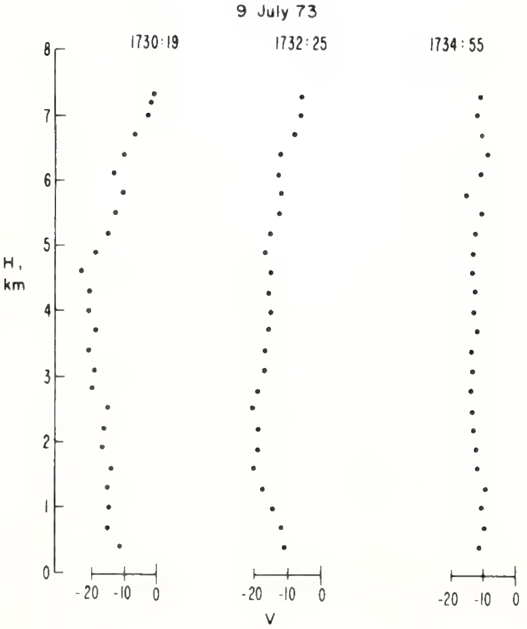

Figure 4b.

Figure 4. Vertical particle velocity profiles. (a) Profiles when strong updrafts were observed and (b) later in the observation period.

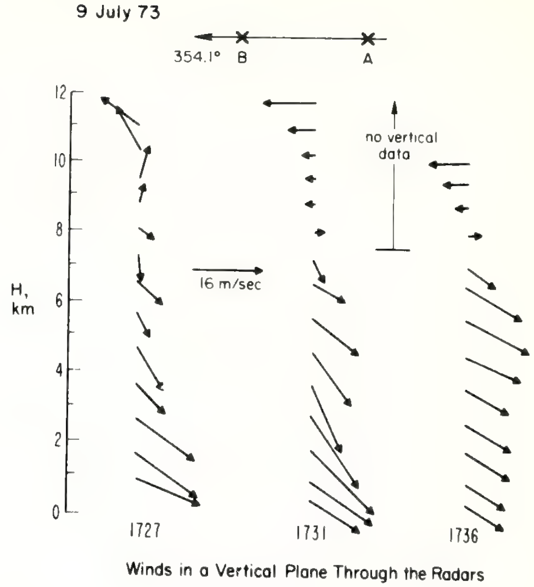

Figure 5. Two-dimensional wind profiles above the zenith-pointing radar taken in a vertical plane through the two radars.

Fig. 6 shows the estimated vertical wind structure during the observation period. No updrafts were measured below 5.6 km (AGL) although the data in 6a indicates the updraft region may extend below this altitude prior to the start of the observations. The highest updrafts occurred at 8-10 km (AGL) and were occurring at the start of observations. By 1728 the updrafts were diminishing, although at 1731 small updrafts were observed at 7.3 km. The slope of the 0 velocity contour in Fig. 6a, denoting the edge of the updraft region, also verifies that the tilt of the updraft is toward the north. If the updraft region is assumed advecting at 9 m sec^{-1} then the slope of the updraft is 70 deg from the horizontal. The largest downdrafts were observed when the updrafts were terminating and occur at the trailing edge of the low level high reflectivity region.

Both Doppler radars provided estimates of the variance of the velocity spectra. These data have not been analyzed in detail; however, the data confirm that a significant contribution to the variance of the spectra of the zenith-pointing radar is from the spread of fall velocities. The scanning radar, in spite of having much larger pulse volumes (and therefore greater shear contribution to the spectral width) measured smaller variances in the lower levels. In the upper levels the scanning radar observed high variance in the updraft regions. A horizontal shear of the updraft, as inferred from the data in Fig. 3a, would contribute a variance of about 16 m^2 sec^{-2} to the spectral width of the zenith-pointing radar. This value is typical of those observed.

5. SUMMARY

The height of the maximum updraft velocities observed was 9 km (AGL) and the updraft was tilted opposite the direction of echo motion.

Low level flow relative to the storm was in the direction of echo motion. Horizontal shear of the updraft as large as $8\text{x}10^{-2}$ was inferred. High spectral variance, observed in the region of strong updrafts, is being investigated.

The desired sampling rate for a zenith-pointing Doppler radar is about 1 velocity estimate every 4 sec. A height gate every 150 m from the minimum altitude to the top of the echo is needed. Data taking should commence as soon as the radar echo is observed to avoid missing the updrafts in the weak echo region. The combination of a dual Doppler system scanning in coplane over a zenith-pointing radar would greatly aid in the interpretation of storm dynamics.

REFERENCES

Atlas, D., R. C. Srivastava, and R. S. Sekhon, 1973: Doppler radar characteristics of precipitation at vertical incidence, Rev. Geophys. and Space Phys., 11(1), 1-35.

Joss, J. and A. Waldvogel, 1970: Raindrop size distribution and Doppler velocities, Preprint Vol., 14th Rad. Meteor. Conf., AMS, 153-156.

Kropfli, R. A. and L. J. Miller, 1974: Dual Doppler radar measurements within a hail producing storm in northeast Colorado, Preprints AMS Cloud Physics Conf., Tucson, Ariz., Oct. 1974.

Lhermitte, Roger M. and L. Jay Miller, 1970: Doppler radar methodology for the observation of convective storms, Preprint Vol., 14th Rad. Meteor. Conf., AMS, 133-138.

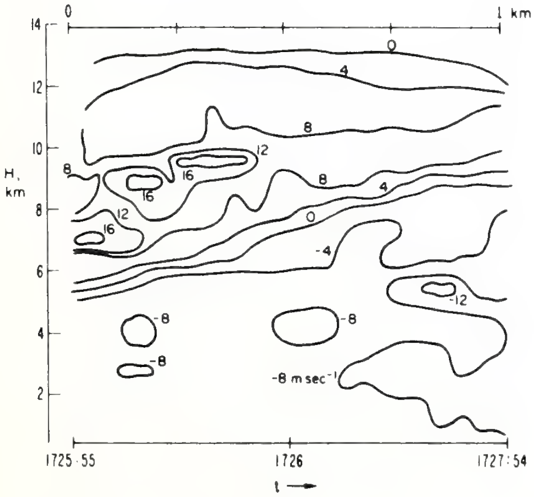

Figure 6a.

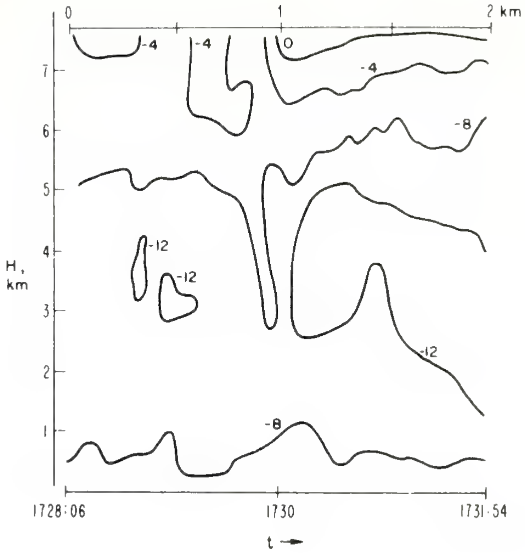

Figure 6b.

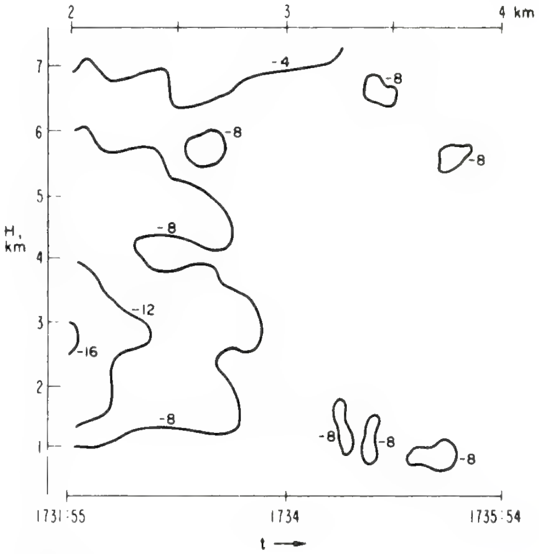

Figure 6c.

Figure 6. Updraft velocity contours estimated from measured particle velocities and the Joss-Waldvogel fall velocity relationship. Horizontal distance scale assumes an echo motion of 9 m sec^{-1}.

Pure and Applied Geophysics 113, 765-785, 1975.

Internal Airflow of a Convective Storm from Dual-Doppler Radar Measurements

By L. J. **Miller**[1])

Abstract

The dual-Doppler radar coplane method of scanning and data reduction has been used to determine the internal airflow and radar reflectivity structure of a convective storm. Cumulus convection growing in a moderately sheared wind environment resulted in a nonsteady, moderate intensity thunderstorm. Precipitation fallout and downward moving air are found downshear of an updraft inclined in the downshear direction. Rapid storm translation, vertical shear of the ambient wind, and slow subcloud ascent of inflow air act to establish this observed draft configuration. The absence of significant cold air outflow and its attendant gust front at the surface is attributed to (i) appreciable inflow of slow moving air into the downdraft at the middle layers and (ii) the fact that the potentially coldest air was located too low to contribute significantly to a deep downdraft circulation.

1. Introduction

Several investigators (e.g., Browning and Donaldson, 1963; Browning, 1964; Marwitz, 1973; Chisholm, 1973) have been able to infer general features of the internal airflow in quasi-steady severe convective storms. Their studies have relied heavily on identification of the draft locations from the radar echo structure along with limited information about the nearby environmental airflow. Schematic models of these inferred flow features have emerged from such efforts, but nothing as yet very quantitative. Furthermore, these kinematic models apply only to the steady, mature stage and reveal little about the growing stage of convective storms. The spatial and temporal evolution of the internal airflow has therefore remained something of a mystery.

Only recently have detailed quantitative measurements of the three-dimensional internal kinematic structure of convective storms been possible through application of multiple Doppler radar techniques (Miller and Frank, 1974; Kropfli and Miller, 1974, 1975a, 1975b; Lhermitte, 1974). Now internal airflow and reflectivity structure revealed by the Doppler measurements can be combined with knowledge of the storm environment to determine the storm-environment interactions. We no longer have to limit our studies to a few 'well organized' storms; we can now broaden our scope of understanding to the variety of storms that nature presents to us.

---

[1]) NOAA/ERL/Wave Propagation Laboratory, Boulder, Colorado, 80302.

Such varied studies are absolutely essential if we are to resolve the differences (or similarities) between observations and theoretical numerical predictions. Oftentimes numerical models (e.g., TAKEDA, 1971; SCHLESINGER, 1973a, 1973b) predict airflow configurations that are qualitatively similar to observations yet there still remain substantial differences. Now that reliable measurements of kinematic quantities are available and are taken at spatial and temporal scales comparable to those of numerical models, more joint modeling-observational investigations are clearly needed.

2. Dual-Doppler radar scanning and data reduction

The coplane method of scanning and data reduction was first proposed by LHERMITTE and MILLER (1970). Later MILLER (1972) recast the governing equations into a cylindrical coordinate system and applied these equations to the determination of two-dimensional quasi-horizontal air motion within a snowstorm that occurred on the plains just east of the Rocky Mountains in Colorado. This preliminary analysis was later extended to the complete three-dimensional air motion by FRISCH *et al.* (1974). Since the coplane method has been thoroughly described, including error estimation, by MILLER and STRAUCH (1974), only a brief summary of the technique is presented here.

The procedure is for two Doppler radars to scan simultaneously a common plane, inclined above the local horizontal and passing through the two radar positions. Both radars scan the storm azimuth sector in each plane using range gating and azimuthal increments to sample the signals scattered back by the precipitation. Figure 1 is a schematic representation of the scanning method. By sequentially incrementing the plane angle a complete three-dimensional scan of the entire storm volume is obtained in a short period. This scan time, 2 to 5 min, is a function of the storm size, desired spatial resolution, and the required accuracy of the Doppler radial velocity estimates.

Returned signals are analyzed for average return power and mean particle radial velocity. Fields of average return power for each radar are converted to conventional radar reflectivity factor. Two radial velocity estimates, one from each radar, are combined after interpolation to common grid points to give a two-dimensional vector particle velocity. This field is then reduced to air motion in the tilted plane by subtraction of the mean still-air fall velocity contribution as a function of spatial position. In practice this contribution is estimated from an empirical power law relationship between radar reflectivity factor and terminal fall velocity (ATLAS *et al.*, 1973). Airflow normal to the plane is obtained by integration along the coplane angle direction of the mass continuity equation for an atmosphere having a locally steady, horizontally homogeneous density field. [In MILLER and STRAUCH (1974) the incompressible form, $\bar{\nabla} \cdot \tilde{V} = 0$, was used. It has been found that for the heights typical of deep, moist

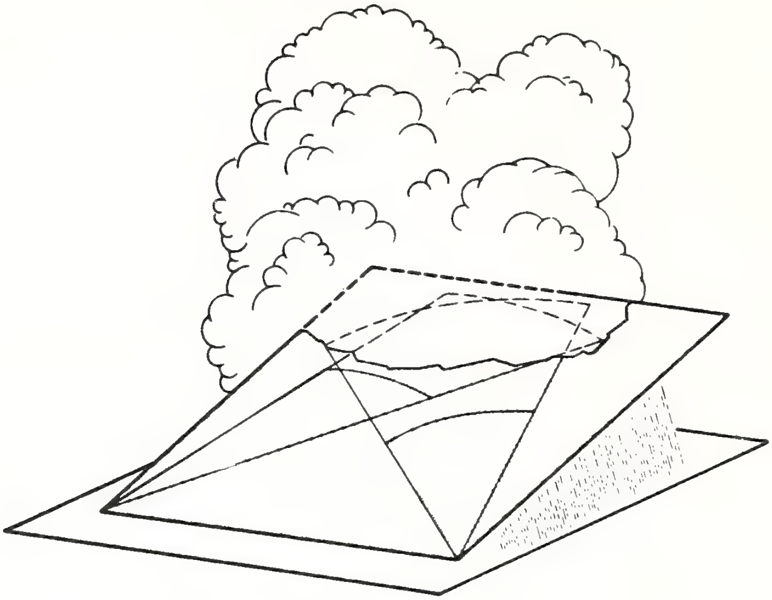

Figure 1
Schematic representation of Doppler radar coplane scan method (from Miller and Strauch, 1974).

convection, failure to account for the vertical variation of air density results in a 10 to 20% bias in the computed vertical air motion.] The surface boundary condition requires that the flow component normal to the zero degree plane be zero. These three coplane air motion components are then reinterpolated and transformed to components at Cartesian grid locations.

3. A case study

A thunderstorm that occurred on 31 July 1973 northwest of the NHRE[2]) surface meso-network in northeast Colorado was scanned by the NOAA/WPL dual-Doppler radar system. This storm never reached a stage of evolution that could be considered truly steady state or severe, but it provided the opportunity for an in-depth study of its convective processes and their temporal behavior. If such relatively moderate rainstorms are omitted from our investigations of convective storms, we run the risk of not clearly revealing the *necessary* conditions that result in more severe convective storms. Preliminary results on this particular storm have been presented elsewhere (Miller and Frank, 1974; Miller *et al.*, 1975). Those papers covered time periods before and after the time of the results presented here.

---

[2]) National Hail Research Experiment, sponsored by the National Science Foundation and managed by the National Center for Atmospheric Research.

Environmental conditions

Early in the day, a 500 mb ridge was located over the western United States with a weak trough extending from the Great Lakes to the Texas Panhandle. There was a weak vorticity maximum over Colorado with northwesterly flow aloft at a speed of 25 m $\sec^{-1}$. Surface dew point temperatures in excess of 10C existed across the NHRE surface meso-network. Deep convection was possible but with capping near 200 mb. This area of northeast Colorado is relatively flat (ground level ~ 1.5 km above mean sea level) and produces many convective hailstorms. These storms are generally not accompanied by extremely high winds or tornadoes and are usually less severe than their counterparts further east on the High Plains of the United States.

The rawinsonde released from Grover, Colorado, at 1329 (all times MDT) was used to determine the local storm environmental conditions. Since Grover was about 25 km downshear and southeast (low level relative upwind side) of the storm, the sounding was reasonably representative of the unperturbed environment.

From the sounding (Fig. 2) it can be seen that a 10 mb superadiabatic layer existed

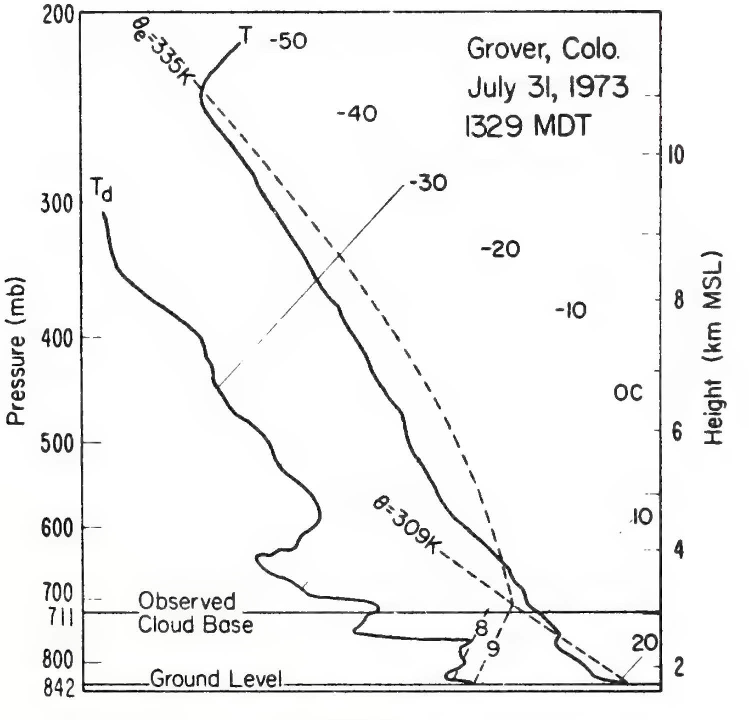

Figure 2

Temperature (T) and dew-point temperature (T_d) profiles from Grover 1329 MDT radiosonde release. Isotherms (deg Celsius) are the thin solid lines that slope upward to the right and water vapor mixing ratio (g/kg) isopleths are the dashed lines, 8 and 9. The trajectory of parcel ascent along the dry (θ = 309K) and the moist (θ_e = 335K) adiabats is shown.

at the surface. Above this layer the atmosphere was nearly dry adiabatic to 780 mb where there was a weak temperature inversion. As shown, a parcel lifted dry adiabatically from the surface arrives at its condensation level colder than the environment. However, such negative buoyancy can be easily overcome by the conversion of potential energy to kinetic energy of the parcel in the region below the inversion. The positive area on the diagram below the inversion exceeds the negative area above it so that air can be carried well above the level of free convection (parcel warmer than its environment) at 650 mb. Continued moist adiabatic parcel ascent above this point would yield a parcel temperature excess of 3.5C at 500 mb. Convection on this day was thermally driven rather than mechanically forced. This distinction is important because MARWITZ (1973) reports that inflow air in most severe storms that occur in this area is negatively buoyant below cloud base. He finds that significant nonhydrostatic pressure perturbations are needed to drive the updraft below cloud base. This is certainly true for his case studies but is not indicated for this particular storm.

The environmental wind sounding showed surface winds generally from the south veering to northwesterly above the observed cloud base at 3 km (all heights above mean sea level). Subcloud mean winds were from 240 deg at 3 m $\sec^{-1}$; cloud layer (from 3 to 11 km) mean winds were from 305 deg at 13 m $\sec^{-1}$. Midtropospheric (3 to 9 km) environmental wind shear had a magnitude of $2.3 \times 10^{-3} \sec^{-1}$ and was oriented along 275 deg. There was an elevated layer of rather slow moving air ($\sim$ 8 m $\sec^{-1}$) centered at 6 km. If this low-speed, middle-level air were to participate in the downdraft circulation, cold air outflow might have low horizontal momentum.

NORMAND (1946) first emphasized the contribution of cold dry air taken into convective storms at upper levels, in particular the downdraft, for maintenance of storm circulations. Recent schematic models (NEWTON, 1963; BROWNING, 1964; FANKHAUSER, 1971) have re-emphasized the role of middle level potentially cold and dry air for invigoration of the downdraft. For this case, environmental equivalent potential temperature (θ_e) decreased from a maximum value of 335K at the surface to a minimum of 320K at a height of only 3.5 km. Above this minimum, θ_e again increased, but more slowly, reaching a value of 332K at 11 km near the top of the radar echo. The potentially coldest air was, therefore, just above cloud base and could not contribute significantly to a deep downdraft circulation. The observed internal kinematic structure will be shown to be consistent with these environmental conditions.

Radar echo evolution

At 1402 the first observations by the NHRE 10 cm weather radar at Grover, Colorado, were made of a radar cell located 35 km NNE of the radar site. Because this cell was partially outside the range of the 3 cm Doppler radars, their operators chose to scan a new cell $\sim$ 25 km SW of the older cell. Figure 3 shows three quasi-horizontal (1.9 deg constant elevation scans from Grover) contoured fields of radar reflectivity at times 1402:13, 1421:45, and 1439:29. At these ranges from Grover, located at (0, 0)

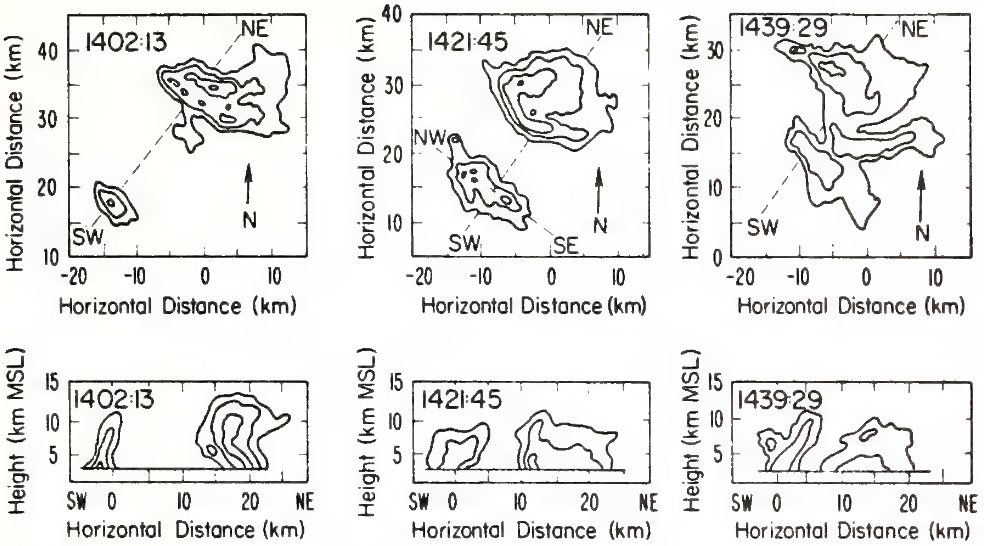

Figure 3

Constant elevation scans near cloud base and vertical slices along the dashed lines (SW–NE) of 10 cm radar reflectivity factor. The outer contour is at 20 dBZ and the interval is 10 dBZ. Grover, Colorado, site of the 10 cm radar is located at (0, 0). Doppler radar data are oriented in the SW–NE, NW–SE coordinate system, time 1421:45.

in this coordinate system, the scans are very close to the cloud base. Contours are $\mathrm{dBZ} \equiv 10 \log Z/1mm^6\,\mathrm{m}^{-3}$. Note that there are two small regions of reflectivity slightly higher than 50 dBZ in the northern cell at the two earliest times. Reflectivity in vertical planes oriented SW–NE were synthesized from a series of constant elevation scans by the Grover radar. At 1402:13 the northern cell had a large precipitation overhang on its southwest side. By 1421:45 this overhang had collapsed and the southern cell was now leaning toward the northeast. The northern cell continued to dissipate, and by 1439:29 the two cells had merged into one storm complex.

The northern cell had been moving slowly southward at about 4 m sec^{-1} prior to this merging. With mean low level winds from the southwest, low level air entered the northern cell on its right forward flank. By the method of MARWITZ *et al.* (1972) this side was tentatively identified, from the precipitation overhang and large horizontal reflectivity gradient, as the most likely location of the updraft for the northern cell. Hence, the southern cell, which was scanned by the two Doppler radars and for which internal flow data are discussed here, grew above the older inflow region. Both radar cells continuously propagated into the area between them and eventually merged.

Internal structure

Before the two radar cells merged, four successive volume scans of the southernmost cell were made with two Doppler radars. A detailed description of the internal airflow at an earlier time, 1416:55, was presented by Miller and Frank (1974) and some of those earlier results are used here to contruct a more complete history of the temporal evolution of the southern cell before merging.

Displays of 3 cm radar reflectivity and vertical air motion are shown in Figs. 4a–e at various horizontal levels of the storm volume. These data have a grid size of 600 m.

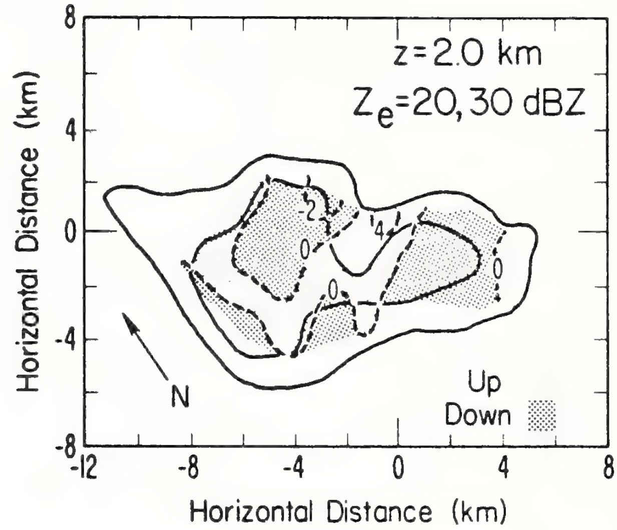

Figure 4a

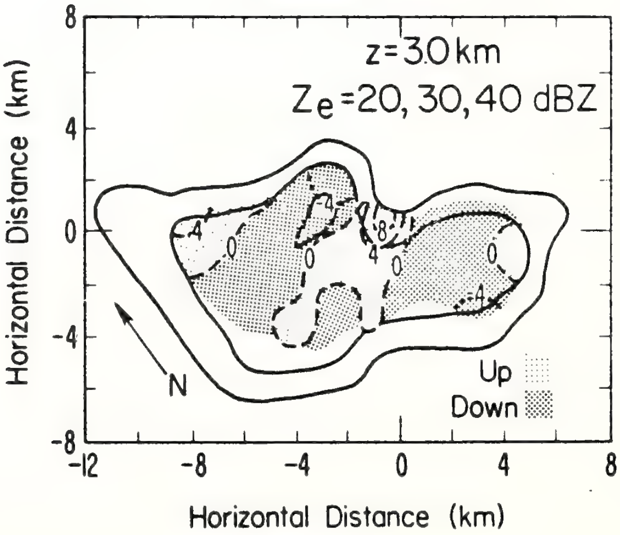

Figure 4b

Figures 4a–e

Horizontal planes of 3 cm radar reflectivity and vertical air motion at heights, z, above mean sea level. The outer reflectivity contour is 20 dBZ and the spacing is 10 dBZ. Up and downdrafts are contoured and shaded.

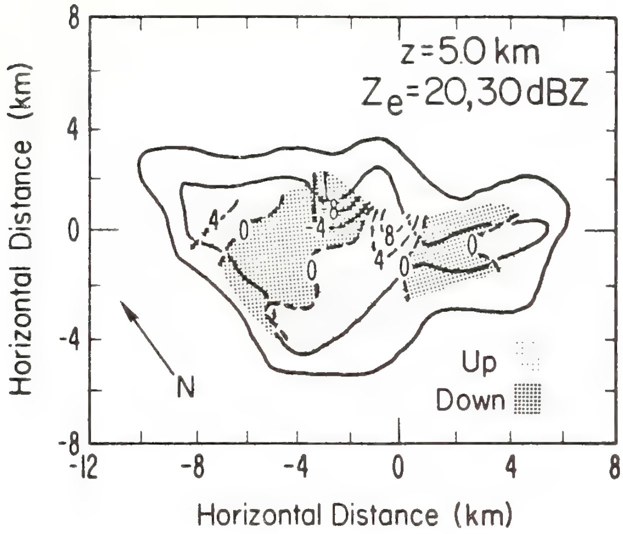

Figure 4c

Raw radar data used to construct these fields were acquired in about 2½ min centered at 1423:50. In the subcloud region 500 m above the ground (Fig. 4a) the downdraft was rather weak, i.e., -2 m sec^{-1}. The downdraft was, however, more intense above this layer, reaching a magnitude slightly greater than 12 m sec$-^{1}$ at 9.5 km near the echo top. From the Thunderstorm Project, Byers and Braham (1949) reported similar large downdraft speeds high in precipitating clouds over Ohio and Florida. Such large downdraft speeds may be due in part to the descent of updraft air that has overshot its equilibrium level near the storm top. At no level was the downdraft core ever

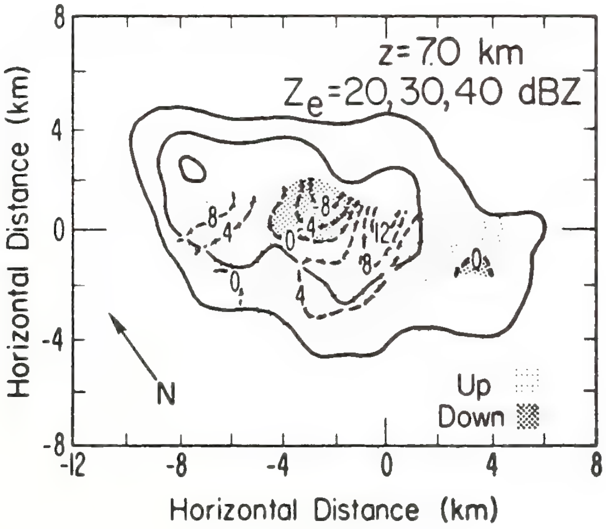

Figure 4d

located within the highest reflectivity regions; in fact, maximum downdrafts were consistently located near the edges of the radar echo. With precipitation content proportional to reflectivity, such a downdraft location indicates that cooling by evaporation at the edge of the precipitation shaft was more important than gravitational loading within the shaft in the initiation and maintenance of the downdraft. SCHLESINGER (1973a) indicated a downdraft was similarly located near the edge of the cloud in his two-dimensional model of deep, moist convection. He also attributed this location to the dominance of evaporative cooling in the downdraft circulation.

Two updraft cores with speeds greater than 4 m $\sec^{-1}$ are found above cloud base (Fig. 4b), one on the northern end of the cell and the other on the east side near the notch in the reflectivity. The northern updraft is believed to be part of a broader updraft on the northwest side. The protuberance shown on the 10 cm radar display in Fig. 3 at 1421:45 near coordinates (−13, 22) apparently was not completely scanned by the 3 cm Doppler radars. The vertical extent and persistence of the echo here as observed on the 10 cm radar suggest that it was being actively supported by a vigorous updraft. This draft had sufficient downshear tilt (i.e., toward the southeast at increasing altitude) for the edge of it to be seen in the Doppler data, particularly at 7 km (Fig. 4d) and above. If the precipitation in this draft had been supercooled liquid water, which was probably not the case (T in cloud ~ −15C at 7 km), updrafts (inferred from reflectivity) in excess of 9 m $\sec^{-1}$ would have been required to prevent precipitation fallout. This is only a rough estimate of the necessary updraft speeds outside the area observed since insufficient information is available to know what still-air fall speeds might be expected if the precipitation was comprised of ice (most likely graupel) particles. The Doppler results show the updraft, on the east side, to be the more vigorous reaching a value slightly in excess of 12 m $\sec^{-1}$ at 9.5 km (Fig. 4e). Note that the upper

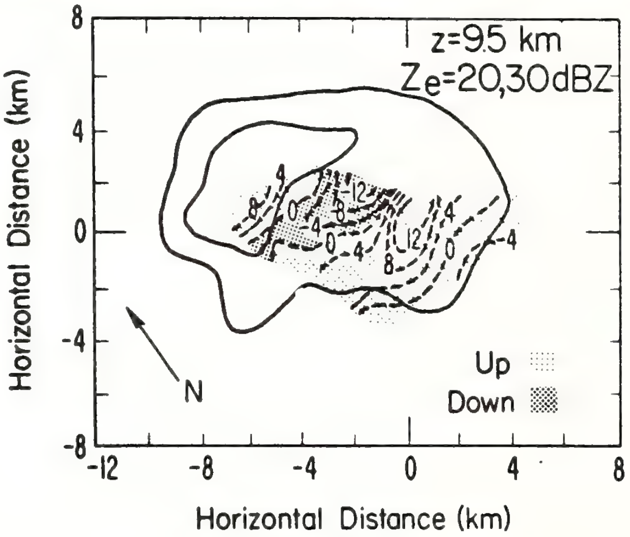

Figure 4e

levels are still dominated by updrafts which indicates that the cell had not yet begun to decay. This updraft was rapidly weakening particularly in the low levels as seen in a subsequent volume scan $2\frac{1}{2}$ min later. The low level relative flow indicates that precipitation was continually falling into air that eventually entered the updrafts. Some evaporative cooling would be expected since this air was not saturated so that thermal buoyancy would decrease, eventually leading to decay of the updraft. As the draft is shut off from the bottom, reduced speeds would be found later at ever increasing altitudes.

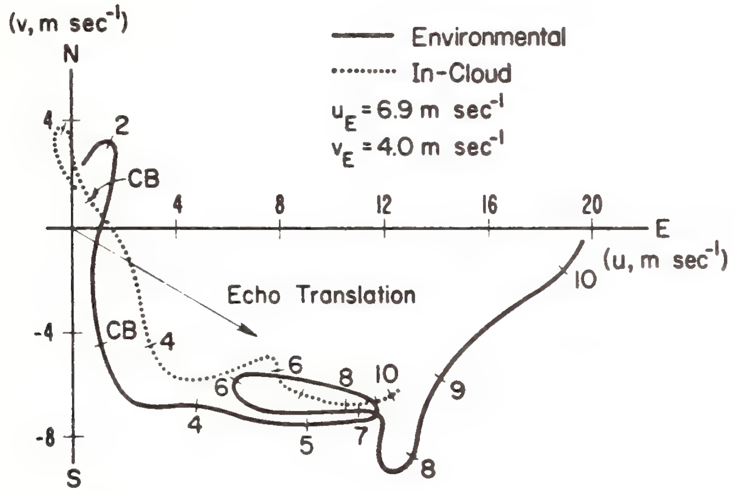

Figure 5

Hodograph of environmental (solid) and in-cloud (dotted) airflow. Lines are the locii of the end-points of the vector winds. Heights are in kilometers above mean sea level with cloud base (CB) at 3 km. The echo was moving toward the southeast with components (u_E, v_E).

A hodograph of the environmental winds from the Grover sounding and in-cloud winds averaged over the entire horizontal extent of the southern cell is shown in Fig. 5. In-cloud horizontal winds closely follow the environmental wind direction but they are generally slower in speed. A mean echo translation from 305 deg at 8 m sec^{-1} must be subtracted from flow relative to the ground to obtain flow relative to the southern radar cell. This cell translation is dramatically different from that of the northernmost cell which was from 360 deg at 3 m sec^{-1}. Both radar cells did, nonetheless, grow in what seems to be the same environment, most notably the same ambient wind field. Differences in the internal flow configuration relative to the ambient winds may have contributed to these differences. Further research is clearly needed, particularly comparing the internal structure of severe and non-severe convective storms and how the structure is related to environmental conditions. Such comparisons cannot be made here because of missing detailed information about the northern cell.

The horizontal displays of relative flow (Figs. 6a–e) are at the same heights as those of the reflectivity and vertical air motion. The outer 20 dBZ reflectivity contour has been repeated for reference. Outside the area where vertical air motion was computed with the standard coplane method, the horizontal air motion was estimated by neglecting the horizontal contribution of the air motion component normal to the plane. Since

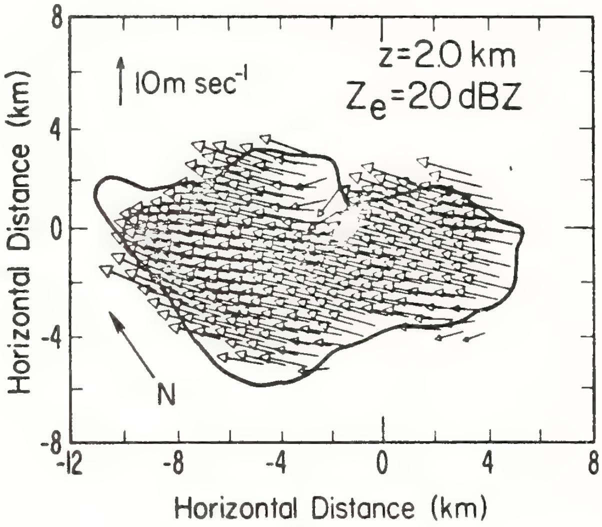

Figure 6a

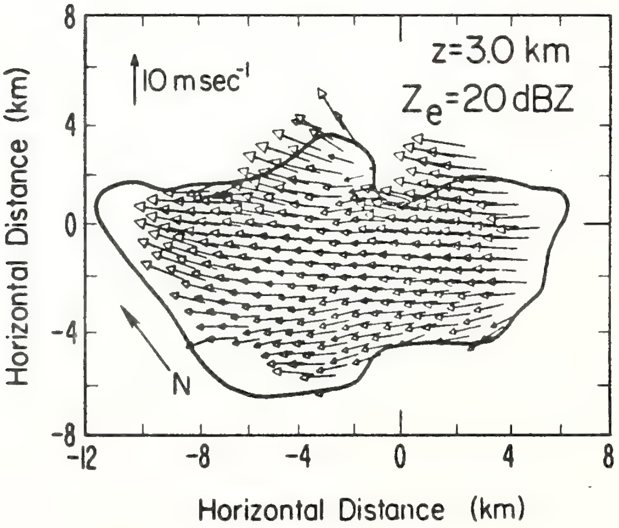

Figure 6b

Figure 6a–e
Horizontal airflow relative to the moving storm at heights, z, above mean sea level. The outer 20 dBZ 3 cm reflectivity contour is shown for reference. Arrow lengths inside the radar echo are proportional to relative wind speed.

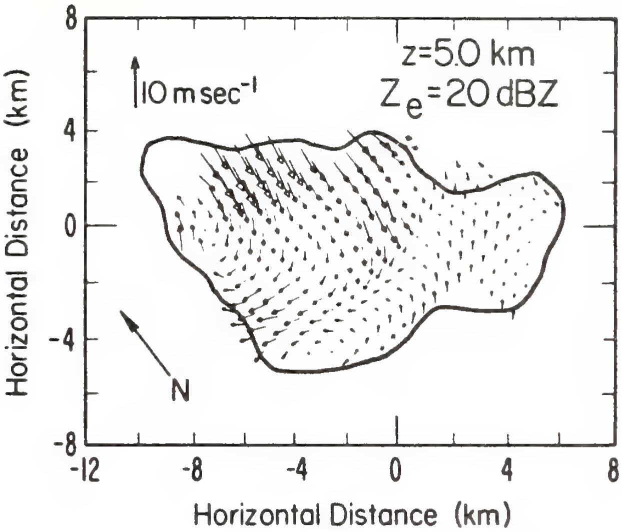

Figure 6c

this normal component enters the horizontal estimate weighted by the sine of the original tilt angle, the contribution of a 10 m sec^{-1} normal component is at most 2 m sec^{-1} at the angles involved (< 12 deg). Reasonable continuity of the horizontal flow across the transitional area where estimates were obtained by the two slightly different methods suggests that the contribution was generally even smaller and hence could safely be neglected.

The airflow at cloud base (Fig. 6b) and the airflow at 2 km (Fig. 6a) were essentially in the same direction, with the flow at cloud base being somewhat slower on the average.

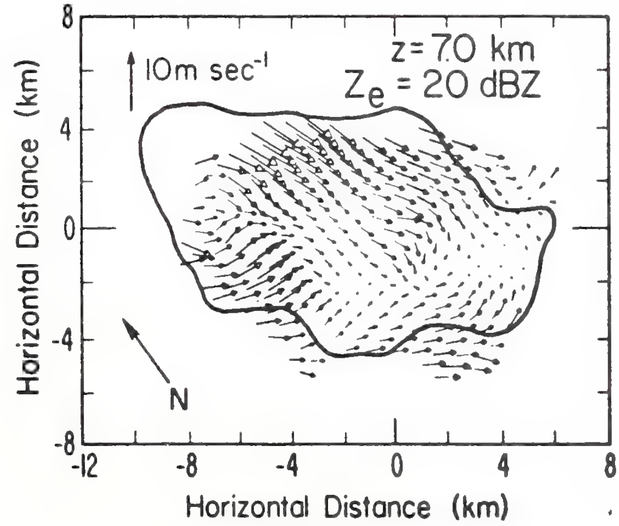

Figure 6d

Air approached the storm from the right front flank. Flow reversed direction above cloud base and nearly paralleled the ambient wind through the rest of the cloud depth. At midcloud (Fig. 6c) the confluence line is mostly a reflection of the horizontal flow required to satisfy mass continuity. Midcloud was near the level of greatest expected thermal buoyancy and just above the highest reflectivity values so that the updraft was probably being invigorated by the unloading of precipitation. Beginning at 7 km near the top of the echo, the updraft on the upshear side of the storm began diverging as vertical momentum was converted to horizontal momentum of the upper level outflow. At 9.5 km (Fig. 6e) the main precipitation column was slightly north of the peak divergence. This region would have appeared visually as a cloud turret on the upstream side of the storm opposite the anvil outflow side.

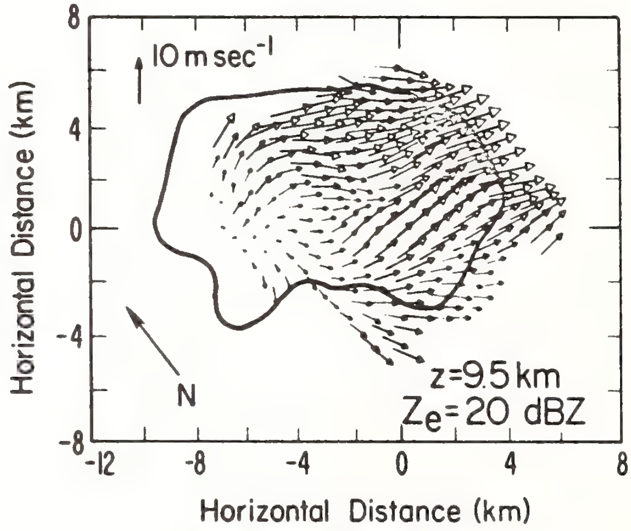

Figure 6e

Vertical planes containing reflectivity contours and relative airflow in these planes are shown in Figs. 7 and 8. These views are oriented, respectively, along (NW–SE) and normal (SW–NE) to the in-cloud mean airflow direction. The direction of the mid-tropospheric environmental wind shear vector is 30 deg to the left of the NW–SE plane when looking in the downwind (to the right in Fig. 7) direction. Each plane has its horizontal distances measured from the intersection of the dashed lines in Fig. 3 or the (0, 0) coordinate of Figs. 4 and 6.

The most striking feature of the relative airflow along the mean flow direction (Fig. 7) is the existence of two horizontal vortices rotating in the same direction. Note also the severe upshear tilt of the updraft in the subcloud region. Above cloud base both updraft and reflectivity slope downshear, with downdraft and precipitation located on the downshear side of the updrafts. The air near 4 km had a small horizontal relative speed across the storm. Recall that equivalent potential temperature in the environment was lowest at 3.5 km. The potentially coldest air, therefore, could not overtake the storm and therefore could not participate in the downdraft circulation except through turbulent mixing at the cloud boundaries. As previously stated, no vigorous downdraft was found in the lower half of the storm.

Rapid translation of the storm core downshear meant that the cloud tended to overtake the low level inflow air before this air had ascended to cloud base. At a storm translation speed of 8 m $\sec^{-1}$, the low-level air would be approaching the updraft at a relative speed of nearly 10 m $\sec^{-1}$. With an average subcloud lifting of about 2 to 4 m $\sec^{-1}$ air would reside in the subcloud region for some 400 to 700 sec. Air lifted at cloud edge would then move horizontally 4 to 7.5 km relative to the storm. At a reduced ascent rate of 1 to 2 m $\sec^{-1}$ this air would enter cloud base even nearer the back of the radar cell. These ascent rates and draft locations are reasonably

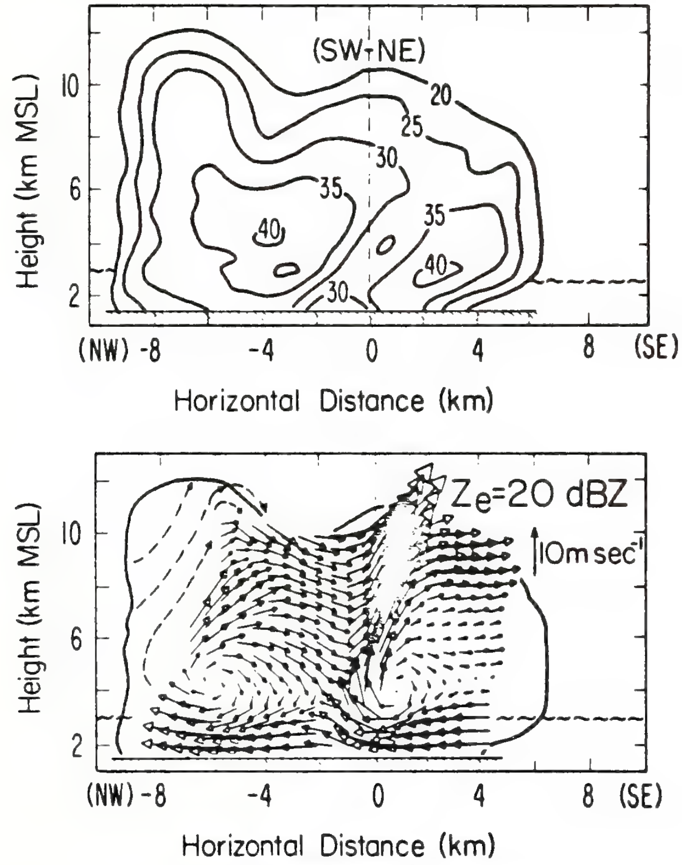

Figures 7a–b

Vertical planes of 3 cm radar reflectivity (*a*) and relative airflow (*b*) in the plane oriented (left-to-right) along the mean flow direction. Arrow lengths are proportional to relative wind speed. Relative streamlines (dashed lines) approximate the flow on the upshear side of the storm. Cloud base is shown at 3 km.

consistent with the observed updrafts at 6 and 14 km from the leading edge 20 dBZ reflectivity contour. Rain was continually falling into subcloud air during its horizontal traverse thereby lowering its temperature and raising its water vapor mixing ratio through evaporation. The storm was moving too fast for the drafts to be located near the forward flank in the same manner as those found in the schematic models of severe convective storms previously cited. These models generally show an updraft rooted near the forward flank in the subcloud region and inclined upshear through a substantial depth of cloud with heavy precipitation and downdraft on the upshear side or on a lateral flank of the updraft.

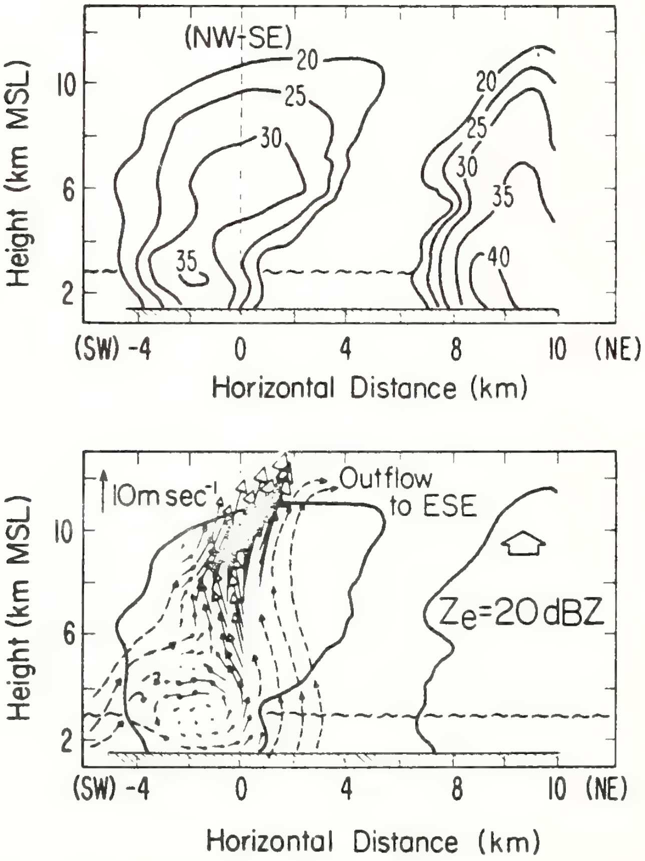

Figures 8a–b

Vertical planes of 3 cm radar reflectivity (*a*) and relative airflow (*b*) in a plane oriented normal to the mean flow. The viewer is looking in the mean upwind direction. Reflectivity contours on the right are from 10 cm radar scans. Dashed streamlines approximate the flow outside the area containing reliable airflow values. The broad arrow on the right represents a decaying updraft.

The three-dimensional character of the vortex associated with the eastern updraft is seen in Fig. 8. The northern cell 10 cm reflectivity configuration has been added to show its position at the time of the Doppler data. Note that the southern cell strongly leans toward the older cell. For this reason and because of the observed updraft location, it is probable that this whole area between the cells was mostly upward moving air at one time. Weak updrafts might still exist in the upper levels of the northern cell; however, nothing but downdrafts should be found in its low layers at this time. Precipitation drag aloft coupled with decreased thermal buoyancy below probably led to the rapid decay of the broader updraft.

Vertical profiles of averaged kinematic quantities

Areal averages of several kinematic quantities were computed at each horizontal level of four successive volume scans of the storm. These scans were centered at times 1415:34, 1418:16, 1423:50, and 1426:42, henceforth referred to as times A, B, C, and D. Such averages and their temporal evolution can serve as input data in the parameterization of cumulus convection and its interaction with the environment in larger scale atmospheric models. However, it must be re-emphasized that these computed averages apply only to the regions of precipitation-sized particles. At time C, the average horizontal area containing precipitation was 113 km^2. In this area, horizontal velocity estimates were obtained over 94 km^2 and vertical velocity estimates were obtained over 46 km^2 which included 26 km^2 of updraft and 20 km^2 of downdraft.

Average divergences of the horizontal winds are shown in Fig. 9. The subcloud layer shows a trend from convergent flow at time A to divergent flow at time D.

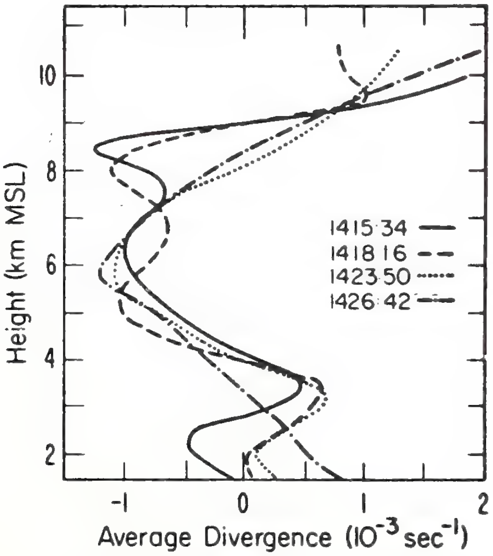

Figure 9

Horizontal wind divergence averaged over the echo area at each vertical height.

Environmental air was converging into the storm through much of the cloud depth and spent air was being exhausted above 8 to 9 km into the anvil outflow. Note that the level of near-zero relative airflow at about 4 km has nearly zero divergence which gives credence to the hypothesis that the potentially coldest air (θ_e = 320K) was able to participate in the downdraft circulation through turbulent mixing at the cloud boundary, but not through substantial relative inflow.

Relative vorticity profiles (Fig. 10) show little consistency. Valid observations are: (i) the storm rotated generally anticyclonically; (ii) vorticity seemed to be increasing in the layer 3 to 6 km; (iii) vorticity seemed to be decreasing in the layer 6 to 10 km. These observations are tentatively interpreted as implying that vorticity is being locally generated, redistributed, and destroyed. More intense convective storms might appear on the synoptic scale as sources or sinks of environmental relative vorticity (Reed and Johnson, 1974); however, the vorticity profiles are too variable for them to be conclusive.

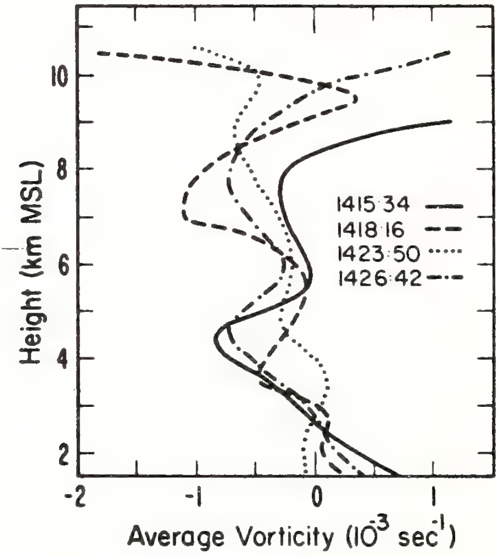

Figure 10

Areal averaged vertical component of relative vorticity. Positive vorticity is associated with cyclonic rotation about the vertical axis.

Mean draft profiles, both up and down, at each of the four times are displayed in Fig. 11. The most striking feature is the simultaneous lessening of both updraft and downdraft intensities at nearly all heights through time. The storm seemed to function in a way which tried to maintain locally compensating vertical air motions. It is not presently clear whether this is a general property of many precipitating convective storms or merely a property of this particular class of storm.

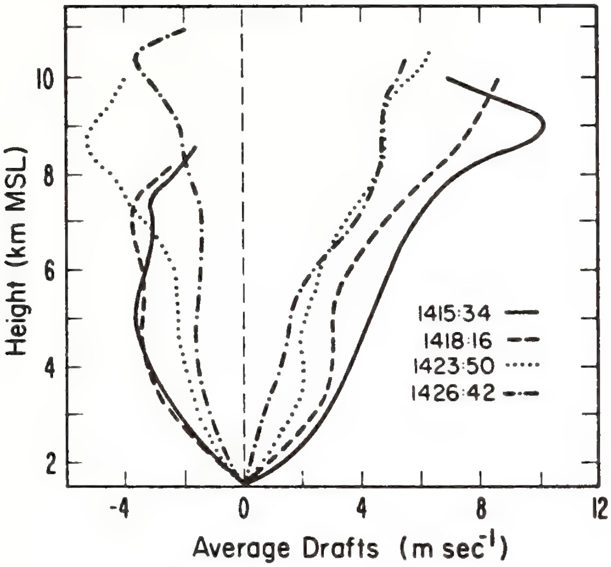

Figure 11
Areal averaged drafts, up (right) and down (left).

Air mass and moisture flux

Cloud base air mass and moisture flux quantities were estimated for this storm. The limitation of having updraft speed estimates over only one-half the echo area at cloud base and also the likelihood of major updraft flux outside detectable echo make the flux estimates somewhat suspect. However, every effort was taken to ensure that reasonable adjustments were made so that values reported here are at least within a factor of two of the true values. At other heights similar adjustments could not be made with any confidence so that entrainment rates for this storm could not be computed. These results are listed in Table 1 along with results averaged for eight hailstorms from the same region as this study, and small, air-mass thunderstorms studied in the Thunderstorm Project. The fluxes reported here agree fairly well with the air-mass thunderstorm results and are about an order of magnitude smaller than the flux values of the hailstorm. This latter point in itself is not surprising; however, the average updraft speed differs from the hailstorm by a factor of only two or less. On the other hand, the hailstorm updraft area is more than five times that of this convective storm (except time C). This suggests that severe convective storms may not have updraft velocities much more intense than less severe storms. However, the updraft areas may be considerably larger, thereby supporting a greater flux of air and moisture.

4. Conclusions

The most obvious conclusion that emerges from this study is that convective storms of moderate intensity need not be configured in the same way as their more severe counterparts. Whether or not these circulation patterns look anything like the growing stage of severe storms remains uncertain. In the cloud layer the updraft was found to tilt downshear with the bulk of the precipitation and downdraft located on its downshear side. A relatively slow ascent rate under a fast-moving storm was partially responsible for this configuration. The air moved a significant horizontal distance beneath this storm before it entered the updraft. The updraft was forced to the back of the storm away from the leading cloud edge. It may be that, if the flow reverses direction too low in the storm, there is insufficient time for substantial water drop growth and fallout on the middle level upshear side of the updraft. Precipitation must then fall predominantly on the downshear side thereby isolating the updraft from its low-level source of warm moist air. This precipitation does not necessarily cause the downdraft but it coincides with it.

These observations of airflow configuration are very similar to theoretical results TAKEDA (1971) obtained in a numerical experiment on the effects of the vertical profile of ambient wind on a precipitating convective cloud. Though some of the assumptions in his model may be somewhat unrealistic, the resultant draft and precipitation configuration of TAKEDA's case B3, which assumed a wind profile much like the one here, are most like the present observations.

Substantial inflow of the potentially coldest air in the midtroposphere seems to be necessary for vigorous lower level downdrafts. Weak relative airflow at the level of lowest equivalent potential temperature apparently prevented this air from entering the storm circulation in significant amounts. Furthermore, precipitation drag did not seem to be important to the initiation or maintenance of the downdraft. The region of significant convergence of environmental air into the storm was characterized by relatively slow moving air. This air, believed to have participated in the downdraft

Table 1

Air and moisture flux estimates at cloud base for this study (rows A–D), for average of 8 NE Colorado hailstorms (AUER *and* MARWITZ, *1968*), *and for small air-mass thunderstorms* (BRAHAM, *1952, as cited in* AUER and MARWITZ)

Type	Time	Updraft speed (m sec^{-1})	Updraft area (km^2)†)	Air mass flux (10^6 kg sec^{-1})	Moisture flux (10^6 kg sec^{-1})‡)
Present	A	2.8	12	> 30	> 0.2
	B	2.7	12	> 30	> 0.2
	C	1.8	40	> 60	> 0.4
	D	0.8	15	> 10	> 0.1
Hailstorm		4.0	85	310	3.1
Air-mass thunderstorms		?	?	50	0.6

†) For the present study this is the adjusted area so that flux quantities must be considered as a lower bound to the true flux.

‡) Moisture flux for the present study was computed using a mean subcloud water vapor mixing ratio of 8 g/kg.

circulation, had insufficient horizontal momentum on arrival at the surface to generate a surface gust front.

Acknowledgements

This study is a culmination of many hours of dedicated effort by many members of the Meteorological Radar Program of this laboratory. Notable among these are Messrs. R. G. Strauch and H. W. Frank in the experimental program and Messrs. N. Kohn and F. Merrem in the computer programming. Upper air rawinsonde and 10 cm radar data were provided by NCAR staff members of NHRE, notably Mr. F. Robitaille and Dr. P. Eccles. The author is indebted to Ms. L. Murdock and Drs. E. Gossard and K. Browning for their critical reviews of the manuscript.

REFERENCES

D. ATLAS, R. C. SRIVASTAVA, and R. S. SEKHON (1973), *Doppler radar characteristics of precipitation at vertical incidence*, Rev. Geophys. Space Physics *11*, 1–35.

A. H. AUER, JR. and J. D. MARWITZ (1968), *Estimates of air and moisture flux into hailstorms on the high plains*, J. Appl. Meteor. *2*, 196–198.

R. R. BRAHAM, JR. (1952), *The water and energy budgets of the thunderstorm and their relation to thunderstorm development*, J. Meteor. *9*, 227–242.

H. R. BYERS and R. R. BRAHAM, JR. (1949), *The thunderstorm*, U.S. Government Printing Office, Washington, D.C., 287 pp.

K. A. BROWNING (1964), *Airflow and precipitation trajectories within severe local storms which travel to the right of the winds*, J. Atmos. Sci. *21*, 634–639.

K. A. BROWNING and R. J. DONALDSON (1963), *Airflow and structure of a tornadic storm*, J. Atmos. Sci. *20*, 533–545.

A. J. CHISHOLM (1973), *Alberta hailstorms. Part I: Radar case studies and airflow models*, Meteor. Mono. *14*, AMS Boston, 1–36.

J. C. FANKHAUSER (1971), *Thunderstorm-environment interactions determined from aircraft and radar observations*, Mo. Wea. Rev. *99*, 171–192.

A. S. FRISCH, L. J. MILLER, and R. G. STRAUCH (1974), *Three-dimensional air motion measured in snow*, Geophys. Res. Letters *1*, 86–89.

R. A. KROPFLI and L. J. MILLER (1974), *Dual-Doppler radar measurements within a hail producing storm in northeast Colorado*, Preprints, AMS Conf. on Cloud Physics, 277–282.

R. A. KROPFLI and L. J. MILLER (1975a), *Thunderstorm flow patterns in three dimensions*, Mo. Wea. Rev. *103*, 70–71.

R. A. KROPFLI and L. J. MILLER (1975b), *Thunderstorm flow patterns in three dimensions from dual-Doppler radar*, Preprints, AMS 16th Radar Meteor. Conf., 121–127.

R. M. LHERMITTE (1974), *Dual Doppler radar study of south Florida convective storms*, Preprints, AMS Conf. on Cloud Physics, 328–332.

R. M. LHERMITTE and L. J. MILLER (1970), *Doppler radar methodology for the observation of convective storms*, Preprints, AMS 14th Radar Meteor. Conf., 133–138.

J. D. MARWITZ, A. H. AUER, and D. L. VEAL (1972), *Locating the organized updraft on severe thunderstorms*, J. Appl. Meteor. *11*, 236–238.

J. D. MARWITZ (1973), *Trajectories within the weak echo regions of hailstorms*, J. Appl. Meteor. *12*, 1174–1182.

L. J. MILLER (1972), *Dual-Doppler radar observations of circulation in snow conditions*, Preprints, AMS 15th Radar Meteor. Conf., 309–314.

L. J. Miller and H. W. Frank (1974), *Three-dimensional air motion within a northeast Colorado rainstorm*, Preprints, AMS Conf. on Cloud Physics, 321–327.

L. J. Miller, J. D. Marwitz, and J. C. Fankhauser (1975), *Kinematic structure of a Colorado thunderstorm*, Preprints, AMS 16th Radar Meteor. Conf., 128–133.

L. J. Miller and R. G. Strauch (1974), *A dual Doppler radar method for the determination of wind velocities within precipitating weather systems*, Remote Sensing of Environ. *3*, 219–235.

C. W. Newton (1963), *Dynamics of severe convective storms*, Meteor. Mono. *5*, AMS Boston, 33–58.

C. W. B. Normand (1946), *Energy in the atmosphere*, Q. J. R. Meteor. Soc. *72*, 145–147.

R. J. Reed and R. H. Johnson (1974), *The vorticity budget of synoptic-scale wave disturbances in the tropical western Pacific*, J. Atmos. Sci. *31*, 1784–1790.

R. E. Schlesinger (1973a), *A numerical model of deep moist convection: Part I. Comparative experiments for variable ambient moisture and wind shear*, J. Atmos. Sci. *30*, 835–856.

R. E. Schlesinger (1973b), *A numerical model of deep moist convection: Part II. A prototype experiment and variations upon it*, J. Atmos. Sci. *30*, 1374–1391.

T. Takeda (1971), *Numerical simulation of a precipitating convective cloud: The formation of a 'long-lasting' cloud*, J. Atmos. Sci. *28*, 350–376.

(Received 31st March 1975)

Proceedings 16th AMS Radar Meteorology Conference, 128-133, April 1975.

KINEMATIC STRUCTURE OF A COLORADO THUNDERSTORM

L. J. Miller
NOAA/ERL/Wave Prop. Lab., Boulder CO 80302

J. D. Marwitz
Dept of Atmos. Sci., Univ. of Wyo., Laramie WY 82071

J. C. Fankhauser
NCAR, Boulder CO 80302

1. INTRODUCTION

On 31 July 1973, a thunderstorm complex developed along the Nebraska-Wyoming border and moved toward the south at ~ 4 m sec^{-1}. While the complex was centered ~ 20 km north of Grover, Colorado, the storm was observed by both NCAR and University of Wyoming aircraft as well as by two NOAA/WPL Doppler radars. These data systems along with the mesonet and rawinsonde networks were operating as part of NHRE*.

Miller and Frank (1974) have synthesized a portion of the dual-Doppler data and some of the chaff data. Their analysis was concentrated on an earlier time, 1414-19 (all times MDT) when the thunderstorm complex consisted of the original storm plus a newly formed radar echo located ~ 15 km SW of the original cell. By 1530 the new cell dominated the local circulation and the original cell had dissipated. In this paper the data are centered at 1443. A complete synthesis of the available storm data is planned for the near future.

2. DATA SYSTEMS

2.1 Rawinsondes and Mesonet

When research aircraft were flying, rawinsondes were released at ~ 90 min intervals beginning at 1200 from 5 stations in the NHRE operational area. The westernmost station was Grover (GRO) where the NHRE headquarters was located. Mesonet stations located at each of the rawinsonde sites recorded temperature, relative humidity, pressure, wind speed and direction on analog strip charts. The instruments were carefully calibrated on a daily basis.

2.2 NCAR Queen Air (N304D)

The NCAR Queen Air (N304D) aircraft data system recorded the state parameters of pressure, temperature, and dew point plus horizontal winds using a Doppler navigation system. From calibration flights the derived parameters of equivalent potential temperature (θ_e), potential temperature (θ) and mixing ratio (w) were determined to be accurate to ± 0.6 K, ± 0.4 K, and ± 0.2 gm/kg, respectively. The vector error of the horizontal wind was shown to be ~ 1 m sec^{-1} (Biter et al., 1974 and Duchon, 1973). The horizontal wind data were filtered as described by Foote and Fankhauser (1973).

N304D was flown at constant pressure (776 mb) and along a series of constant headings in such a manner that the visual cloud boundary was circumnavigated 3 times during the period 1430 to 1550. Data from the first circuit (1432-56) are presented here. The pressure altitude (2.3 km MSL or 0.7 km AGL) was approximately midway between ground and cloud base. When an aircraft is flown at constant pressure altitude, heading and manifold pressure, the increasing and/or high values of true airspeed (TAS) are indicative of ascending air motion and decreasing and/or low values of TAS are indicative of descending air motion. Since the manifold pressure was not recorded, it was not possible to quantify the vertical air motion. High and low values of TAS were, therefore, only qualitative indicators of ascending and descending air motion, respectively.

2.3 Wyoming Queen Air (10UW)

The Wyoming Queen Air (10UW) began flying in the updrafts at 1410 and continued until after 1600. The accuracies of the state parameters were essentially the same as 304D's. In 1973 the 10UW had no capabilities for measuring horizontal winds. However, the aircraft and computer controlled digital data system did contain several features which were quite useful when flying in the updrafts near cloud base. These were as follows: an event system capable of recording 10 separate events for each crew member; a real-time data display of corrected and derived state parameters which included θ_e, θ, and w; a chaff port for releasing individual packets of slow fall (~ 0.3 m sec^{-1}) chaff into a parcel of air whose state parameters were measured and a storm avoidance X-band radar.

2.4 Chaff Data

The track of a slow fall chaff packet has been shown to be the trajectory of an air parcel whose initial state parameters are known (Marwitz, 1973). The procedure consisted of automatically tracking 10UW in the range gate of an M-33 track radar (X-band) located at GRO. When the chaff was released, the range gate was stopped by the radar operators for a few seconds while the aircraft flew away from the chaff. The radar operators then reacquired the chaff and returned the radar to the automatic tracking mode. Beginning in 1973 the x, y, and z positions of the range gate were recorded on tape at 5 sec intervals. Prior to 1973 the spherical coordinates of the chaff were manually recorded at 30 sec intervals. The analog resolvers in the M-33 made the conversion from spherical to Cartesian coordinates. Each recorded position of the chaff was plotted and a smoothed curve was fitted by eye to the data. The data were clearly superior to previous chaff data.

---

*National Hail Research Experiment sponsored by the National Science Foundation and managed by the National Center for Atmospheric Research.

2.5 NOAA/WPL Dual-Doppler

The two NOAA/WPL 3 cm mobile Doppler radars were located, respectively, 30 km east and 60 km southeast of the storm complex center. Several three-dimensional scans of the storm cells were made starting at 1414 and ending at 1547. Reported here are results from the time period 1441-46.

A detailed discussion of the dual-Doppler coplane method of scanning and data reduction can be found in Miller and Strauch (1974). Briefly, the procedure is for 2 radars to simultaneously scan a common plane passing through the 2 radar positions and inclined above the local horizontal. Each radar scans the storm sector of each plane in a range-gated, azimuthal increment fashion. The Doppler shifted return signal is analyzed for mean particle radial velocity and return power estimates. Two radial velocity estimates, one from each radar, are combined with the mass continuity equation and an independent estimate of mean particle fall velocity to obtain 3 air motion components in a cylindrical coordinate system. These 3 components are then transformed to Cartesian components.

3. RESULTS

3.1 Composite Data

Fig. 1a contains the θ_e, θ, and w from GRO at 1400, the track and relative horizontal winds from 304D and the 3 cm reflectivity at this level ($\sim$ 2 km MSL). Segments along the path of 304D and regions determined by 10UW measurements at cloud base where θ_e was high ($\theta_e \geq 335$ K) are delineated. A plan view of 3 chaff tracks--1428 (2), 1437 (3) and 1505 (4)--relative to the storm are shown. Regions of updraft derived from the Doppler data are presented in Fig. 1a and horizontal relative winds are contained in Fig. 1b.

The radar data are located 1 km below cloud base (3 km MSL) and 0.5 km above the local ground level (1.6 km MSL). Contours of reflectivity are at 5 dBz increments starting at 15 dBZ. The stippled areas in Fig. 1a are updrafts and the clear areas inside 15 dBZ are downdrafts. Only weak (< 1.5 m sec^{-1}) drafts are evident at this level. Note the close proximity of areas of high θ_e to the internal locations of the updrafts.

There are only 2 areas of significant divergent flow below cloud base (Fig. 1b), one region on the west flank of each cell. One possible explanation for the absence of significant downdrafts in the subcloud layer is as follows: As will become evident, this storm complex was structured such that the precipitation fell out downwind of the updraft. Without precipitation falling into cool, dry air moist adiabatic descent of downdraft air might not be maintained. The tendency toward dry adiabatic descent of the intruding middle level air parcels would eventually lead to their being slightly warmer than the environmental air at lower levels. This process would decelerate the downdraft implying the possibility of little or no downdraft at the surface. Such an argument is also consistent with the fact that the air moved horizontally across the precipitation zone from south to north relatively undisturbed (the horizontal momentum was nearly the same on the inflow and outflow sides of the storm).

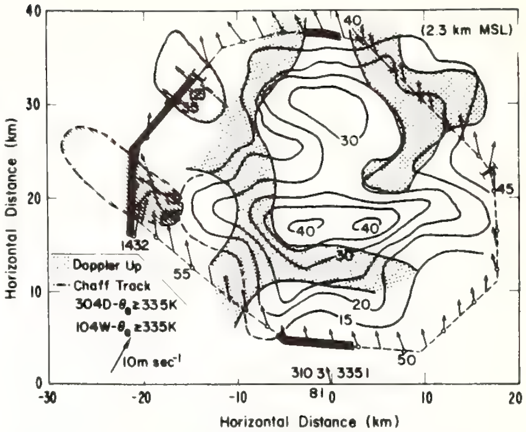

Figure 1a. Composite of 3 cm radar echo at 5 dB contour increments, 304D track and horizontal relative winds, Doppler derived internal updrafts (0-1.5 m sec^{-1}), regions of $\theta_e \geq 335$ K, and plan views of 3 chaff tracks. The values of θ (upper left), θ_e (upper right), and w (lower left) are shown for 1400 MDT at GRO (0, 0). Horizontal distances are from GRO with north at the top of each figure.

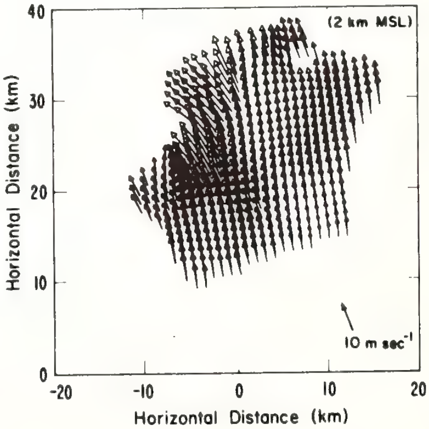

Figure 1b. Relative horizontal air motion near the flight level of 304D.

3.2 GRO Sounding with Chaff Data

Shown in Fig. 2 are the 1329 GRO sounding and chaff-track data. The subcloud rawinsonde data have been slightly modified to be consistent with the mesonet data from GRO. This was done because of the excellent calibration of the mesonet data. It may be seen that 304D was flying ~ 10 mb below the inversion and dry layer at 765 mb. Below the inversion the winds were from the southwest and turned to the northwest and west above the inversion. Environmental wind shear of 2.4×10^{-3} sec^{-1} existed in the cloud layer. The 3 packets of chaff were released in air which originated from near the surface and which had up to 2C of negative thermal buoyancy. Two of the packets rose to 5.5 km MSL before their tracks were terminated. Parcel theory (no entrainment) predicts ~ 3C positive buoyancy at this level. The maximum updrafts varied from 6 to 11 m/s and from 0.5 to 1.5 km above cloud base. These vertical velocities and buoyancies of the chaff are similar to previous such data (Marwitz, 1973).

3.3 Derived Parameters from 304D

Shown in Fig. 3 are the derived parameters of θ_e, θ, and w from 304D for the period 1430 to 1500. The "Begin" and "End" times for the first circuit by 304D (see Fig. 1) are indicated. The periods prior to 1436 and after 1444 have high values of θ_e, while the period from 1436 to 1444 has low values of θ_e. The high values of θ_e indicate this air originated from near the surface, while the low values of θ_e indicate origination from above cloud base. These values of θ_e were in phase with TAS with the highest values of both parameters being observed near 1434. The high θ_e values were, therefore, in ascending air and the low values were in descending air.

3.4 Doppler Radar Results

Contours of reflectivity are shown in Fig. 4 at a number of horizontal levels from cloud base to near the top of the radar echo. Each cell is tilted toward the south with a significant echo overhang on the SW side of the southern cell. The lines marked AA' and BB' are locations of the vertical planes shown in Figs. 7 and 8. Numbered crosses are the relative locations of chaff packets at those heights. The eastern side at the upper levels was not scanned because of the closeness of the storm complex to the radars.

Vertical air motion is displayed in Fig. 5 at the same heights as the reflectivity. Several important features of the vertical air motion are evident. The largest updraft values as determined from chaff trajectories are found outside the 15 dBZ contour. Downdrafts are found near the edges of rather than within the precipitation. This seems to be a consequence of evaporative erosion of the precipitation boundaries. The up/downdrafts were never structured in a way that middle level dry air could have moved very far into the precipitation before evaporation began to cool the air and initiate the downdraft. The > 8 m sec^{-1} updraft speeds in the northern cell (7.5 km MSL) are associated with an updraft located upshear of the cell and tilted in the downshear direction. Chaff packet 2 did indeed overtake the storm even though it was released NW of the cells moving southward. Non-hydrostatic pressure gradients must have existed here to accelerate the air to enable it to overtake the storm.

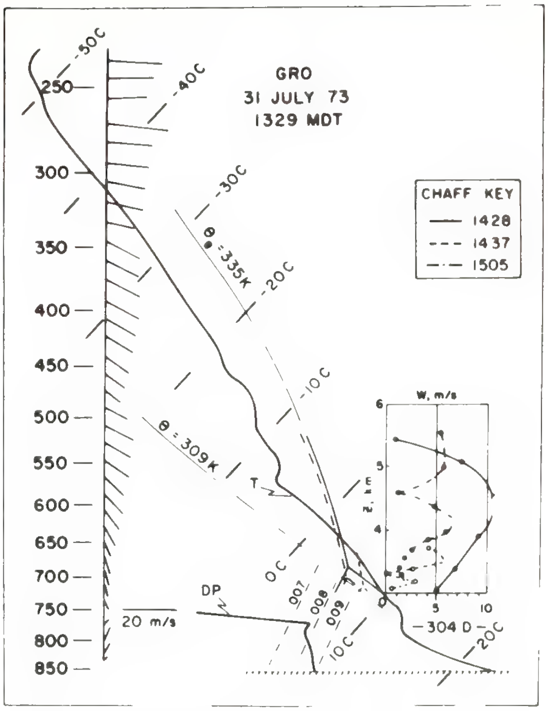

Figure 2. GRO sounding for 1329 and chaff data for 1428, 1437, and 1505. θ, w, and p are noted for each air parcel in which chaff packet was released. The updraft profiles for each chaff track are presented on the same vertical scale as the GRO sounding. The data are spaced at 1 min intervals along the chaff tracks.

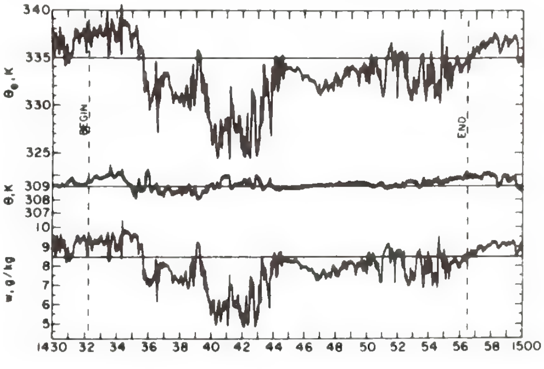

Figure 3. Analog traces of θ_e, θ, and w from 304D during first circuit.

There is a rather abrupt transition in the relative flow from southerly below to westerly above cloud base as seen in Fig. 6. Anticyclonic vorticity (-3.5×10^{-3} sec^{-1}) is found near the middle of the 4.5 km MSL level. Cyclonic vorticity (4×10^{-3} sec^{-1}) is located south of the anticyclonic vortex. These vortices have nearly vertical axes and maintain the same magnitude of vorticity through much of the echo above cloud base.

There is divergent flow at cloud base on both the NE and NW sides of the northern cell. These outflow regions are well correlated with the lower θ_e values at times 1436 and 1442 (Fig. 3) on the 304D circuit. Cloud base is about the lowest level of any appreciable downdrafts.

Vertical slices of reflectivity and air motion in the plane along AA' are shown in Fig. 7. The 20 dBZ contour is repeated in Fig. 7 for easier reference. Fig. 8 (vertical plane along BB') shows the downshear tilt of the updraft outside the 20 dBZ contour (chaff packet 2). Extrapolation of this chaff trajectory places it in good agreement with the internal flow pattern.

4. CONCLUSIONS

a. Subcloud inflow into the storm

The data from the GRO rawinsonde (Fig. 2), from N304D (Figs. 1 and 3) and from 10UW (Fig. 1) rather clearly show that the air feeding this storm had its origin from near the surface and was entering the storm on the upshear (W to NW) side of the storm. The rawinsonde and 10UW data indicated that the air at cloud base was negatively thermally buoyant by 1 to 2C and yet the chaff continued to rise. Marwitz (1973) and Foote and Fankhauser (1973) have noted similar negative buoyancies at cloud base. Grandia and Marwitz (1974) have shown that the chaff rises in the presence of negative thermal buoyancies due to a positive vertical pressure perturbation gradient. The existence of such perturbations may also affect the horizontal motions of the chaff. It may be noted that the earliest chaff packet (1428) moved toward the SE even though its original momentum was toward the NNW. The chaff packets released at 1437 and 1505 continued to move toward the NNW even though environmental air above cloud base was from the opposite direction. A lack of form and entrainment drag and an effect from pressure perturbations are indicated for this storm.

b. Internal Structure

There are 4 important observations in the Doppler data:

1) Precipitation falls out downshear from a downshear-tilted updraft rather than upshear from an upshear tilted updraft.

2) No significant downdraft speeds are found near or below cloud base.

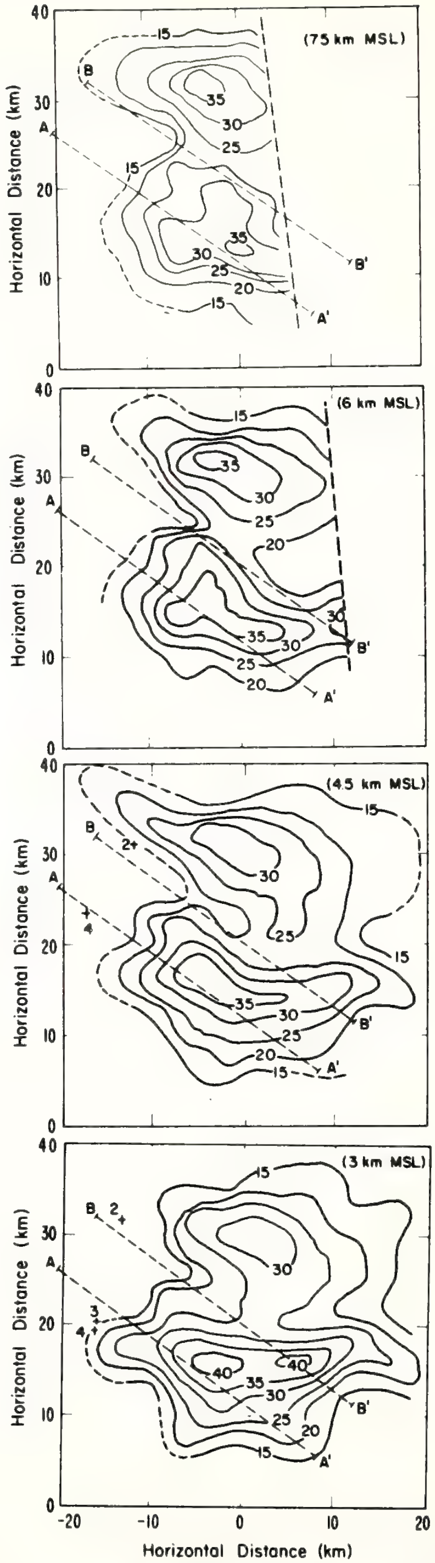

Figure 4. Horizontal planes at 4 levels starting at cloud base (3 km MSL) and spaced by 1.5 km of 3 cm reflectivity (dBZ) and chaff positions at these levels. The lines AA' and BB' are the locations of the vertical planes shown in Figs. 7 and 8.

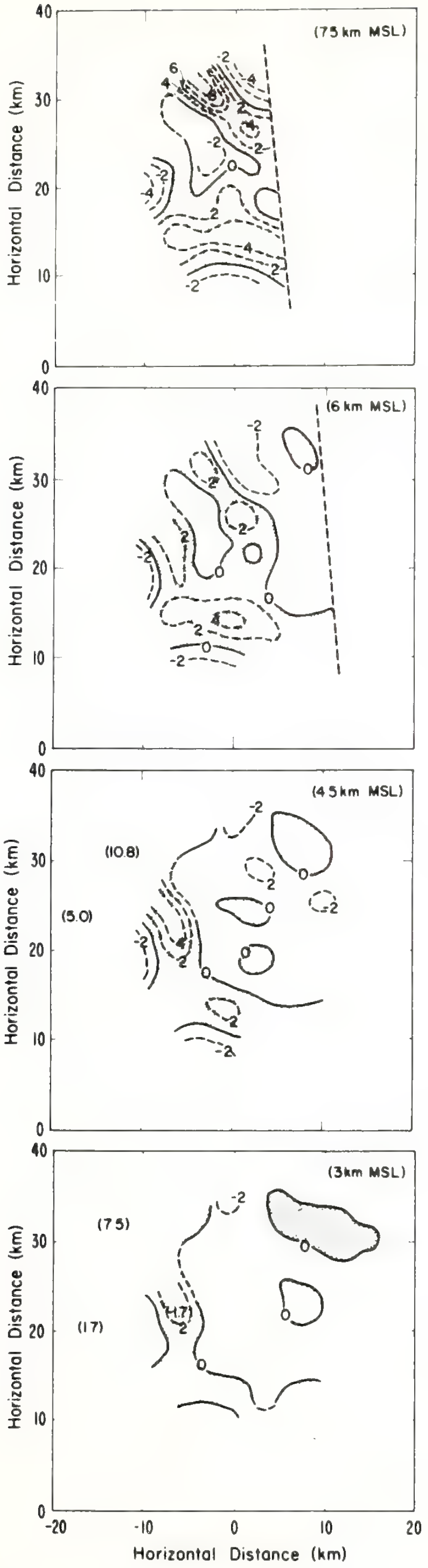

Figure 5. Vertical air motion at the same levels as Fig. 4. The numbers in parentheses are chaff derived vertical air motions at (or near) these levels. The contour interval is 2 m sec^{-1}.

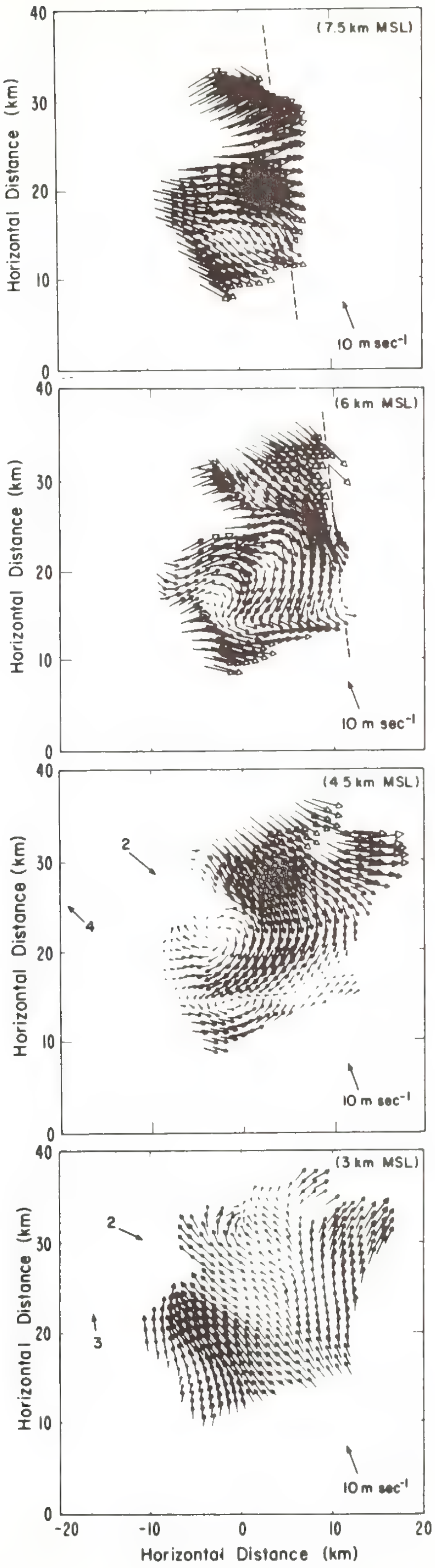

Figure 6. Relative horizontal air motion at the levels of Fig. 4. The numbered vectors to the west are chaff derived relative horizontal air motions.

3) Air in the lowest 500 m moves horizontally across the storm relatively undisturbed.

4) Air is only weakly lifted out of the subcloud layer as evidenced by small (< 1 m sec^{-1}) updrafts in this layer.

The up and downdrafts appear not to be configured in a way which allows the usual more severe storm to develop (Browning, 1964; Kropfli and Miller, 1975; Marwitz, 1972). An updraft which tilts downshear will have precipitation falling out on the downshear side. This configuration does not permit fallout into intruding dry middle level air. Evaporative cooling, therefore, did not produce a strong downdraft.

Such a storm configuration as observed here would at first glance require that the storm not advect. Pressure perturbations could, however, accelerate the air locally so that it can overtake the storm as the storm moves in the general downshear direction. This overtaking is clearly shown in the trajectory of the chaff released at 1428. In addition, air can move beneath and through the precipitation and still be lifted in the backside (relative to the storm motion) as shown in the Doppler data at 500 m AGL. The relatively moist layer beneath the 765 mb temperature inversion may have played a role in this process.

REFERENCES

Biter, C., C. Wade, and A. Rodi, 1974: Field calibration and intercomparison of aircraft meteorological measurements, to be published.

Browning, K. A., 1964: Airflow and precipitation trajectories within severe local storms which travel to the right of the winds, J. Atmos. Sci., 21, 634-639.

Duchon, C. E., 1973: Interaircraft calibration experiment, Final Report NCAR Subcontract 183-71, Univ. of Oklahoma, Norman, Okla., 63 pp.

Foote, G. B. and J. C. Fankhauser, 1973: Airflow and moisture budget beneath a northeast Colorado hailstorm, J. Appl. Meteorol., 12, 1330-1353.

Grandia, K. L. and J. D. Marwitz, 1974: Observational investigations of entrainment within the weak echo region, Monthly Wea. Rev. (in press).

Kropfli, R. A. and L. J. Miller, 1975: Thunderstorm flow patterns in three dimensions from dual-Doppler radar, Preprint Vol., AMS 16th Radar Meteorol. Conf., Houston, Texas, 21-23 April 1975.

Marwitz, J. D., 1973: Trajectories within the weak echo regions of hailstorms, J. Appl. Meteorol., 12, 1174-1182.

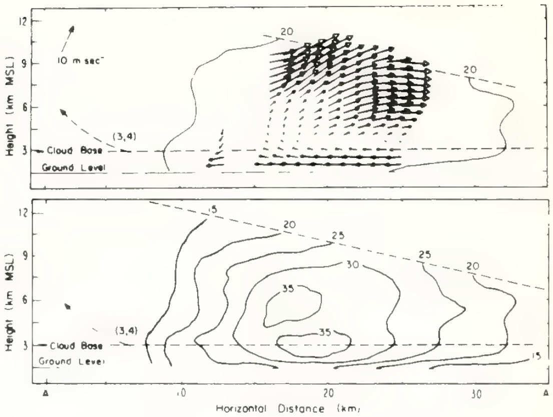

Figure 7. Vertical planes containing 3 cm reflectivity (7a) and relative air motion in this plane (7b). Projections of chaff trajectories nearest this plane are also shown. This plane is oriented along A (NW) to A' (SE) on the south side of the southernmost radar cell.

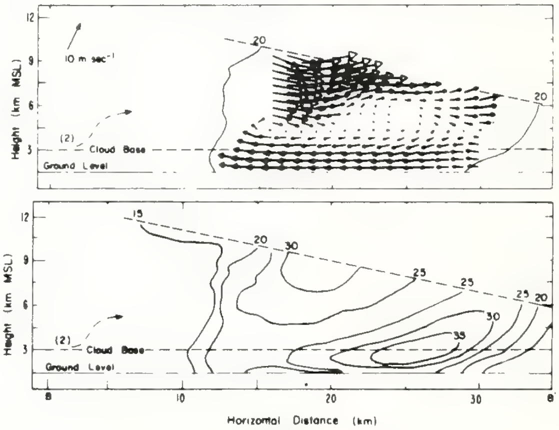

Figure 8. The same as Fig. 7 except along BB' on the north side of the southern cell.

Marwitz, J. D., 1972: The structure and motion of severe hailstorms, Parts I, II, and III, J. Appl. Meteorol., 11, 166-201.

Miller, L. J. and R. G. Strauch, 1974: A dual-Doppler radar method for the determination of wind velocities within precipitating weather systems, Remote Sensing of Environ., 3, 217-233.

Miller, L. J. and H. W. Frank, 1974: Three-dimensional air motion within a northeast Colorado rainstorm, Preprint Vol., AMS Conf. on Cloud Physics, 321-327.

Proceedings AMS Conference on Cloud Physics, 321-327, October 1974.

THREE-DIMENSIONAL AIR MOTION WITHIN A NORTHEAST COLORADO RAINSTORM

L. J. Miller and H. W. Frank

NOAA/ERL, Wave Propagation Laboratory
Boulder, Colorado 80302

1. INTRODUCTION

In recent years multiple Doppler radar systems have emerged as instruments capable of revealing the detailed air motion structure within convective precipitating weather systems. Knowledge of these in-cloud wind fields is prerequisite to any complete understanding of the dynamical and many of the microphysical processes occurring in convective storms. A dual Doppler technique of radar scanning and data reduction (Miller and Strauch, 1974) has been successfully used by the Meteorological Radar Program of this laboratory in air motion studies for the past two years.

During the 1973 summer field program of the National Hail Research Experiment* (NHRE), two 3-cm mobile Doppler radars were located in the NHRE project area in Northeastern Colorado. On 31 July a nearly stationary storm complex which developed in the area of coverage of these radars was scanned for about 1-1/2 hr. Air motion and radar reflectivity fields obtained in a 5 min period of new growth on the right flank of an older cell are presented here. Additional data throughout the lifetime of this complex exists but was not available at the time of this writing.

2. DUAL DOPPLER SCANNING AND DATA REDUCTION

The dual Doppler coplane method of scanning and data reduction is described in detail in Miller and Strauch (1974). A brief summary of the technique is presented here. The procedure is for two radars to simultaneously scan a common plane, inclined above the local horizontal and passing through the radar positions. The radars scan the storm azimuth sector in each plane using range gating and azimuthal increments.

The Doppler return signals are Fourier analyzed for estimates of the mean particle radial velocities within the pulse volumes of interest. Two such estimates, one from each radar, are combined to give a two-dimensional vector particle velocity. This field is then reduced to air motion in the plane by subtraction of the mean fall velocity contribution as a function of position and radar reflectivity factor. Air motion normal to the plane is obtained from an integration in cylindrical coordinates of the mass continuity equation for an incompressible atmosphere. These three coplane air motion components are then re-interpolated and transformed to Cartesian components at Cartesian grid locations.

The major assumptions implicit in this dual Doppler data reduction technique are:

1) Precipitation particles are tracers of the air motion.
2) Particle fall speeds can be estimated from the radar reflectivity factor with sufficient accuracy.
3) Linear interpolations of measured values to common grid locations are valid.
4) The mass continuity equation for an incompressible atmosphere is applicable at the scale sizes and heights observed by the radars.
5) The velocity fields are stationary for the scan time (~ 2-1/2 min for this study) of a series of planes covering the vertical extent of the radar echo.

3. SYNOPTIC SITUATION AND STORM ENVIRONMENT

On the morning of 31 July 1973, a 500 mb ridge was located over the western United States with a trough extending from the Great Lakes to the Texas Panhandle. There was a weak vorticity maximum over Colorado with northwesterly flow aloft at a speed of 25 m sec^{-1}. Surface dew points across the NHRE network were in the middle to upper 50's. Deep convection was possible but with sharp capping near 200 mb.

The rawinsonde released from Grover, Colorado, at 1329 (all times MDT) is used to define the storm environmental conditions. The surface temperature was 70 deg F with a dew point temperature of 54 deg F. An approximately 10 mb thick superadiabatic layer existed at the surface (842 mb) with a nearly adiabatic layer above it to 710 mb. Observed* cloud base was indeed at 711 mb or near 3 km MSL. The surface water vapor mixing ratio was 10.7 g/kg and the subcloud layer average mixing ratio was 6.75 g/kg.

Low level winds were light and variable from an average direction of 260 deg and speed of 3 m sec^{-1} in the subcloud layer. Winds veered nearly 150 deg in this layer. Through the depth of the cloud (3 km to 13 km MSL) the wind speed increased from 3 m sec^{-1} at cloud base to 25 m sec^{-1} at cloud top. This amount of wind shear, $2.2x10^{-3}$ sec^{-1}, and light winds in the subcloud layer are characteristic environmental conditions which lead to multicell storm formation (Marwitz, 1972). The winds in the cloud layer backed some 50 deg with height indicating cold air advection aloft.

---

*Sponsored by the National Science Foundation and managed by the National Center for Atmospheric Research.

*Private communication, J. D. Marwitz, Univ. of Wyoming.

The melting level was at 4.2 km MSL and the -10 deg C level was at 5.6 km MSL. Cloud top temperatures were colder than -50 deg C. A parcel lifted moist adiabatically from cloud base would have had a temperature excess of 6 deg C at the 500 mb level.

4. STORM EVOLUTION

At 1200 there were towering cumulus NW of Grover, Colorado, with one small radar echo 80 km to the NW. By 1345 another cell amost 15 km in diameter, having a maximum radar reflectivity factor of 45 dBz ($dBz \equiv 10 \log Z/1\ mm^6\ m^{-3}$) at cloud base, was located 33 km north of Grover. Radar locations are shown in Fig. 1 on the 1421 slant range PPI from the Grover 10 cm radar. The new growth to the southwest of the older northern cell was scanned by the WPL dual Doppler radar system beginning at 1414.

The echo complex was moving slowly toward the south at less than 3 m sec^{-1}, the northern cell had a low level relative inflow from the SW at 4.7 m sec^{-1} towards its right forward flank. New growth began at about 1345 in this inflow region and is shown as the cell SW of the large cell at time 1407:34 in Fig. 2. As evidenced by the succeeding cloud base slant range PPI's from the Grover 10 cm radar, growth progressed in the downshear direction at a rapid rate (~ 11 m sec^{-1}) from 1407 to 1422, but more slowly (~ 4 m sec^{-1} overall) after this time.

The dashed lines marked 1427, 1437, and 1505 are horizontal trajectories of chaff packets released from the Univ. of Wyoming Queen Air aircraft flying near cloud base. These chaff results are summarized in Table I. The line enclosing the UWER (unbounded weak echo region) is the expected location of the main updraft deduced from the radar echo structure. However, as seen from the chaff data, updrafts of 5-10 m sec^{-1} must have existed well outside this UWER. By 1500 the new precipitation region of the southernmost cell had partly blocked the inflow region to the northern cell.

5. VERTICAL AIR MOTION AND RADAR REFLECTIVITY STRUCTURE

Horizontal fields at the ground of radar reflectivity factor, horizontal divergence, and streamlines inferred from the Doppler measurements are shown in Fig. 3. The first section (Fig. 3a) is centered on time 1415:24 (A) whereas the second one (Fig. 3b) is centered on time 1418:06 (B), 2 min, 42 sec later. Contours of radar reflectivity factor are at 5 dBz increments. The abscissa is nearly parallel to the cloud layer mean environmental air flow. Streamlines are drawn relative to the ground since this individual cell had no discernible advection, only propagation in the downshear direction. The cross-hatched region is an area of convergence and as such delineates the base of the updraft

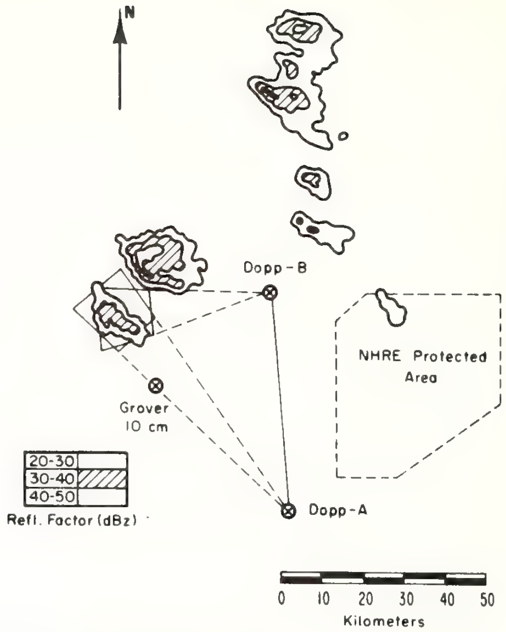

Fig. 1. Plan view of radar positions in NHRE project area. The slant range PPI showing echo locations and dual Doppler scanning area is from the Grover 10-cm radar at 1422.

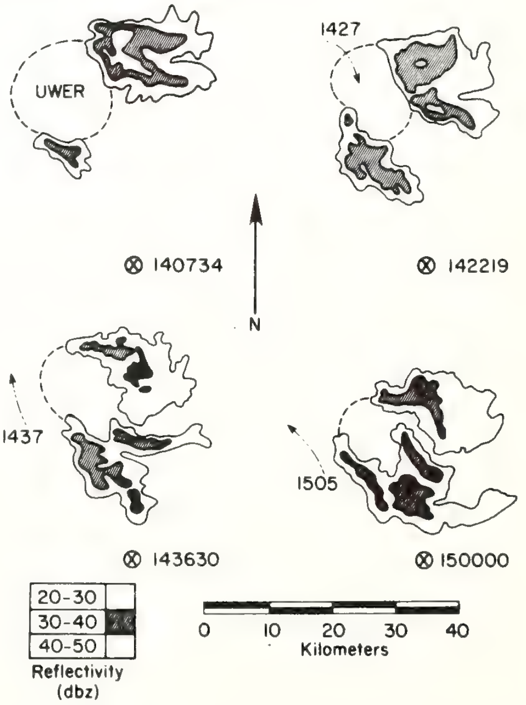

Fig. 2. Four 10-cm radar slant range PPI's taken near cloud base. Times for each frame are marked near Grover (circled X). The dashed lines 1427, 1437, and 1505 are horizontal trajectories of chaff released at cloud base. The unbounded weak echo region (UWER) is the expected updraft location deduced from the radar structure.

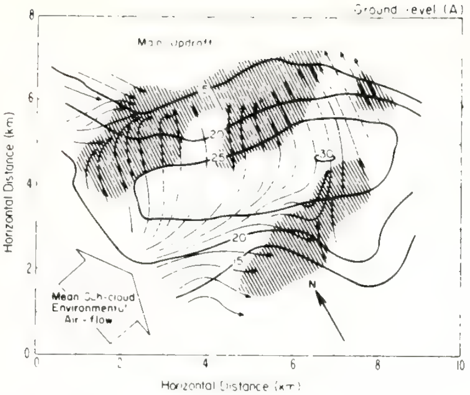

Fig. 3a. 1415:24 MDT (A).

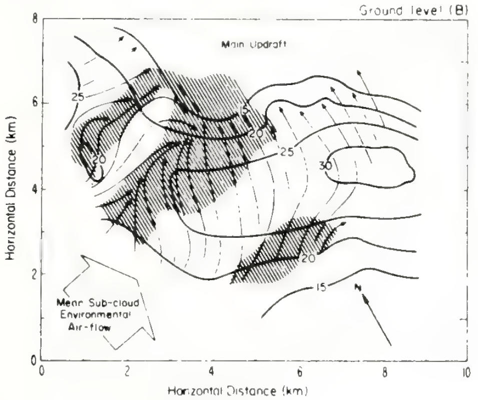

Fig. 3b. 1418:06 MDT (B).

Fig. 3. Ground level Doppler 3-cm radar reflectivity contours, air motion streamlines, and convergence zone (cross-hatched) at times (A) and (B).

which protrudes into the region of precipitation. Only a small portion of the main, approximately 10 km diameter, updraft had sufficient radar return to be detected.

At time (A) the maximum convergence at the surface was 10×10^{-3} sec^{-1} and was located near the top (in Fig. 3a) 15 dBz reflectivity contour. Divergence of 4.6×10^{-3} sec^{-1} was located in the lower left portion near the 20 dBz contour. There was also another divergence peak of 4.3×10^{-3} sec^{-1} slightly upshear from the reflectivity maximum (30 dBz contour). There was net divergence of 0.48×10^{-3} sec^{-1} at the surface but net convergence of 0.36×10^{-3} sec^{-1} throughout the depth of the storm. In the second time interval (B) the peak divergence and convergence values were nearly the same as at time (A), but the mean value of net divergence at the surface had decreased to 0.05×10^{-3} sec^{-1}. However, net convergence into the storm was slightly higher than before and had a value of 0.65×10^{-3} sec^{-1}.

As shown by the streamlines, low level inflow air passed through the precipitation and was lifted in the main updraft at the backside of the cell. Cooling from evaporation of rain in this inflow air will act to decrease its buoyancy and possibly destroy the updraft. There are two possible interpretations of the convergence area toward the right of the downshear direction: 1) low level convergence beneath a new updraft or 2) convergence associated with a part of the old updraft having a precipitation induced downdraft embedded within it (the area enclosed by the 25 dBz contour of reflectivity). The latter interpretation is favored since the new cell grew in what appears to be a broad cloud base updraft as seen from the chaff data.

Radar reflectivity and vertical air motion in horizontal planes beginning at cloud base (~ 1500 m AGL) are shown in Fig. 4. The crosshatched areas are updrafts and the clear area in between is a region of downdraft. Dual Doppler measurements were not available in the areas away from the main body of the cell. These regions near the detected updrafts are most likely updrafts and should be interpreted as such. Peak values of the vertical air motion are given to the nearest meter per second at their respective locations. For example, the peak updraft at 3 km AGL (time A) was 9 m sec^{-1} and the peak downdraft was -5 m sec^{-1}.

Table I. Chaff data* from 31 July 1973.

Time (MDT)	Release height (km MSL)	Horizontal velocity (direction/m sec^{-1})	Vertical velocity	
			Peak (m sec^{-1})	Height (km MSL)
1427	3.7	SE/15	11	4.6
1437	3.4	NW/4	5	4.3
1505	3.6	NW/7	8 and 11	4.4 and 5.8

*Private communication, J. D. Marwitz, Univ. of Wyoming.

Table II. Draft peak values and areal averages for times 1415:24 (A) and 1418:06 (B).

Time	Altitude (m AGL)	Maximum updraft (m sec^{-1})	Maximum downdraft (m sec^{-1})	Average vertical air motion (m sec^{-1})
A	1500	7	-3	-0.5
	3000	9	-5	-0.7
	4500	9	-5	-0.9
B	1500	5	-5	-0.4
	3000	6	-5	-0.3
	4500	7	-9	1.3

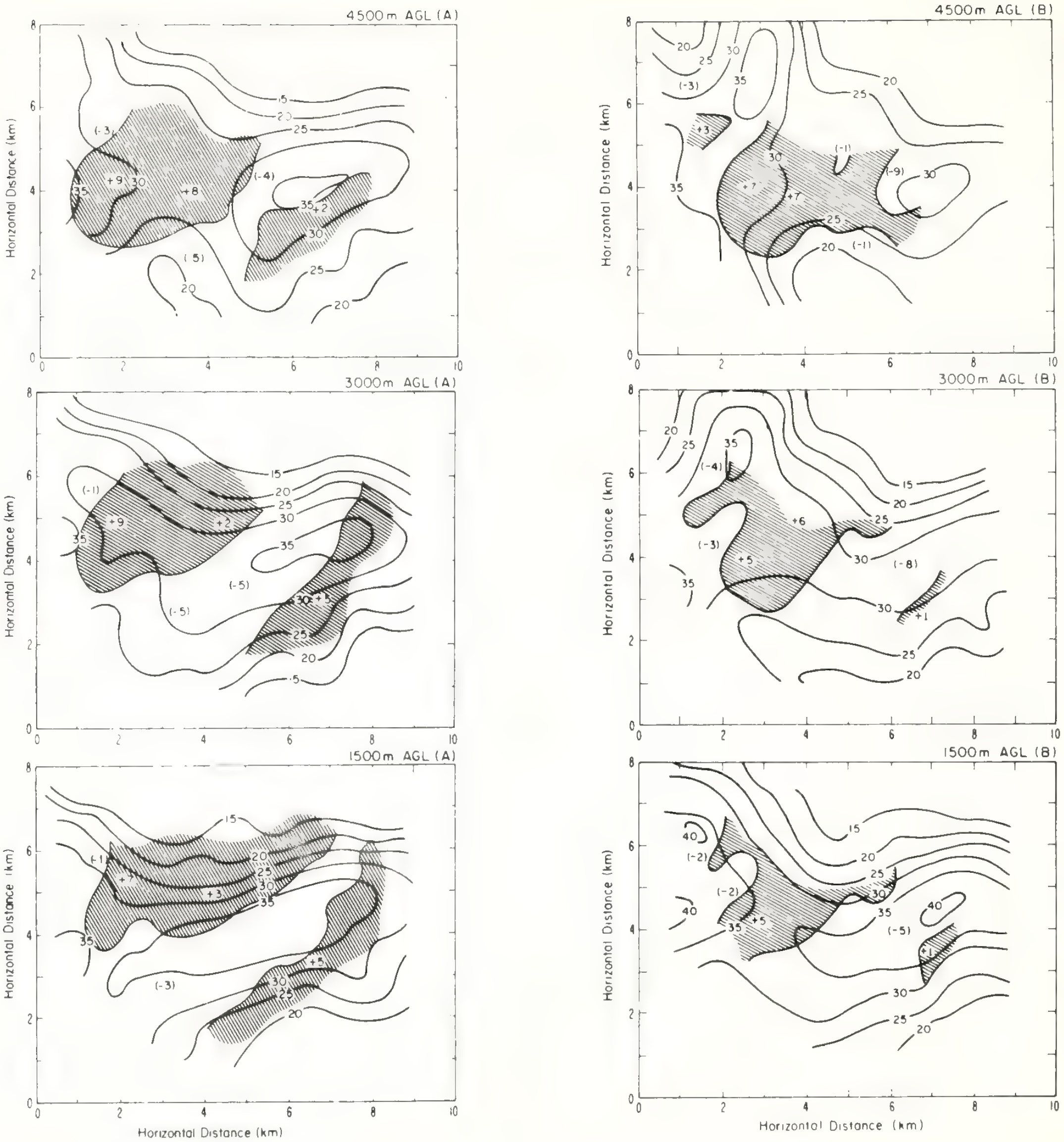

Fig. 4. Radar reflectivity contours and vertical air motion in horizontal planes from cloud base (1500 m AGL) to 4.5 km AGL. The updrafts are the cross-hatched areas and the downdraft is the clear area between these areas. Numbers in parantheses are peak downdraft values and numbers in the cross-hatching are peak updraft values.

All levels at cloud base and above show a general intensification of the downdraft accompanied by a weakening of the updraft. This is evident in both the peak values as well as the areal extent of each draft. These results are summarized in Table II for the two different scan times. The most likely mechanisms which caused this trend were evaporative cooling and gravitational loading of the updraft by the precipitation.

6. HORIZONTAL AIR MOTION

Horizontal vector air motion in horizontal planes spaced by 1500 m starting at the ground are shown in Fig. 5. A 10 m sec^{-1} scaled vector is located in the upper right hand corner of each frame for easy reference. Again those frames marked (A) are for the earlier Doppler time and those marked (B) are for the later time. There is close agreement in the patterns at the successive times thereby lending credence to the data reduction technique. The flow field is seen to advect in the direction of the cloud layer mean winds. This is particularly noticeable at the surface and at cloud base.

The significant features apparent in these flow fields are:

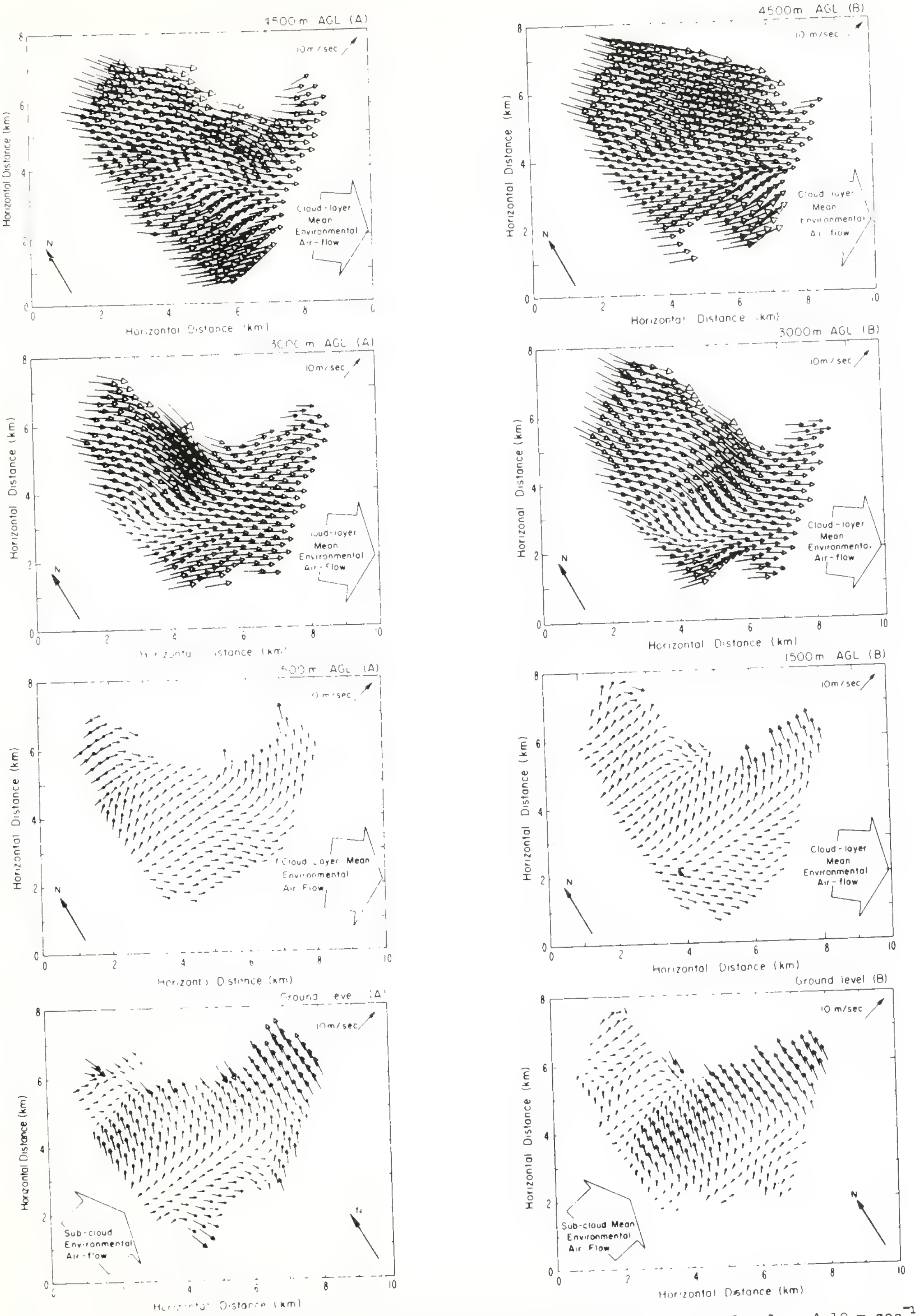

Fig. 5. Horizontal vector air motion in horizontal planes from ground to upper levels. A 10 m sec^{-1} scaled vector is in the upper right corner of each frame.

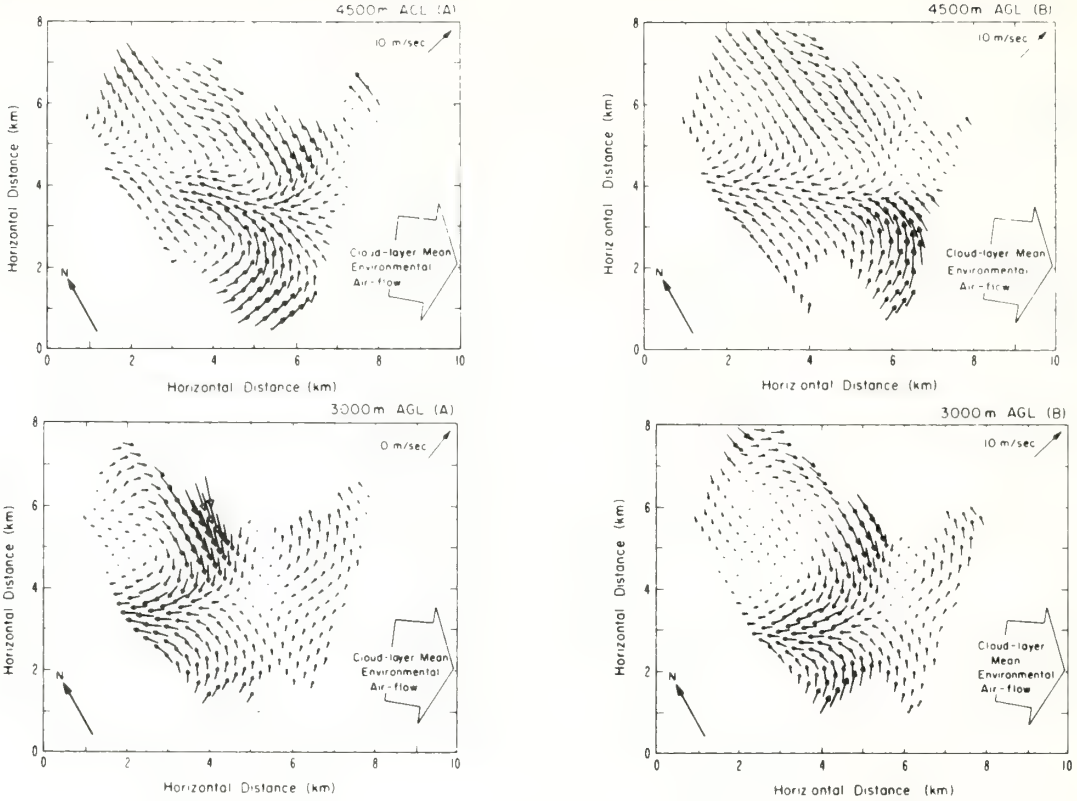

Fig. 6. Horizontal vector air motion after removal of the mean ambient wind at that particular level. Horizontal planes here correspond to the same frames in Fig. 5.

1) Low level environmental flow beneath cloud base is significantly distorted by the up and downdrafts.

2) The entire subcloud layer is apparently a region of inflow into the main updraft.

3) Air motion within the cloud layer is generally along the direction of the environmental flow in this layer.

4) There is deflection of the flow around the main updraft as shown by the cyclonic curvature in the region near the top portion of the 3 and 4.5 km AGL frames.

When the mean ambient wind at a particular level is subtracted from the in-cloud air motion at that level, some rather dramatic smaller scale air motion structure is revealed. Examples of these detailed flow patterns are shown in Fig. 6 for the 3 and 4.5 km levels at times (A) and (B). The high speed tongue of the updraft has anticyclonic curvature whereas the downdraft region has cyclonic curvature. The confluence line is located above the low level high reflectivity zone and oriented parallel to the mean environmental air flow in the cloud layer. This line does not seem to be close enough to downstream from an obstacle (the high reflectivity region on the left side of the upper level frames) in a uniform flow to be considered as a wake line. However, it does bear a remarkable similarity to such a flow regime.

Vertical profiles of the environmental winds from the 1329 Grover RAOB and average in-cloud winds obtained from the Doppler measurements are displayed in Fig. 7. In the subcloud layer the environmental and in-cloud winds are in close agreement. Through the depth of the cloud layer, however, the in-cloud winds are consistently less than the environmental winds. Note that from about 3.5 km AGL to 5.5 km AGL the Ft. Morgan (70 km SW of Grover) rawinsonde data has been added. The sharp decrease in the wind speed in this layer obtained from the Grover RAOB is believed to be a result of the balloon having passed through the storm outflow region. Humidity data indicated a slightly more moist, but unsaturated layer here. The environmental wind direction just below cloud base where the Doppler winds and environmental winds had the same speed was 357 deg. If this is more than just coincidence, the storm complex was advecting along the direction of the cloud base winds.

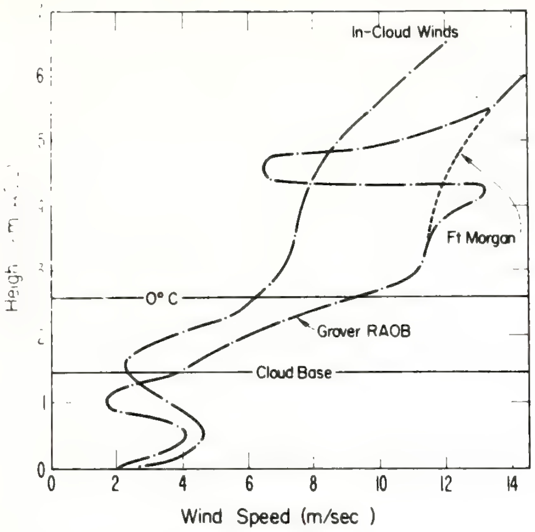

Fig. 7. Vertical profiles of the areal mean, Doppler inferred in-cloud air motion and the environmental winds from the Grover (and Ft. Morgan) rawinsondes. These profiles are separated in time by about 45 min.

7. SUMMARY AND DISCUSSION

Two coplane scans by a dual Doppler radar system taken less than 3 min apart have been used to infer the three-dimensional air motion and its evolution within a rainstorm. Some of the more important observations are:

1) Precipitation from a growing cell on the right forward flank of an older cell falls into the low level inflow region of the older cell.

2) Subcloud layer winds in the precipitation region are in close agreement with the environmental winds.

3) Cloud layer winds within the precipitation zone are consistently lower than the environmental winds in the same layer. However, the environmental and in-cloud air is moving in the same general direction.

4) Downdrafts show significant intensification in a very short period of time, 4 m $\sec^{-1}$ increase in less than 3 min. Updrafts show a 2-3 m $\sec^{-1}$ decrease in the same time interval.

5) The updraft is rotating anticyclonically in the upper levels whereas the downdraft is rotating cyclonically.

6) A confluence line exists above the low level high reflectivity area and is oriented parallel to the cloud layer mean environmental flow.

7) A high reflectivity region and its associated downdraft occur on the downshear side of the updraft. This is consistent with such two-dimensional numerical models of precipitating convective clouds as Takeda's (1971).

8) New growth occurring ahead of or within the older updraft possibly has a new updraft associated with it. This kind of discrete propagation of both radar echo and updraft is very similar to Hane's (1973) two-dimensional squall line thunderstorm model.

Further analysis of available Doppler data is expected to reveal many more features of this air motion. The complete history of this non-steady state, precipitating convective system air motion should help to confirm or reject earlier hypotheses about the wind structure deduced from radar reflectivity. In addition, numerical models can be tested with measurements of the air motion within the cloud at a scale comparable to the models.

Acknowledgements

The authors wish to express their thanks to the rest of the WPL/Meteorological Radar Program staff, notable among whom was R. G. Strauch, without whose assistance the field operation and data reduction could not have been accomplished.

References

Hane, C. E., 1973: The squall line thunderstorm: Numerical experimentation. J. Atmos. Sci., 30, 1672-1690.

Marwitz, J. D., 1972: The structure and motion of severe hailstorms. Part II: Multicell storms. J. Appl. Meteorol., 11, 180-188.

Miller, L. J. and R. G. Strauch, 1974: A dual-Doppler radar method for the determination of wind velocities within precipitating weather systems, submitted to Remote Sensing of Environ.

Takeda, T., 1971: Numerical simulation of a precipitating convective cloud: The formation of a "long-lasting" cloud. J. Atmos. Sci., 28, 350-376.

Proceedings 16th AMS Radar Meteorology Conference, 83-88, April 1975.

DOPPLER RADAR MEASUREMENTS OF TURBULENCE, SHEAR, AND DISSIPATION RATES IN A CONVECTIVE STORM

R. G. Strauch, A. S. Frisch, and W. B. Sweezy

NOAA/ERL/Wave Propagation Laboratory
Boulder, Colorado 80302

1. INTRODUCTION

Recent research with Doppler radar has emphasized the utilization of the first moment of the Doppler velocity spectrum to infer air motions in convective storms. The dual-Doppler radar method uses the first moment measurements from separated radars to estimate the three-dimensional wind field throughout the storm as, for example, in Kropfli and Miller (1975). Regions of high wind shear, updrafts, inflow, etc., are clearly defined with the dual-Doppler technique. A single Doppler radar can measure the reflectivity factor, radial velocity, and variance of the radial velocity throughout the storm echo. In some cases it is possible to deduce the approximate air motions inside the storm from the radial velocity field measured by a single Doppler radar. However, there has been relatively little use made of the second moment of the Doppler spectrum, except for zenith pointing radars (Battan, 1974). In this paper we present data derived from the second moment of the velocity spectrum taken by a radar that scanned a convective storm at low elevation angles. Measurements of the radial velocity field and radar reflectivity depict the structure of the storm and the radial wind shear. In addition, we have supporting data from a zenith pointing radar that enables us to relate the observed second moments to the location of the storm updrafts.

2. VARIANCE OF THE DOPPLER SPECTRUM

There are 3 major contributors to the variance or second moment of the Doppler spectrum for a narrow beamwidth radar: wind shear, turbulence, and the spread of particle fall speeds. Lhermitte (1963) has shown that the spread of fall velocities in rain, σ_D^2, is about 1 m^2 sec^{-2} and is nearly independent of rainfall rates. If the precipitation is observed at low elevation angles, θ, (less than 15 deg) then the contribution to the second moment is $\sigma_D^2 \sin^2 \theta$ or at most about 1/16 m^2 sec^{-2} and can usually be neglected. If hail is present, then the fall speed spread may be as great as 20 m^2 sec^{-2} (Battan, 1974) with a contribution of 1.3 m^2 sec^{-2} to the variance measured by a radar observing the hail at a 15 deg elevation angle. In the data we used the fall speed spread was neglected because the high variance values that were observed by the zenith pointing radar occurred where the scanning radar elevation angle was less than 8 deg. If the variance measured by the zenith pointing radar is attributed entirely to the spread of fall velocities, then the fall speed variance measured by the scanning radar would be at most 0.4 m^2 sec^{-2} over a small region and generally less than 0.2 m^2 sec^{-2}.

The variance contribution due to wind shear across the beam is given by

$$\sigma_s^2 = (0.3\ k\ R\ \theta)^2$$

where k is the shear across the beam (sec^{-1}), R is the range and θ is the one way, half-power beamwidth. The variance contribution for shear along the beam is given by

$$\sigma_s^2 = \frac{(kh)^2}{12}$$

where h is the radar range resolution (Sirmans and Doviak, 1973). Thus there are 3 shear components to be considered; one along the beam k_R, and two orthogonal components across the beam, k_V and k_H. Since the scanning Doppler radar measures the mean radial velocity throughout the storm, each of these shear contributions can be evaluated. (For purposes of this paper, we are defining "wind shear" as those components of wind variability that exist on scale sizes that can be measured by the mean radial velocity field.) The shear contribution to the velocity variance is given by

$$\sigma_s^2 = \left(k_H^2 + k_V^2\right)(0.3\ R\ \theta)^2 + \frac{k_R^2\ h^2}{12}$$

for low elevation angles. We estimate the shear contribution by calculating the 3 shear components from finite differences of the mean radial velocity measurements. The antenna beamwidth is 0.9 deg and the range for the data used is 40 to 55 km. The radar range resolution is 75 m, so the variance caused by shear across the beam will usually be much greater than that caused by shear along the beam.

The contribution to the velocity variance due to turbulence is not as well known. (We are classifying those components of wind variability that cannot be resolved by the radar as "turbulence.") Lhermitte (1972) tabulates the turbulence contribution to the variance as 0.1 to 0.5 m^2 sec^{-2} for "light turbulence" and 6 to 20 m^2 sec^{-2} for "strong turbulence." Sirmans and Doviak (1973) take 4 m^2 sec^{-2} as an average value in a convective storm. Data from the National Severe Storms Project (Steiner and Rhyne, 1962) show rms velocity fluctuations greater than 4 m sec^{-1} on scale sizes from 30 m to 3 km in thunderstorm penetrations with aircraft. Data from zenith pointing radars can be used to deduce the turbulent contribution only if the drop size distribution is known. Large variance values measured by zenith pointing radars are invariably attributed to the distribution of the fall speeds of hail. Donaldson and Wexler (1968) suggest that velocity variances observed with a zenith pointing radar greater than 4 m^2 sec^{-2} are likely indicators of damaging hail, severe turbulence, or both. If the variance of the velocity spectrum is measured by a radar scanning at low elevation angles where the variance caused by fall speed spread is negligible, and if the shear contribution is negligible or can be found from the velocity field, then the variance due to turbulence can be evaluated.

3. DISSIPATION ESTIMATES

The problem with using the variance of the Doppler spectrum (corrected for shear and fall speed spread) as the measure of air turbulence is that the variance is a function of the pulse volume (Frisch and Clifford, 1974) as well as the turbulent motions. A more useful quantity for characterizing the inertial subrange turbulence is the turbulent dissipation rate, ϵ. This quantity can be estimated from the variance of the Doppler spectrum if the outer scale of the inertial subrange is larger than the largest dimension of the radar pulse volume (Frisch and Clifford, 1974).

The dissipation rate is a measure of the turbulent intensity (Trout and Panofsky, 1969) and regions of large ϵ are regions of strong turbulence. The three-dimensional field of ϵ and its temporal evolution in a storm would be an important measure of the internal energy transfers that occur. It would also allow prediction of how seed material would diffuse if injected into various parts of the storm (Kyle, 1974). A real-time display of the dissipation rate is needed if seeding aircraft are to inject seed material for optimum diffusion in the storm and at the same time avoid hazardous flight conditions.

Measurement of the dissipation rate using Doppler radar is described by Gorelik and Mel'nichuk (1963, 1968) for a zenith pointing radar where the pulse length is larger than the beamwidth. Frisch and Clifford (1974) applied the technique to the convective boundary layer and derived expressions for the pulse volume effects. In both of these papers, the radar-measured velocity variances were assumed to be caused by air turbulence--shear and fall speed spreading was negligible. The turbulence was much less than would be expected in a convective storm. Frisch and Clifford used chaff tracers in the boundary layer and measured dissipation rates up to 30 cm^2 sec^{-3}.

The expression derived by Frisch and Clifford, applicable to the present case where the beamwidth is much greater than the pulse length, is

$$\epsilon \doteq \frac{1}{\alpha} \left[\frac{\sigma_T^{\,2}}{1.28\ A} \right]^{3/2} \qquad (1)$$

$\sigma_T^{\,2}$ is the portion of the variance of the Doppler spectrum caused by air turbulence, A is the universal constant ($A \approx 0.47$, Lumley and Panofsky, 1964) and α is the width parameter of the Gaussian beamwidth. For the radar used in these experiments, $\alpha = 0.0094$ R. The largest beam dimension is about 800 m. We apply the technique at altitudes greater than 1 km and assume the outer scale exceeds the maximum beam dimensions.

4. RESULTS

The dissipation rates in a convective storm were estimated using data acquired during the 1973 field program of the National Hail Research Experiment (NHRE). Radar reflectivity, radial velocity, and velocity variance in a vertical plane parallel to the direction of echo motion are shown in Fig. 1 for a storm that occurred on 9 July 1973. This storm produced pea-sized hail, mixed with rain, at the ground. A few larger hailstones, up to 1.5 cm in diameter, were noted. Echo motion is toward the right (nearly south) at 9 m sec^{-1}. The radial velocity measurements are absolute values. The radar that acquired the data was located about 50 km north of the storm and used a maximum elevation angle of 15 deg. The back portion of the main updraft of the storm, measured with a zenith pointing Doppler radar, is shown by the shaded area (Merrem and Strauch, 1974). Peak updrafts of 20 m sec^{-1} were measured. Radial velocity contours show the feeding air moving against the echo motion, mid-level entrainment of dry air from the backside, and a strong outflow, opposite to the direction of echo motion, at the top of the storm. The gust front and updraft region are clearly depicted by the radial velocity contours. Variance contours show a distinct high variance core at mid-level. This core persists from about 4 to 8 km altitude, and is located just ahead of the highest reflectivity region. The vertical section shown is not through the center of the core. Mid-level contours in a horizontal plane, shown in Fig. 2, reveal high variance values in a region about 5 km in diameter, just ahead of the high reflectivity core. Data from the zenith pointing radar indicate that the high variance values are located at the interface between the updraft and downdraft. Radial velocity contours at 5 km altitude show strong convergence in the feeding air and the mid-level entrainment from the backside. The variance of the Doppler spectrum is less than 1 m^2 sec^{-2} in portions of the backside of the storm and as large as 20 m^2 sec^{-2} at the core of the storm.

If we attribute the entire measured variances to wind shear across the beam, then the variance contours labeled 2, 6, 10, and 14 m^2 sec^{-2} in Figs. 1 and 2 would (approximately) correspond to shear contours of 5.8×10^{-3}, 10^{-2}, 1.3×10^{-2}, and 1.6×10^{-2} sec^{-1}. On the other hand, if we attribute the entire measured variance to turbulence, the contours would correspond (approximately) to dissipation rates of 130, 685, 1470, and 2440 cm^2 sec^{-3}. These values of shear and dissipation would be upper limit values since the actual measured values are caused by both shear and turbulence.

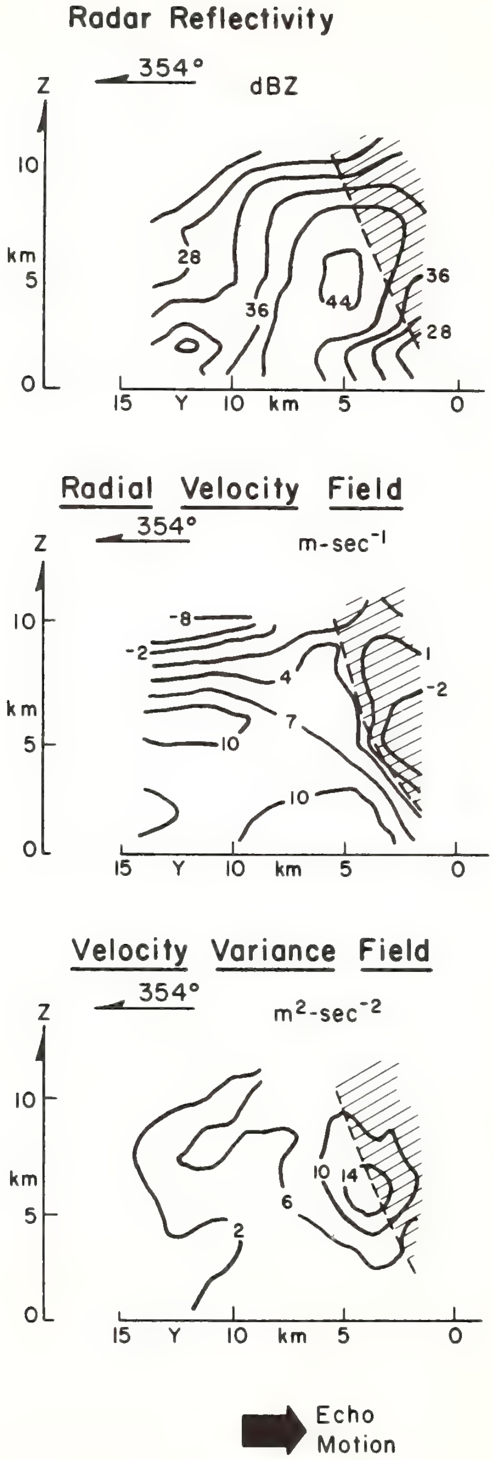

Figure 1. Contours of radar reflectivity, radial velocity and velocity variance in a vertical plane parallel to the echo motion. Positive radial velocity is in the direction of echo motion. Shaded region is the trailing edge of the updraft.

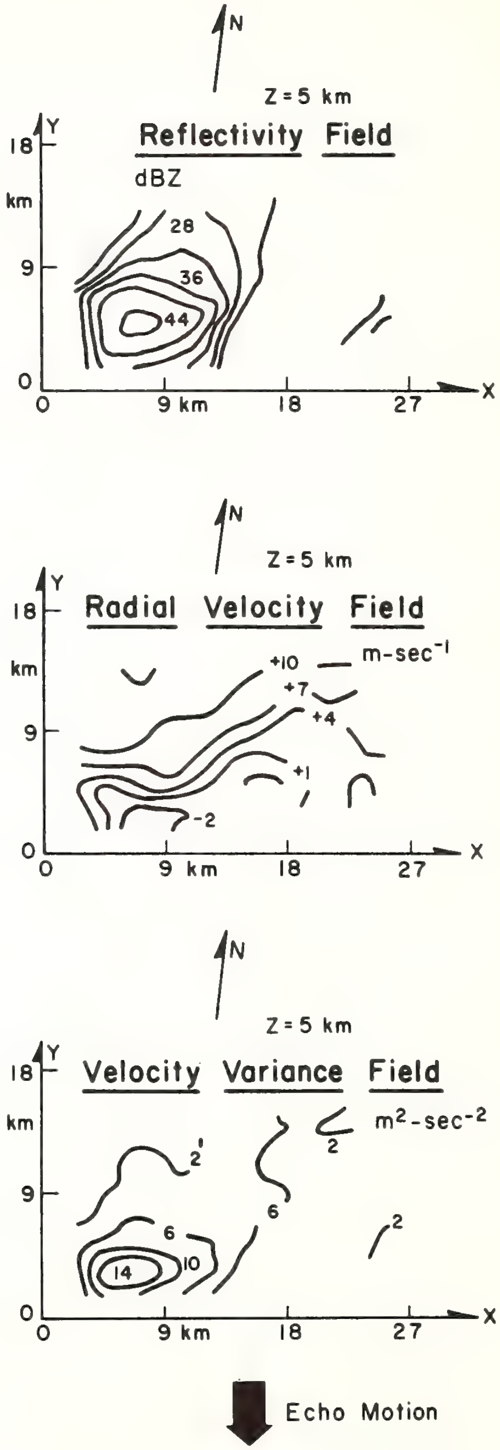

Figure 2. Radar reflectivity, radial velocity and velocity variance at 5 km altitude. Data are measured with a 3 cm radar located about 55 km north-northwest of the storm. Positive radial velocity is in the direction of echo motion.

The shear contributions to the variance of the Doppler spectrum are the result of gradients of the radial velocity. We can estimate the variance that is caused by shear from the radial velocity fields. The shear along the beam, k_R, and the vertical component of the shear across the beam, k_V, can be estimated from the radial velocity displayed in vertical planes, and shear across the beam in the horizontal direction, k_H, can be estimated from the radial velocity displayed in horizontal planes. Since the beamwidth is much larger than the range resolution, the variance caused by radial gradients of the radial velocity will be negligible compared to the variance caused by gradients normal to the beam axis. For example, a radial gradient of 10^{-2} sec^{-1} contributes only 0.05 m^2 sec^{-2} to Doppler variance, whereas the same gradient across the beam contributes 5.5 m^2 sec^{-2} to the Doppler variance if the range is 50 km.

The radial velocity contours in Fig. 1 indicate the highest values of k_V occurred at the back of the storm as a result of the shear created by the mid-level entrainment into the storm and the upper level outflow opposite to the direction of storm motion. Peak values of k_V noted in Fig. 1 are about 6×10^{-3} sec^{-1}. The radial gradient is a maximum in the region where the feeding air and air overtaking the storm from the backside create strong convergence. Values of k_R greater than 10^{-2} sec^{-1} are measured. Note that the radar was located nearly due north of the storm which was moving south and the highest velocities and gradients are in the radial direction. Radial velocity contours in Fig. 2 indicate the cross beam shear, k_H, is very small at 5 km altitude except at the southwest edge of the region scanned. Maximum values of k_H of 4×10^{-3} sec^{-1} are noted.

Turbulent dissipation rates are calculated in several regions of the storm using Eq. 1 with the measured velocity variances corrected for the shear contribution. (The various factors that contribute to the measured variance are assumed independent so the total variance is the sum of the components.) Fig. 3 lists the calculated dissipation rates for the vertical plane shown in Fig. 1 and for the horizontal plane at 5 km altitude shown in Fig. 2. The 44 dBZ reflectivity contour is shown as a solid curve and the 14 m^2 sec^{-2} variance contour is shown as a dashed curve. The dissipation rate was estimated only if the shear component of variance was less than half the measured variance. Since the region of high measured variance is a region of high shear along the beam but relatively low shear across the beam, the shear contribution to the measured variance is relatively unimportant in this region. Therefore the core of high measured variance is also a core of high dissipation rate, and the high dissipation rates extend from about 4 to 8 km altitude in the interface between the updraft and downdraft.

The dissipation rates vary by two orders of magnitude for different areas in the storm. At the backside of the storm the dissipation rates are similar to those measured by Frisch and Clifford in the boundary layer, < 30 cm^2 sec^{-3}, while in the most turbulent region the rates are greater than 2000 cm^2 sec^{-3}. The very highest dissipation rates are 3600 cm^2 sec^{-3} and considerably exceed values usually associated with severe clear air turbulence.

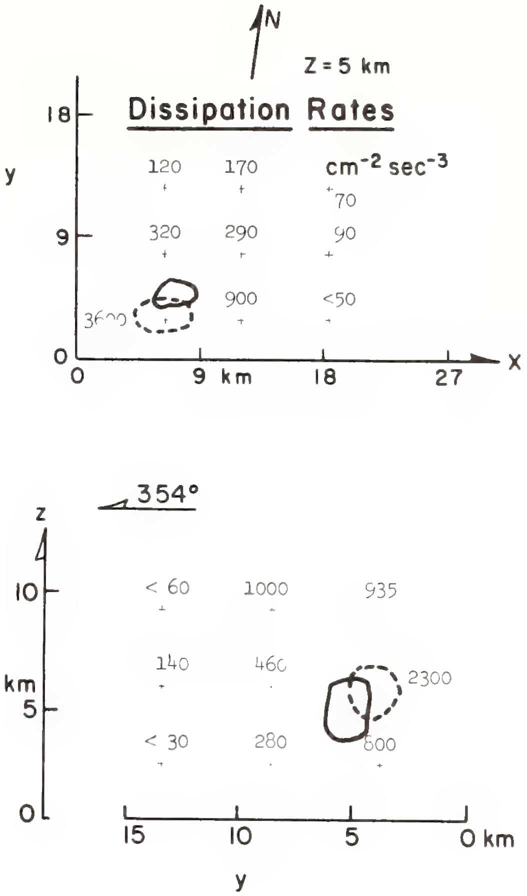

Figure 3. Dissipation rates at 5 km altitude (top) and in the vertical plane shown in Fig. 1 (bottom). The solid contour is 44 dBZ reflectivity and the dashed contour is 14 m^2 sec^{-2} variance. Upper limit of the dissipation rate is estimated when shear contribution to the variance is more than half the total variance.

The results obtained by the scanning radar indicate that significant spectral broadening due to turbulence can occur for a zenith pointing radar. If we have a dissipation rate of 2000 cm^2 sec^{-3} in a region 6 km above the radar, then the velocity variance caused by turbulence will be 4.8 m^2 sec^{-2} for a radar with a range resolution of 75 m and a 1 deg beamwidth. Therefore large variances measured by a zenith pointing radar should not be totally attributed to the fall speed spread of hail.

5. DISCUSSION

Dissipation rates measured by aircraft in clear air turbulence are summarized by Trout and Panofsky (1969) for different levels of intensity. The highest dissipation rate they report is 1160 cm^2 sec^{-3} with a geometric mean of 675 cm^2 sec^{-3} for "severe turbulence." They believe the average estimates to be conservative and may easily be incorrect by 50%. The dissipation rates we calculate using the Doppler radar measurements for a convective storm range from their classifications for "light turbulence" to greater than their numbers for "severe turbulence." Aircraft measurements, with in situ sensors, may be expected to be more accurate than the radar technique, but during the time required for the aircraft to make a single pass through the storm, the radar can obtain estimates throughout the entire storm. For example, the radar data we have used were acquired in 160 sec. In addition, the probability that the aircraft will locate the most turbulent region of a storm is less than unity, and the desirability of doing so is questionable. Kyle (1974) used an aircraft measurement to arrive at an average dissipation rate of 512 cm^2 sec^{-3} throughout the height of a storm to compute the diffusion of seed material. An aircraft flying through the storm we have studied could measure this average value, depending on the track and record length used, but the radar measurements indicate the distribution with height is not constant, and the diffusion for this storm should be modeled considering a small but intense turbulent region at mid-level.

The accuracy of the dissipation rates derived from the radar measurements depends on the accuracy of the measured velocity variance and the accuracy of the assessment of the fall speed spread and shear contributions to the variance. In the data we have used, the fall speed contribution to the variance is at most 0.4 m^2 sec^{-2} and would have negligible effect on the measurements of the highest dissipation rates. In the less turbulent regions of the storm, the fall speed contribution is less than 0.1 m^2 sec^{-2} and would also be negligible. The shear contribution we used would generally be underestimated because it is calculated from velocity fields after the measured velocity fields are interpolated into Cartesian coordinates. The interpolation process reduces peak gradients. The region of highest variance, however, is also a region where little cross-beam shear is measured, and the shear along the beam would have to be about 10^{-1} sec^{-1} to significantly change the highest dissipation rates. The highest measured shear along the beam was only 10^{-2} sec^{-1}. In less intense parts of the storm the gradients should be adequately represented by the interpolated velocity fields. The velocity variance is also interpolated to grid points and we used the smoothed values to calculate dissipation rates rather than the second moments of selected individual spectra used by Frisch and Clifford (1974). The estimate of the second moment of the Doppler spectrum in the presence of noise usually uses a threshold (Campbell et al., 1971) to separate signal from noise. In practice this leads to an underestimation of the second moment. Our method employs a velocity window to select the signal spectra and we manually scan the result to insure the computer algorithm has operated as intended. The Doppler spectra in the high variance region are generally flat and broad. A flat spectrum of width ΔV m sec^{-1} leads to a second moment of $\frac{(\Delta V)^2}{12}$ m^2 sec^{-2} so the signal power extends over about 15 m sec^{-1} for the highest variances measured. This is about one-half the unambiguous velocity interval for our radar.

6. CONCLUSION

The three-dimensional scalar field of velocity variance, measured in a convective storm by a Doppler radar scanning at low elevation angles, depicts areas in the storm where high shear or severe turbulence will be found. Shear of the radial velocity can be estimated from the gradients of the radial velocity field, so the contribution of shear to the velocity variance field can be assessed. Turbulent dissipation rates can be derived from the portion of the variance that is not related to the shear. Dissipation rates derived from the Doppler velocity variance for a northeast Colorado thunderstorm range from rates associated with little or no turbulence to rates associated with severe turbulence. The high dissipation rates were found in the mid-level of the storm at the trailing edge of the updraft. Remote measurement of the dissipation rate throughout the storm provides essential data for calculating the diffusion of seed material injected along a line or at a point. The velocity variance field is also potentially important in identifying hazardous areas for aircraft.

REFERENCES

Battan, L. J., 1974: Doppler radar observations of a hailstorm, Sci. Rep. #28, Univ. of Arizona, Feb 1974.

Campbell, R. B., F. E. Compton, V. Friedman, and H. L. Groginsky, 1971: Doppler signal processing and instrumentation for modified "Porcupine" C-band pulse-Doppler radar, AFCRL-71-0318, May 1971.

Donaldson, R. J. and R. Wexler, 1968: Flight hazards in thunderstorms determined by Doppler velocity variance, J. Appl. Meteorol., 8, 128-133.

Frisch, A. S. and S. Clifford, 1974: A study of convection by a stable layer using Doppler radar and acoustic echo sounder, J. Atmos. Sci., 31, 1622-1628.

Gorelick, A. G. and Yu. V. Mel'nichuk, 1963: Radar study of dynamic process in the atmosphere, Tr. Vses, Nav. Meteorol. Souesh, No. 5.

Gorelick, A. G. and Yu. V. Mel'nichuk, 1968: A new method for measuring dissipation rate of turbulence in clouds and precipitation using conventional radar, Proc. Third All-Union USSR Radar Meteorol. Conf., 150-156.

Kropfli, R. A. and L. J. Miller, 1975: Thunderstorm flow patterns in three dimensions from dual-Doppler radar, *Preprint Vol., AMS 16th Radar Meteorol. Conf.*, Houston, Tex., 21-23 Apr 1975.

Kyle, T. G., 1974: The dispersal of seeding material in the updraft of storms, *Preprint Vol., AMS 14th Conf. on Weather Modification*, 18-21 Nov 1974, 69-72.

Lhermitte, R. M., 1963: Motions of scatterers and the variance of the mean intensity of weather radar signals, *Sperry Rand Res. Center, 5PRC-RR-63-57*.

Lhermitte, R. M., 1972: Probing of atmospheric motion by airborne pulse Doppler radar techniques, *J. Appl. Meteorol.*, *10*, 234-246.

Lumley, J. L. and H. A. Panofsky, 1964: *The Back Structure of Atmospheric Turbulence*, Wiley, London, 239 pp.

Merrem, F. H. and R. G. Strauch, 1974: Observation of a hailstorm with two Doppler radars, *Preprint Vol., AMS Conf. on Cloud Physics*, Tucson, Ariz., 21-24 Oct 1974, 287-291.

Sirmans, D. and R. J. Doviak, 1973: Meteorological radar signal estimation, *NOAA TM ERL-NSSL-64*, US Dept of Commerce.

Steiner, R. and R. H. Rhyne, 1962: Some measured characteristics of severe storm turbulence, *Natl. Severe Storms Project Report No. 10*, US Dept of Commerce.

Trout, D. and H. A. Panofsky, 1969: Energy dissipation near the tropopause, *Tellus*, 21, 355-358.

J. Fluid Mech. (1975), *vol.* 72, *part* 4, *pp.* 673–694
Printed in Great Britain

On higher-order spectra of turbulence

By C. W. VAN ATTA
Scripps Institution of Oceanography, University of California, La Jolla
AND J. C. WYNGAARD
Air Force Cambridge Research Laboratories, Bedford, Massachusetts 01731†

(Received 21 January 1975 and in revised form 3 June 1975)

Measurements of higher-order spectra of turbulent velocity fluctuations in the atmospheric boundary layer over the open ocean and land produce the interesting result that, in the wavenumber range designated originally by Kolmogorov as an inertial subrange, the functional dependence of the spectra on wavenumber is practically independent of the order of the spectrum. These results confirm the observation of Dutton & Deaven that their extension by a dimensional similarity argument of the original Kolmogorov theory to higher-order spectra was not valid. In the present work, we derive an alternative generalization of the Kolmogorov ideas for spectra of arbitrary order. The results of this generalization describe the dependence upon wavenumber of the available data quite well. We also present theoretical calculations based on a Gaussian model for the fluctuating velocity field which furnish quantitative predictions for spectra of arbitrary order that are also in good agreement with the measurements, both in functional form and in absolute value.

Comparison of results based on the Gaussian model with laboratory measurements obtained in a free shear layer shows that the Gaussian theory predicts accurately all the available normalized higher-order spectra for all frequencies. When the corresponding measured higher-order moments are close to those expected for a Gaussian process, the Gaussian theory also correctly predicts the absolute magnitudes of the higher-order spectra.

1. Introduction

Interest in measurements of higher-order statistical functions of turbulent velocity fluctuations in fluid turbulence is partially based on the hope that their determination will provide crucial tests of theories which differ little for lower-order quantities, but which provide wildly conflicting results for higher-order functions. The simplest and most extensive theoretical predictions available are for turbulence in flows with very large values of the Reynolds number. The largest Reynolds numbers achieved in experiments have been obtained in flows of geophysical interest in the atmosphere and oceans.

A great number of measurements of energy spectra (the lowest-order spectral statistic) have been made, but only recently has interest arisen in higher-order spectra, of squares and higher powers of fluctuating turbulent variables. There has been considerable interest in such spectra in statistical communication problems for some time, however.

---

† Present address: Wave Propagation Laboratory, N.O.A.A., Boulder, Colorado 80302.

The term 'higher-order spectra' has been previously used in several different ways in the turbulence literature. In the present work it has the same meaning as in the atmospheric work of Dutton & Deaven (1972) and in the laboratory study of Champagne, Pao & Wygnanski (1976). Here the nth-order spectrum is defined as the power spectrum of the nth power of the fluctuating velocity. This definition differs from another one in common use, namely that the order of the spectrum denotes the number of frequency or wavenumber variables of which the spectrum is a function, and also the dimension of the corresponding displacement vector in its Fourier transform, the $(n+1)$th-order correlation. General characteristics of such polyspectra have been described in detail by Brillinger & Rosenblatt (1967). These include bispectra, which are functions of two frequency variables, trispectra, which are functions of three frequency variables, etc. In the present work, we are not concerned with this latter type of higher-order spectrum, and shall be dealing only with power spectra of powers of the fluctuating velocity.

Dutton & Deaven (1972) considered the behaviour of spectra of algebraic powers of the velocity fluctuations of up to fourth order. Defining $\phi_n(k)$ to be such that $\phi_n(k)\,dk$ is the spectral contribution to $\langle u^{2n}\rangle$ from the wavenumber interval k to $k+dk$ we have

$$\langle (u^n - \langle u^n\rangle)^2\rangle = \langle u^{2n}\rangle - \langle u^n\rangle^2 \equiv \int_{-\infty}^{\infty} \phi_n(k)\,dk. \tag{1}$$

In analogy with Kolmogorov's (1941) development of the second-order structure function and corresponding spectrum ϕ_1, Dutton & Deaven argued that for large Reynolds numbers an inertial subrange of wavenumbers might exist in which all $\phi_n(k)$ depend only upon the wavenumber k and the mean rate ϵ of dissipation of turbulent kinetic energy per unit mass.

Assuming, in analogy with Kolmogorov's original inertial-subrange analysis (which results in $\phi_1(k) = \alpha\epsilon^{\frac{2}{3}}k^{-\frac{5}{3}}$), that $\phi_n(k) = \alpha_n\epsilon^{\gamma}k^{\lambda}$, dimensional analysis yields $\gamma = \frac{2}{3}n$, $\lambda = -\frac{1}{3}(2n+3)$ and

$$\phi_1 \sim k^{-\frac{5}{3}}, \quad \phi_2 \sim k^{-\frac{7}{3}}, \quad \phi_3 \sim k^{-3}, \quad \phi_4 \sim k^{-\frac{11}{3}}, \quad \text{etc.} \tag{2}$$

Dutton & Deaven computed higher-order spectra of up to fourth order ($n = 4$) for all three velocity components from samples of atmospheric turbulence obtained at four different altitudes with instrumented aircraft. The lower-altitude data (250 and 750 ft), obtained over the Kansas plains, were considered as examples of boundary-layer turbulence, while the higher-altitude data (60 000 and 30 000 ft) were characteristic of clear-air turbulence (CAT) over the Sierra Nevada and severe CAT near Grand Junction, Colorado, respectively. The behaviour for $n \geqslant 2$ described by (2) was not observed in any of these cases. As shown in the example of their data replotted in figure 5, rather than increasing in slope with increasing order for the higher frequency range, the higher-order spectra either retained an approximately $-\frac{5}{3}$-power law or decreased somewhat in slope. This behaviour led Dutton & Deaven to conjecture that "it is clear that the $-\frac{5}{3}$ power law generally observed in atmospheric turbulence in the range 100 to 1000 m does not indicate an inertial range in which spectral properties [of higher-order spectra] depend only on $\langle\epsilon\rangle$ and k". This conjecture served as the basic stimulus for the present investigation. If the analysis leading to (2) were correct, it would appear to weaken the foundations of Kolmogorov's inertial-subrange theory sufficiently to require a complete reassessment of the underlying concepts of an energy cascade as first proposed by Richardson (1920).

In the present paper, we propose an alternative extension of Kolmogorov's ideas, which describes the available data quite well. The key factor in the present dimensional argument is an order-dependent dissipation term ϵ_n, which appears in the dynamical equation for $\langle u^{2n}\rangle$.

As noted by Dutton & Deaven, the probability density of the velocity fluctuations in atmospheric turbulence is generally not even approximately Gaussian. In clear-air turbulence, there are clearly more large gusts and more nearly zero values than would be expected if the density were Gaussian. The lower-altitude boundary-layer data appear to fit a Gaussian distribution much more closely. One knows that the distribution cannot, in principle, be exactly Gaussian. If it were, the probability densities of velocity derivatives would also necessarily be Gaussian, in direct conflict with an extensive body of experimental and theoretical evidence. The grid-turbulence measurements of Townsend (1947) furnish an example of a velocity field for which the one-point density $p(u)$ is very nearly Gaussian, but for which the density $p(\partial u/\partial t)$ of its derivative is clearly non-Gaussian. Later work by Frenkiel & Klebanoff (1967) and by Van Atta & Chen (1968) showed that for grid turbulence a Gaussian distribution could be used to predict even-order single- and multi-point moments of the velocity field to very high order with only a small error. The Gaussian assumption is thus a good approximation for the calculation of certain statistical properties of the velocity field, like even-order moments of the velocity, while it is not a good approximation for other properties, like velocity derivatives. It is of course also of no use whatever for multi-point odd-order moments (e.g. triple correlations), which are all identically zero for a multivariate Gaussian distribution.

Champagne *et al.* (1976) used measurements of higher-order spectra ($n \leqslant 4$) in a turbulent mixing layer to determine the contributions of various frequencies to higher moments of the velocity fluctuations. There was relatively little evidence of inertial-subrange behaviour in their ϕ_1 spectra, but they noted that, in the approximately $k^{-\frac{5}{3}}$ region of their first-order energy spectrum, the higher-order spectra did not follow the behaviour predicted by (2), but became somewhat less steep with increasing order.

The question naturally arises as to whether the Gaussian assumption for the probability density of the velocity fluctuations leads to realistic predictions for higher-order spectra of the velocity, and how these would compare with measured spectra and those predicted from the extended Kolmogorov arguments. In the present work we shall see that in the inertial subrange the Gaussian assumption produces results for higher-order spectra that are in excellent agreement with the experiments of Dutton & Deaven and with some new spectral measurements obtained in the atmospheric boundary layer over the open ocean. Comparison with some lower Reynolds number laboratory data of

Champagne *et al.* (1976) shows that the results of the Gaussian calculations are in close absolute agreement with the measured results when the measured higher-order moments are close to the values expected for a Gaussian distribution.

2. Theory

In this section, we present two distinct theoretical attempts to determine the form of higher-order spectra in the inertial subrange. The first is a dimensional argument which can predict only the functional variation with wavenumber or frequency of higher-order spectra. The second analysis, based on an assumption of Gaussianity, predicts the same wavenumber variation, but has the distinct advantage of yielding quantitative predictions for the spectral levels.

2.1. *The maintenance of $\langle u^{2n}\rangle$ and implications for higher-order spectra*

The conservation equations which identify the mechanisms which maintain higher moments in turbulence follow directly from the Navier–Stokes equation. We shall show that these moment equations also suggest which parameters govern the inertial-range behaviour of higher-order spectra.

We start from

$$\partial\langle u_\alpha^{2n}\rangle/\partial t = 2n\langle u_\alpha^{2n-1}\,\partial u_\alpha/\partial t\rangle, \tag{3}$$

where $\mathbf{u} = (u, v, w)$ is the turbulent velocity vector. An equation for the right side of (3) can be derived from the $\partial u_\alpha/\partial t$ equation:

$$u_{\alpha,t} + U_{\alpha,j}u_j + u_{\alpha,j}U_j + u_{\alpha,j}u_j - \langle u_{\alpha,j}u_j\rangle = -p_{,\alpha} + \nu u_{\alpha,jj}. \tag{4}$$

Here $\mathbf{U}$ is the mean velocity vector, p the fluctuating kinematic pressure and ν the kinematic viscosity. A subscript comma denotes differentiation and repeated non-Greek indices are summed. Multiplying (4) by $2nu_\alpha^{2n-1}$ and averaging gives

$$\begin{aligned}\partial\langle u_\alpha^{2n}\rangle/\partial t = {} & \underbrace{-2nU_{\alpha,j}\langle u_j u_\alpha^{2n-1}\rangle}_{\text{shear production}} \underbrace{-U_j\langle(u_\alpha^{2n})_{,j}\rangle}_{\text{advection}} \underbrace{-\langle(u_\alpha^{2n}u_j)_{,j}\rangle}_{\text{turbulent transport}} \\ & \underbrace{+2n\langle u_\alpha^{2n-1}\rangle\langle(u_\alpha u_j)_{,j}\rangle}_{\text{turbulent production}} \underbrace{-2n\langle u_\alpha^{2n-1}p_{,\alpha}\rangle}_{\text{pressure interaction}} \underbrace{+2n\nu\langle u_\alpha^{2n-1}u_{\alpha,jj}\rangle}_{\text{viscous effects}}.\end{aligned} \tag{5}$$

Equation (5) shows that $\langle u_\alpha^{2n}\rangle$ is maintained by a variety of terms. Their relative importance can be determined from scaling arguments of the type used, for example, in Tennekes & Lumley (1972, p. 63) and by considering the form of the $\langle u_\alpha^{2n}\rangle$ equation in special cases. Taking the scaling arguments first, we note that the time rate of change term is at most of order

$$\frac{\partial}{\partial t}\langle u_\alpha^{2n}\rangle \sim \frac{q^{2n}}{l/q} \sim \frac{q^{2n+1}}{l}, \tag{6}$$

where q and l are velocity and length scales of the energy-containing eddies. The first four terms on the right side can also be shown to be at most of this order.

To evaluate the viscous term we start by noting that molecular diffusion of $\langle u_\alpha^{2n}\rangle$ is negligible in large Reynolds number turbulence:

$$\nu\langle(u_\alpha^{2n})_{,jj}\rangle \sim \frac{\nu q^{2n}}{l^2} \sim \frac{q^{2n+1}}{l}\frac{\nu}{lq} \sim \frac{q^{2n+1}}{l}R_l^{-1}, \tag{7}$$

where $R_l = ql/\nu$ is a turbulence Reynolds number. We exploit this result by writing

$$(\nu l/q^{n+1})\,\langle (u_\alpha^{2n})_{,jj}\rangle \simeq 0 \tag{8}$$

and manipulating this to get

$$\langle u_\alpha^{2n-1} u_{\alpha,jj}\rangle = -(2n-1)\,n^{-2}\,\langle u^n_{\alpha,j} u^n_{\alpha,j}\rangle. \tag{9}$$

Using (9), the viscous term in the $\langle u_\alpha^{2n}\rangle$ budget (5) becomes

$$2n\nu\langle u_\alpha^{2n-1} u_{\alpha,jj}\rangle = -2\nu(2n-1)\,n^{-1}\langle u^n_{\alpha,j} u^n_{\alpha,j}\rangle, \tag{10}$$

which shows that it is always negative and hence represents viscous destruction.

To determine the magnitude of the viscous destruction, we note that

$$\langle u^n_{,j} u^n_{,j}\rangle = n^2 \langle u^{n-1} u^{n-1} u_{,j} u_{,j}\rangle. \tag{11}$$

We have dropped the subscript α since the arguments for this term will hold for any component. The higher-order spectral results show that the dominant Fourier modes of $u^{n-1}u^{n-1}$ lie in the energy-containing (small wavenumber) range, and earlier work (e.g. Wyngaard & Pao 1972) shows that those of $u_{,j}u_{,j}$ lie in the large wavenumber range. It is believed (see, for example, Tennekes & Lumley 1972) that these two ranges approach statistical independence as the turbulence Reynolds number (and hence their separation) increases. We write, therefore,

$$\langle u^{n-1}u^{n-1}u_{,j}u_{,j}\rangle \sim \langle u^{n-1}u^{n-1}\rangle\,\langle u_{,j}u_{,j}\rangle \sim q^{2n}/\lambda^2, \tag{12}$$

where $\lambda = (\nu l/q)^{\frac{1}{2}}$ is the Taylor microscale. Our estimate for viscous destruction then is, from (10)–(12),

$$\nu\langle u^n_{\alpha,j} u^n_{\alpha,j}\rangle \sim \nu q^{2n}/\lambda^2 \sim q^{2n+1}/l, \tag{13}$$

which indicates that viscous destruction is of the order of the largest terms in the budget.

The dominant role of viscosity can also be inferred directly in special cases. For example, in a boundary layer over a flat surface and for $\alpha = 2$ (the lateral direction), the shear production, advection and turbulent production terms in (5) all vanish. Turbulent transport only moves $\langle u_\alpha^{2n}\rangle$ around in space, since it integrates to zero over the whole flow. In this flow, then, the pressure and viscous terms are the dominant source and sink, respectively, for $\langle v^{2n}\rangle$.

The dominant role of viscous destruction has direct implications for higher-order spectra. If we use a Fourier–Stieltjes representation for the nth moment,

$$u^n - \langle u^n\rangle = \int e^{i\mathbf{k}.\mathbf{x}} dZ_n(\mathbf{k}), \quad \langle dZ_n(\mathbf{k})\, dZ_n^*(\mathbf{k})\rangle = \phi_n(\mathbf{k})\, d\mathbf{k}, \tag{14}$$

then it follows that

$$\left.\begin{aligned} \langle (u^n - \langle u^n\rangle)^2\rangle &= \int \phi_n(\mathbf{k})\, d\mathbf{k}, \\ \langle (u^n - \langle u^n\rangle)_{,j}\rangle\,\langle (u^n - \langle u^n\rangle)_{,j}\rangle &= \int k^2 \phi_n(\mathbf{k})\, d\mathbf{k}. \end{aligned}\right\} \tag{15}$$

We can also write

$$\langle (u^n - \langle u^n\rangle)_{,j}(u^n - \langle u^n\rangle)_{,j}) = (u^n_{,j} u^n_{,j}\rangle - \langle u^n_{,j}\rangle\,\langle u^n_{,j}\rangle. \tag{16}$$

The second term on the right side of (16) is smaller than the first by a factor

$\lambda^2/l^2 \sim R_l^{-1}$ and can be neglected. It follows that the viscous destruction rate of $\langle u^{2n} \rangle$ (call it ϵ_{2n}) is

$$\epsilon_{2n} = \frac{2(2n-1)}{n} \nu \int k^2 \phi_n(\mathbf{k})\, d\mathbf{k}. \tag{17}$$

We said earlier that the dominant contributions to ϵ_{2n} come from the largest wavenumbers. If there is an inertial range where $\phi_n \sim k^{-m}$, it follows that $m < 2$.

The budget for the odd moment $\langle u^{2n+1} \rangle$ is derived in the same way. It reads

$$\begin{aligned}\partial\langle u_\alpha^{2n+1}\rangle/\partial t = &-\underbrace{(2n+1)\, U_{\alpha,j} \langle u_j u_\alpha^{2n} \rangle}_{\text{shear production}} - \underbrace{U_j \langle (u_\alpha^{2n+1})_{,j} \rangle}_{\text{advection}} - \underbrace{\langle (u_\alpha^{2n+1} u_j)_{,j} \rangle}_{\text{turbulent transport}} \\ &+ \underbrace{(2n+1)\langle u_\alpha^{2n} \rangle \langle (u_\alpha u_j)_{,j} \rangle}_{\text{turbulent production}} - \underbrace{(2n+1)\langle u_\alpha^{2n} p_{\ \alpha} \rangle}_{\text{pressure interaction}} \\ &- \underbrace{(2n+1)\,\nu \langle (u_\alpha^{2n})_{,j} u_{\alpha,j} \rangle}_{\text{viscous effects}}.\end{aligned} \tag{18}$$

The dominant terms here are of order q^{2n+2}/l. If the correlation between u_α^{2n} and u_α extends throughout the k range, then the viscous term is of the same order:

$$\nu \langle (u_\alpha^{2n})_{,j} u_{\alpha,j} \rangle \simeq \nu \frac{q^{2n}}{\lambda} \frac{q}{\lambda} \approx \frac{q^{2n+2}}{l}. \tag{19}$$

Note that the viscous term can be expressed in terms of the higher-order cospectrum:

$$(2n+1)\,\nu \langle (u_\alpha^{2n})_{,j} u_{\alpha,j} \rangle = (2n+1)\,\nu \int k^2 C_0(u_\alpha^{2n}, u_\alpha)\, d\mathbf{k} = \epsilon_{2n+1}. \tag{20}$$

Viscous destruction will be confined to the high-k range, and hence will be significant if the cospectrum falls slower than k^{-2} in the inertial range.

The picture we have roughly sketched suggests that the familiar ideas about the maintenance of velocity variance in large R_l turbulence, and the roles the various scales of motion play, can be generalized to higher moments. Production occurs mainly in the energy-containing (low k) range, with viscous destruction confined to large k. If R_l is so large that these ranges are sufficiently separated, we expect an intermediate, inertial range where only transfer from smaller to larger k occurs.

Direct application of the Kolmogorov arguments to these higher-order spectra gives

$$\left.\begin{aligned} C_0(u^{2n}, u) &= f(\epsilon, k) = \epsilon^{\frac{1}{3}(2n+1)} k^{-(\frac{4}{3}+\frac{2}{3}n)}, \\ \phi_n &= g(\epsilon, k) = \epsilon^{\frac{2}{3}n} k^{-(\frac{2}{3}n+1)}. \end{aligned}\right\} \tag{21}$$

These are clearly incorrect: the slopes are too steep compared with experimental values and the cospectrum does not change sign under co-ordinate reflexion as it must.

A natural extension of the Kolmogorov ideas, and one which recognizes the importance of viscous destruction for higher moments, is

$$C_0(u^{2n}, u) = f(\epsilon, \epsilon_{2n+1}, k), \quad \phi_n = g(\epsilon, \epsilon_{2n}, k). \tag{22}$$

If ϕ_n and C_0 depend in the same way on their arguments, the simplest forms with the required property under co-ordinate reflexion are

$$C_0(u^{2n}, u) \simeq \epsilon_{2n+1} \epsilon^{-\frac{1}{3}} k^{-\frac{5}{3}}, \quad \phi_n \simeq \epsilon_{2n} \epsilon^{-\frac{1}{3}} k^{-\frac{5}{3}}. \tag{23}$$

This predicts that the coherence between u^{2n} and u in the inertial range is independent of the wavenumber. It is also interesting to note the similarity between the higher-order predictions of (23) and that of Corrsin (1951) for the inertial-range spectral level of a passive scalar θ:

$$\phi_\theta \sim N\epsilon^{-\frac{1}{3}}k^{-\frac{5}{3}}, \tag{24}$$

where N is the rate of destruction of scalar variance.

2.2. *Higher-order inertial-subrange spectra for a Gaussian variable*

The dimensional arguments given in §2.1 can predict only the functional dependence of the higher-order spectra on the wavenumber, and not their magnitudes. In this section, an alternative analysis, based on the assumption of Gaussianity, yields predictions for all spectral levels, and gives the same dependence upon wavenumber, which is invariant for all higher-order spectra.

For convenience of comparison with the raw experimental data, the following theoretical development is carried out in terms of spectra that are a function of the frequency f (measured in Hz), rather than in terms of a spatial wavenumber k. Since the measured velocity fluctuations are assumed to be stationary random functions of the time t, comparisons with the predictions of the Gaussian theory can be made without recourse to an assumed relation between f and k. However, when the analytical results are compared with predictions like (2) and (23), it is to be understood that Taylor's hypothesis (see Hinze 1959, p. 40) in the form $k = f/U$ has been invoked, where U is the mean flow velocity.

If a stationary random function of time $u(t)$ is normally distributed, then the higher-order spectra ϕ_n of $u^n(t)$ defined by (1) can all be computed in principle from a knowledge of only the first-order spectrum ϕ_1, or its corresponding correlation function $R(\tau)$. This result follows from the fact that, for a Gaussian process, the joint statistics of the bivariate distribution for $u(t)$ and $u(t+\tau)$ are completely determined by the correlation function $R(\tau) = \langle u(t)\,u(t+\tau)\rangle$. Given the two-sided power spectrum $\phi_1(f)$ of $u(t)$, we wish to find the power spectrum $\phi_n(f)$ of $u^n(t)$. The power spectrum $\phi_n(f)$ will be equal to the inverse Fourier transform of the correlation function $\langle u^n(t)\,u^n(t+\tau)\rangle$:

$$\phi_n(f) = \int_{-\infty}^{\infty} \langle u^n(t)\,u^n(t+\tau)\rangle\, e^{-i2\pi f\tau}\,d\tau. \tag{25}$$

For odd powers of $u(t)$, we have (see, for example, Rice 1973)

$$\langle u^{2n+1}(t)\,u^{2n+1}(t+\tau)\rangle = \sum_{k=0}^{n} \frac{[(2n+1)!]^2\,R^{2k+1}(\frac{1}{2}R(0))^{2n-2k}}{(2k+1)!\,[(n-k)!]^2},$$

where
$$R(0) = \int_{-\infty}^{\infty} \phi_1(f)\,df = \langle u^2(t)\rangle$$

is the variance. For even n, say $n = 2m$, a similar calculation yields

$$\langle u^{2m}(t)\,u^{2m}(t+\tau)\rangle = \sum_{k=0}^{m} \frac{[(2m)!]^2\,R^{2m-2k}(\frac{1}{2}R(0))^{2k}}{(k!)^2\,(2m-2k)!}.$$

The higher-order spectra of a Gaussian variable are thus given by

$$\phi_{2n+1}(f) = \int_{-\infty}^{\infty} d\tau\, e^{-i2\pi f\tau} \sum_{k=0}^{n} \frac{[(2n+1)!]^2 R(\tau)^{2k+1}(\tfrac{1}{2}R(0))^{2n-2k}}{(2k+1)!\,[(n-k)!]^2} \quad \text{(odd powers of } u(t)\text{)}, \tag{26}$$

$$\phi_{2m}(f) = \int_{-\infty}^{\infty} d\tau\, e^{-i2\pi f\tau} \sum_{k=0}^{m} \frac{[(2m)!]^2 R(\tau)^{2m-2k}(\tfrac{1}{2}R(0))^{2k}}{(k!)^2\,(2m-2k)!} \quad \text{(even powers of } u(t)\text{)}. \tag{27}$$

The manipulation of these relations that follows makes use of the convolution relation for the Fourier transform of powers of the correlation function:

$$\begin{aligned}\int_{-\infty}^{\infty} R^m(\tau)\, e^{-i2\pi f\tau}\, d\tau &= \int_{-\infty}^{\infty} df_1 \cdots \int_{-\infty}^{\infty} df_{m-1}\, \phi_1(f_1) \cdots \phi_1(f_{m-1})\, \phi_1(f-f_1 \cdots f_{m-1}) \\ &= (m-1)\text{-fold convolution of } \phi_1(f).\end{aligned} \tag{28}$$

In the general case, evaluation of the higher-order spectra of a Gaussian variable requires either analytical or numerical evaluation of the integrals in (26) and (27), or evaluation of the convolution integrals in (28). These operations require that the entire spectrum or correlation function be specified. However, for the present atmospheric data, we are mainly interested in the behaviour of the spectra in the inertial subrange. As observed by Kaimal *et al.* (1972), first-order spectra obtained from different experiments and under different conditions show a wide systematic variation for low frequencies, depending on the degree of stability and other external parameters, but their forms and magnitudes in the inertial subrange follow a universal scaling. An asymptotic analysis for large frequencies, applying only to the inertial subrange, appears desirable.

To carry out the analysis, one needs a spectral form which reduces to the Kolmogorov spectrum for large frequencies or wavenumbers. A suitable form, due to von Kármán and discussed by Hinze (1959, p. 199), is

$$\phi_1(f) = b\lambda^{\frac{5}{3}}/[1+(\lambda f)^2]^{\frac{5}{6}}. \tag{29}$$

It seems likely that other model spectra which have a $k^{-\frac{5}{3}}$ behaviour in the inertial subrange would also be suitable for the present purpose. The von Kármán spectrum has the advantage of possessing a simple and convenient correlation function (see appendix), which makes it fairly easy to carry out an asymptotic analysis for large f. From (29), the mean square of the velocity fluctuations is

$$\langle u^2 \rangle \equiv R(0) = b\lambda^{\frac{2}{3}}[\Gamma(\tfrac{1}{2})\,\Gamma(\tfrac{1}{3})/\Gamma(\tfrac{5}{6})] = 4{\cdot}20 b\lambda^{\frac{2}{3}}. \tag{30}$$

The higher-order spectra for odd powers of $u(t)$ are then given by

$$\phi_{2m+1}(f) = [(2m+1)!]^2 \sum_{k=0}^{m} \left(\frac{4{\cdot}20 b\lambda^{\frac{2}{3}}}{2}\right)^{2m-2k} \frac{(2k\text{th convolution of } \phi_1)}{(2k+1)!\,[(m-k)!]^2}.$$

For large values of f, keeping only the leading term in the $2k$th convolution of ϕ_1 gives (see appendix)

$$\begin{aligned}2k\text{th convolution of } \phi_1(f) \sim{}& b(b\lambda^{\frac{2}{3}})^{2k}(4{\cdot}20)^{2k}(2k+1)\, f^{-\frac{5}{3}} \\ &+ (\text{higher-order terms in } f).\end{aligned}$$

So for large f, the dependence on f will be the same ($\phi_n \sim f^{-\frac{5}{3}}$) for higher-order spectra of all orders. We then have for large f

$$\phi_{2m+1}(f) \sim [(2m+1)!]^2 bf^{-\frac{5}{3}} \left(\frac{4{\cdot}20b\lambda^{\frac{2}{3}}}{2}\right)^{2m} \sum_{k=0}^{m} \frac{1}{k!(\frac{1}{2})_k[(m-k)!]^2}.$$

The summation term can be written as

$$\begin{aligned}\sum_{k=0}^{m} \frac{(-1)^{2k}(-m)_k(-m)_k}{k!(\frac{1}{2})_k(m!)^2} &= \frac{F(-m,\ -m;\ \frac{1}{2};\ 1)}{(m!)^2} \\ &= \frac{\Gamma(\frac{1}{2})\,\Gamma(\frac{1}{2}+2m)}{(m!)^2\,\Gamma(\frac{1}{2}+m)\,\Gamma(\frac{1}{2}+m)} = \frac{(\frac{1}{2})_{2m}\,2^{2m}}{[(2m)!]^2}.\end{aligned}$$

Finally, for the power spectra of odd powers of $u(t)$ we have

$$\phi_{2m+1}(f) \sim b(4{\cdot}20b\lambda^{\frac{2}{3}})^{2m}(2m+1)^2[1 \times 3 \times 5 \times \ldots \times (4m-1)]f^{-\frac{5}{3}} \qquad (m = 1, 2, \ldots). \tag{31}$$

A similar analysis for even powers of $u(t)$ produces the result

$$\begin{aligned}\phi_{2m}(f) \sim{} & (\text{d.c. spike}) + b(4{\cdot}2b\lambda^{\frac{2}{3}})^{2m-1} \\ & \times (2m)^2[1 \times 3 \times 5 \times \ldots \times (2m-1)\,(2m+1) \times \ldots \times (4m-3)]f^{-\frac{5}{3}}.\end{aligned} \tag{32}$$

Equations (31) and (32) may be combined to obtain a single expression valid for arbitrary powers (both even and odd) of u:

$$\begin{aligned}\phi_n(f) \sim{} & (\text{d.c. spike if } n \text{ is even}) \\ & + b(4{\cdot}2b\lambda^{\frac{2}{3}})^{n-1} n^2[1 \times 3 \times 5 \times \ldots \times (2n-3)]f^{-\frac{5}{3}},\end{aligned} \tag{33}$$

where the final product in brackets is replaced by 1 when $n = 1$.

From (29) and (33), the non-dimensionalized ratio of the higher-order spectra to the first-order spectrum is simply

$$\phi_n(f)/[R(0)^{n-1}\phi_1(f)] = n^2[1 \times 3 \times 5 \times \ldots \times (2n-3)]. \tag{34}$$

Note that this ratio is independent of the parameters b and λ and of the dimensions used for the velocity u and other multiplicative constants in the spectra or frequency variable.

3. Comparison of atmospheric experimental data with theory

The raw computed spectra shown in figures 1 and 2 were compared with the dimensional theory of §2.1 and with the asymptotic theory of §2.2. These are spectra of the longitudinal component $u(t)$ of the fluctuating velocity obtained in the atmospheric boundary layer over the open ocean at a height of 3 m above the mean water surface level. The data were obtained during steady trade wind conditions from FLIP, the stable floating instrument platform of the Scripps Institution of Oceanography, during the Barbados Oceanographic and Meteorological Experiment (BOMEX), in May 1969. The mean velocity was 7·2 m/s. The fluctuating velocity was measured with a single vertically oriented hot wire 5 μm in diameter and 1 mm long. This hot wire was operated in the constant-resistance

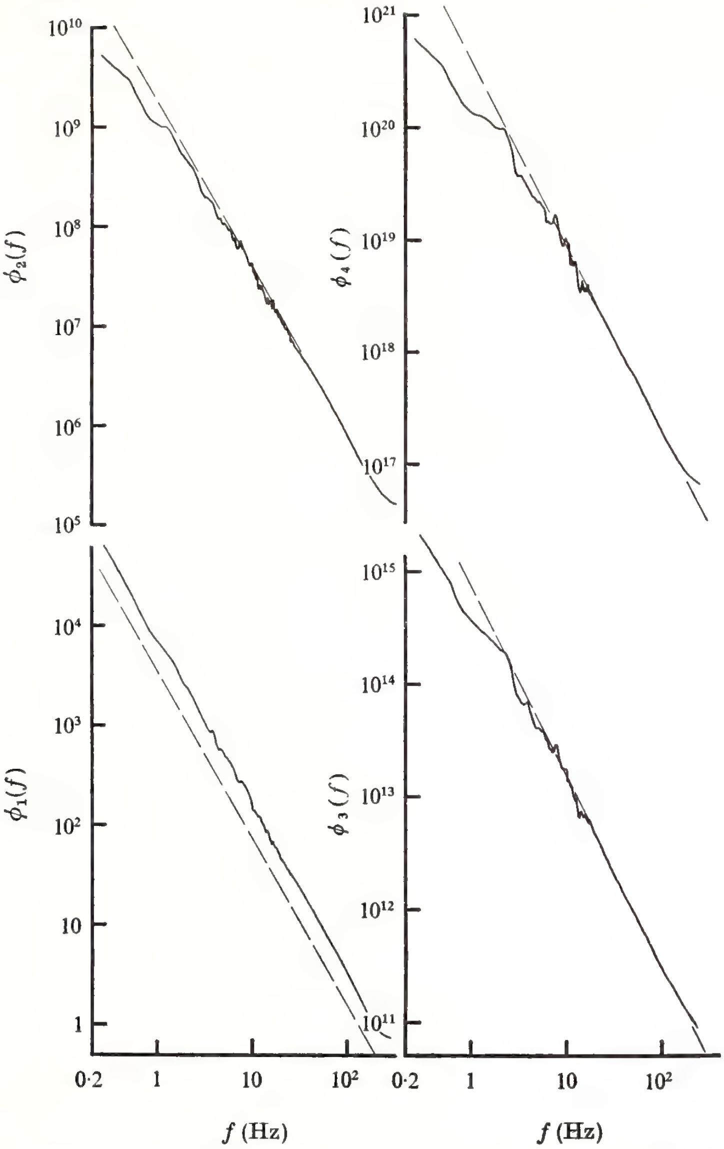

FIGURE 1. First-, second-, third- and fourth-order spectra of $u(t)$ measured in the atmospheric boundary layer over the open ocean. Dashed lines, which have a slope of $-\frac{5}{3}$, are higher-order inertial-subrange spectra predicted by asymptotic Gaussian theory. Dashed $-\frac{5}{3}$ line in ϕ_1 plot is not a fit to data. Note large range of the magnitudes of the higher-order spectra.

mode using a DISA 55D05 anemometer, and the anemometer output was linearized with a DISA 55D10 linearizer. The linearized hot-wire signal was FM tape recorded and later played back and sampled in the laboratory with a 12-bit analog-to-digital converter at a rate of 521·5 samples/s. Further details of the experimental conditions and apparatus, calibrations and data sampling have been given by Van Atta & Chen (1970) and Van Atta & Park (1972) in studies of

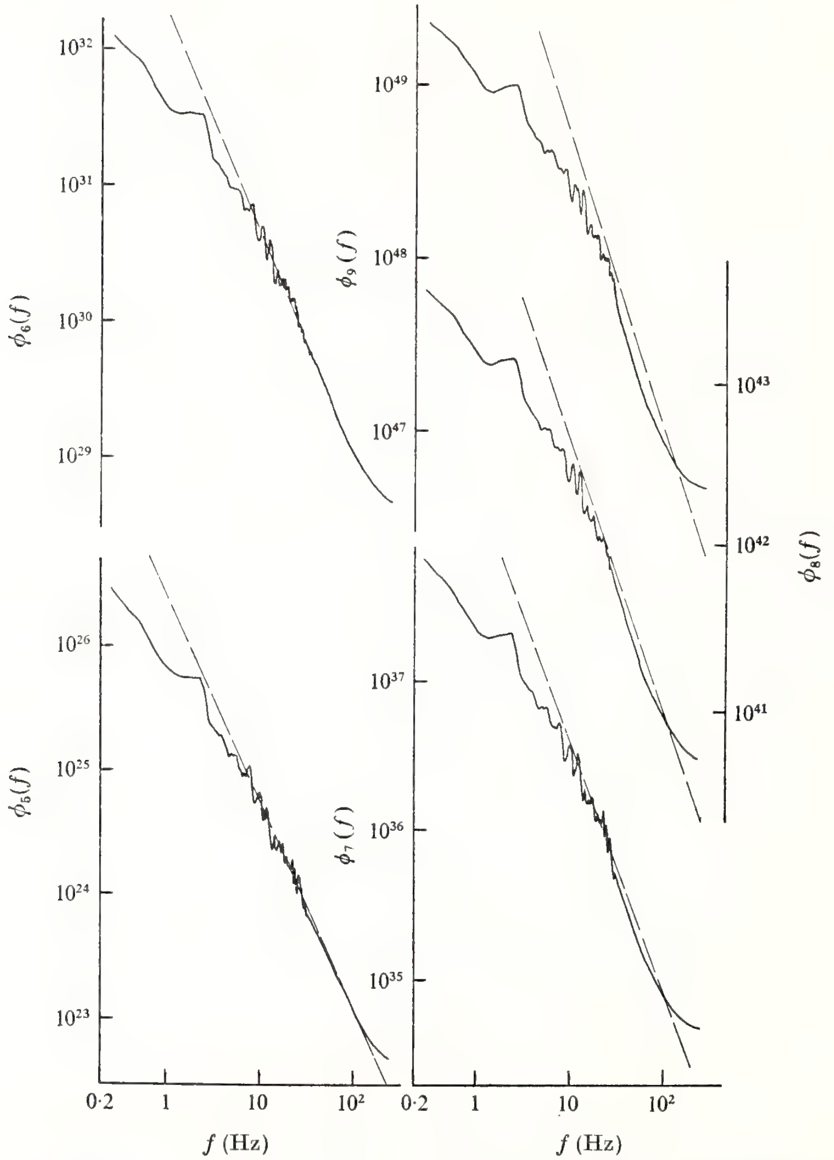

FIGURE 2. Fifth-, sixth-, seventh-, eighth- and ninth-order inertial-subrange spectra of $u(t)$ measured in the atmospheric boundary layer over the open ocean. Dashed lines have same meaning as in figure 1.

structure functions in the inertial subrange. The present spectra were obtained using fast Fourier transforms of 100 digital records, each of which contained 2048 samples. Individual record averages of u^n were used for the mean values $\langle u^n \rangle$. For atmospheric data, individual record averages of such short length will fluctuate considerably around the long-term average. Use of the long-term averages to compute the fluctuations and spectral levels in each record will produce errors in the measured higher-order spectra that depend on the values of lower-order spectra. For example, if in a given record the local record mean differs from the long-term mean by u_0, i.e. $u(t) = u_0 + \tilde{u}$, where $\langle \tilde{u} \rangle = 0$, then

$$\phi_{2(u^2,u^2)}(f) = \phi_{2(\tilde{u}^2,\tilde{u}^2)}(f) + 4u_0^2\phi_{1(\tilde{u},\tilde{u})}(f) + 2u_0(S_{\tilde{u},\tilde{u}^2}(f) + S_{\tilde{u}^2,\tilde{u}}(f)),$$

where $S_{\tilde{u},\tilde{u}^2}$ is the cross-spectrum of $\tilde{u}$ and $\tilde{u}^2$. The measurement of ϕ_2 is thus contaminated by terms that are proportional to ϕ_1 and S. For measurements of ϕ_1, the value of u_0 affects only the zero-frequency spectral value $\phi(0)$. For laboratory data, the record length can normally be chosen to be considerably longer (say by a factor of 10 or 20) than the integral time scale of the fluctuations, and the spectral contamination problem is negligible because of the small size of the residual u_0. Attention was first drawn to this kind of problem by Chen (1969) in connexion with correlation measurements, for which record means are not appropriate. A discussion of similar questions concerning cross-spectral measurements has been given by Helland (1974).

The data shown in figures 1 and 2 are spectral averages over 100 records. In these data, a clear $-\frac{5}{3}$-power-law range in the spectra is apparent for all spectra of up to sixth order, but for higher orders it is not as clearly defined, partly owing to an increasing oscillation in the spectra near 30 Hz. The effect of aliasing in the high frequency tails of the spectra also becomes more apparent as the order is increased. The slopes of the dashed lines ($-\frac{5}{3}$) are those predicted both by the asymptotic Gaussian theory and the present extension of Kolmogorov's dimensional theory [equation (33)]. The dashed lines also denote the absolute spectral values predicted by the Gaussian theory (except in figure 1*a*). The present theories both represent the data fairly well. The present generalized Kolmogorov theory clearly provides a good representation of the data, in contrast to the earlier proposal for inertial-subrange behaviour by Dutton & Deaven [equation (2)]. The frequency below which the spectra depart from an approximately $-\frac{5}{3}$ slope increases monotonically with increasing order. For high frequencies, the measured spectra are thus in qualitative agreement with the Gaussian asymptotic theory and with the trends observed by Dutton & Deaven.

The asymptotic theory was compared quantitatively with the present experiments by using the measured lower-order spectra to determine the constants b and λ and then comparing the measured higher-order spectra with their predicted magnitudes obtained using the same values of b and λ. The data for the frequency range 10–100 Hz were used in determining b and λ. A fit to the data for ϕ_1 in figure 1 gives $b = 7194$, corresponding to a value of $\phi_1 = 155$ at $f = 10$ Hz. Using this value of b, the values of λ determined from ϕ_2 and ϕ_3 are $\lambda = 2{\cdot}6$ and $3{\cdot}0$, respectively. The average of these two values, $\lambda = 2{\cdot}8$, was then used with $b = 7194$ to predict the values of the higher-order spectra using (33).

The fits for the lower-order spectra and the predicted spectra for higher orders are indicated by the dashed lines in figures 1 and 2 for $2 \leqslant n \leqslant 9$. In most cases the predicted spectral levels indicated by the dashed lines pass directly through the measured spectral values, and are in fact close approximations to the measured spectra for each value of n. In view of the large changes in the absolute spectral level with increasing n, the agreement between the asymptotic formula (33) and the measured spectra in the $-\frac{5}{3}$ range appears to be quite good. For

$n = 8$ and 9, the predicted levels are a bit high. For the largest values of n the spectra are also becoming progressively more ragged and the $-\frac{5}{3}$ range is not clearly defined. From the present data, one may conclude that, for the spectra of up to and including seventh order, the measured spectra in the inertial range are in good agreement with theoretical predictions for higher-order spectra of a Gaussian variable.

For the present data, the extent of the $-\frac{5}{3}$-slope region in the spectra is less for all higher-order spectra than for the first-order spectrum. For comparison with the low-frequency ends of spectra predicted using the von Kármán form for ϕ_1, the complete higher-order spectra for $n \leqslant 4$ were determined numerically. Using the normalized correlation function [see equation (A 1) of the appendix]

$$R(\tau)/R(0) = 2^{\frac{2}{3}}(2\pi\tau/\lambda)^{\frac{1}{3}}\, K_{\frac{1}{3}}(2\pi\tau/\lambda)/\Gamma(\tfrac{1}{3})$$

the expressions in (26) and (27) were numerically evaluated using a fast-Fourier-transform routine. These numerical results also served as a further check on the asymptotic theory for large f. The second-order spectrum was also evaluated using a direct numerical convolution, as a further check on the calculations performed via sums of Fourier transforms of powers of the correlation function. It did not appear practical to attempt to obtain ϕ_n for $n > 2$ by numerically evaluating the multiple convolutions of (28). The results of these calculations, which are applicable for arbitrary values of b and λ, are shown in figure 3. The numerical results are in good agreement with the asymptotic theory, and show that for a von Kármán spectrum the asymptotic theory is a good approximation down to dimensionless frequencies $F = f\lambda$ of about 10, the lower limit being a weakly increasing function of the order of the spectrum. This latter behaviour is consistent with that observed in the data.

The measured probability density of the velocity fluctuations is shown in figure 4. Although the distribution is decidedly non-Gaussian, the deviations from Gaussianity are small enough so that the first few moments are of the same order of magnitude as those for a Gaussian distribution. For a Gaussian distribution, and therefore also for the numerically determined spectra in figure 3, the values of the moments are given by $\langle u^{2n}\rangle/\langle u^2\rangle^n = 1 \times 3 \times 5 \times \ldots \times (2n-1)$. In view of (1), the ratios of the areas under all the higher-order spectral curves are therefore fixed. However, as the order increases, the moments will rapidly deviate from those expected for a Gaussian density. As is well known, experimental values of such moments are a strong function of the type of flow, stability and the position of measurement in the flow (e.g. the distance from the boundary in a boundary layer). The present good agreement between the Gaussian calculations of ϕ_n and experimental values in the inertial subrange indicates that the major contribution to non-Gaussian behaviour of the higher-order moments comes from the non-universal low-frequency end of the first-order and higher-order spectra. Higher-order moments and the corresponding low-frequency portion of the higher-order spectra have not been determined for the present atmospheric data. This would require lower sampling rates and considerably longer samples of data than were used for the inertial-subrange spectral calculations.

The Dutton & Deaven data are most easily compared with the asymptotic

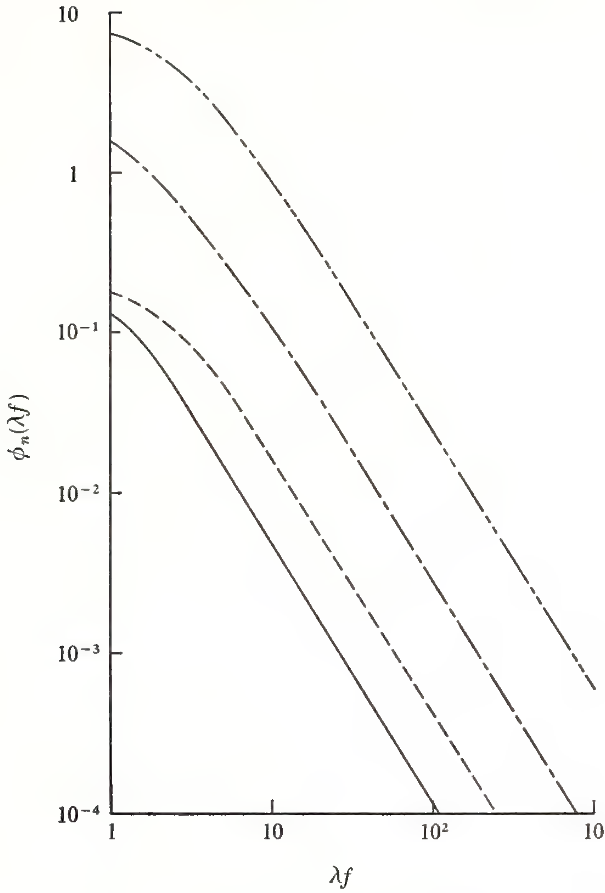

FIGURE 3. Numerically computed first-, second-, third- and fourth-order spectra obtained using Gaussian theory and normalized correlation function of von Kármán spectrum. Note departure from inertial-subrange behaviour for low frequencies and decrease in extent of inertial-subrange $(-\frac{5}{3})$ behaviour as order of spectrum increases. ——, ϕ_1; – – –, ϕ_2; — · —, ϕ_3; — ·· —, ϕ_4.

theory using (34). In processing their data, Dutton & Deaven worked with the velocity normalized with its variance, i.e. $u/R_u(0)^{\frac{1}{2}}$, $v/R_v(0)^{\frac{1}{2}}$, etc., and the spectral data they presented are also given in terms of the velocity components normalized with their variances. For this reason, the ratio of any of their spectral results to their first-order spectrum corresponds exactly to the definition of the dimensionless spectrum given in (34). We therefore can simply multiply their first-order spectrum by 4, 27 and 60 in order to compare their experimental results with the asymptotic theory for ϕ_2, ϕ_3 and ϕ_4, respectively. Results of this comparison are illustrated in figure 5, which is a replot of the Dutton & Deaven LO-LOCAT 750 ft data. These data exhibited the most regular behaviour in the inertial subrange, and appear to be the most suitable of their data for the present comparison. The asymptotic theory predicts the magnitudes of the higher-order spectra quite well, and the agreement is as good as one could hope for, considering the relatively small extent of the inertial subrange covered by the data. These measured spectra

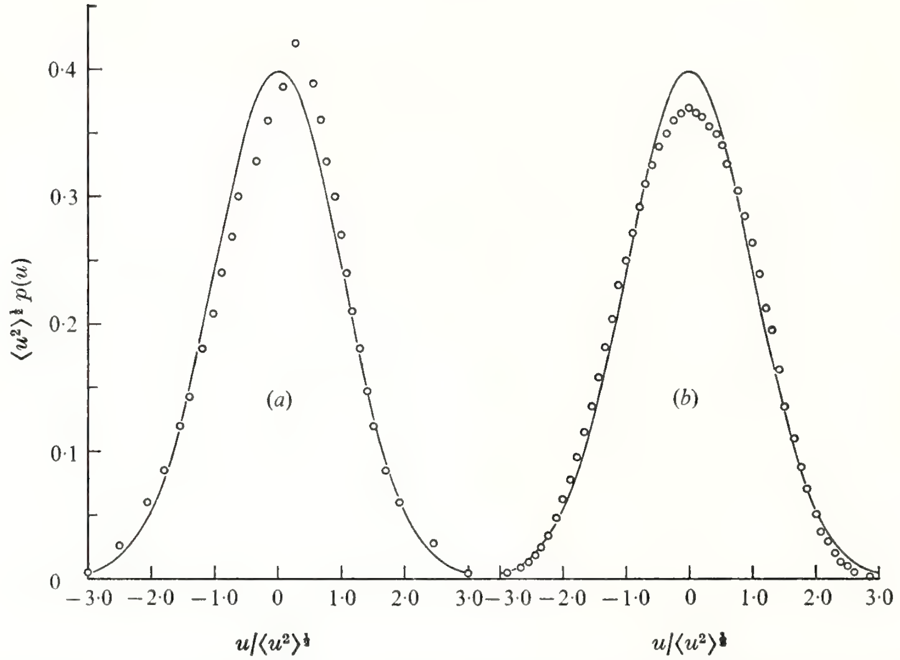

FIGURE 4. Probability densities of $u(t)$ for present atmospheric boundary-layer data and mixing-layer centre-line data of Champagne *et al.* (*a*) Atmospheric boundary layer over the open ocean. (*b*) Two-dimensional mixing layer. ——, Gaussian distribution.

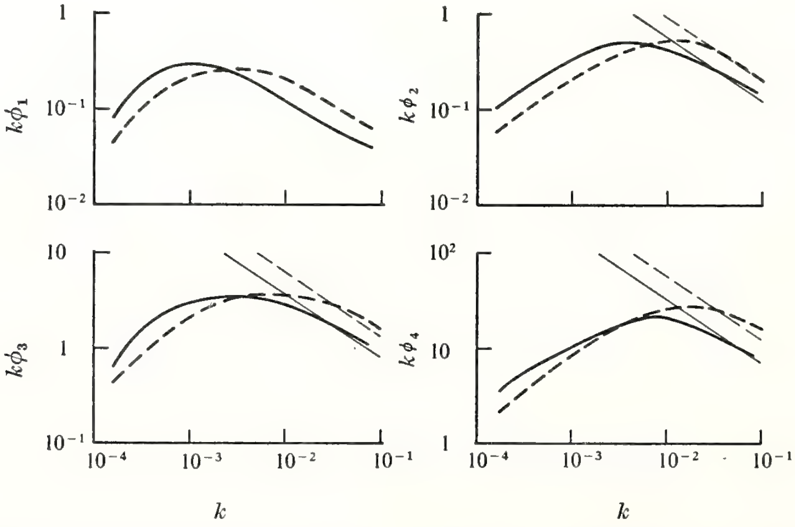

FIGURE 5. First-, second-, third- and fourth-order spectra $k\phi_n(k)$ obtained by Dutton & Deaven for the LO-LOCAT 750 ft (altitude) data. The straight lines, which have a slope of $-\frac{2}{3}$, are higher-order inertial-subrange spectra predicted by asymptotic Gaussian theory using the von Kármán spectral form. Note that in these co-ordinates the $-\frac{2}{3}$ slope corresponds to the $-\frac{5}{3}$ power law of Kolmogorov theory. ——, u, longitudinal component of velocity; – – –, v, lateral component of velocity.

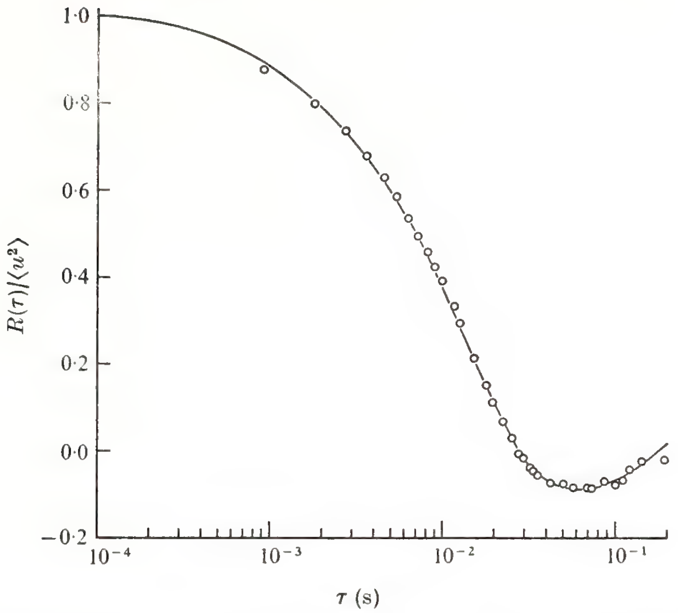

FIGURE 6. Curve fit to plane-mixing-layer correlation-function data used for numerical computations of higher-order spectra shown in figure 7. ——, curve fit; ○, data of Champagne *et al.*

also exhibit the trend that the inertial-subrange spectral behaviour begins at a higher frequency as the order of the spectrum increases. This is consistent with the trend in the BOMEX data and with that predicted by the calculations using the von Kármán spectral model.

4. Comparison of Gaussian theory with some laboratory data

Laboratory measurements on the centre-line of a plane mixing layer of spectra of $u^n(t)$ up to fourth order have been made recently by Champagne *et al.* (1976). Their measurements were motivated by a need to determine whether the frequency response of their analog and digital measuring instruments and computational techniques was adequate for determining the higher-order moments of $u(t)$. Since raising a signal to a power (e.g. squaring) produces sum and difference frequencies, this operation produces higher-order spectral energy at frequencies considerably exceeding the usual Nyquist frequency. As discussed by Van Atta (1974), if the first-order spectrum does not fall sufficiently rapidly, higher-order spectral mass can be lost if the data are processed according to the usual Nyquist criterion. Champagne *et al.* found that in their case this was not a serious problem, and that their measured spectra gave an accurate measure of the contributions of various frequency components to the higher-order moments. Their first-order spectrum exhibited a small interval of roughly $f^{-\frac{5}{3}}$ behaviour. They noted that in this frequency interval their higher-order spectra did not follow the trend predicted by (2), but rather the spectra became somewhat less steep (on a log–log plot) as the order increased.

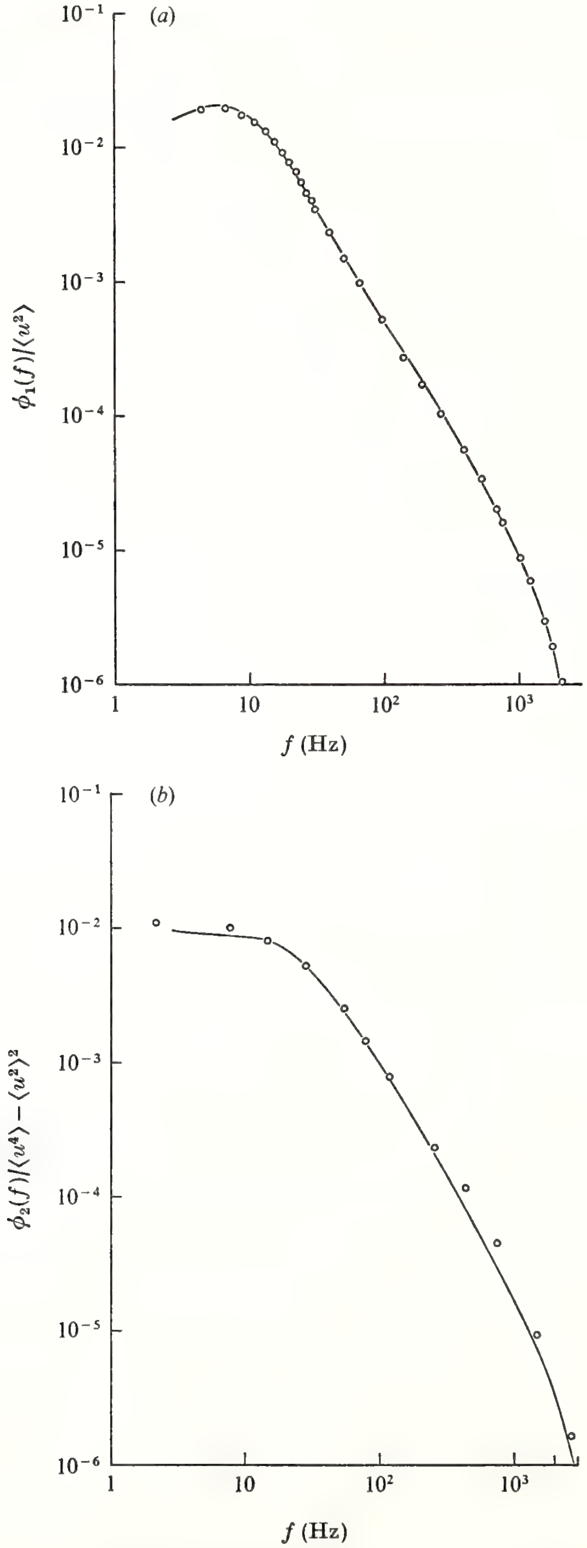

FIGURES 7(a, b). For legend see next page.

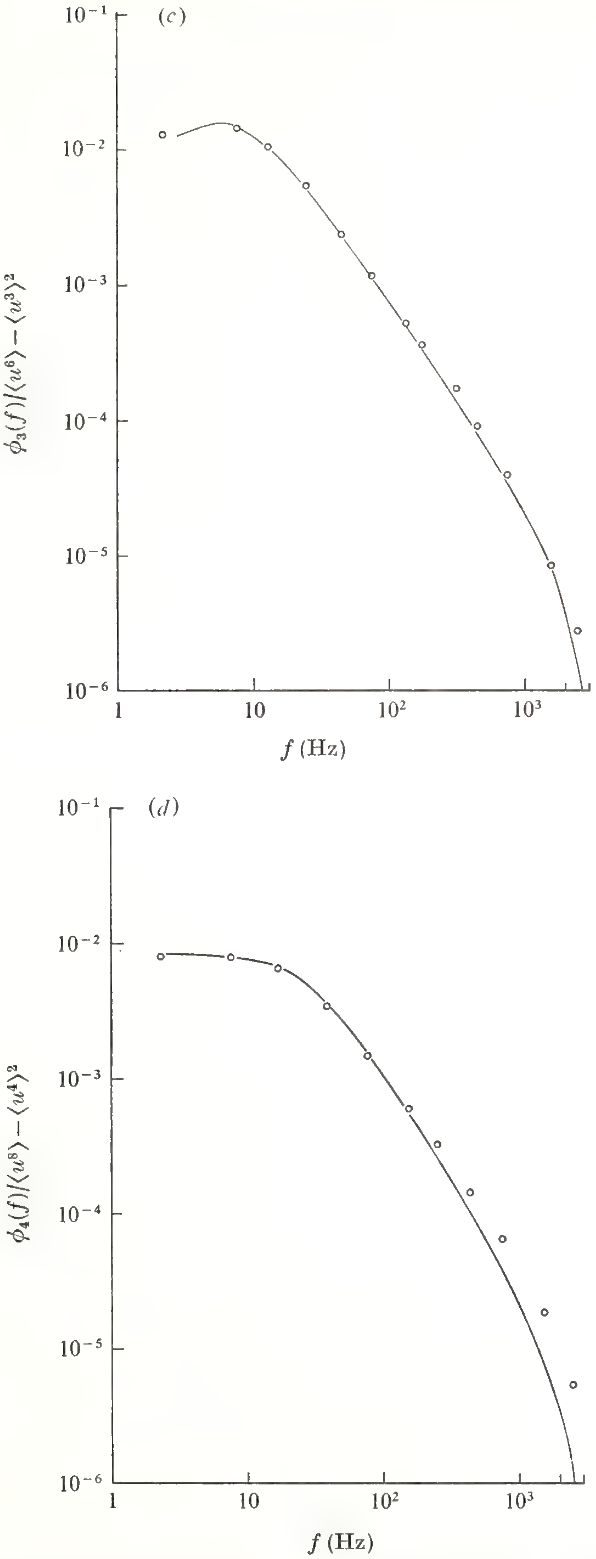

FIGURE 7. (*a*) First-, (*b*) second-, (*c*) third- and (*d*) fourth-order normalized spectra for plane-mixing-layer centre-line data. ——, numerical Fourier transform using correlation-function curve fit of figure 6; ○, data of Champagne *et al.*

Theoretical higher-order spectra for the mixing-layer data were computed from (26) and (27), using a three-section polynomial curve fit to the measured correlation function as input to the same program as was used to produce the data in figure 3. The curve fit shown in figure 6 was used to generate 4096 points of the correlation function. Some numerical experimentation with the curve fit for small time lags τ was necessary in order to fit accurately the high-frequency end of the first-order spectrum, as only a few points were available for the measured correlation function for small τ. These correlation data were then raised to the appropriate powers and fast Fourier transformed to generate the terms in (26) and (27). Since spectra up to only fourth order were computed, this procedure required a maximum of two Fourier transforms for each higher-order spectrum computed. The resulting spectra are shown in figures 7 (*a*)–(*d*). The computed results for ϕ_1 are in close agreement with the measured spectrum, indicating that the fit to the correlation function is adequate, and that the results for the higher orders can be trusted. As shown in figures 7 (*b*), (*c*) and (*d*), normalized spectra of second, third and fourth order computed using the Gaussian formulation all lie rather remarkably close to the measured values of these spectra. The agreement becomes somewhat poorer as the order of the spectrum increases, and also noticeably degrades with increasing frequency for ϕ_3 and ϕ_4. One would expect the discrepancies between theoretical and experimental higher-order spectra to increase with increasing order, as the difference between the measured moments and those for a Gaussian random function increases as the order increases. The measured values of the first few higher-order moments for the mixing-layer data are $\langle u^3\rangle/\langle u^2\rangle^{\frac{3}{2}} = -0{\cdot}035$, $\langle u^4\rangle/\langle u^2\rangle^2 = 2{\cdot}6$, $\langle u^5\rangle/\langle u^2\rangle^{\frac{5}{2}} = -0{\cdot}16$, $\langle u^6\rangle/\langle u^2\rangle^3 = 10{\cdot}2$, $\langle u^7\rangle/\langle u^2\rangle^{\frac{7}{2}} = -0{\cdot}27$ and $\langle u^8\rangle/\langle u^2\rangle^4 = 52$, compared with corresponding Gaussian values of 0, 3, 0, 15, 0 and 105, respectively. The measured probability density, shown in figure 5, is quite symmetrical and to a low-order approximation is fairly well described by the Gaussian probability density.

In terms of an absolute-magnitude comparison like that made in §3 for the atmospheric inertial-subrange spectra, the unnormalized theoretical and measured values of ϕ_2 are in very good agreement, while in the low-frequency range, which produces the largest contributions to the moments, the theoretical and measured values of ϕ_3 and ϕ_4 are roughly in the ratios 3/2 and 2/1, respectively. This is the spectral equivalent of the difference between the directly measured higher-order moments and the corresponding Gaussian values. For these data then, the Gaussian assumption provides an accurate representation for third- and fourth-order spectra only in the normalized representation in which the total area under the spectral curves is equal to one.

5. Discussion and conclusions

The original Kolmogorov argument asserts that, if the energy spectrum ϕ_1 has a range in which it depends solely on ϵ and the wavenumber k, then it must have the form $\phi_1 = \alpha_1 \epsilon^{\frac{2}{3}} k^{-\frac{5}{3}}$ in that range. Dutton & Deaven proposed that, if the Kolmogorov argument could be extended in the sense that nth-order spectra ϕ_n also had a range in which they depended only on ϵ and k, then they must have the form given by (2). This expression is in serious conflict with the observations of Dutton & Deaven ($n \leqslant 4$) and the present data ($n \leqslant 9$). Hence we conclude that the Dutton & Deaven extension of the Kolmogorov argument is not valid. The present theoretical generalization (§2.1) of the Kolmogorov dimensional argument is based on the dissipation terms in the dynamical equations for $\langle u^{2n} \rangle$ and $\langle u^{2n+1} \rangle$. The resulting predicted variation of the higher-order spectra with wavenumber is consistent with the experimental results. The Gaussian theory is also in good qualitative and quantitative agreement with the experiments.

The good agreement of the normalized mixing-layer spectral data with the Gaussian calculations shows that the Gaussian formulation can be used to predict accurately entire spectra of arbitrary order from the first-order spectrum or correlation function when the higher-order moments are known and the probability density is approximately Gaussian. Good absolute spectral agreement is obtained when the moments are close to those for a Gaussian distribution. Further measurements of this kind in other flows, especially a flow like grid turbulence, in which the probability density is more closely Gaussian, might serve as an interesting test of the order to which the Gaussian theory can furnish valid predictions for the ϕ_n.

We wish to thank Dr S. O. Rice, Dr K. N. Helland and Dr T. T. Yeh for much help with the analysis and computing done at UCSD, and Dr F. H. Champagne for kindly furnishing tabulated data for the BSRL plane-mixing-layer experiment. The research was supported by National Science Foundation Grant GK-43643X and the Advance Research Projects Agency of the Department of Defense and monitored by ONR under Contract N00014-69-A-0200-6054.

Appendix. Derivation of asymptotic form of the *n*th-order convolution of the von Kármán spectrum

Define $C_n(f)$ as the n-fold convolution of $(1+x^2)^{-\frac{5}{6}}$. The zeroth-order convolution is the spectrum itself, i.e. $C_0(f) = (1+f^2)^{-\frac{5}{6}}$. From Watson (1944, p. 185), the correlation function is

$$R(\tau) = \int_{-\infty}^{\infty} \frac{e^{-i2\pi\tau x}}{(1+x^2)^{\frac{5}{6}}}\,dx = \frac{2^{\frac{2}{3}}\Gamma(\frac{1}{2})}{\Gamma(\frac{5}{6})}\,|2\pi\tau|^{\frac{1}{3}} K_{\frac{1}{3}}(|2\pi\tau|), \tag{A 1}$$

where $K_{\frac{1}{3}}$ is the modified Bessel function of order $\frac{1}{3}$. Then

$$\begin{aligned} C_n(f) &= \int_{-\infty}^{\infty} e^{i2\pi f\tau}[R(\tau)]^{n+1}\,d\tau \\ &= c^{n+1}\frac{1}{\pi}\,\mathrm{Re}\int_0^{\infty} e^{izf}\,[z^{\frac{1}{3}}K_{\frac{1}{3}}(z)]^{n+1}\,dz, \end{aligned} \tag{A 2}$$

where $z = 2\pi\tau$ and $c = 2^{\frac{2}{3}}\pi^{\frac{1}{2}}/\Gamma(\frac{5}{6})$. From Watson (1944, p. 202), for large z

$$K_{\frac{1}{3}}(z) \sim (\pi/2z)^{\frac{1}{2}}\,e^{-z}(1-5/(72z)+\ldots). \tag{A 3}$$

Because of (A 3), the conditions for Jordan's lemma are satisfied, and we can swing the path of integration up along the imaginary z axis and, letting $z = iy$, we have

$$C_n(f) = \frac{c^{n+1}}{\pi} \operatorname{Re} \int_0^\infty i\, e^{-yf}[(iy)^{\frac{1}{3}} K_{\frac{1}{3}}(iy)]^{n+1}\, dy. \tag{A 4}$$

Because of the exponential factor in the integrand, for large values of f the major contribution to the integral comes from small values of iy, and an asymptotic result for large f can be obtained by expanding the integrand for small values of $\xi = \frac{1}{2}iy$.

From the definition of $K_{\frac{1}{3}}$ (e.g. Watson 1944, pp. 77, 78)

$$z^{\frac{1}{3}} K_{\frac{1}{3}}(z) = \frac{\pi}{3^{\frac{1}{2}}} [z^{\frac{1}{3}} I_{-\frac{1}{3}}(z) - z^{\frac{1}{3}} I_{\frac{1}{3}}(z)].$$

Keeping the first few terms in the summations for $I_{\frac{1}{3}}$ and $I_{-\frac{1}{3}}$ and regrouping gives

$$z^{\frac{1}{3}} K_{\frac{1}{3}}(z) = b[1 - a\xi^{\frac{2}{3}} + \tfrac{3}{2}\xi^2 - \tfrac{3}{4}a\xi^{\frac{8}{3}} + \ldots]$$

and

$$\begin{aligned}[z^{\frac{1}{3}} K_{\frac{1}{3}}(z)]^{n+1} = d^{n+1}\Bigg[& 1 - a(n+1)\xi^{\frac{2}{3}} + \tfrac{1}{2}n(n+1)\, a^2 \xi^{\frac{4}{3}} \\ & + \xi^2 \left(\tfrac{3}{2}(n+1) - \frac{(n+1)\, n(n-1)}{3!} a^3 \right) + \xi^{\frac{8}{3}} \\ & \times \Bigg(- \tfrac{3}{4}(n+1)a - \tfrac{3}{2}n(n+1)a \\ & + \frac{(n+1)\, n(n-1)(n-2)}{4\,!} a^4 \Bigg) + \ldots \Bigg],\end{aligned} \tag{A 5}$$

where $\xi = \frac{1}{2}iy$, $a = 3\Gamma(\frac{2}{3})/\Gamma(\frac{1}{3})$ and $d = 2^{\frac{1}{3}}\pi/3^{\frac{1}{2}}\Gamma(\frac{2}{3})$. From (A 4) and (A 5),

$$\begin{aligned}C_n(f) = [2\pi^{\frac{3}{2}}/3^{\frac{1}{2}}\Gamma(\tfrac{5}{6})\, \Gamma(\tfrac{2}{3})]^{n+1} \frac{3^{\frac{1}{2}}}{2\pi} \int_0^\infty dy\, e^{-yf} & [a(n+1)\, (\tfrac{1}{2}y)^{\frac{2}{3}} - \tfrac{1}{2}n(n+1) \\ & \times a^2 (\tfrac{1}{2}y)^{\frac{4}{3}} - (\tfrac{1}{2}y)^{\frac{8}{3}} (\tfrac{3}{4}a(n+1)\, (2n+1) - \tfrac{1}{24}a^4 (n+1)\, n(n-1)\, (n-2)) + \ldots].\end{aligned}$$

Integrating term by term yields an asymptotic series for large f:

$$\begin{aligned}C_n(f) \sim [\pi^{\frac{1}{2}}\Gamma(\tfrac{1}{3})/\Gamma(\tfrac{5}{6})]^n\, & [(n+1)f^{-\frac{5}{3}} - 2^{-\frac{2}{3}} n(n+1) f^{-\frac{7}{3}} \\ & + \tfrac{5}{6}\{-(2n+1) + \tfrac{1}{18}n(n-1)\, (n-2)\, a^3\} f^{-\frac{11}{3}} + \ldots],\end{aligned}$$

or

$$C_n(f) \sim (4{\cdot}20)^n\, [(n+1)f^{-\frac{5}{3}} - n(n+1) f^{-\frac{7}{3}}/1{\cdot}59 + \ldots].$$

REFERENCES

Brillinger, D. R. & Rosenblatt, M. 1967 Computation and interpretation of k-th order spectra. In *Spectral Analysis of Time Series* (ed. B. Harris), pp. 189–232. Wiley.

Champagne, F. H., Pao, Y. H. & Wygnanski, I. J. 1976 On the two-dimensional mixing region. *J. Fluid Mech.* (In press.)

Chen, W. Y. 1969 Spectral energy transfer and higher-order correlations in grid turbulence. Ph.D. thesis, University of California, San Diego.

Corrsin, S. C. 1951 On the spectrum of isotropic temperature fluctuations in an isotropic turbulence. *J. Appl. Phys.* **22**, 469.

Dutton, J. A. & Deaven, D. G. 1972 Some properties of atmospheric turbulence. In *Statistical Models and Turbulence. Lecture Notes in Physics*, vol. 12 (ed. M. Rosenblatt & C. W. Van Atta), pp. 402–426. Springer.

Frenkiel, F. N. & Klebanoff, P. S. 1967 Higher-order correlations in a turbulent field. *Phys. Fluids*, **10**, 507–520.

Helland, K. N. 1974 Energy transfer in high Reynolds number turbulence. Ph.D. thesis, University of California, San Diego.

Hinze, J. O. 1959 *Turbulence*. McGraw-Hill.

Kaimal, J. C., Wyngaard, J. C., Izumi, Y. & Coté, O. R. 1972 Spectral characteristics of surface layer turbulence. *Quart. J. Roy. Met. Soc.* **98**, 563–589.

Kolmogorov, A. N. 1941 The local structure of turbulence in an incompressible fluid for very large Reynolds numbers. *Dokl. Akad. Nauk S.S.S.R.* **30**, 301–305.

Oboukhov, A. M. 1941 On the distribution of energy in the spectrum of turbulent flow. *Dokl. Akad. Nauk S.S.S.R.* **32**, 19.

Oboukhov, A. M. 1962 Some specific features of atmospheric turbulence. *J. Fluid Mech.* **13**, 77–81.

Rice, S. O. 1973 Distortion produced by band limitation of an FM wave. *Bell Syst. Tech. J.* **52**, 605–626.

Richardson, L. F. 1920 The supply of energy to and from atmospheric eddies. *Proc. Roy. Soc.* A **97**, 354.

Tennekes, H. & Lumley, J. L. 1972 *A First Course in Turbulence*. M.I.T. Press.

Townsend, A. A. 1947 The measurement of double and triple correlation derivatives in isotropic turbulence. *Proc. Camb. Phil. Soc.* **43**, 560–570.

Van Atta, C. W. 1974 Sampling techniques in turbulence measurements. *Ann. Rev. Fluid Mech.* **6**, 75–91.

Van Atta, C. W. & Chen, W. Y. 1968 Correlation measurements in grid turbulence using digital harmonic analysis. *J. Fluid Mech.* **34**, 497–515.

Van Atta, C. W. & Chen, W. Y. 1970 Structure functions of turbulence in the atmospheric boundary layer over the ocean. *J. Fluid Mech.* **44**, 145–160.

Van Atta, C. W. & Park, J. 1972 Statistical self-similarity and inertial subrange turbulence. In *Statistical Models and Turbulence. Lecture Notes in Physics*, vol. 12 (ed. M. Rosenblatt & C. W. Van Atta), pp. 402–426. Springer.

Watson, G. N. 1944 *Theory of Bessel Functions*. Cambridge University Press.

Wyngaard, J. C. & Pao, Y. H. 1972 Some measurements of the fine structure of large Reynolds number turbulence. In *Statistical Models and Turbulence. Lecture Notes in Physics*, vol. 12 (ed. M. Rosenblatt & C. W. Van Atta), pp. 384–401. Springer.

Reviews of Geophysics and Space Physics 13, 716-720, July 1975.

Progress in Research on Boundary Layers and Atmospheric Turbulences

J. C. Wyngaard

Air Force Cambridge Research Laboratories, Hanscom Air Force Base, Massachusetts 01731

INSTRUMENTATION AND EXPERIMENTAL TECHNIQUES

The potential of remote probing techniques, both acoustic and electromagnetic, for research in atmospheric turbulence has become apparent recently. Acoustic wind sounding devices, both one-dimensional [*Beran et al.*, 1971] and three-dimensional [*Beran et al.*, 1974; *Mahoney et al.*, 1973] have been built. This 'acoustic radar' is sensitive to both temperature and velocity fluctuations [*Cronenwett et al.*, 1972], and much of its early use has been for monitoring the height and structure of low-level inversions [*Wyckoff et al.*, 1973]. Early work has also dealt with measurements of temperature fluctuations and wind speed and direction profiles for use in gravity wave studies [*Beran et al.*, 1973]. *Emmanuel et al.* [1972] observed breaking Helmholtz waves near an inversion, and *Hooke et al.* [1972] discussed planetary boundary layer (PBL) waves detected with an acoustic sounder and a microbarograph array. The performance of acoustic probes in turbulence is not yet fully understood but is under intensive investigation.

Theoretical work has been done on sound wave pulse propagation in turbulence with a mean wind [*E.H. Brown*, 1972], on the spectral broadening of a pulse [*Brown and Clifford*, 1973], on the acoustic scattering from a moving turbulent medium [*Clifford and Brown*, 1974], and on refractive effects in monostatic sounding [*Georges and Clifford*, 1972] and bistatic sounding [*Georges and Clifford*, 1974]. It appears that some of the differences between calculated and observed echo properties are difficult to reconcile theoretically [*Beran et al.*, 1973], and side-by-side comparisons with conventional instruments will be required for a full assessment of acoustic probe performance.

Copyright © 1975 by the American Geophysical Union.

High-resolution FM radar has been successfully used to detect the structure of elevated inversions and accompanying wave motions and convective structure within the PBL [*Bean et al.*, 1971, 1973*a*; *Browning et al.*, 1973*a*, *b*]. *Richter et al.* [1973] and *Noonkester et al.* [1974] used radar and lidar simultaneously in PBL research. Optical techniques have been developed for measuring horizontal wind divergence near the surface [*Kjelaas and Ochs*, 1974]. *Hosler and Lemmons* [1972] described a remote radiometric technique for detecting the height of an elevated inversion in fair weather. A very complete status report on remote probing techniques was given by *Little* [1972].

Progress in tower-based instrumentation has been steady but less dramatic. There are some new instruments, such as that of *Elliott* [1972*a*] for measuring fluctuating static pressure within a turbulent flow. Updated sonic anemometers were reported by *Kaimal et al.* [1974] and *Mitsuta* [1974]. *Wesely et al.* [1972] improved the three-component pressure sphere anemometer, and *Yap et al.* [1974] tested a yaw sphere-thermometer combination which measures sensible heat flux. *Shaw et al.* [1973] developed a wide acceptance angle split film anemometer for use within plant canopies, and *Lynch and Bradley* [1974] tested a new surface drag meter which gives the surface friction velocity for boundary layer studies. Propeller anemometers continued to receive attention; *Hicks* [1972] and *McBean* [1972] analyzed their suitability as tower-based turbulence sensors, and *Fichtl and Kumar* [1974] and *Drinkrow* [1972] discussed their response characteristics. A 1970 joint comparison experiment

[*Tsvang et al.*, 1973] showed generally good agreement among sonic and propeller anemometers and gave useful insight into the dependence of turbulence statistics on instrument differences and data processing techniques. *Smith* [1974] compared sonic and thrust anemometers and found good agreement in speed and stress measurements. Some aspects of the nonlinear response of cup anemometers and their effect on speed measurements were discussed by *Hyson* [1972] and *Wyngaard et al.* [1974*a*]. For detailed reviews of contemporary instrumentation and techniques for surface layer turbulence measurements over land see *Kaimal* [1975]; over sea, *Friehe et al.* [1975].

Delicate instrumentation once seen only in the laboratory now is routinely used outdoors; hot wire anemometers and thermometers, for example, are well established. Equivalent bandwidth measurements can be made with larger diameter wires for velocity than for temperature because of the bandwidth gains in constant temperature anemometry circuitry. According to *Friehe et al.* [1975], 4-μ-diameter hot wires are typically used for velocity fine structure measurements, with 25-μ-diameter hot film probes sometimes preferred for their stability of calibration. *Boston and Burling* [1972] used 0.25-μ-diameter Pt wires to measure temperature fine structure in the surface layer. The spatial and temporal resolution of these fine wires, and their parasitic sensitivity to velocity, has been studied by *Wyngaard* [1971*a*, *b*] and *Larue et al.* [1974]. With the increasing activity in fine structure research the digital processing techniques reviewed by *Van Atta* [1974] and the data processing hazards discussed by *Tennekes and Wyngaard* [1972] are of interest.

Turbulence measurements from aircraft, which can require an inertial platform [*Lilly and Lenschow*, 1974], have given high-quality data [*Pennell and LeMone*, 1974] with less statistical uncertainty than one expects from fixed instruments, because the higher aircraft speed reduces the required averaging time [*Wyngaard*, 1973]. Some of the tradeoffs in measuring fine structure from aircraft are discussed by *Sheih* [1972*a*].

PBL Studies

Busch [1973] and *Panofsky* [1973, 1974] have done in-depth surveys of recent research on the structure of the lower portion of the planetary boundary layer (PBL). Perhaps the most complete flux profile data are those of *Businger et al.* [1971], whose reduced von Karman constant (0.35 rather than 0.40) is consistent with predictions by *Tennekes* [1973*b*]. New evidence in support of the traditional value has since been reported by *Pruitt et al.* [1973]. *McCarl et al.* [1973], using measurements up to 150 m, found general agreement with previous flux profile relations at lower levels.

Knowledge of turbulence structure in the lowest 30 m has been considerably refined. Turbulence energy budget studies [*Wyngaard and Coté*, 1971; *McBean et al.*, 1971; *Garratt*, 1972] show that energy flux divergence is large under unstably stratified conditions, and the first study suggests that the pressure work term (not measured directly) is also large, a result which was not evident from previous work. A pioneering attempt to measure pressure statistics directly was made by *Elliott* [1972*b*] under near-neutral conditions. Turbulent fluxes were measured directly via correlation techniques [*Haugen et al.*, 1971], were inferred from spectral measurements and turbulence budget assumptions [*Hicks and Dyer*, 1972; *Stegen et al.*, 1973], or were inferred from simple scalar measurements [*Tillman*, 1972]. Flux measurements at points separated by a few meters vertically and larger distances horizontally were found to track well, supporting the use of single-point fluxes in similarity analyses. Direct flux measurements were also made over the sea [*Pond et al.*, 1971; *Dunckel et al.*, 1974] and over ice [*Banke and Smith*, 1971, 1973; *Smith*, 1972; *Thorpe et al.*, 1973]. The now routine availability of turbulent fluxes has allowed detailed analyses of turbulence structure in the Monin-Oboukhov (M-O) similarity framework [*Wyngaard et al.*, 1971*c*; *McBean*, 1971; *Arya*, 1972] and detailed studies of transport processes [*McBean*, 1973, 1974]. There is now widespread support for the M-O similarity hypothesis and general agreement on many of the universal functions, although some statistics, notably those involving horizontal wind fluctuations, seem not to follow the M-O predictions. It seems that for these quantities the depth of the PBL might also have an influence, although this is difficult to establish experimentally. *Taylor* [1971*b*], *Brutsaert* [1972], *Lettau* [1973], and *Kaimal* [1973] have studied aspects of surface layer structure under stable stratification, and *Businger and Arya* [1974] have discussed the steady state structure of the stable PBL.

Many studies of spectra in the surface layer have been done [*Phelps and Pond*, 1971; *McBean and Miyake*, 1972; *Kaimal et al.*, 1972; *Wyngaard and Coté*, 1972; *Smedman-Hogstrom*, 1973; *Sharan and Wickerts*, 1974], and there is now general agreement on shapes and stability dependence. The Taylor conversion from frequency to wave number spectra received some support [*Powell and Elderkin*, 1974]. Experimental evidence supporting local isotropy has accumulated, and the inertial range velocity spectral (Kolmogorov) constant seems settled between 0.5 and 0.6. The temperature constant has more spread, with dissipative range measurements [e.g., *Boston and Burling*, 1972] being about twice those from inertial range data [*Kaimal et al.*, 1972; *Pacquin and Pond*, 1971] for unknown reasons. *Frenzen* [1973] has related the von Karman and Kolmogorov constants through the turbulence energy budget in the surface layer.

While most surface layer research has assumed horizontally homogeneous conditions, studies have been made of the structure over inhomogeneous surfaces. *Hsu* [1971], *Echols and Wagner* [1972], and *Panofsky and Petersen* [1972] have discussed observations of mean wind profiles in the response region of water-land flow. The data are generally consistent with model predictions, such as the K theory versions of *Taylor* [1971*a*] and *Panchev et al.* [1971], turbulence closure models [*Peterson*, 1971; *Shir*, 1972; *Peterson and Taylor*, 1973; *Rao et al.*, 1974*a*]. The flow over a step change in surface moisture was studied numerically by *Rao et al.* [1974*b*]. In general, this problem area suffers somewhat from the situation described by *Bradshaw* [1972] as 'too many computers chasing too few facts.' Detailed measurements of inhomogeneous surface layer flows, along the lines of the laboratory studies of *Antonia and Luxton* [1971, 1972], would be valuable now.

Flow structure in the PBL is sensitive to many more influences than that in the surface layer, but recent experimental and theoretical work has extended the frontiers here as well. Some remarkably detailed studies of PBL turbulence structure have been made from aircraft; *Panofsky and Mazzola* [1971], *Warner* [1971, 1972, 1973], *Bean et al.* [1972], *Taylor* [1972], *Donelan and Miyake* [1973], and *Pennell and LeMone* [1974] have presented statistics of velocity, temperature, and humidity fluctuations over both land and sea. *Thompson* [1972], *Rayment* [1973], *Gjessing et al.* [1973], and *Caughey and Readings* [1974] have presented measurements made from a tethered balloon, and *Coulman* [1973] measured PBL temperature structure from a free-flying balloon. *Carson and Smith* [1973] deduced from the Leipzig data that wind shear and stress vectors are parallel, as assumed in K theory. Baroclinic wind structure has been considered by *Bernstein* [1973], *Hoxit* [1974], and *Brummer et al.* [1974] and has been simply parameterized for the convective case by *Arya and Wyngaard* [1975]. Here again most work has dealt with the horizontally homogeneous case, but *Lenschow* [1974] has presented aircraft measurements of the boundary layer response to cold air flow over a warmer lake. *Fiedler and Panofsky* [1972] have proposed an effective roughness length for inhomogeneous terrain. The complex PBL in the Atlantic trade region was discussed by *Augstein et al.* [1974], who identified five distinct sublayers between the surface and the trade inversion. This situation features baroclinicity, cumulus convection, and subsidence as well as mechanical turbulence and dry convection and will continue to be intensively studied because of its importance for larger-scale motions. Encouraging progress has been made in parameterizing some aspects of the problem; *Betts* [1973], for example, discusses a simple model for nonprecipitating cumulus convection.

Mollo-Christiansen [1971] has suggested that the study of the dynamics of discrete flow structures can provide insight into the physics of turbulent flow, and opportunities along this line exist in the PBL. *LeMone* [1973] considered the dynamics of horizontal roll vortices and found they are maintained by inflectional instability and buoyancy. *Angell* [1971, 1972] reported observations of these vortices, and their stability has been analyzed by *Kaylor and Faller* [1972] and *R. A. Brown* [1972]. Some aspects of convective plumes were discussed by *Telford* [1972], *Frisch and Businger* [1973], and *Kaimal* [1974]. *Fitzjarrald* [1973] and *Sinclair* [1973] analyzed measurements of dust devils.

Significant advances have been made in parameterization of the convective PBL. Combinations of acoustic, radar, and aircraft observations [*Konrad and Robison*, 1973; *Rowland*, 1973; *Robison and Konrad*, 1974; *Frisch and Clifford*, 1974] have revealed convective structure, shown the influence of an inversion lid, and given support to the structure shown by the three-dimensional numerical simulations of *Deardorff* [1972*a*]. *Lenschow* [1974] has compiled data from several experiments and suggested a model of the turbulence energy budget. Parameterizations were made for convective layer growth [*Tennekes*, 1973*c*; *Stull*, 1973; *Carson*, 1973; *Carson and Smith*, 1974], for the countergradient heat flux [*Deardorff*, 1972*b*], for entrainment effects on stress profiles [*Deardorff*, 1973*a*], and for stress maintenance in convection [*Wyngaard et al.*, 1974*b*]. Parameterization of PBL processes is necessary in general circulation models, as discussed by *Tennekes* [1974], and *Deardorff* [1972*c*] has proposed stability-dependent models for that purpose. Similarity theories for the PBL have evolved considerably; some have ignored the influence of inversion lids [*Zilitinkevich*, 1972], but there is increasing evidence of their role in convective structure, and recent efforts [*Zilitinkevich and Deardorff*, 1974; *Melgarejo and Deardorff*, 1974] include them. Nevertheless the similarity picture remains somewhat unclear, with some data [*Clarke and Hess*, 1973] indicating that the neutral height scale (u_*/f) rather than the inversion height remains the significant scale in convective conditions, while model studies [*Deardorff*, 1972*a*; *Wyngaard et al.*, 1974*c*] show the opposite. Geostrophic wind shear (baroclinic) effects could be the cause of some of the discrepancies between model predictions and observations, and recent attention has been given to this case [*Schwerdtfeger*, 1972; *Hess*, 1973; *Thompson*, 1974; *Arya and Wyngaard*, 1975]. *Csanady* [1974] and *Brown* [1974] have simply parameterized the effect of an inversion of a neutral PBL and show that it can radically change its structure from that of an unconstrained Ekman layer. It seems likely that much of the frequent lack of correspondence of PBL models and observations is also due to the influence of advective and diurnal changes, and as suggested by *Pasquill* [1972], this should be a productive area for future experimentation. There have been a number of K theory numerical studies of such effects [*Mak*, 1972, 1974; *Mahrt*, 1972; *Sheih*, 1972*b*; *Arya*, 1973; *Young*, 1973].

The turbulence modeling area is developing rapidly and has given much insight into PBL structure. *Deardorff* [1974] has continued his three-dimensional simulations with a study of the evolution of a convective PBL, and *Wyngaard and Coté* [1974] have found very similar structure from a higher-order closure turbulence model. *Shir* [1973], *Lewellen and Teske* [1973], and *Mellor* [1973] have also applied the latter type of model to the PBL, and *Mellor and Yamada* [1974] have simulated the diurnal evolution of the PBL with a hierarchy of such models. *Delage* [1974] has used a simplified model of this general class to study the evolution of the nocturnal case. *Orlanski et al.* [1974] have included the boundary layer in a two-dimensional mesoscale model and concluded that it responds realistically to diurnal forcing. It is hoped that future experimental and modeling work will be coordinated to the extent possible, because each area has reached the point where it depends crucially on the other. Such a study of the nocturnal PBL would be valuable at this time.

Existing knowledge of PBL structure has been used to advantage in a number of problems affected by turbulence. The relatively frequent occurrence (compared to a Gaussian process) of large strain rates in turbulent fine structure was used to predict significant increases in droplet collection efficiencies in only weakly turbulent clouds [*Tennekes and Woods*, 1973]. *Wesely and Alcaraz* [1973] and *Wyngaard et al.* [1971*d*] used surface layer similarity theory to predict the refractive index structure near the ground. The statistics of energy containing range velocity shear, important in structural applications, have been studied by *Fichtl* [1971, 1972] and *Kumar* [1974], and *Monahan and Armendariz* [1971] discussed gust factors in the lowest 150 m.

Encouraging progress has also been made in the laboratory simulation of atmospheric flow. *Caldwell et al.* [1972] set up a turbulent Ekman layer in a rotating apparatus and found good agreement, in similarity coordinates, with field data. A laboratory convection tank has proved to have turbulence structure like that of the convective PBL [*Willis and Deardorff*, 1974] and should prove useful in simulation studies. Diffusion experiments have already been done in the tank [*Deardorff and Willis*, 1974]. *Fanaki* [1971] discussed a water tunnel simulation of the unstable boundary layer, and *Sadeh et al.* [1971] have modeled flow over high roughness elements in a wind tunnel. *Snyder* [1972] has reviewed similarity criteria for fluid model simulations of atmospheric flow. *Dessens* [1972], *Wan and Chang* [1972], and *Ward* [1972] have explored various aspects of tornado dynamics through laboratory models.

CLEAR AIR TURBULENCE, GRAVITY WAVES, AND STABLE LAYERS

Intensive work has been done recently on the structure of turbulence in elevated inversion layers such as those which often cap the PBL. Much of the recent activity is due to recent advances in remote probing techniques, which are thoroughly reviewed by *Ottersten et al.* [1973]. *Metcalf and Atlas* [1973] used high-resolution radars and aircraft measurements to infer details of turbulence structure in breaking Kelvin-Helmholtz waves in such an inversion layer. *Browning et al.* [1973*a*], *Readings et al.* [1973], and *Rayment and Readings* [1974] have also studied the dynamics of elevated inversion layers. *Gossard et al.* [1973] used radar to study atmospheric wave structure and suggested that the multiple-layer returns are caused by reduced Richardson number due to wave-induced shear as well as background shear. *Kerman* [1974] has studied the maintenance of breaking waves in an inversion by considering the turbulence energy budget. *Bean et al.* [1973*b*] used remote and tower measurements to relate wave motion aloft to turbulent activity within the PBL. *Hooke et al.* [1973] observed the generation of a gravity wave by shear instability in the PBL and measured directly the wave phase velocity and the vertical fluxes of energy and momentum in the wave.

Radar and aircraft measurements have also allowed some detailed analyses of clear air turbulence (CAT) structure. *Browning* [1971] discussed the structure near large amplitude (200 m) Kelvin-Helmholtz (K-H) billows at heights between 5 and 11 km and found every occurrence closely associated with well-defined local wind shear maxima as large as 9 m/s per 200 m. *Browning et al.* [1973*b*] presented more details of billow structure. *Hardy et al.* [1973] discussed observations of two-dimensional K-H billows near an upper level frontal zone, and CAT studies have also been made by *Axford* [1971], *Delay and Dutton* [1971], *Kropfli* [1971], *Reed and Hardy* [1972], and *Boucher* [1973]. *Woodman and Guillen* [1974] and *Lilly and Lester* [1974] discussed turbulence observations in the stratosphere. *Lilly et al.* [1974] have derived eddy diffusivities from stratospheric turbulence data, and *Axford* [1973] reported on turbulence on the tropopause surface which is closely correlated with wave activity. Mountain lee waves and their associated turbulence have been studied by *Lilly and Kennedy* [1973], *Vezee et al.* [1973], and *Lester and Fingerhut* [1974]. *Dutton and Deaven* [1972] discussed detailed CAT statistics.

Analytical work on internal waves has been compared to radar observations by *Gossard et al.* [1971] and *Gossard* [1974]. There have been a number of studies of the hydrodynamic stability of a stratified free shear layer [*Maslowe and Thompson*, 1971; *Breeding*, 1971; *Gage*, 1972; *Dudis*, 1972]. *Howard and Maslowe* [1973] have done a useful review of work in this area. *Hines* [1971] has discussed generalizations of the Richardson criterion for the onset of turbulence, *Orlanski* [1972] has studied the breaking of internal gravity waves, and *Orlanski and Ross* [1973] have simulated their generation and breaking with a two-dimensional numerical model.

TURBULENCE STRUCTURE AND CLOSURE THEORY

Direct calculation of three-dimensional homogeneous isotropic turbulence, by solution of the Navier-Stokes equations, was reported by *Orszag and Patterson* [1972] and extended to turbulent shear flow by *Orszag and Pao* [1974]. The calculations were carried out within a sphere in wave number space, with Fourier modes beyond a maximum wave number magnitude not allowed. This restricts the turbulence Reynolds number R_λ, and the calculations to date have been in the range $R_\lambda \approx 20$–40.

This restriction is not as serious as it might seem, because the energy-containing structure of turbulent flows is observed to become Reynolds number independent fairly quickly. Thus moderate Reynolds number turbulence calculations are very important and have already been used to assess various closure approximations in isotropic turbulence models [*Herring and Kraichnan*, 1972]. They tested Kraichnan's direct interaction approximation, Herring's test field model, and other closure schemes and found that all gave adequate qualitative description of the evolution of energy and vorticity spectra at low and moderate R_λ. *Herring et al.* [1973] have also used direct solution of the Navier-Stokes equations at $R_\lambda \approx 40$ to study the evolution of an initial velocity difference variance (error energy) in decaying isotropic turbulence. They found the error energy grew in time even when it was initially confined to the viscous range, which has implications for the predictability of turbulent flow. They found the direct interaction approximation also gave reasonable results. Much of the recent progress in these turbulence simulations is due to the development of fast efficient numerical techniques (see *Orszag and Israeli* [1974] for a review and more references). Work has also continued with heuristic models of spectral energy transfer in turbulence. *Panchev and Syrakov* [1971] used a Heisenberg transfer assumption and calculated velocity and temperature spectra in stratified flow, and *Lin* [1972] calculated one-dimensional velocity spectral shape in the inertial and dissipative ranges.

The dynamics of two-dimensional turbulence has received attention because of its relevance to large-scale atmospheric motions and their predictability. *Lilly* [1972*a*, *b*] has shown that idealized numerical simulations of a two-dimensional turbulence bear a useful resemblance to atmospheric flow, and his 1973 calculations also tend to confirm *Lorenz*'s [1972] conclusions about the loss of predictability of large-scale flow. *Leith* [1971] has also viewed the predictability of planetary scale motion in the context of two-dimensional turbulence, and *Leith and Kraichnan* [1972] used a test field model to compute the growth of prediction error for inertial range turbulence in two and three dimensions. They found the initial uncertainty at large wave number spreads through the entire inertial range according to a similarity law. *Charney* [1971] has shown that quasi-geostrophic flow can strongly resemble two-dimensional turbulence, and *Thompson* [1973] derived some properties of two-dimensional turbulence through a similarity argument for its spectrum.

Considerable success has also been had with three-dimensional numerical simulations on coarser grids which do not resolve all turbulent activity, thus requiring parameterization of the subgrid turbulence. *Deardorff's* [1972*a*] three-dimensional simulations of neutral and convective PBL structure used local eddy viscosity assumptions on the subgrid scale, and his more recent work [*Deardorff*, 1973*b*, 1974] used conservation equations for the subgrid turbulence. In most of these simulations most of the turbulence activity is resolved directly, but stable thermal stratification can cause trouble by decreasing turbulence scales to subgrid size.

A third type of turbulence model now widely used is the 'higher-order closure' or 'transport' model. Here equations for second-order single-point turbulence moments are closed approximately and carried along with the mean field equations. In this approach the average structure (means, second moments) is calculated, in contrast to the first two methods, which give the instantaneous details of the randomly fluctuating flow. *Bradshaw* [1972] has surveyed recent transport model developments. The fidelity of a transport model hinges on its closure assumptions, which typically are physically plausible but difficult to justify from first principles. *Lumley and Khajeh-Nouri* [1974] have attempted systematic closure via a functional expansion technique. While the rational formulation of transport models needs continued attention, existing models have had impressive successes in reproducing measured flow structure and can provide substantially better predictions than eddy diffusivity models. *Hanjalic and Launder* [1972] have calculated several shear flows, and *Donaldson* [1973] discussed simulation of both laboratory and atmospheric flow. *Shir* [1973], *Lewellen and Teske* [1973], *Mellor* [1973], *Wyngaard et al.* [1974*b*, 1974*c*], and *Wyngaard and Cote'* [1974] have done PBL simulations. *Daly* [1974] calculated convection between parallel plates, and *Naot et al.* [1973] used the transport approach to calculate two-point correlations.

The flurry of activity on turbulent fine structure in the late 1960's, stimulated by Kolmogorov's refined theory of the structure of dissipative range turbulence, has subsided somewhat. One refinement was the hypothesis that the distribution of any locally averaged positive quantity such as dissipation rate should be log normal in large R_λ turbulence. *Mandelbrot* [1972] has noted some deficiencies of this hypothesis and suggested some further refinements, and *Kraichnan* [1974] has also critically examined Kolgomorov's theories. *Chen* [1971] showed geophysical fine structure data which support the log normal hypothesis. *Gibson and Masiello* [1972] found approximately log normal distributions for squared temperature and velocity derivatives in flow over the ocean, and *Kuo and Corrsin* [1971] found roughly log normal distributions for velocity derivatives in laboratory turbulence. *Wyngaard and Pao* [1972] reported several statistical properties of dissipative structure which are consistent with the refined theory. *Van Atta and Park* [1972] analyzed velocity difference statistics and found them not consistent with a self-similarity hypothesis but instead behaving in ways consistent with the Kolomogorov refined theory. *Van Atta* [1971] has also calculated some of the effects of the refined theory on inertial range statistics of a scalar and finds some of them strong enough to warrant attention. *Tennekes* [1973*a*] has reviewed many of the consequences of the refined theory and concluded that while it does predict many of the observed features, there are still many unresolved issues.

While the recognition that geophysical flows provide unique sources of large R_λ data has been the key to recent advances here, the near inaccessibility of many important fine structure statistics to current instruments is a continuing limitation. Instrumentation advances here would be particularly welcome and might well generate another wave of interest in turbulent fine structure.

MODELING THE PLANETARY BOUNDARY LAYER – EXTENSION TO THE STABLE CASE

J. C. WYNGAARD*

Air Force Cambridge Research Laboratories, Hanscom AFB, Mass., U.S.A.

(Received 26 June, 1975)

Abstract. A higher-order-closure model, which contains equations for turbulence covariances as well as the mean field, was developed and used to investigate the structure of the stably-stratified planetary boundary layer. The calculated surface-layer profiles of wind shear, temperature gradient, and dissipation rate agree well with the 1968 Kansas data. A simulation of the evolution of the nocturnal PBL reproduces fairly accurately some observations from the 1973 Minnesota experiments.

1. Introduction

This paper presents an extension of our planetary boundary layer (PBL) simulations to the stably stratified case. The numerical model used is of the second moment, or 'higher-order-closure' variety. Earlier studies concerned the steady-state structure of the neutral and convective cases (Wyngaard *et al.*, 1974), stress maintenance under convective conditions in the barotropic (Wyngaard *et al.*, 1974) and baroclinic (Arya and Wyngaard, 1975) PBL, and the evolution of a convective PBL (Wyngaard and Coté, 1974).

Through higher-order-closure models, one hopes to obtain a better representation of the physics of turbulence than is possible with eddy diffusion approximations. This can lead to more accurate mean-field predictions and to heretofore unavailable information on the detailed structure of the turbulence field. We do not mean to suggest that the higher-order-closure approach is directly useful today on the meso- or regional scale; this requires two- or three-dimensional models and thus can quickly get out of hand computationally. It seems more likely that higher-order-closure calculations will be useful in generating turbulence parameterizations for use in the larger scale models.

Higher-order-closure modeling rests, as pointed out by Lumley and Khajeh-Nouri (1974), on an article of faith: if a crude assumption for second moments predicts the mean field adequately, then perhaps a crude assumption for third moments will predict second moments adequately. Evidence is rapidly accumulating that second-moment predictions can be quite good (see Launder *et al.*, 1975, for recent laboratory flow simulations and more references). Unfortunately, however, there is little theoretical guidance for the rational, systematic formulation of closure approximations. As discussed by Bradshaw (1972), one can check the effects of closure assumptions by comparing calculations with detailed measurements, but rarely are there data suitable for

---

* Present address: NOAA Wave Propagation Laboratory, Boulder, Colo. 80302.

Boundary-Layer Meteorology 9 (1975) 441–460. *All Rights Reserved*
Copyright © 1975 by D. Reidel Publishing Company, Dordrecht-Holland

testing the closure assumptions themselves. Not surprisingly, then, models change as new flows are calculated and compared with data.

The model presented here is an outgrowth of that used in our earlier work. Closure refinements were made to allow a reasonable simulation of the stable boundary layer, which includes reproducing some of its well measured characteristics as well as some new data from the 1973 Minnesota experiments. The model predictions for the neutral and convective PBL remain substantially as reported earlier. We continue to stress that the model is evolving, however, and will probably need further refinements as new situations are modeled.

2. The Model

We consider horizontally homogeneous flow, with the mean velocity $U_i=(U, V, O)$ and mean potential temperature Θ governed by

$$\begin{aligned} &\frac{\partial U}{\partial t} + \frac{\partial}{\partial z}\overline{uw} = f(V - V_g), \\ &\frac{\partial V}{\partial t} + \frac{\partial}{\partial z}\overline{vw} = f(U_g - U), \\ &\frac{\partial \Theta}{\partial t} + \frac{\partial}{\partial z}\overline{\theta w} = 0. \end{aligned} \tag{1}$$

Here f is the Coriolis parameter $2\omega \sin\phi$, where ω is the Earth's rotation rate and ϕ is latitude. Velocity and temperature fluctuations are denoted by $u_i=(u, v, w)$ and θ, respectively. The geostrophic wind components are defined by

$$\begin{aligned} &U_g = -\frac{1}{f}\frac{\partial P}{\partial y}; \quad V_g = \frac{1}{f}\frac{\partial P}{\partial x}, \\ &G = (U_g^2 + V_g^2)^{1/2}, \end{aligned} \tag{2}$$

with P the mean kinematic pressure, and are assumed independent of height z. We ignore moisture and radiative flux divergence.

The turbulence covariance equations are

$$\begin{aligned} \frac{\partial}{\partial t}\overline{u_i u_k} + U_{i,j}\overline{u_j u_k} + U_{k,j}\overline{u_j u_i} + (\overline{u_i u_j u_k})_{,j} = -(\overline{u_k p_{,i}} + \overline{u_i p_{,k}}) + \\ + (\overline{u_k \theta} g_i + \overline{u_i \theta} g_k)/T - 2\bar{\varepsilon}/3\delta_{ik} - 2\omega\varepsilon_{ijl} n_j \overline{u_l u_k} - 2\omega\varepsilon_{klm} n_l \overline{u_m u_i}, \end{aligned} \tag{3}$$

$$\frac{\partial}{\partial t}\overline{\theta^2} + 2\Theta_{,j}\overline{u_j \theta} + (\overline{\theta^2 u_j})_{,j} = -2\bar{\varepsilon}_\theta, \tag{4}$$

$$\frac{\partial}{\partial t}\overline{\theta u_i} + U_{i,j}\overline{\theta u_j} + \Theta_{,j}\overline{u_i u_j} + (\overline{\theta u_i u_j})_{,j} = -\overline{\theta p_{,i}} + \frac{g_i}{T}\overline{\theta^2} - 2\omega\varepsilon_{ijk} n_j \overline{u_k \theta}, \tag{5}$$

where p is the fluctuating kinematic pressure, T is mean temperature, $\bar{\varepsilon}$ is the dissipation rate of turbulence kinetic energy per unit mass, $\bar{\varepsilon}_\theta$ is the corresponding quantity for temperature variance, n_i is the unit vector along the Earth's rotation axis, and g_i is the acceleration of gravity vector. Differentiation is indicated by a comma and repeated indices are summed.

No approximations beyond those customarily made for dissipative terms in high Reynolds number turbulence (see Tennekes and Lumley, 1972) have been made in deriving the second-moment Equations (3) – (5). Unfortunately, however, the set cannot be solved as written because it contains unknowns of yet higher order. To close the system, we will approximate the unknowns in terms of the mean field and the second moments.

Starting with the stress Equation (3), we rewrite the pressure covariances in the form suggested by Lumley (1975):

$$-(\overline{u_k p_{,i}} + \overline{u_i p_{,k}}) + \tfrac{2}{3}(\overline{u_j p})_{,j}\,\delta_{ik} = A_{ik}. \tag{6}$$

By taking the divergence of the equation for u_i, one finds the following equation for pressure fluctuations:

$$\nabla^2 p = -\,(u_{i,j}u_{j,i} - \overline{u_{i,j}u_{j,i}}) - 2U_{i,j}u_{j,i} + \frac{g_i}{T}\theta_{,i} - 2\omega\varepsilon_{ijk}n_j u_{k,i}. \tag{7}$$

The terms on the right side of Equation (7) are called the turbulence, mean strain, buoyancy, and rotation contributions, respectively. Since the solution for p can be expressed in terms of an integral of the right-side of Equation (7) over the entire flow, one can write a formal expression for A_{ik} as a flow integral of turbulence moments by combining Equations (6) and (7). One can see that A_{ik} will have contributions from third moments of u_i; from products of mean strain and second moments; from the velocity-temperature covariance; and from a rotation term involving second moments of u_i. The moments involve quantities at two spatial points.

This presents a severe closure problem which is met by parameterizing A_{ik}. We assume that

$$A_{ik} = A_{ik}\left(\overline{u_iu_j}, \bar{\varepsilon}, U_{i,j}, \frac{g_i}{T}, \overline{\theta u_i}\right) \tag{8}$$

and require, in accordance with Equation (6), that $A_{ii}=0$ and $A_{ik}=A_{ki}$. We used the form

$$\begin{aligned} A_{ik} = &-\frac{C}{\tau}\left(\overline{u_iu_k} - \frac{2E}{3}\delta_{ik}\right) + C_1E\,(U_{i,k} + U_{k,i}) + \\ &+ C_2\,(\overline{u_iu_j}U_{k,j} + \overline{u_ku_j}U_{i,j} - \tfrac{2}{3}\delta_{ik}\overline{u_mu_j}U_{j,m}) + \\ &+ C_3\left(\frac{g_i}{T}\overline{\theta u_k} + \frac{g_k}{T}\overline{\theta u_i} - \tfrac{2}{3}\frac{g_j}{T}\overline{\theta u_j}\delta_{ik}\right), \end{aligned} \tag{9}$$

where $2E=\overline{u_iu_i}$ is twice the turbulent kinetic energy, $\tau=2E/\bar{\varepsilon}$ is a turbulence time scale, and C, C_1, C_2, and C_3 are constants.

The C term, the only one used in our earlier studies, represents the effects of the turbulence term in Equation (7). It is usually credited to Rotta (1951) and called a 'return to isotropy' term; it destroys off-diagonal stresses and drives the diagonal ones toward equality. The C_1 and C_2 terms represent mean strain effects while C_3 parameterizes the buoyancy.

We established values for C and C_1 through our usual procedure of forcing the model to yield a constant-stress, neutral surface layer. When the boundary conditions discussed later are applied and turbulent flux divergence terms.dropped, the resulting algebraic set can be solved to give

$$\begin{aligned} C &= 6.67(1 - C_2), \\ C_1 &= 0.23(1 - C_2). \end{aligned} \tag{10}$$

We chose values of $C_2 = 0.3$, $C_3 = -0.5$ by optimizing the fit of model calculations to stable surface-layer data, as discussed in detail later. The model results for the PBL do not seem unduly sensitive to values of C_1, C_2, and C_3; in fact, the neutral and unstable PBL structure from the present model differs little from that with these constants zero.

For the pressure covariance in the heat-flux Equation (5), we assume

$$\overline{p_{,i}\theta} = \overline{p_{,i}\theta}\left(\overline{u_i u_j},\ \bar{\varepsilon},\ U_{i,j},\ \frac{g_i}{T},\ \overline{\theta u_i},\ \overline{\theta^2}\right). \tag{11}$$

We used the parameterization

$$\overline{p_{,i}\theta} = d\,\frac{\overline{\theta u_i}}{\tau} + a_1 \frac{g_i}{T}\overline{\theta^2} + a_2 U_{i,j}\overline{\theta u_j}, \tag{12}$$

which includes turbulence, mean strain, and buoyancy effects. Our expressions (9) and (12) for the pressure covariances are very similar to those suggested by Launder (1975).

We set $d = 9.7$ by forcing the $\overline{\theta w}$-equation to satisfy observations in the neutral surface-layer limit, as discussed in our earlier work (Wyngaard *et al.*, 1974). We used $a_2 = -0.5$ as suggested by Launder (1975). We can get some insight into the appropriate value of a_1 by considering the exact expression for the buoyant contribution to $\overline{p_{,i}\theta}$. In free turbulence (i.e., away from the surface), we can relate our parameterization in Equation (12) to the exact form through

$$a_1 \frac{g_i}{T}\overline{\theta^2} = -\frac{g_j}{4\pi T}\int\limits_{\mathrm{Vol}} \frac{(\overline{\theta'\theta})_{,i'j'}}{|\mathbf{x} - \mathbf{y}|}\, d_{\mathrm{Vol}}, \tag{13}$$

where primed and unprimed terms are evaluated at $\mathbf{y}$ and $\mathbf{x}$, respectively, and the integration is over all $\mathbf{y}$. In homogeneous turbulence, the temperature covariance in Equation (13) can be related to the temperature spectrum by

$$\overline{\theta'\theta} = \int e^{i\boldsymbol{\kappa}\cdot(\mathbf{x}-\mathbf{y})}\Phi(\boldsymbol{\kappa})\, \mathrm{d}\boldsymbol{\kappa}, \tag{14}$$

which gives, upon substitution and integration (see Crow, 1968)

$$a_1 \frac{g_i}{T}\overline{\theta^2} = \frac{g_j}{T}\int \frac{\kappa_i \kappa_j}{\kappa^2}\,\Phi(\kappa)\,\mathrm{d}\kappa\,. \tag{15}$$

If the field is isotropic, Equation (15) gives $a_1 = \frac{1}{3}$. In the isotropic limit, therefore, the buoyancy parameterization in Equation (12) is exact. In reality, stable stratification should restrict eddy size in the vertical, thereby distorting constant Φ surfaces from spherical and giving larger intercepts on the vertical wavenumber axis compared to the horizontal. This should increase a_1 toward its upper limit of 1.0. Note that in this limit, the buoyant contribution to the pressure covariance exactly cancels the direct buoyant production of $\overline{\theta w}$.

It was found necessary to make a_1 larger in stably stratified conditions, as suggested above, in order to eliminate spurious generation of heat flux by temperature fluctuations. We used the simple model

$$\begin{aligned} &a_1 = 0.5\,, \qquad Ri < 0\,,\\ &a_1 = 0.5 + 1.5\,Ri^2 - Ri^3\,, \qquad 0 < Ri < 1\,,\\ &a_1 = 1.0\,, \qquad Ri > 1\,, \end{aligned} \tag{16}$$

where $Ri = (g/T)\,\Theta_{,3}/(U_{,3}^2 + V_{,3}^2)$ is the gradient Richardson number. This form for a_1 was chosen simply because it approaches both the neutral limit and the cutoff value with zero slope. In the usual range ($Ri < 0.25$), a_1 varies only from 0.50 to 0.58.

The dissipation-rate equation, which in large Reynolds number turbulence takes the form (with ν the kinematic viscosity)

$$\frac{\partial\bar{\varepsilon}}{\partial t} + (\overline{\varepsilon u_j})_{,j} = -2\nu\overline{u_{i,k}u_{i,j}u_{j,k}} - 2\nu^2\overline{u_{i,kj}u_{i,kj}} = \text{Imbalance} \tag{17}$$

is perhaps the most difficult to parameterize. Its right side should presumably reflect the influence of energy-containing range processes, even though dissipation is confined to the smallest scales, because $\bar{\varepsilon}$ is determined by the energy cascade from the larger eddies. One can find little fundamental guidance for parameterizing these effects, however. We used

$$\text{Imbalance} = \frac{-\bar{\varepsilon}^2}{2E}\left\{4 + B\,\frac{\overline{u_i u_j}\,U_{i,j}}{\bar{\varepsilon}} - C\,\frac{\frac{g_i}{T}\overline{\theta u_i}}{\bar{\varepsilon}} - D\,\frac{\left(\frac{g_i}{T}\overline{\theta u_i}\right)^2}{\bar{\varepsilon}^2}\right\}, \tag{18}$$

with $B = 3.5$, $C = 1.0$, $D = 2.0$. This gave neutral and unstable PBL structure virtually identical to that of our earlier model ($B = C = 3.0$, $D = 0$) but substantially better predictions of the stable surface layer.

Turbulent transport was parameterized as before, with the gradient diffusion model

$$\overline{fu_i} = -a_t\,\overline{f}_{,j}\,\overline{u_j u_i}\,\tau\,, \tag{19}$$

where f is any turbulence quantity except $u_i u_j$; for that we used

$$\overline{(u_i u_k + \tfrac{2}{3} p \delta_{ik})\, u_j} = - a_t \overline{(u_i u_k)}_{,m}\, \overline{u_m u_j}\, \tau \tag{20}$$

in keeping with Equation (6). The constant a_t was unchanged at $(4-B)/12.1$ in the $\bar{\varepsilon}$ equation and 0.15 in the others. The final approximation is that for $\bar{\varepsilon}_\theta$:

$$\bar{\varepsilon}_\theta = 1.4 \frac{\overline{\theta^2}}{\tau}. \tag{21}$$

These approximations thus close the set of 14 equations: 3 for the mean wind and temperature, 6 for $\overline{u_i u_j}$, 3 for $\overline{\theta u_i}$, and one each for $\overline{\theta^2}$ and $\bar{\varepsilon}$. We solved the set numerically using the DuFort-Frankel (1953) method on a logarithmic, 50-point grid between 1 and 1000 m. Unless stated otherwise, we used west winds, 45 N latitude, v. Karman's constant $k = 0.35$, a roughness length $z_0 = 0.01$ m, and $G = 10$ m s^{-1}.

At the upper boundary, a simulated inversion at height z_i, all mean gradients and turbulence quantities were held at zero. At the lower boundary, the variables were required to follow Monin-Obukhov similarity. For neutral and stable conditions, and in coordinates aligned with the mean wind, we specified

$$\begin{aligned}
&-\overline{uw}/u_*^2 = 1.0, && \overline{vw}/u_*^2 = \overline{uv}/u_*^2 = 0, \\
&\overline{u^2}/u_*^2 = 4.0, && \overline{v^2}/u_*^2 = \overline{w^2}/u_*^2 = 1.75, \\
&\overline{\theta^2}/T_*^2 = 4.0, && U = \frac{u_*}{k}\left(Ln \frac{z}{z_0} + 4.7 \frac{z}{L}\right), \\
&V = 0, && \varepsilon = -\overline{u_i u_j}\, U_{i,j} + \frac{g_i}{T} \overline{\theta u_i}, \\
&\overline{\theta u}/u_* T_* = 3.0, && \overline{\theta v}/u_* T_* = 0 \quad \overline{\theta w} = -u_* T_* = Q_0, \\
&L = \frac{-T u_*^3}{k Q_0 g}, && \Theta(t) \text{ prescribed.}
\end{aligned} \tag{22}$$

For unstable conditions, the neutral values were used for all but $\bar{\varepsilon}$ and the velocity variances; for the latter we specified

$$\begin{aligned}
\overline{u^2} &= 4.0 u_*^2 + 0.2 w_*^2, \\
\overline{v^2} &= 1.75 u_*^2 + 0.2 w_*^2, \\
w_* &= \left(\frac{g}{T} Q_0 z_i\right)^{1/3}
\end{aligned} \tag{23}$$

3. Stable PBL Simulations

3.1. SOME GENERAL PROPERTIES

The structure of the evolving nocturnal PBL was explored with the model by starting from initial conditions typical of a decaying convective PBL at the instant of transition (vanishing surface heat flux). We used the same model for simulating the evolution of the convective layer, specifying a sinusoidal variation of the surface heat flux and an 11-hr heating period. This gave a moderately convective PBL with $u_* = 0.4$ m s^{-1} and $z_i/L = -10$ near midday. After transition, the cooling rate near the lower boundary, rather than the surface heat flux, was specified. An alternative is to use a surface energy budget and thus avoid specifying either the heat flux or the cooling rate.

Figure 1 shows the calculated history of the surface friction velocity u_* for various cooling rates. A rate of 2 C hr^{-1} at 1 m, typical over agricultural sites in clear weather, decreases u_* (and the surface wind speed) by a factor of three within a few hours, according to the model. Meanwhile, the angle α between the surface and geostrophic winds increases sharply, as shown in Figure 2.

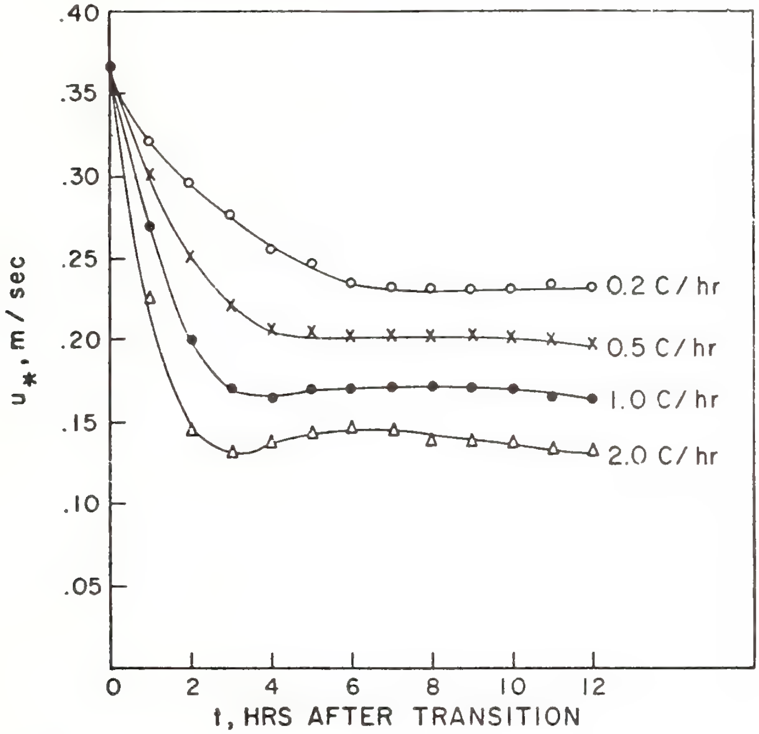

Fig. 1. Evolution of the surface friction velocity for various cooling rates at 1 m. $G = 10$ m s^{-1}, 45 N latitude, $z_0 = 0.01$ m, and initial conditions from simulated decaying convective layer.

The rapid change in the surface wind vector after transition is easily explained with the mean momentum equations. In coordinates aligned with the geostrophic wind, these are

$$\frac{\partial U}{\partial t} = -\frac{\partial}{\partial z}\overline{uw} + fV,$$
$$\frac{\partial V}{\partial t} = -\frac{\partial}{\partial z}\overline{vw} + f(U_g - U). \qquad (24)$$

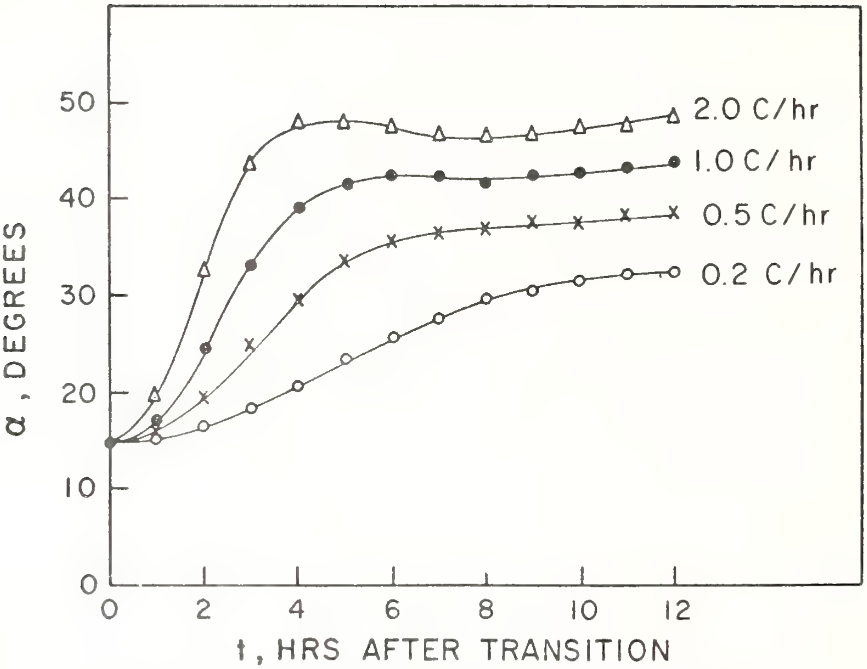

Fig. 2. Evolution of angle between surface and geostrophic winds.

The results indicate that near the surface and immediately after transition, the frictional (stress gradient) term dominates the first equation and causes U to decrease rapidly. At this time the frictional term is typically twice as large as it is near midday. While the $\overline{uw}$-profile at transition retains the nearly linear shape characteristic of convective conditions, the vertically propagating stable stratification caused by the surface cooling decreases $\overline{uw}$ magnitudes aloft more rapidly than at the surface, thus significantly increasing the stress gradient. The terms in the lateral momentum equation are much more closely matched, but the geostrophic departure term does slightly exceed the friction. Thus near the surface after transition, U drops sharply while V slowly increases in magnitude, causing the surface wind speed to decrease and the cross-isobaric angle to increase.

Above the stable layer, the calculated stress gradients decay to negligible levels within a few hours. The mean momentum equations then reduce to, for our idealized case, with steady G and horizontal homogeneity,

$$\begin{aligned} \frac{\partial}{\partial t}(U - U_g) &= f(V - V_g), \\ \frac{\partial}{\partial t}(V - V_g) &= f(U_g - U), \end{aligned} \tag{25}$$

so that U and V oscillate about U_g and V_g, respectively. In coordinates such that

$V_g = 0$, the following simple equation governs the mean wind speed S:

$$\frac{\partial S}{\partial t} = f\frac{G}{S}V. \tag{26}$$

In the idealized mid-afternoon convective PBL, the $\overline{uw}$-profile decreases essentially linearly from $-u_*^2$ at the surface to zero at z_i, the height of the inversion base. (This assumes negligible mean momentum change across the inversion; if not, the momentum entrainment process will distort the stress profiles, as shown by Deardorff (1973)). Our mid-afternoon estimate for fV is then

$$fV \simeq \frac{u_*^2}{z_i}. \tag{27}$$

Since fV does not change rapidly after transition, it should remain positive, and Equation (26) then predicts increasing wind speeds aloft after sundown; this is commonly referred to as the nocturnal jet, and the speeds can be supergeostrophic.

Even over homogeneous terrain, the evolution of the jet is probably influenced by at least two other effects – advection and turbulence. If the advective term in Equation (26) is of the order of the retained term, we have

$$U_i S_{,i} \simeq \frac{S \Delta S}{l} \simeq fV, \tag{28}$$

and if we use Equation (27) for a crude estimate of fV, we find

$$l \simeq \frac{S}{u_*}\frac{\Delta S}{u_*} z_i. \tag{29}$$

Using typical values of $S/u_* = 25$, $u_* = 0.4$ m s^{-1}, $\Delta S = 1$ m s^{-1}, $z_i = 1.5$ km, we find $l = 10^2$ km. This means that a 1 m s^{-1} change in S over a horizontal distance of 100 km, probably not an unusual situation even over homogenous surfaces, creates an advective term as large as the single term we kept. A second complication is that significant frictional forces can exist due to wave motions and associated intermittent turbulence. In practice then, the nocturnal jet may evolve in a somewhat different manner than implied by Equations (25) and (26).

The calculated surface heat flux histories are shown in Figure 3. With the prescribed constant cooling rate, the initial increase in Q_0 is linear; when the thermal stratification becomes strong enough to affect the flow, a feedback effect limits the heat transfer. For strong cooling rates, there is a secondary recovery in Q_0 which might be associated with the increasing wind speed in the nocturnal jet. Figure 4 shows the evolution of the Obukhov length L.

The model indicates, through Figures 1–4, that the nocturnal PBL can approach a steady state a few hours after transition. Turbulence is confined to a layer of thickness h which we have arbitrarily taken as the height where stress has decreased to 5% of its surface value. Figure 5 shows typical turbulence profiles within this layer. The

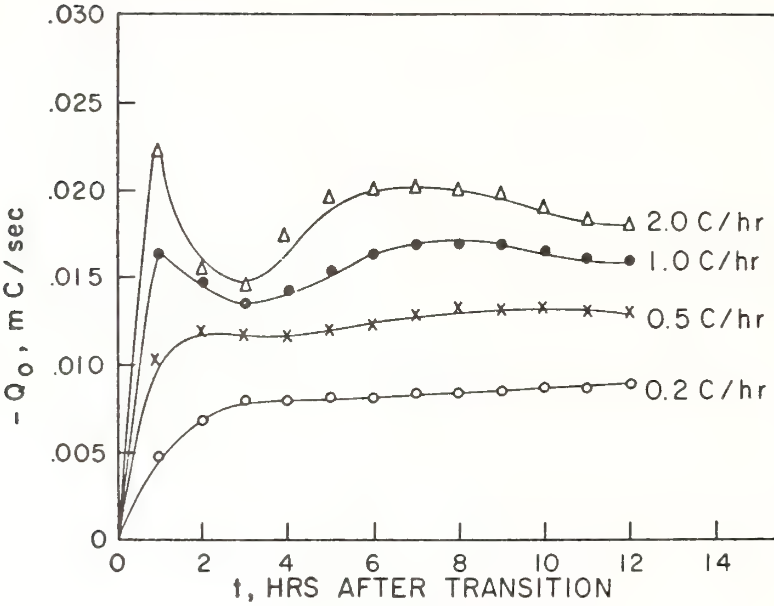

Fig. 3. Evolution of surface heat flux.

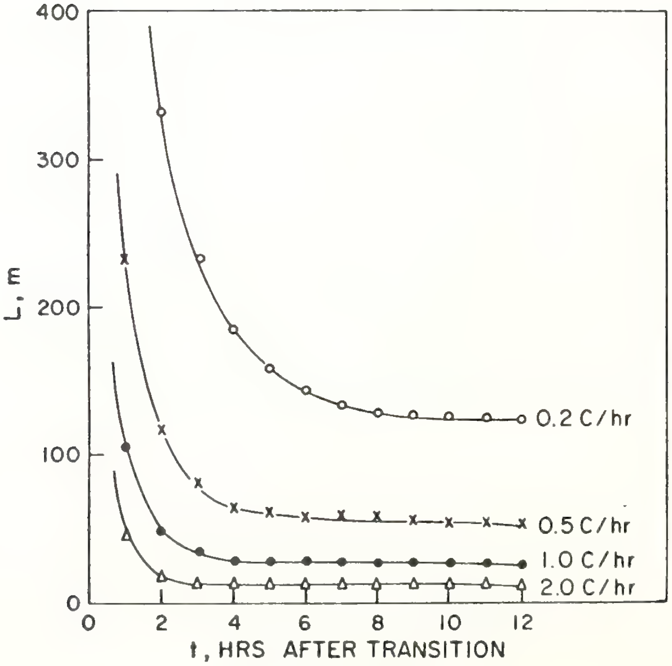

Fig. 4. Evolution of Obukhov length.

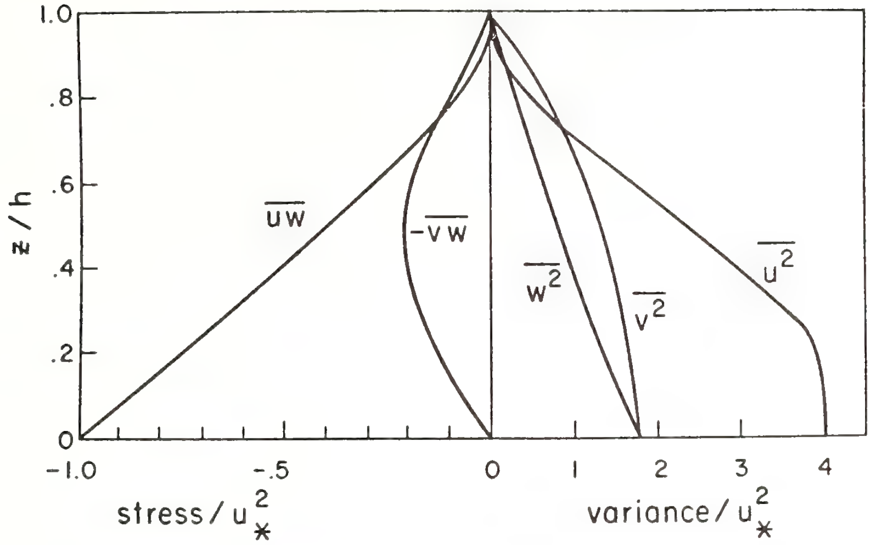

Fig. 5. Turbulence profiles within steady-state stable PBL.

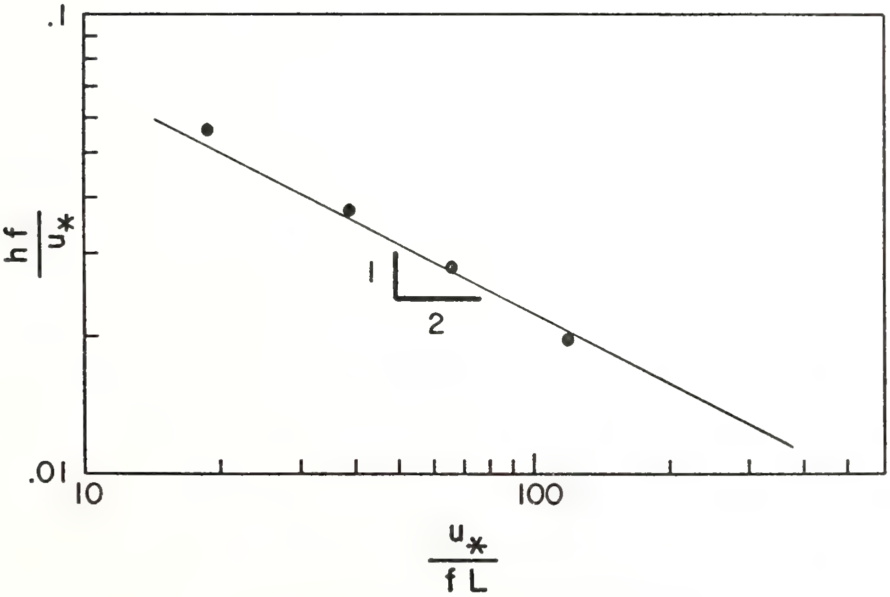

Fig. 6. Stability dependence of depth of stable PBL.

vertical heat flux profile is not shown but also decreases essentially linearly to zero at $z=h$.

The model predictions for h are plotted in dimensionless form in Figure 6. The line through the data is

$$\frac{hf}{u_*} = 0.22\left(\frac{u_*}{fL}\right)^{-1/2}, \tag{30}$$

which is the power law predicted on dimensional grounds by Zilitinkevich (1972). Businger and Arya (1974) also obtained this power law with a K-model, but find a constant factor about twice ours.

The profiles of two Richardson numbers,

$$R_i = \frac{\frac{g}{T}\Theta_{,3}}{U_{,3}^2 + V_{,3}^2} \qquad R_f = \frac{\frac{g}{T}\overline{\theta w}}{\overline{u_i u_j}\, U_{i,j}} \tag{31}$$

are shown in Figure 7. Near the surface they should be functions only of z/L, and recasting them in terms of z/h leaves a h/L dependence (or equivalently, a $u_*/(fL)$ dependence) as shown in Figure 7 near the origin. The calculations suggest a similar dependence exists near the top of the layer as well.

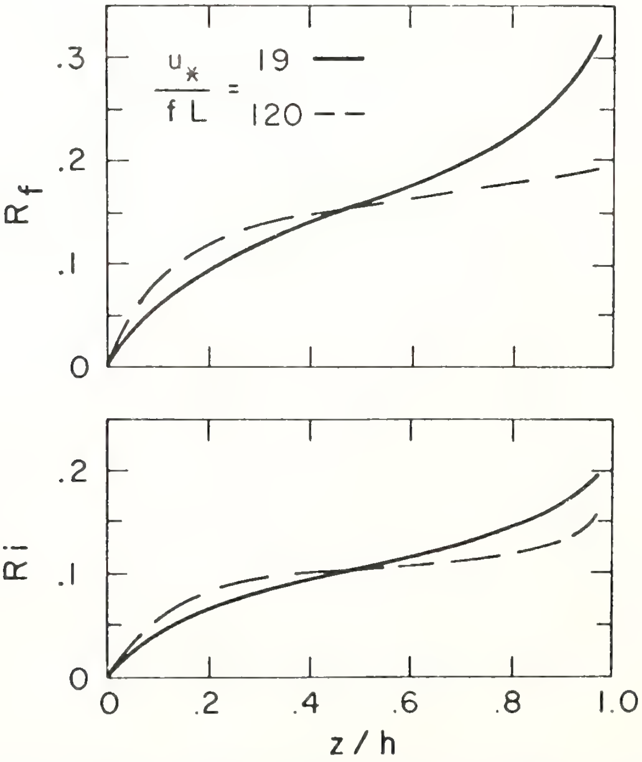

Fig. 7. Variation of gradient and flux Richardson numbers with height in the stable PBL.

While many of these results are difficult to test, there are abundant measurements of mean wind speed and temperature in the nocturnal surface layer. The 1968 Kansas data, for example, show that (Businger *et al.*, 1971)

$$\begin{aligned} \frac{kz}{u_*} U_{,3} &= \phi_m = 1 + 4.7 \frac{z}{L}, \\ \frac{kz}{T_*} \Theta_{,3} &= \phi_h = 0.74 + 4.7 \frac{z}{L}, \end{aligned} \tag{32}$$

within the first 30 m or so. These are compared with the model predictions in Figure 8. The ϕ_h data agree remarkably well, while the ϕ_m values from the model tend to be about 20% higher than the observations. The model Ri values near the surface are therefore probably low by about 30%.

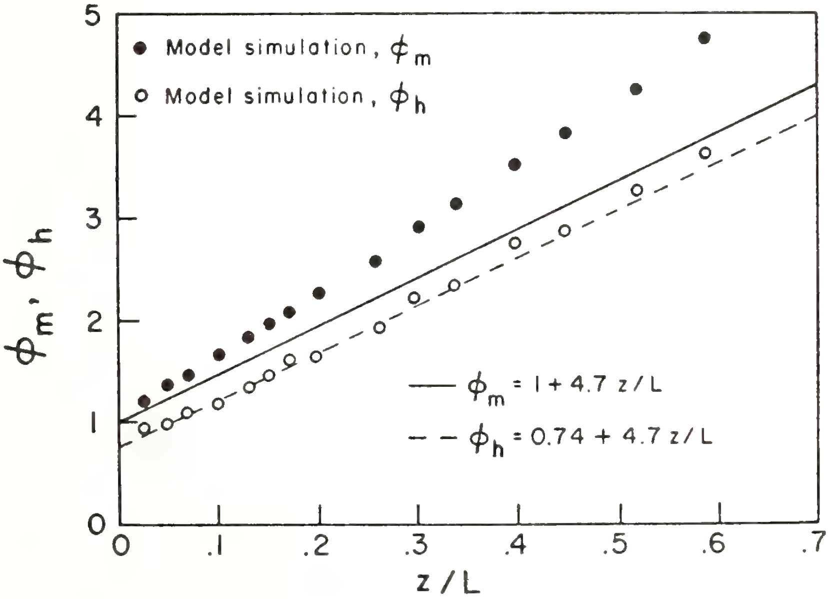

Fig. 8. Comparison of dimensionless wind shear (ϕ_m) and temperature gradient (ϕ_h) profiles in stable surface layer with those observed in Kansas experiments.

The dimensionless dissipation rate ϕ_ε is shown in Figure 9. If in the stable surface layer the flux divergence term in the turbulent kinetic energy budget is negligible, the steady-state budget reduces to

$$\frac{k_z}{u_*^3} \bar{\varepsilon} = \phi_\varepsilon = \phi_m - \frac{z}{L} = 1 + 3.7 \frac{z}{L}. \tag{33}$$

Direct ϕ_ε measurements seem to be slightly higher than indicated by Equation (33) (Wyngaard and Coté, 1971), but not conclusively so because of the experimental dif-

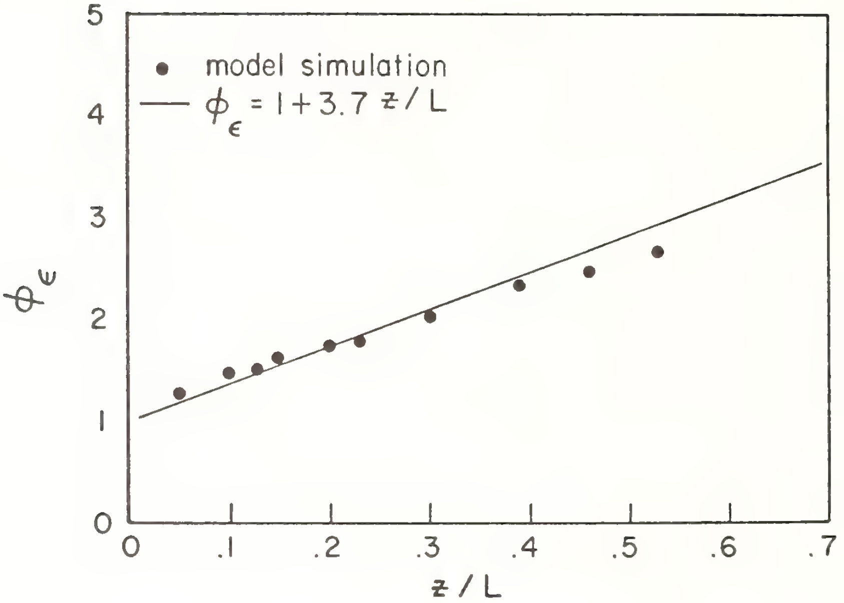

Fig. 9. Comparison of dimensionless dissipation-rate (ϕ_ϵ) profile in stable surface layer with a transport-free prediction based on Kansas observations.

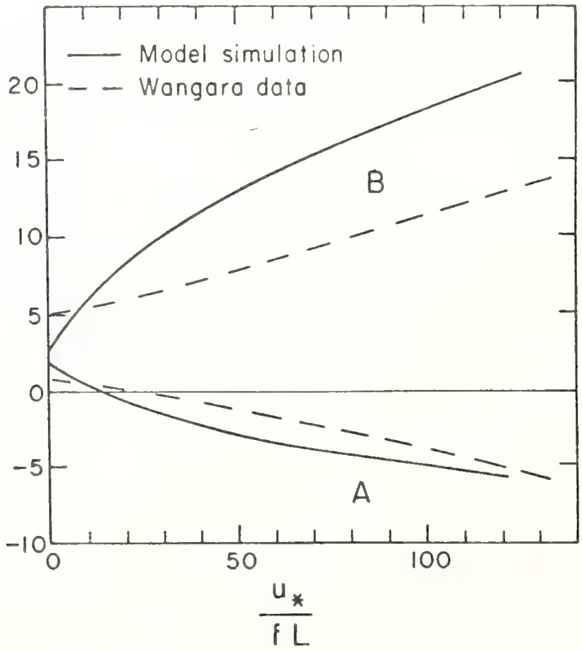

Fig. 10. Results for geostrophic drag law parameters compared with Wangara data.

ficulties and the sparse data. The model results in Figure 9 agree quite well with Equation (33).

Our final result of a general nature concerns the geostrophic drag law. It is usually written in coordinates aligned with the surface wind as

$$\begin{aligned} A\left(\frac{u_*}{fL}\right) &= ln\left(\frac{u_*}{fz_0}\right) - k\,\frac{U_g}{u_*}, \\ B\left(\frac{u_*}{fL}\right) &= -K\,\frac{V_g}{u_*}, \end{aligned} \tag{34}$$

although sometimes A and B are interchanged. Our results are shown in Figure 10 along with the trends of the Wangara data as reported by Businger and Arya (1974).

3.2. COMPARISON WITH 1973 MINNESOTA DATA

We have also tested some of the model predictions for an evolving nocturnal PBL against data from the 1973 Minnesota experiments. A discussion of this program, and the results from tethered balloon and tower measurements in the convective PBL, are presented by Kaimal *et al.* (1975). During the evening runs, the turbulence was

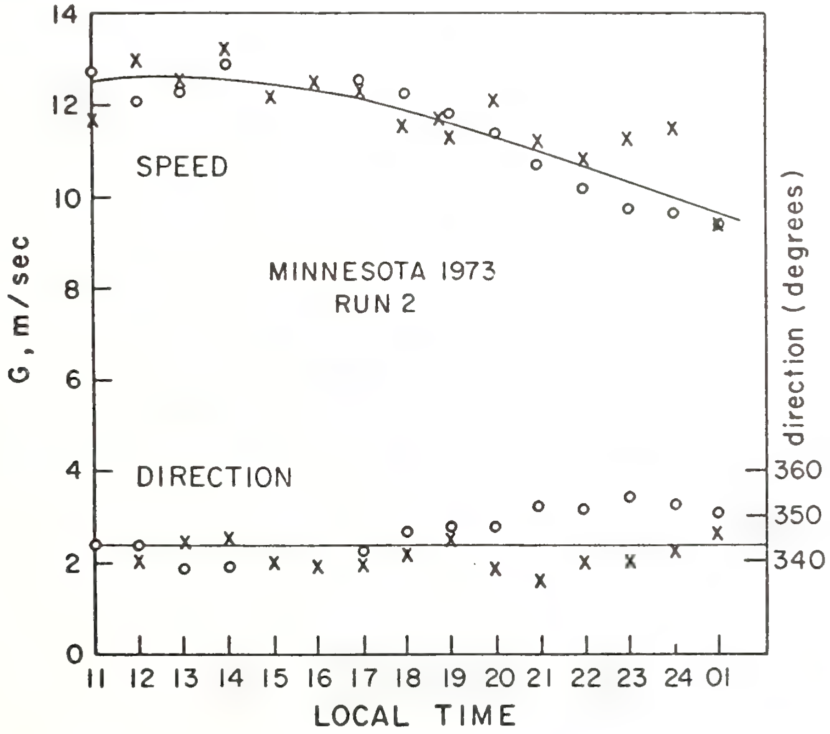

Fig. 11. History of surface geostrophic wind for run 2 of the 1973 Minnesota experiments as observed from two sets of stations (× and ○).

virtually extinguished within a few hours due to the high surface cooling rates and decreasing surface geostrophic wind speed. We chose run 2, where these effects were least, for simulation.

We concentrated our comparison on turbulence properties in the tower layer. We chose this layer because short (15-min) averaging periods were needed for the non-stationary field data in the early evening hours. This is not long enough for statistically stable averages above a few tens of meters height, so the 15-min data from the tethered balloon tend to be unusable due to scatter.

The surface geostrophic wind history for the run was found from the data of Figure 11. The components of the horizontal mean pressure gradient were found from 2-point differences in hourly surface pressure observations taken to 0.1 mb. Two sets of stations were used, one oriented N–S, E–W, the other NE–SW, NW–SE, with the separations ranging from 350 to 580 km. The smooth curves faired through the points in Figure 11 were used as the geostrophic wind input to the model. After transition (1845 local time) the cooling rate at 1 m was fixed at the observed value of 2.75 C hr^{-1}. As with our simulations mentioned earlier, the initial conditions for the model study of run 2 were generated from a simulation of the convective PBL of that day.

The calculated u_* history, Figure 12, agrees well with the observations, which were terminated about 4 h after transition because the turbulence levels were too low. The vertical heat flux at 4 m, Figure 13, shows the characteristic rapid increase after transition followed by a drop as stability suppresses the turbulence and limits the heat transfer. The experimental points in Figure 13 are somewhat scattered and probably

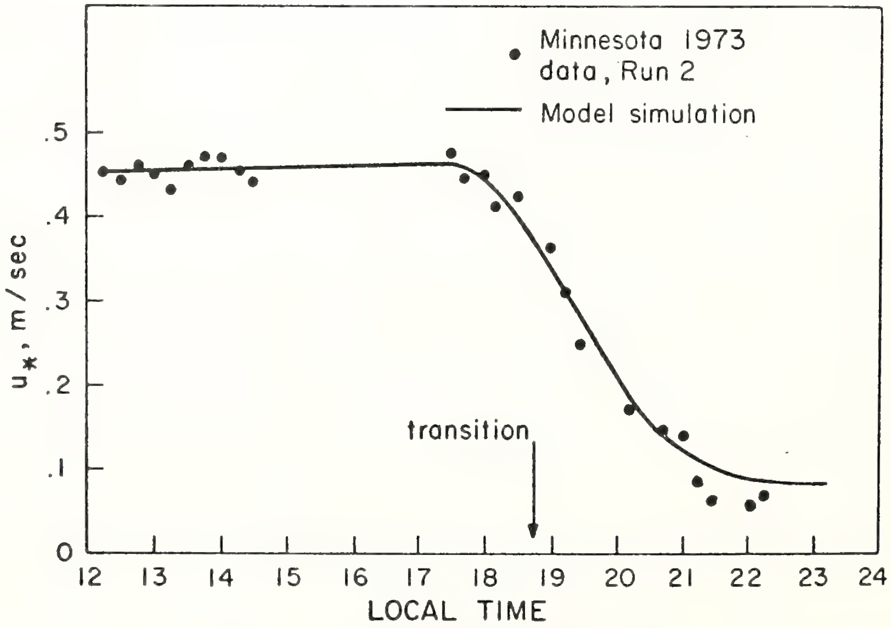

Fig. 12. Calculated and observed u_* for run 2.

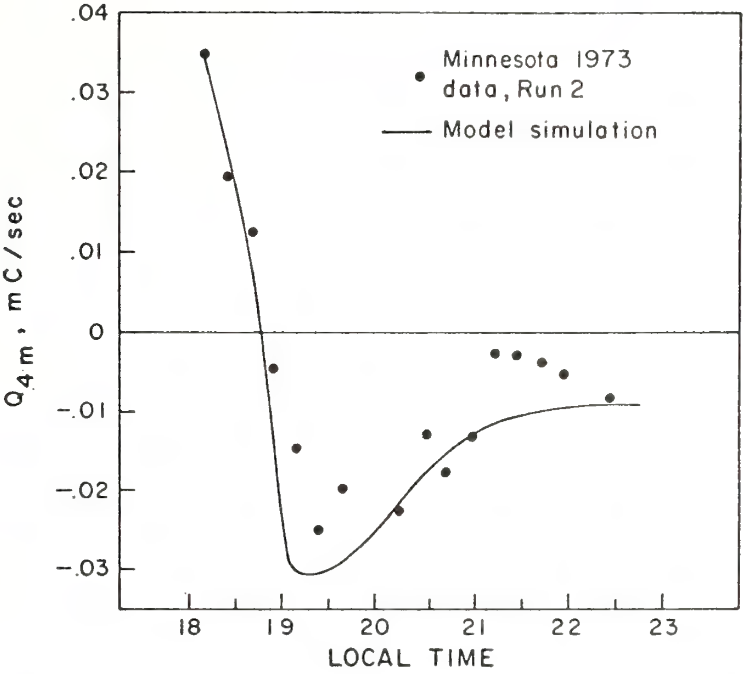

Fig. 13. Vertical heat flux at 4 m compared with data from run 2.

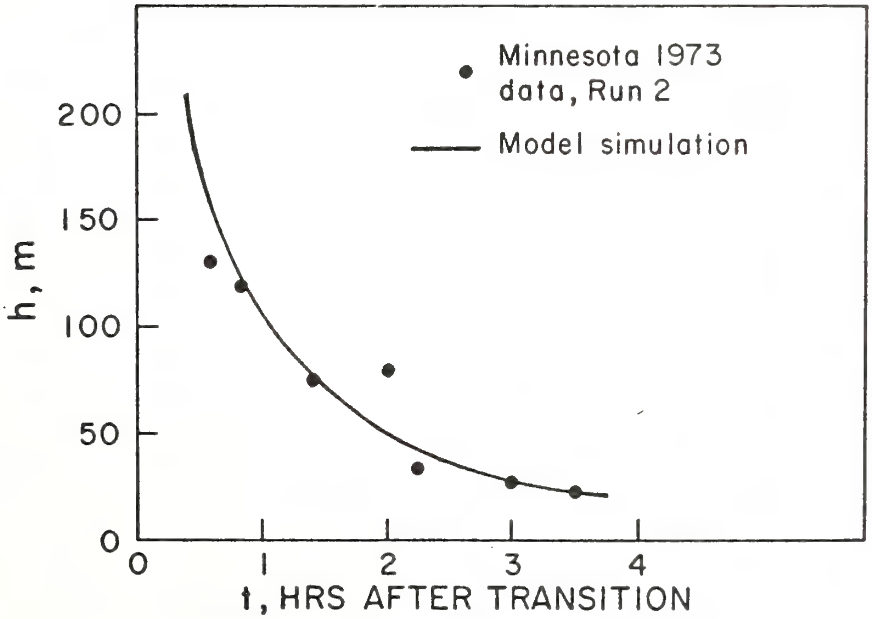

Fig. 14. The evolution of the height where vertical heat flux vanished in run 2, compared with observations.

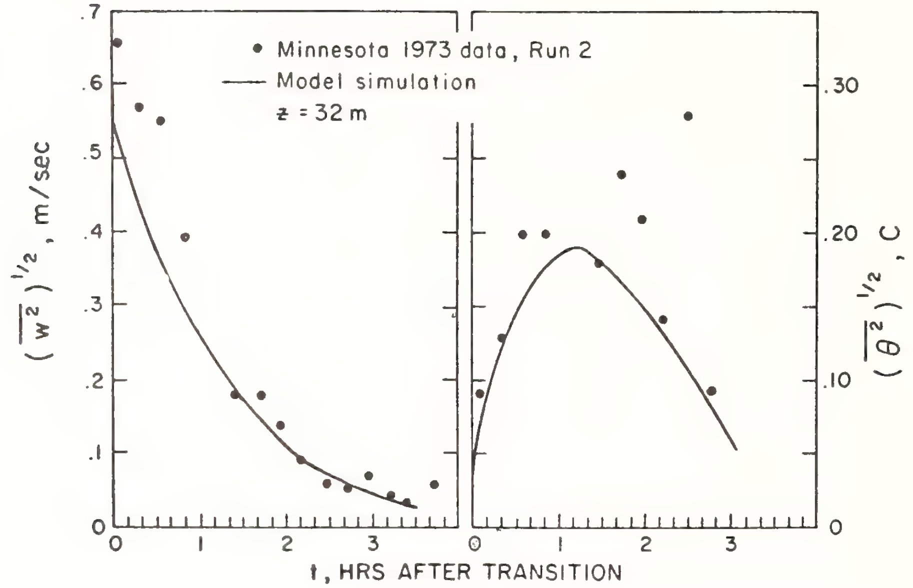

Fig. 15. Histories of vertical velocity and temperature fluctuation levels at 32 m, run 2, compared with observations.

consistently low by about 10% because of path-averaging losses in the 20-cm sonic anemometer, but again the overall agreement with the calculations is good.

Heat flux was also measured at 32 m on the tower and 61 m on the balloon cable, so we could plot heat-flux profiles and determine the height where the flux vanished. Figure 14 shows these data, along with the model calculations which behave in the same way.

Figure 15 compares representative turbulence quantities at 32 m. The predicted rms vertical velocity behavior is very much like the observations, with the most significant difference the mismatch at transition. The agreement in the temperature is not quite as good.

4. Summary and Conclusions

Judging from the good agreement between the calculations and the surface-layer data from Kansas and Minnesota, the model predicts the structure of turbulence from neutral to moderately stable stratification fairly well.

Observations indicate that the extremely stable stratification at greater heights in the nocturnal PBL is accompanied by unusual flow structure. Some of the most detailed observations in very stable conditions come not from the atmosphere but from the thermocline in the ocean (Woods, 1969), and reveal a complicated microstructure in the velocity and temperature profiles. Stewart (1969) speculates this is a mechanism that maintains the local *Ri* value at some critical level, independent of the macroscopic value. Woods' observations also show that internal waves traveling along stable sheets occasionally become unstable and break into isolated patches of turbulence which at any instant cover only a few percent of the surface area of a sheet. Presumably this turbulence is responsible for virtually all of the scalar diffusion. Stewart points out that the waves themselves, as well as the turbulent patches, can transport momentum. Evidently, these wave momentum fluxes can be large; Beran *et al.* (1973) measured values on the order of 10^3 $(\text{cm s}^{-1})^2$ at 300 m in the nocturnal PBL.

Our model does not predict the local structure, of course, but rather the average over an ensemble of realizations or over a large, horizontally homogeneous plane. One would not expect these averages to display the dramatic microstructure observed locally. But since turbulence under extremely stable conditions is so conspicuously different in some respects from that in neutral and unstably stratified flows, one wonders if the closure parameterizations are as effective. One also suspects that the neglected effects of wave motions, such as local turbulence generation and direct momentum transport, could be important. Hopefully, further theoretical and experimental studies of the upper portions of the nocturnal PBL will help to answer these questions.

Acknowledgments

The author is grateful to Owen Coté for many helpful discussions, to Y. Izumi for his compilation of the 1973 Minnesota data, and to the other members of the Boundary Layer Branch for providing a stimulating and productive atmosphere during the course of this work.

References

Arya, S. P. S. and Wyngaard, J. C.: 1975, 'Effect of Baroclinicity on Wind Profiles and the Geostrophic Drag Law for the Convective Planetary Boundary Layer', *J. Atmos. Sci.* **32**, 767–778.

Beran, D. W., Hooke, W. H., and Clifford, S. F.: 1973, 'Acoustic Echo-Sounding Techniques and Their Application to Gravity-Wave, Turbulence, and Stability Studies', *Boundary-Layer Meteorol.* **4**, 133–154.

Bradshaw, P.: 1972, 'The Understanding and Prediction of Turbulent Flow', *Aero. J.* **76**, 403–418.

Businger, J. A., Wyngaard, J. C., Izumi, Y., and Bradley, E. F.: 1971, 'Flux-Profile Relationships in the Atmospheric Surface Layer', *J. Atmos. Sci.* **28**, 181–189.

Businger, J. A. and Arya, S. P. S.: 1974, 'Height of the Mixed Layer in the Stably Stratified Planetary Boundary Layer', in *Advances in Geophysics* **18A**, Academic Press, New York, pp. 73–92.

Crow, S. C.: 1968, 'Viscoelastic Properties of Fine-Grained Incompressible Turbulence', *J. Fluid Mech.* **33**, 1–20.

Deardorff, J. W.: 1973, 'An Explanation of Anomalously Large Reynolds Stresses Within the Convective Planetary Boundary Layer', *J. Atmos. Sci.* **30**, 1070–1076.

Kaimal, J. C., Wyngaard, J. C., Haugen, D. A., Izumi, Y., Coté, O. R., and Caughey, S. J.: 1975, 'Turbulence Structure in a Convective Boundary Layer', to be submitted for publication.

Launder, B. E.: 1975, 'On the Effects of a Gravitational Field on the Turbulent Transport of Heat and Momentum', *J. Fluid. Mech.* **67**, 569–581.

Launder, B. E., Reece, G. J., and Rodi, W.: 1975, 'Progress in the Development of a Reynolds-Stress Turbulence Closure', *J. Fluid Mech.* **68**, 537–566.

Lumley, J. L.: 1975, 'On the Pressure Strain Correlation', *Physics Fluids* **18**, 750.

Lumley, J. L. and Khajeh-Nouri, B.: 1974, 'Computational Modeling of Turbulent Transport', in *Advances in Geophysics* **18A**, Academic Press, New York, pp. 169–192.

Rotta, J. C.: 1951, 'Statistische Theorie nichthomogener Turbulenz', *Z. Phys.* **129**, 547.

Stewart, R. W.: 1969, 'Turbulence and Waves in a Stratified Atmosphere', *Radio Science* **4**, 1269–1278.

Tennekes, H. and Lumley, J. L.: 1972, 'A First Course in Turbulence', MIT Press, Cambridge, 300 pp.

Woods, J. D.: 1969, 'On Richardson's Number as a Criterion for Laminar-Turbulent-Laminar Transition in the Ocean and Atmosphere', *Radio Science* **4**, 1289–1298.

Wyngaard, J. C. and Coté, O. R.: 1971, 'The Budgets of Turbulent Kinetic Energy and Temperature Variance in the Atmospheric Surface Layer', *J. Atmos. Sci.* **28**, 190–201.

Wyngaard, J. C. and Coté, O. R.: 1974, 'The Evolution of a Convective Planetary Boundary-Layer – a Higher-order-closure Model Study', *Boundary-Layer Meteorol.* **7**, 289–308.

Wyngaard, J. C., Coté, O. R., and Rao, K. S.: 1974, 'Modeling the Atmospheric Boundary Layer', in *Advances in Geophysics* **18A**, Academic Press, New York, pp. 193–211.

Wyngaard, J. C., Arya, S. P. S., and Coté, O. R.: 1974, 'Some Aspects of the Structure of Convective Planetary Boundary Layers', *J. Atmos. Sci.* **31**, 747–754.

Zilitinkevich, S. S.: 1972, 'On the Determination of the Height of the Ekman Boundary Layer', *Boundary-Layer Meteorol.* **3**, 141–145.

Journal of Geophysical Research 79, 3015-3018, July 1974.

Results of Field Testing a Two-Wavelength Optical Distance-Measuring Instrument

G. M. B. Bouricius and K. B. Earnshaw

Environmental Research Laboratories, NOAA, Boulder, Colorado 80302

A two-color optical distance-measuring instrument has been developed and field tested. Results show that the instrument has a short-term (1 day) precision of 1 part in 10^7 and a long-term (months) precision of 2 parts in 10^7 without requiring atmospheric temperature measurements. Simultaneous measurements taken with a model 4 geodimeter and with the two-color instrument show that the two-color instrument has an improvement of a factor of 10 in the standard deviation over the older model 4. An analysis of the variances of the measurements shows that no significant increase in precision of distance measurements can be made with this particular model 4 instrument even with greatly improved temperature measurements. Only an instrument with inherently greater precision can benefit from greatly improved temperature measurements.

Many electromagnetic techniques for making precise geodetic distance measurements are described in the literature [*Earnshaw and Owens*, 1967; *Wood and Thompson*, 1970; *Bender*, 1967; *Bean and Dutton*, 1966]. The accuracy of these techniques is invariably limited by lack of knowledge of the average refractive index of the air along the path. As was pointed out by *Bender and Owens* [1965], simultaneous measurement with two colors of light can provide the correction necessary to account for the refractive index. An instrument using two microwave-modulated laser beams has been under development for several years at the Wave Propagation Laboratory (WPL) of the Environmental Research Laboratories of NOAA. Because the theory of operation of this particular instrument has been adequately reported [*Earnshaw and Hernandez*, 1972], it is the purpose of this paper to describe only the more important improvements in the instrument and the latest results of field testing.

The instrument has demonstrated a long-term precision of 2×10^{-7} (in this paper precision means the ratio of the standard deviation of a variable to the variable) and a short-term precision at least 10 times better than can be obtained by using a model 4 (laser) geodimeter and estimating the refractive index correction from temperature measurements at the two end points.

INSTRUMENT

The instrument, shown in Figure 1, uses two laser light sources. The red light is a helium-neon CW laser operating at a vacuum wavelength of 6329.9 Å and producing approximately 7.0 mW of radiant power in a beam that has a divergence of 1.3 mrad. The blue light is a helium-cadmium CW laser operating at a vacuum wavelength of 4416.8 Å and radiating approximately 15 mW in a beam that has a divergence of 0.8 mrad.

The two laser beams are joined in a Wollaston prism and passed through a KH_2PO_4 (KDP) crystal modulator. The modulator changes the polarization of the optical beams at a microwave frequency of approximately 2.7 GHz. The light is then propagated over a path to be measured, reflected from a polarization-preserving telescope, and returned over the path to the modulator where a modulation phase comparison is made.

By changing the frequency of modulation the modulation wavelength can be adjusted so that the optical path length will contain exactly an even number of half wavelengths. In practice the modulation frequency of each laser beam is continuously adjusted to achieve this balance because the atmosphere (and hence the optical path length) is continuously changing.

The instrument is self-balancing; updating of the two multiplexed modulation frequencies for red and blue light occurs 250 times/s. Counters that determine the average modulation frequencies during each measurement interval (normally 10 s) are used to average the path length fluctuations for both red and blue light.

DISTANCE MEASURING

The apparent distance measurements are made by substituting the measured red and blue modulation frequencies into the following equations:

For red apparent length

$$n_R L = I_R (C/f_R)^{1/2} - k_R \tag{1}$$

For blue apparent length

$$n_B L = I_B (C/f_B)^{1/2} - k_B \tag{2}$$

where L is the true length, n_R and n_B are the average group indices of refraction along the path for red and blue light, I_R and I_B are the number of modulation wavelengths along the path for red and blue light, (C/f_R) and (C/f_B) are the modulation wavelengths in vacuum for red and blue light, and k_R and k_B are the path length corrections for optical components in the red and blue light beams.

The geometrical distance is calculated by using the difference in the two apparent path lengths to correct the red apparent length for the apparent extra length caused by the atmosphere. The corrected length is thus given by

$$L = n_R L - A(n_B L - n_R L) \tag{3}$$

where

$$A = (n_R - 1)/(n_B - n_R) \tag{4}$$

In a dry atmosphere of standard composition the correction factor A depends only on the two optical wavelengths and is known to high accuracy [*Owens*, 1967]. Temperature measurements are not needed. However, water vapor changes the composition of the atmosphere and therefore affects the

Copyright © 1974 by the American Geophysical Union.

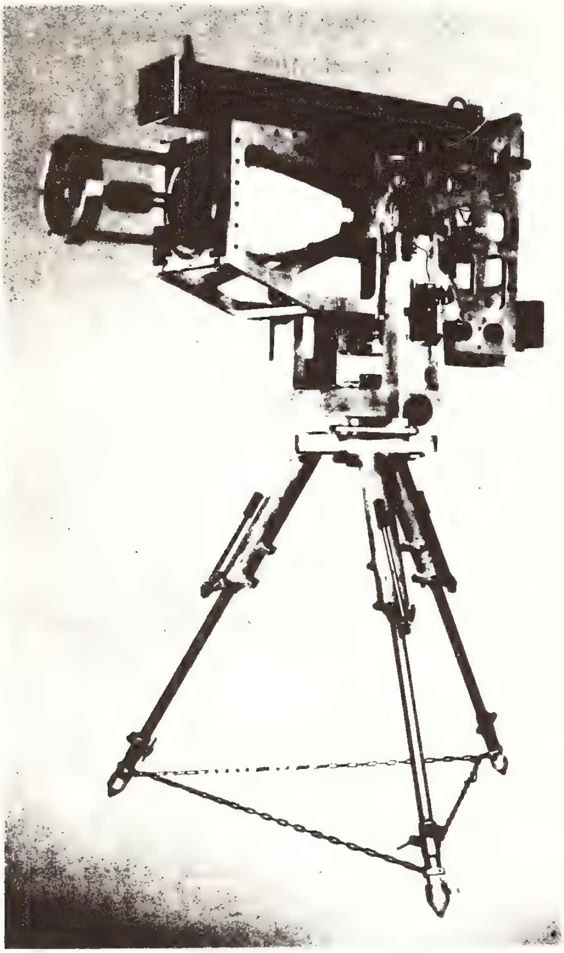

Fig. 1. Two-laser microwave-modulated distance-measuring instrument.

value of *A* necessary for the true correction of distances. Fortunately, the dependence of *A* on water vapor pressure is small, so that a very accurate value of water vapor pressure is not needed. For example, if the path-averaged water vapor pressure measurement is in error by 3 mbar, the error in corrected distance will be less than 3×10^{-7}.

Since the last report [*Earnshaw and Hernandez*, 1972] on this developmental instrument several major improvements have been made in the field installations and in the electronic and data-handling systems. Poured concrete pillars, whose foundations extend into the ground about 1 m below frost line, have replaced the temporary retroreflector supports. Poured concrete foundations also now support the tripod of the instrument head. These changes, along with the installation of precision levels and optical plummets, now provide a fixed base line suitable for observations extending over months and years.

The electronic system has been completely redesigned and rebuilt to reduce noise, to allow common electronics to be used for both optical signals, and to provide signal amplitude aperturing that prevents low-amplitude and noise signals and large saturating signals from affecting the self-balancing circuits.

A dedicated minicomputer has been interfaced with the instrument to provide automatic data logging and more recently to provide computed distance printout.

Field Test Results

At the end of June 1972 the instrument was set up at the Table Mountain Research Facility north of Boulder, Colorado, to determine long-term stability. The instrument was tested at various times from July 1972 through January 1973 under a wide range of meteorological conditions. Figure 2 shows the daily average distance as a function of date. The long-term average distance is 616899.04 ± 0.13 cm.

To test the influence of several factors on distance measurement, scatter diagrams were made of individual distance measurements as they relate to dew point, atmospheric pressure, instrument frame temperature, and air temperature. Only the air temperature, measured 2 m above the ground at the instrument end of the path, seemed to be related to the measured distance; this relationship is shown in Figure 3. The installation of the signal-aperturing system was completed after the bulk of the data reported here was collected, and it is believed that this result may be caused by lower signal-to-noise ratios at higher temperatures. Data taken subsequently will show whether this apparent temperature dependence has been removed or reduced. Alternatively, this temperature dependence may indicate a systematic bias in the formulas that we have adopted for the refractive index of air. The bias could be removed either by making better determinations of the refractivity of air or perhaps more practically by using the observed temperature regression to remove the effect from future observations. Whether it is removed or not, the observed bias contributes only slightly to the variance of the measurements.

Late in October of 1972 we had the opportunity to make a direct comparison between the WPL two-wavelength instrument and a model 4 geodimeter operated by personnel from the National Oceanic Service (NOS). The NOS geodimeter was set up to measure a path parallel to our path, offset laterally by about 3 m. Simultaneous measurements were made with the two instruments with a cyclic schedule of 3 hours of continuous operation followed by 1 hour of rest. Measurements began at 0600 hours and concluded at 2400 hours.

Figure 4 shows the point-by-point distance measurements obtained during this comparison experiment as a function of the time of day. Curve 1 was obtained by using data from the WPL instrument and using the dew point and average of the pressures as measured at each end of the path. Curve 2 was obtained by using data from the NOS geodimeter and using

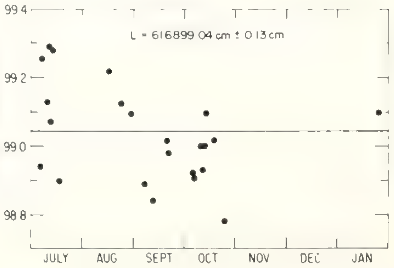

Fig. 2. Daily average distance as a function of time. This is a long-term stability test.

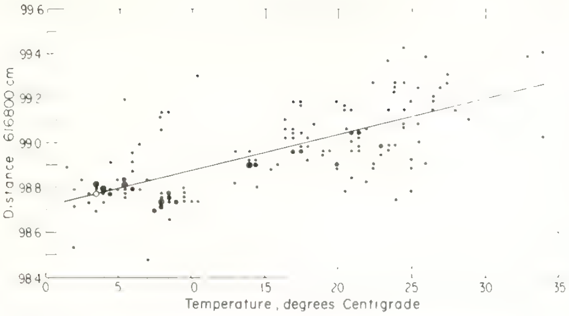

Fig. 3. Distance as a function of temperature measured 2 m above the ground at one end of the path. The individual distance measurements not daily averages are used.

the average temperatures and pressures as measured at each end of the path.

The 0.73-cm difference in average path length measurements is not unexpected; in fact, the determination of this offset was one of the important reasons for conducting this experiment. The reasons for this offset are: (1) the instrument telescope-folding lengths are difficult to measure accurately and may be in error, (2) the center of polarization modulation in the crystal is not known precisely, and (3) the indices of refraction, used for correcting the modulator crystal length, are of unknown precision. The difference is a correction to the instrument constant that in no way affects the precision of the measurements. Another immediately apparent difference is the relatively smooth curve of the WPL measurement, showing a standard deviation of 0.05 cm, or $^1/_{10}$ of the 0.48-cm standard deviation of the NOS geodimeter measurement curve.

Because the WPL instrument measurements are insensitive to temperature and because the geodimeter measurements use the average of the two end point temperatures as a necessary datum, we attempted to reduce the standard deviation of the geodimeter data by using a path averaged temperature derived from the two-color data. The path-averaged temperature may be obtained from the WPL measurements by dividing the optical path length of either color by the long-time average length to obtain the index of refraction. Using the measured total pressure and water vapor pressure, we can find the corresponding temperature necessary to produce this index of refraction. When these WPL-derived temperatures are used with the geodimeter data, curve 3 is obtained.

Because we believe the temperature derived from the WPL instrument to be a better estimate of actual path-averaged temperature than can be obtained from end point temperatures, it is interesting to note that use of these better temperature values improves the standard deviation of the geodimeter measurements only slightly (curves 2 and 3). An analysis of the variance of the distance measurements has been made to help in understanding these results.

For a given set of length measurements the total variance may be considered to be composed of two parts: instrumental and meteorological (principally owing to uncertainties in path-averaged temperature).

To obtain data from which we can derive a distance, simultaneous measurements are taken at two wavelengths, red and blue. We may either combine these measurements in the two-wavelength formula for distance or use them separately in a one-wavelength distance formula.

Because the two-wavelength formula, (3), is insensitive to temperature, the total measurement variance is attributed to the instrument. From this fact we obtain the instrumental variances of the individual red distance and blue distance measurements. From the individual red distance and blue distance total variances we remove the instrumental variances to obtain the meteorological variances. Using the same sets of meteorological data with geodimeter distance measurements, we obtain total variances from which we subtract the meteorological variances to obtain the geodimeter instrumental variances. Variances that should be identical but are not have been averaged. This is as far as we feel justified in going at this time. Table 1 is a summary of the results.

CONCLUSIONS

Long-term tests under varying meteorological conditions have now shown that the two-wavelength instrument is capable of measuring a distance of several kilometers with a precision of about 2 parts in 10^7 without requiring temperature measurements. The precision of the instrument is made possible by using two wavelengths and a high frequency of modulation. To obtain this precision, each of the two identical length-measuring channels must have a precision of 1 part in 10^8 because the distance formula contains a term that is the difference of the optical distances (red and blue) multiplied by 20. Thus either channel used alone can produce length measurements whose precision depends only upon the precision of the measurements of meteorological data.

Short-term tests extending throughout a day show the two-

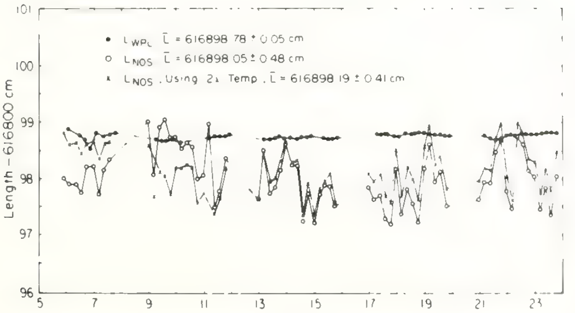

Fig. 4. Point-by-point distance measurements taken during a 1-day comparison test of the two-wavelength instrument and a model 4 geodimeter.

TABLE 1. Analysis of Variance Results

Laboratory Supplying Distance Data	Temperature Data Source	Total Variance of Measurement, cm²	Variance of Instrument, cm²	Variance Resulting From Meteorological Factors, cm²
WPL*	...	$(0.0505)^2$	$(0.0505)^2$	0
WPL†	A	$(0.051)^2$	$(0.0017)^2$	$(0.0509)^2$
WPL†	B	$(0.715)^2$	$(0.0017)^2$	$(0.733)^2$
WPL†	C	$(0.315)^2$	$(0.0017)^2$	$(0.323)^2$
NOS	A	$(0.414)^2$	$(0.411)^2$	$(0.0509)^2$
NOS	B	$(0.783)^2$	$(0.275)^2$	$(0.733)^2$
NOS	C	$(0.475)^2$	$(0.348)^2$	$(0.323)^2$

Average variance for NOS instrument is $(0.345)^2$.

*Using two wavelengths.

†The total variance of the measurement was determined separately from red light data and from blue light data, and the average is tabulated.

A, temperature derived from WPL two-wavelength measurements; B, average of the path end temperature taken at a height of 2 m; and C, average of the path end temperature taken at a height of 9 m.

wavelength instrument capable of measuring distance with a precision of 1 part in 10^7.

It is interesting to observe that the instrument variance of the model 4 geodimeter is very nearly the same as the temperature variance of averaged end point measurements. If better temperature measurements are not available, almost no distance measurement precision could be gained by improving the instrument. In addition, it is obvious that no significant increase in precision of distance measurements can be made with this particular instrument even with greatly improved temperature measurements such as might be obtained by flying the path with an airplane or helicopter.

REFERENCES

Bender P. L., Laser measurements of long distances, *Proc. IEEE, 55,* 1039–1045, 1967.

Bender, P. L., and J. C. Owens, Correction of optical distance measurements for the fluctuating atmospheric index of refraction, *J. Geophys. Res., 70,* 2461–2462, 1965.

Bean, B. R., and E. J. Dutton, The radio refractive index of air, *Nat. Bur. Stand. Rep. 92,* pp. 1–22, U.S. Govt. Print. Office, Washington, D.C., 1966.

Earnshaw, K. B., and E. N. Hernandez, Two-laser optical distance-measuring instrument that corrects for the atmospheric index of refraction, *Appl. Opt., 11,* 749–754, 1972.

Earnshaw, K. B., and J. C. Owens, A dual-wavelength optical distance-measuring instrument which corrects for air density, *IEEE J. Quantum Electron., 3,* 544-550, 1967.

Owens, J. C., Optical refractive index of air: Dependence on pressure, temperature and composition, *Appl. Opt., 6,* 51–59, 1967.

Wood, L. E., Progress in electronic surveying, *Eos Trans. AGU, 52,* IUGG 17–21, 1971.

Wood, L. E., and M. C. Thompson, Jr., Differential phase technique for measuring atmospheric refractivity, in *Proceedings of Electro-Optical Systems Design Conference, September 22–24, 1970,* pp. 921–926, Industrial and Scientific Conference Management, Inc., Chicago, Ill., 1970.

(Received August 15, 1973;
revised March 27, 1974.)

NOAA Technical Report ERL 341-WPL 42

July 1975

FINAL REPORT AND OPERATIONS MANUAL FOR MICROWAVE MODULATED, DUAL OPTICAL DISTANCE-MEASURING INSTRUMENT

K. B. Earnshaw, G. M. B. Bouricius, and K. P. Moran

The accuracy of optical distance measurements on horizontal paths is limited at present by uncertainty in knowledge of the average air density along the path. This report describes the development and testing of a prototype instrument capable of significantly greater accuracy, probably as high as 0.1 ppm. The instrument makes simultaneous measurements of transit time using two superimposed beams of light which have different optical wavelengths but which are modulated at a common microwave frequency. From the difference in transmit time for the two colors, plus the absolute transit time for either one, the average refractive index along the path and hence the true geodetic path length can be determined. Tests over a 6.2 -km path have given a standard error of 0.3 ppm in corrected distance, and it is believed that even better results can be obtained. The system is described in detail, including proposed modifications that would significantly increase its accuracy and range.

Acoustic antennas for atmospheric echo sounding

F. F. Hall Jr. and J. W. Wescott

Wave Propagation Laboratory, NOAA Environmental Research Laboratories, Boulder, Colorado 80302

(Received 31 January 1973; revised 26 February 1973)

Utilization of acoustic waves for atmospheric studies through echo sounding requires an efficient antenna with high on-axis gain and suppressed sidelobes. The antenna pattern for a piston source, as it influences the evaluation of the acoustic radar equation, is calculated and the effective gain factor obtained. Existing microwave antennas and optical searchlights have been adapted for acoustic use and their performance measured. A conical horn-reflector antenna made of fiberglass gives excellent performance in the frequency region 1–5 kHz after being coated with a viscous dampening tar to shorten vibration time. This damping allows reception of weak echoes with minimum delay following the transmission of a high-power acoustic pulse from the antenna. Septum dampers have been used successfully on parabolic-dish antennas. Antenna beam patterns have been measured on an outdoor range, with some measurements being made across a canyon to avoid multipath ground-reflection effects. Mainlobe to 90° sidelobe ratios are 40 to 50 dB. The measured antenna pattern for the horn-reflector antenna agrees closely with predictions for a perfect piston source. The parabolic-dish antennas produce a more complex diffraction pattern. Absorbing cylindrical antenna enclosures have been found effective in further reducing sidelobe reception by 10 to 20 dB, in agreement with predictions. Attention to antenna design allows acoustic echo-sounder operation in a noisy urban environment, and keeps noise pollution from the sounder pulses below the annoyance threshold.

Subject Classification: 28.55, 28.20; 85.90.

INTRODUCTION

In this paper we consider how the measured gain or directivity factor pattern of an acoustic antenna is used in evaluating the echo-sounding equation. We report on fabrication techniques and testing methods found useful when working with highly directional horns and dishes in the atmosphere.

Acoustic echo sounding has been shown to be a valuable new technique for investigating the structure and dynamics of the lower atmosphere.[1–4] To take full advantage of this remote sensing method, it is important to have available acoustic antennas producing sharply defined highly directive beams with minimized sidelobes. Much of the echo sounding is done with the main beam of the antenna pointed vertically, while most of the unwanted background noise originates from the surface of the earth. In this case, it is most important to minimize the reception of unwanted sound at 90° to the main lobe. This also serves to reduce the noise pollution which the pulses from the sounder might contribute to the environment. For some operations, it may be desired to tilt the main beam to elevation angles as low as 30°. Thus, it is sometimes desirable to minimize sidelobes even at this small angle from the main beam.

In order to perform quantitative measurements of the atmospheric parameters contributing to the scattering of acoustic energy, it is also necessary to know accurately the gain characteristics of the antenna.

In the sections which follow, the antenna gain factor for a piston source is evaluated as it enters into the acoustic echo sounding equation. Then, measured gain patterns for several different antennas are presented. And finally, antenna efficiency is discussed.

I. THE METEOROLOGICAL ACOUSTIC ECHO-SOUNDING EQUATION

Acoustic echo sounders probe the atmosphere by transmitting a pulse of acoustic power P of time duration t. The power P_r scattered back from the atmosphere is given by the meteorological acoustic echo-sounding equation[2]

$$P_r = P\sigma(ct/2)AR^{-2}L \,, \tag{1}$$

where σ is the scattering function (fraction of power backscattered per unit solid angle per unit volume), c is the velocity of sound, A is the collecting area of the receiving antenna, R the range to the scattering volume, and L is a compensation factor which accounts for changing antenna gain across the beam as well as atmospheric attenuation. In the atmosphere, the scattering structure contributing to σ is distributed throughout the volume insonified by the beam. Because of varying gain at angles of azimuth θ and elevation φ from the main axis of the beam, the scatterers will receive a power dependent upon their position. Consider the antenna to have an on-axis gain which is a factor $G(0)$ greater than an omnidirectional source. If the antenna acts as a perfect piston source, the angular dependence of gain $G(\theta, \varphi)$ may be predicted by diffraction theory. The acoustic-system compensation factor L may be considered the product of a term attributable to the antenna gain pattern L_a and the round-trip atmospheric attenuation factor L_k, or

$$L = L_a L_k \,. \tag{2}$$

The power backscattered by the total insonified volume located within a cone of some entirely general semiangle θ_0, and with antenna gain averaged over this cone as $G(\theta_0)_{av}$, is

$$P_\sigma = (P/8)\,G(\theta_0)_{av}\,\theta_0^2\,ct\sigma L_k^{1/2} \,, \tag{3}$$

where the atmospheric attenuation is along a one-way path, thus explaining the square root on the final term.

If we now define $G(\theta, \varphi)$ in terms of the on-axis gain $G(0)$ and the response representing the fraction of on-axis gain R,

$$G(\theta, \varphi) = G(0)R(\theta, \varphi) \,, \tag{4}$$

Copyright © 1974 by the Acoustical Society of America

or, integrating over the beam pattern for $0 < \theta < \theta_0$, assuming θ is small,

$$\int_0^{\omega_0} G(\theta, \varphi)\, d\omega = G(0) \int_0^{2\pi} \int_0^{\theta_0} R(\theta, \varphi)\, \theta d\theta d\varphi \ . \tag{5}$$

For a perfect circular piston source,[5] the fraction of the power radiated within the cone is

$$\int_0^{\omega_0} G(\theta, \varphi)\, d\omega = G(0) \int_0^{2\pi} \int_0^{\theta_0} \left[\frac{2J_1(2\pi a\theta/\lambda)}{(2\pi a\theta/\lambda)}\right]^2 \theta d\theta d\varphi \ , \tag{6}$$

where $J_n(x)$ is the Bessel function of order n, a is the radius of the antenna aperture, and λ the acoustic wavelength. The use of the baffled piston function $[2J(x)/x]^2$ is used to illustrate the similarity to the electromagnetic case without anticipating exact correspondence. The right-hand side of Eq. 6 may be integrated to

$$\int G(\theta, \varphi)\, d\omega = \frac{G(0)\,\lambda^2}{\pi a^2}\left[1 - J_0^2\left(\frac{2\pi a\theta_0}{\lambda}\right) - J_1^2\left(\frac{2\pi a\theta_0}{\lambda}\right)\right] . \tag{7}$$

The function in the brackets is available in tabular form[5] and is designated $L(\theta_0)$. Noting that πa^2 is the antenna-aperture area A, and that the left side of Eq. 7 may be rewritten in terms of an average gain over the cone of semiangle,

$$G(\theta_0)_{av} = \frac{G(0)\,\lambda^2 L(\theta_0)}{\pi\theta_0^2 A} \ . \tag{8}$$

Then, the power backscattered from the insonified volume defined by the pulse length and the cone of semiangle θ_0, obtained by combining Eqs. 3 and 8, becomes

$$P_\sigma = \frac{PG(0)\lambda^2 L(\theta_0)\, ct\sigma L_k^{1/2}}{8\pi A} \ . \tag{9}$$

The available acoustic power from the receiving antenna is given by

$$P_r = \frac{P_\sigma A}{R^2}\, R(\theta_0)_{av} L_k^{1/2} \ , \tag{10}$$

but since the same receiver is used for transmitting and receiving,

$$R(\theta_0)_{av} = \frac{\lambda^2 L(\theta_0)}{\pi\theta_0^2 A} \ . \tag{11}$$

Combining Eqs. 9 and 11 with Eq. 10, the final form for the meteorological acoustic echo-sounding equation is

$$P_r = \frac{Pct\sigma AL_k}{2R^2}\left[\frac{G(0)\,\lambda^4 L^2(\theta_0)}{4\pi^2\theta_0^2 A^2}\right] . \tag{12}$$

This is equivalent to Eq. 1 with the "beam-shape compensation factor" term in brackets replacing the antenna factor term L_a lumped in L, as indicated in Eq. 2. In selecting the cone semiangle θ_0, we are guided by radar-meteorology practice for axially symmetric beams, where a Gaussian function is usually employed as closely approximating the gain polar diagram.[6] For such a Gaussian beam, the angle at which transmitted power is half the maximum value, the so-called half-power point, defines a beam within which lies 80% of the total transmitted power. Neglecting greater angles results in an overall error of but 1 dB.[7] From a plot[5] of the quantity $L^2(\theta_0)/\theta_0^2$, as applies for a piston source, it is found that a 1-dB error in beam energy occurs for a value of $(2\pi a\theta_0/\lambda) = 3$. For an antenna with $a = 0.6$ m, used at a frequency of 2 kHz, the beam-shape compensation factor assumes a value of 0.237. If the beam half-power point for a piston antenna is used instead of the 1-dB error, then the compensation factor is 0.370, similar to the factor 0.43 for a uniform illuminated square aperture.[8]

II. ACOUSTIC ANTENNA GAIN-PATTERN TESTS

Two types of antennas have been tested and used in our Atmospheric Acoustics Program. These are (1) conical horn reflectors, and (2) prime-focus paraboloids. The configuration of the horn-reflector antenna is shown in Fig. 1. When mounted as shown, the antenna can be directed to different elevation angles. The electrodynamic acoustic transducer is bolted to a conical adapter which serves as a direct coupling to the conical section of the antenna, providing a good impedance match to the atmosphere while shielding the omnidirectional characteristic of the transducer. The radius of the antenna aperture is 0.6 m, with the conical section being approximately 1.5 m long.

This antenna was designed for microwave use at X band and has fiberglass walls 0.5 cm thick. The exterior of the antenna shown in Fig. 1 has been coated with an additional 0.5-cm thickness of viscous epoxy to provide greater mass and reduce structural vibration time. A second antenna of this type was given an additional 1-cm-thick coat of asphaltic mastic, resulting in further reduction of vibration. This damping is important since the transducer serves as a microphone receiver only 100 msec after a high-power acoustic pulse is transmitted.

In order to measure the gain pattern of the horn-reflector acoustic antenna, two such units were placed 30 m apart, well away from reflecting structures. The separation distance used insured that we were measuring the farfield diffraction pattern, except at frequencies above 4 kHz, where we were in the outer limits of the transition field. One antenna was rotated in azimuth, as it radiated a constant acoustic power level. The signal level received by the other antenna was recorded as a function of the transmitting antenna azimuth.

Although the antennas were elevated about 3 m above ground, and there was some depression of the terrain between the antennas, there were nonetheless some ground-reflection effects present. The standing waves produced by these reflections were studied by probing the line-of-sight path between the antennas with a sound-level meter. The maximum fluctuation of sound pressure along the path was about 6 dB. These fluctuations were considered acceptable, especially since even higher-amplitude standing waves had been measured during similar tests across a shallow ravine. Wind and temperature effects sometimes produced very large fluctuations in received signal level, often as much as 20 dB. Accordingly, data were taken only during calm or near-calm conditions in order to minimize meteorological influences.

The results of the horn-reflector antenna measurements are presented in the polar diagrams, Fig. 2. The important sidelobes to consider for vertical sounding lie in the range 70°–90° from the main lobe. The 20° spread above the horizon is to allow for atmospheric refraction of sound waves during strong temperature inversions. The plotted results represent the average of many independent measurements of the gain pattern.

Using a sound-level meter, the transmitting pressure levels were measured across the aperture of the antenna and found to be extremely uniform. It is not surprising, therefore, that the measured patterns closely resemble the predicted diffraction pattern for a piston source, represented by the term in the brackets in Eq. 6.

The measured 90° sidelobe suppression ranged from 38 dB at 1 kHz to 50 dB at 5 kHz. In order to operate an acoustic echo sounder in noisy urban environments, it is desirable to improve this rejection figure to 70 or even 90 dB, so that unwanted sound does not enter the antenna and also to minimize noise pollution from the transmitted pulses.[9] Analytical studies showed that placing about the antenna an absorbing cylindrical cuff with a height several times the aperture diameter should achieve a 20-dB additional attenuation of the 90° sidelobe. A cylindrical absorber, 3 m in diameter and extending to 2.5 m above the horn-reflector aperture, was constructed of stacked haybales. The measured additional sidelobe suppression at 90° with the haybale cylinder surrounding the antenna ranged from 22 dB at 2 kHz to 32 dB at 4 kHz, in close accordance with theoretical calculations.[10] The 80° sidelobes were suppressed between 16 and 20 dB with this same shield.

In addition to the horn-reflector antenna, experiments have been performed with the electrodynamic transducer mounted at the focus of paraboloids. In one configuration, a searchlight mirror 1.5 m in diameter is used, as shown in Fig. 3. The searchlight was modified by painting the mirror black (to avoid an accidental solar furnace effect), by mounting the mirror and transducer support on rubber shims (to isolate the structures acoustically from the searchlight frame), by applying a 2.5-cm-thick fiberglass spacer and a 0.5-mm-sheet lead-septum damper to the rear of the mirror, and by lining the cylindrical structure around the mirror with convoluted open-cell polyurethane plastic foam.

The gain patterns for the searchlight acoustic antenna are shown in Fig. 4. The best sidelobe suppression, and most narrow main lobe, were obtained with the geometrical focus of the mirror inside of the exponential impedance-matching horn attached to the transducer. Thus, the transducer aperture was 6 cm farther from the mirror than the proper geometrical focus. The position was not highly critical with movement of ±2 cm, producing just detectable changes in the polar diagram. This type of antenna was operated near a noisy interstate highway in downtown Denver and provided clearly defined acoustic echoes of temperature inversions to heights of 700 m.

A second type of parabolic antenna was constructed using a 1.2-m-diameter microwave dish, shown in Fig. 5. A fiberglass–lead septum also serves to damp this antenna, with a silicone-rubber-doped canvas boot extending around the edge of the dish to prevent moisture from entering the septum. Moisture might freeze, reducing the effectiveness of the viscously coupled damper. The plywood enclosures, shown on three sides of the antenna in Fig. 5, completely encircle the unit in operation, with a lining of open-cell polyurethane, 1.2 m in height, to improve sidelobe suppression. The polar diagrams for this antenna are shown in Fig. 6. Two such units are in operation in an acoustic echo-sounding system at the University of Alaska and are providing good results.

Arrays of electrodynamic loudspeakers have also been used successfully for acoustic echo sounding.[3] We have not yet examined carefully the properties of such arrays, so that comparisons between the performance of single transducer–reflector arrangements—discussed in this paper—and horn arrays cannot be made at this time.

III. EFFICIENCY MEASUREMENTS

Future acoustic echo-sounder design improvements may lead to equipment able to detect smaller echoes than those presently measured. Especially important will be improvements in antenna characteristics, rather than changes in the electronic circuits which follow the antenna. The improvements involve: (1) An increase in the forward (main lobe) gain of the antenna relative to an isotropic receiver; (2) Further suppression of antenna sidelobe response; And (3) an increase in efficiency of the transducer coupled to the antenna.

Making the antenna aperture ever larger is not likely to produce corresponding dependable increases in antenna gain because of acoustic wavefront distortions produced by wind and temperature fluctuations in the atmosphere. For any given carrier frequency, as antenna-aperture size increases, the main beam width decreases. A half-power beam width of less than about 4° or 5° probably is not desirable, since the strong refracting effects of temperature and wind gradients in the atmosphere may cause backscattered wavefronts to return at angles up to several degrees off the beam axis.

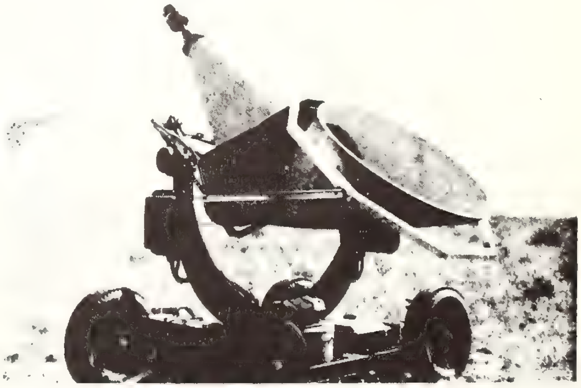

FIG. 1. Conical horn-reflector-type antenna used for acoustic echo sounding.

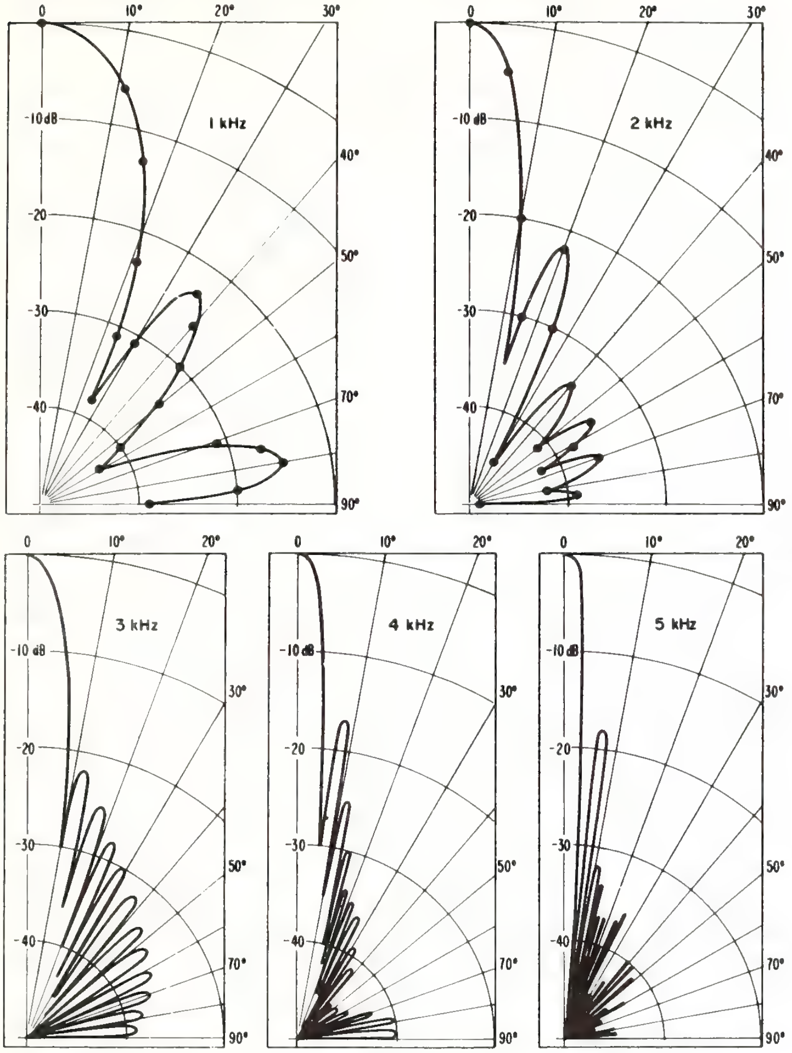

FIG. 2. Polar diagrams of the gain pattern of the conical horn-reflector acoustic antenna for five different frequencies.

Also, large-aperture antennas are usually not portable, and are difficult and unwieldy to steer. For the above reasons, and because the polar diagrams of Figs. 2, 4, and 6 indicate adequately narrow beam widths at all frequencies above 1 kHz, it is concluded that the present antenna-aperture diameter of 1.2 m is near optimum for lower atmospheric studies if the antenna is diffraction limited.

It may be possible to achieve an effective increase in overall antenna-transducer system gain by improving the efficiency with which received acoustic energy is converted by the antenna transducer to an electrical signal. Figure 7 shows the overall receiving efficiency of two antenna-transducer combinations when the antenna aperture is illuminated by a plane wave at an rms acoustic pressure of 1 dyne/cm^2. Both curves are for the same horn-reflector antenna, but the Altec-Lansing 291-16A transducer achieves a flatter frequency response than was obtainable with the University ID-40 transducer. Note that the ID-40 curve of Fig. 7 shows an

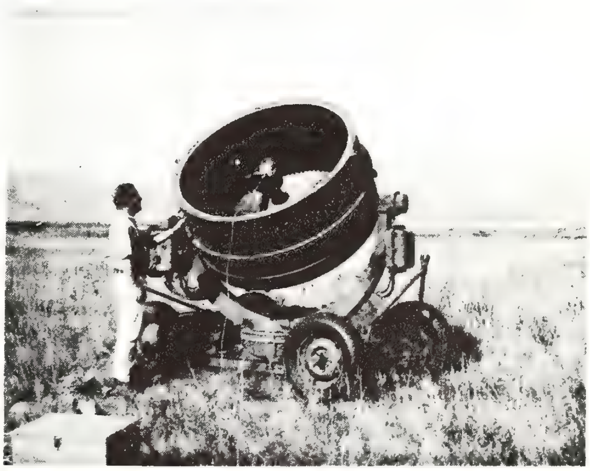

FIG. 3. Modified 1.5-m searchlight acoustic antenna.

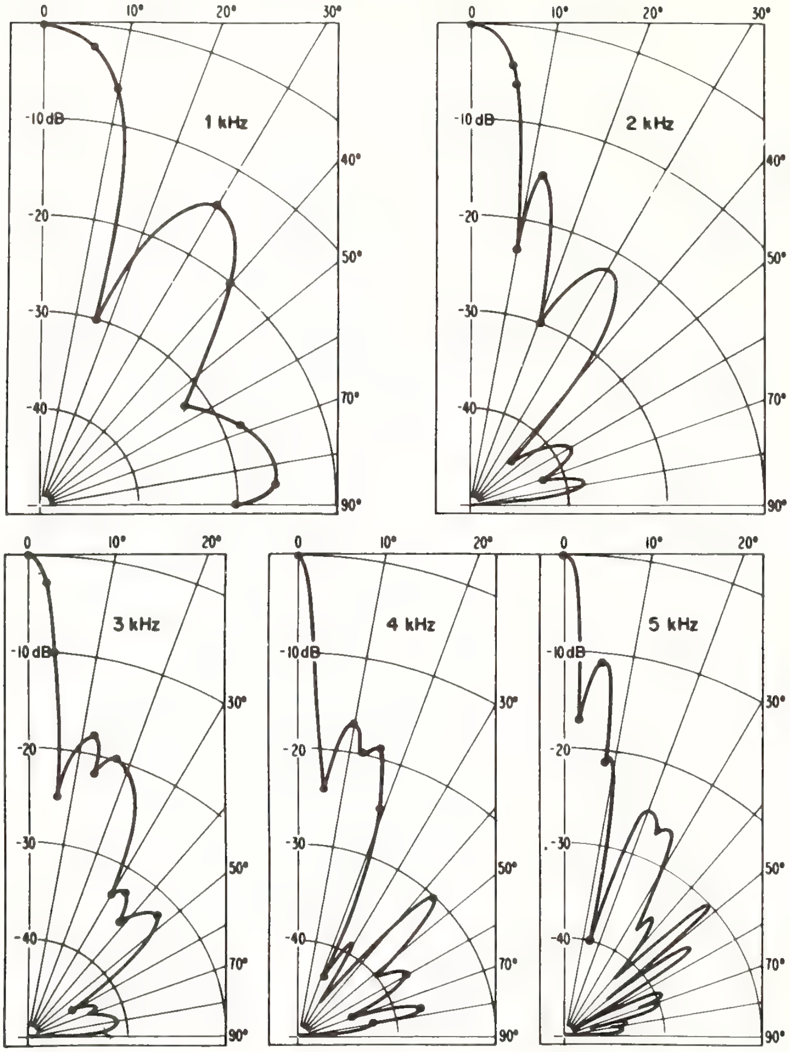

FIG. 4. Polar diagrams of the gain pattern of the 1.5-m searchlight acoustic antenna.

efficiency peak of about 30% at a frequency of slightly less than 2 kHz. The less spectrally dependent receiving efficiency of the 291-16A transducer coupled to the horn-reflector antenna is only about 10% at frequencies up to 3 kHz and declines with slight irregularities to about 1% at 5 kHz. It should be possible to increase the efficiency to about 50% at 2 kHz by carefully matching the throat impedance of the antenna to the acoustic-input impedance of the transducer and by further damping and stiffening of the antenna surfaces.

Figure 8 shows the overall transmitting efficiency of the horn-reflector antenna-transducer system when 1 W rms of electrical power is applied to the 291-16A transducer. Efficiencies at this power level are, in general, above 50% at frequencies from 1 to 2 kHz, 10% from 2 to 3.5 kHz, and roughly 3% at higher frequencies up to 6 kHz. These efficiencies, especially at the lower frequencies, are deemed to be satisfactory. Transmitting efficiencies, at any rate, are almost certain to improve automatically as the previously discussed improvements

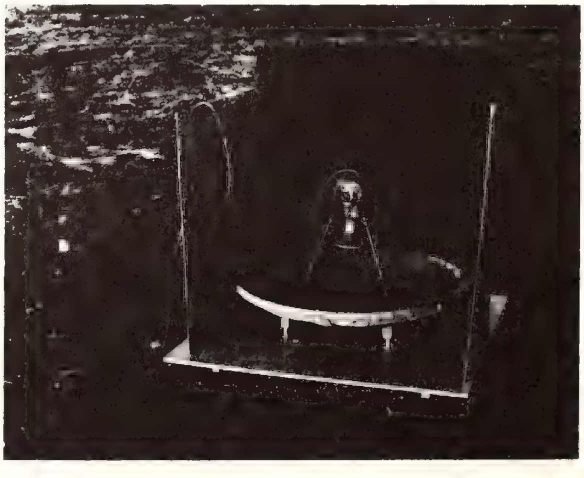

FIG. 5. Modified 1.2-m microwave dish antenna, showing transducer and impedance matching horn at the focus, and with a partial absorbing cuff in place.

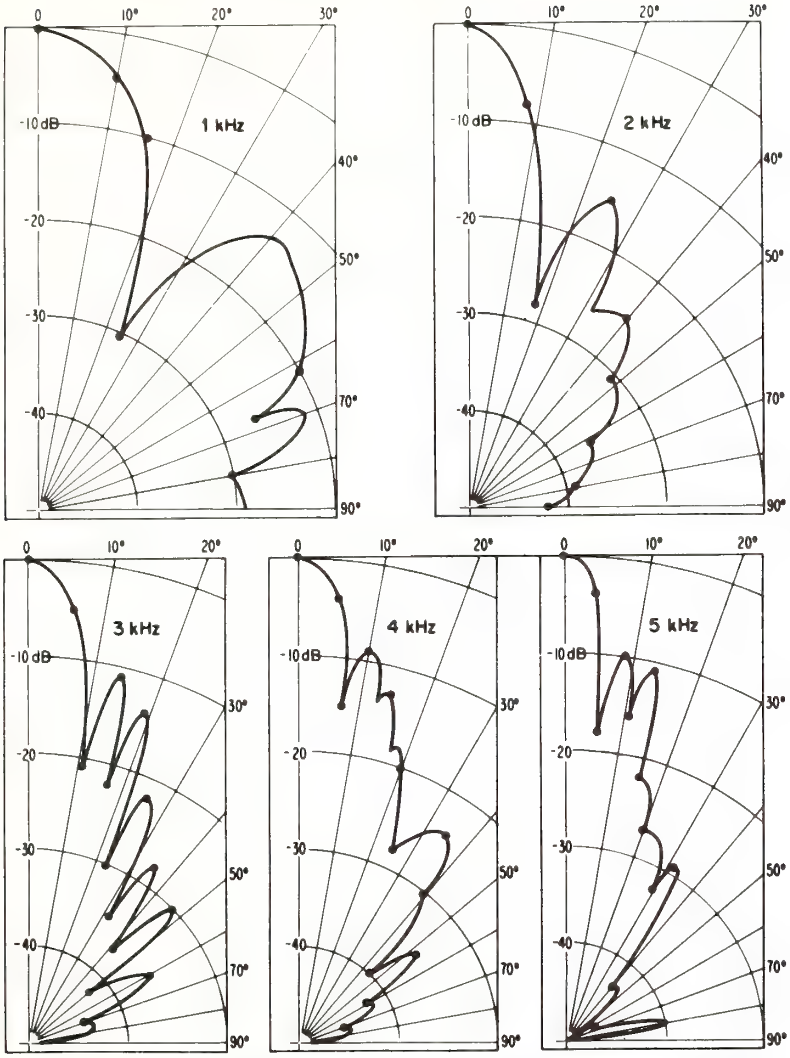

FIG. 6. Polar diagram of the gain pattern of the 1.2-m microwave dish.

in receiving efficiency are achieved.

The reason for the increased transmitting efficiency, as compared to receiving efficiency at frequencies below 2 kHz for the 291-16A transducer, is not understood. It is believed that the absolute accuracy of the measurements, averaging several spectral runs together, is within 3 dB. Possibly, a slight friction in the voice-coil suspension could account for the apparent nonreciprocity between receiving and transmitting.

Further suppression of antenna sidelobe response appears to offer the most promise for increasing the ratio of echo signal to ambient noise when receiving, and for minimizing sidelobe radiation noise-pollution levels when transmitting. It is obvious from the polar dia-

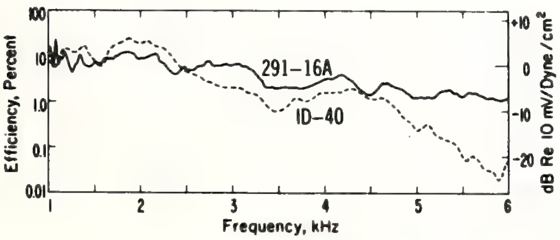

FIG. 7. Receiving efficiency of two transducers with the conical horn-reflector antenna.

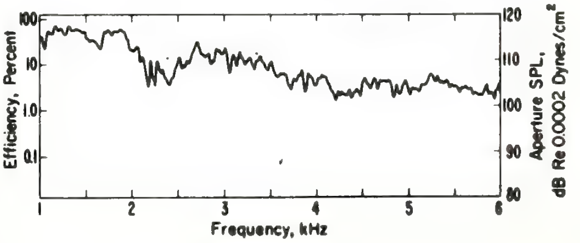

FIG. 8. Transmitting efficiency of the 291-16A transducer with the conical horn-reflector antenna.

grams of Fig. 2 that sidelobes at angles of 70° to 90° from the main beam become progressively smaller as the echo carrier frequency is increased. It is thus advantageous to use as high a carrier frequency as possible consistent with recognizing that absorption and scattering attenuation losses increase with frequency.

IV. CONCLUSIONS

It is possible to fabricate relatively efficient highly directional acoustic antennas by using structures originally intended for microwave or optical use, if proper attention is given to vibration damping, proper transducer to reflector impedance matching, and sidelobe suppression absorbing cuffs. Careful measurement of the beam shape of the antenna allows calculating the antenna gain factor. This factor enters into the meteorological acoustic sounding equation, permitting quantitative determination of the returned acoustic power scattered from atmospheric structure.

ACKNOWLEDGMENTS

Many of the antenna polar-diagram measurements were performed by B. C. Willmarth and the modification of the antennas to improve their acoustical properties was accomplished by R. D. Dickason. This work was supported by NOAA research funds and also, in part, by the Environmental Protection Agency and the National Science Foundation.

[1] L. G. McAllister, "Acoustic sounding of the lower troposhere," J. Atmos. Terr. Phys. 30, 1439–1440 (1968).

[2] C. G. Little, "Acoustic methods for the remote probing of the lower atmosphere," Proc. IEEE 57, 571–578 (1969).

[3] L. G. McAllister, J. R. Pollard, A. R. Mahoney, and P. J. R. Shaw, "Acoustic sounding—A new approach to the study of atmospheric structure," Proc. IEEE 57, 579–587 (1969).

[4] D. W. Beran, C. G. Little, and B. C. Willmarth, "Acoustic Doppler measurements of vertical velocities in the atmosphere," Nature 230, 160–162 (1971).

[5] M. Born and E. Wolf, *Principles of Optics* (Macmillan, New York, 1964), pp. 395–398.

[6] J. R. Probert-Jones, "The radar equation in meteorology," Q. J. R. Meteorol. Soc. 88, 485–495 (1962).

[7] L. J. Battan, *Radar Meteorology* (U. Chicago P., Chicago, 1959), p. 66.

[8] K. L. Bowles, G. R. Ochs, and J. L. Green, J. Res. Natl. Bur. Stand. D 66, 395–407 (1962).

[9] W. R. Simmons, J. W. Wescott, and F. F. Hall Jr., "Acoustic echo sounding as related to air pollution in urban environments," NOAA Technical Report ERL 216-WPL-17 (Boulder, Colorado, May 1971), 77 pp.

[10] O. N. Strand, "Numerical study of the gain pattern of a shielded acoutsic antenna," J. Acoust. Soc. Am. 49, 1698–1703 (1971).

3rd AMS Symposium on Meteorology Observations and Instrumentation, 175-178, February 1975.

SENSITIVE MICROBAROGRAPHS USED TO STUDY ATMOSPHERIC GRAVITY WAVES

William H. Hooke

Wave Propagation Laboratory
NOAA Environmental Research Laboratories
Boulder, Colorado

The Geoacoustics Research Program Area of NOAA's Wave Propagation Laboratory is responsible for the development of pressure-measurement techniques and their application to the study of severe weather, atmospheric gravity waves and infrasound, and turbulence. The basic instrument we have developed for our experimental studies is a variable-capacitance type of differential pressure sensor, which we normally use in conjunction with an acoustic high-pass filter to detect and measure atmospheric pressure changes in the period range from 1 second to greater than 1000 seconds, but which we have modified in certain applications to measure pressure fluctuations at periods as short as 0.25 seconds or as long as several hours. The system noise level at short periods is as low as 0.001 microbar, providing a sensitivity some 10^5 times greater than standard drum recording microbarographs (which might more properly be termed millibarographs). Most recently, we have incorporated a variable reluctance type of pressure transducer in this system, improving system linearity and simplifying its design; in addition, we have incorporated design advances such as a temperature-independent acoustic resistor. Although the basic instrument has been in use for some 25 years, few details of its construction and operation have appeared in the open literature. The interested reader is referred to Cordero *et al.* (1957), Cook and Bedard (1971), Georges and Young (1972), and Bedard (1973, 1975a) for discussion of some aspects of the instrument and its operation as well as further references. Testing and calibrating these instruments requires special procedures. We maintain an extensive facility for this work, utilizing both static and dynamic techniques, as well as field pressure calibration devices. One version of the instrument and probe together with some of its associated electronics and a field calibration unit is shown in Figure 1.

In this paper, we review briefly our application of this instrument, used either singly, in arrays, or in conjunction with other meteorological sensors (including various remote-sensing techniques) to study atmospheric gravity waves and to use atmospheric gravity waves as tools to probe the atmosphere. We conclude with a short mention of the microbarograph's potential usefulness for other meteorological applications, including studies of turbulence, thermal plumes, and other boundary-layer and mesoscale phenomena.

Used by itself, a single microbarograph provides information on the frequency spectra of pressure fluctuations at the instrument location, but gives little information on the physical nature of the atmospheric motions which give rise to the pressure spectra. Specifically, the data from a single microbarograph do not differentiate unambiguously between pressure fluctuations arising from wavelike motions, coherent over distances of several wavelengths, propagating with well-defined phase and group speeds, and interacting only weakly with the medium through which they propagate, and turbulent motions, interacting strongly with the medium and exhibiting minimal coherence over distances comparable to their own length scale. Some information is provided by any peakedness of the observed pressure spectra, since sharp peaks suggest motions of a wave type, but this information is only qualitative; certainly the absence of any peaks in the spectra does not rule out the possibility that a broad spectrum of weakly interacting waves is present. Data from a single instrument do not provide properties of fundamental interest such as wave phase and group speeds, wavenumber spectra, or wave dispersion.

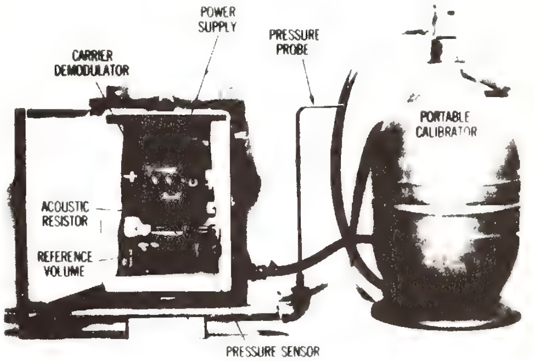

Figure 1. Photograph of the microbarograph and associated electronics, pressure-sensing probe, and calibrator used in conjunction with a sonic anemometer to measure turbulent pressure-velocity correlations in the atmospheric boundary layer. The microbarograph and probe were mounted on a 1500 ft. tower.

Used in arrays of three or more (microbarographs spaced at distances the order of 100 m to 100 km, depending upon the application), the microbarographs can provide this additional information. By analyzing the cross-correlation between pressure fluctuations at pairs of microbarographs and the time difference required to maximize this cross-correlation, we can distinguish waves having wavelengths the order of the array size or greater from turbulent motions on similar scales, since turbulence is found to be poorly correlated over the array. By analyzing the correlated part of the pressure fluctuations we can extract wavenumber spectra as well as horizontal wave phase speeds and azimuths of propagation as functions of frequency, thus giving the wave dispersion and simultaneously providing clues concerning the nature of the wave sources and the propagation medium. Young and Hoyle (1975) have developed computer software for this purpose, making the digital analysis of array data routine. We have used both digital and analog array-processing techniques in a number of studies of acoustic-gravity wave propagation in the atmosphere, including recent analyses of the infrasound generated by thunderstorms (Georges and Young, 1972; Georges, 1973), infrasound generated by the airflow over mountains (Bedard, 1975b), infrasound generated by impulsive sources such as explosions (Young, 1975), gravity waves generated by shear instability in the tropospheric airflow (Keliher, 1975; Hooke *et al.*, 1975), and gravity waves excited by thunderstorms (Kjelaas *et al.*, 1975a).

Whether used singly or in arrays, these microbarographs are useful adjuncts to other meteorological instruments, including remote sensing systems such as FM-CW radars, acoustic echo sounders, and high power clear-air radars. The simplest application of this type is the combined use of a single microbarograph with a single anemometer. Together these two instruments can be used to measure wave phase speeds and direction of propagation through the use of the so-called wave impedance relation. This equation follows directly from the horizontal equation of motion stating that the wave phase speed Ω/k relative to the background medium is given by (Gossard and Munk, 1954)

$$\frac{\Omega}{k} = \frac{1}{\rho_o}\frac{\Delta p}{\Delta u} \quad , \qquad (1)$$

where Ω is the wave intrinsic frequency, measured by an observer moving with the mean wind at the height of the observation, k is the horizontal wavenumber, ρ_o is the unperturbed atmospheric density, Δp is the wave-associated pressure perturbation, and Δu is the wave-associated velocity perturbation. As explained by Gossard and Munk, the vector sense of the velocity perturbations relative to the maximum algebraic pressure perturbation yields the azimuth of wave propagation, and adding the mean wind in the direction of wave propagation to both sides of equation (1) yields the wave phase speed relative to an observer fixed with respect to the ground. While the wave impedance relation has been found to be a useful means for determining wave phase speeds and propagation directions (see, e.g., Gossard and Munk, 1954; Gossard, 1962; Gossard *et al.*, 1970; Hooke *et al.*, 1973; Gossard and Sweezy, 1974), it has been subject to direct verification in relatively few instances (see, e.g., Hooke *et al.*, 1972; Kjelaas *et al.*, 1975a,b); more extensive comparisons between wave parameters deduced by this means and by the direct analysis of array data are urgently needed. Often a scale analysis of the Navier-Stokes equations shows that for mesoscale motions (spatial scales λ such that $1 \text{ km} < \lambda < 10^3$ km and periods τ such that $3\text{x}10^2 \text{ sec} < \tau < 3\text{x}10^3$ sec) the approximations implicit in equation (1) (neglect of Coriolis, viscous, and nonlinear terms) are valid, but *a priori* in any specific case there must always remain cause for doubt. In any event, use of the impedance relation and data from instruments located at a single point provide no direct, definitive information on wave coherence, etc., so that application of the technique has been limited to those special "events" demonstrating sharp spectral peaks. In practice the use of the impedance relationship is often made more difficult by the presence of high wavefrequency-wavenumber noise in the wind data. Recently we have been able to improve on this situation somewhat by using as our anemometer the laser transverse-wind sensor described by Lawrence *et al.* (1972); this approach provides valuable spatial filtering, as discussed by Kjelaas *et al.* (1974).

In more sophisticated applications microbarographs may be used in arrays to supplement data gathered from other meteorological sensors. Acoustic echo sounders provide an excellent case in point. A typical output of such sounders is a facsimile record showing the acoustic echo intensity as a function of height and time over the sounder location. By itself, such a record provides only acoustic backscatter echo intensity (which may be related to the structure constant of thermal inhomogeneity in the atmosphere) plus displacement spectra revealed by undulations of strata of strong echo returns (Figure 2). Addition of data from arrays of microbarographs supplement the facsimile record as shown in Figure 2 by providing the wave parameters of interest (e.g., the dominant wavelengths and periods as indicated by the table). These results, together with the results from similar cases are discussed in more detail by Beran *et al.* (1972) as well as by Hooke *et al.* (1972). Similar supplementary data are also extremely useful in conjunction with the output from FM-CW radars, which as typically used, takes the form of height-time information over the sounder location.

Microbarograph arrays have been used in this manner to detect wave motions as high as ten kilometers in the atmosphere, provided only that the wave amplitudes and wavelengths are sufficiently large. Thus Hooke and Hardy (1975) show that a microbarograph array in Washington, D. C. was able to detect a gravity-wave system generated by shear instability in a layer between 8 and 9 km above the earth's surface and detected at that height by a clear-air radar at Wallops Island (Figure 3). Statistical studies (e.g., Flauraud *et al.*, 1954; Claerbout, 1967; Claerbout and Madden, 1968; Madden and Claerbout, 1968; Herron and Tolstoy, 1969; Herron *et al.*, 1969; Keliher, 1975) have indicated that a substantial fraction of the mesoscale gravity waves detected at the earth's surface at temperate latitudes in wintertime are generated by shear instability in the tropospheric airflow, suggesting that this technique may be suitable for detection of clear-air turbulence (CAT).

Thus far we have focused our attention on the use of microbarographs to determine "kinematic" wave parameters such as frequency, wavelength, phase velocity, and the like. However, the instruments may also be used to measure "dynamic" parameters as well, including specifically wave amplitude and energy flux, the latter being given by the pressure-velocity correlation $\overline{\Delta p \Delta u}$ (where the superbar indicates an average over the wave period). Hooke *et al.* (1973) used the instrument in this application in conjunction with a bivane anemometer to verify that shear instability was the source mechanism for a gravity-wave observed in the planetary boundary layer at Haswell,

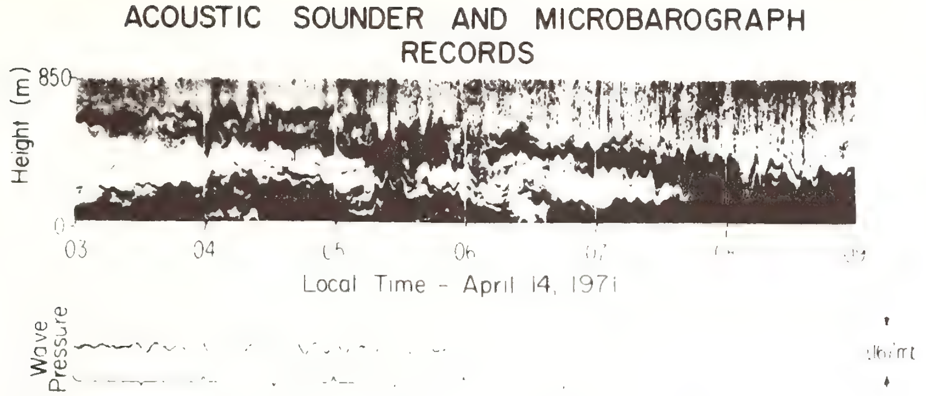

v (m/sec)	17	10	undetermined	10	undetermined	7
τ (sec)	600	500		450		480
λ (km)	10.2	5.0		4.5		3.4
Azimuth	265°	295°		250°		250°

WAVE PARAMETERS

Figure 2. Atmospheric gravity waves revealed by the acoustic echo sounder as undulations in the strata of strong echo returns in the stable planetary boundary layer. The white line superimposed on the facsimile record is the pressure trace from a nearby microbarograph. The microbarograph was part of a four-element array; the four pressure traces, superimposed and time shifted to provide maximum cross-correlation, are also shown. The wave parameters thus deduced are indicated in the table.

Colorado in November 1971, measuring an energy flux the order of 10^3 ergs cm^{-2} sec^{-1} directed away from the shear zone in this case. Further measurements of pressure-velocity correlations during wave events were made in a subsequent Haswell experiment in the spring of 1974, but these data are only just now being analyzed. Thus it does appear that with proper probe design to minimize contamination of pressure data by Bernoulli pressures $\rho_0 u^2$ occurring in the flow, that the pressure-velocity correlation can be accurately measured in the planetary boundary layer (as it has been measured in the surface boundary layer by Elliott, 1972a,b).

Up to this point, we have concentrated on the use of microbarographs to study atmospheric gravity waves. We now turn to use of the observed waves to study atmospheric temperature and wind structure. Kjelaas *et al.* (1975b) have recently demonstrated that wave observations combining acoustic-echo sounder and microbarograph data can be used to determine prevailing wind components in the direction of wave propagation. In addition, it appears possible, at least in principle, to deduce atmospheric temperature structure in the daytime troposphere under situations likely to favor severe convective storm development by proceeding as follows. One might idealize the temperature structure prevailing at such times by a three-layer model in which the temperature height profile of the bottom layer (the convective boundary layer) is adiabatic, of height H, and surmounted by an inversion layer of zero thickness characterized by a discontinuity in potential temperature which we express as $\Delta(\ell n \Theta)$. If the Brunt-Väisälä frequency of the air above

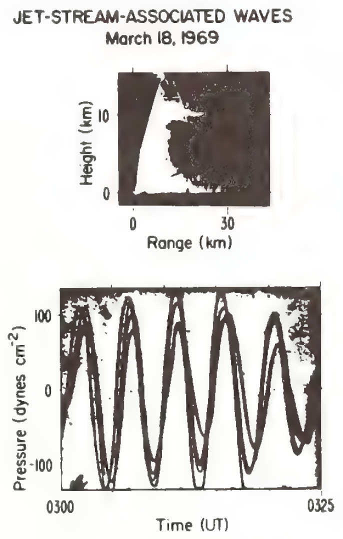

WALLOPS ISLAND
RADAR (NASA)
0323 U.T
λ = 15 km
V = 44-50 m sec^{-1}
(τ) = 300-340 sec
(A) = 270°
(from Reed and Hardy)

WASHINGTON, D.C
Microbarograph
Array (NOAA)
λ = 14 km
V = 47 m sec^{-1}
τ = 300 sec
A = 284°

Figure 3. A gravity-wave event occurring just after 0300 UT, together with the values for the horizontal wavelength λ, horizontal phase speed V, period τ, and azimuth from which the wave was propagating A.

is given by N, the wave dispersion equation is given by (Gossard, 1960, 1962)

$$\left(\frac{\omega}{k}\right)^2 = \frac{g\Delta(\ell n\Theta)}{k\ \coth(kH) + k[1-N^2/\omega^2]^{\frac{1}{2}}} \quad , \qquad (2)$$

where g is the acceleration of gravity and ω is the wavefrequency measured by an observer fixed with respect to the ground (here $\omega = \Omega$, since we assume that the winds are zero). By measuring ω/k at several frequencies ω, it is possible in principle to solve for $\Delta(\ell n\Theta)$, H, and N. However, the effects of winds and wind shear remain unknown. It should be clear that the above examples are merely specific illustrations of the more general inversion procedure that could be applied to gravity wave spectra.

Finally, it should be noted that the instrument is also suitable for the study of a wide range of natural and artificial meteorological phenomena. These include measurements of pressure velocity correlations arising from turbulence and contributing through their divergence to turbulent kinetic energy budgets, studies of updraft motions such as thermal plumes and thunderstorm updrafts (such studies are either underway or contemplated in cooperation with other groups), CAT detection, and monitoring of aircraft wake vortices.

References

Bedard, A. J., Jr., 1973: The design of a temperature-independent DC flow resistor. *Fluidics Quart.*, 5, 31-50.

Bedard, A. J., Jr., 1975a: The DC pressure summator: theoretical operation, experimental tests and possible practical uses. (Paper in preparation)

Bedard, A. J., Jr., 1975b: Infrasound, subsonic pressure disturbances and airflow over mountains. (Paper in preparation)

Beran, D. W., W. H. Hooke, and S. F. Clifford, 1973: Acoustic echo sounding techniques and their application to gravity wave, turbulence and stability studies. *Boundary-Layer Meteorology*, 4, 133-153.

Claerbout, J. F., 1967: Electromagnetic effects of atmospheric gravity waves. M.I.T. Ph.D. thesis, June.

Claerbout, J. F., and T. R. Madden, 1968: Electromagnetic effects of atmospheric gravity waves. *Proc. Acoustic-Gravity Wave Symp.*, T. M. Georges, Ed., U. S. Gov't. Printing Office, 135-155.

Cook, R. K., and A. J. Bedard, Jr., 1971: On the measurement of infrasound. *Geophys. J. Roy. Astron. Soc.*, 26, 5-11.

Cordero, F., H. Matheson, and D. P. Johnson, 1957: A nonlinear instrument diaphragm. *J. Res. Nation. Bur. Stds.*, 58, 333-337.

Elliott, J. A., 1972a: Instrumentation for measuring static pressure fluctuations within the atmospheric boundary layer. *Boundary-Layer Meteor.*, 2, 476-495.

Elliott, J. A., 1972b: Microscale pressure fluctuations measured within the lower atmospheric boundary layer. *J. Fluid Mech.*, 53, 351-383.

Flauraud, E. A., A. H. Mears, F. A. Crowley, Jr., and A. P. Crary, 1954: Investigation of microbarometric oscillations in eastern Massachusetts. AFCRC Tech. Rept. 54-11.

Georges, T. M., 1973: Infrasound from convective storms: examining the evidence. *Rev. Geophys. Space Sci.*, 11, 571-594.

Georges, T. M., and J. M. Young, 1972: Passive sensing of natural acoustic-gravity waves at the earth's surface. *Remote Sensing of the Troposphere*, V. E. Derr, Ed., Chapt. 21, U. S. Gov't. Printing Office.

Gossard, E. E., and W. H. Munk, 1954: On gravity waves in the atmosphere. *J. Meteor.*, 11, 259-269.

Gossard, E. E., 1960: Spectra of atmospheric scalars. *J. Geophys. Res.*, 65, 3339-3351.

Gossard, E. E., 1962: Vertical flux of energy into the lower ionosphere from internal gravity waves generated in the troposphere. *J. Geophys. Res.*, 67, 745-757.

Gossard, E. E., J. H. Richter, and D. Atlas, 1970: Internal waves in the atmosphere from high-resolution radar measurements. *J. Geophys. Res.*, 75, 3523-3536.

Gossard, E. E., and W. B. Sweezy, 1974: Dispersion and spectra of gravity waves in the atmosphere. *J. Atmos. Sci.*, 31, 1540-1548.

Herron, T. J., and I. Tolstoy, 1969: Tracking jet stream winds from ground level pressure signals. *J. Atmos. Sci.*, 26, 266-269.

Herron, T. J., I. Tolstoy, and D. W. Kraft, 1969: Atmospheric pressure background fluctuations in the mesoscale range. *J. Geophys. Res.*, 74, 1321-1329.

Hooke, W. H., J. M. Young, and D. W. Beran, 1972: Atmospheric waves observed in the planetary boundary layer using an acoustic sounder and a microbarograph array. *Boundary-Layer Meteor.*, 2, 371-380.

Hooke, W. H., F. F. Hall, Jr., and E. E. Gossard, 1973: Observed generation of an atmospheric gravity wave by shear instability in the mean flow of the planetary boundary layer. *Boundary Layer Meteor.*, 5, 29-42.

Hooke, W. H., and K. R. Hardy, 1975: Further study of the atmospheric gravity waves over the eastern seaboard on March 18, 1969. *J. Appl. Meteor.*, (in press).

Hooke, W. H., B. Stankov, and J. M. Young, 1975: (Paper in preparation)

Keliher, T. E., 1975: Comparison of microbarograph detected gravity waves and predictions from dynamically unstable wind-shear layers. (Paper in preparation)

Kjelaas, A. G., E. E. Gossard, J.M. Young, and W. R. Moninger, 1975a: Dispersion and spectra of gravity waves generated by a convective storm. *Tellus*,,(in press).

Kjelaas, A. G., D. W. Beran, W. H. Hooke, and B. R. Bean, 1975b: Waves observed in the planetary boundary layer using an array of acoustic sounders. *J. Atmos. Sci.*, (in press).

Lawrence, R. S., G. R. Ochs, and S. F. Clifford, 1972: The use of scintillations to measure average winds across a light beam. *Appl. Optics*, 239-243.

Madden, T. R., and J. F. Claerbout, 1968: Jet-stream-associated gravity waves and implications concerning jet stream stability. *Proc. Acoustic-Gravity Wave Symp.*, T. M. Georges, Ed., U.S. Gov't. Print. Office, 121-134.

Young, J. M., 1975: (Paper in preparation)

Young, J. M., and W. Hoyle, 1975: Multidimensional spectral array processing techniques. (Paper in preparation)

Applied Optics 13, 2100-2104, September 1974.

Prepulse Enhancement of Flashlamp Pumped Dye Laser

Michael H. Ornstein and Vernon E. Derr

A simple technique has been developed that increases the power output of a conventional flashlamp pumped dye laser by typically one order of magnitude and, for some dyes, much more. This is achieved by igniting a low-energy prepulse discharge through the flashlamp just prior to firing the main flashlamp discharge.

I. Introduction

The tuneable dye laser[1] has emerged as one of the most versatile laser systems for spectroscopic research both in the laboratory and in the field. Recently Cohen, Derr, McNice, and Cupp have used a dye laser to measure Mie scattering intensities from monodispersed particles as a function of wavelength with application to lidar determination of aerosol size distributions in the atmosphere.[2] In a novel application, Hongsuk H. Kim has used an airborne dye laser for mapping phytoplankton distributions across Lake Ontario by detecting laser induced fluorescence in chlorophyll $-a$.[3]

Although organic dyes can be made to lase with relative ease by laser pumping with pulsed lasers (e.g., ruby or nitrogen lasers)[4] and recently even on a continuous basis for the most efficient dyes using an argon-ion laser as pump,[5,6] the greater simplicity, higher average power output, and wider wavelength range obtained by flashlamp pumping of the dye have stimulated much effort to develop high repetition rate, high power flashlamp pumped systems. This paper describes a simple method for substantially increasing the power output of a conventional flashlamp pumped dye laser. As a secondary effect, lower power input to the flashlamp is possible without reducing laser power, thus lengthening flashlamp lifetime.

II. Theoretical Considerations

It is well known[1,7] that intersystem transitions from lasing singlet states to metastable triplet states reduce the power output from most organic dye lasers by depleting the population of the upper level of the laser transition and also by permitting triplet state absorption at the laser wavelength. For this reason the design of flashlamp driving circuits for such lasers must feature low inductance and fast rise time characteristics so laser action can occur on an equal or faster time scale than intersystem transitions. Flashlamp rise times on the order of 1 μsec or less are typically required. To achieve these fast rise times the inductance of all circuit parameters must be taken into account and minimized, including the inductance of the flashlamp plasma itself. In any well-designed discharge circuit the inductance of the flashlamp is in fact a primary contributor to circuit inductance and places a lower limit on rise time of the discharge.

The analysis of a flashlamp discharge circuit is of course complicated by the fact that during the discharge the flashlamp is a highly nonlinear circuit element. Consider a single mesh flashlamp discharge circuit whose equivalent circuit can be expressed as a simple series connection of a charged capacitor C, an inductance L, a resistive loss in the flashlamp, and a switch to complete the circuit. If the flashlamp were a linear resistor R, the discharge would be described by the equation

$$L(dI/dt) + RI + 1/C \int_0^t I\, dt = V, \qquad (1)$$

and the rise time for a low inductance circuit would be approximately $\tau = L/R$. In an actual flashlamp the situation is more complicated. Experiments by Goncz[8] have shown that in the high current regime (20–17,000 A) the volt-ampere characteristic of the lamp is well represented by the expression

$$V_{\text{Lamp}} = \beta I^{1/2}, \qquad (2)$$

where $\beta = 1.13\, d/A^{1/2}$ (d = arc length and A = cross section area of the flashlamp). Further it has been demonstrated[9,10] that during the initiation of the flash, the discharge does not fill the cross section of the lamp uniformly from the start. Instead a very thin streamer is initiated between electrodes, which then proceeds to grow in diameter to eventually fill the entire lamp cross section. During this initial

---

The authors are with NOAA Environmental Research Laboratories, Boulder, Colorado 80302.

Received 25 March 1974.

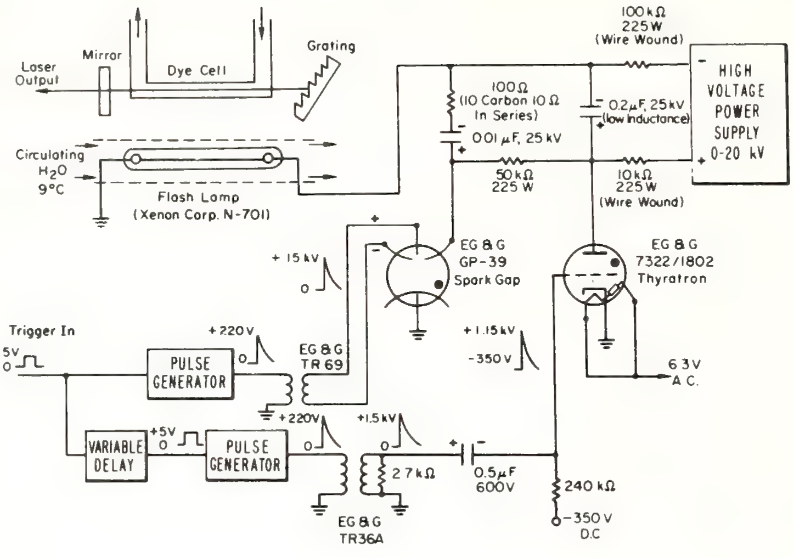

Fig. 1. Flashlamp firing circuit.

growth, the inductance of the plasma is much larger than its quasi-steady state value when the discharge fills the entire cross section. During this growth period, which takes typically several microseconds, the discharge is more accurately described by

$$L\left(\frac{dI}{dt}\right) + \beta_{\rm eff} I^{1/2} + \frac{1}{c}\int_0^t I\,dt = V. \qquad (3)$$

where Eq. (2) has been used as the resistive characteristics of the lamp and where

$$\beta_{\rm eff} = \beta + [(dL)/(dt)]I^{1/2}. \qquad (4)$$

The second term in Eq. (4) takes into account the changing inductance of the lamp. Computer solutions to the above equations have been obtained by Markiewicz and Emmett[11] for the special case of L = constant. Their solutions indicate the same qualitative features that one would deduce from the simpler Eq. (1). Fast rise time depends on small L and large $\beta_{\rm eff}$.

Referring to Eq. (4) above, we note that during the initial growth of the plasma streamer $\beta_{\rm eff}$ is small since dL/dt is a negative number during this period. Also L is large during this initial period. Both of these factors tend to increase the rise time of the flash. With the above analysis in mind, we decided to try to decrease the rise time of the flashlamp by eliminating (or at least by decreasing) the initial growth period of the discharge. This was accomplished by initiating a low-energy discharge (prepulse) of about 2 μsec decay constant in the flashlamp just prior to firing the main high-energy discharge through the lamp. The prepulse discharge does not have sufficient light output to significantly alter the populations of the energy levels of the dye, yet the prepulse should significantly reduce, if not eliminate, the growth period for the plasma to fill the cross section of the lamp when the main discharge is fired.

III. Electronics

Figure 1 shows a schematic diagram of the flashlamp firing circuit. The flashlamp used in this experiment was a Xenon Corporation N-701 xenon-filled linear lamp (10-cm arc length, 3-mm inner diameter). The lamp was cooled by circulating deionized water through a quartz jacket surrounding the tube. The cooling water was maintained at 9°C in an external refrigerated reservoir. The prepulse circuit consisted of a 0.01-μF, 25-kV capacitor (Capacitor Specialists, Inc. =25W126TN) in series with an EG & G spark gap and a 100-Ω pulse shaping resistor. When the spark gap is triggered, the 0.01 μF capacitor charged to the high-voltage supply potential is momentarily switched in parallel across the flashlamp. The main discharge circuit, connected in parallel with the prepulse circuit, consisted of a coaxial 0.2 μF capacitor (Tobe Deutschman Laboratories, special order, $L \approx 10$ nh) in series with an EG & G thyratron. The thyratron switch was chosen for the original design of the laser due to its generally greater reliability over a spark gap. The spark gap was used in the prepulse circuit because of its simplicity of installation and its availability. No adverse affects have as yet been encountered with the spark gap after several hundred thousand shots, but some precautions are required in connecting it in the circuit. The configuration indicated in Fig. 1 was found most successful. If the principal electrodes of the gap are reversed from that shown, or if the secondary of the trigger transformer is not floated, discharge current will be drawn through the trigger transformer. The trigger polarity indicated is recommended by the manufacturer. The high-voltage power supply is isolated from the discharge circuits

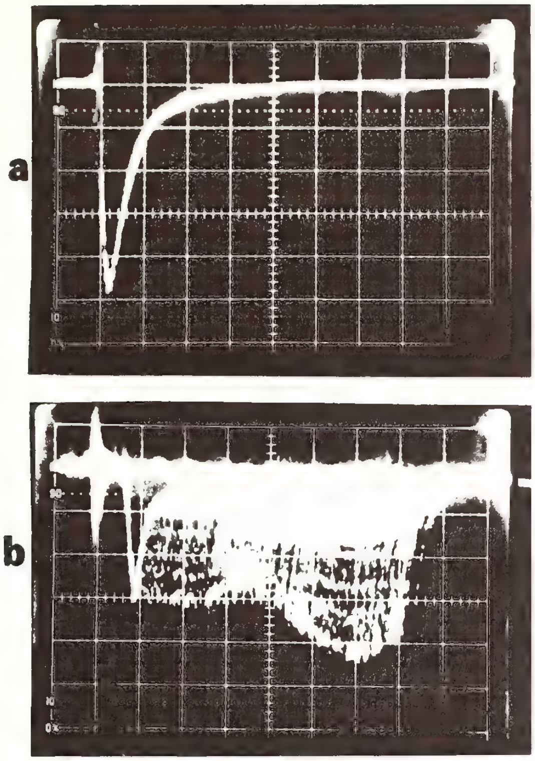

Fig. 2. (a) Flashlamp output (prepulse only). (b) Flashlamp output (main discharge during prepulse). Delay between pulses varied from ≈ 2 μsec to ≈ 14 μsec. Horizontal scale = 2 μsec/cm (all traces).

during the pulse by wire wound power resistors in the charging circuit. The precise values of these resistors are not critical as they are used more for their inductance than their resistance. The 50-kΩ power resistor was used to prevent discharge of the main-pulse capacitor (0.2 μF) through the spark gap during the prepulse. A variable time delay was incorporated in the trigger circuits to allow triggering of the main discharge anywhere from ≈ 2 μsec to ≈ 14 μsec after firing the prepulse. As will be shown in Section IV, an optimum delay time between prepulse and main pulse was found that gave maximum enhancement to the laser output.

A bothersome problem was encountered with the above circuit when it was first constructed in that feed-through from the prepulse discharge was capacitively coupled from the plate of the thyratron to its trigger grid, causing the thyratron sometimes to fire on the prepulse instead of on the delayed trigger. This problem was corrected by a −350V dc bias on the grid of the thyratron, which was enough offset to prevent the feedback voltage from firing the thyratron.

One final remark regarding the circuit is worth noting. Originally the negative side of the high-voltage supply was grounded for safety. However, this presented a complete circuit from the positive terminal of the supply though the spark gap to the negative terminal. Under these conditions it was found that the spark gap would occasionally not turn off after discharging to 0.01-μF capacitor, but would maintain a current for as much as a second. This interferes with rapid firing of the flashlamp and may have a deleterious effect on life of the gap. An attempted solution to this problem was to float the high-voltage supply. Even with this, the above effect was sometimes observed. The problem was finally traced to the fact that the water used to cool the flashlamp created a 50-kΩ conductive path around the flashlamp, which was enough to complete the high-voltage circuit. To correct this, a deionization filter was installed in a bypass loop for the circulating water. This maintained the leakage resistance of the water at about one MΩ, which was enough to prevent the sustained discharge of the gap. Some leakage resistance across the lamp is beneficial to ensure that the high voltage will appear across the spark gap and thyratron prior to discharge.

IV. Results

In Fig. 2 are shown some oscillograms of the flashlamp output. This data was obtained by detecting the light output from the flashlamp by an RCA 1P28 photomultiplier placed near the lamp. The output from the photomultiplier went directly into an FET source follower preamp and then to a Tektronix 453A oscilloscope. The limiting bandwidth of the detection electronics was about 10 MHz. The oscilloscope trace for all pulses in Fig. 2 was triggered by the initial 5-V trigger pulse shown in Fig. 1 and hence was independent of any delay in the sparkgap or thyratron firing circuits. Fig. 2(a) shows a trace of the prepulse flash alone (horizontal scale = 2 μsec/cm). The prepulse had a duration of about 1 μsec (FWHM) with a tail of ≈ 2 μsec decay constant and a peak current of about 100 A at 10 kV. Figure 2(b) shows the flashlamp output from the main discharge fired during the prepulse. This oscillogram is a time exposure of many shots as the time delay between the prepulse and the main pulse was continuously varied from ≈ 2 μsec to ≈ 14 μsec delay. Neutral density filters were used to attenuate the light to keep from saturating the photomultiplier tube.

An interesting feature of Fig. 2(b) is the appearance of maxima and minima of light output vs delay time. An optimum delay time of about 12 μsec is indicated for this circuit configuration. The precise physical reason for this structure was not investigated in detail, but we surmise that it is probably associated with an oscillatory expansion and contraction of the plasma shock wave of the prepulse discharge.

Figure 3(a) shows a superposition of the flashlamp output from the main discharge fired alone without the prepulse (smaller signal) and fired during the prepulse with 12 μsec delay (larger signal). For the traces in Fig. 3, the delayed sweep feature of the

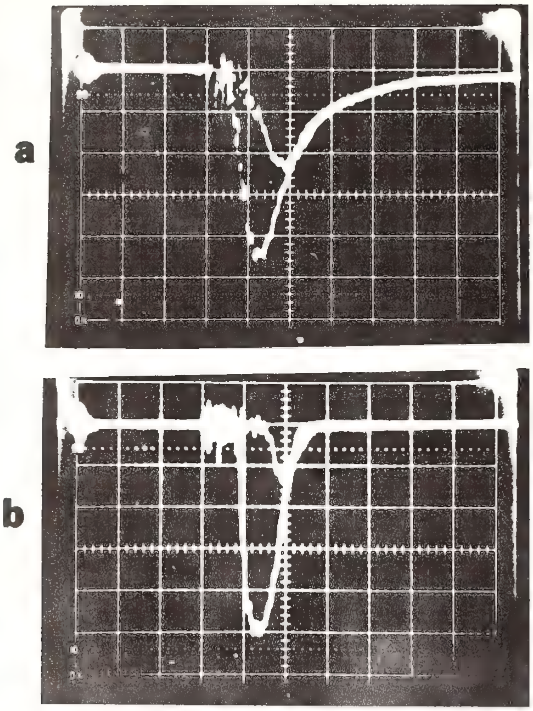

Fig. 3. (a) Flashlamp output from main discharge without prepulse (smaller signal) and with prepulse (larger signal). (b) Laser output using Rhodamine 6G without prepulse (smaller signal) and with prepulse (larger signal).
Horizontal scale = 0.5 μsec/ cm (all traces).

453A oscilloscope was used with about 10 μsec delay so the horizontal scale could be expanded to 0.5 μsec/cm. The rise time of the light output (10–90% intensity) decreases from about 500 nsec without the prepulse to about 200 nsec with the prepulse. A second important feature is the occurrence of over 100% increase in light output from the lamp when the prepulse is used. This is presumably due to the decreased resistance of the plasma when the discharge streamer is already expanded prior to firing the main pulse.

Both of the above effects, decreased rise time of the flashlamp pulse and greater light output, are instrumental in increasing the power output of the laser. Figure 3(b) shows superimposed traces of the laser output form the dye rhodamine 6G (5×10^{-4} M dissolved in H_2O + 5% Ammonyx LO) without the prepulse (smaller signal) and with the prepulse (larger signal). The high-voltage supply to the flashlamp was set at 12 kV for these pulses. For this voltage there is almost a five-fold enhancement of the laser output from rhodamine 6G. It was found that as the dye aged, the enhancement factor increased (the laser output with prepulse decreases more slowly with dye age than the power decrease without prepulse). This was generally true for all the dyes tested. Rhodamine 6G was used for the comparison in Fig. 3(b) because the signals could easily be shown on the same scale. For some of the dyes tested, the enhancement was so large that the two signals could not conveniently be shown on the same scale.

Rhodamine 6G is well known to be one of the most efficient laser dyes available, and hence we did not expect a dramatic improvement in efficiency for this dye. The faster rise time is probably not of too much significance for this dye, but the greater efficiency in conversion of electrical energy to light output is of significance even for this dye and is responsible for the increased power output shown in Fig. 3(b).

To check the improvement for some of the less efficient dyes, we ran some tests on two other dyes, esculin and 1-2-dihydro-4-methoxybenzo /c/ xanthylium fluoroborate, which lase in the blue and green wavelength ranges, respectively. Table I lists the ratio of laser power with the prepulse to laser power without the prepulse for the several dyes tested. As noted above, the enhancement factor increased as the dye aged. The minimum and maximum enhancements for several runs are listed in the table. The enhancement was quite dramatic for the latter two dyes, being consistently over a factor of 10 and as high as a factor of 50 for esculin. Along with the increased power output, the wavelength range (also indicated in Table I) over which the laser output could be tuned by rotating the grating was increased by using the prepulse.

The prepulse enhancement of laser power was observed to be a function of power supply voltage, decreasing gradually as power supply voltage was increased. This is of course reasonable since at lower voltage, nearer laser threshold, the increased light output and faster rise time has a greater effect. Nevertheless, even at 15 kV the laser power was increased by almost a factor of 7 for esculin and almost a factor of 2 for rhodamine 6G. However, at these higher voltages flashlamp life is significantly reduced. One of the significant advantages of using the prepulse is that the same laser power output is obtained at much lower driving voltage with the

Table I. Laser Power Enhancement Using Prepulse

Dye	Enhancement ratio (at HV = 12 kV) (min)	(max)	Wavelength range (Å) (at HV = 15 kV) Without prepulse	With prepulse
Rhodamine 6G (5×10^{-4} M, H_2O + 5% am LO)	2.6	5.8	5871–6154	5860–6210
1,2-dihydro-4-methoxybenzo c xanthylium fluoroborate (1×10^{-4} M, H_2O)	15	16	5051–5578	5021–5633
Esculin (1×10^{-3} M, H_2O + 5% am LO)	9	50	4464–4877	4433–5051

Table II. Prepulse Enhancement of Laser Power vs Flashlamp Voltage

Flashlamp voltage (kV)	Rhodamine 6G (λ = 5940 Å) (5×10^{-4} M, H_2O + 5% am LO) laser power (kW) Without prepulse	With prepulse	Esculin (λ = 4690 Å) (1×10^{-3} M, H_2O + 5% am LO) laser power (kW) Without prepulse	With prepulse
8.0	0.9	1.60	...	...
9.0	1.25	5.25	...	...
10.0	2.75	8.9	...	...
11.0	4.9	12.4	0.12	2.5
12.0	6.4	16.3	0.31	2.8
13.0	7.75	17.9	0.81	5.6
14.0	9.5	18.1	1.25	7.3
15.0	11.75	18.6	1.50	10.0

prepulse than is required without the prepulse, thus lengthening flashlamp lifetime, one of the major expense factors in the dye laser system. Another advantage is that the average power of the laser can be significantly increased since higher repetition rates are possible before overheating the lamp. Table II lists the laser power as a function of power supply voltage for rhodamine 6G and for esculin. (Laser power was measured with a Scientech calorimeter power meter.) For both dyes more laser power was obtained at 11 kV with the prepulse than was obtained at 15 kV without the prepulse.

We wish to express our indebtedness to G. T. McNice for many enlightening and useful discussions regarding the design and construction of the prepulse circuit. We also wish to acknowledge the assistance of Michael Maish in constructing and debugging the timing circuits.

This research was conducted while M. H. Ornstein was holding an NRC–NOAA Resident Research Associateship.

References

1. B. B. Snavely, Proc. IEEE **57**, 1374 (1969).
2. A. Cohen, V. E. Derr, G. T. McNice, and R. E. Cupp, Appl. Opt. **12**, 779 (1973).
3. Hongsuk H. Kim, Appl. Opt. **12**, 1454 (1973).
4. H. Samelson, Electronics **41**, 142 (1968).
5. M. Hercher and H. A. Pike, IEEE J. Quantum Electron. **QE-7**, 9, 473 (1971).
6. S. A. Tuccio and F. C. Strome, Appl. Opt. **11**, 64 (1972).
7. P. P. Sorokin *et al.*, J. Chem. Phys. **48**, 4726 (1968).
8. H. J. Goncz, J. Appl. Phys. **36**, 742 (1965).
9. G. W. LeCompte and H. E. Edgerton, J. Appl. Phys. **27**, 1427 (1956).
10. M. Cloupeau, Compt. Rend. **244**, 2033 (1957).
11. J. P. Markiewicz and J. L. Emmett, J. Quantum Electron. **QE-2**, 707 (1966).

NOAA Technical Memorandum ERL WPL-11

September 1974

THE NOAA PASSIVE OPTICAL CROSSWIND MONITOR

G. R. Ochs, G. F. Miller, and E. J. Goldenstein

We describe an optical instrument that measures crosswinds by observing the scintillation of naturally illuminated scenes. Operating instructions, adjustment procedures, and circuit diagrams are included.

NOAA Technical Report ERL 298-WPL 31

May 1974

DEVELOPMENT OF A PORTABLE ACOUSTIC ECHO SOUNDER

Edward J. Owens

There has been increasing interest in developing a small, inexpensive device for monitoring atmospheric temperature fluctuations by measuring the backscattered echoes of acoustic tone bursts with an acoustic echo sounder. Much of the theory and engineering design for such a device was developed during construction of the NOAA MARK II Acoustic Echo Sounder (Simmons, Wescott, and Hall, 1971). The MARK II system was not portable, but rather utilized standard-sized, laboratory-quality, commercially available electronic instruments for their precision and flexibility. This flexibility was desirable during research stages where a wide range of environmental field conditions was encountered. The total estimated cost of equipment for a single-channel MARK II system mounted in a 5-ft relay rack was $34,000. This report describes a portable, lower cost acoustic echo sounder recently developed at NOAA.

NOAA Technical Memorandum ERL WPL-12

June 1975

NOAA MARK VII ACOUSTIC ECHO SOUNDER

Edward J. Owens

The NOAA Mark VII portable Acoustic Echo Sounder which consists of a central unit, power amplifier, facsimile recorder, and 4-ft parabolic reflector antenna and which is used to monitor atmospheric temperature structure (inversions and convective plumes) to a height of 1360 m, by measuring backscattered echoes from acoustic tone bursts, is described. The theory and operation of the system are covered in detail. Complete instructions for initial set-up, adjustment and calibration, startup, shutdown, and maintenance are given. Appendices include wiring diagrams, design and operation of electronics subsystems, modifications to system, parts lists, and schematic diagrams of circuits.

Digital data acquisition for laser scattering spectroscopy using the scattered-to-incident light intensity ratio

R. L. Schwiesow and M. J. Post

Wave Propagation Laboratory, Environmental Research Laboratories, National Oceanic and Atmospheric Administration, Boulder, Colorado 80302

(Received 7 September 1973; and in final form, 25 February 1974)

We describe a digital data acquisition system for laser scattering spectroscopy, which measures the ratio of the scattered signal to either the incident laser power on the sample cell or the total signal incident at the spectrometer entrance aperture. The incident reference that is not used to form the ratio is used to check stability of the scattering sample. This report outlines the philosophy of the technique and gives components and circuit diagrams for its implementation. Digital measurement of light intensity is based on photon counting methods.

INTRODUCTION

The basis of scattering spectroscopy involves measuring the ratio of scattered intensity to incident intensity as a function of scattered wavelength. The simplest, least satisfactory approach is to assume that the incident intensity is constant in time. The scattered signal is then taken to represent the scattered-to-incident ratio. Topp and Schmid[1] introduced a significant improvement with a sophisticated fast *analog* dividing technique to compensate for incident intensity (or "source") fluctuations. This dividing circuit was used before the signal was time integrated, since division after smoothing was shown to degrade signal-to-noise. The analog technique necessitated converting an essentially digital signal (individual photons impinging on a photocathode) into an analog one. In effect, this decreased the signal-to-noise ratio by eliminating the accuracy of counting, for example, one photon out of 50 000, a resolution nearly impossible to attain in measuring current or voltage.

We have developed a data acquisition system that preserves and utilizes the digital nature of the photomultiplier signal while simultaneously compensating for *both* source and sample fluctuations. In addition, the system provides synchronism between data recording and spectrometer scanning and produces data output in computer-compatible format.

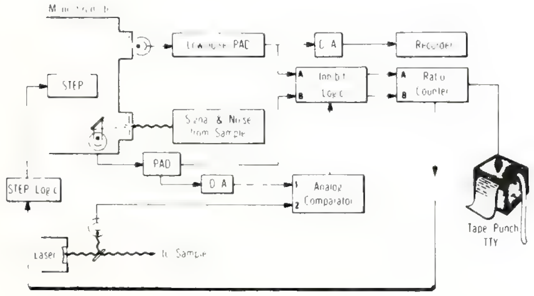

FIG. 1. Block diagram of digital data acquisition system based on measurement of intensity ratios. The scattered signal and two reference photoreceptors are shown schematically. PAD units are preamplifier, amplifier and discriminator combinations. The D/A units represent digital-to-analog converters or counting ratemeters.

The purpose of this paper is to present the concepts used in the system and to depict components developed for their implementation.

SYSTEM CONCEPT

A representation of the overall data system is shown in Fig. 1. The basic data are the ratios of scattered-to-incident light (to within an undetermined multiplicative constant that is characteristic of the system) as the monochromator wave number is changed. The use of an internal reference standard allows determination of the multiplicative instrument constant without an absolute intensity measurement.

Scattered energy is measured digitally by the total number of photon counts registered in channel A of the counter. A preamplifier–amplifier–discriminator setup (abbreviated PAD in Fig. 1) standardizes the photocathode pulses, and a D/A converter allows visual monitoring of scattered power.

Incident energy is determined by the total number of photon counts from the behind-the-slit intensity monitor. An additional illuminator monitor is positioned at the laser output. This analog signal is directly proportional to laser power. A voltage-to-frequency converter can be used to convert the laser monitor to a digital signal which can be processed in the same manner as the behind-the-slit reference signal.

Computation of the ratio of scattered energy to incident energy is done by the ratio counter, which produces a binary coded decimal output representing the ratio of photon counts in channel A to the number of counts in channel B. The counter determines a ratio by counting photons in the A channel until a preset number of counts (for example 10^6) is recorded in the B channel. The time required to fill the reference count requirement is inversely proportional to the incident power level. If we assume the limiting noise of the system is shot noise (Poisson statistics), then a constant uncertainty in reference energy level is assured, in spite of possible wide variations in power. This is because the total number of reference counts is independent of the incident power level. For the same reason, the statistical noise level

Copyright © 1975 by the American Institute of Physics

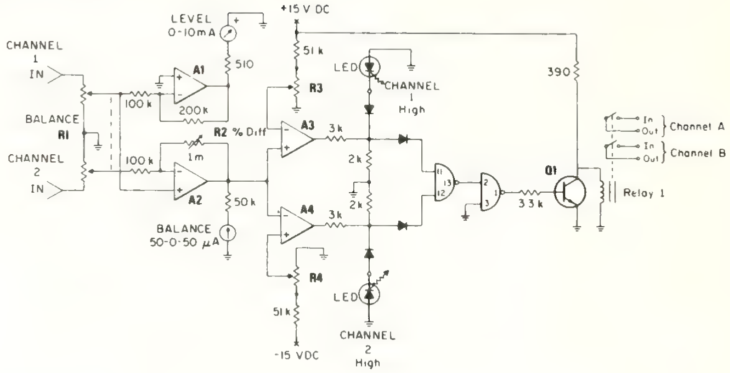

FIG. 2. Circuit diagram for the comparator/inhibitor module. The controlled switch serves to allow or prevent data taking by the ratio counter.

in the scattering spectrum will be independent of source power, resulting in greater spectral uniformity.

Since the data taking rate is not constant, but dependent on illumination level, the monochromator cannot be driven independently. Instead, when the reference channel is full, a pulse from the ratio counter initiates data recording (on punched paper tape) and triggers stepping the spectrometer by a preset (but variable) increment of wave number.

Digital data acquisition based on scattered-to-incident energy *ratios* allows great freedom in the operation of the experiment. Laser alignment may be peaked in the middle of a run, for example. Temporary interruptions of the illumination path do not affect the spectra.

Computing scattering ratios compensates for source fluctuations and adjustments, but it does not correct for changes in the sample condition, system misalignment or optical path attenuation between scatterer and monochromator. Particularly in fluids, the motion of unavoidable particulates through the focused laser beam causes scattering signal changes. If the particulate enters the beam in a region that is imaged on the monochromator entrance slit, an increase of many orders of magnitude in laser-frequency scattering will occur. This increase appears through instrumental scattering as a false increase in off-frequency spectral scattering, although laser power may be constant. If the particulate intercepts the small-diameter beam before the region imaged into the spectrometer, a sharp decrease in effective source intensity will cause a spurious reduction in scattered spectral signal to be recorded.

To eliminate effects from such changes, the reference signals from the monochromator entrance slit, D/A converted, and the laser are compared in an analog comparator. When these initially balanced source signals are unbalanced by a preset (but variable) percentage, the comparator signals an inhibit logic circuit which opens the input to *both* channels A and B of the ratio counter, thereby interrupting data taking. When the two reference levels are again within the balance limits, the data channels are reconnected to the ratio counter.

The diagram of Fig. 1 shows the monochromator reference level as the primary input to the measurement of the intensity ratio, with the source monitor serving to monitor particulate scattering in the sample. For some applications, such as absolute scattering cross section measurements, it is possible to use a voltage-to-frequency converter on the output of the laser monitor and use this signal as the channel B reference for determination of scattering-to-source intensity ratio.

In our application, the digital spectra generated by the system in Fig. 1 are computer processed to yield Raman cross sections, depolarization ratios, and integrated spectral areas above the baseline, corrected for instrumental quantum efficiencies. Basic data information includes the starting and ending wave number values and the record of scattered photon counts for each wave number increment (for a fixed reference count level). In practice, a reference sample spectrum is scanned before and after the spectral line of the sample gas.

SYSTEM COMPONENTS

Preamplifier, Amplifier, Discriminator Units

The low-noise preamplifier, amplifier and discriminator units used on the scattered intensity channel are adapted from commercial nuclear spectroscopy electronics. While highly linear, count rates are limited to approximately 50 kHz or less. A number of satisfactory photon counting systems are now commercially available. The signal processing for the behind-the-slit reference monitor is taken from the circuits of Miller.[2]

Digital-to-Analog Converters

The digital-to-analog converters are conventional *RC* type linear ratemeters. These units are widely available commercially or can be built in the laboratory.

Comparator-Inhibitor Module

This comparison unit checks that the primary and auxiliary source reference signals are proportional to each other, and permits both reference and scattered photon counts to be, or prevents them from being, registered on the ratio counter.

The comparator/inhibitor circuit is shown in Fig. 2. When operating, one first sets the difference potentiometer R_2 to some desired value corresponding to the maximum allowable percentage differences between channels. Positive analog inputs on channels 1 and 2 (which correspond to

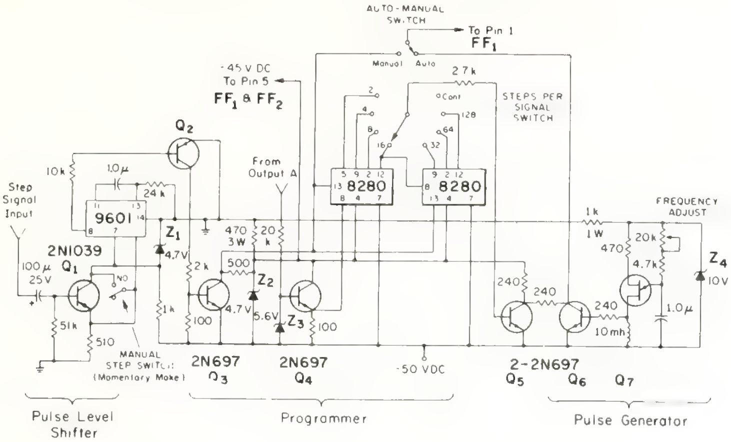

FIG. 3. Program circuit for the spectrometer stepping drive. The variable number of steps per data increment allows adjustment for optimum data density.

power levels, for instance) should be several volts. These voltages are balanced by adjusting the oppositely wired dual potentiometer R_1 to center the -50–0–50 μA balance meter. Next, the readings on the two 2 kΩ, ten-turn potentiometers are matched to the reading on the 0–10 mA level meter, where 0 reading corresponds to chassis ground and 10 corresponds to a value of 2 kΩ. This insures that percentage rather than absolute differences at the analog inputs will affect the operation of the inhibit circuit.

After these initial adjustments, if either channel 1 or channel 2 changes signal level, a positive or negative voltage will appear on the output of A_2, the magnitude of which is determined by the setting of the "percent difference" potentiometer R_2. If the absolute value of this voltage is greater than the magnitude of the voltage set by the two ten-turn potentiometers, either A_3 or A_4 will switch from negative saturation to positive saturation. An OR gate, composed of two NAND gates, senses such a change and goes positive. This is the inhibit signal which opens the relays that connect A and B inputs and outputs. The light-emitting diodes indicate which channel is high. Ordinary incandescent lights in combination with diodes and resistors may be substituted for the light-emitting diodes.

The settings of R_2 are calibrated by setting the potentiometer to various positions and observing what percentage difference in level at either channel is required to produce an inhibit signal. The various positions and values are marked on the chassis.

Power requirements are ±15V dc at 50 mA and +5V dc at 100 mA.

Ratio Counter

The two-channel counter is a commercial unit, which serves as the heart of the data collection system. This counter displays the ratio of A channel counts to B channel counts. The counter also triggers logic that controls both the spectrometer scan and data recording operations, based on the total number of reference photon counts. When the reference channel B is filled, the spectrometer is driven a preset number of steps while the number of scattered photon counts is punched on paper tape.

Stepper Drive

Figures 3 and 4 are schematics of the circuit used to drive the three-wire stepping motor, which scans the spectrometer. The switching voltage sequence required for the two motor windings is comparable to two square waves 90° out of phase. Motor direction is reversed by shifting one sequence 180° relative to the other (switching leads). The waveforms are generated by the flip-flop configuration prior to the final transistor power switches.

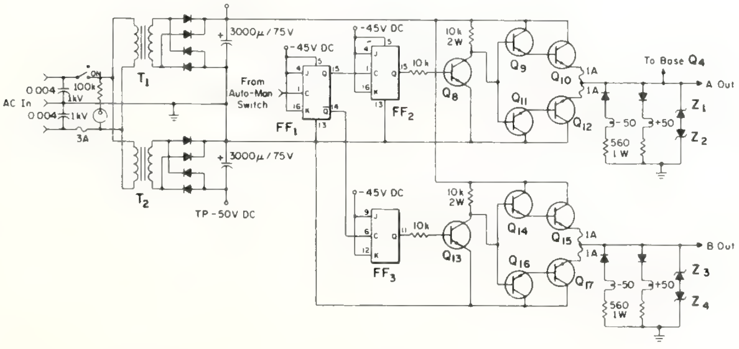

FIG. 4. Power supply and switch for the spectrometer stepping drive. This unit is controlled by the program circuit of Fig. 3.

A negative 5 V pulse of less than 200 msec duration is needed to trigger the 9601 one-shot multivibrator from the step signal input, or it may be triggered by depressing the manual step switch. If the normal–auto switch is in the "normal" mode, the pulse from the one-shot causes the first 7476 J–K flip-flop to change states, which in turn causes one of the outputs to switch from +50 V to −50 V, or vice versa. If the switch is in the "auto" position, the one-shot pulse clears the 8280 decade counters and connects the pulse generator to the flip-flop thru Q6. Each time the generator pulses thereafter the outputs and the counters increment by one. When the counter output, selected by the "steps per signal" switch, goes to logical 1, the preset number of steps have occurred, and Q5 disconnects the pulse generator from the flip-flop. This stops the outputs from changing states until the next pulse from the one-shot causes the sequence to repeat itself.

The 20 kΩ potentiometer associated with Q7 is a trimpot used to adjust the generator frequency from 20 to 100 Hz. The 28 V lamps on the output indicate the state of the outputs, while the back-to-back Zener diodes protect the power transistors from inductive loads. A reversing switch may be added to switch output leads in order to reverse direction of the motor.

Any switching transistors may be used for Q_1 and Q_3–Q_6. Q_2 must be rated for 60 V while the output transistors must be capable of handling 100 V at 300 mA. The four output transistors are mounted on heat sinks. Transformers T_1 and T_2 are rated 36 V rms at 1 A.

Detectors

The scattered light photomultiplier is suitably chosen for the specific spectroscopic experiment. We have found that a low-fluorescence quartz beamsplitter and 1P28 photomultiplier are suitable for the total scattered intensity monitor behind the spectrometer entrance slit. The incident intensity monitor at the laser follows standard practice, with a polarizer selecting the principal polarization direction of the laser, and an opal glass diffuser spreading the signal into a solid state photodetector–operational-amplifier combination.

[1] J. A. Topp and W. J. Schmid, Rev. Sci. Instrum. **42**, 1683 (1971).
[2] S. A. Miller, Rev. Sci. Instrum. **39**, 1923 (1968).

A sensitive two-frequency radiometer for remote sensing of temperature profiles

J. B. Snider

NOAA/Wave Propagation Laboratory, Boulder, Colorado 80302

(Received 7 March 1974; and in final form, 19 April 1974)

The design and operating characteristics of a two-frequency radiometer operating in the 50–60 GHz band are described. The system was developed as a remote sensor of the vertical temperature profile in the lower atmosphere. Recent applications of the system as a temperature probe are summarized.

1. INTRODUCTION

The use of radiometric measurements in the 50–60 GHz frequency region to infer the vertical temperature profile of the lower atmosphere has developed within the past few years.[1–3] A number of experiments and theoretical studies have considered various methods of inverting radiometric data to retrieve temperature profiles. In particular, the single-frequency angle-scan and multispectral approaches have been examined by the Wave Propagation Laboratory[4]; it has been shown that a two-frequency radiometer operated in the angle-scan mode will yield profile retrievals with greater accuracy than a single-frequency angle-scan system, and as accurate as a considerably more expensive and complicated four-frequency angle-scan radiometer. As a result of this finding, and with the availability of suitable low-noise broadband mixers, a two-frequency radiometer was built in the Wave Propagation Laboratory. Detailed results of an experiment using the radiometer to estimate atmospheric temperature profiles have been recently published.[5] In this paper the design and field performance of the radiometer are described.

2. RADIOMETER DESIGN

The major operating requirements for the radiometer in order of priority were as follows.

(1) The radiometer shall operate at two frequencies simultaneously using a single antenna.

(2) The spacing between the two operating frequencies shall be variable from 500 MHz to 2 or 3 GHz. Operation over this range shall be possible by simply retuning the local oscillators and without adjusting or changing radiometer components.

(3) The system shall be capable of operating over the 50–60 GHz range with changes in waveguide components and local oscillators permitted if necessary.

(4) The rms sensitivity shall be at least 0.25 K for a 30 sec integration time.

The prime requirement of simultaneous operation at two frequencies was achieved by use of a switchable four-port ferrite circulator. This approach makes use of the fact that the transmission direction in the circulator, i.e., direction of energy flow with lowest loss, may be switched by applying a dc bias of the correct polarity. Application of this property results in a system consisting, in effect, of two independent radiometers connected to a common antenna and calibration system.

Operation of the system may be understood by reference to the block diagram (Fig. 1), and the following discussion. During measurements, atmospheric radiation collected by the antenna is coupled to the radiometer through the waveguide switch and directional coupler. During calibration, the radiometer input is switched from the antenna to the input termination to establish a known temperature reference. The linearity and calibration of the instrument are then checked by coupling different amounts of noise into the system from the gaseous discharge noise generator via the precision attenuator and directional coupler. Up to this point, the operation of the radiometer is straightforward and follows customary practice.

We now discuss the manner in which simultaneous operation at two frequencies is achieved. The ferrite circulator is constructed so that without a dc bias current applied the low-attenuation signal paths are from port 1 to port 4 and from port 3 to port 2. Thus, the signal from the directional coupler flows through the circulator to mixer 2 via port 4 and the isolator. Similarly, the signal from the circulator termination flows from port 3 to mixer 1 via port 2. When a dc bias current of the correct polarity is applied to the circulator, the signal from the directional coupler flows to mixer 1 via port 2 and the isolator, while the signal from the termination now flows to mixer 2. In practice, the bias is applied to the circulator as a square wave. Hence, the two mixers are alternately connected to the directional coupler and the termination; as in the standard Dicke[6] system, the radiometer outputs are proportional to the difference in the noise temperature emitted by the termination connected to the circulator and the noise temperature incident from the directional coupler. The isolators connected between the circulator and mixers are included to prevent possible impedance modulation of the signal by local oscillator energy that might be reflected from the circulator output ports to the mixer inputs.

The mixers are broadband low noise units connected in the pushpull or balanced configuration; the devices were purchased from Aerojet General Corporation. The intermediate frequency (i.f.) amplifiers were supplied integrally with the mixers and are noise-matched to the mixer to obtain the optimum noise figure for the combination. The

Copyright © 1974 by the American Institute of Physics

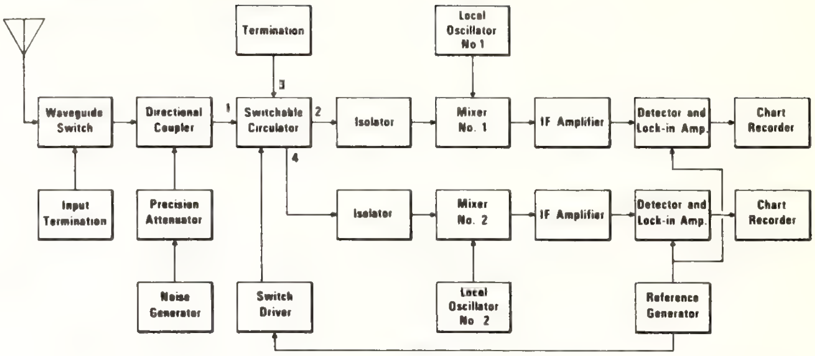

FIG. 1. Block diagram of two-frequency microwave radiometer for remote sensing of temperature profiles.

i.f. amplifier passband is flat within ±1 dB from 10 to 110 MHz; since no preselection is employed, both side bands are amplified. The noise figure for the mixer–i.f. combination is less than 8.5 dB over the 50–60 GHz frequency band.

Radiometer operating frequencies are determined by two klystron oscillators; no klystron frequency control is employed except that inherently provided by the use of regulated power supplies for all klystron voltages. Each local oscillator subsystem consists of the klystron, a wavemeter, a variable attenuator for varying the power supplied to the mixer diodes, and a mixer drive monitor. Diode bias voltage (proportional to mixer power) is indicated on a single digital voltmeter which is switched between the four diodes that comprise the two balanced mixers. The digital voltmeter is also used in combination with each absorption-type wavemeter to indicate the klystron oscillation frequency. Klystron frequencies are checked during measurements; in general, frequency changes during a 45 min period are not detectable.

The wavemeters were calibrated against a 52.75 GHz source derived from the fifth harmonic of a 10.55 GHz crystal-controlled solid-state multiplier. Although only a single point calibration was achieved in this manner, we assume the same wavemeter error exists over the operating bandwidth of the radiometer. The estimated accuracy of the wavemeter calibration is ±40 MHz; this figure includes an uncertainty of ±10 MHz in the harmonic calibration technique and an allowance of ±30 MHz for random errors. Since the change in zenith brightness temperature with frequency is approximately 54 K/GHz in the 54 GHz region, the wavemeter uncertainty produces a possible error of ±2.1 K at 90° elevation angle when translated to brightness temperature. At lower elevation angles and as the operating frequency approaches the O_2 resonance at 60 GHz, the possible error decreases since the change of brightness temperature with frequency decreases.

The reference signal for the lock-in amplifiers (synchronous detectors) is generated by a single audio oscillator which also serves as the trigger to the square wave generator that switches the ferrite circulator. A 180° phase reversal is used in the reference signal of one lock-in amplifier so that both radiometer channels have the same output polarity. The dc outputs from the lock-in amplifiers are recorded on strip-chart recorders; in addition, an interface unit (not shown) provides a ±1 V dc output for magnetic tape recording.

All radiometer components, except for power supplies, lock-in amplifiers, and recorders are located in a housing mounted on the system antenna (Fig. 2). Those waveguide components whose self-generated noise temperatures affect the radiometer output are housed in a temperature-controlled insulated compartment to minimize the variation in self-generated noise. The waveguide temperature at six different locations is measured by thermistors and recorded automatically on a digital printer at 5 min intervals. These temperatures, along with the waveguide loss factors (which were measured in the laboratory) are combined in the data reduction process to correct for self-generated noise.

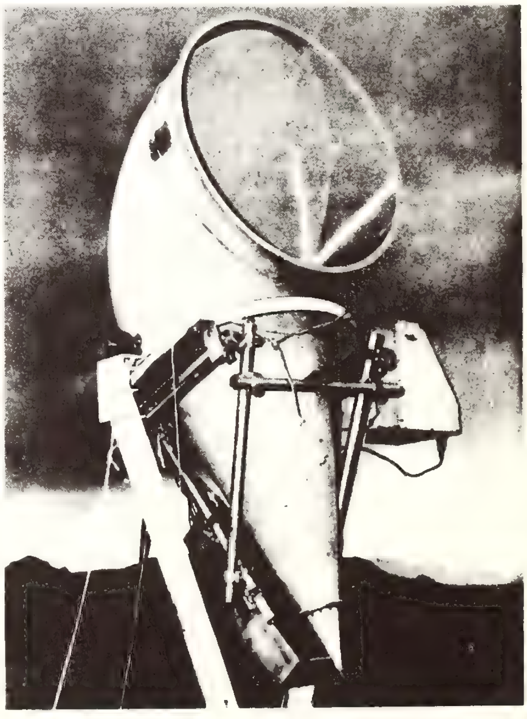

FIG. 2. Microwave radiometer and antenna installed in elevation over azimuth pedestal.

The radiometer antenna is a conical horn reflector with a 1.2 m aperture installed in an elevation over azimuth mount. Antenna mount axes are individually controlled, and the elevation and azimuth angles displayed at the radiometer operating position. The half-power antenna beamwidth is approximately 0.3° at 54 GHz; primary polarization antenna power patterns were measured to facilitate calculation of brightness temperature.

We derive brightness temperature from antenna temperature using a simple conversion factor based upon our antenna characteristics and a mean brightness temperature profile. The process converts antenna temperature measured at a given elevation angle to a value of brightness temperature at the same elevation angle. The conversion factor was calculated by numerically integrating

$$T_a(\theta)=\frac{1}{4\pi}\int_{4\pi} G(\Omega)T_b(\Omega)d\Omega, \qquad (1)$$

where $T_a(\theta)$ is the antenna temperature at elevation angle θ, and $T_b(\Omega)$ and $G(\Omega)$ are the brightness temperature and antenna directive gain, respectively, as a function of solid angle Ω; the integration is performed over 4π steradians. Mean brightness temperature profiles at the operating frequencies are computed from past radiosonde data for the area in which measurements are to be made. We assume that the ground is a black body radiating at the surface temperature of the mean brightness temperature profile. The conversion factor is the difference between mean brightness temperature and the integrated antenna temperature at the same elevation angle.

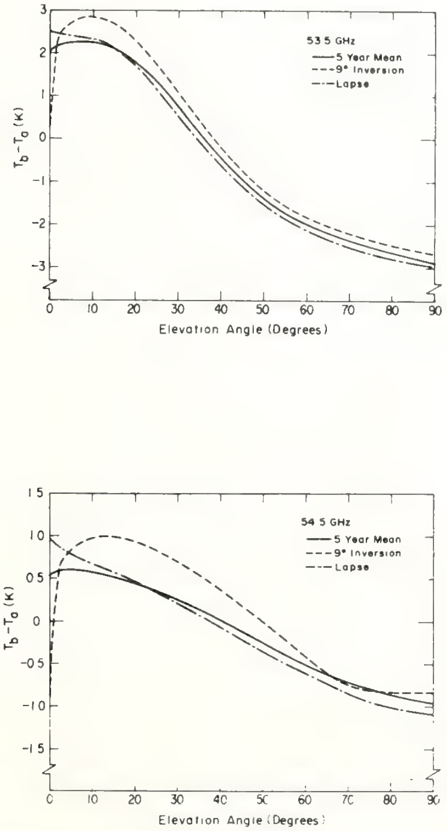

FIG. 3. Brightness temperature conversion factor for different temperature profiles.

A brightness temperature measurement is now given by

$$T_{bm}(\theta)=T_{am}(\theta)+[T_b(\theta)-T_a(\theta)], \qquad (2)$$

where $T_{bm}(\theta)$ and $T_{am}(\theta)$ are the measured brightness and antenna temperatures, respectively, at elevation angle, θ, and the quantity in brackets is the conversion factor.

To estimate the error in the conversion factor caused by an incorrect choice for the mean brightness temperature, we evaluated Eq. (1) for measured profiles consisting of (i) a strong ground-based inversion, and (ii) a 9°C/km lapse rate. From Fig. 3 we see that the conversion factor for the individual profiles may differ from that for the mean profile by approximately 1 K at the low elevation angles with the largest differences occurring for the intense temperature inversion. This result indicates that retrieved profiles containing temperature inversions may be subject to a slightly greater error than lapse profiles.

The absolute accuracy of an antenna temperature measurement based upon uncertainties in line loss values, waveguide physical temperature, the radiometer noise level, etc. is estimated to be ±4.5 K. Adding the uncertainty in converting antenna to brightness temperature, the absolute accuracy of a brightness measurement varies from approximately (−5.8)–(+4.5) K at 0° elevation angle to ±4.6 K at 90° elevation. In practice the absolute accuracy can be made somewhat better than just stated through the technique of using the atmospheric radiation at 0° elevation angle as a calibration point; this procedure is valid since the 0° brightness and surface temperatures are essentially equal in the 50–60 GHz region. With this technique, an absolute accuracy figure of ±3 K appears reasonable.

3. RADIOMETER PERFORMANCE

The rms sensitivity of both radiometer channels is conservatively estimated to be 0.25 K for a 10 sec integration time; this value is determined by dividing the peak to peak fluctuation of the radiometer output (in temperature units) by four. The experimental sensitivity is consistent with the theoretical value for a balanced radiometer computed from[7]

$$\Delta T_{\rm rms}=\frac{\pi}{\sqrt{2}}\frac{T_s}{\sqrt{B\tau}}, \qquad (3)$$

where $\Delta T_{\rm rms}$ is the minimum detectable temperature change, T_s is the system operating temperature, B is the effective noise bandwidth, and τ is the integration time. The factor $\pi/\sqrt{2}$ is the modulation constant used for square-wave switching and sine-wave detection waveforms. System operating temperature is given by

$$T_s=T_a+\tfrac{1}{2}(F-1)290, \qquad (4)$$

where T_a is the antenna temperature and F is the radiometer noise factor. The $(\frac{1}{2})$ multiplier in Eq. (4) is included because the radiometer noise temperature is effectively halved since the noise power in both signal and image passbands contributes to the radiometer output.[8] Substituting system characteristics

$$T_a = 250\ \mathrm{K} \qquad F = 13.8 \qquad B = 100\ \mathrm{MHz} \qquad \tau = 10\ \mathrm{sec}$$

into Eqs. (2) and (3) yields a theoretical sensitivity of 0.15 K. This system cannot be operated in a balanced condition as a consequence of its two-frequency capability. Therefore, the actual sensitivity can be expected to be slightly worse than predicted by Eq. (3). Characteristics of the radiometer are summarized in Table I.

An inconvenient operational problem with the present instrument is a slow variation in the i.f. gain caused by thermal radiation from the klystron local oscillators. The problem occurs only during the day when ambient temperatures are 25°C or higher. Fortunately, the gain varies systematically with the temperature proximate to the i.f. amplifiers. By monitoring the latter temperature with a thermistor, changes in the radiometer's input–output characteristic can be followed.

While the gain variation might be reduced by installation of suitable thermal barriers between the i.f. amplifiers and klystrons, a more viable solution would be to replace the klystrons with low-power solid-state sources. Use of solid-state local oscillators would also eliminate the need for high voltages and the attendant problems with moisture and arcing. An additional advantage of solid-state local oscillators is an improved frequency stability that would decrease the measurement error caused by uncertainty in indicated operating frequency (see above).

4. APPLICATIONS

The two-frequency system has been used to estimate vertical temperature profiles up to a height of 3 km from 53.5 and 54.5 GHz measurements.[5] Temperature profiles were derived from the radiometric measurements using minimum variance statistical inversion techniques.[1,5] An average rms difference of 2.0 K between temperature profiles measured by radiosondes and that inferred from the radiometer data was obtained for 13 soundings containing a variety of profiles. The radiometer easily indicated the presence or absence of ground-based inversions. In addition, brightness temperature recorded at a fixed antenna elevation angle correlated well with temperatures recorded at specific levels on an instrumented tower.

TABLE I. Summary of two-frequency microwave radiometer characteristics.

LO center frequencies	Variable, 50–60 GHz
Frequency separation	250 MHz–2 GHz
I.f. passband (2 dB)	10–110 MHz
Sensitivity ($\tau = 10$ sec)	0.25 K
System noise figure[a]	11.4 dB
Mixer noise figure	8.0 dB
Antenna beamwidth (3 dB)	0.3°
Estimated absolute accuracy	±3.0 K

[a] System noise figure is referred to the antenna input port.

A second experiment was performed to investigate the ability of the radiometer to monitor temperature fluctuations in the first few hundred meters above the earth's surface. For this study, the radiometer was operated at 58 and 60 GHz; the frequency change was accomplished by changing the circulator, isolators, and the klystrons. The system sensitivity was essentially the same as at the lower frequencies. Although the radiometer data have not been inverted to recover temperature profiles, radiometric and theoretical brightness temperatures compare well. Further, direct radiometric measurements correctly indicate the gross temperature structure of the lower atmosphere.

[1] E. R. Westwater, Mon. Wea. Rev. **100**, No. 1, 15 (1972a).
[2] G. F. Miner, D. D. Thornton, and W. J. Welch, J. Geophys. Res. **77**, 975 (1972).
[3] W. D. Mount, B. R. Fow, C. V. Wick, and C. M. Maloy, "Three Radiometric Data Analysis Techniques for Measuring Air Temperature Profiles," Sperry Rand Research Center, Sudbury, MA., Contract No. CPA 22-69-116, prepared for the Division of Meteorology, Air Pollution Control Office, Environmental Protection Agency, Durham, N.C., 1969.
[4] J. B. Snider, J. Appl. Meteor. **11**, 958 (1972).
[5] E. R. Westwater, J. B. Snider, A. V. Carlson, and J. R. Yoder, "Experimental Determination of Temperature Profiles by Ground-Based Radiometry," US Department of Commerce, NOAA Technical Report No. ERL 289-WPL-27, US Government Printing Office, Washington, D.C., 1973.
[6] R. H. Dicke, Rev. Sci. Instrum. **17**, 268 (1946).
[7] J. D. Kraus, *Radio Astronomy* (McGraw–Hill, New York, 1966).
[8] P. D. Strum, Proc. IRE **46**, 43 (1958).

The Annals of Statistics
1974, Vol. 2, No. 5, 935-949

COEFFICIENT ERRORS CAUSED BY USING THE WRONG COVARIANCE MATRIX IN THE GENERAL LINEAR MODEL

BY OTTO NEALL STRAND

Wave Propagation Laboratory, Boulder, Colorado

A method is derived to place an approximate bound on the mean-square error incurred by using an incorrect covariance matrix in the Gauss-Markov estimator of the coefficient vector in the full-rank general linear model. The bound thus obtained is a function of the incorrect covariance matrix $\tilde{S}$ actually used, the Frobenius norm of $S - \tilde{S}$, where S is the correct covariance matrix, and the basis matrix ϕ. This estimate can therefore be computed from known or easily-approximated data in the usual regression problem. All mathematics related to the method is derived, and numerical examples are presented.

1. Introduction. In this paper we are concerned with the full-rank general linear model

$$y = \phi\alpha + e \tag{1.1}$$

where

y is an $n \times 1$ vector of real measurements,
ϕ is an $n \times p$ real matrix of rank $p, p < n$,
α is an unknown $p \times 1$ real vector of coefficients,
e is an $n \times 1$ random real column vector of measurement errors,

such that

$$E(e) = 0 \quad \text{and} \tag{1.2}$$

$$E(ee^T) = S\,. \tag{1.3}$$

Here S is assumed strictly positive definite, $E(\cdot)$ is the expected-value operator, and the superscript ^{T} denotes matrix transposition.

It is well known that the optimum linear unbiased estimate of α (i.e., that estimate having the smallest expected mean-square error) is achieved when the residuals are weighted in accordance with S^{-1}. However, in practice S is not known, but one only has an approximation $\tilde{S}$ to S and perhaps a reasonable bound on the departure of $\tilde{S}$ from S. If one uses $\tilde{S}$ in place of S, one will ordinarily incur an error in the estimated coefficient vector α. In this paper we develop a method of placing an approximate bound on the expected mean-square value of this error. This bound is a function of the basis matrix ϕ, the

---

Received April 1973; revised January 1974.

AMS 1970 *subject classifications.* Primary 15A60; Secondary 62F10.

Key words and phrases. Covariance matrix, expected mean-square error, incorrect covariances, matrix trace expressions.

approximate covariance matrix $\tilde{S}$ and a norm of the departure of $\tilde{S}$ from the true covariance matrix S. Several authors [1], [3], [4], [5], [6], [8], [10], have recently investigated questions closely related to this. However, although these papers are of theoretical interest, they do not provide readily usable estimates of the error to be expected in α for a given size error in S. The present paper differs from these others in that it attacks the mean-square error expression directly to provide an estimate of the maximum possible expected mean-square error in terms of quantities that are often available; that is, in terms of ϕ, $\tilde{S}$ and a bound on the Frobenius norm of $S - \tilde{S}$.

In the following sections we begin by obtaining covariance and mean-square error expressions (Section 2), show how to maximize the mean-square error in α for a given covariance-matrix error norm (Section 3), show how to determine the required maximal eigenvalue (Section 4), apply the theory to regression errors for unit-weight least squares (Section 5), and finally, present numerical illustrations (Section 6).

2. Covariance and mean-square error results. The results in the first part of this section are well known and are easily derived by taking expected values and traces. We therefore do not include derivations. In this paper we assume that both $\tilde{S}$ and S are *strictly* positive definite and that $\tilde{S}$ and ϕ are known. The *optimum* or *Gauss–Markov* estimate of α is given by $\hat{\alpha}$, where

$$\hat{\alpha} = (\phi^T S^{-1} \phi)^{-1} \phi^T S^{-1} y \, . \tag{2.1}$$

Furthermore,

$$E(\hat{\alpha}) = \alpha \, , \tag{2.2}$$

so that α is unbiased. The covariance matrix of $\hat{\alpha}$ is

$$S_{\hat{\alpha}-\alpha} = (\phi^T S^{-1} \phi)^{-1} \, . \tag{2.3}$$

(Whenever convenient, we denote the covariance matrix of a random vector v by S_v.) Now suppose that, instead of using the correct covariance matrix S, we use the incorrect covariance matrix $\tilde{S}$ in the estimation. Then we form the corresponding estimate

$$\tilde{\alpha} = (\phi^T \tilde{S}^{-1} \phi)^{-1} \phi^T \tilde{S}^{-1} y \, , \tag{2.4}$$

where the only difference between (2.1) and (2.4) is that S is replaced by $\tilde{S}$ in the latter. Again we have

$$E(\tilde{\alpha}) = \alpha \tag{2.5}$$

and this time

$$S_{\tilde{\alpha}-\hat{\alpha}} = V - (\phi^T S^{-1} \phi)^{-1} \tag{2.6}$$

where

$$V = (\phi^T \tilde{S}^{-1} \phi)^{-1} \phi^T \tilde{S}^{-1} S \tilde{S}^{-1} \phi (\phi^T \tilde{S}^{-1} \phi)^{-1} = S_{\tilde{\alpha}-\alpha} \, . \tag{2.7}$$

It follows from (2.6) and (2.7) that

(2.8) $$S_{\tilde{\alpha}-\alpha} = S_{\tilde{\alpha}-\hat{\alpha}} + S_{\hat{\alpha}-\alpha} \,.$$

By taking traces we obtain

(2.9) $$E[(\tilde{\alpha} - \alpha)^T(\tilde{\alpha} - \alpha)] = E[(\tilde{\alpha} - \hat{\alpha})^T(\tilde{\alpha} - \hat{\alpha})] + E[(\hat{\alpha} - \alpha)^T(\hat{\alpha} - \alpha)] \,.$$

It is also covenient to write

(2.10) $$\operatorname{tr} S_{\tilde{\alpha}-\hat{\alpha}} = \operatorname{tr} P_1 S - \operatorname{tr} (\phi^T S^{-1} \phi)^{-1}$$

and

(2.11) $$\operatorname{tr} S_{\tilde{\alpha}-\alpha} = \operatorname{tr} P_1 S$$

where

(2.12) $$P_1 = \tilde{S}^{-1}\phi(\phi^T\tilde{S}^{-1}\phi)^{-2}\phi^T\tilde{S}^{-1}$$

and we note that P_1 involves only the basis matrix ϕ, which is assumed known, and the known incorrect covariance matrix $\tilde{S}$. Throughout this paper we shall be concerned with $\operatorname{tr} S_{\tilde{\alpha}-\hat{\alpha}}$ (as given by (2.10)) as a measure of the departure of $\tilde{\alpha}$ from the optimum solution $\hat{\alpha}$.

It is apparent from (2.10) that the nonlinear dependence of the term $\operatorname{tr} [(\phi^T S^{-1} \phi)^{-1}]$ on the (unknown) correct covariance matrix S presents difficulties which must be overcome. For this purpose we let

(2.13) $$S = \tilde{S} + \Delta S \,,$$

where ΔS is a symmetric error matrix. Further define the Frobenius (or Euclidean) norm of any square matrix A by

(2.14) $$||A||^2 = \operatorname{tr} A^T A \,.$$

Equation (2.14) defines the only type of matrix norm to be used in this paper.

Since S itself is not known, we will assume that a number $\varepsilon > 0$ is known such that

(2.15) $$||\Delta S|| \leqq \varepsilon \,.$$

An important restriction is made at the outset: the number ε must be sufficiently small that for every ΔS satisfying (2.15), the matrix S in (2.13) is strictly positive definite. Since the eigenvalues of $\tilde{S}$ are all positive by hypothesis, and since the eigenvalues of $\tilde{S} + \Delta S$ are continuous functions of ΔS, and furthermore all $\tilde{S} + \Delta S$ are symmetric (having real eigenvalues), it follows that as ΔS is continuously varied in compliance with (2.15), the eigenvalues of $\tilde{S} + \Delta S$ move continuouly along the real axis and that the set of admissible ε has the form $\{\varepsilon \mid 0 < \varepsilon < \varepsilon_0 \text{ for some } \varepsilon_0 > 0\}$. What we do not permit is for any eigenvalue of $\tilde{S} + \Delta S$ to touch or cross the origin as ΔS varies arbitrarily over all symmetric matrices satisfying (2.15). In what follows we will assume that this restriction is satisfied unless a specific statement to the contrary is made. It will be discovered that many of the arguments in this paper depend on the interaction of P_1 (see (2.12)) and P_2, defined below:

$$P_2 = \tilde{S}^{-1} - \tilde{S}^{-1}\phi(\phi^T\tilde{S}^{-1}\phi)^{-1}\phi^T\tilde{S}^{-1} . \tag{2.16}$$

Note that P_2 also involves only known quantities. The following identities follow readily from (2.12) and (2.16):

$$\begin{aligned}
&P_1^T = P_1 \quad \text{and} \quad P_2^T = P_2 \\
&\phi^T P_2 = P_2\phi = 0 \\
&\phi^T P_1 \phi = I_p = p \times p \quad \text{identity} \\
&\text{rank } P_1 = p \\
&P_2\tilde{S}P_1 = P_1\tilde{S}P_2 = 0 \\
&P_2\tilde{S} \quad \text{and} \quad \tilde{S}P_2 \quad \text{are idempotent,} \\
&\text{i.e.,} \quad (P_2\tilde{S})^2 = P_2\tilde{S} \quad \text{and} \quad (\tilde{S}P_2)^2 = \tilde{S}P_2 \\
&\phi(\phi^T\tilde{S}^{-1}\phi)^{-1}\phi^T = \tilde{S} - \tilde{S}P_2\tilde{S} .
\end{aligned} \tag{2.17}$$

In the special case $\tilde{S} = I$, some of the relationships (2.17) may be written as

$$\begin{aligned}
&P_2P_1 = P_1P_2 = 0 \\
&P_2^j = P_2 , \qquad j = 1, 2, 3, \cdots \\
&\phi(\phi^T\phi)^{-1}\phi^T = I - P_2 .
\end{aligned} \tag{2.18}$$

It follows from the continuity of the eigenvalues of S as functions of the coefficients ΔS_{ij} that the set $E = \{\Delta S \,|\, S \text{ is strictly positive definite}\}$ is an open set in the sense that if $\Delta S \in E$ then for each $i \leqq j$ the element $\Delta S_{ij} \equiv \Delta S_{ji}$ can be varied within an open interval without causing ΔS to depart from E. Thus every $\Delta S \in E$ is an interior element.

If $\Delta S \in E$, then the matrix $I + P_2\Delta S$ is nonsingular. This will be established by proving that if v is an n-tuple, then

$$(I + P_2\Delta S)v = 0 \quad \text{implies} \quad v = 0 . \tag{2.19}$$

Suppose (2.19) is satisfied; then by (2.13),

$$[(I - P_2\tilde{S}) + P_2S]v = 0 . \tag{2.20}$$

Since $P_2\tilde{S}$ is idempotent (see 2.17) we may multiply (2.20) on the left by $P_2\tilde{S}$ to get

$$P_2\tilde{S}P_2Sv = 0 . \tag{2.21}$$

Since $\tilde{S}P_2$ is also idempotent, we may multiply (2.21) on the left by $\tilde{S}$ to get $\tilde{S}P_2Sv = 0$, from which

$$P_2Sv = 0 , \quad \text{since} \quad \tilde{S} \quad \text{is nonsingular.} \tag{2.22}$$

Substituting (2.22) into (2.20) gives

$$v = P_2\tilde{S}v . \tag{2.23}$$

We calculate $v^T S v = v^T S P_2 \tilde{S} v = (P_2 S v)^T \tilde{S} v = 0$. Since S is strictly positive definite by hypothesis, this implies $v = 0$.

We are now ready to state and prove a theorem that greatly simplifies the study of the expected mean-square departure of $\tilde{\alpha}$ from $\hat{\alpha}$.

THEOREM 2.1. *If* $\tilde{S} + \Delta S = S$ *is a strictly positive definite matrix, then*

$$E[(\tilde{\alpha} - \hat{\alpha})^T(\tilde{\alpha} - \hat{\alpha})] = \operatorname{tr} P_1 S - \operatorname{tr} (\phi^T S^{-1} \phi)^{-1} \tag{2.24}$$
$$\equiv \operatorname{tr} [P_1 \Delta S P_2 \Delta S (I + P_2 \Delta S)^{-1}] ,$$

where P_1 *is given by* (2.12), P_2 *is given by* (2.16), *and* ΔS *is given by* (2.13). *The equality of the second and third members of* (2.24) *holds whether* S *is strictly positive definite or not.*

PROOF. We first note the useful identity

$$(I + R)^{-1} = \textstyle\sum_{j=0}^{k} (-R)^j + T_k \tag{2.25}$$

where $k = 0, 1, 2, \cdots$, $T_k = (-R)^{k+1}(I + R)^{-1} \equiv (I + R)^{-1}(-R)^{k+1}$, R is any square matrix for which $I + R$ is nonsingular. Formula (2.25) is easily established by pre- or post-multiplication by $I + R$. We calculate from (2.13)

$$(\phi^T S^{-1} \phi)^{-1} = (\phi^T \tilde{S}^{-1} \phi)^{-1} (I - A)^{-1} \tag{2.26}$$

where

$$A = \phi^T \tilde{S}^{-1} \Delta S(\ + \tilde{S}^{-1} \Delta S)^{-1} \tilde{S}^{-1} \phi (\phi^T \tilde{S}^{-1} \phi)^{-1} , \tag{2.27}$$

and from (2.16)

$$(I + \tilde{S}^{-1} \Delta S)^{-1} = (I + P_2 \Delta S)^{-1} (I - B) \tag{2.28}$$

where

$$B = \tilde{S}^{-1} \phi (\phi^T \tilde{S}^{-1} \phi)^{-1} \phi^T \tilde{S}^{-1} \Delta S (I + \tilde{S}^{-1} \Delta S)^{-1} . \tag{2.29}$$

Applying (2.25) to (2.26) with $k = 0$ and $R = -A$ gives

$$(\phi^T S^{-1} \phi)^{-1} = (\phi^T \tilde{S}^{-1} \phi)^{-1} + (\phi^T \tilde{S}^{-1} \phi)^{-1} A (I - A)^{-1} . \tag{2.30}$$

Substituting (2.28) and (2.29) into (2.27) gives

$$A = \phi^T \tilde{S}^{-1} \Delta S (I + P_2 \Delta S)^{-1} \tilde{S}^{-1} \phi (\phi^T \tilde{S}^{-1} \phi)^{-1} [I - A] . \tag{2.31}$$

Substituting (2.31) into (2.30) and taking traces gives

$$\operatorname{tr} (\phi^T S^{-1} \phi)^{-1} = \operatorname{tr} [P_1 \tilde{S} + P_1 \Delta S (I + P_2 \Delta S)^{-1}] . \tag{2.32}$$

Applying (2.25) with $R = P_2 \Delta S$ and $k = 0$, and noting (2.13), shows that (2.32) is equivalent to (2.24).

Note that the proof just given holds for any symmetric matrix ΔS for which the indicated inverses exist. In fact, the identity of the second and third members of (2.24) is valid even when the resulting matrix S is not positive definite, and this fact was demonstrated numerically for randomly-chosen symmetric matrices ΔS. Expression (2.24) is the basis for the analysis of this paper.

The objective is to find a maximum for the mean-square error expression (2.24) under the assumption that $||\Delta S||$ is fixed.

3. Maximization of mean-square error for a given covariance-matrix error norm. We begin by maximizing the expression (2.24) under the assumption that

$$||\Delta S||^2 = \operatorname{tr}\{(\Delta S)^T \Delta S\} = \varepsilon^2 . \tag{3.1}$$

Since all admissible ΔS must be symmetric, we require the further constraint

$$\Delta S_{ij} = \Delta S_{ji} \quad \text{for} \quad i < j , \quad \text{where} \quad \Delta S = (\Delta S_{ij}) . \tag{3.2}$$

In accordance with the method of Lagrange, we require that the quantity $G(\Delta S)$ be stationary, where

$$\begin{aligned} G(\Delta S) = {} & \operatorname{tr}\{P_1 \Delta S P_2 \Delta S (I + P_2 \Delta S)^{-1}\} \\ & - \lambda[\operatorname{tr}\{(\Delta S)^T \Delta S\} - \varepsilon^2] - \textstyle\sum_{j=2}^{n} \sum_{i=1}^{j-1} \mu_{ji}(\Delta S_{ji} - \Delta S_{ij}) \end{aligned} \tag{3.3}$$

and λ and the μ_{ij} are Lagrange multipliers. We may differentiate the first trace in (3.3) as follows. If we denote this trace by $f(\Delta S)$, then

$$\begin{aligned} & f(\Delta S + H) - f(\Delta S) \\ & \quad = \operatorname{tr}[P_2 \Delta S (I + P_2 \Delta S)^{-1} P_1 H + (I + P_2 \Delta S)^{-1} P_1 \Delta S P_2 H \\ & \qquad - (I + P_2 \Delta S)^{-1} P_1 \Delta S P_2 \Delta S (I + P_2 \Delta S)^{-1} P_2 H + O(H^2)] . \end{aligned}$$

Differentiating the linear terms with respect to H (note the well-known formula $(d/dH)[\operatorname{tr} BH] = B^T$), simplifying and applying the condition $\Delta S = \Delta S^T$ gives

$$\begin{aligned} & (d/d\Delta S) \operatorname{tr}\{P_1 \Delta S P_2 \Delta S (I + P_2 \Delta S)^{-1}\} \\ & \qquad = (I + P_2 \Delta S)^{-1} Q(\Delta S)(I + \Delta S P_2)^{-1} \end{aligned} \tag{3.4}$$

where

$$Q(\Delta S) = P_1 \Delta S P_2 + P_2 \Delta S P_1 + P_2 \Delta S P_1 \Delta S P_2 . \tag{3.5}$$

Also,

$$(d/d\Delta S) \operatorname{tr}\{(\Delta S)^T \Delta S\} = 2\Delta S \tag{3.6}$$

and

$$(d/d\Delta S)[\textstyle\sum_{j=2}^{n} \sum_{i=1}^{j-1} \mu_{ji}(\Delta S_{ji} - \Delta S_{ij})] = M = (M_{ij})$$

where

$$\begin{aligned} M_{ij} & = -\mu_{ji} \quad & i < j \\ & = 0 & i = j \\ & = \mu_{ij} & i > j . \end{aligned} \tag{3.7}$$

Thus $M = -M^T$ so that M is skew symmetric. The stationarity condition $(d/d\Delta S)[G(\Delta S)] = 0$ and the symmetry of ΔS together imply that M is also symmetric; consequently $M = 0$ and all μ_{ij} are zero. We therefore obtain the equation

$$T_{\mathrm{NL}}(\Delta S) = \lambda \Delta S \tag{3.8}$$

where the constraint (3.2) has been imposed, the subscript NL denotes "nonlinear," and

$$2T_{\mathrm{NL}}(\Delta S) = (I + P_2 \Delta S)^{-1} Q(\Delta S)(I + \Delta S P_2)^{-1} \tag{3.9}$$

where $Q(\Delta S)$ is defined by (3.5).

Up to this point no approximations have been made. Two formidable difficulties become apparent. First, it is not clear that solving (3.8) to maximize (2.24) using the equality constraint $||\Delta S|| = \varepsilon$ will necessarily suffice for the inequality constraint $||\Delta S|| \leqq \varepsilon$. Furthermore, solving the nonlinear eigenvalue problem (3.8) would itself be a formidable task. We therefore resort to an approximation which consists of maximizing the leading term of (2.24). Applying identity (2.25) with $k = 0$ and $R = P_2 \Delta S$ to (2.24) gives

$$E\{(\bar{\alpha} - \hat{\alpha})^T (\bar{\alpha} - \hat{\alpha})\} = \operatorname{tr}\{P_1 \Delta S P_2 \Delta S [I - P_2 \Delta S (I + P_2 \Delta S)^{-1}]\} \tag{3.10}$$

so that the error committed by using a second-degree approximation is

$$\text{Error} = -\operatorname{tr}\{P_1 \Delta S (P_2 \Delta S)^2 (I + P_2 \Delta S)^{-1}\}\ . \tag{3.11}$$

Since (3.11) is of degree 3 or higher in $P_2 \Delta S$, it can be ignored for sufficiently small ΔS. Of course, if (3.11) could be bounded in a satisfactory manner, a rigorous upper bound to (2.24) could be obtained. Otherwise the bound is only approximate. However, even a rough upper bound on the expected mean-square error is often useful. The situation is similar to that occurring when one uses differentials to estimate errors in a function of several variables.

Dropping third and higher-degree terms from (2.24) gives the simpler problem

$$\operatorname{tr}\{P_1 \Delta S P_2 \Delta S\} = \text{maximum} \tag{3.12}$$

under the constraints $||\Delta S|| = \varepsilon$ and $\Delta S = \Delta S^T$ as in (3.2). It will be seen that the resulting maximum will also suffice for the inequality constraint. Carrying out the differentiation gives the following equation corresponding to (3.8):

$$\tfrac{1}{2}(P_1 \Delta S P_2 + P_2 \Delta S P_1) = \lambda \Delta S\ . \tag{3.13}$$

We present some facts about expressions (2.24) and (3.12) and the solutions of (3.8) and (3.13).

First, if S if strictly positive definite, then

$$\operatorname{tr}\{P_1 \Delta S P_2 \Delta S\} \geqq 0 \quad \text{for all symmetric matrices} \quad \Delta S\ . \tag{3.14}$$

This follows from (2.12) and the fact that P_2 is nonnegative definite by writing

$$\operatorname{tr}\{P_1 \Delta S P_2 \Delta S\} = \operatorname{tr}\{[\Delta S \tilde{S}^{-1} \phi (\phi^T \tilde{S}^{-1} \phi)^{-1}]^T P_2 [\Delta S \tilde{S}^{-1} \phi (\phi^T \tilde{S}^{-1} \phi)^{-1}]\} \geqq 0\ . \tag{3.15}$$

The right-hand side of the exact expression (2.24) is also nonnegative, as it is a mean-square error.

It follows readily from (2.24) that the two types of symmetric matrices

$$\Delta S = \phi A \phi^T \tag{3.16}$$

where A is any symmetric $p \times p$ matrix and

$$\Delta S = k \cdot \tilde{S} \tag{3.17}$$

where k is any constant for which S is positive definite, are such that

$$E\{(\tilde{\alpha} - \hat{\alpha})^T(\tilde{\alpha} - \hat{\alpha})\} = 0 \,. \tag{3.18}$$

These are special cases in which the expected mean-square error is not increased by an error, ΔS, in the covariance matrix. If $\tilde{S} = I$, such cases are easily characterized.

Theorem 3.1. *If* $\tilde{S} = I$ *and* S *is strictly positive definite, then* (3.18) *holds if and only if*

$$P_1 \Delta S P_2 = 0 \tag{3.19}$$

or equivalently

$$\phi^T \Delta S P_2 = 0 \,. \tag{3.20}$$

In case ΔS satisfies (3.19), then both (2.24) and the leading term tr $\{P_1 \Delta S P_2 \Delta S\}$ vanish, and both (3.8) and (3.13) are satisfied with $\lambda = 0$.

Proof. Suppose (3.18) holds. Then, since tr $\{P_1 \Delta S P_2 \Delta S (I + P_2 \Delta S)^{-1}\}$ is zero, it is an unconstrained minimum, and according to the discussion in Section 2, ΔS is an interior point of the set E. Thus ΔS satisfies (3.8) with $\lambda = 0$. Recalling that $I + P_2 \Delta S$ and $I + \Delta S P_2 = (I + P_2 \Delta S)^T$ are nonsingular matrices and cancelling the inverses gives

$$Q(\Delta S) = 0 \,. \qquad \text{(See (3.5).)} \tag{3.21}$$

Pre-multiplying by $I - P_2$ and noting (2.18) gives $P_1 \Delta S P_2 = 0$, and (3.13) is satisfied with $\lambda = 0$. Conversely, if $P_1 \Delta S P_2 = 0$, then both (2.24) and the leading term vanish and both (3.8) and (3.13) are satisfied with $\lambda = 0$.

We note that ΔS as given by (3.16) and (3.17) both satisfy (3.19) when $\tilde{S} = I$. It is known [8], that the most general assignment of ΔS for which (3.18) holds (when $\tilde{S} = I$) has the form

$$\Delta S = \phi A \phi^T + x B x^T + r \cdot I \tag{3.22}$$

where r is a scalar, A and B are arbitrary symmetric matrices and x is an n-tuple such that $x^T \phi = 0$. It is easily verified that (3.22) satisfies (3.19).

If the simplified equation (3.13) is satisfied, and $\tilde{S} = I$, then the last member of (2.24) reduces to (3.12) even if $\lambda \neq 0$. Because of this, one might expect that the corresponding solution of (3.13) would solve (3.8). Unfortunately, this is not the case. To see this, note that if X is a symmetric solution to (3.13), $\lambda \neq 0$ and S is strictly positive definite, then

$$P_2 X P_2 = 0 \,. \tag{3.23}$$

If $X \neq 0$ also satisfies (3.8), we have

$$P_1 X P_2 + P_2 X P_1 + P_2 X P_1 X P_2 = 2\lambda (I + P_2 X) X (I + X P_2) \,. \tag{3.24}$$

Pre-multiplication by P_2 gives

$$P_2XP_1 = 2\lambda P_2(I + P_2X)X \tag{3.25}$$

and post-multiplication of (3.25) by P_2 gives $P_2(I + P_2X)XP_2 = 0$ or

$$P_2XP_2 = -P_2X^2P_2 . \tag{3.26}$$

According to (3.23) this implies

$$P_2X^2P_2 = (P_2X)(P_2X)^T = 0 , \tag{3.27}$$

from which $P_2X = 0$ and therefore $P_2XP_1 = P_1XP_2 = 0$ which, according to (3.13), is a contradiction unless $\lambda = 0$. Thus, even when $\tilde{S} = I$, a solution of (3.13) only approximates the maximum expected mean-square error in α.

We continue the discussion of the approximate problem (3.12). Multiplying by $\Delta S \equiv \Delta S^T$ and taking the trace gives

$$\operatorname{tr}\{P_1XP_2X\} = \lambda\varepsilon^2 \tag{3.28}$$

if X is a solution of (3.12) under the stated constraints. Thus (3.12) will be maximized by substituting the maximal λ for which (3.13) has a solution into (3.28). It follows from (3.15) that the desired solution for λ must be positive. Since (3.28) defines an increasing function of ε^2, this value of λ will then maximize (3.12) under the constraint $||\Delta S||^2 \leqq \varepsilon^2$. In the next section we derive a method of solving (3.13). Because of the fact that the unknown element, ΔS, is a *matrix* and not an n-tuple, (3.13) is not (as it stands) a vector-matrix characteristic equation. However, it will be discovered in the next section that (3.13) represents a characteristic equation in a space whose elements are $n \times n$ symmetric matrices.

4. Determination of maximal operator eigenvalue. Let $\mathscr{H}$ be the set of all $n \times n$ real symmetric matrices. We denote elements of $\mathscr{H}$ by capital letters $X, Y, \cdots$. (These are elements such as ΔS in (3.13).) Clearly $\mathscr{H}$ is a linear manifold. We define the *inner product* of elements of $\mathscr{H}$ by the formula

$$(X, Y) = \operatorname{tr} XY^T = \operatorname{tr} XY = \operatorname{tr} YX . \tag{4.1}$$

With the definition (4.1) $\mathscr{H}$ is a finite-dimensional Hilbert space. Taking as a basis the set of matrices having ones in two symmetrically-placed locations and zeros elsewhere, together with matrices having a single one on the diagonal and zeros elsewhere, shows that $\mathscr{H}$ has dimension $n(n + 1)/2$.

Consider the operator T defined by the left-hand side of (3.13).

$$TX \equiv \tfrac{1}{2}[P_1XP_2 + P_2XP_1] , \qquad X \in \mathscr{H} . \tag{4.2}$$

Since TX is again a real symmetric $n \times n$ matrix, T maps $\mathscr{H}$ into $\mathscr{H}$. It is easily verified that T is linear. (It is also true that T_{NL} (see (3.8)) maps $\mathscr{H}$ into $\mathscr{H}$, although the mapping is nonlinear.) Now if $X, Y \in \mathscr{H}$, then

$$\begin{aligned}(TX, Y) &= \operatorname{tr}[\tfrac{1}{2}(P_1XP_2 + P_2XP_1)Y] \\ &= \operatorname{tr}\{X[\tfrac{1}{2}(P_2YP_1 + P_1YP_2)]\} = (X, TY) .\end{aligned} \tag{4.3}$$

Therefore T is self adjoint. Since $(TX, X) = \operatorname{tr}(P_1XP_2X) \geqq 0$ for all $X \in \mathscr{H}$ (see (3.15)), it follows that T is nonnegative definite. Thus T is a *compact, self-adjoint nonnegative definite* operator defined on $\mathscr{H}$.

Equation (3.13) may be written in the form

$$TX = \lambda X \tag{4.4}$$

and what we require to solve (3.13) for λ to use in (3.28) is a *maximal eigenvalue* of the operator T. We may invoke the theory of such operators [9], and state that there exists a maximal positive λ which provides a nontrivial solution to (4.4) (and hence (3.13)) and that any matrix X which corresponds to the maximal λ in (4.4) will cause

$$(TX, X) = \operatorname{tr}[P_1XP_2X] \tag{4.5}$$

to be a maximum for a given $||X|| = ||\Delta S|| = \varepsilon$.

We develop a method for finding the required maximal λ. It follows from the theory of operators such as T [9] that any element $X_0 \in \mathscr{H}$ can be written in the form

$$X_0 = \alpha_1 H_1 + \alpha_2 H_2 + \cdots + \alpha_k H_k + \alpha_{k+1} H_{k+1} + \cdots + \alpha_p H_p + Q \tag{4.6}$$

where

$$\begin{array}{lll} TH_i = \lambda H_i\,, & & i = 1, 2, \cdots k \\ TH_i = \lambda_{i-k} H_i\,, & & i = k+1, \cdots p \\ TQ = 0\,, & \text{all } H_i \text{ are orthonormal,} & \\ & \text{and } \lambda > \lambda_1 \geqq \lambda_2 \cdots \geqq \lambda_{p-k} > 0\,. & \end{array} \tag{4.7}$$

Here we deliberately single out the subspace of eigenelements associated with the maximal eigenvalue λ. Numerical experiments have shown that this subspace may be multidimensional. Although this does not affect the validity of the theory, it must be provided for in the derivation. We develop a slight generalization of the *power* method of von Mises [7], similar to a method often employed for matrix eigenvalue problems. Assume that X_0 is such that

$$\textstyle\sum_{i=1}^{k} \alpha_i^2 \neq 0 \qquad \text{in (4.6)} \tag{4.8}$$

and repeatedly apply the operator T to X_0. For $j \geqq 1$ the result is

$$\begin{aligned} T^j X_0 = \lambda^j \Big[& (\alpha_1 H_1 + \alpha_2 H_2 + \cdots + \alpha_k H_k) \\ & + \left(\frac{\lambda_1}{\lambda}\right)^j \alpha_{k+1} H_{k+1} + \cdots + \left(\frac{\lambda_{p-k}}{\lambda}\right)^j \alpha_p H_p \Big]. \end{aligned} \tag{4.9}$$

The *Rayleigh quotient* for the operator T with argument $V \in \mathscr{H}$ is:

$$R = (TV, V)/(V, V)\,. \tag{4.10}$$

Letting R_j be the Rayleigh quotient for T with argument T^jX_0 gives

$$R_j = (T^{j+1}X_0, T^jX_0)/(T^jX_0, T^jX_0)\,. \tag{4.11}$$

Evaluating (4.11) with the help of (4.9) and the orthonormality of the H_i gives

$$R_j = a_j/b_j \qquad \text{where}$$

$$a_j = \lambda^{2j+1}\left[\textstyle\sum_{i=1}^{k} \alpha_i^2 + \sum_{i=1}^{p-k} \alpha_{k+i}^2(\lambda_i/\lambda)^{2j+1}\right] \tag{4.12}$$

$$b_j = \lambda^{2j}\left[\textstyle\sum_{i=1}^{k} \alpha_i^2 + \sum_{i=1}^{p-k} \alpha_{k+i}^2(\lambda_i/\lambda)^{2j}\right] .$$

Since $0 < \lambda_i < \lambda$, $i = 1, 2, \cdots, (p-k)$, it follows from (4.12) and (4.8) that:

$$\lim_{j\to\infty} R_j = \lambda . \tag{4.13}$$

Furthermore, the limit

$$X = \lim_{j\to\infty} T^j X_0/\|T^j X_0\| \tag{4.14}$$

is an element such that $TX = \lambda X$. (See (4.9).) In practical computations we take X_0 as a symmetric matrix whose entries are obtained from a random number generator. We cease applying T to X_0 as soon as R_j and R_{j+1} agree to the desired precision. As a check, the corresponding element $T^j X_0/\|T^j X_0\|$ then approximates an element X for which the maximum in (3.12) is actually achieved. Substituting λ into (3.28) gives the desired bound on the expected mean-square error in the estimate of α. In summary, we have the following approximate error bound, for which (3.12) is maximized,

$$E[(\hat{\alpha} - \tilde{\alpha})^T(\tilde{\alpha} - \hat{\alpha})] \leqq \lambda\varepsilon^2 \tag{4.15}$$

where S and $\tilde{S}$ are strictly positive definite, and $\|\Delta S\| = [\operatorname{tr} \Delta S^2]^{\frac{1}{2}} \leqq \varepsilon$.

Finally, note that any solution of (3.13) (whether $\tilde{S} = I$ or not) is orthogonal in $\mathscr{H}$ to ΔS as given by either (3.16) or (3.17). To see this, calculate (assuming 3.13)

$$\operatorname{tr} \{\phi A \phi^T \Delta S\} = \tfrac{1}{2} \operatorname{tr} \{\phi A \phi^T [P_2 \Delta S P_1 + P_1 \Delta S P_2]\} = 0$$

and

$$\operatorname{tr} \{k \tilde{S} \Delta S\} = \frac{k}{2} \operatorname{tr} \{P_2 \tilde{S} P_1 + P_1 \tilde{S} P_2\} = 0 .$$

In Section 6 we shall give more details on the numerical computation of λ and X. First, however, we present an interesting special case in which λ can be calculated explicitly.

5. Regression errors caused by using equal-weight least squares instead of Gauss–Markov estimation in the linear model.

In many applications of the full-rank general linear model it is convenient to estimate coefficients by simply requiring that the equally-weighted sum of the squares of the residuals be a minimum. This procedure is often used even when the data are correlated and have unequal variances, so that the results thus obtained are not optimum. However, the non-optimum estimate obtained in this way is entirely satisfactory if the resulting errors are sufficiently small. In this paper we apply the theory already developed to establish a remarkably simple approximate upper bound on such errors. So far we have been mainly concerned with coefficient errors, i.e., errors in α. However, in many applications it is more meaningful to study errors in $\phi\alpha$, as these errors often represent the error incurred when the estimate is actually used. For example, in the case of polynomial regression one is usually much more interested in the quality of the fit than in the coefficient errors, as the latter are not invariant under scaling. In this section errors in $\phi\alpha$ will be called *regression errors*, in contrast to errors in α, which have been called *coefficient errors*. The use of unit-weight least squares amounts to assuming $\tilde{S} = I$. (The modification in case $\tilde{S} = \sigma^2 I$ is immediate.) We therefore state the main result as follows.

THEOREM 5.1. *If* $\tilde{S} = I$ *and* $\|\Delta S\| = \|S - I\| \leqq \varepsilon$, *then the regression error vector* $\phi(\tilde{\alpha} - \hat{\alpha})$ *is such that*

$$E\{[\phi(\tilde{\alpha} - \hat{\alpha})]^T[\phi(\tilde{\alpha} - \hat{\alpha})]\} \leqq \varepsilon^2/2 + O(\varepsilon^3) . \tag{5.1}$$

PROOF. First note that, in accordance with the propagation of covariances and formula (2.6),

$$\begin{aligned} E\{[\phi(\tilde{\alpha} - \hat{\alpha})]^T[\phi(\tilde{\alpha} - \hat{\alpha})]\} &= \operatorname{tr} \phi S_{\tilde{\alpha}-\hat{\alpha}} \phi^T \\ &= \operatorname{tr} \phi^T S \phi (\phi^T\phi)^{-1} - \operatorname{tr} \phi^T\phi(\phi^T S^{-1}\phi)^{-1} . \end{aligned} \tag{5.2}$$

If A is any nonsingular $p \times p$ matrix and one replaces ϕ by ϕA in (5.2), he finds that the expected mean-square regression error (5.2) is unchanged. Since $(\phi^T\phi)^{-1}$ is strictly positive definite, there exists [2] a nonsingular $p \times p$ matrix W such that $(\phi^T\phi)^{-1} = W^T W$. If we put $\psi = \phi W^T$, then $\psi^T\psi = I$. However, if we replace ϕ by ψ, so that $\phi^T\phi = I$, then coefficient errors and regression errors are identical. Therefore we may obtain the desired expected mean-square regression error from (2.10) by simply imposing the condition $\phi^T\phi = I$. If this is done, (5.2) then reduces to (2.10), and the coefficient-error theory may be used to majorize the error as given by (5.2). Thus we assume $\phi^T\phi = I$ and proceed to solve (3.13) for λ. Multiplying (3.13) on the left by P_1 and on the right by P_2, noting that both P_1 and P_2 are now idempotent, gives

$$\tfrac{1}{2} P_1 \Delta S P_2 = \lambda P_1 \Delta S P_2 . \tag{5.3}$$

According to Theorem 3.1, the maximal λ will occur when $P_1 \Delta S P_2 \neq 0$ unless the mean-square error (5.2) is identically zero for all admissible ΔS. In the first case, $\lambda = \frac{1}{2}$ and Theorem 5.1 is proved. In the second case, Theorem 5.1 is trivially true. Although it is not needed for the proof, one can construct an example showing that the second case cannot occur for $1 \leqq p \leqq n - 1$.

In the following section we indicate the nature of the numerical verifications that have been obtained.

6. Numerical illustrations. In the numerical work reported here all computations were performed in double precision. Whenever no particular assumption is made regarding a variable (such as ϕ, ΔS, etc.), we assigned the values by the use of a Gaussian random-number generator. The resulting values were rounded in the computer before they were used in such a way that the values given below are *exactly* those actually used to at least single-precision accuracy, or to about 11 significant figures. It is realized that the determination of λ to an accuracy of two digits would suffice for most applications; however, the more accurate values are given to show the ease of obtaining the λ to great accuracy by the method of Section 4. The exactness of the fundamental formula (2.24) was verified numerically by many computations.

EXAMPLE 1. (See 1.1.) $n = 4$, $p = 3$, $\varepsilon = .01$, $\tilde{S} = I$,

$$\phi = \begin{bmatrix} .008 & .845 & -.362 \\ .388 & .903 & -.796 \\ -.286 & -.520 & -.691 \\ -.373 & -1.387 & -.157 \end{bmatrix} . \tag{6.1}$$

Three random choices of X_0 were chosen and λ was computed by the method of Section 4 as

$$\lambda = 6.26055201920083 . \tag{6.2}$$

This exact value was obtained after 13 to 14 iterations from each of the three randomly-chosen X_0. In this particular case the eigenspace associated with λ appears to be one-dimensional, i.e., $k = 1$ in (4.6). The normalized eigenmatrix obtained was

$$X = \begin{bmatrix} .50630972 & -.12855536 & -.18828182 & .27563970 \\ -.12855536 & -.13497855 & .28344970 & -.27880171 \\ -.18828182 & .28344970 & -.26125714 & .19105482 \\ .27563970 & -.27880171 & .19105482 & -.11007403 \end{bmatrix} . \tag{6.3}$$

Either this matrix or its negative was obtained exact to the number of decimals given for all three random choices of X_0. The corresponding error bound (4.15) or (3.28) is:

$$E\{(\tilde{\alpha} - \hat{\alpha})^T(\tilde{\alpha} - \hat{\alpha})\} \leqq \varepsilon^2\lambda = 6.26 \cdots \times 10^{-4} . \tag{6.4}$$

Note that for other small assumed values of ε we need only multiply λ by ε^2. Thus for $\varepsilon = .1$ we have a bound of $6.26 \cdots \times 10^{-2}$ corresponding to (6.4). A random sample of five symmetric error matrices ΔS for which $||\Delta S|| = .01$ was taken and the actual expected mean-square error for each was calculated by (2.10) and (2.24). The maximum actual expected mean-square error achieved by any ΔS was about 15 % of the bound (6.4). It will be noticed throughout the numerical examples that the chances of obtaining a matrix ΔS which approximates the bound are not great. This is apparently related to the extensive nature of the space for which the increase in expected mean-square error is zero. (See (3.22), for instance.) The bound of (6.4) was actually achieved by $\varepsilon^2 X$, where X is given by (6.3).

EXAMPLE 2. $n = 11$, $p = 4$, $\varepsilon = .01$, $\tilde{S} = I$. The matrix ϕ is not reproduced here, but was obtained from the random-number generator. With three randomly-chosen starting elements X_0, the maximal eigenvalue λ was obtained to an accuracy of at least 15 significant figures after 58 to 66 iterations. The X obtained was different in each case, indicating $k > 1$ in (4.6). One of the X's was substituted into (2.10) and (2.24) to verify that the maximum, $\lambda\varepsilon^2$, was actually achieved. In a random sample of 30 symmetric matrices ΔS for which $||\Delta S|| = .01$, it was found that the largest actual expected mean-square error was about 35 % of the bound.

Cases were computed in which $\tilde{S} \neq I$ was determined by calculating $A^T A$, where A is a randomly-chosen triangular matrix. In many of these cases it was seen that calculating the bound $\varepsilon^2\lambda$ gave a value that was within a couple of percent of the expected mean-square error obtained when X was substituted into (2.24). This indicated that a reasonable bound could probably be obtained by dropping 3rd and higher degree terms in ΔS from (2.24).

As a check of the results of Section 5, a sample of 200 symmetric matrices ΔS was obtained by using the random-number generator. The resulting matrices were normalized to have $||\Delta S|| = 10^{-3}$ and $||\Delta S|| = 10^{-2}$ for each ΔS. The basis ϕ was chosen from a table of orthogonal polynomials such that $\phi^T\phi = I$, $p = 3$, $n = 11$, and (5.2) was computed for each ΔS (both normalizations). The largest actual relative mean-square regression error (5.2) was 70.4 % of $||\Delta S||^2/2$.

7. Summary. A rational procedure has been developed for finding an approximate bound on the expected mean-square error caused by using an incorrect covariance matrix to estimate the coefficient vector in the general linear model. A new expression (Theorem 2.1) for this mean-square error was derived. The matrices P_1 and P_2 ((2.12) and (2.16), respectively) were defined, and it was found that their properties greatly aided in the derivation. The method of Lagrange was employed to maximize the expected mean-square error under the constraints that $||\Delta S|| = \varepsilon$ and that ΔS was symmetric. A necessary and sufficient condition that $E[(\tilde{\alpha} - \hat{\alpha})^T(\tilde{\alpha} - \hat{\alpha})] = 0$ was derived (Theorem 3.1). A second-degree approximation to the nonlinear expected mean-square error was introduced. In Section 4 a method was derived to solve for the required eigenvalue for the approximation; it was found that the theory of self-adjoint, nonnegative definite, compact operators played an essential role in the derivation, which involved the (finite-dimensional) Hilbert space whose elements are symmetric matrices. In Section 5 we derived a simple approximate upper bound for the expected mean-square regression error caused by wrongly using unit-weight least squares; it was possible to obtain the explicit solution $\lambda = \frac{1}{2}$ in this case. In Section 6 numerical results were presented to illustrate the practical computation of the error bounds.

REFERENCES

[1] CLEVELAND, W. S. (1971). Projection with the wrong inner product and its application to regression with correlated errors and linear filtering of time series. *Ann. Math. Statist.* **42** 616–624.

[2] FADDEEVA, V. N. (1959). *Computational Methods of Linear Algebra.* Dover, New York. 81–85.

[3] GOLUB, G. H. (1963). Comparison of the variance of minimum variance and weighted least squares regression coefficients. *Ann. Math. Statist.* **34** 984–991.

[4] GRENANDER, U. (1954). On the estimation of the regression coefficients in the case of an auto-correlated disturbance. *Ann. Math. Statist.* **25** 252–272.

[5] KRUSKAL, W. (1968). When are Gauss–Markov and least squares estimators identical? A coordinate-free approach. *Ann. Math. Statist.* **39** 70–75.

[6] MAGNESS, T. A. and MCGUIRE, J. B. (1962). Comparison of least squares and minimum variance estimates of regression parameters. *Ann. Math. Statist.* **33** 462–470.

[7] RALSTON, A. (1965). *A First Course in Numerical Analysis.* McGraw-Hill, New York. 474–480.

[8] RAO, C. R. (1967). Least squares theory using an estimated dispersion matrix and its application to measurement of signals. *Fifth Berkeley Symp. Math. Statist. Prob.* **1** 355–371. Univ. of California Press.

[9] RIESZ, F. and SZ-NAGY, B. (1955). *Functional Analysis.* Ungar, New York. Chapter VI.

[10] Watson, G. S. (1967). Linear least-squares regression. *Ann. Math. Statist.* **38** 1679–1699.

ENVIRONMENTAL RESEARCH LABS
U. S. DEPARTMENT OF COMMERCE
NATIONAL OCEANIC AND
ATMOSPHERIC ADMINISTRATION
BOULDER, COLORADO 80302

SIAM J. NUMER. ANAL.
Vol. 11, No. 4, September 1974

THEORY AND METHODS RELATED TO THE SINGULAR-FUNCTION EXPANSION AND LANDWEBER'S ITERATION FOR INTEGRAL EQUATIONS OF THE FIRST KIND†

OTTO NEALL STRAND‡

Abstract. For the Fredholm integral equation of the first kind, written notationally as $Kf = g$, $g \in L_2[0, 1]$, we study the behavior of the iteration

$$\hat{f}_k = \hat{f}_{k-1} + DK^*(g - K\hat{f}_{k-1}), \qquad k = 1, 2, \cdots,$$

both with respect to its convergence properties and its response to singular functions of K. Here K^* is the adjoint of K, $\hat{f}_0$ is a suitable starting function and D is a fixed linear operator to be chosen. The general theory of singular functions is interpreted and extended for the study of the iteration, and a quantitative method of choosing D to shape the response to singular functions of K is derived. Several specific matrix and integral-equation examples are presented.

1. Introduction. In 1951 Landweber [12] proposed an iterative method for solving the integral equation of the first kind:

$$\int_0^1 K(x, y)f(y)\,dy = g(x), \qquad 0 \leqq x \leqq 1, \tag{1}$$

where $K(x, y)$ is an L_2-kernel and $g \in L_2[0, 1]$. If we write (1) in the abbreviated operator form

$$Kf = g \tag{2}$$

where the operator K is defined by the left-hand side of (1),[1] then Landweber's iteration takes the form

$$\hat{f}_k = \hat{f}_{k-1} + K^*(g - K\hat{f}_{k-1}), \qquad k = 1, 2, \cdots. \tag{3}$$

Here K^* is the *adjoint* operator to K (defined in § 2) and $\hat{f}_0$ is a suitable starting function. Landweber showed that the sequence $\{\hat{f}_k\}_{k=1}^{\infty}$ had limiting properties similar to those of the sequence generated by truncating the singular-series expansion. Because of the prevalence of the integral equation of the first kind in physical applications (see, for example, [5], [20] and [31], there has been much recent interest in methods similar to Landweber's. Most recent work is of two types: *theoretical* [2], [6], [9], [11] and [14], in which methods closely related to (3) are examined with respect to their behavior as $k \to \infty$ when the solution to (2) exists, and *empirical* [3], [7] and [21], in which generalizations to (3) are made and, although the convergence properties are not studied, convincing empirical evidence is given that the methods are successful in practice. The theoretical

---

† Received by the editors May 17, 1972, and in revised form December 20, 1972.

‡ Environmental Radiometry, National Oceanic & Atmospheric Administration, Environmental Research Laboratories, Boulder, Colorado 80302, and Colorado State University, Fort Collins, Colorado. This paper is from a thesis submitted to the Graduate Faculty of Colorado State University in partial fulfillment of the requirements for the degree of Doctor of Philosophy. This research was supported by the National Aeronautics and Space Administration–Manned Spacecraft Center under Contract T-4727A.

[1] For simplicity, we make no distinction between almost-everywhere equivalence and true equality, but simply denote both by the equals sign. We sometimes write L_2 for $L_2[0, 1]$.

methods are not adequate in themselves for the practical inversion problem, as they do not treat the usual case in which g (in (2)) is a measured function with error. In the present paper we derive both the convergence properties and the response with respect to singular functions of K after a finite number of steps for the iteration

$$\hat{f}_k = \hat{f}_{k-1} + DK^*(g - K\hat{f}_{k-1}), \qquad k = 1, 2, \cdots, \tag{4}$$

where D is a linear operator to be specified below. The generalization (4) was suggested by recent successful empirical methods published by Smith [21], Fleming and Smith [7], and Conrath and Revah [3], although the present method actually differs from these in the choice of D. One main purpose of the current paper is to study (4) with respect to its response to singular functions of the operator K after a finite number k of iterations and to show how to construct D and choose k to provide a desired response.

Before describing the proposed method and new theory related to it, we first summarize and interpret the classical theory of singular-function expansions as related to integral equations of the first kind. Such expansions have been used in the matrix-approximation case by Baker et al. [1], and more recently by Hanson [10], among others. In the present paper we interpret and extend the theory of singular-function expansions as required (§ 2), apply this theory to equation (4) (§ 3), show how to shape the "response" curve (§ 4), and finally present illustrative results (§ 5).

2. Singular functions and integral equations of the first kind. We consider the Fredholm integral equation of the first kind as given in (1), or in abbreviated form as (2). All the developments to be presented will hold for compact operators K and elements g of a real separable Hilbert space (for this more general treatment, see Strand [23]). However, our arguments here are confined to the integral operator defined above, although the corresponding matrix results are freely used.

We define the *adjoint operator* K^* by

$$K^*g = \int_0^1 K(x, y)g(x)\,dx, \qquad g \in L_2[0, 1]. \tag{5}$$

With the usual L_2 inner product, if $f \in L_2[0, 1]$, then

$$\begin{aligned} \langle Kf, g \rangle &= \int_0^1 \int_0^1 K(x, y)f(y)g(x)\,dy\,dx \\ &= \int_0^1 f(y)\,dy \int_0^1 K(x, y)g(x)\,dx = \langle f, K^*g \rangle. \end{aligned} \tag{6}$$

In the case of a real matrix operator A, we define $A^* = A^T =$ the transpose of A; an equation analogous to (6) is then satisfied.

In the practical problem to be considered, (1) is used to infer $f(y)$ from measurements made of $g(x)$. This so-called inversion problem is ill-posed, and several methods have been proposed to replace (1) by a well-posed problem [8], [15], [19], [24], [25], [27] and [30]. The successful methods all have one feature in common: either explicitly or implicitly they incorporate desired properties of f in addition to its ability to satisfy (1). For example, the method may force f to be smooth, or it may impose conditions such as boundedness, having a known statistical distribution, or being a linear combination of certain well-chosen functions. When no conditions are stated other than (1), and $g(x)$ is obtained by measurement with error, there is *always* ambiguity in the f to be found; that is, there are many functions f which satisfy (1) to within measurement error. For example, the ambiguity asserts itself in the Phillips–Twomey–Tikhonov method, [15], [27] and [25], by the presence of a smoothing parameter to which a value must be arbitrarily assigned. In the present case it will be seen that the ambiguity is in the choice of the "correct" number of singular functions to be used in the expansion. The criterion to be used in this paper is as follows: when f is approximated by a linear combination of the first N singular functions (defined below), the approximation will be considered to provide desirable smoothing when N is chosen as the smallest value consistent with $\|Kf - g\|$ being comparable in size to measurement error. This is the condition used by Hanson [10] and Baker et al. [1].

The definitions, concepts and proofs of classical theorems summarized here may be found in an excellent book by Smithies [22, Chap. 8]. We present proofs only where they are needed. For a compact operator K, a *singular system* $(u_n, v_n; \mu_n)$ is defined as follows: $(u_n; \mu_n^2)$, $n = 1, 2, \cdots$, is a characteristic system of KK^* and $(v_n; \mu_n^2)$ is a characteristic system of K^*K. Thus

$$\begin{aligned} &\mu_n^2 KK^* u_n = u_n, && n = 1, 2, \cdots, \\ &\mu_n^2 K^*K v_n = v_n, && n = 1, 2, \cdots, \end{aligned} \tag{7}$$

where we suppose without loss of generality that $0 < \mu_1 \leqq \mu_2 \leqq \cdots$. The μ_n's are called *singular values* and the u_n's and v_n's are called *singular functions* of K. For convenience we also define

$$\lambda_n = 1/\mu_n^2, \qquad n = 1, 2, \cdots; \tag{8}$$

then

$$\lambda_1 \geqq \lambda_2 \geqq \cdots > 0.$$

The terminology *high order harmonics* will be used to describe singular functions u_n (or v_n) associated with large singular values μ_n. The functions u_n are related to the corresponding v_n by the formulas:[2]

$$\begin{aligned} u_n &= \mu_n K v_n, && n = 1, 2, \cdots, \\ v_n &= \mu_n K^* u_n, && n = 1, 2, \cdots. \end{aligned} \tag{9}$$

---

[2] The reader who is accustomed to matrices should note the reciprocal nature of the μ_n defined here, and that the λ_n are conventional eigenvalues of KK^* or K^*K.

As usual, we assume that $\{u_n\}$ and $\{v_n\}$ are orthonormal sets. It is known [18, Chap. 6] that there are only two possibilities: either $\mu_n \to \infty$ as $n \to \infty$ or there are only finitely many u_n and v_n.

The fundamental theorem concerning the existence of an L_2-solution to (1) was first proved by Picard [16] over 60 years ago. We state it as the following theorem.

THEOREM 1. *Let* $(u_n, v_n; \mu_n)$ *be a singular system for the operator* K *and let* $g \in L_2$. *Then the equation* (2) $Kf = g$ *has an* L_2-*solution if and only if*

$$\text{(a)} \qquad \sum_{n=1}^{\infty} \mu_n^2 |\langle g, u_n\rangle|^2 < \infty$$

and

(b) *whenever* u *is such that* $K^*u = 0$, *then* $\langle g, u\rangle = 0$.
Under these conditions a solution f *can be written as*[3]

$$\text{(10)} \qquad \underset{N\to\infty}{\text{l.i.m.}}\, f_N,$$

where

$$\text{(11)} \qquad f_N = \sum_{n=1}^{N} \langle g, u_n\rangle \mu_n v_n.$$

THEOREM 2. *If* $v \in L_2$, *then* $Kv = 0$ *if and only if* $\langle v, v_n\rangle = 0$ *for all* n. *Similarly if* $u \in L_2$, *then* $K^*u = 0$ *if and only if* $\langle u, u_n\rangle = 0$ *for all* n.

(This is Smithies' Theorem 8.3.1, [22, p. 145].)

THEOREM 3. *If* $v \in L_2$ *and* $g = Kv$, *then*

$$\text{(12)} \qquad g = \sum_{n=1}^{\infty} \langle g, u_n\rangle u_n = \sum_{n=1}^{\infty} \frac{\langle v, v_n\rangle}{\mu_n} u_n.$$

Similarly, if $u \in L_2$ *and* $f = K^*u$, *then*

$$\text{(13)} \qquad f = \sum_{n=1}^{\infty} \langle f, v_n\rangle v_n = \sum_{n=1}^{\infty} \frac{\langle u, u_n\rangle v_n}{\mu_n}.$$

(This is Smithies' Theorem 8.3.2, [22, p. 145].)

The *range* of the operator K will be denoted by $R(K)$: similarly, the range of K^* is denoted by $R(K^*)$. The following corollaries to Theorem 1 easily follow.

COROLLARY 1.1. *Suppose* $\mu_n \to \infty$ *as* $n \to \infty$. *Let* $g \in R(K)$ *and* $\varepsilon > 0$ *be arbitrary. Then there exists a function* $g' \in L_2$ *such that*:

$g' \notin R(K)$,

g' *satisfies condition* (b) *of Theorem* 1 *and*

$\|g - g'\| < \varepsilon$.

---

[3] The manner of convergence in (10) can be stated in slightly stronger form. but such a version is not needed here. All subsequent infinite series of elements of L_2 are to be interpreted as limits in the mean. For convenience, we write all sums over the singular functions as infinite series. Proper interpretation should be made if the spectrum is finite.

Proof. Let $\{a_n\}_{n=1}^{\infty}$ be a sequence of real numbers such that $\sum_{n=1}^{\infty} |a_n|^2 < \varepsilon^2$, but $\sum_{n=1}^{\infty} \mu_n^2 a_n^2$ diverges. Because $\mu_n \to \infty$ by hypothesis, such a sequence can always be constructed. By the Riesz–Fischer theorem there exists an L_2-function g'' defined by $g'' = \sum_{n=1}^{\infty} a_n u_n$. Put $g' = g + g''$. Since g'' does not satisfy condition (a) of Theorem 1, neither does g'. Now suppose $u \in L_2$ such that $K^*u = 0$. Then $\langle u, u_n \rangle = 0$ for all n and

$$\langle g', u \rangle = \langle g, u \rangle + \lim_{N \to \infty} \sum_{n=1}^{N} a_n \langle u_n, u \rangle. \tag{14}$$

Since $\langle g, u \rangle = 0$ by hypothesis, it follows from (14) that $\langle g', u \rangle = 0$ in accordance with condition (b) of Theorem 1. Finally, by Parseval's equation,

$$\|g - g'\|^2 = \sum_{n=1}^{\cancel{N}\infty} |a_n|^2 < \varepsilon^2.$$

We define U as the *space spanned* by $\{u_n\}$, i.e., the set consisting of all linear combinations of the form $\sum_{n=1}^{N} \alpha_n u_n$, together with all mean-square limits of such combinations. In an analogous manner we define V as the *space spanned* by $\{v_n\}$. It follows from (12) and (13) that

$$R(K) \subset U \quad \text{and} \quad R(K^*) \subset V. \tag{15}$$

Note that any element $\bar{h} \in L_2$ can be uniquely decomposed as

$$\bar{h} = h + h^{\perp}, \tag{16}$$

where $h \in U$, $h^{\perp} \in U^{\perp}$ and we define

$$U^{\perp} = \{p \in L_2 | \langle p, u_n \rangle = 0 \text{ for all } n\}.$$

The element h is called the *projection* of $\bar{h}$ onto U. We shall sometimes write $P_U \bar{h}$ to denote h. The only element common to U and $U^{\perp}$ is the zero element. (To see this note that any element $u \in U$ has the form $u = \sum_{n=1}^{\infty} \langle u, u_n \rangle u_n$, but if $u \in U^{\perp}$, then all $\langle u, u_n \rangle = 0$.) In an analogous manner we define V and $P_V \bar{h}$ for $\bar{h} \in L_2$. The decomposition used here is similar to that employed by Kammerer and Nashed [11].

We present one more easy corollary to Theorem 1.

COROLLARY 1.2. *If $\mu_n \to \infty$ as $n \to \infty$, then $R(K)$ is not closed.*

Proof. The sequence $\{t_N\}_{N=1}^{\infty}$, where $t_N = \sum_{n=1}^{N} a_n u_n$, a_n as in Corollary 1.1, has no limit in $R(K)$, although $\{t_N\}_{N=1}^{\infty}$ is a Cauchy sequence in L_2 and in fact has a limit in U. It can be shown that $\overline{R(K)} = U$ and $\overline{R(K^*)} = V$. The following theorem is essential to an understanding of the convergence properties of the iteration (4).

THEOREM 4. *Consider the equation*

$$K^*Kf = K^*\bar{g}, \quad \textit{where } \bar{g} \in L_2. \tag{17}$$

Let $\bar{g}$ be projected onto U as $\bar{g} = g + g^{\perp}$, $g \in U$, $g^{\perp} \in U^{\perp}$. Then:

(a) *Equation* (17) *is consistent in L_2 if and only if $g \equiv P_U \bar{g} \in R(K)$.*

(b) *The set of solutions of* (17) *does not depend on $g^{\perp}$.*

(c) *Any two solutions of* (17) *differ by an element of $V^{\perp}$.*

(d) *If f is a solution of* (17), *then so is $f + f^{\perp}$, where f is an arbitrary element of $V^{\perp}$.*

(e) *If* (17) *is consistent, then there is a unique solution $\tilde{f}$ such that $\tilde{f} \in V$.*

Proof. (a) If $g \in R(K)$, then f exists such that $Kf = g$ and $K^*Kf = K^*g = K^*(g + g^{\perp}) = K^*\bar{g}$ by Theorem 2. Conversely, suppose (17) has an L_2-solution f. Then $K^*Kf = K^*\bar{g} = K^*g$ and $K^*(Kf - g) = 0$. According to Theorem 2 this implies $Kf - g \in U^{\perp}$. Since $Kf \in R(K) \subset U$ and $g \in U$ by the projection, it follows that $Kf - g \in U$. Since $Kf - g$ is an element of both U and $U^{\perp}$, it follows that $Kf = g$.

(b) This follows from the fact that $K^*(g + g^{\perp}) = K^*g$ for any $g^{\perp} \in U^{\perp}$.

(c) Let f_1 and f_2 be solutions of (17). Then, by subtraction, $K^*K(f_1 - f_2) = 0$ and for $n = 1, 2, \cdots$ we have

$$\langle f_1 - f_2, v_n \rangle = \mu_n^2 \langle f_1 - f_2, K^*Kv_n \rangle = \mu_n^2 \langle K^*K(f_1 - f_2), v_n \rangle = \mu_n^2 \langle 0, v_n \rangle = 0.$$

(d) By Theorem 2, $K^*K(f + f^{\perp}) = K^*Kf = \bar{g}$.

(e) Let $\tilde{f}_1 \in V$ and $\tilde{f}_2 \in V$ be solutions of (17). Then $\tilde{f}_1 - \tilde{f}_2$ is an element of both V and $V^{\perp}$ by (c) and consequently $\tilde{f}_1 = \tilde{f}_2$.

According to this theorem, if $g \in R(K)$, then every solution f of (17) has the form

$$f = \tilde{f} + f^{\perp}, \tag{18}$$

where $\tilde{f}$ is a fixed element of V (which depends on g), and $f^{\perp}$ is an arbitrary element of $V^{\perp}$. It follows from (18) that

$$\|f\|^2 = \|\tilde{f}\|^2 + \|f^{\perp}\|^2 \geqq \|\tilde{f}\|^2 \quad \text{for all } f \text{ satisfying (17).} \tag{19}$$

Because of this, $\tilde{f}$ (which is also the Picard sum (10)) is called the *least squares solution of minimum norm* for $Kf = \bar{g}$. It will presently be seen that Landweber's iteration converges to $\tilde{f}$ if $P_U\bar{g} \in R(K)$ and the starting function f_0 is an element of V. The convergence of certain other iterative processes to $\tilde{f}$ has recently been studied (in greater generality than is done here) by Kammerer and Nashed [11].

We now consider the case in which the right-hand side of (2) is a measured function with error. In practice, measurements are taken for only a finite number of x-values; however, in the arguments presented here we consider measurements for a *continuum* of x-values,[4] and define the error function as $\varepsilon(x)$. It is assumed that the physical (or other) process being described by (2) has been correctly formulated, so that the equation has a solution in the absence of error. Note that the results of any simplifying assumptions inherent in the derivation of (2) from physical reasoning can be lumped into $\varepsilon(x)$ along with the other errors. Thus, we are confronted with the equation

$$Kf = g + \varepsilon, \tag{20}$$

---

[4] In the examples we also consider a matrix case with a finite number of x-values. For the general case of compact operators and (finite- or infinite-dimensional) Hilbert spaces, see Strand [23]

where $g \in R(K)$ and ε is an error function. In view of Corollary 1.1, it is not reasonable to expect $g + \varepsilon$ to satisfy the conditions of Theorem 1. Furthermore, *g and ε can never be separated from each other.* Therefore, the problem we are given normally has no solution at the outset; however, we can still make an estimate of the solution of $Kf = g$, and the quality of this estimate would be expected to depend on the size of the error function, ε. Such an estimate can be made by simply taking f_N (equation (11)) as the estimator. This is the estimate used by Hanson [10] and Baker et al. [1]. The estimator f_N will be called the *truncated Picard series* or the *expansion in terms of the first N harmonics.* Note that it is inherent in the measurement process that

$$\|\varepsilon\|^2 \geqq \|g + \varepsilon\|^2 - \sum_{n=1}^{\infty} |\langle g + \varepsilon, u_n\rangle|^2. \tag{21}$$

This follows from (15), as any component of $g + \varepsilon$ orthogonal to U is necessarily pure error. A good estimation process should remove the effect of such components of error.

To facilitate the discussion, let

$$\begin{aligned} U_N &\equiv \text{algebraic span of } u_1, u_2, \cdots, u_N \equiv \operatorname{asp}\{u_1, \cdots, u_N\}, \\ V_N &\equiv \operatorname{asp}\{v_1, \cdots, v_N\}, \end{aligned} \tag{22}$$

from which (see (9) and (15))

$$U_N \subset R(K) \subset U \quad \text{and} \quad V_N \subset R(K^*) \subset V. \tag{23}$$

Further define

$$g_N = \sum_{n=1}^{N} \langle g, u_n\rangle u_n \quad \text{for } g \in L_2. \tag{24}$$

Then from (9) and (11)

$$Kf_N = g_N. \tag{25}$$

Consider the truncated Picard-series approximation to the solution $\tilde{f}$ of (17) as defined in Theorem 4:

$$f_N = \sum_{n=1}^{N} \langle g, u_n\rangle \mu_n v_n + \sum_{n=1}^{N} \langle \varepsilon, u_n\rangle \mu_n v_n.$$

If $\tilde{f}$ is the full Picard-series solution of $Kf = g$, then

$$\tilde{f} - f_N = \sum_{n=N+1}^{\infty} \langle g, u_n\rangle \mu_n v_n - \sum_{n=1}^{N} \langle \varepsilon, u_n\rangle \mu_n v_n.$$

From this, we obtain

$$\|\tilde{f} - f_N\|^2 = \sum_{n=1}^{N} |\langle \varepsilon, u_n\rangle|^2 \mu_n^2 + \sum_{n=N+1}^{\infty} |\langle g, u_n\rangle|^2 \mu_n^2. \tag{26}$$

Since $0 < \mu_1 \leqq \mu_2 \leqq \cdots$, we have

$$\sum_{n=1}^{N} |\langle \varepsilon, u_n\rangle|^2 \mu_n^2 \leqq \mu_N^2 \cdot \sum_{n=1}^{N} |\langle \varepsilon, u_n\rangle|^2 \leqq \mu_N^2 \|\varepsilon\|^2. \tag{27}$$

Note that equality can be achieved in (27) if ε is a multiple of u_N. From (26) and (27) we therefore obtain the following (sharp) error bound:

$$\|\tilde{f} - f_N\| \leqq \left[\mu_N^2\|\varepsilon\|^2 + \sum_{n=N+1}^{\infty} |\langle g, u_n\rangle|^2\mu_n^2\right]^{1/2}. \tag{28}$$

This error estimate can never be computed without more information about the unknown function $\tilde{f}$ as the true right-hand side g cannot be found in the presence of error. However, in the commonly-occurring case where the spectrum is infinite, (28) does give a qualitative picture of the behavior of the error in estimating $\tilde{f}$ as N is increased. For small N the remainder series

$$\sum_{n=N+1}^{\infty} |\langle g, u_n\rangle|^2\mu_n^2$$

predominates. As N is increased, this series decreases, but even a moderate component of ε in the "direction" of u_N is magnified by larger and larger factors μ_N^2, so that the norm $\|\tilde{f} - f_N\|$ finally becomes unacceptably large. If the spectrum is not infinite but is such that some of the μ_N are large, similar considerations apply. Inequality (28) also illustrates the indeterminate nature of the integral equation of the first kind. This ambiguity is not caused by the method of solution, but is inherent in the original equation (20). As was mentioned earlier, other methods are confronted with a similar ambiguity. Finally, note that if $P_U(g + \varepsilon)$ is not an element of $R(K)$, then condition (a) of Picard's theorem cannot be satisfied by $P_U(g + \varepsilon)$ so that $\|f_N\| \to \infty$ as $N \to \infty$. In the present case, the cutoff level

$$\mu_N^2 = 1/a, \tag{29}$$

say, must be assigned before the solution becomes well-defined. In the absence of a priori knowledge about $\tilde{f}$, one of the following three procedures for determining N might be reasonable, but must be used with caution. We assume in I and III below that $\|\varepsilon\|$ is approximately known.

I. Increase N until the residual function $R_N = (g + \varepsilon)_N - (g + \varepsilon)$ *barely* satisfies

$$\|R_N\| \leqq \|\varepsilon\|. \tag{30}$$

Some idea of the error in estimating $\tilde{f}$ is then obtained by setting the remainder series to zero to get (roughly):

$$\|\tilde{f} - f_N\| \leqq \mu_N \cdot \|\varepsilon\|. \tag{31}$$

II. Take N as the smallest integer such that R_N appears to be a random function. One may then assign to $\|\varepsilon\|$ a value equal to twice the root-mean-square value of R_N, and estimate the error by (31).

III. Determine beforehand the largest error Δf that can be tolerated. Then assume the remainder series in (28) is negligible, so that N is determined approximately from

$$\mu_N^2 = \|\Delta f\|^2/\|\varepsilon\|^2. \tag{32}$$

A procedure similar to this has also been proposed by Twomey [29].

None of the three procedures described above is entirely satisfactory; they all suffer from the same shortcoming: the assumption that the remainder series is negligible. Cases can arise in which, for increasing N, the remainder series is still large when the possible value of $\mu_N^2 \cdot \|\varepsilon_N\|^2$ has increased to an unacceptable value. Although procedure III attempts to make the remainder series as small as possible consistent with an acceptable error in f, it is clear that it will not always succeed. Procedure I can fail because, due to the increasing nature of the μ_n, it is easily possible for R_N to satisfy (30) even though the remainder series is large. Procedure II has essentially the same limitation. Some sort of asymptotic estimate of the terms in the remainder series, or some a priori knowledge of the harmonic structure of the correct solution, would, or course, improve the situation greatly. Finding the proper cutoff level (29) is essentially a problem in filtering which must be faced if optimum or near-optimum results are to be obtained. We assume in the next section that a cutoff level has been determined, so that N is to be chosen from an equation of the form (29), where a is known. We also assume that the equation $Kf = g$ has been normalized so that $0 < 1/\mu_1^2 = \lambda_1 \leqq 1$. This inequality can always be guaranteed in the integral-equation case after dividing both sides of (1) by

$$\left[\int_0^1 \int_0^1 K^2(x, y)\, dx\, dy\right]^{1/2} \tag{33}$$

and in the matrix case after dividing by $[\text{trace } A^T A]^{1/2}$. For purposes of study (§ 3), we often normalize $K(x, y)$ such that $\lambda_1 = 1$.

3. The generalized Landweber iteration. Let $f_0 \in L_2[0, 1]$ and consider the iteration

$$\hat{f}_k = \hat{f}_{k-1} + DK^*(g - K\hat{f}_{k-1}), \qquad k = 1, 2, \cdots, \tag{4}$$

where D is an operator to be specified. In this section and the following section we prove the general convergence properties of the iteration (4) and study its behavior as applied to singular functions for various values of the μ_N and a certain restricted class of operators D. A systematic procedure is then developed to choose the operator D to approximate a cutoff of harmonics in accordance with (29). The study of the resulting "response" to various harmonics is analogous to the study of frequency response in ordinary Fourier analysis. An advantage of using a "shaped" iteration process is that it provides a specified singular-function expansion without the necessity of obtaining the singular functions u_n and v_n. The analysis also provides a new quantitative method of studying the effects of iterative procedures, and a method of designing the response (after a specified finite number of iterations) to achieve a desired effect.

We begin by restricting the class of operators D. First note from (4) that D needs to be defined only on the set of elements of the form K^*u, $u \in L_2$. Since $R(K^*) \subset V$ (see (23)) and since $\{v_n\}$ is an orthonormal basis for V, the definition of D is complete if the image under D of each singular function v_n is specified. Sufficient generality for the purposes of this paper is achieved by letting

$$Dv_n = p_n v_n, \qquad n = 1, 2, \cdots, \tag{34}$$

where we assume that $0 < p_n\lambda_n < 2$ for all n and that the sequence $\{p_n\}_{n=1}^{\infty}$ is bounded. In practice (§4) we shall let $D = F(K^*K)$, where $F(\lambda)$ is a rational fraction and $0 < \lambda F(\lambda) < 2$ for all $\lambda \leqq \lambda_1$. Clearly this choice will satisfy (34). It can be seen that the operator D defined by (34) maps V into V; that is, if $v = \sum_{n=1}^{\infty} \alpha_n v_n$, then

$$Dv = \sum_{n=1}^{\infty} \alpha_n p_n v_n \in V, \tag{35}$$

because the boundedness of the p_n implies $\sum_{n=1}^{\infty} \alpha_n^2 p_n^2 < \infty$.

Before studying the response we first derive the kth iterate of (4) and prove some general convergence theorems. Following Landweber's general approach [12], let

$$\gamma_k = \hat{f}_k - \hat{f}_{k-1}, \qquad k = 1, 2, \cdots. \tag{36}$$

Then

$$\hat{f}_k = \hat{f}_0 + \sum_{i=1}^{k} \gamma_i. \tag{37}$$

By (4),

$$\gamma_k = DK^*(g - K\hat{f}_{k-1}),$$

$$\gamma_k - \gamma_{k-1} = -DK^*K\gamma_{k-1}.$$

From this,

$$\gamma_k = (I - DK^*K)\gamma_{k-1},$$

and consequently,

$$\gamma_k = (I - DK^*K)^{k-1}\gamma_1, \qquad k = 1, 2, \cdots. \tag{38}$$

Summing (38) as a geometric progression in accordance with (37) gives

$$\hat{f}_k = \hat{f}_0 + \left\{\frac{I - (I - DK^*K)^k}{DK^*K}\right\} DK^*(g - K\hat{f}_0), \tag{39}$$

where the operator in braces in (39) represents that polynomial in DK^*K obtained by canceling DK^*K from the numerator and denominator. We are now prepared to state and prove the main theorems concerning the convergence of (4). They may be summarized by the statement that $\hat{f}_k$ converges as $k \to \infty$ if and only if the projection of g onto U is in $R(K)$. If $\hat{f}_k$ does not converge, then $\|\hat{f}_k\| \to \infty$ as $k \to \infty$.

THEOREM 5. *Let the operator D be defined as in* (34) *with* $0 < \lambda_n p_n < 2$ *for all* n, *and suppose that the sequence* $\{p_n\}$ *is bounded. Let* $\bar{g} = P_U\bar{g} + g^{\perp} = g + g^{\perp}$, $g \in U$, $g^{\perp} \in U^{\perp}$, *where we assume* $g \in R(K)$. *Let* $\hat{f}_0$ *be any element of* L_2, *where* $\hat{f}_0 = P_V\hat{f}_0 + f^{\perp} = f + f^{\perp}$, $f \in V$, $f^{\perp} \in V^{\perp}$. *Then*

$$\lim_{k\to\infty} \hat{f}_k = \tilde{f} + f^{\perp}, \tag{40}$$

where $\tilde{f}$ *is the least-squares solution of minimum norm for* $Kf = \bar{g}$.

Proof. According to (39),

$$\hat{f}_k = f + f^{\perp} + \left\{\frac{I - (I - DK^*K)^k}{DK^*K}\right\} DK^*(\bar{g} - Kf - Kf^{\perp}),$$

$$\hat{f}_k = f^{\perp} + \left[f + \left\{\frac{I - (I - DK^*K)^k}{DK^*K}\right\} DK^*(g - Kf)\right]. \tag{41}$$

Since the bracketed quantity in (41) is exactly the result of applying k iterations to $f \in V$ with a right-hand side $g \in R(K) \subset U$, we need only show that

$$\lim_{k \to \infty} \hat{f}_k = \tilde{f}$$

whenever $\hat{f}_0 \in V$ and $g \in R(K)$. Under these assumptions, we have $K\tilde{f} = g$ and $\hat{f}_k = \hat{f}_0 + \{I - (I - DK^*K)^k\}(\tilde{f} - \hat{f}_0)$ or

$$\hat{f}_k = \tilde{f} - (I - DK^*K)^k(\tilde{f} - \hat{f}_0) \tag{42}$$

and the proof reduces to showing that

$$\lim_{k \to \infty} \|(I - DK^*K)^k(\tilde{f} - \hat{f}_0)\| = 0. \tag{43}$$

Because $\tilde{f} - \hat{f}_0 \in V$, the series

$$\sum_{n=1}^{\infty} |\langle \tilde{f} - \hat{f}_0, v_n \rangle|^2 \tag{44}$$

is convergent and

$$\tilde{f} - \hat{f}_0 = \sum_{n=1}^{\infty} \langle \tilde{f} - \hat{f}_0, v_n \rangle v_n. \tag{45}$$

Then, since the v_n are eigenfunctions of K^*K, and since the operator $(I - DK^*K)^k$ is continuous,

$$\begin{aligned} (I - DK^*K)^k(\tilde{f} - \hat{f}_0) &= \sum_{n=1}^{\infty} \langle \tilde{f} - \hat{f}_0, v_n \rangle (I - DK^*K)^k v_n \\ &= \sum_{n=1}^{\infty} \langle \tilde{f} - \hat{f}_0, v_n \rangle (1 - p_n\lambda_n)^k v_n. \end{aligned} \tag{46}$$

Assume that $\varepsilon > 0$ is given. Because of the convergence of (44), there exists N_0 so large that

$$\sum_{n=N_0+1}^{\infty} |\langle f - \hat{f}_0, v_n \rangle|^2 < \varepsilon^2/2. \tag{47}$$

Since $0 < \lambda_n p_n < 2$ by hypothesis, we have

$$|1 - \lambda_n p_n| < 1 \quad \text{for all } n \tag{48}$$

and

$$\begin{aligned} \sum_{n=N_0+1}^{\infty} &|\langle (I - DK^*K)^k(\tilde{f} - \hat{f}_0), v_n \rangle|^2 \\ &= \sum_{n=N_0+1}^{\infty} |1 - \lambda_n p_n|^{2k} |\langle \tilde{f} - \hat{f}_0, v_n \rangle|^2 \\ &\leqq \sum_{n=N_0+1}^{\infty} |\langle \tilde{f} - \hat{f}_0, v_n \rangle|^2 < \varepsilon^2/2, \end{aligned} \tag{49}$$

where inequality (49) holds for every k. On account of the strict inequality (48), there exists k_0 so large that

$$\sum_{n=1}^{N} |\langle (I - DK^*K)^k(\tilde{f} - \hat{f}_0), v_n\rangle|^2 = \sum_{n=1}^{N} |1 - \lambda_n p_n|^{2k} |\langle \tilde{f} - \hat{f}_0, v_n\rangle|^2 < \varepsilon^2/2 \tag{50}$$

for all $k > k_0$, since the sum here is finite.

Combining (49) and (50) and noting that $(I - DK^*K)^k$ maps V into V gives

$$\|(I - DK^*K)^k(\tilde{f} - \hat{f}_0)\| = \left[\sum_{n=1}^{\infty} |\langle (I - DK^*K)^k(\tilde{f} - \hat{f}_0), v_n\rangle|^2\right]^{1/2} < \varepsilon \quad \text{for all } k > k_0. \tag{51}$$

In Theorem 5 it is necessarily true that $\lim_{n\to\infty} \lambda_n p_n = 0$ if $\lambda_n = 1/\mu_n^2 \to 0$ as $n \to \infty$ because the p_n are bounded by hypothesis. By operating on v_n we see that $\|I - DK^*K\| \geqq 1$ if the μ_n are unbounded. To show that this means $\|I - DK^*K\| = 1$, let $\bar{f}$ be any element of L_2 and project $\bar{f}$ as $\bar{f} = P_V\bar{f} + f^\perp = f + f^\perp$, $f \in V$, $f^\perp \in V^\perp$. Then

$$\begin{aligned}\|(I - DK^*K)\bar{f}\|^2 &= \sum_{n=1}^{\infty} |\langle f, v_n\rangle|^2 \cdot |1 - \lambda_n p_n|^2 + \|f^\perp\|^2 \\ &\leqq \sum_{n=1}^{\infty} |\langle f, v_n\rangle|^2 + \|f^\perp\|^2 = \|\bar{f}\|^2.\end{aligned}$$

It can be shown that if $\|I - DK^*K\| < 1$ (a condition one might be tempted to impose judging from the appearance of (39)), then the number of u_n (and v_n) is necessarily finite and DK^*K has a bounded inverse. A proof and discussion of this result for the general compact-operator case is given by Strand [23].

COROLLARY 5.1. *Let D be defined as in* (34) *where $0 < p_n v_n < 2$ and the p_n are bounded. Let $\hat{f}_{01}$ and $\hat{f}_{02}$ be arbitrary elements of V. Then for the sequences $\{\hat{f}_{k1}\}_{k=1}^{\infty}$ and $\{\hat{f}_{k2}\}$ generated by* (4) *with starting functions $\hat{f}_{01}$ and $\hat{f}_{02}$, respectively, we have*

$$\lim_{k\to\infty} \|\hat{f}_{k1} - \hat{f}_{k2}\| = 0\,. \tag{52}$$

Remark. If the iteration (4) converges to $\tilde{f}$ for one starting function in V, it converges to $\tilde{f}$ for any other starting function in V. Equation (52) is valid whether $\hat{f}_{k1}$ and $\hat{f}_{k2}$ define separate convergent sequences or not. Thus, if (4) diverges for any starting function in V, it diverges for all starting functions in V.

Proof. By (39) and by subtraction,

$$(\hat{f}_{k1} - \hat{f}_{k2}) = (\hat{f}_{01} - \hat{f}_{02}) + \left\{\frac{I - (I - DK^*K)^k}{DK^*K}\right\} DK^*[0 - K(\hat{f}_{01} - \hat{f}_{02})]. \tag{53}$$

Since (53) is the same as (39) applied to $Kf = 0$ with a starting function $\hat{f}_{01} - \hat{f}_{02} \in V$, and since for this equation $\tilde{f} = 0$, (52) follows from Theorem 5.

THEOREM 6. *Let the operator D be defined as in* (34) *with $0 < p_n\lambda_n < 2$ for all n, and suppose that the sequence $\{p_n\}$ is bounded. Let $\tilde{g} = P_U\tilde{g} + g^\perp = g + g^\perp$,*

$g \in U$, $g^{\perp} \in U^{\perp}$, where $g \notin R(K)$. Then if (4) *is applied to $Kf = \bar{g}$, we have $\|f_k\| \to \infty$ as $k \to \infty$.*

Proof. By Corollary 5.1 we may take $\hat{f}_0 = 0$ and consider the sequence

$$\hat{f}_k = \left\{ \frac{I - (I - DK^*K)^k}{DK^*K} \right\} DK^*g. \tag{54}$$

Because $g \in U$ by hypothesis, we have

$$g = \sum_{n=1}^{\infty} \langle g, u_n \rangle u_n \tag{55}$$

and by condition (a) of Picard's theorem (note that (b) is satisfied by any element of U), the series

$$\sum_{n=1}^{\infty} |\langle g, u_n \rangle|^2 \mu_n^2 \tag{56}$$

diverges. Substitute (55) into (54):

$$\hat{f}_k = \left\{ \frac{I - (I - DK^*K)^k}{DK^*K} \right\} DK^* \left[\sum_{n=1}^{\infty} \langle g, u_n \rangle u_n \right]. \tag{57}$$

The operator $\{[I - (I - DK^*K)^k]/DK^*K\}DK^*$ is bounded and therefore continuous for every finite k, as it has the form $P(DK^*K)DK^*$, where P is a polynomial of degree $(k - 1)$. (The norm of this operator can be expected to grow with k.) Thus we may operate termwise in (57) to obtain

$$\hat{f}_k = \sum_{n=1}^{\infty} \langle g, u_n \rangle \left\{ \frac{I - (I - DK^*K)^k}{DK^*K} \right\} DK^*u_n. \tag{58}$$

Substituting (9) $u_n = \mu_n K v_n$ and noting that the v_n are eigenfunctions of K^*K gives

$$\hat{f}_k = \sum_{n=1}^{\infty} [1 - (1 - p_n\lambda_n)^k] \mu_n \langle g, u_n \rangle v_n, \tag{59}$$

valid for every finite k. Let N be any (large) positive integer. Then since $0 < p_i\lambda_i < 2$, $i = 1, 2, \cdots, N$, where the inequalities are strict, there exists k_N so large that

$$[1 - (1 - p_1\lambda_1)^{k_N}], \cdots, [1 - (1 - p_N\lambda_N)^{k_N}]$$

are all greater than 1/2. Thus, for $k \geqq k_N$,

$$\begin{aligned} \|\hat{f}_k\|^2 &\geqq \sum_{n=1}^{N} [1 - (1 - p_n\lambda_n)^k]^2 \mu_n^2 |\langle g, u_n \rangle|^2 \\ &\geqq \frac{1}{4} \sum_{n=1}^{N} \mu_n^2 |\langle g, u_n \rangle|^2. \end{aligned}$$

Since this latter series diverges (see (56)), it follows that $\|\hat{f}_k\|^2 \to \infty$ as $k \to \infty$.

Qualitative remarks. It follows from Theorem 6 that applying the iteration (4) to a right-hand side, $\bar{g}$ for which $P_U\bar{g} \notin R(K)$ will produce unbounded iterates $\hat{f}_k$ as $k \to \infty$ for any starting function $\hat{f}_{01}$ whatsoever. By Corollary 5.1 use of a *different* starting function $\hat{f}_{02}$ will give iterates that become indistinguishable from those resulting from $\hat{f}_{01}$ for large k. Recalling that the L_2-norm of a function $f \in L_2$ is $\int_0^1 [f(y)]^2\,dy$ shows that the functional values *must become large* in absolute value for large k. Thus, if $P_U\bar{g} \notin R(K)$, absurd results can be guaranteed for sufficiently large k. For this reason, difficulty can be expected as $k \to \infty$ if the right-hand side of (1) has been contaminated with error. In practice, this will be true even if the spectrum is not infinite, but contains some large μ_n. The situation is analogous to that which occurs with an asymptotic series. In spite of the fact that $\hat{f}_k$ becomes infinite as $k \to \infty$, one may obtain a reasonable estimate of $\bar{f}$ by properly choosing a finite value of k together with an appropriate choice of D. In fact, if the resulting estimate approximates a truncated Picard series for which eigenfunctions of K^*K having $1/\mu_i^2 = \lambda_i < a$ are excluded, then the error in $\hat{f}_k$ will be governed by inequality (28) and a useful approximation becomes possible if a has been properly chosen. The iteration (4) is essentially a smoothing process for which the amount of smoothing is inversely related to the number of iterations.

In the next section we derive a method for approximating a Picard series truncated at $\lambda = a$ by the use of (4). Such an approximation has an added advantage of not requiring the calculation of any singular functions u_n or v_n.

4. "Shaping" the response to the various harmonics. In this section we treat the iteration number k as a finite positive integer and develop a rational method of determining the operator D. Recall our assumption that

$$Dv_n = p_n v_n, \qquad 0 < p_n\lambda_n < 2, \tag{34}$$

where the p_n are bounded. We assume for convenience that $\lambda_1 = 1$. The Picard series for $Kf = g$, truncated to eliminate all λ_n such that $\lambda_n = 1/\mu_n^2 < a$, can be written as

$$\sum_{\lambda_n \geqq a} \langle g, u_n\rangle \mu_n v_n = \sum_{n=1}^{\infty} \langle g, u_n\rangle \mu_n H_a(\lambda_n) v_n, \tag{60}$$

where

$$H_a(\lambda) = \begin{cases} 1, & \lambda \geqq a, \\ 0, & \lambda < a. \end{cases} \tag{61}$$

In this paper we use an extremely simple method of achieving (34): we let

$$D = F(K^*K), \tag{62}$$

where $F(\lambda)$ is a polynomial or rational fraction and

$$0 < \lambda F(\lambda) < 2 \quad \text{for} \quad 0 < \lambda \leqq 1. \tag{63}$$

Then D complies with (34) with

$$p_n = F(\lambda_n), \qquad n = 1, 2, \cdots. \tag{64}$$

Comparison of (59) and (60) shows that a truncation at $\lambda_n = a$ is achieved for all $k \geqq 1$ if $\lambda F(\lambda) = H_a(\lambda)$ and that (59) will approximate (60) for a given k if the function

$$R_k(\lambda) = 1 - [1 - \lambda F(\lambda)]^k, \qquad 0 < \lambda \leqq 1, \tag{65}$$

approximates the Heaviside step function $H_a(\lambda)$.

In a forthcoming paper Crone [4] defines a numerical filter for which the filter function $\lambda F(\lambda)$ is a rational fraction. He studies a filtering process analogous to Twomey's method [27] and does not study iterative procedures. Mateer [13] defines the smoothing inherent in the original Twomey method [27] by an analysis of a rational-fraction response with no iteration, as does Twomey in a later paper [28]. In the present paper we first study cases in which $\lambda F(\lambda)$ is a *polynomial*, and in Example 4, § 5, we study the iterated Twomey process for which $\lambda F(\lambda)$ is a certain rational fraction. It will be seen that many choices are possible. If $\lambda F(\lambda)$ closely approximates $H_a(\lambda)$, then the desired response is achieved in one iteration; otherwise, as will be seen, a judiciously chosen polynomial $\lambda F(\lambda)$ will be such that the response is improved with subsequent iterations. The curve defined by (65) completely determines the singular-function response of the solution after k iterations and will be called the *response curve after k iterations* associated with $D = F(K^*K)$. Now for any fixed k (with the general definition (34) of D) the effect on the solution of the harmonic u_n will become negligible as $\lambda_n \to 0$, as the corresponding term of the solution has magnitude (see (59))

$$\{1 - [1 - \lambda_n p_n]^k\} \cdot \frac{1}{\sqrt{\lambda_n}} = k\lambda_n^{1/2} p_n + O(\lambda_n^{3/2}) \to 0 \tag{66}$$

as $\lambda_n \to 0$, since the p_n are bounded. Note that the choice of the polynomial $\lambda F(\lambda)$ does not depend on the operator K, but only on the cutoff value a; however, for any operator K, the operator function $F(K^*K)$ will have to be evaluated. In the matrix case the computation is particularly simple, as D is computed by matrix addition and multiplication, and the matrix DA^T is formed once, where the equation to be solved is $Af = g$. Then DA^T is repeatedly used in the iteration

$$\hat{f}_k = \hat{f}_{k-1} + DA^T(g - A\hat{f}_{k-1}). \tag{67}$$

Several comments about the practical determination of $\lambda F(\lambda)$ and the resulting response curve $R_k(\lambda)$ are in order.

Figures 1 and 2 represent response curves arising from the same polynomial $\lambda F(\lambda)$, but drawn with two different abscissa scales. Figure 1 illustrates the fact that any oscillation of $\lambda F(\lambda)$ about 1 is quickly removed in the response curves for subsequent iterations. When the response appears to have leveled off as in Fig. 2, $k = 25$, $\lambda \geqq 0.007$, say, then $R_k(\lambda) = 1$ to many decimals. For a given polynomial $\lambda F(\lambda)$, the choice of k is made as a compromise between distortion of desired harmonics (k too small) and too much response to unwanted harmonics (k too large). Since the exact value of a is usually not critical, a rounded cutoff in $R_k(\lambda)$ causes no difficulty in practice.

Figure 3 illustrates the fact that $\lambda F(\lambda)$ should not be negative for any λ between 0 and 1 unless it is known that no $\lambda_n = 1/\mu_n^2$ lies in the set $\{\lambda : \lambda F(\lambda) < 0\}$ or unless a very small number k of iterations is contemplated and the resulting

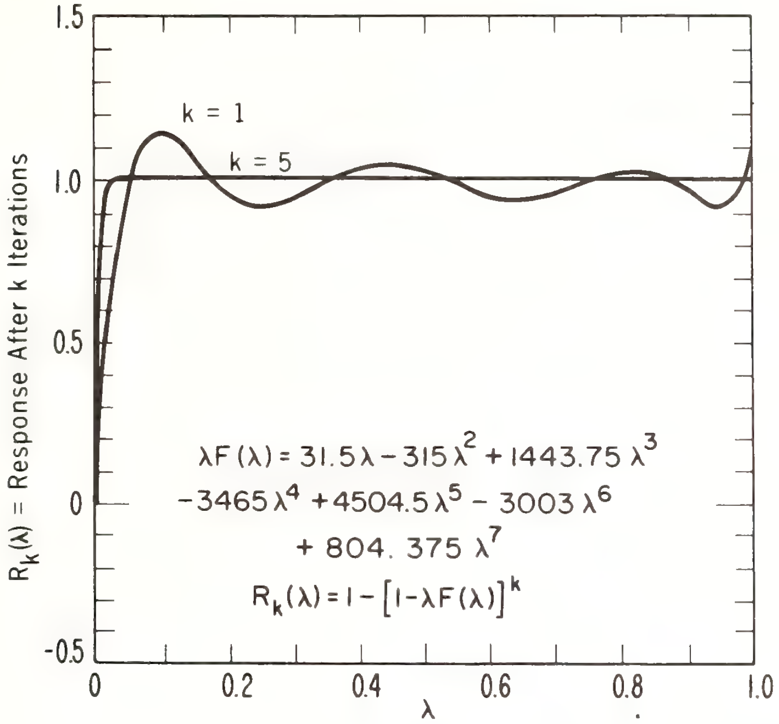

FIG. 1. *Response curves for the 7th degree polynomial obtained using $a = 0$ in (69)*

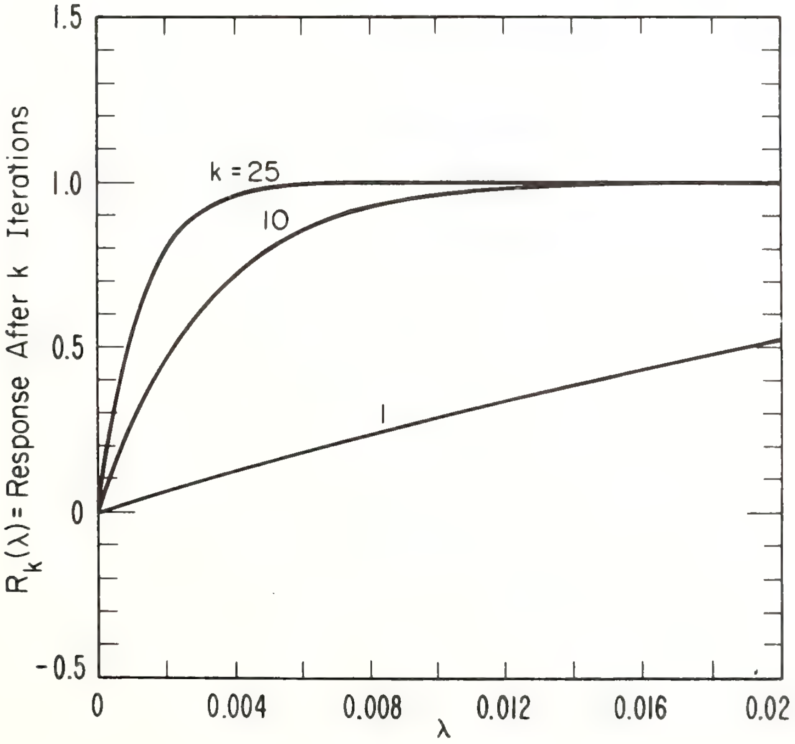

FIG. 2. *Response curves for $\lambda F(\lambda)$ as in Fig. 1*

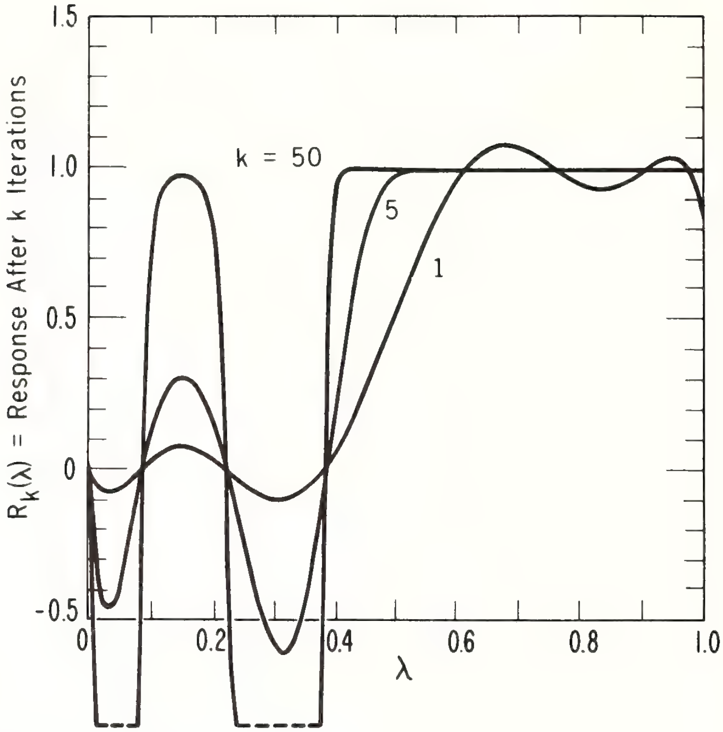

FIG. 3. *Response curves for the 7th degree polynomial obtained using* $a = 0.5$ *in* (69)

response curve is satisfactory. Clearly the response curves in Fig. 3 deteriorate rapidly as k is increased. Similar considerations would apply for $\lambda F(\lambda) > 2$; however, this latter situation is much easier to avoid in approximating $H_a(\lambda)$.

Finding an optimum polynomial for a given a and for a given k is a nontrivial problem. However, satisfactory polynomials for studying the response were obtained by using a mean-square approximation to $H_a(\lambda)$. It was assumed that

$$P(\lambda) = \lambda F(\lambda) = a_1\lambda + a_2\lambda^2 + \cdots + a_m\lambda^m \tag{68}$$

and the criterion

$$\int_0^a P^2(\lambda)\,d\lambda + \int_a^1 [1 - P(\lambda)]^2\,d\lambda = \text{minimum} \tag{69}$$

was used. An ill-conditioned coefficient matrix similar to Hilbert's matrix was encountered in solving for the a_i. This matrix was inverted analytically by using Cauchy's theorem for determinants [17, p. 263]. Double-precision programming was used for all numerical work presented in this paper, so that roundoff errors can be ignored. For $a \to 0$ in (69), a useful polynomial is obtained for small a. In fact, the polynomial $\lambda F(\lambda)$ of Figs. 1 and 2 was obtained in this manner. The cutoff value of $R_k(\lambda)$ can then be largely controlled by adjusting k. For larger a (say $a = 0.5$), (69) gives a polynomial which is negative for some λ as in Fig. 3.

The response can be improved by squaring $\lambda F(\lambda)$ or raising it to some higher even power (see Fig. 4). The resulting operator function is easy to implement in the matrix case. Care must be taken to see that the resulting response for $k = 1$ does not approach or exceed 2 for any λ_i.

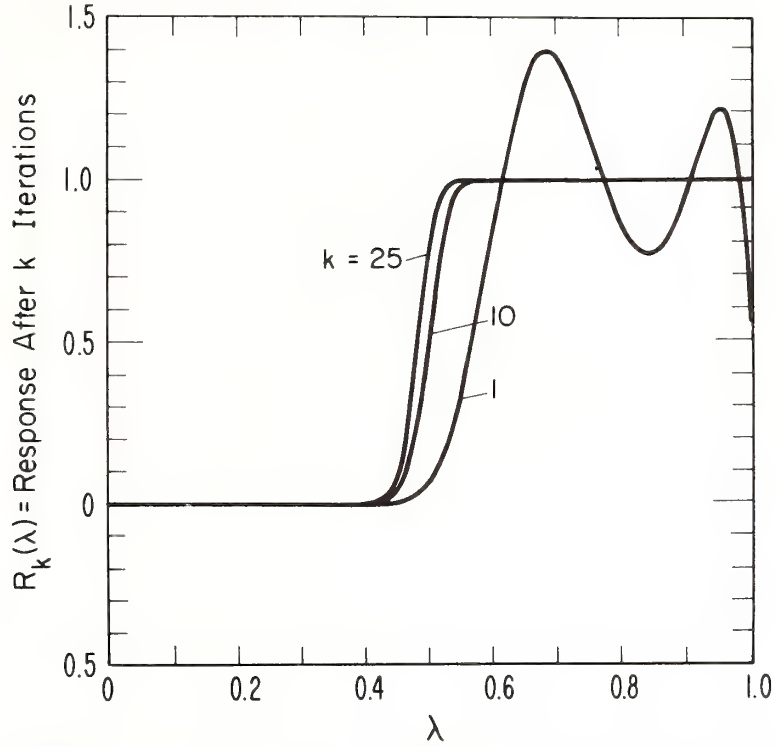

FIG. 4. *Response curves resulting from replacing* $\lambda F(\lambda)$ *by* $[\lambda F(\lambda)]^4$ *for the conditions of Fig. 3*

A study of optimum response polynomials could be made, and tables of coefficients could be constructed, but this has not yet been done. In the next section we present examples illustrating the theory and methods of this paper.

5. Examples.

Example 1. *The original Landweber iteration.* In Landweber's original iteration [12], we have $D = I$, from which

$$\lambda F(\lambda) = \lambda. \tag{70}$$

The response curves $R_k(\lambda)$ are plotted for $k = 1, 10, 20$ and 50 in Fig. 5. It is clear that if high order harmonics contribute substantially to g (equation (20)), then the approach of Landweber's original iteration to a reasonable approximation to $\tilde{f}$ will necessarily be extremely slow.

Example 2. *An underdetermined matrix system.* Consider the linear system defined by

$$\begin{aligned} x_1 - 0.1\ x_2 + 0.2\ x_3 \qquad &= 1, \\ 2x_2 + 0.1\ x_3 - 0.1x_4 &= 2, \\ -0.1x_1 + 0.01x_2 + 0.03x_3 + 0.5x_4 &= 1. \end{aligned} \tag{71}$$

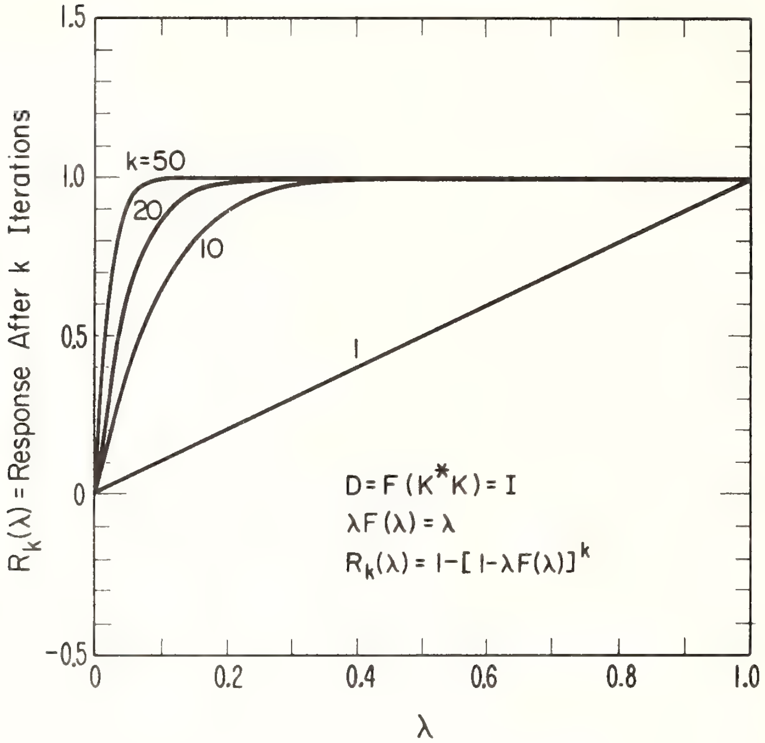

FIG. 5. *Response curves for the original Landweber iteration*

This system has an infinite number of solutions; however the finite singular-function approximations to the vector $x = (x_1, x_2, x_3, x_4)^T$ are easily obtained. We have (after normalization obtained by dividing both sides of (71) by $\sqrt{\lambda_1}$):

$$\lambda_1 = 1, \quad \lambda_2 = 0.260706 \cdots, \quad \lambda_3 = 0.0617974 \cdots.$$

The projection of x onto the algebraic span of all three singular vectors (i.e., the pseudo-inverse solution) is

$$\begin{aligned} x_1 &= 1.011807332 \cdots, & x_2 &= 1.083452084 \cdots, \\ x_3 &= 0.482689377 \cdots, & x_4 &= 2.151731062 \cdots. \end{aligned} \tag{72}$$

The matrix D was determined from the 7th degree polynomial given in Figs. 1 and 2. After 20 iterations agreement with (72) was obtained to 19 decimal places. This is the expected result, as the response curve indicates a cutoff of harmonics far below 0.0617 $\cdots$.

The projection of x onto the *first* singular value (i.e. v_1 for which $\lambda_1 = 1$) is

$$\begin{aligned} x_1 &= -0.0285144395 \cdots, & x_2 &= 0.95899692417 \cdots, \\ x_3 &= 0.0419700695 \cdots, & x_4 &= -0.049156595 \cdots. \end{aligned} \tag{73}$$

The polynomial $\lambda F(\lambda) = \lambda^{20}$ was used. This polynomial has unit response at $\lambda = 1$ and has small response for smaller λ. Clearly the best response to obtain the projection onto v_1 only is given after the *first* iteration. Agreement with (73) to 10 decimals was achieved for $k = 1$.

The projection of x onto the first *two* singular functions is

$$x_1 = 0.9140919429\cdots, \quad x_2 \doteq 0.975574185\cdots, \tag{74}$$
$$x_3 = 0.230338174\cdots, \quad x_4 = -0.111642995\cdots.$$

The polynomial $\lambda F(\lambda)$ was obtained by raising the 15th-degree polynomial obtained from (69), $a = 0.22$, to the 4th power. The response for the squared polynomial is indicated in Fig. 6. Thus the polynomial used has a root near $0.0617\cdots$, so that the response to v_3 is small, as indicated. After 20 iterations agreement with (74) was obtained to about 8 decimal places.

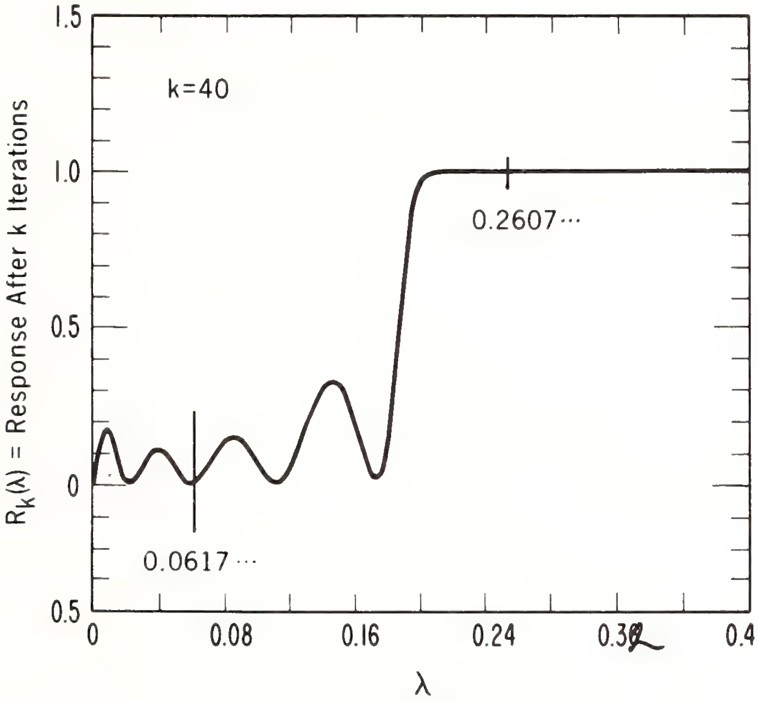

FIG. 6. *Response curve obtained by squaring $\lambda F(\lambda)$ as obtained from* (69) *with $a = 0.22$, degree* 15

In practice, of course, the spectrum of the operator is not known, but this example illustrates the correspondence between the behavior of the iteration and its response curve.

Example 3. Consider the integral equation defined by

$$Kf \equiv \int_0^1 T(x,y)f(y)\,dy = g(x), \qquad g \in L_2[0,1], \tag{75}$$

where

$$T(x,y) = \begin{cases} (1-x)y, & 0 \leqq y \leqq x \leqq 1, \\ x(1-y), & 0 \leqq x \leqq y \leqq 1. \end{cases} \tag{76}$$

The operator K defined by (75) has been studied by Tricomi [26, §§ 3.10, 3.15]. He shows that the singular values and functions are given by

$$1/(\lambda_n)^{1/2} = \mu_n = n^2\pi^2 \tag{77}$$

and

$$u_n \equiv v_n = \sqrt{2}\sin(n\pi x), \qquad 0 \leqq x \leqq 1, \quad n = 1, 2, \cdots. \tag{78}$$

Consequently, if $a_n = \langle g, u_n\rangle = \sqrt{2}\int_0^1 g(x)\sin n\pi x\,dx$, then condition (a) of Picard's theorem (Theorem 1) is $\sum_{n=1}^{\infty} n^4 a_n^2 < \infty$. The results given below follow from Tricomi's results and/or the definition of $T(x, y)$.

First,

$$K^* = K, \tag{79}$$

that is, K is symmetric, and

$$\left[\int_0^1\int_0^1 T^2(x, y)\,dx\,dy\right]^{1/2} = 1/\sqrt{12} \tag{80}$$

(see (33)). Any function $g(x)$ which does not vanish at $x = 0$ and $x = 1$ cannot belong to U and hence is not an element of $R(K)$. If $P(y)$ is a polynomial

$$P(y) = a_0 + a_1 y + \cdots + a_n y^n, \tag{81}$$

then

$$(KP)(x) = b_1 x + b_2 x^2 + \cdots + b_p x^p + b_{p+1}x^{p+1} + b_{p+2}x^{p+2}, \tag{82}$$

where

$$b_m = -\frac{a_{m-2}}{m(m-1)}, \qquad m = 2, 3, \cdots, n + 2, \tag{83}$$

and

$$b_1 = -\sum_{j=2}^{p+2} b_j.$$

If we consider the polynomial $P(y)$ abstractly as a $(p + 1)$-tuple

$$P = (a_0, a_1, \cdots, a_p),$$

then

$$KP = (0, b_1, b_2, \cdots, b_{p+2})$$

is a $(p + 3)$-tuple.

The objective of this example is to study the application of the iteration (4) to a certain polynomial $Q(x)$ given below. As in Example 1, the operator D is taken as the 6th-degree polynomial in $K^*K = K^2$ resulting from $\lambda F(\lambda)$ as defined in Figs. 1 and 2. It would appear that applying operators of high degree in K^2 to a given polynomial $P(y)$ would cause the resulting n-tuple of coefficients to become unmanageably long; however, a little numerical experimentation (with the help of a computer) shows that the higher order coefficients rapidly become small for the images of high powers of K. It was therefore practical to truncate all p-tuples of coefficients to contain no more than a certain number, $p_{\max}$, of components. As a check, $p_{\max}$ was varied between 40 and 50; there was no significant change in the result after 10 iterations. In this example we are concerned with the polynomial

$$g = Q(x) = \frac{x}{30}(3 - 5x^2 + 3x^4 - x^5) \tag{84}$$

in (75). First, in accordance with (33) and (80) we divide by $1/\sqrt{12}$, replacing K by $K\sqrt{12}$ and g by $g\sqrt{12}$ in (75). It follows readily upon integration by parts that

$$g(x) = 24\sqrt{24} \sum_{n=1}^{\infty} l_n u_n(x), \tag{85}$$

where $u_n(x)$ is given by (78) and

$$l_n = [1 - (-1)^n]/n^7\pi^7. \tag{86}$$

Furthermore, $g = Kf$, where

$$f(y) = y - 2y^3 + y^4 = 24\sqrt{2} \sum_{n=1}^{\infty} l_n \cdot n^2\pi^2 v_n(y). \tag{87}$$

In this example g satisfies Picard's theorem. The polynomial $P(y)$ has been chosen so that most of the solution is contained in the first harmonic, that is, to a fair approximation

$$f(y) \cong \frac{96}{\pi^5} \sin \pi y. \tag{88}$$

Note that for the system presently being considered,

$$\lambda_n = 12/n^4\pi^4 = 1/\mu_n^2. \tag{89}$$

The L_2-norm of any polynomial $h(y) = \sum_{j=0}^{p} a_j y^j$ is easily computed from the formula

$$\|h\|^2 = \sum_{i=0}^{p} \sum_{j=0}^{p} a_i a_j/(i + j + 1). \tag{90}$$

All formulas were implemented in a double-precision computer program. For the error-free right-hand side g we obtained

$$\begin{aligned} \|g\| &= 0.077857023200967 \cdots, \\ \|f\| &= 0.221825041882897 \cdots = \left(\frac{107}{126} - \frac{4}{5}\right)^{1/2}. \end{aligned} \tag{91}$$

To generate error functions ε, random numbers were generated and added to the coefficients of $1, x, \cdots, x^6$ in (84). The resulting error norm $\|\varepsilon\|$ was computed from (90).

In order to obtain the projections of the perturbed right-hand sides onto U, the following recursion formula (easily derived by integration by parts) was used:

$$\langle x^k, u_n \rangle = \langle x, u_n \rangle - \frac{k(k-1)}{n^2\pi^2} \langle x^{k-2}, u_n \rangle, \qquad k = 2, 3, \cdots, \tag{92}$$

where

$$\langle x, u_n \rangle = \frac{\sqrt{2}(-1)^{n+1}}{n\pi}$$

and

$$\langle 1, u_n \rangle = \frac{\sqrt{2}}{n\pi}[1 - (-1)^n].$$

The projections of given polynomials were then computed by linear superposition of the results of (92). As a check, agreement with (85) was noted for $\|\varepsilon\| = 0$. Typical results of the singular-function projections and corresponding truncated Picard-series solutions are summarized in Table 1. In rows 1 to 4 of this table, the following coefficient errors were used to define ε:

$$(93) \qquad \begin{aligned} \Delta a_0 &= 1.0931587909 \times 10^{-3}, & \Delta a_4 &= 1.6763942336 \times 10^{-3}, \\ \Delta a_1 &= -7.5369385118 \times 10^{-4}, & \Delta a_5 &= 2.8982549939 \times 10^{-4}, \\ \Delta a_2 &= 1.6284123052 \times 10^{-3}, & \Delta a_6 &= 6.7137026479 \times 10^{-4}. \\ \Delta a_3 &= -2.6160019297 \times 10^{-3}, & & \end{aligned}$$

TABLE 1
Singular-function projection errors for Tricomi's example

$\|\varepsilon\|$	N	$\lambda_N = 1/\mu_N^2$	Remainder Sum of Squares	Error Estimate (28)	Actual Error $\|\tilde{f} - f_N\|$
*1.1100 − 3	1	1.23918 − 1	8.3853 − 7	3.29 − 3	2.73 − 3
1.1100 − 3	2	7.6995 − 3	8.3853 − 7	1.27 − 2	2.84 − 3
1.1100 − 3	3	1.5209 − 3	5.2293 − 9	2.85 − 2	1.08 − 2
1.1100 − 3	49	2.1370 − 8	1.3913 − 18	7.59	0.64
1.1100 − 2	1	1.23918 − 1	8.3853 − 7	3.15 − 2	2.57 − 2
8.6936 − 4	1	1.23918 − 1	8.3853 − 7	2.64 − 3	1.59 − 3
1.2659 − 4	2	7.6995 − 3	8.3853 − 7	1.71 − 3	1.13 − 3
3.0348 − 3	1	1.23918 − 1	8.3853 − 7	8.67 − 3	6.96 − 3

* 1.1100 − 3 denotes 1.1100×10^{-3} and similarly for other numbers in this table.

The coefficient errors for the results reported in the fifth row of Table 1 are exactly 10 times those reported above. The reason for the slight lack of proportionality in the reported errors is that these quantities contain both truncation error and error propagated through the solution. As a check on the program, proportionality of changes in both the projected unknown and the result of (4) after 10 iterations to a direct error magnification was observed.

Table 2 presents typical results of the iteration and indicates the correlation between the residual norms

$$(94) \qquad \|(g + \varepsilon) - K\hat{f}_k\| = \|r_k\|$$

and the errors $\|\tilde{f} - \hat{f}_k\|$ after k iterations. The results show a behavior quite similar to that of the error in an asymptotic series: at first the error decreases; then it reaches a minimum, and finally it increases as the residuals are decreased. Similar behavior was also observed for the truncated Picard series and the error

TABLE 2

Error norms $\|f - f_k\|$ and residual norms $\|r_k\|$ relative to $g + \varepsilon$ for selected iteration numbers and randomly chosen error functions ε

Iteration number, k	$\|\varepsilon\| = 0$		$\|\varepsilon\| = 2.60 - 3$		$\|\varepsilon\| = 1.11 - 3$	
	$\|f - \hat{f}_k\|$	$\|r_k\|$	$\|f - \hat{f}_k\|$	$\|r_k\|$	$\|f - \hat{f}_k\|$	$\|r_k\|$
1	*2.64 − 2	9.25 − 3	2.03 − 2	9.15 − 3	2.92 − 2	9.38 − 3
2	3.24 − 3	1.10 − 3	9.99 − 3	1.82 − 3	7.21 − 4	1.28 − 3
3	8.76 − 4	1.34 − 4	8.46 − 3	1.42 − 3	3.06 − 3	6.39 − 4
5	7.20 − 4	2.80 − 5	1.08 − 2	1.34 − 3	3.11 − 3	6.02 − 4
10	5.67 − 4	2.20 − 5	1.45 − 2	1.24 − 3	4.54 − 3	5.57 − 4
15	4.47 − 4	1.73 − 5	1.72 − 2	1.18 − 3	5.95 − 3	5.26 − 4
20	3.53 − 4	1.36 − 5	1.95 − 2	1.14 − 3	7.16 − 3	5.04 − 4
25	2.80 − 4	—	2.14 − 2	—	8.18 − 3	—

Iteration number, k	$\|\varepsilon\| = 6.17 - 4$		$\|\varepsilon\| = 1.11 - 2$		$\|\varepsilon\| = 1.27 - 4$	
	$\|f - \hat{f}_k\|$	$\|r_k\|$	$\|f - \hat{f}_k\|$	$\|r_k\|$	$\|f - \hat{f}_k\|$	$\|r_k\|$
1	2.77 − 2	9.32 − 3	5.53 − 2	1.21 − 2	2.61 − 2	9.24 − 3
2	1.98 − 3	1.19 − 3	2.43 − 2	6.33 − 3	3.50 − 3	1.10 − 3
3	1.68 − 3	4.54 − 4	2.99 − 2	6.09 − 3	1.00 − 3	1.50 − 4
5	1.64 − 3	4.18 − 4	3.48 − 2	5.88 − 3	1.07 − 3	6.97 − 5
10	2.72 − 3	3.85 − 4	4.95 − 2	5.47 − 3	1.17 − 3	6.68 − 5
15	3.76 − 3	3.63 − 4	6.30 − 2	5.19 − 3	1.23 − 3	6.54 − 5
20	4.63 − 3	3.48 − 4	7.45 − 2	4.99 − 3	1.28 − 3	6.43 − 5
25	5.37 − 3	—	8.42 − 2	—	1.33 − 3	—

* 2.64 − 2 denotes 2.64×10^{-2} and similarly for other numbers in this table.

Note: Omitted entries were not computed.

bound (28). In this example, at least, the solution would not be far from optimum if the iteration were stopped at the smallest value of k for which the residual norm (94) is less than $\|\varepsilon\|$ in accordance with procedure I, § 2. The case $\varepsilon = 0$ is interesting. The error in f after several iterations remains comparable in size to that resulting from an expansion for $N = 1$ (this error is the square root of the remainder series). This is because the expansion (87) contains only *odd* terms, so that the next lower effective eigenvalue for the response is 0.0015209. Reference to Fig. 2 shows that the response to the corresponding eigenfunction is only starting to appear after 25 iterations. The inequality (21) was also verified by summing 49 terms for this example. The difference between the two sides of (21) depends, of course, on the extent to which the error function ε is orthogonal to U. The removal of error components orthogonal to U in the iteration is illustrated by the fact that all iterated solutions $\hat{f}_k$ vanish for $y = 0$ and $y = 1$. Finally, we emphasize that this example is quite special in that the solution is mainly concentrated in the first eigenfunction; in practice one would not expect to be so fortunate. However, it illustrates the concepts involved for a true integral equation rather than a matrix approximation.

Example 4. The iterated Twomey–Tikhonov solution. In the matrix case an inversion is often easily performed provided that the matrix to be inverted is well-conditioned. If the given system has the matrix form

$$Af = g$$

we may set

$$D = (A^T A + \gamma I)^{-1},$$

where $\gamma > 0$. In this case the first iteration (4) with starting vector f_0 gives exactly the same solution as Twomey's method [27] with trial vector f_0. For this choice of D,

$$\lambda F(\lambda) = \frac{\lambda}{\gamma + \lambda}$$

and the resulting response curve (65) is

$$R^k(\lambda) = 1 - \left[1 - \frac{\lambda}{\lambda + \gamma}\right]^k = 1 - \left(\frac{\gamma}{\gamma + \lambda}\right)^k. \tag{95}$$

From this,

$$p_n = \frac{1}{\lambda_n + \gamma}, \qquad n = 1, 2, \cdots,$$

which is in compliance with (34). It follows from Theorem 5 that if $f_0 \in V$, then the iteration converges to the least squares solution of minimum norm of $Af = g$ whenever it exists, irrespective of the choice of γ. For a given γ and k we may get an approximate value for the resulting cutoff value a by setting $R_k(a) = \frac{1}{2}$ and solving for a. This gives

$$a = (2^{1/k} - 1)\gamma \sim \frac{0.69\gamma}{k} \quad \text{for large } k. \tag{96}$$

Note that a is directly proportional to γ for a fixed iteration number k. For $k = 1$ we have $a = \gamma$. If the desired cutoff value is known, as in (29), we can choose γ somewhat larger than the given a and then iterate enough to bring the response up to 1 for the harmonics to be retained and to bring a as computed from (96) down to the desired value. Some typical response curves for $\gamma = 0.05$ are shown in Fig. 7 for $0 \leqq \lambda \leqq 0.2$.

The iterated Twomey–Tikhonov solution was applied to the matrix case of Example 1, using $\gamma = 0.05$, as in Fig. 7. Agreement with the pseudo-inverse solution was obtained to 6 places after 20 iterations, to 10 places after 30 iterations, and to 12 places after 40 iterations. These results appear to be in agreement with the response indicated in Fig. 7. Faster convergence to the pseudo-inverse solution could, of course, be obtained by using a smaller value of γ. Finally, we note that Shaw [20] has proposed a statistically-motivated generalization of the iterated Twomey–Tikhonov process.

Summary. The iteration method of Landweber has been generalized to provide a "shaped" response with respect to the singular functions of the operator.

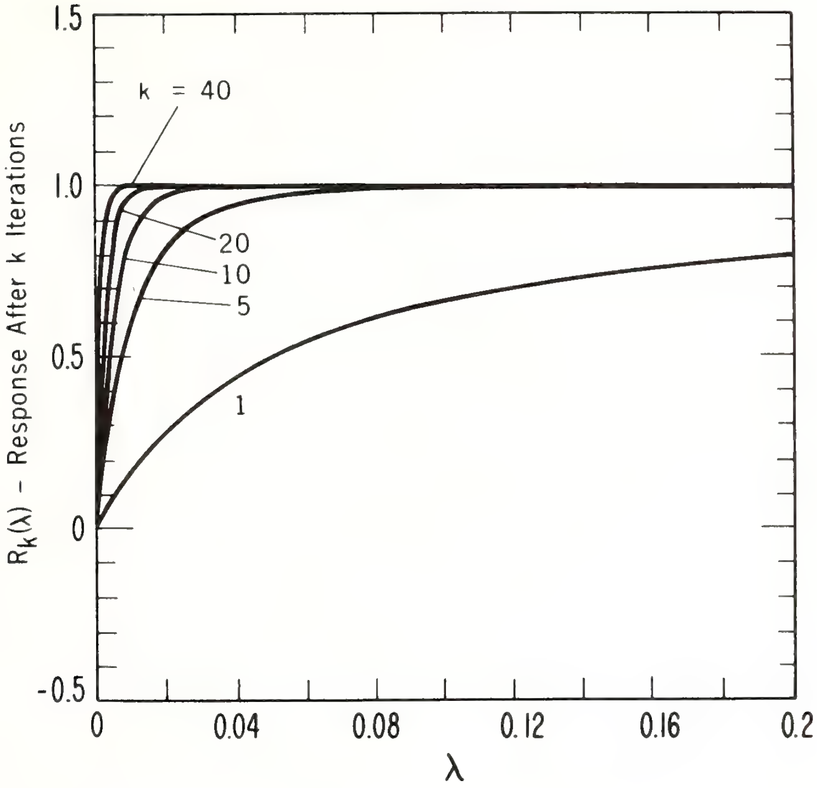

FIG. 7. *Response curves for the iterated Twomey–Tikhonov process,* $\gamma = 0.05$

This shaped response provides a method of smoothing by approximating a truncated Picard-series solution of the integral equation of the first kind. The relevant theory has been developed as needed, and several examples have been given. The type of analysis presented here is recommended, when applicable, in preference to empirical usage of iteration schemes with no assurance as to their true behavior with respect to the unknown. The method of Twomey [27] can be treated as a special-case first iteration, as is shown in Example 4. The use of polynomial response curves eliminates any need for operator inversion, but in the matrix case, at least, this may not always be a great advantage. The pseudo-inverse matrix solution to an underdetermined system of linear equations can be obtained by the method given here, as is indicated in Examples 2 and 4.

Acknowledgments. The author gratefully acknowledges many valuable and stimulating conversations with Dr. Patricia M. Prenter. Her constructive criticism improved the paper considerably. Henry E. Fleming suggested Tricomi's example as one in which both the solution and the spectrum could easily be obtained. Dr. Paul Wacker read the manuscript with exceptional competence and care. The author also thanks one of the referees, who made suggestions that contributed substantially to the finished form of §§3 and 4.

REFERENCES

[1] C. T. H. Baker, L. Fox, D. F. Mayers and K. Wright, *Numerical solution of Fredholm integral equations of the first kind*, Comput. J., 7 (1964), pp. 141–148.

[2] A. B. Bakusinski, *A general method of constructing regularizing algorithms for a linear incorrect equation in Hilbert space*, Ž. Vyčisl. Mat. i Mat. Fiz., 7 (1967), pp. 672–677 = U.S.S.R. Comput. Math and Math. Phys., 7 (1967), pp. 279–287.

[3] B. J. Conrath and J. Revah, *A review of nonstatistical techniques for the estimation of vertical atmospheric structure from remote infrared measurements*, Mathematics of Profile Inversion, Proc. of a Workshop held at Ames Research Center, Moffett Field, Calif. 94055, July 12–16, 1971, L. Colin, ed., NASA Tech. Memo. X-62,150, Aug. 1972.

[4] L. Crone, *The singular value decomposition and cheap numerical filtering*, to appear.

[5] J. V. Dave, *Determination of size distribution of spherical polydispersions using scattered radiation data*, Appl. Optics, 10 (1971), pp. 2035–2044.

[6] J. B. Diaz and F. T. Metcalf, *On iteration procedures for equations of the first kind, $Ax = y$, and Picard's criterion for the existence of a solution*, Math. Comp., 24 (1970), pp. 923–935.

[7] H. E. Fleming and W. L. Smith, *Inversion techniques for remote sensing of atmospheric temperature profiles*, Proc. 5th Symposium on Temperature, its Measurement and Control in Science and Industry, Washington, D.C., 1971.

[8] J. N. Franklin, *Well-posed stochastic extensions of ill-posed linear problems*, Programming Rep. 135, Calif. Institute of Technology, Willis H. Booth Computing Center. (Invited address presented to SIAM, April 19, 1969.)

[9] V. M. Fridman, *The method of successive approximations for a Fredholm integral equation of the first kind*, Uspehi Mat. Nauk, 11 (1956), pp. 223–224.

[10] R. J. Hanson, *A numerical method for solving Fredholm integral equations of the first kind*, this Journal, 8 (1971), pp. 616–622.

[11] W. J. Kammerer and M. Z. Nashed, *Iterative methods for best approximate solutions of integral equations of the first and second kinds*, MRC Tech. Summ. Rep. 1117, Mathematics Research Center, Madison, Wisc., 1971.

[12] L. Landweber, *An iteration formula for Fredholm integral equations of the first kind*, Amer. J. Math., 73 (1951), pp. 615–624.

[13] C. L. Mateer, *On the information content of umkehr observations*, J. Atmos. Sci., 22 (1965), pp. 370–381.

[14] W. V. Petryshyn, *On a general iterative method for the approximate solution of linear operator equations*, Math. Comp., 17 (1963), pp. 1–10.

[15] D. L. Phillips, *A technique for the numerical solution of certain integral equations of the first kind*, J. Assoc. Comput. Mach., 9 (1962), pp. 84–97.

[16] E. Picard, *Sur un théorème générale relatif aux équations integrales de première espèce et sur quelques problèmes de physique mathématique*, R. C. Mat. Palermo, 29 (1910), pp. 615–619.

[17] A. Ralston, *A First Course in Numerical Analysis*, McGraw-Hill, New York, 1965.

[18] F. Riesz and B. Sz. Nagy, *Functional Analysis*, Frederick Ungar, New York, 1955.

[19] C. D. Rodgers, *Satellite infrared radiometer—a discussion of inversion results*, Memo. 66.13, Clarendon Lab., Oxford University, Oxford, 1966.

[20] C. B. Shaw, Jr., *Improvement of the resolution of an instrument by numerical solution of an integral equation*, J. Math. Anal. Appl., 37 (1972), pp. 83–112.

[21] W. L. Smith, *Iterative solution of the radiative transfer equation for the temperature and absorbing gas profile of an atmosphere*, Appl. Optics, 9 (1970), pp. 1993–1999.

[22] F. Smithies, *Integral Equations*, Cambridge University Press, London, 1958.

[23] O. N. Strand, *Theory and methods for operator equations of the first kind*, Doctoral thesis, Colorado State Univ., Fort Collins, 1972.

[24] O. N. Strand and E. R. Westwater, *Minimum-rms estimation of the numerical solution of a Fredholm integral equation of the first kind*, this Journal, 5 (1968), pp. 287–295.

[25] A. N. Tikhonov, *Solution of incorrectly formulated problems and the regularization method*, Soviet Math. Dokl., 4 (1963), pp. 1035–1038.

[26] F. G. Tricomi, *Integral Equations*, John Wiley, New York, 1957.

[27] S. Twomey, *On the numerical solution of Fredholm integral equations of the first kind by the inversion of the linear system produced by quadrature*, J. Assoc. Comput. Mach., 10 (1963), pp. 79–101.

[28] ———, *The application of numerical filtering to the solution of integral equations encountered in indirect sensing measurements*, J. Franklin Inst., 279 (1965), pp. 95–109.

[29] ———, *Indirect measurements of atmospheric temperature profiles from satellites. II: Mathematical aspects of the inversion problem*, Monthly Weather Rev., 94 (1966), pp. 363–366.

[30] G. Wahba, *On the numerical solution of Fredholm integral equations of the first kind*, Rep. UWIS-DS-69-217, Dept. of Statistics, Univ. of Wisconsin, Madison, 1969.

[31] E. R. Westwater, *Ground-based determination of low altitude temperature profiles by microwaves*, Monthly Weather Rev., 100 (1972), pp. 15–23.

NOAA Technical Report ERL 295-WPL 28

December 1973

EXPECTED ACCURACY OF TROPOPAUSE HEIGHT AND TEMPERATURE AS DERIVED FROM SATELLITE RADIATION MEASUREMENTS

Otto Neall Strand
NOAA/ERL

This report presents a numerical simulation study of the accuracy to be expected in determining the height and temperature of the tropopause from infrared radiation data obtained by satellite with the Vertical Temperature Profile Radiometer (VTPR). Two methods of analysis are used. First, Backus-Gilbert averaging kernels are constructed and the inherent resolution of the integral-equation inversion program is thereby determined. Then a statistical regression study is made to determine the extent to which the tropopause parameters can be recovered as functions of eight radiances. Numerical results are presented for height resolution and various regressions.

NOAA Technical Report ERL 309-WPL 34

November 1974

A GENERALIZED INVERSION PROGRAM

Ed R. Westwater and Otto Neall Strand

ABSTRACT

A generalized inversion computer program is described for deriving a profile (i.e., a vector of functional values) from a finite set of imperfect measurements. The program assumes the observations are related to the profile by a nonlinear first kind operator equation. The method of solving the nonlinear equations is to iterate the solution of their linear approximation. Linear equations can be solved with this method in one iteration. The program described here uses either the Backus-Gilbert technique or the generalized Landweber inversion technique to solve the linear approximation at each stage of the iteration process. The computer programs described here are available from the authors on request.

Proceedings of 16th AMS Radar Meteorology Conference, 278-281, April 1975.

BEAM PATTERN MEASUREMENTS FOR LARGE ACOUSTIC ANTENNAS

B. C. Willmarth, E. H. Brown,
J. T. Priestley, and D. W. Beran

Wave Propagation Laboratory
NOAA Environmental Research Laboratories
Boulder, Colorado 80302

1. INTRODUCTION

Remote sensing of the clear atmosphere with acoustic devices has become an increasingly valuable method for a variety of research and operational tasks. The recent development of the atmospheric echosonde has evolved from rudimentary equipment to sophisticated antenna-computer combinations. Each stage of the development of the echosonde has added to the realization that the antenna is the system component which often places the most severe limitations on maximum performance. Following a discussion of the importance of good beam pattern measurements and consideration of some practical and theoretical problems, we present a method for rapidly making accurate in situ beam pattern measurements. Some effects of poor beam patterns are: loss of accuracy in positioning targets (and consequent inaccuracies in resolving Doppler vectors), degradation of signal-to-noise ratios, and increased interference introduced through minor lobes.

Recent experimental testing of a Doppler echosonde wind measuring system at an airport site using the antenna configuration shown in Figure 1 (Beran 1974; Beran et al. 1974) stressed the importance of the antenna. Results from this bistatic wind measuring system suggested that success depended on careful control of both transmitter and receiver beams through proper design. Achievement of optimum beam shape, output power, and signal-to-noise ratio required large antennas - approximately 3 meters in diameter. Emplacement of the antennas in bunkers with openings flush with the surrounding terrain (Figure 2) brought additional improvement by reducing the effect of wind noise and ambient background in the sidelobes.

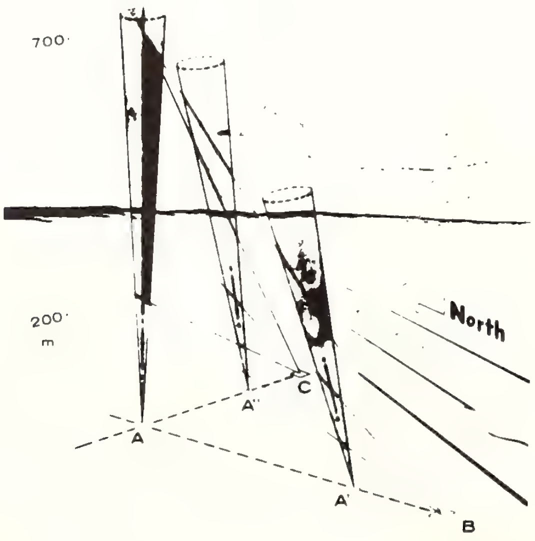

Figure 1. Multi-transmitter bistatic antenna configuration (Beran et al., 1974)

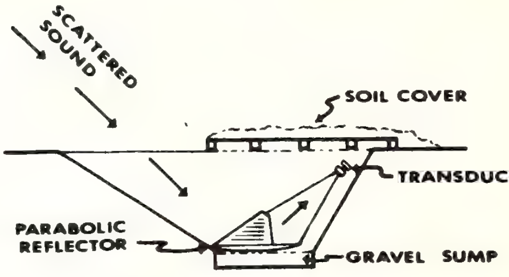

Figure 2. Bunker installation with a horn reflector antenna

The development of a large 10 x 10 meter acoustic array for atmospheric research at 80 Hz encountered similar problems. The size of these antennas precludes the use of laboratory-type beam pattern measurements, and interaction with rough terrain prevents sufficiently accurate theoretical calculations.

The directivity index (or antenna gain factor) alone is not adequate for good system design, because it gives little information about minor lobe structure. Total beam patterns have typically been measured by aiming the antenna horizontally and making farfield measurements (Hall and Wescott, 1974). (Where possible, this was done across a small valley to reduce ground effects.) Some large antennas now in use or under development are set on the ground or in bunkers. Not only are they too large (4 to 10 meters in diameter) to be tilted to a horizontal position, but the ground is an effective part of the antenna and its contributions to the total pattern must be known.

In principle, a complete set of careful nearfield measurements of both amplitude and phase determines the farfield beam pattern of intensity. Computer programs are available to make such determinations in the laboratory. However, the cost of a portable system which could measure echosonde antennas in the field would be prohibitively expensive. Therefore, a continuing need exists for practical methods for direct field measurements of farfield beam patterns of echosonde antennas. Among specifications for such a system are: provision for adjustments of probe location to a number of known positions in the farfield pattern, a minimum of supporting structures that might produce interference or standing waves, and easy portability for moving to various antenna emplacement sites.

2. THEORY

2.1 Farfield. Custom divides the field of antenna into three regions: the nearfield, the transition regions, and the farfield. Fresnel diffraction predominates in the nearfield, and Fraunhofer diffraction in the farfield. The transition region extends roughly four times the length of the nearfield. The equation $L = kD^2/\lambda$, with L the pathlength, D the antenna diameter, and λ the acoustic wavelength, defines the beginning of the farfield. The conventional choice $k = 2$ permits a 22.5° variation in phase over an antenna in a receiving mode. Differing applications may indicate other appropriate choices. Here, the large sizes and distances involved have suggested the choice $k = 1$, corresponding to a maximum phase variation of 45°.

2.2 Turbulence Effects. The real atmosphere is almost always turbulent causing, in turn, random fluctuations of the acoustic refractive index. The resulting perturbations in an echosonde system constitute, at the same time, signal and noise: sound scattered out of the beam carries information on the turbulence in the layer under study; the perturbations in the echosonde beam by intervening turbulence contaminate the desired signal. The effects of the intervening turbulence appear in two ways: smearing of the beam energy in space - that is, beam spreading; and, smearing in time - that is random roughening of the phase surfaces. Since Brown and Keeler (1975) study the latter effect in another article in these Proceedings, this paper considers only the beam spreading (other than in assuming the existence of a phase coherence length ρ_o).

A piston source gives a simple, instructive model for understanding the behavior of more complicated antennas. Such a source has a beam power pattern dependent on the function $(2J_1(kr)/kr)^2$, with $k = 2\pi/\lambda$ the wave number and r the radius of the antenna. Then, the half-power points lie at the beam half-angle $\theta = 0.305\lambda/r$. In the absence of turbulence, any increase in the antenna radius r produces a decrease in the beam half-angle θ, and increases the signal-to-noise ratio by lowering the amount of ambient noise received from side lobes.

Early work of Tatarskii (1961) and Fried (1967) suggested that the addition of turbulence spoiled the simple picture above, and that a limiting antenna diameter existed for which increases in diameter would not lower the beam width or increase the signal-to-noise ratio. However, later work of Lutomirski and Yura (1971) showed that this was unduly restrictive - that for path lengths within some critical distance Z_c, increasing antenna diameters would always improve beam patterns and signal-to-noise ratios.

Because of the obvious importance of the critical distance Z_c in echosonde antenna design, we calculate some typical values for this parameter. For typical vertical atmospheric echosonde beams the calculation becomes more complicated than that of Lutomirski and Yura (1971) for homogeneous turbulence due to the variation of the refractive index structure constant C_n with height. In an obvious extension of their work, we write for the critical distance for a beam observed at a height Z above a transmitter on the ground

$$Z_c^{-1} = 0.066\, \pi^2 k^2 \cdot \frac{1}{Z} \int_0^Z ds\, C_n^2(s) \int_0^\infty d\kappa\, \kappa \left[\kappa^2 + 4\pi^2/L_o^2(s)\right]^{-11/6} \qquad (1)$$

where $L_o(s)$ is the outer scale of turbulence. Using the order-of-magnitude approximations $C_n^2(s) = C_{no}^2\, s^{-4/3}$ and $L_o(s) = s$, where C_{no}^2 is the structure constant at one meter, gives

$$Z_c^{-1} = 4.679 \times 10^{-6}\, f^2 Z^{1/3}\, C_{no}^2 \qquad (2)$$

where f is frequency, and sound velocity was taken as 340 m/s. A typical maximum value of C_{no}^2 is $C_{no}^2 = 10^{-6}\ m^{-2/3}$. Then, for $Z = 1$ km, and for four typical frequencies covering the ordinary range of echosonde use, the critical distance Z_c becomes as shown in the following table:

TABLE 1

f(Hz)	Z_c(m)
500	85,470
1000	21,372
2000	5,343
4000	1,336

Clearly, the beam spreading effects of turbulence on optimum antenna diameters will not be limiting for echo sounding within the atmospheric boundary layer. As mentioned earlier, the effects of phase coherence length are studied elsewhere.

3. INSTRUMENTATION AND TECHNIQUES

Instrumentation for making beam pattern measurements consists simply of a microphone and associated sound level indicator, and a mechanical support and positioning system for the probe. The probe might be either the sound source or the microphone, the latter being preferred. The sound source should be capable of either tone-burst or continuous operation, and an oscilloscope should be available to observe the microphone output.

Figure 3 illustrates the basic probe-support system used in a measurement at WPL. If the distance from the antenna (A) to the probe

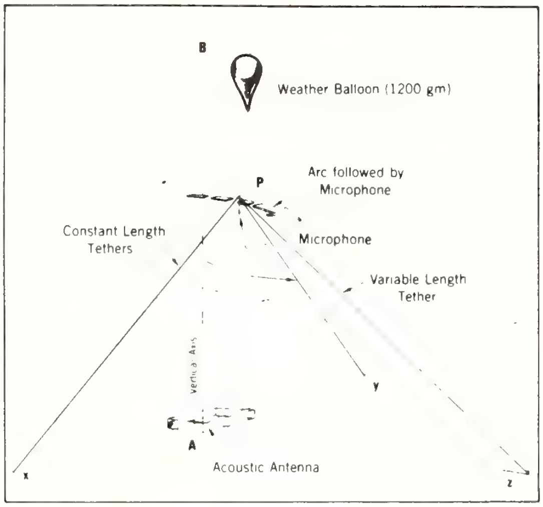

Figure 3. Schematic of basic probe-support system used at WPL

(P) is called "L", then anchor points X, Y, and Z are at distance L from the antenna. The constant length tethers X-P and Y-P will each be 1.41 x L in length. A fourth line, opposite line Z-P, may be needed to keep tension on the variable length tether when the probe approaches the zenith. The symetrical configuration described here was primarily used for convenience of calculating the position of the probe. There is no reason why an asymetrical arrangement could not be used for measuring other portions of a beam pattern. Tethering the balloon at some distance above the probe serves two purposes. First, it permits some lateral drift of the balloon in light breezes without seriously disturbing the position of the probe. If the mean wind is strong enough to make the balloon unmanageable it will also cause large fluctuations in acoustic signal level over a fixed path, and for these reasons measurements should be made under calm weather conditions. Second, it reduces interference caused by sound reflected from the balloon. These two purposes are best served by a long line from probe to balloon, but a long line also places the balloon at a high angle to the antenna when the probe is at a low angle. If the antenna has high directivity the balloon would then be in a much stronger sound field than the probe, and sound reflected from it may then become a significant source of interference.

At this time not enough is known about reflections from balloons to accurately predict the strength of this interference. It is therefore desirable to observe the microphone output on an oscilloscope while driving the source with short tone-bursts. The strength of the echo signal can then be compared with the strength of direct pulse. If the echo is 20 dB below the direct signal (one tenth the amplitude) it can cause ± 1 dB error, and amplitude scintillation caused by other atmospheric effects often exceeds this. The microphone used in our experiment was omnidirectional. A directional microphone may reduce interference, but care must be taken to keep it aimed at the antenna.

A test of this technique was made at WPL in 1974 using a transmitting antenna with a 1.2 m aperture. The microphone, suspended 20 m below a balloon, was fixed in an arc of 20 m radius. A wave analyzer band-pass filtered and rectified the output of the microphone preamp. The log output of this wave analyzer was then recorded on strip charts. While operating the transmitter in the tone-burst mode, the probe was swept through an arc from zenith to horizon. Since no significant echoes were observed on a monitor oscilloscope, measurements were continued in the CW mode.

4. RESULTS

A polar plot of the beam pattern resulting from measurements made at 2000 Hz is shown in Figure 4. The variable tether line (PZ in Figure 1) was fixed at ≃ 3 m increments. The points with error bars represent the measurements recorded at each of these fixed positions. The variable tether line was then released at a controlled rate and the resulting probe sweep was recorded. The solid line in Figure 4 was taken from the

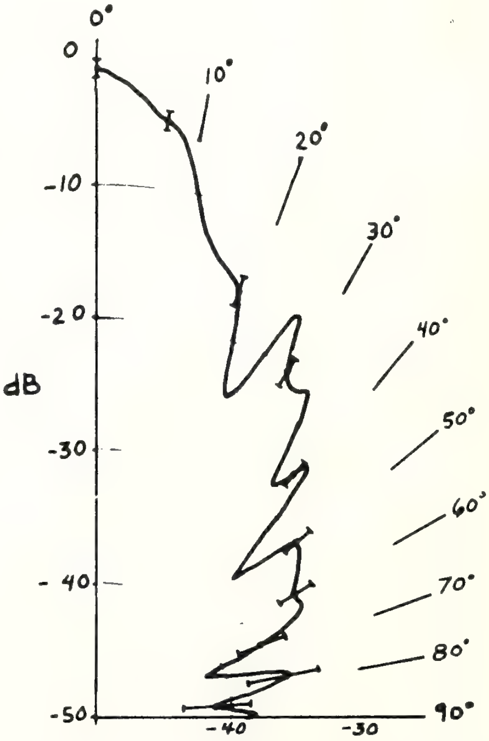

Figure 4. Acoustic antenna beam pattern obtained with system shown in Figure 3

controlled sweep data by interpolating between the levels recorded at the fixed positions. Since the antenna is not of a very sophisticated design, the beam pattern is only moderately good - dropping only 40 dB at 90 degrees. However, the results are approximately as expected from previous antenna measurements. We expect the application of the method to larger and more carefully designed antennas to give much sharper beam patterns. Clearly, however, use of this beam pattern measuring method can become of utmost importance in evaluating and modifying various antenna designs.

CONCLUSIONS

We have developed an inexpensive effective and sufficiently accurate method for measuring the beam patterns of large echosonde antennas in situ (thus, including automatically, effects of surrounding terrain). In brief, the method consists of moving a microphone probe, controlled by a system of a supporting balloon and fixed and variable tethers, through a precise arc in the farfield of the antenna.

ACKNOWLEDGMENTS

The authors wish to acknowledge the support of Mr. Larry Vohs and Mr. Edward Owens during field tests. Financial support for this work was provided partially by the FAA for the development of an acoustic Doppler wind measuring system.

REFERENCES

Beran, D. W., 1974: Remote sensing wind and wind shear systems. Rept. No. FAA-RD-74-3, DOT/FAA Systems Research and Development Service, Washington, D. C. 20591.

Beran, D. W., F. F. Hall, B. C. Willmarth, R. J. Keeler, and D. Hunter, 1974: Operational test results of acoustic Doppler wind shear detector. Preprint, Sixth Conf. on Aerospace & Aeronautical Meteorology, Amer. Met. Soc., pp 412-417.

Brown, E. H., and R. J. Keeler, 1975: Applications of propagation parameters to atmospheric echosondes. Proc. 16th Conf. on Radar Meteorology (see this volume).

Fried, D. L., 1967: Optical heterodyne detection of an atmospherically distorted signal wave front. Proc. IEEE, 55, p 57.

Hall, F. F., and J. W. Wescott, 1974: Acoustic antennas for atmospheric echo sounding. J. Acoust. Soc. Am., 56, No. 5, 1376-1382.

Lutomirski, R. F., and H. T. Yura, 1971: Wave structure functions and mutual coherence functions of an optical wave in a turbulent atmosphere. J. Opt. Soc. Amer., 61, 482-487.

Tatarskii, V. I., 1961: Wave Propagation in a Turbulent Medium. McGraw-Hill, New York, (transl. by R. S. Silverman).

NOAA Technical Report ERL 345-WPL 43

August 1975

COMPUTER PROGRAMS FOR MULTIDIMENSIONAL SPECTRA ARRAY PROCESSING

Jessie M. Young and Wayne A. Hoyle

ABSTRACT

We have combined a number of Fortran routines to phase-steer and process outputs from a planar array of sensors. The array is used as an analyzer to obtain an array-enhanced plane-wave signal estimate and spectra as a function of frequency and spatial frequencies and to follow variations as the chosen analyzing time segment is advanced. The programs feature:

(1) Near optimum use of Fast Fourier Transform (FFT) techniques to compute correlations, convolutions, and steered array signal spectra.

(2) An algorithm to obtain power density in the phased array signal from K sensors in K summation terms that is equivalent to the (K-1) K/2 terms necessary with pairwise cross-correlations.

(3) A wide choice of frequency bandwidths within the Nyquist interval. If the entire Nyquist band is chosen, results are equivalent to time-domain cross-correlation processing.

(4) Presentation of results in the form of microfilm plots that facilitate quantitative and qualitative deductions about the three-dimensional spectra of the input data and how they change with time.

The programs were originally developed to process pressure signatures from wide-band transient infrasound in frequency bands where dispersion is relatively small. They have also proved useful for processing atmospheric gravity waves. The methods should be potentially useful for the analysis of electromagnetic waves as well as sound and gravity waves in the atmosphere and the oceans.

☆U.S. Government Printing Office: 1976-677-347/1286 Region 8

PENN STATE UNIVERSITY LIBRARIES
A000072832837